Digitized by Arya Samaj Foundation Chennai and eGangotri

CC-0. In Public Domain. Gurukul Kangri Collection, Haridwar

Digitized by Siddhanta eGangotri Gyaan Kosha
Collection, Haridwar

Digitized by Arya Samaj Foundation Chennai and eGangotri
111939
CC-0. In Public Domain. Gurukul Kangri Collection, Haridwar

Digitized by Arya Samaj Foundation Chennai and eGangotri

CC-0. In Public Domain. Gurukul Kangri Collection, Haridwar

Digitized by Arya Samaj Foundation Chennai and eGangotri

CC-0. In Public Domain. Gurukul Kangri Collection, Haridwar

Digitized by Arya Samaj Foundation Chennai and eGangotri

ISSN 0304-42

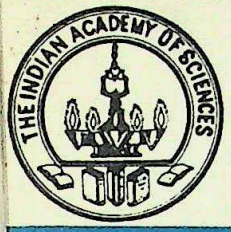

Volume 34 Number 1 January 1990

39 L.

Pramāṇa

journal of physics

11939

published by
INDIAN ACADEMY OF SCIENCES
in collaboration with
INDIAN PHYSICS ASSOCIATION
and
INDIAN NATIONAL SCIENCE ACADEMY

CC-0. In Public Domain. Gurukul Kangri Collection, Haridwar

Digitized by Arya Samaj Foundation Chennai and eGangotri

Pramāṇa – journal of physics

Editor

R Rajaraman
Indian Institute of Science, Bangalore

Associate Editor

Rajaram Nityananda
Raman Research Institute, Bangalore

Editorial Board

C V K Baba, *Tata Institute of Fundamental Research, Bombay*
M Barma, *Tata Institute of Fundamental Research, Bombay*
D D Bhawalkar, *Centre for Advanced Technology, Indore*
Deepak Kumar, *Jawaharlal Nehru University, New Delhi*
P K Kaw, *Institute for Plasma Research, Gandhinagar*
H R Krishnamurthy, *Indian Institute of Science, Bangalore*
H S Mani, *Indian Institute of Technology, Kanpur*
N Mukunda, *Indian Institute of Science, Bangalore*
T Padmanabhan, *Tata Institute of Fundamental Research, Bombay*
J C Parikh, *Physical Research Laboratory, Ahmedabad*
T G Ramesh, *National Aeronautical Laboratory, Bangalore*
Probir Roy, *Tata Institute of Fundamental Research, Bombay*
A K Sood, *Indian Institute of Science, Bangalore*
R Srinivasan, *Indian Institute of Technology, Madras*

Editor of Publications of the Academy

G Srinivasan
Raman Research Institute, Bangalore

Subscription Rates
(Effective from 1989)

All countries except India	1 year	3 years	5 years
(Price includes AIR MAIL charges)	US$ 175	$ 470	$ 700
India	1 year Rs. 100	10 years Rs. 500	

All correspondence regarding subscription should be addressed to The **Circulation Department** of the Academy

---

Editorial Office

Indian Academy of Sciences, C V Raman Avenue
P.B. No. 8005, Bangalore 560 080, India

Telephone: 34 25 46
Telex: 0845-2178 ACAD IN

© 1990 by the Indian Academy of Sciences. All rights reserved.

The "Notes on the preparation of papers" are printed in the last issue of every volume.

CC-0. In Public Domain. Gurukul Kangri Collection, Haridwar

Digitized by Arya Samaj Foundation Chennai and eGangotri

Pramāṇa – journal of physics

Volume 34

1990

Published by The Indian Academy of Sciences
Bangalore 560 080

CC-0. In Public Domain. Gurukul Kangri Collection, Haridwar

Digitized by Arya Samaj Foundation Chennai and eGangotri

Pramāṇa – journal of physics

Editor

R Rajaraman
Indian Institute of Science, Bangalore

Associate Editor

Rajaram Nityananda
Raman Research Institute, Bangalore

Editorial Board

C V K Baba, *Tata Institute of Fundamental Research, Bombay*
M Barma, *Tata Institute of Fundamental Research, Bombay*
D D Bhawalkar, *Centre for Advanced Technology, Indore*
Deepak Kumar, *Jawaharlal Nehru University, New Delhi*
P K Kaw, *Institute for Plasma Research, Gandhinagar.*
H R Krishnamurthy, *Indian Institute of Science, Bangalore*
H S Mani, *Indian Institute of Technology, Kanpur*
N Mukunda, *Indian Institute of Science, Bangalore*
T Padmanabhan, *Tata Institute of Fundamental Research, Bombay*
J C Parikh, *Physical Research Laboratory, Ahmedabad*
T G Ramesh, *National Aeronautical Laboratory, Bangalore*
Probir Roy, *Tata Institute of Fundamental Research, Bombay*
A K Sood, *Indian Institute of Science, Bangalore*
R Srinivasan, *Indian Institute of Technology, Madras*

Editor of Publications of the Academy

G Srinivasan
Raman Research Institute, Bangalore

Subscription Rates

(Effective from 1989)

	1 year	3 years	5 years
All countries except India (Price includes AIR MAIL charges)	US$ 175	$ 470	$ 700
India.....	1 year Rs. 100	10 years Rs. 500	

All correspondence regarding subscription should be addressed to The **Circulation Department** of the Academy

---

Editorial Office

Indian Academy of Sciences, C V Raman Avenue,
P.B. No. 8005, Bangalore 560 080, India

Telephone: 34 25 46
Telex: 0845-2178 ACAD IN

© 1990 by the Indian Academy of Sciences. All rights reserved.

"Information for contributors" is printed in the last issue of every volume.

CC-0. In Public Domain. Gurukul Kangri Collection, Haridwar

Digitized by Arya Samaj Foundation Chennai and eGangotri

Regd. No. KRN-A 64

Pramāṇa journal of physics Vol. 34 (No. 1), January 1990

Contents

String cosmology in Bianchi I space-time . . . . . *A Banerjee, Abhik Kumar Sanyal and Subenoy Chakraborty* 1

Orthogonality constrained general variational calculation of excited state wavefunctions and energies: A new strategy. . . . . *Priyatosh Dutta and S P Bhattacharyya* 13

Structure factor of charged colloidal suspensions using Brownian-dynamics simulation: Comparison of Yukawa and Sogami pair potentials . . . . . *B V R Tata, A K Sood and R Kesavamoorthy* 23

Positron annihilation in copper . . . . *V Sundararajan and D G Kanhere* 33

Effect of variation of dielectric constant on the magnetic field modulation of exciplex luminescence . . . . *Deb Narayan Nath and Mihir Chowdhury* 51

Effect of annealing on the opto-electronic properties of $Cu_{0\cdot9}In_{1\cdot0}Se_{2\cdot0}$ films . . . . . *R P Sharma, Pankaj Garg and J C Garg* 67

Time-resolved spectra of coumarin 30–rhodamine 6G dye mixture . . . . . *R D Singh, D Mohan, A K Sharma and N V Unnikrishnan* 77

Comments and Addenda

Comment on a solution of Altarelli–Parisi equations . . . . . *D K Choudhury and A Saikia* 85

High energy elastic e^+–O_2 scattering . . . . . *K N Joshipura* 87

Indexed in CURRENT CONTENTS

Edited and published by G Srinivasan for the Indian Academy of Sciences, Bangalore 560 080. Typeset at Thomson Press (I) Ltd., New Delhi 110 001 and printed at Macmillan India Press, Madras 600 041.

CC-0. In Public Domain. Gurukul Kangri Collection, Haridwar

Digitized by Arya Samaj Foundation Chennai and eGangotri

CC-0. In Public Domain. Gurukul Kangri Collection, Haridwar

Digitized by Arya Samaj Foundation Chennai and eGangotri

Regd. No. KRN-A 64

Pramāṇa journal of physics Vol. 34 (No. 2), February 1990

Contents

On mass-independence of the minimal subtraction scheme in dimensional regularization II . . . . . *Satish D Joglekar* 91

Phenomenology of the proton spin. . . . . *M V N Murthy and V Ravindran* 103

Bonding potential between two ^{12}C nuclei . . . . . *P Sarangi, S Ali and L Satpathy* 111

Interaction of strong laser beam with He-atom using non-perturbative Floquet method . . . . *Man Mohan, Vinod Prasad and Bhupat Sharma* 117

Thermodynamic properties of hard ellipsoid square-well fluid . . . . . *A K Singh, T K Dey and S K Sinha* 123

Electron crystallization using localized representation . . . . . *K Iyakutti and Jean Louis Calais* 133

Indentation studies on alkaline earth fluoride crystals at elevated temperatures . . . . . *K Kishan Rao and D B Sirdeshmukh* 151

Ultrasonic absorption studies in solutions of ortho and para hydroxy benzoic acid in dioxan . . . . . *V Balasubramanian and A Srinivasa Rao* 157

Rotational analysis of 3664 Å band of NiCl . . . . . *A B Darji and M B Suresh Kumar* 165

Indexed in CURRENT CONTENTS

Edited and published by G Srinivasan for the Indian Academy of Sciences, Bangalore 560 080. Typeset at Thomson Press (I) Ltd., New Delhi 110 001 and printed at Macmillan India Press, Madras 600 041.

CC-0. In Public Domain. Gurukul Kangri Collection, Haridwar

Digitized by Arya Samaj Foundation Chennai and eGangotri

CC-0. In Public Domain. Gurukul Kangri Collection, Haridwar

Digitized by Arya Samaj Foundation Chennai and eGangotri

Regd. No. KRN-A 64

Pramāṇa journal of physics Vol. 34 (No. 3), March 1990

Contents

Triad of homogeneous and inhomogeneous three particle Lippmann–Schwinger equations . . . . . *Suprokash Mukherjee* 173

Stability of the *S* matrix pole . . . . . *G Rajasekaran and S S Vasan* 183

A relation between X-ray diffraction based liquid structure and packing coefficient . . . . . *A Mikusińska-Planner* 193

Convexity of internal energy of cubic crystal deformed to orthorhombic structure . . . . . *K P Thakur, R K Jha and O P Thakur* 201

Anharmonic effects on lattice resonant modes of impure metallic crystals . . . . . *S K Roy and N Kundu* 217

The Young-Hoshino pseudopotential for lithium: calculations of structure and thermodynamics . . . . . *T Das and R N Joarder* 225

Melting temperatures of some alkali halide mixed crystal systems . . . . . *D B Sirdeshmukh, K G Subhadra and K A Hussain* 235

Electrical conductivity, thermoelectric power and figure of merit of doped Bi-Sb tapes produced by melt spinning technique . . . . . *T K Dey* 243

Design and the operational characteristics of a 16 μm CF_4 laser . . . . *P K Gupta, V P Singhal, N S Shikarkhane, S Sinha, S Sasikumar, U Nundy and U K Chatterjee* 249

Indexed in CURRENT CONTENTS

Edited and published by G Srinivasan for the Indian Academy of Sciences, Bangalore 560 080. Typeset at Thomson Press (I) Ltd., New Delhi 110 001 and printed at Macmillan India Press, Madras 600 041.

CC-0. In Public Domain. Gurukul Kangri Collection, Haridwar

Digitized by Arya Samaj Foundation Chennai and eGangotri

STATEMENT ABOUT OWNERSHIP AND OTHER PARTICULARS ABOUT

Pramāṇa - Journal of Physics

1. Place of Publication	..	Bangalore
2. Periodicity of Publication	..	Monthly
3. Printer's Name	..	G Srinivasan Indian Academy of Sciences Bangalore 560 080
4. and 5. Publisher and Editor	..	G Srinivasan
6. Nationality	..	Indian
7. Address	..	Indian Academy of Sciences P B No. 8005, C. V. Raman Avenue Bangalore 560 080
8. Name and Address of the Owner	..	Indian Academy of Sciences Bangalore 560 080

I, G Srinivasan, hereby declare that the particulars given above are true to the best of my knowledge.

Dated 1st March 1990

G Srinivasan
Signature of Publisher

CC-0. In Public Domain. Gurukul Kangri Collection, Haridwar

Digitized by Arya Samaj Foundation Chennai and eGangotri

Regd. No. KRN-A 64

Pramāṇa journal of physics Vol. 34 (No. 4), April 1990

Contents

Layered superconductors with anisotropic energy gap: specific heat and infrared absorption . . . . . *Sudhanshu S Jha* 259

Field and temperature dependence of intergranular hysteresis in $YBa_2Cu_3O_7$ *Shailendra Kumar, G Ravikumar, P K Mishra, P Chaddah, B A Dasannacharya, Ram Prasad and N C Soni* 279

Electrical resistivity of the alkaline earth metals Ca, Sr and Ba in the 50–300K temperature region . . . . . *O Akinlade, U Marte and L A Hussain* 289

Elastic behaviour of lead fluoride under pressure . . . . . *R K Singh and C N Rao* 297

Computation of small angle neutron scattering functions for molecules of arbitrary shapes . . . . . *F U Ahmed, P Martel and A M Khan* 303

NMR investigations of molecular motions in *p-n*-hexyloxybenzylidene-*p'*-*n*-propylaniline. . . . . *K Usha Deniz and S R Kasturi* 313

Study of electric potentials across a moving solid-liquid interface . . . . . *A K Bhuniya, N Prasad, Lakshman Pandey and P Ramachandrarao* 325

Evaluation of downstream-mixing scheme for 9.4-μm CO_2 gasdynamic laser . . . . . *P Chakravarty, N M Reddy and K P J Reddy* 333

Beam propagation method and its application to integrated optic structures and optical fibers . . . . . *Shiva Kumar, T Srinivas and A Selvarajan* 347

Differential temperature sensors method for simultaneous determination of thermal conductivity and diffusivity . . . . . *L S Verma, A K Shrotriya, Ramvir Singh and D R Chaudhary* 359

Rapid Communications

Mössbauer study of the stability of quasicrystalline phases: $Al_{78}Fe_{22}$ and $Al_{82}Fe_{18}$ . . . . . *K R P M Rao* L369

Detection limits of high temperature superconducting materials on various substrates by energy dispersive X-ray fluorescence and proton induced X-ray emission methods. . . . . *M Lal, H N Bajpai, D Joseph and R K Choudhury* L377

Indexed in CURRENT CONTENTS

Edited and published by G Srinivasan for the Indian Academy of Sciences, Bangalore 560 080. Typeset at Thomson Press (I) Ltd., New Delhi 110 001 and printed at Macmillan India Press, Madras 600 041.

CC-0. In Public Domain. Gurukul Kangri Collection, Haridwar

Digitized by Arya Samaj Foundation Chennai and eGangotri

CC-0. In Public Domain. Gurukul Kangri Collection, Haridwar

Digitized by Arya Samaj Foundation Chennai and eGangotri

Regd. No. KRN-A 64

Pramāṇa journal of physics Vol. 34 (No. 5), May 1990

Contents

Spherical shells of positive density – can they be of non-positive mass? . . . . . *A K Raychaudhuri and S Banerjee* 383

Spherically symmetric solutions with heat flow in general relativity . . . . . *A Banerjee, S B Dutta Choudhury and B K Bhui* 397

Wave function with second order correction and inflationary solutions in quantum cosmology . . . . . *Subenoy Chakraborty* 403

Cosmological models consistent with supersymmetric compactification of superstring theories . . . . . *Sanjay Kumar, S Mahajan, A Mukherjee, N Panchapakesan and R P Saxena* 415

Spherically symmetric anisotropic and inhomogeneous cosmological models . . . . . *J Krishna Rao* 423

Q matter in the field of an abelian dyon admitting parity violating anomalous couplings. . . . . *C Wolf* 433

The wavefunction envelope in one-dimensional random potentials. . . . . *A Mookerjee and A M Jayannavar* 441

The effect of the relativistic Hartree-Fock-Roothaan momentum distribution in the binary encounter approximation for inner shell ionization . . . . . *V Kumar, S N Chatterjee and B N Roy* 447

Indexed in CURRENT CONTENTS

Edited and published by G Srinivasan for the Indian Academy of Sciences, Bangalore 560 080. Typeset at Thomson Press (I) Ltd., New Delhi 110 001 and printed at Macmillan India Press, Madras 600 041.

CC-0. In Public Domain. Gurukul Kangri Collection, Haridwar

Digitized by Arya Samaj Foundation Chennai and eGangotri

CC-0. In Public Domain. Gurukul Kangri Collection, Haridwar

Digitized by Arya Samaj Foundation Chennai and eGangotri

Regd. No. KRN-A 64

Pramāṇa journal of physics Vol. 34 (No. 6), June 1990

Contents

Wavelength dependence of phase conjugate reflectivity in absorbing media and thermal grating studies by four wave mixing. . . . . *R Krishna Mohan, B Raghavendra Prasad, C K Subramanian and P S Narayanan* 461

Analysis of the absorption mechanism during laser-metal interaction. . . . . *B S Yilbas, R Davies, Z Yilbas and A Koc* 473

Anisotropic ESR parameters of Cu(II) complexes in solutions and dynamics of solvent coordination: use of "minimum linewidths" . . . . . *B S Prabhananda* 491

A quantitative study of diffracted X-ray intensities from type I natural diamond crystals by high resolution X-ray diffractometry and comparison with nearly perfect silicon single crystals. . . . . *Krishan Lal, S Niranjana N Goswami and Ajit Ram Verma* 507

Diffraction properties of one-dimensional finite size Fibonacci quasilattice *V S K Balagurusamy, S Baranidharan, E S R Gopal and V Sasisekharan* 525

Generation of aperiodic tilings with fivefold symmetry by the method of intersecting decagons and diffraction from finite size tilings . . . . . *S Baranidharan, E S R Gopal and V Sasisekharan* 537

Vibrational spectra of $Na_4P_2O_7 \cdot 10H_2O$. . . . . *V Ramakrishnan, S Narayana Kalkura and P Rajagopal* 555

Comments on the Meyer–Neldel rule in amorphous semiconductors . . . . . *K L Narasimhan* 561

A study of absorption characteristics in polyimide and polyimide fluoro-carbon-2 polymer film . . . . . *M M Hossain* 565

A theoretical study of surface plasmon cross coupling in asymmetric corrugated metal films . . . . . *M B Pande and S Dutta Gupta* 575

(*Continued on inside back cover*)

Indexed in CURRENT CONTENTS

Edited and published by G Srinivasan for the Indian Academy of Sciences, Bangalore 560 080. Typeset at Thomson Press (I) Ltd. New Delhi 110 001 and printed at Macmillan India Press, Madras 600 041.

CC-0. In Public Domain. Gurukul Kangri Collection, Haridwar

Digitized by Arya Samaj Foundation Chennai and eGangotri

(*Continued from back cover*)

Fluorescence quantum yield of rhodamine 6G using pulsed photoacoustic technique. . . . . *P Sathy, Reji Philip, V P N Nampoori and C P G Vallabhan* 585

Subject index 591

Author index 595

CC-0. In Public Domain. Gurukul Kangri Collection, Haridwar

Digitized by Arya Samaj Foundation Chennai and eGangotri

Pramāṇa – J. Phys., Vol. 34, No. 1, January 1990, pp. 1–11. © Printed in India.

String cosmology in Bianchi I space-time

A BANERJEE, ABHIK KUMAR SANYAL and SUBENOY CHAKRABORTY*

Department of Physics, * Department of Mathematics, Jadavpur University, Calcutta 700032, India

MS received 1 April 1989; revised 21 July 1989

Abstract. Some cosmological solutions of massive strings are obtained in Bianchi I space-time following the techniques used by Letelier and Stachel. A class of solutions corresponds to string cosmology associated with/without a magnetic field and the other class consists of pure massive strings, obeying the Takabayashi equation of state $\rho = (1 + W)\lambda$.

Keywords. String; space-time; magnetic field; cosmology; string-dust system; Bianchi I.

PACS Nos 98·90; 04·20

1. Introduction

At the early stage of the universe a phase transition occurs as the temperature lowers below some critical temperature, and this can give rise to various topologically stable defects of which strings are of most important whose world sheets are two dimensional time-like surfaces (Kibble 1976). It has been noted (Kibble 1976) that the existence of a large scale network of strings in the early universe does not contradict the present-day observations of the universe and further the vacuum strings (Zeldovich 1980) can generate density fluctuations sufficient to explain the galaxy formation.

These strings have stress energy and they couple to the gravitational field so that it may be interesting to study the gravitational effects which arise from strings.

This has been already done by several authors, (Vilenkin (1981), Gott (1985), Garfinkle (1985), although the general relativistic treatment of strings was pioneered by Letelier (1979) and Stachel (1980). Letelier (1983) presented some cosmological solutions of massive strings in Bianchi I and Kantowski-Sachs space-time.

In geometrical string (massless) models, infinite number of degrees of freedom are possessed by each string for which the end points move at the speed of light. This problem is resolved by considering the realistic (massive) string model of Takabayashi (1976). The energy-momentum tensor for the massive strings has been first formulated by Letelier (1979), who considered the massive strings being formed by geometric strings with particles attached along its extension. Its application to general relativity first appeared in Letelier (1983), while Stachel (1980) considered massless strings. So the total energy-momentum tensor for a cloud of massive strings can be written as

$$T_\mu^\nu = \rho \cdot V_\mu \cdot V^\nu - \lambda \cdot x_\mu \cdot x^\nu, \tag{1}$$

where ρ is the rest energy density for a cloud of strings with particles attached to

CC-0. In Public Domain. Gurukul Kangri Collection, Haridwar

Digitized by Arya Samaj Foundation Chennai and eGangotri

them (p-strings). Thus we have

$$\rho = \rho_p + \lambda, \tag{2}$$

ρ_p being the particle energy density and λ being the string's tension density. V^μ is the four velocity for the cloud of particles and x^μ is the four vector representing the string's direction which essentially is the direction of anisotropy. Thus,

$$V_\mu \cdot V^\mu = -1 = -x_\mu \cdot x^\mu \text{ and } V_\mu \cdot x^\mu = 0, \tag{3}$$

in $(-, +, +, +)$ signature.

In the present paper, we study the string cosmology in axially symmetric Bianchi I space-time both in the presence and absence of a source-free magnetic field. The evolution of a string-dust system may be interesting in the presence of the cosmic magnetic field.

Melvin (1975) in his cosmological solution for dust and electromagnetic field argues that the presence of magnetic field is not as unrealistic as it appears to be, because for a large part of the history of evolution matter was highly ionized, and matter and field were smoothly coupled. Later during cooling as a result of expansion the ions combined to form neutral matter.

Since the number of unknown parameters appearing in the model exceeds the number of field equations by one, we require one more equation to find the exact solutions. This additional equation is an assumed relation between the metric coefficients in the first case, where the string universe is associated with a magnetic field. In the second case where there is no magnetic field we have assumed an equation of state $\rho = (1 + W)\lambda$, ($W > 0$, is a constant), which is known as Takabayashi string (or P-string).

Since there is no direct evidence of strings in the present day universe, we are, in general, interested in constructing models of a universe that evolves purely from the era dominated by either geometric string or massive strings and ends up in a particle dominated era with or without remnants of strings.

2. Einstein's field equations.

We consider an axially symmetric Bianchi I metric, which is

$$ds^2 = -dt^2 + \exp(2\alpha)\,dx^2 + \exp(2\beta)(dy^2 + dz^2), \tag{4}$$

where, $\alpha = \alpha(t)$ and $\beta = \beta(t)$.

Now, the energy-momentum tensor for the string dust with a magnetic field along the direction of the string, i.e. the x-direction is given by

$$T_\mu{}^\nu + E_\mu{}^\nu = \rho \cdot V_\mu V^\nu - \lambda \cdot x_\mu x^\nu + \frac{1}{4\pi}(F_\mu{}^\alpha F^\nu{}_\alpha - \tfrac{1}{4} F_{\alpha\beta} F^{\alpha\beta} \cdot \delta_\mu{}^\nu). \tag{5}$$

In the above, $T_\mu{}^\nu$ is the stress-energy tensor for a string-dust system, $E_\mu{}^\nu$ is that for the magnetic field and $F_{\alpha\beta}$ is the electromagnetic field tensor. The other terms have already been explained in the previous section. In the co-moving co-ordinate system $V^\mu = \delta_0{}^\mu$ and

$$T_0{}^0 = -\rho, \quad T_1{}^1 = -\lambda, \quad T_2{}^2 = T_3{}^3 = 0 = T_\mu{}^\nu \text{ (for } \mu \neq \nu). \tag{6}$$

CC-0. In Public Domain. Gurukul Kangri Collection, Haridwar

Digitized by Arya Samaj Foundation Chennai and eGangotri

Further, since the magnetic field is being assumed in the x-direction F_{23} is the only non-zero component of the electromagnetic field tensor. Maxwell equation $F_{[\mu\nu,\alpha]} = 0$ and $(F^{\mu\nu}\cdot(-g)^{1/2})_{,\mu} = 0$, now lead to the result (remembering that $(-g)^{1/2}$ is a function of time only)

$$F_{23} = A, \tag{7}$$

A being a constant quantity. So, the components of stress energy tensor for the electromagnetic field are

$$E_0^0 = E_1^1 = -E_2^2 = -E_3^3 = -\frac{A^2}{8\pi}\exp(-4\beta). \tag{8}$$

Now, choosing units such that $8\pi\sigma = 1$, the surviving. Components of Einstein field equations

$$R_\mu{}^\nu - \tfrac{1}{2}\delta_\mu{}^\nu\cdot R = -(T_\mu{}^\nu + E_\mu{}^\nu), \tag{9}$$

are

$$2\dot{\alpha}\dot{\beta} + \dot{\beta}^2 = \rho + \frac{A^2}{8\pi}\exp(-4\beta), \tag{10}$$

$$2\ddot{\beta} + 3\dot{\beta}^2 = \lambda + \frac{A^2}{8\pi}\exp(-4\beta), \tag{11}$$

$$\ddot{\alpha} + \dot{\alpha}^2 + \ddot{\beta} + \dot{\beta}^2 + \dot{\alpha}\dot{\beta} = -\frac{A^2}{8\pi}\exp(-4\beta). \tag{12}$$

The proper volume R^3, expansion scalar θ and shear scalar σ^2 are respectively given by,

$$R^3 = \exp(\alpha + 2\cdot\beta),$$

$$\theta = v^a_{;a} = \dot{\alpha} + 2\dot{\beta} = 3\cdot\frac{\dot{R}}{R}, \tag{13}$$

$$\sigma^2 = \sigma_{\mu\nu}\cdot\sigma^{\mu\nu} = \dot{\alpha}^2 + 2\dot{\beta}^2 - \tfrac{1}{3}\cdot\theta^2, \tag{14}$$

where,

$$\sigma_{\mu\nu} = \tfrac{1}{2}[V_{\mu;\nu} + V_{\nu;\mu} + V_\mu V^\alpha V_{\nu;\alpha} + V_\nu\cdot V^\alpha\cdot V_{\mu;\alpha}] - \tfrac{1}{3}\theta(g_{\mu\nu} + V_\mu\cdot V_\nu), \tag{15}$$

Now, one can directly obtain the Ray Chaudhuri's equation (Ray Chaudhuri 1979) from the above set of field equations (10) to (12) and using (14) and (15) as,

$$\dot{\theta} = -\tfrac{1}{3}\cdot\theta^2 - 2\sigma^2 = \tfrac{1}{2}\cdot\rho_p - \frac{A^2}{8\pi}\exp(-4\beta), \tag{16}$$

where,

$$R_{\mu\nu}\cdot V^\mu V^\nu = -\frac{\rho_p}{2} - \frac{A^2}{8\pi}\exp(-4\beta). \tag{17}$$

Now in view of all the three (strong, weak and dominant) energy conditions (Wald

CC-0. In Public Domain. Gurukul Kangri Collection, Haridwar

Digitized by Arya Samaj Foundation Chennai and eGangotri

(1984)), one finds $\rho \geqslant 0$ and $\rho_p \geqslant 0$, together with the fact that the sign of λ is unrestricted, it may take values positive, negative or zero as well. This implies in view of (16) that even the existence of the strings is unable to halt the collapse. From the above energy conditions we find that λ might even take the negative value and therefore Einstein's equation (9) with $\lambda < 0$, is the equation for an anisotropic fluid with pressure different from zero along the direction of x^μ.

3. Exact solutions of Einstein's field equations

Since we have a set of three field equations (10)–(12), with four unknown parameters, viz. α, β, ρ, λ the reduction of one unknown enables us to obtain a set of exact solutions. This is achieved in the present case by assuming the following relation between the metric co-efficients

$$\alpha = a\beta, \tag{18}$$

Where a is a constant. In view of this (12), reduces to the following form,

$$(a+1)\ddot{\beta} + (a^2 + a + 1)\dot{\beta}^2 = -\frac{A^2}{8\pi}\exp(-4\beta).$$

For $a \neq -1$ ($a = -1$ implies $\dot{\beta}$ is imaginary) the above equation can be written as an integral equation

$$\int \mathrm{d}\left[\dot{\beta}^2 \exp\left(2\cdot\left(\frac{a^2+a+1}{a+1}\right)\beta\right)\right]$$
$$= -\frac{A^2}{4\pi(a+1)}\int \exp\left(2\cdot\left(\frac{a^2-a-1}{a+1}\right)\beta\right)\mathrm{d}\beta + k,$$

where k is constant of integration. So one obtains

$$\dot{\beta}^2 = k\exp\left[-2\cdot\left(\frac{a^2+a+1}{a+1}\right)\cdot\beta\right] - \frac{A^2}{81T(a^2-a-1)}\exp(-4\beta),$$

which can again be written in an integral form as

$$\int \frac{\exp(2\beta)\mathrm{d}\beta}{\left[k\cdot\exp\left(-2\cdot\left(\frac{a^2-a-1}{a+1}\right)\cdot\beta\right) - \frac{A^2}{8\pi(a^2-a-1)}\right]^{1/2}} = \pm(t-t_0), \tag{19}$$

where t_0 is another integration constant. We shall solve the above integral for two different cases, $(a^2-a-1)/(a+1) = -1$ and 2. For other cases the solutions either will not be obtained in closed form or 'a' will become imaginary.

Case 1.

$$\frac{a^2-a-1}{a+1} = -1 \tag{20}$$

i.e. $a = 0$, and hence $\alpha = 0$. It gives a very special form of Bianchi 1 metric. So now,

CC-0. In Public Domain. Gurukul Kangri Collection, Haridwar

Digitized by Arya Samaj Foundation Chennai and eGangotri

(19) can be immediately integrated to yield,

$$\exp(2\cdot\beta) = k\cdot(t-t_0)^2 - \frac{A^2}{8\cdot\pi\cdot k}. \tag{21}$$

ρ and λ can now be obtained from (10) and (11) respectively as

$$\rho = k \Big/ \left[k(t-t_0)^2 - \frac{A^2}{8\pi k} \right], \tag{22}$$

$$\lambda = \left[k^2\cdot(t-t_0)^2 - 3\cdot\frac{A^2}{8\pi} \right] \Big/ \left[k\cdot(t-t_0)^2 - \frac{A^2}{8\cdot\pi\cdot k} \right]^2, \tag{23}$$

and,

$$\rho_p = \rho - \lambda = \left(\frac{A^2}{4\pi}\right) \Big/ \left[k(t-t_0)^2 - \frac{A^2}{8\pi k} \right]^2. \tag{24}$$

Finally, R^3, θ and σ can be obtained from (13) to (16) respectively as

$$R^3 = k\cdot(t-t_0)^2 - \frac{A^2}{8\cdot\pi\cdot k}, \tag{25}$$

$$\theta = 2\cdot k\cdot(t-t_0)/R^3, \tag{26}$$

and

$$\sigma^2 = \tfrac{1}{6}\cdot[2\cdot k\cdot(t-t_0)/R^3]^2. \tag{27}$$

From the above solutions we observe that at the initial epoch, $(t-t_0)^2 = (A^2)/(8\pi k^2)$, the string model starts with an initial singularity $R^3 \to 0$, while ρ, ρ_p, λ, θ, σ^2 etc. diverge. This is a line singularity, since, $\exp(2\alpha) \to 1$ and $\exp(2\beta) \to 0$. At a later instant when $(t-t_0)^2 = 3A^2/8\pi\cdot k^2$ we have $\lambda = 0$ and $\rho = \rho_p$. So at this epoch strings vanish and we are left with a dust filled universe with a magnetic field. At this stage

$$\rho = \frac{4\cdot\pi\cdot k^2}{A^2}, \quad R^3 = \frac{A^2}{4\cdot\pi\cdot k}, \quad \theta = \frac{2}{A}(6\pi)^{1/2} \quad \text{and} \quad \sigma^2 = \frac{2\cdot\pi\cdot k^2}{3\cdot A^2},$$

i.e. all these parameters are of finite magnitude. In this solution matter is directly related with the magnetic field as is noted in (24). When the magnetic field is absent, the matter is also absent and the solution reduces to that of pure geometric string distribution.

Case 2.

$$\frac{a^2 - a - 1}{a+1} = 2. \tag{28}$$

i.e.

$$a = \frac{3 \pm (21)^{1/2}}{2}.$$

For this case integral (19) can at once be evaluated to yield

$$\exp(2\beta) = \left[\frac{8\cdot\pi\cdot k}{A^2}(5 \pm (21)^{1/2}) - \frac{A^2}{2\cdot\pi}\cdot\frac{(t-t_0)^2}{(5\pm(21)^{1/2})} \right]^{1/2}. \tag{29}$$

CC-0. In Public Domain. Gurukul Kangri Collection, Haridwar

Digitized by Arya Samaj Foundation Chennai and eGangotri

From (29) it is evident that the arbitrary constant k must be positive in this case, so we replace k by m^2 in the following. The other parameters can be obtained as before.

$$\rho = \frac{\frac{9+2\cdot(21)^{1/2}}{(5+(21)^{1/2})^2}\cdot\frac{A^2}{16\pi^2}(t-t_0)^2 - (5+(21)^{1/2})m^2}{\left[\frac{8\cdot\pi\cdot m^2}{A^2}\cdot(5+(21)^{1/2}) - A^2(t-t_0)^2/2\cdot\pi\cdot(5+(21)^{1/2}\right]^2}. \tag{30}$$

The positivity of ρ which follows from the energy conditions demands that one has to choose the positive sign before $(21)^{1/2}$ in the solution (29). With this choice the other parameters are obtained explicitly as follows,

$$\lambda = -\frac{(9+(21)^{1/2})m^2 - \frac{(4+(21)^{1/2})}{(5+(21)^{1/2})^2}\cdot\frac{A^2}{16\pi^2}(t-t_0)^2}{\left[\frac{8\cdot\pi\cdot m^2}{A^2}(5+(21)^{1/2}) - \frac{A^2\cdot(t-t_0)^2}{2\cdot\pi\cdot(5+(21)^{1/2})}\right]^2}, \tag{31}$$

$$\rho_p = \frac{4m^2 + \frac{A^4}{16\pi^2\cdot(5+(21)^{1/2})}\cdot(t-t_0)^2}{\left[\frac{8\cdot\pi\cdot m^2}{A^2}(5+(21)^{1/2}) - A^2\cdot(t-t_0)^2/(2\pi\cdot(5+(21)^{1/2}))\right]^2}, \tag{32}$$

$$R^3 = \left[\frac{8\cdot\pi\cdot m^2}{A^2}\cdot(5+(21)^{1/2}) - \frac{A^2\cdot(t-t_0)^2}{2\cdot\pi\cdot(5+(21)^{1/2})}\right]\times\frac{(7+(21)^{1/2})}{8}, \tag{33}$$

$$\theta = -\left(\frac{7+(21)^{1/2}}{5+(21)^{1/2}}\right)\cdot\frac{A^2}{8\cdot\pi}\cdot\left[\frac{(t-t_0)}{\frac{8\cdot\pi\cdot m^2}{A^2}(5+(21)^{1/2}) - \frac{A^2\cdot(t-t_0)^2}{2\cdot\pi\cdot(5+(21)^{1/2})}}\right], \tag{34}$$

$$\sigma^2 = \left(\frac{7+(21)^{1/2}}{(5+(21)^{1/2})^2}\right)\cdot\frac{A^2}{48\cdot\pi^2}\left[\frac{(t-t_0)}{\frac{8\cdot\pi\cdot m^2}{A^2}(5+(21)^{1/2}) - \frac{A^2\cdot(t-t_0)^2}{2\cdot\pi\cdot(5+(21)^{1/2})}}\right]. \tag{35}$$

So, we get the complete set of solutions. Now, it is evident from (29) that

$$U^2 < \frac{16\cdot\pi^2\cdot m^2}{A^4}(5+(21)^{1/2})^2,$$

where $U = t_0 - t$, so when $t < t_0$, we have $U > 0$, and $\theta > 0$, i.e. the expanding model. Towards the past U^2 increases and at an epoch $t = -t_s$, we find

$$U_s^2 = (t_s + t_0)^2 = \frac{16\cdot\pi^2}{A^4}(5+(21)^{1/2})^2,$$

which shows the existence of a singularity of a finite past. At t increases, U^2 decreases and we have the regularity condition satisfied when t approaches t_0 that is $U^2 \to 0$. This gives the upper limit to the expansion, as is evident from (34). At a subsequent stage the motion reverses from a maximum volume and $t > t_0$ so that the system

CC-0. In Public Domain. Gurukul Kangri Collection, Haridwar

Digitized by Arya Samaj Foundation Chennai and eGangotri

contracts ($\theta < 0$). As t increases, evidently U^2 increases and approaches the singularity when $t = t_s + 2t_0$.

One must clearly mention in this context that the field equations without any contribution from the magnetic field can however, be integrated to yield solutions, which are not special cases of those given above.

Assuming (18), the field equation (12) would reduce to the following form

$$\ddot{\beta} + K\dot{\beta}^2 = 0, \quad K = \frac{a^2 + a + 1}{a + 1} \tag{36}$$

which has a general solution

$$\exp(2\cdot\beta) = [C\cdot(t - t_0)]^{2/K}, \; C \text{ is a constant.} \tag{37}$$

So,

$$\exp(2\cdot\alpha) = [C\cdot(t - t_0)]^{(2a/K)}. \tag{38}$$

Thus all other physical parameters can be obtained in a straightforward manner as,

$$R^3 = [C\cdot(t - t_0)]^{(2+a)/K}, \tag{39}$$

$$\rho = (2a + 1)/(t - t_0)^2, \tag{40}$$

$$\lambda = 1/(t - t_0)^2, \tag{41}$$

$$\rho_p = 2a/(t - t_0)^2, \tag{42}$$

$$\theta = (a + 2)/(t - t_0), \tag{43}$$

$$\sigma^2 = \tfrac{2}{3}\cdot(a - 1)^2/(t - t_0)^2. \tag{44}$$

From the above solutions, we note that at the initial epoch, $t = t_0$, $R^3 \to 0$, while ρ, λ, ρ_p, θ, σ^2 etc diverge, and $\exp(2\alpha)$, $\exp(2\beta) \to 0$ – the point singularity. This is the starting point of the string model. Again at a later stage, when $t \to \infty$, R^3 also tends to infinity but all other physical parameters become insignificant. It is interesting to note that for a pure geometric string ($\rho_p = 0$) model, we have to take the value of $a = 0$. For this case the universe starts with strings and ends up at a stage when the massive strings themselves disappear without any remnant.

4. P-string solutions in the absence of magnetic field

In this section we consider a string-dust system in the absence of the magnetic field, in which case the field equations take the following form,

$$2\cdot\dot{\alpha}\dot{\beta} + \dot{\beta}^2 = \rho, \tag{45}$$

$$2\cdot\ddot{\beta} + 3\cdot\dot{\beta}^2 = \lambda, \tag{46}$$

$$\ddot{\alpha} + \ddot{\beta} + \dot{\alpha}^2 + \dot{\beta}^2 + \dot{\alpha}\dot{\beta} = 0. \tag{47}$$

Here also, in order to obtain the exact solutions of the above set of field equations,

CC-0. In Public Domain. Gurukul Kangri Collection, Haridwar

Digitized by Arya Samaj Foundation Chennai and eGangotri

we require one more equation. Let that be an equation of state for Takabayashi string (i.e. *P*-string), which is

$$\rho = (1 + W)\lambda, \tag{48}$$

where $W > 0$ is a constant. This is analogous to choosing an equation of state between the matter density and the string's tension density in the form $\rho_p = W \cdot \lambda$. This equation of state for Takabayashi string is interesting for the two limiting cases viz. for infinitesimally small value of W on the one hand and for infinitely large value of W on the other. When W is very small only geometric strings appear and for very large W, particles dominate over strings.

In view of (48), one can reduce the set of equations (45) to (47) into a single nonlinear differential equation in β, as

$$\frac{\dddot{\beta}}{\dot{\beta}} + W\frac{\ddot{\beta}^2}{\dot{\beta}^2} + \left(\frac{6W^2 + 15W + 10}{2(W+1)}\right)\ddot{\beta} + \frac{3}{4}\left(\frac{3W^2 + 6W + 4}{W+1}\right)\dot{\beta}^2 = 0. \tag{49}$$

This equation can be solved with a special technique of substitutions which is as follows. We first replace $\dot{\beta}^2$ by y and then substitute z for $y_\beta{}^2 \cdot y^W$ and so the above equation (49) becomes

$$y^{-W/2} \cdot z_y + \kappa \cdot (Z)^{1/2} + l \cdot y^{(W/2+1)} = 0, \tag{50}$$

where,

$$\kappa = \frac{6W^2 + 15W + 10}{W+1} \text{ and } l = 3\frac{(3W^2 + 6W + 4)}{W+1}. \tag{51}$$

Now, again replacing $y^{(W/2+1)}$ by U and z by V^2 and considering $V = AU$, A being a constant, (50) takes the following form

$$(W+2)A + \kappa + \frac{l}{A} = 0,$$

which immediately yields the value of the constant A, which is

$$A = -3, \text{ or } A = -\left(\frac{3W^2 + 6W + 4}{(W+1)(W+2)}\right), \tag{52}$$

κ and l being substituted from (51), so now one obtains

$$A = \frac{V}{U} = -\frac{(z)^{1/2}}{y^{(W/2+1)}} = \frac{Y_\beta}{Y},$$

and hence

$$\ln Y = A \cdot \beta + m,$$

where m is a constant of integration. Now replacing Y by $\dot{\beta}^2$ the above equation can be solved to obtain

$$\exp(2 \cdot \beta) = \exp(-2m/A) \cdot (-2/(A \cdot (t - t_0')))^{(4/A)}. \tag{53}$$

CC-0. In Public Domain. Gurukul Kangri Collection, Haridwar

Digitized by Arya Samaj Foundation Chennai and eGangotri

In view of (53) one can easily find out the other parameters from (45) to (47) as

$$\exp(2\alpha) = n\cdot(t-t_0)^{-2((A+WA+3W+2))/A}, \tag{54}$$

$$\rho = \frac{4}{A^2}\cdot(W+1)\cdot(3+A)\cdot(t-t_0)^{-2}, \tag{55}$$

$$\lambda = \frac{4}{A^2}\cdot(3+A)\cdot(t-t_0)^{-2}, \tag{56}$$

$$\rho_p = \frac{4}{A^2}\cdot W\cdot(3+A)\cdot(t-t_0)^{-2}, \tag{57}$$

where n is yet another constant of integration. Finally, R^3, θ and σ^2 can be obtained from (13) to (15) as

$$R^3 = \left(n\cdot\left(-\frac{2}{A}\right)\cdot\frac{4}{A}\cdot\exp(-2m/A)\right)\cdot(t-t_0)^{-(A+WA+3W+6)/A}, \tag{58}$$

$$\theta = -\left(\frac{A+WA+3W+6}{A}\right)\cdot(t-t_0)^{-1}, \tag{59}$$

$$\sigma^2 = 2\frac{(A+WA+3W)^2}{3A^2}(t-t_0)^{-2}. \tag{60}$$

Now for $A=-3$, ρ, λ, ρ_p all become zero and

$$\begin{aligned}
&\exp(2\beta) = \exp(2m/3)(2/(3\cdot(t-t_0)))^{-4/3} = m_1(t-t_0)^{4/3},\\
&\exp(2\alpha) = n\cdot(t-t_0)^{-2/3},\\
&R^3 = (n)^{1/2}\cdot(2/3)^{-4/3}\cdot\exp(2m/3)\cdot(t-t_0) = l_1\cdot(t-t_0),\\
&\theta = (t-t_0)^{-1},\\
&\sigma^2 = \tfrac{2}{3}\cdot(t-t_0),
\end{aligned} \tag{61}$$

where, m_1, l_1 are constants depending on m and n. Now absorbing the constants m_1 and n into the metric co-efficients by suitable choice of spatial co-ordinates and defining a new time co-ordinate $\bar{t} = t - t_0$, it is possible to write the metric (2.1) in the following form

$$ds^2 = -d\bar{t}^2 + \bar{t}^{2p_1}dx^2 + \bar{t}^{2p_2}dy^2 + \bar{t}^{2p_3}dz^2,$$

where

$$p_1 = -1/3,\ p_2 = p_3 = 2/3.$$

From the above it is evident that

$$p_1 + p_2 + p_3 = 1 = p_1^2 + p_2^2 + p_3^2.$$

So this metric is the well-known Kasner metric for a flat, homogeneous anisotropic

CC-0. In Public Domain. Gurukul Kangri Collection, Haridwar

Digitized by Arya Samaj Foundation Chennai and eGangotri

empty space. It may be noted that Letelier (1983) could not find any solution though he concluded that the anisotropy of the universe decreases as the universe expands. Again for

$$A = -\left(\frac{3W^2+6W+4}{(W+1)\cdot(W+2)}\right) = -\mu \text{ (say)},$$

we find,

$$\exp(2\cdot\beta) = m_2\cdot(t-t_0)^{(4/\mu)},$$

$$\exp(2\cdot\alpha) = n\cdot(t-t_0)^{(4W\cdot n/(\mu\cdot(W+2)))},$$

$$\rho = \frac{4\cdot(3W+2)\cdot(W+1)^2\cdot(W+2)}{(3W^2+6W+4)^2}\cdot(t-t_0)^{-2}, \tag{62}$$

$$\lambda = \frac{4\cdot(3W+2)}{\mu\cdot(3W^2+6W+4)}\cdot(t-t_0)^{-2},$$

$$\rho_p = \frac{4\cdot W\cdot(3W+2)}{\mu\cdot(3W^2+6W+4)}\cdot(t-t_0)^{-2},$$

$$R^3 = l_2\cdot(t-t_0)^{((3W+4)/(\mu\cdot(W+2)))},$$

$$\theta = \frac{(3W+4)}{(W+2)\cdot\mu}\cdot(t-t_0)^{-1},$$

$$\sigma^2 = (8/(3\mu^2\cdot(W+2)^2))\cdot(t-t_0)^2,$$

where m_2 and l_2 are constants depending on m, n and w.

So (62) is the set of solutions obtained for Takabayashi string. Here we observe that at the initial epoch when $t\to t_0$, $\exp(2\alpha)$, $\exp(2\beta)$ and hence R^3 all tend to zero giving rise to a point singularity, and all other parameters viz., ρ, ρ_p, λ, θ, σ^2, etc diverge. As $t\to\infty$, $\exp(2\alpha)$, $\exp(2\beta)$ and $R^3\to\infty$ while all other parameters become insignificant.

5. Conclusion

The present work extends the work of Letelier given earlier. In addition, we have considered a source-free magnetic field, the reason for which has been discussed in the introduction, we have obtained three sets of solutions with a special choice of metric coefficients, viz., $\alpha = a\beta$. For a particular value of a we observe that our model starts from a string dominated era, but at a later instant strings vanish and the universe becomes particle dominated. Here, the gravitational field is coupled to the magnetic field such that in the absence of the magnetic field the system reduces to pure geometric strings. For a different value of a we find that there is an upper limit for the expansion of the string universe and one cannot obtain a physical model in the absence of the magnetic field. We have also presented solutions for vanishing magnetic field and it is observed that the string distribution cannot go over to a particle dominate era at any stage of the evolution, unlike the result obtained by

CC-0. In Public Domain. Gurukul Kangri Collection, Haridwar

Digitized by Arya Samaj Foundation Chennai and eGangotri

Letelier. At the end an explicit solution for Takabayashi strings has been presented which represents a system of massive strings.

References

Garfinkle D 1985 *Phys. Rev.* **D32** 1323
Gott J R 1985 *Astrophys. J.* **288** 422
Kibble T W S 1976 *J. Phys.* **A9** 1387
Letelier P S 1979 *Phys. Rev.* **D20** 1294
Letelier P S 1983 *Phys. Rev.* **D28** 2414
Melvin M A 1975 *Ann. New York Acad. Sci.* **262** 253
Ray Chaudhuri A 1979 *Theoretical Cosmology*, (Oxford: Clarendon Press)
Stachel J 1980 *Phys. Rev.* **D21** 2171
Takabayashi T 1978 *Q. Mech. Determinism, Causality and Particles*, (ed.) M Flato (Holland: Reidel Dorbrecht) p. 179
Vilenkin A 1981 *Phys. Rev.* **D24** 2982
Wald R M 1984 *General Relativity*, The Univ. of Chicago Press
Zeldovich Ya B 1980 *Mon. Not. R Astron. Soc.* **192** 663

CC-0. In Public Domain. Gurukul Kangri Collection, Haridwar

Digitized by Arya Samaj Foundation Chennai and eGangotri

CC-0. In Public Domain. Gurukul Kangri Collection, Haridwar

Digitized by Arya Samaj Foundation Chennai and eGangotri

Pramāṇa – J. Phys., Vol. 34, No. 1, January 1990, pp. 13–21. © Printed in India.

Orthogonality constrained general variational calculation of excited state wavefunctions and energies: A new strategy

PRIYATOSH DUTTA and S P BHATTACHARYYA

Department of Physical Chemistry, Indian Association for the Cultivation of Science, Jadavpur, Calcutta 700 032, India

MS received 29 March 1988; revised 24 July 1989

Abstract. A viable strategy is developed for the general variational calculation of excited state wavefunctions which are constrained to remain *orthogonal* to all the lower-lying states of the same *symmetry*. A key element of the strategy is to employ the penalised functional procedure for enforcing the relevant orthogonality constraints and the method of steepest descent to locate the constrained minima with respect to all variables, linear as well as nonlinear. The workability of the algorithm is tested by applying the technique for the optimization of nonlinear parameters in trial functions for the 2*s* state of H atom and singlet 1*s*2*s* states of helium atom and some isoelectronic ions.

Keywords. Constrained variation; variational calculation of excited states; orthogonality constrained variation; penalised functional method.

PACS No. 31·15

1. Introduction

The Ritz variational principle asserts that for any arbitrary trial function ($\tilde{\psi}$) satisfying the appropriate boundary conditions, the energy expectation value $\tilde{E}$ is an upper bound to the exact ground state energy (E_0) of the system (Epstein 1974) described by the hamiltonian $\hat{H}$ (viz.)

$$\tilde{E} = \langle \tilde{\psi} | \hat{H} | \tilde{\psi} \rangle / \langle \tilde{\psi} | \tilde{\psi} \rangle \geqslant E_0.$$

The upper boundedness of $\tilde{E}$ is no longer valid for variationally computed excited state energies unless the trial function ($\tilde{\psi}$) is constrained to be orthogonal to all the lower-lying states of the same symmetry. However, if the trial space is linear, the Hyllerass Undheim Macdonald (HUM) theorem guarantees the upper boundedness of the computed energies (Hylleraas and Undheim 1930; Macdonald 1933; Epstein 1974). The required linearity of the trial space can be easily satisfied by taking the trial function in the form of a linear combination of a linearly independent set of basis functions and varying only the linear parameters in the trial function. The basis functions may contain nonlinear parameters which are held fixed during the variation. This restriction on the variational freedom affects the flexibility of the trial function, for it is well known that several linear parameters are generally required to mimic the effects of variation of a single nonlinear parameter. It would be desirable therefore to have a method which permits one to perform a general variational calculation on an excited state without sacrificing the orthogonality of the computed excited state

CC-0. In Public Domain. Gurukul Kangri Collection, Haridwar

Digitized by Arya Samaj Foundation Chennai and eGangotri

wavefunctions to the lower-lying states of the same symmetry. If the lower-lying exact eigenstates of $\hat{H}$ are known, orthogonality constrained variation ensures strict upperboundedness of the computed excited state energies in spite of variations of the non-linear parameters. The same is not true when only approximate lower state functions are available. Nevertheless, one can try to optimize the non-linear variational parameters for a manifold of states (ground and several excited states of the same symmetry) at the same level of sophistication or approximation by resorting to the use of orthogonality constrained variation method. This would amount to the optimization of the 'Ritz basis vectors' for a manifold of states which could enhance the convergence of a subsequent linear variational calculation within the same manifold.

In quantum theoretical calculation of atomic and molecular electronic structure, the ground and lowest electronic state of each symmetry is commonly described by approximate wavefunctions determined variationally by applying the SCF method. The result of an SCF calculation provides the 'parent configuration' which is usually supplemented by invoking the linear variation method (cf HUM theorem) in the manifold of electronic states generated by the SCF orbitals (The so called CI method). The convergence of CI expansion is generally very slow. The same two step heirarchy (viz. SCF + CI) can, in principle, be adopted to describe an arbitrary excited state as well. But the scheme in this case is much less well defined. This is because the 'parent excited state configuration' may not be amenable to SCF calculation. CI expansion around a 'non-parent configuration' is rather inefficient.

The MC-SCF method on the other hand invokes a nonlinear variational strategy werein the CI expansion coefficients and orbital forms are both optimized. The nonlinear orbital optimization step is, however, plagued by problems originating from variational collapse and manifested in 'root-flipping' (Docken and Hinze 1972; Chang and Schwarz 1977; Werner and Meyer 1981). The search for alternative techniques which avoid the problem of variational collapse while performing nonlinear variational calculations on excited states, although cursory, can be found in literature. These invariably involve either the application of the Hylleraas perturbation variation method (Sinanoglu 1961; Miller 1966; Chang 1980) or the use of orthogonality constrained variation method. Although the basic philosophy underlying the latter method has been well known, practical computational difficulties have led researchers in the field to consider the method as more or less untractable (Chang 1980). Nevertheless, few attempts in this direction can be found in the literature (Weber and Handy 1969; Wang et al 1973; Hendekovic 1983). It appears that these methods have never been numerically evaluated or persued seriously. Our purpose in this communication has been to explore a new strategy for tackling the orthogonality constrained variational method –a strategy that is computationally easy to handle and leads to a tractable numerical recipe. In what follows we first describe the algorithm. The workability of the algorithm is then tested by applying the method to some model problems. Possible avenues of improving the algorithm are suggested.

2. The method

Let $\phi_1, \phi_2, \phi_3 \cdots \phi_{n-1}$ be the first $(n-1)$ eigenstates (exact or approximate) of a given hamiltonian $\hat{H}$. Let the corresponding energies be $\varepsilon_1, \varepsilon_2, \varepsilon_3, \ldots, \varepsilon_{n-1}$. $\tilde{\psi}$ is the trial

CC-0. In Public Domain. Gurukul Kangri Collection, Haridwar

Digitized by Arya Samaj Foundation Chennai and eGangotri

wavefunction for the nth eigenstate of $\hat{H}$ which is constrained to remain orthogonal to $\phi_1, \phi_2, \ldots, \phi_{n-1}$ during variation. The constraint conditions are therefore

$$\langle \hat{\psi} | \phi_k \rangle = \langle \phi_k | \hat{\psi} \rangle = 0 \text{ for } k = 1, 2, 3, n-1. \tag{1}$$

Some of the conditions in (1) may be automatically satisfied for reasons of symmetry (eg $\hat{\psi}$, ϕ_k belong to two different irreducible representations of the symmetry group to which $\hat{H}$ belongs). For the sake of generality we assume that all the constraint conditions in (1) are non-trivial. Having explicated the constraint conditions we may now define an $(n-1)$ fold constrained energy functional as follows (Fiacco and McCormik 1968; Morrison 1969; Fiacco 1970; Das and Bhattacharyya 1985, 1986, 1987).

$$\tilde{\mathscr{F}}_c(\xi) = \{\varepsilon_c(\xi) - \varepsilon_1\}^2 + \sum_{k=1}^{n-1} \lambda_k g_k(\langle \tilde{\psi} | \phi_k \rangle). \tag{2}$$

In (2) ε_1 is a lower bound to the constrained energy $\bar{\varepsilon}(\xi)$. The g_k $(\langle \tilde{\psi} | \phi_k \rangle)$ s are appropriate penalty functions such that,

$$g_k(\langle \tilde{\psi} | \phi_k \rangle) = 0 \quad (k = 1, 2, \ldots, n-1),$$

only when all the constraints in (1) are satisfied. If the constraints are violated, g_ks rise sharply and $g_k(\langle \tilde{\psi} | \phi_k \rangle) > 0$ if the kth constraint is violated. A variety of functional forms can be chosen for g_k', the simplest of which is

$$g_k(\langle \tilde{\psi} | \phi_k \rangle) = [\langle \tilde{\psi} | \phi_k \rangle]^2$$

λ_ks are penalty weight factors of appropriate magnitudes and dimensions. The minimum of $\tilde{\varepsilon}_c(\xi)$ then corresponds to a set of values for $(\xi) = (\xi_c)$ such that

$$\langle \tilde{\psi}(\xi_c) | \phi_k \rangle = 0 \quad \text{for } k = 1, 2, \ldots, n-1 \text{ and } \varepsilon(\xi) = \varepsilon_1 = \varepsilon_c(\xi).$$

The constrained variational parameters are therefore determined by the stationary condition of $\mathscr{F}(\xi)$ for arbitrary variation $\delta\xi$ in ξ (viz).

$$\delta\mathscr{F}(\xi) = 0, \quad \text{which immediately leads to}$$

$$2[\{\varepsilon(\xi) - \varepsilon_1\}](\partial\varepsilon/\partial\xi)\delta\xi + 2\sum_{k=1}^{n-1} \lambda_k [g_k(\langle \tilde{\psi} | \phi_k \rangle)(\partial g_k/\partial\xi)]\delta\xi = 0$$

since $\delta\xi$ is arbitrary, we have, from the preceding equation

$$2[\varepsilon(\xi) - \varepsilon_1](\partial\varepsilon/\partial\xi) + 2\sum_{k=1}^{n-1} \lambda_k [g_k(\langle \tilde{\psi} | \phi_k \rangle)(\partial g_k/\partial\xi)] = 0. \tag{3}$$

Instead of trying to solve (3) for $\xi = \xi_c$ directly, a more viable strategy would be to seek the minimum of $\mathscr{F}(\xi)$ by adopting a direct functional minimization procedure. One way to do this is to invoke the method of steepest descent (SD) for the minimization of $\mathscr{F}(\xi)$. Since it is, in any case, going to be an iterative process, we must have a well defined scheme of estimating (or updating) the lower bound ε_1 to $\bar{\varepsilon}(\xi)$ at any specific stage of the iterative process. A convenient way of doing this is to adopt the following approach (Morrison 1969). Let ε_1^i be a lower bound to the

CC-0. In Public Domain. Gurukul Kangri Collection, Haridwar

Digitized by Arya Samaj Foundation Chennai and eGangotri

constrained energy ε^i at the ith stage of the iterative process. Let the constrained functional have the value S_i at this stage. The lower bound for the next cycle is then updated by taking

$$\varepsilon_1^{i+1} = \varepsilon_1^i + \eta(S_i)^{1/2} \tag{4}$$

where

$$S_i = \mathscr{F}_c^i(\xi) = (\varepsilon_1^i - \varepsilon^i)^2 + \sum_k g_k(\langle \tilde{\psi}_i | \phi_k \rangle) \tag{5}$$

η is a damping parameter which should lie in the range $0 < \eta \leqslant 1$. An appropriate choice of η is very important for the achievement of smooth convergence (see later). When an appropriate value of η has been chosen, we may try to locate the constrained minimum in the following way.

Let $\xi_1^0, \xi_2^0, \ldots, \xi_n^0$ be the starting set of parameters in the trial wave function ($\tilde{\psi}$). Taylor's expansion of $\mathscr{F}(\xi_k)$ around ξ_k^0 gives us

$$\mathscr{F}(\xi_k) = \mathscr{F}(\xi_k^0) + (\partial \mathscr{F}/\partial \xi_k)_{\xi_k = \xi_k^0} \delta\xi_k + \cdots$$

If one sets $\delta\xi_k = -\lambda (\partial \mathscr{F}/\partial \xi_k)_{\xi_k = \xi_k^0}$ where λ is an appropriately small positive scalar, $\mathscr{F}(\xi_k) < \mathscr{F}(\xi_k^0)$ is ensured. Although a sufficiently small λ will ensure minimization of $\mathscr{F}(\xi_k)$, the best or steepest rate of descent can be achieved by further minimizing $\mathscr{F}(\xi_k)$ with respect to the step length parameter λ (Mcweeny 1960, 1968). This, however, requires an explicit knowledge of the second derivative of $\mathscr{F}(\xi)$ with respect to ξ.

3. Results and discussion

The workability of the algorithm is amply demonstrated by the following numerical examples. The examples belong to two distinct categories described earlier.

3.1 *Where the exact lower state wavefunctions of the same symmetry are known*

The example under this category belongs to the class of problems where the exact wavefunctions for the $(n-1)$ lower lying states are available. The hydrogen atom is a case in point. The exact ground state of H atom is given by

$$\psi_0(r) = \frac{1}{\sqrt{\pi}} \exp(-r).$$

Let the trial wavefunction for the $2s$ state be chosen in the form

$$\bar{\psi}_{2s}(r) = \bar{\psi}_1(r) = N(1 + \beta r/2) \exp(-\alpha r/2).$$

The form chosen for $\tilde{\psi}_1$ has been deliberately made to make it coincide with that of the exact ψ_{2s}; for our basic purpose is to demonstrate the ability of our algorithm to prevent variational collapse even in the worst case and optimize the nonlinear parameters simultaneously.

If one tries to minimize the energy $E_{2s}(\alpha, \beta) = \langle \tilde{\psi}_1 | H | \tilde{\psi}_1 \rangle / \langle \tilde{\psi}_1 | \tilde{\psi}_1 \rangle$ directly, without enforcing the constraint $\langle \tilde{\psi}_1 | \psi_0 \rangle = \langle \psi_0 | \tilde{\psi}_1 \rangle = 0$, one anticipates variational collapse to the ground state to occur whichever set of α, β one starts with as $\tilde{\psi}_1(r) = \psi_0(r)$ for

CC-0. In Public Domain. Gurukul Kangri Collection, Haridwar

Digitized by Arya Samaj Foundation Chennai and eGangotri

Table 1. Comparison of the results obtained by applying the unconstrained and an orthogonality constrained variational procedure to the 2*s* state of *H* atom ($\tilde{\psi}_{2s} = \exp(-\alpha r/2)\cdot(1+\beta r/2)$; convergence criterion are the same in each case).

Method	Starting values of variational parameters		Optimized values* of variational parameters	Starting values of energy (E_0) and overlap (S_0) with the ground state	Final values of energy (E) and overlap (S) with the ground state
	α_0	β_0	α'/β'	E_0(a.u)/S_0	E(a.u)/S
UVM	0·75	−0·25	0·99487/ $1{\cdot}0867\times10^{-16}$		−0·49566/ 0·99406
OCVM	0·75	−0·25	0·5031/ −0·5093	−0·46875/ 0·9596	−0·12494/ $-0{\cdot}970\times10^{-11}$

$\alpha' = \alpha/2$, $\beta' = \beta/2$

$\alpha=2$, $\beta=0$. This is what happens when we attempt an unconstrained minimization of $\mathscr{F}(\xi)$ in our model which amounts to setting all the λ_ks equal to zero in (2). Table 1 displays the initial values of α, β as well as the initial energy and overlap of trial $\tilde{\psi}_1$ with the exact ground state wavefunction ψ_0 and the corresponding quantities at convergence. The collapse is evident. The corresponding quantities for the constrained variational optimization of $E_{2s}(\alpha,\beta)$ are also reported in the same table for comparison. It is clear that our orthogonality constrained model for the variational determination of non-linear (as well as linear) parameters characterizing the excited state wavefunction prevents variational collapse completely and produces energies which are upperbound to the exact energies of the corresponding excited states, when exact lower state wavefunctions are known. In the present case, we could recover the exact energy of the 2*s* state since the analytical form of the trial 2*s* state wavefunction coincided with the known one.

3.2 *Constrained minimization when only approximate lower state wavefunctions are known*

This is the situation one normally expects to encounter. The questions that naturally arise are (i) whether the method proposed can operate with equal facility in a case where exact lower state wavefunctions are not available to start with; (ii) whether the computed energies retain their upperbound character; (iii) what can be done to improve the quality of the results. To investigate these points we take up the singlet (1*s*2*s*) states of helium or helium-like atoms as examples. Two different types of basis sets are employed. In the first, we approximate the ground state by the Hylleraas–Eckert wave function ($\tilde{\psi}_0$) (Eckert 1930) which has two adjustable non-linear parameters α_0 and β_0

$$\tilde{\psi}_0(r_1,r_2) = N_0\{\exp[-(\alpha_0 r_1+\beta_0 r_2)]+\exp[-(\beta_0 r_1+\alpha_0 r_2)]\}.$$

The approximate trial wavefunction (space part) for the singlet (1*s*2*s*) state ($\tilde{\psi}_1$) is also chosen in the same form:

$$\tilde{\psi}_1(r_1,r_2) = N_1[\mathscr{U}_{1s}(\alpha',r_1)\mathscr{V}_{2s}(\beta',r_2)+\mathscr{U}_{1s}(\beta',r_1)\mathscr{V}_{2s}(\alpha',r_2)]$$

CC-0. In Public Domain. Gurukul Kangri Collection, Haridwar

Digitized by Arya Samaj Foundation Chennai and eGangotri

where

$$\mathscr{U}_{1s}(\alpha', r) = N_{1s}\exp(-\alpha' r) \text{ and}$$

$$\mathscr{V}_{2s}(\beta', r) = N_{2s}(1 + \beta' r/2)\exp(-\beta' r/2)$$

N_0, N_1, N_{1s} and N_{2s} are the corresponding normalization constants. In our orthogonality constrained variational model the functional (penalised) to be minimized is

$$\mathscr{F}(\alpha', \beta', \alpha^0, \beta^0) = \{\varepsilon(\alpha', \beta') - \varepsilon_1\}^2 + \lambda[S(\alpha', \beta', \alpha^0, \beta^0)]^2$$

where

$$S(\alpha', \beta', \alpha^0, \beta^0) = \langle \tilde{\psi}_0(r_1, r_2) | \tilde{\psi}_1(r_1, r_2) \rangle .$$

The minimization is to be done with respect to α' and β', while α^0 and β^0 are held constant. Table 2 reports the orthogonality constrained optimal values of α', β' the computed energy and overlap with the ground state wavefunction ($\tilde{\psi}_0$). It is clear that $\tilde{\psi}_1$ is orthogonal to $\tilde{\psi}_0$ and $\tilde{E}_1'$ is upperbound to the exact energy (Sharma and Coulson 1961). The unconstrained variational results are also included in table 2 for comparision. The computed energy $\tilde{E}_1$ is slightly lower than the constrained energy ($\tilde{E}_1'$) although no sign of variational collapse is evident in $\tilde{E}_1$ (unconstrained). In fact the form of the trial wavefunction ($\tilde{\psi}_1$) has been so chosen as to prevent the possibility of a complete collapse onto the ground state. It is however, clear from table 2 that $\tilde{\psi}_1$ (unconstrained) is not orthogonal to $\tilde{\psi}_0$ ($S \simeq 10^{-3}$). Thus our method is capable of generating a manifold of completely optimized and rigorously orthonormal set of basis vectors of a particular symmetry. One can use these vectors for further linear variational calculations which should lead to faster convergence as no a priori structure has been assumed for the Ritz-basis vectors. They have been fully optimized for the particular manifold consistent with the orthogonality requirement.

Table 3 presents another set of results for the singlet $1s2s$ states of a few members of the He isoelectronic sequence with a different choice of the basis functions. The

Table 2. Comparison of the results obtained by applying the unconstrained and an orthogonality constrained variational procedure to the singlet $1s2s$ state of helium atom ($^1\tilde{\psi}_{1s2s}$ and $\tilde{\psi}_{1s2s}$ are approximated by the corresponding Hyllearaas-Eckert function).*

Method	Starting values of variational parameters α_1^0	β_1^0	Optimized values of variational parameters α_1/β_1	Starting values of energy (E_a) and overlap (S_0) E_0(a.u)/S_0	Final values of energy (E) and overlap (S) E(a.u)/S
UVM	2·15	1·20	1·83649/ 1·50295		−2·05879/ −0·00129
OCVM	2·15	1·20	1·84593/ 1·49522	−2·01796 $4{\cdot}74 \times 10^{-2}$	−2·05859/ $-1{\cdot}94 \times 10^{-12}$
Exact results (Sharma and Coulson)					−2·147294

*Eckert 1932

CC-0. In Public Domain. Gurukul Kangri Collection, Haridwar

Digitized by Arya Samaj Foundation Chennai and eGangotri

Table 3. Comparison of the results obtained by applying the unconstrained and an orthogonality constrained variational procedure to the singlet $1s2s$ states of helium atom and some isoelectronic ions.

Z	OCV Energy of singlet $1s2s$ state (a.u)	Overlap with ψ_0	Exact[a] energy (singlet $1s2s$) (a.u)	Exact[b] energy (ground state) (a.u)	Unconstrained energy (singlet $1s2s$) (a.u)
2	−2·010336	$3{\cdot}6\times10^{-5}$	−2·14729	−2·9037	−2·80827
3	−4·318752	$2{\cdot}6\times10^{-5}$	−5·04115	−7·2799	−7·07201
4	−6·503459	$3{\cdot}2\times10^{-5}$	−9·18466	−13·6555	−13·28465
5	−10·21153	$4{\cdot}5\times10^{-5}$	−14·57809	−22·0309	−21·44574
6	−13·11626	$4{\cdot}24\times10^{-5}$	−21·22136	−32·4062	−31·55516

[a]Ref. Coulson and Sharma (1962)
[b]Ref. Scherr and Knight (1963)

trial wavefunction (space part) $\psi\,(r_1, r_2)$ is of the form

$$\tilde{\psi}(r_1, r_2) = N\{\phi_{1s}(r_1)\phi_{2s}(r_2)\}$$

where ϕ's are the appropriate ($1s$ or $2s$) single ξ-slater type of orbitals. The corresponding ground state ($\tilde{\psi}_0$) is also represented by variationally determined antisymmetrized product of single ξ-$1s$ slater orbitals. The reason behind this particular choice of $\tilde{\psi}\,(r_1, r_2)$ and $\tilde{\psi}_0(r_1, r_2)$ lies in the possibility of a complete variational collapse of $\tilde{\psi}\,(r_1, r_2)$ onto $\tilde{\psi}_0(r_1, r_2)$ during the optimization of ξ-parameters. This could happen since $\phi_{2s}(r_1)$ is nodeless and has a non-zero overlap with $\phi_{1s}(r_1)$. Perusal of table 3 clearly shows that the constrained calculations on the singlet $1s2st$ state successfully avoid variational collapse onto the ground state while the unconstrained variational calculations invariably lead to collapse of the $1s2s$ wavefunction onto the ground state. We may say that these constrained wave functions represent the best possible single ξ-STO based wavefunctions for the singlet $1s2s$ states consistent with the requirement of orthogonality with the corresponding approximate ground state. The computed energies are no doubt upper bounds to the exact energies. But they are a bit too high. This is not unexpected because of the very limited variational freedom enjoyed by the single-ξ STO based wavefunction for the singlet $1s2s$ state subject to the orthogonality constraint. A linear combination of such functions is required to improve the situation. We are exploring this possibility at present.

4. General features of the algorithm

We have made a preliminary study of the convergence behaviour of our algorithm. Our experience so far has been that a smooth and monotonic convergence can be achieved by our algorithm in all cases if η in (4) is properly chosen. The only requirement on η is that it should be a small positive scalar. Irrespective of the starting point the orthogonality constrained variational determination of the excited state wavefunction proceeds smoothly and converges to the same point, showing its stability. The constrained (penalised) functional value also decreases monotonically as the required orthogonality condition is satisfied more and more strictly with the increase.

CC-0. In Public Domain. Gurukul Kangri Collection, Haridwar

Digitized by Arya Samaj Foundation Chennai and eGangotri

in the number of steepest descent iterations. The rate of convergence is slow as is expected of the steepest descent procedure. We are exploring some avenues for convergence acceleration in the framework of the steepest descent based procedures (Bevington 1969). The slow convergence is more than compensated by the extreme simplicity of the algorithm. The algorithm does not loose its simplicity with an increase in the number of constraints. Although we have employed the steepest descent technique for minimizing the penalised functional, one can invoke any other suitable unconstrained minimization technique. The relative merits and demerits of these different techniques in the present context are under evaluation. The numerical stability of the algorithm is excellent since we have always been able to reach the same constrained minimum quite independent of the starting point. The algorithm is thus expected to be useful in a two step hierarchy where the Ritz basis vectors of a particular manifold of excited states are first optimized subject to the orthogonality constraint and then a further linear variation is performed within the same manifold. Our algorithm can be used, in principle, with the two step manifold energy minimization procedure suggested recently by Hendekovic (1982) essentially on the basis of max-min theorem (Gould 1966; Epstein 1974). However no numerical data on the performance of this method is available for comparison. The one-step method proposed by Weber and Handy (1969) which involves the application of Ritz variational principle to an appropriately projected hamiltonian $\bar{H}$ is much more cumbersome. For the first excited state having the same symmetry as the ground state (ϕ_0) the projected hamiltonian is given by

$$\bar{H} = (1 - P)H(1 - P)$$

where

$$P = |\phi_0\rangle\langle\phi_0| + |H\phi_0\rangle\langle H\phi_0|$$

The method is hardly tractable in view of its requirement to calculate the matrix elements of H^2 and H^3. Its generalization to handle higher than the first excited state of the same symmetry appears to be almost impossible. In comparison, our algorithm does not increase in complexity when one goes to higher excited states of a particular symmetry.

5. Scope of improvement of the algorithm

It may be noted that $\tilde{\psi}_1$ (constrained) is orthogonal to $\tilde{\psi}_0$. But since $\tilde{\psi}_0$ is not the exact ground state of H, the optimized $\tilde{\psi}_1$ (constrained) is not necessarily decoupled with $\tilde{\psi}_0$. That essentially means,

$$\langle\tilde{\psi}_1|\tilde{\psi}_0\rangle = 0, \quad \text{but } \langle\tilde{\psi}_1|\hat{H}|\tilde{\psi}_0\rangle \neq 0.$$

An obvious way of improving our results will be to incorporate the decoupling condition as an additional constraint and replace the two-step strategy by a single step one. Unlike the method of Weber and Handy (1969) this will not require the calculation of matrix elements of $\hat{H}^2$ or $\hat{H}^3$. On the other hand, this would certainly lead to a viable, if not better, alternative to the linear variational method (Wang *et al* 1973). Another area of improvement is in the choice of the penalty functions. We have so far used the simplest possible form of $g_k\langle\tilde{\psi}|\phi_k\rangle$. Better choice of g_k may

CC-0. In Public Domain. Gurukul Kangri Collection, Haridwar

Digitized by Arya Samaj Foundation Chennai and eGangotri

enhance the convergence rate achievable by the algorithm. Finally, we have used the simplest possible forms of trial functions for the excited states in our exploratory calculation and chosen the ground state accordingly. We can make systematic improvements in both and improve both the upperbounds. We will address ourselves to some of these aspects in a future communication (Datta and Bhattacharyya 1989).

111939

Acknowledgements

The computations have been carried out on a SIRIUS-32 minicomputing facility created under a CSIR (Government of India, New Delhi) sponsored research project.

References

Bevington P R 1969 in Data Reduction in Physical Science (New York: Mcgraw Hills) p 215
Chang T and Schwarz W H E 1977 *Theor. Chim. Acta* **44** 45
Chang T 1980 *Int. J. Quantum Chem.* **18** 43
Das K K and Bhattacharyya S P 1986 *Chem. Phys. Letts.* **125** 225
Das K K, Khan P and Bhattacharyya S P 1985 *Pramana – J. Phys.* **25** 281
Das K K, Khan P and Bhattacharyya S P 1987 *Pramana – J. Phys.* **28** 51
Datta P and Bhattacharyya S P 1989 (To be submitted)
Docken K and Hinze J 1972 *J. Chem. Phys.* **57** 4928
Eckert C E 1930 *Phys. Rev.* **32** 820
Epstein S T 1974 *in variational method in Quantum Chemistry* (A.P. New York)
Fiacco A V 1970 *J. Opt. Theor. Appl.* **6** 252
Fiacco A V and McCormic G P 1968 *in nonlinear programming: Sequential Unconstrained minimization Techniques*, (New York: Wiley)
Gould S H 1966 *in variational methods for eigenvalue Problems* (Toronto: University of Toronto press) ch. 2, sec. 6
Hendekovic J 1982 *Chem. Phys. letts.* **90** 198
Hylleraas E A and Undheim B 1930 *Z. Phys.* **65** 759
Macdonald J K L 1933 *Phys. Rev.* **43** 830
Mcweeny R 1960 *Rev. Mod. Phys.* **32** 335
Mcweeny R 1968 *Symp. Far. Soc.* **2** 7
Miller W H 1966 *J. Chem. Phys.* **44** 2198
Morrison D D 1969 *S I A M J Numer. Anal.* **5** 83
Scherr C W and Knight R E 1963 *Rev. Mod. Phys.* **35** 436
Sharma C S and Coulson C A 1962 *Proc. Phys. Soc. (London)* **80** 81
Sinanoglu O 1961 *Phys. Rev.* **122** 491
Wang P S C, Benston M L and Chong D P 1973 *J. Chem. Phys.* **59** 1721
Weber T A and Handy N C 1969 *J. Chem. Phys.* **50** 2214
Werner H J and Meyer W 1981 *J. Chem. Phys.* **24** 5794

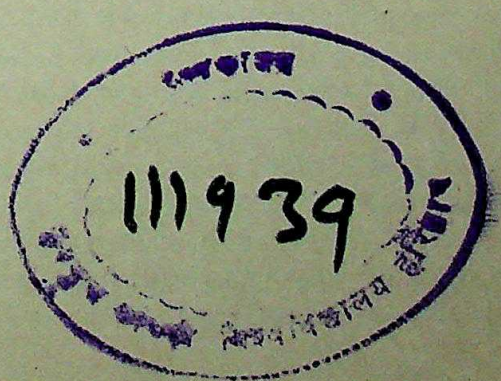

CC-0. In Public Domain. Gurukul Kangri Collection, Haridwar

Digitized by Arya Samaj Foundation Chennai and eGangotri

CC-0. In Public Domain. Gurukul Kangri Collection, Haridwar

Digitized by Arya Samaj Foundation Chennai and eGangotri

Pramāṇa – J. Phys., Vol. 34, No. 1, January 1990, pp. 23–31. © Printed in India.

Structure factor of charged colloidal suspensions using Brownian–dynamics simulation: Comparison of Yukawa and Sogami pair potentials

B V R TATA, A K SOOD* and R KESAVAMOORTHY

Materials Science Division, Indira Gandhi Centre for Atomic Research, Kalpakkam 603 102, India

*Present address: Department of Physics, Indian Institute of Science, Bangalore 560 012, India

MS received 8 May 1989; revised 18 September 1989

Abstract. Static structure factors $S(Q)$ are obtained for dilute charged colloidal systems using Brownian dynamics simulation method for the widely used screened Coulomb repulsive Yukawa potential and the recently proposed Sogami pair potential. The latter potential has, in addition to the usual repulsive part, an attractive term which is necessary to understand the reentrant phase transition reported in these colloids. It is shown for the first time that $S(Q)$ obtained using the Sogami potential for parameters favourable for liquid-like order agrees well with that measured experimentally. Thus it appears that the Sogami potential explains features of a homogeneous liquid as well as phase separated states, whereas Yukawa potential does not.

Keywords. Computer simulation: structure factor: colloids.

PACS Nos 82·70; 61·20

1. Introduction

Electrostatically stabilized aqueous colloidal systems can develop structural orders similar to those in atomic liquids (Pusey 1979; Tata *et al* 1987), crystalline solids (Williams and Crandall 1974) and even glasses (Pusey and van Megen 1987; Lindsay and Chaikin 1982; Kesavamoorthy *et al* 1988) when suitably deionized. The unique feature of these systems is that one can alter the strength and range of interparticle interaction simply by changing the impurity ion concentration n_i and the particle (also called polyball or macroion) concentration n_p, making them model systems to study the co-operative behaviour in condensed matter. It is widely believed that the particles interact predominantly via repulsive screened Coulomb Yukawa potential $U(r) \simeq \exp(-Kr/r)$, (for a review, see Castillo *et al* 1984). Here K is the inverse Debye screening length. There also exists a primary minimum (Castillo *et al* 1984) in the inter particle interaction due to London-van der Waals attraction, which gives rise to irreversible aggregation (flocculation), when n_i is large. However, for suspensions with low n_i this minimum is not important due to Coulomb barrier. So far Yukawa potential is used to explain ordering phenomena in colloids. Using this potential it has been shown that the static structure factors for liquid like ordered suspensions, computed using rescaled-mean spherical approximation (RMSA) (Hansen and Hayter 1982) and hypernetted chain (HNC) approximation (Schaefer 1977) agree well with the experiments (Hartl *et al* 1983; Tata *et al* 1986). The Monte Carlo (MC) (van Megen

CC-0. In Public Domain. Gurukul Kangri Collection, Haridwar

Digitized by Arya Samaj Foundation Chennai and eGangotri

and Snook 1977) and Brownian dynamics (BD) simulations (Gaylor *et al* 1981) have been done with Yukawa potential to calculate static and dynamic properties of these colloids and the results agree with the light scattering experiments. Recently Arora *et al* (1988) have observed a reentrant phase transition in these colloids, wherein a non-interacting homogeneous suspension phase separates into a rare (low polyball concentration) and a dense (high polyball concentration) phases as the impurity concentration n_i is reduced. This suspension once again becomes homogeneous (with liquid or crystalline-like order) on further reduction of n_i. This phenomena cannot be explained on the basis of the pure repulsive interparticle interaction. Since a purely repulsive interaction between particles confined in a given volume cannot lead to inhomogeneous phases except the crystalline-liquid transition observed in a system of hard spheres, an attractive part in $U(r)$ is a must. Based on free energy calculation, Arora *et al* (1988) showed that the observed phase transition can be understood by considering Sogami potential (Sogami 1983; Sogami and Ise 1984) which has the usual screened Coulomb repulsion and also an attractive part leading to a secondary minimum. The formalism of Sogami and Ise (1984) has been questioned by Overbeek (1987), subsequently Ise *et al* (1988a) have in turn shown flaws in the treatment of Overbeek. A number of other experimental results viz. the coexistence of ordered and disordered phases (Ise 1986), observation of Ostwald ripening in the growth of colloidal crystals (Ito *et al* 1989) and the existence of stable voids in colloidal crystals (Ise *et al* 1988b) also suggest the existence of a secondary minimum in the effective pair potential (Ise *et al* 1988).

As pointed out earlier, apart from the phase separated states colloidal suspensions also exhibit homogeneous liquid-like and crystalline-like ordered states. To confirm whether Sogami potential leads to these structural orders (for some physically reasonable parameters), we obtain $S(Q)$ of a suspension of colloidal particles interacting via Sogami potential. As analytical calculations of $S(Q)$ using Sogami potential on the lines similar to that of RMSA (routinely used for Yukawa potential) is difficult, we use BD simulation to obtain pair correlation function ($g(r)$) and mean square displacement ($r^2(t)$). $S(Q)$ is obtained by Fourier transforming $g(r)$. Yukawa potential is also used in simulation for the sake of comparison. $S(Q)$ obtained using Sogami potential agrees equally well with the experimental $S(Q)$. MC simulations are also carried out for the same parameters and compared with the BD results.

This paper is organized as follows. In §2 we present both Yukawa and Sogami pair potentials with a brief discussion of their origin. Details of BD simulation is presented in §3. Section 4 deals with the results and discussion. We end this paper with conclusions given in §5.

2. Pair potentials

2.1 *Yukawa potential*

For the aqueous monodispersed colloidal system consisting of polystyrene spheres (polyballs) of radius a, charge Ze, the screened Coulomb Yukawa pair potential between ith and jth particles is given by (Verwey and Overbeek 1948)

$$U_Y(r_{ij}) = Z^2e^2[\exp(Ka)/(1+Ka)]^2 \exp(-Kr_{ij})/\varepsilon r_{ij} \tag{1}$$

CC-0. In Public Domain. Gurukul Kangri Collection, Haridwar

Digitized by Arya Samaj Foundation Chennai and eGangotri

where K is inverse screening length given by

$$K^2 = 4\pi e^2 \left(n_p Z + \sum_\beta n_\beta Z_\beta^2 \right) \Big/ \varepsilon k_B T. \tag{2}$$

The first term in (2) arises due to $n_p Z$ counter-ions coming from particles with concentration n_p and the second term is the contribution of the impurity ions of βth type with the concentration n_β and charge eZ_β. In all our calculations the impurities are considered as monovalent ($Z_\beta = \pm 1$), hence $n_i = \sum_\beta n_\beta$. ε is the dielectric constant of the medium and taken to be equal to 78·0 at room temperature $T(=298°\,\mathrm{K})$. A detailed discussion on the range of validity of this potential is given in the recent work of Robbins *et al* (1988).

2.2 *Sogami potential*

For the system considered above Sogami obtained an effective pair potential $U_s(r)$ given by (Sogami 1983; Sogami and Ise 1984)

$$U_S(r_{ij}) = Z^2 e^2 (\sinh Ka/Ka)^2 [A \exp(-Kr_{ij})/r_{ij} - B \exp(-Kr_{ij})]/\varepsilon \tag{3}$$

where $A = 1 + Ka \coth(Ka)$, $B = K/2$ and K is given by (2).

The attractive term leads to a secondary minimum in $U_s(r)$ whose position ($R_{\min}$)

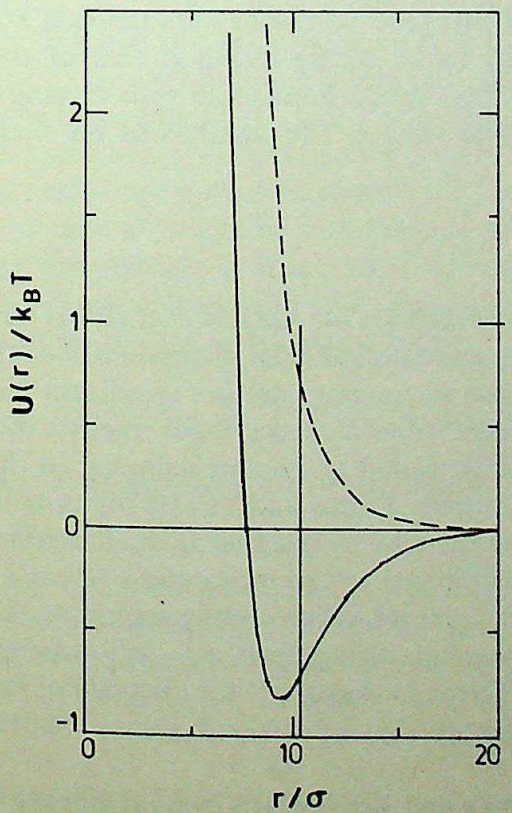

Figure 1. Pair potential $U(r)$ in units of $k_B T$ vs distance of separation r in units of σ. Continuous line is Sogami potential for $\sigma = 0{\cdot}109\,\mu$m, $n_p = 1{\cdot}33 \times 10^{12}\,\mathrm{cm}^{-3}$, $Z = 600$ with $n_i = 1{\cdot}75 \times 10^{15}\,\mathrm{cm}^{-3}$ and dotted line is Yukawa potential for $n_i = 2{\cdot}1 \times 10^{15}\,\mathrm{cm}^{-3}$ with n_p and Z same as above. The vertical line is at interparticle separation $2a_s = 10{\cdot}35\sigma$.

CC-0. In Public Domain. Gurukul Kangri Collection, Haridwar

Digitized by Arya Samaj Foundation Chennai and eGangotri

depends on n_p and n_i and is given by

$$R_{\min} = [C + 1 + \{(C+1)(C+3)\}^{1/2}]/K \tag{4}$$

where $C = A - 1$. Sogami potential has been derived from the Gibbs free energy which takes into account counterion-counterion and polyball-polyball interaction. The degrees of freedom of counterions are integrated out to give an effective pair potential $U_s(r)$. Figure 1 shows the $U_y(r)$ and $U_s(r)$ used in the calculation. Marked on figure 1 is the line at $r = 2a_s$. It can be noted that the interaction at $r = 2a_s$ is repulsive in one case and attractive in the other case.

3. Simulation details

Simulations at constant volume and constant temperature are performed for a colloidal system with particle density n_p. N particles are taken in a cubic cell with cube length L given by $L^3 = N/n_p$. The periodic boundary conditions are used to remove the surface effects and simulate an infinite system. The number of particles chosen in the simulation were $N = 128$ and 250. The results are same for both the values, consistent with the earlier observation that $N > 100$ does not change the results (Gaylor *et al* 1981). All the results presented in this paper correspond to $N = 250$. The potential is cut-off at $r = L/2$ at which $U(r = L/2) \leqslant 10^{-4}\, k_B T$, which is comparable to the cut-off value used in simulation of Lennard-Jones systems (Rahman 1964). The small value of $U(r)$ at the cut-off suggests that the Ewald summation is not required for computing the total energy. The initial configuration is that of the particles arranged on the body centered cubic(bcc) lattice. Simulation with starting configuration being random also gave the same results. The simulations are performed on Norsk Data 560CX computer.

3.1 *Brownian dynamics simulation*

Based on BD algorithm of Ermak and Yeh (1974), Gaylor *et al* (1981) have applied the BD computer simulation to dilute aqueous colloidal dispersions. For these dilute suspensions, many body hydrodynamic interactions are not significant (Gaylor *et al* 1981, van Megen *et al* 1985). The dynamics of each particle is governed by the Langevin equation in which the random force is related to viscous damping of the medium through the fluctuation dissipation theorem. Ermak and Yeh (1974) formalism allows one to obtain the new positions of the particles by integrating the Langevin equation over a time step Δt, which is large compared to the momentum relaxation time τ_R but is small compared to the time τ_e over which the configuration of the particles appreciably changes. The momentum relaxation time $\tau_R = m/f$, where m is the mass of particle and the friction coefficient $f = 6\pi\eta a$, η is the viscosity of the medium. For polystyrene particle of diameter $\sigma(=2a) = 0{\cdot}109$ μm and $\eta = 0{\cdot}01089$ Poise, $\tau_R = 6{\cdot}4 \times 10^{-10}$ s.

We have used the algorithm of Ermak and Yeh (1974) which provides the following equations to generate the particle trajectories and velocities

$$\mathbf{r}_i(t + \Delta t) = \mathbf{r}_i(t) + \mathbf{R}_i(\Delta t) + \mathbf{F}_i(t)\Delta t/\gamma \tag{5}$$

CC-0. In Public Domain. Gurukul Kangri Collection, Haridwar

Digitized by Arya Samaj Foundation Chennai and eGangotri

$$\mathbf{v}_i(t+\Delta t) = \mathbf{v}_i(t)\exp(-\Delta t/\tau_R) + \mathbf{V}_i + [\mathbf{F}_i(t+\Delta t) - \mathbf{F}_i(t)\exp(-\Delta t/\tau_R)]/\gamma \quad (6)$$

where $\mathbf{r}_i(t)$, $\mathbf{v}_i(t)$ are the position and velocity of the ith particle at time t respectively. The $\mathbf{R}_i(\Delta t)$ is the Gaussian random displacement representing the net effect of the collisions of the ith particle with other particles in the time interval Δt, and $\mathbf{V}_i$ is the Gaussian random velocity of the ith particle. $\mathbf{F}_i(t)$ is the direct force on the ith particle due to remaining particles in the system i.e.,

$$\mathbf{F}_i = -\sum_{j\neq i} \frac{\partial U(r_{ij})}{\partial r_{ij}} \frac{\mathbf{r}_{ij}}{r_{ij}}. \quad (7)$$

The random displacements $\mathbf{R}_i$ and the random velocities $\mathbf{V}_i$ are generated by employing central limit theorem. Here M random numbers having uniform distribution in the range 0 to 1 are selected and their sum S is calculated. This sum S is Gaussian distributed with mean $M/2$ and variance $M/12$ and the required Gaussian variate $\zeta(t)$ (here $\zeta = X$, Y or Z component of $\mathbf{R}_i$ or $\mathbf{V}_i$) with zero mean and variance α is obtained as

$$\zeta(t) = \sqrt{\alpha}\{(S/\sqrt{M/12}) - \sqrt{3/M}\}. \quad (8)$$

The variance for random displacement is $\alpha_R = 6D_0\Delta t$, where D_0 is the diffusion coefficient of the particle ($D_0 = k_BT/f$) and the variance in random velocity $\alpha_v = 3\ k_BT/m$.

As discussed above the time step chosen in BD algorithm should be such that $\tau_R \ll \Delta t \ll \tau_e$. For our system $\tau_R = 6{\cdot}4 \times 10^{-10}$ s. Since there is no unambiguous way of estimating τ_e, we tried time steps from $\Delta t = 10^{-7}$ to 10^{-3} s and monitored the total energy. It was found that for $\Delta t \leqslant 10^{-4}$ s the total energy is conserved with root mean squared deviation of $\sim 0{\cdot}7\%$ whereas for $\Delta t > 10^{-4}$ s the total energy is not conserved and showed wide excursions. Hence $\Delta t = 10^{-4}$ s has been chosen in our simulations. Using the value of D_0 it can be seen that the paticle on the average moves $\sim 4\%$ of the average interparticle distance $2a_s$ $(=2(3/4\pi n_p)^{1/3})$ in time Δt. After reaching equilibrium $g(r)$ was obtained (for $r = L/2$) using the standard methods (Rahman 1964). The structure factor $S(Q)$ is calculated using

$$S(Q) = 1 + 4\pi n_p \Delta r \sum_{l=1}^{l_{\max}} (g(l\Delta r) - 1) l\Delta r \sin(Ql\Delta r)/Q \quad (9)$$

for those values of wavevector Q which satisfy

$$Q = 2\pi(n_1, n_2, n_3)/L \quad (10)$$

where n_1, n_2, n_3 are integers and $l_{\max} = L/(2\Delta r)$. This constraint on Q is introduced by the finite size of the system. The same constraint limits the range of $g(r)$ to $r \leqslant L/2$ and can introduce spurious oscillations or distortions in the small Q region of the computed $S(Q)$ using (9).

4. Results and Discussion

The parameters entering the pair potentials, (1) for Yukawa and eq (3) for Sogami are σ, n_p, n_i and Z. The particle diameter σ is $0{\cdot}109$ μm, and the particle concentration

CC-0. In Public Domain. Gurukul Kangri Collection, Haridwar

Digitized by Arya Samaj Foundation Chennai and eGangotri

in the suspension can be determined accurately by weight method (Tata *et al* 1987) and was found to be $n_p = 1{\cdot}33 \times 10^{12}\,\mathrm{cm}^{-3}$ for which we have measured $S(Q)$ by angle resolved Rayleigh scattering (Tata *et al* 1987). The accurate determination of the quantities n_i and Z are experimentally difficult (Robbins *et al* 1988). The charge Z for the diameter 0·109 μm particle has been reported to be 600 ± 100 (Lindsay and Chaikin 1982) and hence $Z = 600$ is taken in all our calculations. The experimental $S(Q)$ was fitted to the calculated $S(Q)$ using RMSA for the Yukawa potential (Hansen and Hayter 1982; Härtl *et al* 1983) with n_i as the fitting parameter. The peak position and peak height of the first peak in $S(Q)$ are chosen as criteria for judging the best fit. The best fit of calculated $S(Q)$ to the experimental data was obtained for $n_i = 2{\cdot}1 \times 10^{15}\,\mathrm{cm}^{-3}$. The impurity ion concentration was estimated from the conductivity measurements and found to be $(1{\cdot}9 \pm 0{\cdot}4) \times 10^{15}\,\mathrm{cm}^{-3}$. It is interesting to note that the fitted value of n_i matches well with the measured one.

The same value of n_i in the Sogami potential (eq (3)) was used to compute $g(r)$ and $S(Q)$ by BD simulation. It was found that the calculated $S(Q)$ does not match well with the experiment. But a good agreement with the experiment was obtained for $n_i = 1{\cdot}75 \times 10^{15}\,\mathrm{cm}^{-3}$. A small difference in n_i (note this n_i value is also within the experimental accuracy) for Yukawa and Sogami potentials is not surprising since K enters both the potentials in slightly different ways. Hence the results will be presented for Sogami potential with $n_i = 1{\cdot}75 \times 10^{15}\,\mathrm{cm}^{-3}$.

In BD simulation the total potential energy is monitored to find out whether equilibrium has been reached or not. Typically 700 time steps have taken to reach the equilibrium. The relative error in the energy after reaching equilibrium is 0·85%. In addition to energy the virial pressure and velocity distribution of particles are also monitored as a check for equilibrium state. After 700 time steps the virial pressure remained constant with relative error being 0·53% and velocity distribution remained Maxwellian. The interval $\Delta r = 0{\cdot}16$ was used to calculate $g(r)$ and particle coordinates generated from 350 time steps were used for averaging. The $g(r)$s thus obtained for Sogami (continuous line) as well as Yukawa (dotted line) pair potentials are shown in figure 2(a). Since Δr chosen is very small the $g(r)$ obtained looks almost continuous curve. Figure 2(b) presents $S(Q)$s calculated using (9). Also shown are the experimental data with error bars. One can see from figure 2(b) that the calculated $S(Q)$ for Yukawa potential (dotted line) matches with the experiment. Also note that the calculated $S(Q)$ for Sogami potential (continuous line) also agrees equally well with the experimental $S(Q)$. To compare the equilibrium BD results with other simulation techniques conventional Monte-carlo simulations (based on Metropolis method, see for example Binder 1979; Hansen and McDonald 1986) were also carried out for same parameters of the suspension. The step size of 0·56 was chosen such that trial rejection rate was $45 \pm 5\%$. The calculations are started with initial configuration being the particles occupying a bcc lattice and first 100,000 configurations are discarded to allow the system to equilibrate. The total potential energy and virial pressure of the system is monitored to find out whether equilibrium has been reached or not. After reaching equilibrium typically 150,000 configurations are generated to determine $g(r)$. The relative error in energy as well as in virial pressure are same as that in BD simulation. The errors of this magnitude are normal for a liquid-like ordered suspension. Figure 3 shows calculated $S(Q)$s for the Sogami potential using MC and BD simulations. It is not surprising to find that both the calculated $S(Q)$s agree. At this stage one can compare the total computation time needed to calculate

CC-0. In Public Domain. Gurukul Kangri Collection, Haridwar

Digitized by Arya Samaj Foundation Chennai and eGangotri

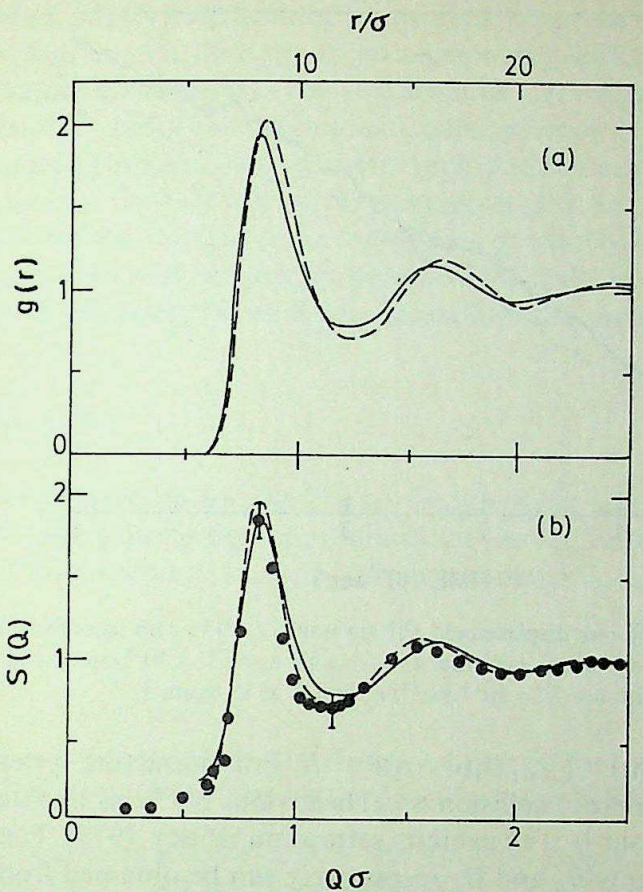

Figure 2. (a) Pair distribution functions $g(r)$ vs r (in units of σ) calculated from BD simulation for Sogami potential (——) with $n_i = 1{\cdot}75 \times 10^{15}\,\mathrm{cm}^{-3}$ and Yukawa potential (– – –) with $n_i = 2{\cdot}1 \times 10^{15}\,\mathrm{cm}^{-3}$. n_p and Z as mentioned in figure 1. (b) Structure factors $S(Q)$ vs Q (in units of σ^{-1}) calculated using eq. (9) and $g(r)$s of figure 2(a) for Sogami (——) and Yukawa (– – –) potentials. The parameters are same as for figure 2a. Experimental $S(Q)$ (·····) is also shown for comparison.

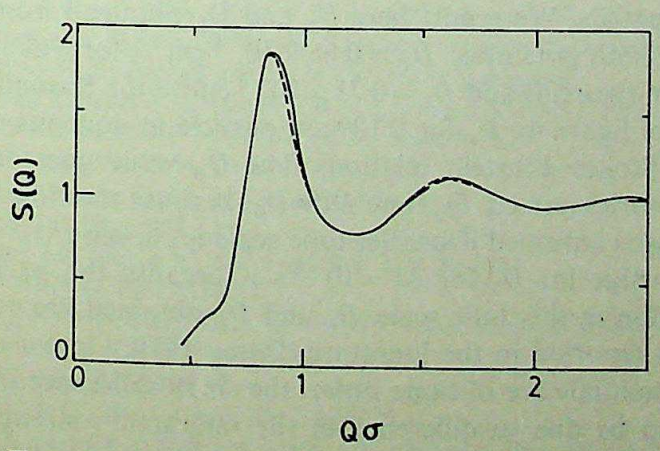

Figure 3. Comparison of structure factors $S(Q)$ vs Q (in units of σ^{-1}) calculated from MC (——) and BD (– – –) for Sogami potentials with $n_i = 1{\cdot}75 \times 10^{15}\,\mathrm{cm}^{-3}$, n_p and Z as in figure 1.

$S(Q)$. The CPU time for MC was 5 h and for BD was 3 h, on Norsk Data System, which clearly demonstrates that BD simulation saves a lot of computation time.

The dynamic light scattering experiments give a direct estimate of mean square

CC-0. In Public Domain. Gurukul Kangri Collection, Haridwar

Digitized by Arya Samaj Foundation Chennai and eGangotri

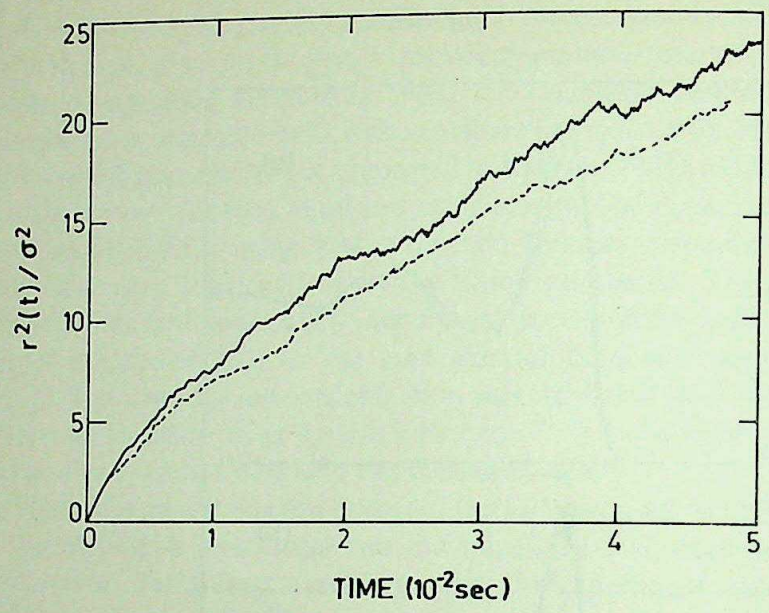

Figure 4. Mean square displacement $r^2(t)$ (in units of σ^2) vs t (in seconds) calculated from BD simulation for Sogami potential (——) with $n_i = 1{\cdot}75 \times 10^{15}\,\mathrm{cm}^{-3}$ and for Yukawa potential (– – –) with $n_i = 2{\cdot}1 \times 10^{15}\,\mathrm{cm}^{-3}$, n_p and Z as in figure 1.

displacement defined as $r^2(t) = \sum_{i=1}^{N} (r_i(t) - r_i(0))^2/N$. For interacting system the short time ($t < \tau_c$, where τ_c is the mean collision time) behaviour of $r^2(t)$ is like free diffusion and the long time behaviour ($t > \tau_c$) exhibits saturation (Pusey 1979). The short and long time diffusion constants D_S and D_L respectively can be obtained from the slope of $r^2(t)$ vs t plot in the short and long times (Pusey 1978). Using 500 time steps of BD simulation data $r^2(t)$ is calculated for both the potentials and is shown in figure 4. This behaviour of $r^2(t)$ is expected for a liquid-like ordered suspension (Gaylor *et al* (1981)). One can notice from figure 4 that $r^2(t)$ calculated for a colloidal system interacting with Sogami potential also agrees well qualitatively and the difference in long time behaviour of $r^2(t)$ is due to the difference in the magnitude of interaction strengths of the two potentials. We report here D_S and D_L obtained from figure 4. $D_S = 2{\cdot}4 \times 10^{-8}\,\mathrm{cm}^2/\mathrm{s}$ for both potentials. $D_L = 0{\cdot}66 \times 10^{-8}\,\mathrm{cm}^2/\mathrm{s}$ for Yukawa potential (from dashed curve of figure 4) and $D_L = 0{\cdot}71 \times 10^{-8}\,\mathrm{cm}^2/\mathrm{s}$ for Sogami potential (from continuous curve of figure 4). D_0 for $0{\cdot}109\,\mu\mathrm{m}$ particle in aqueous medium is $3{\cdot}68 \times 10^{-8}\,\mathrm{cm}^2/\mathrm{s}$ (from Stokes–Einstein relation). The D_0 value goes as input in generating particle trajectories (see eq. 5). Here $D_S \neq D_0$, because the time scale used here is 10^{-4} s. However we confirmed if smaller time scale is chosen ($\Delta t = 10^{-6}$ s) we obtain $D_S \simeq D_0$. Lower value for D_S for $\Delta t = 10^{-4}$ s is because the particles start experiencing the interaction in this time scale. D_S and D_L obtained are comparable with macroscopic values reported in the literature (Pusey 1978; Gaylor *et al* 1981). D_L value for both the potentials are of same order, the small difference in D_L value for both potentials could be due to difference in the interaction strengths of the potentials. Careful dynamic light scattering measurements and accurate determination of n_i can perhaps be used to find out which potential fits better to the experiment.

5. Conclusions

We have shown that the static structure factor $S(Q)$ obtained based on the Sogami

CC-0. In Public Domain. Gurukul Kangri Collection, Haridwar

Digitized by Arya Samaj Foundation Chennai and eGangotri

pair potential, which has a secondary minimum, agrees well with the experimental data. It is also shown that the mean square displacement calculated for Sogami potential agrees qualitatively. The two features viz. the earlier mentioned reentrant phase transition and above mentioned homogeneous liquid like ordering can be understood using Sogami potential. Although Yukawa can explain the second feature it cannot explain the first feature. This suggests that Sogami potential is perhaps a better choice for the charged colloidal systems. It will be interesting to examine some more dynamical as well as static properties of the colloids with Sogami potential and compare with the experiments. Such calculations are underway.

Acknowledgements

We thank G Amarendra and the Theory Group of our laboratory for their invaluable help in developing the computer programs for the MC and BD methods respectively. Thanks are also due to A K Arora for helpful discussions.

References

Arora A K, Tata B V R, Sood A K and Kesavamoorthy R 1988 Phys. Rev. Lett. **60** 2438
Binder K 1979 in *Monte Carlo Methods in Statistical Physics* (Ed) K Binder (New York: Springer-Verlag) p. 1
Castillo C A, Rajagopalan R and Hirtzel C S 1984 *Rev. Chem. Engg.* **2** 237
Ermak D L and Yeh Y 1974 *Chem. Phys. Lett.* **24** 243
Gaylor K, Snook I and van Megen W 1981 *J. Chem. Phys.* **75** 1682
Hansen J P and Hayter J B 1982 *Mol. Phys.* **46** 651
Hansen J P and McDonald I R 1986 *Theory of Simple Liquids*, 2nd ed. (London: Academic)
Hartl W, Versmold H and Witting U 1983 *Mol. Phys.* **50** 815
Ise N 1986 *Angew. Chem. Int. Ed. Engl* **25** 323
Ise N, Matsuoka H, Ito K, Yoshida H and Yamanaka J 1988a in *Symposium on 'Ordered particles and polymer colloids'* Fall meeting of the American Chemical Society, Los Angeles, Sept. 1988
Ise N, Matsuoka H and Ito K 1988b in *Proc. of XIX Yamada Conference on 'Ordering and Organisation in Ionic Solutions'* (Kyoto 1987) (Eds) N Ise and I Sogami (Singapore: World Scientific)
Ito K, Okumura H, Yoshida H and Ise N 1989 (to be published)
Kesavamoorthy R, Sood A K, Tata B V R and Arora A K 1988 *J. Phys.* **C21** 4737
Lindsay H M and Chaikin P M 1982 *J. Chem. Phys.* **76** 3774
Overbeek J T G 1987 *J. Chem. Phys.* **87** 4406
Pusey P N 1979 *Philos. Trans. R. Soc.* **A293** 429
Pusey P N 1978 *J. Phys.* **A11** 119
Pusey P N and van Megen W 1987 *Phys. Rev. Lett.* **59** 2083
Rahman A 1964 *Phys. Rev.* **A136** 405
Robbins M O, Kremer K and Grest G S 1988 *J. Chem. Phys.* **88** 3286
Schaefer D W 1977 *J. Chem. Phys.* **66** 3980
Sogami I 1983 *Phys. Lett.* **A96** 199
Sogami I and Ise N 1984 *J. Chem. Phys.* **81** 6320
Tata B V R, Kesavamoorthy R and Arora A K 1986 *Mol. Phys.* **57** 369
Tata B V R, Kesavamoorthy R and Sood A K 1987 *Mol. Phys.* **61** 943
van Megen W and Snook I 1977 *J. Chem. Phys.* **66** 813
van Megen W, Ottewill R H, Owens S M and Pusey P N 1985 *J. Chem. Phys.* **82** 508
Verwey E J W and Overbeek J G 1948 *Theory of the Stability of Lyophobic Colloids* (Amsterdam: Elsevier)
Williams R and Crandall S 1974 *Phys. Lett.* **A97** 289

CC-0. In Public Domain. Gurukul Kangri Collection, Haridwar

Digitized by Arya Samaj Foundation Chennai and eGangotri

CC-0. In Public Domain. Gurukul Kangri Collection, Haridwar

Digitized by Arya Samaj Foundation Chennai and eGangotri

Pramāṇa – J. Phys., Vol. 34, No. 1, January 1990, pp. 33–49. © Printed in India.

Positron annihilation in copper

V SUNDARARAJAN and D G KANHERE
Department of Physics, University of Poona, Pune 411 007, India

MS received 16 June 1989

Abstract. Electron momentum distribution in copper is studied through the angular correlation of positron annihilation radiation, by employing self-consistent linear combination of Gaussian orbitals band structure method. The two-photon momentum density is presented and analysed through three dimensional plots and angular momentum decomposed contributions. Calculation of two-dimensional angular correlation has been carried out in the independent particle approximation. The results for the analysis using Lock, Crisp and West theorem and the reciprocal form factors are also presented. The present theoretical results are compared with the experimental ones wherever possible, and the agreement in general, is good.

Keywords. Positron annihilation; angular correlation; copper.

PACS Nos 71·25; 78·70

1. Introduction

In recent years two experimental techniques namely, the measurement of Compton profiles (CP) and angular correlations of positron annihilation radiation (ACPAR) have emerged as powerful tools to study the ground state electronic structure of solids (Williams 1977; Brandt and Dupasquier 1983). Both the techniques probe electronic structure in momentum space and yield complementary information about electron momentum density (EMD). While CP which is related directly to EMD, serves as a useful technique to investigate the nature of the electron wavefunctions (Cooper 1985), the ACPAR measurements, especially with modern high resolution 2-dimensional (2D) machines (Berko and Mader 1975; West *et al* 1981 and Manuel 1983), yield a rich data about Fermi surface (FS) topology and are sensitive to conduction electron states as seen by positron (Berko 1983). Thus a careful comparison of theoretical calculations and the experimental data for both the techniques can provide much insight into the nature of electron states, electron-electron correlations, electron-positron correlations as well as about FS features. This has been demonstrated by recent works on Cu (Bauer and Schneider 1983, 1984a, b, 1985 and Pattison *et al* 1982) and Ni (Rollason *et al* 1987 and Sundararajan *et al* 1988) for CP and on a number of transition metals for ACPAR (Singh and Singru 1982, 1983; Genoud *et al* 1988; Singh *et al* 1986 and Matsumoto and Wakoh 1988).

The transition metals have attracted considerable interest due to the localized nature of the *d*-electrons, high degree of *sp-d* hybridization and complicated FS topology (Mijnarends 1983). The density functional (DF) theory with its impressive achievements in explaining ground state properties provides a natural and computationally tractable framework for CP and ACPAR calculations. Let us recall

CC-0. In Public Domain. Gurukul Kangri Collection, Haridwar

Digitized by Arya Samaj Foundation Chennai and eGangotri

that EMD is related, via Fourier transform, to the full two-particle density matrix, while the DF guarantees its diagonal elements only i.e., the charge density. Indeed the work of Bauer and Schneider (1984a, 1985) on Cu and that of Rollason *et al* (1987) on Ni have demonstrated that a careful comparison between high accuracy experimental CP and DF calculations reveals the inadequacy of the local density approximation (LDA).

The sensitivity of these experimental techniques, especially the positron annihilation technique, makes it mandatory to employ an accurate band structure method for theoretical calculations and over the years a number of band structure methods like APW (Loucks 1966), KKR (Kaiser *et al* 1986), LMTO (Singh and Jarlborg 1985) have been used. Almost all theoretical calculations for ACPAR are performed within the independent particle approximation (IPA). Such calculations missout the electron-positron correlations. To get a clear picture of EMD it is desirable to calculate the electronic structure, and related properties in momentum space, both for ACPAR and CP cases by using the same theoretical method and same electron wavefunction. The present investigation aims at calculating these properties by employing *ab initio*, all electron, self-consistent, linear combination of Gaussian orbitals (LCGO) method developed by Callaway and co-workers (Wang and Callaway 1978). We have chosen the LCGO method because of several advantages that it offers. Firstly, apart from being all electron and self-consistent, there are no shape dependent approximations e.g. Muffin-tin type. Secondly, the Gaussian nature of the basis function allows analytic evaluation of the Fourier transforms enabling us to obtain momentum density for large momentum values without loss of accuracy.

It has been realized that the comparison between experiment and theory can be fruitfully carried out by comparing not only the profiles and their anisotropies but also via Fourier transformed profiles called reciprocal form factors (Bauer and Schneider 1984a, 1985; Pattison *et al* 1982; Schulke 1977; Pattison and Williams 1976 and Singh *et al* 1985). It has a number of advantages: (1) This function emphasizes the band nature of the electrons because, the core contribution becomes negligible after about 3 a.u. (2) Any deviation between the theoretical and experimental value at $z = R$, the lattice translation vector, reflects upon the differences between the occupancy functions for the interacting and non-interacting electrons. (3) These functions are related to the off-diagonal elements of the two-particle density matrix and hence, should offer a test for density functional theory. (4) Lastly, for a metal like copper, comparison of the zero crossings of the B functions with that of the free electron case would indicate the influence of the anisotropic FS and d-wavefunctions and deviation from free electron-like behaviour.

In ACPAR the folding procedure introduced by Lock, Crisp and West (Lock *et al* 1973 and Lock and West 1975) and its extension to 2D ACPAR (Berko 1979) are turning out to be very powerful.

In the light of these developments, we have investigated the following properties: (a) TPMD, ACPAR and their anisotropies; (b) 2D ACPAR and LCW analysis; (c) Reciprocal form factors.

We have also calculated the EMD and CP using LCGO wavefunctions. The calculated profiles agree very well with CPs reported by Bagayoko *et al* (1980). Our work differs only in the lattice constant. We have used the lattice constant of 6·822 a.u. Pattison *et al* (1982) and Bauer and Schneider (1984a, b, 1985) have reported a detailed investigation of the CP for copper. Their work gave a definitive indication of

CC-0. In Public Domain. Gurukul Kangri Collection, Haridwar

Digitized by Arya Samaj Foundation Chennai and eGangotri

the inadequacy of the LDA and also brought out the need for an accurate theoretical calculation of EMD and CP. The recent experimental developments in CP and the status of the theory have been reviewed by Cooper (1985). In the present work the emphasis is on the application of LCGO method to positron annihilation and only the differences between EMD and TPMD are pointed out wherever appropriate.

The one-dimensional (1D) ACPAR has been reviewed by Mijnarends (1979). Cushner *et al* (1970) have reported their 1D ACPAR measurements along with their model calculation. Berko (1983) has reviewed the measurements of 2D ACPAR in copper. Recently, Matsumoto and Wakoh (1988) have compared their theoretical 2D ACPAR results with the experimental work of Haghgooie *et al* (1978) and Berko *et al* (1977). They have included electron-positron correlation effects by state dependent and character dependent enhancement factors. The present report is the first one to apply LCGO method for positron wavefunction and ACPAR calculations (Sundararajan *et al* 1988). It is hoped that this work would provide accurate profiles for meaningful quantitative comparison.

The organization of the paper is as follows. In §2 a brief outline of the LCGO formulation alongwith the relevant numerical details are given and §3 presents our results and §4 gives the summary.

2. Theory

In this section we give a brief outline of the formulation used, alongwith the definitions of the relevent quantities calculated for CP and ACPAR. The electron wavefunctions and energy bands have been calculated by self-consistent LCGO method (Wang and Callaway 1978). In this approach the Bloch functions for band index n and state $\mathbf{k}$ at position $\mathbf{r}$ are expanded as linear combination of Gaussian orbitals.

Thus,

$$\psi_n(\mathbf{k},\mathbf{r}) = \sum_i C_{ni}(\mathbf{k})\phi_i(\mathbf{k},\mathbf{r}) \tag{1}$$

where

$$\phi_i(\mathbf{k},\mathbf{r}) = (N)^{-1/2}\sum_\mu \exp(i\mathbf{k}\cdot\mathbf{R}_\mu)u_i(\mathbf{r}-\mathbf{R}), \tag{2}$$

u_i's are the individual Gaussian orbitals, $\mathbf{R}_\mu$ is the lattice vector, and N is the number of cells in the crystal volume. The expansion coefficients $C_{ni}(\mathbf{k})$ and energy eigenvalues are calculated by diagonalizing the density functional hamiltonian in the above mentioned Gaussian basis set. We have obtained self-consistency on 89 $\mathbf{k}$ points in the irreducible part of the Brillouin zone (BZ) using von Barth-Hedin exchange correlation potential as parametrized by Rajagopal *et al* (1980). The final band structure is calculated at 505 k points in the irreducible wedge of the BZ.

Positron wavefunction is also calculated under the framework of LCGO. It is written as

$$\psi_+(\mathbf{r}) = \sum_j C_j(\mathbf{k}_+ = 0)\phi_j(\mathbf{r}). \tag{3}$$

Since it gets annihilated in its ground state with $\mathbf{k}_+ = 0$ we have calculated the positron wavefunction, using the self-consistent electron potential by subtracting the exchange correlation part and changing its sign. The positron basis set consisted of 7*s*

CC-0. In Public Domain. Gurukul Kangri Collection, Haridwar

Digitized by Arya Samaj Foundation Chennai and eGangotri

functions. Our positron wavefunction (Sundararajan *et al* 1988) compares favourably with the previous calculation by Bross and Stohr (1974), using modified augmented plane wave method but, has a slightly higher value around 1 a.u. as compared to the wavefunction obtained by Mijnarends (1983) using symmetrized plane wave method. However, $\psi_+(r)$ calculated using the same potential under plane wave approximation is found to differ very little from the LCGO wave function.

Using electron and positron wavefunctions thus obtained, the TPMD and ACPAR can be calculated as

$$\rho^{2\gamma}(\mathbf{p}) = \sum_{n\mathbf{k}}^{\text{occ}} |F_{\mathbf{k}}^{n}(\mathbf{p})|^2 f(\mathbf{k}, n)\delta(\mathbf{k} - \mathbf{p} + \mathbf{G}), \tag{4}$$

$$N_{\hat{k}}(q) = \text{const} \times \int \mathrm{d}\mathbf{p}\rho^{2\gamma}(\mathbf{p})\delta(q - \mathbf{p}\cdot\hat{k}) \tag{5}$$

where $f(\mathbf{k}, n)$ is the Fermi-Dirac distribution function and $F_{\mathbf{k}}^{n}(\mathbf{p})$ is the electron-positron overlap integral,

$$F_{\mathbf{k}}^{n}(\mathbf{p}) = \int \exp(-i\mathbf{p}\cdot\mathbf{r})\psi_+(\mathbf{r})\psi_n(\mathbf{k}, \mathbf{r}). \tag{6}$$

The TPMD is calculated up to 4 a.u. by considering 113 G vectors. This generates about 42237 points in 1/48th part of the **p** space. The ACPAR values are calculated along the three symmetry directions.

It is instructive to decompose the TPMD into its *s*-, *p*- and *d*-components. Such a decomposition would provide more insight into the relative importance of the angular momentum of the electronic states. We can write the *l*-decomposed TPMD as

$$\rho_l^{2\gamma}(\mathbf{p}) = \sum_{n\mathbf{k}}^{\text{occ}} \left| \sum_{\mathbf{G}''} \sum_{i}^{n_l} \sum_{j} C_{ni}(\mathbf{k}) C_j(0) \chi_i(\mathbf{k} + \mathbf{G} - \mathbf{G}'') \chi_j(\mathbf{G}'') \right|^2 \delta(\mathbf{k} - \mathbf{p} + \mathbf{G}) \tag{7}$$

where $\mathbf{G} = \mathbf{G}' + \mathbf{G}''$. $\mathbf{G}'$ is the reciprocal lattice vector for the electron and $\mathbf{G}''$ for that of the positron. The above equation gives the pure *l*-component of TPMD wherein n_l is the number of *l*-type orbitals used. We used 13*s*, 10*p*, 5*d* and 1*f* functions as the basis set. χ_i and χ_j are the Fourier transforms of the electron and positron basis functions respectively and written as (Rath *et al* 1973)

$$\chi_i(p) = \Omega^{-1/2} \int \exp(-i\mathbf{p}\cdot\mathbf{r}) u_i(\mathbf{r})\, \mathrm{d}\mathbf{r}. \tag{8}$$

Ω is the unit cell volume. The *l*-decomposed TPMD is calculated and presented along the $\langle 100 \rangle$, $\langle 110 \rangle$ and $\langle 111 \rangle$ directions along with the total.

We now turn to the calculations of 2D ACPAR expressed as

$$N(p_y, p_z) = \int \rho^{2\gamma}(\mathbf{p})\, \mathrm{d}p_x \tag{9}$$

where p_x is the direction of integration. The above quantity was calculated for three integration directions. The 2D ACPAR curves $N(p_y, p_z)$ thus calculated have been remapped from the *p* space to the *k* space using the LCW folding procedure governed

CC-0. In Public Domain. Gurukul Kangri Collection, Haridwar

Digitized by Arya Samaj Foundation Chennai and eGangotri

by the relation,

$$\tilde{N}(k_y, k_z) = \sum_{\mathbf{H}} N(p_y + H_y, p_z + H_z) \tag{10}$$

where H_y and H_z are the components of the full reciprocal lattice vectors on the (p_y, p_z) plane. The $\tilde{N}(k_y, k_z)$ distributions so obtained can be compared with the experimental results. Recently the validity of the LCW theorem for the analysis of ACPAR data has been examined by Singh and Singru (1984), Rabou and Mijnarends (1984) and Kaiser *et al* (1986, 1987). The work of Kaiser *et al* (1986) in particular, has shown that a realistic application of the LCW theorem to ACPAR data should be carried out in terms of the Bloch **k**-space density $\rho^{2\gamma}(\mathbf{k})$ which, in turn, requires a proper band structure calculation of $\rho^{2\gamma}(\mathbf{p})$.

Yet another useful way to compare theory and experiment is via Fourier transform of the momentum density i.e., $B(\mathbf{r})$ functions, which are also called the reciprocal form factors (Shulke 1977; Pattison and Williams 1976),

$$B(\mathbf{r}) = (2\pi)^{-3/2} \int \exp(-i\mathbf{p}\cdot\mathbf{r})\rho(\mathbf{p})\,\mathrm{d}\mathbf{p}. \tag{11}$$

Where $\rho(\mathbf{p})$ is the EMD. It has been shown that

$$B_{\hat{k}}(0,0,z) = (2\pi)^{-1/2} \int \exp(-izq) J_{\hat{k}}(q)\,\mathrm{d}q \tag{12}$$

in which, $J_{\hat{k}}(q)$ is the CP along the direction $\hat{k}$. Similarly, for $N_{\hat{k}}(q)$,

$$B^{2\gamma}_{\hat{k}}(0,0,z) = (2\pi)^{-1/2} \int \exp(izq) N_{\hat{k}}(q)\,\mathrm{d}q. \tag{13}$$

In the rest of the paper $B(0,0,z)$ and $B^{2\gamma}(0,0,z)$ would be denoted respectively as $B^{CP}(z)$ and $B^{2\gamma}(z)$ or as B^{CP} and $B^{2\gamma}$, depending on the context.

Equations (1) to (13) form the basis of our calculations and the results obtained are presented in the next section.

3. Results and discussion

As mentioned in the introduction, the self-consistent electron wavefunctions and the positron wavefunction calculated in IPA have been used to investigate a number of properties relevant for CP and ACPAR studies. Specifically, we present our results for TPMD, 1D ACPAR, 2D ACPAR, $B^{2\gamma}$ and $B^{2\gamma}$ functions. Since a detailed analysis of the differences between experimental and theoretical CP has been presented by Bauer and Schneider, our emphasis in this report will be on TPMD and 1D and 2D ACPAR.

3.1 *TPMD*

Conventionally, the TPMD is presented and discussed in terms of band by band contributions along three symmetry directions. Our calculations for EMD as well as TPMD depict the familiar nature along three directions showing the drops or

CC-0. In Public Domain. Gurukul Kangri Collection, Haridwar

Digitized by Arya Samaj Foundation Chennai and eGangotri

discontinuities at Fermi momentum with corresponding Umklapp images (Mijnarends 1973; Kanhere and Singru 1977 and Mijnarends and Singru 1979). Bross (1982) has shown the momentum density as a function of p_x in the plane $p_z = 0{\cdot}05(2\pi/a)$ for different values of p_y. Such a graph gives information on the discontinuities and the anisotropic nature of the momentum density. However, to gain more insight into the nature of TPMD, it is instructive to plot its sections by symmetry planes as 3*D* perspective plots. Figures 1(a) and 1(b) show such 3*D* plots of the section of TPMD by (100) and (110) planes respectively. The corresponding zone structure is also shown with the same scale and with the same perspective view. The anisotropic nature of the momentum density is immediately clear by examination of these figures. The differences in the Umklapp contribution in these planes are also apparent. For example, in (100) the first drops in figure 1(a) clearly depict the FS structure in the first BZ. But its Umklapp images in the 2nd zone are dominant only in ⟨100⟩ direction. The effect of neck can be clearly seen in figure 1(b) i.e., in the section by (110) plane. It is interesting to note that only near ⟨111⟩ line the drops are absent including the discontinuities due to Umklapp process. Amongst all the three sections the higher zone effects are more prominent in (110) plane and least in (111) plane (not shown). A comparison of EMD plots (not shown) with TPMD plots shows that TPMD has very similar features as that of EMD. However, the first zone drops are much sharper and the Umklapp contribution is less prominent in TPMD. This is to be expected because, the different angular momentum components of the electron wavefunctions viz. *s*, *p*, *d* are spanned differently by positron.

This aspect can be brought out more clearly by making angular momentum decomposition of EMD and TPMD (eq. (7)). Such a decomposition of TPMD is shown in figures 2(a)–2(c) for the three symmetry directions. In each of these figures the total TPMD is shown by unlabelled line while *s*-, *p*- and *d*-components by labelled lines. It may be mentioned that the *s*-, *p*- and *d*-contributions will not add up to the total TPMD, since the total TPMD contains the hybridization terms also. We can somewhat quantify the relative contributions by the ratio of the weighted area under each component to the total area. Table 1 presents these ratios for both EMD and TPMD. A comparison of the *s*-, *p*- and *d*-contributions for the three directions indicates that the *d*-contribution is the least along ⟨111⟩ direction. This is reflected in the high momentum components along ⟨100⟩ and ⟨110⟩ directions. A comparison of EMD and TPMD through the figures in table 1 shows that the relative contribution from *d*-component reduced for the case of positron in all the three directions as compared to EMD. In both the cases there is a relatively high *p*-component along ⟨111⟩ direction indicating dominant *p*-character of the wavefunctions especially near the neck. It may be pointed out that the width of the *d*-band is smallest for copper and it lies well below the Fermi level, while for other 3*d* metals the Fermi level lies in the midst of the *d*-band complex (Kanhere and Singru 1977). The angular momentum decomposition analysis along the lines presented here would be fruitful for the systematic understanding of the *d*-band contribution when applied to other 3*d*-metals.

3.2 *ACPAR and LCW theorem*

The present work is the first in applying the LCGO method to positron annihilation studies. A preliminary report of the 1D ACPAR and its anisotropies has been presented elsewhere (Sundararajan *et al* 1988). Comparison of the theoretical

CC-0. In Public Domain. Gurukul Kangri Collection, Haridwar

Digitized by Arya Samaj Foundation Chennai and eGangotri

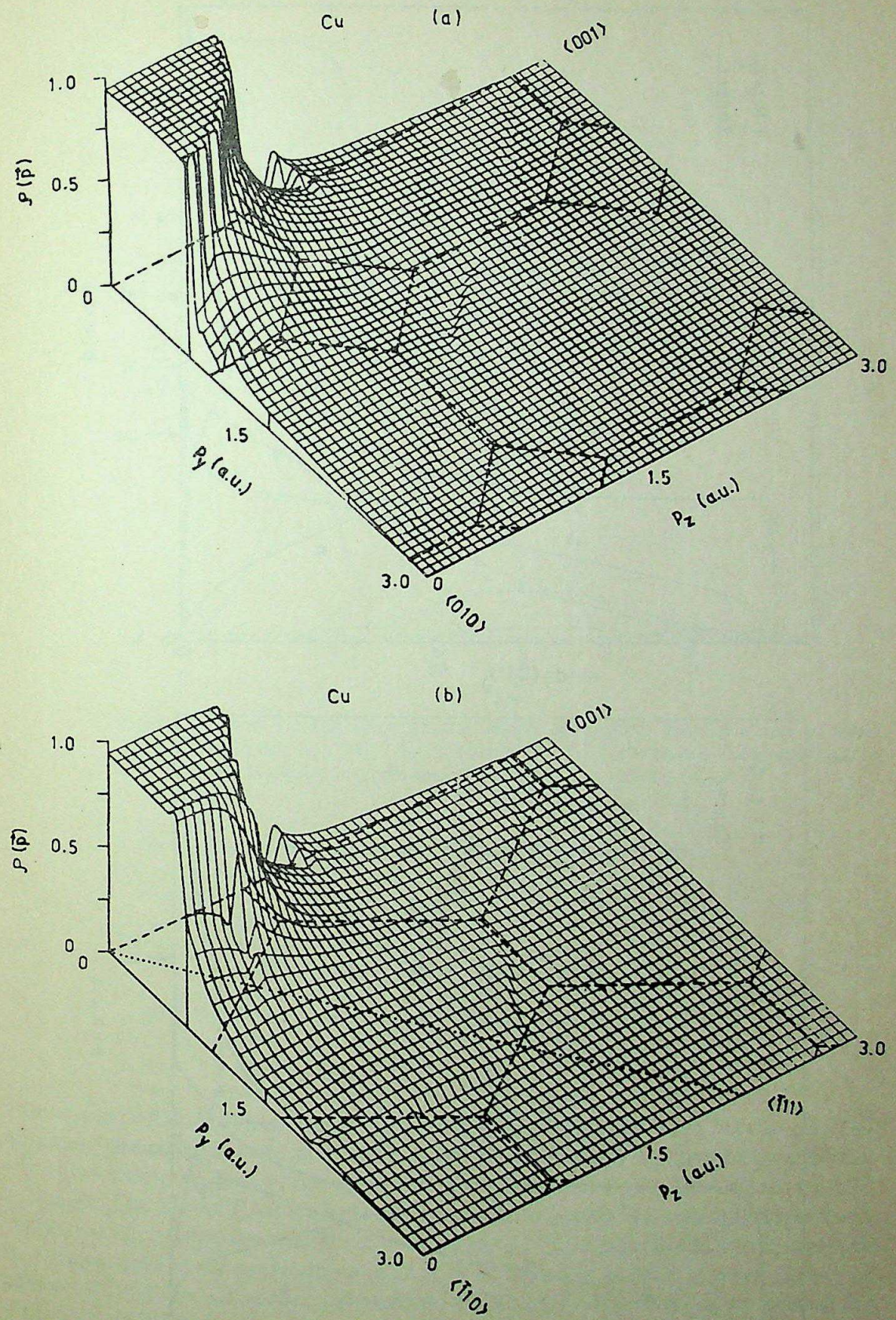

Figure 1. Sections of band TPMD for copper by the planes (**a**)(100) and (**b**)(110). The corresponding zone structure is also displayed. Dotted line in (b) shows the Λ line in the (110) plane.

CC-0. In Public Domain. Gurukul Kangri Collection, Haridwar

Digitized by Arya Samaj Foundation Chennai and eGangotri

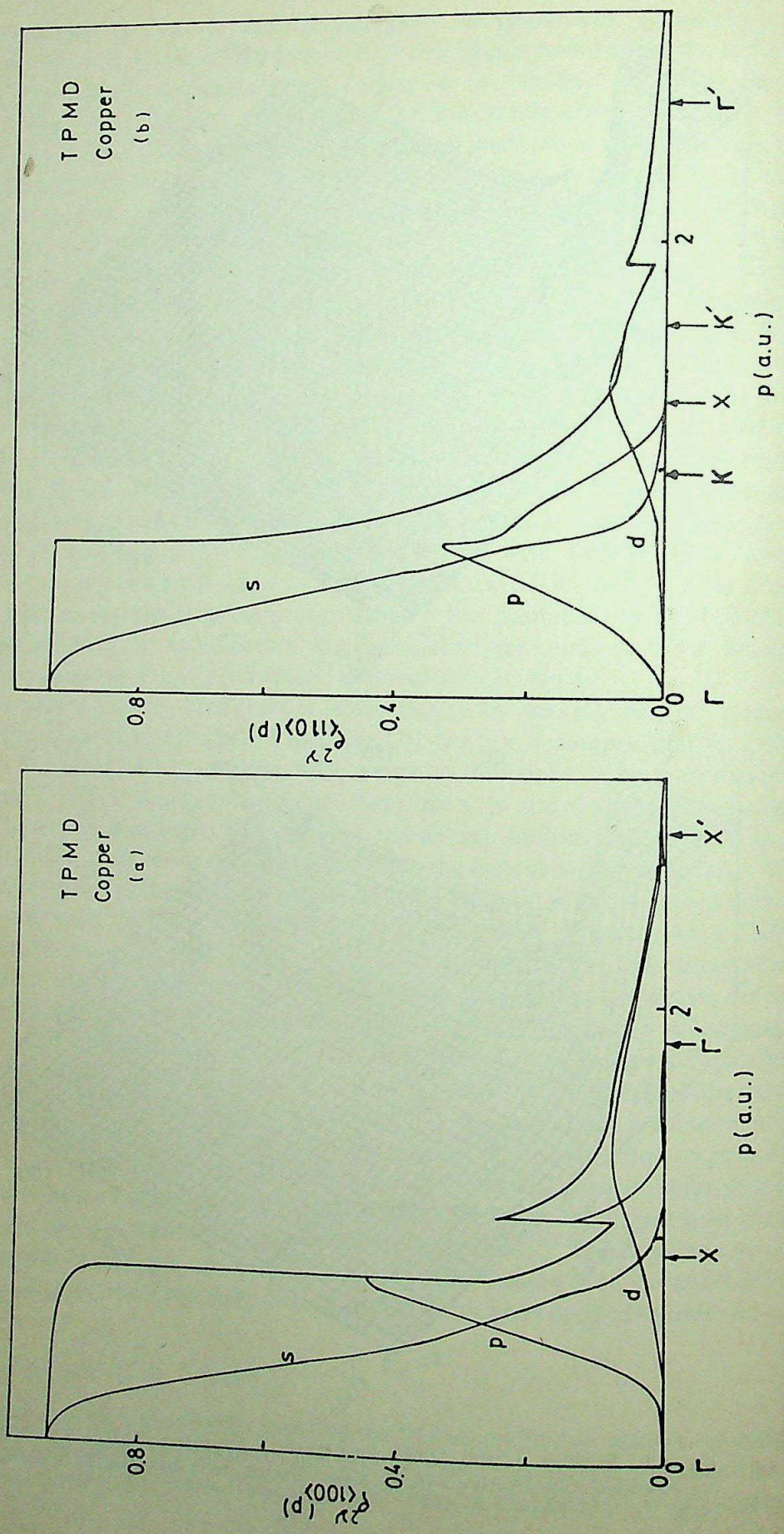

CC-0. In Public Domain. Gurukul Kangri Collection, Haridwar

Digitized by Arya Samaj Foundation Chennai and eGangotri

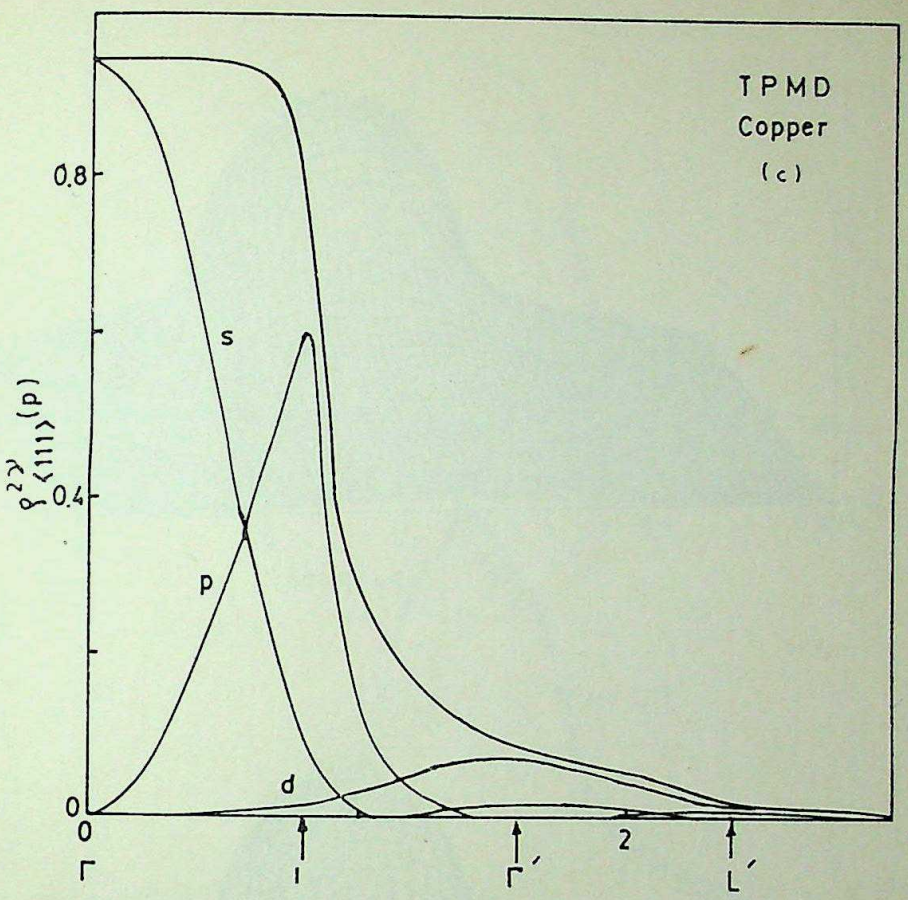

Figure 2. Band TPMD alongwith the angular momentum decompositions on three symmetry directions (**a**) ⟨100⟩, (**b**) ⟨110⟩ and (**c**) ⟨111⟩. Unlabelled line corresponds to total EMD. Individual *s*, *p*, *d* contributions are shown by labelled lines.

Table 1. Ratio of the weighted areas of pure *s*-, *p*-, *d*-contributions to the total momentum density.

Direction	*s*		*p*		*d*	
	EMD	TPMD	EMD	TPMD	EMD	TPMD
⟨100⟩	0·056	0·137	0·052	0·131	0·833	0·559
⟨110⟩	0·053	0·135	0·059	0·167	0·850	0·554
⟨111⟩	0·065	0·117	0·104	0·284	0·789	0·434

anisotropies with the experimental (Cushner *et al* 1970) ones were very good. The remaining discrepancies are attributed to the electron-positron correlation effects.

In this section we discuss the 2D ACPAR results obtained by the LCGO method for copper. The 2D ACPAR surfaces are presented in figures 3(a) and 3(b) respectively for the two integration directions viz. ⟨100⟩ and ⟨111⟩. In general the agreement with the experimental surfaces (Haghgooie *et al* 1978; Berko *et al* 1977) is good. It may be mentioned that, in an earlier calculation of 2D ACPAR using APW method by Wakoh *et al* (1979), for the case of ⟨100⟩ two small horns due to neck in the FS are prominently seen. In the present case they are less pronounced and are comparable with the experimental result. The agreement of the features in ⟨111⟩ direction with the

CC-0. In Public Domain. Gurukul Kangri Collection, Haridwar

Digitized by Arya Samaj Foundation Chennai and eGangotri

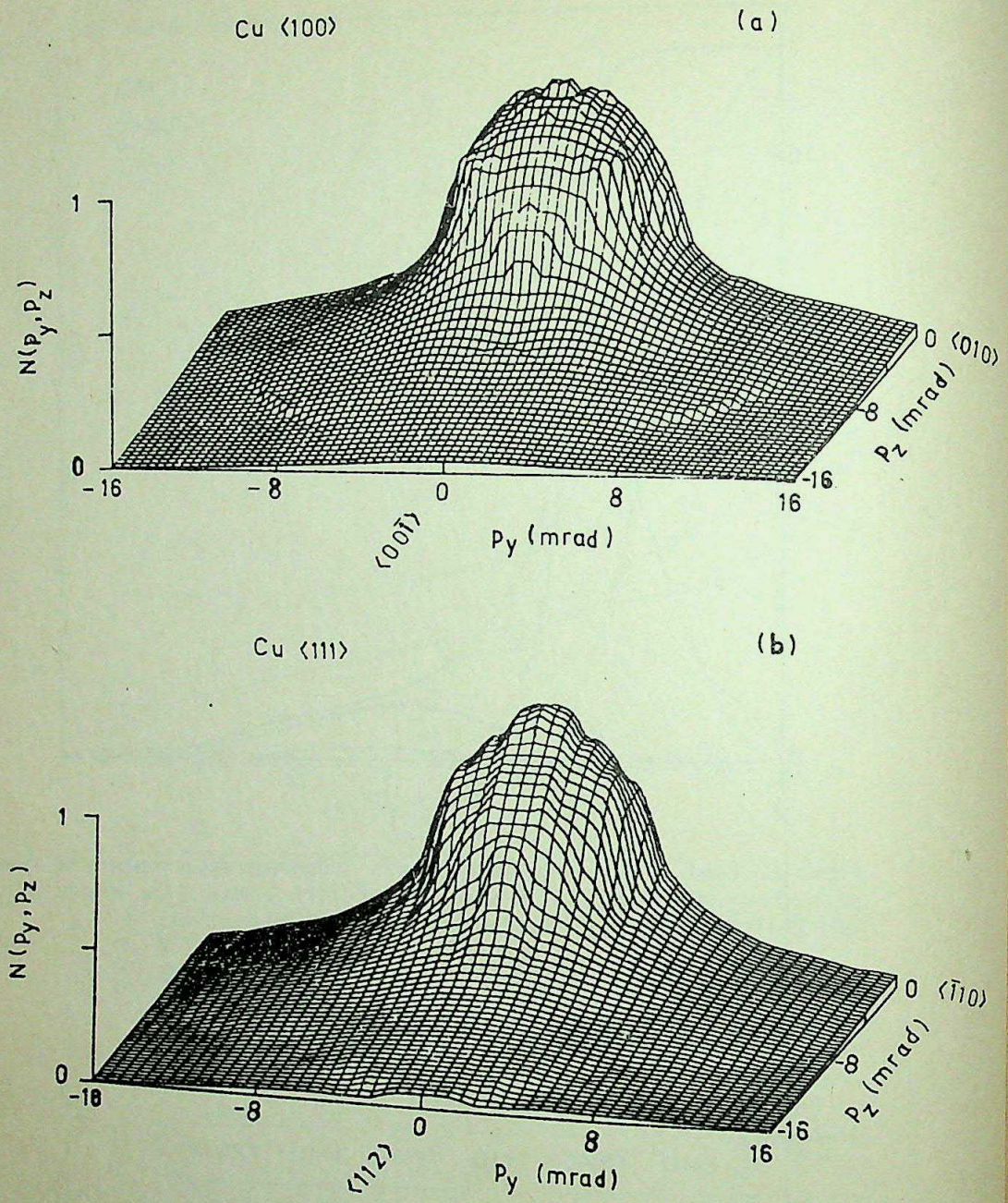

Figure 3. Theoretical band 2D ACPAR plots along the three integration directions (a) ⟨100⟩ and (b) ⟨111⟩.

experimental ones is also good, especially, the neck in the FS is clearly visible. The comparison of the results, in the three integration directions, among themselves reveal the anisotropic nature of the 2D ACPAR surface. Another observation worthy of mention here is that, theoretical surfaces show sharper structures than the experiments (Singh and Singru 1982, 1983). It is expected that the inclusion of the electron-positron enhancement effects should make these structures less sharp.

In the work of Matsumoto and Wakoh (1988), APW results have been compared with the experiment (Haghgooie *et al* 1978 and Berko *et al* 1977) through the cross-sections of 2D ACPAR surface for ⟨100⟩ and ⟨111⟩ integration directions. A similar comparison is presented in figures 4(a)–4(c). For this purpose, we added 0·2 times the

CC-0. In Public Domain. Gurukul Kangri Collection, Haridwar

Digitized by Arya Samaj Foundation Chennai and eGangotri

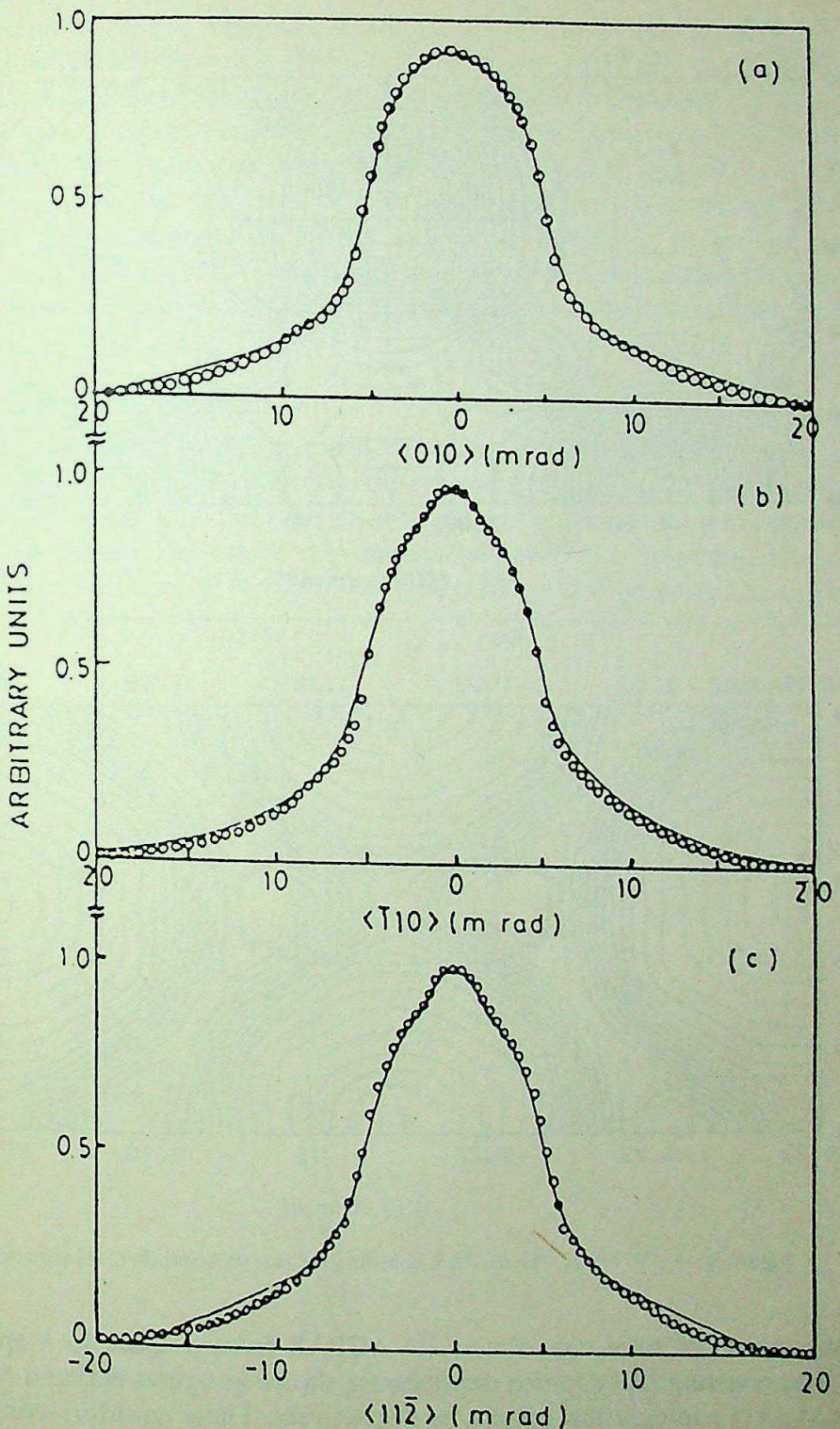

Figure 4. The cross sections of 2D ACPAR. **(a)** along the ⟨010⟩ direction and $P_{\langle 010\rangle}=0$, **(b)** along the ⟨$\bar{1}$10⟩ direction and $P_{\langle 11\bar{2}\rangle}=0$ and **(c)** along the ⟨11$\bar{2}$⟩ direction and $P_{\langle 110\rangle}=0$. Continuous curve – theory, circles – experiment.

core contribution, as done by them, to the band result and then convoluted with the experimental resolution function. The core 2D ACPAR is calculated using the density functional wavefunctions obtained through the LCGO method. The agreement with the experiment is very good but for minor differences.

CC-0. In Public Domain. Gurukul Kangri Collection, Haridwar

Digitized by Arya Samaj Foundation Chennai and eGangotri

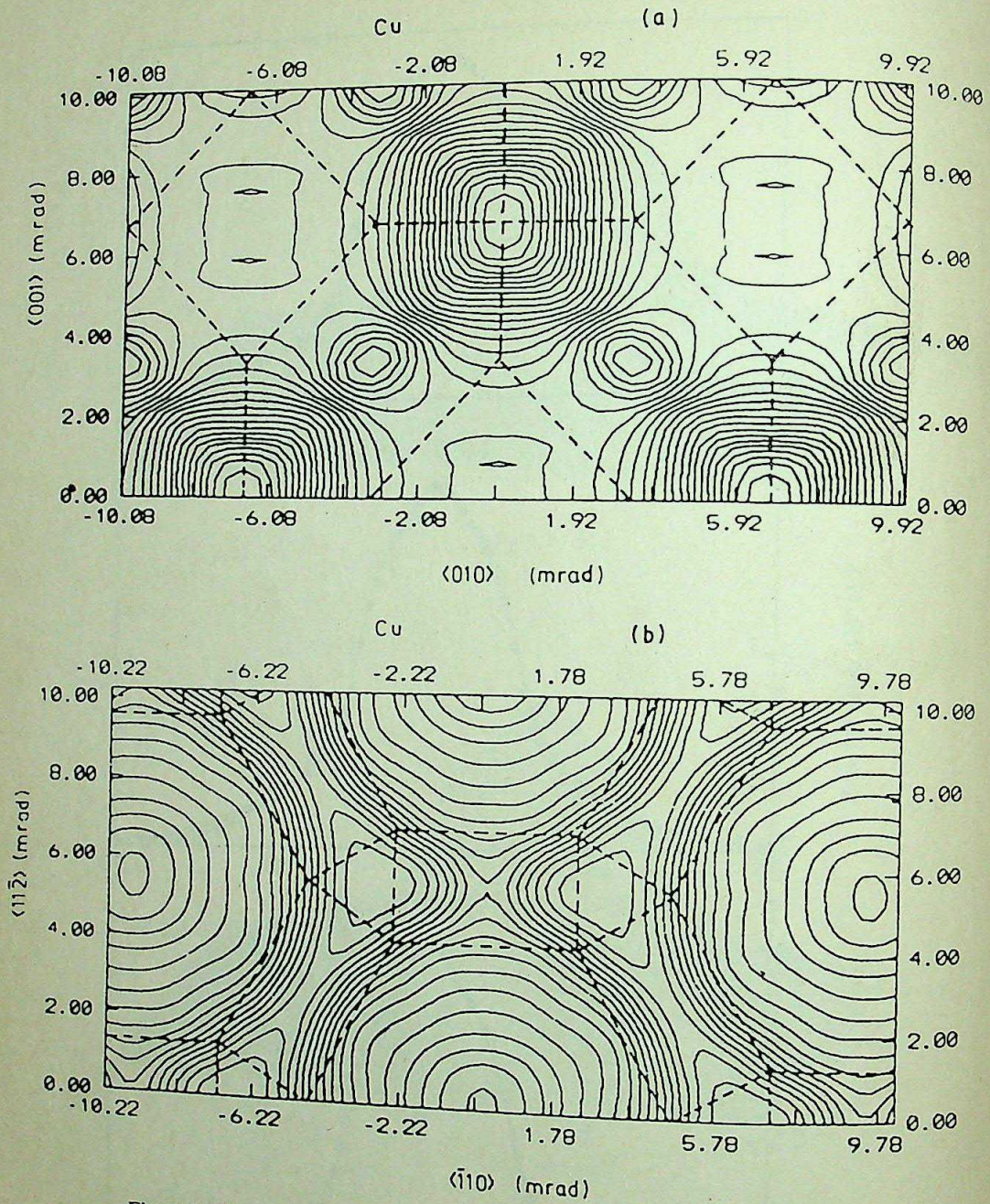

Figure 5. LCW folded 2D ACPAR contours for (**a**) (100) and (**b**) (111) planes.

We remapped the total convoluted 2D ACPAR from p space to k space using eq. (10). The resulting LCW folded densities are shown in figures 5(a) and 5(b) for the ⟨100⟩ and ⟨111⟩ integration directions respectively. These contours compare well with the experiment as well as with the APW calculation of Matsumoto and Wakoh (1988). The projection of the BZ corresponding to the (100) and (111) planes are superimposed by dotted lines which guide us to give an idea of the FS shape as reflected by LCW folded density.

It may be mentioned that the present 1D and 2D ACPAR results do not correct for the electron-positron correlation via the enhancement factors. We are unable to carry out such an analysis meaningfully because of the non-availability of the experimental

CC-0. In Public Domain. Gurukul Kangri Collection, Haridwar

Digitized by Arya Samaj Foundation Chennai and eGangotri

data in terms of tables. This still leaves us an option of taking into account the enhancement effects by using one of the schemes proposed by Kahana (1963), Mijnarends and Singru (1979) or Matsumoto and Wakoh (1987). However, the utility of such a procedure in the absence of experimental numerical data is somewhat limited since, only qualitative comparison is then possible. Moreover, a number of workers have reported the enhancement factor analysis on 3*d*-metals. Their work indicate that the enhancement factors are state, character or energy dependent (Matsumoto and Wakoh 1987 and Singh *et al* 1986). It is hoped that the present data would be useful to experimentalists for detailed electron-positron correlation analysis.

3.3 *Reciprocal form factors*

We present our results on $B^{CP}(z)$ and $B^{2\gamma}(z)$ along the three directions in figures 6(a)–6(c) Both the CP and ACPAR include the core contributions. The arrows indicate the lattice translation vectors and their projections on the direction under consideration. In table 2 we present the values of these vectors and the corresponding values for B functions. Our value for $B^{CP}(z)$ at $z = R_{110}$ is 0·141 as compared to the experimental

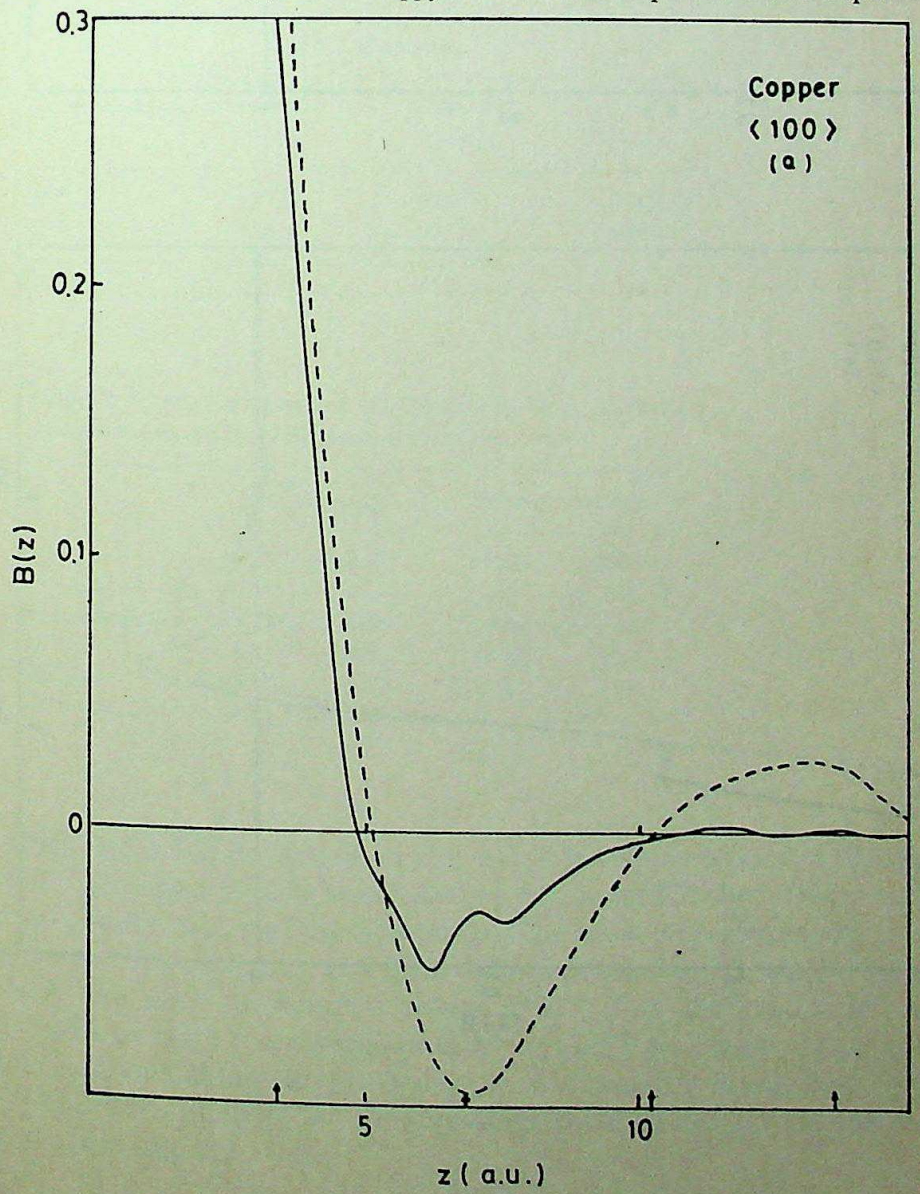

CC-0. In Public Domain. Gurukul Kangri Collection, Haridwar

Digitized by Arya Samaj Foundation Chennai and eGangotri

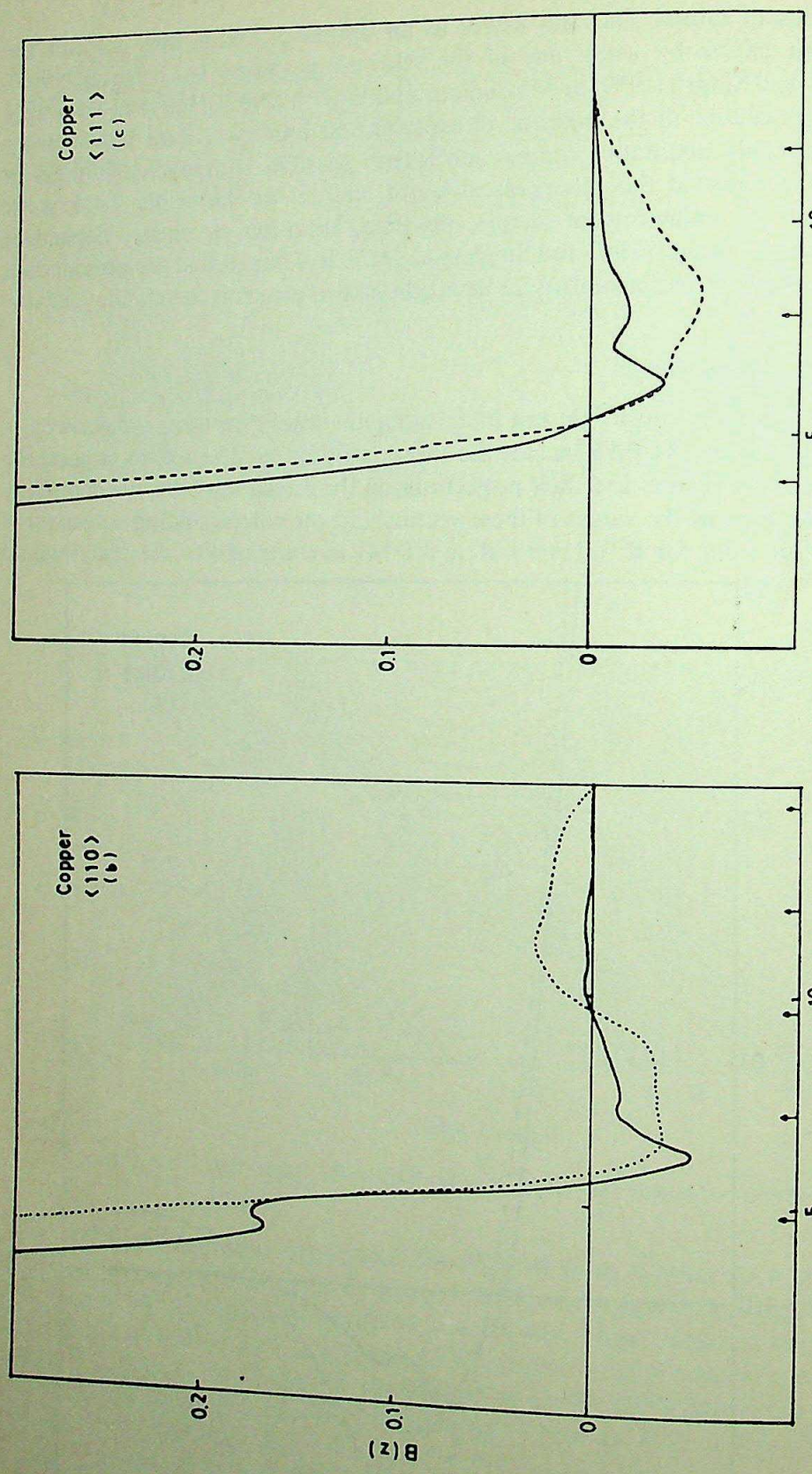

Figure 6. $B^{CP}(z)$–continuous curve, $B^{2'}(z)$–dashed curve, along the three symmetry directions (**a**) $\langle 110 \rangle$, (**b**) $\langle 110 \rangle$ and (**c**) $\langle 111 \rangle$. Both the functions include core contribution and are convoluted by the respective experimental resolution functions. The arrows indicate the positions of the lattice vectors.

CC-0. In Public Domain. Gurukul Kangri Collection, Haridwar

Digitized by Arya Samaj Foundation Chennai and eGangotri

Table 2. Distances of lattice vectors and their projections on each of the symmetry direction and the corresponding values of the B function. The directions of the projected lattice vector is also indicated.

	⟨100⟩ Direction		
distances (a.u.)	3·411 ⟨110⟩	6·822 ⟨100⟩	10·233 ⟨110⟩
B^{CP}	0·2913	−0·0284	0·0008
$B^{2\gamma}$	0·3701	−0·0951	−0·0006

	⟨110⟩ Direction			
distances (a.u.)	2·416 ⟨011⟩	4·832 ⟨110⟩	7·248 ⟨011⟩	9·664 ⟨110⟩
B^{CP}	0·5115	0·1415	0·0128	0·0019
$B^{2\gamma}$	0·7771	0·1394	−0·0337	−0·0014

	⟨111⟩ Direction		
distances (a.u.)	3·9306 ⟨110⟩	7·8612 ⟨110⟩	11·7918 ⟨111⟩
B^{CP}	0·1725	0·0183	−0·00131
$B^{2\gamma}$	0·2524	−0·0524	−0·0107

Table 3. Zero crossings of the reciprocal form factors alongwith free electron values (distances are in a.u.).

	First crossing		Second crossing	
	⟨100⟩	⟨110⟩	⟨100⟩	⟨100⟩
Free electron	5·73	6·66	9·86	11·45
B^{CP}	4·85	5·50	10·48	9·54
$B^{2\gamma}(z)$	5·15	5·73	10·28	9·69

(Bauer and Schneider 1985) value of 0·112 + 0·007. A comparison of ⟨110⟩ direction for B^{CP} and $B^{2\gamma}$ shows additional hump around 4·5 a.u. for CP case. This is attributed to the overlap of d-lobes along that direction. As the positron preferentially senses the delocalized conduction electrons, and since the d-bands are well below the FS and are almost atomic like, such an hump is absent in $B^{2\gamma}$. This also causes $B^{2\gamma}$ to have appreciable value at large z as compared to B^{CP}. Table 3 gives zero crossings for the reciprocal form factors alongwith the free electron values. It is found that, $B^{2\gamma}$ values are nearer to the corresponding B^{CP} zero crossings, but the nature of the curve is close to the free electron-like behaviour.

CC-0. In Public Domain. Gurukul Kangri Collection, Haridwar

include core contribution and are convoluted by the respective experimental resolution functions. The arrows indicate the positions of the lattice vectors.

Digitized by Arya Samaj Foundation Chennai and eGangotri

4. Summary

We have reported the calculation of EMD and TPMD in copper using the self-consistent LCGO method within a single theoretical framework. The present study is the first to report the positron annihilation characteristics using LCGO method. The results for TPMD have been presented by taking its sections by the symmetry planes. Such 3D plots yield information about the nature of the FS. Comparison of the angular momentum decomposition of the EMD and the TPMD substantiates the fact that the positron preferentially annihilates with free *sp*-electrons rather than with the localized *d*-electrons. The 2D ACPAR surfaces and their cross-sections compare well with the experimental ones and also provide rich information about the FS topologies. This is greatly supported by the LCW folding procedure. The theoretical LCW-folded 2D ACPAR contours also compare well with the experimental ones and with the calculation by the APW method. The discrepancies that appear in these comparisons are attributed to the electron-positron correlation effects. The present results obtained within IPA would be useful in quantifying these effects with the help of experimental data.

Acknowledgements

We are thankful to Prof. R M Singru for illuminating discussions and Dr. Anjali Kshirsagar for critical examination of the manuscript. We are thankful to National Informatics Centre, Pune and Bhabha Atomic Research Centre, Bombay for computational facilities. Financial support from the Department of Science and Technology and Department of Atomic Energy, India, is thankfully acknowledged.

References

Bagayoko D, Laurent D G, Singhal S P and Callaway J 1980 *Phys. Lett.* **A76** 187
Bauer G E W and Schneider J R 1983 *Z. Phys.* **B54** 17
Bauer G E W and Schneider J R 1984a *J. Phys. Chem. Solids* **45** 675
Bauer G E W and Schneider J R 1984b *Phys. Rev. Lett.* **52** 2061
Bauer G E W and Schneider J R 1985 *Phys. Rev.* **B31** 681
Berko S 1979 *Positron Annihilation* (eds) R R Hasiguti and K Fujiwara (Sendai: Japanese Inst Metals) p. 65
Berko S 1983 *Positron Solid State Physics* (eds) W Brandt and A Dupasquier (Amsterdam: North-Holland) p. 64
Berko S and Mader J J 1975 *Appl. Phys.* **5** 287
Berko S, Haghgooie M and Mader J J 1977 *Phys. Lett.* **A63** 335
Brandt W and Dupasquier A 1983 *Positron Solid State Physics* (Amsterdam: North-Holland)
Bross H 1982 *J. Phys. F: Met. Phys.* **12** 2249
Bross H and Stohr H 1974 *Appl. Phys.* **3** 307
Cooper M J 1985 *Rep. Prog. Phys.* **48** 415
Cushner S, Erskine J C and Berko S 1970 *Phys. Rev.* **B1** 2852
Genoud P, Singh A K, Manuel A A, Jarlborg T, Walker E, Peter M and Weller M 1988 *J. Phys. F* **18** 1933
Haghgooie M, Mader J J and Berko S 1978 *Phys. Lett.* **A69** 293
Kahana S 1963 *Phys. Rev.* **129** 1622
Kaiser J H, West R N and Shiotani N 1986 *J. Phys. F* **16** 307
Kaiser J H, Walters P A, Bull C R, West R N and Shiotani N 1987 *J. Phys. F* **17** 1243
Kanhere D G and Singru R M 1977 *J. Phys. F* **7** 2603

CC-0. In Public Domain. Gurukul Kangri Collection, Haridwar

Digitized by Arya Samaj Foundation Chennai and eGangotri

Lock D G, Crisp V H C and West R N 1973 *J. Phys. F* **3** 561
Lock D G and West R N 1975 *Appl. Phys.* **6** 249
Loucks T L 1966 *Phys. Rev.* **144** 504
Manuel A A 1983 *Positron Solid State Physics* (eds) W Brandt and A Dupasquier (Amsterdam: North-Holland) p. 581
Matsumoto M and Wakoh S 1987 *J. Phys. Soc. Jpn* **56** 3566
Matsumoto M and Wakoh S 1988 *Physica* **B149** 57
Mijnarends P E 1973 *Physics* **63** 237
Mijnarends P E 1979 *Positrons in Solids* (ed.) P Hautojarvi (Berlin: Springer-verlag) p. 25
Mijnarends P E 1983 *Positron Solids State Physics* (eds) W Brandt and A Dupasquier (Amsterdam: North-Holland) p. 146
Mijnarends P E and Singru R M 1979 *Phys. Rev.* **B19** 6038
Pattison P, Hansen N K and Schneider J R 1982 *Z. Phys.* **B46** 285
Pattison P and Williams B 1976 *Solid State Commun.* **20** 585
Rabou L and Mijnarends P E 1984 *Solid State Commun.* **52** 933
Rajagopal A K, Singhal S P and Kimball J in Rajagopal A K 1980 *Adv. Chem. Phys.* **41** 59
Rath J, Wang C S, Tawil R A and Callaway J 1973 *Phys. Rev.* **B8** 5139
Rollason A J, Schneider J R, Laundy D S, Holt R S and Cooper M J 1987 *J. Phys. F* **17** 1105
Schulke W 1977 *Phys. Status Solidi* **B82** 229
Singh A K and Singru R M 1982 *J. Phys. F* **12** 685
Singh A K and Singru R M 1983 *J. Phys. F* **13** 2189
Singh A K and Singru R M 1984 *J. Phys. F* **14** 1751
Singh A K and Jarlborg T 1985 *J. Phys. F* **15** 727
Singh A K, Manuel A A, Jarlborg T, Mathys Y, Walker E and Peter M 1986 *Helv. Phys. Acta* **59** 410
Singh A K, Manuel A A, Singru R M and Peter M 1985 *Helv. Phys. Acta* **58** 640
Sundararajan V, Asokamani R and Kanhere D G 1988 *Phys. Rev.* **B38** 12653
Sundararajan V, Kanhere D G and Callaway J 1988 *Phys. Lett.* **A133** 521
Wakoh S, Berko S, Haghgooie M and Mader J J 1979 *J. Phys. F* **19** L231
Wang C S and Callaway J 1978 *Comput. Phys. Commun.* **14** 327
West R N, Mayers J and Walters P A 1981 *J. Phys.* **E14** 478
Williams B 1977 *Compton Scattering* (London: McGraw-Hill)

CC-0. In Public Domain. Gurukul Kangri Collection, Haridwar

Digitized by Arya Samaj Foundation Chennai and eGangotri

CC-0. In Public Domain. Gurukul Kangri Collection, Haridwar

Digitized by Arya Samaj Foundation Chennai and eGangotri

Pramāṇa – J. Phys., Vol. 34, No. 1, January 1990, pp. 51–66. © Printed in India.

Effect of variation of dielectric constant on the magnetic field modulation of exciplex luminescence

DEB NARAYAN NATH and MIHIR CHOWDHURY

Department of Physical Chemistry, Indian Association for the Cultivation of Science, Jadavpur, Calcutta 700 032, India

Ms received 1 June 1989; revised 19 September 1989

Abstract. The effect of variation of dielectric constant on the relative magnetic field effect in singlet luminescence has been studied using a typical exciplex system at a saturating field. The study indicates strong specificity in the perturbation of the magnetic field effect by alcoholic solvents. In contrast to alcohols where relative singlet magnetic field effect is of the order of 2% only, the magnetic field effect in non-alcoholic medium reaches as high as 9%. Moreover, dielectric constant variation in alcohols yields curves which are distinctly different from those in non-alcoholic media. It turns out that this dependence of magnetic field effect on dielectric constant is similar in all non-alcoholic solvent mixtures. An analytical study based on Hong and Noolandi's solution of Smoluchowski equation has been made. Derived expressions can interpret experimental curves reasonably well.

Keywords. Radical pair reactions; magnetic field effect; exciplex luminescence; solvent effect of molecular interactions.

PACS Nos 82·30; 82·50; 75·20; 78·55; 31·70

1. Introduction

The phenomenon of magnetic effect on electron-spin-nonconserving chemical processes such as radical pair (RP) recombination has received considerable attention in recent years. The field has been competently reviewed by various workers (Atkins and Lambert 1975; Atkins 1976; Buchachenko 1976; Sagdeev *et al* 1977; Turro and Kraeutler 1980; Turro 1983; Gould *et al* 1984; Salikhov *et al* 1984; Basu *et al* 1988b; Steiner and Ulrich 1989). Exciplex luminescence in moderately polar solvent is one of the convenient ways to monitor the magnetic effect on the recombination of photo-generated radical ion pairs (RIP) (Petrov *et al* 1981) and two such magnetically sensitive exciplex systems have recently been studied by us (Nath and Chowdhury 1984a, b; Nath *et al* 1986, 1989; Basu *et al* 1987a, b, 1988a, b, 1989a, b). Following photo-excitation of one of the two partners of the exciplex, an electron is transferred from the donor to the acceptor to form solvent-separated radical ion pairs (SSIP) which then recombine to produce luminescent contact ion pair (CIP) or exciplex. A small fraction of the singlet-born RIPs, however, diffuses out to a domain where the exchange interaction between them is negligibly small and undergoes irreversible, hyperfine interaction (HFI)-induced intersystem crossing to the triplet state. A part of those still remaining in the singlet state after a diffusional excursion may recombine to form luminescent exciplex. A small magnetic field can lift the S-T degeneracy of the well-separated RIP to an extent greater than the widths of the levels and thus

CC-0. In Public Domain. Gurukul Kangri Collection, Haridwar

Digitized by Arya Samaj Foundation Chennai and eGangotri

may cause a significant decrease in the rate of HFI-induced RIP intersystem crossing process. The suppression of the ISC process in the RIP by the small magnetic field, in turn, increases the singlet RIP recombination yield causing the exciplex luminescence to be magnetically sensitive. The diffusion provides the RIP the necessary time required for the comparatively slow spin-evolution process to occur and thus plays a major role in controlling the magnitude of the effect. For charged RIPs, the modification of the potential energy surface by electrostatic solvent interaction is large and this can cause an order of magnitude change in the diffusion rate. The purpose of this paper is to investigate the effect of dielectric constant (ε) variation on the magnetic effect of the pyrene-N,N-dimethylaniline (Py-DMA) system and explain the curves from a schematic theoretical model.

In order to find out whether any other specific property of the solvent, apart from ε, needs to be considered for cage effect of RIP, we have studied the magnetic effect in several iso-dielectric solvent mixtures. Our experiments show that the presence or absence of alcohols makes a significant difference. The ε variation in non-alcoholic media yields curves which are independent of the specific nature of the molecules comprising the solvent mixture, but this curve is distinctly different in the case of alcoholic media.

The analysis of the magnetic field effect requires an accurate knowledge of the HFI-induced spin motion, electrochemical potential induced spatial motion and the coupling between the two. A realistic formulation of the problem involves separate diffusion equation for singlet and triplet states, and a quantum mechanics based kinetic equation for singlet-triplet interconversion. Solutions for the coupled system of partial differential equations are not available, but can be computed. Freed and Pederson (1976) used the computational approach using finite difference algorithm for uncharged radicals. Schulten and Schulten (1977) and Werner *et al* (1977) have used the same approach for the ion pair case. Schulten and Epstein (1979) used a Monte Carlo path integral method. Mauzerall and Ballard (1982) used computed solutions with finite difference equations under more realistic conditions. In this paper we have attempted an analytical formulation of the magnetic effect on exciplex luminescence.

2. Experimental

An improved phase sensitive detection technique has been employed by us to study the magnetic field effect on exciplex luminescence and this has been described in detail in our previous works (Nath and Chowdhury 1984a, b). The lifetimes were measured with our correlated single-photon-counting set-up (Nath and Chowdhury 1984a; Nath *et al* 1986; Basu *et al* 1989a, b). Commercially available compounds of the highest quality were purified by zone refining (pyrene) and vacuum distillation (DMA). Trans-anethole (AN) and 9-cyanophenanthrene (CNP) were obtained from Aldrich (99% purity) and were used without further processing. Spectra-grade solvents methanol, 1-propanol, tetrahydrofuran (THF), dimethylformamide (DMF), acetone, ethylacetate, benzene, acetonitrile were used after distillation in inert atmosphere. The working samples were made with fixed acceptor and donor concentrations of [Py]:[DMA] = 10^{-4} M:6×10^{-2} M for Py-DMA exciplex system and [CNP]:[AN] = 10^{-3} M:8×10^{-2} M for CNP-AN exciplex system. All the samples

CC-0. In Public Domain. Gurukul Kangri Collection, Haridwar

Digitized by Arya Samaj Foundation Chennai and eGangotri

were deoxygenated by either freeze-pump-thaw technique or by bubbling pure, dry nitrogen for 45 min and were used within one hour after preparation. Several checks were made during experiments for the possible degradation of the sample.

3. Results

Figure 1 shows the dependence of relative magnetic effect $\Delta\phi/\phi$ (ϕ = exciplex luminescence, $\Delta\phi$ = enhancement in presence of a saturating magnetic field of 240 G) on the ε for Py-DMA system when ε has been varied using various compositions of the following non-alcoholic solvent pairs: THF and DMF, ethylacetate and DMF, ethylacetate and acetonitrile, THF and acetonitrile, THF and acetone, acetone and DMF etc; and mixtures of methanol and *n*-propanol for alcoholic environment. Figure 2 shows the same for the total luminescence ϕ in a typical non-alcoholic environment (THF-DMF mixtures) and in mixtures of methanol and *n*-propanol. When ε has been varied using mixtures of different alcohols the data closely correspond to those reported by Petrov *et al* (1981) for alcoholic solvents. While ϕ decreases monotonically with increase in ε, $\Delta\phi/\phi$ shows a maxima at an intermediate dielectric constant ($\varepsilon = 29$). The $\Delta\phi/\phi$ versus ε plots for non-alcoholic solutions, however, differ markedly from the plot in alcoholic solution. The salient features of the curves are: (a) The $\Delta\phi/\phi$ versus ε curve in non-alcohols shows a rapid increase after the onset at $\varepsilon = 9$, followed by a slow decrease with increase in ε. In alcohols $\Delta\phi/\phi$ shows a gradual increase, followed by a decrease with increase in ε. (b) The peak position of $\Delta\phi/\phi$ versus ε curve *does not depend on the nature of the non-alcoholic solvent chosen or the exciplex system*; this stays within the limit $15 < \varepsilon < 20$ for different choice of components. Similarly, the basic nature of the ϕ versus ε curve remains the same for

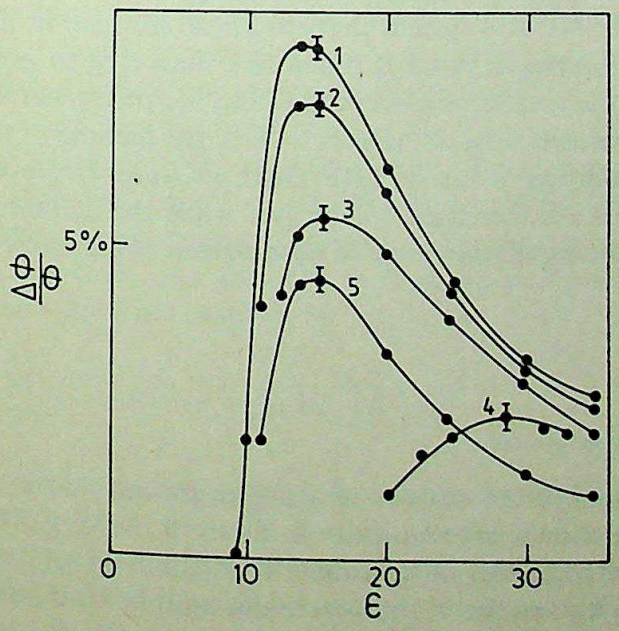

Figure 1. Change in $\Delta\phi/\phi$ with ε. Curves 1 to 4 stand for Py-DMA exciplex in THF/DMF, ethylacetate/DMF, ethylacetate/acetonitrile and 1-propanol/methanol mixed solvents respectively. Curve 5 stands for CNP-AN system in THF/DMF. The relative errors in the data-points are shown by vertical bars.

CC-0. In Public Domain. Gurukul Kangri Collection, Haridwar

Digitized by Arya Samaj Foundation Chennai and eGangotri

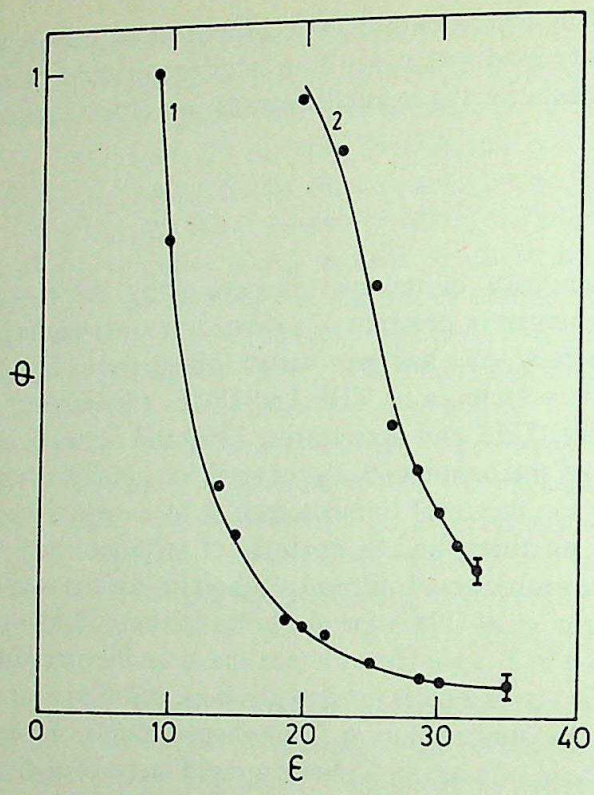

Figure 2. Change in ϕ with variation in ε for Py-DMA system in THF/DMF (curve 1) and in 1-propanol/methanol (curve 2). The scale of ϕ has been adjusted so that for THF/DMF $\phi = 1$ at $\varepsilon = 9$.

non-alcoholic solvent mixtures. But the $\Delta\phi/\phi$ versus ε curve in alcohol does not display any system-independent characteristic. While the peak for Py-DMA system occurs at $\varepsilon = 29$, that for the CNP-AN system shifts to $\varepsilon > 40$ (Basu *et al* 1987b; Nath *et al* 1989). (c) In alcohols the $\Delta\phi/\phi$ value is much less than that in non-alcohols. (d) In isodielectric situation the total luminescence (ϕ) and life-time (τ) of the exciplex is larger in alcohol. Our experiment shows, when $\varepsilon = 28{\cdot}5$, the lifetime of the exciplex is 17 ns in alcohol, while this drops to 4 ns in THF/DMF mixture. However, for both alcohols and non-alcohols, as ε is increased τ decreases while the lifetime for pyrene decay remains the same ($\simeq 3$ ns) over the range of observation of magnetic field effect.

4. Discussion

4.1 *Description of the proposed model*

The potential energy diagrams of the various uncharged ground and excited states and charged RIP states are shown schematically in figure 3. At large inter-radical distances ($r > 6A^0$) the potential energy of the singlet RIP (solid curve) is represented by Coulombic interaction. At smaller r, however, the simple Coulombic energy diagram is modulated by the presence of an activation barrier (E_a, E'_a) which arises due to the specific interaction of the solvent molecules with the radicals. This barrier originates from the work done in the reorientation of the solvent molecules in the process of SSIP$\rightleftharpoons$CIP interconversion.

CC-0. In Public Domain. Gurukul Kangri Collection, Haridwar

Digitized by Arya Samaj Foundation Chennai and eGangotri

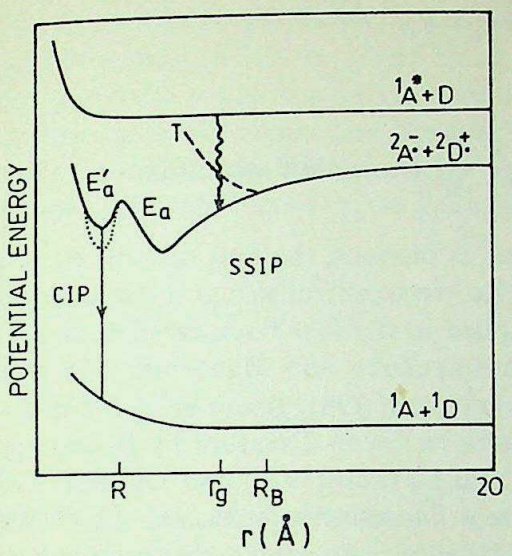

Figure 3. Schematic representation of the dependence of energy levels of the ($^2Py^- + {}^2DMA^+$). RIP system on the inter-radical distance (r) in a moderately polar solvent. The dashed curve represents the triplet state of the RIP and the dotted curve represents the possible CIP stabilisation in the case of alcoholic solvents to account for the anomalous effect in alcohols (see text and figure 10).

The energy of the RIP state depends on the orientation of polar solvent molecules surrounding it. The orientation of solvent molecules is fluctuating and for some specific orientations the RIP energy may degenerate with the initial $^1A^* + D$ state making the radiationless transition facile. We consider a simple model where direct transition to the RIP state is assumed to take place only at r_g where r_g is greater than the reaction distance R. The idea of long-range electron transfer is in conformity with Staerk *et al* (1985) and Petrov *et al* (1981) conclusion. Lastly, we have assumed a minimum inter-radical distance R_B, characterized by $\omega_{HFI} = V_{ST}(R_B)$, below which spin-evolution cannot occur. To have observable magnetic effect it is essential for the RIP to undergo diffusional excursion in the domain $r > R_B$.

Extensive work has been reported on the theory of diffusion controlled reactions, the classical Smoluchowski equation being the starting point of all such pursuits (Mauzerall 1980; Calef and Deutch 1983; Newton and Sutin 1984; Hynes 1985). Most of the theoretical developments, however, pertain to neutral species. The diffusion process of oppositely charged RIP in their mutual potential field (F) according to Smoluchowski equation is given by

$$\frac{d\rho}{dt} = \nabla\left\{D\left(\nabla\rho + \frac{\rho}{kT}\nabla F\right)\right\}, \tag{1}$$

where ρ is the probability per unit volume for finding two radicals at a relative distance r at a time t; D is the mutual diffusivity of two radicals, k, the Boltzman constant, T, the absolute temperature, F, the potential over the surface governing the radical motion. The following boundary conditions are pertinent to the problem at hand:

$$\text{at } t = 0; \quad \rho \to \frac{\delta(r - r_g)}{4\pi r_g^2}$$

CC-0. In Public Domain. Gurukul Kangri Collection, Haridwar

Digitized by Arya Samaj Foundation Chennai and eGangotri

i.e. RIPs are generated at a distance $r_g > R$;

$$\text{at } r \to \infty, \quad \rho \to 0; \tag{2}$$

$$\text{at } r \to R \text{ (reaction radius); } D\left(\frac{\delta\rho}{\delta r} + \frac{\rho}{kT}\frac{\delta F}{\delta r}\right) \to h\rho. \text{ (diffusive flux).}$$

While the second boundary condition is obvious, the first and the third conditions need a few comments: (a) Evidence for electron transfer at a distance greater than molecular contact distance R, as implied in the first boundary condition of (2), has been provided by various workers (Carapellucci and Mauzerall 1975; Brugger *et al* 1981; Borsenberger *et al* 1978; Crawford *et al* 1981; Boxer *et al* 1983). Evidence for electron tunnelling in molecular system has been discussed by Brockelhurst (1973), Miller (1975), Libby (1977), Chance and Devault (1979) and Devault (1980). In our system, the quenching constant of pyrene fluorescence yields a r_g of $8A^0$ (Weller 1967). (b) The third boundary condition of (2) contains an adjustable parameter h defined by

$$h = \kappa U_0/4 \tag{3}$$

where U_0 is an effective velocity of crossing the potential barrier at the reaction radius and κ is a transmission coefficient. In our system κ is governed ultimately by the interconversion rates CIP$\rightleftharpoons$SSIP. The condition $h = \infty$ means a perfectly absorbing sink, as assumed commonly, while $h = 0$ corresponds to non-reaction. If some of the CIPs formed from SSIP dissociate back, instead of irreversibly and radiatively coming down to the ground state, h will be finite.

(c) It is to be noted that in practice, fixing a value for R depends on our knowledge of F. In all our analysis we have considered F to be represented by a pure Coulombic potential and thus the minimum R one can choose in a working theoretical model is the SSIP minima, below which the Coulombic model fails. If, however, we assume that the activation barrier induced perturbation is negligible and the Coulombic law extends all the way up to CIP minima then R can be conceptually taken as the CIP minima. In such a case the disappearance of RP through transitions to the ground state will be irreversible, and h will be given by the sum of radiative and non-radiative decay rates of the CIP or exciplex. The point we would like to emphasize that the interpretation of h will depend on the choice of R in the model.

Onsager (1934, 1938) was the first to modify the Smoluchowski equation to describe Brownian motion of ions under the influence of an external field and their own Coulomb attraction. Debye (1942) generalized Smoluchowski's result for steady-state reaction rate to include the effect of potential interaction. The stationary solutions of modified Smoluchowski equation for ion pair in presence of scavenger and/or electric field have been obtained in elegant ways by Monchik (1956), Berlin *et al* (1980), Sano and Baird (1982), Sano (1983), Tachiya (1978, 1979), Raaen and Hemmer (1982), Naqui *et al* (1979), Waldenstrom *et al* (1981). Non-stationary solutions describing time-evolution of the neutralization process have been obtained mostly by numerical techniques (Fries and Patey 1984; Rzad and Bakale 1973; Ludwig 1969; Abell and Mozumder 1972; Abell *et al* 1972; Hummel and Infelta 1974) and such a numerical approach has been attempted by Schulten and Schulten (1977) and Schulten and Epstain (1979) to discuss magnetic effect in geminate recombinations of RIPs. Approximate analytical methods for the time-dependent equation have been suggested by Montroll (1946), Mozumder (1968, 1974). Belloni *et al* (1977), Deutch (1972) and

CC-0. In Public Domain. Gurukul Kangri Collection, Haridwar

Digitized by Arya Samaj Foundation Chennai and eGangotri

Berlin (1976). *Exact analytical solution for Coulomb field* has been obtained and applied by Hong and Noolandi (1978a, b, c) and Sano and Tachiya (1979).

The exact analytical solution is given in terms of the Laplace transform variable S. The long-time behaviour can be described by simple expressions and is particularly easy to handle. In the long time limit (for $Dt \gg r_g^2, r_c^2$), the evolution of the reactivity $R(t)$ and the survival probability $\Omega(t)$ are given by Hong and Noolandi (1978a, b, c) as

$$R(t) = \frac{r_c}{(4\pi Dt^3)^{1/2}} \frac{U(r_g)}{[U(\infty)]^2}, \tag{4}$$

$$\Omega(t) = \frac{U(r_g)}{U(\infty)} \left[1 + \frac{r_c}{U(\infty)(\pi Dt)^{1/2}} \right] \tag{5}$$

where the Onsager radius $r_c = e^2/\varepsilon kT = \frac{547{\cdot}2}{\varepsilon} A^0$ at room temperature, (6)

and

$$U(r) = \exp(r_c/r) + [(Dr_c/hR^2) - 1]\exp(r_c/R). \tag{7}$$

The yield of free ions is simply the survival probability at infinite time and is given by

$$Y = \frac{U(r_g)}{U(\infty)}. \tag{8}$$

In the present case of exciplex fluorescence from CIP, the total exciplex fluorescence yield (ϕ) is given by

$$\phi = 1 - Y = 1 - \frac{U(r_g)}{U(\infty)} \tag{9}$$

assuming negligible role of other modes of decay of RIP.

As mentioned before, the diffusion process and the spin rephasing dynamics are decoupled in our model. For calculating ϕ, we limit ourselves to the Smoluchowski equation with complete neglect of the spin hamiltonian while, to calculate the enhancement in magnetic field ($\Delta\phi$), we attribute a phenomenological leakage to its expressions. However, such an assumption is justified because ϕ is substantially higher than $\Delta\phi$. Thus, we treat the intersystem crossing phenomenologically as a leakage to the triplet surface (linear with time) represented by (figure 4)

$$\rho_T = At \quad \text{for } t < 10\,\text{ns}$$

$$\rho_T = A_{sat} \quad \text{for } t \geqslant 10\,\text{ns}, \tag{10}$$

where A is the HFI induced ISC rate in absence of magnetic field. The simple expression (10) is assumed on the basis of the theoretical computation of Werner *et al* (1977) for the Py-DMA system. Actually, however, ρ_T will deviate from (10) at small times, but the computed curve, as reproduced in figure 4 shows that the deviations from (10) are too small to change the conclusions arrived at finally. The time t at which the saturation occurs is assumed to be independent of the magnetic field; a justification for this has been provided in our earlier paper (Basu *et al* 1989a, b). We further assume that the S-T degeneracy extends up to the reaction radius i.e. $R_B = R$.

CC-0. In Public Domain. Gurukul Kangri Collection, Haridwar

Digitized by Arya Samaj Foundation Chennai and eGangotri

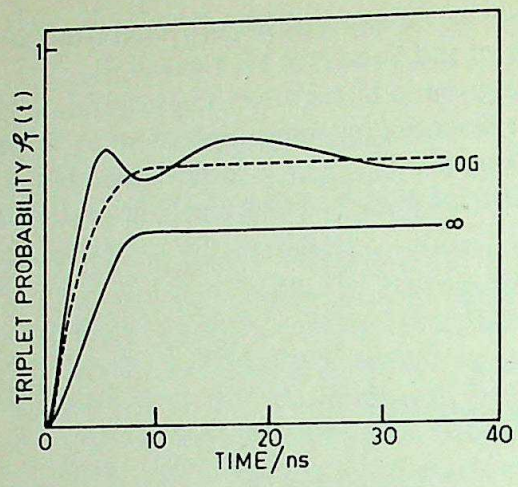

Figure 4. Time-evolution of the hyperfine interaction induced triplet probability $\rho_T(t)$ for the ($^2Py^- + {}^2DMA^+$). RIP system in absence (0 G) and in presence of saturating magnetic field (∞ G) as calculated by Werner *et al* (1977). The linearly approximated time-evolution curve is shown as the dashed line.

Assuming that an exciplex can be formed from a singlet RIP only, the rate of exciplex formation in absence of external magnetic field is given by

$$\chi(t, B=0) = (1 - At)R(t). \tag{11}$$

In the presence of a saturating magnetic field $S \rightarrow T_{\pm 1}$ channels are blocked and ISC rate reduces to $A/3$; the exciplex formation rate is thus given by

$$\chi(t, B=B_S) = \{1 - (A/3)t\}R(t). \tag{12}$$

So the time-dependent magnetic field induced enhancement is given by

$$\Delta\chi(t) = (2/3)AtR(t). \tag{13}$$

Equations (11) to (13) hold for $t < t'$; $t' \simeq 10$ ns. For $t > t'$,

$$\Delta\chi(t) = (2/3)A_{sat}R(t). \tag{14}$$

Thus, the total magnetic field induced enhancement is given by

$$\Delta\phi = \frac{2}{3}\frac{Ar_c}{(4\pi D)^{1/2}}\frac{U(r_g)}{[U(\infty)]^2}\left[\int_0^{t'} t^{-1/2}\,dt + \int_{t'}^{\infty}(A_{sat}/A)t^{-3/2}\,dt\right]. \tag{15}$$

The integrals within the third bracket are finite and there is no need of truncation as required in many approaches. Convergence could also have been ensured by introducing a finite lifetime of the RIP state due to the effect of the scavengers or non-radiative processes. It may be noted that after a long time the recombination is a homogeneous process with hardly any magnetic effect. Thus we get

$$\Delta\phi = \tfrac{2}{3}AB\frac{r_c}{(4\pi D)^{1/2}}\frac{U(r_g)}{[U(\infty)]^2} \tag{16}$$

CC-0. In Public Domain. Gurukul Kangri Collection, Haridwar

Digitized by Arya Samaj Foundation Chennai and eGangotri

where B stands for the integrals within the bracket. From (9) the total luminescence yield (ϕ) is given by

$$\phi = \frac{1 - \exp(r_c/r_g)}{1 + (\bar{\alpha} r_c/R^2 - 1)\exp(-r_c/R)} \tag{17}$$

where

$$\bar{\alpha} = (D/h) \times 10^8 = 10^9/\mathrm{h} \tag{18}$$

for $D = 10^{-5}\,\mathrm{cm}^2/\mathrm{s}$; R, r_g and r_c are in A^0 unit and h is given in cm/s. From (17), (16) and (9) we obtain

$$\frac{\Delta\phi}{\phi} = \frac{2}{3}\frac{AB}{(4\pi D)^{1/2}}\frac{r_c(1-\phi)}{1-\exp(-r_c/r_g)} \tag{19}$$

$$= \tfrac{2}{3} \times \text{constant} \times \frac{r_c}{1-\exp(-r_c/r_g)} \times \left[\frac{(\bar{\alpha} r_c/R^2 - 1)\exp(-r_c/R) + \exp(-r_c/r_g)}{1 + (\bar{\alpha} r_c/R^2 - 1)\exp(-r_c/R)}\right]. \tag{20}$$

[The factor A is effectively constant for a particular donor-acceptor system; the form of the time integral B used in (15) also renders it independent of solvent composition. For the sake of simplicity, we also neglect any effect of variation in D through the factor $1/(4\pi D)^{1/2}$, because in different solvent mixtures the order of D remains the same; effect of its variation is further reduced by the square-root dependence. That is why the second term in the right-hand-side of (20) is taken as a constant.]

The variation of ϕ and $\Delta\phi/\phi$ with ε can be studied with various fitting values for R, r_g and $\bar{\alpha}$. In the case of $\Delta\phi/\phi$, we consider the variation of the bracketted term (20) only.

4.2 *Computed curves and its comparison with experiment*

4.2.1 *Theoretical fit of the experimental ϕ versus ε curves*: In trying to achieve an empirical fit, we have kept in mind the restriction $r_g > R$ of our model. The effect of variation of r_g, R and $\bar{\alpha}$, one at a time, on ϕ versus ε curve is shown in figure 5. Generally ϕ remains unity up to a threshold value of ε, after which it drops to a saturation value. As r_g increases, the threshold shifts towards lower value. The slope of the curve is insensitive to variation of r_g, particularly at large R and $\bar{\alpha}$. In comparison to r_g-variation, R-variation is more pronounced. As R increases, the slope is slightly affected, but the threshold ε rapidly decreases. On the other hand, the variation of $\bar{\alpha}$ affects the slope of the curve and not so much the threshold ε.

Figure 6 shows the best theoretical fit for ϕ versus ε curve in THF/DMF mixed solvents with parameter values $R = 6A^0$, $r_g = 8A^0$, $\bar{\alpha} = 1000$. The fit is more-or-less unique with respect to the values of R and $\bar{\alpha}$, but it is not sensitive to r_g for assumed R and $\bar{\alpha}$. From (18) the estimated value of the boundary parameter h is 1 cm/s.

Figure 7 shows the theoretical fit for ϕ versus ε in alcoholic solvents with a set of parameters ($r_g = 4A^0$, $R = 2{\cdot}5A^0$, $\bar{\alpha} = 900$). A characteristic feature in this case is that unlike non-alcohols, the fit is not unique with respect to the value of $\bar{\alpha}$. For example, almost equivalent fit can also be obtained with the following sets of parameters

CC-0. In Public Domain. Gurukul Kangri Collection, Haridwar

Digitized by Arya Samaj Foundation Chennai and eGangotri

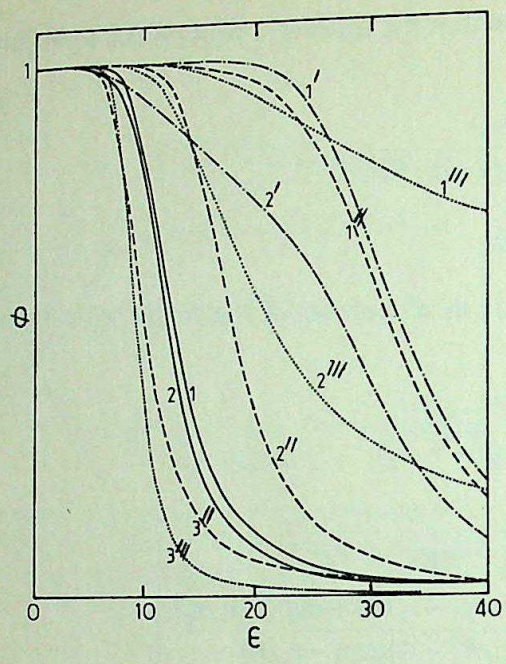

Figure 5. Theoretical ϕ versus ε curve for Py-DMA system. Curves with (———) represent $r_g = 4A^0$ (1) and $20A^0$ (2) with $R = 6A^0$, $\bar{\alpha} = 1000$; (—·—·—) curves for $r_g = 4A^0$ (1′) and $20A^0$ (2′) with $R = 2A^0$, $\bar{\alpha} = 1000$; (— — —) curves represent variation of R for $2A^0$ (1″), $4A^0$ (2″) and $8A^0$ (3″) with $r_g = 8A^0$ and $\bar{\alpha} = 1000$; (····) curves are for $\bar{\alpha} = 10$ (1‴), 100 (2‴) and 10000 (3‴) keeping $r_g = 8A^0$ and $R = 6A^0$.

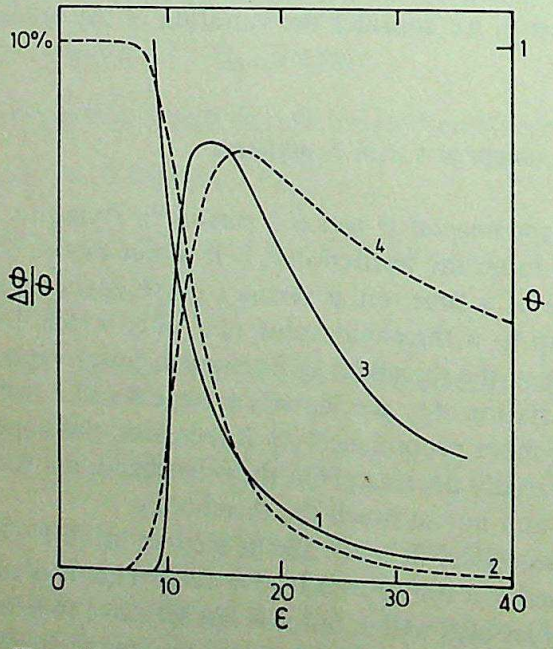

Figure 6. Comparison of the theoretical $\Delta\phi/\phi$ versus ε (plot 4) and ϕ versus ε (plot 2) curves (dotted lines) for Py-DMA exciplex with the best curves (plots 3 and 1) drawn through experimental points (solid lines) in THF/DMF. Parameter values for the theoretical curves are $R = 6A^0$, $r_g = 8A^0$, $\bar{\alpha} = 1000$.

CC-0. In Public Domain. Gurukul Kangri Collection, Haridwar

Digitized by Arya Samaj Foundation Chennai and eGangotri

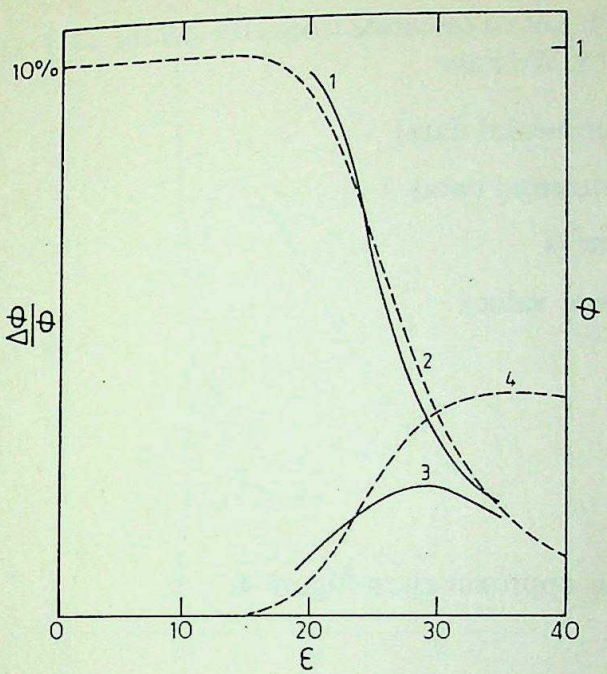

Figure 7. Comparison of the theoretical $\Delta\phi/\phi$ versus ε (plot 4) and ϕ versus ε (plot 2) curves (dotted lines) for Py-DMA exciplex with the best curves (plots 3 and 1) drawn through experimental points (solid lines) in 1-propanol/methanol. Parameter values for the theoretical curves are $R = 2{\cdot}5A^0$, $r_g = 4A^0$, $\bar{\alpha} = 1000$.

($r_g = 8A^0$, $R = 2A^0$, $\bar{\alpha} = 3000$); ($r_g = 8A^0$, $R = 2{\cdot}8A^0$, $\bar{\alpha} = 500$). However, all the fits demand R to be less than $3A^0$. A value of r_g less than $8A^0$ gives a slightly better fit. A study of figures 6 and 7 leads to the conclusion that parameter R carries the information for the behavioral difference between alcohols and non-alcohols (see later).

4.2.2 *Theoretical fit of the experimental $\Delta\phi/\phi$ versus ε curves*: Figures 6 and 7 also contain the theoretical $\Delta\phi/\phi$ versus ε curves corresponding to the set of parameters which fit ϕ versus ε curves nicely. The initial rising part of the curve matches well with the experimental curve for both alcohols and non-alcohols. The general features of the variation (e.g. maxima etc.) are also reproduced. However, in the theoretical curve $\Delta\phi/\phi$ drops more slowly with increase in ε (for $\varepsilon > 15$ in non-alcohols and $\varepsilon > 30$ in alcohols) in comparison to the experiment. One of the possible causes of the anomaly might be our assumption that the spin-evolution rate is independent of r_g once r_g is greater than R. In reality, however, this may not hold, specially for a low value of R; ISC is probably operative only for $r > R_B$. If that be the case, $\Delta\phi$ is contributed to only by those RIPs which are in the diffusion domain $r > R_B$ (figure 3) whereas ϕ receives contribution from the entire diffusion domain. The increase in outward diffusion process with increase in ε, which reduces the recombination, will then affect $\Delta\phi$ *more* in comparison to ϕ causing $\Delta\phi/\phi$ to decrease faster than the theoretical curve.

CC-0. In Public Domain. Gurukul Kangri Collection, Haridwar

Digitized by Arya Samaj Foundation Chennai and eGangotri

4.2.3 *Estimate of the order of A*: Let us calculate from (19) AB for THF/DMF mixed solvent corresponding to $\varepsilon = 15$. We have

$$\Delta\phi/\phi = 0{\cdot}081 \text{ (experimental data)}$$

$$\phi = 0{\cdot}26 \text{ (experimental data)}$$

$$D = 3 \times 10^{-5}\,\text{cm}^2/\text{s}$$

$$r_g = 8A^0 \text{ (assumed value)}$$

and

$$r_c = 36{\cdot}48A^0.$$

Expression (19) yields

$$AB = 8{\cdot}63 \times 10^3\,\text{s}^{-1/2}.$$

Considering (15) and the linear approximation (figure 4)

$$A_{sat} = At,$$

we get

$$B = [2t^{1/2}]_0^{t'} + t'[-2t^{1/2}]_{t'}^{\infty}$$

$$= 4t'^{1/2}$$

$$= 4 \times 10^{-4}\,\text{s}^{1/2}$$

Thus

$$A = 0{\cdot}2 \times 10^8\,\text{s}^{-1}.$$

The order matches nicely with the HF-induced ISC rate in Py-DMA system.

4.2.4 *Non-typical behaviour of alcoholic solvents*: The alcohols can influence magnetic field effect either by altering the static potential energy surface of the RIP, particularly at small inter-radical distances, or by reduction of effective HFI through dynamic involvement (Nath *et al* 1989). Here, we will only discuss the significance of the parameters in relation to the static potential energy surface. The first point we would like to make is that the difference in $\Delta\phi/\phi$ versus ε curve between alcoholic an non-alcoholic solvents is arising through the solvent effect on ϕ itself. Since the parameter $\bar{\alpha}$ may vary with ε, a better alternative is to use the experimental ϕ in the expression of $\Delta\phi/\phi$ (19). The $\Delta\phi/\phi$ versus ε curves so obtained for non-alcohols and alcohols are shown in figure 8 ($r_g = 8A^0$) and figure 9 ($r_g = 4A^0$) respectively. The ϕ versus ε curve for alcoholic solvent differs drastically from that for non-alcoholic solvent; hence, $\Delta\phi/\phi$ versus ε curve also shows non-typical features. The difference of $\Delta\phi/\phi$ at isodielectric solvent mixtures arises mainly due to the factor $(1-\phi)$.

The essential difference between non-alcohols and alcohols, with respect to the parameter values for a good fit, is that for non-alcohols the required R is $6A^0$ whereas alcohols demand distinctly lower values of R i.e. $R < 3A^0$. As the whole analysis is based on a purely Coulombic potential, the fit with $R \simeq 2{\cdot}8A^0$ for alcohols may be interpreted as that the Coulombic potential is valid up to an inter-radical distance of $\simeq 3A^0$ which nearly corresponds to the CIP minima. The boundary parameter h in such a situation should be interpreted as an irreversible radiative and non-radiative decay rate of the exciplex. The experimental observation that the life time τ also

CC-0. In Public Domain. Gurukul Kangri Collection, Haridwar

Digitized by Arya Samaj Foundation Chennai and eGangotri

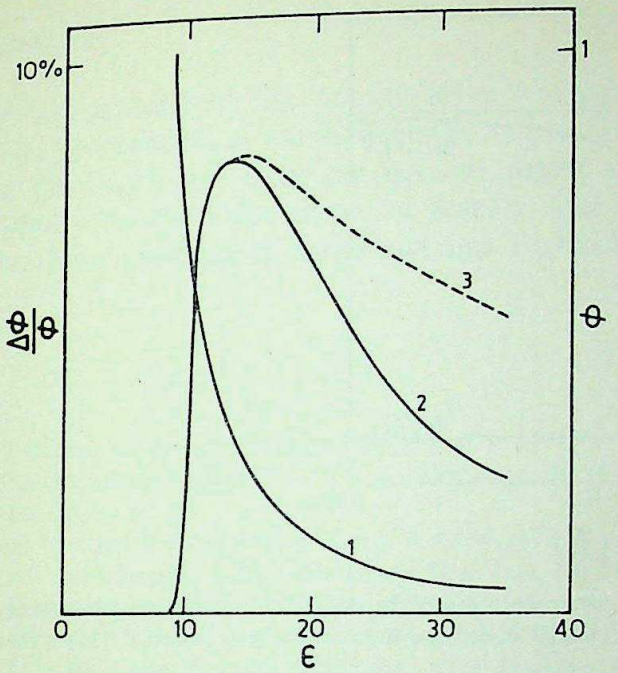

Figure 8. Theoretical $\Delta\phi/\phi$ versus ε curve (dotted curve 3) for Py-DMA exciplex in THF/DMF evaluated with experimental ϕ values (curve 1) following (19). Curve 2 represents $\Delta\phi/\phi$ versus ε curve drawn through experimental points.

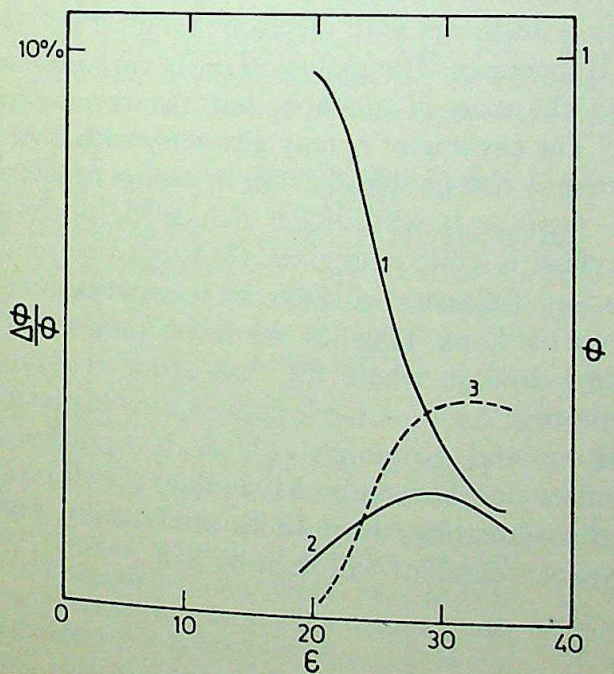

Figure 9. Theoretical $\Delta\phi/\phi$ versus ε curve (dotted curve 3) for Py-DMA exciplex in 1-propanol/methanol evaluated with the experimental ϕ values (curve 1) in (19). Curve 2 represents $\Delta\phi/\phi$ versus ε curve drawn through experimental points.

increases in alcohol agrees with the assumption that energetically the CIP is lower than the SSIP in this medium. Figure 10 gives a qualitative presentation of the schematic potential energy diagram of the RIP in alcohols on the basis of the above argument.

CC-0. In Public Domain. Gurukul Kangri Collection, Haridwar

Digitized by Arya Samaj Foundation Chennai and eGangotri

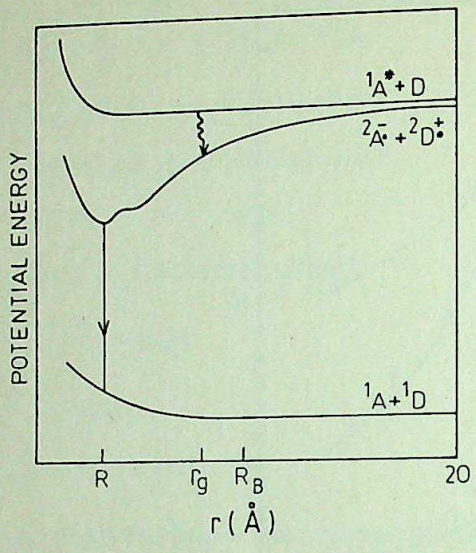

Figure 10. Schematic representation of the dependence of the singlet-state potential energy of the (^{2}Py$^-$ + ^{2}DMA$^+$). RIP system on the inter-radical distance (r) in a moderately polar alcoholic solvent.

4.2.5 *A few additional comments on further improvement of the crude theory may be pertinent*: (1) In the experiment D decreases with increase in ε for THF/DMF mixed solvents whereas for alcohols it increases. The inclusion of its variation in the factor $1/(4\pi D)^{1/2}$ improves the fit in the case of alcohols but the reverse happens for THF/DMF mixed solvents. (2) The parameter r_g may also vary with ε. At low values of ε the charge transfer distance may reduce slightly. The inclusion of this variation in (19), through the factor $r_c/(1-\exp(r_c/r_g))$, will further reduce the slope of the $\Delta\phi/\phi$ versus ε curve. However, this effect is quite negligible. (3) It is to be noted that our starting eq. (4) is valid only for $t > r_c^2/D$ (Basu *et al* 1989a, b). In practice, for THF/DMF mixture at $\varepsilon = 9$, this reduces to $t > 12$ ns. Thus, at the lower limit of ε the starting equation is only valid at a time domain where ISC has attained saturation. This introduces an error in our theoretical $\Delta\phi/\phi$. A more complicated expression, such as the exact one derived by Hong and Noolandi (1978a, b, c) through Laplace transformation or the approximate one derived by Mozumder (1974) on the basis of prescribed diffusion, is needed for treating short times analytically. However, the simplicity of the present analytical treatment will then be lost.

5. Conclusion

We have tried to develop an analytical working model for ε-variation of magnetic effect. Considering the simplicity of the model and lack of our knowledge of parameters, the success achieved is satisfying. However, a more solid conclusion requires more substantial effort. A rigorous analysis where the spin dynamics and the diffusion dynamics are coupled will certainly give a better picture of the phenomenon. However, such an analysis will be vastly more complicated where a numerical approach needs to be followed.

CC-0. In Public Domain. Gurukul Kangri Collection, Haridwar

Digitized by Arya Samaj Foundation Chennai and eGangotri

Acknowledgements

The authors are grateful to Dr. Samita Basu for experimental assistance, helpful discussion and preparation of the manuscript and to Dr. Debshankar Ray for useful suggestions. The work has been carried out under the INDO-US project CE-2 sponsored jointly by the Department of Science and Technology, Government of India and National Institute of Standards and Technology, USA.

References

Abell G C and Mozumder A 1972 *J. Chem. Phys.* **56** 4079
Abell G C, Mozumder A and Magee J L 1972 *J. Chem. Phys.* **56** 5422
Atkins P W 1976 *Chem. Br.* 214
Atkins P W and Lambert T-P 1975 *Annu. Rep. Chem. Soc.* **A72** 67
Basu S, Kundu L and Chowdhury M 1987a *Chem. Phys. Lett.* **141** 115
Basu S, Nath D N and Chowdhury M 1987b *J. Chem. Soc. Faraday Trans. II* **83** 1325
Basu S, Nath D N and Chowdhury M 1988a *J. Lumin.* **40 & 41** 252
Basu S, Nath D N and Chowdhury M 1988b *Proc. Natl. Acad. Sci. (India)* **A54** 830
Basu S, Chakraborty T and Chowdhury M 1989a *J. Indian Chem. Soc.* **66** 599
Basu S, Nath D N and Chowdhury M 1989b *Chem. Phys. Lett.* **161** 449
Beecroft R A, Davidson R S, Goodwin D, Pratt J E, Chewter L A and Phillips D A 1982 *Chem. Phys. Lett.* **93** 468
Belloni J, Billiau F, Cordier P, Delaire J, Delcourt M O and Magat M 1977 *Faraday Discuss. Chem. Soc.* **63** 58
Berlin Yu A 1976 *Dokl. Akad. Nauk. SSR* **228** 628
Berlin Yu A, Cordier P and Delaire J A 1980 *J. Chem. Phys.* **73** 4619
Borsenberger P M, Contois L E and Hoesterey D C 1978 *J. Chem. Phys.* **68** 637
Boxer S G, Chidsey C E D and Roelofs M G 1983 *Annu. Rev. Phys. Chem.* **34** 389
Brockelhurst B 1973 *Chem. Phys.* **2** 6
Brugger P A, Infelta P P, Braun A M and Gratzel M 1981 *J. Am. Chem. Soc.* **103** 320
Buchachenko A L 1976 *Russ. Chem. Rev.* **45** 761
Calef D F and Deutch J M 1983 *Annu. Rev. Phys. Chem.* **34** 493
Carapellucci P A and Mauzerall D 1975 *Ann. NY Acad. Sci.* **244** 214
Chance B and Devault D (eds) 1979 *Tunnelling in Biological Systems* (New York: Academic Press)
Crawford M K, Wang Y and Eisenthal K B 1981 *Chem. Phys. Lett.* **79** 529
Debye P 1942 *Trans. Electrochem. Soc.* **82** 265
Deutch J M 1972 *J. Chem. Phys.* **56** 6076
Devault D 1980 *Q. Rev. Biophys.* **13** 387
Freed J H and Pedersen J B 1976 *Adv. Magn. Reson.* **8** 1
Fries P H and Patey G N 1984 *J. Chem. Phys.* **80** 6253
Gould I R, Turro N J and Zimmt M B 1984 *Adv. Phys. Org. Chem.* **20** 1
Hong K M and Noolandi S 1978a *J. Chem. Phys.* **68** 5163
Hong K M and Noolandi S 1978b *J. Chem. Phys.* **68** 5172
Hong K M and Noolandi S 1978c *J. Chem. Phys.* **69** 5026
Hummel A and Infelta P P 1974 *Chem. Phys. Lett.* **24** 559
Hynes J T 1985 *Annu. Rev. Phys. Chem.* **36** 573
Libby W F 1977 *Annu. Rev. Phys. Chem.* **28** 105
Ludwig P K 1969 *J. Chem. Phys.* **50** 1787
Mauzerall D 1980 *Annu. Rev. Phys. Chem.* **31** 345
Mauzerall D and Ballard S G 1982 *Annu. Rev. Phys. Chem.* **33** 377
Miller J R 1975 *Science* **189** 221
Monchik L 1956 *J. Chem. Phys.* **24** 381
Montroll E W 1946 *J. Chem. Phys.* **14** 202
Mozumder A 1968 *J. Chem. Phys.* **48** 1659
Mozumder A 1974 *J. Chem. Phys.* **61** 780

CC-0. In Public Domain. Gurukul Kangri Collection, Haridwar

Digitized by Arya Samaj Foundation Chennai and eGangotri

Naqui K R, Waldenstrom S and Monk K J 1979 *J. Chem. Phys.* **71** 73
Nath D N and Chowdhury M 1984a *Chem. Phys. Lett.* **109** 13
Nath D N and Chowdhury M 1984b *Indian J. Pure Appl. Phys.* **22** 687
Nath D N, Basu S and Chowdhury M 1986 *J. Indian Chem. Soc.* **63** 56
Nath D N, Basu S and Chowdhury M 1989 *J. Chem. Phys.* (in press)
Newton M and Sutin N 1984 *Annu. Rev. Phys. Chem.* **35** 437
Onsager L 1934 *J. Chem. Phys.* **2** 599
Onsager L 1938 *Phys. Rev.* **54** 554
Petrov N Kh, Sushin A I and Frankevich E L 1981 *Chem. Phys. Lett.* **82** 339
Raaen S and Hemmer P C 1982 *J. Chem. Phys.* **76** 2569
Rzad S J and Bakale G 1973 *J. Chem. Phys.* **59** 2768
Sagdeev R Z, Salikhov K M and Molin Yu N 1977 *Russ. Chem. Rev.* **46** 297
Salikhov K M, Molin Yu N, Sagdeev R Z and Buchachenko A L 1984 *Spin polarization and magnetic effects in radical reactions* (ed.) Yu N Molin (Amsterdam: Elsevier)
Sano H 1983 *J. Chem. Phys.* **78** 4423
Sano H and Baird J K 1982 *J. Chem. Phys.* **77** 6236
Sano H and Tachiya M 1979 *J. Chem. Phys.* **71** 1276
Schulten K and Epstein I R 1979 *J. Chem. Phys.* **71** 309
Schulten Z and Schulten K 1977 *J. Chem. Phys.* **66** 4616
Staerk H, Künhle W, Treichel R and Weller A 1985 *Chem. Phys. Lett.* **118** 19
Steiner U E and Ulrich T 1989 *Chem. Rev.* **89** 51
Tachiya M 1978 *J. Chem. Phys.* **69** 2375
Tachiya M 1979 *J. Chem. Phys.* **70** 238
Turro N J 1983 *Proc. Natl. Acad. Sci., USA* **80** 609
Turro N J and Kraeutler 1980 *Acta Chem. Res.* **13** 369
Waldenstrom S, Naqui K R and Mork K J 1981 *J. Chem. Phys.* **74** 6535
Weller A 1967 *Fast reaction and primary processes in chemical kinetics* (ed.) S Claesson (New York: Wiley-Interscience) p. 413
Werner H J, Schulten Z and Schulten K 1977 *J. Chem. Phys.* **67** 646

CC-0. In Public Domain. Gurukul Kangri Collection, Haridwar

Digitized by Arya Samaj Foundation Chennai and eGangotri

Pramāṇa – J. Phys., Vol. 34, No. 1, January 1990, pp. 67–75. © Printed in India.

Effect of annealing on the opto-electronic properties of $Cu_{0·9}In_{1·0}Se_{2·0}$ films

R P SHARMA, PANKAJ GARG and J C GARG
Department of Physics, University of Rajasthan, Jaipur 302 004, India

MS received 11 November 1988; revised 7 September 1989

Abstract. The influence of annealing on the structure and opto-electronic properties of $Cu_{0·9}In_{1·0}Se_{2·0}$ films prepared by solution growth technique has been studied. The films annealed at 500–520°C in air, vacuum (10^{-4} torr), In-vapour and Se-vapour show polycrystalline chalcopyrite structure with orientation perpendicular to the (220) plane. Films annealed in Se-vapour at 500°C for 30 min have maximum grain size (560 Å), minimum optical energy gap, maximum absorption coefficient, lowest resistivity, maximum photosensitivity and thus are suitable for photovoltaic applications. Annealing in In-vapour or in vacuum changes *p*-type $CuInSe_2$ into *n*-type which possibly arises due to the increase in Se vacancies.

Keywords. Annealing effect; $CuInSe_2$.

PACS Nos 78·65; 73·50.

1. Introduction

$CuInSe_2$ has become an important semiconductor for solar cell applications (Mikelson and Chen 1982; Kazmerski *et al* 1983). The opto-electronic properties of $CuInSe_2$ polycrystalline thin films as well as single crystals have been studied extensively. It is known that chalcopyrite and sphalerite structure of $CuInSe_2$ films depend on the growth conditions of films (Piekoszewski *et al* 1980; Tomlinson *et al* 1980; Gorska *et al* 1980; Bates *et al* 1982). However, films prepared by spray pyrolysis (Dushan *et al* 1986; Mooney and Lamoreaux 1986) and laser irradiations (Laude *et al* 1986) were only single phase chalcopyrite in nature. Recently, Sharma and Garg (1989) studied the structural, optical and electrical properties of non-stoichiometric $CuInSe_2$ films and observed that opto-electronic properties are sensitive to Cu/In ratio and films of ratio equal to 0·9 have chalcopyrite structure, large grain size, low resistivity and high photosensitivity. According to Kazmerski *et al* (1983) the heat treatment of $CuInSe_2$ films in oxygen, nitrogen and argon at 200°C shows an improvement in absorption properties of the films. The effect of air annealing (200°C) on the spectral response of CdS/$CuInSe_2$ thin films solar cells were investigated by Noufi *et al* (1985) and found an increase in efficiency of the cells. Single crystals (Migliorato *et al* 1975; Masse and Redjai 1984) of $CuInSe_2$ were found to be *p*-type when annealed under Se-vapour, whereas crystals annealed under In-vapour or in vacuum were *n*-type. However studies on the post deposition heat treatment of non-stoichiometric films in different ambients are rarely found in the literature and are important both for device optimisation as well as temperature stability of ternary chalcopyrite phase.

In the present paper, we report the results of our investigations on the effect of

CC-0. In Public Domain. Gurukul Kangri Collection, Haridwar

Digitized by Arya Samaj Foundation Chennai and eGangotri

annealing in different ambients on the opto-electronic properties of $Cu_{0\cdot9}In_{1\cdot0}Se_{2\cdot0}$ films.

2. Experimental procedure

The solution growth technique used to deposit non-stoichiometric films of $CuInSe_2$ is described by Garg *et al* (1988). The process involves the reaction of Cu^+ with In^{3+} and Se^{2-} ions in deionized water solution. Elemental selenium (99·95%) is dissolved in an aqueous solution of sodium sulphite (pH > 9) at 90°C to form a partial unstable Na_2SeSO_3 compound. The solution is mixed with tetraamine copper and then added to a solution containing a complex ion of indium and citrate. In the solution, unstable Na_2SeSO_3 yields Se^{2-} and SO_3^{2-} ions. Sulphite ions reduce $Cu(NH_3)_4^{2+}$ and generate Cu^+ ions. The temperature of solution is held at 40°C for about 12 h, and uniform films of $CuInSe_2$ are obtained on glass substrates at 30Å min^{-1}. As deposited films (grown in same batch) were annealed in a vacuum tight chamber at 500–520°C in air, vacuum (10^{-4} torr), indium-vapour and selenium-vapour for 30 min separately, in identical sealed enclosures fitted with digital copper alumel thermocouple to record the temperature. Structural characterization of the films was carried out using XRD technique. The optical transmittance and reflectance of films at various wavelengths were measured using the Hitachi 330 spectrophotometer. The electical properties of the films were determined from d.c. Hall measurements using vander pauw geometry with evaporated indium ohmic contacts. To measure the photosensitivity of the films, current in dark and under illumination was measured by conventional method using digital multimeter (HIL). The temperature was determined by surface thermocouple probe with a digital indicator (HIL) of 1°C accuracy. The resistivity of the annealed films was measured by two probe electrical method.

3. Results and discussion

Figures 1(a) and 1(b) show the X-ray diffraction profile for films of $Cu_{0\cdot9}In_{1\cdot0}Se_{2\cdot0}$ annealed in vacuum, air, In-vapour and Se-vapour respectively. The positions, relative intensities and identifications of the peaks indicate that all the films were polycrystalline and single phase chalcopyrite with the orientation perpendicular to the (220) plane. The lattice constants and grain size estimated from graphs are presented in table 1. The different values of c and a results from the shift of (220) peak and may be attributed to the change in the stoichiometry of films caused by Se deficiency through annealing. It can be seen from the above table that annealed Cu-deficient ($Cu_{0\cdot9}In_{1\cdot0}Se_{2\cdot0}$) films irrespective of annealing ambients, have single phase chalcopyrite structure. Our earlier investigations (Sharma and Garg 1989) show that reduction of Cu: In ratio from one favour the formation of single phase chalcopyrite structure. Further, it is to be noted that films annealed in Se-vapour have maximum grain size. The present results are consistent with those reported by Kazmerski *et al* (1976), Varela *et al* (1985), Pamplin and Feigelson (1979) and Cammy *et al* (1984).

Figure 2 depicts transmittance spectra of samples annealed in air, vacuum, Se-vapour and In-vapour respectively. The observed sharp absorption edge in all the

CC-0. In Public Domain. Gurukul Kangri Collection, Haridwar

Digitized by Arya Samaj Foundation Chennai and eGangotri

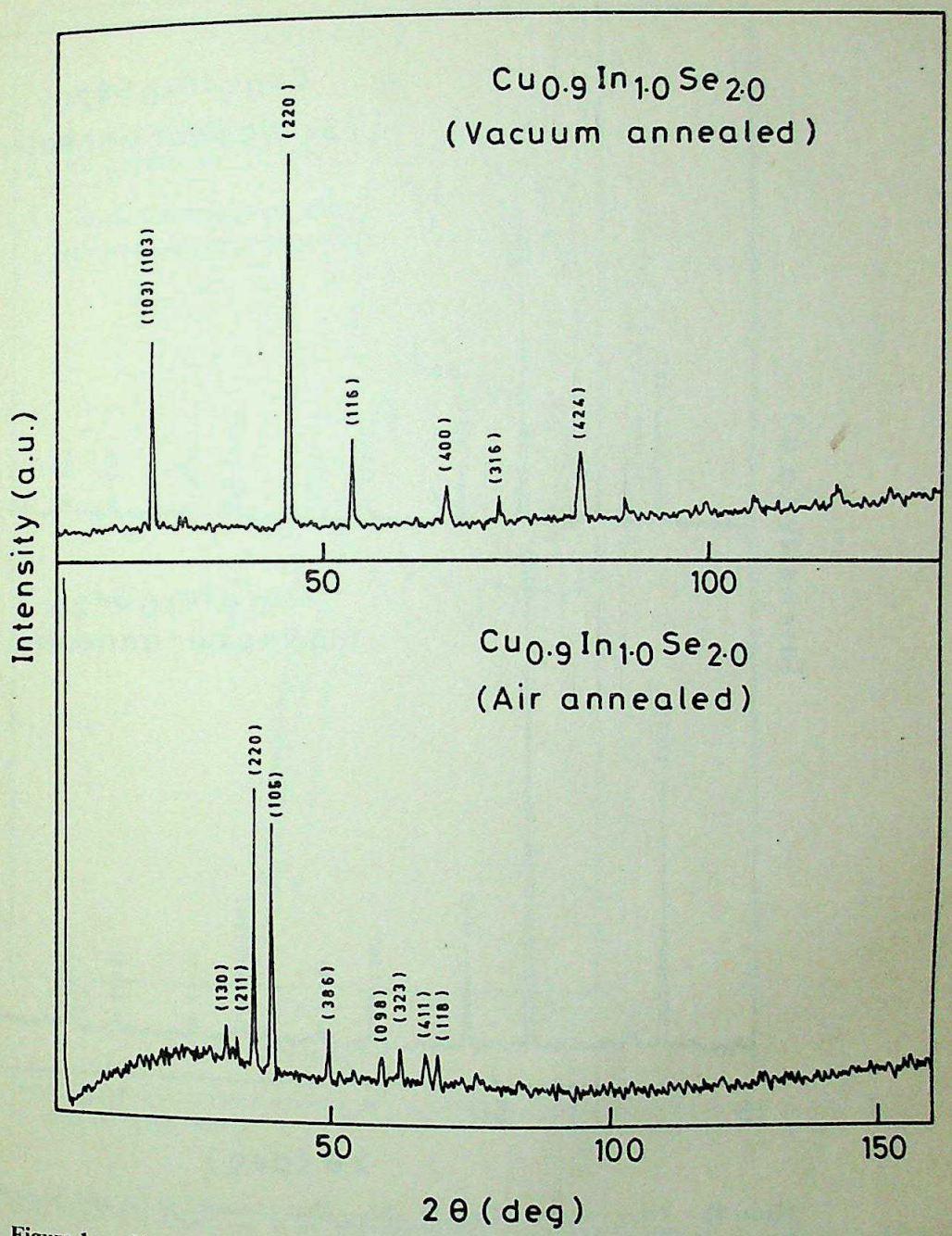

Figure 1a. X-ray pattern of $Cu_{0\cdot9}In_{1\cdot0}Se_{2\cdot0}$ films annealed in air and vacuum.

Table 1. XRD results of Cu_{09} $In_{1\cdot0}$ $Se_{2\cdot0}$ films annealed in different ambients.

Parameters	Vacuum	Air	In-vapour	Se-vapour
a (A°)	5·88	5·74	5·79	5·80
c (A°)	11·77	11·88	11·62	11·20
Grain size (A°)	499·00	502·00	541·00	560·00
Structure	Chalcopyrite	Chalcopyrite	Chalcopyrite	Chalcopyrite

CC-0. In Public Domain. Gurukul Kangri Collection, Haridwar

Digitized by Arya Samaj Foundation Chennai and eGangotri

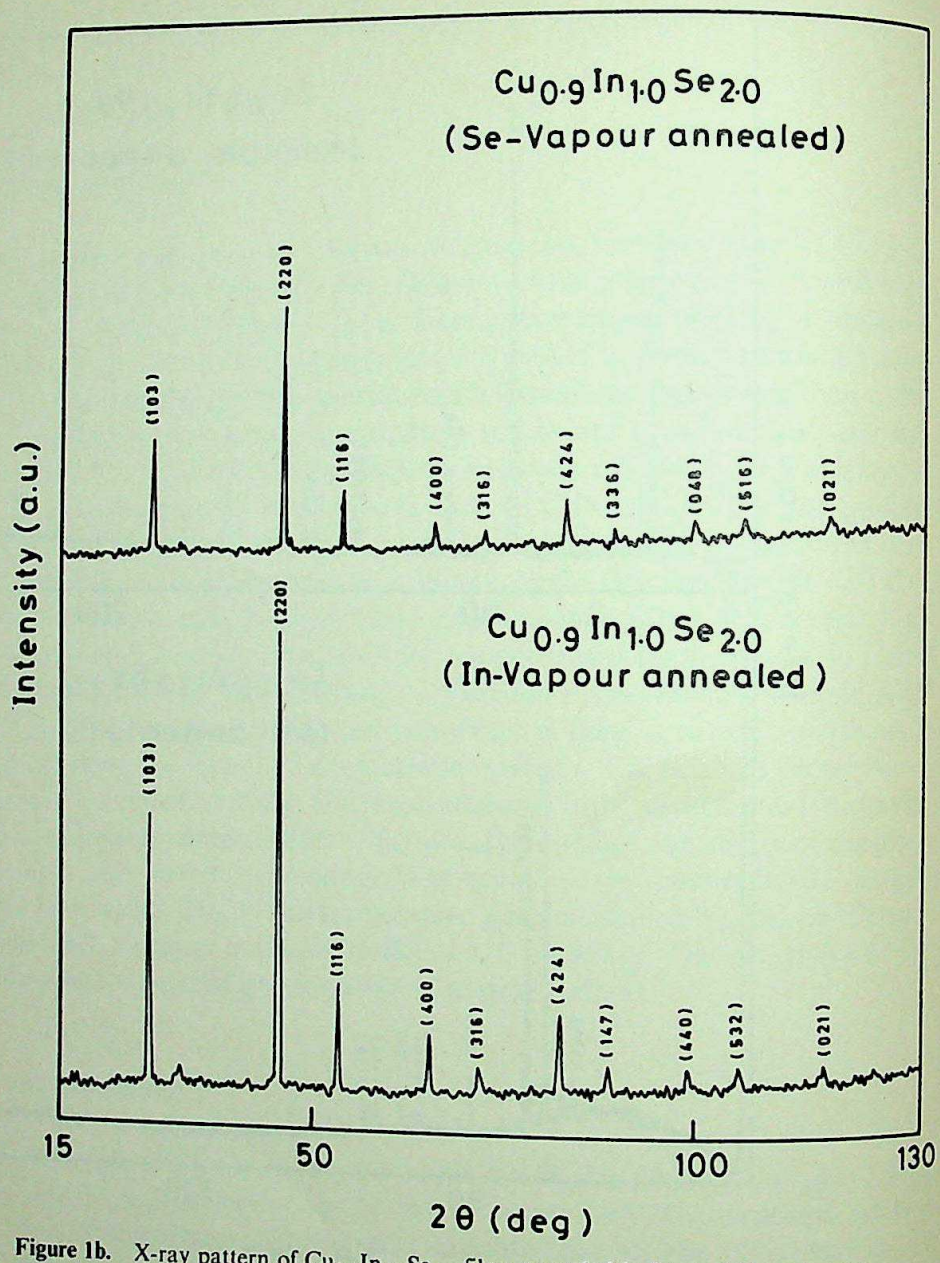

Figure 1b. X-ray pattern of $Cu_{0\cdot9}In_{1\cdot0}Se_{2\cdot0}$ films annealed in In- and Se-vapours.

spectra suggest the presence of direct band gap and single phase. The optical absorption coefficient α of the films has been calculated at various wavelengths from the relation:

$$\alpha = \frac{4\pi K}{\lambda}, \tag{1}$$

where K is the extinction coefficient in the fundamental absorption region and λ is the wavelength in the same region. The value of K at different wavelengths has been computed from observed optical transmittance and reflection spectra and film thickness determined by interferometer technique, following the standard procedure reported by Rastogi and Salcalachen (1982), after applying necessary correction in observed transmission for attenuation by reflection behind the substrate (Berming

CC-0. In Public Domain. Gurukul Kangri Collection, Haridwar

Digitized by Arya Samaj Foundation Chennai and eGangotri

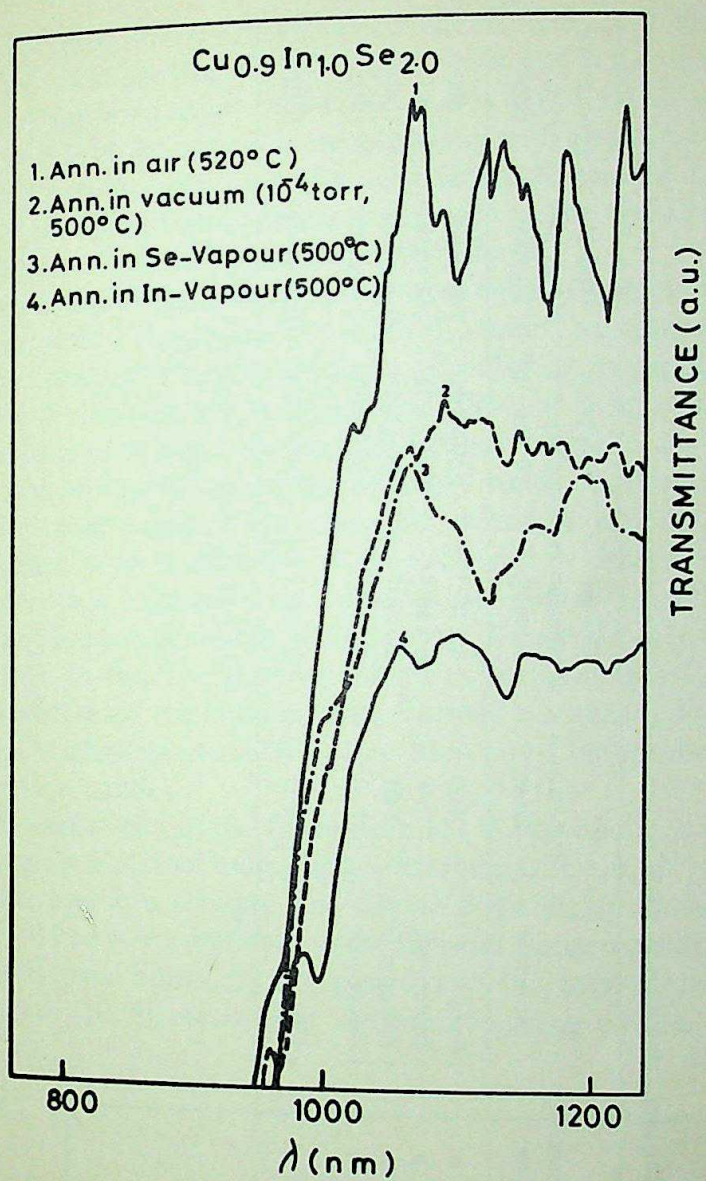

Figure 2. Transmittance spectra of $Cu_{0·9}In_{1·0}Se_{2·0}$ films annealed in air, vacuum, Se-and In-vapours respectively.

1963). The calculated values of α at wavelengths corresponding to absorption edge for films annealed in different ambients only are given in table 2. It can be seen that the films annealed in Se-vapour have highest absorption coefficient in comparison to vacuum and In-vapour annealed films. Since the films annealed in Se-vapour have maximum grain size, one may infer that annealing in Se-vapour results in improvement of the compositional uniformity both across and through polycrystalline thin films. On the other hand heating in vacuum/In-vapour, causes Se desorption near the film surface, causing a related degradation in the film absorptance (Kazmerski *et al* 1983).

The direct transition in a semiconductor is related by the relation:

$$\alpha = A(h\nu)^{-1}(h\nu - Eg)^{1/2}, \tag{2}$$

where A is a constant, $h\nu$ is the photon energy and Eg is the optical band gap of the semiconductor. The band gap Eg of different samples has been deduced from the

CC-0. In Public Domain. Gurukul Kangri Collection, Haridwar

Table 2. Properties of annealed $Cu_{0.9}In_{1.0}Se_{2.0}$ thin films at 300 K.

Annealing ambient	Annealing temperature T_A (°C)	Thickness t (μm)	Conductivity type	Structure	Resistivity ρ (Ω cm)	Carrier concentration h(cm^{-3})	Absorption coefficient α ($10^4\ cm^{-1}$)	Optical energy gap Eg (eV)	Absorption edge λ (nm)
As-deposited	50	2·0	p	Mixed	1600	4×10^{18}	1·25 ± 0·02	1·45 ± 0·02	800
Air	520	1·5	p	Chalcopyrite	500	6×10^{18}	1·30 ± 0·02	1·09 ± 0·02	1040
Se-vapour	500	2·0	p	Chalcopyrite	1·00	8×10^{19}	3·00 ± 0·03	0·96 ± 0·02	1060
In-vapour	500	2·2	n	Chalcopyrite	1·20	7×10^{17}	2·50 ± 0·02	1·14 ± 0·02	1010
Vacuum (10^{-4} torr)	500	1·6	n	Chalcopyrite	5·00	5×10^{17}	2·80 ± 0·02	1·00 ± 0·02	1030

Digitized by Arya Samaj Foundation Chennai and eGangotri

CC-0. In Public Domain. Gurukul Kangri Collection, Haridwar

Digitized by Arya Samaj Foundation Chennai and eGangotri

intercepts obtained after extrapolation of the straightline section of $(\alpha h\nu)^2$ vs $h\nu$ curve. A curve $(\alpha h\nu)^2$ vs $h\nu$ for $Cu_{0\cdot9}In_{1\cdot0}Se_{2\cdot0}$ film annealed in Se-vapour is shown in figure 3 which is the representative of all the curves obtained in the present study. The calculated values of the optical band gap along with annealing ambients are presented in table 2. It is to be seen that film annealed in Se-vapour has lowest optical band gap and is a manifestation of better grain size i.e., improvement in the compositional uniformity of the film surface as suggested above.

The dependence of electronic properties of the films on the annealing ambients are presented in table 2. It can be seen from the table that films annealed in Se–vapour have *p*-type conductivity whereas films annealed in In-vapour-vacuum have *n*-type conductivity. Following Masse and Redjai (1984), the annealing in Se-vapour induces the disappearing of defects involving Se-vacancy, increases the concentration of cation vacancies and interstitial Se atoms, and may reduce the concentration of interstitial cations. The large conductivity observed in our Se-vapour annealed samples may therefore result from a decrease of Se-vacancies or interstitial cations or from an increase of cation vacancies or interstial Se atoms. Since interstitial cations are unstable, they are less probable in the process. Annealing in In-vapour/vacuum results in an increase in the Se-vacancies which in turn changes $CuInSe_2$ from *p*-type to *n*-type and decreases the conductivity. Further our results are consistent with those reported by Migliorata *et al* (1975), and Shih and Champness (1984) in single crystal stoichiometric $CuInSe_2$.

The photosensitivity of the films annealed in Se-vapour, is found to be maximum. Figure 4 depicts a plot of long photosensitivity(*s*) versus $10^3/T$ of the films annealed in Se-vapour and is a straight line whose slope yields a thermal activation energy $Ea = 0{\cdot}33 \pm 0{\cdot}01$ eV. To understand the thermal assisted conduction in polycrystalline $CuInSe_2$ films grain boundary trapping theory has been proposed by Seto (1975) and Baccarani *et al* (1978). According to them, trapping centres at the grain boundary

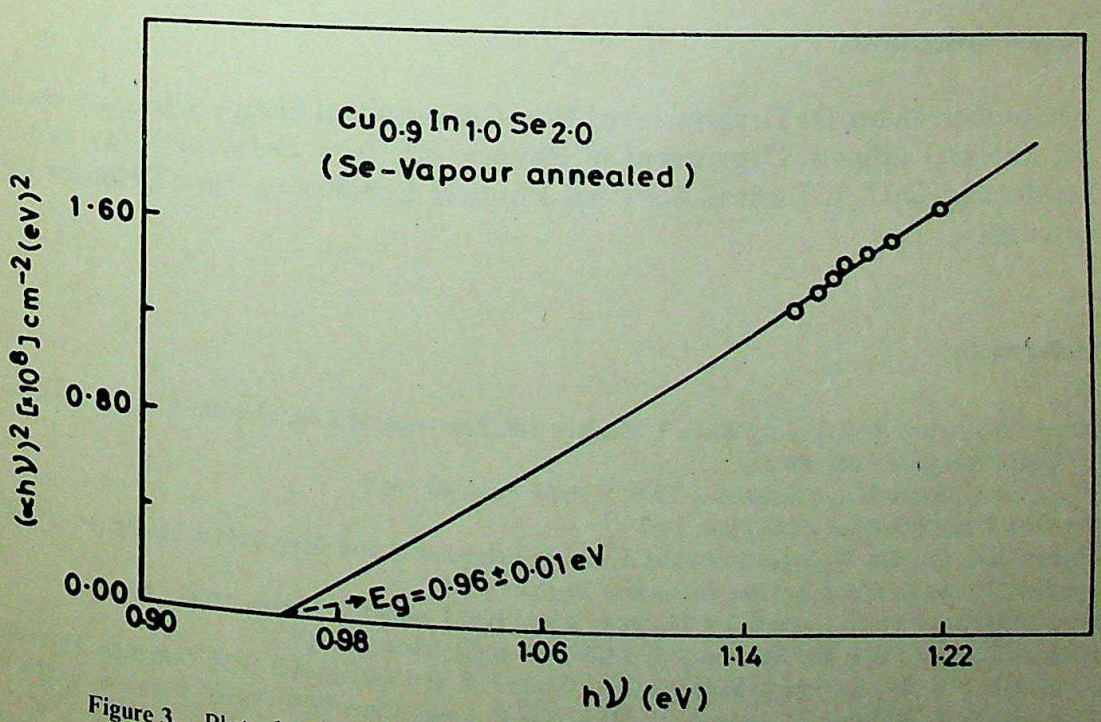

Figure 3. Plot of $(\alpha h\nu)^2$ versus $h\nu$ for $Cu_{0\cdot9}In_{1\cdot0}Se_{2\cdot0}$ film annealed in Se-vapour.

CC-0. In Public Domain. Gurukul Kangri Collection, Haridwar

Digitized by Arya Samaj Foundation Chennai and eGangotri

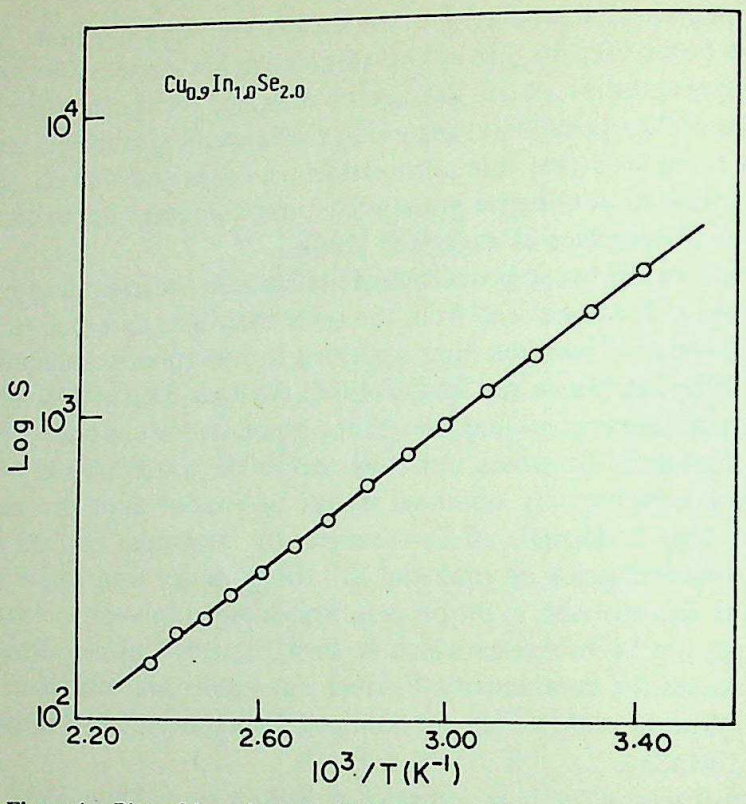

Figure 4. Plot of log photosensitivity versus $10^3/T$ for $Cu_{0.9}In_{1.0}Se_{2.0}$ film annealed in Se-vapour.

capture free carriers and these charged centres create barriers and carrier transport is influenced by these barriers.

Acknowledgements

The authors thank the Department of Non-Conventional Energy Sources, New Delhi, for financial support, Department of Physics, IIT, New Delhi for X-ray diffraction results and Dr A C Rastogi, National Physical Laboratory, New Delhi for helpful discussion.

References

Bates C W, Nelson Jr K F, Atig, Raza S, Mooney J B, Recktenwald J M, Macintash L and Lamoreaux R 1982 *Thin Solid Films* **88** 279

Baccarani G, Ricco B and Spadini G 1978 *J. Appl. Phys.* **49** 5565

Berming P H 1963 *Phys. Thin Films* **1** 69

Cammy R A, Clayton W, Bates Jr, Anaba A, Anani, Belgacem H and Greg S 1984 *Appl. Phys. Lett.* **45** 890

Dushan, Zhao and Guomin 1986 *Taijannerg Xuebao* **7** 114

Gorska M, Beaulieu R, Loferski J J, Roesscer B and Bell J 1980 *Sol. Energy Mater.* **2** 343

Garg J C, Sharma R P and Sharma K C 1988 *Thin Solid Films* **164** 269

Kazmerski L L, Ayyagari M S, Sanborn G A, White F R and Merrill A J 1976 *Thin Solid Films* **37** 323

Kazmerski L L, Hallendt M, Ireland J J, Mickelson R A and Chen W S 1983 *J. Vacsci Sci. Tech.* **2** 395

Laude L D, Joliet M C and Antoniadise 1986 *Sol. Cell.* **16 (1–4)** 199

CC-0. In Public Domain. Gurukul Kangri Collection, Haridwar

Digitized by Arya Samaj Foundation Chennai and eGangotri

Masse G and Redjai E 1984 *J. Appl. Phys.* **56** 1154
Migliorato P, Shay J L, Kasper H M and Wagner S 1975 *J. Appl. Phys.* **46** 1777
Mickelson R A and Chen W S 1982 in *Proc. 15th IEEE Photovoltaic Special Conference* San Deigo, New York pp. 800
Mooney J B and Lamoreaux R 1986 *Sol. Cell.* **16 (1–4)** 211
Noufi R, Souza, Oster P and Wald C 1985 *Sol. Cell.* **15(1)** 87
Piekoszewski J, Loferski J J, Beaulieu R, Beal J, Rocessler B, and Shew Chum 1980 *J. Sol. Energy Mater.* **2** 363
Pamplin B and Figelson 1979 *Thin Solid Films* **60** 141
Rastogi A C and Salkalachen S 1982 *Thin Solid Films* **97** 191
Seto J Y W 1975 *J. Appl. Phys.* **46** 5247
Sharma R P and Garg J C 1989 *Indian J. Pure Appl. Phys.* (in press)
Shih I and Champness C H 1984 in *Proc. III Int. Symp. on industrial uses of Se and Te*, Stockholm, Sweden, p. 388
Tomlinson R D, Armour D G, Hill A E, Samaan A and Abdul Hussien N A K 1980 *Jpn. J. Appl. Phys.* **19(19–3)** 15
Varela M, Bertran E, Esteve J and Morenza J L 1985 *Thin Solid Films* **130** 155

CC-0. In Public Domain. Gurukul Kangri Collection, Haridwar

Digitized by Arya Samaj Foundation Chennai and eGangotri

CC-0. In Public Domain. Gurukul Kangri Collection, Haridwar

Digitized by Arya Samaj Foundation Chennai and eGangotri

Pramāṇa – J. Phys., Vol. 34, No. 1, January 1990, pp. 77–83. © Printed in India.

Time-resolved spectra of coumarin 30-rhodamine 6G dye mixture

R D SINGH, D MOHAN, A K SHARMA and N V UNNIKRISHNAN*
Department of Physics, Maharshi Dayanand University, Rohtak 124001, India
*Department of Material Science, Mahatma Gandhi University, Kottayam 686562, India

MS received 9 March 1989; revised 30 September 1989

Abstract. The effect of acceptor concentration on the energy transfer from Coumarin 30 (donor) to Rhodamine 6G (acceptor) has been studied. The nature of energy transfer reaction has been studied through lifetime measurements by recording the time-resolved fluorescence decay curves. The energy transfer parameters calculated were used to confirm the occurrence of energy transfer on the basis of the emission-reabsorption effect.

Keywords. Time-resolved spectra; energy transfer; fluorescence; Coumarin-Rhodamine mixture.

PACS No. 42·55

1. Introduction

Excitation transfer in laser dye mixtures has earlier been used to achieve better dye laser performance at the desired wavelengths (Morey 1972; Drake *et al* 1972; Cox and Matise 1980; Berlman *et al* 1973). The mechanism responsible for the intermolecular singlet-singlet electronic energy transfer in dye mixture can be directly determined by lifetime measurements. The studies so far reported in this field have been based on the indirect method of optical gain studies. We have studied the energy transfer mechanism in coumarin 30-rhodamine 6G (C 30-Rh 6G) dye mixture in ethanol by using a laser fluorimeter developed in the laboratory. The dependence of lifetime on dye concentration of the two dye molecules C 30 and Rh 6G in alcoholic solutions of methanol and ethanol, and ethylene glycol has also been studied. An attempt was also made to study the energy transfer mechanism in ethylene glycol, but it was not found to be a good solvent due to the Cage effect (Turro 1967).

The fluorescence lifetime studies in nanosecond range are commonly performed by phase-shift measurements, mode-locked laser systems or single-photon counting technique. Of these methods, the phase-shift measurements provide good speed and accuracy, but offer limited capabilities for the resolution of multiple components. The mode-locked laser systems provide good time resolution in picosecond range, but suffer from poor signal-to-noise ratio. The photon-counting system, on the other hand, operate with excellent signal-to-noise ratio, a wide dynamic range of time, and picosecond lifetime measurement capabilities. A brief account of the single-photon counting system used in the present investigation is shown in figure 1, the details of which have been reported earlier (Bhatti *et al* 1985).

CC-0. In Public Domain. Gurukul Kangri Collection, Haridwar

Digitized by Arya Samaj Foundation Chennai and eGangotri

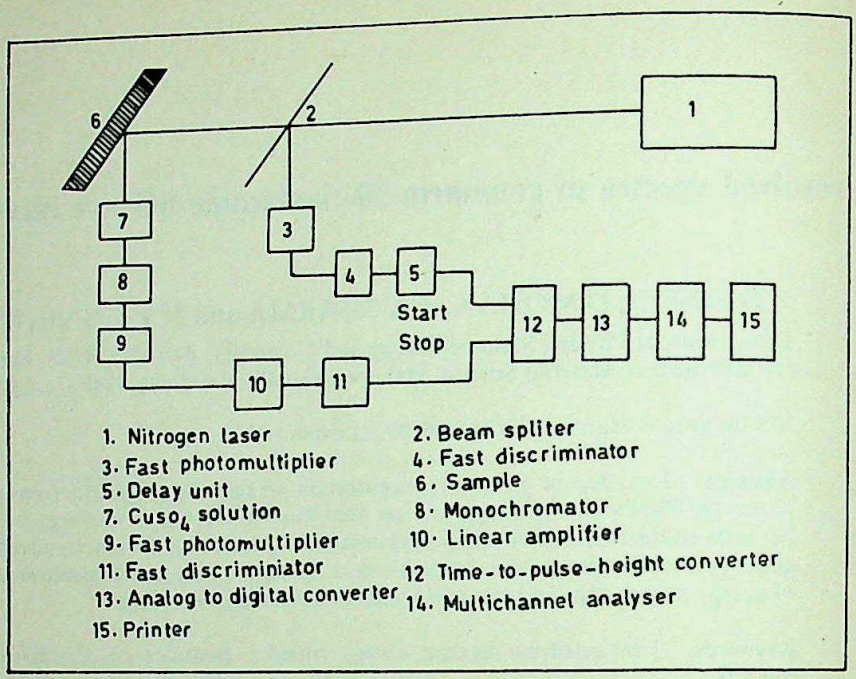

Figure 1. Laser fluorimetric system for subnanosecond life time measurements.

2. Experimental details

The system consists of a pulsed N_2 laser (CEL model NL 103), which delivers pulses of 200 kW peak power and 10 ns duration, and a time-correlated single-photon counting electronics. The output of the N_2-laser is divided into two parts by a beam splitter. One of it is used to excite the sample and the other is used as a reference pulse in the start channel. The fluorescence emission from the sample is directed on to the slit of the monochromator and the signal coming out of it is detected by a fast photomultiplier (Phillips XP 2020). A cuvette of $CuSO_4$ solution inserted between the sample and the monochromator absorbs the scattered and reflected ultraviolet laser radiation. The long optical path of the fluorescent radiation through the glass optics of the monochromator further reduces the presence of the UV radiation, if any. The output signal of the photomultiplier is suitably amplified, discriminated and then delivered to the TPHC as a stop pulse.

The other part of the laser beam divided by the beam splitter is used to illuminate the photocathode of a photomultiplier identical to the one used in the stop channel. The signal from this photomultiplier tube, after discrimination is fed to the start input of the time-to-pulse height converter (TPHC) via a nanosecond delay unit. The TPHC produces an output pulse with a height proportional to the time interval between the start and the subsequent stop pulse. The analog output of the TPHC is converted into digital form by analog-to-digital converter (ADC). The multichannel analyser accumulates the data from ADC and its display on the MCA screen shows a histogram of the accumulated counts (as ordinate) and time (as abscissa), which is equivalent to the fluorescence decay curve. To accurately interpret the decay curve from the data, the time axis of the MCA is calibrated from the shifts produced in the signal peak due to a known delay introduced in the start channel. With the system in the normal mode (TPHC started with reference pulses and stopped with fluorescence

CC-0. In Public Domain. Gurukul Kangri Collection, Haridwar

Digitized by Arya Samaj Foundation Chennai and eGangotri

pulses), the limited effects to the data collection rate are the reset time of the TPHC and the conversion time of the electronics consisting of TPHC, ADC and MCA. The interchange of start and stop pulses (reverse mode) as proposed by Hagen *et al* (1970) proved to be advantageous in the present case, as the data accumulation time decreased appreciably. In this mode, the data collection rate is limited only by the percentage of data loss. Also the maximum starting rate is no longer limited by the reset time of the TPHC, ADC and MCA. The possible disadvantage of operation in this mode is the reversal of time scale of MCA. Also some experience of inserting the delay in the stop channel is needed.

In general, the probability of multiphoton events is very low in both these cases (normal as well as reverse modes). This is accomplished by attenuating the light intensity reaching the photomultipliers, so that these events are extremely rare. However, the limited rate of data collection associated with this approach increases the time required to record the spectrum. The precision of measurements in single photon counting technique, on the other hand, is determined by the data collection rate. Therefore, the attenuation had to be optimized in the present case. Further, to reduce the error caused by multiple photon events, the rate of photon being counted should be about 10% of the experimental repetition rate. Under these circumstances the probability of observing two photons in a single experiment is only 5%. Since the N_2-laser has a large photon flux, the data collection rate of 10% could very easily be achieved by reducing the excitation intensity even for samples having considerably low quantum yield.

3. Results and discussion

The results of the lifetime measurements are summarized in figure 2 for pure Rh 6G and in figure 3 for pure C 30 solutions. The behaviour of lifetime at lower concentration is probably due to the effect of radiation trapping, i.e., the self-absorption reemission, which tends to enhance the lifetime. After attaining the maximum, the value of lifetime starts decreasing in all cases because of concentration quenching. In Rh 6G in ethylene glycol and methanolic solutions, the peak position is shifted towards lower concentration side vis-a-vis ethanolic solutions. This can be understood in terms of the solvent effect reported by Masilamani and Sivaram (1982) and Ramakrishnan *et al* (1980). Another interesting feature of these curves is the slight increase in lifetime values at higher concentration of 10^{-2} M using ethylene glycol and methanol. This may be attributed to the formation of excimers at higher concentration. Such an increase in lifetime values at higher concentration has not been reported earlier, perhaps because lifetime studies in dye solutions made so far were primarily dependent on the indirect method of change in optical gain values with concentration. It has been studied by Arbeloa *et al* (1988) that the fluorescence quantum yield of Rh 6G decreases in concentrated ethanolic solutions where aggregates are present. They suggested that the fluorescence yield depends upon the degree of aggregation of molecules in the excited state and the excitation energy migrates between the monomers until it arrives at an aggregate that acts as an energy trap. The formation of non-fluorescent aggregates of Rh 6G has also been expected by Terada and Muto (1986) in their investigation. Thus, the increase in lifetime and the reduction in fluorescence yield at higher concentration can be understood by studying the rate of formation of exciplexs

CC-0. In Public Domain. Gurukul Kangri Collection, Haridwar

Digitized by Arya Samaj Foundation Chennai and eGangotri

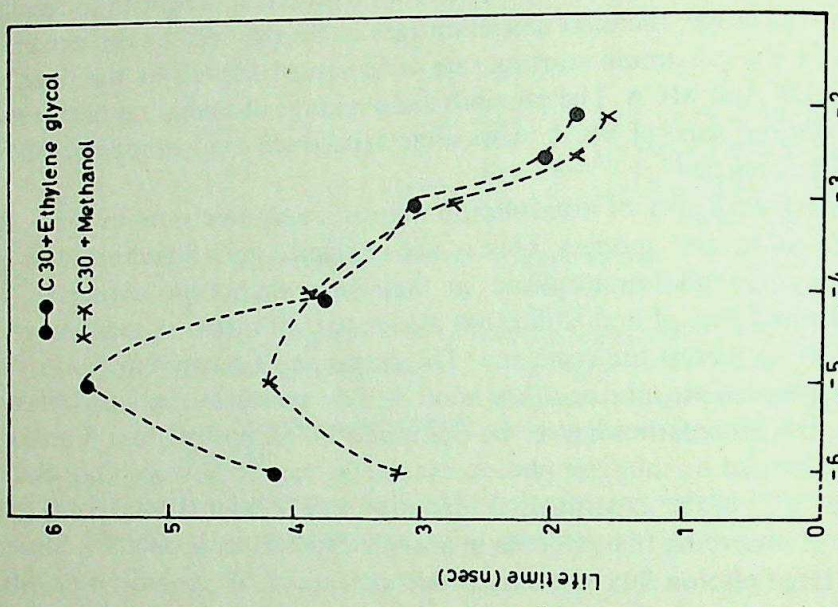

Figure 3. Concentration dependence of fluorescence life time of C 30 in methanol and ethylene glycol.

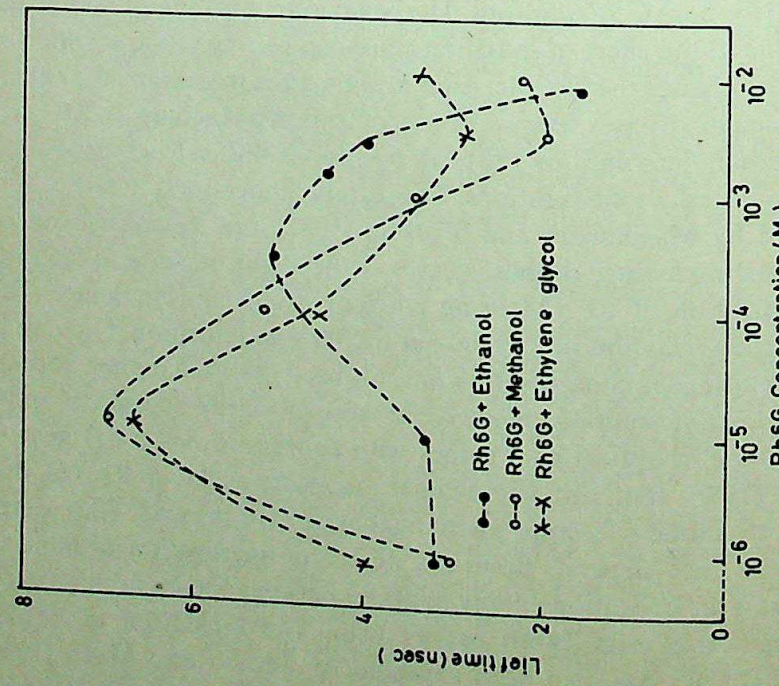

Figure 2. Concentration dependence of fluorescence life time of Rh 6G in ethanol, methanol and ethylene glycol.

CC-0. In Public Domain. Gurukul Kangri Collection, Haridwar

Digitized by Arya Samaj Foundation Chennai and eGangotri

as well as extent of monomer-aggregates energy transfer. Another possible explanation for the increase in lifetime values at higher concentration could be due to intersystem crossing, photoquenching (Speiser *et al* 1973; Speiser 1974; Speiser and Bromberg 1975; Speiser and Katraro 1978) or internal conversion. Of these, the first one does not seem to play an important role because it leads to a change in lifetime values by several orders of magnitude. The second one, which is different from bleaching effect as discussed by Speiser *et al* (1973) produces a large reduction in the magnitude of the output signal. The possibility of intersystem crossing as discussed by Atkinson, which becomes important at higher concentration cannot, however, be ruled out as the frequency of the pumping beam is quite high in comparison to that of the fluorescent signal. Atkinson *et al* (1974) have also argued in favour of internal conversion taking place at higher concentration. Urisu and Kajiyama (1976), while studying the dependence of peak gain on the concentration of Rh 6G have also reported an abnormal behaviour when the concentration reaches 10^{-2} M or more, without assigning any reason for it.

The experimentally obtained lifetime values of C 30 as donor (1×10^{-3} M) with varying concentration of Rh 6G as acceptor have been presented in table 1. The study shows significant change from τ_{f0} the measured lifetime of C 30 in the absence of Rh 6G, only when the acceptor concentrations become relatively high. At lower acceptor concentrations ($\sim 10^{-6}$ M), the change from τ_{f0} is very small indicating the dominance of radiative type energy transfer in this mixture (table 1). This result agrees with the prediction that at low acceptor concentration radiative transfer (trivial process) is the main process and the probability of non-radiative transfer (Forster type) is very small.

To evaluate the energy transfer parameters, the measured lifetimes from table 1 were fitted to the Stern–Volmer equation (Turro 1967)

$$1/\tau_f = K_{D\,A}[A] + 1/\tau_{f0} \tag{1}$$

where τ_f is the donor lifetime in the presence of the acceptor, $[A]$ is the acceptor concentration and $K_{D\,A}$ is the excitation transfer rate.

Figure 4 presents a plot of τ_f^{-1} versus Rh 6G concentration. The plot is linear in nature apparently obeying the Stern–Volmer expression for bimolecular quenching. It also gives an evidence of the fact that there is a competition between a bimolecular process of energy transfer and a unimolecular process of fluorescence. The critical

Table 1. Variation in the donor lifetime with the acceptor concentration in ethanolic solutions for fixed donor concentration (1×10^{-3} M).

Acceptor concentration (M)	Donor lifetime (ns)	$1/\tau_f$ ($\times 10^9 s^{-1}$)
0	$6{\cdot}92 \rightarrow \tau_{f0}$	–
1×10^{-6}	$5{\cdot}50 \rightarrow \tau_f$	0·18
5×10^{-6}	$5{\cdot}02 \rightarrow \tau_f$	0·20
1×10^{-5}	$4{\cdot}62 \rightarrow \tau_f$	0·22
5×10^{-5}	$4{\cdot}01 \rightarrow \tau_f$	0·25
1×10^{-4}	$3{\cdot}61 \rightarrow \tau_f$	0·28
3×10^{-4}	$3{\cdot}49 \rightarrow \tau_f$	0·29

CC-0. In Public Domain. Gurukul Kangri Collection, Haridwar

Digitized by Arya Samaj Foundation Chennai and eGangotri

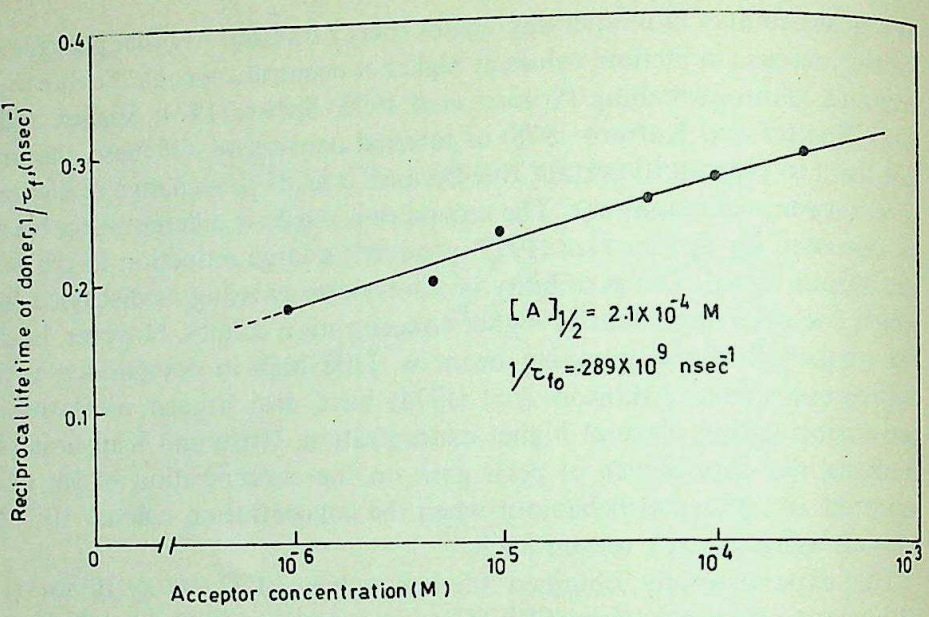

Figure 4. Stern Volmer Plot for C 30–Rh 6G dye mixture in ethanol.

separation, R_0, of donor and acceptor molecules for which the energy transfer from excited donor (D^*) to acceptor (A) and the emission from excited donor are equally probable, can be calculated from the expression

$$R_0 = \{3000/4N[A]_{1/2}\}^{1/3} = 7{\cdot}35/\{[A]_{1/2}\}^{1/3} \tag{2}$$

where $[A]_{1/2}$ is the "half quenching concentration" at which $\tau_f = \frac{1}{2}\tau_{f0}$ and N is the Avogadro's number. Using figure 4 the value of $[A]_{1/2}$ was found to be $2{\cdot}1 \times 10^{-4}$ M. This corresponds to an average of one molecule of the acceptor in a sphere with radius R_0 having excited donor at the centre.

On the basis of the method described above, the values of $K_{D\,A}$ and R_0 were $0{\cdot}68 \times 10^{12}\,S^{-1}$ and 124 Å respectively. The value of $K_{D\,A}$ is much larger than those for collisional transfer. Also the value of R_0 is larger as compared to that of collisional transfer where R_0 values are reported to be in the range 1–10 Å. Similarly it is larger compared to that for resonance transfer where it ranges from 10–90 Å. Thus the present value is typical of the so-called trivial mechanism (emission-reabsorption effect) characterized by critical distance of the order of several angstroms. The results, however, agree with those obtained by Urisu and Kajiyama (1976) using optical gain studies. The results indicate that the energy transfer processes between unlike molecules can be studied by lifetime measurements. However, the reliability of the experimental data, depends largely on the sensitivity and accuracy of the detection system. In the present case, since the accuracy of the laser fluorimeter is in the subnanosecond range and the donor lifetimes are in the nanosecond range, τ_{f0} and $K_{D\,A}$ have been obtained much more accurately.

Acknowledgement

The work was supported by a grant from CSIR, New Delhi.

CC-0. In Public Domain. Gurukul Kangri Collection, Haridwar

Digitized by Arya Samaj Foundation Chennai and eGangotri

References

Arbeloa Lopez F, Ojeda Ruiz P and Arbeloa Lopez I 1988 *J. Photochem. Photobiol.* **45** 313
Atkinson G H, Parmenter C S and Scheyler M W 1974 *Creation and detection of the excited state* (ed.) W R Ware. (New York: Marcel Dekker Inc.) Vol. 3, p. 72
Berlman I B, Rokni H and Goldshmidt C R 1973 *Chem. Phys. Lett.* **22** 458
Bhatti H S, Unnikrishnan N V and Singh R D 1985 *Indian J. Pure Appl. Phys.* **23** 42
Cox A J and Matise B K 1980 *Chem. Phys. Lett.* **76** 125
Drake J M, Ton E M and Morse R I 1972 *IEEE J. Quantum Electron.* **QE-8** 92
Hagen G R, Wallin B W and Tytle F E 1970 *Rev. Sci. Instrum.* **50** 64
Masilamani V and Sivaram B M 1982 *J. Lumin.* 147
Morey W W 1972 *IEEE J. Quantum Electron.* **QE-8** 818
Ramakrishnan P, Sivaram B M and Srinivasan M 1980 *Indian J. Phys.* **B54** 52
Speiser S, van der Werf R and Komman deur J 1973 *Chem. Phys.* **1** 297
Speiser S 1974 *Chem. Phys.* **6** 479
Speiser S and Bromberg A 1975 *Chem. Phys.* **9** 191
Speiser S and Katraro R 1978 *Opt. Commun.* **27** 287
Terada M and Muto J 1986 *Opt. Commun.* **59** 199
Turro N J 1967 *Molecular photochemistry* (New York: Benjamin) p. 95
Urisu T and Kajiyama K 1976 *J. Appl. Phys.* **47** 3559

CC-0. In Public Domain. Gurukul Kangri Collection, Haridwar

Digitized by Arya Samaj Foundation Chennai and eGangotri

CC-0. In Public Domain. Gurukul Kangri Collection, Haridwar

Digitized by Arya Samaj Foundation Chennai and eGangotri

Pramāṇa – J. Phys., Vol. 34, No. 1, January 1990, pp. 85–86. © Printed in India.

Comment on a solution of Altarelli Parisi equations

D K CHOUDHURY and A SAIKIA
Department of Physics, University of Gauhati, Guwahati 781 014, India

MS received 27 September 1989

Abstract. We show that the assumptions of factorizability of the structure function $F(x,t)$ in x and t and the equality of t evolution of the singlet and gluon distributions are not necessary to obtain the approximate solutions of Altarelli–Parisi equations derived by us recently.

Keywords. Structure function; Altarelli–Parisi equations.

PACS No. 12·35

In a recent paper (Choudhury and Saikia 1989), we have shown that the Altarelli–Parisi (AP) equations (Altarelli and Parisi 1977) can be recasted as

$$\frac{\partial F_2^{NS}}{\partial t}(x,t) = \frac{4}{25t}\Bigg[(3+4\ln(1-x))F_2^{NS}(x,t) + 2\int_x^1 \frac{dw}{(1-w)}\{(1+w^2)F_2^{NS}(x/w,t) - 2F_2^{NS}(x,t)\}\Bigg] \tag{1}$$

and

$$\frac{\partial F_2^{S}}{\partial t}(x,t) = \frac{4}{25t}\Bigg[(3+4\ln(1-x))F_2^{S}(x,t) + 2\int_x^1 \frac{dw}{(1-w)}\{(1+w^2)F_2^{s}(x/w,t) - 2F_2^{S}(x,t)\} + 6\int_x^1 (w^2+(1-w)^2)G(x/w,t)dw\Bigg] \tag{2}$$

where we considered the number of flavours to be four and $t = \ln Q^2/\Lambda^2$.

Let us consider the trial solutions of (1) and (2) to be

$$F_2^{NS}(x,t) = F_2^{NS}(x,t_0)\left(\frac{t}{t_0}\right)^{\beta(x)} \tag{3}$$

and

$$F_2^{S}(x,t) = F_2^{S}(x,t_0)\left(\frac{t}{t_0}\right)^{\gamma(x)} \tag{4}$$

respectively. Here $t_0 = \ln Q_0^2/\Lambda^2$ and $\beta(x)$ and $\gamma(x)$ are some functions of x only.

CC-0. In Public Domain. Gurukul Kangri Collection, Haridwar

Digitized by Arya Samaj Foundation Chennai and eGangotri

Putting (3) in (1), we obtain

$$\beta(x)F_2^{NS}(x,t) = \frac{4}{25}\Bigg[(3+4\ln(1-x))F_2^{NS}(x,t) + 2\int_x^1 \frac{dw}{(1-w)}\{(1+w^2)F_2^{NS}(x/w,t) - 2F_2^{NS}(x,t)\}\Bigg]$$

or,

$$\left[\frac{25}{4}\beta(x) - (3+4\ln(1-x))\right]F_2^{NS}(x,t) = 2\int_x^1 \frac{dw}{(1-w)}\{(1+w^2)F_2^{NS}(x/w,t) - 2F_2^{NS}(x,t)\}. \tag{5}$$

Solving the above equation, at $t = t_0$ we obtain

$$\beta(x) = \frac{4}{25}\left[2\int_x^1 \frac{dw}{(1-w)}\left\{(1+w^2)\frac{F_2^{NS}(x/w)}{F_2^{NS}(x)} - 2\right\} + 3 + 4\ln(1-x)\right] \tag{6}$$

where $F_2^{NS}(x) = F_2^{NS}(x,t_0)$.

The integral which occurred in (6) is same as $I^{NS}(x)$ defined in (18) of our previous work (Choudhury and Saikia 1989)

$$\beta(x) = \tfrac{4}{25}[3 + 4\ln(1-x) + 2I^{NS}(x)]$$

which is nothing but $H^{NS}(x)$ of our previous work (eq(26)).

Similarly, putting (4) in (2), we can show that $\gamma(x)$ is equal to $H^S(x)$ of the previous work (eq (27)).

Hence, without assuming (12), (13), (14), (17) of the previous work we arrive at the same result, considering $\beta(x)$ and $\gamma(x)$ to be dependent on x only. Thus neither the factorizability of the structure function nor the equal rate of t-evolution of the singlet and gluon distributions is necessary to derive our previous result. We however note that the trial solutions (3) and (4) are valid only in leading logarithmic approximation (LLA) but not with higher order effects. With such effects, $\beta(x)$ and $\gamma(x)$ should have t-dependence as well.

One of us (DKC) acknowledges the receipt of the Thawani Research Fellowship of the Assam Science society.

References

Choudhury D K and Saikia A 1989 *Pramana – J. Phys.* **33** 359
Altarelli G and Parisi G 1977 *Nucl. Phys.* **B126** 298

CC-0: In Public Domain. Gurukul Kangri Collection, Haridwar

Digitized by Arya Samaj Foundation Chennai and eGangotri

Pramāṇa – J. Phys., Vol. 34, No. 1, January 1990, pp. 87–90. © Printed in India.

High energy elastic $e^+ - O_2$ scattering

K N JOSHIPURA and S MOHANAN
Department of Physics, Sardar Patel University, Vallabh Vidyanagar 388 120, India

MS received 14 August 1989; revised 20 November 1989

Abstract. Theoretical differential cross-sections are obtained for the elastic scattering of fast ($E_i \geq 200$ eV) positrons by oxygen molecules. Employing the independent atom model, the atomic scattering amplitudes are calculated with the (static + polarization) model potentials, in the partial wave analysis (PWA). Comparisons made with the theory and experiments on the incident electrons, show significant differences at small angles.

Keywords. Positron scattering; static potential; polarization potentials; partial waves.

PACS No. 34·80

1. Introduction

This paper is an addendum to the previous paper on $e^- - O_2$ scattering (Joshipura 1989, to be referred to as paper I). There have been recent experiments on inelastic collisions of positrons with oxygen molecules (e.g. Katayama *et al* 1987), but there are hardly any data on elastic $e^+ - O_2$ scattering, especially at intermediate and high energies. With positrons of intermediate and high energies, whereas the positronium formation may be ignored, considerable differences compared to electron scattering are still expected. The nature and extent of these differences, depend on the projectile energy for a particular target, hence the present investigation. The calculations of paper I are refined presently in two ways viz., by choosing an improved atomic static potential and by employing a better partial wave treatment of the long range polarization potential. Comparisons of our positron results are made with theory and experiments on incident electrons.

2. Theoretical calculations

Concentrating on the problem of positron scattering by atomic oxygen, we write the total interaction as a sum of static and polarization potentials, i.e.

$$V(r, k_i) = V_{st}(r) + V_{pol}(r, k_i). \tag{1}$$

The first term of (1) is obtained following Salvat *et al* (1987), who have calculated and parametrized the Dirac-Hartree-Fock-Slater screening functions for neutral atoms from $Z = 1$ to 92. Thus, we have,

$$V_{st}(r) = \frac{8}{r}[0{\cdot}0625 \exp(-14{\cdot}823r) + 0{\cdot}9375 \exp(-2{\cdot}0403r)]. \tag{2}$$

CC-0. In Public Domain. Gurukul Kangri Collection, Haridwar

Digitized by Arya Samaj Foundation Chennai and eGangotri

The polarization potential is the same as in paper I. We may add here that, if the incident particles are electrons, a term V_{ex} corresponding to the exchange effect must be added in (1). Now, with the optical potential described heretofore, the Schrödinger scattering equation is solved numerically to obtain phase-shifts δ_l in the partial wave analysis (PWA). For the long range polarization potential the first few phase-shifts ($l \sim 10$) are determined through the Numerov method for the scattering solution and the higher partial wave phase-shifts are obtained analytically, following the Born approximations calculated by Wadehra (1986). After having obtained the partial wave scattering amplitudes for positrons incident on oxygen atoms, the independent atom model (see paper I) is employed to calculate the DCS of e^+–O_2 scattering.

3. Results and discussion

Though our aim is to obtain the DCS of positrons on O_2 molecules, we have also calculated the same for incident electrons, to afford comparison. We have exhibited in figures 1 and 2 the e^+ and e^- DCS at 200 and 500 eV respectively. In figure 2, the curves represent theoretical results on positrons alone.

The PWA calculations for electrons, including exchange (Riley and Truhler 1975), show a fair agreement with the measured data of Daimon *et al* (1982) as well as Iga *et al* (1987). At 200 eV the results of Iga *et al* (1987) are not available. Because of the success with electrons, we expect our theoretical results on positrons to be reliable.

The most remarkable feature of our results is the behaviour of the positron

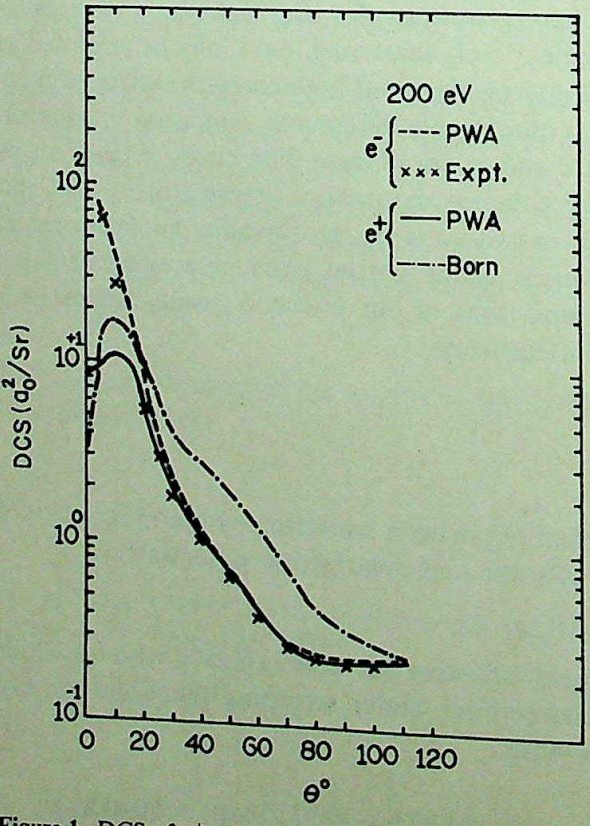

Figure 1. DCS of e^+ and e^- scattering from O_2 at 200 eV.

CC-0. In Public Domain. Gurukul Kangri Collection, Haridwar

Digitized by Arya Samaj Foundation Chennai and eGangotri

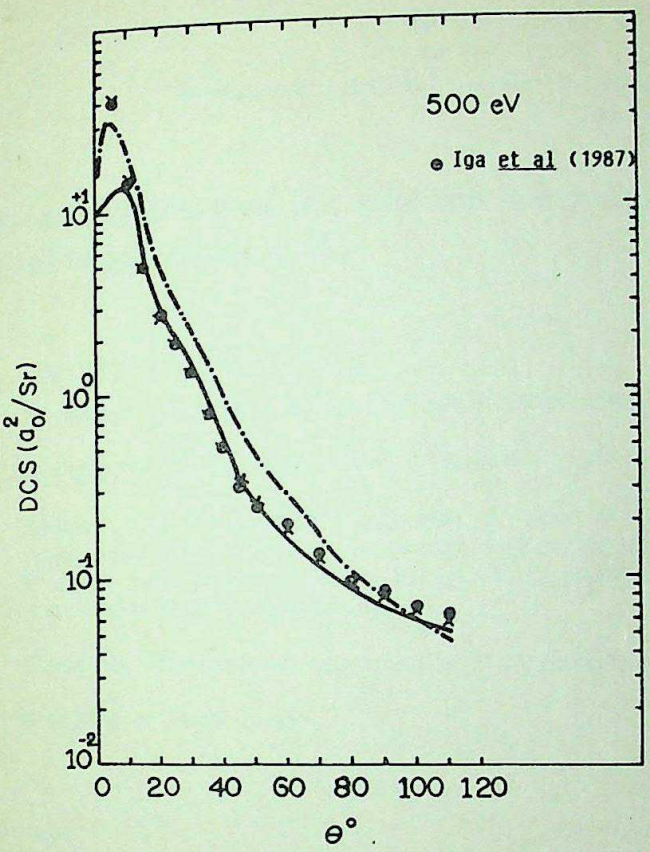

Figure 2. DCS of e^+ and e^- scattering from O_2 at 500 eV.

cross-sections towards the forward direction. Unlike the electron DCS, the positron DCS are not sharply peaked in the forward direction, since in the case of positrons, the static and the polarization potentials have opposite signs. The polarization effect, in itself, is maximum in the forward direction, at a given energy. The difference between e^+ and e^- cross-sections, which also depends on energy, is appreciable up to the angle of about 20° at 200 eV and about 10° at 500 eV. At intermediate and large angles, the e^+ and the e^- DCS tend to merge. At energies $E_i < 200$ eV a dip in the DCS curves is observed near $\theta = 85°$. Also shown in our figures are the Born approximation results for positrons. These are higher than the PWA results, except for very small angles at 200 eV.

Thus, in this paper high energy elastic DCS for e^+–O_2 scattering are presented. Notably the basic atomic interaction of electrons or positrons considered here does not include an imaginary part representing absorption effects.

This research was financed in part by the Department of Atomic Energy, Government of India.

References

Daimon H, Hayashi S, Kondow T and Huchitsu K 1982 *J. Phys. Soc. Jpn.* **51** 2641
Iga I, MuTao L, Nagueira J C and Barbieri R S 1987 *J. Phys.* **B20** 1095
Joshipura K N 1989 *Pramāṇa – J. Phys.* **32** 139

CC-0. In Public Domain. Gurukul Kangri Collection, Haridwar

Digitized by Arya Samaj Foundation Chennai and eGangotri

Katayama Y, Sucka O and Mori S 1987 *J. Phys.* **B20** 1645
Riley M E and Truhler D G 1975 *J. Chem. Phys.* **63** 2182
Salvat F, Martinez J D, Mayol R and Paralleda J 1987 *Phys. Rev.* **A36** 467
Wadehra J M 1986 *J. Phys.* **B19** L761

CC-0. In Public Domain. Gurukul Kangri Collection, Haridwar

Digitized by Arya Samaj Foundation Chennai and eGangotri

Pramāṇa – J. Phys., Vol. 34, No. 2, February 1990, pp. 91–101. © Printed in India.

On mass-independence of the minimal subtraction scheme in dimensional regularization II

SATISH D JOGLEKAR
Department of Physics, Indian Institute of Technology, Kanpur 208016, India

MS received 17 July 1989; revised 27 September 1989

Abstract. A self-contained argument is given for the mass independence of the renormalization constants in the minimal subtraction scheme in dimensional regularization in a two mass theory (Yukawa theory). An extension to a theory containing more mass parameters seems straightforward.

Keywords. Dimensional regularization; renormalization.

PACS Nos 11·10; 11·15

1. Introduction

It is well known from 't Hooft's work ('t Hooft 1973) that the renormalization constants in the minimal subtraction scheme (henceforth abbreviated as MS scheme) in dimensional regularization are independent of the mass parameter(s) of the theory. This fact has been well-exploited in writing down renormalization group equation (RGE) and *solving it* (formally) *exactly* without making any approximations in the process ('t Hooft 1973; Gross 1975). This is not possible for RGE's in other (mass dependent) schemes nor for Callan-Symanzik equations (Callan 1972; Symanzik 1971) where approximations have to be made before actually proceeding to the solution of the relevant equation. In addition mass-independent MS scheme leads to many powerful and elegant results and great simplification in formal proofs (See e.g. (Gross 1975). A similar approach has been suggested by Weinberg (1973).

However, a simple but *complete* and *self-contained* qualitative understanding of the mass independence has not been available. In 't Hooft's work ('t Hooft 1973; 't Hooft and Veltman 1972) one needs to go over lengthy mathematical steps before arriving at mass-independence and the proof is not transparent.

With this in view, we gave (Joglekar 1987) an *independent* simple and a *self-contained* argument for the mass-independence of the MS scheme for the case of $\lambda\phi^4$ theory, which contains a single mass parameter. The arguments given by 't Hooft (1973) and by Collins and Macfarlane (1974) heavily rely on 't Hooft's claim that the divergences in the dimensional regularization are polynomials in mass parameters of the theory. This fact which makes the proof a mass independence of work of 't Hooft (1973) and Collins and Macfarlane (1974) simple is by no means transparent from 't Hoofts (1973) work.

With this in view, we have generalized the work of Joglekar (1987) to a two mass theory in which we do not assume polynomial nature of divergences with respect to

CC-0. In Public Domain. Gurukul Kangri Collection, Haridwar

Digitized by Arya Samaj Foundation Chennai and eGangotri

mass parameters. It should be noted that there is a great deal of qualitative difference between a single mass theory of Joglekar (1987) and a two-mass (or a multi-mass) theory in this context. In a single mass theory the dependence of a dimensionless renormalization constant on mass m can be easily pinned down to the form (Collins and Macfarlane 1974) $\sum_s a_s (\ln(m/\mu))^s$, making it easy to deal with it. On the other hand in a two mass theory a dimensionless renormalization constant could depend, a priori, on the mass parameters m, M (and μ) through an infinite variety of functions. [Examples: $((m^2 - M^2)/(m^2 + M^2))^p$, $(\ln(\sqrt{m^2 + M^2})/\mu)^n$ etc.]. In this work, we have succeeded in proving mass-independence of the renormalization constants by completely bypassing the question of the kind of possible dependence of renormalization constants on the two mass parameters.

The proof given here is certainly not as simple as that in Joglekar (1987) for a single mass theory, but we believe it to be as simple as it could be in the present context. Its generalization to a multi mass theory seems reasonably straightforward, though it is not attempted here.

2. Preliminaries

We shall deal with a concrete case of a two mass theory, viz. Yukawa theory. It is described by a Lagrange density

$$\mathscr{L} = \bar{\psi}(i\partial\!\!\!/ - m_0)\psi + \tfrac{1}{2}\partial^\mu\phi\partial_\mu\phi - \tfrac{1}{2}M_0^2\phi^2 - \frac{\lambda_0}{4!}\phi^4 + ig_0\bar{\psi}\gamma_5\psi\phi$$

$$S \equiv \int \mathrm{d}^N x \mathscr{L} \tag{1}$$

Here ψ and ϕ are bare fields, m_0 and M_0 are bare masses and λ_0 and g_0 are bare coupling constants.

We shall be using the minimal subtraction scheme (MS scheme) in dimensional regularization ('t Hooft and Veltman 1972) to renormalize Green's functions of the theory and of operators. The renormalization transformations are ($\varepsilon \equiv 4 - n$):

$$\begin{aligned} &\psi = Z_\psi^{1/2}\psi^R \quad \phi = Z_\phi^{1/2}\phi^R \\ &g_0 = Z_g g\mu^{\varepsilon/2} \quad \lambda_0 = [\lambda Z_\lambda + \delta\lambda(g^2)]\mu^\varepsilon \\ &m_0 = m + \delta m_0 \quad M_0^2 = M^2 + \delta M_0^2 \end{aligned} \tag{2}$$

where μ is the arbitrary mass scale in dimensional regularization and $\delta\lambda$ is chosen to be independent of λ. We shall show that δm_0 and δM_0^2 in (2) are such that

$$m_0 = Z_m m \quad M_0^2 = ZM^2 + \tilde{Z}m^2. \tag{3}$$

The Lagrange density of (1) can be reëxpressed in terms of renormalized quantities as

$$\begin{aligned} \mathscr{L}[\psi, \phi, m_0, M_0^2, g_0, \lambda_0] &\equiv \mathscr{L}[\psi^R, \phi^R, m, M, g\mu^{\varepsilon/2}, \lambda\mu^{\varepsilon/2}] + \mathscr{L}_{\text{c.t.}} \\ &\equiv \mathscr{L}^R + \mathscr{L}_{\text{c.t.}} \end{aligned} \tag{4}$$

CC-0. In Public Domain. Gurukul Kangri Collection, Haridwar

Digitized by Arya Samaj Foundation Chennai and eGangotri

The unrenormalized but dimensionally regularized Green's functions are generated by

$$W^{UR}[\eta, \bar{\eta}, J; \lambda_0, g_0; m_0, M_0^2, \varepsilon]$$
$$\equiv \frac{1}{N} \int D\psi\, D\bar{\psi}\, D\phi \exp i \int \mathrm{d}^n x [\mathscr{L} + \bar{\psi}\eta + \bar{\eta}\psi + J\phi] \tag{5}$$

whereas the renormalized Green's functions are generated by

$$W^R[\eta^R, \bar{\eta}^R, J^R; \lambda, g; m, M^2, \mu, \varepsilon]$$
$$\equiv \frac{1}{N'} \int D\psi^R\, D\bar{\psi}^R\, D\phi^R \exp i \int \mathrm{d}^n x [\mathscr{L}^R + \mathscr{L}_{\text{c.t.}} + \bar{\psi}^R \eta^R + \bar{\eta}^R \psi^R + J^R \phi^R] \tag{6}$$

N' in (6) is a quantity depending on coupling constants, masses, μ, ε so adjusted that $W^R[\mathscr{J}^R = 0] = 1$. Here $\mathscr{J}$ denotes collectively the sources. Further one has $W^{UR} = W^R$.

The renormalized and unrenormalized connected Green's functions are respectively generated by $Z^R = -i \ln W^R$ and $Z^{UR} = -i \ln W^{UR}$, with $Z^R = Z^{UR}$.

For an operator $O[\psi, \bar{\psi}, \phi]$ we define $\langle\langle O \rangle\rangle$ and $\langle O \rangle$ by

$$\langle\langle O \rangle\rangle = \frac{1}{N} \int D\psi\, D\bar{\psi}\, D\phi O[\psi, \psi, \phi] \exp i \int \mathrm{d}^n x [\mathscr{L} + \bar{\psi}\eta + \bar{\eta}\psi + J\phi]$$
$$= W \langle O \rangle \tag{7}$$

$\langle\langle O \rangle\rangle$ and $\langle O \rangle$ generate the Green's functions and the connected Green's functions with one insertion of O. We further define operator insertion at momentum q by

$$\langle O(q) \rangle = \left\langle \int \mathrm{d}^n x \exp(iq.x) O \right\rangle \tag{8}$$

with $\langle O_0 \rangle = \langle O(q = 0) \rangle$. It should, further, be noted that $\langle O(q) \rangle$ regarded as a functional of field expectation values $\langle \phi \rangle = \delta Z / \delta J$ etc. generates unrenormalized proper vertices with one insertion of $O(q)$.

We note that equations of motion imply that

$$\left\langle \frac{\delta S}{\delta \phi} \phi \right\rangle = -J \langle \phi \rangle = -J \frac{\delta Z^{UR}}{\delta J} = -J^R \frac{\delta Z^R}{\delta J^R} = \text{finite} = \left\langle \frac{\delta S}{\delta \phi} \phi \right\rangle^R \tag{9}$$

and similar equations for fermion fields.

We introduce the notation $F = -i\bar{\psi}\psi$ and $S = (-i/2)\phi^2$. Then*

$$\frac{\partial W^{UR}}{\partial m_0} = \langle\langle F_0 \rangle\rangle^{UR}; \quad \frac{\partial W^{UR}}{\partial M_0^2} = \langle\langle S_0 \rangle\rangle^{UR} \tag{10a}$$

* In differentiating W^{UR} or W^R with respect to m_0 (or m) both the functional integral and the normalization factor N' (or N) get differentiated. As $W^R[\mathscr{J}^R = 0] = 1$, $(\partial W^R / \partial m)|_{\mathscr{J}^R = 0} = 0$. Thus the vacuum diagrams arising from one insertion of $\bar{\psi}\psi$ are subtracted out by the term arising from the differentiation of N.

CC-0. In Public Domain. Gurukul Kangri Collection, Haridwar

Digitized by Arya Samaj Foundation Chennai and eGangotri

and*

$$\frac{\partial W^R}{\partial m} = \langle\langle F_0 \rangle\rangle^R; \quad \frac{\partial W^R}{\partial M^2} = \langle\langle S_0 \rangle\rangle^R. \tag{10b}$$

3. Certain observations

In this section, we make a number of observations in the form of lemmas which are helpful in later sections. Many of them are evident by an inspection of Feynman graphs.

Lemma A. The unrenormalized proper vertices of the theory exist at $m_0 = 0 = M_0$ provided the external momenta are off-shell (Proof: Off-shell moments avoid infrared divergences).

This ensures that the limits $m_0 \to 0$ and/or $M_0^2 \to 0$ exist for the off-shell proper vertices.

Lemma B. The unrenormalized off-shell proper vertices of $S = -\frac{i}{2}\phi^2$ and $F = -i\bar{\psi}\psi$ at nonzero momentum q exist at $m_0 = 0$ and $M_0^2 = 0$. (Proof: Off-shell momenta and $q \neq 0$ avoid infrared divergences).

This ensures that the limits $m_0 \to 0$ and/or $M_0^2 \to 0$ exist for these proper vertices at $q \neq 0$.

Lemma C. The unrenormalized off-shell proper vertices generated by two insertions of F viz $\langle F(q), F(q') \rangle$ exist at $m_0 = 0$ and $M_0^2 = 0$ if $q \neq 0$ and $q' \neq 0$. (Proof: off-shell momenta and $q \neq 0$ and $q' \neq 0$ avoid infrared divergences).

Lemma D. The operators F and S satisfy relations of the sort

$$\langle S \rangle^{UR} = Z' \langle S \rangle^R \tag{11a}$$

$$\langle F \rangle^{UR} = T' \langle F \rangle^R + Z_1' \langle S \rangle^R \tag{11b}$$

Relations (11a) and (11b) define the renormalization constants Z', T', Z_1' uniquely in the MS scheme as can be seen by an order by order expansion.

Proof. This follows from (i) power counting (ii) scalar nature of F and S (iii) pseudo-scalar nature of ϕ.

Z' and T' are dimensionless and Z_1' has dimensions of mass. These relations can be inverted to yield

$$\langle S \rangle^R = Z \langle S \rangle^{UR} \tag{12a}$$

$$\langle F \rangle^R = T \langle F \rangle^{UR} + Z_1 \langle S \rangle^{UR} \tag{12b}$$

with

$$Z' = Z^{-1}, \quad T' = T^{-1} \quad \text{and} \quad Z_1 = -T' Z_1' Z'^{-1} \tag{12c}$$

*These relations become obvious in the context of MS scheme from relations such as (45) and (48).

CC-0. In Public Domain. Gurukul Kangri Collection, Haridwar

Digitized by Arya Samaj Foundation Chennai and eGangotri

From (12b) we define $F^R = TF + Z_1 S$. Now $\langle F^R(q)F^R(q)\rangle_c$ (subscript "c" for connected) generates connected Green's functions of two insertions of F at momenta q and q' respectively. These Green's functions are "partially renormalized" in the sense that each operator F is a renormalized operator, but they need additional subtractions as $x \to y$ in $\langle F^R(x)F^R(y)\rangle_c$. By power counting these subtractions are needed* only for the 2 scalar Green's function of $\langle F^R(q)F^R(q')\rangle_c$. Hence a relation of the sort given below exists:

$$\langle F^R(q)F^R(q')\rangle_c^R = \langle F^R(q)F^R(q')\rangle_c + K(\varepsilon)\langle S(q+q')\rangle. \tag{13}$$

Now noting that

$$\langle F^R(q)F^R(q')\rangle = \langle F^R(q)\rangle\langle F^R(q')\rangle + \langle F^R(q)F^R(q')\rangle_c \tag{14}$$

and that $\langle F^R(q)\rangle$ is always finite, (13) yields,

$$\begin{aligned}\langle F^R(q)F^R(q')\rangle^R &= \langle F^R(q)\rangle\langle F^R(q')\rangle + \langle F^R(q)F^R(q')\rangle_c^R \\ &= \langle F^R(q)\rangle\langle F^R(q')\rangle + \langle F^R(q)F^R(q')\rangle_c + K(\varepsilon)\langle S(q+q')\rangle \\ &= \langle F^R(q)F^R(q')\rangle + K(\varepsilon)\langle S(q+q')\rangle. \end{aligned}\tag{15}$$

Lemma E. Eq. (15) is valid and $K(\varepsilon)$ is dimensionless (as seen by power counting).

Lemma F. The renormalization constants Z', T', Z_1', Z, T, Z_1 and K have a smooth limit as $m_0 \to 0$ and/or $M_0^2 \to 0$.

Proof. This follows from Lemmas A, B and C. For example, the renormalization constant Z' can be determined (successively in higher and higher loop approximation) by considering the divergent part of $\langle S(q)\rangle^{UR}$ with $q \neq 0$. This is so because by power counting Z' is independent of q. But by Lemma B, $\langle S(q)\rangle^{UR}$ exists at $m_0 = 0 = M_0^2$ and Z' must have a smooth limit as $m_0 \to 0$ and/or $M_0^2 \to 0$. In a similar fashion Lemma B implies a smooth limit for T' and Z_1' (and hence via Eq. (12c) for Z, T and Z_1). Lemma C implies a smooth limit for K as $m_0 \to 0$ and/or $M_0^2 \to 0$.

Lemma G. The renormalization constants Z_φ, Z_ψ, Z_λ $\delta\lambda$ and Z_g; δm_0, δM_0^2 have a smooth limit as $m_0 \to 0$ and/or $M_0^2 \to 0$.

Proof. This follows from the Lemma A and the logic used in Lemma F.

Lemma H. *If* a dimensionless renormalization constant Z_0 depends on a *single* mass,

---

*The case of no external lines will not need to be considered here. If one were to consider (13) with zero external lines, there would be additional counterterms of the form $f(q^2, m, M^2, \varepsilon)$, which are independent of J, on the right hand side of (13).

When one considers a quantity of the kind $\langle F^R(x)F^R(y)\rangle_c$, internal subtractions are already made for those proper subdiagrams which contain insertion of only *one* operator $F(x)$ or $F(y)$. But this object develops a singularity as $x \to y$ indicating a need for additional subtraction in primitively divergent proper subgraphs containing both $F(x)$ and $F(y)$. By power counting only such graphs with two external scalars can contain (momentum independent) divergences. Hence the counterterm needed will be of the form $K(\varepsilon)S = K(\varepsilon)(-(i/2))\phi^2$. This leads to relation (13) in the momentum space.

CC-0. In Public Domain. Gurukul Kangri Collection, Haridwar

Digitized by Arya Samaj Foundation Chennai and eGangotri

say m, then in the r loop approximation it must be expressible as

$$Z_0(m) = \sum_{s=0}^{r-1} b_s \left(\ln \frac{m}{\mu} \right)^s \tag{16}$$

Proof. This follows from the Lemma D and E of Joglekar (1987).

Lemma I. If a dimensionless renormalization constant Z_0 depends on a single mass, say m, and has a smooth limit as $m_0 \to 0$ then it is mass-independent.

Proof. The proof proceeds by induction. The result is trivially true in the zero loop approximation. Let us assume the result in the $(r-1)$ loop approximation. Then by Lemma H

$$Z_{0[r]} = Z_{0[r-1]} + a^r \sum_{s=0}^{r-1} b_s \left(\ln \frac{m}{\mu} \right)^s$$

$$= Z_{0[r-1]} + a^r \sum_{s=0}^{r-1} b_s \left(\ln \frac{m_0}{\mu} \right)^s + 0(a^{r+1}).$$

Here $Z_{0[r]}$ denotes the renormalization constant Z_0 up to r loop approximation and a is the loop expansion parameter. $Z_{0[r]}$ has a smooth limit as $m_0 \to 0$ iff $b_s = 0$ $s = 1, 2, .., r-1$. Hence $Z_{0[r]}$ is mass independent.

4. A useful theorem

In this section we shall prove a very useful theorem. Let $X = \sum_{n=0} a^n x_n$ and $Y = \sum_{n=0} a^n y_n$ have MS-structure [i.e. x_0, y_0 are finite and x_n's and y_n's$(n \neq 0)$ have only poles in ε, and a is the loop expansion parameter].

Theorem. A relation

$$X\langle F \rangle^{UR} + Y\langle S \rangle^{UR} = \text{finite} \tag{17}$$

implies

$$X = x_0 T \quad \text{and} \quad Y = x_0 Z_1 + y_0 Z. \tag{18}$$

Proof. We introduce the notation $X_{[n]} = \sum_{m=0}^{n} a^m x_m$ etc.

(i) First consider the case $x_0 = 0$. Consider the relation (17) in one loop approximation:

$$x_1\langle F \rangle_0 + y_0\langle S \rangle_1^{UR} + y_1\langle S \rangle_0 = \text{finite}$$

i.e.

$$y_0\langle S \rangle_1^{UR} = -x_1\langle F \rangle_0 - y_1\langle S \rangle_0 + \text{finite} \tag{19}$$

whereas (12b) leads to

$$y_0\langle S \rangle_1^{UR} = -y_0 z_1 \langle S \rangle_0 + \text{finite}. \tag{20}$$

As $\langle F \rangle_0$ and $\langle S \rangle_0$ are linearly independent, comparison of (19) and (20) implies that

$$x_1 = 0 \quad y_1 = y_0 z_1 \tag{21}$$

CC-0. In Public Domain. Gurukul Kangri Collection, Haridwar

Digitized by Arya Samaj Foundation Chennai and eGangotri

which agrees with (18) to one loop order.

Now let us assume the result of (18) up to $(n-1)$ loop approximation: i.e.

$$X_{[n-1]} = 0 \quad \text{and} \quad Y_{[n-1]} = y_0 Z_{[n-1]}. \tag{22}$$

Then

$$X_{[n]} = x_n a^n \quad \text{and} \quad Y_{[n]} = y_0 Z_{[n]} + (y_n - y_0 z_n) a^n. \tag{23}$$

Now in the n-loop approximation (17) reads

$$x_n \langle F \rangle_0 + y_0 Z_{[n]} \langle S \rangle^{UR}_{[n]} + (y_n - y_0 z_n) \langle S \rangle_0 = \text{finite}. \tag{24}$$

Now using the fact that (i) $Z_{[n]} \langle S \rangle^{UR}_{[n]}$ is finite up to n-loop approximation [see (12a)] (ii) x_n, y_n Z_n contain only poles (iii) $\langle F \rangle_0$ and $\langle S \rangle_0$ are linearly independent one obtain

$$x_n = 0 \quad \text{and} \quad y_n = y_0 z_n \tag{25}$$

proving (18) in n-loop approximation, etc.

(ii) Now consider the case $x_0 \neq 0$. We can rewrite (17) using (12a) as

$$X \langle F \rangle^{UR} + (Y - y_0 Z) \langle S \rangle^{UR} = \text{finite}. \tag{26}$$

Dividing throughout by x_0, we have

$$X' \langle F \rangle^{UR} + Y' \langle S \rangle^{UR} = \text{finite} \tag{27}$$

with

$$X = x_0 X' \quad \text{and} \quad Y' = (1/x_0)(Y - y_0 Z) \quad \text{with} \quad y'_0 = 0. \tag{28}$$

Equation (18) then requires that we prove

$$X' = T \quad \text{and} \quad Y' = Z_1. \tag{29}$$

Consider (27) in one loop approximation:

$$\langle F \rangle^{UR}_1 + x'_1 \langle F \rangle_0 + y'_1 \langle S \rangle_0 = \text{finite}. \tag{30}$$

Comparing this with (12b) in the one loop approximation (Z_1 vanishes in the tree approximation)

$$\langle F \rangle^{UR}_1 + t_1 \langle F \rangle_0 + z_{1(1)} \langle S \rangle_0 = \text{finite} \tag{31}$$

one obtains

$$x'_1 = t_1 \quad \text{and} \quad y'_1 = z_{1(1)} \tag{32}$$

proving (29) to one loop order.

Next, we assume the result of (29) to $n-1$ loop approximation, viz:

$$X'_{[n-1]} = T_{[n-1]} \quad \text{and} \quad Y'_{[n-1]} = Z_{1[n-1]} \tag{33}$$

so that

$$\begin{aligned} X'_{[n]} &= T_{[n]} + a^n (x'_n - t_n); \\ Y'_{[n]} &= Z_{1[n]} + a^n (y'_n - z_{1n}). \end{aligned} \tag{34}$$

CC-0. In Public Domain. Gurukul Kangri Collection, Haridwar

Digitized by Arya Samaj Foundation Chennai and eGangotri

Equation (27), in n loop approximation, reads

$$T_{[n]}\langle F\rangle^{UR}_{[n]} + (x'_n - t_n)\langle F\rangle_0 + Z_{1[n]}\langle S\rangle^{UR}_{[n]} + (y'_n - z_{1n})\langle S\rangle_0 = \text{finite}. \tag{35}$$

Using Eq. (12b), this reduces to

$$(x'_n - t_n)\langle F\rangle_0 + (y'_n - z_{1n})\langle S\rangle_0 = \text{finite}. \tag{36}$$

This, as in (24), yields

$$x'_n = t_n \quad \text{and} \quad y'_n = z_{1n} \tag{37}$$

proving (29) to n loop approximation, etc.

5. Proof of mass-independence

Consider first

$$\begin{aligned}\text{finite} &= \left.\frac{\partial W^R}{\partial M^2}\right|_{\mathscr{J}^R, m, \lambda, g, \mu} = \left.\frac{\partial W^{UR}[\mathscr{J}; \lambda_0, g_0, m_0^2, M_0^2, \varepsilon]}{\partial M^2}\right|_{\mathscr{J}^R, m, \lambda, g, \mu} \\ &= \frac{\partial m_0}{\partial m}\frac{\partial W^{UR}}{\partial m_0} + \frac{\partial M_0^2}{\partial M^2}\frac{\partial W^{UR}}{\partial M_0^2} + \frac{\partial \lambda_0}{\partial M^2}\frac{\partial W^{UR}}{\partial \lambda_0} + \frac{\partial g_0}{\partial M^2}\frac{\partial W^{UR}}{\partial g_0} \\ &\quad + \sum_{\mathscr{J}} \int \frac{\partial \mathscr{J}^{UR}}{\partial M^2}\frac{\delta W^{UR}}{\delta \mathscr{J}^{UR}}\,\mathrm{d}^n n. \end{aligned} \tag{38}$$

Using (9), (10a) and similar results one obtains

$$\begin{aligned}\text{finite} &= \frac{1}{W^R}\frac{\partial W^R}{\partial M^2} = \frac{\partial m_0}{\partial M^2}\langle F_0\rangle + \frac{\partial M_0^2}{\partial M^2}\langle S_0\rangle + \mu^{\varepsilon}\left[\lambda\frac{\partial Z_\lambda}{\partial M^2} + \frac{\partial \delta\lambda}{\partial M^2}\right] \\ &\quad \times \left\langle -\frac{i}{4!}\int \phi^4\,\mathrm{d}^n x\right\rangle + \mu^{\varepsilon/2} g \frac{\partial Z_g}{\partial M^2}\left\langle i\int \bar\psi\gamma_5\psi\phi\,\mathrm{d}^n x\right\rangle \\ &\quad + \frac{1}{2}\frac{\partial \ln Z_\phi}{\partial M^2}\left\langle -\int \frac{\delta S}{\delta\phi}\phi\,\mathrm{d}^n x\right\rangle + \frac{1}{2}\frac{\partial \ln Z_\psi}{\partial M^2}\left\langle -\int\left(\bar\psi\frac{\delta S}{\delta\bar\psi} - \frac{\delta S}{\delta\psi}\psi\right)\mathrm{d}^n x\right\rangle. \end{aligned} \tag{39}$$

Consider (39) in the one loop approximation. We note that all factors of operators on the right hand side except $\partial M_0^2/\partial M^2$ vanish in the tree approximation. Hence, one has

$$\begin{aligned}\langle S_0\rangle_1 &= -\left(\frac{\partial M_0^2}{\partial M^2}\right)_1\langle S_0\rangle_0 - \left(\frac{\partial m_0}{\partial M^2}\right)_1\langle F_0\rangle_0 \\ &\quad - \mu^{\varepsilon}\left[\lambda\frac{\partial Z_\lambda}{\partial M^2} + \frac{\partial\delta\lambda}{\partial M^2}\right]_1\left\langle\frac{-i}{4!}\int\phi^4\mathrm{d}^n x\right\rangle_0 \\ &\quad - \mu^{\varepsilon/2} g\left[\frac{\partial Z_g}{\partial M^2}\right]_1\left\langle i\int\bar\psi\gamma_5\psi\phi\,\mathrm{d}^n x\right\rangle_0 \end{aligned}$$

CC-0. In Public Domain. Gurukul Kangri Collection, Haridwar

Digitized by Arya Samaj Foundation Chennai and eGangotri

$$+\frac{1}{2}\left[\frac{\partial}{\partial M^2}\ln Z_\phi\right]_1\left\langle -\int\frac{\delta S}{\delta\phi}\phi\,\mathrm{d}^n x\right\rangle_0$$
$$-\frac{1}{2}\left[\frac{\partial}{\partial M^2}\ln Z_\psi\right]_1\left\langle -\int\left(\bar\psi\frac{\delta S}{\delta\bar\psi}-\frac{\delta S}{\delta\psi}\psi\right)\mathrm{d}^n x\right\rangle + \text{finite.} \tag{40}$$

But S is a dimension two (multiplicatively renormalizable) operator and hence $\langle S\rangle_1$ cannot contain counterterms of dimension higher than two. This immediately implies that

$$\frac{\partial m_0}{\partial M^2}=0=\frac{\partial Z_\lambda}{\partial M^2}=\frac{\partial\delta\lambda}{\partial M^2}=\frac{\partial Z_g}{\partial M^2}=\frac{\partial}{\partial M^2}Z_\psi=\frac{\partial}{\partial M^2}Z_\phi \tag{41}$$

and using (12a)

$$\frac{\partial M_0^2}{\partial M^2}=Z \tag{42}$$

in *one* loop approximation. Now, one assumes the results of (41) and (42) to $(n-1)$ loop approximation. Then

$$\left[\frac{\partial M_0^2}{\partial M^2}\right]_{[n]}=Z_{[n]}+\left\{\left[\frac{\partial M_0^2}{\partial M^2}\right]_n - Z_n\right\}a^n. \tag{43}$$

When this is used in (39) and use is made of (12a), (39) in the n loop approximation yields, as before, (41) and (42) in the n loop approximation. Hence the proof is complete by induction.

From (41) it follows that m_0 is only a function of m and on dimensional grounds it can be expressed as

$$m_0=Z_m(m)m. \tag{44}$$

Equation (41) also implies that Z_λ, $\delta\lambda$, Z_g, Z_ψ, Z_ϕ are dimensionless constants depending only on m and by lemma G they have a smooth limit as $m_0\to 0$. Hence by lemma I, they are mass independent. Hence it remains to show the mass-independence of $Z_m(m)$ and Z and $\tilde Z$ of (3). Analogous to (39) one can obtain

$$\text{finite}=\frac{1}{W^R}\frac{\partial W^R}{\partial m}=\frac{\partial m_0}{\partial m}\langle F_0\rangle^{UR}+\frac{\partial M_0^2}{\partial m}\langle S_0\rangle^{UR} \tag{45}$$

where use has been made of the mass independence of Z_ϕ, Z_ψ, $\delta\lambda$, Z_λ and Z_g. Equation (45) when compared to (17) yields [from (18)]:

$$\frac{\partial m_0}{\partial m}=T \quad\text{and}\quad \frac{\partial M_0^2}{\partial m}=Z_1. \tag{46}$$

Now from (44), $\partial m_0/\partial m$ is a renormalization constant that is a function of m alone and by lemma F, it has a smooth limit as $m_0\to 0$. Hence by lemma I it is mass independent. Hence,

$$\frac{\partial m_0}{\partial m}=\text{constant}\equiv Z_m. \tag{47}$$

CC-0. In Public Domain. Gurukul Kangri Collection, Haridwar

Digitized by Arya Samaj Foundation Chennai and eGangotri

This proves first of (3) and mass independence of Z_m.

Finally we shall prove second of (3) and mass independence of Z' and $\tilde{Z}$. To this end, we note that (39) now becomes, (using 42)

$$\frac{\partial W^R}{\partial M^2} = Z\langle S_0\rangle W^R = Z\langle\langle S_0\rangle\rangle. \tag{48}$$

Differentiating with respect to M^2 once

$$\begin{aligned}\text{finite} = \frac{\partial^2 W^R}{\partial (M^2)^2} &= Z\frac{\partial M_0^2}{\partial M^2}\frac{\partial}{\partial M_0^2}\langle\langle S_0\rangle\rangle + \frac{\partial Z}{\partial M^2}\langle\langle S_0\rangle\rangle \\ &= Z^2\langle\langle S_0, S_0\rangle\rangle + \frac{\partial Z}{\partial M^2}\langle\langle S_0\rangle\rangle \\ &= \langle\langle S_0^R, S_0^R\rangle\rangle + \frac{\partial Z}{\partial M^2}\langle\langle S_0\rangle\rangle. \end{aligned} \tag{49}$$

By power counting and the logic of the kind used in Lemma E, $\langle\langle S_0^R, S_0^R\rangle\rangle$ is finite. Hence

$$\frac{1}{W^R}\frac{\partial Z}{\partial M^2}\langle\langle S_0\rangle\rangle = \text{finite} = \frac{\partial Z}{\partial M^2}\langle S_0\rangle. \tag{50}$$

Hence the theorem of §4 implies (Here $y_0 = 0$)

$$\frac{\partial Z}{\partial M^2} = 0. \tag{51}$$

Thus Z is only a function of m. But by lemma F, Z has a smooth limit as $m_0 \to 0$. Hence by lemma I, Z is mass independent. Equation (42), then implies

$$M_0^2 = ZM^2 + A(m). \tag{52}$$

Equation (45), with the help of (46) and (12b) can be cast in the form

$$\frac{\partial W^R}{\partial m} = \langle\langle F_0^R\rangle\rangle = \left\langle\!\!\left\langle TF_0 + \frac{\partial M_0^2}{\partial m}S_0\right\rangle\!\!\right\rangle. \tag{53}$$

Differentiating (53) with respect to m once more and noting the mass independence of T, we obtain*

$$\frac{1}{W^R}\frac{\partial^2 W^R}{\partial m^2} = \langle F_0^R, F_0^R\rangle + \frac{\partial^2 M_0^2}{\partial m^2}\langle S_0\rangle = \text{finite}. \tag{54}$$

---

*The equation below can be made valid even with zero external lines provided suitable counterterms are included in the definition of $\langle F_0^R, F_0^R\rangle$ with zero external lines. These counterterms can be generated out of the derivatives of N' of (6), much as in footnote in p. 93. We, however, need this equation only with *nonzero* external lines.

CC-0. In Public Domain. Gurukul Kangri Collection, Haridwar

Digitized by Arya Samaj Foundation Chennai and eGangotri

As M_0^2 as a function of m and M has the MS form, so does $\partial^2 M_0^2/\partial m^2$. Hence,

$$\frac{1}{W^R}\frac{\partial^2 W^R}{\partial m^2} = \langle F_0^R, F_0^R\rangle + \frac{\partial^2 M_0^2}{\partial m^2}\langle S_0\rangle = \langle F_0^R, F_0^R\rangle^R. \tag{55}$$

Comparison of (55) with (15) yields

$$\frac{\partial M_0^2}{\partial m^2} = K. \tag{56}$$

Using (52),

$$\frac{\mathrm{d}A(m)}{\mathrm{d}m^2} = K. \tag{57}$$

Thus K is a dimensionless renormalization constant depending only on m and by lemma F, it has smooth limit as $m_0 \to 0$. Hence, by lemma I, K is mass independent. Hence (57) implies

$$A(m) = \tfrac{1}{2} Km^2 \equiv \tilde{Z}m^2 \tag{58}$$

(Here use is made of the fact that $A(m)$ has dimension two). Equations (52) and (58) now imply that

$$M_0^2 = ZM^2 + \tilde{Z}m^2$$

with Z and $\tilde{Z}$ mass-independent. This completes the proof.

References

Callan C G 1972 *Phys. Rev.* **D5** 3202
Collins J C and Macfarlane 1974 *Phys. Rev.* **D10** 1201
Gross D 1975 in *Methods in field theory* Les Houches lectures, (eds) R Balian and J Zinn-Justin
't Hooft 1973 *Nucl. Phys.* **B61** 455
't Hooft and Veltman M 1972 *Nucl. Phys.* **B44** 189
Joglekar S D 1987 *Phys. Rev.* **D35** 759
Symanzik S 1971 *Commun. Math. Phys.* **23** 49
Weinberg S 1973 *Phys. Rev.* **D8** 3497

CC-0. In Public Domain. Gurukul Kangri Collection, Haridwar

Digitized by Arya Samaj Foundation Chennai and eGangotri

CC-0. In Public Domain. Gurukul Kangri Collection, Haridwar

Digitized by Arya Samaj Foundation Chennai and eGangotri

Pramāṇa – J. Phys., Vol. 34, No. 2, February 1990, pp. 103–109. © Printed in India.

Phenomenology of the proton spin

M V N MURTHY and V RAVINDRAN
The Institute of Mathematical Sciences, Madras 600 113, India

MS received 8 August 1989

Abstract. We analyze the various inputs that go into computing the recently measured first moment of the proton spin structure function $g_1^p(x)$. The basic inputs are the various valence and sea quark polarisations and the gluonic contribution coming through axial anomaly. We show that the quark model predictions for valence quark polarisations, suitably modified to accommodate Bjorken sum rule, are consistent with measured value of moment of the spin structure function.

Keywords. Structure functions; polarization; sum rules; quantum chromodynamics.

PACS Nos 12·38; 13·60; 14·80; 13·88

1. Introduction

The European Muon Collaboration (Ashman *et al* 1988) has recently measured the asymmetry in polarized muon deep inelastic scattering on polarized protons. The measured asymmetry together with the data on unpolarized proton structure function directly leads to the determination of the spin structure function of the proton $g_1^p(x)$. We are interested in the first moment of this structure function,

$$G_p = \int \mathrm{d}x g_1^p(x) = 0{\cdot}114 \pm 0{\cdot}012\,(\text{stat.}) \pm 0{\cdot}026\,(\text{syst.}), \tag{1}$$

where x is the Bjorken scaling variable. This result is in disagreement with the Ellis-Jaffe sum rule (Ellis and Jaffe 1974) which predicts,

$$G_p = \frac{1}{12} G_A \left[1 + \frac{5}{3} \frac{3F - D}{F + D} \right] = 0{\cdot}2 \pm 0{\cdot}005, \tag{2}$$

where $G_A = 1{\cdot}254 \pm 0{\cdot}006$ is the neutron β decay coupling constant and F and D are SU(3) couplings, $F/D = 0{\cdot}632 \pm 0{\cdot}024$ (Gaillard and Sauvage 1984). Much of the controversy generated regarding the spin structure of the proton has its origin in this discrepancy (see for example, Soffer 1989; Jaffe and Manohar 1989).

Bjorken's (1966) analysis relates the first moment G_p to a weighted sum of axial vector matrix elements of various quark flavours $(u, d, s, \ldots)$ between proton states,

where $$G_p = \tfrac{1}{18}[4\Delta u + \Delta d + \Delta s], \tag{3}$$

$$\Delta q = -S^\mu \langle P, S | \bar{q} \gamma_\mu \gamma_5 q | P, S \rangle. \tag{4}$$

CC-0. In Public Domain. Gurukul Kangri Collection, Haridwar

Digitized by Arya Samaj Foundation Chennai and eGangotri

Here q is any quark flavour and S^μ is the spin vector of the proton. In general G_p gets contribution from both flavour singlet as well as non-singlet current matrix elements. The flavour non-singlet part of G_p can be related to,

$$G_A = \Delta u - \Delta d = F + D \tag{5}$$

$$G_8 = \Delta u + \Delta d - 2\Delta s = 3F - D. \tag{6}$$

The Ellis-Jaffe sum rule is obtained by setting $\Delta s = 0$ in which case G_A, F/D values are sufficient to determine G_p. On the other hand using the measured values of G_A, F/D and G_p one obtains,

$$\Delta u = 0{\cdot}74 \pm 0{\cdot}08, \quad \Delta d = -0{\cdot}51 \pm 0{\cdot}08, \quad \Delta s = -0{\cdot}23 \pm 0{\cdot}08. \tag{7}$$

As a result $\Sigma = \sum \Delta q_i \cong 0, i = u, d, s$, which has aroused much interest in the high energy physics community. A naive interpretation of this would be that quarks together carry very little of the proton spin. An even more surprising result is that the strange quark contribution is substantial which could imply large violation of the OZI rule (Ellis *et al* 1988). At the outset these conclusions rebel against well known results from the quark models based on the $SU(3)_f$ flavour symmetry where quarks are expected to carry nearly 75 per cent of the proton polarization.

In a recent paper by Gupta *et al* (1989), it has been argued that the non-zero value of Δs need not be in contradiction with known hadronic physics. The matrix elements in (3) and (4) are essentially non-perturbative and can be computed using the method of QCD sum rules. The method yields,

$$\Delta u = 0{\cdot}8, \quad \Delta d = -0{\cdot}45, \quad \Delta s = -0{\cdot}165, \tag{8}$$

within errors consistent with (7). With QCD radiative corrections these values yield G_p in good agreement with EMC measurements. It was also noted in the above analysis that the large non-zero value of Δs could be a result of the role of axial anomaly in singlet axial vector matrix elements. This, for example, contributes through the use of phenomenological values of chiral symmetry breaking parameter $\langle q\bar{q}\rangle$ which arises from anomaly in instanton based models of QCD vacuum. It is also worth pointing out that the importance of such an anomaly in preventing large isospin violations in Bjorken sum rule (eq. (5)) was first pointed out by Gross *et al* (1979)). In a series of papers recently, Altarelli and Ross (1988), Efremov and Teryaev (1988) and Carlitz *et al* (1988) have also emphasized the role of axial anomaly in understanding the spin structure of the proton. These authors explicitly show how gluons contribute to the first moment via the axial anomaly. A similar analysis through the QCD evolution equations had been carried out earlier by Bajpai and Ramachandran (1980) who overlooked the contribution of the anomaly but predicted large sea and gluon polarization.

The objective of the present paper is to carry out a consistent phenomenological analysis in the light of above investigations. This we try to achieve by separately analyzing the various singlet, non-singlet and gluonic contributions to the axial matrix element. The main result is that predictions from the quark model wave functions for the valence quark polarizations can be consistent with the EMC measurement.

CC-0. In Public Domain. Gurukul Kangri Collection, Haridwar

Digitized by Arya Samaj Foundation Chennai and eGangotri

2. The model

Following Altarelli and Ross (1988) (see also Efremov and Teryaev 1988 and Carlitz *et al* 1988), we write,

$$\Delta u = \Delta u_v + \Delta u_\sigma + \Delta G, \tag{9}$$

$$\Delta d = \Delta d_v + \Delta d_\sigma + \Delta G, \tag{10}$$

$$\Delta s = \Delta s_\sigma + \Delta G, \tag{11}$$

where we have separately identified the contributions from valence (v) and sea quarks (σ). It has been argued in the above references that the gluonic contribution

$$\Delta G = -\frac{\alpha_s}{2\pi}\Delta g, \quad \Delta g = \int \mathrm{d}x[g_+(x) - g_-(x)], \tag{12}$$

where Δg the moment of the spin dependent gluon density, arises through the Adler-Bell-Jackiw axial vector anomaly. However there is some disagreement (Jaffe and Manohar 1989) as to whether this gluonic contribution is calculable using perturbative QCD. For our purposes we treat ΔG as a phenomenological parameter which measures the gluonic contribution to the axial matrix elements.

As advertised our objective is to use the theoretically determined values of Δq_i (eq. (8)) or equivalently the experimentally determined values (eq. (7)) and check the consistency of various inputs Δq_v, Δq_σ and ΔG with known physics. To do this we first note that we have no information on ΔG, it is a phenomenological input to the flavour singlet part of Δq. Similarly we have no information of the sea quark spin densities. However proceeding in analogy with the unpolarized case we set,

$$\Delta u_\sigma = \Delta d_\sigma = \frac{1}{k}\Delta s_\sigma = \Delta\sigma. \tag{13}$$

The equivalence of u, d quark contributions avoids any isospin violation in the Bjorken sum rule for G_A. For a SU(3) symmetric sea $k=1$. However it is well known that in the unpolarized case the strange sea distribution is about 1/2 of the u, d, distributions (Abramowicz 1983). The factor k takes care of the break down of the SU(3) symmetry or equivalently the quark mass effects.

Next we consider the valence quark contribution. Using the $\mathrm{SU(3)_{flavour}} \times \mathrm{SU(2)_{spin}}$ wave function of the proton we obtain (Mani and Noman 1981),

$$\tilde{u}_v(x) = \tfrac{2}{3}u_v(x) \tag{14}$$

$$\tilde{d}_v(x) = -\tfrac{1}{3}d_v(x) \tag{15}$$

where $\tilde{q}_v(x)$ ($q_v(x)$) is the spin dependent (spin independent) quark density and the weights on the right hand side are obtained by constructing the probabilities for u or d quarks to have spin parallel or anti parallel to the proton spin (Close 1979). With these definitions,

$$\Delta u_v = \int \mathrm{d}x\tilde{u}_v(x) = 4/3$$

$$\Delta d_v = \int \mathrm{d}x\tilde{d}_v(x) = -1/3$$

CC-0. In Public Domain. Gurukul Kangri Collection, Haridwar

Digitized by Arya Samaj Foundation Chennai and eGangotri

and through Bjorken sum rule we have

$$G_A = \Delta u - \Delta d = \Delta u_v - \Delta d_v = 5/3$$

which is the standard SU(3) value in disagreement with the experimental value ($\cong 5/4$).

To avoid this problem we use the Carlitz-Kaur model (Carlitz and Kaur 1976; Kaur 1977) where the valence quark spin densities are diluted due to their interaction with the gluons and the sea. As a result,

$$\begin{aligned} \tilde{u}_v(x) &= (u_v(x) - \tfrac{2}{3} d_v(x)) \cos 2\theta \\ \tilde{d}_v(x) &= -\tfrac{1}{3} d_v(x) \cos 2\theta \end{aligned} \tag{16}$$

where $\cos 2\theta$, a function of Bjorken x, is the spin dilution factor. A parametrization of $\cos 2\theta$ is then obtained using Regge arguments at small x. The large x ($x \to 1$) behaviour of $\tilde{u}_v(x)$ and $\tilde{d}_v(x)$ should be similar to $u_v(x)$ and $d_v(x)$ due to the constraint

$$|\tilde{u}_v(x)/u_v(x)|, \quad |\tilde{d}_v(x)/d_v(x)| \leqslant 1.$$

The effect of the spin dilution factor will therefore be seen only at small x and $\cos 2\theta \to 1$ as $x \to 1$. Later we demonstrate that even a simple model in which

$$\begin{aligned} \tilde{u}_v(x) &= \tfrac{2}{3} u_v(x) \cos 2\theta \\ \tilde{d}_v(x) &= -\tfrac{1}{3} d_v(x) \cos 2\theta \end{aligned} \tag{17}$$

yields results identical to the Carlitz–Kaur model.

In the next section we consider the phenomenological implications of the various inputs.

3. Phenomenology

First we compute the valence quark contribution to Δq. Recently Gupta *et al* (1989) have given parametrizations of $u_v(x)$ and $d_v(x)$ and $\cos 2\theta$ and various other distributions which fit the $g_1^p(x)$ given by EMC (Ashman *et al* 1988). We concentrate on the valence and $\cos 2\theta$ distributions given by them. The two sets of distributions given by them are,

Set I: ($Q_0^2 = 5\,\text{GeV}^2$, $\Lambda_{\text{QCD}} = 200\,\text{MeV}$)

$$\begin{aligned} x u_v(x) &= 1{\cdot}78 x^{0{\cdot}5}(1 - x^{1{\cdot}51})^{3{\cdot}5} \\ x d_v(x) &= 0{\cdot}67 x^{0{\cdot}4}(1 - x^{1{\cdot}51})^{4{\cdot}5} \\ \cos 2\theta &= [1 + 0{\cdot}258\ (1-x)^{1/2}/x^{0{\cdot}1}]^{-1} \end{aligned} \tag{18}$$

Set II: ($Q_0^2 = 15\,\text{GeV}^2$, $\Lambda_{\text{QCD}} = 90\,\text{MeV}$)

$$\begin{aligned} x u_v(x) &= 2{\cdot}75 x^{0{\cdot}588}(1 - x)^{2{\cdot}69} \\ x d_v(x) &= 8{\cdot}53 x^{1{\cdot}03}(1 - x)^{6{\cdot}87} \\ \cos 2\theta &= [1 + 0{\cdot}2656(1 - x^{1/2}/x^{0{\cdot}1}]^{-1} \end{aligned} \tag{19}$$

CC-0. In Public Domain. Gurukul Kangri Collection, Haridwar

Digitized by Arya Samaj Foundation Chennai and eGangotri

In addition we also consider a third set, with $u_v(x)$ and $d_v(x)$ as given by Diemoz *et al* (1988) (see also Gluck *et al* 1988).

Set III: ($Q_0^2 = 10\,\text{GeV}^2$, $\Lambda_{\text{QCD}} = 200\,\text{MeV}$)

$$xu_v(x) = 2{\cdot}26x^{0{\cdot}54}(1-x)^{2{\cdot}52}[1 - 1{\cdot}617(1-x) + 3{\cdot}647(1-x)^2 - 1{\cdot}998\,(1-x)^3]$$

$$xd_v(x) = 0{\cdot}57(1-x)xu_v(x). \tag{20}$$

The corresponding $\cos 2\theta$ for set three is taken to be

$$\cos 2\theta = [1 + \eta(1-x)^2/\sqrt{x}]^{-1}, \quad \eta = 0{\cdot}078.$$

a form suggested by Carlitz and Kaur (1976) (see also Kaur (1977)) based on Regge arguments. The moments Δu_v and Δd_v calculated based on the above parametrizations are given in table 1. It is easily seen that the moments are not only independent of the various parametrizations but are insensitive to the details of the model, Carlitz-Kaur or the modified SU(3) model of eqs (17) on the other. Notice that if $\cos 2\theta = 1$, Δu_v and Δd_v given by either of these models are identical and collapse to the naive SU(3) values. The effect of spin dilution factor is therefore to reduce G_A from 5/3 of SU(3) to approximately 5/4 closer to the experimental value.

An important point that emergies from table 1 is that $\Delta u_v/\Delta d_v = -4$ which is exactly the ratio predicted by the naive SU(3). This should not be surprising since we know that the SU(3) predictions for ratios elsewhere (like magnetic moment of baryons, the F/D ratio, etc.,) have been found to be accurate. In fact if the ratios of u and d matrix elements were to be renormalized differently by the effect of sea quarks and gluons such that the ratios differed from SU(3) predictions, it would imply catastrophic isospin violations not found elsewhere. We can therefore safely choose, based on the analysis above,

$$\Delta u_v \cong 1, \quad \Delta d_v \cong -0{\cdot}25. \tag{21}$$

Similar numbers have been obtained by Fritzsch (1988) where the reduction of G_A from 5/3 to 5/4 has been attributed to the effect of sea quarks and gluons. These

Table 1. First moment of valence quark spin distribution functions

Input		Carlitz-Kaur	SU(3) modified
Set I	Δu_v	1·0	1·0
	Δd_v	−0·25	−0·25
Set II	Δu_v	1·013	1·003
	Δd_v	−0·245	−0·245
Set III	Δu_v	1·004	0·99
	Δd_v	−0·24	−0·24

Modified $SU(3)$ distributions of (17) with spin dilution factor.

CC-0. In Public Domain. Gurukul Kangri Collection, Haridwar

Digitized by Arya Samaj Foundation Chennai and eGangotri

however contribute differently to u and d quarks implying isospin violation, which we have avoided above.

Next we consider the sea quark contribution constrained according to (13). In the simplest case we can take the OZI rule to be exact for axial vector current matrix elements and set $\Delta s_\sigma = 0$. This would imply either $k=0$ or $\Delta\sigma = 0$. The former is unlikely since for the unpolarized distributions k is approximately 1/2 from CDHS parametrizations (Abramowicz *et al* 1983). If the latter is taken to be correct, then the non-zero value of Δs arises entirely from gluons. Using the theoretical values given in (8), and using (9–11), we find

$$\Delta G \cong -0{\cdot}165, \quad \Delta u_v \cong 0{\cdot}965, \quad \Delta d_v \cong -0{\cdot}285. \tag{22}$$

The valence quark contribution is not far off from (21). On the other hand if we take $\Delta s_\sigma \neq 0$ and using the valence quark contribution from (21) as input in (9–11), we obtain,

$$\begin{aligned} \Delta u &= 1 + \Delta\sigma + \Delta G, \\ \Delta d &= -0{\cdot}25 + \Delta\sigma + \Delta G, \\ \Delta s &= k\Delta\sigma + \Delta G, \end{aligned} \tag{23}$$

where $0 \leqslant k \leqslant 1$. The case $k=1$ corresponds to SU(3) symmetric sea which yields $G_A = 1{\cdot}25$ and $G_8 = \Delta u + \Delta d - 2\Delta s = 0{\cdot}75$. Experimentally the value of G_B is close to 0·685 using the measured value of F/D (Gaillard and Sauvage 1984). For $k < 1$, we obtain

$$G_8 = 0{\cdot}75 + 2\Delta\sigma(1-k) = 0{\cdot}685. \tag{24}$$

For $k \cong 1/2$ as in the unpolarized case $\Delta\sigma \cong -0{\cdot}07$ and $\Delta s_\sigma \cong -0{\cdot}035$ which is consistent with the Regge bound (Anselmino *et al* 1988) on the strange quark polarization,

$$\| \Delta s_\sigma \| \leqslant 0{\cdot}072 \pm 0{\cdot}030. \tag{25}$$

A slightly different bound $\| \Delta s_\sigma \| \leqslant 0{\cdot}052^{+0{\cdot}023}_{-0{\cdot}052}$ has been quoted by Soffer (1989). The value of Δs_σ is consistent with either of these two bounds. The corresponding value of $\Delta G \cong -0{\cdot}13$ is slightly different from the $SU(3)$ symmetric case (eq. (22)).

In both cases discussed above the sign of the gluon contribution turns out to be negative. Following Altarelli and Ross (1988), if $\Delta G = -\alpha_s \Delta g/2\pi$, then the gluon polarization is in turn positive. Recently Cheng and Li (1989) have challenged the sign of Δg as obtained. Using the anomalous divergence equations to constrain the size of ΔG, they claim that the resulting sign of ΔG is positive; in fact,

$$\Delta G = 0{\cdot}16 \pm 0{\cdot}08. \tag{26}$$

They also conclude from this that it spells trouble for naive quark model. We show below that if any, the positive value of ΔG results in a large violation of the bound on the strange quark polarization, eq (25). Substituting the mean value of ΔG in (23) we find, without affecting the values of Δu_v and Δd_v,

$$\Delta\sigma = -0{\cdot}36, \quad \Delta s_\sigma = -0{\cdot}325, \tag{27}$$

CC-0. In Public Domain. Gurukul Kangri Collection, Haridwar

Digitized by Arya Samaj Foundation Chennai and eGangotri

or analogously $k \cong 0{\cdot}9$ which is very close to the SU(3) symmetric case with $k=1$. However such large strange sea polarization violates the Regge bound but is still consistent with quark model estimates.

4. Conclusions

We have recalculated the valence quark contribution Δu_v and Δd_v to the axial vector matrix elements of u and d quarks Δu and Δd consistent with the Bjorken sum rule. The ratio $\Delta u_v/\Delta d_v = -4$ obeys the SU(3) prediction. Keeping this as the input to the first moment of the proton spin structure function, we have reanalyzed the phenomenology of proton spin. We find that the gluonic contribution ΔG to be negative, as claimed by Altarelli and Ross (1988), in order to satisfy the Regge bound on the strange quark polarization. On the other hand Cheng and Li (1989) find ΔG to be positive which result they claim is just the wrong sign to accommodate naive quark model predictions. We find, however the quark model predictions for valence Δu_v and Δd_v can be accommodated with positive ΔG while violating the bound on strange quark polarisation.

Acknowledgements

One of us (MVN) thanks J Pasupathy for many valuable discussions and helpful comments. We also thank D Indumathi for going through the manuscript.

References

Ashman J *et al* [EMC] 1988 *Phys. Lett.* **B206** 364
Abramowicz H *et al* 1983 *Z. Phys. C* **17** 283
Altarelli G and Ross G G 1988 *Phys. Lett.* **B212** 391
Anselmino M, Ioffe B L and Leader E 1988 *Santa Barbara Preprint* NSF-ITP-88-94
Bajpai R P and Ramachandran R 1980 *Phys. Lett.* **B97** 125
Bjorken J D 1966 *Phys. Rev.* **148** 1467
Carlitz R D, Collins J and Mueller A H 1988 *Phys. Lett.* **B214** 229
Carlitz R D and Kaur J 1977 *Phys. Rev. Lett.* **38** 673
Cheng T P and Li L F 1989 *Phys. Rev. Lett.* **62** 1441
Close F E 1979 *An introduction to quarks and partons.* (London: Academic Press) p. 294
Diemoz M, Ferroni F, Longo E and Martinelli G 1988 *Z. Phys.* **C39** 21
Efremov A V and Teryaev D V 1988 *Dubna Preprint*-JINR EZ-88-287
Ellis J and Jaffe R L 1974 *Phys. Rev.* **D9** 1444, Erratum **D10** 1669
Ellis J, Gabathuler E and Karliner M 1988 *Preprint CERN*-TH-5188
Fritzsch H 1988 *Preprint MPI*-PAE/pTh-45/88
Gaillard J M and Sauvage G 1984 *Ann. Rev. Nucl. Part. Sci.* **34** 351
Gluck M, Godbole R and Reya E 1988 *Preprint* DO-Th-88/18
Gross D J, Treiman S B and Wilczek F 1979 *Phys. Rev.* **D19** 2188
Gupta S, Murthy M V N and Pasupathy J 1989 *Phys. Rev.* **D39** 2547
Gupta S, Pasupathy J and Szwed 1989 *Preprint* Un. Bielefeld
Jaffe R L and Manohar A 1989 *Preprint* CTP-1706
Kaur J 1977 *Nucl. Phys.* **B128** 219
Mani H S and Noman M 1981 *Phys. Rev.* **D24** 1223
Soffer J 1989 *Preprint* CPT-89/P.2220

CC-0. In Public Domain. Gurukul Kangri Collection, Haridwar

Digitized by Arya Samaj Foundation Chennai and eGangotri

CC-0. In Public Domain. Gurukul Kangri Collection, Haridwar

Digitized by Arya Samaj Foundation Chennai and eGangotri

Pramāṇa – J. Phys., Vol. 34, No. 2, February 1990, pp. 111–115. © Printed in India.

Bonding potential between two ^{12}C nuclei

P SARANGI*, S ALI+ and L SATPATHY*

*Institute of Physics, Sachivalaya Marg, Bhubaneswar 751 005, India
+Department of Physics, University of Dacca, Dacca 2, Bangladesh

MS received 18 September 1989; revised 21 November 1989

Abstract. The potential between two ^{12}C nuclei in linear chain configuration has been calculated microscopically using the Ali-Bodmer α-α potential. This potential shows a pocket and compares well in the tail region with the phenomenological potential extracted before, from the data on the quasi-molecular resonances of the $^{12}C+^{12}C$ system. This provides support to the diatomic like rotation-vibration picture of quasi-molecular states.

Keywords. Bonding potential; quasimolecular resonances.

PACS No. 25·70

Eventhough more than twenty five years have passed since the discovery of the nuclear quasi-molecular states in the $^{12}C+^{12}C$ system in 1960 by Bromley *et al* (1960), the mechanism of the phenomena has not yet been clearly established. During these years, such states have been observed in many other combinations of projectile and target nuclei. The general features of these states are that they show resemblance to the rotation-vibration spectra generally observed in a diatomic molecule. It was first suggested by Iachello (1981) that dipole degree of freedom characterized by the distance between the two nuclei could play important role in the mechanism. So the internuclear potential $V(R)$, where R is the distance between the two centres of the nuclei would govern the physics of these states. The analysis of the experimental data shows that the moment of inertia is very large, which correspond to a stretched out configuration suggestive of a very long range potential. Such long range is not in any way compactible with the usual optical potential of the $^{12}C+^{12}C$ system. This has been a quite puzzling problem in this area of heavy-ion physics. Satpathy *et al* (1983, 1986) had attempted to obtain this potential by using the data of the quasi-molecular states in the framework of a quantum mechanical two-body problem. They had supposed that the effective potential between two ^{12}C ions comprising both Coulomb and nuclear part could be represented by a four parameter Morse type potential. By fitting the energies of more than 20 quasi molecular states with the eigenvalue expression, parameters of the potential were determined. This potential was found to have a range of the order of 15 fm. The potential, besides fitting the data, suggests a possible mechanism (Satpathy *et al* 1986) of the quasi molecular states, according to which, the two nuclei when come closer by overcoming Coulomb barrier, or by sub-barrier tunnelling, they form a composite system, and in the effort to separate, they undergo a strong prolate deformation in the exit channel. Because of this strong prolate deformation, a broad Coulomb barrier is formed, which inhibits separation. Hence, they undergo rotation and vibration like a diatomic molecule and generate molecular resonance states.

CC-0. In Public Domain. Gurukul Kangri Collection, Haridwar

Digitized by Arya Samaj Foundation Chennai and eGangotri

Finally they separate with restoration of original shape after a long time in the exist channel. Thus, it is desirable to see that such a long range potential between two ^{12}C nuclei found above, really originates at a more microscopic level. It is known that the first 0^+ excited state of ^{12}C at 7·65 MeV has the configuration in which three α-particles form a linear chain. Feshbach (1976) had suggested long back, that this linear chain state may play an important role in explaining the mechanism of the quasi-molecular states. Hence, it is very much desirable to see if, the potential between two ^{12}C in linear chain configuration has a pocket to sustain resonances, and if, it resembles the phenomenological potential extracted by Satpathy and Faessler (1983). Previously Faessler *et al* (1984) have calculated this potential in the framework of α-cluster model, using the Brink-Boeker and Volkov effective interactions. They have found that their calculated potential has a long range with a pocket and resembles the phenomenological potential in the tail region. Considering the importance of this problem, we intend to calculate this potential using the Ali-Bodmer (1969) α-α potential, which was obtained by fitting the experimental phase-shifts and had been widely used (Afzal *et al* 1969; Portilho and Coon 1979; Portilho *et al* 1983). The Ali-Bodmer α-α potential is given by

$$V_{\alpha\alpha}(r) = V_r \exp(-\mu_r^2 r^2) - V_a \exp(-\mu_a^2 r^2) \tag{1}$$

where $V_r = 475$ MeV, $V_a = 130$ MeV, $\mu_r^2 = 0{\cdot}49\,\text{fm}^{-2}$ and $\mu_a^2 = 0{\cdot}2256\,\text{fm}^{-2}$. To this potential, Portilho *et al* (1983) have added a three-body term given by

$$V_{\alpha\alpha\alpha}(\mathbf{r}_1, \mathbf{r}_2, \mathbf{r}_3) = V_0[\exp(-\lambda(r_{12}^2 + r_{13}^2)) + \exp(-\lambda(r_{12}^2 + r_{23}^2)) + \exp(-\lambda(r_{13}^2 + r_{23}^2)] \tag{2}$$

where, $V_0 = -75$ MeV and $\lambda = 0{\cdot}21792\,\text{fm}^{-2}$. In our investigation, we have taken the nuclear part $V_N(r)$ as the combination of the above two potentials.

$$V_N(r) = V_{\alpha\alpha}(r) + V_{\alpha\alpha\alpha}(\mathbf{r}_1, \mathbf{r}_2, \mathbf{r}_3). \tag{3}$$

Since we are considering only the linear chain state for the two ^{12}C nuclei, the configuration chosen is the one as shown in figure 1, where R denotes the separation between the centres of the two carbon nuclei and r denotes the separation between two adjacent α-particles.

The calculation has been performed in two steps. In the first step, we determine the wavefunction and energy of an isolated C-nucleus in this linear chain state. We choose a variational wavefunction which includes correlation such that it does not allow overlap of any pair. This is given by

$$\phi(x_1, x_2, x_3) = S\Big[(x_1 - x_2)^4 (x_1 - x_3)^4 (x_2 - x_3)^4 \times \exp(-\alpha(x_1 - x_2)^2 - \alpha(x_2 - x_3)^2 - \frac{\alpha}{4}(x_1 - x_3)^2\Big]. \tag{4}$$

Since α-particles are bosons, therefore, S is the symmetrization operator, which ensures that ϕ remains symmetric under the exchange of co-ordinates of any two α-particles.

CC-0. In Public Domain. Gurukul Kangri Collection, Haridwar

Digitized by Arya Samaj Foundation Chennai and eGangotri

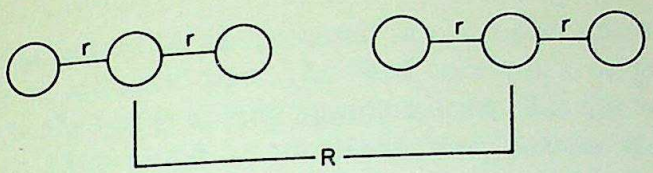

Figure 1. A schematic diagram of the linear chain configuration for the nuclear molecular resonance in ^{24}Mg formed by a ^{12}C-^{12}C collision.

This wave function has one parameter α, which was determined by minimizing the energy

$$E = \langle \phi | H | \phi \rangle / \langle \phi | \phi \rangle \tag{5}$$

where H is the Hamiltonian defined as

$$H = T - T_{cm} + V_N + V_C \tag{6}$$

where V_C is the Coulomb interaction and T_{cm} is the centre of mass energy. The values of E and α so obtained are 1·03 MeV and 0·19 respectively. If we take the ground state energy to be 7·25 MeV calculated by Portilho *et al* (1983) using the same potential which had agreed quite well with the experiment, then the energy of the first excited 0^+ states comes to 8·28 MeV in our calculation. This agrees reasonably well with the experimental value of 7·65 MeV. Portilho *et al* (1983) obtained a value of 9·33 MeV for this state using the same potential. Using our wavefunction we calculated the mean square distance $\langle (x_1 - x_2)^2 \rangle^{1/2}$ between two adjacent α-particles to be 3·31 fm. Thus the length of the C chain comes out to be 6·62 fm. In the study of this state by Friedrich *et al* (1971) using the Brink-Boeker force in the framework of α-cluster model, the length of the chain was obtained as about 7·7 fm.

In the second step of our calculation we determine the interaction potential between two C-ions, which is given by

$$V(R) = \langle \psi(R) | H | \psi(R) \rangle - \langle \psi(R = \infty) | H | \psi(R = \infty) \rangle. \tag{7}$$

Here $\psi(R)$ represents the wavefunction of the two carbon nuclei separated by a distance R. $\psi(R)$ in the frozen density approximation has been taken to be

$$\psi(R) = [\phi(x_1, x_2, x_3)\phi(x_4, x_5, x_6)]\delta \times \left[R - \frac{x_1 + x_2 + x_3}{3} - \frac{x_4 + x_5 + x_6}{3} \right] \tag{8}$$

where the ϕ's are defined in (4). In figure 2, we have compared our calculated potential with the phenomenological potential of Satpathy *et al* (1983, 1986) and the results of Faessler *et al* (1984). The solid curve is the pure nuclear part obtained in references [Satpathy and Faessler 1983; Satpathy *et al* 1986]. The broken curve is the nuclear part of the potential calculated by Faessler *et al* 1984 using the Brink–Boeker force in the framework of α-cluster model. In our calculation we have switched off the Coulomb term in (6) to get the corresponding nuclear part which has been shown as dotted curve in figure 2. Thus our potential agrees with the phenomenological potential in the tail region. It is also quite similar to the potential obtained by Faessler *et al* (1984). In figure 3, we have presented our results obtained with the inclusion of the

CC-0. In Public Domain. Gurukul Kangri Collection, Haridwar

Digitized by Arya Samaj Foundation Chennai and eGangotri

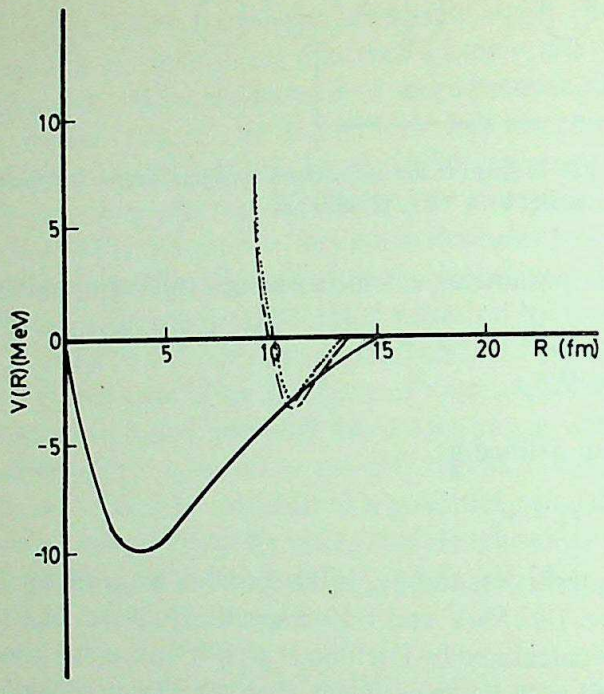

Figure 2. The interaction potential between two ^{12}C nuclei calculated using the Ali-Bodmer α-α potential (dotted curve) together with the phenomenological potential of Satpathy and Faessler (full curve) and the calculated potential of Faessler *et al* using the Brink-Boeker force (broken curve).

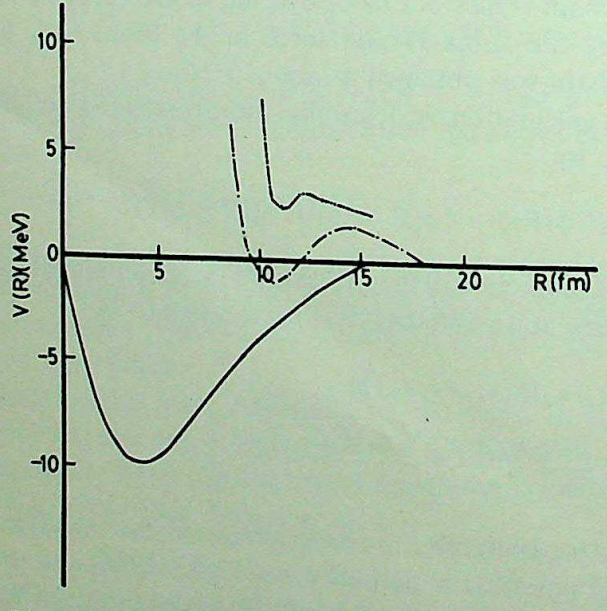

Figure 3. The full curve is as in figure 2. The chain curve is calculated by Faessler *et al* using the Volkov force together with Coulomb potential and the dotted curve is the present result obtained using the α-α potential along with the Coulomb interaction.

Coulomb potential represented by the dotted curve. The chain curve is the result obtained by Faessler *et al* (1984) using the Volkov force and the Coulomb interaction. Although somewhat shallower, we find a pocket in our potential. This potential is positive throughout, however because of the presence of the pocket it can have, in principle, bound states as well as resonances.

CC-0. In Public Domain. Gurukul Kangri Collection, Haridwar

Digitized by Arya Samaj Foundation Chennai and eGangotri

The general feature of our potential in the figure has a hard core of long range followed by an attractive part. The hard core has a range of about 8 fm, which is mainly due to the frozen density approximation. But the total range of the potential is more than 13 fm found in our calculation. Besides this long range, it is quite interesting to note that the potential does show a pocket which is very essential for the sustenance of quasi-molecular resonances.

The quasi-molecular states are manifested in low energy experiment, in which the projectile has energy whose value is about the Coulomb barrier of the projectile and target nuclei. The outer region of the potential is explored in the process. So, the physics of the phenomena is mainly governed by that region of the potential. Hence, our potential calculated here, although differ very substantially from the phenomenological one found by Satpathy *et al* (1986) in the core region, provides support for the mechanism.

In conclusion we would like to say that the mechanism of quasi-molecular states which has emerged in our previous study is being corroborated by the present calculation. It is quite satisfying that starting from a totally different approach and using α-α potential determined from experimental data, we obtain an interaction potential between two ^{12}C nuclei in linear chain configuration, which is quite similar to that of Faessler *et al* (1984) calculated with effective nucleon-nucleon potentials. This enhances our confidence on the diatomic like rotation-vibration mechanism of the quasi-molecular states in the $^{12}C + ^{12}C$ system proposed earlier.

References

Afzal S A, Ahmal A A Z and Ali S 1969 *Rev. Mod. Phys.* **41** 247

Ali S and Bodmer A R 1966 *Nucl. Phys.* **80** 99

Bromley D A, Kurehrer J A and Almavist E 1960 *Phys. Rev. Lett.* **4** 365

Faessler A, Wadia W, Rashdan M and Ismail M 1984 *J. Phys.* **G10** L35

Feshbach H 1976 *J. Phys.* (*Paris*) *Colloq.* **37** 177

Friedrich H, Satpathy L and Weiguny A 1971 *Phys. Lett.* **B36** 189

Iachello F 1981 *Phys. Rev.* **C23** 2778

Portilho O and Coon S A 1979 *Z. Phys.* **A290** 93

Portilho O, Agrello D A and Coon S A 1983 *Phys. Rev.* **C27** 2923

Satpathy L and Feassler A 1983 *Bhubaneswar Preprint* IP/BBSR/83-19

Satpathy L, Sarangi P and Feassler A 1986 *J. Phys.* **G12** 201

CC-0. In Public Domain. Gurukul Kangri Collection, Haridwar

Digitized by Arya Samaj Foundation Chennai and eGangotri

CC-0. In Public Domain. Gurukul Kangri Collection, Haridwar

Digitized by Arya Samaj Foundation Chennai and eGangotri

Pramāṇa – J. Phys., Vol. 34, No. 2, February 1990, pp. 117–122. © Printed in India.

Interaction of strong laser beam with He-atom using non-perturbative Floquet method

MAN MOHAN*, VINOD PRASAD† and BHUPAT SHARMA†

*Department of Physics, K.M. College, University of Delhi, Delhi 110007, India
†Department of Physics and Astrophysics, University of Delhi, Delhi 110007, India

MS received 15 March 1989; revised 12 October 1989

Abstract. Non-perturbative Floquet method is used to investigate the interaction of strong linearly polarized light with He-atom. In the calculations, six lowest singlet target states and fifteen photon states are taken for absolute convergence. For allowed transitions, accurate oscillator strengths using configuration interaction wave-functions are used. A number of interesting features such as nonlinear effects at high intensities, line broadening, a dynamic Stark effect are obtained and explained.

Keywords. Photon states; oscillator strengths; target states.

PACS No. 32·80

1. Introduction

Recently there has been considerable attention in the study of interaction of intense laser beam with multielectron atoms (Lambropoulos and Tang 1987; Perry and Szoke 1988) due to its importance in the production of powerful lasers and laser fusion reactions. Here in this paper we have used the Floquet theory (non-perturbative) for the calculation of multi-photon excitation of the He-atom. The Floquet theory (Shirley 1965; Moloney and Faisal 1979; Leasure and Wyatt 1979; Chu 1986) relates the solution of Schrödinger equation with a periodic Hamiltonian (laser + atom system) to the solution of another Schrödinger equation with a time-independent Hamiltonian represented by an infinite matrix (called a Floquet matrix). In the present calculations we have included lowest six singlet states of target atom and fifteen photon states (i.e. $N = 0, \pm 1, \pm 2, \pm 3, \pm 4, \pm 5, \pm 6, \pm 7$) for absolute convergence.

2. Floquet theory formalism

The Schrödinger equation for a quantum mechanical system in an external field, which is periodic function of time with period T, can be written (in a.u.) as

$$i(\partial\psi_p/\partial t) = H\Psi_p(\mathbf{r}, t) \tag{1}$$

where $H = H_0 - \mu(\mathbf{r}).\ \mathbf{E}_0 \cos \omega t$; H_0 is the Hamiltonian for the isolated atom, $\mu(r)$ is the atomic dipole moment function, $|\mathbf{E}_0|$ is the amplitude and ω is the frequency of the field.

CC-0. In Public Domain. Gurukùl Kangri Collection, Haridwar

Digitized by Arya Samaj Foundation Chennai and eGangotri

We can expand the total wavefunction $\Psi_p(\mathbf{r}, t)$ of the system in terms of field free atomic eigenfunctions

$$\Psi_p(\mathbf{r}, t) = \sum_{q=1}^{N} a_{qp}(t)\chi_q(\mathbf{r}) \tag{2}$$

when the e.m. field is turned off adiabatically, the wavefunction of the system becomes the usual stationary states, hence,

$$\Psi_p(\mathbf{r}, t) = \chi_q(\mathbf{r}). \tag{3}$$

Substituting (2) into (1) and using the orthogonality conditions for the atomic states, we obtain

$$i\frac{\partial a_{qp}}{\partial t} = E_q^0 a_{qp}(t) - |\mathbf{E}_0| \cos \omega t \sum_{s=1}^{N} V_{qs} a_{sp}(t) \tag{4}$$

where

$$V_{qs} = \langle \chi_q(\mathbf{r}) | \mu(\mathbf{r}) \cdot \hat{E}_0 | \chi_s(\mathbf{r}) \rangle \tag{4a}$$

is the dipole matrix element and $\hat{E}_0$ is a unit vector in the direction of $\mathbf{E}_0$. In the matrix notation the above equation can be written as

$$i(\partial A/\partial t) = H_c(t)A(t), \tag{5}$$

where $H_c(t)$ is a periodic function of time with period $T = 2\pi/w$ i.e. $H_c(t) = H_c(t+T)$. According to Floquet theory (5) admits the following solution

$$A^F(t) = \Phi(t) \exp(-i\mu t), \tag{6}$$

where $\Phi(t)$ is another periodic function of time, and μ is the diagonal matrix called the characteristic exponent.

According to Shirley (1965), the Fourier series expansions of $A^F(t)$ and $H_c(t)$ are given by

$$A^F(t) = \sum_{m=-\infty}^{+\infty} f_{r,l}^m \operatorname{emp}(im\omega t) \exp(-i\mu_l t) \tag{7}$$

and

$$H_c(t) = (H_c)_{r,l} = \sum_{m=-\infty}^{+\infty} \mathscr{H}_{r,l}^m \exp(im\omega t) \tag{8}$$

where $f_{r,l}^m$ and $\mathscr{H}_{r,l}^m$ are the Fourier amplitudes corresponding to a particular value of m. Here the indices r and l range over the atomic states and the Fourier index m indicates the photon number.

Substituting (7) and (8) in (5) yield the following eigenvalue equation for the Fourier components $f_{r,l}^m$ and the characteristic value μ_l i.e.

$$\sum_j \sum_n (\mathscr{H}_{r,j}^{m-n} + n\omega\delta_{rj}\delta_{nm}) f_{rl}^n = \mu f_{r,l}^m. \tag{9}$$

Once the eigenvalue $f_{r,l}^m$ corresponding to the eigenvalue μ_l are found by diagonalizing the Floquet matrix H_F (the terms within the bracket of (9)), the transition amplitude can be determined from (7). More explicitly the transition probability from

CC-0. In Public Domain. Gurukul Kangri Collection, Haridwar

Digitized by Arya Samaj Foundation Chennai and eGangotri

the initial atomic state $|i\rangle$ to final atomic state $|j\rangle$ is given by (Shirley 1965; Leasure and Wyatt 1979; Moloney and Faisal 1979)

$$P_{i\to j}(t,t_0)=|\langle j|U(t,t_0)|i\rangle|^2 \tag{10}$$

where $U(t,t_0)$ is the evolution operator.

For continuous coherent operation of the laser, we average (10) over $t-t_0=T$, and obtain the long time average transition probability as

$$\bar{P}_{i\to j}=\lim_{T\to\infty}\frac{1}{T}\int_0^T P_{ij}(\tau)\,d\tau$$
$$=\sum_n\sum_{\mu_l}|f^n_{i,\mu_l}f^0_{j,l}|^2. \tag{11}$$

The determination of $\bar{P}_{i\to j}$ requires the construction of the Floquet Hamiltonian H_F which involves the dipole-matrix element between the various target levels. We have used the recent calculations (Berrington *et al* 1985; Berrington and Kingston 1987) for the evaluation of accurate dipole matrix elements from oscillator strengths for the He-atom. The sophisticated configuration interaction wavefunctions, needed to evaluate oscillator strengths have been obtained by using CI V3 code (Hibbert 1975). The theoretical energies obtained for six lowest singlet levels and the oscillator strengths for different allowed transitions between them are shown in tables 1 and 2 respectively. In our calculations we have truncated the Floquet Hamiltonian H_F to

Table 1. Excitation energies (in eV) for $n=1$, $n=2$ and $n=3$ states in He atom relative to groundstate 1^1S.

State	Thresholds (eV)
1^1S	0·0
2^1S	20·617
2^1P^o	21·219
3^1S	22·921
3^1D	23·075
3^1P^o	23·088

Table 2. Oscillator strength for allowed transitions among the lowest six states in the He atom.

Transitions	f(length)
$1^1S\to 2^1P^o$	0·2145
$1^1S\to 3^1P^o$	0·0006
$2^1S\to 2^1P^o$	0·3662
$2^1S\to 3^1P^o$	0·1755
$2^1P^o\to 3^1S$	0·0514
$2^1P^o\to 3^1D$	0·7254
$3^1S\to 3^1P^o$	0·5663
$3^1P^o\to 3^1D$	0·0221

CC-0. In Public Domain. Gurukul Kangri Collection, Haridwar

Digitized by Arya Samaj Foundation Chennai and eGangotri

contain fifteen Floquet photon blocks ($N=0, \pm1, \pm2, \pm3, \pm4, \pm5, \pm6, \pm7$) as described by Mohan and Sharma (1986) although the results were found to be converged after truncating H_F by including only seven photon blocks.

Using the standard diagonalization routines from SSP Library, the Floquet Hamiltonian H_F of dimension (90×90) is diagonalized to yield the characteristic Floquet exponents and the corresponding Fourier components defined by (9). These are then substituted into (11) to yield infinite-time average transition probability.

3. Results and discussion

The results for the $(s^2)1^1S \rightarrow (1s2p)2^1P^\circ$ transition are shown in figure 1 with the variation of laser frequency (in cm^{-1}) for several laser intensities. Clearly the probability $\bar{P}_{1\rightarrow3}$ at $I = 10^6$ cm^{-2}, increases quite steadily from $\omega = 161470{\cdot}0\,cm^{-1}$ to, $\omega = 161491{\cdot}8\,cm^{-2}$ where it has an extremum value. However, with further increase in the frequency, the probability $\bar{P}_{1\rightarrow3}$ decreases. At a higher intensity $I = 10^7$ Wcm^{-2}, the probability $\bar{P}_{1\rightarrow3}$ has the similar variation except the extremum occurs at $\omega = 161491{\cdot}6\,cm^{-1}$. Thus, the shifting of resonance by $\Delta\omega = 0{\cdot}2\,cm^{-1}$ with increase of laser power 10^1 Wcm^{-2}, is a clear indication of the dynamic Stark shift which increases with increasing intensity of the laser beam. Further broadening of overall probability curve at $I = 10^8$ Wcm^{-2} as compared to that at $I = 10^6$ Wcm^{-2} shows that the line broadening effect is much more pronounced in He atom at high intensities as also shown by others (Geltman 1980; Mohan and Sharma 1986).

In figure 2 we have shown the variation of $(1s2p)2^1p^0 \rightarrow (1s3d)\ 3^1D$ transition probability with frequency of the laser beam. Comparison of the two figures shows

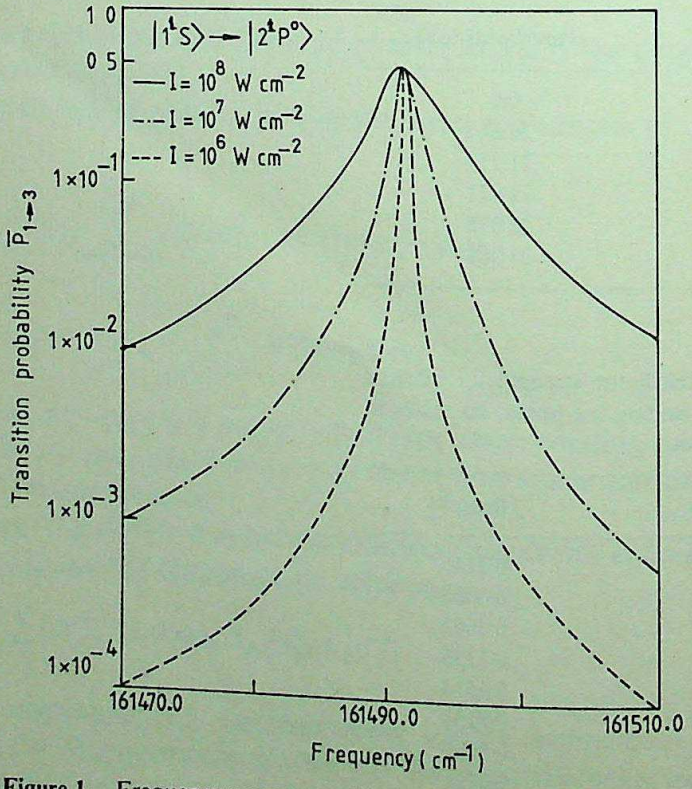

Figure 1. Frequency versus transition probability $\bar{P}_{1-3}$.

CC-0. In Public Domain. Gurukul Kangri Collection, Haridwar

Digitized by Arya Samaj Foundation Chennai and eGangotri

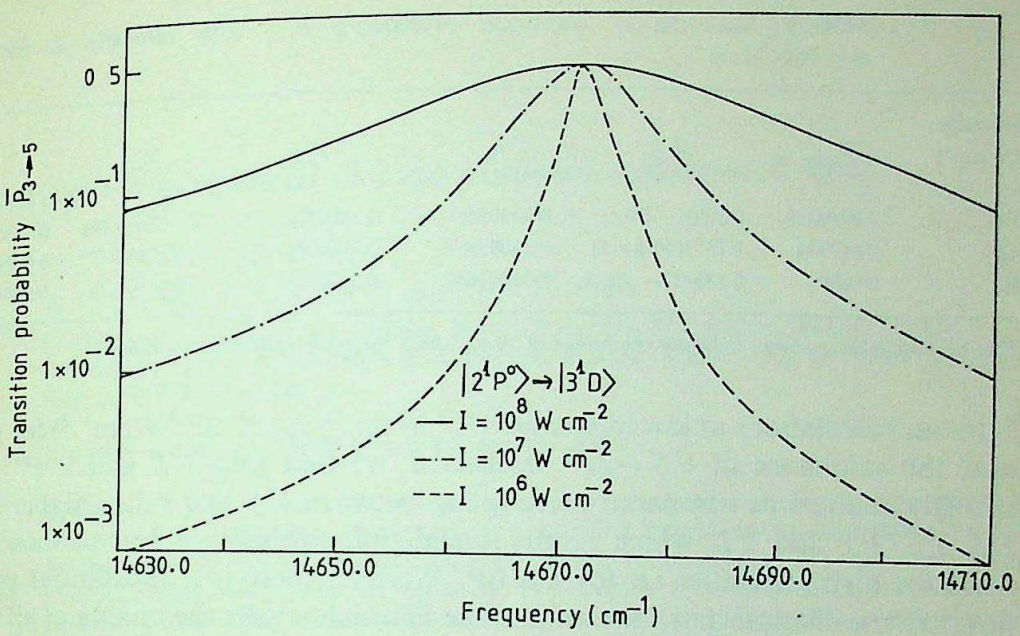

Figure 2. Frequency versus transition probability $\bar{P}_{3-5}$.

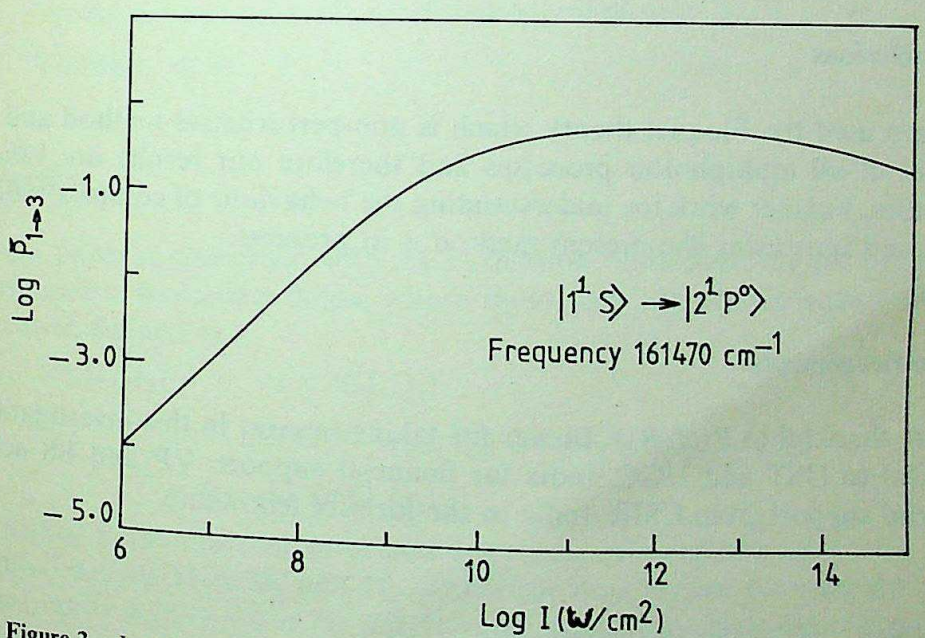

Figure 3. Log intensity versus log transition probability $\bar{P}_{1-3}$.

the asymmetrical behaviour for transition $1^1S \to 2^1P^0$ at laser intensities 10^7 W/cm^2 and 10^8 W/cm^2. This is due to low coupling between 1^1S and 2^1P^0 with respect to the coupling between 2^1P^0 and 3^1D. This asymmetrical behaviour becomes more pronounced with increase of laser intensity.

Figure 3 shows the variation of transition probability $\mathbf{P}_{1-3}$ for the $1^1S \to 2^1P^0$ transition with intensity I (W/cm^2) at $\omega = 161470\,\text{cm}^{-1}$. Here the probability varies linearly with intensity up to $10^{10}\,\text{Wcm}^{-2}$ as expected from perturbation theory. However, as the intensity of the field is increased further, the probability reaches to the saturation value up to $10^{13}\,\text{Wcm}^{-2}$. Beyond $I \geqslant 10^{14}\,\text{Wcm}^{-2}$ there is a decline in probability showing the nonlinear effect at high intensity.

CC-0. In Public Domain. Gurukul Kangri Collection, Haridwar

Digitized by Arya Samaj Foundation Chennai and eGangotri

Table 3. Variation of transition probability $\bar{P}_{i\to j}$ with intensity I, for frequency $\omega = 161470\,\text{cm}^{-1}$.†

Intensity I(W/cm^2)	$\bar{P}_{1\to1}$	$\bar{P}_{1\to2}$	$\bar{P}_{1\to3}$	$\bar{P}_{1\to4}$	$\bar{P}_{1\to5}$	$\bar{P}_{1\to6}$
10^6	0·9999023	0·5501(−14)	0·976055(−4)	0·210658(−13)	0·2721(−14)	0·53851997(−12)
10^{10}	0·667904	0·18716854(−6)	0·330954(0)	0·716908(−8)	0·92546(−7)	0·47642(−8)
10^{14}	0·6069	0·235957(−2)	0·379416(0)	0·515699(−3)	0·1633(−2)	0·9054(−2)

†The number in parentheses indicates the power of 10 by which the entry should be multiplied.

In our calculations at low intensities ($10^6\,\text{Wcm}^{-2} \leqslant I \leqslant 10^{13}\,\text{Wcm}^{-2}$) for frequency near the resonance of $1^1S \to 2P^0$ transition, we find that 1^1S and 2^1P^0 levels are strongly coupled as compared to coupling between 1^1S and other higher levels e.g. 2^1S, 3^1S, 3^1P and 3^1D, which results a negligible probability flow to these channels while for high intensities i.e. for $I \geqslant 10^{14}\,\text{Wcm}^{-2}$, there is a substantial probability flow to these channels (also shown in table 3) which results the mixing of all the levels. This mixing leads finally to drop in the probability for $1^1S \to 2^1P^0$ transition.

4. Conclusions

We have used the Floquet theory which is non-perturbative method and takes into account of all multiphoton processes and therefore our results are valid for high intensities. Further work for understanding the behaviour of complex-multi-electron atoms and ions using the present method is in progress.

Acknowledgements

We are thankful to Prof. S N Biswas for taking interest in this investigation. MM is thankful to DST and UGC, India for financial support. VP and BS acknowledge financial support from CSIR, India in the form of fellowship.

References

Berrington K A, Burke P G, Freitas L C G and Kingston A E 1985 *J. Phys.* **B18** 4135
Berrington K A and Kingston A E 1987 *J. Phys.* **B20** 6631
Chu S I 1986 *Adv. At. Mol. Phys.* **21** 197
Geltman S 1980 *J. Phys.* **B13** 115
Hibbert A 1975 *Comput. Phys. Commun.* **9** 141
Lambropoulos P and Tang X 1987 *J. Opt. Soc. Am.* **B4** 821
Leasure S C and Wyatt R E 1979 *Chem. Phys. Lett.* **61** 625
Mohan M and Sharma B 1986 *Chem. Phys. Lett.* **B12** 38
Moloney J V and Faisal F H M 1979 *J. Phys.* **B12** 2829
Perry M D and Szoke A 1988 *Phys. Rev. Lett.* **60** 1270
Shirley J H 1965 *Phys. Rev.* **B138** 979

CC-0. In Public Domain. Gurukul Kangri Collection, Haridwar

Digitized by Arya Samaj Foundation Chennai and eGangotri

Pramāṇa – J. Phys., Vol. 34, No. 2, February 1990, pp. 123–131. © Printed in India.

Thermodynamic properties of hard ellipsoid square-well fluid

A K SINGH*, T K DEY and S K SINHA

Department of Physics, L S College, Bihar University, Muzaffarpur 842001, India
*Permanent address: Department of Physics, S R K Goenka College, Bihar University, Sitamarhi 843301, India

MS received 24 June 1987; revised 5 September 1989

Abstract. The perturbation theory with non-spherical reference system is used for molecular fluid with angle-dependent square-well type potential. Simple analytic expressions are given for the thermodynamic properties such as the equation of state, excess free energy per particle, internal energy and internal heat capacity. The effects of anisotropy on the thermodynamic properties are discussed. The anisotropy effects increase with increase of density and decrease of temperature and depends on the anisotropy parameter x_0.

Keywords. Perturbation theory; equation of state; excess free energy; internal energy; internal heat capacity; anisotropy parameter; hard ellipsoid.

PACS No. 61·25

1. Introduction

The present paper is concerned with the evaluation of thermodynamic properties of axially symmetric molecular fluids, whose molecules interact via square-well (SW) type potential, defined as

$$\begin{aligned} u(r,\Omega_1\Omega_2) &= \infty, \quad r < \sigma(\Omega_1\Omega_2) \\ &= -\varepsilon(\Omega_1\Omega_2), \quad \sigma(\Omega_1\Omega_2) < r < \lambda\sigma(\Omega_1\Omega_2) \\ &= 0, \quad r > \lambda\sigma(\Omega_1\Omega_2), \end{aligned} \tag{1}$$

where $\sigma(\Omega_1\Omega_2)$ is the distance of closest approach between two molecules and λ is the potential cut off. Here Ω_1 and Ω_2 denote the orientations of molecules 1 and 2, respectively and $r = |\bar{r}_1 - \bar{r}_2|$. In (1), $\varepsilon(\Omega_1\Omega_2)$ and $\sigma(\Omega_1\Omega_2)$ are angle-dependent strength and range parameters respectively. They are assumed to be of forms (Berne and Pechukas 1972)

$$\varepsilon(\Omega_1\Omega_2) = \varepsilon_0[1 - x^2(\hat{e}_1\cdot\hat{e}_2)^2]^{-1/2}, \tag{2}$$

$$\begin{aligned} \sigma(\Omega_1\Omega_2) = \sigma_0[1 - x\{&(\hat{r}\cdot\hat{e}_1)^2 + (\hat{r}\cdot\hat{e}_2)^2 \\ &- 2x(\hat{r}\cdot\hat{e}_1)(\hat{r}\cdot\hat{e}_2)(\hat{e}_1\cdot\hat{e}_2)\}\{1 - x^2(\hat{e}_1\cdot\hat{e}_2)^2\}^{-1}]^{-1/2}, \end{aligned} \tag{3}$$

where $\hat{e}_1$ and $\hat{e}_2$ are unit vectors along the symmetry axes of two interacting molecules and $\hat{r}$ the unit vector along the intermolecular axis **r**. Here ε_0 and σ_0 are constants with units of energy and length respectively, and

$$x = (x_0^2 - 1)/(x_0^2 + 1) \tag{4}$$

CC-0. In Public Domain. Gurukul Kangri Collection, Haridwar

Digitized by Arya Samaj Foundation Chennai and eGangotri

is an anisotropy parameter, x_0 being the length ($2a$) to width ($2b$) ratio of the molecule and $\sigma_0 = 2b$. The SW potential is the simplest model which takes into account strong anisotropy in both intermolecular repulsion and attraction and represents, at least qualitatively, the shape of the molecular core.

At present one of the most successful approaches for dealing with molecular fluids is the perturbation theory (Gray and Gubbins 1984). For molecular fluid, whose molecules interact via the angle-dependent pair potential, the perturbation expansion is made about the hard-convex body reference system (Boublik 1976). Recently Boublik (1987) has used the Barker-Henderson (BH) theory in the macroscopic compressibility approximation (Barker and Henderson 1967; Fischer 1980) to calculate the equilibrium properties of the molecular fluids. One may, however, expect to obtain better results by using the local compressibility approximation (Barker and Henderson 1967) in place of the macroscopic compressibility.

In this work we generalize the BH perturbation theory in the local compressibility (l.c.) approximation for non-spherical molecule fluids employing the hard convex body as reference.

In §2 we discuss the second order perturbation theory of hard convex-molecule fluids. The properties of the reference system are given and the angle-integrations of the perturbation parts are performed. Section 3 is devoted to the square-well type of fluid. Analytic expressions for the first and second perturbation corrections to the free energy and pressure are reported there. Results and discussions are presented in §4.

2. Perturbation expansion

We divide the pair potential $u(r\Omega_1\Omega_2)$ as

$$u(r\Omega_1\Omega_2) = u_{hc}(r\Omega_1\Omega_2) + u_p(r\Omega_1\Omega_2), \tag{5}$$

where

$$\begin{aligned} u_{hc}(r\Omega_1\Omega_2) &= \infty, \quad r < \sigma\,(\Omega_1\Omega_2) \\ &= 0, \quad r > \sigma\,(\Omega_1\Omega_2) \end{aligned} \tag{6}$$

is the hard-convex (HC) potential treated as a reference potential and $u_p(r\Omega_1\Omega_2)$ is perturbation. (Here $r = |\bar{r}_1 - \bar{r}_2|$.)

Using this division of pair potential in the Barker-Henderson-like (BH) perturbation theory in the l.c. approximation, the free energy per particle is given by

$$\begin{aligned} \beta f = \beta f_{hc} &+ \tfrac{1}{2}\beta\rho \int d\bar{r} \langle g_{hc}(r\Omega_1\Omega_2) u_p(r\Omega_1\Omega_2)\rangle \\ &- \tfrac{1}{4}\beta\rho \left(\frac{\partial\rho}{\partial P_{hc}}\right) \frac{\partial}{\partial\rho}\left[\rho \int d\bar{r} \langle g_{hc}(r\Omega_1\Omega_2) u_p^2(r\Omega_1\Omega_2)\rangle\right], \end{aligned} \tag{7}$$

where $g_{hc}(r\Omega_1\Omega_2)$ is the pair correlation function (PCF) of the HC fluid and $\rho \equiv N/V$ is the number density. Here $\langle \cdots \rangle$ represents an unweighted average over the molecular orientations Ω_1 and Ω_2 for the quantity within the angular bracket i.e.

$$\langle \cdots \rangle = \frac{1}{\Omega^2} \int d\Omega_1 \int d\Omega_2 (\cdots). \tag{8}$$

CC-0. In Public Domain. Gurukul Kangri Collection, Haridwar

Digitized by Arya Samaj Foundation Chennai and eGangotri

Ω is the normalisation constant. For the linear molecules $\Omega = 4\pi$ and

$$d\Omega_i = \sin\theta_i \, d\theta_i \, d\phi_i.$$

The thermodynamic properties of the HC fluid can be calculated from the equation of state (Singh and Singh 1986; Singh *et al* 1988)

$$\frac{\beta P_{hc}}{\rho} = 1 + \frac{2\eta(2-\eta)}{(1-\eta)^3} F_1(x), \tag{9}$$

where

$$F_1(x) = (1-x^2)^{-1/2}\left[1 - \tfrac{1}{6}x^2 - \tfrac{1}{40}x^4 - \tfrac{1}{112}x^6 + \cdots\right] \tag{10}$$

and

$$\eta = \rho V_{hc} = \pi\rho\sigma_0^3 x_0/6 \quad \text{(for hard ellipsoids)}$$
$$= \tfrac{1}{12}\pi\rho\sigma_0^3 (3x_0 - 1) \quad \text{(for prolate hard spherocylinder),}$$

V_{hc} being the volume of a hard non-sphere molecule. Then the expression for free energy per particle of the HC fluid is (Singh *et al* 1988)

$$\beta f_{hc} = \frac{\eta(4-3\eta)}{(1-\eta)^2} F_1(x). \tag{11}$$

Using (9), the compressibility equation for the HC fluid is given by

$$\left(\frac{\partial\rho}{\partial P_{hc}}\right) = \frac{\beta}{a_{hc}}, \tag{12}$$

where

$$a_{hc}(x) = 1 + \frac{2\eta(4-\eta)}{(1-\eta)^4} F_1(x). \tag{13}$$

In order to evaluate the perturbation correction terms, we use the decoupling approximation (Parson 1979) and write

$$g_{hc}(r\Omega_1\Omega_2) = g_{hc}(r/\sigma(\Omega_1\Omega_2)) = g_{hs}(r^*), \tag{14}$$

where $g_{hs}(r^*)$ is the PCF for the hard sphere (HS) system at the packing fraction $\eta = \rho v_{hc}$. In the decoupling approximation, the orientational and positional degrees of freedom are completely decoupled. Then the free energy per particle of the system is expressed in a simpler form

$$\beta f - \beta f^c = \frac{12(1-x^2)^{-1/2}}{T^*}\eta \int_1^\infty dr^* r^{*2} u_p^*(r^*) g_{hs}(r^*)$$
$$- \frac{6\Delta(x)}{T^{*2} a_{hc}} \eta \frac{\partial}{\partial\eta}\left[\eta \int_1^\infty dr^* r^{*2} u_p^{*2}(r^*) g_{hs}(r^*)\right], \tag{15}$$

where

$$\Delta(x) = (1-x^2)^{-1/2}\Omega^{-2} \int d\Omega_1 \int d\Omega_2 \, (1 - x^2\cos^2\theta_{12})^{-1/2}$$
$$= (1-x^2)^{-1/2}\left[1 + \tfrac{1}{6}x^2 + \tfrac{3}{40}x^4 + \tfrac{5}{112}x^6 + \cdots\right], \tag{16}$$

$T^* = kT/\varepsilon_0 \equiv (\beta\varepsilon)^{-1}$ and $u_p^* = u_p/\varepsilon_0$

CC-0. In Public Domain. Gurukul Kangri Collection, Haridwar

Digitized by Arya Samaj Foundation Chennai and eGangotri

3. Square-well potential

For the square-well potential (Eq. (1)), u_p^* is given by

$$u_p^*(r^*) = -1, \quad 1 \leqslant r^* \leqslant \lambda$$
$$= 0, \quad r^* \geqslant \lambda, \tag{17}$$

where λ determines the width of the well in relation to the hard core. This is a very useful model for testing theory of fluids, as the complicating effects of a soft core are not present for this model. Since the classical square well potential with $\lambda = 1{\cdot}5$ is a qualitatively reasonable model for real simple fluids (Henderson *et al* 1976), we choose $\lambda = 1{\cdot}5$ in our calculations. In this case, (15) reduces to

$$\beta f - \beta f_{hc} = \beta f_1 + \beta f_2, \tag{18}$$

where

$$\beta f_1 = -\frac{12\eta(1-x^2)^{-1/2}}{T^*} Q(\eta) \tag{19}$$

$$\beta f_2 = -\frac{6\eta\Delta(x)}{T^{*2} a_{hc}} \frac{\partial}{\partial\eta}[\eta Q(\eta)], \tag{20}$$

where

$$Q(\eta) = \int_1^\lambda \mathrm{d}r^* r^{*2} g_{hs}(r^*), \tag{21}$$

which can be solved analytically to give (Ponce and Renon 1976)

$$Q(\eta) = \tfrac{1}{3}\left[\lambda^3 + \left(\frac{1-a_{hs}}{8\eta a_{hs}}\right)\right], \tag{22}$$

where $a_{hs} = (\partial P_{hs}/\partial\rho)$, which can be obtained from (13) by putting $F_1(x) = 1$ i.e.

$$a_{hs} = 1 + \frac{2\eta(4-\eta)}{(1-\eta)^4}. \tag{23}$$

Substituting (22) in (19) and (20) we obtain an analytic expression for the free energy of the square-well molecular fluid

$$\beta f = \beta f_{hc} + \frac{f_1^*}{T^*} + \frac{f_2^*}{T^{*2}}, \tag{24}$$

where

$$f_1^* = -4\eta\left[\lambda^3 + \left(\frac{1-a_{hs}}{8\eta a_{hs}}\right)\right](1-x^2)^{-1/2} \tag{25}$$

$$f_2^* = -2\eta a_{hc}^{-1}\left[\lambda^3 - \tfrac{1}{8}a_{hs}^{-2}\left(\frac{\partial a_{hs}}{\partial\eta}\right)\right]\Delta(x). \tag{26}$$

Other thermodynamic properties such as equation of state, internal energy and internal heat capacity can be obtained from (24) using the standard thermodynamic relations.

CC-0. In Public Domain. Gurukul Kangri Collection, Haridwar

Digitized by Arya Samaj Foundation Chennai and eGangotri

Expanding the equation of state $\beta P/\rho$ in power of η, we obtain expressions for the second and third virial coefficient for the molecular square well fluid

$$B_2 = b_0\left[1-(\lambda^3-1)\left\{\frac{(1-x^2)^{-1/2}}{T^*}+\frac{\Delta(x)}{2T^{*2}}+\cdots\right\}\right] \tag{27}$$

$$B_3 = b_0^2\left[\frac{5}{8}+\frac{2}{T^{*2}}\left\{\left((\lambda^3-1)F_1(x)-\frac{17}{16}\right)\right.\right.$$
$$\left.\left.-\frac{17}{16}T^*(1-x^2)^{-1/2}\right\}\right], \tag{28}$$

where

$$b_0 = 4v_{hc} = \frac{2\pi}{3}\sigma_0^3 x_0 \quad \text{(hard ellipsoid)}$$

$$= \frac{\pi}{3}\sigma_0^3(2x_0-1) \quad \text{(hard prolate spherocylinder).} \tag{29}$$

For hard sphere ($x_0 = 1$), $b_0 = 2\pi\sigma_0^3/3$ and $F_1(x) = \Delta = 1$ and (27) and (28) reduce to (Ponce and Renon 1976)

$$B_2 = b_0\left[1-(\lambda^3-1)\left(\frac{1}{T^*}+\frac{1}{2T^{*2}}+\cdots\right)\right] \tag{30}$$

$$B_3 = b_0^2\left[\frac{5}{8}+\frac{2}{T^{*2}}\{(\lambda^3-1)-\tfrac{17}{16}(1+T^*)\}\right]$$

The theory developed here for the S W fluid is valid for molecules of oblate ($x_0 < 1$) as well as prolate ($x_0 > 1$) shapes of arbitrary symmetry. $x_0 = 1$ corresponds to the simple fluid whose molecules are spherically symmetric.

4. Results and discussion

In this section we calculate the thermodynamic properties such as equation of state, excess free energy per particles, the internal energy and internal heat capacity of the SW molecular fluid for different values of anisotropy parameter x_0 (i.e. $0 < x_0 < 3{\cdot}0$).

The Monte Carlo values of the thermodynamic properties such as pressure and free energy of the SW fluid with $\lambda = 1{\cdot}5$ are available only for $x_0 = 1{\cdot}0$, where the agreement was found to be good (Ponce and Renon 1976). This method is expected to provide good results even for other values of x_0. We calculate the results for $\lambda = 1{\cdot}5$, which is qualitatively a reasonable model for simple fluids.

Figure 1 shows the values of f_1^* and f_2^* as a function of parameter x_0 at $\eta = 0{\cdot}3$ and $0{\cdot}4$ for $\lambda = 1{\cdot}5$ using (25) and (26), respectively. They are maximum at $x_0 = 1{\cdot}0$ and decreases steadily as x_0 moves away from $1{\cdot}0$. For a given η each of f_1^* and f_2^* has the same value at $x_0 = l$ and $x_0 = l^{-1}$ (l being any value of $x_0 > 1{\cdot}0$). For example f_1^* at a given η has the same value at $x_0 = 2{\cdot}0$ and $x_0 = 0{\cdot}50$.

The values of the equation of state, $\beta P/\rho$, are reported in figure 2 as a function of x_0 for $\eta = 0{\cdot}45$ at the isotherms $T^* = 2{\cdot}0$, $1{\cdot}333$, $1{\cdot}0$ and $0{\cdot}667$. At high temperatures

CC-0. In Public Domain. Gurukul Kangri Collection, Haridwar

Digitized by Arya Samaj Foundation Chennai and eGangotri

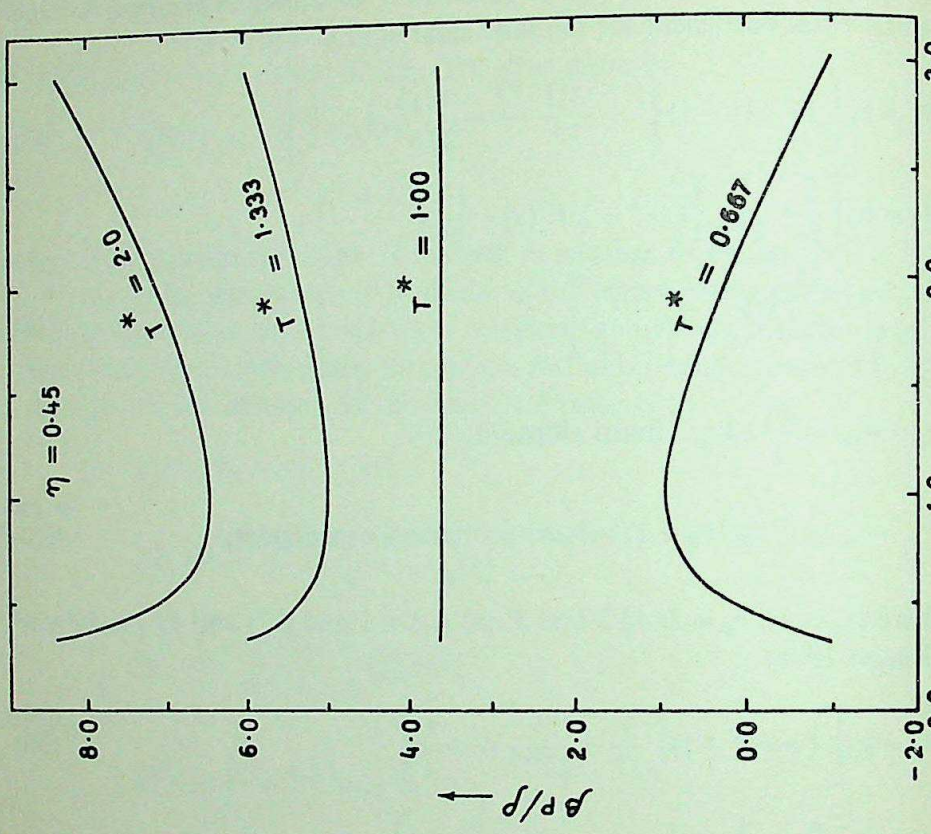

Figure 2. The equation of state, $\beta P/\rho$ of the hard ellipsoid S W fluid with $\lambda = 1{\cdot}5$ as a function of χ_0 for $\eta = 0{\cdot}45$ at $T^* = 2{\cdot}0$, 1·333, 1·0 and 0·667.

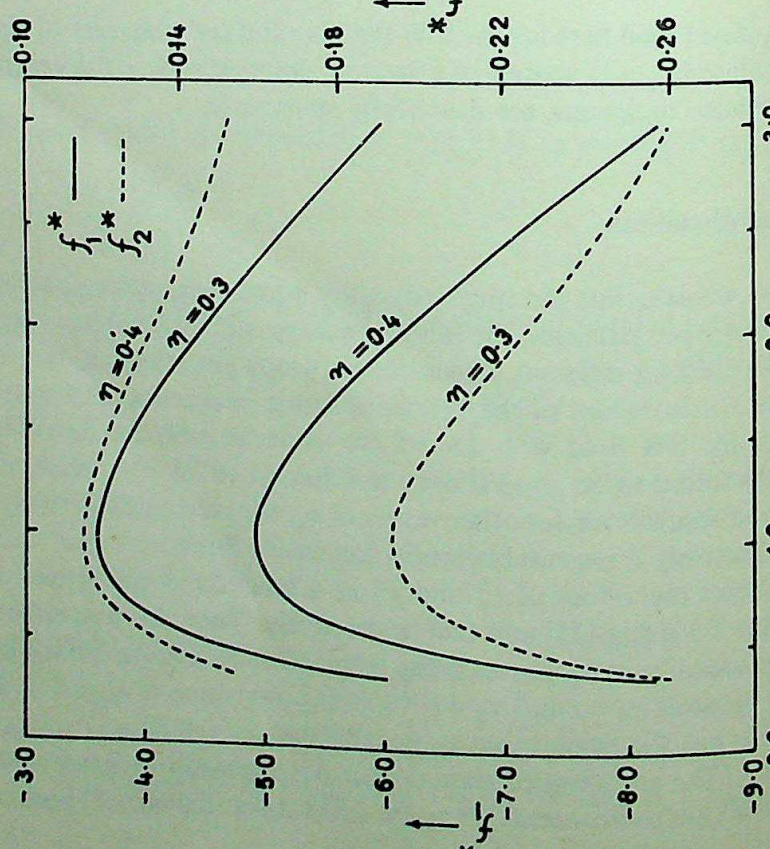

Figure 1. Values of f_1^* and f_2^* of the hard ellipsoid S W fluid with $\lambda = 1{\cdot}5$ as a function of χ_0 for $\eta = 0{\cdot}3$ and 0·4.

CC-0. In Public Domain. Gurukul Kangri Collection, Haridwar

Digitized by Arya Samaj Foundation Chennai and eGangotri

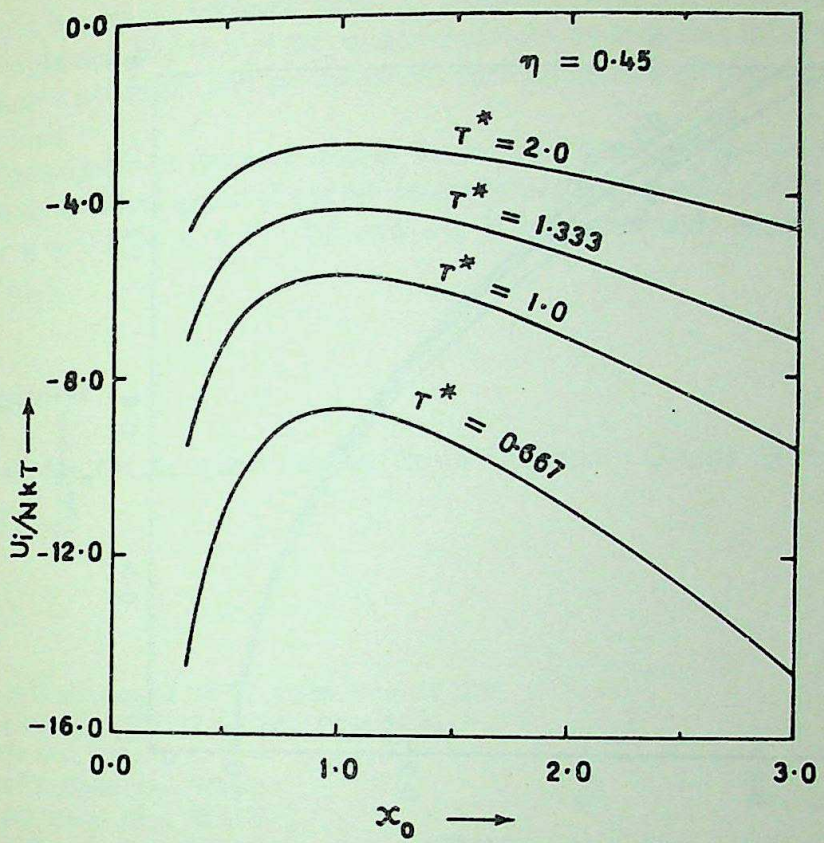

Figure 3. The internal energy, $U_i/N\ kT$ of the hard ellipsoid S W fluid with $\lambda = 1{\cdot}5$ as a function of x_0 for $\eta = 0{\cdot}45$ at $T^* = 2{\cdot}0$, 1·333, 1·0 and 0·667.

$T^* \geqslant 1{\cdot}0$, $\beta\ P/\rho$ is minimum at $x_0 = 1{\cdot}0$ and increases steadily as x_0 moves away from 1·0. However the rate of variation of $\beta\ P/\rho$ with x_0 decreases with decrease of T^* and at low temperature $T^* < 1{\cdot}0$ $\beta\ P/\rho$ begins to decrease as x_0 goes away from 1·0. To explain this behaviour, we consider the contributions of the hard core potential and perturbation corrections which are of opposite signs. However the magnitudes of these contributions increase as x_0 moves away from 1·0. At high temperatures $T^* > 1{\cdot}0$ the hard-core contribution is dominant and $\beta\ P/\rho$ increases when x_0 moves away from 1·0. On the other hand at low temperatures it is perturbation effect which dominates and $\beta P/\rho$ decreases when x_0 goes away from 1·0. For a given η, $\beta P/\rho$ has the same value at $x_0 = l$ and $x_0 = l^{-1}$. However it is clear from the expressions of $\beta P_{hc}/\rho$, P_1^* and P_2^* that for a given reduced density $\rho^* = \rho\sigma_0^3$, it cannot have the same value at $x_0 = l$ and $x_0 = l^{-1}$.

Figure 3 demonstrates the variation of the internal energy $U_i/N\ kT$ as a function of x_0 for $\eta = 0{\cdot}45$ at $T^* = 2{\cdot}0$, 1·333, 1·0 and 0·667. It is maximum at $x_0 = 1{\cdot}0$ and decreases steadily as x_0 moves away from 1·0. Here U_i is the excess internal energy with respect to the ideal gas at the same temperature and density. Like the equation of state the internal energy is also symmetric about $x_0 = 1{\cdot}0$, i.e. it has the same value at $x_0 = l$ and $x_0 = l^{-1}$.

In figure 4 the values of the excess free energy per particle, βf, are plotted as a function of $1/T^*$ for $\eta = 0{\cdot}4$ at $x_0 = 1{\cdot}0$, 1·5 and 2·0. The excess free energy increases with increase of temperature and also depends on x_0. At high temperature ($1/T^* \lesssim 0{\cdot}5$), βf is minimum and increases as x_0 increases from 1·0, where as at lower temperature

Figure 1. Values of f_1^* and f_2^* of the hard ellipsoid S W fluid with $\lambda = 1{\cdot}5$ as a function of x_0 for $\eta = 0{\cdot}3$ and 0·4.

Figure 2. The equation of state, $\beta P/\rho$ of the hard ellipsoid S W fluid with $\lambda = 1{\cdot}5$ as a function of x_0 for $\eta = 0{\cdot}45$ at $T^* = 2{\cdot}0$, 1·333, 1·0 and 0·667.

CC-0. In Public Domain. Gurukul Kangri Collection, Haridwar

Digitized by Arya Samaj Foundation Chennai and eGangotri

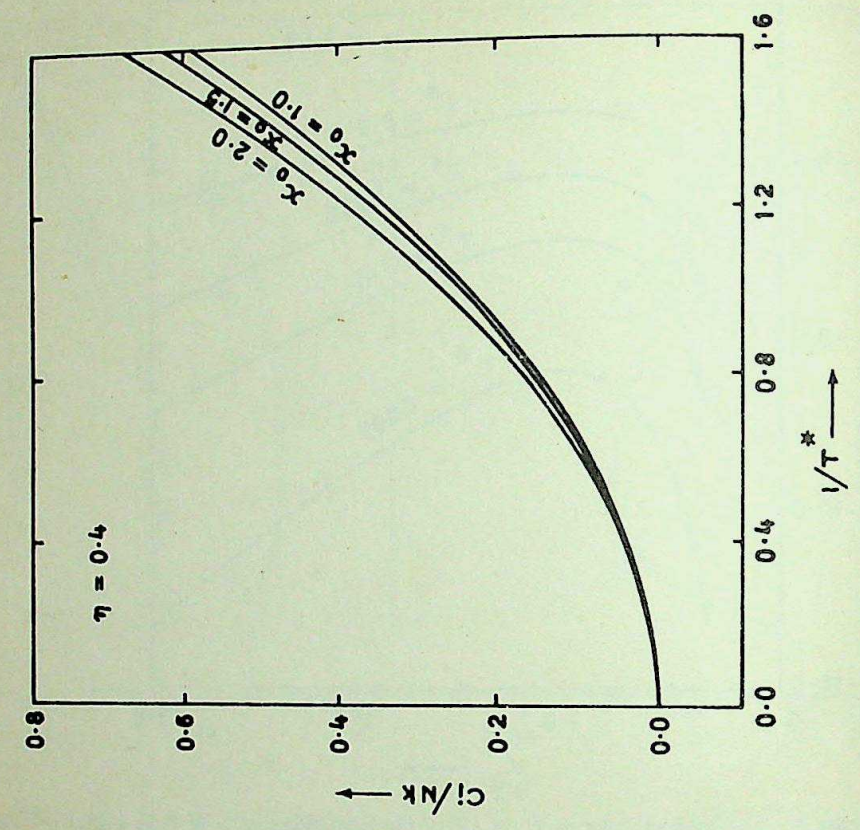

Figure 4. The excess free energy per particle βf of hard ellipsoid SW fluid with $\lambda = 1{\cdot}5$ as a function of $1/T^*$ for $\eta = 0{\cdot}4$ at $x_0 = 1{\cdot}0$, 1·5 and 2·0.

Figure 5. The internal heat capacity, C_i/Nk of the hard ellipsoid SW fluid with $\lambda = 1{\cdot}5$ as a function of $1/T^*$ for $\eta = 0{\cdot}4$ at $x_0 = 1{\cdot}0$, 1·5 and 2·0.

CC-0. In Public Domain. Gurukul Kangri Collection, Haridwar

Digitized by Arya Samaj Foundation Chennai and eGangotri

$(1/T^* \gtrsim 0{\cdot}5)$ it begins to decrease when x_0 increases from 1·0. This behaviour of βf can also be explained, like that of the equation of state, by considering the contributions of the hard-core potential and perturbation corrections, which are of opposite signs in this case also.

Figure 5 demonstrates the variation of the internal heat capacity (i.e. heat capacity with respect to the ideal gas at the same density and temperature) C_i/Nk as a function of $1/T^*$ for $\eta = 0{\cdot}4$ at $x_0 = 1{\cdot}0$, 1·5 and 2·0. It increases with decrease of T^* and increase of x_0.

Acknowledgement

We acknowledge the financial support from University Grants Commission, New Delhi.

References

Barker J A and Henderson D 1967 *J. Chem. Phys.* **47** 2856
Berne B J and Pechukas P 1972 *J. Chem. Phys.* **56** 4213
Boublik T 1976 *Mol. Phys.* **32** 1737
Boublik T 1987 *J. Chem. Phys.* **87** 1751
Fischer J 1980 *J. Chem. Phys.* **72** 5371
Gray C G and Gubbins K E 1984 *Theory of Molecular Physics* (Oxford: Clarendon press) p. 248
Henderson D, Madden W G and Fitts D D 1976 *J. Chem. Phys.* **64** 5026
Parson J D 1979 *Phys. Rev.* **A19** 1225
Ponce L and Renon H 1976 *J. Chem. Phys.* **64** 638
Singh U P and Singh Y 1986 *Phys. Rev.* **A33** 2725
Singh T P, Sinha J P and Sinha S K 1988 *Pramana – J. Phys.* **31** 289

CC-0. In Public Domain. Gurukul Kangri Collection, Haridwar

Digitized by Arya Samaj Foundation Chennai and eGangotri

CC-0. In Public Domain. Gurukul Kangri Collection, Haridwar

Digitized by Arya Samaj Foundation Chennai and eGangotri

Pramāṇa – J. Phys., Vol. 34, No. 2, February 1990, pp. 133–149. © Printed in India.

Electron crystallization using localized representation

K IYAKUTTI and JEAN LOUIS CALAIS*

School of Physics, Madurai Kamaraj University, Madurai 625021, India
*Department of Quantum Chemistry, University of Uppsala, Box 518 S 751 20, Uppsala, Sweden

MS received 11 August 1989; revised 9 November 1989

Abstract. The character of the ground state of the electron crystal—an electron gas with periodic density and/or spin density is investigated. Calculations for non-magnetic, ferromagnetic and anti-ferromagnetic electron crystals based on the Koster-Kohn variational principle for direct calculation of Wannier functions are presented. The Wannier function is approximated by a symmetrically orthonormalized Gaussian. The orbital exponent of the Gaussian is used as a variational parameter. The effect of the positive background is suitably taken into account. The results of our calculation support Wigner's prediction of electron crystallization.

Keywords. Electron crystal; Wigner lattice; Wannier function; localized representation; Gaussians.

PACS Nos 71·50; 71·45

1. Introduction

For a long time it has been believed that the ground state of the electron gas need not be of normal type. Wigner (1934, 1938) first suggested that the electron gas at the low density limit will favour a crystalline state and the electrons will occupy the sites of a body centred cubic lattice. In recent years there has been some experimental evidence for electron crystallization (Crandall and Williams 1972; Grimes and Adams 1979; Cole *et al* 1981; Mehrotra *et al* 1982; Gallet *et al* 1982; Koji Kajita 1985). It is reported (Care and March 1975) that it is possible to envisage electron crystallization in the following systems: (1) highly compensated semiconductors (2) inversion layers in silicon devices (3) outside suitable metal surfaces. We shall briefly summarize below the evidence for the electron crystallization in these areas: there are doubtless some others, perhaps more definitive, that are going to come to light as interest in this field grows.

In doped semiconductors one can control the free carrier density by compensating the material, and hence arrange, say, to have one electron per n donors, where n can easily be made 100. Thus, in this way one can readily simulate a really low electron density system. From various experiments it is known that, in such a system, the application of modest magnetic fields can alter crucially the Hall conducting properties. These results were interpreted by Durkan *et al* (1968), Durkan and March (1968) and Rosenbaum *et al* (1985) in terms of a Wigner transition. Subsequent experiments on electrical condition by Somerford (1971) are in general accord with such a description (Care and March 1971) and some high frequency experiments

CC-0. In Public Domain. Gurukul Kangri Collection, Haridwar

Digitized by Arya Samaj Foundation Chennai and eGangotri

purport to reveal a frequency to be associated with the Wigner lattice (Biskupski *et al* 1973).

On Si inversion layer, beautiful experiments have been carried out at Cambridge (Pepper *et al* 1974) in MOS and MNOS devices. Briefly, the MOS devices have led to a definite confirmation of the essential features of Anderson localization due to disorder. But in MNOS devices the disorder is minimized. There seems to be some evidence for a Wigner type transition, of a two dimensional kind, though as yet unexplained effects occur. This is also a promising area for further work regarding electron crystallization.

The region of conduction electron spill-out from metal surfaces is becoming quite clear in a number of applications. By now, in an electron gas frame work, density profiles exist which allow relatively successful calculation of a number of surface properties: work functions (Smith 1969) surface energies (Lang and Kohn 1970) and ion-ion interaction energies (Brown *et al* 1974). In this latter paper it had been pointed out that in the tail of this distribution where the electron density is really low, Coulomb repulsion effects might lead to a tendency to Wigner lattice formation. Recently Koji Kajita (1985) has observed Wigner crystallization of two dimensional electrons formed on the surface of solid neon. Another technique which is developing very fast in the study of surface properties is the low energy positron technique (Mills 1978). Here the formation of positronium on the surface of the metal mainly depends upon the low density electron spilled out from the surfaces. So the study about the positronium on the metal surface may throw light on the nature of electron density distribution. One can also estimate the positron life time in such a system and monitor the Wigner transition (Majumdar and Ramakrishnan 1973); Crandall and Williams (1972) and Crandall (1973) considered the possibility of a two dimensional Wigner crystallization in the electron trapped on the surface of liquid helium. This was experimentally first observed by Grimes and Adams (1979) and more recently by others (Mehrotra *et al* 1982; Gallet *et al* 1982).

On the theoretical side there have been efforts to understand, the character of the ground state of the electron crystal—an electron gas with periodic density. Care and March (1975) have reviewed the various theoretical work available at that time. After that there have been many theoretical discussions about electron crystallization. Shore *et al* (1978) have studied Wigner crystallization using density functional theory. Nagai and Fukuyama (1982, 1983) have investigated theoretically Wigner crystal in magnetic field. All the above calculations do not deal with the different magnetic states of the electron crystal. Only the calculations by Carr (1961) and Edwards and Hillel (1968) contain the discussion about the ferromagnetic and antiferromagnetic state of the electron crystal. Carr (1961) had shown that for $r_s < 27$, the system is antiferromagnetic and for $r_s > 27$, it is ferromagnetic. Edwards and Hillel's results show that for $10 < r_s < 40$, it is antiferromagnetic and for $r_s > 40$, it is ferromagnetic. We have reinvestigated this problem by representing, in a more suitable way, the localized electrons by Wannier function which has not been attempted earlier. Edwards and Hillel have used variational approach to the Hartree-Fock approximation and the corresponding orbitals are Bloch states. They have considered only a simple cubic lattice with cubic Fermi surface. We have considered b.c.c. lattice with spherical as well as cubic Fermi surfaces. Our calculation is in a localized representation of electrons by Wannier function which amounts to a certain infinite expansion of plane waves with fixed coefficients, but with one undetermined parameter for the whole

CC-0. In Public Domain. Gurukul Kangri Collection, Haridwar

Digitized by Arya Samaj Foundation Chennai and eGangotri

function. We present calculations for nonmagnetic, ferromagnetic and antiferromagnetic electron crystals.

In §2 we give our formalism of the theory. In §3 we give our treatment of the positive background. Section 4 will contain the special treatment of the antiferromagnetic crystal case. In §5 we present our numerical results and discussion.

2. Theoretical formalism

a) *Direct calculation of Wannier functions for an electron crystal*

The calculation is based on the Koster–Kohn (1953, 1974) variational principle for direct calculation of Wannier functions. We start out from sets of OAO's (orthonormalized atomic orbitals) as basis functions and these are completely orthonormal. The unknown Wannier function is expanded in these basis functions as

$$W(\mathbf{m},\mathbf{r}) = \sum_i \phi_i(\mathbf{m},\mathbf{r}) C_i. \tag{1}$$

The Wannier functions thus obtained are automatically orthonormal. We then extremise the functional

$$\varepsilon = \int W^*(\mathbf{r}) H_{\text{eff}} W(\mathbf{r})\, d\mathbf{r} \tag{2}$$

and in this we choose the effective Hartree-Fock operator.

The Hartree-Fock effective operator, H_{eff}, is characterized by the state under consideration which is a determinant filled with Bloch orbitals and spin functions in some way. To characterize the state we need the transformations

with
$$W = \psi U^+ \quad \psi = WU \tag{3}$$

$$U(\mathbf{m},\mathbf{k}) = \frac{1}{\sqrt{N}} \exp(2\pi i \mathbf{k}\cdot\mathbf{m}). \tag{4}$$

We have considered the three cases NC (non-magnetic crystal), FC (ferromagnetic crystal) and AC (anti-ferromagnetic crystal). Like Edwards and Hillel (1968) we have

$$\rho_{NC}(X,X') = \rho_{NC}(\mathbf{r},\mathbf{r}')\,[\alpha\alpha' + \beta\beta'] \tag{5a}$$

$$\rho_{FC}(X,X') = \rho_{FC}(\mathbf{r},\mathbf{r}')\alpha\alpha' \tag{5b}$$

$$\rho_{AC}(X,X') = \rho^+_{AC}(\mathbf{r},\mathbf{r}')\alpha\alpha' + \rho^-_{AC}(\mathbf{r},\mathbf{r}')\beta\beta' \tag{5c}$$

and in terms of the Wannier function

$$\rho_{NC}(\mathbf{r},\mathbf{r}') = \sum_{\mathbf{m},\mathbf{m}'} W_{NC}(\mathbf{m},\mathbf{r}) R_{NC}(\mathbf{m},\mathbf{m}') W^*_{NC}(\mathbf{m},\mathbf{r}') \tag{6}$$

$$\rho_{FC}(\mathbf{r},\mathbf{r}') = \sum_{\mathbf{m},\mathbf{m}'} W_{FC}(\mathbf{m},\mathbf{r}) R_{FC}(\mathbf{m},\mathbf{m}') W^*_{FC}(\mathbf{m},\mathbf{r}') \tag{7}$$

$$\rho^{\pm}_{AC}(\mathbf{r},\mathbf{r}') = \sum_{\mathbf{m},\mathbf{m}} W_{AC}(\mathbf{m},\mathbf{r}) R^{\pm}_{AC}(\mathbf{m},\mathbf{m}') W^*_{AC}(\mathbf{m},\mathbf{r}'). \tag{8}$$

CC-0. In Public Domain. Gurukul Kangri Collection, Haridwar

Digitized by Arya Samaj Foundation Chennai and eGangotri

We have

$$R_{NC}(\mathbf{m},\mathbf{m}') = \frac{1}{N}\sum_{k}^{k_{NC}} \exp\left(2\pi i\mathbf{k}\cdot(\mathbf{m}-\mathbf{m}')\right)$$

$$= V_{oa}\int_{FSNC} \exp\left(2\pi i\mathbf{k}\cdot(\mathbf{m}-\mathbf{m}')\right) \mathrm{d}V_k \tag{9}$$

and similar for the FC and special case is needed for AC.

b) *Densities in the Wannier representation*

To study the translational properties in the three cases we consider the densities ($[\mathbf{r}=\mathbf{r}']$; j = NC, FC, AC)

$$\rho_j(\mathbf{r}) = \rho_j(\mathbf{r},\mathbf{r}')$$

$$\rho_j(\mathbf{r}-\mathbf{n}) = \sum_{\mathbf{m},\mathbf{m}'} W_j(\mathbf{m},\mathbf{r}-\mathbf{n})R_j(\mathbf{m},\mathbf{m}')W_j^*(\mathbf{m},\mathbf{r}-\mathbf{n}) \tag{10}$$

$$= \sum_{\mathbf{m},\mathbf{m}'} W_j(\mathbf{m}+\mathbf{n},\mathbf{r})R_j(\mathbf{m},\mathbf{m}')W_j^*(\mathbf{m}'+\mathbf{n},\mathbf{r}). \tag{11}$$

From (9) we see that, at least for NC and FC we have

$$R_j(\mathbf{p}-\mathbf{n},\mathbf{p}'-\mathbf{n}) = R_j(\mathbf{p},\mathbf{p}') \text{ with } \mathbf{p}=\mathbf{m}+\mathbf{n} \tag{12}$$

and so

$$\rho_j(\mathbf{r}-\mathbf{n}) = \rho_j(\mathbf{r}). \tag{13}$$

We further notice that

$$\int \rho_{NC}(\mathbf{r},\mathbf{r})\,\mathrm{d}\mathbf{r} = \frac{N}{2} \tag{14a}$$

$$\int \rho_{FC}(\mathbf{r},\mathbf{r})\,\mathrm{d}\mathbf{r} = N \tag{14b}$$

$$\int \rho_{AC}(\mathbf{r},\mathbf{r})\,\mathrm{d}\mathbf{r} = \frac{N}{2}. \tag{14c}$$

To calculate R_j, we must decide which shape of the Fermi surface (FS) we are going to use. For high densities a sphere seems to be natural, whereas for low densities a cube would seem to be more reasonable. Since we are going to present our calculations for both the above cases, here also we outline the calculation of R_j for both cases of FS. Now we will consider only NC and FC states.

From (14) we can write

$$\sum_{\mathbf{m}} R_{NC}(\mathbf{m},\mathbf{m}) = \frac{N}{2}$$

$$\sum_{\mathbf{m}} R_{FC}(\mathbf{m},\mathbf{m}) = N. \tag{15}$$

Combining (9) with the above equations and integrating over a cube gives

$$R_j^{(c)}(\mathbf{m},\mathbf{m}') = V_{oa}\prod_{i=1}^{3}\frac{\sin\pi b_j(m_i-m_i')}{\pi(m_i-m_i')} \tag{16}$$

CC-0. In Public Domain. Gurukul Kangri Collection, Haridwar

Digitized by Arya Samaj Foundation Chennai and eGangotri

and integrating over a sphere gives

$$R_j^{(S)}(\mathbf{m},\mathbf{m}') = \frac{4\pi}{3} k_{Fj}^3 V_{oa}\, q(2\pi k_{Fj}|\mathbf{m}-\mathbf{m}'|) \tag{17}$$

where $q(x) = 3(\sin x - x\cos x)/x^3$, k_{Fj} is the radius of the spherical FS and b_j is the cube edge of the cubic FS and V_{oa} is the volume per electron.

3. Treatment of the positive background

The Hartree-Fock effective operator for a normal system with nuclei and electrons is

$$H_{\text{eff}}(1) = \tfrac{1}{2}\Delta_1 - \sum_g \frac{Z_g}{|\mathbf{r}-\mathbf{R}_g|} + \int \frac{\mathrm{d}X_2(1-P_{12})\rho(X_2,X_2)}{r_{12}} \tag{18}$$

For any extended system (solid or large molecule) great care is needed in evaluating matrix elements of the long range electro-static part

$$V_c(\mathbf{r}_1) = -\sum_g \frac{Z_g}{|\mathbf{r}_1-\mathbf{R}_g|} + \int \frac{\rho(X_2,X_2)}{r_{12}}\mathrm{d}X_2 \tag{19}$$

so that the large parts are cancelled out (Lowdin 1956; Delhalle 1978; Delhalle *et al* 1980; Monkhoest and Schwalm 1981). The two extreme cases of positive charge distributions are uniform distribution and point like nuclei. All the real situations lie between the above extreme cases. In the present problem we have taken the first extreme case and also a case where the positive charge distribution approximately represents the real situation.

a) *Non-uniform positive background and charge neutrality problem*

For the electron crystal it is desirable to have a distribution of positive charge which does not have to be uniform (Overhauser 1978; Hall 1981). We denote this distribution by $P(\mathbf{r})$ and partition it like $\rho(r)$

$$P(\mathbf{r}) = \sum_{\mathbf{m}}^{B\cdot K} P_m(\mathbf{r}). \tag{20}$$

The total amount of positive charge must equal the number of electrons.

$$\int P(\mathbf{r})\,\mathrm{d}V = N. \tag{21}$$

We must also require, however that each unit cell is neutral, i.e.,

$$\text{i.e.} \qquad \int_{V_m} [P_m(\mathbf{r}) - \rho_m(\mathbf{r})]\,\mathrm{d}V = 0 \tag{22}$$

$$\int P_m(\mathbf{r})\,\mathrm{d}V = N_m. \tag{23}$$

CC-0. In Public Domain. Gurukul Kangri Collection, Haridwar

Digitized by Arya Samaj Foundation Chennai and eGangotri

In a crystal both $\rho(\mathbf{r})$ and $P(\mathbf{r})$ have the periodicity of the lattice. We can then expand

$$\bar{\rho}(\mathbf{r}) = \rho(\mathbf{r}) - P(\mathbf{r}) \tag{24}$$

in a Fourier series labelled by the reciprocal lattice vectors $\mathbf{K}$

$$\bar{\rho}(\mathbf{r}) = \sum_{\mathbf{K}} \bar{\rho}_{\mathbf{K}} \exp(i\mathbf{K}\cdot\mathbf{r}). \tag{25}$$

In calculating the Fourier coefficients $\bar{\rho}_{\mathbf{K}}$ it is sufficient, because of the periodicity of $\bar{\rho}(\mathbf{r})$, to integrate over one of the unit cells.

$$\begin{aligned}\bar{\rho}_{\mathbf{K}} &= \frac{1}{V}\int \bar{\rho}(\mathbf{r}) \exp(-i\mathbf{K}\cdot\mathbf{r})\, \mathrm{d}V \\ &= \frac{1}{V_{\mathrm{oa}}}\int_{V_{\mathrm{oa}}} \bar{\rho}(\mathbf{r}) \exp(-i\mathbf{K}\cdot\mathbf{r})\, \mathrm{d}V.\end{aligned} \tag{26}$$

The charge neutrality implies that

$$\begin{aligned}\int_V \bar{\rho}(\mathbf{r})\, \mathrm{d}V = 0 &= \sum_{\mathbf{K}} \bar{\rho}_{\mathbf{K}} \int \exp(i\mathbf{K}\cdot\mathbf{r})\, \mathrm{d}V \\ &= V\bar{\rho}_0\end{aligned} \tag{27}$$

i.e.,

$$\bar{\rho}_0 = 0. \tag{28}$$

We therefore write

$$\bar{\rho}(\mathbf{r}) = \sum_{\mathbf{K}}{}' \bar{\rho}_{\mathbf{K}} \exp(i\mathbf{K}\cdot\mathbf{r}). \tag{29}$$

In the electron gas $\rho(\mathbf{r}) = n = \text{constant}$ and $P(\mathbf{r})$ is chosen to be the same constant so that $\bar{\rho}(\mathbf{r}) = 0$, $V_c(\mathbf{r}_1) = 0$, $E_c = 0$. In the present case where $\rho(\mathbf{r})$ varies periodically, we can reach the same goal by choosing $P(\mathbf{r}) = \rho(\mathbf{r})$. That also implies charge neutrality.

We can also imagine less drastic assumptions, in the sense that the condition

$$\int \bar{\rho}(\mathbf{r})\, \mathrm{d}V = 0 \tag{30}$$

can be satisfied without requiring

$$\bar{\rho}(\mathbf{r}) = 0 \text{ for all } \mathbf{r}. \tag{31}$$

We can choose $P(\mathbf{r}) = \text{constant}\ (=n)$ eventhough $\rho(\mathbf{r})$ varies. Then

$$\int_{V_{\mathrm{m}}} P_{\mathrm{m}}(\mathbf{r})\, \mathrm{d}V = PV_{\mathrm{oa}} = \int_{V_{\mathrm{m}}} P_{\mathrm{m}}(\mathbf{r})\, \mathrm{d}V = N_{\mathrm{m}} = 1 \tag{32}$$

$$P = \frac{1}{V_{\mathrm{oa}}} = \frac{N}{NV_{\mathrm{oa}}} = \frac{N}{V} = n.$$

With this choice the constant n can be regarded as the zeroth Fourier component in

CC-0. In Public Domain. Gurukul Kangri Collection, Haridwar

Digitized by Arya Samaj Foundation Chennai and eGangotri

the expansion of the electron density

$$\rho(\mathbf{r}) = \bar{\rho}(\mathbf{r}) + P(\mathbf{r}) = \bar{\rho}(\mathbf{r}) + n$$
$$= n + \sum_{\mathbf{K}}{}' K \exp(i\mathbf{K}\cdot\mathbf{r}) = \sum_{\mathbf{K}} \rho_{\mathbf{K}} \exp(i\mathbf{K}\cdot\mathbf{r}). \tag{33}$$

The Fourier components of the density

$$\rho_{\mathbf{K}} = \frac{1}{V_{oa}} \int \rho(\mathbf{r}) \exp(-i\mathbf{K}\cdot\mathbf{r})\, dV \tag{34}$$

can be calculated by means of Cartesian coordinates when $\rho(\mathbf{r})$ is obtained from a superposition of Gaussians.

Using the Fourier representation of r_{12}^{-1}, we get for $V_c(\mathbf{r}_1)$

$$V_c(\mathbf{r}_1) = 4\pi \sum{}' \rho_{\mathbf{K}} \frac{\exp(i\mathbf{K}\cdot\mathbf{r})}{K^2}. \tag{35}$$

In the present calculation we need the matrix element of $V_c(\mathbf{r}_1)$ with respect to the trial Wannier function.

What follows below is for the non-magnetic case. Similar results are obtained for the other cases with suitable modifications of relevant quantities. The orbital part of the Fock-Dirac density matrix is in terms of the Wannier functions,

$$\rho(\mathbf{r}, \mathbf{r}) = \sum_{\mathbf{m},\mathbf{n}}^{B\cdot k} W(\mathbf{m}, \mathbf{r}) R_w(\mathbf{m}, \mathbf{n}) W^*(\mathbf{n}, \mathbf{r}). \tag{36}$$

The actual calculation of the Fourier components (34) from (36) will proceed differently depending on the actual form of the Wannier functions.

We first study a general aspect which may be useful in actual situations. We introduce the notation

$$a(\mathbf{r}) = W(0, \mathbf{r}) \tag{37}$$

for the Wannier function centred at the origin. For calculation of $\rho(\mathbf{r})$ we need the quantities

$$\Gamma_K(\mathbf{m}, \mathbf{n}) = \frac{1}{V_{oa}} \int_{V_{oa}} \exp(i\mathbf{K}\cdot\mathbf{r}) W(\mathbf{m}, \mathbf{r}) W^*(\mathbf{n}, \mathbf{r})\, dV$$
$$= \frac{1}{V_{oa}} \int \exp(i\mathbf{K}\cdot\mathbf{r}) a(\mathbf{r}) a^*(\mathbf{r} + \mathbf{m} - \mathbf{n})\, dV. \tag{38}$$

The Fourier transform of the function $a(\mathbf{r})$ is essentially what Slater (1965) calls the momentum eigen-functions, i.e., the expansion coefficients in the expansion of the Bloch function in plane waves.

$$a^T(\mathbf{q}) = \int \exp(i\mathbf{q}\cdot\mathbf{r}) a(\mathbf{r})\, dV \tag{39a}$$

$$a(\mathbf{r}) = \frac{1}{8\pi^3} \int \exp(-i\mathbf{q}\cdot\mathbf{r}) a^T(\mathbf{q})\, d\mathbf{q} \tag{39b}$$

$$= \frac{\sqrt{V_{oa}}}{8\pi^3} \int \exp(i\mathbf{q}\cdot\mathbf{n}) A(\mathbf{q})\, d\mathbf{q}, \quad \mathbf{q} = \mathbf{k} + \mathbf{k} \tag{39c}$$

CC-0. In Public Domain. Gurukul Kangri Collection, Haridwar

Digitized by Arya Samaj Foundation Chennai and eGangotri

Thus

$$a^T(\mathbf{r}) = \sqrt{V_{oa}}\, A(-\mathbf{q}) \tag{39d}$$

$$\rho_{\mathbf{K}} = \frac{1}{8\pi^3}\int d\mathbf{q} A(\mathbf{q}) A^*(\mathbf{K}+\mathbf{q}) f(\mathbf{q})$$

with

$$f(\mathbf{q}) = \sum_{\mathbf{m}'}^{Bk} R_w(\mathbf{m}') \exp(-i\mathbf{q}\cdot\mathbf{m}'). \tag{40}$$

The Fourier transform of GTO is known analytically. In Shavift's notation (Shavift 1962)

$$G_i(r_A) = \exp(-\alpha i|\mathbf{r}-\mathbf{A}|^2) \tag{41}$$

$$[G_i(r_A)]^T(\mathbf{q}) = \int \exp(i\mathbf{q}\cdot\mathbf{r}) G_i(r_A)\, dV$$

$$= \exp(i\mathbf{q}\cdot\mathbf{A})\left(\frac{\pi}{\alpha_i}\right)^{3/2} \exp(-q^2/4\alpha_i). \tag{42}$$

When the WF is a linear combination of GTO's the integration in (40) reduces to integration over a product of two functions of type (42) and $\exp(-i\mathbf{q}\cdot\mathbf{m}')$.

The numerical results using the above formalism is presented in §5. As pointed out earlier we have also done numerical calculation, as a special case, assuming uniform positive background where $V_c(\mathbf{r}_1)=0$. These two results are compared in §5.

4. Antiferromagnetic crystal

As we indicated in §2 the anti-ferromagnetic crystal case requires a special treatment. We can assume that the crystal structure is made up of two inter-penetrating sublattices. 1. Sub-lattice formed out of the corner atoms of the lattice. 2. Sub-lattice formed out of the body centred atom of the b.c.c lattice (figure 1).

If there are N electrons in the b.c.c lattice then each sublattice will have $N/2$ electrons. The sub-lattice Bloch-type orbitals are defined as (Larson and Thorson 1966)

$$\chi(\mathbf{k}) = \frac{1}{\sqrt{2}}[\psi(\mathbf{k}) + \psi(\bar{\mathbf{k}})]$$

$$\bar{\chi}(\mathbf{k}) = \frac{1}{\sqrt{2}}[\psi(\mathbf{k}) - \psi(\bar{\mathbf{k}})] \tag{43}$$

where $\bar{\mathbf{k}} = \mathbf{k} + \mathbf{K}$ and

$$\rho^{+}_{AC}(\mathbf{r},\mathbf{r}') = \sum_{k}^{k^{+}_{AC}} \chi(\mathbf{k},\mathbf{r})\chi^*(\mathbf{k},\mathbf{r}')$$

$$\rho^{-}_{AC}(\mathbf{r}',\mathbf{r}') = \sum_{k}^{k^{-}_{AC}} \bar{\chi}(\mathbf{k},\mathbf{r})\bar{\chi}^*(\mathbf{k},\mathbf{r}'). \tag{44}$$

It is interesting to point out that the above particular kind of Fock-Dirac matrix (44)

CC-0. In Public Domain. Gurukul Kangri Collection, Haridwar

Digitized by Arya Samaj Foundation Chennai and eGangotri

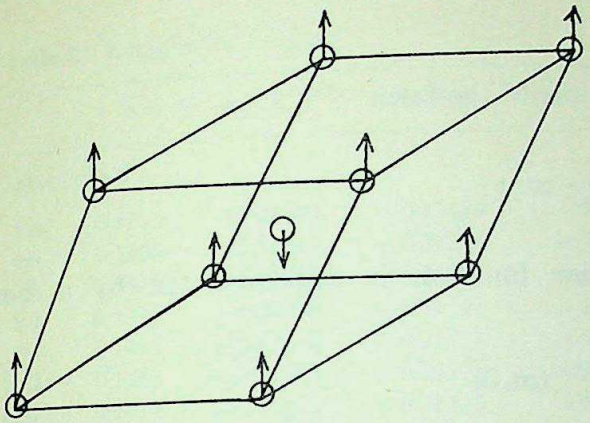

Figure 1. Wigner crystal AC case.

that we use here corresponds to a special case of the AMO method, namely the 'Most alternating' one, with $\theta = 0$, ie., $\theta = \pi/4$ (Calais and Sperber 1973). We have

$$\rho_{AC} = \rho^{+}_{AC} + \rho^{-}_{AC}.$$

In terms of Wannier functions

$$\rho_{AC} = \tfrac{1}{2} \sum_{\mathbf{m},\mathbf{m}'} W_{AC}(\mathbf{m}, \mathbf{r}) [R^{+}_{AC} + R^{-}_{AC}] W^{*}_{AC}(\mathbf{m}, \mathbf{r}') \tag{45}$$

with

$$R^{+}_{AC}(\mathbf{m}, \mathbf{m}') = \frac{2}{N} \left[\sum_{k}^{k^{+}_{AC}} \exp(2\pi i k(m - m'))(1 - \exp(-2\pi i K m) + \exp(2\pi i K m') + \exp(2\pi i K(m - m'))) \right] \tag{46}$$

$$R^{-}_{AC}(\mathbf{m}, \mathbf{m}') = \frac{2}{N} \left[\sum_{k}^{k^{-}_{AC}} \exp(2\pi i k(m - m'))(1 - \exp(-2\pi i K m) - \exp(2\pi i K m') + \exp(2\pi i K(m - m'))) \right]. \tag{47}$$

The final expressions for $R^{+}_{AC}(\mathbf{m}, \mathbf{m}')$ for both spherical and cubic Fermi surfaces are found to be:

Cubic F.S. case

$$R^{+}_{AC}(\mathbf{m}, \mathbf{m}') = V_{oa} + \prod_{j=1}^{3} \frac{\sin b^{+}_{FAC}(m_j - m_{j'})}{\pi(m_j - m_j)} \times (2 + \exp(2\pi i K m') + \exp(-2\pi i K m')). \tag{48}$$

Spherical F.S. case

$$R^{+}_{AC}(\mathbf{m}, \mathbf{m}') = V^{+}_{oa} 4\pi k^{+3}_{FAC} q(2\pi i K m) \times (2 + \exp(2\pi i K m') + \exp(-2\pi i K m')). \tag{49}$$

We get similar expressions for $R^{-}_{AC}(\mathbf{m}, \mathbf{m}')$. The numerical results are presented in §5 along with the other cases.

CC-0. In Public Domain. Gurukul Kangri Collection, Haridwar

Digitized by Arya Samaj Foundation Chennai and eGangotri

5. Results and discussion

We have chosen single Gaussians of the form

$$\phi(r) = \left(\frac{2\alpha}{\pi}\right)^{3/4} \exp(-\alpha r^2)$$

as our orbitals. The Wannier function is approximated by a symmetrically orthonormalized Gaussian

$$W(\mathbf{r}) = \sum_{\mathbf{m}} \phi(\mathbf{m}, r)\Delta^{-1/2}(\mathbf{m}, 0) \tag{50}$$

where Δ is the overlap matrix (Lowdin 1956) $\Delta^{-1/2}$ is calculated by means of a method given by one of the authors (Calais and Appel 1964). We then extremize the functional given by (2), with the appropriate H_{eff}. The orbital exponent of the Gaussian is used as a variational parameter. As discussed in §3, first a calculation is performed for the case where a complete cancellation between the Coulomb term and the uniform positive background is assumed. Energies were calculated as a function of r_s, the electron density parameter. For all the three cases (NC, FC and AC) calculations were done for both cubic and spherical Fermi surfaces. The results are presented in tables 1 to 6. The results of the calculations for the 2nd case where we have taken the contribution from the positive background are also presented graphically in figure 2. In the figure for FC case the difference in the energies between spherical FS and cubic FS is small so we have given only one graph. In the figures and in the tables $E\Lambda$ is the Hartree-Fock ground state energy for the non-magnetic electron gas given by

$$E_G = \frac{0{\cdot}458}{r_s}\left(\frac{2{\cdot}413}{r_s} - 1\right) \text{ Rydberg}$$

Table 1. Energies corresponding to NC case.

r_s	α	E_G (R_{yd})	E (R_{yd})	$(E - E_G)/\lvert E_G\rvert$
Spherical FS				
9·0	0·042	−0·03725	−0·05148	−0·38231
10·0	0·039	−0·03475	−0·05239	−0·50765
11·0	0·037	−0·03250	−0·05281	−0·62490
12·0	0·036	−0·03049	−0·05298	−0·73748
15·0	0·035	−0·02562	−0·05304	−1·07042
20·0	0·035	−0·02013	−0·05350	−1·63439
Cubic FS				
8·0	0·0450	−0·03998	−0·04945	−0·23689
9·0	0·0425	−0·03724	−0·05131	−0·37767
10·0	0·0400	−0·03475	−0·05232	−0·50569
11·0	0·0375	−0·03250	−0·05279	−0·62419
12·0	0·0350	−0·03049	−0·05295	−0·73676
15·0	0·0350	−0·02562	−0·05304	−1·07042
20·0	0·0350	−0·02013	−0·05305	−1·63439

CC-0. In Public Domain. Gurukul Kangri Collection, Haridwar

Digitized by Arya Samaj Foundation Chennai and eGangotri

Table 2. Energies for FC case

r_s	α	E_G (R_{yd})	E (R_{yd})	$(E-E_G)/\|E_G\|$
Spherical FS				
5·0	0·1395	−0·04740	−0·21199	−3·47229
6·0	0·1420	−0·04563	−0·21216	−3·64862
7·0	0·1415	−0·04287	−0·21220	−3·94907
8·0	0·1415	−0·03998	−0·21221	−4·30724
9·0	0·1415	−0·03725	−0·21221	−4·69730
10·0	0·1415	−0·03475	−0·21221	−5·10668
11·0	0·1415	−0·03250	−0·21221	−5·52862
12·0	0·1415	−0·03049	−0·21221	−5·95919
15·0	0·1415	−0·02562	−0·21221	−7·28214
Cubic FS				
5·0	0·1485	−0·04740	−0·21088	−3·44903
6·0	0·1425	−0·04563	−0·21207	−3·64683
7·0	0·1415	−0·04287	−0·21220	−3·94898
8·0	0·1415	−0·03998	−0·21220	−4·30722
9·0	0·1415	−0·03725	−0·21221	−4·69730
10·0	0·1415	−0·03475	−0·21221	−5·10668
11·0	0·1415	−0·03250	−0·21221	−5·52861
12·0	0·1415	−0·03049	−0·21221	−5·95919
15·0	0·1415	−0·02562	−0·21221	−7·28215

Table 3. Energies for AC case.

r_s	α	$E_G(R_{yd})$	E (R_{yd})	$(E-E_G)/\|E_G\|$
Cubic FS				
6·0	0·0360	−0·04564	−0·05713	−0·25184
7·0	0·0268	−0·04288	−0·05671	−0·32256
8·0	0·0175	−0·03998	−0·06565	−0·64189
9·0	0·0129	−0·03725	−0·07365	−0·97743
10·0	0·0105	−0·03475	−0·06576	−0·89226
11·0	0·0355	−0·03250	−0·05304	−0·63207
12·0	0·0355	−0·03049	−0·05305	−0·73979
15·0	0·0355	−0·02562	−0·05305	−1·07050
20·0	0·0355	−0·02014	−0·05305	−1·63444
Spherical FS				
5·0	0·116	−0·04740	0·00043	1·00908
6·0	0·088	−0·04564	−0·02492	0·45384
7·0	0·070	−0·04288	−0·03821	0·10887
8·0	0·059	−0·03998	−0·04539	−0·13543
9·0	0·049	−0·03725	−0·04930	−0·32366
10·0	0·044	−0·03475	−0·05136	−0·47809
11·0	0·040	−0·03250	−0·05238	−0·61153
12·0	0·037	−0·03049	−0·05283	−0·73242
13·0	0·036	−0·02869	−0·05299	−0·84683
14·0	0·036	−0·02707	−0·05304	−0·95879
15·0	0·036	−0·02562	−0·05305	−1·07042
20·0	0·036	−0·02014	−0·05305	−1·63446

CC-0. In Public Domain. Gurukul Kangri Collection, Haridwar

Digitized by Arya Samaj Foundation Chennai and eGangotri

Table 4. Energy values for NC Case (with non-uniform positive background).

r_s	α	$E_G\ (R_{yd})$	$E\ (R_{yd})$	$(E-E_G)/\lvert E_G\rvert$
Spherical FS				
9·0	0·0390	−0·03725	−0·05088	−0·36610
10·0	0·0360	−0·03475	−0·05141	−0·47951
11·0	0·0330	−0·03250	−0·05142	−0·58189
12·0	0·0305	−0·03049	−0·05108	−0·67514
13·0	0·0285	−0·02869	−0·05054	−0·76131
14·0	0·0270	−0·02707	−0·04987	−0·84215
15·0	0·0255	−0·02562	−0·04917	−0·91896
16·0	0·0245	−0·02430	−0·04844	−0·99254
18·0	0·0230	−0·02203	−0·04699	−1·13298
20·0	0·0220	−0·02014	−0·04566	−1·26756
Cubic FS				
9·0	0·0405	−0·03725	−0·05067	−0·36038
10·0	0·0365	−0·03475	−0·05136	−0·47789
11·0	0·0335	−0·03250	−0·05144	−0·58254
12·0	0·0310	−0·03049	−0·05115	−0·67739
13·0	0·0285	−0·02869	−0·05064	−0·76500
14·0	0·0270	−0·02707	−0·05002	−0·84728
15·0	0·0260	−0·02562	−0·04934	−0·92559
16·0	0·0250	−0·02430	−0·04864	−1·00082
18·0	0·0235	−0·02203	−0·04726	−1·14496
20·0	0·0225	−0·02014	−0·04599	−1·28385

Table 5. Energies corresponding to FC case (with non-uniform positive background).

r_s	α	$E_G\ (R_{yd})$	$E\ (R_{yd})$	$(E-E_G)/\lvert E_G\rvert$
Spherical FS				
6·0	0·1215	−0·04564	−0·20656	−3·52599
7·0	0·1125	−0·04288	−0·20208	−3·71300
8·0	0·1055	−0·03998	−0·19724	−3·93285
9·0	0·1015	−0·03725	−0·19257	−4·17012
10·0	0·0990	−0·03475	−0·18835	−4·42012
11·0	0·0980	−0·03250	−0·18468	−4·68174
12·0	0·0980	−0·03049	−0·18158	−4·95470
14·0	0·1005	−0·02708	−0·17693	−5·53440
16·0	0·1040	−0·02431	−0·17403	−6·15920
18·0	0·1095	−0·02203	−0·17251	−6·82919
20·0	0·1140	−0·02014	−0·17203	−7·54252
Cubic FS				
5·0	0·1380	−0·04740	−0·20855	−3·39975
6·0	0·1240	−0·04564	−0·20656	−3·52599
7·0	0·1135	−0·04288	−0·20248	−3·72228
8·0	0·1070	−0·03998	−0·19788	−3·94881
9·0	0·1030	−0·03725	−0·19343	−4·19318
10·0	0·1010	−0·03475	−0·18942	−4·45102
11·0	0·1000	−0·03250	−0·18596	−4·72096
12·0	0·1005	−0·03049	−0·18304	−5·00251
14·0	0·1025	−0·02708	−0·17868	−5·59918
16·0	0·1060	−0·02431	−0·17599	−6·23982
18·0	0·1105	−0·02203	−0·17459	−6·92363
20·0	0·1150	−0·02014	−0·17416	−7·64747

CC-0. In Public Domain. Gurukul Kangri Collection, Haridwar

Digitized by Arya Samaj Foundation Chennai and eGangotri

Table 6. Energies corresponding to AC case (with non-uniform positive background).

r_s	α	E_G (R_{yd})	E (R_{yd})	$(E-E_G)/\|E_G\|$
Cubic FS				
6·0	0·0360	−0·04564	−0·05713	−0·25182
7·0	0·0270	−0·04288	−0·05670	−0·32243
8·0	0·0175	−0·03998	−0·06565	−0·64188
9·0	0·0130	−0·03725	−0·07356	−0·97481
10·0	0·0105	−0·03475	−0·06576	−0·89224
11·0	0·0315	−0·03250	−0·05216	−0·60457
12·0	0·0305	−0·03049	−0·05171	−0·69582
13·0	0·0295	−0·02869	−0·05118	−0·78389
14·0	0·0280	−0·02708	−0·05055	−0·86702
16·0	0·0260	−0·02431	−0·04917	−1·02259
18·0	0·0255	−0·02203	−0·04809	−1·18243
20·0	0·0250	−0·02014	−0·04724	−1·34591
Spherical FS				
5·0	0·1150	−0·04740	0·00131	1·02754
6·0	0·0865	−0·04564	−0·02379	0·47875
7·0	0·0680	−0·04288	−0·03681	0·14148
8·0	0·0555	−0·03998	−0·04373	−0·09367
9·0	0·0465	−0·03725	−0·04734	−0·27095
10·0	0·0400	−0·03475	−0·04706	−0·41199
11·0	0·0350	−0·03250	−0·04969	−0·52870
12·0	0·0310	−0·03049	−0·04965	−0·62829
13·0	0·0280	−0·02869	−0·04922	−0·71537
14·0	0·0255	−0·02708	−0·04855	−0·79309
16·0	0·0220	−0·02431	−0·04688	−0·92860
18·0	0·0190	−0·02203	−0·04508	−1·04625
20·0	0·0180	−0·02013	−0·04334	−1·15232

In table 7 we have given R matrices values for the three cases.

All our calculations predict energies which are well below the usual groundstate energy E_G. From the tables the following points may be observed.

The values of α, for all the cases quickly converge to certain values when r_s increases. Also the change in the ground state energy is small as r_s increases. For the uniform positive background case for NC and FC the energies for spherical FS are slightly lower than the energies corresponding to cubic FS. A similar feature has been observed in the ferromagnetic state of an electron gas by Calais and Sykja (1982). In AC the situation is entirely different. For this the cubic Fermisurface case has lower energy and also the curve has a minimum corresponding to $r_s = 9$. Among all the three crystals' cases the FC case has the lowest energy.

It is of importance to note the special character of the AC curves. As pointed out here the cubic fermisurface has less energy than the spherical Fermisurface. This is not something out of the way. A similar result was reported by Calais and Sperber (1973) in their calculation for Lithium crystal. The minimum in the curve for AC alone is to be noted. This situation strongly predict a crystallization in antiferromagnetic phase. This is also called the Wigner crystal. When the positive background is assumed to be non uniform, it contributes to the ground state energy. From tables

CC-0. In Public Domain. Gurukul Kangri Collection, Haridwar

Digitized by Arya Samaj Foundation Chennai and eGangotri

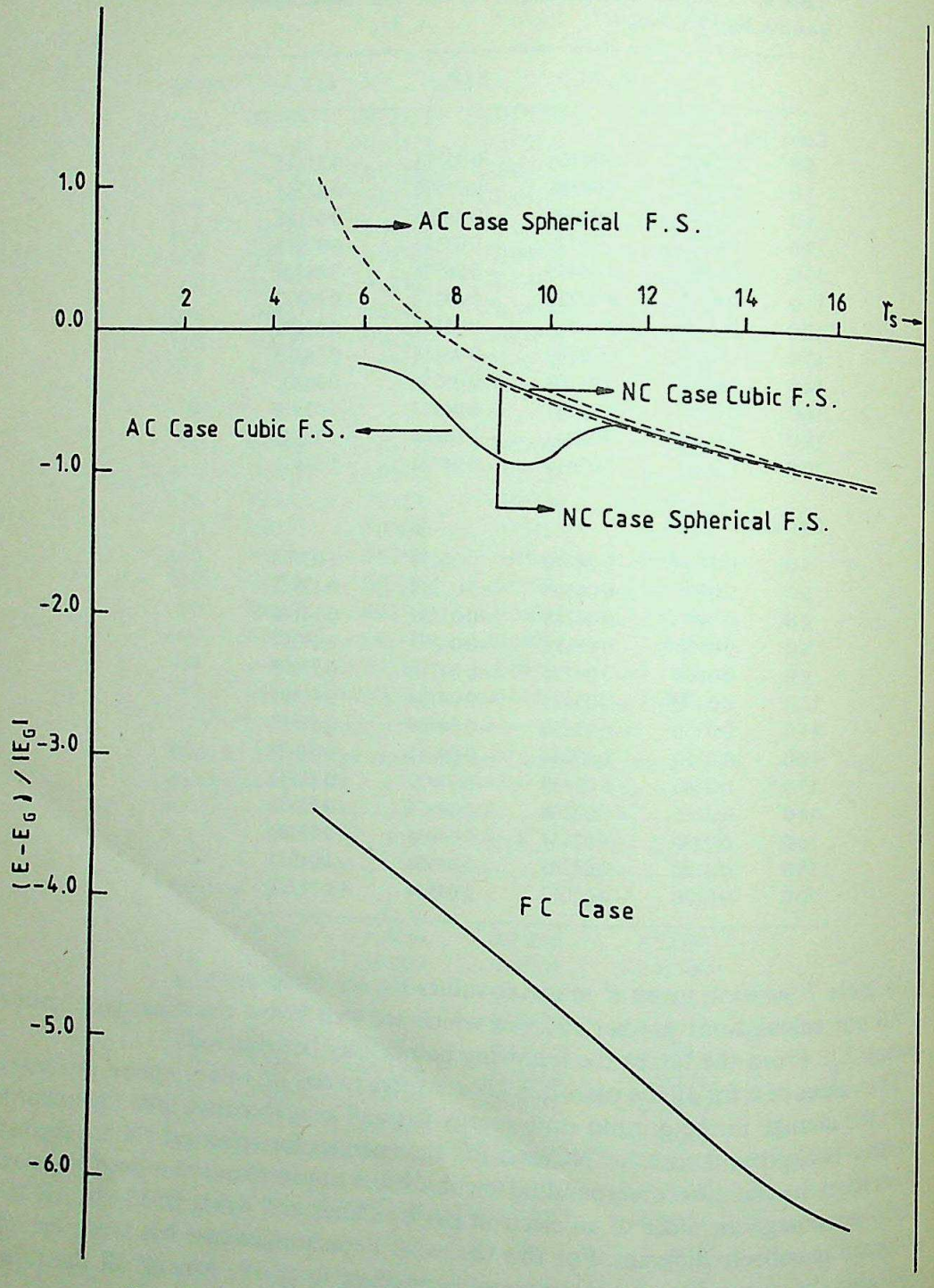

Figure 2. $(E-E_G)/|E_G|$ vs r_s for different crystals (Present work).

4 to 6 we see that the contribution from positive background has slightly lifted up the E values. Also for all the three cases the energies corresponding to cubic FS are lower than the spherical FS energies. This situation is similar to what has been observed by Carr (1961) and Edwards and Hillel (1968).

For comparison, we have plotted the results of Edwards and Hillel (1968) in figure 3. Our results agree with their results that at low densities the ground state is

CC-0. In Public Domain. Gurukul Kangri Collection, Haridwar

Digitized by Arya Samaj Foundation Chennai and eGangotri

Table 7 *R-Matrices*

	NC-Cubic F.S	
0·500000	0·000000	0·129006
0·000000	0·500000	0·129006
0·129006	0·129006	0·50000
	NC Spherical F.S	
0·500000	0·054443	0·119014
0·054443	0·500000	0·119014
0·119014	0·119014	0·500000
	FC Cubic F.S	
1·000000	−0·184126	0·099738
−0·184126	1·000000	0·099738
0·099738	0·099738	1·000000
	FC Spherical F.S	
1·000000	0·049364	0·038594
−0·049364	1·000000	0·038594
0·038594	0·038594	1·000000
	AC Cubic F.S	
1·000000	0·000000	0·000516
0·000000	1·000000	0·000000
0·000516	0·000000	1·000000
	AC Spherical F.S	
1·000000	0·000000	0·615025
0·000000	1·000000	0·000000
0·615025	0·000000	1·000000

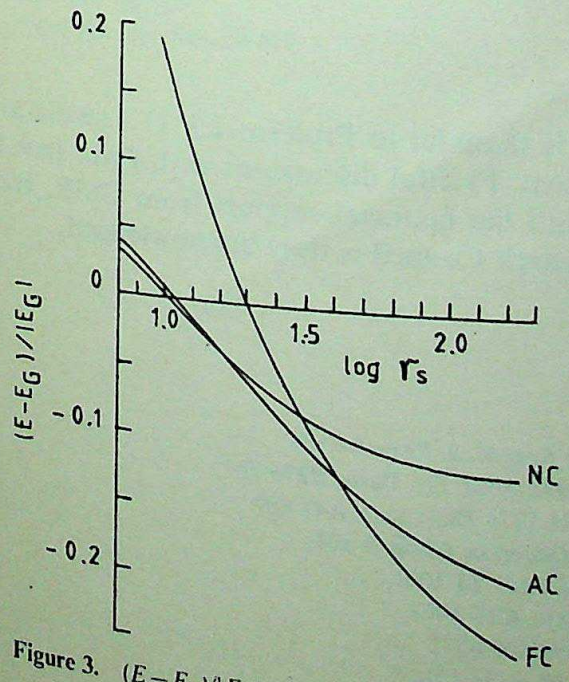

Figure 3. $(E-E_G)/|E_G|$ vs r_s for different crystals (Edwards and Hillel's work).

CC-0. In Public Domain. Gurukul Kangri Collection, Haridwar

Digitized by Arya Samaj Foundation Chennai and eGangotri

Table 8. Comparision of α values for AC with α value from Wigner's Theory

r_s	$\alpha = \frac{1}{2r_s^{3/2}}$	α (calculated)
6·0	0·0340	0·0360
7·0	0·0270	0·0268
8·0	0·0221	0·0175
9·0	0·0185	0·0129
10·0	0·0158	0·0105

ferromagnetic crystal. They have predicted crystalline antiferromagnetic state over a large intermediate density range. But in our case corresponding to AC case for cubic FS we get a minimum (figure 2) which in an indirect way may indicate a crystalline antiferromagnetic state at that density. It occurs around $r_s = 10$, which is the lower limit for the density range for antiferromagnetic crystalline state in their calculation.

Wigner in his paper has pointed out that for sufficiently large r_s the wave function of the crystallized electron should be a Gaussian. He gets this result since he is considering zero-point vibration. Wigner claims that the orbital exponent of the Gaussion α (=his $(\alpha/2)$) should go like

$$\frac{1}{2r_s 3/2}.$$

We find in AC case for cubic fermisurface the values of α are found to behave as indicated above. The numbers are given in table 8. It is worth to mention again that only for this case we got a minimum in the $(E-E_G)/|E_G|$ vs r_s curve and also it corresponds to the interesting case of Wigner crystallization.

Acknowledgements

One of the authors K Iyakutti is thankful to Professors P O Lowdin and Osvaldo Goscinski for their encouragement. Fruitful discussions with Prof. Jens Peder Dhal is acknowledged with thanks and the financial support from CSIR, India and the Swedish National Sciences Research Council is duly acknowledged.

References

Ando T, Fowler A B and Stern F 1982 *Rev. Mod. Phys.* **54** 589
Biskupski G, Dubois H and Ferre D 1973 *Acad. Sci.* Paris, **B276** 781
Brown J S, Brown R C and March N H 1974 *Phys. Lett.* **A47** 489
Calais J L and Sperber G 1973 *Int. J. Quantum. Chem.* 7 501
Calais J L and Appel K 1964 *J. Maths. Phys.* **51** 1001
Calais J L and Besnik Sykja 1982 *J. Phys.* **C15** 3093
Care C M and March N H 1971 *J. Phys.* **C4** L372
Care C M and March N H 1975 *Adv. Phys.* **24** 101
Carr W J 1961 *J. Phys. Rev.* **122** 1437

CC-0. In Public Domain. Gurukul Kangri Collection, Haridwar

Digitized by Arya Samaj Foundation Chennai and eGangotri

Cole T, MeCombe B D, Quinn J I and Kalia R V 1981 *Phys. Rev. Lett.* **46** 1096
Crandall R S 1973 *Phys. Rev.* **A8** 2136
Crandall R S and Williams R 1971 *Phys. Rev. Lett.* **A34** 404
Crandall R S and Williams R 1972 *Phys. Rev.* **A5** 2183
Delhalle J 1978 *Int. J. Quantum Chem.* **13**, 605
Delhalle J, Piela L, Bredas J L and Andre J M 1980 *Phys. Rev.* **B22** 6254
de Llano M and Plastino A 1971 *Kinam* **1** 201
Durkan J, Elliott R J and March N H 1968 *Rev. Mod. Phys.* **40** 812
Durkan J and March N H 1968 *J. Phys.* **C1** 118
Edwards S F and Hillel A J 1968 *J. Phys.* **C1** 61
Gallet F, Deville G, Valdes A and Williams F I B 1982 *Phys. Rev. Lett.* **49** 212
Grimes C C and Adams G 1979 *Phys. Rev. Lett.* **42** 795
Hall G L 1981 *J. Maths. Phys.* **22** 2996
Koji Kajita 1985 *J. Phys. Soc. Jpn.* **54** 4092
Kohn W 1973 *Phys. Rev.* **B7** 4388
Kohn W 1974 *Phys. Rev.* **B10** 382
Kostor G F 1953 *Phys. Rev.* **89** 67
Lang N D and Kohn W 1970 *Phys. Rev.* **B1** 4555
Larson E G and Thorson W R 1966 *J. Chem. Phys.* **45** 1539
Lowdin P O 1956 *Adv. Phys.* **5** 1
Majumdar C K and Ramakrishnan T V 1973 *Phys. Rev.* **B7** 1850
Mehrotra R, Guenin B M and Dahm A J 1982 *Phys. Rev. Lett.* **48** 641
Mills A P 1978 *Phys. Rev. Lett.* **41** 1828
Monkhoest H J and Schwalm W A 1981 *Phys. Rev.* **B23** 1729
Overhauser A W 1978 *Adv. Phys.* **27** 343
Pepper M, Pollitt S I, Adkins C J and Oakley R E 1974 *Phys. Lett.* **A47** 71
Rosenbaum T E, Field S B, Nelson A and Littlewood P B 1985 *Phys. Rev. Lett.* **54** 241
Shavift I 1962 *Methods Comp. Phys.* (Academic Press) Vol. II.
Shore H B, Zaremba E, Rose J H and Sander L 1978 *Phys. Rev.* **B18** 6506
Shore H B, Zaremba E, Rose J H and Sander L 1980 *Phys. Rev.* **B21** 3037
Slater J C 1965 *Quantum theory of atoms and molecules*, (New York: McGraw Hill) Vol. II
Smith J R 1969 *Phys. Rev.* **181** 522
Somerford D J 1971 *J. Phys.* **C4** 1570
Tatsuzo Nagai and Hidetoshi Fukuyama 1982 *J. Phys. Soc. Jpn.* **51** 3431
Tatsuzo Nagai and Hidetoshi Fukuyama 1983 *J. Phys. Soc. Jpn.* **52** 44
Wigner E 1934 *Phys. Rev.* **46** 1002
Wigner E 1938 *Trans. Faraday Soc.* **34** 678

CC-0. In Public Domain. Gurukul Kangri Collection, Haridwar

Digitized by Arya Samaj Foundation Chennai and eGangotri

CC-0. In Public Domain. Gurukul Kangri Collection, Haridwar

Digitized by Arya Samaj Foundation Chennai and eGangotri

Pramāṇa – J. Phys., Vol. 34, No. 2, February 1990, pp. 151–156. © Printed in India.

Indentation studies on alkaline earth fluoride crystals at elevated temperatures

K KISHAN RAO and D B SIRDESHMUKH
Department of Physics, Kakatiya University, Warangal 506 009, India

MS received 12 May 1989; revised 11 October 1989

Abstract. Indentations have been made on the (111) planes of CaF_2, SrF_2 and BaF_2 at various temperatures up to 700°C. By etching the crystals, the indentation dislocation rosettes (IDRs) have been recorded and the relative hardness is estimated from the dimensions of the IDRs. The hardness of all these crystals falls with temperature according to the equation $H = A\exp(-BT)$. Dramatic changes are observed in the shape of the IDR at elevated temperatures indicating activation of new slip systems.

Keywords. Hardness; indentation; slip; fluorite type crystals.

PACS Nos 62·20, 61·70

1. Introduction

The hardness of a crystal is generally determined by indenting its surface with a precision-cut diamond under an applied load. The hardness is calculated from the dimensions of the indentation figure. During indentation, dislocations are generated by the deformation due to indentation. When an indented crystal surface is etched, these dislocations reveal themselves in the form of an array of etch pits. Such an array is referred to as an Indentation Dislocation Rosette (IDR). It has been pointed out that the dimensions of the IDR are related to the hardness of the crystal (Gridneva *et al* 1979). Direct measurements on the indentation provides values of hardness. A study of the IDR provides the value of relative hardness i.e., hardness of a sample in terms of the hardness of a standard. Besides, the IDRs provide information about the mobility of dislocations and slip systems. The design of a simple instrument for determination of relative hardness based on measurements on IDRs was discussed in an earlier paper (Kishan Rao and Sirdeshmukh 1984, hereinafter referred as I). Using this instrument, the variation of hardness with temperature of some alkali halides was studied (Kishan Rao and Sirdeshmukh 1985 hereinafter referred as II).

These studies have now been extended to another interesting class of crystals – the alkaline earth fluorides. The alkaline earth fluorides – CaF_2, SrF_2 and BaF_2 are ionic crystals with high melting points and have the cubic fluorite structure. These crystals have applications in infrared optics, in thin film dielectric devices and they display superionic conduction at high temperatures. Because of the simplicity of structure and bonding and the varied applications, these crystals have been the subject of a large amount of experimental as well as theoretical work (Hayes 1974). However, there is very little work on hardness and much less on its temperature variation. The

CC-0. In Public Domain. Gurukul Kangri Collection, Haridwar

Digitized by Arya Samaj Foundation Chennai and eGangotri

microhardness of CaF_2, SrF_2 and BaF_2 was determined by Kishan Rao and Sirdeshmukh (1983) by the Vickers indentation method at room temperature. The temperature variation of hardness of CaF_2 was studied by Boyarskaya *et al* (1981) and Jain and Rawat (1982a) by the Vickers indentation method up to 500°C; in both the investigations, the hardness was found to decrease with increasing temperature. In BaF_2, Liu and Li (1964) recorded the IDR at room temperature; there is no work on the temperature variation of hardness. On SrF_2, there is no work on the temperature variation of hardness nor has the IDR been observed at any temperature.

In the present investigation, a systematic study has been made of the indentation on CaF_2, SrF_2 and BaF_2 at elevated temperatures. The study has yielded information on the temperature variation of hardness and also on the slip activation process at high temperatures.

2. Experimental

The crystals used in this study were supplied by Optovac in the form of cylinders, 10 mm in diameter, from which plates 2 mm thick with (111) faces were cleaved out. The design features of the instrument for indentation at room temperature and elevated temperatures have been described in I and II. The indented surfaces were etched with nitric acid to reveal the dislocation etch pits and IDRs. For obtaining clear etch pits, the normality of nitric acid and the time of etching had to be chosen after some trials. The optimum values of the normalities and etching times were 0·2 N and 60 min for CaF_2, 0·1 N and 40 min for SrF_2 and 0·1 N and 30 s for BaF_2. The etch pits on the (111) face are in the form of equilateral triangles with their sides along the $\langle 110 \rangle$ directions.

In I, it was shown that a relation between the hardness and linear dimension of the IDR exists in crystals with diamond structure. It was assumed in I and II that the same relation exists in crystals with the NaCl structure. It is now assumed that the relation holds in the crystals with the CaF_2 structure also.

As shown in II, the relative hardness is calculated from the relation:

$$H_t = H_{RT} l^2_{RT} / l_t^2 \qquad (1)$$

where H_{RT} and H_t are the hardness values at room temperatures and temperature t and l_{RT} and l_t are the linear dimensions of the IDR at the respective temperatures. Values of 185, 163 and 149 (in units of kg/mm^2) obtained in the earlier work (Kishan Rao and Sirdeshmukh 1983) have been used for H_{RT} of CaF_2, SrF_2 and BaF_2 respectively.

A detailed discussion of the slip systems in the CaF_2 structure will be given in the next section. Here, it is sufficient to note that the IDR due to the primary slip system is triangular with its sides along the $\langle 110 \rangle$ directions. The length of the side of the triangle is taken as the linear dimension of the IDR. It will be mentioned later that at elevated temperatures, the secondary slip system introduces a change in the shape of the IDR but for purposes of hardness measurement, the IDR due to primary slip alone is considered.

CC-0. In Public Domain. Gurukul Kangri Collection, Haridwar

Digitized by Arya Samaj Foundation Chennai and eGangotri

3. Results and discussion

3.1 *Temperature variation of hardness*

The values of the relative hardness of CaF_2, SrF_2 and BaF_2 at different elevated temperatures, determined by the method described in §2 are shown in figure 1. In SrF_2 and BaF_2, the measurements were made up to 700°C; in CaF_2, the measurements could not be made above 400°C due to reasons discussed later in this section. In all the three crystals, the hardness decreases with temperature. The fall in hardness is fast up to about 200°C and thereafter, it is slow. The pattern of temperature variation of hardness is similar in the three crystals. Further, the temperature variation of hardness of CaF_2 determined in this study is close to the results obtained by Boyarskaya *et al* (1981) and Jain and Rawat (1982a) by the direct vickers indentation method. SrF_2 is harder than BaF_2 up to 250°C but at higher temperatures, it becomes relatively softer.

Neither Boyarskaya *et al* (1981) nor Jain and Rawat (1982a) have discussed their results on CaF_2 quantitatively. In II, it was shown that a good fit to experimental data was provided by the relation.

$$H = A\exp(-BT) \tag{1}$$

where A and B are constants characteristic of the crystal. It has been verified that the hardness values in figure 1 are represented well by (1). Plots of $\log H$ vs T are linear. From a least-squares fitting of the data, values of A and B have been obtained. The values of A and B for CaF_2, SrF_2 and BaF_2 are (6·58, 0·0055), (7·26, 0·0073) and (5·95, 0·0045) respectively. These values are of the same order as in the alkali halides (II).

3.2 *The shape of the indentation dislocation rosette*

A visual examination of the indentation dislocation rosette (IDR) provides consider-

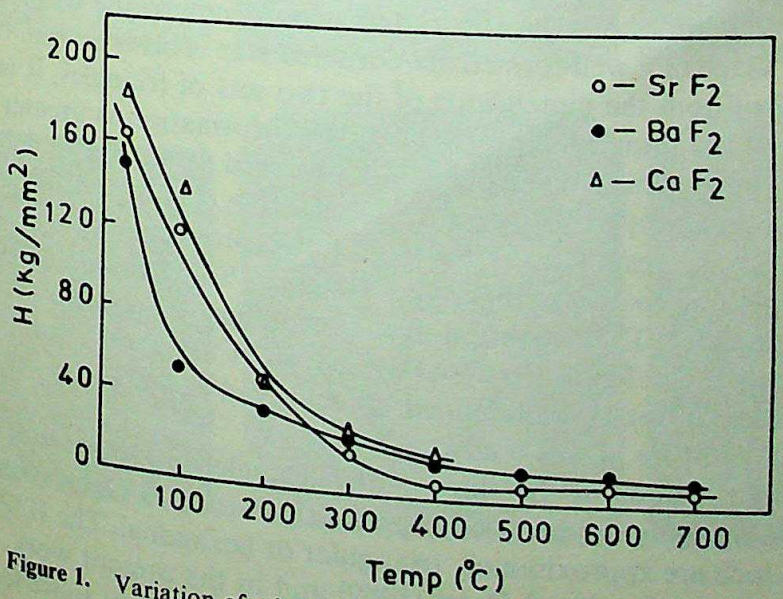

Figure 1. Variation of relative hardness (H) with temperature (T).

CC-0. In Public Domain. Gurukul Kangri Collection, Haridwar

Digitized by Arya Samaj Foundation Chennai and eGangotri

able information regarding the slip process. Thus, Boyarskaya *et al* (1975) observed that the IDR on the (111) face of NaCl has its arms along the ⟨110⟩ direction at room temperature and along the ⟨121⟩ directions at 160°C. A change in the mode of deformation was proposed to explain the observed change in the shape of the IDR. Similarly, Kishan Rao and Sirdeshmukh (II) observed that the IDR on the (100) face of NaCl is well-defined up to 400°C but becomes an isotropic cluster of dislocation etch pits at higher temperatures. This was attributed to the activation of new glide systems.

The slip systems for the CaF_2 structure are discussed by Chin (1975). The primary slip system is $\{001\}\langle\bar{1}10\rangle$; the glide traces of this system on the (111) face are along $\langle 0\bar{1}1\rangle$. There is also a secondary slip system $\{110\}\langle\bar{1}10\rangle$; the corresponding glide traces on the (111) plane are along the $\langle\bar{1}10\rangle$ and $\langle\bar{1}\bar{1}2\rangle$ directions. Evans *et al* (1966) have suggested that in CaF_2 in addition to the primary slip system, the secondary slip also gets activated at 200°C. Boyarskaya *et al* (1981) do not make any comment except that the dislocation mobility in CaF_2 increases sharply at a temperature of 0·35 T_m, where T_m is the melting point. Jain and Rawat (1982b) observed a transition at 200°C in the surface distortion features on (111) faces of CaF_2 studied with Fizeau fringe pattern technique. Some interesting observations made in the present study are discussed below.

The IDRs on the (111) planes of the alkaline earth fluorides at some select temperatures are shown in figure 2. For convenience, we shall discuss the observations on SrF_2 and BaF_2 first and take up CaF_2 in the end. From figure 2a, it can be seen that the IDR on SrF_2 at room temperature is essentially triangular with its sides along the ⟨110⟩ directions. These three ⟨110⟩ directions are identified with the $\langle 0\bar{1}1\rangle$ glide traces of the primary slip planes. There is a feeble protrusion (figure 2a) in the sides of the IDR due to the secondary slip system. These protrusions become clear at about 300°C indicating that the secondary slip system is fully activated. These protrusions form a second triangle with sides along the $\langle\bar{1}10\rangle$ glide traces of the secondary slip system. There is no dislocation motion along the $\langle\bar{1}\bar{1}2\rangle$ directions. As the temperature increases, both the slip systems contribute to the deformation and the IDR has the shape of a well-formed six-cornered star. This is seen in the IDR at 500°C in figure 2a. From the dimensions of the two sets of triangles, it is seen that the contribution of the primary slip system to the deformation is greater than that of the secondary slip system. These features are observed up to 700°C, the maximum temperature of observation in the present investigation. It may be mentioned that for the relative hardness results discussed in §3.1, measurements were made only on the triangular IDR due to the primary slip system. The results on BaF_2 are very similar to those on SrF_2. The activation of the secondary slip system takes place at 200°C itself (although in figure 2b the IDR at 300°C is shown for the sake of uniformity in presentation). A well-defined six-cornered IDR persists up to 700°C, the maximum temperature in this study.

In CaF_2, the protrusions in the sides of the triangle due to secondary slip are clearly seen at room temperature itself (figure 2c). Patel and Desai (1969) refer to IDRs on CaF_2 which are approximately triangular or hexagonal. The IDRs recorded at room temperature by Patel and Desai (1969) and in the present work reveal that the secondary slip system is already participating in deformation at room temperature. At relatively elevated temperatures, the IDRs are triangular with some distortion due to the secondary slip contribution. But surprisingly, this lasts only up to 400°C. At

CC-0. In Public Domain. Gurukul Kangri Collection, Haridwar

Digitized by Arya Samaj Foundation Chennai and eGangotri

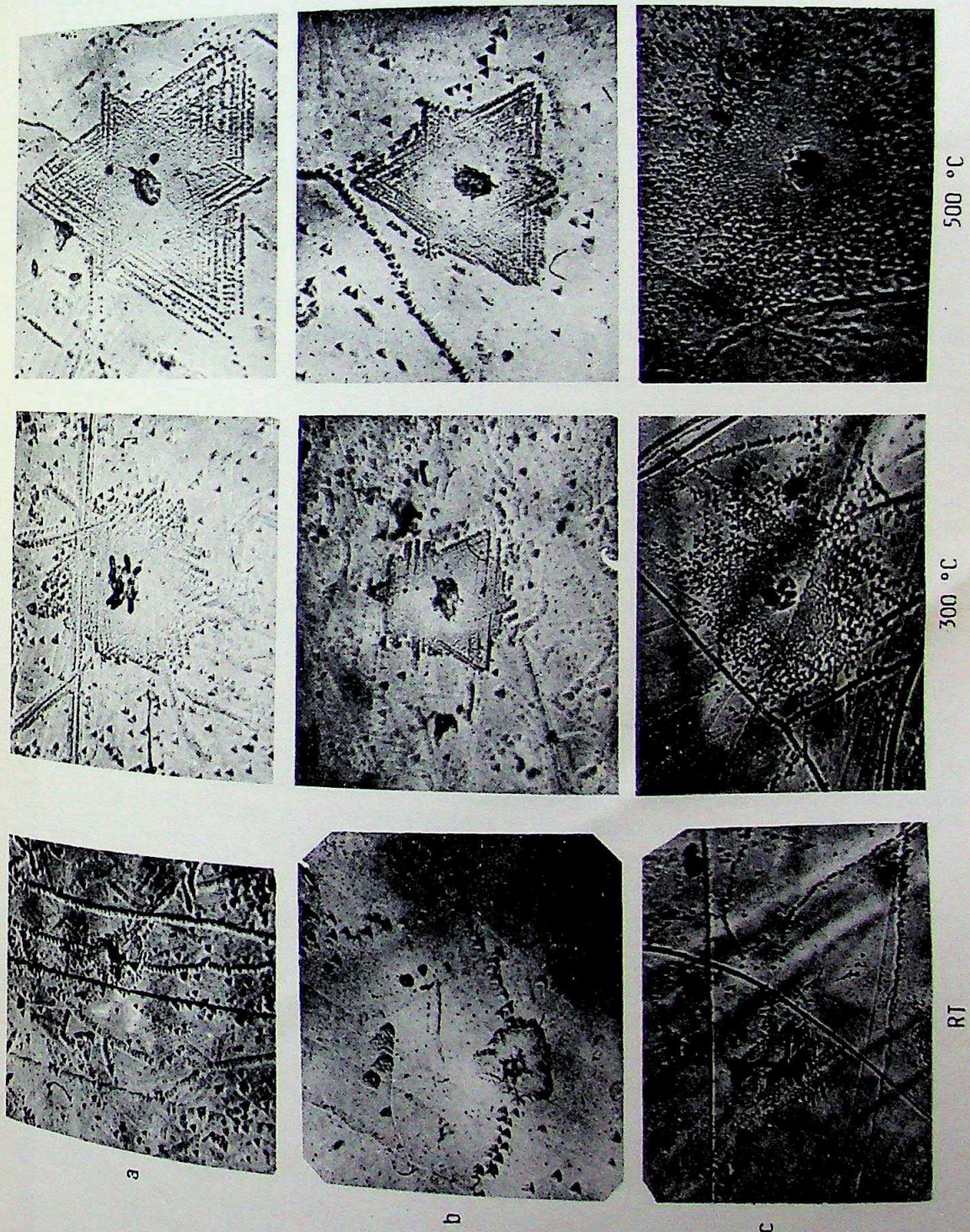

Figure 2. IDR patterns for (a) SrF_2, (b) BaF_2 and (c) CaF_2 crystals at different temperatures, X200.

CC-0. In Public Domain. Gurukul Kangri Collection, Haridwar

Digitized by Arya Samaj Foundation Chennai and eGangotri

higher temperatures the IDR is neither triangular nor six-cornered but is a mere cluster of etch pits as seen from the IDR at 500°C (figure 2c). The motion of dislocations is no longer restricted to the glide traces of either slip systems. Apparently there is cross slip and activation of a number of new, as yet, unidentified, slip systems. A similar effect was observed in NaCl (II).

Thus, the present results show that activation of the secondary slip system takes place at 300°C in SrF_2 at 200°C in BaF_2 and at about the room temperature in CaF_2. Further there is evidence that a very large number of slip systems are getting activated in CaF_2 at a temperature of about 400°C resulting in dislocation motion almost in all directions. Such an effect could not be observed in SrF_2 and BaF_2 up to 700°C but may take place at higher temperatures.

Acknowledgements

Thanks are due to the referees for numerous useful suggestions. One of the authors (KKR) is thankful to UGC, New Delhi for financial support.

References

Boyarskaya Y S, Shutova S S and Zhitaru R P 1975 *Phys. Status Solidi* **A30** K7
Boyarskaya Y S, Grabko D Z and Dintu M P 1981 *Cryst. Res. Technol.* **16** 441
Chin G Y 1975 *Deformations in Ceramic Materials* (NY: Plenum Pub. Corp.)
Evans A G, Roy C and Pratt P L 1966 *Proc. Br. Ceram. Soc.* **6** 173
Gridneva I V, Millman Y V, Trefilow V I and Chugunova S I 1979 *Phys. Status Solidi* **A54** 195
Hayes W 1974 *Crystals with Fluorite Structure* (Oxford: Clarendon Press)
Jain G C and Rawat P N 1982a *Indian J. Phys.* **A56** 76
Jain G C and Rawat P N 1982b *Bull. Mater. Sci.* **4** 589
Liu T S and Li C H 1964 *J. Appl. Phys.* **35** 3325
Kishan Rao K and Sirdeshmukh D B 1983 *Bull. Mater. Sci.* **5** 449
Kishan Rao K and Sirdeshmukh D B 1984 *Pramana – J. Phys.* **23** 251
Kishan Rao K and Sirdeshmukh D B 1985 *Pramana – J. Phys.* **24** 887
Patel A R and Desai C C 1969 *Indian J. Pure Appl. Phys.* **7** 562

CC-0. In Public Domain. Gurukul Kangri Collection, Haridwar

Digitized by Arya Samaj Foundation Chennai and eGangotri

Pramāṇa – J. Phys., Vol. 34, No. 2, February 1990, pp. 157–163. © Printed in India.

Ultrasonic absorption studies in solutions of ortho and para hydroxy benzoic acid in dioxan

V BALASUBRAMANIAN and A SRINIVASA RAO*

Department of Physics, Bharathidasan Government College for Women, Pondicherry 605 003, India
*Raman School of Physics, Pondicherry University, JIPMER Campus, Pondicherry 605 006, India

MS received 27 April 1989; revised 2 September 1989

Abstract. Ultrasonic absorption was measured in ortho and para hydroxy benzoic acid (OHBA and PHBA) in dioxan at room temperature for various solute concentrations. The variation of ultrasonic absorption in both solutions with the solute concentration showed two maxima, one at lower solute concentration and the other at higher solute concentration. The first maximum is explained as due to formation of hydrogen bonds between the O–H groups of OHBA and PHBA molecules and the oxygen of dioxan molecules and the second maximum as due to the COOH group of the OHBA/PHBA molecules and oxygen of dioxan molecules. In both systems the measured absorption is explained on the basis of Hall's two-state model.

Keywords. Ultrasonic absorption; hydrogen bond; volume viscosity; relaxation time.

PACS No. 62·80

1. Introduction

Earlier studies carried out by Anbanandan *et al* (1976) in solutions of *o*-hydroxy benzoic acid (OHBA) and *p*-hydroxy benzoic acid (PHBA) in dioxan indicated the possibility of hydrogen bonding in these solutions. Ultrasonic velocity was studied by Sosamma *et al* (1988) in the same solutions at various solute concentrations ranging from 0·01–0·10 mole fraction at various temperatures. The variation of ultrasonic velocity in both solutions with solute concentration showed two velocity maxima, one at lower solute concentration and another at higher solute concentration. The maxima were explained as due to the formation of hydrogen bonds between the solute and solvent molecules. To obtain additional information on the molecular interactions in these systems we have carried out ultrasonic absorption studies in OHBA and PHBA solutions in dioxan and the results are reported in this paper.

2. Theoretical aspects

The classical absorption may be obtained from Stoke's–Kirchoff's equation as

$$(\alpha/f^2)_{cl} = \frac{8\pi^2\eta_s}{3\rho C^3} + \frac{2\pi^2 K(\gamma-1)}{\rho C^3 \gamma C_v}, \qquad (1)$$

*To whom all correspondence should be addressed

CC-0. In Public Domain. Gurukul Kangri Collection, Haridwar

Digitized by Arya Samaj Foundation Chennai and eGangotri

where ρ is the density of the medium, C the sound velocity in the medium, γ the ratio of two specific heats, C_v the specific heat at constant volume, K the coefficient of thermal conductivity and η_s is the coefficient of shear viscosity. The contribution due to the second term in (1) is negligible for liquids of low thermal conductivity.

The measured ultrasonic absorption $(\alpha/f^2)_{obs}$ is considered as the sum of classical absorption $(\alpha/f^2)_{cl}$ and structural absorption $(\alpha/f^2)_{st}$. The excess absorption is defined as

$$(\alpha/f^2)_{ex} = (\alpha/f^2)_{obs} - (\alpha/f^2)_{cl}. \tag{2}$$

The excess absorption measured in water was explained using Hall's two-state model (Narayana *et al* 1975). The $(\alpha/f^2)_{ex}$ value was theoretically calculated to be:

$$(\alpha/f^2)_{ex} = 2\pi^2 \rho C \beta_r \tau, \tag{3}$$

where τ is the relaxation time, β_r, the relaxing part of the compressibility, C the velocity of sound and ρ the density of the liquid.

The structural relaxation time τ was related to the molar volume (V) and the free energy difference (ΔF) as follows

$$\tau = \frac{V\eta_s}{R_g T\left[1 + \exp\dfrac{\Delta F}{K_B T}\right]}, \tag{4}$$

where η_s is the shear viscosity, T the temperature, R_g the gas constant and K_B the Boltzmann constant.

The volume viscosity may be estimated from the relation

$$\eta_V = 4\eta_s/3\left[\frac{(\alpha/f^2)_{obs} - (\alpha/f^2)_{cl}}{(\alpha/f^2)_{cl}}\right], \tag{5}$$

where η_s is the shear viscosity.

The relaxing part of compressibility (β_s) is related to η_V and τ by an expression developed by Litovitz and Davis (1965)

$$\eta_v = \beta_r \tau/\beta_0^2 \tag{6}$$

where β_0 is the static compressibility. For viscoelastic liquids, the relaxation time may be related to the static compressibility (β_0) and the two viscosities η_v and η_s

$$\tau = \beta_0[\eta_v + \tfrac{4}{3}\eta_s] \tag{7}$$

3. Materials and methods

Ultrasonic absorption in OHBA and PHBA in dioxan was measured at a frequency of 10 MHz using a pulse echo interferometer at a temperature of $30 \pm 0{\cdot}1°C$. A cylindrical cell fabricated by the author (Balasubramanian 1988) in this laboratory was used for this purpose. The accuracy in the measurement of velocity is 0·1% and absorption is 0·03% respectively. The absorptions are represented as $Npm^{-1}s^2$. The

CC-0. In Public Domain. Gurukul Kangri Collection, Haridwar

Digitized by Arya Samaj Foundation Chennai and eGangotri

Table 1. Ultrasonic absorption and related parameters for the solution of *o*-hydroxy benzoic acid in dioxan.

X M.F	C ms^{-1}	$\rho \times 10^{-3}$ $kg.m^{-3}$	$\beta_s \times 10^{10}$ m^2N^{-1}	$(\alpha/f^2)_{obs}$	$(\alpha/f^2)_{cl}$	$(\alpha/f^2)_{ex}$	η_S Poise	η_V Poise	$\tau \times 10^{11}$ s	ΔF k_{cal}/M	$\beta_r \times 10^{10}$ m^2N^{-1}
				$\times 10^{15}$ $Npm^{-1}s^2$							
0·01	1326·1	1·027	5·537	175·92	12·62	163·30	0·01148	0·19815	1·182	1·527	5·140
0·02	1323·7	1·029	5·547	175·92	13·14	162·78	0·01192	0·19679	1·180	1·633	5·131
0·03	1322·0	1·032	5·546	175·92	13·77	162·15	0·01247	0·19581	1·178	1·106	5·113
0·04	1327·9	1·033	5·490	230·89	13·64	217·25	0·01253	0·19966	1·188	1·107	5·065
0·05	1335·6	1·039	5·395	282·19	13·94	268·25	0·01311	0·33645	1·909	0·546	5·130
0·06	1334·7	1·042	5·387	250·46	14·27	236·19	0·01344	0·29645	1·694	1·007	5·078
0·07	1325·3	1·045	5·449	230·89	16·35	214·54	0·01511	0·26432	1·550	1·526	5·063
0·08	1342·2	1·051	5·284	300·71	17·32	283·39	0·01679	0·36611	2·053	1·102	4·979
0·09	1328·4	1·055	5·374	255·74	20·90	234·84	0·01963	0·29409	1·713	1·990	4·958
0·10	1330·2	1·058	5·342	249·58	25·11	224·47	0·02376	0·28315	1·682	2·489	4·804

For explanation of symbols, see text

Table 2. Ultrasonic absorption and related parameters for the solution of *p*-hydroxy benzoic acid in dioxan.

X M.F	C ms^{-1}	$\rho \times 10^{-3}$ $kg.m^{-3}$	$\beta_s \times 10^{10}$ m^2N^{-1}	$(\alpha/f^2)_{obs}$	$(\alpha/f^2)_{cl}$	$(\alpha/f^2)_{ex}$	η_S Poise	η_V Poise	$\tau \times 10^{11}$ s	ΔF k_{cal}/M	$\beta_r \times 10^{10}$ m^2N^{-1}
				$\times 10^{15}$ $Npm^{-1}s^2$							
0·01	1346·7	1·037	5·317	219·02	12·66	206·36	0·01219	0·26479	1·494	1·049	5·011
0·02	1345·7	1·039	5·312	220·56	13·23	207·33	0·01274	0·26612	1·509	1·068	4·973
0·03	1348·1	1·042	5·280	225·28	14·57	210·71	0·01414	0·27253	1·539	1·396	4·922
0·04	1359·9	1·044	5·179	229·87	15·22	214·65	0·01518	0·28551	1·588	1·514	4·823
0·05	1354·4	1·045	5·214	216·18	17·53	198·65	0·01729	0·26143	1·483	2·015	4·792
0·06	1366·3	1·047	5·116	219·94	18·28	201·66	0·01855	0·27283	1·522	2·128	4·692
0·07	1366·9	1·052	5·087	218·46	20·33	198·13	0·02076	0·26970	1·513	2·403	4·613
0·08	1386·8	1·056	4·924	230·98	21·81	209·17	0·02334	0·29847	1·623	2·523	4·458
0·09	1377·1	1·060	4·974	223·37	24·38	198·99	0·02564	0·27908	1·558	2·829	4·433
0·10	1380·1	1·065	4·929	224·28	25·39	198·89	0·02701	0·28209	1·528	2·935	4·372

For explanation of symbols, see text

viscosities of the solutions were determined using ostwalds viscometer with an accuracy of 0·04% in a constant temperature bath at 30+0·1°C. The densities were measured using a pyknometer with an accuracy of 0·005%. All the measured and calculated parameters are shown in tables 1 and 2. The variation of the parameters with concentration is shown in figures 1–4.

4. Results

4.1 *OHBA in dioxan*

It can be seen from figure 1A that in solutions of OHBA in dioxan, the ultrasonic absorption initially increases with increase in solute concentration, attains a maximum value at solute concentration of 0·05 mole fraction (cm_1), then decreases with further increase of solute concentration attaining a second maximum at a solute concentration of 0·08 mole fraction (cm_2). The excess absorption calculated for these solutions also

CC-0. In Public Domain. Gurukul Kangri Collection, Haridwar

Digitized by Arya Samaj Foundation Chennai and eGangotri

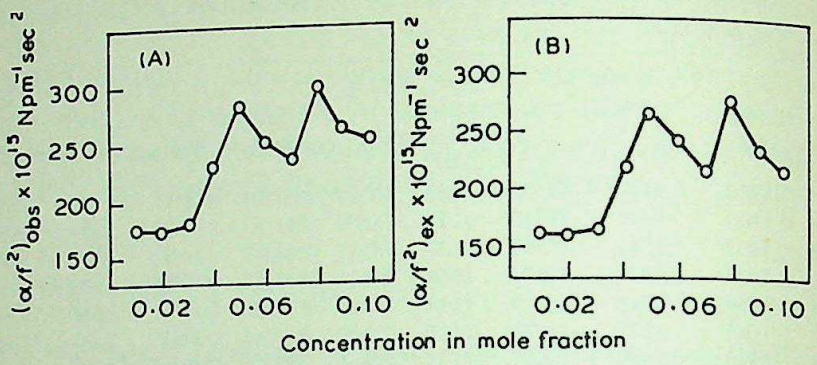

Figure 1.

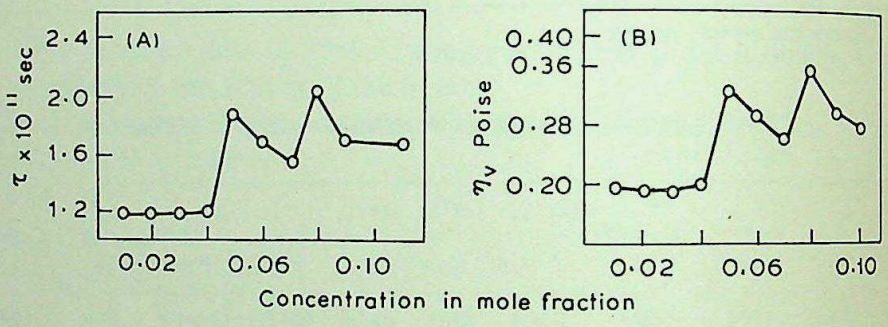

Figure 2.

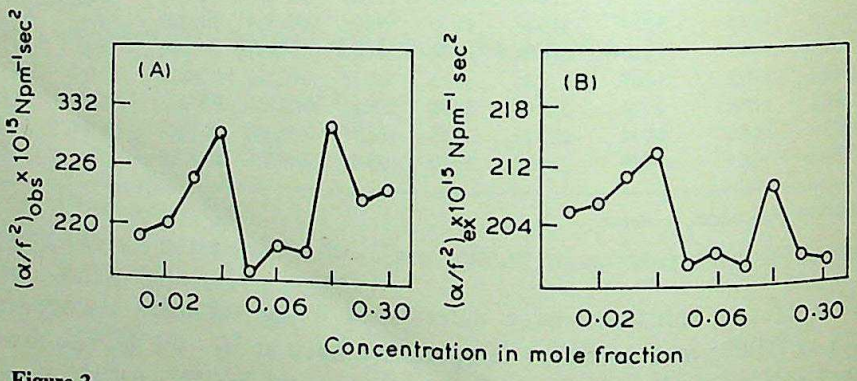

Figure 3.

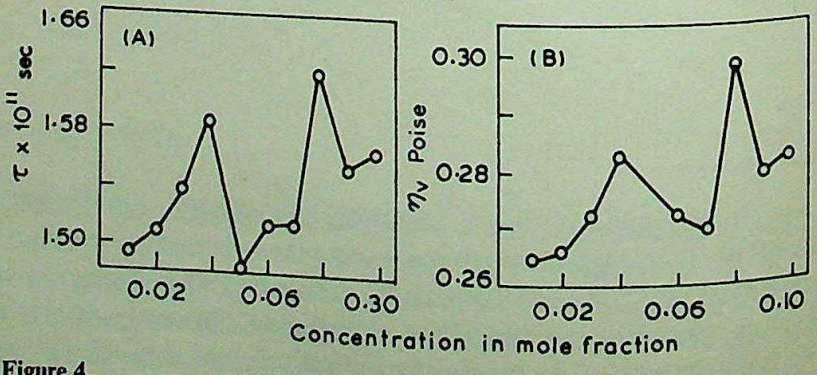

Figure 4.

CC-0. In Public Domain. Gurukul Kangri Collection, Haridwar

Digitized by Arya Samaj Foundation Chennai and eGangotri

shows two maxima at 0·05 mf (cm_1) and at 0·08 mf (cm_2) with increase in concentration of OHBA in dioxan (figure 1B).

4.2 *PHBA in dioxan*

The variation of ultrasonic absorption with solute concentration in the solutions of PHBA in dioxan is shown in figure 3A and it can be seen that the behaviour is similar to the one observed in the solution of OHBA in dioxan, with the exception that the absorption maxima occur at different solute concentrations. The first maximum (cm_3) occurs at 0·04 mf and the second (cm_4) at 0·08 mf of solute concentration. The excess absorption calculated for these solutions also shows two maxima at 0·04 mf and at 0·08 mf with increase in concentration of PHBA in dioxan (figure 3B).

5. Discussion

The ultrasonic absorption in both the systems initially increases with increase in solute concentration and reaches a maximum value and then decreases (figures 1A and 2A). The mole fraction of the solute which corresponds to the maximum absorption may be called the critical concentration. The maximum absorption at critical concentration indicates that the solution is highly structured. The present study confirms the two maxima observed in the velocity studies in the same systems by Sosamma *et al* (1988). The first maximum is explained as due to the formation of hydrogen bond between the O–H groups of OHBA/PHBA molecules and the oxygen atom of the dioxan molecules. A similar explanation may also hold good for the first maximum observed in the absorption vs concentration curves. The formation of hydrogen bonds is likely to make the solution highly structured and such a solution generally absorbs more ultrasound energy (Srinivasa Manja and Srinivasa Rao 1986). The second maximum is explained as due to the formation of hydrogen bond between COOH monomers of OHBA/PHBA molecules and oxygen of the dioxan molecules. The same explanation may also hold good for the second maxima observed in the present curves.

In both the systems of OHBA and PHBA in dioxan, the experimentally observed ultrasonic absorptions are higher than the classical absorption for all concentrations (tables 1 and 2). The values of $(\alpha/f^2)_{ex}$ are found to be 4–6 times the value of classical absorption. This indicates that the absorption of ultrasonic waves in the solution of OHBA in dioxan is not only due to shear viscosity but also due to some other effects. Probably the major contribution comes from structural effects.

The decrease in the absorption above 0·05 mole fraction in both systems can be explained as follows. Formation of strong hydrogen bonds generally increases the inter proton distance between adjacent hydrogen bonds, thereby weakening the intermolecular forces of the bulk solutions (Lippincott and Srinivasa Rao 1964). This may be the reason for the decrease of ultrasonic absorption above 0·05 mole fraction of solute concentration in both the systems studied.

To obtain further confirmation that the ultrasonic absorption maximum at cm_1 is due to the phenolic hydroxyl groups, the ultrasonic absorption was experimentally measured in solutions of benzoic acid in dioxan in the solute concentration range 0·01 to 0·1 mole fraction. In this solution only one maximum is observed at 0·07 mole

CC-0. In Public Domain. Gurukul Kangri Collection, Haridwar

Digitized by Arya Samaj Foundation Chennai and eGangotri

fraction of solute concentration. The absence of velocity maximum at the lower solute concentration is due to the fact that benzoic acid molecules do not possess any phenolic hydroxyl group. This confirms that the absorption maximum observed in both solutions of OHBA/PHBA in dioxan (cm_1) is due to the formation of hydrogen bonds between phenolic O–H groups of the above acid and the oxygen of dioxan molecules.

The decrease in ultrasonic absorption above the solute concentration of 0·08 mole fraction in both systems may be interpreted as due to weakening of hydrogen bonds in solutions formed between monomers and dioxan molecules. It is probable that at concentration cm_2 all the molecules are broken into monomers and hydrogen bonds are formed. It is also likely that the solute molecules above the critical concentration (cm_2) may stay in dimer form. These dimers are fairly large in size compared to dioxan molecules and have to be accommodated in the liquid and this may cause some structural changes resulting in weakening of intermolecular forces. This is probably the reason for the decrease in ultrasonic absorption observed above the concentration cm_2 in both the system studied.

The concentration at which first maximum was observed is at 0·05 mole fraction for OHBA and at 0·04 mole fraction for PHBA at 307K. This difference in value of concentration may be due to the fact that the phenolic group in PHBA is not chelated and hence it is more free to form hydrogen bonds than the phenolic group of *o*-hydroxy benzoic acid. Hence the hydrogen bonds are likely to be formed in solutions of PHBA in dioxan at a lower solute concentration as compared to OHBA in dioxan.

The two state model of Hall was applied by Srinivasa Manja *et al* (1985) to the solutions of certain carboxylic acids in dioxan. The two states in these solutions are: (1) dimer carboxylic acid molecules and (2) carboxylic acid monomers hydrogen bonded to dioxan molecules.

There will be an equilibrium between dimers and monomers hydrogen bonded to dioxan molecules at a given temperature. A compression during the wave propagation will produce a change in the number of molecules in both the states caused by the breaking of intermolecular hydrogen bonds. This structural change lags behind the acoustical pressure which is the cause of the absorption. The model was applied to methanol and ethanol at elevated pressures to explain the excess absorption (Narayana *et al* 1975).

The two-state model of Hall was applied to the present system at the first critical concentration (cm_1) where the phenolic O–H of hydroxy benzoic acid forms hydrogen bonds with dioxan. The two states are free OHBA molecules and hydrogen bonded OHBA – dioxan complexes through the O–H group.

The values of β_r and τ are calculated using the theory of structural relaxation developed by Hall (1948) and these are shown in tables 1 and 2. The calculated values appear to be reasonable and this indicates that Hall's two-state model may also be applied for dilute solutions.

The two-state model can also be applied for the maxima obtained at higher concentration. The second maximum (cm_2) at 0·08 mole fraction of solute concentration of OHBA is due to the formation of hydrogen bonds between carboxylic acid group (COOH) and the free oxygen atoms of the dioxan molecules. Since the situation is similar to the two state model of Hall which was proposed to explain the excess absorption in liquid water, the same model is extended here also to explain the excess absorption due to the formation of hydrogen bonds between the carboxylic acid of

CC-0. In Public Domain. Gurukul Kangri Collection, Haridwar

Digitized by Arya Samaj Foundation Chennai and eGangotri

o-hydroxy benzoic acid and dioxan at higher concentration. The two states assumed for the mixture at higher concentration are the dimeric state of the carboxylic acid (COOH) of the ortho hydroxy benzoic acid and the hydrogen bonded state between the monomeric carboxylic acid group with dioxan.

It is likely that the two states described for cm_1 may also be present at this concentration, but their number may not be significant as the hydrogen bonds between monomeric carboxylic acid and dioxan are stronger as revealed in the velocity studies (Nambinarayanan 1981; Srinivasa Manja and Srinivasa Rao 1986; Sosamma *et al* 1988).

The variation of ultrasonic absorption with concentration for solutions of PHBA in dioxan and the other calculated parameters are shown in the table 2. It can be seen from figure 3A that in the solutions of PHBA in dioxan, the absorption co-efficient attains maximum at 0·04 and at 0·08 mole fraction. The two-state model of Hall was also applied to these cases.

Tables 1 and 2 show that in both cases of OHBA and PHBA in dioxan, the relaxation times increase with concentration, show a maximum at the critical concentration and then decrease. The same trend is observed in the second critical concentration (0·08) for *o*-hydroxy and *p*-hydroxy benzoic acid.

Tables 1 and 2 also show that the free energy difference for the two states are 0·56 kcal/mol at 0·05 mole fraction, 1·10 kcal/mol for 0·08 mole fraction of the OHBA in dioxan and 1·51 kcal/mol at 0·04 mole fraction at 2·52 kcal/mol at 0·08 mole fraction of PHBA in dioxan. The increase of free energy indicates that the hydrogen bonds formed at the higher concentrations (cm_1) of *o*- and *p*-hydroxy benzoic acids are stronger (Glasstone 1956).

Finally it may be mentioned that the present absorption studies generally support the results obtained by Sosamma *et al* (1988) and indicate the usefulness of ultrasonic studies in the study of molecular interaction in liquid mixture. It is also possible to study chelation in these molecules by ultrasonic methods.

References

Anbanandan D, Krishnan B and Srinivasa Rao A 1976 *Indian J. Chem.* **14** 277

Balasubramanian V 1988 *Molecular acoustical studies in some aqueous and non-aqueous solutions*, Ph.D thesis, University of Madras, Madras

Glasstone 1956 *Text book of physical chemistry* (London: Macmillan)

Hall L 1948 *Phys. Rev.* **73** 775

Lippincott E R and Srinivasa Rao A 1964 *J. Chem. Phys.* **41** 3006

Litovitz T A and Davis C M 1965 in *Physical acoustics, Principles and methods* (ed.) W P Mason (New York: Academic Press) Vol. 2

Nambinarayanan T K 1981 *Ultrasonic studies on the nature of molecular interaction in some solution*, Ph.D thesis, University of Madras, Madras

Narayana K L, Mallikarjuna Swamy K, Sriramamurthy J and Sitaramaswamy P 1975 *Nuovo Cimento*, **B25** 199

Sosamma G, Nambinarayanan T K and Srinivasa Rao A 1988 *Indian J. Phys.* **B62** 31

Srinivasa Manja K 1985 *Ultrasonic studies on the nature of molecular interactions in some aqueous, non-aqueous solutions and liquid crystals*. Ph.D. thesis, Madras University, Madras

Srinivasa Manja K and Srinivasa Rao A 1985 *Pramāṇa – J. Phys.* **26** 459

CC-0. In Public Domain. Gurukul Kangri Collection, Haridwar

Digitized by Arya Samaj Foundation Chennai and eGangotri

CC-0. In Public Domain. Gurukul Kangri Collection, Haridwar

Digitized by Arya Samaj Foundation Chennai and eGangotri

Pramāṇa – J. Phys., Vol. 34, No. 2, February 1990, pp. 165–171. © Printed in India.

Rotational analysis of 3664 Å band of NiCl

A B DARJI and M B SURESH KUMAR
Department of Physics, M S University of Baroda, Baroda 390 002, India

MS received 4 May 1989; revised 1 December 1989

Abstract. Nickel chloride was excited in a high frequency discharge source and the band at 3664 Å was photographed at an inverse dispersion of 0·59 Å/mm on a two metre plane grating spectrograph. The rotational analysis was carried out and the molecular constants of the upper state are reported. The rotational isotopic shifts due to ^{37}Cl support the rotational analysis. The electronic transition involved is identified to be $\beta\ ^2\Delta_{5/2} \rightarrow X_1\ ^2\Delta_{5/2}$.

Keywords. Rotational analysis; molecular constants; isotopic shifts; electronic transition.

PACS No. 33·20

1. Introduction

The emission spectrum of nickel chloride was first reported by More (1938) and later studied by others (Krishnamurthy 1952; Reddy and Rao 1960; Rao *et al* 1962; Rao and Rao 1969; Darji and Shah 1980; Gopal 1981; Gopal and Joshi 1981, 1982, 1983; Shah *et al* 1983). From these studies several fragmentary systems are reported. But only two band systems have been identified as $F^2\Delta \rightarrow X^2\Delta$ (6395–6930 Å) and $G^2\Delta \rightarrow X^2\Delta$ (7270–7750 Å) (Rao and Rao 1969). However from the study of poorly resolved rotational structure of the bands of F and G systems electronic transitions $F^2\Delta_{5/2} \rightarrow X^2\Delta_{5/2}$ and $G^2\Delta_{5/2} \rightarrow X^2\Delta_{5/2}$ have been suggested by them. The electronic transitions are not yet ascribed to the remaining systems of NiCl from the study of rotational structure of the bands. The nature of the ground state of NiCl is also not yet established unambiguously. Further the various band systems of this molecule are designated differently by different workers. The spectrum of NiCl is complex due to the large number of electronic transitions between closely spaced high multiplicity molecular states. This gives rise to many sub-systems overlapping with each other. Thus only a few bands have rotational structure free from overlapping and suitable for rotational analysis. This makes the study of the spectrum of NiCl more difficult. However the complex nature of the spectrum of NiCl involving transitions between high multiplicity energy states demands careful investigation. The present paper reports, for the first time, a rotational analysis of the (0, 0) band of $\beta \rightarrow X$, system at 3664 Å reported by Darji and Shah (1980). From the analysis of this band the rotational constants have been evaluated and the nature of electronic transition responsible for the emission of this band system has been discussed.

CC-0. In Public Domain. Gurukul Kangri Collection, Haridwar

Digitized by Arya Samaj Foundation Chennai and eGangotri

2. Experimental details

The spectrum of NiCl molecule in the region 3600–3800 Å has been excited in a high frequency discharge source using a pure sample (BDH) of dehydrated nickel chloride. The characteristic light blue colour of the discharge was maintained bright in which the bands developed strong in intensity. The (0,0) band at 3664 Å was recorded on Kodak 103–0 spectroscopic plates in the 7th order of the two metre plane grating spectrograph (Carl–Zeiss) at an inverse dispersion of 0·59 Å/mm with a fine slit of 20 μm. Standard method was used to measure the plates using Abbe comparator. The accuracy of the measurement is up to $\pm 0{\cdot}05\,cm^{-1}$ for sharp and unblended lines. To pick up the branches, intensity records of the rotational lines obtained by microdensitometer coupled with a potentiometric recorder were employed.

3. Results and discussion

The O–O band of $\beta \rightarrow X$ system at 3664 Å photographed at high resolution and reproduced as seen on the negative (figures 1 a and b) reveals the presence of only two branches identified as R and P which are blended at low J values. As an intense Q branch is not seen the electronic transition should be of the type $\Delta\Lambda = 0$. The rotational analysis was carried out following the standard method (Herzberg 1950) of forming combination differences. The $\Delta_2 F''(J)$ values of this band when compared with those of the lower state of F and G systems, reported by Rao and Rao (1969), and also with the L_1 system reported by Darji and Sureshkumar (in press) were found to agree well i.e. the systems F, G, L_1 and β have a common lower state and is designated as $X_1{}^2\Delta_{5/2}$ as suggested by Rao and Rao (1969). Since a Q branch is not seen the transition should be $\beta^2\Delta_{5/2} \rightarrow X_1{}^2\Delta_{5/2}$. J assignments and vacuum wave numbers of the rotational lines are given in table 1, and the rotational constants obtained by the least squares fitting of the lines are given in table 2, together with the ground state constants reported by Rao and Rao (1969). The rotational lines of the isotopic molecule $Ni^{37}Cl$ have also been observed (see figure 1 and table 1) and the isotopic shifts support the analysis.

Table 1. Rotational constants of 3664 Å band of NiCl.

State	Constants	New values	Values reported by previous workers (Rao and Rao 1969)
$\beta^2\Delta_{5/2}$	B'_0	$0{\cdot}15575\,(\pm 21)\,cm^{-1}$	—
	D'_0	$1{\cdot}638 \times 10^{-7}\,cm^{-1}$	—
	r'_0	$2{\cdot}2293\,(\pm 15)$ Å	—
	I'_0	$179{\cdot}65\,(\pm 24) \times 10^{-40}\,gcm^2$	—
$X_1{}^2\Delta_{5/2}$	B''_0	$0{\cdot}16712\,(\pm 23)\,cm^{-1}$	$0{\cdot}167\,cm^{-1}$
	D''_0	$1{\cdot}607 \times 10^{-7}\,cm^{-1}$	$2{\cdot}0 \times 10^{-7}\,cm^{-1}$
	r''_0	$2{\cdot}1521\,(\pm 15)$ Å	2·137 Å
	I''_0	$167{\cdot}43\,(\pm 23) \times 10^{-40}\,gcm^2$	$167{\cdot}56 \times 10^{-40}\,gcm^2$
	ν_0	$= 27282{\cdot}81\,cm^{-1}$	

CC-0. In Public Domain. Gurukul Kangri Collection, Haridwar

Digitized by Arya Samaj Foundation Chennai and eGangotri

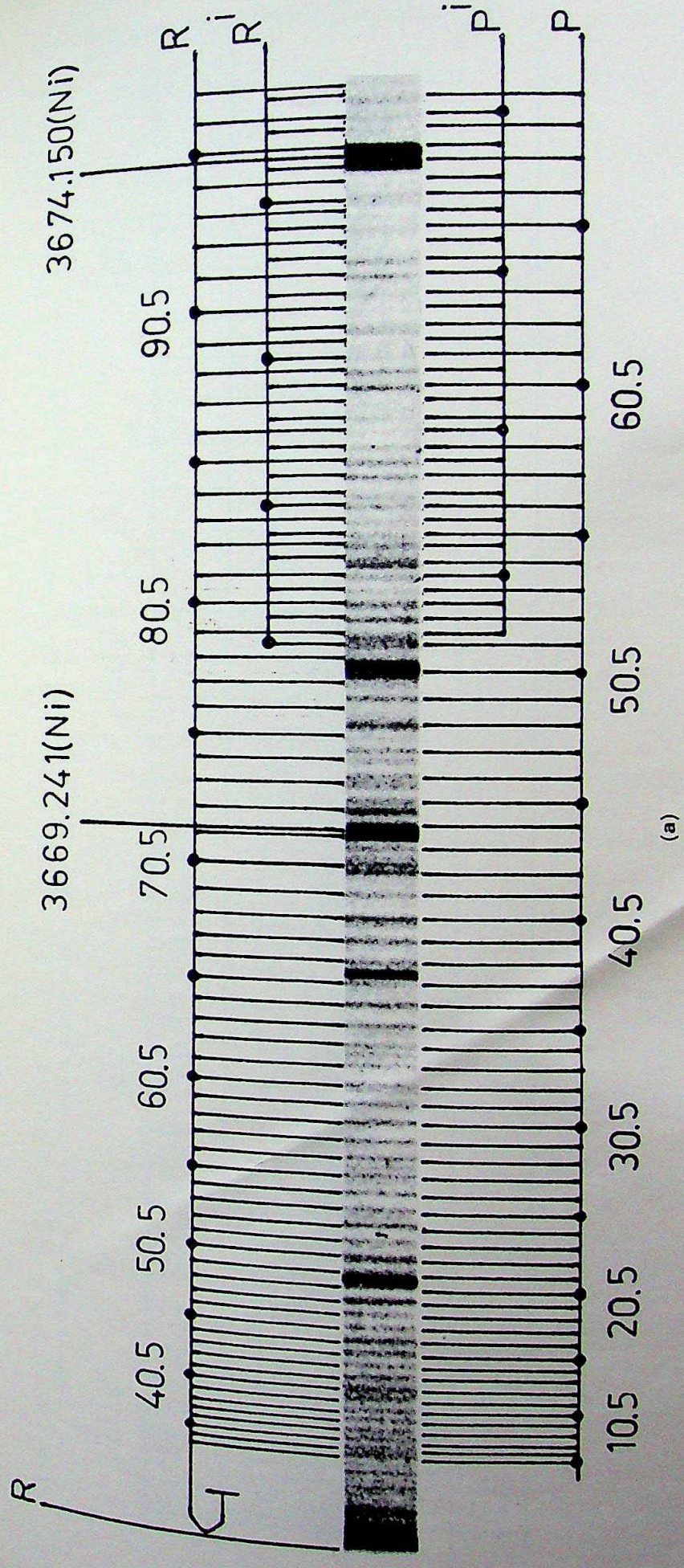

CC-0. In Public Domain. Gurukul Kangri Collection, Haridwar

Digitized by Arya Samaj Foundation Chennai and eGangotri

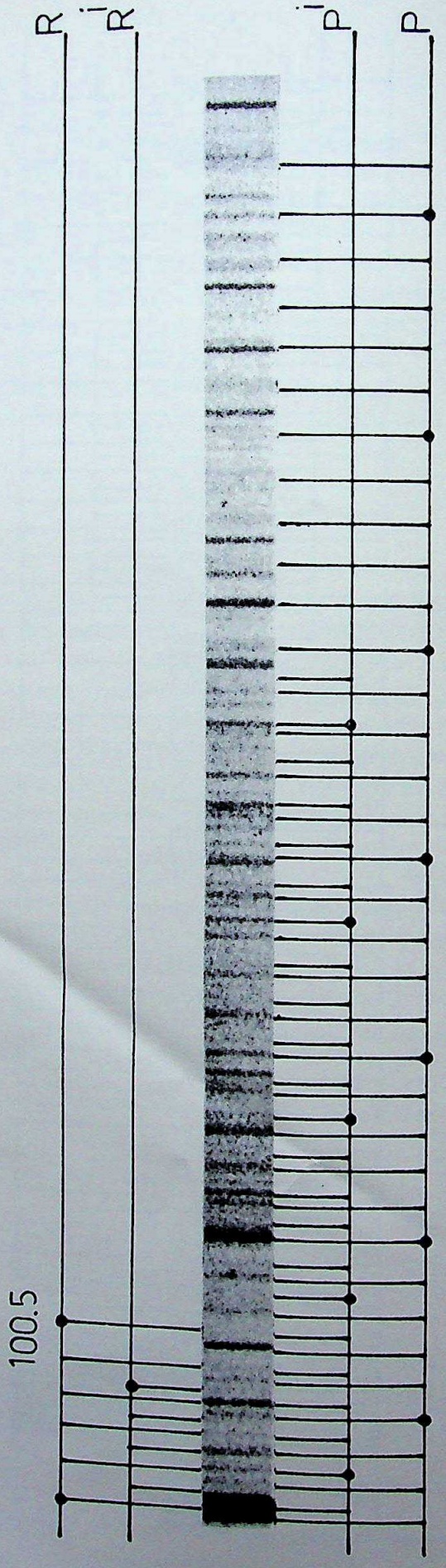

Figure 1a and b. Rotational structure of 3664 Å band of NiCl at 0·59 Å/mm.

CC-0. In Public Domain. Gurukul Kangri Collection, Haridwar

Digitized by Arya Samaj Foundation Chennai and eGangotri

Table 2. Data on the 3664 Å band of NiCl (cm^{-1}).

$J-\frac{1}{2}$	$R(J)$	$P(J)$	$R(J)^i$	$P(J)^i$
1	2	3	4	5
10		27277·80		
11		77·12		
12		76·59		
13		75·94		
14		75·32		
15		74·56		
16		74·03		
17		73·24		
18		72·52		
19		71·79		
20		70·99		
21		70·15		
22		69·45		
23		68·54		
24		67·67		
25		66·67		
26		65·86		
27		64·88		
28		63·93		
29		62·95		
30		61·99		
31		60·94		
32		59·88		
33	27280·29	58·87		
34	79·83	57·74		
35	79·34	56·72		
36	78·80	55·53		
37	78·36	54·41		
38	77·75	53·23		
39	77·12	52·06		
40	76·59	50·84		
41	75·94	49·57		
42	75·32	48·34		
43	74·63	46·99		
44	74·03	—*		
45	73·24	44·36		
46	72·52	43·13		
47	71·79	41·65		
48	70·99	40·28		
49	70·15	38·85		
50	69·45	—*		
51	68·54	35·91		
52	67·67	34·57		
53	66·77	33·02		
54	65·86	31·56	27234·85	
55	64·88	29·89	33·95	
56	63·93	28·37	32·19	
57	62·95	26·74	30·73	
58	61·99	25·16	29·25	
59	60·94	23·53	27·55	
60	59·88	21·88	25·98	
			24·32	

(*continued*)

CC-0. In Public Domain. Gurukul Kangri Collection, Haridwar

Digitized by Arya Samaj Foundation Chennai and eGangotri

Table 2. (*continued*)

$J-\frac{1}{2}$	$R(J)$	$P(J)$	$R(J)^i$	$P(J)^i$
1	2	3	4	5
61	58·87	20·17		22·38
62	57·74	18·54		20·62
63	56·72	16·89		18·85
64	55·53	14·96		17·23
65	54·41	13·31		15·42
66	53·23	11·42		13·75
67	52·06	—*		12·02
68	50·84	07·96		10·32
69	49·57	06·02		—*
70	48·23	04·06		06·72
71	—*	02·11		04·77
72	45·59	200·16		02·95
73	43·96	197·92		200·91
74	42·83	96·22		199·07
75	41·16	93·90		96·85
76	39·98	92·16		95·40
77	38·31	89·86		93·07
78	—*	88·00		91·38
79	35·40	85·67		89·14
80	33·70	83·55	27235·91	87·08
81	32·19	81·39	34·08	85·21
82	30·73	79·15	33·05	82·88
83	29·12	79·97	31·23	80·47
84	27·47	74·72	29·75	78·40
85	25·82	72·56	27·96	76·49
86	24·12	70·27	26·74	74·09
87	22·46	67·96	24·82	72·08
88	20·70	65·59	23·25	69·62
89	18·95	63·26	21·88	67·36
90	17·32	61·01	20·17	65·23
91	15·42	58·49	18·34	
92	13·85	56·36	18·34	
93	12·02	53·80	14·96	
94	10·45	51·67	13·48	
95	08·50	49·18	11·72	
96	06·72	46·80	09·60	
97	04·77	44·74	07·96	
98	02·95	41·83	05·68	
99	100·91	39·18	04·26	
100	99·07	36·80	02·31	

*Superposed by atomic line.

References

Darji A B and Suresh Kumar M B 1990 *Indian J. Pure Appl. Phys.* (in Press)
Darji A B and Shah N R 1980 *Indian J. Pure Appl. Phys.* **18** 802
Gopal R 1981 *Curr. Sci.* **50** 584
Gopal R and Joshi M M 1981 *Indian J. Phys.* **B55** 368
Gopal R and Joshi M M 1982 *Indian J. Pure Appl. Phys.* **20** 280
Gopal R and Joshi M M 1983 *Indian J. Pure Appl. Phys.* **21** 595

CC-0. In Public Domain. Gurukul Kangri Collection, Haridwar

Digitized by Arya Samaj Foundation Chennai and eGangotri

Herzbrg G 1950 *Molecular spectra and molecular structure spectra of diatomic molecule* (New York: Van Nostrand) Vol 1
Krishnamurthy V G 1952 *Indian J. Phys.* **26** 207
More K R 1938 *Phys. Rev.* **54** 122
Rao S V, Reddy S P and Rao P T 1962 *Z. Phys.* **166** 261
Rao N V K and Rao P T 1969 *Curr. Sci.* **38** 589
Reddy S P and Rao P T 1960 *Proc. Phys.* (*London*) **75** 275
Shah P M, Darji A B and Shah N R 1983 *Indian J. Pure Appl. Phys.* **21** 617
Youngner P and Winans J G 1960 *J. Mol. Spectrosc.* **4** 23

CC-0. In Public Domain. Gurukul Kangri Collection, Haridwar

Digitized by Arya Samaj Foundation Chennai and eGangotri

CC-0. In Public Domain. Gurukul Kangri Collection, Haridwar

Digitized by Arya Samaj Foundation Chennai and eGangotri

Pramana – J. Phys., Vol. 34, No. 3, March 1990, pp. 173–182. © Printed in India.

[illegible]

Triad of homogeneous and inhomogeneous three particle Lippmann–Schwinger equations

SUPROKASH MUKHERJEE
Saha Institute of Nuclear Physics, Calcutta 700 009, India

MS received 2 May 1988; revised 29 September 1989

Abstract. A general distribution theoretic treatment of the convergence of sequences involving wave functions show that the problem of non-uniqueness does not exist for the solutions of the Lippmann–Schwinger equation for multichannel scattering, in the eigenfunction space.

Keywords. Scattering theory; Lippmann–Schwinger equation; non-uniqueness problem in multi channel scattering.

PACS Nos 25·10; 2140

1. Introduction

It was shown (Mukherjee 1978, 1981 a, b, c; 1982) that the solution $\Psi_\alpha(E_\alpha + io) >$ of Lippmann–Schwinger (LS) equation for multichannel scattering, at an energy E_α, is unique. The analysis used, however, was not rigorous and a few authors (Adhikari 1980; Adhikari and Glockle 1980; Levin and Sandhas 1984; Gerjuoy and Adhikari 1984; 1985) tried to counter these arguments, but their criticisms being just as poor, not much was actually achieved either way.

In §2 we discuss a higher level of rigour, using either L_2-theory of scattering for wave packets or distribution theoretic treatments for energy eigenfunctions. An attempt is made to show that some of the results, which are actually valid only in L_2-theory of scattering are taken to be valid in spaces other than L_2 and that these have led to some of the popular misunderstanding of some of the results of scattering theory. In the end we show that most of the results derived by Mukherjee (1978, 1981a, b, c; 1982) heuristically earlier remains valid if interpreted properly, using the distribution theoretic analysis.

2. Results of distribution theoretic limits

We discuss here the sense in which the equations of multichannel scattering like (see eqs A(12)–A(20) of Appendix)

$$|\Psi_\alpha^{\pm}(E_\alpha)\rangle = |\phi_\alpha(E_\alpha)\rangle + G_\alpha(E_\alpha \pm io)\bar{V}_\alpha|\Psi_\alpha \pm (E_\alpha)\rangle \tag{1}$$

are valid, where the channel wave functions $|\phi_\alpha(E_\alpha)\rangle$ is an improper state and also

CC-0. In Public Domain. Gurukul Kangri Collection, Haridwar

Digitized by Arya Samaj Foundation Chennai and eGangotri

the sense in which the limit $\varepsilon \to 0$ is performed on vector sequence like

$$|\psi_\alpha^{\pm}(E_\alpha)\rangle = \lim_{\varepsilon \to 0} |\psi_\alpha(E_\alpha \pm i\varepsilon)\rangle \tag{2}$$

where

$$|\Psi_\alpha(E_\alpha \pm i\varepsilon)\rangle = \pm i\varepsilon G(E_\alpha \pm i\varepsilon)|\phi_\alpha(E_\alpha)\rangle. \tag{3}$$

It must be noticed that strong or weak limits of vector sequences are useful and well defined concepts in normed spaces (e.g. Hilbert space); but these theories cannot be applied to evaluate limits of vector sequence as in (2), for $|\phi_\alpha(E_\alpha)\rangle$ of (3) is an improper state vector and hence not normalizable. Formal algebraic manipulation of (3) yields (eq. A(13)):

$$|\Psi_\alpha(E_\alpha \pm i\varepsilon)\rangle = |\phi_\alpha(E_\alpha)\rangle + G_\alpha(E_\alpha \pm i\varepsilon)\bar{V}_\alpha|\Psi_\alpha(E_\alpha \pm i\varepsilon)\rangle \tag{4}$$

but passing from (4) to (1) as limit $\varepsilon \to 0$ is not at all straight forward when the vector sequences (2) are not members of Hilbert space. The question, therefore, arises as to the meaning one can assign to the multichannel Lippmann–Schwinger eq. (1) where scattering states are defined through limits in (2) of vector sequence involving improper states, when it is noted that its counterpart in Hilbert space (i.e. LS-equation in H^1 of A(3)) exists in the sense of strong limit for a large class of potential (Reed and Simon 1979). An additional problem arises in (1) due to presence of Dirac delta functions in the momentum of spectator particles in the Green's function in (1), which necessitates the use of distribution theory for treatment of these equations. From treatment (Faddeev 1964) of three body scattering by Faddeev, one has (in the notation of Faddeev (1964))

$$\Psi_\alpha^{\pm}(k_\alpha, p_\alpha, p_\alpha^0) = \lim_{\varepsilon \to 0} \langle k_\alpha, p_\alpha | i\varepsilon G(E_\alpha + i\varepsilon)|\phi_\alpha(E_\alpha)\rangle \tag{5}$$

$$= \hat{\psi}_\alpha(k_\alpha)\delta(p_\alpha - p_\sigma^0) + \left(\frac{k_0^2}{2m_\alpha} + \frac{p_\alpha^2}{2n_\alpha} - E_\alpha\right)^{-1} \sum_\beta K_{\beta\alpha}(k_\alpha, p_\alpha, p_\alpha^0). \tag{6}$$

Here the channel state, in three body system, is $|\phi_\alpha(E_\alpha)\rangle = |\psi_\alpha\rangle|p_\alpha\rangle^0$; the Fourier component $\hat{\psi}_\alpha(k_\alpha) = \langle k_\alpha|\psi_\alpha\rangle$; k_α is the relative momentum of αth pair with reduced mass m_α binding energy-ε_α and wave function $|\psi_\alpha\rangle$, p_α^0 is the momentum of the third particle (with reduced mass n_α) from the centre of mass of the pair; $E_\alpha = -\varepsilon_\alpha + (p_\alpha^{02}/2n_\alpha)$. The singularity structure of the matrix element of Green's functions was shown by Faddeev to be of the form (§§V, IX of Faddeev (1964)):

$$\langle k_\alpha, p_\alpha|G(z)|\phi_\alpha(E_\alpha)\rangle = \langle k_\alpha, p_\alpha|G_\alpha(z) + G_0(z)\sum_\beta M_{\beta\alpha}(z)G_0(z)|\phi_\alpha(E_\alpha)\rangle$$
$$+ \langle k_\alpha, p_\alpha|\{G_0(z)\sum_{\beta\neq\alpha} t_\alpha(z) + \Sigma M_\beta(z)G_0(z)\}|\phi_\alpha(E_\alpha)\rangle \tag{7}$$

$$= \frac{1}{i\varepsilon}F_1(z) + F_2(z) \tag{8}$$

with $z = E + i\varepsilon$, and

$$\langle k_\alpha, p_\alpha|M_{\beta\alpha}(z)G_0(z)|\phi_\alpha(E_\alpha)\rangle = \frac{K_{\beta\alpha}(k_\alpha, p_\alpha, p_\alpha^0)}{Z - E_\alpha}. \tag{9}$$

CC-0. In Public Domain. Gurukul Kangri Collection, Haridwar

Digitized by Arya Samaj Foundation Chennai and eGangotri

Thus the singularity structure of the above matrix element of Green's function of $1/i\varepsilon$ type with the numerical sequence $F_1(z)$ and $F_2(z)$ as well behaved as $\varepsilon \to 0$. From A(12) and A(13) we get

$$|\Psi_\alpha(E_\alpha + i\varepsilon)\rangle = |\phi_\alpha(E_\alpha)\rangle + G_\alpha(E_\alpha + i\varepsilon)\bar{V}_\alpha[i\varepsilon G_\alpha I E_\alpha + i\varepsilon)|\phi_\alpha(E_\alpha)\rangle]. \tag{10}$$

As mentioned earlier, the matrix element $\langle k_\alpha, p_\alpha|G_\alpha(E_\alpha + i\varepsilon)\bar{V}_\alpha|k_\alpha, p_\alpha\rangle$ has Dirac delta function, in momentum of spectator particle (see §§II to IV of Faddeev (1964)), which has no meaning in L_1 or L_2 space, so that (10) can be handled rigorously from the standpoint of distribution theory only. For a wide class of potentials v_α including singular ones, suitable test functions ω of compact support in C_0^∞ (R^6) or Schwartzian space $S(R^6)$, $\langle\omega|G_\alpha(E_\alpha + io).\ \bar{V}_\alpha|k'_\alpha,\ p'_\alpha\rangle = \omega_1(k'_\alpha, p'_\alpha)$ can also be used as a test function in momentum space (see Gelfand *et al* (1966); Richtmyer (1978), Kanwal (1983)) which would be then sufficient to handle the Dirac delta function of (6) so that $\langle\omega_1(k'_\alpha, p'_\alpha)|\Psi_\alpha^\pm(k'_\alpha, p'_\alpha, p_\alpha^0\rangle$ coming from the last square bracket of (10), by virtue of (5), remain well defined for the distribution theoretic treatment. Since the finite contribution to $\langle\omega_1|i\varepsilon G(E_\alpha + i\varepsilon)|\phi_\alpha(E_\alpha)$ comes only from $F_1(7)$ of (8) as $\varepsilon \to 0$, we may rewrite the distribution theoretic limit of (2) through (10) as

$$|\Psi_\alpha(E_\alpha + io)\rangle = D\text{-}\lim_{\varepsilon\to 0} |\Psi_\alpha(E_\alpha + i\varepsilon)\rangle \tag{11}$$

$$= |\phi_\alpha(E_\alpha)\rangle + D\text{-}\lim_{\varepsilon\to 0} G_\alpha(E_\alpha + i\varepsilon)\bar{V}_\alpha \cdot D\text{-}\lim_{\varepsilon\to 0} |\Psi_\alpha(E_\alpha + io)\rangle \tag{12}$$

$$= |\phi_\alpha(E_\alpha)\rangle + G_\alpha(E_\alpha + io)\bar{V}_\alpha|\Psi_\alpha(E_\alpha + io)\rangle \tag{13}$$

where the distribution theoretic limit, denoted by D-lim, is defined in Appendix B. Clearly, the only surviving term in the numerical sequence $\langle\omega|\Psi_\alpha(E_\alpha + i\varepsilon)\rangle$ comes from $F_1(z)$ of (8), so that the limit of the product of terms on the right side of (12) reduces to the product of their respective limits, provided the limits are both taken in the distribution theoretic sense and this in turn leads to the multi channel Lippmann–Schwinger equation (13) whose validity is, therefore, established only in the distribution theoretic sense for a wide class of potentials. Further, by (3),

$$(E_\alpha - H)|\Psi_\alpha(E_\alpha \pm i\varepsilon)\rangle = \pm i\varepsilon|\phi_\alpha(E_\alpha)\rangle \tag{14}$$

since for test function, in C_0^∞ (R^6) $S(R^6)$, $\lim_{\varepsilon\to 0}\langle\omega|i\varepsilon|\phi_\alpha(E_0)\rangle = 0$, we have from (14)

$$(E_\alpha - H)|\Psi_\alpha^\pm(E_\alpha)\rangle = 0 \tag{15}$$

as distribution theoretic limit, so that the $|\Psi_\alpha^\pm(E_\alpha)\rangle$, which is the solution of the LS-equation (13) is also the distribution theoretic solution of Schrödinger equation (15) as is also seen by evaluating $\langle\omega|E_\alpha - H|\psi_\alpha^\pm(E)\rangle = 0$, as applied to eq. (13). It is in this sense the multichannel wave functions $|\Psi_\alpha^\pm(E_\alpha)\rangle$ are the eigenfunctions of the total Hamiltonian H. In single channel case, the LS-equation A(9) in eigenfunction space, is valid for Rollnick class of potentials or locally square integrable class of potentials, while in general A(9) is valid also in distribution theoretic sense for much wider class of potentials. In contrast, the multichannel LS-equation (13) is valid only in distribution theoretic sense, also for a wider class of potentials including singular ones with integrable singularities, in Schwartzian, compact or other suitable space of test functions (Kanwal 1983).

CC-0. In Public Domain. Gurukul Kangri Collection, Haridwar

Digitized by Arya Samaj Foundation Chennai and eGangotri

Since the multichannel wave function $|\Psi_\alpha^{\pm}(E_\alpha)\rangle$ is to be defined as limit $\varepsilon \to 0$ of (2) in the distribution theoretic sense we should make similar treatment to different terms of equation (A14):

$$|\Psi_\alpha(E_\alpha \pm i\varepsilon)\rangle = i\varepsilon G_\beta(E_\alpha \pm i_\varepsilon)|\phi_\alpha(E_\alpha)\rangle + G_\beta(E_\alpha \pm i\varepsilon)\bar{V}_\beta|\Psi_\alpha(E_\alpha \pm i\varepsilon)\rangle. \tag{16}$$

The distribution theoretic treatment of the first term on the right side of equation (A19) for $\varepsilon \to 0$ can be shown give a single layer surface distribution in general, instead of Kronecker delta function as appears in Lippmann's identity in A(19).

It is noted that $i\varepsilon\ G_\beta\ (E_\alpha + i\varepsilon)$, $\varepsilon \neq 0$, has ("in some sense") an infinite number of eigenstates $|\xi_\beta(E_\alpha, f)\rangle$ belonging to the eigenvalue unity and that the following holds, (in obvious notations):

$$i\varepsilon G_\beta(E + i\varepsilon)|\xi_\beta(E,f)\rangle = |\xi_\beta(E,f)\rangle \tag{17}$$

where (Baumgartel *et al* 1983)

$$|\xi_\beta(E,f)\rangle = p_\beta(E)|f\rangle \tag{18}$$

$$p_\beta(x) = S\text{-}\lim_{\varepsilon \to 0} \frac{1}{2\pi i}\{G_\beta(x - i\varepsilon) - G_\beta(x + i\varepsilon)\} = \delta(x - E_\beta) \tag{19}$$

where $|f\rangle$ is any vector in the Hilbert space H^1. Expanding (see Prugovecki 1981) the Green's functions in terms of the eigenfunctions $|\phi_\beta(E_\beta)\rangle$ of H_β, the vectors $|\xi_\beta(E_\beta, f)$ can be expressed, by the Radon transform (Gelfand *et al* 1966) of $|f\rangle$ over the surface $S_\beta\ (E_\beta)$ of a sphere in momentum variable k_j, where one of the degrees of freedom is frozen by the constraint (see (A7))

$$E_{\beta'} = E_\beta = \sum \frac{h^2}{2\mu_j} k_j^2 - \sum \varepsilon_j^\beta \tag{20}$$

and we have

$$|\xi_\beta(E_\beta, f)\rangle = \int |\phi_\beta(E'_\beta)\rangle\, \mathrm{d}^3k_1 a^3k_2 \cdots \delta(E'_\beta - E_\beta)\langle \phi_\beta(E'_\beta)|f\rangle \tag{21a}$$

$$= \delta(E_\beta - H_\beta)|f\rangle. \tag{21b}$$

As $|f\rangle$ runs over the Hilbert space H^1, the eigenvectors $|\xi_\beta(E_\beta, f)\rangle$ spans an infinite dimensional linear manifold $M_\beta(E_\beta)$ (of codimension $(n-1)$ in momentum space, being constrained by (23)) onto which H^1 is mapped by $p_\beta(E_\beta)$.

In distribution theory (Kanwal 1983), a single layer surface distribution $\delta(S)\, f$ is defined by the surface integral, over the surface S,

$$\langle \omega|f\rangle_S = \langle \omega|\delta(S)f\rangle = \int_S \omega f \mathrm{d}S \tag{22}$$

whenever the surface integral (22) is found to exist for all test functions ω in a suitable space, like C_0^∞ or Schwartzian. Now

$$\hat{A}_\beta(E'_\beta; \varepsilon, E_\beta, f) = \langle \phi_\beta(E'_\beta)|i\varepsilon G_\beta(E_\beta + i\varepsilon)|f\rangle$$

$$= \frac{i\varepsilon}{E_\beta + i\varepsilon - E'_\beta}\langle \phi_\beta(E'_\beta)|f\rangle \tag{23}$$

$$\underset{\varepsilon \to 0}{\to} {}^{\delta}E_\beta, E'_\beta \langle \phi_\beta(E'_\beta)|f\rangle. \tag{24}$$

CC-0. In Public Domain. Gurukul Kangri Collection, Haridwar

Digitized by Arya Samaj Foundation Chennai and eGangotri

In a straightforward way we have the following (using $\hat{f}=\langle\phi_\beta(E_\beta)|f\rangle$, $\hat{\omega}=\langle\phi_\beta(E_\beta)|\omega\rangle$):

$$I_\beta(E_\beta,\omega,f)=\lim_{\varepsilon\to 0}\langle\xi_\beta(E_\beta,\omega)|i\varepsilon G_\beta(E_\beta+i\varepsilon)|f\rangle \tag{25}$$

$$=\lim_{\varepsilon\to 0}\int\langle\omega|\phi_\beta(E'_\beta)d^3k_1^1a^3k_2^1\cdots\delta(E'_\beta-E_\beta)\hat{A}_\beta(E'_\beta,\varepsilon,E_\beta,f)\rangle \tag{26}$$

$$=\lim_{\varepsilon\to 0}\int_{S_\beta(E_\beta)}\langle\omega|\phi_\beta(E'_\beta)\rangle a^3k_1^1a^3k_2^1\cdots\hat{A}_\beta\,(E_\beta;\varepsilon,E_\beta,f) \tag{27}$$

$$=\langle\hat{\omega}|\hat{A}_\beta(\quad;\varepsilon,E_\beta,f)\rangle_{S_\beta(E_\beta)} \tag{28}$$

$$=\langle\hat{\omega}|\hat{f}\rangle_{S_\beta(E_\beta)}. \tag{29}$$

The surface integrals in (25)–(29) are over a surface $S_\beta\,(E)$ of a $(n-1)$ sphere in momentum variables, constrained by $\sum(k^2/(2m))=E_\beta+\sum\varepsilon^\alpha$, correspond to a restriction mapping of $L_2(R^n,n)$. Although $M(R^n,n-1)$ has a Lebesgue measure zero in $L_2(R^n,n)$, it does not imply that the above surface integrals in $M(R^n,n-1)$ are zero. In fact, for the non-trivial existence of the single layer surface distribution, it is enough that the surface integrals in (25)–(29) exist for all test functions ω or $\hat{\omega}$ in suitable test space. Further, the above discussion can clearly be repeated for $|f\rangle$ replaced by $|\phi_\alpha(E_\alpha)\rangle$, when ω or $\hat{\omega}$ is taken to belong to suitable class of test functions for which the above surface integrals in (25)–(29) exist; we get from (28)–(29), for

$$E_\beta=E_\alpha,\ \langle\hat{\omega}|\hat{A}_\beta(\quad;\varepsilon,E_\beta,\phi_\alpha(E_\alpha))_{S_\beta(E_\beta)}$$
$$=\langle\hat{\omega}|\phi_\alpha(E_\alpha)\rangle_{S_\beta(E)_\alpha} \tag{30}$$

so that we may write, (by B(1)–B(3) and (22))

$$D\text{-}\lim_{\varepsilon\to 0}i\varepsilon G_\beta(E_\alpha+i_\varepsilon)|\phi_\alpha(E_\alpha)\rangle=\delta(S_\beta(E_\alpha))|\phi_\alpha(E_\alpha)\rangle \tag{31}$$

From (16) we then have, in distribution theoretic limit,

$$|\Psi_\alpha^\pm(E_\alpha)\rangle=\delta(S_\beta(E_\alpha))|\phi_\alpha(E_\alpha)\rangle+G_\beta(E_\alpha\pm io)\bar{V}_\beta|\Psi_\alpha^\pm(E_\alpha)\rangle. \tag{32}$$

The single layer surface distribution of (31) on the surface $S_\beta(E_\alpha)$ correspond to the projection operator $P_{\beta\alpha}(E_\alpha)$ of (A20) obtained heuristically earlier and it shows also that the limit $\omega\to 0$ in (A20) is to be taken only in the distribution theoretic sense to arrive at the correct result. The result in (31) is distinctly different from the Kronecker delta function of Lippmann's identity. The point is that for the non-trivial existence of the surface integral and equation (30), it is enough to have $E_\beta=E_\alpha$, which will of course be true for $\beta=\alpha$, but E_β may be equal to E_α (see (A7)) even when $\beta\neq\alpha$. This in turn means that (30) or the surface distribution (31) does not yield a Kronecker delta (e.g. ${}^\delta\beta\alpha$ as in (A19)), but behaves more like ${}^\delta E_\beta$, E_α instead, as in (24) and this makes a lot of difference in the context of the non-uniqueness problem in multichannel scattering theory. The $P_{\beta\alpha}\,(E_\alpha)$ of the heuristic treatment in A(20) also point in the same direction. It implies, as emphasised earlier, that equation (A21) or (32) above is no longer a homogeneous equation for $\beta\neq\alpha$ as in (A18), and hence there is no problem of non-uniqueness in the solution of multichannel Lippmann–Schwinger equation in the eigenfunction space, for a three body scattering problem. The above result is

CC-0. In Public Domain. Gurukul Kangri Collection, Haridwar

Digitized by Arya Samaj Foundation Chennai and eGangotri

easily extended to many body multichannel scattering and one can similarly conclude that the Lippmann–Schwinger equation in many particle multichannel scattering problem is valid in the sense of distribution theory, and there is no problem of non-uniqueness of its solution as envisaged earlier.

Appendix A

In this appendix we quote without proof a few results of non-relativistic scattering theory for ready reference for our discussion.

In the Hilbert space theory of multichannel scattering, the channel scattering states $|f_{\pm}^{\alpha}\rangle$ are given by (see Prugovecki 1981; Reed and Simon 1979) the following strong limits:

$$|f_{\pm}^{\alpha}\rangle = S\text{-}\lim \Omega_{\pm}^{\alpha}(\varepsilon)E_{m_{\pm}^{\alpha}}|f\rangle = \underset{\varepsilon\to 0}{S\text{-}\lim} \pm i\varepsilon \int \exp(\pm\varepsilon\tau)\exp(iHt)$$

$$\times \exp(iH_{\alpha}t)E_{M_{\pm}^{\alpha}}|f\rangle \,dt \tag{A1}$$

$$= \underset{\varepsilon\to 0^{+}}{S\text{-}\lim} \pm i\varepsilon \int_{-\infty}^{+\infty} G(\lambda+i\varepsilon)d_{\lambda}(\varepsilon_{H_{\alpha}}(\lambda))E_{M_{\pm}^{\alpha}}|f\rangle \tag{A2}$$

$$|f_{\pm}^{\alpha}\rangle = E_{M_{\pm}^{\alpha}}|f\rangle + S\text{-}\lim \int_{-\infty}^{+\infty} G_{\alpha}(\lambda+i\varepsilon)(H-H_{\alpha})d_{\lambda}(\varepsilon_{H}(\lambda))|f_{\pm}^{\alpha}\rangle. \tag{A3}$$

In (A1)–(A3), $H = H_{\alpha} + \bar{V}_{\alpha} = H_0 + V$; $V = V_{\alpha} + \bar{V}_{\alpha} = V_{\beta} + \bar{V}_{\beta}$ where H_0 and V are total kinetic and potential energy operators, respectively; $H_{\alpha} = H_0 + V_{\alpha}$ = Hamiltonian for the α-channel with its potential V_{α}; the α-channel Green's function is $G = (Z - H_{\alpha})^{-1}$; $G(Z) = (Z-H)^{-1}$; $E_{M_{\pm}^{\alpha}}$ is the projection operator on to the subspace M of Hilbert space H^1 consisting only of those vectors for which the strong limits in (A1)–(A3) exist; $\varepsilon_H(\lambda)$ and $\varepsilon_{H_{\alpha}}(\lambda)$ are, respectively, the spectral projection operators for the Hamiltonian H and H_{α} giving rise to the Bochner integrals in (A1)–(A3). The equation (A3) is the Lippmann–Schwinger (LS) equation in the Hilbert space H^1, and both the range and the domain space of the scattering operator $\Omega_{\pm}^{\alpha}(\varepsilon)$ are Hilbert spaces (Reed and Simon 1979). This implies that $|f\rangle$ cannot be replaced by the channel state $|\Phi_{\alpha}(E_{\alpha})\rangle$ the eigenstate of H_{α}, for the subspace $M_{\pm}^{\alpha}$ is a Hilbert space and $\phi_{\alpha}(E_{\alpha})$ is not normalizable as H_{α} contains the kinetic energy operators for the free propagations of the centre of mass motions of bound group of particles forming clusters constituting the channel α:

$$E_{\alpha}|\phi_{\alpha}(E_{\alpha})\rangle = H_{\alpha}|\phi_{\alpha}(E_{\alpha})\rangle = (H_0 + V_{\alpha})|\phi_{\alpha}(E_{\alpha})\rangle \tag{A4}$$

$$= \sum_{i=1}^{n_{\alpha}} \left\{ T_i + \sum_{j=1}^{n_{\alpha}} h_j^{\alpha} \right\} |\Phi_{\alpha}(E_{\alpha})\rangle. \tag{A5}$$

Here α-channel is formed from a group of η_{α}-clusters, with internal Hamiltonian $h_j^{\alpha}(j = 1, z, \ldots, n_{\alpha})$ with its eigenfunction χ_j^{α} and internal energy $-\varepsilon_j^{\alpha}$, with T_i as the kinetic energy operator of centre of mass motion of the i *th* group of bound particles moving with momentum $\hbar\vec{k}_i$. In obvious notation, the following may be written:

$$|\Phi_{\alpha}(E_{\alpha})\rangle = \prod_{j=1}^{n_{\alpha}} |\chi_j^{\alpha}\rangle \prod_{j-1}^{n_{\alpha}} |k_j\rangle \tag{A6}$$

CC-0. In Public Domain. Gurukul Kangri Collection, Haridwar

Digitized by Arya Samaj Foundation Chennai and eGangotri

$$E_\alpha = -\sum \varepsilon_j^\alpha + \sum \frac{\hbar^2}{2\mu_j} k_j^2 \tag{A7}$$

$$T_i|\vec{k}_i\rangle = \frac{\hbar^2}{2\mu_i}|\vec{k}_i\rangle; \quad h_j^\alpha|\chi_j^\alpha\rangle = -\varepsilon_j^\alpha|\chi_j^\alpha\rangle. \tag{A8}$$

Since $|\phi_\alpha(E_\alpha)\rangle$ of (6) contains the non-normalizable improper states (plane wave, $|\vec{k}_i\rangle$), it cannot be used for $|f\rangle$ in (1)–(3), as strong limits are defined for normalizable states only. The LS-equation (3) in L_2-space and its single channel version, is known to exist for a wide class of potential (Reed and Simon 1979).

Side by side with the LS-equation in L_2-space, we have the old familiar (Schiff 1968) LS-equation for the scattering states $\Psi^\pm(k, r; E)$, in single-channel case:

$$\Psi^\pm(k, r; E) = \phi(k, r; E) + \int G_0^\pm(r, r'; E) V(r') \Psi^\pm(k, r', E)\, \mathrm{d}^3 r'. \tag{A9}$$

The space where (A9) is valid is not a L_2 space and here the unperturbed state $\phi(k, r; E)$ and the scattering state $\Psi^\pm(k, r; E)$ are not L_2 objects and (in some sense) also the eigenstates of H_0 and H, respectively, for the energy eigenvalue $E = (h^2k^2/2m)$, written formally as

$$(H_0 - E)\phi(k, r; E) = 0 \tag{A10}$$

$$(H - E)\Psi^\pm(k, r; E) = 0 \tag{A11}$$

corresponding to the absolutely continuous part of the spectrum of the Hamiltonians. Such functions $\Psi_\pm(k, r; E)$ from eigenfunction space which is not a L_2 space. The solution $\Psi_\pm(k, r; E)$ of (A9) is also a solution of the Schrödinger equation (A11) in classical function theoretic sense, only for a very restricted class of potentials. For wide class of potentials, the solution of the LS-equation (A9) is also a solution of the Schrödinger equation (A11) in the distribution theoretic sense only (see Reed and Simon 1979). In the single channel version of (A3) in two body L_2 theory of scattering, the LS-equation is

$$|f_\pm\rangle = E_m|f\rangle + S\text{-}\lim_{\varepsilon \to 0^+} \left\{ \int_{-\infty}^{+\infty} G_0(\lambda + i\varepsilon)(H - H_0) d_\lambda(\varepsilon_H(\lambda)) \right\} |f_\pm\rangle. \tag{A3'}$$

It is shown by Prugovecki (1981) that only for a restricted class of potential the LS-equation (A3′) in Hilbert space for single channel case leads to the existence of LS-equation (A9) in the eigenfunction space of the Hamiltonian H for the absolutely continuous part of its spectrum. But it may be emphasised that, in single channel case the LS-equation (A3′) and (A9) exist independently of each other, under a very general condition and that (A9) does not have to exist if and when the single channel version (A3′) in L_2 space does.

The situation in multichannel case is, however, more complicated, because the analysis of single channel case cannot be carried over verbatim in multichannel case and hence the equations corresponding to (A9) for multichannel case is not obtainable from (A3), for condition on potential only.

However, in the heuristic treatment of three body scattering theory (Sandhas 1976; Levin 1984), one writes for scattering wave function ($\alpha \neq \beta \neq \gamma \neq 0$):

$$|\Psi_\alpha(E_\alpha \pm i\varepsilon)\rangle = \pm i\varepsilon G(E_\alpha \pm i\varepsilon)|\phi_\alpha(E_\alpha)\rangle \tag{A12}$$

CC-0. In Public Domain. Gurukul Kangri Collection, Haridwar

Digitized by Arya Samaj Foundation Chennai and eGangotri

$$|\Psi_\alpha(E_\alpha \pm i\varepsilon)\rangle = |\phi_\alpha(E_\alpha)\rangle + G_\alpha(E_\alpha \pm i\varepsilon)\bar{V}_\alpha|\Psi_\alpha(E_\alpha \pm i\varepsilon)\rangle \tag{A13}$$

$$|\Psi_\alpha(E_\alpha \pm i\varepsilon)\rangle = \pm i\varepsilon G_\beta(E_\alpha \pm i\varepsilon)|\phi_\alpha(E_\alpha)\rangle + G_\beta(E_\alpha \pm i\varepsilon)\bar{V}_\beta|\Psi_\alpha(E_\alpha \pm i\varepsilon)\rangle \tag{A14}$$

where the total wave function, defined by

$$|\Psi_\alpha^{\pm}(E_\alpha)\rangle = \lim_{\varepsilon \to 0} |\Psi_\alpha(E_\alpha \pm i\varepsilon)\rangle \tag{A15}$$

is considered (in some sense) to be the eigenfunction of the total Hamiltonian H:

$$(E_\alpha - H)|\Psi_\alpha^{\pm}(E_\alpha)\rangle = 0 \tag{A16}$$

with outgoing (+) or incoming (−) wave boundary condition. The limits performed formaly in A(12)–(A14) one writes (Sandhas 1976; Levin 1984):

$$|\Psi_\alpha^{\pm}(E_\alpha)\rangle = |\phi_\alpha(E_\alpha)\rangle + G_\alpha(E_\alpha \pm io)\bar{V}_\alpha|\Psi_\alpha^{\pm}(E_\alpha)\rangle \tag{A17}$$

$$|\Psi_\alpha^{\pm}(E_\alpha)\rangle = \delta_{\alpha\beta}\,|\phi_\alpha(E_\alpha)\rangle + G_\beta(E_\alpha \pm io)\bar{V}_\beta|\Psi_\alpha^{\pm}(E_\alpha)\rangle \tag{A18}$$

where one uses the "Lippmann's Identity" given by

$$\lim_{\eta \to 0} |A_\beta(\eta, E_\alpha, \phi_\alpha(E_\alpha)) = \lim_{\eta \to 0} i\eta G_\beta(E_\alpha + i\eta)|\phi_\alpha(E_\alpha)\rangle$$

$$= \delta_{\alpha\beta}|\phi_\alpha(E_\alpha)\rangle. \tag{A19}$$

The simultaneous existence of the triad of inhomogeneous equation (A17), for $\alpha, \beta, \gamma \neq 0$, along with the homogeneous equation (A18) (for $\alpha \neq \beta$), precipitate the solution of LS-equation (A17). This is because, from any solution of the inhomogeneous equation one can obtain infinity of other solution by adding an arbitrary linear combination of the solutions of homogeneous equation. It was shown (Mukherjee 1981a) that the root cause of this non-uniqueness problem is the use of Lippmann's identity (A19) and that the correct evaluation of the limit in (A19) gives, instead of the crucial Kronecker delta function $\delta_{\alpha\beta}$ of (A19), a projection operator $P_{\beta\alpha}(E)$ defined by

$$\lim_{\eta \to 0} i\eta G_\beta(E_\alpha + i\eta)|\phi_\alpha(E_\alpha)\rangle = P_{\beta\alpha}(E_\alpha)|\phi_\alpha(E_\alpha)\rangle$$

$$= \lim_{\eta \to 0} \int_{E_\alpha - \eta}^{E_\alpha + i\eta} |\phi_\beta(E)\rangle\, d\rho(E)\, \langle \phi_\beta(E)|\phi_\alpha(E_\alpha)\rangle. \tag{A20}$$

It can be shown that $P_{\beta\alpha}(E_\alpha) = 1$ when $\alpha = \beta$, and for $\alpha \neq \beta$, $P_{\beta\alpha}(E_\alpha)$ is non zero in a suitable hyperspace so that instead of (A18) one gets

$$|\Psi_\alpha^{\pm}(E_\alpha)\rangle = P_{\beta\alpha}(E_\alpha)|\phi_\alpha(E_\alpha)\rangle + G_\beta(E_\alpha + io)\bar{V}_\beta|\Psi_\alpha^{\pm}(E_\alpha)\rangle. \tag{A21}$$

Since $P_{\beta\alpha}(E_\alpha)$ is a projection operator, and does not behave like Kronecker delta function $\delta_{\alpha\beta}$, (A21) does not reduce to a homogeneous equation for $\alpha \neq \beta$, so that we no longer have simultaneous existence of homogeneous and inhomogeneous equation and, with that, have no longer the problem of non-uniqueness of the solution of LS-equation (A17). It should further be noted that there is no problem of non-uniqueness in the complex energy plane, for (A12) to (A14) are trivially equal to each

CC-0. In Public Domain. Gurukul Kangri Collection, Haridwar

Digitized by Arya Samaj Foundation Chennai and eGangotri

other for $\varepsilon \neq 0$, and they do not even form a set of independent equations, being one equation written in three different forms only. It can be shown that our equation (21) merely assures that the same is true for (A12)–(A14) in the limit $\varepsilon \to 0+$. But if one uses the Lippmann's identity in the limit of $\varepsilon \to 0$ it changes the situation completely by giving rise to independent triad (A17) and (A18) giving rise to the above mentioned non-uniqueness problem. One can give other examples of problems created by use of Lippmann's identity, like appearance of spurious solutions of Weinberg's equation of scattering and similar other equations (Glockle 1973), and it can be shown in a similar way that these spurious solutions do not appear when the projection operator $P_{\beta\alpha}(E_\alpha)$ is used instead of the Kronecker delta $\delta_{\alpha\beta}$ in Lippmann's identity.

Appendix B

The distribution theoretic limit of a vector sequence, defined as

$$D\text{-}\lim_{\varepsilon \to 0} |f(\varepsilon)\rangle = |f\rangle \tag{B1}$$

is said to exist (see Gelfand *et al* 1966; Kanwal 1983) when one or both of the two following equalities exist

$$\langle \omega | D\text{-}\lim_{\varepsilon \to 0} |f(\varepsilon)\rangle = \lim_{\varepsilon \to 0} \langle \omega | f(\varepsilon)\rangle = \langle \omega | f\rangle \tag{B2}$$

or

$$\lim_{\varepsilon \to 0} \langle \hat{\omega} | f(\varepsilon)\rangle = \lim_{\varepsilon \to 0} \langle \hat{\omega} | f(\varepsilon)\rangle = \langle \omega | \hat{f}\rangle = \langle \hat{\omega} | f\rangle \tag{B3}$$

and equation (B2) and/or (B3) exist for all test functions or their Fourier transform $\hat{\omega}$, in a suitable space of test functions like $S(R^n)$ or $C_0^\infty(R^n)$ or on some of their submanifolds The distribution theoretic $|A\rangle = |B\rangle$ means $\langle \omega | A\rangle = \langle \omega | B\rangle$ for all such ω in a test space.

Let $f(z)$, with $z = \mathrm{d}/\mathrm{d}x$, is a function of differential operator giving rise to the differential equation

$$\left\{ E - f\left(\frac{\mathrm{d}}{\mathrm{d}x}\right) \right\} |Y\rangle = 0 \tag{B4}$$

subject to some boundary condition. Then $|\psi\rangle$ is said to be the distributional solution of the differential equation (B4), when

$$\left\langle \omega \middle| \left(E - f\left(-\frac{\mathrm{d}}{\mathrm{d}x} \right) \right) \middle| \psi \right\rangle = 0 \tag{B5}$$

for all test function ω in a suitable space like compact space $C_0^\infty(R)$ or Schwartzian space $S(R^2)$ etc. There are interesting situations when the distributional solution, of equation (B5) exist when the classical solution, of equation (B4) does not exist.

References

Adhikari S K 1980 *Phys. Lett.* **A95** 21
Adhikari S K and Glockle W 1980 *Phys. Rev.* **C21** 54

CC-0. In Public Domain. Gurukul Kangri Collection, Haridwar

Digitized by Arya Samaj Foundation Chennai and eGangotri

Baumgartel H and Wollenberg M 1983 *Mathematical Scattering Theory*, Birkhawser Verlag
Faddeev L D 1964 *Mathematical Problems of Quantum Theory of Scattering for Three Particle System*, Translated by J B Sykes AERE Harwell Berkshire UK
Gerjuoy E and Adhikari S K 1984 *Phys. Lett.* **A105** 203
Gerjuoy E and Adhikari S K 1985 *Phys. Rev.* **A31** 2005
Gelfand I M, Graev M I and Vilenkin N Ya 1966 *Generalise function* (New York: Academic Press) Vol 5
Kanwal R P 1983 *Generalised Function* (New York: Academic Press)
Levin F S and Sandhas W 1984 *Phys. Rev.* **C29** 1617
Mukherjee S 1978 *Phys. Lett.* **B80** 73
Mukherjee S 1981a *Phys. Lett.* **A81** 207
Mukherjee S 1981b *Phys. Lett.* **A83** 1
Mukherjee S 1981c *Pramana – J. Phys.* **16** 81
Mukherjee S 1982 *Pramana – J. Phys.* **18** 495
Prugovecki E 1981 *Quantum Mechanics in Hilbert Space* 2nd ed. (New York: Academic Press)
Reed M and Simon B 1979 *Methods of Modern Mathematical Physics* (Academic Press) Vol III
Richtmyer R D 1978 *Principles of Advanced Mathematical Physics* (Berlin: Springer Verlag) Vols I and II
Sandhas W 1976 *Few body dynamics* (Ed.) A N Mitra (North Holland)
Schiff L I 1968 *Quantum Mechanics* (New York: McGraw Hill)

CC-0. In Public Domain. Gurukul Kangri Collection, Haridwar

Digitized by Arya Samaj Foundation Chennai and eGangotri

Pramāṇa – J. Phys., Vol. 34, No. 3, March 1990, pp. 183–192. © Printed in India.

Stability of the S matrix pole

G RAJASEKARAN* and S S VASAN

*Tata Institute of Fundamental Research, Homi Bhabha Road, Bombay 400 005, India
*On leave of absence from the Institute of Mathematical Sciences, Madras 600 013, India
Department of Theoretical Physics, University of Madras, Guindy Campus, Madras 600025, India

MS received 5 June 1989; revised 4 December 1989

Abstract. We show how the position and residue of the S matrix pole can remain stable under changes in the form of the parametrization of the S matrix elements. We also derive a relation among the shifts in the Breit–Wigner resonance parameters under the same changes and verify the relation numerically for the case of $\Delta(1232)$. Despite its stability, the pole does not provide a unique definition of the resonance because of the existence of shadow poles.

Keywords: Scattering theory; S matrix; resonance poles; Δ (1232) resonance; Breit–Wigner formula; shadow poles.

PACS Nos 03·80; 11·20; 11·80

1. Introduction

The problem of characterizing the properties of a resonance or an unstable particle has attracted much attention in the past. This problem is particularly relevant for hadrons many of which are very short-lived and so occur as resonances with large widths. A question of practical importance is how to define the mass of the resonance and its width. There is no unique set of values for the resonance mass and width. Depending on the resonance formula used to fit the scattering amplitude, one gets different values for these parameters. Thus, for instance, in the case of $\Delta(1232)$, the best known hadronic resonance, the mass and width are found to shift by as much as 10 MeV and 40 MeV respectively, when different parametrizations or different formulae are used to describe the resonant amplitude.

Some time ago it was pointed out by Ball *et al* (1972, 1973) that the position of the pole of the scattering amplitude in the second sheet of the complex energy plane is much less dependent on the resonance formula used. To a certain extent this was found to be true for the residue at the pole also. In the example of $\Delta(1232)$, the real and imaginary parts of the pole position were in fact found to change by less than 1 MeV. This stability property of the pole is now well-known and the Particle Data Groups (Aguilar-Benitez *et al* 1986; Yost *et al* 1988) quote the real and imaginary parts of the pole (wherever known) in addition to the conventional mass and width of the hadron. This striking property of the pole of the scattering amplitude gives added support to the view that a resonance or an unstable particle must be defined by the pole of the S matrix.

Although the stability property of the pole is now well-known, so far it seems to

CC-0. In Public Domain. Gurukul Kangri Collection, Haridwar

Digitized by Arya Samaj Foundation Chennai and eGangotri

be based only on empirical observation. Our purpose is to provide a theoretical foundation for it. We give a simple but general proof for the stability of the position and residue of the pole under certain conditions. Our method also allows us to obtain a relation between the shifts in the Breit–Wigner mass and width parameters. The shifts in the mass and the energy-dependent width function are found to be so correlated that the shift in the pole position is zero.

In §2, the proof of the stability of the position and residue of the S matrix pole is given, while §3 is devoted to the derivation of the relations between the shifts of the Breit–Wigner parameters. In §4, we discuss the examples of various forms of parametrization used for the case of the resonance $\Delta(1232)$ which illustrate the stability of the pole. The numerical comparison of the data with our relation between shifts of the Breit–Wigner parameters is also presented in this section. In the final section, the loss of the uniqueness of the S matrix pole because of the existence of "shadow poles" is briefly discussed.

2. Stability of the pole parameters

Let us define the T matrix in terms of the S matrix by

$$T = \frac{i}{2}(1 - S). \tag{1}$$

We consider two-body reactions in a single partial wave. Also, except in the final section where the discussion is relevant to multichannel scattering, in the rest of the paper we consider only single-channel scattering. However, the formulae will be written in such a way that they will be valid for multichannel case also. Let W be the energy in the c.m. system. If W_p is the position of a resonance pole in an unphysical sheet of the complex W plane, we may write

$$T(W) = \frac{R}{W - W_p} + C(W) \tag{2}$$

in the vicinity of the resonance. Here R is the residue matrix and $C(W)$ is the nonpole term which is finite at W_p. It is more convenient for our purposes to consider $T^{-1}(W)$ which has only a zero at W_p:

$$T^{-1}(W) = (W - W_p)\{R + (W - W_p)C\}^{-1}. \tag{3}$$

Consider now two different parametrizations $T_1(W)$ and $T_2(W)$ of the scattering amplitude given by two different formulae. Examples of such parametrizations will be given in §4. Since we may always put the amplitude in the form (2) in the neighbourhood of a resonance pole, we may write

$$T_1(W) = \frac{R_1}{W - W_{p_1}} + C_1(W)$$
$$T_2(W) = \frac{R_2}{W - W_{p_2}} + C_2(W). \tag{4}$$

CC-0. In Public Domain. Gurukul Kangri Collection, Haridwar

Digitized by Arya Samaj Foundation Chennai and eGangotri

Let us suppose that both parametrizations provide equally good fits to the experimental data according to some suitably chosen criterion. We may then expect that the differences

$$\begin{aligned} \delta T(W) &\equiv T_2(W) - T_1(W) \\ \delta W_p &\equiv W_{p2} - W_{p1} \\ \delta R &\equiv R_2 - R_1 \\ \delta C(W) &\equiv C_2 - C_1 \end{aligned} \tag{5}$$

are small enough so that second and higher orders of these differences may be ignored. In that case the differences may be computed as if they were ordinary differentials. We interpret $\delta W_p, \delta R, \delta C(W)$ as the changes in W_p, R and $C(W)$ respectively introduced by a change in the parametrization of the scattering amplitude.

For the sake of clarity, we shall first present our results in the form of two theorems

Theorem 1. *If the first order difference in $T^{-1}(W)$ is zero for a region near W_p, then so is the first order difference in the pole position W_p.*

Theorem 2. *If the first order differences in both $T^{-1}(W)$ and $(\partial/\partial W)T^{-1}(W)$ are zero, then so are the first order differences in W_p and the pole residue R.*

The proof is straightforward. From (3), the first order difference is

$$\delta T^{-1} = -\delta W_p\{R + (W - W_p)C\}^{-1} + (W - W_p)\delta\{R + (W - W_p)C\}^{-1} \tag{6}$$

where the differences are to be taken at fixed W. Putting

$$\delta T^{-1}(W_p) = 0 \tag{7}$$

we get

$$\delta W_p = 0 \tag{8}$$

which proves theorem 1.

To prove theorem 2, we differentiate (3) and get

$$\frac{\partial T^{-1}}{\partial W} = \{R + (W - W_p)C\}^{-1} + (W - W_p)\frac{\partial}{\partial W}\{R + (W - W_p)C\}^{-1}. \tag{9}$$

Hence the first order difference of the derivative of T^{-1} is

$$\begin{aligned} \delta\frac{\partial T^{-1}}{\partial W} &= \delta\{R + (W - W_p)C\}^{-1} - \delta W_p\frac{\partial}{\partial W}\{R + (W - W_p)C\}^{-1} \\ &\quad + (W - W_p)\delta\left[\frac{\partial}{\partial W}\{R + (W - W_p)C\}^{-1}\right]. \end{aligned} \tag{10}$$

We now demand the vanishing of $\delta T^{-1}(W_p)$ as well as

$$\delta\frac{\partial T^{-1}}{\partial W}(W_p) = 0. \tag{11}$$

CC-0. In Public Domain. Gurukul Kangri Collection, Haridwar

Digitized by Arya Samaj Foundation Chennai and eGangotri

Since the condition $\delta T^{-1}(W_p) = 0$ led to the vanishing of δW_p, we get from (10)

$$[\delta\{R + (W - W_p)C\}^{-1}]_{W_p} = 0$$

which implies

$$[\delta\{R + (W - W_p)C\}]_{W_p} = 0.$$

This leads to

$$[\delta R - \delta W_p C + (W - W_p)\delta C]_{W_p} = 0.$$

Again making use of the vanishing of δW_p, we get the required result:

$$\delta R = 0. \tag{12}$$

We now come to the physical interpretation of the theorems. If the scattering amplitude in the neighbourhood of the resonance is known to sufficient accuracy from experimental data, and different parametrizations are used to fit the same data, then it is reasonable to suppose that $\delta T^{-1}(W_p)$ is vanishingly small for any two parametrizations which provide equally good fits to the amplitude. (Recall the meaning of the difference δT^{-1} given by (5).) Our theorem 1 then says that δW_p tends to zero, i.e., the pole position is well-determined.

If further the experimental data are so accurately known and the parametrizations provide such good fits that even the first derivative of the scattering amplitude in the neighbourhood of the resonance is well represented (so that $\delta(\partial T^{-1}/\partial W)\,(W_p)$ can be set equal to zero), then, according to our theorem 2, the residue also is well determined. Because of the more stringent condition for the stability of the residue, it is clear that the stability of the pole position will be on a better footing when one looks at the results of actual fits to the data.

3. Shift of the Breit-Wigner parameters

Since in almost all phenomenological work on resonances, the Breit–Wigner formula, or some modification thereof, is utilized, it will be useful and instructive to deduce the consequences of the theorems of the last section for the Breit-Wigner parameters. The shifts in the Breit–Wigner mass and width parameters caused by a change in the type of parametrization will be found to be related.

The Breit–Wigner formula for the T matrix element near a resonance can be written as

$$T(W) = \frac{\frac{1}{2}F(W)}{W_0 - W - (i/2)\Gamma(W)} + B(W). \tag{13}$$

Here W_0 is the resonance energy or mass taken to be real. In general, F and Γ are energy-dependent quantities. B is a background term. In the multichannel case F and B are to be interpreted as matrices in the channel space.

Let us now relate the Breit–Wigner parameters W_0 and Γ to the pole parameters of the last section. The pole position W_p is determined by the equation

$$W_0 - W_p - \frac{i}{2}\Gamma(W_p) = 0. \tag{14}$$

CC-0. In Public Domain. Gurukul Kangri Collection, Haridwar

Digitized by Arya Samaj Foundation Chennai and eGangotri

The residue of the right hand side of (13) at this pole is given by

$$R = \frac{\frac{1}{2}F(W_p)}{1 + (i/2)\Gamma'(W_p)} \tag{15}$$

where the prime denotes differentiation with respect to W:

$$\Gamma'(W_p) = [\partial\Gamma(W)/\partial W]_{W_p}.$$

Calculating the first order differences from (14) and (15), we get the formulae

$$\delta W_p = \{\delta W_0 - \tfrac{1}{2}i\delta\Gamma(W_p)\}\{1 + \tfrac{1}{2}i\Gamma'(W_p)\}^{-1} \tag{16}$$

and

$$\delta R = \{1 + (i/2)\Gamma'(W_p)\}^{-2}[\tfrac{1}{2}\{1 + (i/2)\Gamma'(W_p)\}\delta F(W_p) - (i/4)\delta\Gamma'(W_p)F(W_p) + \{\tfrac{1}{2}(1 + (i/2)\Gamma'(W_p))F'(W_p) - (i/4)\Gamma''(W_p)F(W_p)\}\delta W_p]. \tag{17}$$

Using (16) and (17), it is now easy to state the theorems of the last section in terms of Breit–Wigner parameters. If $\delta T^{-1}(W_p) = 0$, then

$$\delta W_0 = \tfrac{1}{2}i\delta\Gamma(W_p). \tag{18}$$

If, in addition, $\delta(\partial T^{-1}/\partial W)\,(W_p) = 0$, then

$$\{1 + (i/2)\Gamma'(W_p)\}\delta F(W_p) = (i/2)\delta\Gamma'(W_p)F(W_p). \tag{19}$$

Eqs (18) and (19) are the desired relations between the shifts in the Breit–Wigner parameters.

In spite of their simplicity these relations are quite remarkable. Especially interesting is the appearance of i in both relations. This emphasizes the known fact that $\Gamma(W)$ evaluated at the complex pole W_p is complex. Since δW_0 is real, (18) implies that the shift in the width $\delta\Gamma(W_p)$ caused by any change in the type of parametrization is necessarily purely imaginary.

In the next section we shall study how well the relation (18) is satisfied when applied to various parametrizations that have been used to fit the $\Delta(1232)$ resonance.

4. Application to $\Delta(1232)$

In this section we apply our formulae to the $\Delta(1232)$ resonance and provide concrete illustration of the ideas of the foregoing sections.

For comparison with our formulae, only those fits satisfying the following two criteria should be chosen: (i) the fits should be to the same data, and (ii) the fits should be equally good, in the sense that χ^2 per degree of freedom should be comparable. We have chosen the following parametrizations of the best studied hadronic resonance, the $\Delta^{++}(1232)$:

(a) *Breit–Wigner I* (*Söding et al* 1972; *Barbaro–Galtieri* 1973): In this parametrization, the P_{33} partial wave amplitude in the pion-nucleon channel is taken to be a resonant term plus a nonresonant background:

$$T = \left(\frac{W_0\Gamma}{W_0^2 - W^2 - iW_0\Gamma}\right)\exp(2i\delta_B) + \exp(2i\delta_B)\sin\delta_B \tag{20}$$

CC-0. In Public Domain. Gurukul Kangri Collection, Haridwar

Digitized by Arya Samaj Foundation Chennai and eGangotri

with

$$\Gamma = \Gamma_0 \left(\frac{q}{q_0}\right)^3 \left(\frac{1+q_0^2 r^2}{1+q^2 r^2}\right) \tag{21}$$

$$\delta_B = \tan^{-1} aq^3. \tag{22}$$

W and q are the c.m. energy and momentum respectively. W_0, Γ_0, r and a are adjustable parameters.

(b) *Breit–Wigner II* (*Cheng and Lichtenberg* 1973). This has the same expression for T as Breit–Wigner I, but with

$$\Gamma = \Gamma_0 \left(\frac{q}{q_0}\right)^3 \left(\frac{W_0}{W}\right)^2 \tag{23}$$

$$\delta_B = \tan^{-1} a\left(\frac{q}{W}\right)^3 \tag{24}$$

(c) *Polynomial* (*Söding et al* 1972; *Barbaro–Galtieri* 1973): In this fit the amplitude is written as

$$T = \frac{q^3}{q^3 \cot\delta - iq^3} \tag{25}$$

with

$$q^3 \cot\delta = \sum_{n=1}^{4} a_n q^{2n-2} \tag{26}$$

(d) *Extended Chew-Low* (*Vasan* 1976): This parametrization is defined by

$$T = q^3\{\mu'^3(1-A\omega) - iq^3 + \frac{\omega}{\lambda'}(1-A\omega)(1+B\omega+C\omega^2)\}^{-1} \tag{27}$$

where $\omega = W - M\ (1-\frac{1}{2}\beta)$, M is the proton mass and $\beta = 0{\cdot}00277$. Despite its appearance, this form has only three adjustable parameters A, B and C since it is semitheoretical. The parameters μ' and λ' are related to the π^+ mass μ and the pseudovector pion-nucleon coupling constant f by the following equations

$$\mu' = \mu\left(1 - \frac{\mu^2}{4M^2} + \frac{1}{2}\beta\right)^{1/2},$$

$$\lim_{\omega\to 0} \frac{\omega T}{q^3} = \frac{4f^2}{3\mu^2}\left(1 + \frac{19}{20}\frac{\mu^2}{M^2}\right)$$

(e) *Breit–Wigner III* (*Vasan* 1976): T and Γ are as in (a) but δ_B as in (b).

For all the parametrizations above, the resonance energy or mass W_0 is defined to be the energy at which the resonant part of the amplitude T is equal to i. The width parameter Γ_0 is defined by the relation

$$\Gamma_0 = -2\left\{\frac{\partial}{\partial W}(T^{-1}+i)\right\}^{-1}_{W=W_0}. \tag{28}$$

CC-0. In Public Domain. Gurukul Kangri Collection, Haridwar

Digitized by Arya Samaj Foundation Chennai and eGangotri

We have considered fits to two different sets of πN P_{33} phase shift data. One set consists of 14 data points from Carter 71 partial wave analysis (Carter *et al* 1971). The other set consists of 11 points from the more accurate data of Carter 73 analysis (Carter *et al* 1973). The parametrizations (a) to (c) above were fitted to the Carter 71 data while (d) and (e) were, to the Carter 73 data. The values of the parameters in the various fits are as follows:

Fits to Carter 71 data:

Breit–Wigner I: $W_0 = 1234\,\text{MeV}$, $\Gamma_0 = 120\,\text{MeV}$,
$r = 0{\cdot}89\,\text{f}$, $a = 0{\cdot}028\,\text{fm}^3$

Breit–Wigner II: $W_0 = 1243{\cdot}3\,\text{MeV}$, $\Gamma_0 = 152{\cdot}2\,\text{MeV}$,
$a = 27{\cdot}67$

Polynomial: $a_1 = 1{\cdot}78\,\text{f}^{-3}$, $a_2 = -0{\cdot}41\,\text{f}^{-1}$, $a_3 = -0{\cdot}53\,\text{f}$,
$a_4 = -0{\cdot}13\,\text{f}^3$, $W_0 = 1231{\cdot}4\,\text{MeV}$, $\Gamma_0 = 112\,\text{MeV}$

Fits to Carter 73 data:

Extended Chew–Low: $A = 3{\cdot}41\,\text{GeV}^{-1}$, $B = -2{\cdot}35\,\text{GeV}^{-1}$,
$C = 8{\cdot}28\,\text{GeV}^{-2}$, $W_0 = 1230{\cdot}6\,\text{MeV}$,
$\Gamma_0 = 114{\cdot}5\,\text{MeV}$, $\mu' = 139{\cdot}3\,\text{MeV}$,
$\frac{1}{\lambda'} = 0{\cdot}187\,\text{GeV}^2$

Breit–Wigner III: $W_0 = 1234{\cdot}0\,\text{MeV}$, $\Gamma_0 = 124\,\text{MeV}$,
$r = 0{\cdot}842\,\text{f}$, $a = 9{\cdot}23$.

In table 1, the values of W_0 and Γ_0 for the various parametrizations are collected together for convenience. The first three lines a) to c) refer to fits to Carter 71 data while the last two lines d) and e) refer to fits to Carter 73 data. These fits satisfy the two criteria mentioned in the beginning of this section. The rather large shifts in W_0 and Γ_0 as one goes from one parametrization to another can be noted. The pole position W_p is also presented in the same table. The remarkable stability in both the

Table 1. Mass, width and pole positions for various parametrizations of $\Delta(1232)$.

Parametrization	χ^2/d.f	W_0 (MeV)	Γ_0 (MeV)	W_p (MeV)	$\Gamma(W_p)$ (MeV)
a) B-W I	9·7/10	1234·0	120	1211·2–50·0*i*	98·1–47·3*i*
b) B-W II	16/11	1243·3	152·2	1210·7–50·7*i*	98·9–66·3*i*
c) Poly.	12·2/10	1231·4	112	1211·3–50·2*i*	98·7–42·0*i*
d) E.C-L	5·4/8	1230·6	114·5	1209·5–50·5*i*	99·2–43·8*i*
e) B-W III	5·0/7	1234·0	124	1209·7–50·3*i*	98·7–50·3*i*

CC-0. In Public Domain. Gurukul Kangri Collection, Haridwar

Digitized by Arya Samaj Foundation Chennai and eGangotri

Table 2. Comparison of the mass shift with the shift in the width function.

Parametrization	δW_0 (MeV)	$\frac{i}{2}\delta\Gamma(W_p)$ (MeV)
Breit–Wigner I Breit–Wigner II	9·3	$9{\cdot}5 + 0{\cdot}4i$
Polynomial Breit–Wigner II	11·9	$12{\cdot}2 + 0{\cdot}1i$
Extended Chew-Low Breit–Wigner III	3·4	$3{\cdot}2 + 0{\cdot}2i$

real and imaginary parts of W_p is obvious. It is interesting to note that the pole position is apparently stable even when the data are changed! In the last column of this table, we give the value of the width function at the pole, $\Gamma(W_p)$, which will be needed for verifying our relation (18).

The verification of the relation (18) is presented in Table 2. To minimize unknown effects in the numerical comparison of the fits to our formulae, we have compared two fits (to the same data) having appreciably different values for the parameters W_0 and Γ_0. The shifts δW_0 and $\delta\Gamma(W_p)$ are calculated as differences between the parametrizations indicated in the first column of table 2. A look at the second and third columns shows that the relation $\delta W_0 = i\delta\Gamma(W_p)/2$ is well satisfied. It is seen that the large imaginary part of $\delta\Gamma(W_p)$ is taken care of by the extra factor i. As δW_p is not zero, though very small, we cannot expect strict equality of the two sides of the relation. As seen from table 1, the pole position W_p is determined at best with an error of 0·5 MeV. Hence, the agreement between the two columns of table 2 should be considered quite satisfactory. This good agreement of our relation (18) with data supports the arguments made in proving the stability of the pole position since both derivations are based essentially on the same logic.

We have not displayed any numerical verification of relation (19) (which would indicate that δR tends to zero) because we do not feel that the fits determine the residue R well enough for the application of our first order formula to be meaningful. It may be recalled that relation (19) implies that the fits are a good representation of not only the amplitude T but also the derivative $\partial T/\partial W$.

5. Discussion

The aim of our work has been to demystify the pole and provide a simple understanding of the stability of the pole, under different parametrizations of the scattering amplitude. We have shown that the pole position has a first order stability under variations of the forms of parametrizations, provided the experimental data in the neighbourhood

CC-0. In Public Domain. Gurukul Kangri Collection, Haridwar

Digitized by Arya Samaj Foundation Chennai and eGangotri

of the pole are equally well fitted by the various parametrizations. Under the same conditions we have also derived a relation between the shifts of the Breit–Wigner parameters and this relation is found to agree well for the actual shifts found in the parametrizations fitted to $\Delta(1232)$.

Because of its stability, the position of the pole seems to be the best way of characterizing the properties of the resonant state – the real and imaginary parts of the pole position playing the roles of the conventional mass and width of the resonance. However, here we would like to draw attention to a basic issue. There is in fact no unique correspondence between a resonance and a single pole of the multichannel S matrix. It has been known for quite some time that a single pole of the S matrix in a particular Riemann sheet of the complex energy plane is in general followed by a retinue of poles, called shadow poles, existing in the other Riemann sheets (Dalitz and Rajasekaran 1963; Eden and Taylor 1963; Ross 1963; Amati 1963). Experimental evidence for the existence of these shadow poles has recently been found. Shadow poles exist and their positions have been determined in the case of $J^P=\frac{3}{2}^+$ resonance in the $(n\alpha, \mathrm{d}t)$ channels of nuclear physics (Hale *et al* 1987) and in the case of the isoscalar $J^P=0^+$ state $f_0(975)$ (formerly S (975)) in the $(\pi\pi, K\bar{K})$ channels of particle physics (Au *et al* 1987). Thus, in principle, a resonance is represented by a system of poles in various Riemann sheets and often there is no a priori justification for choosing one among them for characterizing the resonance.

In many physical situations, one of the poles may be nearest to the physical region where the experimental data on the scattering exist. Since our stability argument depended on the nearness of the pole to the region where experimental data are fitted, it is clear that only this nearby pole is expected to be stable and thus, for most practical purposes, the real and imaginary parts of this pole do have some significance. But, from a fundamental point of view, all the poles of the S matrix on the various Riemann sheets are equal manifestations of the resonance phenomenon and none is to be singled out as having a closer relationship with the resonance.

There does exist a pole which is of special significance and that is the pole of the K matrix. A single and unique pole of the K matrix in fact replaces or represents the whole system of shadow poles of the S matrix (Rajasekaran 1965). However, the determination of the K matrix and its pole from the experimental data being more indirect, the position of the K matrix pole is not expected to be so stable.

Finally, we must point out that there are certain important exceptional situations where shadow poles do not exist (Rajasekaran 1972). The question of the existence or nonexistence of shadow poles is in fact intimately connected to hadron dynamics and contains information about the nature of the hadron: whether it is a normal bound state of quarks or whether it is a "molecule" of other hadrons. The nucleon and $\Delta(1232)$ are examples of the former while deuteron and possibily Λ (1405) are examples of the latter (Rajasekaran 1972; Dalitz 1982). A fuller discussion of this problem is outside the scope of the present paper and is reserved for a future publication.

To sum up, poles of the S matrix may be the best candidates for the definition of unstable particles. One can even mathematically prove the stability of the poles under changes in the parametrization of the scattering amplitude. But, because of the existence of the shadow poles there is no unique correspondence between particle and pole. For each particle in general, there may be a retinue of poles in various Riemann sheets. The existence or nonexistence of shadow poles is related to deeper questions of dynamics.

CC-0. In Public Domain. Gurukul Kangri Collection, Haridwar

Digitized by Arya Samaj Foundation Chennai and eGangotri

References

Aguilar–Benitez M *et al* (Particle Data Group) 1986 *Phys. Lett.* **B170** 1

Amati D 1963 *Phys. Lett.* 7 290

Au K L, Morgan D and Pennington M R 1987 *Phys. Rev.* **D35** 1633

Ball J S, Campbell R R, Lee P S and Shaw G L 1972 *Phys. Rev. Lett.* **28** 1143

Ball J S, Lee P S and Shaw G L 1973 *Phys. Rev.* **D7** 2789

Barbaro–Galtieri A 1973 *in Properties of the Fundamental Interactions*, (Ed) A Zichichi (International School of Subnuclear Physics, Erice) p. 533

Carter A A, Williams J R, Bugg D V, Bussey P J and Dance D R 1971 *Nucl. Phys.* **B26** 445

Carter J R, Bugg D V and Carter A A 1973 *Nucl. Phys.* **B58** 378

Cheng T-Y and Lichtenberg D B 1973 *Phys. Rev.* **D7** 2249

Dalitz R H and Rajasekaran G 1963 *Phys. Lett.* 7 373

Dalitz R H *et al* 1982 *in Proc. of The International Conference on Hypernuclear and Kaon Physics*, (Ed) B Povh (Heidelberg: Max Planck Institute) p. 201

Eden R J and Taylor J R 1963 *Phys. Rev. Lett.* **11** 516

Hale G M, Brown R E and Jarmie N 1987 *Phys. Rev. Lett.* **59** 763

Rajasekaran G 1965 *Nuovo Cimento* **37** 1004

Rajasekaran G 1972 *Phys. Rev.* **D5** 610

Ross M 1963 *Phys. Rev. Lett.* **4** 473

Söding P *et al* (Particle Data Group) 1972 *Phys. Lett.* **B39** 105

Vasan S S 1976 *Nucl. Phys.* **B106** 535

Yost G P *et al* (Particle Data Group) 1988 *Phys. Lett.* **B204** 1

CC-0. In Public Domain. Gurukul Kangri Collection, Haridwar

Digitized by Arya Samaj Foundation Chennai and eGangotri

Pramāṇa – J. Phys., Vol. 34, No. 3, March 1990, pp. 193–199. © Printed in India.

A relation between X-ray diffraction based liquid structure and packing coefficient

A MIKUSINSKA-PLANNER

Optics Laboratory, Institute of Physics, A Mickiewicz University, Grunwaldzka 6, PL-60780 Poznań, Poland

MS received 15 March 1989; revised 28 August 1989.

Abstract. A relation between the liquid structure and the molecules packing coefficient has been derived on the grounds of the experimental results of X-ray diffraction studies. The packing coefficient k was assumed to be a criterion of correctness of the structural models of 2-methyl-1-propanol and 2-methyl-2-propanol based on experimental results. This coefficient was estimated from the specific volumes of molecules V_0, volumes of elementary pseudocells V and the number of molecules comprised into these pseudocells. The volumes V of pseudocells were estimated from the same X-ray diffraction pattern as was used for determination of the liquid structure. The determined values of the packing coefficient support the chain-like structure of associates of liquid 2-methyl-1-propanol and reject the chain-like structure for liquid 2-methyl-2-propanol.

Keywords. X-ray scattering pattern; molecules packing coefficient; structural model of the liquid.

PACS Nos 78·70; 61·20

1. Introduction

Although no rigorous periodic internal structure exists in liquids, they still reveal some tendency towards ordering, namely, their molecules are statistically densely arranged and some intermolecular distances are distinguished. As a result of the statistical arrangement of molecules, a liquid subjected to X-ray investigation reveals a spherical symmetry. The diffraction patterns show more or less broadened rings. These patterns are the basic experimental data both for the formulation of the structural model of the liquid (Mikusińska-Planner 1979, 1983) and for estimation of the packing coefficient (Mikusińska-Planner 1986).

A structural model of a liquid is found from the analysis of radial functions of electron, atom or molecular density obtained by Fourier inversion of the experimental scattering data. However, as the X-ray patterns obtained for liquid are broadened, they are not as convenient for numerical analysis as the patterns obtained for crystals. Therefore structural information inferred from X-ray diffraction patterns for liquids is based on the model-theoretical interpretations. Assuming the most probable model of intermolecular interactions for which the calculated scattering pattern agrees best with the experimental one, we can estimate the number of molecules x per an elementary pseudocell. The volume of this cell, $\bar{V}$, is found from the radius of the so-called first coordination sphere $\bar{R}$, according to the spherical relation:

$$\bar{V} = 4\pi \bar{R}^3/3. \tag{1}$$

CC-0. In Public Domain. Gurukul Kangri Collection, Haridwar

Digitized by Arya Samaj Foundation Chennai and eGangotri

The notion of a spherical elementary pseudocell is justified by the spherically-symmetric distribution of molecules in the liquid, which is confirmed by the broadened rings in the diffraction pattern. The mean value of the radius $\bar{R}$ is approximately determined from the position of the main maximum in X-ray scattering pattern

$$\bar{R} \approx 7{\cdot}72/s(\max) - 0{\cdot}3, \tag{2}$$

where $s(\max) = 4\pi \sin\theta(\max)/\lambda$, 2θ the angle of scattering and λ the X-ray scattering wavelength. The correcting factor 0·3 for molecular liquids has been found empirically (Voigtlaender-Tetzner 1958).

By analogy with the packing coefficient defined for crystals (Van Meerssche and Feneau-Dupont 1976) we can define the corresponding packing coefficient of molecules in liquids

$$k = V_0/(\bar{V}/x), \tag{3}$$

where V_0 is the specific volume of the molecule and $\bar{V}/x$ is the volume available for one molecule in a pseudocell. The determined value k is correct only when it falls within the range $0{\cdot}51 \leqslant k \leqslant 0{\cdot}58$ as the values $k > 0{\cdot}58$ correspond to the crystal phase and the values $k < 0{\cdot}51$ to the gas phase (Kozhin 1968). The right coefficient value is, however, obtained only when the assumed model of intermolecular liquid structure in a given liquid is correct. If this model is not correct, the number of molecules, x, in one elementary pseudocell is wrongly estimated and the value of the k coefficient goes beyond the limit of values admissible for liquid phase.

2. Specific volume of molecules

The specific volume of a molecule may be found from its chemical structure, the length of bonds and van der Waals radii of atoms and functional groups. As an example we shall estimate it for a molecule of 2-methyl-1-propanol. Its shape and dimensions required are given in figure 1. The figure presents three orthogonal projections of $(CH_3)_2CHCH_2OH$ molecule model onto three mutually orthogonal planes. The shape of the molecule can be approximated by a sphere and limited by three radii r_1, r_2, r_3 making the mean radius of

$$\bar{r} = (r_1 + r_2 + r_3)/3 = 3{\cdot}03 \text{ Å}, \tag{4}$$

where $r_1 = 3{\cdot}00$ Å, $r_2 = r_3 = 3{\cdot}05$ Å. The real radius of the molecule, r_0, is however, significantly shorter than $\bar{r} = 3{\cdot}03$ Å. The latter is henceforth called the maximum radius of the molecule $\bar{r} = r_{max}$. The maximum radius r_{max} determines the maximum volume of the molecule, $V_0 = 116{\cdot}5$ Å^3. The areas of the model projections onto the three orthogonal planes (figure 1) were found to make only 76·85% of the area of sphere determined by the maximum radius $r_{max} = 3{\cdot}03$ Å. Thus, the spherical volume corresponding to the real molecule is

$$V_0 = (76{\cdot}85 \times 116{\cdot}5/100)\text{ Å}^3 = 89{\cdot}5\text{ Å}^3. \tag{5}$$

The real specific radius r_0 of a 2-methyl-1-propanol molecule is therefore 2·77 Å.

CC-0. In Public Domain. Gurukul Kangri Collection, Haridwar

Digitized by Arya Samaj Foundation Chennai and eGangotri

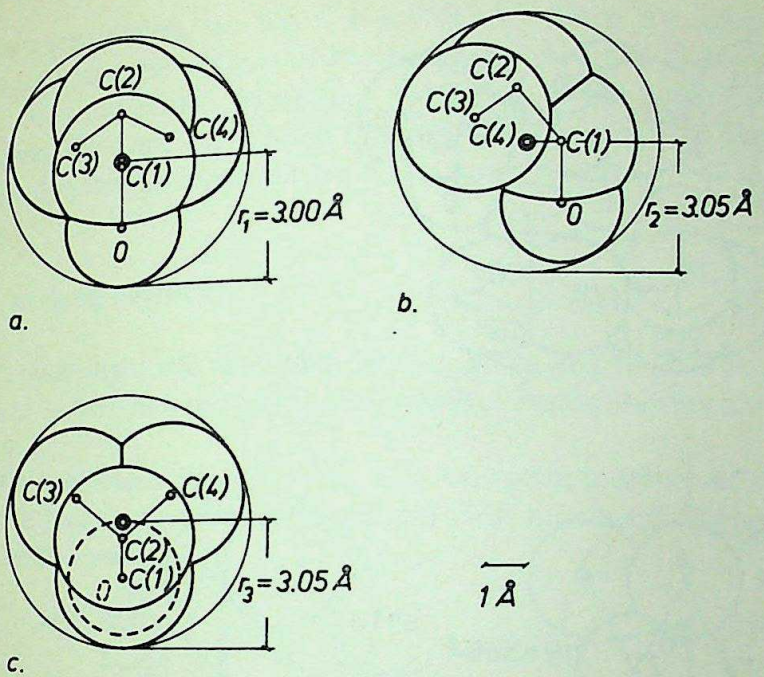

Figure 1. A model of 2-methyl-1-propanol molecule projected onto three orthogonal planes.

Table 1. Specific radii and volumes of molecules.

Alcohol	$\bar{r}_0$	$\bar{V}_0$
2-methyl-1-propanol	2·7 Å	82·4 Å^3
2-methyl-2-propanol	3·03 Å	116·5 Å^3

Taking into account the earlier results of specific radii of molecules reported by other authors (Vyrodov *et al* 1964) $r_{\text{theor}} = 2{\cdot}69$ Å and $r_{\text{vol}} = 2{\cdot}64$ Å, the mean value of a 2-methyl-1-propanol molecule is estimated to be

$$\bar{r}_0 = (r_0 + r_{\text{theor}} + r_{\text{vol}})/3 = 2{\cdot}7 \text{ Å}. \tag{6}$$

The r_{theor} is the so-called kinetic radius of the molecule and r_{vol} is the radius obtained from summing up the volume elements of the molecule.

The resultant mean value of the radius $\bar{r}_0 = 2{\cdot}7$ Å determines the mean value of the specific volume of a 2-methyl-1-propanol molecule as, $\bar{V}_0 = 82{\cdot}4$ Å^3. Table 1 presents the values of the specific radii and volumes of 2-methyl-1-propanol molecule and, for the sake of comparison, 2-methyl-2-propanol molecule (Mikusińska-Planner 1986).

3. Configuration of molecules in liquid 2-methyl-1-propanol

Assuming the model of intermolecular interaction in liquid 2-methyl-1-propanol proposed by Mikusińska-Planner (1979) we can show schematically the chain arrangement of molecules associated in the way presented in figure 2a*. The central molecule A is connected by a hydrogen bond of a length of $R_{\text{OH...O}} = 2{\cdot}65$ Å with the

CC-0. In Public Domain. Gurukul Kangri Collection, Haridwar

Digitized by Arya Samaj Foundation Chennai and eGangotri

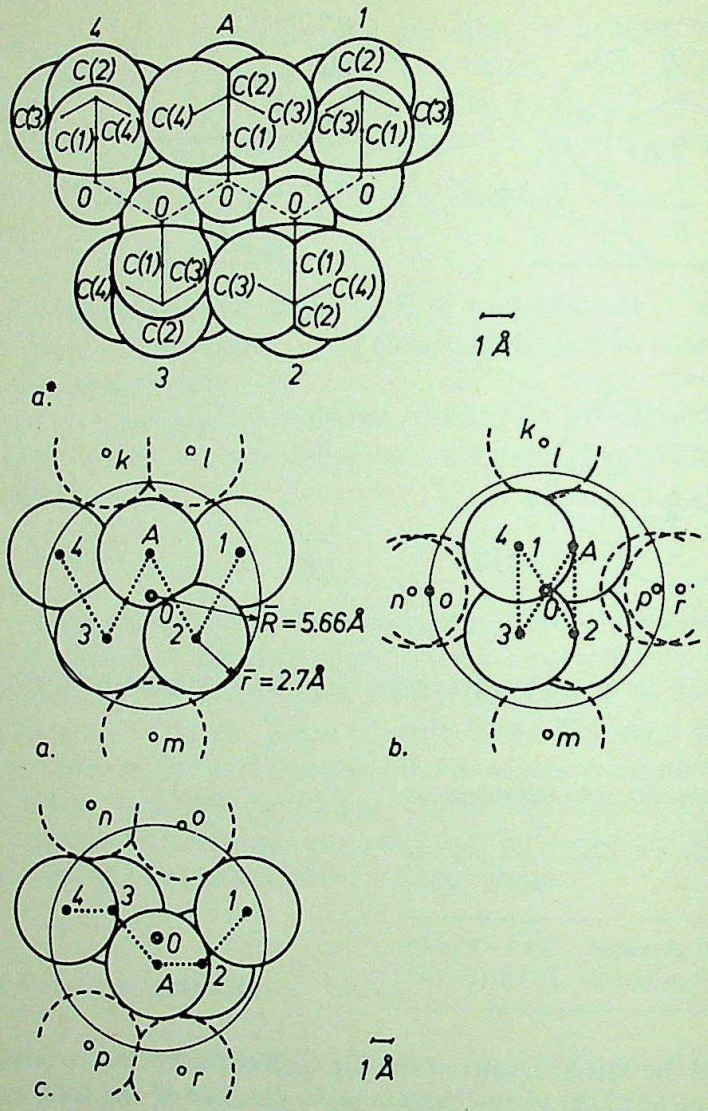

Figure 2. A model of liquid 2-methyl-1-propanol structure projected onto three orthogonal planes a*) projection on the plane of the figure in which the O and C(1) atoms lie a) projection on the plane of the figure which is parallel to the plane determined by the centres of molecules 1, 3, 4 etc. b) and c) projections where the centres of molecules 1, 3 and 4 determined a plane perpendicular to the plane of the figure.

molecules 2 and 3. The molecules A, 1, 2, 3 and 4 form an open chain with a mean angle of 120° between the OH...O bonds. The molecules 1 and 4 have $CH(CH_3)_2$ groups inclined to the plane containing the atoms O and C(1) in the direction opposite to the A molecule. The arrangement of associated molecules in a chain shown in figure 2a* may be illustrated in a simplified way. In figure 2a (and b, c) the molecules are shown as spheres of a radius $\bar{r}_0 = 2{\cdot}7$ Å. In this figure the centres of molecules making a chain are linked with dotted lines. The molecules denoted by A and 2 in the projection a) lie above the plane of the figure whereas the centres of the molecules 1, 3 and 4 lie in this plane. The centre of the associate was assumed to be at O. From this point we drew a circle of the radius $\bar{R}$ equal to the radius of the first coordination sphere. The value of the latter radius was obtained from (2) for $s(\max) = 1{\cdot}295$ Å^{-1} (Mikusińska-Planner 1979) and is, $\bar{R} \approx 5{\cdot}66$ Å. Since $\bar{R}$ determines the volume of

CC-0. In Public Domain. Gurukul Kangri Collection, Haridwar

Digitized by Arya Samaj Foundation Chennai and eGangotri

an elementary pseudocell, we have, $\bar{V} = 759{\cdot}5\,\text{Å}^3$. Since the sphere of the radius $R = 5{\cdot}66\,\text{Å}$ comprises the centres of molecules 1, 2, A, 3 and 4, the projections were drawn only for 5 molecules. Molecules belonging to the neighbouring chaotically distributed associates are denoted in figure 2 broken lines. The centres of adjacent molecules are denoted by small letters k, l, m, n, o, p, r.

4. Molecule packing coefficient

The molecule packing coefficient, k, is defined, according to (3). The specific volumes of molecules of 2-methyl-1-propanol and 2-methyl-2-propanol are already known and given in table 1.

To find the coefficient k, we should also know the number of molecules in the known volume $\bar{V}$ of an elementary pseudocell. This number x may be estimated from (3) which may be rewritten as

$$x = k(\bar{V}/\bar{V}_0). \tag{7}$$

The values of x obtained from (7) for the pseudocell volume $\bar{V} = 759{\cdot}5\,\text{Å}^3$ and the mean specific volume of a molecule $\bar{V}_0 = 82{\cdot}4\,\text{Å}^3$ together with the k values corresponding to the liquid phase, are given in table 2. For the sake of comparison, table 2 also includes the corresponding data for liquid 2-methyl-2-propanol taken from Mikusińska-Planner's (1986) paper.

Considering figure 2 and the data of table 2 on liquid 2-methyl-1-propanol we may expect that the coefficient k falls within the range $0{\cdot}54 \leqslant k \leqslant 0{\cdot}55$, as the number of molecules in the elementary pseudocell is $x = 5$. This supposition has been supported by the analysis of the areas of orthogonal projections of the associate on the plane limited by the radius $\bar{R}$ of the elementary pseudocell (figure 2). The appropriate data for liquid 2-methyl-1-propanol are given in table 3, according to which, the area of the projection that does not fall within the borders of an elementary pseudocell makes 18·9% of the area of projection a) and 19·6% of the area of projection c) of the whole model of the associate of 5 molecules. So an average 19·2% of the area of projection of the model does not fall within the elementary pseudocell. However, the unoccupied space of the pseudocell above and below the model on the projection c) (figure 2c) may be filled with the molecules k, l, m, n, o, p, r of the neighbouring associates, according to figure 2. The areas of the projections of the molecules falling within the area of the pseudocell (table 3) make, on the average, about 17·5% of the area of projection of the model.

Thus, the area of projection of the elementary pseudocell of the volume $\bar{V} = 759{\cdot}5\,\text{Å}^3$ includes 80·8% of the area of projection of the model and 17·5% of the area due to the

Table 2. Number of molecules x of liquid 2-methyl-1-propanol and 2-methyl-2-propanol comprised in an appropriate elementary pseudocell for the admissible packing coefficients.

k	0·51	0·52	0·53	0·54	0·55	0·56	0·57	0·58
$x_{(CH_3)_2CHCH_2OH}$	4·70	4·79	4·88	4·97	5·06	5·16	5·25	5·34
$x_{(CH_3)_3COH}$	3·39	3·46	3·52	3·59	3·66	3·72	3·79	3·86

CC-0. In Public Domain. Gurukul Kangri Collection, Haridwar

Digitized by Arya Samaj Foundation Chennai and eGangotri

Table 3. Areas of the orthogonal projections of the model of liquid 2-methyl-1-propanol associates.

Orthogonal projection of 2-methyl-1-propanol associate model	Areas [Å^2]		
	a	*b*	*c*
The projection of the model of 5-molecule associate	110·0	68·0	81·6
The part beyond the borders of the pseudocell area	20·8	—	16·0
The projections of neighbouring associates falling into the area of the pseudocell	9·2		21·6

molecules k, l, m, n, o, p, r belonging to the neighbouring associates. Altogether it makes 98·3% of the total area of projections required for $x = 5$. The unfilled area making only 1·7% of the total area of the projection can be easily filled by molecules of the vacancy of the structure shown in figure 2b. Thus, consistent with previous suppositions we assume that the molecule packing coefficient $k = 0{\cdot}55$ as the elementary pseudocell comprises 5 molecules of liquid 2-methyl-1-propanol.

5. Discussion

The value of packing coefficient obtained ($k = 0{\cdot}55$) corresponds to the chain structure of associates of liquid 2-methyl-1-propanol. Moreover, a comparison between figures 3a and 3b proves that the chain structure of this compound requires more compact arrangement of molecules than in 2-methyl-2-propanol (figure 3b) (Mikusińska-Planner 1983). This results in a denser filling of a pseudocell with 2-methyl-1-propanol molecules when compared to that of 2-methyl-2-propanol. This is a direct consequence of the fact that $x_{(CH_3)_2CHCH_2OH} > x_{(CH_3)_3COH}$, as the packing coefficient for 2-methyl-2-propanol was found to be $k = 0{\cdot}54$. According to table 2, this value corresponds to $x = 3{\cdot}6$ molecules and as we have shown above, for 2-methyl-1-propanol this value is $x = 5$ molecules.

Determination of the packing coefficient is of great practical importance as it helps to find the right molecular liquid structure. For the sake of illustration let us assume the chain structure of liquid 2-methyl-2-propanol which is in contradiction with the results of Mikusińska-Planner (1983). Figure 3c presents an orthogonal projection of the assumed model onto the plane of the figure which corresponds to the projection of the 2-methyl-1-propanol model shown in figures 2a and 3a.

Orthogonal projections of these models are made for the characteristic parameters of individual liquid. For 2-methyl-2-propanol these parameters are $\bar{r}_0 = 3{\cdot}03$ Å and $\bar{R} = 5{\cdot}7$ Å, after Mikusińska-Planner (1986). The OH...O bond length in the assumed associate would be $\bar{R}_{OH...O} = 2{\cdot}8$ Å and the angle between the directions of the bonds is 120°. As seen from table 2, the maximum number of 2-methyl-2-propanol molecules in the elementary pseudocell is $x = 3{\cdot}86$. On the other hand, for the assumed chain structure of this alcohol $x > 4$ which follows directly from the analysis of the projection in figure 3c and from its comparison with the corresponding projection for 2-methyl-1-propanol (figure 2 and 3a). According to table 2, the value $x > 4$ would

CC-0. In Public Domain. Gurukul Kangri Collection, Haridwar

Digitized by Arya Samaj Foundation Chennai and eGangotri

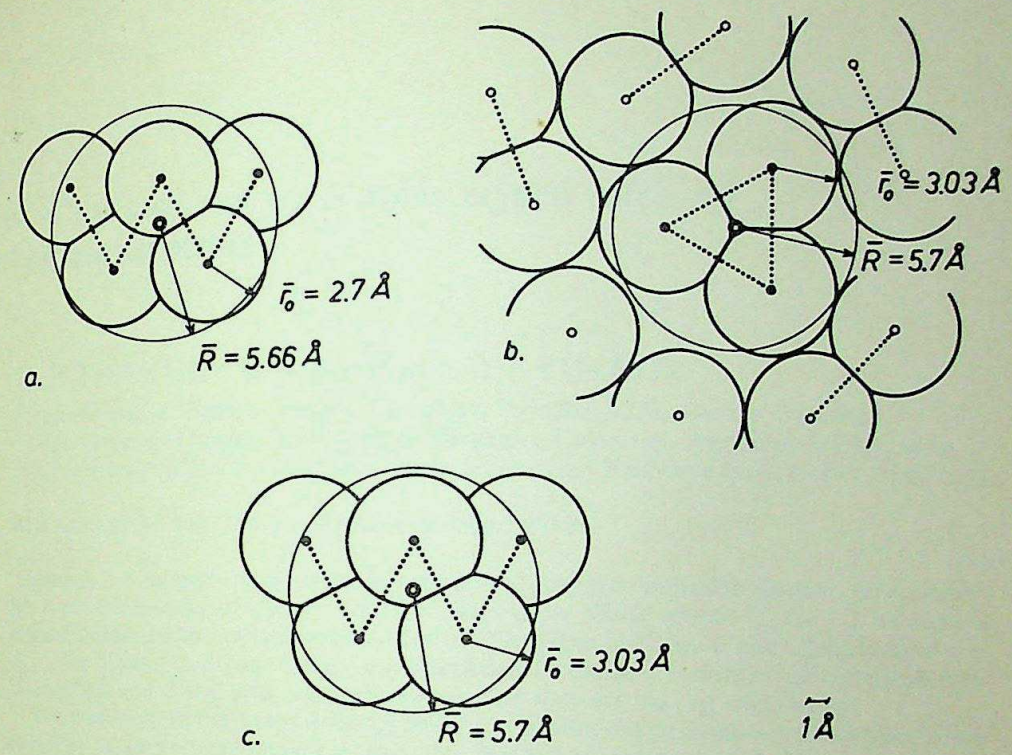

Figure 3. Molecule packing in an elementary pseudocell **a)** Molecules of the chain associate packed into an elementary pseudocell of 2-methyl-1-propanol **b)** Molecules of binary and triple associates packed into an elementary pseudocell of 2-methyl-2-propanol **c)** Molecules of the assumed chain associate packed into a pseudocell of 2-methyl-2-propanol.

give $k > 0{\cdot}58$ which is beyond the liquid phase range. This analysis shows that the packing coefficient value found on the grounds of the liquid structure determined by X-ray diffraction studies is unquestionably and important criterion of correctness of the structure determination.

Acknowledgment

The author is grateful to Professor Marian Surma for helpful correction of the manuscript.

References

Kozhin W M 1968 *Zh. Strukt. Khi.* **9** 671
Mikusińska-Planner A 1979 *Acta Phys. Polon.* **A55** 11
Mikusińska-Planner A 1983 *Acta Crystallogr.* **B39** 394
Mikusińska-Planner A 1983 *Acta Phys. Polon.* **A64** 461
Mikusińska-Planner A 1986 *J. Mol. Liquids* **31** 203
Van Meerssche M and Feneau-Dupont J 1976 *Introduction a la cristallographie et a la chimie structurale* (*Leuven*: OYEZ) chap. 2.2
Voigtlaender-Tetzner G 1958 *Z. Phys.* **150** 215
Vyrodov I P, Budko P S and Dyerkatch L W 1964 *Zh. Phis. Khi.* **38** 232

CC-0. In Public Domain. Gurukul Kangri Collection, Haridwar

Digitized by Arya Samaj Foundation Chennai and eGangotri

CC-0. In Public Domain. Gurukul Kangri Collection, Haridwar

Digitized by Arya Samaj Foundation Chennai and eGangotri

Pramāṇa – J. Phys., Vol. 34, No. 3, March 1990, pp. 201–215. © Printed in India.

Convexity of internal energy of cubic crystal deformed to orthorhombic structure

K P THAKUR[1], R K JHA[2] and O P THAKUR[3]

[1]Department of Physics, Asmara University, P.O. Box 1220, Asmara (Ethiopia)
[2]Department of Physics, TNB College Bhagalpur University, Bhagalpur 812007, India
[3]Department of Physics, Delhi Institute of Technology, Kashmere Gate, Delhi 110006 India

MS received 31 July 1989; revised 3 November 1989

Abstract. A generalized set of strain variables q_r^N, has been defined to develop the expression for a generalized set of second order and third-order elastic moduli C_{rs}^N and C_{rst}^N for a cubic crystal deformed to orthorhombic structure. The Hessain $C_{rs}^N \delta q_r \delta q_s$ and $C_{rst}^N \delta q_r \delta q_s \delta q_t$ ($r = 1, 2 \ldots\ldots 6$; summation convention) are calculated in the new variables and compared with *G*-strength and *S*-strength, for both positive and negative loading environment.

The convexity of the internal energy relative to various choice of strain measure is examined considering up to third degree terms in the internal energy expression. The computational results for *bcc* iron is presented according to the new moduli. The stable ranges thus obtained for iron under hydrostatic compressive and tensile stresses is found to generate the classical stable range, green-stable range and stretch-stable range as the specific cases. However, *bcc* iron does not seem to follow any conventional stable ranges under hydrostatic compression, where the present generalized stable range is found satisfactory.

Keywords. Material strength; elastic constants;

PACS Nos 81·40; 62·20; 03·40

1. Introduction

Studies on ideal crystal strength was initiated in 1940 by Born, which has been extensively studied by Macmillan and Kelly (1972a, b), Milstein (1971, 1973), Thakur (1982a, b, 1985) and Hill (1975) because vast information concerning mechanical behaviour and other elastic constant dependent properties of deformed solids can be gathered from these studies.

The specification of the state of homogeneous strain in a crystal involves any six variables that define the geometry of the primitive cell. Various researchers, in practice, have adopted different sets of generalized co-ordinates q_r ($r = 1, 2, \ldots, 6$), as a measure of pure homogeneous strain for the computation of ideal strength of crystal under load. It will be very interesting to see whether there exists any set of such strain variable which can generate crystal strength (under load) somewhat different (smaller or greater) from the strength obtainable from the other conventional set of variables. Hill (1975) pointed out that a suitable measure of symmetric tensor having smooth monotone scale function $f(\lambda)$ satisfying the condition $f(1) = 0$ and $f'(1) = 1$.

In this paper we have adopted a new generalized set of strain variables, q_r^N, to get the expressions for second-order elastic constant (SOEC), C_{rs}^N, and third-order elastic constants (TOEC), C_{rst}^N, for cubic crystal deformed to orthorhombic structure. The

CC-0. In Public Domain. Gurukul Kangri Collection, Haridwar

Digitized by Arya Samaj Foundation Chennai and eGangotri

new generalized set of strain variables, q_r^N, adopted in this paper represent the generalized form of other conventional sets of strain variables namely (i) the Green's variables used by Born school (Born 1940; Born and Furth 1940; Born and Misra 1940; Misra 1940; Furth 1941), and (ii) the stretch variables used by Macmillan and Kelly (1972a, b, 1973). The rotational symmetry of the new elastic moduli is also examined.

We further compare the strength of loaded crystal determined from new moduli with those due to the conventional ones (i.e., Green and stretch moduli). The role of third order elastic moduli in the determination of stability of loaded crystals is also investigated considering upto the third degree terms in the expansion of energy in Taylor series.

Finally the computational results for a *bcc* iron subjected to hydrostatic compressive and tensile stresses are presented according to the new set of elastic moduli, which are further compared with the results obtained from the Green-moduli and the stretch moduli.

2. Theoretical approach

In the present paper we define a new set of generalized geometric variables according to Hill's (1975) criteria under the summation convention

$$q_{ij}^N = \frac{1}{1+k}[\tfrac{1}{2}(\lambda p_i \lambda p_j - \delta_{ij}) + k(\lambda_{ij} - \delta_{ij})], \tag{1}$$

where δ_{ij} is Kroneker delta, k can assume any suitable value positive or negative, and λ_{ij} are the elements of stretch tensor, a choice of Macmillan and Kelly (1972a, b) for the generalized geometric variables defined by

$$x_i = \sum \lambda_{ij} X_j \quad (i,j = 1,2,3) \tag{2}$$

where X_i and x_i are, respectively, the reference and current rectangular co-ordinates of any lattice vector.

The co-ordinates corresponding to the new set of strain variables (1) may explicitly be expressed by

$$q_1^N = \frac{1}{1+k}[\tfrac{1}{2}(\lambda_1^2 + \lambda_5^2 + \lambda_6^2 - 1) + k(\lambda_1 - 1)], \tag{3}$$

$$q_4^N = \frac{1}{1+k}[(\lambda_2 + \lambda_3)\lambda_4 + \lambda_5\lambda_6 + 2k\lambda_4],$$

where the tensor notation (ij) in (1) are converted into matrix notation (r) according to the following scheme

$$(11)\to 1, \quad (22)\to 2, \quad (33)\to 3, \tag{4}$$
$$(23)\to 4, \quad (31)\to 5, \quad (12)\to 6.$$

For $k=0$, eq. (3) reduces to

$$2q_1^G = \lambda_1^2 + \lambda_5^2 + \lambda_6^2 - 1, \tag{5}$$
$$q_4^G = (\lambda_2 + \lambda_3)\lambda_4 + \lambda_5\lambda_6,$$

CC-0. In Public Domain. Gurukul Kangri Collection, Haridwar

Digitized by Arya Samaj Foundation Chennai and eGangotri

which represents the coordinates, q_r^G, corresponding to the Green's strain tensor adopted by Born School (Born 1940; Born and Furth 1940; Born and Misra 1940; Misra 1940). Again if we put $k=\infty$, (3) reduces to

$$q_1^S = \lambda_1 - 1$$
$$q_4^S = 2\lambda_4 \tag{6}$$

which represents the co-ordinates corresponding to the stretch variables used by Macmillan and Kelly (1972a, b). Thus the present form of the new generalized set of strain variables, q_r^N, is capable of reproducing G-variables, q_r^G, s-variables, q_r^S in special cases. Moreover, (3) can lead to any desired set of strain variables depending upon the choice of the parameter k.

The internal energy E per unit reference cell may be expressed as a function of the geometric variables q_r^N $(r=1,2,\ldots)$

$$E = E(q_1, q_2, \ldots, q_6)$$

and

$$r^2 = \tfrac{1}{4}(l_1^2 a_1^2 + l_2^2 a_2^2 + l_3^2 a_3^2) \tag{7}$$

where a_i $(i=1,2,3)$ represent the vectors coincident with the cell edges whereas their magnitude represent the cell lengths.

The generalized set of elastic moduli C_{rs}, can be defined by

$$C_{rs} = \frac{\partial^2 E}{\partial q_r \partial q_s} \tag{8}$$

where q_r $(r=1,2,\ldots,6)$ are generalized co-ordinates. With the help of eqs (3) and (8), we obtain the expressions for the set of new moduli C_{rs}^N. The new set of elastic moduli thus obtained are

$$C_{iiii}^N = \tfrac{1}{4}(1+k)^2 a_0^4 l_i^4 \left(\frac{\lambda_{ii}}{\lambda_{ii}+k}\right)^2 \frac{\partial^2 E}{(\partial r^2)^2} + \tfrac{1}{2}k(1+k)^2 a_0^2 \frac{l_i^2}{(\lambda_{ii}+k)^3}\frac{\partial E}{\partial r^2} \tag{9a}$$

$$C_{iijj}^N = \tfrac{1}{4}(1+k)^2 a_0^4 l_i^2 l_j^2 \frac{\lambda_{ii}\lambda_{jj}}{(\lambda_{ii}+k)(\lambda_{jj}+k)}\frac{\partial^2 E}{(\partial r^2)^2} \tag{9b}$$

$$C_{ijij}^N = \tfrac{1}{4}(1+k)^2 a_0^4 l_i^2 l_j^2 \frac{(\lambda_{ii}+\lambda_{jj})^2}{(\lambda_{ii}+\lambda_{jj}+2k)^2}\frac{\partial^2 E}{(\partial r^2)^2} + \tfrac{1}{2}a_0^2 \frac{k(1+k)^2}{(\lambda_{ii}+\lambda_{jj}+2k)^2}\left[\frac{l_i^2}{\lambda_{ii}+k}+\frac{l_j^2}{\lambda_{jj}+k}\right]\frac{\partial E}{\partial r^2} \tag{9c}$$

$(i,j=1,2,3;\ i\neq j)$.

These elastic moduli C_{rs}^N have the rotational symmetry.

The derivation of eqs (9) is given in Appendix A. For $k=0$, eqs (9) reduce to

$$C_{iiii}^G = \tfrac{1}{4}a_0^4 l_i^4 \frac{\partial^2 E}{(\partial r^2)^2} \tag{10a}$$

CC-0. In Public Domain. Gurukul Kangri Collection, Haridwar

Digitized by Arya Samaj Foundation Chennai and eGangotri

$$C^G_{iijj} = \tfrac{1}{4} a_0^4 l_i^2 l_j^2 \frac{\partial^2 E}{(\partial r^2)^2} \tag{10b}$$

$$C^G_{ijij} = \tfrac{1}{4} a_0^4 l_i^2 l_j^2 \frac{\partial^2 E}{(\partial r^2)^2} \quad (i,j = 1,2,3;\ i \neq j) \tag{10c}$$

which represents the set of Green moduli, C^G_{rs}, used by Born-School.

Again if we put $k = \infty$ in eqs (9), we find that the C^N_{rs} generate the stretch moduli, C^S_{rs}, a choice of Macmillan and Kelly (1972a, b, 1973).

$$C^S_{iiii} = \lambda_{ii}^2 C^G_{iiii} + \tfrac{1}{2} a_0^2 l_i^2 \frac{\partial E}{\partial r^2} \tag{11a}$$

$$C^S_{iijj} = \lambda_{ii}\lambda_{jj} C^G_{iijj} \tag{11b}$$

$$C^S_{ijij} = \tfrac{1}{4}(\lambda_{ii} + \lambda_{jj})^2 C^G_{ijij} + \tfrac{1}{4}(p^G_{ii} + p^G_{jj}) \quad (i,j = 1,2,3;\ i \neq j) \tag{11c}$$

where $p^G_{ii} = \partial E / \partial q^G_i$.

Thus we see that in special cases the C^N_{rs} can lead to the G-moduli, C^G_{rs}, the S-moduli, C^S_{rs}. Moreover, the set of new moduli, C^N_{rs}, is capable of reproducing any desired set of elastic moduli depending upon the choice of k.

3. Comparison theorem

Following Hill and Milstein (1977) we obtain the differences between S-strength and N-strength of the deformed crystal

$$S - N = p^N_r \left(\frac{\partial^2 q^N_r}{\partial q^s_u \partial q^s_v} \right) \delta q^s_u \delta q^s_v \quad (r,u,v = 1,2,\ldots,6) \tag{12}$$

which with the help of eqs (3) and (6) yield of cubic crystal deformed to orthorhombic structure

$$\begin{aligned} S - N = {} & p^G_1 \left[\frac{\lambda_{11}}{\lambda_{11} + k} \{ (\delta\lambda_{11})^2 + (\delta\lambda_{13})^2 + (\delta\lambda_{12})^2 \} \right] + \cdots + \cdots \\ & + 2p^G_4 \left[\frac{(\lambda_{22} + \lambda_{33})}{(\lambda_{22} + \lambda_{33} + 2k)} \{ (\lambda_{22} + \lambda_{33})\delta\lambda_{23} + \delta\lambda_{12}\delta\lambda_{13} \} \right] \cdot \\ & + \cdots + \cdots \end{aligned} \tag{13}$$

Hill and Milstein (1972) calculated the values of $S - G$

$$\begin{aligned} S - G = {} & p^G_1 [(\delta\lambda_{11})^2 + (\delta\lambda_{13})^2 + (\delta\lambda_{12})^2] + \cdots + \cdots \\ & + 2p^G_4 [(\lambda_{22} + \lambda_{33})\delta\lambda_{23} + \delta\lambda_{13}\delta\lambda_{12}] + \cdots + \cdots \end{aligned} \tag{14}$$

From (13) and (14), we obtain

$$G - N = p^G_1 \left[\{ (\delta\lambda_{11})^2 + (\delta\lambda_{13})^2 + (\delta\lambda_{12})^2 \} \left(\frac{\lambda_{11}}{\lambda_{11} + k} - 1 \right) \right] + \cdots + \cdots + \cdots$$

CC-0. In Public Domain. Gurukul Kangri Collection, Haridwar

Digitized by Arya Samaj Foundation Chennai and eGangotri

$$+ 2p_4^G \left[\left\{ \frac{(\lambda_{22}+\lambda_{33})}{(\lambda_{22}+\lambda_{33}+2k)} - 1 \right\} \{(\lambda_{22}+\lambda_{33})\delta\lambda_{23} + \delta\lambda_{13}\delta\lambda_{12}\} \right]. \quad (15)$$

The simple relations (13), (14) and (15) enable the stability to be compared via the respective convexity criteria. On the considered path of deformation, for positive loads, i.e. $p_1, p_2, p_3 \geqslant 0$ and $k > 0$, we find that the various strengths could be compared as

$$S \geqslant N \geqslant G \quad (16)$$

when $k < 0$ and $p_1, p_2, p_3 \geqslant 0$, we obtain

$$S \geqslant G \geqslant N \quad (17)$$

and when $k = -\lambda_1$ or $k = \lambda_2$ or $k = -\lambda_3$, we obtain

$$G - N = \infty; \quad N = -\infty \quad (18)$$

when $p_1, p_2, p_3 \leqslant 0$ and $k > 0$, we find that

$$G \geqslant S \geqslant N \quad (19)$$

when $k < 0$ and $p_1, p_2, p_3 \leqslant 0$

$$N \geqslant G \geqslant S \quad (20)$$

and when $k = -\lambda_1$ or $k = -\lambda_2$ or $k = -\lambda_3$, we have

$$G - N = -\infty; \quad N = \infty \quad (21)$$

4. Application to BCC iron under hydrostatic stresses

As a specific example we study the mechanics of *bcc* iron subjected to hydrostatic compressive and tensile stresses. The Morse potential as well as the generalized Morse potentials have failed to represent the behaviour of *bcc* iron. However, a recent study (Thakur 1985) has revealed that the generalized logrithmic potential is capable of representing the mechanical behaviour of iron and other *bcc* metals

$$\phi(r) = -\frac{\lambda}{r^3} + B \ln\left(1 + \frac{P}{r^{20}}\right) \quad (22)$$

where A, B and P are potential parameters taken for present computation from Thakur (1985).

We have computed the values of internal energy, stresses, cell lengths, bulk modulus, K, shear moduli μ and μ' and the elastic moduli C_{rs} (Green, stretch and the generalized moduli) of *bcc* iron as a function of lattice deformation. In the stress-free state we obtain for bcc iron

$K = 1{\cdot}69$ mega bar

$\mu = 0{\cdot}51$ mega bar

$\mu' = 1{\cdot}35$ mega bar

CC-0. In Public Domain. Gurukul Kangri Collection, Haridwar

Digitized by Arya Samaj Foundation Chennai and eGangotri

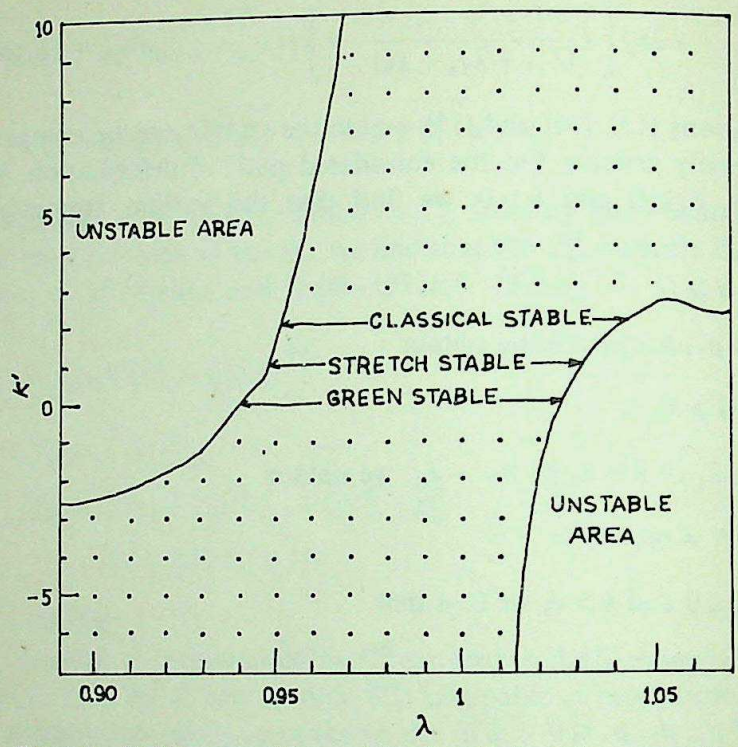

Figure 1. Stable range of iron subjected to hydrostatic compressive and tensile stresses according to present generalized moduli together with the conventional stable ranges (viz. classical, green and stretch).

various computational techniques are described in the literature (Thakur 1982a, b, 1985). The present generalized moduli C_{rs}^{N} are computed as a function of reduced variable

$$K' = \frac{k}{1+k}$$

for a particular lattice deformation.

The stable ranges thus obtained according to the Born criteria is presented in figure 1. Figure 1 also presents the stable ranges obtained from the Green moduli, stretch moduli as also the classical stable range (Thakur 1985).

The stable range obtained from the new strain variables (eq. 1) varies under tension from cell length of $a = 2{\cdot}905$Å to $a = 3{\cdot}06$Å and under compression from $a = 2{\cdot}61$Å to $a = 2{\cdot}767$Å depending upon the choice of strain parameter k'. The values of cell lengths and pressure at the onset of lattice instability (Green, stretch and classical instabilities) for iron under the present study are listed in table 1 together with the values of strain parameter k', for which the generalized results are equivalent to the conventional ones. Figure 1 and table 1 indicate that all the conventional ranges could be generated as the specific cases of our generalized results. Figure 1 also shows that the stable range of *bcc* iron under hydrostatic compression is limited by all the conventional variables. However, in actual practice, iron is stable under hydrostatic compression up to considerably large strain, which is possible only if we consider our generalized variables with $K' < -2{\cdot}6$ (Figure 1).

CC-0. In Public Domain. Gurukul Kangri Collection, Haridwar

Digitized by Arya Samaj Foundation Chennai and eGangotri

Table 1. Cell length (a in Å) and pressure (p in Mbar) at the onset of lattice instability (G-, S-, and N-stabilities) for iron under hydrostatic stresses together with the values of k' for which generalized results are equivalent to the conventional ones.

Stability type	Stability failure under compression			Stability failure under tension			k'
	a	p	Cause	a	p	Cause	
Classical	2·720	0·253	$\mu' = 0$	2·980	−0·205	$\mu = 0$	2
Green	2·690	0·308	$C_{44} = 0$	2·935	−0·129	$C_{11} = C_{12}$	0
Stretch	2·714	0·265	$C_{44} = 0$	2·950	−0·156	$C_{11} = C_{12}$	1

5. Third order elastic constants

In the past few decades the third order elastic constant (TOEC) of crystals has been a topic of extensive study (Birch 1947; Nranyan 1964; Thurston and Brugger 1964) and plays an important role in solid state physics. Brugger (1964) presented a general thermodynamic definition of higher order elastic constant. The most general definition for elastic constants of the nth order is

$$C_{rst\ldots} = \frac{\partial^n E}{\partial q_r \partial q_s \partial q_{t\ldots}}; \quad n \geqslant 2 \tag{23}$$

where $q_r (r = 1, 2, \ldots, 6)$ are the generalized co-ordinates defined earlier, E is the internal energy per unit reference volume and may be expressed as a function of q_r.

From (23) the third order elastic constant, C_{rst}, can be defined by

$$C_{rst} = \frac{\partial^3 E}{\partial q_r \partial q_s \partial q_t}. \tag{24}$$

Taking q_r^N, the new set of generalized variables (eq. 1) for q_r in (24), we generate the expressions for the third order elastic constants, C_{rst}^N,

$$C_{rrr}^N = \tfrac{1}{8} a_0^6 l_r^6 (1+k)^3 \left(\frac{\hat{\lambda}_r}{\hat{\lambda}_r + k}\right)^3 \frac{\partial^3 E}{(\partial r^2)^3} + \tfrac{3}{4} a_0^4 l_r^4 \frac{k(1+k)^3 \hat{\lambda}_r}{(\hat{\lambda}_r + k)} \frac{\partial^2 E}{(\partial r^2)^2}$$
$$- \tfrac{3}{2} k (1+k)^3 \frac{a_0^2 l_r^2}{(\hat{\lambda}_r + k)^5} \frac{\partial E}{\partial r^2} \quad (r = 1, 2, 3) \tag{25a}$$

$$C_{rrs}^N = \tfrac{1}{8} a_0^6 l_r^4 l_s^2 (1+k)^3 \frac{\hat{\lambda}_r^2 \hat{\lambda}_s}{(\hat{\lambda}_r + k)^2 (\hat{\lambda}_s + k)} \frac{\partial^3 E}{(\partial r^2)^3}$$
$$+ \tfrac{1}{4} k l_r^2 l_s^2 a_0^4 (1+k)^3 \frac{\hat{\lambda}_s}{(\hat{\lambda}_r + k)^3 (\hat{\lambda}_s + k)} \frac{\partial^2 E}{(\partial r^2)^2} \quad (r, s = 1, 2, 3;\ r \neq s) \tag{25b}$$

$$C_{rst}^N = \tfrac{1}{8} a_0^6 l_r^2 l_s^2 l_t^2 (1+k)^3 \frac{\hat{\lambda}_r \hat{\lambda}_s \hat{\lambda}_t}{(\hat{\lambda}_r + k)(\hat{\lambda}_s + k)(\hat{\lambda}_t + k)} \frac{\partial^3 E}{(\partial r^2)^3}$$
$$(r, s, t = 1, 2, 3;\ r \neq s \neq t) \tag{25c}$$

CC-0. In Public Domain. Gurukul Kangri Collection, Haridwar

Digitized by Arya Samaj Foundation Chennai and eGangotri

$$C^N_{144} = \tfrac{1}{8}a_0^6 l_1^2 l_2^2 l_3^2 (1+k)^3 \frac{\lambda_1(\lambda_2+\lambda_3)^2}{(\lambda_2+\lambda_3+2k)^2(\lambda_1+k)}\frac{\partial^3 E}{(\partial r^2)^3}$$
$$+\tfrac{1}{4}a_0^4 l_1^2 \frac{k(1+k)^3\lambda_1}{(\lambda_1+k)(\lambda_2+\lambda_3+2k)^2}\left\{\frac{l_2^2}{(\lambda_2+k)}+\frac{l_3^2}{(\lambda_3+k)}\right\}\frac{\partial^2 E}{(\partial r^2)^2} \quad (25d)$$

$$C^N_{166} = \tfrac{1}{8}a_0^6 l_1^4 l_2^2 (1+k)^3 \frac{\lambda_1(\lambda_1+\lambda_2)^2}{(\lambda_1+k)(\lambda_1+\lambda_2+2k)^2}\frac{\partial^3 E}{(\partial r^2)^3}$$
$$+\tfrac{1}{4}a_0^4 l_1^2 \frac{k(1+k)^3\lambda_1}{(\lambda_1+k)(\lambda_1+\lambda_2+2k)^2}\left\{\frac{l_1^2}{(\lambda_1+k)}+\frac{l_2^2}{(\lambda_2+k)}\right\}\frac{\partial^2 E}{(\partial r^2)^2}$$
$$-k(1+k)^3\left[\frac{2(\lambda_1+k)+(\lambda_1+\lambda_2+2k)}{(\lambda_1+k)^3(\lambda_1+\lambda_2+2k)^3}\right]p^G_{11} \quad (25e)$$

The derivation of eqs (25) is given in Appendix A2.

Taking $k=0$ in (25), we obtain the third order Green moduli

$$C^G_{rrr} = \tfrac{1}{8}a_0^6 l_r^6 \frac{\partial^3 E}{(\partial r^2)^3} \quad (r=1,2,3) \quad (26a)$$

$$C^G_{rrs} = \tfrac{1}{8}a_0^6 l_r^4 l_s^2 \frac{\partial^3 E}{(\partial r^2)^3} \quad (r,s=1,2,3;\ r\neq s) \quad (26b)$$

$$C^G_{rst} = \tfrac{1}{8}a_0^6 l_r^2 l_s^2 l_t^2 \frac{\partial^3 E}{(\partial r^2)^3} \quad (r,s,t=1,2,3;\ r\neq s\neq t) \quad (26c)$$

$$C^G_{144} = \tfrac{1}{8}a_0^6 l_1^2 l_2^2 l_3^2 \frac{\partial^3 E}{(\partial r^2)^3} \quad (26d)$$

$$C^G_{166} = \tfrac{1}{8}a_0^6 l_1^4 l_2^2 \frac{\partial^3 E}{(\partial r^2)^3}. \quad (26e)$$

And for $k=\infty$, (25) reduces to the third order stretch moduli

$$C^S_{rrr} = 3\lambda_r C^G_{rr} + \lambda_r^3 C^G_{rrr} \quad (r=1,2,3) \quad (27a)$$
$$C^S_{rrs} = \lambda_s C^G_{rs} + \lambda_r^2\lambda_s C^G_{rrs} \quad (r,s=1,2,3;\ r\neq s) \quad (27b)$$
$$C^S_{rst} = \lambda_r\lambda_s\lambda_t C^G_{rst} \quad (r,s,t=1,2,3;\ r\neq s\neq t) \quad (27c)$$
$$C^S_{144} = \tfrac{1}{4}\lambda_1[C^G_{12} + C^G_{13} + (\lambda_2+\lambda_3)^2 C^G_{144}] \quad (27d)$$
$$C^S_{166} = \tfrac{1}{6}\lambda_1[C^G_{11} + C^G_{12} + (\lambda_1+\lambda_2)^2 C^G_{166}]. \quad (27e)$$

Thus we see that in special cases the C^N_{rst} can lead to the G-moduli, C^G_{rst}, and the S- moduli, C^S_{rst}. Moreover, the set of new moduli C^N_{rst} is capable of reproducing any desired set of third order elastic moduli depending upon the choice of k.

6. Energy convexity

The stability criterion was first initiated by Born (1940) which is popularly known as the Born stability condition. It may be taken to be equivalent to the condition

CC-0. In Public Domain. Gurukul Kangri Collection, Haridwar

Digitized by Arya Samaj Foundation Chennai and eGangotri

that the internal energy function 'E' be locally strictly convex in the arguments. In a deformed state the positive definiteness of the quadratic terms in Taylor's expansion of the internal energy

$$\delta E = p_r \delta q_r + \tfrac{1}{2} C_{rs} \delta q_r \delta q_s + \tfrac{1}{6} C_{rst} \delta q_r \delta q_s \delta q_t + \cdots,$$
$$(r, s, t = 1, 2, \ldots 6, \text{ summation convention}) \tag{28}$$

is taken as the stability criterion.

Under the combined effect of second degree and third degree terms, the stability criterion may routinely be expressed as

$$\left(\sum_{r,s=1}^{6} \tfrac{1}{2} C_{rs} \delta q_r \delta q_s + \sum_{r,s,t=1}^{6} \tfrac{1}{6} C_{rst} \delta q_r \delta q_s \delta q_t \right) > 0. \tag{29}$$

For cubic crystal under lod, deformed to orthorhombic structure, we obtain

$$X^S - X^N = \sum_{i,j,k_1=1}^{3} \frac{\lambda_{ii}}{\lambda_{ii} + k} p_{ii}^G \{(\delta\lambda_{ii})^2 + (\delta\lambda_{ij})^2 + (\delta\lambda_{ik_1})^2\} \quad i \neq j \neq k_1 \tag{30}$$

which for $k = 0$ reduces to

$$X^S - X^G = \sum_{i,j,k_1=1}^{3} p_{ii}^G \{(\delta\lambda_{ii})^2 + (\delta\lambda_{ij})^2 + (\delta\lambda_{ik_1})^2\} \quad i \neq j \neq k_1 \tag{31}$$

where N-stability becomes equal to the G-stability. On the other hand for $k = \infty$, right hand side of (30) vanishes and clearly N-strength and S-strength becomes equal to each other.

Let us write the transformation rule for third order elastic constants as

$$C_{uvw}^S \delta q_u^S \delta q_v^S \delta q_w^S - C_{rst}^N \delta q_r^N \delta q_s^N \delta q_t^N$$
$$= C_{rs}^N \left[\frac{\partial^2 q_r^N}{\partial q_u^S \partial q_w^S} \frac{\partial q_s^N}{\partial q_v^S} + \frac{\partial^2 q_r^N}{\partial q_u^S \partial q_v^S} \frac{\partial q_s^N}{\partial q_w^S} + \frac{\partial^2 q_s^N}{\partial q_v^S \partial q_w^S} \frac{\partial q_r^N}{\partial q_u^S} \right]$$
$$\times \delta q_u^S \delta q_v^S \delta q_w^S + p_r^N \frac{\partial^3 q_r^N}{\partial q_u^S \partial q_v^S \partial q_w^S} \delta q_u^S \delta q_v^S \delta q_w^S \tag{32}$$

with the help of (3) and (6), one can calculate the partial derivatives of the right hand side of (32)

$$X^S - X^N = \frac{3}{(1+k)^2} \sum_{i,j,k_1=1}^{3} \{C_{iiii}^N (\lambda_{ii} + k)\delta\lambda_{ii} + C_{iijj}^N (\lambda_{jj} + k)\delta\lambda_{jj}$$
$$+ C_{iik_1k_1}^N (\lambda_{k_1k_1} + k)\delta\lambda_{k_1k_1}\} \{(\delta\lambda_{ii})^2 + (\delta\lambda_{ij})^2 + (\delta\lambda_{ik_1})^2\}$$
$$i \neq j \neq k_1 \tag{33}$$

where X^S and X^N denotes, respectively, the quantities $C_{uvw}^S \delta q_u^S \delta q_v^S \delta q_w^S$ and $C_{rst}^N \delta q_r^N \delta q_s^N \delta q_t^N$.

From (29) and (33) under considered path of loading

$$S - N = \sum_{i,j,k_1=1}^{3} \frac{1}{2(1+k)} \left[\left\{ p_{ii}^N + C_{iiii}^N \frac{(\lambda_{ii} + k)}{(1+k)} \delta\lambda_{ii} \right.\right.$$

CC-0. In Public Domain. Gurukul Kangri Collection, Haridwar

Digitized by Arya Samaj Foundation Chennai and eGangotri

$$+ C^N_{iijj}\frac{(\lambda_{jj}+k)}{(1+k)}\delta\lambda_{jj} + C^N_{iik_1k_1}\frac{(\lambda_{k_1k_1}+k)}{(1+k)}\delta\lambda_{k_1k_1}\Bigg\}$$

$$\{(\delta\lambda_{ii})^2 + (\delta\lambda_{ij})^2 + (\delta\lambda_{ik_1})^2\}\Bigg] i \neq j \neq k_1 \tag{34}$$

where S and N denotes respectively, the crystal strengths relative to the stretch and new variables, when up to third degree terms in the internal energy expansion, (28), is taken into account. If we put the values of p_{ii} and C^N_{rs} in terms of G-moduli, we reproduce the result in terms of Green's and the stretch variables

$$S - N = \sum_{i,j,k_1=1}^{3} \frac{1}{2(\lambda_{ii}+k)}\Bigg[\Bigg\{\lambda_{ii} + \frac{k(1+k)}{(\lambda_{ii}+k)^2}\Bigg\}p^G_{ii}$$
$$+ C^G_{iiii}(\lambda_{ii})^2\delta\lambda_{ii} + C_{iijj}\lambda_{ii}\lambda_{jj}\delta\lambda_{jj}$$
$$+ C_{iik_1k_1}\lambda_{ii}\lambda_{k_1k_1}\delta\lambda_{k_1k_1}\Big]\{(\delta\lambda_{ii})^2 + (\delta\lambda_{ij})^2 + (\delta\lambda_{ik_1})^2\}$$
$$i \neq j \neq k_1 \tag{35}$$

which for $k = 0$ reduces to

$$S - G = \sum_{i,j,k_1=1}^{3} \tfrac{1}{2}[\{p^G_{ii} + C^G_{iiii}\lambda_{ii}\delta\lambda_{ii} + C^G_{iijj}\lambda_{jj}\delta\lambda_{jj} + C_{iik_1k_1}\lambda_{k_1k_1}\delta\lambda_{k_1k_1}\}$$
$$\times\{(\delta\lambda_{ii})^2 + (\delta\lambda_{ij})^2 + (\delta\lambda_{ik_1})^2\} \quad i \neq j \neq k_1 \tag{36}$$

In this case N-strength becomes equal to G-strength. For $K = \infty$, the right hand side of (35) becomes zero and hence, the N-strength becomes equal to S-strength. Equations (35) and (36) together lead to

$$N - G = \sum_{i,j,k_1=1}^{3}\Bigg[\Bigg\{1 - \frac{\lambda_{ii}}{\lambda_{ii}+k} - \frac{k(1+k)}{(\lambda_{ii}+k)^3}\Bigg\}p^G_{ii}$$
$$+ \{C^G_{iiii}\lambda_{ii}\delta\lambda_{ii} + C^G_{iijj}\lambda_{jj}\delta\lambda_{jj} + C^G_{iik_1k_1}\lambda_{k_1k_1}\delta\lambda_{k_1k_1}\}$$
$$\left(1 - \frac{\lambda_{ii}}{\lambda_{ii}+k}\right)\Bigg]\{(\delta\lambda_{ii})^2 + (\delta\lambda_{ij})^2 + (\delta\lambda_{ik_1})^2\} \quad i \neq j \neq k_1 \tag{37}$$

which vanishes for $k = 0$, reduces to (36) for $k = \infty$ and since in these cases N-strength becomes equal to G-strength and S-strength respectively. We consider the case in which the reference cell is a unit cube which under load gets deformed to orthorhombic structure with cell edges parallel to the symmetry axes. Neglecting for a moment, the third order effect, we reproduce (36) as

$$S - G = \sum_{i,j,k_1=1}^{3} \tfrac{1}{2}p^G_{ii}\{(\delta\lambda_{ii})^2 + (\delta\lambda_{ij})^2 + (\delta\lambda_{ik_1})^2\} \quad i \neq j \neq k_1 \tag{38}$$

when only the second order terms are considered. Comparing the co-efficients of $\{(\delta\lambda_{ii})^2 + (\delta\lambda_{ij})^2 + (\delta\lambda_{ik_1})^2\}$ in (36) and (38), we have three equations of the type

$$p^G_r + C^G_{rr}\lambda_r\delta\lambda_r + C^G_{rs}\lambda_s\delta\lambda_s + C^G_{rt}\lambda_t\delta\lambda_t \geqslant p^G_r \tag{39}$$

$(r, s, t = 1, 2, 3; r \neq s \neq t)$; where (ii)$\rightarrow r$, $(jj)\rightarrow s$, $(k_1k_1)\rightarrow t$

CC-0. In Public Domain. Gurukul Kangri Collection, Haridwar

Digitized by Arya Samaj Foundation Chennai and eGangotri

when the crystal is subjected to a uniaxial deformation, let us examine (39). In this particular mode of loading the axial stretch $\lambda_r \neq 1$ whereas the transverse stretches $\lambda_s = \lambda_t = 1$

$$\text{i.e. } \delta\lambda_r \neq 0, \quad \delta\lambda_s = \delta\lambda_t = 0 \quad (r, s, t = 1, 2, 3;\ r \neq s \neq t)$$

Tensile stresses, $\lambda_r > 1$

In this state of loading the existing term $C^G_{rr}\lambda_r\delta\lambda_r$ in (39) is greater than zero, since C^G_{rr} is itself positive and (38) implies that

$$p^G_r + C^G_{rr}\lambda_r\delta\lambda_r > p^G_r.$$

Hence

$$(S - G) > (S' - G').$$

Moreover, in the current state of positive stress, (36) implies that *S*-strength is greater than *G*-strength.

Compressive stresses

For compressive stress $\lambda_r < 1$, exactly reverse situation arises since $\delta\lambda_r$ makes the term $C^G_{rr}\lambda_r\delta\lambda_r$ less than zero.

With similar arguments (36) implies that *S*-strength is less than *G*-strength in negative loading.

Plane dilation

In plane stress where axial stretch $\lambda_r = 1$ and transverse stretches $\lambda_s = \lambda_t \neq 1$, i.e. $\delta\lambda_r = 0$ and $\delta\lambda_s = \delta\lambda_t \neq 0$. $(r, s, t = 1, 2, 3;\ r \neq s \neq t)$.

In the first case of plane dilation, when $\lambda_r = 1$ and $\lambda_s = \lambda_t > 1$ and the SOEC C^G_{rs} and C^G_{rt} are such that the quantities $(C^G_{rs}\lambda_s\delta\lambda_s + C^G_{rt}\lambda_t\delta\lambda_t)$ in (39) becomes greater than zero, then *S*-strength will be greater than the *G*-strength.

Plane contraction

In the second case of plane contraction, when $\lambda_r = 1$ and $\lambda_s = \lambda_t < 1$ and the SOEC C^G_{rs} and C^G_{rt} are such that the quantities $(C^G_{rs}\lambda_s\delta\lambda_s + C^G_{rt}\lambda_t\delta\lambda_t)$ in (39) becomes less than zero, then *S*-strength will be less than *G*-strength.

Under the same loading paths as illustrated above and with the same reference state one may readily compare the relative stabilities in *S*-variables and *N*-variables (or in *G*-variables and *N*-variables) as in (35) or (38).

7. Summary and conclusion

In this paper a new generalized set of strain variables, q^N_r, has been used for the determination of the new set of second order elastic moduli, C^N_{rs}, and third order elastic moduli, C^N_{rst}. The new generalized set of strain variables q^N_r, and the new set of elastic moduli, C^N_{rs} and C^N_{rst}, reduce respectively to Green's co-ordinate, q^G_r, and

CC-0. In Public Domain. Gurukul Kangri Collection, Haridwar

Digitized by Arya Samaj Foundation Chennai and eGangotri

Green's moduli, C^G_{rs} and C^G_{rst}, after taking $k=0$ in (3), (9) and (25) respectively. After taking $k=\infty$ in these equations, the q^N_r, C^N_{rs} and C^N_{rst} reduce, respectively, to the stretch co-ordinates, q^S_r and the stretch moduli C^S_{rs} and C^S_{rst}. Thus the new co-ordinates q^N_r and new elastic moduli C^N_{rs} and C^N_{rst} are the generalization of the corresponding terms derived from Green and stretch variables.

Also the requisite components obtained from the new co-ordinates, have enabled comparision of theoretical strength of the crystals according to the present scale function with the conventional Green-strength used by Born-School, stretch-strength used by Macmillan and Kelly, for cubic crystals deformed to orthorhombic structure.

From comparision, we conclude that

$$G\text{-strength} \leqslant N\text{-strength} \leqslant S\text{-strength}$$

when load is positive definite and k is positive. But when load is positive and k is negative, it is found that

$$S\text{-strength} \geqslant G\text{-strength} \geqslant N\text{-strength}$$

and when $k=-\lambda_1$, or $k=-\lambda_2$, or $k=-\lambda_3$ and $p_1, p_2, p_3 \geqslant 0$ then N-strength $=-\infty$. But when load is negative, i.e. $p_1, p_2, p_3 \leqslant 0$, outstability condition changes to

(i) $G \geqslant S \geqslant N$, for $k>0$
(ii) $N \geqslant G \geqslant S$, for $k<0$

and (iii) when $k=-\lambda_1$, or $k=-\lambda_2$ or $k=-\lambda_3$ and $p_1, p_2, p_3 \leqslant 0$ then N-strength $=+\infty$.

Further we have estimated lattice stability by comparing directly the convexity criteria relative to various choices of strain measures (G-variables, S-variables and N-variables) when up to third degree terms in the energy expansion are considered.

Finally, we present the computational results for a *bcc* iron subjected to hydrostatic compressive and tensile stresses according to the new set of elastic moduli. The results are summarised in figure 1 and table 1 which indicate that all the conventional stable ranges could be generated as the specific cases of our generalized results. However, the conventional stable ranges fail to represent the state of hydrostatic compression of iron, where only the present study can generate realistic results.

Appendix A

Expressions for C^N_{rs}, eq (9), can be derived using (3), (4), (7) and (8). For example, a detailed derivation of the moduli C^N_{11}, C^N_{12} and C^N_{44} is given here. By the definition (8), we have

$$C^N_{11} = \frac{\partial^2 E}{\partial q^N_1 \partial q^N_1} = \frac{\partial}{\partial q^N_1}\left(\frac{\partial E}{\partial q^N_1}\right) = \frac{\partial}{\partial q^N_1}\left(\frac{\partial E}{\partial r^2}\frac{\partial r^2}{\partial a_1}\frac{\partial a_1}{\partial q^N_1}\right). \tag{A1}$$

Now,

$$\frac{\partial r^2}{\partial a_1} = \tfrac{1}{2} l_1^2 a_1$$

CC-0. In Public Domain. Gurukul Kangri Collection, Haridwar

Digitized by Arya Samaj Foundation Chennai and eGangotri

and
$$\frac{\partial q_1^N}{\partial a_1} = \frac{1}{1+k}\left(\frac{\lambda_1 + k}{a_0}\right) \tag{A2}$$

where
$$\lambda_1 = a_1/a_0. \tag{A3}$$

Hence from (A1), (A2) and (A3) we have

$$C_{11}^N = \tfrac{1}{4} l_1^4 a_0^4 (1+k)^2 \left(\frac{\lambda_1}{\lambda_1 + k}\right)^2 \frac{\partial^2 E}{(\partial r^2)^2} + \tfrac{1}{2} k(1+k)^2 \frac{a_0^2 l_1^2}{(\lambda_1 + k)^3} \frac{\partial E}{\partial r^2}. \tag{A4}$$

Similarly we obtain

$$C_{12}^N = \tfrac{1}{4} a_0^4 (1+k)^2 l_1^2 l_2^2 \frac{\lambda_1 \lambda_2}{(\lambda_1 + k)(\lambda_2 + k)} \frac{\partial^2 E}{(\partial r^2)^2}. \tag{A5}$$

Next for C_{44}^N we have from (8)

$$C_{44}^N = \frac{\partial^2 E}{\partial q_4^N \partial q_4^N} = \frac{\partial}{\partial q_4^N}\left(\frac{\partial E}{\partial \lambda_4}\frac{\partial \lambda_4}{\partial q_4^N}\right) = \frac{\partial}{\partial q_4^N}\left(\frac{\partial E}{\partial \lambda_4}\frac{(1+k)}{(\lambda_2 + \lambda_3 + 2k)}\right)$$

or

$$C_{44}^N = \tfrac{1}{4} a_0^4 l_2^2 l_3^2 (1+k)^2 \frac{(\lambda_2 + \lambda_3)^2}{(\lambda_2 + \lambda_3 + 2k)^2} \frac{\partial^2 E}{(\partial r^2)^2}$$
$$+ \tfrac{1}{2} k(1+k)^2 \frac{a_0^2}{(\lambda_2 + \lambda_3 + 2k)^2}\left[\frac{l_2^2}{(\lambda_2 + k)} + \frac{l_3^2}{(\lambda_3 + k)}\right]\frac{\partial E}{\partial r^2} \tag{A6}$$

Appendix B

Expressions for C_{rst}^N, (25), can be derived using (3), (4), (7), (8) and (9). For example a detail derivation of the C_{111}^N, C_{112}^N, C_{123}^N, C_{144}^N and C_{166}^N are given here.

By the definition (25) we have

$$C_{111}^N = \frac{\partial^3 E}{\partial q_1^N \partial q_1^N \partial q_1^N} = \frac{\partial}{\partial q_1^N}\left(\frac{\partial^2 E}{(\partial q_1^N)^2}\right)$$
$$= \frac{\partial}{\partial q_1^N}\left[\tfrac{1}{4}(1+k)^2 a_0^4 l_1^4 \left(\frac{\lambda_1}{\lambda_1 + k}\right)^2 \frac{\partial^2 E}{(\partial r^2)^2}\right.$$
$$\left. + \tfrac{1}{2} k(1+k)^2 \frac{a_0^2 l_1^2}{(\lambda_1 + k)^3}\frac{\partial E}{\partial r^2}\right]$$
$$= \tfrac{1}{4} a_0^4 l_1^4 (1+k)^2 \left[\left(\frac{\lambda_1}{\lambda_1 + k}\right)^2 \frac{\partial^3 E}{(\partial r^2)^3} \tfrac{1}{2} l_1^2 a_1^2 \frac{a_0(1+k)}{\lambda_1 + k}\right.$$
$$+ \frac{\partial^2 E}{(\partial r^2)^2}\left\{(\lambda_1 + k)^2 \frac{2\lambda_1}{a_0}\frac{a_0(1+k)}{(\lambda_1 + k)} - \lambda_1^2 \frac{2(\lambda_1 + k)}{a_0}\frac{a_0(1+k)}{(\lambda_1 + k)}\right\}\Bigg]$$
$$+ \tfrac{1}{2} k(1+k)^2 a_0^2 l_1^2 \left[\frac{1}{(\lambda_1 + k)^3}\frac{\partial^2 E}{(\partial r^2)^2} \tfrac{1}{2} l_1^2 a_1 \frac{a_0(1+k)}{(\lambda_1 + k)}\right.$$

CC-0. In Public Domain. Gurukul Kangri Collection, Haridwar

Digitized by Arya Samaj Foundation Chennai and eGangotri

$$-\frac{3}{(\lambda_1+k)^4}\frac{1}{a_0}\frac{a_0(1+k)}{(\lambda_1+k)}\frac{\partial E}{\partial r^2}\Bigg]$$

$$=\tfrac{1}{8}a_0^6 l_1^6(1+k)^3\left(\frac{\lambda_1}{\lambda_1+k}\right)^3\frac{\partial^3 E}{(\partial r^2)^3}+\tfrac{3}{4}a_0^4 l_1^4\frac{(1+k)^3\lambda_1 k}{(\lambda_1+k)^4}\frac{\partial^2 E}{(\partial r^2)^2}$$

$$-\tfrac{3}{2}k(1+k)^3\frac{a_0^2 l_1^2}{(\lambda_1+k)^5}\frac{\partial E}{\partial r^2}.$$

For C^N_{112}, we have from (25)

$$C^N_{112}=\frac{\partial^3 E}{\partial q_1^N\partial q_1^N\partial q_2^N}=\frac{\partial}{\partial q_1^N}\left(\frac{\partial^2 E}{\partial q_1^N\partial q_2^N}\right)$$

$$=\frac{\partial}{\partial q_1^N}\left[\tfrac{1}{4}l_1^2 l_2^2 a_0^4(1+k)^2\frac{\lambda_1\lambda_2}{(\lambda_1+k)(\lambda_2+k)}\frac{\partial^2 E}{(\partial r^2)^2}\right]$$

$$=\tfrac{1}{4}a_0^4(1+k)^2 l_1^2 l_2^2\Bigg[\frac{\lambda_1\lambda_2}{(\lambda_1+k)(\lambda_2+k)}\frac{\partial^3 E}{(\partial r^2)^3}\frac{\partial r^2}{\partial a_1}\frac{\partial a_1}{\partial q_1^N}$$

$$+\frac{\partial^2 E}{(\partial r^2)^2}\left\{\frac{(\lambda_1+k)(\lambda_2+k)\lambda_2/a_0\dfrac{a_0(1+k)}{(\lambda_1+k)}-\lambda_1\lambda_2(\lambda_2+k)\dfrac{a_0(1+k)}{(\lambda_1+k)}}{(\lambda_1+k)^2(\lambda_2+k)^2}\right\}\Bigg]$$

$$=\tfrac{1}{4}a_0^4(1+k)^2 l_1^2 l_2^2\Bigg[\frac{\lambda_1\lambda_2}{(\lambda_1+k)(\lambda_2+k)}\tfrac{1}{2}l_1^2 a_1\frac{a_0(1+k)}{\lambda_1+k}\frac{\partial^3 E}{(\partial r^2)^3}$$

$$+(1+k)\left\{\frac{\lambda_1\lambda_2+\lambda_2 k-\lambda_1\lambda_2}{(\lambda_1+k)^3(\lambda_2+k)}\right\}\frac{\partial^2 E}{(\partial r^2)^2}\Bigg]$$

$$=\tfrac{1}{8}a_0^6 l_1^4 l_2^2(1+k)^3\frac{\lambda_1^2\lambda_2}{(\lambda_1+k)^2(\lambda_2+k)}\frac{\partial^3 E}{(\partial r^2)^3}$$

$$+\tfrac{1}{4}l_1^2 l_2^2 a_0^4\frac{(1+k)^3 k\lambda_2}{(\lambda_1+k)^3(\lambda_2+k)}\frac{\partial^2 E}{(\partial r^2)^2}.$$

For C^N_{123}, we have from (25)

$$C^N_{123}=\frac{\partial}{\partial q_1^N}\left(\frac{\partial^2 E}{\partial q_2^N\partial q_3^N}\right)=\frac{\partial}{\partial q_1^N}\left[\frac{1}{4}\frac{l_2^2 l_3^2 a_0^4(1+k)^2\lambda_2\lambda_3}{(\lambda_2+k)(\lambda_3+k)}\frac{\partial^2 E}{(\partial r^2)^2}\right]$$

$$=\tfrac{1}{4}a_0^4 l_2^2 l_3^2(1+k)^2\frac{\lambda_2\lambda_3}{(\lambda_2+k)(\lambda_3+k)}\tfrac{1}{2}l_1^2 a_1\frac{a_0(1+k)}{(\lambda_1+k)}\frac{\partial^3 E}{(\partial r^2)^3}$$

$$=\tfrac{1}{8}a_0^6 l_1^2 l_2^2 l_3^2(1+k)^3\frac{\lambda_1\lambda_2\lambda_3}{(\lambda_1+k)(\lambda_2+k)(\lambda_3+k)}\frac{\partial^3 E}{(\partial r^2)^2}.$$

For C^N_{144}, we have from (25)

$$C^N_{144}=\frac{\partial}{\partial q_1^N}\left(\frac{\partial^2 E}{\partial q_4^N\partial q_4^N}\right)$$

$$=\frac{\partial}{\partial q_1^N}\left[\left(\tfrac{1}{4}a_0^4 l_2^2 l_3^2(1+k)^2\left(\frac{\lambda_2+\lambda_3}{\lambda_2+\lambda_3+2k}\right)^2\frac{\partial^2 E}{(\partial r^2)^2}\right)\right.$$

CC-0. In Public Domain. Gurukul Kangri Collection, Haridwar

Digitized by Arya Samaj Foundation Chennai and eGangotri

$$+\tfrac{1}{2}a_0^2\frac{l_2^2k(1+k)^2}{(\lambda_2+\lambda_3+2k)^2(\lambda_2+k)}\frac{\partial E}{\partial r^2}$$

$$+\frac{1}{2}\frac{a_0^2l_3^2(1+k)^2k}{(\lambda_2+\lambda_3+2k)^2(\lambda_3+k)}\frac{\partial E}{\partial r^2}\Bigg]$$

$$=\tfrac{1}{4}a_0^4(1+k)^2l_2^2l_3^2\left[\left(\frac{\lambda_2+\lambda_3}{\lambda_2+\lambda_3+2k}\right)^2\frac{\partial^3E}{(\partial r^2)^3}\tfrac{1}{2}l_1^2a_1\frac{a_0(1+k)}{(\lambda_1+k)}+0\right]$$

$$+\tfrac{1}{2}a_0^2l_2^2k(1+k)^2\,\tfrac{1}{2}\left[\frac{l_1^2a_1a_0(1+k)}{(\lambda_2+\lambda_3+2k)^2(\lambda_1+k)(\lambda_2+k)}\frac{\partial^2E}{(\partial r^2)^2}\right]$$

$$+\tfrac{1}{2}a_0^2l_3^2k(1+k)^2\left[\frac{1}{2}\frac{l_1^2a_1a_0(1+k)}{(\lambda_2+\lambda_3+2k)^2(\lambda_1+k)(\lambda_3+k)}\frac{\partial^2E}{(\partial r^2)^2}\right].$$

Hence

$$C_{144}^N=\tfrac{1}{8}a_0^6l_1^2l_1^2l_3^2\frac{(1+k)^3\lambda_1(\lambda_2+\lambda_3)^2}{(\lambda_2+\lambda_3+2K)^2(\lambda_1+k)}\frac{\partial^3E}{(\partial r^2)^3}$$

$$+\tfrac{1}{4}a_0^4l_1^2\frac{k(1+k)^3\lambda_1}{(\lambda_1+k)(\lambda_2+\lambda_3+2k)^2}\left[\frac{l_2^2}{\lambda_2+k}+\frac{l_3^2}{\lambda_3+k}\right]\frac{\partial^2E}{(\partial r^2)^2}.$$

References

Birch F, 1947 *Phys. Rev.* **71** 809
Born M, 1940 *Proc. Camb. Philos. Soc.* **36** 160
Born M and Furth R 1940 *Proc. Camb. Philos. Soc.* **36** 454
Born M and Misra R D 1940 *Proc. Camb. Philos. Soc.* **36** 466
Brugger K 1964 *Phys. Rev.* **A133** 1611
Furth R 1941 *Proc. Camb. Philos. Soc.* **37** 34
Hill R 1975 *Math. Proc. Camb. Philos. Soc.* **77** 225
Hill R and Milstein F 1977 *Phys. Rev.* **B15** 3087
Macmillan N H and Kelly A 1972a *Proc. R. Soc. London* **A330** 291
Macmillan N H and Kelly A 1972b *Proc. R. Soc. London* **A330** 309
Macmillan N H and Kelly A 1973 *Mater. Sci. Eng.* **12** 79
Milstein F 1971 *Phys. Rev.* **B3** 1130
Milstein F 1973 *J. Appl. Phys.* **44** 3825
Misra R D 1940 *Proc. Camb. Philos. Soc.* **36** 173
Nranyan A A 1964 *Sov. Phys. Solid State* **5** 129
Thakur K P 1982a *Phys. Rev.* **B26** 3001
Thakur K P 1982b *J. Appl. Phys.* **53** 8722
Thakur K P 1985 *J. Phys.* **F15** 2421
Thurston R N and Brugger K 1964 *Phys. Rev.* **A133** 1604

CC-0. In Public Domain. Gurukul Kangri Collection, Haridwar

Digitized by Arya Samaj Foundation Chennai and eGangotri

CC-0. In Public Domain. Gurukul Kangri Collection, Haridwar

Digitized by Arya Samaj Foundation Chennai and eGangotri

Pramāna – J. Phys., Vol. 34, No. 3, March 1990, pp. 217–224. © Printed in India.

Anharmonic effects on lattice resonant modes of impure metallic crystals

S K ROY and N KUNDU
Department of Physics, Visva-Bharati University, Santiniketan 731 235, India

MS received 2 January 1989; revised 28 November 1989

Abstract. The effect of lattice anharmonicity on the resonant modes of dilute impurities for Au–Cu, Au–Ag and W–Cr metallic systems are studied from the poles of the double time temperature dependent impure Green's function of these crystals. The third order force constants used in the present work are derived assuming the systems to obey the Lennard-Jones potential. The inclusion of lattice anharmonicity has been found to increase the resonant frequency which depends upon the mass defect, force constant change parameter and the impurity concentration terms. Some interesting features about the phase shift and the change in width of the vibrational spectrum are reported at room temperature for the isotopic defects and the defects interacting with host atoms. The results are found to be in qualitative agreement with the experiments on the systems considered.

Keywords. Resonant modes; mass defect; force constant; phase shift.

PACS No. 63·20

1. Introduction

In the harmonic approximation, the normal modes of an impure lattice containing a heavy mass impurity consist of resonant mode and a set of other lattice modes. When the resonance occurs at low frequency as a sharp peak in the density of states, it is a reasonable approach to regard the resonance as being in a single mode (Alexander *et al* 1970, Barker and Sievers 1975).

When the potential energy is purely harmonic the spectrum consists of a sharp line at the resonance frequency. When the anharmonic terms are also included this line may shift, broaden and change in strength. In general the anharmonicity would also induce other lines to appear elsewhere in the spectrum. These are side bands and two phonon transitions which overlap the fundamental or the zero lattice phonon (ZLP) line. The effect of temperature on the impurity induced absorption line has been studied by many workers (Svensson *et al* 1965; Behera and Deo 1967; Weber and Siebert 1968). The contribution of anharmonic terms to the broadening and shifting of absorption lines due to impurity modes have also been discussed by many authors (Maradudin *et al* 1971; Bruesch 1982; Roy 1985; Roy and Kundu 1987) specially with reference to high frequency localized modes treating the anharmonic terms by perturbation theory. In the present work we adopt the Green's function technique (Zubarev 1960; Doniach and Sondheimer 1974) to evaluate the anharmonic effects on the lattice resonant modes for various impure metallic systems considering the effects of force constant change and the impurity concentration. Our calculations follow from simple assumption that the only lattice modes coupled to the resonant

CC-0. In Public Domain. Gurukul Kangri Collection, Haridwar

Digitized by Arya Samaj Foundation Chennai and eGangotri

mode could be represented by a Debye spectrum. This assumption, although was able to explain the width and shift data, where it was found that only low frequency lattice modes were effectively coupled to the resonant modes, gives only qualitative results on the changes in width and shift.

2. Theory

In the present work we propose to study the impurity resonant modes assuming the host atoms to obey the Lennard-Jones potential for simple cubic lattices containing impurities of mass M' which replace the host atoms of mass M.

The Hamiltonian of the impure system in second quantized notation using the well known normal mode transformations (Maradudin *et al* 1971) can be written as

$$H = \hbar \sum_k \omega_k a_k^\dagger a_k + \hbar \sum_{k,q} U(k,q) B_k B_q + \hbar \sum_{k,q} V(k,q) A_k A_q + \hbar \sum_{k,q,p} V'(k,q,p) A_k A_q A_p \tag{1}$$

where A_k and B_k are phonon field and momentum operators which can be written in terms of phonon creation and annihilation operators $a_k^\dagger$, a_k (Roy 1985) and

$$U(k,q) = \frac{\lambda}{4N} \sum_{\alpha,l=1}^{N_d} e_\alpha(k) e_\alpha(q) [\omega_k \omega_q]^{1/2} \exp[i(\mathbf{k}+\mathbf{q})\cdot\mathbf{R}_l] \tag{2}$$

$$V(k,q) = \frac{\tau}{4N} \sum_{\alpha,l=1}^{N_d} e_\alpha(k) e_\alpha(q) [\omega_k \omega_q]^{1/2} \exp[i(\mathbf{k}+\mathbf{q})\cdot\mathbf{R}_l] \tag{3}$$

$$V'(k,q,p) = \frac{\lambda'}{4N} \sum_{\alpha,l=1}^{N} \frac{e_\alpha(k) e_\alpha(q) e_\alpha(p)}{[\omega_k \omega_q \omega_p]^{1/2}} \exp[i(\mathbf{k}+\mathbf{q}+\mathbf{p})\cdot\mathbf{R}_l] \tag{4}$$

where λ and τ are mass and force constant change parameters which can be given as

$$\lambda = (1 - M/M') \tag{5a}$$

$$\tau = \frac{\phi''(i) - \phi''(0)}{\phi''(0)} \tag{5b}$$

and

$$\lambda' = \frac{\phi'''(0)}{3M} (\hbar/2MN)^{1/2}. \tag{5c}$$

Here $\phi''(i)$, $\phi''(0)$ and $\phi'''(0)$ represent the nearest neighbour impurity-host, host-host second order force constants and host-host third order force constant respectively.

It may be noted that in writing (4) we have neglected the anharmonic contribution arising due to impurity part of the potential for it will be negligibly small. The information about the impurity modes can be obtained from the denominator of the fourier transformed impurity Green's function in the matrix form (Tripathi and Behera 1974).

$$\mathbf{G}_{k,q}(\omega) = \delta_{k,-q} G_k^{(0)}(\omega) + \delta_{k,-q} \mathbf{G}_k^{(0)}(\omega) \sum_h \chi(-k,h) \mathbf{G}_{h,q}(\omega) \tag{6}$$

CC-0. In Public Domain. Gurukul Kangri Collection, Haridwar

Digitized by Arya Samaj Foundation Chennai and eGangotri

where $G_k^{(0)}(\omega)$ is the unperturbed Green's function and $\chi(-k, h)$ is the kernel in matrix form (Roy and Kundu 1987). The matrix Green's function can be written in the characteristic form of Dyson's equation by iteration of (6) as (Doniach and Sondheimer 1974)

$$\mathbf{G}_{k,q}(\omega) = \delta_{k,-q}\mathbf{G}_k^{(0)}(\omega) + \delta_{k,-q}\mathbf{G}_k^{(0)}(\omega)\mathbf{\Lambda}(\omega)\mathbf{G}_k^{(0)}(\omega) \tag{7}$$

where $\Lambda(\omega)$ is the modified vertex function given by

$$\Lambda(\omega) = \sum_k \chi(-k, k)[\hat{1} - \mathbf{G}_k^{(0)}(\omega)\chi(-k, h)]^{-1}. \tag{8}$$

3. Impurity resonant modes

For random non interacting impurities at the lattice sites, the Green's function (7) has to be averaged over all possible configurations of the impurities. Following the Langer's method (1961) for averaging of the vertex function in (8) and then solving (7) we get

$$\langle G_{k,q}(\omega)\rangle = \frac{G_k^{(0)}(\omega)}{[\hat{1} - \langle \Lambda q\rangle G_k^{(0)}(\omega)]}. \tag{9}$$

The physically measurable quantities are related to the imaginary part of the impure Green's function $\langle G_{k,q}(\omega + i\varepsilon)\rangle$: which usually gives the observed line shape—a peak distribution around a frequency $\omega = \omega_k$. The impurity modes can be determined by equating to zero the real part of the denominator of (9) considering the cubic anharmonic part and the effect of concentration of the defects in addition to mass and force constant changes. It may be noted that for dilute impurity case we only consider up to the terms linear in concentration ($C_d = N_d/N$) where N_d is the number of impurities in N number of hosts. The ratio of the impurity resonant frequency to the Debye frequency ($\omega_R/\omega_D = X$) may be obtained from the following

where
$$f_h(x) + f_{ch}(x) + f_{h'}(x) + f_{ch'}(x) = (1-\lambda)(1+\tau) \tag{10}$$

$$f_h(x) \simeq 3x^2(\lambda - \tau + \tfrac{5}{4}\lambda\tau) - 3x^3[\tfrac{1}{2}(\lambda - \tau) + \lambda\tau]\ln\left(\frac{1+x}{1-x}\right) \tag{11a}$$

$$f_{ch}(x) \simeq \tfrac{9}{5}(\tau^2 + \lambda^2)C_d\left[1/3 + 2x^2 + \tfrac{7}{4}x^3\ln\left(\frac{1+x}{1-x}\right)\right] - 2\lambda\tau C_d\left[x^2 - \tfrac{3}{4}x^3\ln\left(\frac{1+x}{1-x}\right)\right] \tag{11b}$$

$$f_{h'}(x) \simeq k_\beta T(1-\lambda/3)K\left[\frac{(1-\lambda)}{48} + \frac{(5-7\lambda)}{96}x^2 - \frac{\lambda}{32}x^3\ln\left(\frac{1+x}{1-x}\right)\right] \tag{11c}$$

where
$$f_{ch'}(x) \simeq k_\beta T(1-\lambda/3)K\lambda(1+C_d)x^2$$

$$K = [\phi'''^2_{(0)}/\phi''^3_{(0)}].$$

CC-0. In Public Domain. Gurukul Kangri Collection, Haridwar

Digitized by Arya Samaj Foundation Chennai and eGangotri

The third order force constant appearing in (11c) and (11d) may be obtained by choosing a suitable potential for the system. In this work the third order force constant is evaluated from elastic constants and Bulk modulii using the Lennard-Jones potential for the host impurity systems mentioned, as has been done earlier (Dobrzynski and Maradudin 1973). Equations (11a, b, c, d) represent the harmonic, harmonic with effect of impurity concentration, anharmonic and anharmonic with effect of impurity concentration terms respectively. The above equations together may therefore be taken as the general expression for the impurity resonant mode solution. Equation (11a, b) for isotopic defect ($\tau = 0$) together lead to a well known result (Behera and Deo 1967) on the resonant frequency in the limit of long wave length phonons

$$X^2 \simeq \frac{1 - \frac{3}{5} C_d \lambda \varepsilon}{3\varepsilon(1 + \frac{6}{5}\lambda C_d)} \tag{12}$$

where

$$\varepsilon = \lambda/(1 - \lambda).$$

The consideration of the impurity concentration therefore reduces the resonant frequency of the heavy impurities vibrating in light hosts.

4. Frequency shift and the line width

The frequency shift $\Delta(\omega)$ and the line width $\Gamma(\omega)$ are evaluated from (9) by separating the real and imaginary parts and are given by the following expressions (Fetter and Walecka 1971)

$$\Delta(\omega) = \frac{[1 - \mathrm{Re}\, D_k(\omega + i\varepsilon)]}{[1 - \mathrm{Re}\, D_h(\omega + i\varepsilon)]^2 + [\mathrm{Im}\, D_h(\omega + i\varepsilon)]^2} \tag{13}$$

and

$$\Gamma(\omega) = \frac{2|\mathrm{Im}\, D_k(\omega + i\varepsilon)|\omega = \omega_R}{\left|\frac{\mathrm{d}}{\mathrm{d}\omega}[1 - \mathrm{Re}\, D_k(\omega + i\varepsilon)]\right|_{\omega = \omega_R}} \tag{14}$$

for heavier impurities in lighter solids, the resonant modes lie within the maximum frequency of the host crystal. Although the Debye approximation fails for band edge resonance, one can compare the low frequency resonant modes with the Debye cut off frequency using the Debye approximation for the host. Within the bands of the allowed frequencies of the host crystal the singular points in the frequency spectrum of three dimensional crystal occur and depending upon the impurity mass, the bond shortening and the impurity concentration a critical frequency can be defined at which the frequency spectrum itself is continuous. The typical values of the ratio of line width to the Debye cut off frequency at resonance without and with anharmonicity are 0·30 and 0·312 for Au–Cu system with impurity concentration $C_d = 0{\cdot}93$ At. % and $\tau = 0{\cdot}45$. The τ and ω_D values in our calculations have been selected from the reported results of Grow *et al* 1978 (for Au–Cu, $\omega_D = 2{\cdot}078 \times 10^{13}$ rad/s). At very low frequency the half width goes to zero and the resonance degenerates into a delta function. For the resonance near the band edge the spectrum of mode gives a finite width because of large damping effect whereas above the maximum frequency the

CC-0. In Public Domain. Gurukul Kangri Collection, Haridwar

Digitized by Arya Samaj Foundation Chennai and eGangotri

modes become localized. Many workers (Maradudin 1966; Elliott *et al* 1965) suggested that the resonant mode properties are influenced by lattice anharmonicity to a much larger extent than the local modes. The contribution of the local anharmonicity is neglected from the fact that the local anharmonicity appears as due to the change in third order force constant which has been found to be much smaller than the lattice anharmonicity. Although the contribution of the quartic anharmonic term to the line width and shift would have given a better physical result but because of problems of decoupling the impure Green's function and involvement of heavy computation, the contribution of quartic term to the width and shift are not considered in the present case (Jindal and Kalus 1983).

5. Discussion

The effects of inclusion of anharmonic terms in the potential energy, to the broadening and shifting of the absorption lines due to localized and resonant modes have been widely discussed particularly with reference to high frequency localized modes for ionic crystals (Maradudin 1966; Lowndes 1972). The present calculations are performed for impure metallic crystals where the impurity masses and the impurity-host force constant changes are such that the impurities generate the resonant modes.

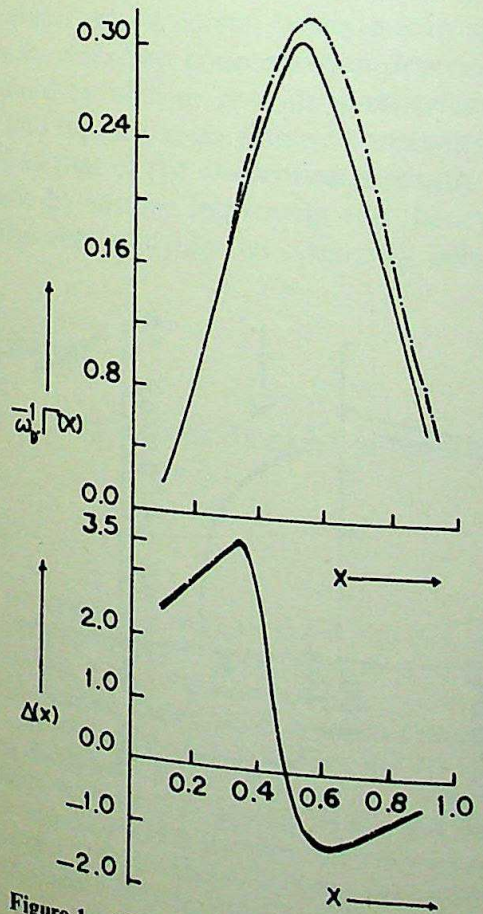

Figure 1. Plot of resonant width and shift for Au–Cu System ($\lambda = 0{\cdot}68$, $\tau = 0{\cdot}45$ and $K = 0{\cdot}18 \times 10^{14}$ erg^{-1}, $C_d = 0{\cdot}93$ At. %). (——) Harmonic effect; (–·–·–) total effect including anharmonicity.

CC-0. In Public Domain. Gurukul Kangri Collection, Haridwar

Digitized by Arya Samaj Foundation Chennai and eGangotri

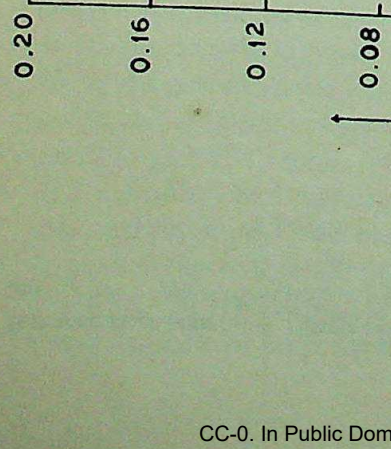

Figure 2. Curves showing the variations of width and shift for Au–Ag System ($\lambda = 0{\cdot}45$, $\tau = 0{\cdot}47$ and $K = 0{\cdot}17 \times 10^{14}\ erg^{-1}$, $C_d = 1{\cdot}0$. At. %). (——) Harmonic effect; (–·–·–) Total effect including anharmonicity.

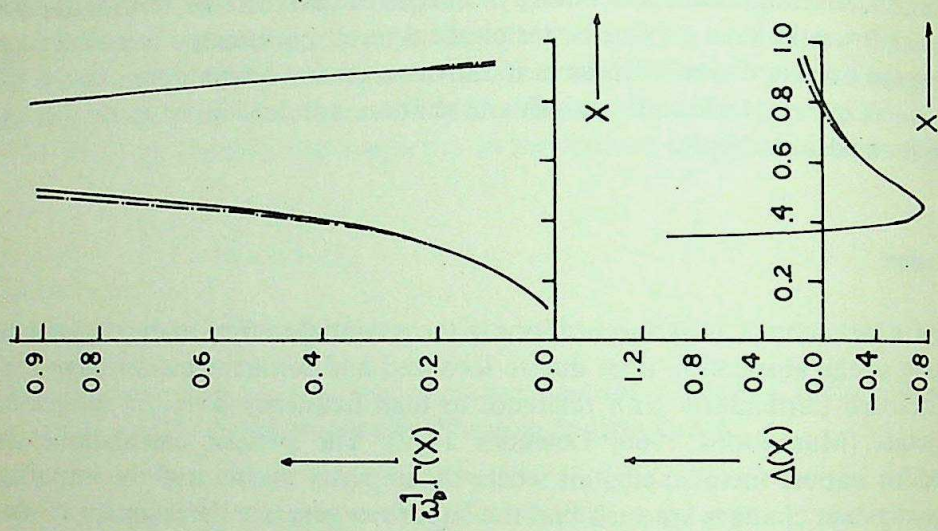

Figure 3. Variations of resonant width and shift for W–Cr System ($\lambda = 0{\cdot}72$, $\tau = 0$ and $K = 0{\cdot}16 \times 10^{14}\ erg^{-1}$, $C_d = 0{\cdot}3$ At. %). (——) Harmonic effect; (–·–·–) Total effect including anharmonicity.

CC-0. In Public Domain. Gurukul Kangri Collection, Haridwar

Digitized by Arya Samaj Foundation Chennai and eGangotri

The resonance frequency values are obtained by solving (10) numerically with the help of (11a-d). The numerical results obtained for three systems Au-Cu, Au-Ag and W-Cr are shown in figures 1 to 3. The results shown for the line widths in different systems are in qualitative agreement with those reported earlier (Svensson *et al* 1965). The inclusion of anharmonic term and the impurity concentrations significantly change the resonant frequencies in different Debye solids which may be attributed to the damping of resonant modes. The damping may be given by the shift of the maxima in each case from the resonance point. The widths corresponding to resonance are represented by the dotted lines in the curves. It is interesting to note that the effect of inclusion of anharmonic term shifts both the line width and the frequency shift to the higher side.

We therefore conclude from calculations on lattice anharmonic effects of the resonant frequency of the impure metallic systems for a definite small concentration of impurity in a metallic system that the anharmonic term increases the line width by a considerable amount and lowers the resonant frequency and also depends on the impurity concentration. Also there is a phase shift between the host and the impurity motion which alters the width of the vibrational spectra. The shift depends on the mass and force constant parameters.

However the correct temperature dependence of these metallic crystals can be obtained and compared with the experimental data by considering a rather real crystal potential with impurity-impurity interactions. At large impurity concentration one has in general a mixed crystal behaviour in which the characteristic absorption of mixed crystals will show concentration dependence. Therefore the theory on impure crystals should be able to provide a criterion to predict one, two or mixed mode behaviour and reproduce the correct concentration dependence of the mode frequencies as well as that of the absorption strength. However, a quantitative comparison can be made by further improving the theory introducing proper metallic crystal potential and also applying the symmetry behaviours of the crystals.

Acknowledgement

One of the authors (NK) is thankful to the CSIR for the financial support.

References

Alexander R W, Hughes A E and Sievers A J 1970 *Phy. Rev.* **B1** 1963
Barker Jr A S and Sievers A J 1975 *Rev. Mod. Phys.* **47** Suppl. 2, 1
Behera S N and Deo B 1967 *Phys. Rev* **153** 728
Bruesch P 1982 *Phonons: Theory and Experiments I* (Berlin: Springer-Verlag) Vol. 34 p. 153
Dobrzynski L and Maradudin A A 1973 *Phys. Rev.* **B7** 1207
Doniach S and Sondheimer E H 1974 *Green's function for solid state Physics* (London: Benjamin) p. 10
Elliott R J, Hayes W, Jodes G D, Macdonald H F and Senett C T 1965 *Proc. R. Soc. (London)* **A289** 1
Fetter A L and Walecka J D 1971 *Quantum theory of many particle systems* (New York: McGraw Hill) p. 119
Grow J M, Howard D G, Nussbaum R H and Takeno M 1978 *Phys. Rev.* **B17** 15
Jindal V K and Kalus J 1983 *J. Phys.* **C16** 3061
Langer J S 1961 *J. Math. Phys.* **2** 584
Lowndes R P 1972 *Phys. Rev.* **B6** 1
Maradudin A A 1966 *Solid State Phys.* (New York: Academic Press) Vol. 19

Figure 2. Curves showing the variations of width and shift for Au–Ag System ($\lambda = 0{\cdot}45$, $\tau = 0{\cdot}47$ and $K = 0{\cdot}17 \times 10^{14}$ erg^{-1}, $C_d = 1{\cdot}0$. At. %). (——) Harmonic effect; (– – –) Total effect including anharmonicity.

Figure 3. Variations of resonant width and shift for W–Cr System ($\lambda = 0{\cdot}72$, $\tau = 0$ and $K = 0{\cdot}16 \times 10^{14}$ erg^{-1}, $C_d = 0{\cdot}3$ At. %). (——) Harmonic effect; (– – –) Total effect including anharmonicity.

CC-0. In Public Domain. Gurukul Kangri Collection, Haridwar

Digitized by Arya Samaj Foundation Chennai and eGangotri

Maradudin A A, Montroll E W, Wiess G H and Ipatova I P 1971 *Solid State Phys.* (New York: Academic press) Suppl. 3 396
Roy S K 1985 *Pramāṇa – J. Phys.* **24** 773
Roy S K and Kundu N 1987 *J. Phys.* **F17** 1051
Svensson E C, Brockhouse B N and Rowe J M 1965 *Solid State Commun.* **3** 245
Tripathi R S and Behera S N 1974 *J. Phys.* **C7** 4470
Weber R and Siebert F 1968 *Z. Physik* **213** 273
Zubarev D N 1960 *Sov. Phys.-Usp.* **3** 320

CC-0. In Public Domain. Gurukul Kangri Collection, Haridwar

Digitized by Arya Samaj Foundation Chennai and eGangotri

Pramāṇa – J. Phys., Vol. 34, No. 3, March 1990, pp. 225–233. © Printed in India.

The Young–Hoshino pseudopotential for lithium: calculations of structure and thermodynamics

T DAS and R N JOARDER
Department of Physics, Jadavpur University, Calcutta 700032, India

MS received 11 September 1989

Abstract. The recently proposed Young–Hoshino model pseudopotential for lithium has been applied to the calculation of structure and thermodynamics. A slight modification of the model potential is necessary and this produces better core size and long range tail of the interionic effective pair potential than the original model.

Keywords. Lithium; pseudopotential; structure; thermodynamics.

PACS No. 61·25

1. Introduction

In the study of physical properties of metals and alloys it is normally required to choose a pseudopotential either in local or non-local form. Lithium is an important exception where the simple pseudopotentials are less successful and therefore this metal plays a role in the research of metals and alloys particularly in the area of liquid alloys (Alblas *et al* 1984; van der Lugt and Geertsma 1984; Ruppersberg and Reiter 1982). Based on physical ideas stronger than those used for constructing local pseudopotentials, Hoshino and Young (1986) proposed a local pseudopotential for Li which after consistent parametrisation have virtues of non-local pseudopotential and produces some of the basic features of metallic Li. This pseudopotential is, however, not suitable for computing atomic properties. We, therefore slightly modify the pseudopotential, based again on physical grounds, and show that better consistencies are thereby brought in the size of the core and tail of the effective interionic potential. We then compute the structure and the thermodynamics of liquid Li through the standard perturbation techniques.

2. Analysis of the model

2.1 *Young–Hoshino (YH) pseudopotential for Li*

Hoshino and Young (1986) proposed a realistic pseudopotential for Li which makes a full self-consistent field potential valid for all electrons and pseudise for s-scattering by introducing a repulsive δ-function located at the origin. Thus in real space,

$$v(r) = v_{\mathrm{HXC}}(r) + \beta\delta(r), \tag{1}$$

CC-0. In Public Domain. Gurukul Kangri Collection, Haridwar

Digitized by Arya Samaj Foundation Chennai and eGangotri

In the q-space the bare ion potential becomes

$$v(q) = -(4\pi Ze^2/q^2)\{3-2(2\alpha)^4/[(2\alpha)^2+q^2]^2 + 2\Gamma\gamma q^2/[q^2+\gamma^2]^2[1+D\exp(-\lambda q^2)] - \beta q^2/4\pi\}, \quad (2)$$

where α, γ, Γ, D and λ are the constants in the full Hartree field (described accurately using exponential form of Slater 1s orbitals) corrected for exchange and correlation in a local density approximation and are obtained as described by Hoshino and Young. The strength parameter $\beta \sim 24$–26 was chosen to describe most of the properties discussed. The electron-ion form factor is given by

$$u(q) = v(q)/\varepsilon(q), \quad (3)$$

where $\varepsilon(q)$ is the appropriate dielectric function of the electron gas. With Ichimaru-Utsumi (1981) local field correction this gives features near $q = 2k_F$, that can be obtained for Li by elaborate non-local pseudopotential calculations (Meyer and Young 1965; Taylor 1982) (figure 1). It produces good liquid resistivity through Ziman formula using experimental structure factor. It is also somewhat in agreement with highly qualitative band gap measurements.

It is, however, to be noted that the form factor takes the form of Harrison's point

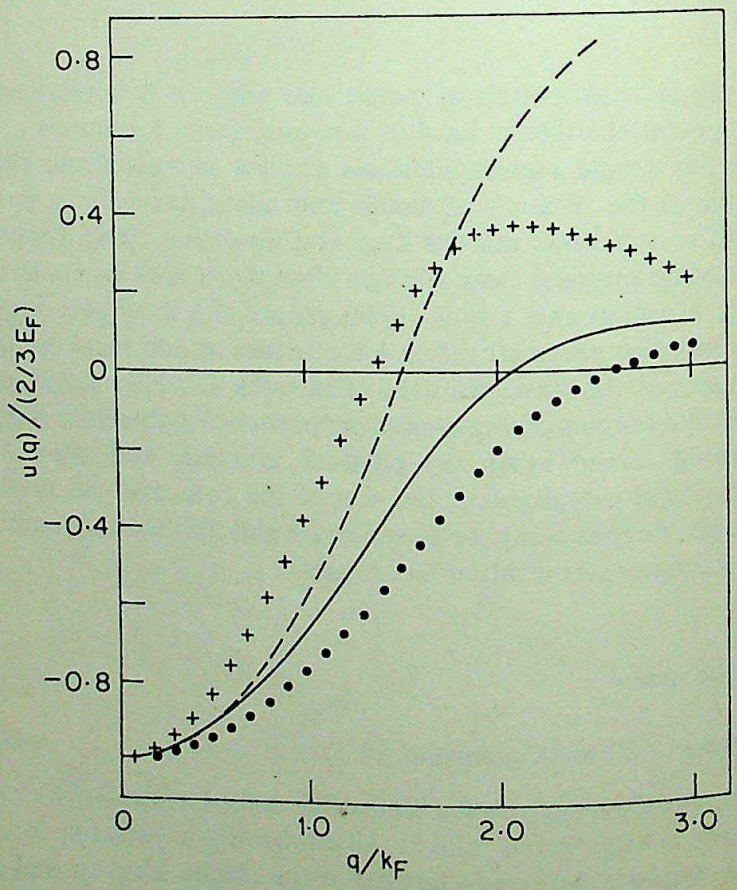

Figure 1. Electron-ion form factor for Li. (- - -) YH model with $\beta = 26$. (——) Modified YH model with $\beta = 26{\cdot}3$ and $r_b = 0{\cdot}44$ au. (···) Ashcroft model with ionic core radius $r_c = 1{\cdot}06$ au (+ + +) Ashcroft model with ionic core radius $r_c = 2{\cdot}00$ au.

CC-0. In Public Domain. Gurukul Kangri Collection, Haridwar

Digitized by Arya Samaj Foundation Chennai and eGangotri

ion model (Harrison 1966) at large q and does not drop to zero at large q as a true form factor is expected to do. This makes the potential unsuitable for computing the atomic properties. The high q values of the form factor decide the core part of the intermolecular interaction and this primarily decides the structure. So, for the calculation of atomic properties, we slightly modify YH pseudopotential at large q based on physical arguments. This brings out, as we shall see later, better consistencies in the size of the core and the tail of the effective pair potential than the original model.

To obtain reasonable values of the form factor at high q we note that the repulsion arising from the conduction electrons are excluded from the core essentially because of the Pauli's principle. This effect has a range r_b ($\sim$ Bohr radius) and may be assumed to fall off exponentially. More specifically, we consider the general Austin–Heine–Sham form (1962) for the unscreened pseudopotential given by

$$\langle \mathbf{k}+\mathbf{q}|v|\mathbf{k}\rangle = \langle \mathbf{k}+\mathbf{q}|v_{\mathrm{HXC}}|\mathbf{k}\rangle + \sum_t \mathbf{f}(\mathbf{k},t)\langle \mathbf{k}+\mathbf{q}|t\rangle\langle t+\mathbf{k}\rangle. \tag{4}$$

The decay of repulsive term at large q comes from the corresponding decay of $\langle \mathbf{k}+\mathbf{q}|t\rangle$. The leading term in a series for $\langle \mathbf{k}+\mathbf{q}|t\rangle$ in $1/q$ will come from the term in the s-state core functions proportional to $\exp(-r/r_b)$, where r_b is a constant. The leading term of $\langle \mathbf{k}+\mathbf{q}|t\rangle$ will take the form

$$\langle \mathbf{k}+\mathbf{q}|t\rangle \propto \int (\sin qr/qr)\exp(-r/r_b)4\pi r^2\,\mathrm{d}r$$

$$\propto 1/[1+(qr_b)^2]^2.$$

This suggests that the last term in the bracket of (2) is modified by $(q^2/4\pi)/(1+q^2r_b^2)^2$. We shall use this simply modified form of YH pseudopotential to study structure and thermodynamic properties of lithium. Clearly, $r_b = 0$ recovers the original model. We use $\beta \sim 26{\cdot}3$ in close agreement with the original model and r_b has been chosen so as to produce a good structure factor peak. This choice of r_b is also in accord with the effective interionic potential. However, some adjustments of r_b is necessary for calculations like electron transports and thermodynamics which is not unexpected for a local model potential (Ashcroft and Langreth 1967).

2.2 *Effective ion–ion potential*

The effective ion–ion potential is given by

$$\Phi(r) = Z^2/r + 1/(2\pi)^3 \int F(q)(\sin qr/qr)4\pi q^2\,\mathrm{d}q, \tag{5}$$

where, Z is the valence (1 for Li) and the energy wave number characteristic, $F(q)$ is given by

$$F(q) = q^2/4\pi(1/\varepsilon(q)-1)v^2(q),$$

where, $\varepsilon(q)$ is the dielectric function given by

$$\varepsilon(q) = 1 + (4\pi/q^2)\chi(q)/[1-(4\pi/q^2)G(q)\chi(q)], \tag{6}$$

with $\chi(q) = (k_F/\pi^2)(1/2 + (1-x)/4x \ln|(1+x)/1-x)|$, $x = q/2k_F$ and $G(q)$ is the local field correction of Ichimaru and Utsumi (1981).

CC-0. In Public Domain. Gurukul Kangri Collection, Haridwar

Digitized by Arya Samaj Foundation Chennai and eGangotri

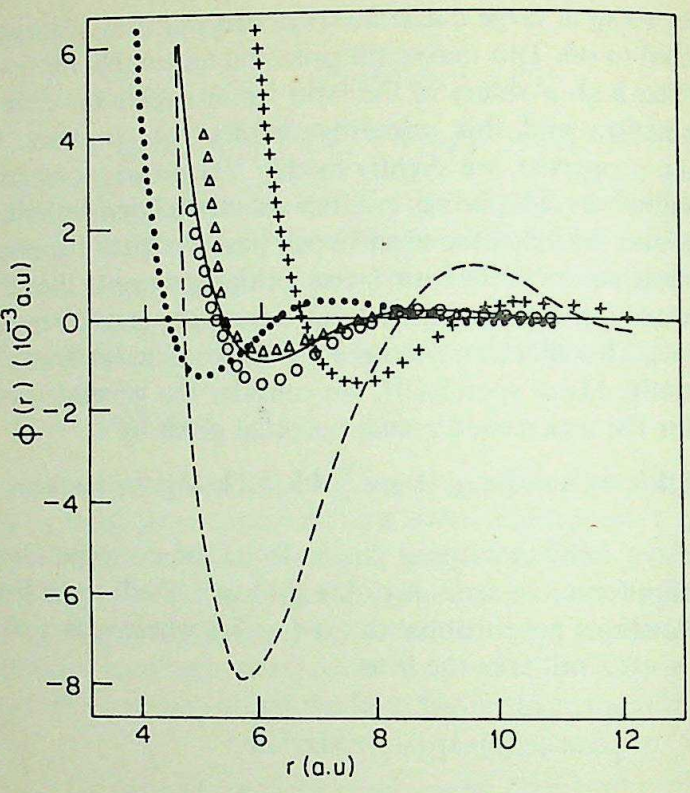

Figure 2. Effective interionic potential for Li. (- - -) as in figure 1. (——) as in figure 1. (○○○) Fully non-local pseudopotential of Day *et al* (1979) (△△△) $-c(r)k_BT$ from calc. $S(q)$, (···) and (+ + +) as in figure 1.

In figure 2 we show the effective interionic potential for Li with $r_b = 0{\cdot}44$ au. The effective potential corresponding to the original YH potential is also shown. Although the position of the first minimum is more or less unaffected, the depth of the potential is considerably reduced. For comparison we give the effective pair potential calculated from a fully first principle non-local pseudopotential of Day *et al* (1979). Clearly this slightly modified YH form agrees better with this than the original YH model. We have also obtained $\Phi(r)$ for large r from the calculated structure factor $S(q)$ through the mean spherical approximation (MSA) relation $\Phi(r) = -k_BTc(r)$, where $c(r)$ is the direct correlation function (DCF) obtained from $S(q)$. This relation is known to be very accurate for large r (Barker and Gaskell 1975). The potential so generated from the calculated $S(q)$ compares well with the $\Phi(r)$ obtained from the model pseudopotential. This is surely a consistency check and choice of r_b is therefore justified. We have not given the corresponding MSA potential from experimental $S(q)$ data because of uncertainties in the low q data of $S(q)$ and $c(r)$ known to be very sensitive to these data. It is however to be noted that the MSA $\Phi(r)$ from experimental $S(q)$ is much better in agreement with the present $\Phi(r)$ than with the original model $\Phi(r)$. $\Phi(r)$ from Ashcroft model with the same screening function but different ionic core radii (fitted to resistivity through Ziman formula, $r_c = 1{\cdot}06$ au and $2{\cdot}00$ au) are also shown, but none agree with the Day *et al* potential.

It is to be noted that the form factor for $r_b = 0{\cdot}44$ au has somewhat different form from $q = k_F$ onwards (figure 1). It corresponds to a band gap considerably less than that from positron-annihilation measurement but these experimental data are highly qualitative (Donaghy and Stewart 1967). The precise quantitative status of the Ziman

CC-0. In Public Domain. Gurukul Kangri Collection, Haridwar

Digitized by Arya Samaj Foundation Chennai and eGangotri

formula for resistivity is also not known. The calculated resistivity and thermoelectric power are 11 μohm cm and 8·6 μ V/° respectively against the experimental values of 24 μ ohm cm and 22 μ V/°. Somewhat smaller value of r_b ($\sim$0·3 au) will improve these values and also the band gap almost in agreement with experiment. In the original model the thermoelectric power, however, comes out to be negative. There have been a variety of form factors for Li and some, for example, Soma (1979), Popovic *et al* (1971), have the forms similar to this modified form and produce very good bulk modulus, cohesive energy, etc. for Li. The form factor which gives elaborate non-local character is in no way better in these calculations.

2.3 *Core size and tail of the potential*

From the effective interionic potential we estimate the effective hardcore diameter, σ for liquid-state ionic collisions using the Ashcroft–Langreth prescription (1967)

$$\Phi(\sigma) - \Phi_{\min} = 3/2k_BT, \tag{7}$$

where, $\Phi_{\min}$ is the minimum of the potential $\Phi(r)$. The relation (7) is known to be quite accurate near the melting point (Hafner 1977; Das *et al* unpublished work). The values of σ, packing fraction $\eta = \pi n\sigma^3/6$, n being the mean ion density, hard sphere structure factor at long wave limit, $S_{hs}(0)$ (through PY equation (Waseda 1980)), excess entropy, S^{ex}/k_B (through Carnahan and Starling equation (Waseda 1980)) are displayed in table 1. The observed structure factors lead us to expect a packing fraction of about 0·43 at $T = 573$ K which is in good agreement with the one obtained from (7) (at m.p. 453 K, it is $\sim$0·46, (Waseda 1980)). Obviously, both $S_{hs}(0)$ and S^{ex}/k_B are reasonable. The original YH potential produces at $T = 453$ K with $\beta = 26$ (best β from core and tail analysis (Hoshino and Young 1986), core size $\sigma = 5{\cdot}15$ and $\eta = 0{\cdot}47$ which

Table 1. Atomic properties of liquid Li at 573 K.

Through core analysis based on AL prescription					Through ORPA caln. of $S(q)$ in long wave limit					
		$\beta = 26{\cdot}3$			$r_b = 0{\cdot}44$ au					
		$-S^{ex}/k_B$					$S(0)$		$\chi_T \times 10^{-11}$ m^2 N	
η	σ(au)	$S_{hs}(0)$	Calc.	Obs.	η	σ(au)	Γ	Calc.	Obs.	Calc.	Obs.
0·42	5·0	0·033	3·42	3·61	0·43	5·1	110	0·03	0·031	8·67	8·69

Through the thermodynamic variational calculation
$\beta = 26{\cdot}3$ $r_b = 0{\cdot}65$ au

η	Γ	Excess entropy $-S^{ex}/k_B$		*Sp. ht. at const. vol. C_V/k_B		Internal energy $-E$(au)	
		Calc.	Obs.	Calc.	Obs	Calc.	Obs.
0·43	90	3·40	3·61	3·40	3·40	0·29	0·26

*In the calculation of charge part, the term containing $(\partial\eta/\partial T)_V$ is neglected since $(\partial\eta/\partial T)_V \ll (\partial\Gamma/\partial T)_V$.

CC-0. In Public Domain. Gurukul Kangri Collection, Haridwar

Digitized by Arya Samaj Foundation Chennai and eGangotri

appears not very unreasonable (through $S_{hs}(0) = 0{\cdot}014$ considerably smaller and $S^{ex}/k_B = -4{\cdot}33$ considerably bigger compared to experimental values). $\beta = 24$ which was the best estimate from band gap considerations, however, does not give good core size and tail of the potential. Ashcroft potentials for $r_c = 1{\cdot}06$ au and $2{\cdot}00$ au, however fail this core analysis (Hoshino and Young 1986).

The overall tail in the present case is quite reasonable. This contention is supported by our calculation of isothermal compressibility (χ_T) in the longwave (LW) limit of structure factor $S(0)$. The tail of the original YH potential was clearly exaggerated because it produces $S(0)$ and hence χ_T in the RPA with $\beta = 26$ considerably larger in magnitude than the observed value. A slightly bigger value of β could give good $S(0)$ and χ_T but corresponding σ and η would be unrealistic. Obviously no Ashcroft potential will suffice in this test (with a choice of arbitrary r_c) as pointed out by Hoshino and Young (1986).

2.4 *Structure factor*

The calculation of structure factor based on this simply modified form of YH potential is surely an interesting exercise. Information about the core is obtainable from the large q behaviour while the small q-behaviour (and at $q = 0$) gives information about the tail of the potential. So the generation of good structure factors in the entire momentum space shows the correctness of the effective interionic potential. Now, various perturbative schemes e.g. WCA, RPA, ORPA with appropriate reference system are available for doing so. Recent investigations show that OCP or a realistic OCP i.e. a CHS system (Chaturbedi *et al* 1981; Pastore and Tosi 1984; Singh and Holz 1984; Das and Joarder 1988) serves as a successful reference system for alkalis. The ORPA calculation of Das and Joarder (1988) for alkalis with Ashcroft potential is very successful in general and we have adopted the same procedure to check the structure factor of Li with this potential. The result is shown in figure 3 and it is clearly very good. One of the best possible calculated structure factors based on the

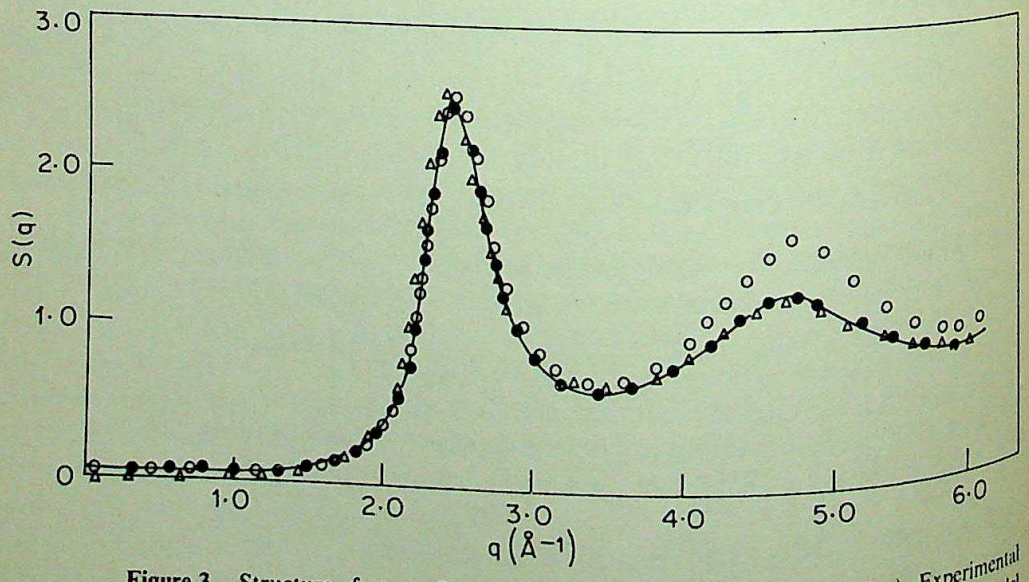

Figure 3. Structure factor, $S(q)$ of liquid Li. (– – –) Calculated (···) Experimental (Ruppersberg and Egger 1975) (○ ○ ○) Best possible calculated based on the original model with $\beta = 17{\cdot}0$ (△ △ △) Reference system.

CC-0. In Public Domain. Gurukul Kangri Collection, Haridwar

Digitized by Arya Samaj Foundation Chennai and eGangotri

original model with $\beta = 17$ and uniform electron gas dielectric function is shown for comparison. Clearly the original model does not work except near the peak. It is much worse than the reference system structure factor which is also shown.

The RPA expression for structure factor is given by

$$S(q) = S_0(q)/[1 + n\beta\tilde{v}(q)S_0(q)], \tag{8}$$

where, $S_0(q)$ is the structure factor of the reference system, $\tilde{v}(q)$ is the electron mediated attraction and other terms have their usual meaning. In ORPA, the attraction is modified in the excluded volume region as followed by Weeks *et al* (1971). The potential $\tilde{v}(r)$ is replaced by an effective potential $\bar{v}(r)$ such that $\bar{v}(r) = \tilde{v}(r)$ for $r > \sigma$. The optimal choice of $\bar{v}(r)$ for $r < \sigma$ in the RPA form of the free energy is based on the requirement that the functional derivative of the free energy with respect to $\bar{v}(r)$ should vanish for $r < \sigma$. For details please see Pastore and Tosi (1984) and Das and Joarder (1988). In the calculation, η was taken to be that for hard sphere system (Singh and Holz 1984; Das and Joarder 1988) and plasma parameter Γ was adjusted to have best reference structure factor. The good $S(0)$ and isothermal compressibility surely support our earlier contention about the present interionic potential. In this connection it is to be mentioned that the difference between $S(0)$'s in RPA and ORPA is quite small ($<5\%$) and this means that the optimization procedure has little effect on $S(0)$ (Das and Joarder 1988).

2.5 *Thermodynamics*

The thermodynamic variational calculation for Li with the simply modified form of YH pseudopotential is performed following the methods discussed by Lai (1985), Ono and Yokoyama (1984), Joarder and Das (1988) and the details are not given here. The basic principle is the Gibbs–Bogoliubov (GB) inequality which gives the free energy of the system given by

$$F \leqslant F_0 + \langle H - H_0 \rangle_0, \tag{9}$$

where, F_0 is the free energy of the CHS reference system and $\langle H - H_0 \rangle_0$ is the ensemble average over all the configurations of the chosen reference system and evaluated with the modified YH potential. F_0 is given by

$$F_0 = 3/2k_BT + V_0 - TS_0, \tag{10}$$

where, V_0 and S_0 are the CHS potential energy and entropy respectively as in Joarder and Das (1988).

Following the same procedure as in Joarder and Das (1988) we minimise the free energy using Γ as a variational parameter. Once the free energy is obtained by the minimization procedure other thermodynamic functions follow directly. Some of the properties calculated are shown in table 1. The r_b value had to be adjusted to have a general consistency in the Γ value with $S(q)$ calculation. In spite of this adjustment the Γ value in the thermodynamic calculation is somewhat less. This difference is not unexpected if we recall the thermodynamic inconsistency (MacGowan 1983) that prevails in such a theory. The calculated properties surely shows the relevance of this simply modified YH pseudopotential in the thermodynamic perturbation study of liquid lithium. It is to be mentioned that the YH pseudopotential in the original

CC-0. In Public Domain. Gurukul Kangri Collection, Haridwar

Digitized by Arya Samaj Foundation Chennai and eGangotri

form cannot be applied with any success for this calculation. With $\beta=17$, Γ comes out to be absurdly small and free energy has very large negative value.

3. Discussion

We have shown in this communciation how YH pseudopotential for Li with a slight modification can be applicable to the calculation of structure and thermodynamics of liquid Li. This form produces an effective pair potential which agrees better with that from the first principle fully non-local pseudopotential of Day *et al* (1979) than the original form. It has the correct core size and reasonably good oscillatory tail. A good agreement in $S(q)$ throughout and the generation of thermodynamic properties through GB principle support this contention. The effective pair potential obtained from Ashcroft model as pointed out by Hoshino and Young cannot produce the correct core size and isothermal compressibility (in RPA) simultaneously with any value of ionic core radius r_c. It is also known that the Ashcroft model is not very suitable for Li in the structure factor calculations (Pastore and Tosi 1984; Das and Joarder 1988). This impasse exists in the original YH pair potential also and probably arises not because of the weak tail of the Ashcroft pair potential as pointed out by Hoshino and Young but because of the details of the potential. Possibly, a modified theory i.e. a theory containing terms other than only RPA is required to describe $S(0)$ or isothermal compressibility in a better way. This is clearly demonstrated here by the use of ORPA with the modified form of YH pair potential though the latter possesses a relatively weak tail-like Ashcroft potential.

In conclusion, we reiterate that YH potential with the slight modification enjoys the desired simplicity and at the same time generates reasonably the properties of this less simple member of alkali series.

Acknowledgements

The Authors gratefully acknowledge the financial support of DST, New Delhi, India.

References

Alblas B P, Van der Marel C, Geertsma W, Mayer J A, Van Oosten A B, Dijkstra J, Stein P G, and Van der Lugt W, 1984 *J. Non-Cryst. Solids* **61 & 62** 201
Ashcroft N W and Langreth D C 1967 *Phys. Rev.* **156** 685
Ashcroft N W and Langreth D C 1967 *Phys. Rev.* **159** 500
Austin B J, Heine V and Sham L J 1962 *Phys. Rev.* **127** 276
Barker M I and Gaskell T 1975 *Phys. Lett.* **A53** 285
Chaturbedi D K, Rovere M, Senatore G and Tosi M P 1981 *Physica* **B111** 11
Das T and Joarder R N 1988 *Phys. Lett.* **A131** 111
Day R S, Sun F and Cutler P H 1979 *Phys. Rev.* **A19** 328
Donaghy J J and Stewart A T 1967 *Phys. Rev.* **164** 391
Hafner J 1977 *Phys. Rev.* **A16** 351
Harrison W A 1966 *Pseudopotentials in the theory of metals* (NY: Benjamin).
Hoshino K and Young W H 1986 *J. Phys.* **F16** 1659
Ichimaru S and Utsumi K 1981 *Phys. Rev.* **B24** 7385

CC-0. In Public Domain. Gurukul Kangri Collection, Haridwar

Digitized by Arya Samaj Foundation Chennai and eGangotri

Joarder R N and Das T 1988 *Phys. Scr.* **37** 762
Lai S K 1985 *Phys. Rev.* **A31** 3886
MacGowan D 1983 *J. Stat. Phys.* **32** 123
Meyer A and Young W H 1965 *Phys. Rev.* **A139** 401
Ono S and Yokoyama I 1984 *J. Phys.* **F14** 2909
Pastore G and Tosi M P 1984 *Physica* **B124** 383
Popovic Z D, Carbotte J P and Piercy G R 1974 *J. Phys.* **F1** 351
Ruppersberg H and Egger H 1975 *J. Chem. Phys.* **63** 4095
Ruppersberg H and Reiter H 1982 *J. Phys.* **F12** 1311
Singh H B and Holz A 1984 *Phys. Rev.* **A28** 1108
Soma M 1979 *Physica* **B97** 76
Taylor R 1982 *Can. J. Phys.* **60** 725
Van der Lugt W and Geertsma W 1984 *J. Non-Cryst. Solids* **61 & 62** 187
Waseda Y 1980 *The structure of non-crystalline materials* (NY: McGraw-Hill)
Weeks J D, Chandler D and Anderson H C 1971 *J. Chem. Phys.* **54** 5237

CC-0. In Public Domain. Gurukul Kangri Collection, Haridwar

Digitized by Arya Samaj Foundation Chennai and eGangotri

CC-0. In Public Domain. Gurukul Kangri Collection, Haridwar

Digitized by Arya Samaj Foundation Chennai and eGangotri

Pramāṇa – J. Phys., Vol. 34, No. 3, March 1990, pp. 235–241. © Printed in India.

Melting temperatures of some alkali halide mixed crystal systems

D B SIRDESHMUKH*, K G SUBHADRA and K A HUSSAIN**

Department of Physics, Kakatiya University, Warangal 506 009, India
**Department of Physics, University Arts & Science College, Kakatiya University, Warangal 506 010, India

MS received 20 April 1989; revised 23 October 1989

Abstract. The melting points in the KCl–KBr, RbCl–RbBr and KBr–RbBr mixed crystal systems have been measured using the microscopic method. In all the three systems, melting points vary nonlinearly with composition, with negative deviations from linearity and maximum deviation at about the equimolar concentration. The observed composition dependence of the melting points is explained qualitatively in terms of the enhanced concentration of point defects and dislocations in mixed crystals.

Keywords. Mixed crystals; alkali halides; melting points.

PACS Nos 64·70; 65·90

1. Introduction

Several physical properties of mixed crystals of the alkali halides have been studied in recent times. While growth and characterisation aspects of alkali halide mixed crystals have been reviewed by Hari Babu and Subba Rao (1974), Sirdeshmukh and Srinivas (1986) reviewed the physical properties of these mixed crystals. However, data on the melting temperatures of mixed crystals are very scanty. The melting of a crystal takes place at a temperature lower than that predicted from any lattice theory. Weyl (1961) suggested that the presence of a large number of vacancies at temperatures close to the melting point is responsible for the lowering of melting point. Since a mixed crystal has, by its very nature, a defect structure, it would be interesting to study the composition dependence of melting temperatures of mixed crystals.

Slagle and McKinstry (1967) quoted the melting temperatures for KCl–KBr mixed crystals from the work of Lifshitz (1955). Cholokov *et al* (1970) referred to the liquidus curve of KCl–RbCl system, but did not give the actual values of the melting point. Srinivas (1984) calculated the melting temperatures of some alkali halide mixed crystal systems from Debye temperature values using Lindemann's formula.

The composition dependence of melting points of the KCl–KBr, RbCl–RbBr and KBr–RbBr systems has been determined in the present study by hot stage microscopy.

*To whom correspondence should be addressed.

CC-0. In Public Domain. Gurukul Kangri Collection, Haridwar

Digitized by Arya Samaj Foundation Chennai and eGangotri

2. Experimental

Mixed crystals of KCl–KBr, RbCl–RbBr and KBr–RbBr with different compositions were prepared by melt growth technique. The starting materials were 99·99% pure AR grade KCl and KBr (supplied by BDH) and RbCl and RbBr (supplied by Fluka). The materials were used in the as supplied form without further purification. The preparation of the mixed crystals was similar to that described by Srinivas and Sirdeshmukh (1985).

In KCl–KBr and RbCl–RbBr mixed crystals, the relative concentrations of chloride and bromide were determined by the potentiometric titration method. The composition of the mixed crystals in the KBr–RbBr system was determined from lattice constants using Vegard's law.

The melting temperatures may be determined by several methods. Pistorius (1966) used the differential thermal analysis (DTA) technique for determining the melting points of alkali halides. Bruton (1974) used a thermobalance and also the DTA technique for the Bi_2O_3–Ti_2O_3 system. In the present work, melting was observed under a microscope. A simple microscope was modified for the purpose by incorporating on the specimen stage a small heater designed to give temperatures up to 1000°C. The salient feature of the heater is good thermal insulation so that the microscope parts are unaffected by the presence of the heater even at 1000°C. A quartz crucible designed so as to just fit into the central region of the heater was inserted into the heater and was used as the sample holder. The change of state of the sample from solid to liquid was visually observed under transmitted light. A chromel-alumel thermocouple could be simultaneously viewed under the microscope. This ensured that the thermocouple was in contact with the sample. The thermo-emf was measured with a $4\frac{1}{2}$ digit millivoltmeter with 0·02% accuracy. The melting point of the crystals studied was determined as the temperature at which the solid is completely converted into liquid. For each sample at least six measurements were made and the average taken. The standard deviation in the melting temperature varied slightly from crystal to crystal, but was always close to ± 2°C.

For standardizing the procedure adopted, the melting temperatures of several standard substances having values between 100°C and 800°C were measured. The results for some of these substances are given in table 1. It is seen that the present results agree reasonably with earlier values.

Table 1. Melting points of some standards.

Substance	t_m °C present	t_m °C from CRC Hand Book*
Acetanilide	109	113
$NaClO_3$	262	248–261
RbBr	693	682
RbCl	718	715
KBr	734	730
KCl	770	776

CRC Handbook of Physics and Chemistry (Chemical Rubber Co., Cleveland, Ohio), 1971.

CC-0. In Public Domain. Gurukul Kangri Collection, Haridwar

Digitized by Arya Samaj Foundation Chennai and eGangotri

Table 2. Accuracy obtained in the experiments on melting point determinations by different workers.

Author	Method	Accuracy
Clark Jr (1959)	DTA	±5 C & ±10 C
Pistorius (1965)	DTA	±5 C to ±8 C
Kruger and Moser (1967)	V shaped tungsten filament in conjunction with a pyrometer	±30 C
Akella *et al* (1973)	DTA	±7 C to ±10 C
Bruton (1974)	thermobalance and DTA	±3 C
Present work	hot stage microscopy	±5 C

As a further check on the accuracy of the results obtained, the melting points of KCl and KBr crystals were also measured by DTA technique. Heating was done in air at the rate of 10°C/min. Melting temperature of 768°C and 740°C were obtained for KCl and KBr respectively by DTA measurements. These are in good agreement with the values obtained in this study by hot stage microscopy (770 C and 734 C).

Different workers have reported different accuracies of measurement (table 2). When the accuracy of the present method was compared with that of other methods, the present procedure seems to be satisfactory as an overall accuracy of ±5°C is obtained in the melting temperatures.

3. Results

The melting points of the mixed crystals in the systems KCl–KBr, RbCl–RbBr and KBr–RbBr have been measured over the whole composition range. These results are given in table 3. These values are also plotted in figure 1. For the KCl–KBr system, the melting points given by Slagle and McKinstry (1967) are also included in the figure. For the other two systems there is no earlier work. The present results for KCl–KBr are in good agreement with those of Slagle and McKinstry within experimental errors. Further, it can be seen from the figure that the variation of melting points with composition is non-linear for all the three systems. The deviations from linearity are negative, i.e. the measured values are below the straight line joining the values of the end members. Further, the maximum deviation occurs at about the equimolar composition. The maximum deviations from linearity are 19 C, 19 C and 16 C in the KCl–KBr, RbCl–RbBr and KBr–RbBr systems respectively. These deviations are much larger than the experimental uncertainty of ±5 C discussed earlier.

4. Discussion

As mentioned in the preceding section, the composition dependence of the melting points (t_m) for the three mixed crystal systems studied viz. KCl–KBr, RbCl–RbBr and KBr–RbBr is nonlinear with negative deviations from linearity. This is similar to the observations by Slagle and McKinstry (1967) in KCl–KBr system and by Singh

CC-0. In Public Domain. Gurukul Kangri Collection, Haridwar

Digitized by Arya Samaj Foundation Chennai and eGangotri

Table 3. Melting points (t_m in °C) of alkali halide mixed crystals.

KCl_xBr_{1-x}				$RbCl_xBr_{1-x}$		$K_xRb_{1-x}Br$	
Mole fraction (x)	t_m present	Mole fraction (x)	t_m Slagle & McKinstry	Mole fraction (x)	t_m present	Mole fraction (x)	t_m present
0·00	734 (730)*	0·00	740	0·00	693 (682)*	0·00	693
0·15	734	0·30	736	0·25	684	0·13	693
0·28	733	0·40	734	0·40	682	0·37	698
0·41	733	0·62	738	0·50	688	0·53	699
0·51	732	0·83	752	0·75	698	0·58	696
0·61	732	1·00	775	0·80	704	0·67	700
0·66	738			1·00	718 (715)*	0·76	713
0·79	754					0·93	726
0·86	759					1·00	734
0·93	765						
1·00	770 (776)*						

*Values from CRC Handbook of Physics and Chemistry (Chemical Rubber Co., Cleveland, Ohio), 1971.

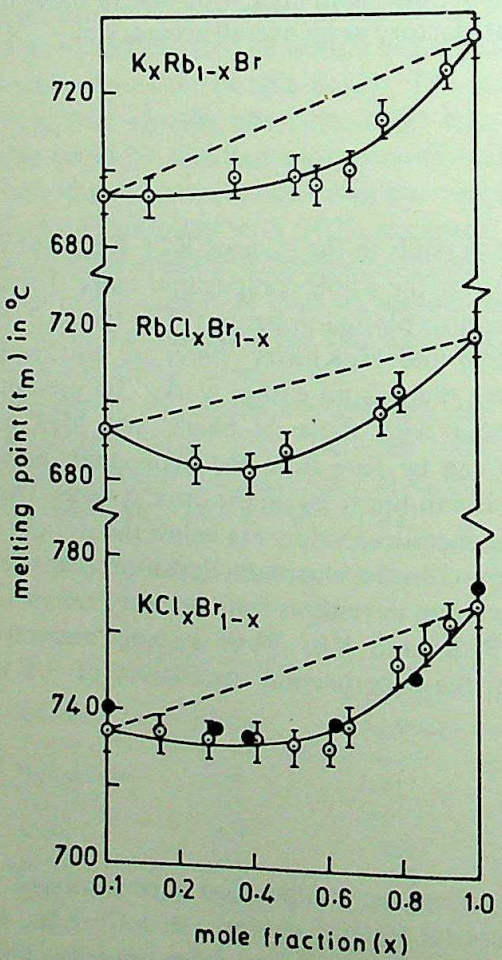

Figure 1. Variation of melting point (t_m) with composition (x) for the KCl–KBr, RbCl–RbBr and KBr–RbBr mixed crystal systems. Dashed lines represent variation expected from additivity rule. ● Slagle and McKinstry (1967); ⊙ Present work.

CC-0. In Public Domain. Gurukul Kangri Collection, Haridwar

Digitized by Arya Samaj Foundation Chennai and eGangotri

(1970) for the AgCl–AgBr system. Thus, while the magnitude of the deviation from linearity differs from system to system, the sign of the deviation seems to be the same for all the mixed crystal systems studied.

Ubblehode (1978) discusses two approaches to the problem of melting viz., the vibrational and the mechanical approach. The former approach is based on Lindemann's (1910) picture of melting. As the temperature increases, the amplitude of atomic vibrations increases and when its value as a fraction of the interatomic distance reaches a critical value, the crystal would become mechanically unstable. An exact verification of this picture has not been possible because of several difficulties. Firstly, the critical value of the amplitude of vibration varies from structure to structure (Shapiro 1970); secondly, the amplitudes of vibration are affected by anharmonicity (Gupta 1983) and thirdly, experimental data on the amplitudes of vibration near melting point are scarce.

An outcome of Lindemann's theory (Lindemann 1910) has been the so called Lindemann melting point formula,

$$\nu = C(T_m/MV^{2/3})^{1/2} \tag{1}$$

where ν is the characteristic frequency, T_m the melting point in °K, M the atomic mass and V the molar volume. This formula can be used either to estimate the characteristic frequency from the melting temperature, or the melting temperature from the characteristic frequency. Adopting the former approach, Ubblehode (1978) calculates the ratio of the characteristic frequency estimated from Lindemann's formula to that calculated from experimental data on specific heats. Ubblehode finds that in most of the crystals for which the calculations were made, the ratio was less than unity. This implies that the observed melting temperatures are lower than that for the ideal lattice.

The mechanical approach is based on Born's stability conditions (Born 1939), according to which for a cubic crystal

$$C_{11} - C_{12} \geqslant 0 \tag{2}$$

and

$$C_{44} \geqslant 0. \tag{3}$$

Here C_{11}, C_{12} and C_{44} are the elastic constants. The melting temperature can be taken as the temperature at which the elastic constants reach this limiting value. Using experimental data on the temperature variation of elastic constants, melting temperatures were estimated in this way for NaCl and KCl by Slagle and McKinstry (1967), for NaI and KI by Barsch and Shull (1971) and for several alkali halides by Jackson and Liebermann (1974). In all these cases, it was observed that the estimated melting point was higher than the experimental melting point. Thus, both the vibrational and mechanical approaches lead us to the conclusion that the melting point of a real crystal is lower than that calculated for a perfect crystal.

According to Weyl (1961) crystals develop a large concentration of lattice vacancies as the temperature approaches the melting point. These vacancies in turn change the nature of binding forces in their vicinity producing fluctuating fissures which permit easy flow. Cahn (1978) has pointed out that melting occurs when the vacancy concentration attains a critical value of 0·37%. A linear correlation has been observed between melting temperature and vacancy formation energy for alkali halides (Barr and Lidiard 1970). According to another defect model of melting (Ubblehode 1965), at high enough temperatures, there is a catastrophic increase in dislocation density

CC-0. In Public Domain. Gurukul Kangri Collection, Haridwar

Digitized by Arya Samaj Foundation Chennai and eGangotri

which leads to the loss of crystallinity. Cahn (1978) discusses a model where both types of defects play a role. The increase in population of dislocations 'cuts the crystal structure to pieces', large number of point defects are created and the combination of liquid-like disorder in dislocation cores and large point defect concentrations destroy crystalline order at an effective melting temperature. Thus, qualitatively at least, the lowering of the melting point from that of an ideal crystal to that of a real crystal seems to be due to the presence of point defects as well as dislocations.

There is considerable evidence to show that the concentration of point defects is greater in mixed crystals than in pure crystals. Evidence to this effect was obtained by Wallace and Flinn (1953) and Wollam and Wallace (1956) in their pyknometric studies on KCl–KBr and NaCl–NaBr systems. Further, Arends *et al* (1965) and Thyagarajan (1966) on the basis of their studies of colour centres in alkali halide mixed crystals observed that the concentration of vacancies is more in mixed crystals than in pure crystals, the concentration being maximum for mixed crystals with equimolar composition. There is also evidence to show that the concentration of dislocations is more in mixed crystals than in pure crystals (Arends *et al* 1965; Subba Rao and Hari Babu 1978 and Hussain *et al* 1988), the crystals with equimolar composition having the maximum dislocation density.

Thus, lattice vacancies and dislocations lower the melting points of pure crystals and because of the comparatively larger concentrations of vacancies and dislocations, the lowering is all the more in mixed crystals. If the defects in mixed crystals (vacancies, as well as, dislocations) were comparable in concentration to those in pure crystals, the composition dependence of melting point might have been additive (linear). The existence of these defects in higher concentration in the mixed crystals results in the depression of the melting point of the mixed crystal in comparison to the value predicted from additivity. This deviation from additivity increases as we approach the equimolar composition from either end resulting in a melting point versus composition curve which is non-linear with negative deviations from linearity. This picture should qualitatively explain the observed composition dependence of melting temperatures of mixed crystals.

Acknowledgement

Thanks are due to the referee for useful suggestions. One of the authors, KAH, thanks the UGC for financial assistance.

References

Akella J, Ganguly J, Grover R and Kennedy G 1973 *J. Phys. Chem. Solids* **34** 631
Arends J, Den Hartog, H W and Decker A J 1965 *Phys. Status Solidi* **10** 105
Barr L W and Lidiard A B 1970 *Physical Chemistry – An advanced treatise* (New York: Academic Press) **10**
Barsch R and Shull H W 1971 *Phys. Status Solidi* **B43** 637
Born M 1939 *J. Chem. Phys.* **7** 591
Bruton T M 1974 *J. Solid State Chem.* **9** 173
Cahn R W 1978 *Nature (London)* **273** 491
Cholokov K S, Novikov E N, Grishukov V A and Botaki A A 1970 *Izv. Vyssh. Uchebn. Zaved., Fiz.* **12** 157
Clark Jr S P 1959 *J. Chem. Phys.* **31** 1526

CC-0. In Public Domain. Gurukul Kangri Collection, Haridwar

Digitized by Arya Samaj Foundation Chennai and eGangotri

Gupta O P 1983 *J. Phys. Soc. Jpn.* **52** 4237
Hari Babu V and Subba Rao U V 1984 *Prog. Cryst. Growth Charac.* **8** 189
Hussian K A, Subhadra K G and Kishan Rao K 1988 *Cryst. Res. Techn.* **23** 171
Jackson J N S and Liebermann R C 1974 *J. Phys. Chem. Solids* **35** 1115
Kruger O L and Moser J B 1967 *J. Phys. Chem. Solids* **28** 2321
Lifshitz G M 1955 *Z. Obschchei Khim* **25** 2417
Lindemann F A 1910 *Z. Phys.* **11** 609
Pistorius C W F T 1965 *J. Chem. Phys.* **43** 1557
Pistorius C W F T 1966 *J. Chem. Phys.* **45** 3513
Singh I 1970 *J. Technol.* **8** 52
Shapiro J N 1970 *Phys. Rev* **B1** 3982
Sirdeshmukh D B and Srinivas K 1986 *J. Mater. Sci.* **21** 4117
Slagle O D and McKinstry H A 1967 *J. Appl. Phys.* **38** 437, 446
Srinivas K 1984 Ph.D. Thesis, Kakatiya University, India
Srinivas K and Sirdeshmukh D B 1985 *Pramana – J. Phys.* **25** 71
Subba Rao U V and Hari Babu V 1978 *Pramana – J. Phys.* **11** 149
Thyagarajan R 1966 *J. Phys. Chem. Solids* **27** 218
Ubblehode A R 1978 *The molten state of matter* (New York: Wiley Interscience)
Wallace W E and Flinn R A 1953 *Nature (London)* **172** 681
Weyl W A 1961 Advances in Chemistry series (New York: American Chemical Society) **33** 72
Wollam J S and Wallace W E 1956 *J. Phys. Chem.* **60** 1654

CC-0. In Public Domain. Gurukul Kangri Collection, Haridwar

Digitized by Arya Samaj Foundation Chennai and eGangotri

CC-0. In Public Domain. Gurukul Kangri Collection, Haridwar

Digitized by Arya Samaj Foundation Chennai and eGangotri

Pramāṇa – J. Phys., Vol. 34, No. 3, March 1990, pp. 243–248. © Printed in India.

Electrical conductivity, thermoelectric power and figure of merit of doped Bi–Sb tapes produced by melt spinning technique

T K DEY
Cryogenic Engineering Centre, Indian Institute of Technology, Kharagpur 721 302, India

MS received 3 August 1989; revised 2 November 1989

Abstract. Temperature dependence of electrical conductivity and thermoelectric power are presented for In and Pb doped Bi + 8·28 at % Sb quenched tapes between 77 and 300K. The results are explained in terms of model for disordered semiconductors. Analysis of our data on electrical conductivity indicates the presence of a temperature independent part and a strongly temperature dependent part. While the T independent part originates from band conduction, the T dependent component could be understood considering the presence of localized states. Thermoelectric figure-of-merit of these tapes are also measured at 300K, which shows a large enhancement (~40%) over that reported earlier on thin Bi–Sb films. This suggests that doped Bi–Sb quenched tapes may be considered as a candidate for material in producing economic and light weight thermoelectric devices.

Keywords. Bismuth–antimony alloy; melt spinning technique; thermoelectric power; figure-of-merit; nearest neighbour hopping; localized states.

PACS Nos 70·20; 72·20

1. Introduction

Existence of a positive energy gap, high carrier mobility and low lattice thermal conductivity are some of the prime requirements for a useful thermoelectric material. This is because the figure-of-merit (Z) of thermoelectric material is expressed as

$$Z = S^2\sigma/K$$

where, S is the Seebeck coefficient, σ is the electrical conductivity and K is the thermal conductivity of the material. Bi–Sb alloys with Sb concentration between 4 and 40 at% meet most of the above requirements and hence, are regarded as an important system for thermoelectric energy conversion (Horst and Williams 1980). Efforts were made with Bi–Sb alloys for making thin film thermoelectric devices in the area of cooling (Trefny 1981), and radiation detector (Chopra and Pandya 1978) etc. Ion beam mixing of Bi–Sb alloys have been reported as a potential method for preparing thin film thermoelectrics (Benenson *et al* 1983; Ibrahim and Thompson 1985).

Melt spinning technique offers an inexpensive way for producing 20 to 30 μm thick Bi–Sb tapes. Most of the studies on this alloy have so far been concentrated either on crystalline bulk alloys (Smith and Wolfe 1962) or on thin films (Garcia *et al* 1972). Therefore, it is of interest to look for the extent to which the splat quenched Bi–Sb tapes prepared by melt spinning are suitable for thermoelectric applications, vis-a-vis thin films. In the present communication, we report our results on temperature

CC-0. In Public Domain. Gurukul Kangri Collection, Haridwar

Digitized by Arya Samaj Foundation Chennai and eGangotri

dependence of electrical resistivity and thermoelectric power (TEP) of Bi–Sb tapes doped with small amount of In and Pb. In addition, room temperature data of figure-of-merit (Z) of these tapes are presented and compared with Z values of Bi–Sb films produced by different techniques.

2. Experimental

In and Pb doped Bi + 8·28 at% Sb tapes were prepared by melt spinning technique described elsewhere (Dey and Ghatak 1989). Electrical resistivity and TEP of these tapes were measured using four probe and differential methods respectively. Details of cryostatic arrangement and the experimental procedures were reported earlier (Dey *et al* 1985).

Figure of merit (Z) of the tapes were measured using modified Herman technique (Herman *et al* 1959; Trefny 1982). This involves the measurement of dc and ac resistivities of the tapes. Dc measurement simulates isothermal condition, while ac measurement with frequency higher than inverse of diffusivity simulates adiabatic condition. This requires frequency of only a few Hz in most cases. In the present study, ρ_{ac} was measured at 73 Hz. From these measurements, the figure of merit (Z) comes out as:

$$Z = (\rho_{ac}/\rho_{dc} - 1)T^{-1}$$

where, ρ_{dc} and ρ_{ac} are the dc and ac resistivities respectively and T is the temperature in K. Several corrections (Trefny 1982) are needed to obtain absolute values of Z. These correction factors are included in Z values reported for our tapes.

3. Results

Electrical resistivity (ρ) and TEP (S) of splat quenched Bi + 8·28 at% Sb tapes doped with small amount of In and Pb are shown in figures 1 and 2 respectively between 77K and 300K. All the tapes show an increase in resistivity with lowering of temperatures and finally approach a saturated value. This behaviour is similar to that reported earlier (Dey and Ghatak 1989) for undoped tapes of Bi–Sb alloys. However, doped tapes show higher resistivities compared to the undoped ones. Similar temperature dependences have been reported for vacuum deposited Bi–Sb films (Inoue *et al* 1979) and on Bi–Sb films deposited by ion beam mixing using Ag^+ and Kr^+ beams (Ibrahim and Thompson 1985). TEP of the tapes decrease with decrease of temperature and shows sign reversal (figure 2). The temperature at which the sign reversal occurs is dependent upon the composition of the tapes. N-type conductivity is apparent near room temperature for all the tapes. This behaviour of TEP is significantly different to that observed earlier for undoped Bi + 8·28 at% Sb tapes, where TEP was found to be negative over the entire temperature range. In addition, doping of Bi–Sb with In and Pb largely increases the magnitude of Seebeck coefficient at 300K. A maximum of $-118\,\mu$v/K has been observed for tapes containing 0·2 at%In, while for the tapes doped with 0·1 at% Pb a maximum of $-102\,\mu$v/K is obtained. These values may be compared with $-94\,\mu$v/K of undoped Bi + 8·28 at% Sb tapes (Dey and Ghatak 1989).

CC-0. In Public Domain. Gurukul Kangri Collection, Haridwar

Digitized by Arya Samaj Foundation Chennai and eGangotri

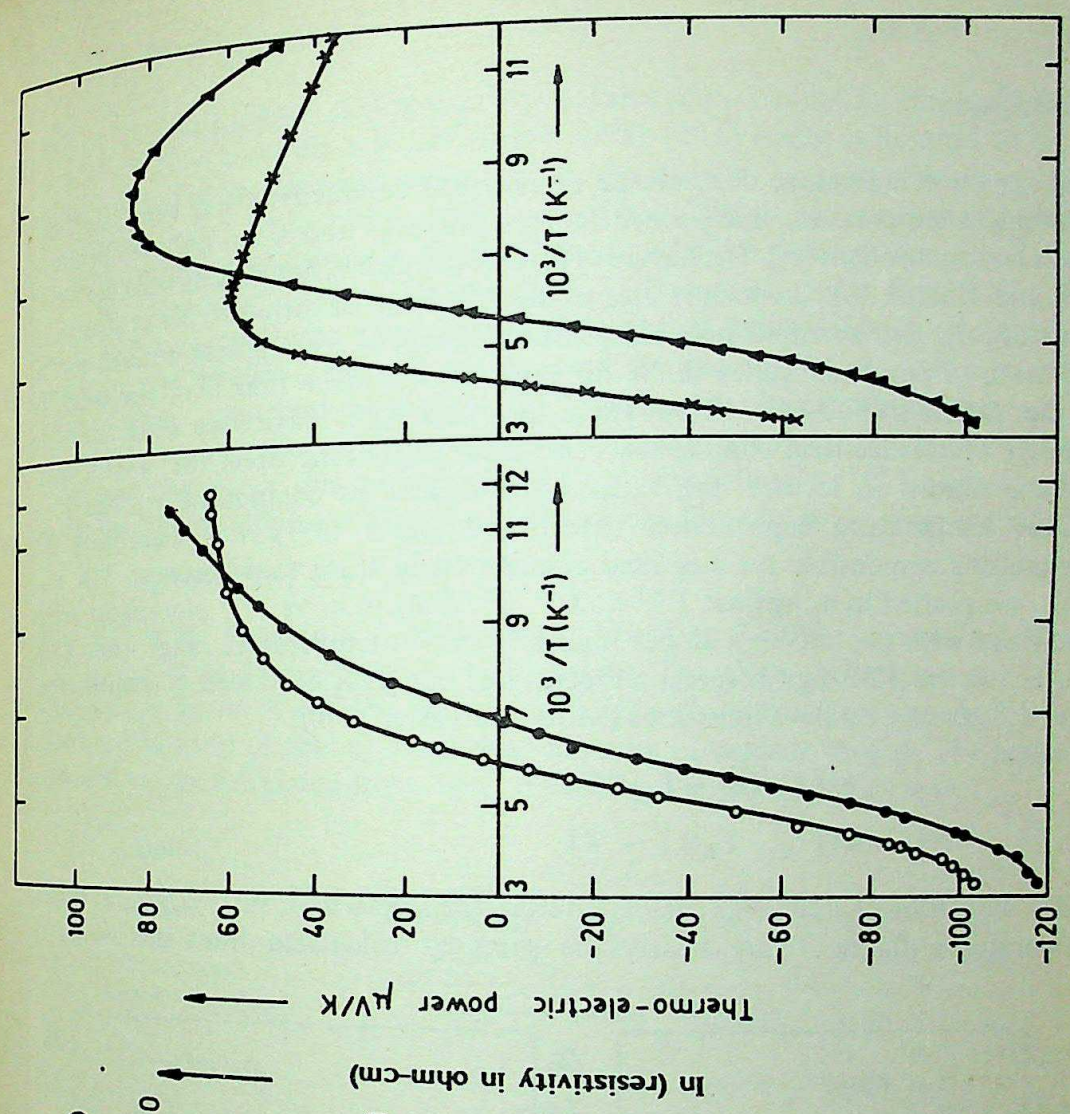

Figure 2. Thermoelectric power as a function of reciprocal temperature for doped Bi + 8·28%Sb quenched tapes. Legends same as in figure 1.

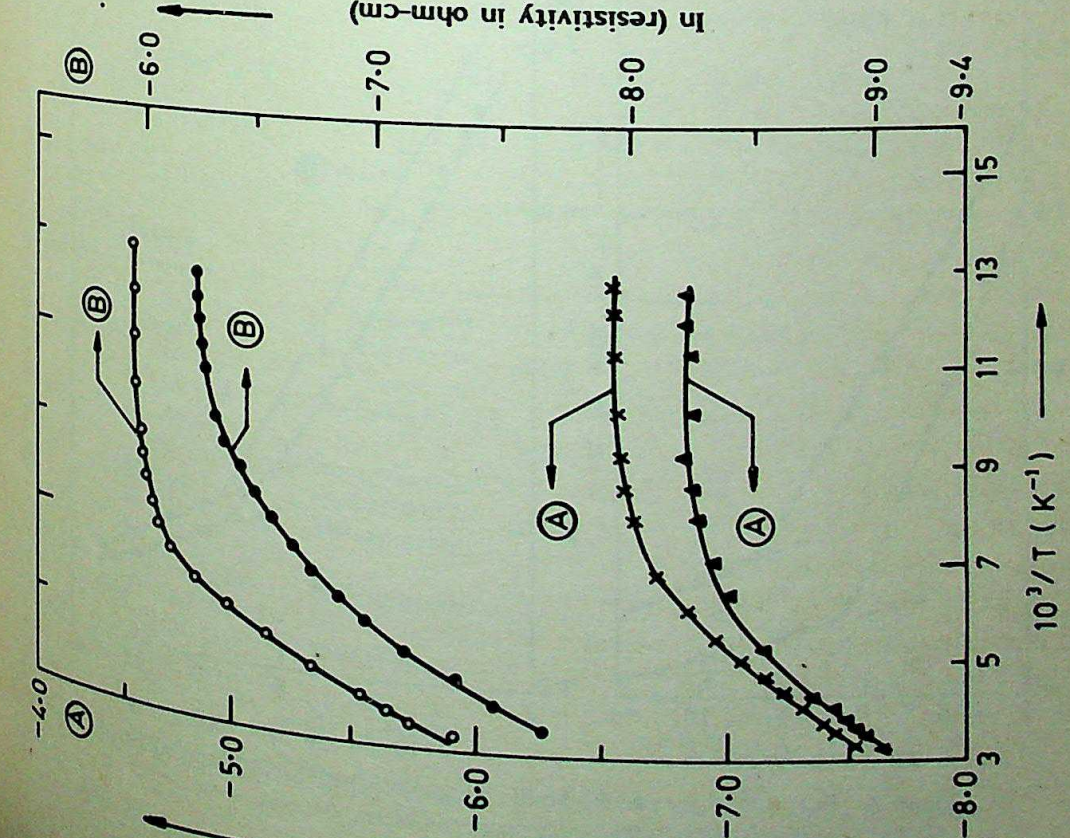

Figure 1. Ln (resistivity) as a function of reciprocal temperature for doped Bi + 8·28 at%Sb quenched tapes. (●) Bi–Sb (0·2 at%In), (○) Bi–Sb (0·3 at%In), (▲) Bi–Sb (0·1 at%Pb), and (×) Bi–Sb (0·2 at%Pb).

CC-0. In Public Domain. Gurukul Kangri Collection, Haridwar

Digitized by Arya Samaj Foundation Chennai and eGangotri

4. Discussion

Data on the temperature dependence of electrical conductivity has been analysed, assuming a temperature independent component (σ_0) and a strongly temperature dependent component (σ_h). The nature of origin of σ_0 and σ_h has already been discussed (Dey and Ghatak 1989), which relates to the formation of various types of structural imperfections due to rapid quenching. Such disorders are reported to lead to the formation of localized states in Bi–Sb tapes and in their thin films prepared by coevaporation (Inoue *et al* 1979). These localized states have very small mobility through which electrical conduction can occur. Depending upon the type of these states available or, formed, the temperature dependent component (σ_h) can have various temperature dependences (Mott and Davis 1971). For identifying the mechanisms responsible for electrical conduction in these tapes between 77K and 300K, we plotted ln σ_h against T^{-1} and $T^{-1/4}$. Only ln σ_h vs T^{-1} plots show linear behaviour with two different slopes (figure 3). In the temperature range from 300K and below the TEP sign reversal temperatures our data on doped quenched tapes can be described by the expressions (Mott and Davis 1970):

$$\sigma_h = \sigma_{ho} \exp[-(E_C - E_F)/kT]$$

$$S = -k/e[E_C - E_F/kT + A].$$

The activation energies (E_σ) calculated from the slopes ln σ_h vs T^{-1} plots at higher temperatures (figure 3) are nearly the same as calculated from the slopes of

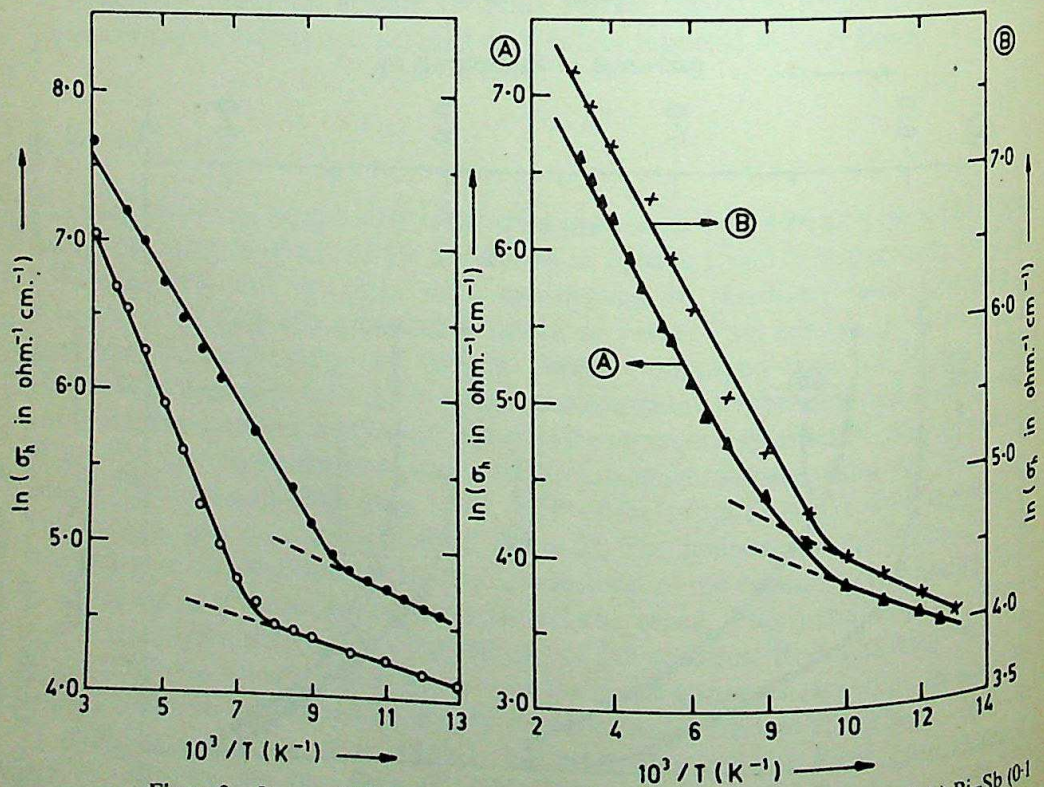

Figure 3. In σ_h vs T^{-1} for (●) Bi–Sb (0·1 at °o In), (○) Bi–Sb (0·3 at °o In), (▲) Bi–Sb (0·1 at °o Pb), (×) Bi–Sb (0·2 at °o Pb), splat quenched tapes.

CC-0. In Public Domain. Gurukul Kangri Collection, Haridwar

Digitized by Arya Samaj Foundation Chennai and eGangotri

TEP vs T^{-1} plots (figure 2). These above features indicate that in this temperature range conduction takes place in only one band and the process is dominated by the carriers excited in the extended states beyond the mobility edge. Further lowering of temperature causes distinct change in slope of $\ln \sigma_n$ (figure 3), which shows that at low temperatures mechanism for electrical conduction is a different one. In addition, it may be noted that the slopes of $\ln \sigma_h$ vs T^{-1} lines are significantly smaller than that at higher temperatures. This clearly indicates that the conduction processes are associated with smaller activation energy. In a disordered system, such a situation can arise when conduction takes place due to either nearest neighbour hopping, or, by variable range hopping of carriers. In the present tapes variable range hopping is absent, since the data in this temperature range do not follow $T^{-1/4}$ dependence. For nearest neighbour hopping of carriers, electrical conductivity is given by the relation

$$\sigma_h = \sigma_{h'0} \exp[-\Delta W/kT]$$

where ΔW is the hopping activation energy. Further, TEP for nearest neighbour hopping should be proportional to temperature. Therefore, the linear region with reduced slope (figure 3) and the linearity of TEP with temperature observed in our tapes are indicative of nearest neighbour hopping of carriers (holes). The hopping activation energy calculated from figure 3 are given in table 1.

Table 1.

Samples (Bi + 8·28 at % Sb + x)	TEP (300 K) μV/K	E_σ (eV)	E_s (eV)	ΔW (eV)	Carrier type
X = 0·2 at % In	−118	0·0400	−0·0417	0·0098	n, $T > 145$ K
					p, $T < 145$ K
X = 0·3 at % In	−104	0·0546	−0·0444	0·0054	n, $T > 166$ K
					p, $T < 166$ K
X = 0·1 at % Pb	−62	0·0452	−0·0450	0·0100	n, $T > 154$ K
					p, $T < 154$ K
X = 0·2 at % Pb	−101	0·0460	−0·0400	0·0132	n, $T > 285$ K
					p, $T < 285$ K

Table 2.

Samples	Method of preparation	Figure of merit $(Z) \times 10^{-4}$ (deg^{-1})
Bi thin film	Ion beam mixing	2·26
$Bi_{87}Sb_{13}$ thin film (Sn doped)	Ion beam mixing	3·33
Bi tapes	Melt spinning	2·46
Bi + 8·28 at % Sb	Melt spinning	3·04
Bi + 8·28 at % Sb (0·2 at % In)	Melt spinning	4·58
Bi + 8·28 at % Sb (0·3 at % In)	Melt spinning	4·80
Bi + 8·28 at % Sb (0·1 at % Pb)	Melt spinning	3·79
Bi + 8·28 at % Sb (0·2 at % Pb)	Melt spinning	4·24

CC-0. In Public Domain. Gurukul Kangri Collection, Haridwar

Digitized by Arya Samaj Foundation Chennai and eGangotri

The results of figure of merit (Z) of our quenched Bi–Sb tapes measured at 300K are given in table 2 along with the Z values for Bi–Sb thin films (Ibrahim and Thompson 1985). Figure of merits (Z) of doped Bi + 8·28 at% Sb tapes are found to exceed that for undoped ones. Further, it is interesting to note that for In doped Bi–Sb tapes an increase of Z value by ~40% over that of Sn doped Bi–Sb films has been observed. Such a large increase in Z observed for doped Bi–Sb quenched tapes results primarily from their higher TEP. However, other feature contributing towards increased Z probably comes from finer grains in liquid quenched tapes, which helps to reduce its thermal conductivity (K) through enhanced phonon-grain boundary scattering (Rowe and Bhandari 1985).

5. Conclusion

Temperature dependence of electrical resistivity and TEP of In and Pb doped Bi–Sb quenched tapes between 77K and 300K have been explained considering the formation of localized states near the band edges. These states are formed as a consequence of various structural disorders associated with rapid quenching. A dominant n-type conduction by carriers excited to the extended state at higher temperatures which makes a transition to P-type hopping near the Fermi level at lower temperatures are concluded from our data. Substantial enhancement of figure of merit has been observed in doped quenched Bi–Sb tapes compared to that for doped Bi–Sb thin films. This suggests that economical device development using Bi–Sb may well be based on quenched tapes processing rather than thin film technology.

Acknowledgements

The author wishes to acknowledge the technical help rendered by Mr D K Paul of Cryogenic Engineering Centre. This work was funded by CSIR (New Delhi).

References

Benenson R E, Tikku V K, Kollewe D and Jin H S 1983 *Nucl. Instrum. Methods* **209/210** 185
Chopra K L and Pandya D K 1978 *Thin Solid Films* **50** 81
Dey T K, Chatterjee C and Duttagupta B 1985 *Proc. Int. Conf. Cryogenics* p. 435
Dey T K and Ghatak S K 1989 *Pramāṇa – J. Phys.* **32** 161
Garcia N, Kao Y H and Strongin M 1972 *Phys. Rev.* **B5** 2029
Herman T C, Chan J H and Logan M J 1959 *J. Appl. Phys.* **30** 1351
Horst R B and Williams L R 1980 *Proc. 3rd Int. Conf. Thermoelectric Energy Conversion* p. 139
Ibrahim A M and Thompson D A 1985 *Nucl. Instrum. Methods* **B7/8** 566
Inoue M, Urai N and Yagi H 1979 *Surf. Sci.* **86** 369
Mott N F and Davis E A 1971 *Electronic Processes in Non crystalline Solids* (Oxford: Clarendon Press) p. 201
Rowe D M and Bhandari C M 1985 *Appl. Phys. Letts.* **47** 255
Smith G E and Wolfe R 1962 *J. Appl. Phys.* **33** 841
Trefny J U 1981 *Proc. 16th Intersoc. Energy Conversion Engg. Conf.* p. 2019
Trefny J U 1982 *Proc. 4th Int. Conf. Thermoelectric Energy Conversion* p. 79

CC-0. In Public Domain. Gurukul Kangri Collection, Haridwar

Digitized by Arya Samaj Foundation Chennai and eGangotri

Pramāṇa – J. Phys., Vol. 34, No. 3, March 1990, pp. 249–257. © Printed in India.

Design and the operational characteristics of a 16 μm CF_4 laser

P K GUPTA, V P SINGHAL, N S SHIKARKHANE, S SINHA, S SASIKUMAR, U NUNDY and U K CHATTERJEE
Laser Division, Bhabha Atomic Research Centre, Bombay 400 085, India

MS received 23 October 1989

Abstract. The design and the operational characteristics of a CO_2 laser pumped CF_4 laser developed at BARC are reported. Output energies of up to 20 mJ have been obtained at 615 cm^{-1} with an absorbed energy conversion efficiency of 10%.

Keywords. 16 μm laser; CF_4 laser; optically pumped molecular gas laser.

PACS No. 42·55

1. Introduction

The CO_2 laser pumped CF_4 laser is an attractive source for generating step tunable, coherent radiation over 15·3–16·3 μm (Gupta and Mehendale 1987). This spectral region overlaps with the ν_3 absorption band of UF_6, which has a well resolved isotopic shift. The development of CF_4 laser has therefore received considerable attention for its use in investigations of multi-photon excitation/dissociation of UF_6 molecules (Tiee and Wittig 1978; Ambartsumyan *et al* 1979; Horsley *et al* 1980; Koren *et al* 1982). We report in this paper the design and operational characteristics of a CO_2 laser pumped CF_4 laser, developd at BARC. Output energies of up to 20 mJ have been obtained at 615 cm^{-1}. The absorbed energy conversion efficiency of 10% obtained in our experiments compares favourably with the best reported for this emission.

2. Basic considerations

A schematic energy level diagram for CF_4 laser (McDowell *et al* 1979) is shown in figure 1. The CO_2 laser pumps the combination band $\nu_2 + \nu_4$ and lasing occurs on the hot band transition $\nu_2 + \nu_4 \rightarrow \nu_2$. The considerable fine structure of the CF_4 laser bands leads to step tunable emission over 80 lines with a frequency tuning discreteness which can be $\lesssim 0{\cdot}1$ cm^{-1} (Grasyuk *et al* 1981). It is pertinent to note here that the CF_4 laser operation is strongly influenced by the characteristics of the pump and the lasing transitions. First, since the pumping is on a dipole forbidden, combination band, the pump absorption is weak. Secondly, the weak pump absorption cannot be offset with an increased operating gas pressure. This is because the lasing band is overlapped with a ground state absorption band ($\nu_0 \rightarrow \nu_4$). Due to anharmonicity, the latter is slightly shifted from the lasing band but its broadening creates a significant cavity loss as the pressure increases, limiting laser operation to relatively low pressures

CC-0. In Public Domain. Gurukul Kangri Collection, Haridwar

Digitized by Arya Samaj Foundation Chennai and eGangotri

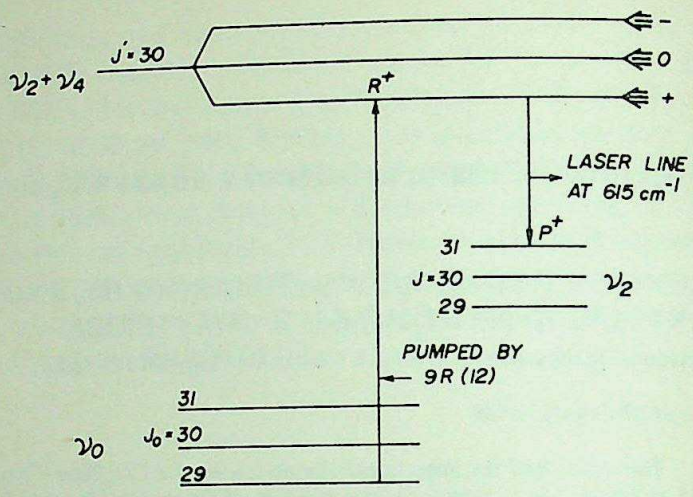

Figure 1. Energy level diagram for the CF_4 laser, with the total angular momentum quantum numbers in the vibrational ground state and in $\nu_2+\nu_4$ and ν_2 denoted by J_0, J' and J respectively. The three Coriolis sublevels of $J=30$ are denoted by −, 0 and +. The CO_2 laser pumps the transition R^+ (29), populating the + level of $J'=30$; stimulated emission occurs from this level to $J=31$ of ν_2, producing the strong laser line P(31) at 615 cm^{-1}.

(typical operating pressure < 10 torr). Thus long gas columns are necessary to ensure that a significant fraction of the pump energy is deposited in the gas. Gas columns of up to 10 m have been used (Jones *et al* 1978). Further, at the typical operating pressures the absorption spectral width (~ 100 MHz) is much narrower than the 3–4 GHz bandwidth of the conventional multimode TEA CO_2 lasers. Efficient optical excitation, therefore, demands spectral narrowing of the CO_2 pump source, to match the frequency, and the frequency spread, of the absorption feature. Since the CF_4 absorption feature responsible for 615 cm^{-1} emission is nearly resonant (frequency offset ~ 19 MHz) with the line centre of the 9R(12) CO_2 laser line, the desired pump frequency control is most readily achieved using a hybrid CO_2 laser (Stein *et al* 1978). Pumping other CF_4 transitions detuned from the CO_2 laser line centre requires off-line centre tuning of the CO_2 laser emission (Stamatakis and Green 1979). It is pertinent to note that spectral control of the TEA CO_2 laser pump is important not from efficiency considerations alone. The use of multimode pump also leads to an extremely erratic CF_4 laser operation. For example in the experiments of Green *et al* (1981) with a 3J multimode CO_2 laser pump and 5 m long CF_4 gas column, a detectable laser emission was observed in only one out of five pump laser pulses. This arises because for a multimode laser the axial mode frequencies and hence the energy absorbed in the gas changes from pulse to pulse. Finally the laser output has a rather strong temperature dependence primarily because, the lower laser level being close to the ground has significant thermal population. The best performance is obtained at the lowest temperatures compatible with the desired vapour pressure (Green 1979).

Thus, the two major requirements for a CF_4 laser are a narrow bandwidth CO_2 laser pump with frequency tuned to the CF_4 absorption feature and a long cryogenic cell.

3. CO_2 Laser pump

A schematic diagram of the home built, CO_2 laser pump system is shown in figure 2. It comprises of a hybrid CO_2 laser oscillator and a UV preionized TEA CO_2

CC-0. In Public Domain. Gurukul Kangri Collection, Haridwar

Digitized by Arya Samaj Foundation Chennai and eGangotri

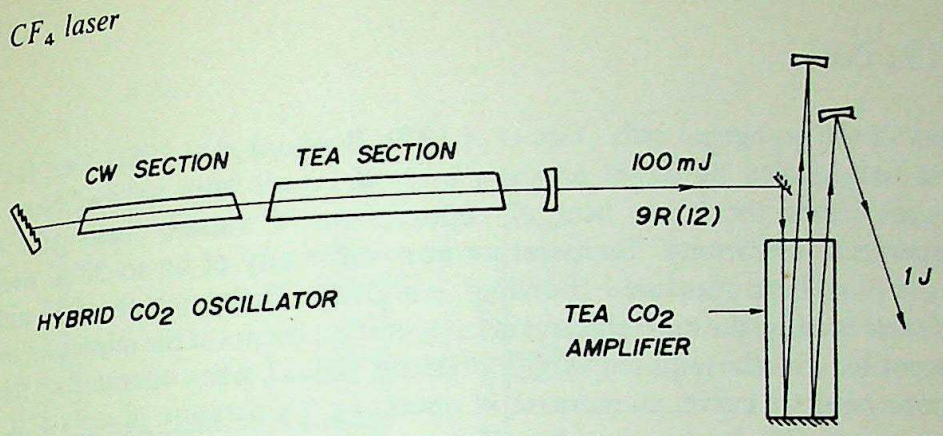

Figure 2. The CO_2 laser pump system.

amplifier. The line tunable, hybrid CO_2 laser oscillator, provided ~ 100 mJ output at a single longitudinal mode near the line center of the 9 μm R(12) line. This output was then amplified to $\gtrsim 1$ J level by making four passes through the 45 cm long TEA CO_2 amplifier having a discharge cross section of 4×4 cm. The beam configuration through the amplifier and the delay between the discharges of the oscillator and the amplifier were optimised for efficient energy extraction. The measured four pass gain of ten was in reasonable agreement with the theoretical estimates based on the configuration used.

A notable feature of the set up was the use of a polythene sheet as the optical window (Shikarkhane *et al* 1988) for the CO_2 amplifier because large aperture (10 cm diameter) conventional optical windows (required to make four passes through the amplifier) were not locally available. The polythene window did not result in any significant degradation of the beam quality of the amplified pulsed output. However, the cw CO_2 laser radiation could not be used for the alignment as it resulted in deformation of the window.

Long term operation of the CO_2 laser system revealed a gradual decay in the hybrid laser output at 9R(12) line. After an operational period of ~ 400 h the hybrid laser output dropped to $\sim 60\%$ of its initial value and more significantly the cw section of the hybrid oscillator could not be made to lase on the 9·6 μm band lines. This was traced to be due to a gradual accumulation of some whitish 'deposits' on the ZnSe Brewster windows, especially the one at the cathode end of the cw discharge section. The deposits were resistant to normal cleaning methods and had an absorption band overlapping the 9 μm CO_2 laser band. The usual window transmission was restored by lapping and repolishing the window. The gases were tested to be free from any contaminants to an impurity level of less than 1% by gas chromatographic analysis. The likely causes for the degradation of the optical quality of the ZnSe windows appear to be sputtering from the aluminium cathode, and laser induced thermochemical changes (Ursu *et al* 1986) which may be accelerated by the ambient humidity and dust. Increasing the distance of the ZnSe window from the cathode to ~ 15 cm and leaving the cw cell in an inert atmosphere have helped improve the performance; the cw output has dropped by only a factor of two after 500 h of operation whereas previously it had stopped lasing after 400 h of operation. More detailed and careful measurements are required to find the exact mechanism for the gradual degradation in the optical quality of the window.

CC-0. In Public Domain. Gurukul Kangri Collection, Haridwar

Digitized by Arya Samaj Foundation Chennai and eGangotri

4. CF_4 Cell

Most of the cryogenic cells (Tiee *et al* 1979; Bonanni *et al* 1981) used for CF_4 laser have been cooled by liquid nitrogen boil off. Apart from an inefficient use of the cryogen (since the latent heat of vaporization is wasted) these cells have poor temperature uniformity. Temperature non-uniformity of up to 30°K over the cold length have been measured (Bonanni *et al* 1981). Better temperature uniformity is desirable because the most efficient laser operation occurs at the minimum temperature compatible with the required vapour pressure. Indeed, when operated on the saturated vapour pressure curve, an increase in operating temperature of only 5° K can result in a drop in CF_4 laser output by a factor of two or three (Green 1979).

The design of a cryogenic cell which can provide temperature uniformity of a few °K over the cold length is shown in figure 3. The cell which is similar to the one developed by Rutt (1985) consists of a 3 m long, 34 mm internal diameter copper tube on which were wound three segments of a teflon insulated heater. The three segments are of equal length ($R = 120\,\Omega$) and connected to separate power supplies. The copper tube was placed in an annular stainless steel liquid nitrogen jacket (the inner and the outer diameters of the two tubes being 81; 89 mm and 128; 142 mm respectively). The liquid nitrogen tank was insulated from the atmosphere by two layers of 6 cm thick freon impregnated polyurethane foam moulded in semi-cylindrical form to fit the tube. Thermal insulation between the variable temperature copper tube and the liquid nitrogen bath was provided by filling the annular space between the two by vermiculite (expanded mica). The latter was purged with dry nitrogen to avoid condensation of atmospheric water vapour in the vermiculite which greatly increases its thermal conductivity. A chromel constantan thermocouple was attached to each of the three heater segments to monitor the cell temperature. Since the liquid nitrogen tank provides a reference temperature, by adjusting the power dissipated in the three heaters the cell temperature was varied from $\sim$90°K to $\sim$230°K. The power dissipated in three heaters was independently adjusted to ensure temperature uniformity over the cold length (inferred from the temperature measured at the three points where the thermocouples were located) of $\sim$5°K. The absence of any significant cold spots was ascertained by measurements of the saturated vapour pressure.

Pumping arrangement. A schematic diagram of the pumping arrangement used for CF_4 laser is shown in figure 4. The CO_2 laser radiation was injected in the cryogenic cell through a Ge Brewster window. The pump radiation was *p* polarized so as to transmit through the Brewster plate without reflection loss. Due to the constraints on the available optics only $\sim$500 mJ of the CO_2 laser radiation could be injected into the CF_4 gas. The pump beam was gently focused in the centre of the cell to result in peak energy fluence of $\sim 1\,J/cm^2$. The 16 μm laser cavity was formed for the orthogonal polarization by the mirror M_1 and the output coupler connected through the reflection at the Brewster surface. Since large gain lengths are involved the CF_4 laser can operate even without feed-back in the amplified spontaneous emission (ASE) mode (figure 4b, c). In the arrangement of figure 4c a fraction of the 16 μm radiation growing in the direction opposite to the pump beam is reflected back by the Ge Brewster window and the mirror M_2 to add to the useful output from the other end of the cell. The 16 μm output was separated from the pump CO_2 radiation via a combination of a LiF reststrahlen filter and a band pass dielectric filter. The latter

CC-0. In Public Domain. Gurukul Kangri Collection, Haridwar

Digitized by Arya Samaj Foundation Chennai and eGangotri

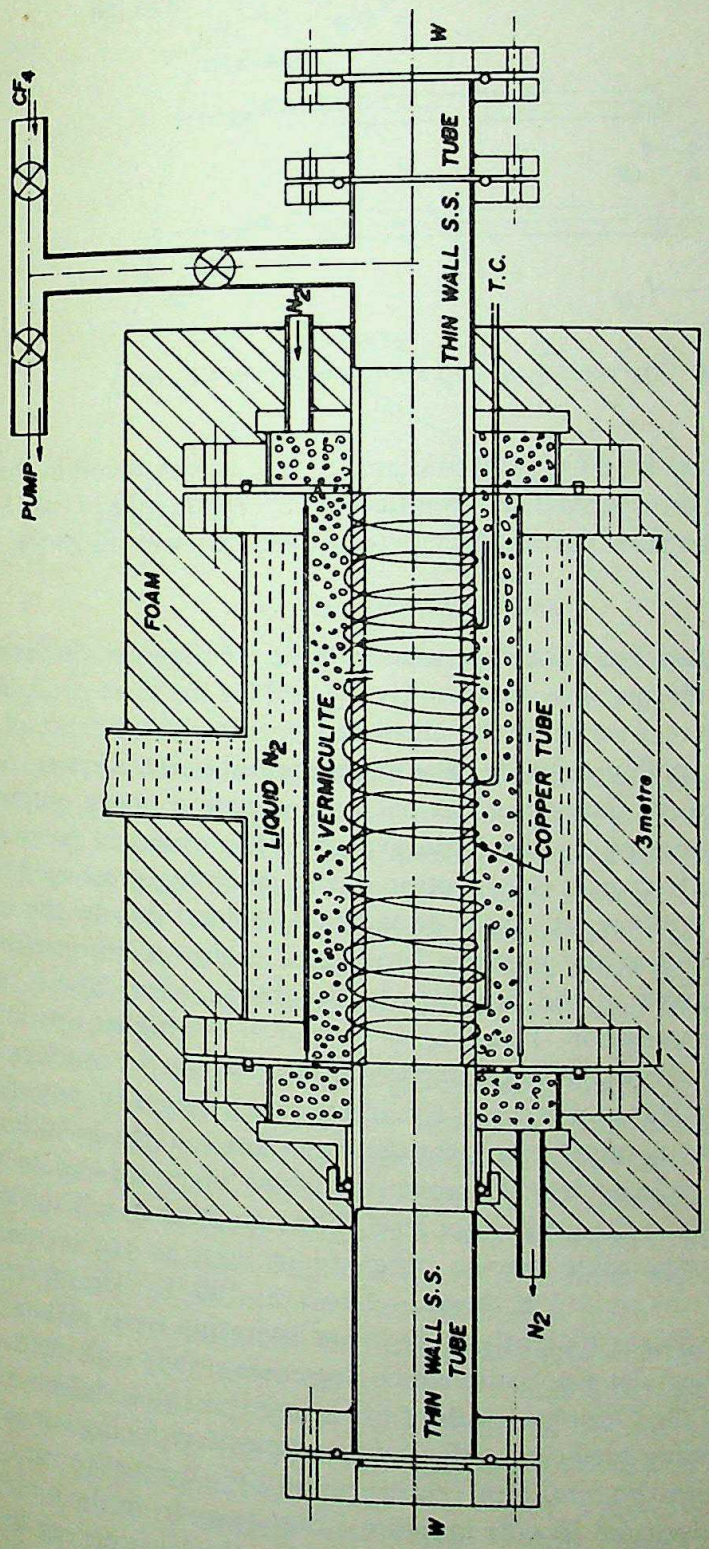

Figure 3. The cryogenic cell.

CC-0. In Public Domain. Gurukul Kangri Collection, Haridwar

Digitized by Arya Samaj Foundation Chennai and eGangotri

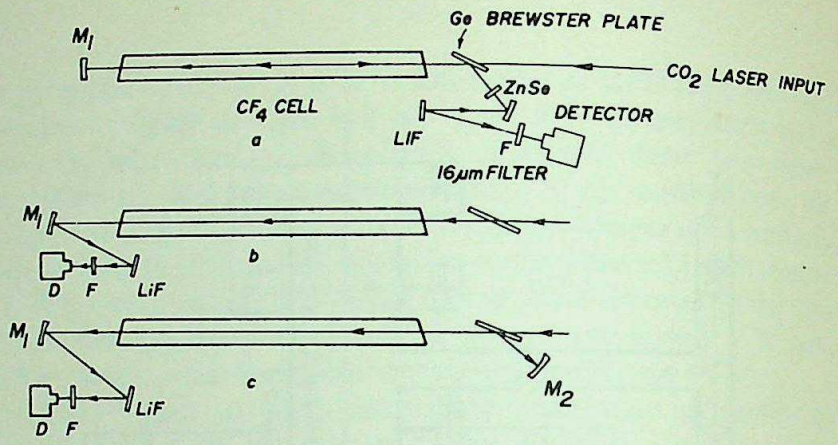

Figure 4. The pumping arrangements used for the CF_4 laser.

had a high rejection for CO_2 radiation and $\sim 70\%$ transmission in the 16 μm range. The combination provided a discrimination of 10^6:1 in favour of the 16 μm radiation. A calibrated molectron pyroelectric detector (J3-05) was used for 16 μm energy measurements.

CF_4 Laser characteristics. The dependence of the CF_4 laser output on the operating temperature and the gas pressure was investigated for the three configurations shown in figure 4. In figure 5 we show the measured pressure dependence of the CF_4 laser output using the configuration 4c. The experimental points shown are average over several pulses and the bars show the per cent variation in the output ($2\sigma/\bar{x}$, where σ is the standard deviation and $\bar{x}$ the average). The observed pressure dependence arises because the laser gain is a function of the operating pressure. It increases with pressure at low pressures (Doppler-broadened regime) due to the increase in the number density and in the pressure broadened region it becomes independent of pressure, the increase in the number density being offset by an increase in the bandwidth of the transition. The drop in output at the higher operating pressure is due to two reasons. First, the increasing loss introduced by the overlapping absorption band. Second, for higher pressures, the input pump intensity may also cease to be sufficient for inverting population over the entire gas column. In such a situation not only is the gain reduced but self absorption also increases due to the significant thermal population in the lower laser level. The reduction in self absorption at lower temperatures is responsible for the observed increase in the maximum operating pressure to ~ 15 torr at 115°K from ~ 9 torr at 190°K. The optimum operating pressure is seen to decrease slightly at the lower operating temperature. This is because maximum gain occurs at a pressure which decreases slowly with decreasing temperature as a result of the Doppler width of the lasing transition decreasing. Further the collisional broadening coefficient will also increase with reducing temperature because at constant pressure, the rotational relaxation time is expected to vary as $T^{1/2}$ (Green 1979). It is also important to note in figure 5 that away from the optimum operating pressure (4–5 torr), the pulse to pulse variation in the laser energy output increases significantly. In particular, CF_4 laser operation near the maximum operating pressure is very erratic with laser action occurring in one pulse out of 5–10 pump pulses. One important reason for this erratic behaviour is that the pump laser frequency is not

CC-0. In Public Domain. Gurukul Kangri Collection, Haridwar

Digitized by Arya Samaj Foundation Chennai and eGangotri

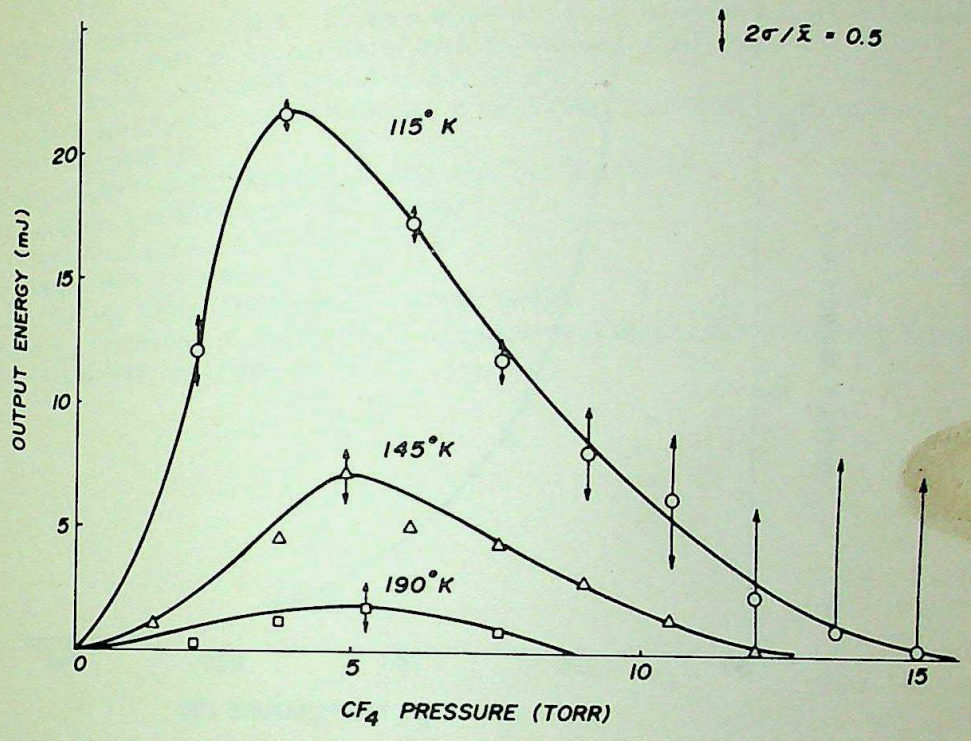

Figure 5. Output energy versus gas pressures at various temperatures for the 16 μm CF_4 laser.

locked and can wander within the gain bandwidth of the low pressure section. The maximum frequency by which the pump laser frequency can get detuned for the CO_2 laser line center is by half the cavity mode spacing for the pump laser ($\sim$50 MHz). The resulting change in the absorbed energy and hence the gain at 16 μm will lead to much larger changes in the laser amplitude for operation close to the lasing threshold and thus at pressures away from the optimum operating pressures. Better amplitude stability will require stabilization of the pump laser frequency to within $\pm$5 MHz (Hawkins *et al* 1985).

In figure 6 we show a plot of the CF_4 laser energy obtained at the optimum (temperature-dependent) pressure against the operating temperature. The output is seen to have a rather strong temperature dependence and increases by a factor of 40 on reduction in temperature from 228°K to 115°K. Under optimum conditions, 5 mJ output was obtained in the oscillator mode (figure 4a) with an uncoated ZnSe window as an output coupler. The energies obtained in the ASE mode were 15 mJ with the arrangement as in figure 4b (mirror M_2 removed) and 20 mJ with the arrangement as in figure 4c. The increased output in the ASE mode is presumably due to the large gain lengths and the use of a lossy cavity for the oscillator (the intracavity Ge Brewster window reflects only 78% of the s polarized 16 μm radiation). In our experiments only $\sim$40% of the CO_2 laser energy was absorbed in the gas column, under the optimum operating conditions ($T = 115$°K, $P \sim 4$ torr). This implies an absorption cross-section, averaged over the pump laser bandwidth, of $\sim 5{\cdot}1 \times 10^{-21}$ cm^2 in reasonable agreement with the other reported values (Bonanni *et al* 1981). Thus in our experiments 20 mJ output is generated at 16 μm with $\sim$200 mJ of the CO_2 laser energy absorbed in the gas. The resulting absorbed energy conversion efficiency of $\sim$10% compares favourably with the best reported values for this emission. (Barnov *et al* 1980; Stein *et al* 1978).

CC-0. In Public Domain. Gurukul Kangri Collection, Haridwar

Digitized by Arya Samaj Foundation Chennai and eGangotri

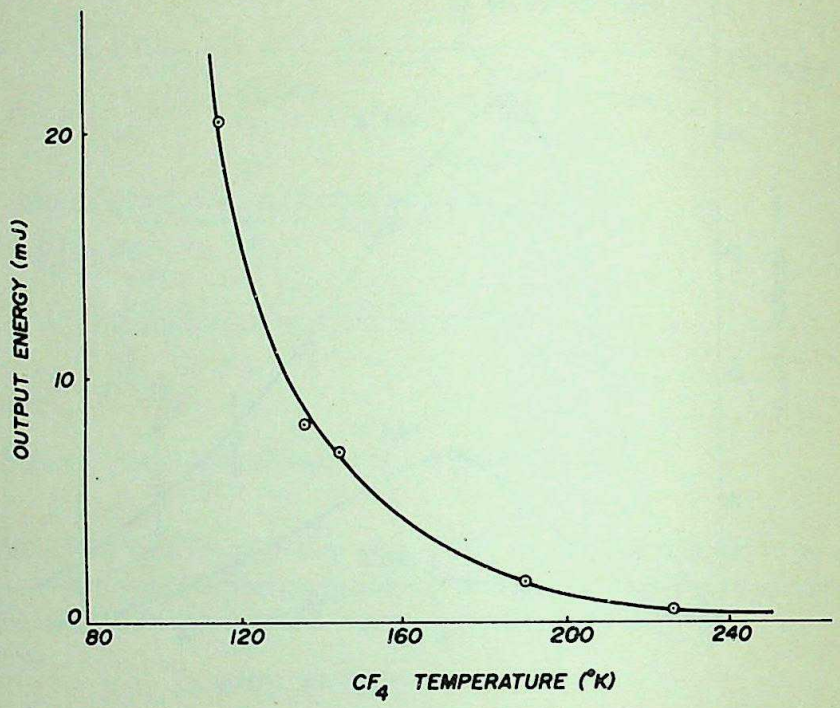

Figure 6. Maximum output energy versus gas temperature for the 16 μm CF_4 laser.

5. Conclusion

To conclude, a CO_2 laser pumped CF_4 laser has been developed at BARC. Output energies of upto 20 mJ have been obtained with an absorbed energy conversion efficiency of $\sim 10\%$.

Acknowledgement

The authors would like to thank Dr K C Rustagi, Dr P R K Rao, Dr J P Mittal and Dr D D Bhawalkar for their help and encouragement at various stages of work.

References

Ambartsumyan R V, Apatin V M, Basov N G, Grasyuk A Z, Dyad'kin A P, and Furzikov N P 1979 *Sov. J. Quantum Electron.* **9** 1546

Barnov V Yu, Kazakov S A, Mezhekov V S, Napartovich A P, Orlov M Yu, Pis'mennyi V O, Starodubtsev A I and Starostin A I 1980 *Sov. J. Quantum Electron.* **10** 47

Bonanni F, Castiglione S, and Salvetti G 1981 *Nuovo Cimento* **B66** 129

Grasyuk A Z, Letokhov V S and Lobko V V 1981 *Prog. Quantum Electron* **6** 245

Green J M 1979 *J. Phys. D.* **12** 489

Green J M, Stamatakis T and Aldcroft D A 1981 *Opt. Commun.* **39** 49

Gupta P K and Mehandale S C 1987 *Hyperfine Interactions* **37** 243

Hawkins K C, Peacock R and Rutt H N 1985 *J. Phys.* **D18** 191

Horsley J A, Rabinovitz P, Stein A, Cox D M, Brickman R O and Kaldor A 1980 *IEEE J. Quantum Electron.* **OE-16** 412

CC-0. In Public Domain. Gurukul Kangri Collection, Haridwar

Digitized by Arya Samaj Foundation Chennai and eGangotri

Jones C R, Telle J M and Buchwald M I 1978 *Digest of technical papers presented at Tenth Int. Quantum Electron. Conf.* Atlanta, Publ. by Optical Soc. of America, Washington, D.C. paper K-7
Koren G, Gerther Y and Shreter U 1982 *Appl. Phys. Lett.* **41** 397
McDowell R S, Patterson C W, Jones C R, Buchwald M I and Telle J M 1979 *Opt. Lett.* **4** 274
Rutt H N 1985 *J. Phys.* **E18** 334
Shikarkhane N S, Nundy U and Chatterjee U K 1988 *Appl. Opt.* **27** 1636
Stamatakis T and Green J M 1979 *Opt. Commun.* **30** 413
Stein A, Rabinowitz P and Kaldor A 1978 *Opt. Lett.* **3** 97
Tiee J J and Wittig C 1978 *Opt. Commun.* **27** 377
Tiee J J, Fischer T A and Wittig C 1979 *Rev. Sci. Instrum.* **50** 958
Ursu I, Mihailescu I N, Nistor L C, Teodorescu V S, Prokhorov A M, Chapliev N I, Konov V I and Starodumov Yu M 1986 *Appl. Phys.* **A40** 227

CC-0. In Public Domain. Gurukul Kangri Collection, Haridwar

Digitized by Arya Samaj Foundation Chennai and eGangotri

CC-0. In Public Domain. Gurukul Kangri Collection, Haridwar

Digitized by Arya Samaj Foundation Chennai and eGangotri

Pramāṇa – J. Phys., Vol. 34, No. 4, April 1990, pp. 259–277. © Printed in India.

Layered superconductors with anisotropic energy gap: specific heat and infrared absorption

SUDHANSHU S JHA
Tata Institute of Fundamental Research, Homi Bhabha Road, Bombay 400 005, India

MS received 7 November 1989

Abstract. New oxide superconductors with layered structure are expected to have anisotropic energy gap in the generalized BCS pairing theory. The gap parameter $2\Delta(\hat{k})$ can be quite different for $\hat{\mathbf{k}}$ perpendicular to the plane of the layers as compared to $\mathbf{k}$ parallel to layer planes. Because of short coherence lengths ξ, quite small compared to the normal state carrier meanfree path l, the effect of these anisotropies do not average out, as in many of the conventional superconductors. For a proper comparison of experimental results with the correct predictions of the pairing theory, a formulation is developed to obtain important physical quantities like specific heat and infrared absorption in the superconducting state of such anisotropic systems. This includes a brief account of the pairing theory generalized to layered crystals with arbitrary number of layers per unit cell, not necessarily equidistant. In an explicit model for the anisotropy of the gap parameter in $\mathbf{k}$-space, with a simple form for the nonspherical Fermi-surface, it is shown that the low-temperature specific heat can have even a linear or a power-law temperature-dependence in the superconducting state. Even if the gap parameter does not vanish anywhere, its smeared-out exponential temperature-dependence may be difficult to be distinguished experimentally from a power-law behaviour. Similarly, it is shown that in the case of appreciable anisotropy, infrared absorption can take place much below the in-plane gap parameter $2\Delta_t(\hat{k}_t)$, where $\mathbf{k}_t$ is the wavevector in the plane of the layers.

Keywords. Layered superconductors; anisotropic energy gap; specific heat; infrared absorption.

PACS Nos 74·20, 74·30, 74·70

1. Introduction

The behaviour of many of the important physical parameters in the superconducting state of the recently discovered high-T_c metallic oxides is known to differ considerably from the predictions of the simple one-parameter, isotropic, weak-coupling BCS model. This need not be very surprising, since these materials have layered structures with large anisotropies in the normal state properties of the relatively low density (~a few times 10^{21} cm^{-3}) carriers, and they have very short anisotropic coherence lengths (3Å to 20Å) in the superconducting state. The mobility of the carriers in the conducting Cu-O layers, which are approximately parallel to the a–b plane of the crystalline unit cell, is much higher than their value in the perpendicular direction (C-axis). Moreover, significant deviations are expected (Jha 1989) because of (i) possible strong-coupling effects in the generalized BCS pairing arising from a net dynamic attractive interaction between the carriers, due to the exchange of lattice phonons and/or electronic excitations in the system, (ii) the possibility of interacting carriers in more than one narrow band or layer, and (iii) possible corrections to the usual

CC-0. In Public Domain. Gurukul Kangri Collection, Haridwar

Digitized by Arya Samaj Foundation Chennai and eGangotri

mean-field results of the theory. Nevertheless, due to the unusual normal and superconducting properties of these metallic oxides, very serious and fascinating attempts have been made to find an alternative to the generalized BCS pairing theory (Anderson 1987; Anderson *et al* 1987), in the form of the resonating-valence-bond (RVB) approach involving very large repulsive intra-atomic carrier-carrier interaction energy U as compared to the band width W of the single-particle electronic states. There are various other bosonic models involving some kind of pairing of fermions followed by Bose-condensation of these pairs, e.g., of possible bound bi-polarons in these materials.

As of now, it is fair to say that starting from a collection of charged fermions, the generalized BCS pairing idea, involving off-diagonal long range order in the two-particle density matrix, seems to be an ideal approach in which the superconducting transition can be demonstrated theoretically without any doubt. In view of this, it is of great interest to examine whether various experimental results on single-crystals of these new high-T_c materials can still be understood, at least in principle, within the framework of an appropriate generalization of the BCS pairing theory. In this connection, as two typical examples, we will consider the behaviour of the electronic specific heat and the infrared absorption in the superconducting state of such materials. Experimentally, it has been found that in many of these materials the electronic specific heat (Phillips *et al* 1987; Ishikawa *et al* 1987; Batlogg *et al* 1987) at low temperatures seems to vary linearly with temperature T, insted of the usual exponential expected in the simple BCS model with a finite gap parameter $\Delta(T)$. Similarly, there seems to be some residual (Schlesinger *et al* 1987; Beyerman *et al* 1987; Sulewski *et al* 1987) absorption of infrared frequencies below the identifiable energy-gap "2Δ", even in the case of experiments done on single crystals, so that the absorption edge is not as sharp as in many of the conventional superconductors (Ginsberg and Hebel 1969). Also, the values of the energy-gap measured in such experiments seem to be somewhat different than their corresponding values obtained in tunnelling experiments. However, even in tunnelling data it is difficult to find real sharp characteristics.

As indicated earlier, the layered structure of the crystal and large anisotropies in various properties can have significant consequences for the nature of superconductivity in these materials. Even when one works within the framework of the mean-field theory of the generalized BCS approach, one can obtain anisotropic gap functions $\Delta(\mathbf{k})$ which may even vanish, depending upon the symmetry of the layers and the crystal, in certain directions or regions of the $\mathbf{k}$-space, e.g., for $\mathbf{k}$ perpendicular to the conducting layers in the high-T_c oxides. In such a case, a power-law behaviour for the electronic specific heat, etc., can result. Note that the conventional argument about the absence of nodes in Δ for the familiar s-wave pairing is no longer valid, because for layered crystals with highly non-spherical Fermi surfaces, a fixed orbital-l is not the correct label to describe pairing. As an approximation, we can still assume isotropy in the 2-dimensional plane of the layers, but not in the direction perpendicular to the planes. We can no longer talk of a s-wave pairing or a d-wave pairing, etc., a concept applicable to the three-dimensional isotropic case. If the gap parameter is small or vanishing in the direction perpendicular to the a-b plane of $\hat{k}$, it is possible to get finite infrared absorption below the larger energy-gap $2\Delta(\hat{k}_t)$ in the a-b plane, depending on the direction of propagation and polarization of the incident radiation.

In what follows, we first describe briefly the recent formulation of the BCS pairing theory in layered crystals, in §2. For allowed pairing within the same conducting

CC-0. In Public Domain. Gurukul Kangri Collection, Haridwar

Digitized by Arya Samaj Foundation Chennai and eGangotri

layer j in any unit cell or within the same band b only, the contributions of quasi-particles in different layers or bands to thermodynamic functions are additive. In view of this, we also examine in §2, the temperature-dependence of specific heat in the superconducting state with anisotropic $\Delta(\mathbf{k})$, consistent with the approximate symmetry for the motion of carriers close to the anisotropic Fermi surface. In an explicit simple model for $\Delta_j(\mathbf{k})$, for $\mathbf{k}$ close to the Fermi surface, where it is assumed to depend only on the direction of $\hat{k}$, the specific heat is calculated analytically to show how the power-law behaviour can be obtained in such a case. The effect of the energy-gap anisotropy on thermodynamic and other properties has been considered extensively in the past for the conventional superconductors (Sheplev 1969). However, in most of these studies the anisotropic part of the gap function is assumed to be small compared to the main isotropic part. This is not necessarily the case in the new superconductors. Moreover, when the coherence length ξ is small compared to the mean free path l due to impurities etc., the effect of anisotropy in many of the physical measurements, e.g., in electromagnetic absorption, does not average out (Anderson 1959), as in most of the conventional superconductors. In §3, we present the calculation of the linear response function for electromagnetic waves in a superconductor with anisotropic energy-gap and nonspherical Fermi surface, valid for the case under discussion in which $\xi \ll l$. By an explicit calculation, we show how the imaginary part of the dielectric function $\varepsilon''_{\mu\nu}(\mathbf{q}, \omega)$, i.e. the real part of the conductivity tensor $\sigma'_{\mu\nu}(\mathbf{q}, \omega)$ can have strength below the larger gap corresponding to $\mathbf{k}$ in the a-b plane. We conclude our discussion in §4.

2. Anisotropic energy-gap and specific heat in layered crystals

Starting with the single-particle electronic-band picture and with Cooper pairing restricted to carriers in the same conducting band only, it is wellknown that the quasi-particle excitations in the superconducting state can be described by the approximate diagonalized Hamiltonian

$$H - \mu N = \langle C \rangle_\mu + \sum_{b\mathbf{k}} E_{b\mathbf{k}} (\gamma^+_{b\mathbf{k}0} \gamma_{b\mathbf{k}0} + \gamma^+_{b\mathbf{k}1} \gamma_{b\mathbf{k}1}) \tag{1}$$

where γ's satisfy the usual Fermion anti-commutation relations and where the quasi-particle energies are given by

$$E_{b\mathbf{k}} = [(\varepsilon_{b\mathbf{k}} - \mu)^2 + \Delta_b^2(\mathbf{k})]^{1/2} \equiv [\xi^2_{b\mathbf{k}} + \Delta_b^2(\mathbf{k})]^{1/2} \tag{2}$$

in terms of the BCS energy-gap parameters $\Delta_b(\mathbf{k}, T)$ and the Bloch energy $\xi_{b\mathbf{k}}$ of the carriers measured from the chemical potential (Fermi energy) μ. In (1), the fixed-μ thermal average

$$\text{with} \qquad \langle C \rangle_\mu = \sum_{b\mathbf{k}} [\xi_{b\mathbf{k}} - E_{b\mathbf{k}} + (\Delta_b^2(\mathbf{k})/2E_{b\mathbf{k}}) \{1 - 2f(E_{b\mathbf{k}})\}] \tag{3}$$

$$f(E) \equiv [1 + \exp \beta E]^{-1}, \quad \beta = 1/k_B T. \tag{4}$$

The coupled BCS equations for the energy-gap functions $\Delta_b(\mathbf{k})$ in the multi-band case were already considered by Suhl *et al* (1959) in terms of the effective interaction parameters $V_{bb'}$. Explicitly, the determination (Jha 1988) of the effective interaction

CC-0. In Public Domain. Gurukul Kangri Collection, Haridwar

Digitized by Arya Samaj Foundation Chennai and eGangotri

functions $V_{bb'}(\mathbf{q}=\mathbf{k}'-\mathbf{k},\omega)$ and the corresponding T_c involves the knowledge of an appropriate inverse dielectric matrix $\varepsilon^{-1}(\mathbf{q}+\mathbf{G}, \mathbf{q}+\mathbf{G}', \omega)$ in the reciprocal G-space of the crystal. Note that, in general, $\Delta_b(\mathbf{k})$ is an anisotropic function of $\mathbf{k}$.

For any 3-dimensional layered crystal, the above multi-band formulation is enough to obtain T_c, $\Delta_b(\mathbf{k}, T)$ and other physical properties of the superconducting material. However, we (Jha 1987) have argued that in highly-layered crystals in which the electronic motion is mostly confined to the plane of the layers, with much larger effective mass in the direction perpendicular to the layers, it is more appropriate to consider effective Cooper pairing of carriers in the same localized layers j only. In other words, to avoid consideration of large matrices in the reciprocal lattice space-G and various local-field corrections in the multi-band theory, the order parameters or the energy-gap parameters are now described by $\Delta_j(\mathbf{k})=\Delta_j(\mathbf{k}_t, k_z)$ where $\mathbf{k}_t$ is the wave vector in the plane of the layers and $k_z=\theta/L$, $0\leqslant\theta\leqslant 2\pi$ is the wavevector in the z-direction, perpendicular to the layer plane, for each of the layers j in the unit cell of length L in the z-direction. Superconductivity in a layered crystal with electronic motion localized in equally-spaced alternate metallic and insulating molecular layers was already investigated by Bulaevskii and Kukharenko (1971). However, we have generalized the formulation to an arbitrary number of layers in any unit cell, which are not necessarily equidistant (Jha 1988). In such an approach, the gap functions Δ_j are determined by the solution of coupled equations

$$\Delta_j(\mathbf{k}_t, k_z) = -\sum_{\mathbf{k}'_t}\sum_{k'_z}\sum_{j'} V^{\text{sup}}_{jj'}(\mathbf{q}_t=\mathbf{k}_t-\mathbf{k}'_t, q_z=k_z-k'_z, \xi_j, \xi_{j'}) \times \Delta_{j'}(\mathbf{k}'_t, k'_z)\tanh(\beta E_{j'\mathbf{k}'})/2E_{j'\mathbf{k}'} \tag{5}$$

where

$$E^2_{j\mathbf{k}} = \xi^2_j(\mathbf{k})+\Delta^2_j(\mathbf{k}) \equiv \xi^2_j(\mathbf{k}_t, k_z)+\Delta^2_j(\mathbf{k}_t, k_z) \tag{6}$$

in terms of the single-particle energies $\xi_j(\mathbf{k})$ of carriers localized in layers j, and where

$$V^{\text{sup}}_{jj'}(\mathbf{q}_t, q_z, \xi, \xi') = V^{(0)}_{jj'}(\mathbf{q}_t, q_z)+\frac{2}{\pi}\int_0^\infty d\omega' \frac{\text{Im}\, V_{jj'}(\mathbf{q}_t, q_z, \omega')}{\omega'+|\xi|+|\xi'|}. \tag{7}$$

In the above equation, $V^{(0)}_{jj'}(\mathbf{q}_t, q_z)$ is the Fourier transform of the bare Coulomb interaction between two carriers in layers j and j' in any unit cell, and $V_{jj'}(\mathbf{q}_t, q_z, \omega)$ is the corresponding effective dynamic interaction in the presence of other electrons and ions. If the z-coordinate of the nth layer is given by

$$z_n = z(N, j) = NL+R_j, \quad R_0=0 \tag{8}$$

where N denotes the unit cell label and j denotes the label for the layer within the unit cell, and where $R_{jj'}=R_j-R_{j'}$ denotes the distance of the jth layer from the j'th layer in the cell, for any function $g(\mathbf{q}_t, z_n-z_{n'})$ we can write

$$g(\mathbf{q}_t, z_n-z_{n'}) \equiv g_{jj'}(\mathbf{q}_t, N-N') = \frac{L}{2\pi}\int_0^{2\pi/L} dq_z g_{jj'}(\mathbf{q}_t, q_z)\exp(i(N-N')Lq_z. \tag{9}$$

For m layers in any unit cell, a simplified diagrammatic perturbation theory can then be used to find the $m\times m$ dynamic interaction matrix V in terms of $V^{(0)}_{jj'}$ and

CC-0. In Public Domain. Gurukul Kangri Collection, Haridwar

Digitized by Arya Samaj Foundation Chennai and eGangotri

2-dimensional electronic layer-polarization functions

$$\Pi_{jj'}(\mathbf{q}_t,\omega)=\delta_{jj'}\pi_j(\mathbf{q}_t,\omega)=\delta_{jj'}\pi_{j+m}(\mathbf{q}_t,\omega). \tag{10}$$

Explicitly, using the matrix notation, one finds

$$V(\mathbf{q}_t,q_z,\omega)=\varepsilon^{-1}(\mathbf{q}_t,q_z,\omega)V^{(0)}(\mathbf{q}_t,q_z) \tag{11}$$

$$\varepsilon(\mathbf{q}_t,q_z,\omega)=I+V^{(0)}(\mathbf{q}_t,q_z)\Pi(\mathbf{q}_t,\omega) \tag{12}$$

where I is the $m\times m$ unit matrix, and

$$V^{(0)}_{jj'}(\mathbf{q}_t,q_z)=\begin{cases}\dfrac{2\pi e^2}{q_t}[P(q_t,q_z)\exp(-q_tR_{jj'})+N(q_t,q_z)\exp(q_tR_{jj'})]; & j>j'\\ \dfrac{2\pi e^2}{q_t}[P(q_t,-q_z)\exp(q_tR_{jj'})+N(q_t,-q_z)\exp(-q_tR_{jj'})]; & j<j'\end{cases} \tag{13}$$

$$P(q_t,q_z)=\exp(iq_zL)[\exp(iq_zL)-\exp(-q_tL)]^{-1} \tag{14}$$

$$N(q_t,q_z)=\exp(-q_tL)[\exp(-iq_zL)-\exp(-q_tL)]^{-1}. \tag{15}$$

Note that $\varepsilon^{-1}(\mathbf{q}_t,q_z,\omega)$ is a $m\times m$ non-diagonal matrix so that even the effective interaction between two carriers in the same layer j depends not only on the polarization function of the same layer but also of other layers in the unit cell. These polarization functions $\pi_j(\mathbf{q}_t,\omega)$ contain contributions from all possible electronic and ionic excitations in the system.

From the above discussions, it is quite clear that for layered crystals, the energy-gap parameters are expected to be highly anisotropic in **k**-space. Whether one uses the multi-band picture or the multi-layer picture, the total contributions to thermodynamic functions are of course additive corresponding to quasi-particles labelled by the band indices b or the layer indices j in (1). For a given form for such a gap function $\Delta(\mathbf{k})$, one has the usual result for the thermodynamic potential

$$\Omega=-\frac{1}{\beta}\ln Z=\frac{2}{\beta}\sum_{\mathbf{k}}\ln[(1-f(E_{\mathbf{k}})]+\langle C\rangle_{\mu} \tag{16}$$

where the partition function

$$Z=\exp(-\beta\Omega)=\mathrm{Trace}\exp(-\beta(H-\mu N)],\quad \Omega=E-TS-\mu N. \tag{17}$$

The entropy per unit volume V is then given by

$$S=-\frac{1}{V}\left[\left(\frac{\partial\Omega}{\partial T}\right)_{V,\mu}\right]=-2k_B\int\frac{\mathrm{d}^3k}{(2\pi)^3}[\ln(1-f(E_{\mathbf{k}}))-\beta E_{\mathbf{k}}f(E_{\mathbf{k}})] \tag{18}$$

from which the specific heat per unit volume can be obtained by the relation

$$C=T\frac{\partial S}{\partial T}=-\beta\frac{\partial S}{\partial\beta}. \tag{19}$$

CC-0. In Public Domain. Gurukul Kangri Collection, Haridwar

Digitized by Arya Samaj Foundation Chennai and eGangotri

If one chooses suitable co-ordinates u and v on the surface of constant single-particle energy $\xi_{\mathbf{k}}=\xi$, so that k_x, k_y, and k_z can be rewritten as functions of u, v and ξ, the integral over d^3k in (18) transforms to

$$\int \frac{\mathrm{d}^3k}{(2\pi)^3} \to \frac{1}{8\pi^3} \int \mathrm{d}u \int \mathrm{d}v \int \mathrm{d}\xi J(u,v,\xi) \equiv \int \mathrm{d}u \int \mathrm{d}v \int \mathrm{d}\xi g(u,v,\xi) \tag{20}$$

where $J(u,v,\xi)$ is the Jacobian determinant

$$J(u,v,\xi) = 8\pi^3 g(u,v,\xi) = \left(\frac{\partial \mathbf{k}}{\partial u} \times \frac{\partial \mathbf{k}}{\partial v}\right) \cdot \frac{\partial \mathbf{k}}{\partial \xi} = \frac{\mathrm{d}^2\sigma_\xi}{|\nabla_{\mathbf{k}}\xi|} \tag{21}$$

in terms of the element of the surface area $\mathrm{d}^2\sigma_\xi$ on the surface $\xi_{\mathbf{k}}=\xi$. In terms of these new variables, $\Delta(\mathbf{k}) \to \Delta(u,v,\xi)$, $E_{\mathbf{k}} \to E(u,v,\xi)$, and the entropy can then be calculated in the form

$$S = H(1) + \int_1^\infty \mathrm{d}\lambda H(\lambda) \tag{22}$$

$$H(\lambda) = 2k_B \int \mathrm{d}u \int \mathrm{d}v \int_{-\mu}^{\infty} \mathrm{d}\xi g(u,v,\xi) \beta E [1 + \exp(\lambda \beta E)]^{-1} \tag{23}$$

$$E = [\xi^2 + \Delta^2(u,v,\xi)]^{1/2}. \tag{24}$$

As it is often the case, if the contributions to S are dominated by the region in ξ near the Fermi surface, i.e. $\xi \simeq 0$, the above general calculation can be simplified considerably. In such a case, one can replace g and Δ in (23) and (24) by their values at the Fermi surface:

$$g(u,v,\xi) \to g(u,v,0) \equiv g_F(u,v) \tag{25}$$

$$\Delta(u,v,\xi) \to \Delta(u,v,0) \equiv \Delta_F(u,v). \tag{26}$$

This leads to the expression

$$S = 2k_B \int \mathrm{d}u \int \mathrm{d}v g_F(u,v) G(u,v) \tag{27}$$

where

$$\begin{aligned} G(u,v) &= 2\beta \int_{\Delta_F}^{\infty} \mathrm{d}E f(E)[E^2 + \xi^2]/\xi \\ &= 2\beta\Delta_\beta^2 \int_0^\infty \mathrm{d}y \frac{\cosh 2y}{[1 + \exp(\beta\Delta_F \cosh y)]} \\ &= 2\beta\Delta_F^2 \sum_{n=1}^{\infty} (-1)^{n-1} K_2(n\beta\Delta_F) \end{aligned} \tag{28}$$

in terms of the modified Bessel function K_2. Note that by definition, the single-spin density of states N_F at the Fermi surface ($\xi=0$) is simply given by

$$\int \mathrm{d}u \int \mathrm{d}v g_F(u,v) = N_F. \tag{29}$$

CC-0. In Public Domain. Gurukul Kangri Collection, Haridwar

Digitized by Arya Samaj Foundation Chennai and eGangotri

For the single-particle carrier energy of the form

$$\xi_k = \frac{\hbar^2 k_X^2}{2m_{XX}} + \frac{\hbar^2 k_Y^2}{2m_{YY}} + \frac{\hbar^2 k_Z^2}{2m_{ZZ}} - \mu \tag{30}$$

it is possible to choose spherical polaral coordinates $\theta = v$, $\phi = u$ on the constant energy surface, so that

$$g_F(u, v)\,du\,dv = \frac{N_F}{4\pi} \sin\theta d\theta\, d\phi \tag{31}$$

$$N_F = \frac{1}{4\pi^2}\left[\frac{2}{\hbar^2}(m_{XX}m_{YY}m_{ZZ})^{1/3}\right]^{3/2} \mu^{1/2} \tag{32}$$

and

$$S = \frac{N_F k_B}{\pi} \int_0^{\pi} \sin\theta\, d\theta \int_0^{2\pi} d\phi \Delta_F^2(\theta, \phi) \sum_{n=1}^{\infty} (-1)^n K_2(n\beta\Delta_F(\theta, \phi)). \tag{33}$$

If one assumes isotropy in the a-b plane, one can take $m_{XX} = m_{YY}$ in (30) and (32). Further, because of the symmetry in the problem, if $\Delta_F(\theta, \phi) = \bar{\Delta}_F(|\cos\theta|)$, i.e. the gap parameter is independent of ϕ and depends only on the magnitude of $\cos\theta$, with $\theta = 0$ along the perpendicular z-axis, the above expression simplifies to

$$S = 2N_F k_B \beta \sum_{n=1}^{\infty} (-1)^{n-1} D_n(\beta) \tag{34}$$

$$D_n(\beta) = 2\int_0^1 dx \bar{\Delta}_F^2(x) K_2(n\beta\bar{\Delta}_F(x)). \tag{35}$$

Note that when $\bar{\Delta}_F(x) = 0$, the above expression leads to the usual linear temperature dependence of the entropy in the normal state, as $T \to 0$,

$$S_{\text{normal}} = \frac{2\pi^2}{3} k_B^2 N_F T \tag{36}$$

since

$$\operatorname*{Lt}_{y\to 0} K_2(ny) = \frac{2}{n^2 y^2}, \quad \sum_{n=1}^{\infty} (-1)^{n-1} \frac{1}{n^2} = \frac{\pi^2}{12}. \tag{37}$$

Similarly, for an isotropic gap $\bar{\Delta}_F(x) = \Delta$ in the superconducting state,

$$S \to 4N_F k_B \beta \Delta^2 \sum_{n=1}^{\infty} (-1)^{n-1} K_2(n\beta\Delta) \tag{38}$$

which varies as $\beta^{1/2}\exp(-\beta\Delta)$ as $T \to 0$, since

$$\operatorname*{Lt}_{y\to\infty} K_2(ny) \to \left(\frac{\pi}{2ny}\right)^{1/2} \exp(-ny). \tag{39}$$

To illustrate the temperature-dependence of the entropy in the more general case of an anisotropic gap, let us assume that $\bar{\Delta}_F(|\cos\theta|)$ has the form

$$\bar{\Delta}_F(|\cos\theta|) = \begin{cases} \Delta_t(1 - p|\cos\theta|), & |\cos\theta| \leqslant \dfrac{1}{p}, \quad p \geqslant 0 \\ 0, & |\cos\theta| > \dfrac{1}{p} \end{cases} \tag{40}$$

CC-0. In Public Domain. Gurukul Kangri Collection, Haridwar

Digitized by Arya Samaj Foundation Chennai and eGangotri

where p is a positive number. Note that for the anisotropy parameter $p<1$, $\bar{\Delta}_F$ does not vanish anywhere, whereas for $p=1$, it vanishes only at points with $\theta=0$ and π, i.e. in directions perpendicular to the layers. For $p>1$, the above model describes regions of vanishing $\bar{\Delta}_F$, close to $\theta=0$ and π. The isotropic case corresponds to $p=0$. In this anisotropic model, (35) and (40) lead to the result, for $0\leqslant p<1$,

$$D_n=\frac{3\pi}{n^3\beta^3 p\Delta_t}[n\beta\Delta_t\{K_2(n\beta\Delta_t)L_1(n\beta\Delta_t)+L_2(n\beta\Delta_t)K_1(n\beta\Delta_t)\}$$
$$-n\beta\Delta_t(1-p)\{K_2(n\beta\Delta_t(1-p))L_1(n\beta\Delta_t(1-p))$$
$$+L_2(n\beta\Delta_t(1-p))K_1(n\beta\Delta_t(1-p))] \tag{41}$$

and for $p\geqslant 1$

$$D_n=\frac{3\pi}{n^3\beta p\Delta_t}[n\beta\Delta_t\{K_2(n\beta\Delta_t)L_1(n\beta\Delta_t)+L_2(n\beta\Delta_t)K_1(n\beta\Delta_t)\}]$$
$$+\frac{4}{n^2\beta^2}\left(1-\frac{1}{p}\right) \tag{42}$$

where $L_n(z)$ is the modified Struve function (Abramowitz and Stegun 1968). In the limiting cases, one has

$$z\to 0\colon K_1(z)\to\frac{1}{z},\quad K_2(z)\to\frac{2}{z^2},\quad L_1(z)\to\frac{2z^2}{3\pi},\quad L_2(z)\to\frac{2z^3}{15\pi}$$
$$z\to\infty\colon K_1(z)\to\left(\frac{\pi}{2z}\right)^{1/2}\exp(-z)\left(1+\frac{3}{8z}+\cdots\right),\quad K_2(z)\to\left(\frac{\pi}{2z}\right)^{1/2}$$
$$\times\exp(-z)\left(1+\frac{15}{8z}+\cdots\right) \tag{43}$$
$$\operatorname*{Lt}_{z\to\infty}L_1(z)\to\operatorname*{Lt}_{z\to\infty}I_{-1}(z)-\frac{2}{\pi}+0\left(\frac{1}{z^2}\right)\to\left(\frac{1}{2\pi z}\right)^{1/2}e^z\left(1-\frac{3}{8z}+\cdots\right)-\frac{2}{\pi}+\cdots$$
$$\operatorname*{Lt}_{z\to\infty}L_2(z)\to\operatorname*{Lt}_{z\to\infty}I_{-2}(z)-\frac{2z}{3\pi}+0\left(\frac{1}{z}\right)\to\left(\frac{1}{2\pi z}\right)^{1/2}e^z\left(1-\frac{15}{8z}+\cdots\right)$$
$$-\frac{2z}{3\pi}+\cdots \tag{44}$$
$$\operatorname*{Lt}_{z\to 0}[K_2(z)L_1(z)+L_2(z)K_1(z)]\to\frac{4}{3\pi} \tag{45}$$
$$\operatorname*{Lt}_{z\to\infty}[K_2(z)L_1(z)+L_2(z)K_1(z)]\to\frac{1}{z}. \tag{46}$$

Thus as $T\to 0$, i.e. $\beta\to\infty$, one has

$$S=2N_F k_B\beta\sum_{n=1}^{\infty}(-1)^{n-1}D_n(\beta\to\infty) \tag{47}$$

CC-0. In Public Domain. Gurukul Kangri Collection, Haridwar

Digitized by Arya Samaj Foundation Chennai and eGangotri

which can be calculated from (41) and (42) by using the limiting values of the functions and expressing $L_n(z)$ in terms of $I_{-n}(z)$ and a power series in z. It can be shown that for $p<1$, i.e. when Δ_F is nonvanishing everywhere, the entropy and specific heat still have temperature-dependences resembling the $\exp(-\beta\Delta_t)$, but for p closer to 1, this can be nearer to a power law behaviour, in practice. In fact, for $p \geqslant 1$, one finds

$$S = 2N_F k_B \beta \sum_{n=1}^{\infty} (-1)^{n-1} \left[\frac{3\pi}{n^3 \beta^3 p \Delta_t} + \frac{4}{n^2 \beta^2} \left(1 - \frac{1}{p} \right) \right], \quad \beta \to \infty, \quad p \geqslant 1 \tag{48}$$

Thus at low temperatures, this leads to the specific heat in the superconducting state which is of the form

$$C_s = \frac{12\pi N_F k_B^3 T^2}{\Delta_t} \sum_{n=1}^{\infty} (-1)^{n-1} \frac{1}{n^3} = \frac{12\pi N_F k_B^3 T^2}{\Delta_t} (0{\cdot}90154), \quad \text{for } p=1 \tag{49}$$

and

$$C_s = \frac{2\pi^2 N_F k_B^2 T}{3} \left(1 - \frac{1}{p} \right) + 0(T^2), \quad \text{for } p > 1. \tag{50}$$

In other words, depending upon the value of the anisotropy parameter p, at low temperatures one can get either a linear temperature-dependence for the specific heat or a higher power law or a smeared out exponential (which may be difficult to be distinguished from a power law behaviour).

Before we conclude this section, it should be emphasized here that the possibility of the spin-singlet or the spin-triplet energy gap vanishing on points or lines of the Fermi surface of a crystalline material, and the consequent T^2 or T^3 power-law behaviour of the low-temperature specific heat have been discussed extensively in recent years, particularly in connection with superconductivity in heavy fermion systems. This has, however, not been appreciated fully in the layered-crystal high-T_c literature, and very often one continues to talk in terms of s-wave or p-wave pairing with a spherical Fermi surface. Our aim here was to examine the expression for the electronic specific heat C_s with a general form of the BCS gap as a function of $\mathbf{k}$, and to introduce an explicit anisotropic model for $\Delta(\hat{k})$ on an ellipsoidal Fermi surface to study the resulting analytic form of C_s as a function of temperature T and the anisotropy parameter p. In light of this analysis, we will discuss some of the available experimental results in high-T_c materials in §4.

3. High frequency electromagnetic response and infrared absorption

For a superconductor with an isotropic gap, an expression for the linear conductivity $\sigma(\mathbf{q}, \omega)$ was first derived by Mattis and Bardeen (1958), and later obtained in more detail by Abrikosov and Gorkov (1959). This calculation has already been described at various other places, including the book by Rickayzen (1965) which has a good discussion of the calculation in the presence of scattering from random impurities in its Appendix IV. In fact, a more general expression for the electromagnetic response function in a superconducting crystal has been derived by Nam (1967), which includes magnetic as well as nonmagnetic impurity scattering. In superconductors, non-magnetic impurity scattering not only leads to the usual relaxation effects in the

CC-0. In Public Domain. Gurukul Kangri Collection, Haridwar

Digitized by Arya Samaj Foundation Chennai and eGangotri

system in the presence of an external e.m. field, but also a change in the superconducting wave function itself if the coherence length ξ is of the order of the mean free path l or larger. In the actual calculation with random impurities and weak scattering, these effects are taken into account by finding the modified quasi-particle propagators as well as the vertex corrections for the interaction of the quasi-particles with the external e.m. wave. Recently, for the case of a spherical Fermi-surface and explicit p-wave ($l=1$) pairings, Klemm *et al* (1988) have obtained the electromagnetic response in the presence of impurity scattering. However, because of the complexity in actual calculations, they have restricted to the case of $\mathbf{q}\rightarrow 0$, where $\mathbf{q}$ is the wavevector of the e.m. wave in the material. This limits its applicability to the case in which $q\xi \ll 1$, and $ql \ll 1$. Also, it cannot be used directly to the case of a nonspherical Fermi surface with gap anisotropies relevant to high-T_c layered materials. In any case, for the situation under consideration here in which $\xi \ll l$, one may be able to avoid this rather tedious calculation by assuming the sample to behave as almost a pure material as far as the superconducting pair wavefunction is concerned. However, as in the normal case, the relaxation effects arising from various elastic and inelastic scattering mechanisms must be included, at least approximately, otherwise the induced current density even in a singly-connected bulk superconductor will not decay to zero in the absence of any dissipation, after the external e.m. field is switched off. In a general density matrix theory of relaxation in any system with Hamiltonian H_0, in the presence of interaction $H_{R'}$ which is responsible for various relaxation mechanisms, and H_A which describes the interaction of the charged system with an external radiation field, one obtains the usual reduced density matrix equation

$$(\partial\rho/\partial t) - (i\hbar)^{-1}[H_0 + H_{A'}\rho] = -\Gamma(\rho),$$

where the relaxation term $\Gamma(\rho)$, linear in ρ, is given by integrals over times t' and t'' of the double commutator involving $H_R(t')$, $H_R(t'')$ and ρ, traced over the states of relaxation agents. Here, a small second-order energy-shift term for the system, arising from the interaction $H_{R'}$ has been neglected. After a sufficiently long time, if the decay of the system to the equilibrium state can be described approximately by a single relaxation time τ_c, one can then often replace $\Gamma(\rho)$ by $(\rho-\rho_0)/\tau_c$. Note that in a normal metal, τ_c^n is usually a very slowly varying function of energy and temperature. However, in the superconducting case τ_c^s is not the same as τ_c^n, as it is evident from an approximate expression for the collision integral in the kinetic equation for a superconductor, introduced by Khalatinikov and Abrikosov (1959) (see §7 of that paper). It is the meanfree path l which remains almost the same in both cases, but

$$\tau_c^n = \tau_c^s[(\xi_k + \Delta_k \partial\Delta/\partial\xi_k)/E_k] = \tau_c^s(v_s/v_n),$$

where v_s and v_n are the velocities of the quasi-particles in the superconducting state and the normal state, respectively. This may also be deduced from the expression (4.12) of Nam's paper for the electromagnetic response function in terms of the imaginary part $\Gamma(\omega)$ of the quasi-particle self-energy arising from various scattering mechanisms and the corresponding pole of the Green function $G(\omega, k)$, at $\omega \simeq E_k - i(\xi_k/E_k)\,\Gamma$, in the limit in which the effect of weak scattering on the real part of the quasi-particle energy is neglected. Thus, following Rickayzen (1965), as long as the scattering is weak, the relaxation effects may be included in our approach by replacing $\Gamma(\rho)$ by $\delta\rho\Omega_c$, where Ω_c is a phenomenological frequency-dependent

CC-0. In Public Domain. Gurukul Kangri Collection, Haridwar

Digitized by Arya Samaj Foundation Chennai and eGangotri

parameter appropriate to $\langle 1/\tau_c^s \rangle$ for the range of energy (of the order of ω) and momenta (of the order of q) involved in the transition process. This procedure, though crude, is expected to give at least a qualitative indication of relaxation effects, in the weak scattering limit.

In the presence of an external transverse electro-magnetic field described by the vector potential $\mathbf{A}(\mathbf{r}, t)$, one has to consider the Hamiltonian

$$H_T = \langle C \rangle_\mu + \sum_{\mathbf{k}} E_{\mathbf{k}} (\gamma_{\mathbf{k}0}^+ \gamma_{\mathbf{k}0} + \gamma_{\mathbf{k}1}^+ \gamma_{\mathbf{k}1}) + H_A \tag{51}$$

$$H_A \simeq \frac{e}{c} \sum_{\mathbf{k},\mathbf{q}\sigma} C_{\mathbf{k}+\mathbf{q}\sigma}^+ C_{\mathbf{k}\sigma} \mathbf{V}_{\mathbf{k}} \cdot \mathbf{A}(\mathbf{q}, t) \tag{52}$$

where for actual intraband transitions among the Bloch states $|\mathbf{k}\rangle$ and $|\mathbf{k}+\mathbf{q}\rangle$

$$\mathbf{V}_k(\mathbf{q}) = \langle \mathbf{k}+\mathbf{q} | \exp(-i\mathbf{q}\cdot\mathbf{r}) \frac{\mathbf{p}}{m} | \mathbf{k} \rangle \tag{53}$$

which can be approximated by the carrier velocity

$$\mathbf{V}_{\mathbf{k}} \cong \mathbf{V}_{\mathbf{k}}(0) = \frac{1}{\hbar} \frac{\partial \xi_{\mathbf{k}}}{\partial \mathbf{k}} \tag{54}$$

and where C's can be transformed into quasi-particle operators γ's by using the Bogoliubov transformation

$$C_{\mathbf{k}\uparrow} = u_{\mathbf{k}} \gamma_{\mathbf{k}0} + v_{\mathbf{k}} \gamma_{\mathbf{k}1}^+; \quad C_{-\mathbf{k}\downarrow} = -v_{\mathbf{k}} \gamma_{\mathbf{k}0}^+ + u_{\mathbf{k}} \gamma_{\mathbf{k}1} \tag{55}$$

$$u_{\mathbf{k}}^2 = \tfrac{1}{2}\left(1 + \frac{\xi_{\mathbf{k}}}{E_{\mathbf{k}}}\right), \quad v_k^2 = \tfrac{1}{2}\left(1 - \frac{\xi_{\mathbf{k}}}{E_{\mathbf{k}}}\right), \quad E_{\mathbf{k}} = +[\xi_{\mathbf{k}}^2 + \Delta^2(\mathbf{k})]^{1/2}. \tag{56}$$

To obtain the linear response function, one has to calculate the expectation value of the current density

$$\mathbf{j}_0(\mathbf{q}) + \mathbf{j}_A(\mathbf{q}, t) = \frac{-e}{mV} \sum_{\mathbf{k}\sigma} C_{\mathbf{k}\sigma} C_{\mathbf{k}+\mathbf{q}\sigma} \mathbf{V}_k - \frac{e^2}{mcV} \sum_{\substack{\mathbf{k}\sigma \\ \mathbf{k}'}} C_{\mathbf{k}+\mathbf{k}',\sigma}^+ C_{\mathbf{k}\sigma} \mathbf{A}(\mathbf{k}'+\mathbf{q}, t) \tag{57}$$

up to terms linear in A. Here, V is the volume of the system. Using the density matrix approach with a phenomenological damping term, it is straightforward to find the required expression in the form

$$j_\mu(\mathbf{q}, \omega) = \frac{i\omega}{c} \sum_\nu \sigma_{\mu\nu}(\mathbf{q}, \omega) A_\nu(\mathbf{q}, \omega) = \frac{\omega^2}{c} \sum_\nu \frac{[\varepsilon_{\mu\nu}(\mathbf{q}, \omega) - \delta_{\mu\nu}]}{4\pi} A_\nu(\mathbf{q}, \omega) \tag{58}$$

where the linear conductivity $\sigma(\mathbf{q}, \omega)$ is given by

$$\sigma_{\mu\nu}(\mathbf{q}, \omega) = \frac{ine^2}{m\omega} \delta_{\mu\nu} - \frac{ie^2}{\omega} \int \frac{\mathrm{d}^3 k}{(2\pi)} V_{\mathbf{k}\mu} V_{\mathbf{k}\nu} R_T(\mathbf{k}, \mathbf{k}-\mathbf{q}, \omega) \tag{59}$$

CC-0. In Public Domain. Gurukul Kangri Collection, Haridwar

Digitized by Arya Samaj Foundation Chennai and eGangotri

with

$$R_T(\mathbf{k},\mathbf{k}-\mathbf{q},\omega,\Omega_c)=\frac{(EE_1-\xi\xi_1-\Delta\Delta_1)}{2EE_1}[1-f(E)-f(E_1)]$$
$$\times(E_1+E+\hbar\omega+i\hbar\Omega_c)^{-1}+(E_1+E-\hbar\omega-i\hbar\Omega_c)^{-1}]$$
$$+\frac{(EE_1+\xi\xi_1+\Delta\Delta_1)}{2EE_1}[f(E)-f(E_1)]$$
$$[(E_1-E+\hbar\omega+i\hbar\Omega_c)^{-1}+(E_1-E-\hbar\omega-i\hbar\Omega_c)^{-1}] \quad (60)$$

and where we have introduced the short hand notations

$$\xi\equiv\xi_{\mathbf{k}}=\varepsilon_{\mathbf{k}}-\mu,\quad \Delta\equiv\Delta(\mathbf{k}),\quad E\equiv E_{\mathbf{k}}=+[\xi_k^2+\Delta^2(\mathbf{k})]^{1/2} \quad (61)$$

$$\xi_1\equiv\xi_{\mathbf{k}-\mathbf{q}}=\varepsilon_{\mathbf{k}-q}-\mu,\quad \Delta_1\equiv\Delta(\mathbf{k}-\mathbf{q}),\quad E_1\equiv E_{\mathbf{k}-\mathbf{q}}$$
$$=+[\xi_{\mathbf{k}-\mathbf{q}}^2+\Delta^2(\mathbf{k}-\mathbf{q})]^{1/2} \quad (62)$$

$$f(E)=[\exp(\beta E_{\mathbf{k}})+1]^{-1},\quad f(E_1)=[\exp(\beta E_{\mathbf{k}-\mathbf{q}}+1]^{-1} \quad (63)$$

As described in §2, we can again replace the integrations over d^3k to integrations over u, v and ξ introduced in (20). However, to be more definite, let us assume that the form of $\xi_{\mathbf{k}}$ and the corresponding Fermi surface are still determined by (30), with $m_{xx}\simeq m_{yy}$. In such a case, one can again introduce spherical polar coordinates $\theta=v$, $\phi=u$ on the constant energy surface $\xi_k=\xi$, so that the velocity components $(1/\hbar)\partial\xi_{\mathbf{k}}/\partial k_i$ of the carriers are given by

$$V_{kX}=\frac{\hbar k_x}{m_{XX}}=\left(\frac{2}{m_{xx}}\right)^{1/2}\sin\theta\cos\phi(\xi+\mu)^{1/2}$$
$$V_{kY}=\frac{\hbar k_y}{m_{YY}}=\left(\frac{2}{m_{YY}}\right)^{1/2}\sin\theta\sin\phi(\xi+\mu)^{1/2} \quad (64)$$
$$V_{kZ}=\frac{\hbar k_z}{m_{ZZ}}=\left(\frac{2}{m_{ZZ}}\right)^{1/2}\cos\theta(\xi+\mu)^{1/2}$$

In terms of the carrier density

$$n=2\int_{-\mu}^{0}\mathrm{d}\xi\int_0^{\pi}\sin\theta\,\mathrm{d}\theta\int_0^{2\pi}\mathrm{d}\phi\frac{N_F}{4\pi}\left(1+\frac{\xi}{\mu}\right)^{3/2}=2\int_{-\mu}^{\infty}\mathrm{d}\xi\int\mathrm{d}u\int\mathrm{d}v g(u,v,\xi) \quad (65)$$

the conductivity tensor $\sigma_{\mu\nu}(\mathbf{q},\omega)$ has the form

$$\sigma_{XX}(\mathbf{q},\omega)=\frac{ine^2}{m_{XX}\omega}-\frac{ine^2}{m_{XX}\omega}D_{XX}(\mathbf{q},\omega)$$
$$\sigma_{YY}(\mathbf{q},\omega)=\frac{ine^2}{m_{YY}\omega}-\frac{ine^2}{m_{YY}\omega}D_{YY}(\mathbf{q},\omega) \quad (66)$$
$$\sigma_{ZZ}(\mathbf{q},\omega)=\frac{ine^2}{m_{ZZ}\omega}-\frac{ine^2}{m_{ZZ}\omega}D_{ZZ}(\mathbf{q},\omega)$$

CC-0. In Public Domain. Gurukul Kangri Collection, Haridwar

Digitized by Arya Samaj Foundation Chennai and eGangotri

where, due to interband terms, m is changed to $m_{\mu\nu}$ in the first term, and, where

$$\omega^{-1}D_{\nu\nu}(\mathbf{q},\omega) = \frac{3}{8\pi}\int_{-\mu}^{\infty} d\xi \int_0^{\pi} d\theta \sin\theta \int_0^{2\pi} d\phi b_\nu b_\nu \left(1+\frac{\xi}{\mu}\right)^{3/2} R_T(\xi,\theta,\phi,q,\omega,\Omega_c)(\omega+i\Omega_c)^{-1} \tag{67}$$

with the electromagnetic absorption due to the second term determined by

$$\mathrm{Re}[\sigma_{\mu\mu}(\mathbf{q},\omega)-\sigma^{(d)}_{\mu\mu}(q,\omega)] = \frac{ne^2}{m_{\mu\mu}\omega}\,\mathrm{Im}\,D_{\mu\mu}(\mathbf{q},\omega) \tag{68}$$

In (67),

$$b_X = \sin\theta\cos\phi, \quad b_Y = \sin\theta\sin\phi, \quad b_Z = \cos\theta. \tag{69}$$

If the direction of the propagation of the incident wave is assumed to be in the Z-direction, i.e. along the C-axis, so that the wave is polarized in the x-y plane, one has to determine D_{XX} and D_{YY} only. These will be equal if the gap-parameter Δ is assumed to be independent of ϕ, and to depend only on $\cos\theta$. In such a case, one finds

$$\omega^{-1}D_{XX}(q\hat{Z},\omega) = \tfrac{3}{8}\int_{-\mu}^{\infty} d\xi \int_{-1}^{+1} dx(1-x^2)\left(1+\frac{\xi}{\mu}\right)^{3/2} R_T(\xi,x,q,\omega,\Omega_c)(\omega+i\Omega_c)^{-1} \tag{70}$$

where

$$x = \cos\theta \tag{71}$$

and where R_T has the same expression as given by (60) but with

$$\xi_1 \simeq \xi - \hbar Q x, \quad Q = V_{FZ}q \tag{72}$$

$$E = +[\xi^2+\Delta^2(x)]^{1/2}, \quad E_1 = [\xi_1^2+\Delta_1^2(x)]^{1/2} \tag{73}$$

for transitions close to the Fermi surface. Note that for $T=0$, $f(E)=f(E_1)=0$, so that the second term in (60) for R_T does not contribute. In this case, the expression for D_{XX} reduces to

$$\omega^{-1}D_{XX}(q\hat{Z},\omega) = \tfrac{3}{8}\int_{-\mu}^{\infty} d\xi \int_{-1}^{+1} dx(1-x^2)\left(1+\frac{\xi}{\mu}\right)^{3/2} \times \tfrac{1}{2}(EE_1-\xi\xi_1-\Delta\Delta_1)/EE_1[(E+E_1+\hbar\omega+i\hbar\Omega_c)^{-1} + (E+E_1-\hbar\omega-i\hbar\Omega_c)^{-1}](\omega+i\Omega_c)^{-1}. \tag{74}$$

In the clean limit in which the mean free path is very large, the electromagnetic absorption can be obtained from the imaginary part of D_{XX} given by (74), in the limit $\Omega_c \to 0^+$. As a simplification, if we also assume that approximately $\Delta_1 \simeq \Delta$, we then obtain

$$\mathrm{Re}\,\sigma_{XX}(q\hat{Z},\omega) \simeq \frac{3\pi ne^2}{8m_{XX}\omega}\int_{-1}^{+1} dx(1-x^2)F_z(x) \tag{75}$$

where

$$F_z(x) = \frac{[E_{m1}E_{m2}+\xi_{m1}\xi_{m2}-\Delta^2(x)]}{|\xi_{m1}E_{m2}-\xi_{m2}E_{m1}|}\,\theta(\omega^2-Q^2x^2-4\Delta^2(x)/\hbar^2) \tag{76}$$

CC-0. In Public Domain. Gurukul Kangri Collection, Haridwar

Digitized by Arya Samaj Foundation Chennai and eGangotri

where the step function

$$\theta(y) = 1, \quad y \geqslant 0$$
$$= 0, \quad y < 0 \tag{77}$$

and where

$$\xi_{m1} = \xi_0 + \frac{\hbar Q}{2} x, \quad \xi_{m2} = -\xi_0 + \frac{\hbar Q}{2} x \tag{78}$$

$$\xi_0 = \frac{\hbar\omega}{2} [\omega^2 - 4\Delta^2/\hbar^2 - Q^2x^2]^{1/2} [\omega^2 - Q^2x^2]^{-1/2} \tag{79}$$

$$E_{m1} = |[\xi_{m1}^2 + \Delta^2(x)]^{1/2}|, \quad E_{m2} = |[\xi_{m2}^2 + \Delta^2(x)]^{1/2}|. \tag{80}$$

For the case of the normal state with $\Delta(x) = 0$ everywhere,

$$F_z(x) \to F_n(x) = 2Qx\delta(\omega - Qx)$$
$$= \frac{2\omega}{Q} \delta(x - \omega/Q) \tag{81}$$

so that

$$\mathrm{Re}\, \sigma_{XX}^n(q\hat{z}, \omega) = \frac{3\pi ne^2}{4m_{XX}Q} \left(1 - \frac{\omega^2}{Q^2}\right) \theta(Q - \omega)$$
$$= \frac{3\pi ne^2}{4m_{XX}qV_{FZ}} \left(1 - \frac{\omega^2}{q^2V_{FZ}^2}\right) \theta(qV_{FZ} - \omega) \tag{82}$$

in this approximation. In fact, if one includes collisions, in the normal state

$$\sigma_{XX}^n(q\hat{z}, \omega) \simeq \frac{3ne^2}{8m_{XX}} \int_{-1}^{+1} \mathrm{d}x(1 - x^2) \left[\frac{2}{(Qx - \omega - i\Omega_c^n)}\right] \tag{83}$$

In the superconducting state, infrared absorption is possible, even at $T = 0\,\mathrm{K}$, if

$$\omega > [Q^2x^2 + 4\Delta^2(x)/\hbar^2]^{1/2}, \quad x = \cos\theta \tag{84}$$

when the incident wave is propagating in the direction of the C-axis, as evident from the expression (76). Here, Q is equal to $V_{FZ}q$ in terms of the carrier Fermi velocity V_{FZ} in the direction of the incident e.m. wave. The minimum value of ω for which absorption can take place is determined by the minimum value of the function

$$f(x) = Q^2x^2 + 4\Delta^2(x)/\hbar^2 \tag{85}$$

If as an illustrative model, we again take the form (40) for $\Delta(x)$, i.e.

$$\Delta(x) = \begin{cases} \Delta_t(1 - p|x|), & x \leqslant \dfrac{1}{p}, \quad p \geqslant 0 \\ 0, & x > \dfrac{1}{p} \end{cases} \tag{86}$$

CC-0. In Public Domain. Gurukul Kangri Collection, Haridwar

Digitized by Arya Samaj Foundation Chennai and eGangotri

the minimum value of $f(x)$ is obtained for

$$|x|_{\min} = \begin{cases} \dfrac{1}{pQ^2 + p^2 g_t^2}, & \text{for } p > p^2 g_t^2 (Q^2 + p^2 g_t^2)^{-1} \\ 1, & \text{for } p \leqslant p^2 g_t^2 (Q^2 + p^2 g_t^2)^{-1} \end{cases} \tag{87}$$

where

$$g_t^2 \equiv 4\Delta_t^2/\hbar^2. \tag{88}$$

In other words, the minimum value of $f^{1/2}(x)$ is given by

$$f_{\min}^{1/2} = \begin{cases} \dfrac{g_t}{[1 + p^2 g_t^2/Q^2]^{1/2}}, & p > p^2 g_t^2 (Q^2 + p^2 g_t^2)^{-1} \\ [Q^2 + g_t^2 (1-p)^2]^{1/2}, & p < p^2 g_t^2 (Q^2 + p^2 g_t^2)^{-1}. \end{cases} \tag{89}$$

Thus, in such a model, infrared absorption can take place for

$$\hbar\omega \geqslant \frac{2\Delta_t}{[1 + 4p^2\Delta_t^2/\hbar^2 q^2 V_{FZ}^2]^{1/2}} \quad \text{for } p > [1 + \hbar^2 q^2 V_{FZ}^2/4p^2\Delta_t^2]^{-1} \tag{90}$$

or

$$\hbar\omega \geqslant 2\Delta_t(1-p)\left[1 + \frac{\hbar^2 q^2 V_{FZ}^2}{4(1-p)^2\Delta_t^2}\right]^{1/2} \quad \text{for } p < [1 + \hbar^2 q^2 V_{FZ}^2/4p^2\Delta_t^2]^{-1}. \tag{91}$$

This implies that depending upon the value of the anisotropy parameter p and the ratio $\hbar Q/\Delta_t = \hbar q V_{FZ}/\Delta_t$, the absorption can take place much below the in-plane gap $2\Delta_t$, provided that $2p\Delta_t/(\hbar q V_{FZ})$ is appreciable. In the isotropic case ($p=0$), there is, of course, no absorption below $2\Delta_t$. At finite temperatures, one can get similar results with additional smearing of the structure below $2\Delta_t$, when $2p\Delta_t/(\hbar q V_{FZ})$ is appreciable. More detailed calculations for finite temperatures can be performed numerically, using (59) to (63), which also include weak collision effects in an approximate way. However, the general conclusion regarding the structure below $2\Delta_t$ will be similar. But, for any actual analysis of the experimental data, one may have to take that into account explicitly.

It is clear that (59)–(63) can also be used to calculate infrared absorption when the incident wave is not necessarily along the Z-direction. For example, at $T = 0\,\mathrm{K}$ and $\Omega_c \to 0$, if the incident wave is propagating along the X-direction (in the plane of the layers) and the wave is polarized either in the Y-direction or the Z-direction, one will get non-vanishing $\sigma_{YY}(q\hat{x}, \omega)$ and $\sigma_{ZZ}(q\hat{x}, \omega)$. The threshold frequency is then determined by the relation

$$\omega \geqslant \left[V_{Fx}^2 q^2 \sin^2\theta \cos^2\phi + \frac{4\Delta^2(\cos\theta)}{\hbar^2}\right]^{1/2} \tag{92}$$

instead of the expression (84). More generally, Δ can, of course, also depend on ϕ.

4. Conclusions and discussion of some experimental results

In this paper, we have considered the problem of calculating thermodynamic quantities like specific heat and nonequilibrium properties like infrared absorption in the

CC-0. In Public Domain. Gurukul Kangri Collection, Haridwar

Digitized by Arya Samaj Foundation Chennai and eGangotri

superconducting state of a material with nonspherical Fermi surface and anisotropic energy gap. It has been argued that such an analysis is necessary for layered oxide-superconductors with anisotropic energy gap and very short coherence lengths, if one is interested in any meaningful comparison of experimental results with the predictions of the generalized BCS pairing theory. It is no longer possible to talk in terms of the 3-dimensional isotropic model for the motion of the carriers. Although, as an approximation, isotropy in the plane of the layers may still be used, it has to be necessarily distinguished from the motion of the carriers perpendicular to the layers. The pairing can no longer be described in terms of pure s-wave or p-wave, etc., since the 3-dimensional orbital l is not a good label any more. The gap parameter in general can be highly anisotropic in the $\mathbf{k}$-space. For example, $\Delta(\mathbf{k})$ with $\hat{k}$ in the plane of the layers may be much larger than $\Delta(\mathbf{k})$ with $\hat{k}$ perpendicular to the layers. Of course, our consideration of the problem is still within the framework of the mean-field theory for the superconducting transition. The corrections to such an approximation are expected to be small if $(k_F\xi)^2$ is still larger than 10 to 100.

The calculation described in the preceding sections for heat capacity in the superconducting state is based on the fact that at finite temperatures the excited states of the system can be described by excitations of quasi-particles with energies $E_{bk}=[\xi_{bk}^2+\Delta_b^2(\mathbf{k})]^{1/2}$, in the multi-band theory or by $E_{jk}=[\xi_{jk}^2+\Delta_j^2(\mathbf{k})]^{1/2}$ in the multi-layer formulation of the generalized BCS pairing theory. In the multi-layer formulation, the effective electron-electron interaction is obtained explicitly in terms of the 2-dimensional layer-polarization functions $\pi_j(\mathbf{q}_t,\omega)$, and pairing is assumed within the same conducting layer only. Of course, the quantity

$$4\pi\chi_j(\mathbf{q}_t,\omega)=\frac{2\pi e^2}{q_t(q_tL/2)}\pi_j(q_t,\omega) \tag{93}$$

is an approximate projection of the three dimensional-band susceptibility function $4\pi\ \chi(\mathbf{q},\omega)$ corresponding to the layer j. In an explicit model for $\Delta(\mathbf{k})$ in the form, $\Delta(\mathbf{k})=\Delta_t(1-p|\cos\theta|)$, for $|\cos\theta|\leqslant 1/p$, $p\geqslant 0$, and $\Delta(\mathbf{k})=0$, for $|\cos\theta|>1/p$, where $\cos\theta$ is the angle between the z-direction (C-axis) and the unit vector $\hat{k}$, with the assumption of an ellipsoidal Fermi surface ($m_{ZZ}\neq m_{XX}\simeq m_{YY}$), the temperature-dependence of the specific heat has been calculated analytically. It is shown that as $T\to 0\,\mathrm{K}$, one can get a linear T-dependence for $p>1$, a T^2-dependence for $p=1$, and a smeared-out exponential dependence for $p<1$. For an appreciable value for the gap anisotropy, it would be difficult to distinguish the smeared-out exponential from a power law.

Soon after the discovery of high-T_c superconductivity in oxide materials, it was reported extensively that the low temperature electronic specific heat in their superconducting state shows an unusual linear temperature variation as $T\to 0\,\mathrm{K}$. This was taken to be an indication of the failure of the BCS pairing theory for such materials, and the possibility of RVB type of superconductivity in which uncharged "spinons" obeying Fermi statistics were supposed to give the usual linear term in C_s and the charged "holons" obeying Bose statistics were supposed to give superconductivity. The coefficient γ^* in $C_s=\gamma^*T$ was found to be of the order of 1–3 $\mathrm{mJ/K^2\,mol}$ in $La_{1\cdot 85}\ Sr_{0\cdot 15}\ CuO_4$ and of the order of 8 to 10 $\mathrm{mJ/K^2\,mol}$ in $Y\ Ba_2Cu_3O_7$ (123 compound). However, more recent experiments by Eckert *et al* (1988) show that in the 123 compound, the most likely cause for the linear term is due to the presence

CC-0. In Public Domain. Gurukul Kangri Collection, Haridwar

Digitized by Arya Samaj Foundation Chennai and eGangotri

of the impurity phase $BaCuO_2$ which happens to have a large normal state γ. New experiments on most of these compounds and on various Bi and Tl-based superconductors (Chakraborty *et al* 1989; Urbach *et al* 1989; Caspary *et al* 1989) seem to indicate that with a few exceptions which need further studies, most likely value of γ^* is close to zero in all these materials, with an upper limit ranging from 0·2 mJ/K^2 mol to 1 mJ/K^2 mol. The difficulty in obtaining good specific heat data to settle this important question whether $\gamma^*=0$ or not, of course, arises due to their extreme sensitivity to material imperfections on the scale of small coherence lengths in these materials. Even if $\gamma^*=0$, the presence of a small T^2 or T^3 term in the intrinsic low temperature electronic specific heat cannot be ruled out experimentally. But, it is quite fair to say that one does not have to abandon the generalized BCS pairing approach to explain such a power-law behaviour. In our explicit model for gap anisotropy discussed earlier, a value of the anisotropic parameter p close to 1 will be sufficient to give such a result. Note that for $\gamma^* \simeq 1$ mJ/K^2 mol and the normal state $\gamma \simeq 10$ mJ/K^2 mol (as in $La_{1\cdot85}Sr_{0\cdot15}CuO_4$), one needs a value of $p \simeq 1\cdot1$ to fit the data. Although, the available experimental data published in the literature are not of such a quality which can be used to find the value of p or the form of a more general structure of the gap by detailed curve-fitting, because of their dependence on sample preparations, etc., the present indication seems to be that $p<1$ in most materials. Any deviation from the experimental temperature-dependence of the intrinsic specific heat arises from the smearing of the exponential due to gap anisotropy and from possible impurity contributions remaining after the subtraction of the phonon contribution (T^3-term).

The calculation for infrared absorption in the superconducting state has been described in this paper only in the limit when the coherence length is small compared to the normal state mean free path, so that the change in the superconducting wave function and vertex corrections to the absorption process due to the impurity scattering, etc., can be ignored. Also, we have ignored the inter-layer or inter-band processes, by finding the electromagnetic response of quasi particles corresponding to a single-layer label j or single-band label b. Of course, this does not imply that interlayer or inter-band interactions are not included in calculating the unperturbed quasi-particle energies and the gap-parameters. Using the model for $\Delta(\hat{k})$ and the Fermi surface similar to that used for the calculation of specific heat, an explicit expression for infrared absorption is obtained in the limit $T \to 0$ K and the collision frequency $\Omega_c \to 0$. It is shown that appreciable absorption can take place below the in-plane gap parameter $2\Delta_t$, if the value of the anisotropy parameter p and the ratio $2\Delta_t/\hbar V_{Fq}q$ are appreciable. Here, V_{Fq} is the Fermi-velocity of the carriers in the direction of the propagation vector q of the incident infrared wave.

The infrared study of reflectivity in superconducting and normal states of high-T_c materials has been made by many groups. Although, the most extensive experimental work exists on $YBa_2Cu_3O_7$ in the form of single crystal as well as polycrystalline material and oriented thin films, one is not able to agree on any unique value for the energy gap even in 123 compound. Sometimes, one finds two gaps (Wieck *et al* 1989) in polycrystalline samples, in the vicinity of 200 cm^{-1} and 580 cm^{-1}, which are attributed to $2\Delta(\hat{k})$ with $\hat{k}$ along the c-axis and in the a-b plane, respectively. For single-crystals, the a-b plane gap was found to be at about 500 cm^{-1} by Schlesinger *et al* (1987). However, they have found it difficult to obtain a realistic value of the gap parameter along the c-axis in the case of single crystals. In any case, from the

CC-0. In Public Domain. Gurukul Kangri Collection, Haridwar

Digitized by Arya Samaj Foundation Chennai and eGangotri

single-crystal reflectivity data, it seems evident that there is always some absorption below the *a-b* plane gap. Usually, the energy gap is identified approximately by using the Mattis-Bardeen expression for electromagnetic response for an isotropic superconductor, in the dirty limit. This implies large scattering rates, not very consistent with normal state conductivity. We feel that the actual shape of the absorption curve below the in-plane gap arises due to the anisotropy of the energy gap. In our model for the anisotropy, this implies the case in which $2\Delta_t p/hV_{Fq}q$ is appreciable. If two energy gaps in the 123 compound as measured by Wieck *et al* (1989) indeed correspond to the *c*-axis and *a-b* plane gaps, it would imply a value of $p \simeq 0{\cdot}65$ in our anisotropy model. However, there may be other valid reasons for the experimental data obtained by Wieck *et al* (1989). At this stage, since there does not seem to be any consensus regarding the exact form of the reflectivity data on single crystals, even with q perpendicular to the *a-b* plane, any numerical analysis of the data to obtain the anisotropy parameter p or the general form of $\Delta(\hat{k})$, even in the case of the 123 compound, seems premature.

In conclusion, we have shown that for any realistic analysis of experimental data obtained for finding the nature of various thermodynamic and nonequilibrium properties in single crystals of layered superconductors, it is necessary to include anisotropy of the gap parameter and the nonspherical nature of the Fermi surface while comparing with the predictions of the generalized BCS theory. In an actual comparison, numerical integrations involving more exact treatment of collisions when $ql \lesssim 1$, and the relaxation of the approximation involving dominant contributions coming from close to the Fermi-surface only may also be necessary, while dealing with high-T_c materials with low carrier densities.

Acknowledgements

I am grateful to Dr R T Collins and Dr Z Schlesinger for many helpful discussions regarding the nature of infrared absorption in the new high-T_c materials, while I was visiting IBM Thomas J Watson Research Center in 1988 summer. I shall also like to thank Drs P Bhattacharyya, S K Malik and E V Sampathkumaran of our Institute for many useful discussions.

References

Abramowitz M and Stegun I A 1968 *Handbook of Mathematical Functions* (Washington DC: NMS) p. 495
Abrikosov A A and Gorkov L P 1959 *Sov. Phys. JETP* **8** 1090
Anderson P W 1959 *J. Phys. Chem. Solids* **11** 26
Anderson P W 1987 *Science* **235** 1196
Anderson P W, Baskaran G, Zou G and Hsu T 1987 *Phys. Rev. Lett.* **57** 2790
Batlogg B, Ramirez A P, Cava R J, Van Dover R B, Reitmann E A 1987 *Phys. Rev.* **B35** 5340
Beyerman W P, Alavi B and Gruner G 1987 *Phys. Rev.* **B35** 8826
Bulaevskii L N and Kukharenko A Yu 1971 *Sov. Phys. JETP* **33** 821
Caspary R, Höhr A, Spille H, Steglich F, Schmidt H, Ahrens R, Roth G, Rietschel H, Yan Y F and Zhao Z X 1989 *Europhys. Lett.* **8** 639
Chakraborty A, Epstein A J, Cox D L, McCarron E M and Farneth W E 1989 *Phys. Rev.* **B39** 12267
Eckert D, Junod A, Graf T and Muller J 1988 *Physica* **C153-155** 1038

CC-0. In Public Domain. Gurukul Kangri Collection, Haridwar

Digitized by Arya Samaj Foundation Chennai and eGangotri

Ginsberg D M and Hebel L C 1969 *Superconductivity* (ed.) R D Parks (New York: Marcel Dekkar) Vol. 1 p. 193
Ishikawa M, Takabatake T and Nakazawa Y 1987 *Physica* **B148** 332
Jha S S 1987 *Pramāṇa – J. Phys.* **29** L615
Jha S S 1988 *Rev. Solid State Sci.* (Singapore: World Scientific) **2** 307
Jha S S 1989 in *Studies of high temperature superconductors* (ed.) A V Narlikar (New York: Nova) Vol. 1 p. 41
Khalatinikov I M and Abrikosov A A 1959 *Adv. Phys.* **8** 45
Klemm R A, Scharnberg K, Walker D and Rieck C T 1988 *Z. Phys.* **B72** 139
Mattis D C and Bardeen J 1958 *Phys. Rev.* **111** 412
Nam S B 1967 *Phys. Rev.* **156** 470
Phillips N E, Fisher R A, Lacy S E, Morcenatc, Olsen J A, Ham W K, Stacy A M, Gordon J E, Tan M L 1987 *Physica* **B148** 332
Rickayzen 1965 *Theory of superconductivity* (New York: John Wiley)
Schlesinger Z, Collins R T, Kaiser D L and Holtzberg F 1987 *Phys. Rev. Lett.* **59** 1958
Sheplev A G 1969 *Sov. Phys. Vspekhi* **11** 690, and other references in the review article
Suhl H, Matthias B T and Walker L R 1959 *Phys. Rev. Lett.* **3** 552
Sulewski P E, Noh T W, Mc Whirter J T, Sievers A J, Russek S E, Buhomann R A, Jec C S, Crow J E, Salomon R E and Myer G 1987 *Phys. Rev.* **B36** 2357
Urbach J S, Mitzi D B, Kapitulnik A, Wei J Y, Morris D E 1989 *Phys. Rev.* **B39** 12391
Wieck A D, Batke E, Merk U, Walker D and Gold A 1989 *Solid State Commun.* **69** 553

CC-0. In Public Domain. Gurukul Kangri Collection, Haridwar

Digitized by Arya Samaj Foundation Chennai and eGangotri

CC-0. In Public Domain. Gurukul Kangri Collection, Haridwar

Digitized by Arya Samaj Foundation Chennai and eGangotri

Pramāṇa – J. Phys., Vol. 34, No. 4, April 1990, pp. 279–287. © Printed in India.

Field and temperature dependence of intergranular hysteresis in $YBa_2Cu_3O_7$

SHAILENDRA KUMAR, G RAVIKUMAR, P K MISHRA, P CHADDAH, B A DASANNACHARYA, RAM PRASAD* and N C SONI*

Nuclear Physics Division, *Metallurgy Division, Bhabha Atomic Research Centre, Bombay 400 085, India

MS received 22 December 1989

Abstract. We have studied the variation of low field magnetization hysteresis in $YBa_2Cu_3O_7$ as a function of the maximum magnetic field applied during a hysteresis cycle ($1\,G < H_{max} < 7{\cdot}3\,G$) and also as a function of temperature ($77\,K < T < 95\,K$). The remnant magnetization is studied as a function of H_{max} and T and the measured dependences are explained using the extended critical state model. The potential of this technique as a contactless method of probing the temperature dependence of J_c is discussed.

Keywords. High temperature superconductors; remnant magnetization; critical current density.

PACS Nos 74·30; 74·60

1. Introduction

Sintered pellets of the ceramic high T_c superconductors are not homogeneous but consist of superconducting grains coupled by intergranular links. The much lower critical current density (J_c) seen in transport measurements on the sintered pellets, as compared to that in single crystal samples, is identified as due to these intergrain links. The isothermal magnetization hysteresis of these sintered pellets shows a low field loop, which disappears on powdering the pellets, and is again attributed to the intergrain links (Grover *et al* 1988; Chaddah *et al* 1989a; Calzona *et al* 1989). The imaginary part (X'') of the susceptibility also shows two peaks as a function of temperature (Chen *et al* 1988; Calzona *et al* 1989) and the low temperature peak disappears on powdering. We have earlier explained the hysteresis of sintered pellets in terms of an extended critical state model (Grover *et al* 1988; Chaddah *et al* 1989a), and related it to the transport J_c and the dimensions of the pellet (Mishra *et al* 1988; Radhakrishnamurthy *et al* 1989).

In this paper we present low field hysteresis measurements on sintered pellets of $YBa_2Cu_3O_7$, as the temperature is varied between 77 K and 90 K and the maximum applied field, H_{max}, varied between 1 G and 7·3 G. The variation of temperature causes a variation in the intergrain transport J_c and thus in the parametric field of the critical state model. This parametric field for a pellet is defined as $H_p^* = \mu_0 J_c D/2$, where D is the dimension of the pellet perpendicular to the field and μ_0 is the permeability of free space. In § 2 we present the experimental details and results, while in § 3 we explain

CC-0. In Public Domain. Gurukul Kangri Collection, Haridwar

Digitized by Arya Samaj Foundation Chennai and eGangotri

these results in terms of a model (Grover *et al* 1988; Chaddah *et al* 1989a). In §4 we discuss the possibility of using such measurements to estimate the temperature dependence of the zero-field J_c in sintered pellets.

2. Experimental set up and results

The hysteresis curves are measured using an AC (317 Hz) susceptibility instrument (Likhite and Radhakrishnamurthy 1966) coupled with a flow type liquid nitrogen cryostat. Figure 1 shows a schematic of the flow type liquid nitrogen cryostat. The $YBa_2Cu_3O_7$ samples were prepared by the conventional sintering route. The sample and a copper constantan thermocouple are encapsulated in a nylon sample holder which is filled with thermally conducting Apiezon N grease. The sample holder rests in a glass tube which is inside a double walled glass tube. The double walled glass tube passes through the secondary coils of the susceptibility instrument. The position of the sample is adjustable with respect to the secondary coils. Temperature is varied in the range of $T = 77$ K to 95 K with $\Delta T = \pm 0{\cdot}5$ K by controlling the rate of flow of the

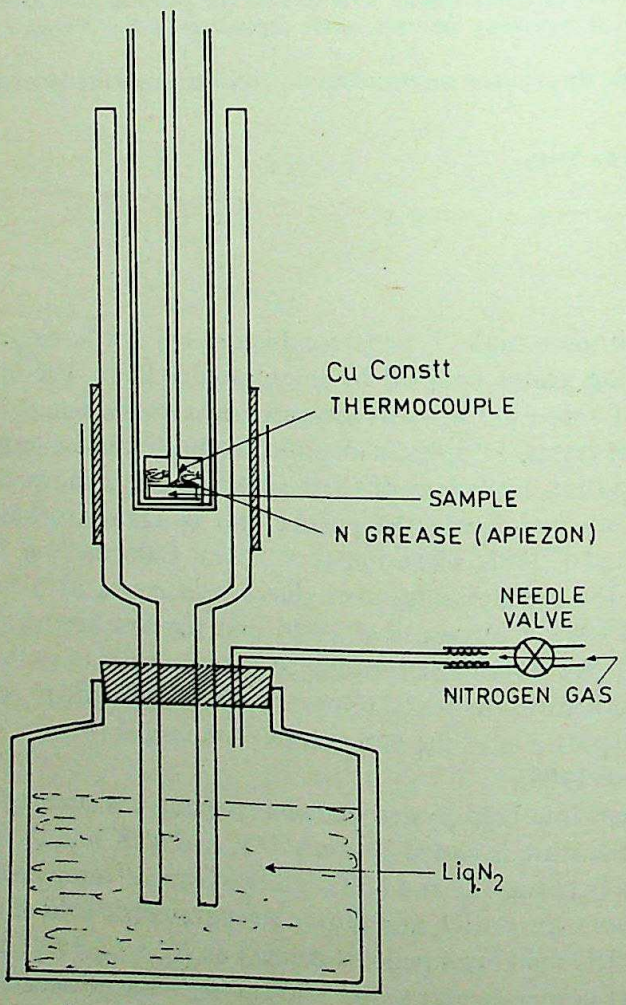

Figure 1. Schematic of flow-type liquid nitrogen cryostat.

CC-0. In Public Domain. Gurukul Kangri Collection, Haridwar

Digitized by Arya Samaj Foundation Chennai and eGangotri

nitrogen gas through liquid nitrogen. Samples in the pellet geometry are used in this study. The maximum cycling field, H_{max}, is varied between 1 and 7·3 G.

Figures 2 and 3 show the hysteresis loops, (for sample 1), for $H_{max} = 2$ G and 7·3 G respectively, at various temperatures. We observe that the remnant magnetization (M_r) which is proportional to the opening in the hysteresis loop at $H = 0$, increases to a maximum and then decreases as the sample is cooled from $T = 90$ K to 77 K. This opening at $H = 0$ is measured directly from the oscilloscope at various temperatures. The relative magnitude of opening at different temperatures is shown in figure 4 for another sample (sample 2) in the range of $H_{max} = 1$ to 6 G.

We make the following observations:

a) For each $H_{max} = H_m$ there exists a temperature $T = T_m$, at which the remnant magnetization (M_r) is maximum. If we now make measurements with the temperature fixed at T_m and vary H_{max}, we find that M_r decreases as H_{max} is reduced below H_m. But as H_{max} increases beyond H_m, M_r stays constant. This feature is clear from figure 4, where the solid line yields this saturation value of M_r for various temperatures.

b) The maximum in M_r shifts to low temperatures for higher H_{max}. The maximum is broader for higher H_{max} (> 3 G).

In the next section we shall explain these results.

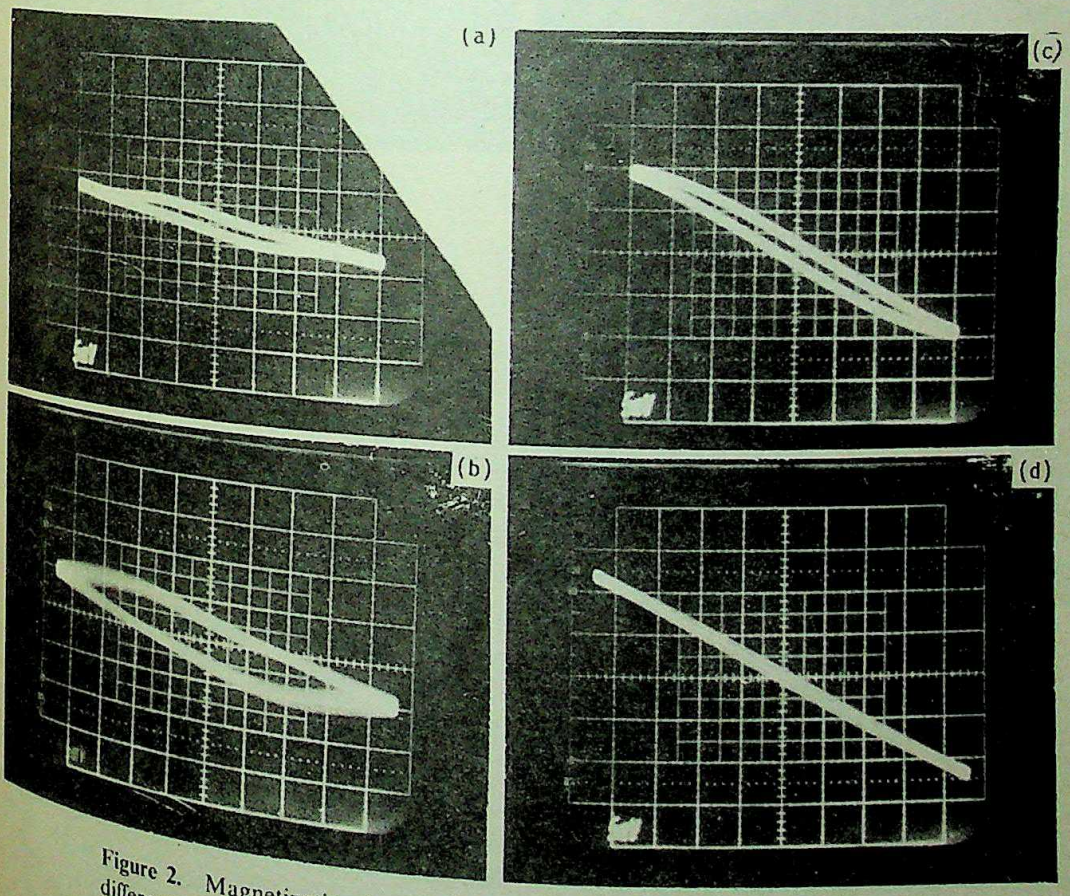

Figure 2. Magnetization hysteresis loops for a $YBa_2Cu_3O_7$ sintered pellet (sample 1) at different temperatures for $H_{max} = 2$ G. The temperatures are **(a)** 88·0 K; **(b)** 87·5 K; **(c)** 86·5 K and **(d)** 80·0 K.

CC-0. In Public Domain. Gurukul Kangri Collection, Haridwar

Digitized by Arya Samaj Foundation Chennai and eGangotri

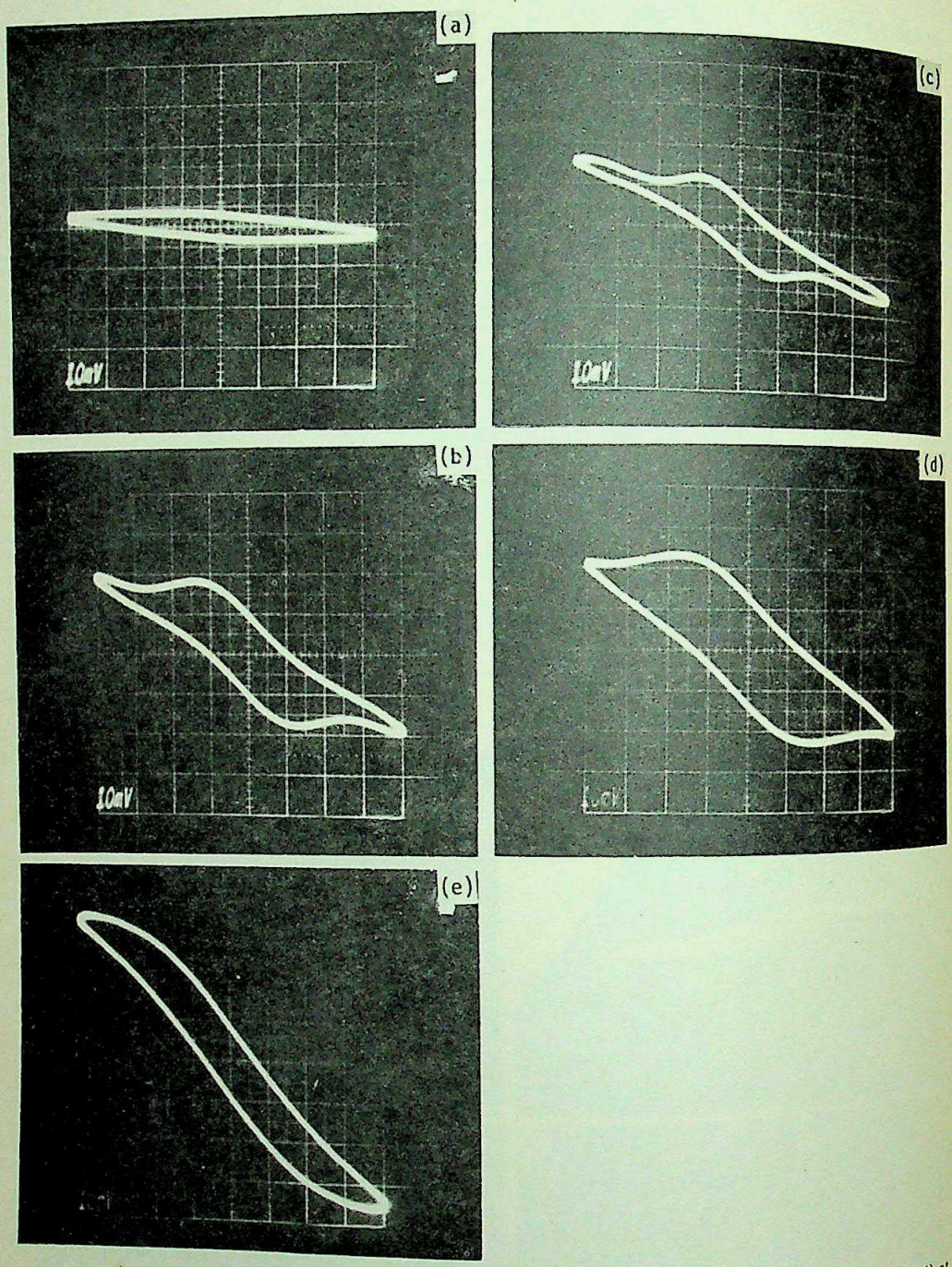

Figure 3. Magnetization hysteresis loops for a $YBa_2Cu_3O_7$ sintered pellet (sample I) at different temperatures for H_{max} of 7·3 G. The temperatures are **(a)** 89·0 K; **(b)** 85·0 K; **(c)** 86·5 K; **(d)** 84·0 K and **(e)** 78·0 K.

CC-0. In Public Domain. Gurukul Kangri Collection, Haridwar

Digitized by Arya Samaj Foundation Chennai and eGangotri

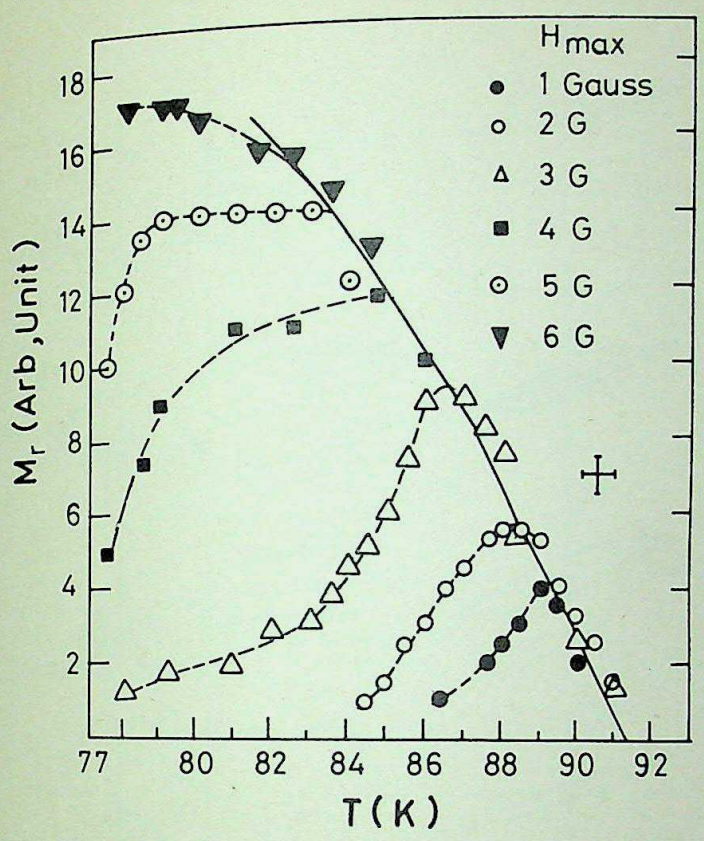

Figure 4. Remnant magnetization (M_r) as a function of temperature for $H_{max} = 1$ G to 6 G of $YBa_2Cu_3O_7$ sample 2. The error bar is indicated. The solid line corresponds to $H_m(T)$ (see text).

3. Extended critical state model

It has been shown earlier (Grover *et al* 1988; Chaddah *et al* 1989a) that the observed low field hysteresis is due to intergranular links when the applied field, H_{max}, is small compared to a parametric field, H_g^*, for a grain. H_g^* depends upon the intragrain critical current density J_{cg} and the grain dimensions and its magnitude is more than 200 G at 77 K in sintered pellets measured by us. We thus note at any given temperature $H_g^* > H_p^*$, and both of them tend to zero, at different rates, as $T \rightarrow T_c$ (Radhakrishnamurty *et al* 1989). Thus, for a fixed H_{max}, there is a temperature above which $H_{max} > H_g^*$ and the hysteresis loop has a contribution from intragrain hysteresis also. This is clearly visible in the data in figures 3(a) and 3(b). The complete loop in figure 3(a) and the narrow tail in figure 3(b) are due to intragrain hysteresis.

Figure 5 shows the qualitative evolution of the hysteresis loop as the temperature is lowered. Once the hysteresis curve shows the shape of figure 5c, the hysteresis is due only to intergrain links. As the temperature is lowered further (for a fixed H_{max}) the observed hysteresis is solely intergranular in origin. The observations (a) and (b) are at such temperatures and will now be explained in terms of the variation of the intergranular transport critical current with temperature. The response of the intergrain regions is characterized by the parametric field

$$H_p^*(T) = 1/2\,\mu_0 J_c(T,0) D \qquad (1)$$

CC-0. In Public Domain. Gurukul Kangri Collection, Haridwar

Digitized by Arya Samaj Foundation Chennai and eGangotri

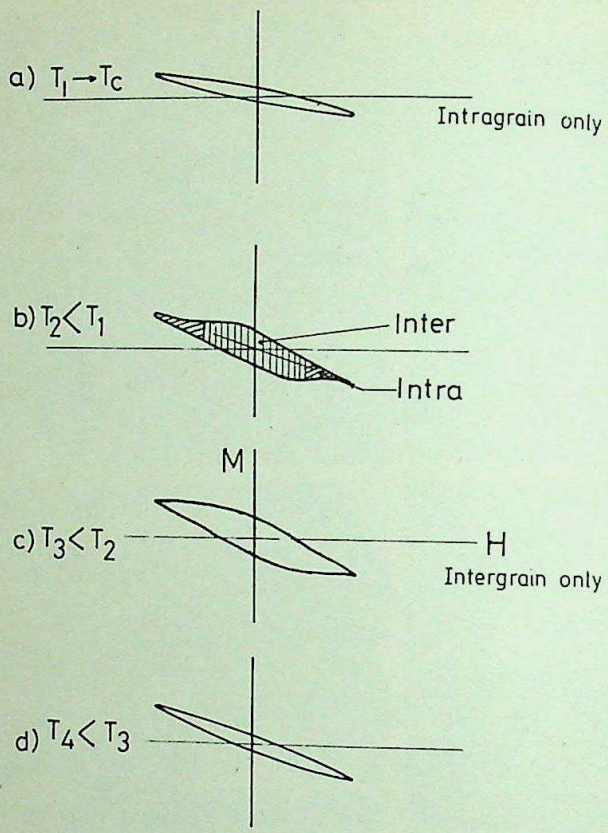

Figure 5. Schematic hysteresis loops as a function of temperature.

where $J_c(T,0)$ is the transport current density in zero field and D is the diameter of the pellet. $J_c(T,H)$ is known to be sharply decaying with field (see Mishra *et al* 1988), and we approximate this decay by

$$J_c(T,H) = J_c(T,0)\exp(-|H|/H_0(T)) \tag{2}$$

where H_0 is an experimental constant that decreases with increasing temperature.

To understand observations (a) and (b), we make the following observations for a general form of $J_c(H)$ that decreases with increasing $|H|$. For a given sample at a constant temperature (i.e. fixed H_p^*), M_r increases up to a certain field H_{II}. When H_{max} increases beyond this H_{II}, the profile of the remnant field in the sample is dictated only by H^* and the H-dependence of J_c, and M_r is independent of H_{max}. This is depicted in figure 6 by drawing schematic field profiles of the remnant field, for various values of H_{max}. These field profiles are obtained by demanding curl $H = J_c$, with the sign of curl H being determined by the sign of the last field change (Chaddah and Ravikumar 1989). H_{II} is the lowest H_{max} for which the remnant field profile peaks at the centre of the sample, and for $J_c(H)$ given by (2) H_{II} is obtained as (Chaddah and Ravikumar 1989).

$$H_{II}(T) = H_0(T)\log[1 + 2H^*(T)/H_0(T)]. \tag{3}$$

This explains our observation (a) and we can identify $H_m(T) = H_{II}(T)$.

To explain observation (b) we note that for a given H_{max}, our above identification corresponds to $H_{max}(T_m) = H_{II}(T_m)$. As H_{max} is held fixed and the temperature is

CC-0. In Public Domain. Gurukul Kangri Collection, Haridwar

Digitized by Arya Samaj Foundation Chennai and eGangotri

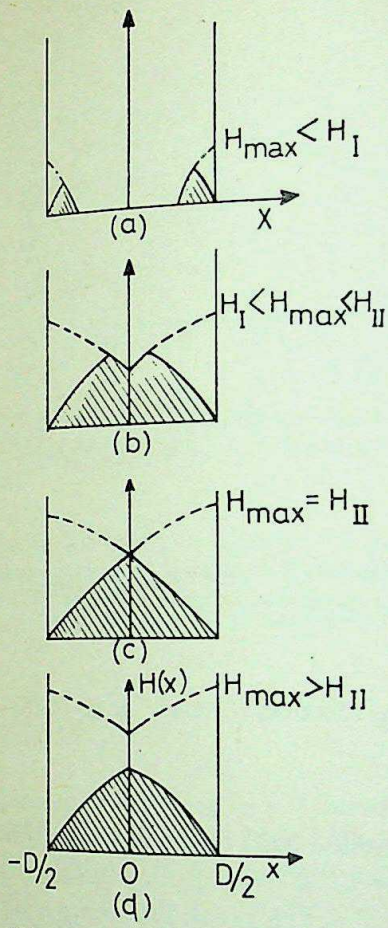

Figure 6. We show (by the dashed lines) the local remnant field profiles ($H(x)$) as the applied field is raised to H_{max} and by the solid lines the field profiles when this field is lowered to zero. The value of M_r is directly proportional to the area of the hatched region for a sample in the shape of a slab. (**a**) to (**d**) corresponds to various values of H_{max}. The curves are schematic corresponding to a $J_c(H)$ that decreases with increasing H. H_I is the value of H_{max} at which the flux first penetrates the entire sample, while H_{II} is defined in the text.

raised, H^* (or $J_c(0)$) is lowered, the hysteresis curve corresponds to the regime $H_{max} > H_{II}$. As depicted in figures 6(d) and 7(b), M_r decreases with decreasing $J_c(0)$. As the temperature is lowered below T_m, $J_c(0)$ and thus H^* increases, and we are now in the regime $H_{max} < H_{II}$. As is schematically depicted by comparing figures 6(a) and 7(a), M_r will decrease in this regime with increasing $J_c(0)$. We thus find that M_r will decrease as temperature is varied on either side of T_m (for fixed H_m) and we can identify $H_{II}(T_m)$ $= H_{max}$. We should mention that the sharpness of the maximum in M_r depends on T_m since H_0 varies with temperature.

Our measurements are on samples of non-zero demagnetization factor N, while the above discussion had assumed $N = 0$. We thus have to make the identification

$$H_{max} = (1 - N) H_{II}(T_m) \tag{4}$$

Since H_{max} and T_m are experimentally determined, $H_{II}(T_m)$ can be obtained from our data provided we can estimate N.

For a sample in the disc geometry, the demagnetization factor N can be

CC-0. In Public Domain. Gurukul Kangri Collection, Haridwar

Digitized by Arya Samaj Foundation Chennai and eGangotri

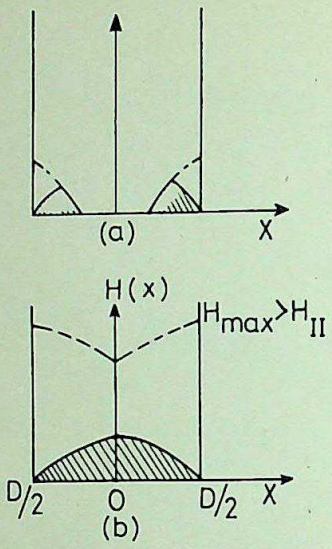

Figure 7. Same as figure 6 but $J_c(0)$ is assumed to be smaller. By comparing 6(a) with 7(a) we note that M_r rises for $H_{max} < H_{II}$, but a comparison of figures 6(**d**) and 7(**b**) shows that M_r decreases for $H_{max} > H_{II}$.

experimentally estimated using the following relation (Grover *et al* 1988)

$$N = (2M_1 - M_2)/(2M_1 + M_2) \tag{5}$$

where M_1 is the magnetization for a fixed applied field perpendicular to the plane of the pellet and M_2 is the magnetization for the same field applied parallel to the plane of the pellet. The applied field is small (1 G at $T = 77$ K) such that there is no hysteresis in the $M - H$ curve. For the sample of volume $= 0{\cdot}40\,\text{cm}^3$ and diameter 0·86 cm, we obtain the value of $N \simeq 0{\cdot}72$ when the field direction is perpendicular to the plane of the pellet.

4. Discussion

We have experimentally determined $H_{II}(T)$, and this is depicted in figure 8. By measuring D we can obtain estimates of $J_c(0)$ provided we know the H-dependence of $J_c(H)$ or the parameter $H_0(T)$. By using (3), we can get the inequality

$$H_{II}(T) < 2H^*(T) \tag{6}$$

where the inequality becomes weaker as $H_0 \to \infty$. H_0 can be determined from the extent of hysteresis at large fields (Chaddah *et al* 1989b), one can then use (1) to estimate $J_c(0)$ at various T. While this can provide a contactless method of estimating $J_c(0)$ as a function of temperature, we have here only confirmed that (1) is consistent with the directly measured $J_c(0)$.

A direct V-I measurement on this sample yields $J_c(0) = 38\,\text{A/cm}^2$ at 77 K. Substituting the pellet dimensions ($D = 8{\cdot}6$ mm) we get $H^*(77\,\text{K}) = 20\,\text{G}$ while our magnetization data shows $H_{II}(77\,\text{K}) = 21{\cdot}5\,\text{G}$. These values satisfy the inequality (6) and provide further justification of our analysis in § 3. They correspond to $H_0 \simeq 20\,\text{G}$ at 77 K, an estimate consistent with our earlier direct measurements (Mishra *et al* 1988).

CC-0. In Public Domain. Gurukul Kangri Collection, Haridwar

Digitized by Arya Samaj Foundation Chennai and eGangotri

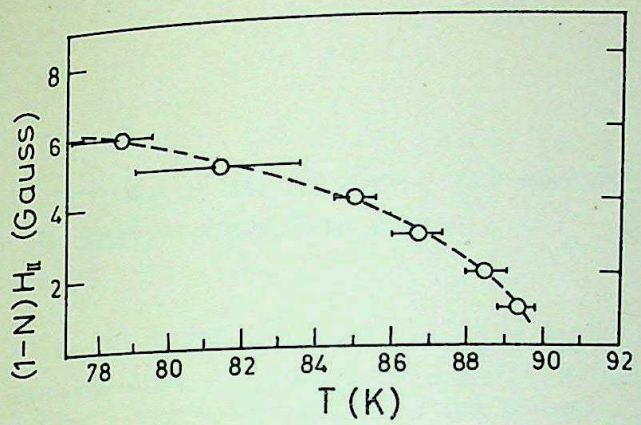

Figure 8. $(1 - N)\, H_{II}$ versus temperature for the sintered $YBa_2Cu_3O_7$ pellet no. 2 as inferred using the data of figure 4. See text for details.

To conclude, we have measured low field hysteresis in $YBa_2Cu_3O_7$ as a function of temperature and cycling field. We have explained this as a response from the intergranular regions and correlated it with the transport J_c.

References

Calzona V, Cimberle M R, Ferdeghini C, Putti M and Siri A S 1989 *Physica* **C157** 425

Chaddah P and Ravikumar G 1989 *Phase Transitions* **19** 37

Chaddah P, Ravikumar G, Grover A K, Radhakrishnamurty C and Subba Rao G V 1989a *Cryogenics* **29** 907

Chaddah P, Bhagwat K V and Ravikumar G 1989b *Physica* **C159** 570

Chen D X, Goldfarb R B, Nogues J and Rao K V 1988 *J. Appl. Phys.* **63** 9809

Grover A K, Radhakrishnamurty C, Chaddah P, Ravikumar G and Subba Rao G V 1988 *Pramāṇa – J. Phys.* **30** 569

Grover A K, Paulose P L, Chaddah P and Ravikumar G 1989 *Pramāṇa – J. Phys.* **33** 297

Likhite S D and Radhakrishnamurty C 1966 *Curr. Sci.* **35** 534

Mishra P K, Ravikumar G, Chaddah P, Dasannacharya B A and Malik M K 1988 *Pramāṇa – J. Phys.* **31** L343

Radhakrishnamurty C, Grover A K, Mishra P K, Chaddah P and Subba Rao G V 1989 *Physica* **C333** 162

CC-0. In Public Domain. Gurukul Kangri Collection, Haridwar

Digitized by Arya Samaj Foundation Chennai and eGangotri

CC-0. In Public Domain. Gurukul Kangri Collection, Haridwar

Digitized by Arya Samaj Foundation Chennai and eGangotri

Pramāṇa – J. Phys., Vol. 34, No. 4, April 1990, pp. 289–295. © Printed in India.

Electrical resistivity of the alkaline earth metals Ca, Sr and Ba in the 50–300K temperature region

O AKINLADE*, U MARTE and L A HUSSAIN

*International Center for Theoretical Physics, Trieste, Italy
*Permanent address: Department of Physics, University of Ibadan, Ibadan, Nigeria

MS received 3 November 1989

Abstract. The computed values of the temperature dependent electrical resistivity is presented for the alkaline earth metals Ca, Sr and Ba. Numerical values of the mean free paths obtained using a finite mean free path approach is also reported. The structure factor has been evaluated using experimental values for the phonon spectra while local model potentials were used for the form factors. Our numerical results compare favourably with experiments.

Keywords. Model potentials; resistivity; mean free path.

PACS No. 72·15

1. Introduction

The alkaline earth metals Ca, Sr and Ba occupy group 2 in the periodic table and the calculation of some of their physical properties could be of considerable interest. Reasons for this include the knowledge that the general features of the electronic structures of these metals are intermediate between those of the simple and the transition metals. It is also known that under normal conditions of pressure and room temperature, Ca and Sr are FCC while Ba exhibits a BCC structure. Ca and Sr also exhibit a BCC structure at high temperatures. Difficulties encountered in the past in growing large single crystals of Ca, Sr and Ba have contributed to an inadequate knowledge of their experimental phonon spectrum. This has in part hampered the theoretical determination of the resistivity.

However in recent times, knowledge of the phonon spectrum has become available for Ca (Stassis *et al* 1983), Sr (Bucheneau *et al* 1984) and Ba (Mizuki *et al* 1983; Bucheneau *et al* 1985). In the present paper, we have used the Ashcroft (1963) and the Heine-Abarenkov (1964) model potentials to compute the electrical resistivity of the aforementioned alkaline earth metals in the 50–300K temperature region by applying the Ferraz-March (1979) method for finite mean free path (l) to the metals. The physical implication is that we have taken into consideration the probable distortion of the Fermi surface in these metals. We have also tried to obtain graphical plots of the variation of resistivity and l with temperature.

A brief theoretical discussion is given in §2. The determination of the structure factor is presented in §3 and §4 contains our results and conclusions.

CC-0. In Public Domain. Gurukul Kangri Collection, Haridwar

Digitized by Arya Samaj Foundation Chennai and eGangotri

2. Theory

Ziman (1960) and Greene and Kohn (1965) have given a general expression of the form given below for the electrical resistivity $\rho(T)$ as a function of temperature T in the pseudopotential formalism

$$\rho(T) = 3/(16n\hbar Ze^2V_f^2K_f^4)\int_0^\infty q^3s(q)|U(q)|^2\theta(q-2K_f)dq. \tag{1}$$

In (1), m is the electronic mass, e the charge on the electron, n the number of ions per unit volume, Z the valency of the metal, K_f the Fermi wave vector, $U(q)$ the pseudopotential form factor, $\hbar = h/2\pi$ here h is the Plancks constant, V_f the Fermi velocity and $s(q)$ is the angular dependent structure factor. θ is the heaviside function. Equation (1) assumes that the Fermi surface is spherical since the q-integration is cut of at $2K_f$.

One would however prefer to leave the structure of the Fermi surface to correct itself relative to the distortion (if it exists). An attempt to take the blurring into consideration in the formulation of resistivity is given by Ferraz and March (1979).

The Ferraz-March approach yields in place of (1)

$$\rho(T) = \frac{3}{16n\hbar Ze^2V_f^2K_f^4}\int_0^\infty q^3s(q)|U(q)|^2\Gamma(q, K_f, l) \tag{2}$$

where $\Gamma(q, K_f, l)$ is given by

$$\Gamma(q, K_f, l) = 2/\pi\{\tan^{-1}(ql) - 0{\cdot}5\tan^{-1}[(2ql)/(1+4(K_fl)^2-(ql)^2] - (\pi/2)\theta[q-(1/l^2+4K_f^2)^{0{\cdot}5}]\}. \tag{3}$$

Here the mean free path l is determined self consistently. The first step being to determine ρ using (1) i.e. with $l=\infty$. l is then recalculated using the Drude expression for the electrical resistivity i.e.

$$\rho = \hbar K_f/(ne^2l). \tag{4}$$

The iteration process begins by obtaining ρ from (1) assuming $l=\infty$, substituting in (4) to obtain l. This value of ρ is then substituted in (2) to obtain ρ and (2) and (4) are iterated until self consistent values of l and ρ are obtained.

3. Structure factor

Although considerable success has been obtained in the experimental determination of the structure factor for a lot of liquid metals (Waseda 1980), the situation is not the same for the solid phases of the metals. One may however use the standard (Van Hove 1954) one phonon approximation for the structure factor given by

$$s(\bar{q}) = \hbar^2/(MK_BT)\sum_p[\bar{q}\cdot\hat{e}_p(\bar{q})]^2/[(e^{\beta\omega p(\bar{q})}-1)(1-e^{-\beta\omega p(\bar{q})})]. \tag{5}$$

Here $\omega_p(\bar{q})$ and $\hat{e}_p(\bar{q})$ are respectively the frequency and polarization vectors of a

CC-0. In Public Domain. Gurukul Kangri Collection, Haridwar

Digitized by Arya Samaj Foundation Chennai and eGangotri

phonon of branch (p) and wave vector $\bar{q}$, $\beta = \hbar/K_B T$, K_B is the Boltzman constant and T is the temperature.

The $\omega_p(\bar{q})$ are obtained using the Born-Von Karman model in which they are expressed in terms of experimental values of the interplanar force constants $\Phi_n(T)$ (Woods *et al* 1962) as

$$\omega^2(T) = M^{-1} \sum_{n=1}^{N} \Phi_n(T)[1 - \cos(n\pi q/q\,\text{max})] \tag{6}$$

where M is the mass of the atom and the sum over n is taken over N planes of atoms.

The structure factor $s(q)$ is obtained using

$$s(q) = 1/(4\pi) \int s(\bar{q})\, d\Omega. \tag{7}$$

For $\bar{q}$ in (5) we have used [100], [110], and [111] directions since these are symmetry directions for which experimental values of force constants can easily be obtained.

The structure factor $s(q)$ in (7) was evaluated using a modified form of the Houston's (1948) 3-term integration procedure.

4. Results and discussion

We present for the first time the numerical results for the temperature variation of resistivity for the alkaline earth metals Ca, Sr and Ba using the self consistent theory explained above.

The parameters R_C and A used in the Ashcroft and Heine-Abarenkov potentials are chosen in such a way that the self consistent values of the calculated resistivity reproduce the experimental results at the highest temperature under consideration. The values are shown in table 1 below and could be used for calculation of other properties which require the use of the model potentials.

As stated earlier, the calculation of the resistivity depends on the model potential and the structure factor. For the determination of the phonon frequencies in (6), we have used experimental force constants provided in (Stassis *et al* 1983), for Ca, (Bucheneau *et al* 1983) for Sr and Ba and (Mizuki *et al* 1985) again for barium. The reason for using two different tables of force constants in Barium is to test two different methods of determining the lattice dynamics of the metals investigated, one using polycrystalline samples (Bucheneau *et al* 1984), and the other (Stassis *et al* 1983; Mizuki *et al* 1985) using single crystals. However as can be observed from figure 3, the results are not remarkably different.

In figures 1, 2, 3 we show plots of temperature variation of electrical resistivity for Ca, Sr and Ba respectively. For the first two metals we have used the two model

Table 1. R_C and A in the Ashcroft and Heine Abarenkov potentials respectively.

	Ca	Sr	Ba
R_C(a.u)	0·7	0·6	1·56
A(a.u)	0·865	0·2	—

CC-0. In Public Domain. Gurukul Kangri Collection, Haridwar

Digitized by Arya Samaj Foundation Chennai and eGangotri

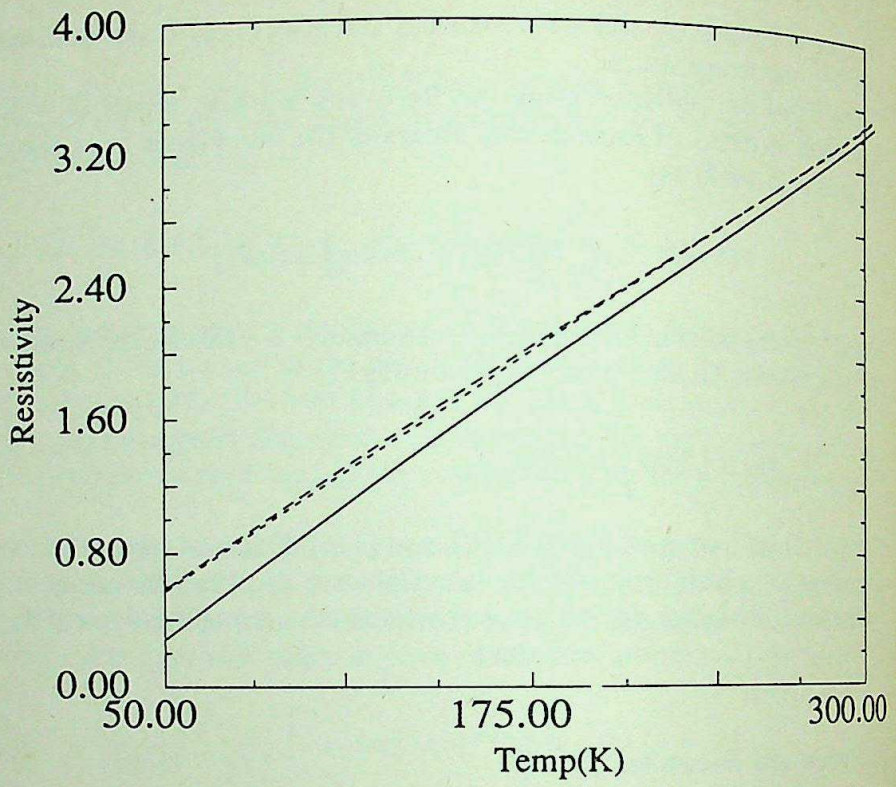

Figure 1. Graphs of resistivity in $\mu\Omega$-cm vs temperature (K) for calcium. ——Experiment; ---Calculated using Ashcroft potential; -- Calculated using Heine-Abarenkov potential.

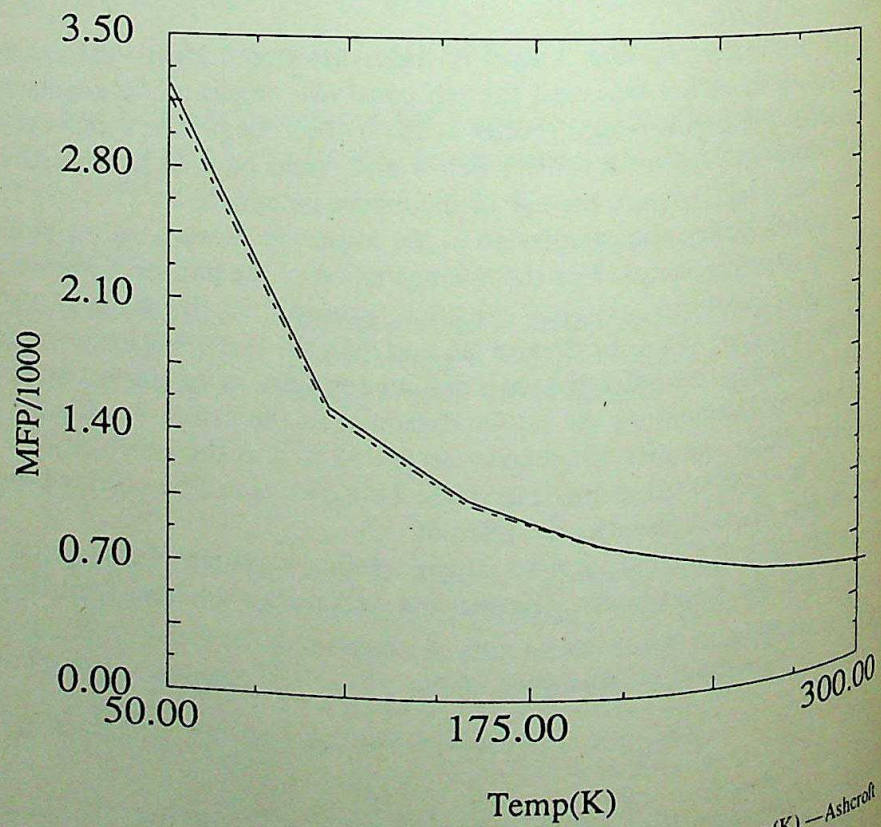

Figure 2. Graphs of calculated mean free path (atomic units) vs temperature (K).—Ashcroft Potential; ---Heine Abarenkov potential.

CC-0. In Public Domain. Gurukul Kangri Collection, Haridwar

Digitized by Arya Samaj Foundation Chennai and eGangotri

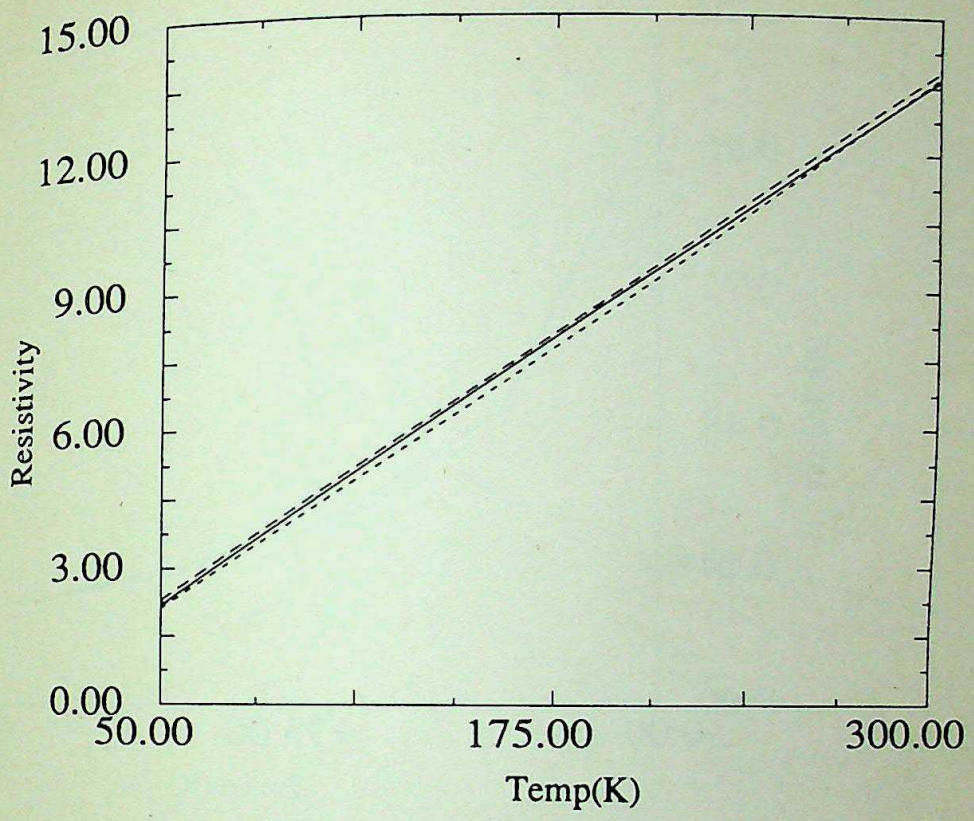

Figure 3. As in figure 1 but for strontium.

potentials while for Ba, we have used only the Ashcroft potential, the reason for this being that the fit for A obtained using the Heine Abarenkov potential was too high.

The experimental results are taken from (Cook *et al* 1975) for Ca (Cook and Van Der Meer 1973) for Sr and Ba.

A close observation of our graph indicates that the results are very good for Sr, reasonable especially at high temperatures for Ca but poor for Ba.

We attribute deviations where they exist to the possibility that the local pseudopotential formulation used could be too simple for the metals. One reason for this being that we have not taken into consideration the proximity of d bands to the Fermi level in other words the effect of hybridization with d states. It is possible that using a non local pseudopotential that takes these factors into consideration could yield better results.

Also presented in figures 4–6 are the computed variations of mean free path with temperature for the elements under investigation. This is in contrast to our earlier work on alkali metals (Akinlade and Hussain 1989) in which we used the value of the mean free path at just one point to compute the thermopower.

One observes that l tends to have a very high value at low temperature which implies that the average distance between successive collisions is long, after which l tends to a constant value at high temperatures. Thus it is reasonable to assume at high temperatures that the finite mean free path is constant.

It is also observed that l decreases with increase in atomic number of the metal. l is highest in Ca and least in Ba, the ratio being about the order of magnitude of 10.

In conclusion we state that the fair results demonstrate the adequacy of the Ferraz-March approach for the class of metals investigated.

CC-0. In Public Domain. Gurukul Kangri Collection, Haridwar

Digitized by Arya Samaj Foundation Chennai and eGangotri

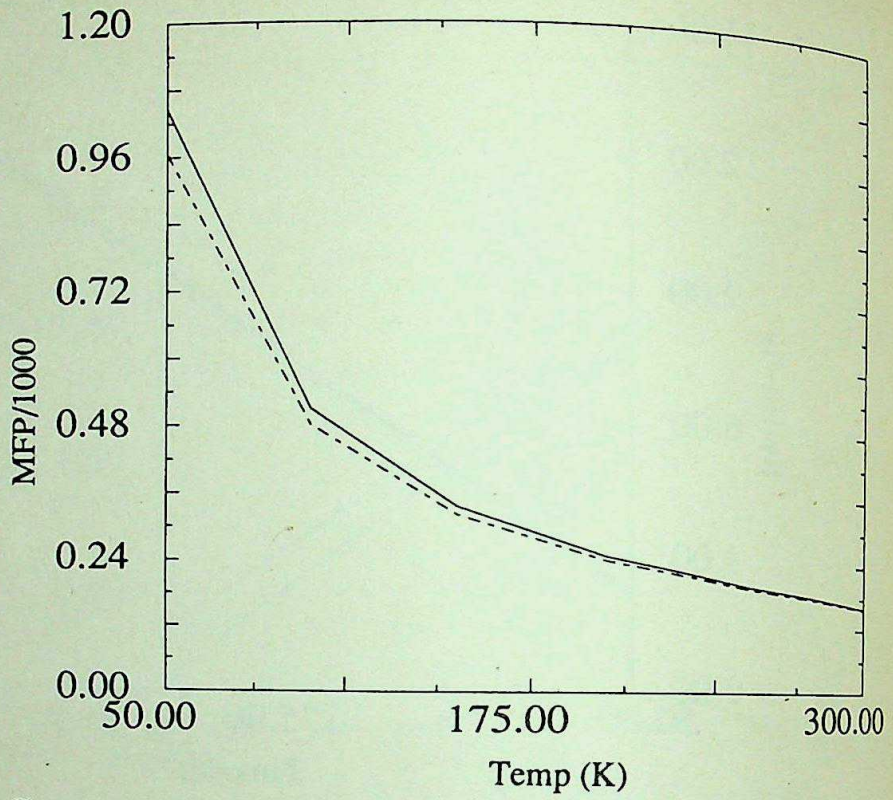

Figure 4. As in figure 2 but for strontium.

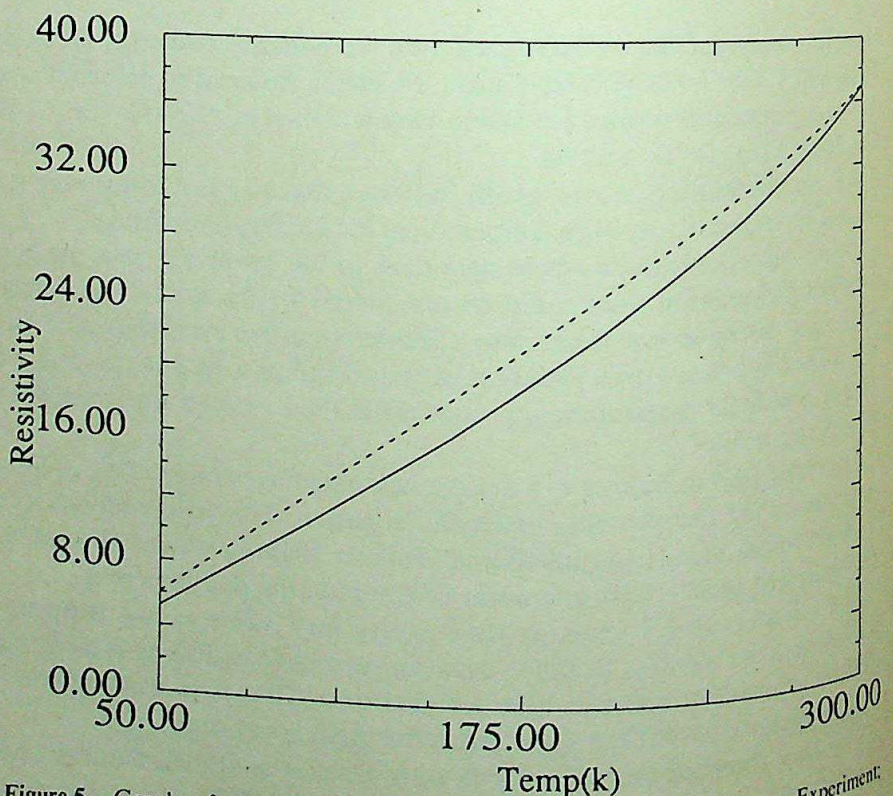

Figure 5. Graphs of resistivity in $\mu\Omega$-cm vs temperature (K) for barium. ——Experiment; – – –Calculated using Heine-Abarenkov potential.

CC-0. In Public Domain. Gurukul Kangri Collection, Haridwar

Digitized by Arya Samaj Foundation Chennai and eGangotri

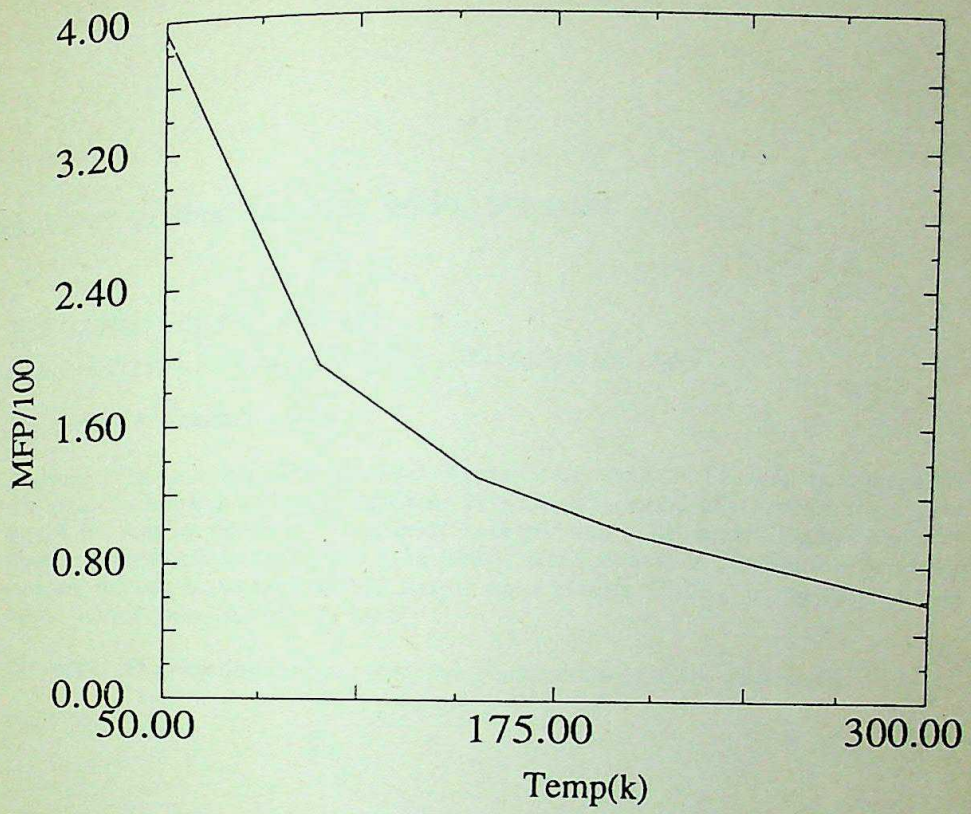

Figure 6. Graph of mean free path (atomic units) vs temperature (K).——Heine Abarenkov potential.

Acknowledgements

One of the authors (OA) would like to thank the organisers of the condensed matter workshop, the International Atomic Energy Agency and UNESCO for hospitality at the International Centre for Theoretical Physics, Trieste.

References

Akinlade O and Hussain L A 1989 *Czech. J. Phys.* **B39** 766
Ashcroft N W 1963 *Phys. Lett.* **23** 48
Bucheneau U, Heiroth M and Schober H R 1984 *Phys. Rev.* **B30** 3502
Cook J G, Laubitz M J and Van Der Meer M P 1975 *Can. J. Phys.* **53** 486
Cook J G and Van Der Meer M P 1973 *J. Phys.* **F3** L130
Ferraz A and March N H 1979 *Phys. Chem. Liq.* **8** 271
Greene M P and Kohn W 1965 *Phys. Rev.* **137** A513
Heine V and Abarenkov I 1964 *Philos. Mag.* **9** 451
Houston W V 1948 *Rev. Mod. Phys.* **20** 161
Mizuki J, Chen Y, Ho K M and Stassis C 1985 *Phys. Rev.* **B32** 666
Stassis C, Zaretsky J, Misemer D K, Skriver H L, Harmon B N and Nicklow R M 1983 *Phys. Rev.* **B27** 3303
Van Hove L 1954 *Phys. Rev.* **95** 249
Waseda Y 1980 *The structure of non-crystalline materials* (New York: McGraw Hill) p. 252–291
Woods A D B, Brockhouse B N, March R H, Stewart T and Bowers R 1962 *Phys. Rev.* **128** 1112
Ziman J M 1960 *Electrons and phonons* (Oxford: Clarendon Press) Ch. 9

CC-0. In Public Domain. Gurukul Kangri Collection, Haridwar

Digitized by Arya Samaj Foundation Chennai and eGangotri

CC-0. In Public Domain. Gurukul Kangri Collection, Haridwar

Digitized by Arya Samaj Foundation Chennai and eGangotri

Pramāṇa – J. Phys., Vol. 34, No. 4, April 1990, pp. 297–302. © Printed in India.

Elastic behaviour of lead fluoride under pressure

R K SINGH and C N RAO
School of Physics, Barkatullah University, Bhopal 462 026, India

MS received 18 December 1989

Abstract. The variation of the second-order elastic constants (SOECs) and the longitudinal and shear modulii with hydrostatic pressure for the lead fluoride (PbF_2) has been investigated for the first time by means of a three-body force potential (TBP) model. The significance of three-body interactions (TBI) has been clearly demonstrated in reproducing the elastic constant variations and the pressure derivatives of SOECs of PbF_2. The equation of state for this crystal has also been reported.

Keywords. Fluorite; anharmonic; three-body interactions; Cauchy discrepancy.

PACS No. 62·20

1. Introduction

Recently, the equation of state and anharmonic elastic properties of the fluorite crystals have been extensively studied by several theoretical (Goyal and Sharma 1988; Goyal *et al* 1988; Gupta *et al* 1987; Rimai and Sladek 1980) and experimental (Rimai and Sladek 1979; Wong and Schuele 1968; Derrington *et al* 1976) workers. Most of these theoretical investigations are confined to three fluorite crystals (CaF_2, SrF_2 and BaF_2) without giving much attention to lead fluoride (PbF_2), which is an important member of the fluorite family and exhibits many interesting temperature and pressure dependent elastic properties (Samara 1976). The most remarkable among them are the transition to superionic state at moderately elevated temperatures between 600 and 800 k, the ferroelectric transition (Samara 1976) below room temperature, the first order transition to orthorhombic structure at 4 kbar and the large Cauchy discrepancy (Srinivasan 1968; Ramachandran and Srinivasan 1972). Earlier, the pressure derivatives of SOECs of PbF_2 were calculated from the shell model (Srinivasan 1968; Ramachandran and Srinivasan 1972) without much success. This might be so because the shell model (Srinivasan 1968) is inadequate to account for the Cauchy discrepancy which owes its origin to three-body interactions (Singh 1982).

Motivated from the above necessity and the facts brought out by Srinivasan (1968) and Singh (1982), the present authors have tried to predict, probably for the first time, the pressure variations of the second-order elastic constants (SOECs) of PbF_2 using the three-body interaction potential (TBP) which has currently been found to explain the temperature variations (Singh *et al* 1989) of SOECs in fluorite crystals. To demonstrate the effects of TBI, we have computed elastic constant variations from two models I and II developed with and without the inclusion of TBI effects. It has been found that model I has given much better agreement with the experimental data (Rimai and Sladek 1980) than that obtained from model II. This clearly indicates the

CC-0. In Public Domain. Gurukul Kangri Collection, Haridwar

Digitized by Arya Samaj Foundation Chennai and eGangotri

significance of the TBI effects in the prediction of pressure variations of SOECs in PbF_2 crystal.

The essentials of TBP model and the method of computations are given in §2. The results and their discussions have been presented in §3.

2. TBP model and method of computations

The stability of a particular lattice structure is well known to be achieved at the minimum value of the Gibbs free energy (G) defined as

$$G = U + PV = U(r) + 2r^3P \tag{1}$$

for the fluorite structure crystals at the pressure, P, volume V and temperature $T = 0°K$. Here, U is the lattice energy consisting of the long-range Coulomb and three-body interactions (Singh 1982) and the short-range van der Waals (vdW) attraction (Tosi 1964) and overlap repulsion effective up to the second neighbour ions (Benson and Dempsey 1962). Its relevant expression is given by Singh *et al* (1989)

$$\begin{aligned} U(r) = &-\sum_{ij}\frac{Z_iZ_je^2}{r_{ij}}\left(1+\sum_k f(r_{ik})\right)-\sum_{ij}c_{ij}r_{ij}^{-6}-\sum_{ij}d_{ij}r_{ij}^{-8} \\ &+8b\beta_{ij}\exp(r_i+r_j-r_{ij})/\rho_{ii}+6b\beta_{ii}\exp(2r_i-k_2r_{ij})/\rho_{ii} \\ &+6b\beta_{jj}\exp(2r_j-k_1r_{ij})/\rho_{jj}+12b\beta_{jj}\exp(2r_j-k_2r_{ij})/\rho_{jj} \end{aligned} \tag{2}$$

with $Z_i(Z_j)$ as the ionic charges for fluorites, c_{ij} and d_{ij} as the vdW dipole-dipole and dipole-quadrupole interaction coefficients (Pauling 1960), b and ρ_{ij} as the range and hardness parameters, $r_i(r_j)$ as the ionic radii of ions $i(j)$ and $f(r_{ik})$ as the TBI parameter (Singh 1982). The details of the first term are reviewed elsewhere (Singh 1982).

The TBP model described above contains only two parameters (b and $f(r)$) as the values of relaxed hardness parameters (ρ_{ij}) are known (Shanker and Singh 1982). The values of these two parameters (b and $f(r)$) are determined from the equilibrium condition

$$(r\,dU(r)/dr)r = r_0 = 0 \tag{3}$$

and the analytical expression (Cochran 1971)

$$f(r_{ik}) = f_0\exp(-r_{ik}/\rho_{ik}) \tag{4}$$

respectively corresponding to those nearest neighbour separations (r) for which the Gibbs free energy given by (1) is minimum. Here, f_0 is a constant and for PbF_2 its value is $-29{\cdot}8$ (Shanker and Singh 1982). In model II, the value of the parameter b will be obtained from (3) by regarding the TBI parameter $f(r)$ and its derivatives to be zero.

The values of the present model parameters (b, $f(r)$) as listed in table 1 have been determined from the above mentioned procedure by making use of the input data listed by Singh *et al* (1989) for PbF_2. The values of the vdW coefficients required for these calculations have been estimated by us using the variational approach of Slater and Kirkwood (1931). The values of the second-order elastic constants have been

CC-0. In Public Domain. Gurukul Kangri Collection, Haridwar

Digitized by Arya Samaj Foundation Chennai and eGangotri

Table 1. Values of model parameters at different pressures (the units in kbar).

Parameters	$P=0{\cdot}0$	$P=1{\cdot}0$	$P=2{\cdot}0$	$P=3{\cdot}0$	Ref. Model
r (Å)	2·572*	2·507	2·491	2·480	I
r (Å)	2·572*	2·474	2·473	2·471	II
b (10^{-19} J)	0·841	0·841	0·841	0·841	I
b (10^{-19} J)	1·044	1·044	1·044	1·044	II
$f(r)(10^{-2})$	−0·60	−0·61	−0·64	−0·67	I

*Experimental value (Palchoudhari and Bichile 1987)

Table 2. Values of pressure derivatives of elastic constants at 1 kbar.

			Other theoretical results		
Expt.[a]	Model I	Model II	(a)	(b)	(c)
dC_{11}/dp 7·40	6·33	4·90	3·90	3·54	4·27
dC_{12}/dp 7·00	5·77	4·25	5·30	5·37	6·83
dC_{44}/dp 0·94	1·35	1·81	0·30	−0·19	−0·51
dC_L/dp 8·14	7·40	6·38	4·90	4·26	4·09
dC_s/dp 0·20	0·28	0·32	−0·70	−0·92	−1·05

[a]Rimai and Sladek 1980; [b]Ramachandran and Srinivasan 1972; Srinivasan 1968; [c]Shanker and Singh 1982.

calculated at different hydrostatic pressures (P) using their expressions reported by Bedi and Verma (1979).

To demonstrate the effects of TBI, we have calculated the variations of SOEC with pressure (P) from two models I (and II) with (and without) TBI effects and depicted them in figure 1 and compared them with their available experimental data (Rimai and Sladek 1980). To guide further merit of the models I and II, we have computed the pressure derivatives of SOECs (dC_{11}/dp, dC_{12}/dp and dC_{44}/dp) and their combinations (dC_L/dp and dC_s/dp) at 1 kbar using their expressions given by Bedi and Verma (1979). We have reported their values in table 2 and compared them with their experimental data (Rimai and Sladek 1980) available only at 1 kbar and other theoretical results (Rimai and Sladek 1980; Shanker and Singh 1982; Srinivasan 1968; Ramachandran and Srinivasan 1972). Here, $C_L = \frac{1}{2}(C_{11} + C_{12} + 2C_{44})$ and $C_s = \frac{1}{2}(C_{11} - C_{12})$.

3. Results and discussion

It is obvious from the results presented in figure 1 that the TBI play an important role in the description of the pressure variations of the SOECs and their longitudinal and shear modulii of PbF_2 crystal. It is evident from figure 1 that the variations obtained from model I are in better agreement with their experimental data than those achieved from model II. This relative success demonstrates the significance of TBI effects.

CC-0. In Public Domain. Gurukul Kangri Collection, Haridwar

Digitized by Arya Samaj Foundation Chennai and eGangotri

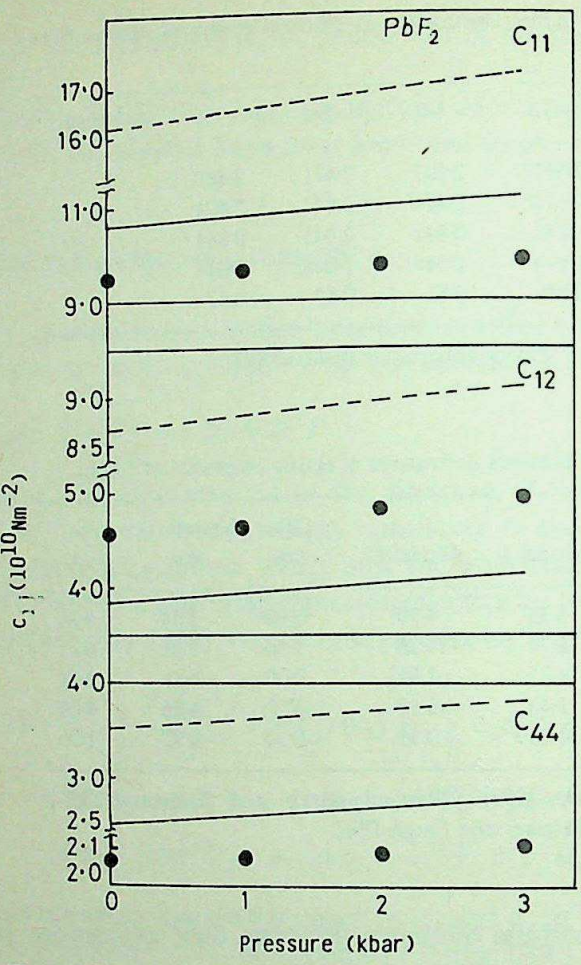

Figure 1. The pressure variations of elastic constants up to 3 kbar. The closed circles represents the experimental data (Rimai and Sladek 1980) while the smooth and broken curves correspond to those obtained from models I and II, respectively.

It has been found that SOECs increase linearly with pressure and they do not show any anomalous behaviour as exhibited in the study of their temperature variations (Singh *et al* 1989). PbF_2 crystal might exhibit interesting features beyond 3 kbar as it undergoes a structural phase transition from fluorite to orthorhombic phase at about 4 kbar. However, investigations beyond 3 kbar could not be possible due to lack of adequate data for its second phase.

Besides, we have depicted the variation of relative volume ratios $[V(P)/V(0)]$ at pressures P and zero in figure 2. This ratio, which gives the equation of state of PbF_2, is found to decrease with pressure and follow the trend similar to that obtained by Wong and Schuele (1968) from the Murnaghan logarithmic equation.

The importance of the role of TBI has been further emphasized from table 2 in which the pressure derivatives of the SOECs and their combinations obtained for PbF_2 from model I are in much closer agreement with their experimental data (Rimai and Sladek 1980) than those obtained from the model II and the shell model (Rimai and Sladek 1980) and earlier TBI model (Shanker and Singh 1982). These deviations clearly show that the present two-body potential and the earlier models are inadequate to predict the pressure dependance of the SOECs in PbF_2 crystal. This is in keeping with the conclusion drawn by Rimai and Sladek (1980). The main reason for the

CC-0. In Public Domain. Gurukul Kangri Collection, Haridwar

Digitized by Arya Samaj Foundation Chennai and eGangotri

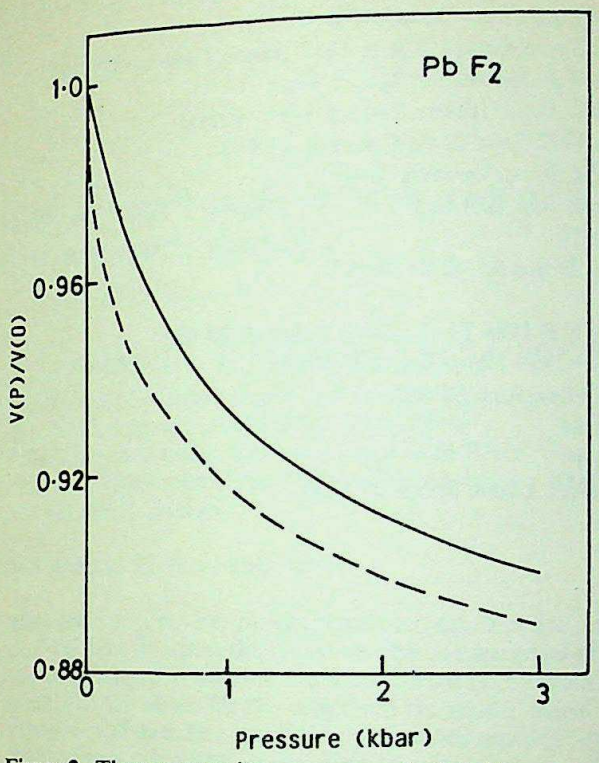

Figure 2. The compression curves as calculated from models I (smooth curve) and II (broken curve) for PbF_2 crystal.

better agreements from TBP model I as compared to those of Shanker and Singh (1982) is that firstly, it uses those values of vdW coefficients which are obtained from Slater-Kirkwood variational approach (1931) which is considered to be a superior method (Singh *et al* 1984). Secondly, it estimates the pressure derivatives of SOECs at 1 kbar at which experimental data are available.

On the basis of the overall achievements, it may be concluded that the present three-body potential model is adequately suitable for the description of the pressure variations and derivatives of the SOECs of the PbF_2 crystal. This TBP model has a promise for such successful description in other members of the fluorite crystal family.

Acknowledgements

The authors are thankful to the Madhya Pradesh Council of Science and Technology (MAPCOST) Bhopal for the financial support to this project.

References

Bedi S S and Verma M P 1979 *Phys. Status Solidi* **B94** 294
Bedi S S and Verma M P 1982 *Phys. Status Solidi* **A97** 203
Benson G C and Dempsey E 1962 *Proc. R. Soc.* (*London*) **A266** 344
Cohran W 1971 *Crit. Rev. Solid State Sci.* **2** 1
Derrington C E, Navarotsky R and O'Keefe M 1976 *Solid State Commun.* **18** 47
Goyal R P, Gupta O P and Gupta B R K 1988 *Phys. Status Solidi* **B146** 475
Goyal S C and Sharma A K 1988a *Solid State Commun.* **66** 741

CC-0. In Public Domain. Gurukul Kangri Collection, Haridwar

Digitized by Arya Samaj Foundation Chennai and eGangotri

Goyal S C and Sharma A K 1988b *Phys. Status Solidi* **B145** 435
Gupta O P, Goyal R P, Adhikari R S and Gupta B R K 1987 *Nuovo Cimento* **D9** 1937
Palchoudhari S and Bichile G K 1987 *J. Mater. Sci. Lett.* **6** 856
Pauling P 1960 *The nature of chemical bond* (Ithaca: Cornell Univ. Press)
Ramachandran V and Srinivasan R 1972 *Solid State Commun.* **11** 973
Rimai D S and Sladek R J 1979 *Solid State Commun.* **31** 473
Rimai D S and Sladek R J 1980 *Phys. Rev.* **B21** 843
Samara G A 1976 *Phys. Rev.* **B13** 4529
Shanker J and Singh J P 1982 *Phys. Status Solidi* **B110** 697
Singh R K 1982 *Phys. Rep.* **85** 259
Singh R K, Agnihotri N and Sanyal S P 1984 *Phys. Status Solidi* **B123** 453
Singh R K, Rao C N and Sanyal S P 1989 *Phys. Rev.* **B39** 13493
Slater J C and Kirkwood J G 1931 *Phys. Rev.* **37** 682
Srinivasan R 1968 *Phys. Rev.* **165** 1054
Tosi M P 1964 *Solid State Phys.* **16** 1
Wong C and Schuele D E 1968 *J. Phys. Chem. Solids* **29** 1309

CC-0. In Public Domain. Gurukul Kangri Collection, Haridwar

Digitized by Arya Samaj Foundation Chennai and eGangotri

Pramāṇa – J. Phys., Vol. 34, No. 4, April 1990, pp. 303–312. © Printed in India.

Computation of small angle neutron scattering functions for molecules of arbitrary shapes

F U AHMED[1], P MARTEL[2] and A M KHAN[3]

[1]Institute of Nuclear Science and Technology, Atomic Energy Research Establishment, P.O. Box 3787, Ramna, Dhaka 1000, Bangladesh
[2]Chalk River Nuclear Laboratories, Chalk River, Ontario KOJ 1JO, Canada
[3]Physics Department, University of Dhaka, Dhaka 1000 Bangladesh and Bangladesh Centre for Advanced Studies

MS received 27 November 1989

Abstract. A computer program has been developed to analyze small angle neutron scattering (SANS) data by using the Debye method of spherical modification proposed by Glatter. In the calculational procedure the model shape is emulated with a large number of overlapping small spheres which fill the volume of the model shape. A technique is described for fitting experimental data to a resolution-broadened model scattering function. At each stage of the iterative procedure the radius of gyration is computed. The program is able to calculate the scattering function of the mixture of two different molecules. This facility even allows one to calculate the scattering function of the mixture of monomer and dimer of a particular molecule in aqueous solution. In case a portion of the molecule has a different weight from the rest, the program has a variation to calculate the scattering function of that model as well.

Keywords. Computation; small angle neutron scattering; arbitrary molecules.

PACS No. 61·20

1. Introduction

The small angle neutron scattering (SANS) technique is nowadays considered a very useful technique in understanding and determining the shape and dimension of complex molecules. Although the method is somewhat analogous to X-ray scattering, there are certain definite advantages this method has over the X-ray techniques e.g. the lower absorption cross section of neutrons than that of X-rays. Moreover thermal neutron scattering amplitudes do not decrease with scattering angles unlike in X-rays. Since the scattering around the centre is particularly independent of the short range order of the atoms, SANS has turned out to be an effective means for studying the dimensions and form of colloidal particles.

The general approach in the study and interpretation of small angle scattering (SANS) data of condensed matter involves the comparison of observed SANS data with some model function (Sjoberg 1978). This comparison is usually done in two ways, either with smeared scattering curves (Sjoberg 1978; Martel *et al* 1980) or with desmeared scattering curves (Glatter 1977, 1980). In either case one has to know the corresponding model functions. While the model functions for a sphere can be calculated analytically, scattering amplitudes of simple triaxial bodies e.g. ellipsoids, prisms and cylinders can be calculated for any specified orientation. However, the spatial average for orientation has to be performed numerically which is time

CC-0. In Public Domain. Gurukul Kangri Collection, Haridwar

Digitized by Arya Samaj Foundation Chennai and eGangotri

consuming. Such semianalytical calculations were done by Porod (1948), Mittelbach and Porod (1961) and Mittelbach (1962). Unfortunately, there are a large number of complex biological molecules which cannot be approximated by simple triaxial models.

Glatter (1977) in his paper had presented a powerful technique for analyzing small angle scattering data from monodisperse suspension of molecules of arbitrary shape. In his method, any arbitrary shape is filled with large number of small spheres and the scattering functions are calculated by means of the Debye equation (Debye 1915). However, Glatter had given no prescription for fitting the model calculations to the experimental data by convoluting the theoretical values with the resolution functions. We have therefore combined his calculational procedure with an iterative least squares procedure which determines various parameters by fitting different models to variance-weighted data. The outline of the method and the user guide were briefly reported elsewhere (Ahmed and Martel 1986).

2. Methodology

Small angle scattering is broadened by the finite resolution of the apparatus, because the perfectly collimated X-ray or neutron beams are impossible to obtain in practice. There are two philosophies for analyzing small angle scattering data. According to the Austrian School, as typified by the papers of Glatter (1977, 1980), the experimental data should be deconvoluted to obtain data which is directly comparable with theoretical scattering functions. Sjoberg (1978) and others (Martel *et al* 1980) suggest that the theoretical scattering function should be convoluted with the known experimental resolution for comparison with the data.

The scattering function of a sphere can be calculated analytically and this function is independent of orientation. As mentioned earlier the scattering functions of simple bodies such as ellipsoids, cylinders etc. can be calculated analytically but the orientational average (Sjoberg 1978; Glatter 1980) is necessary for their random orientations. In the present method of calculation the scattering function depends upon the distances between the centres of the small spheres. The following conditions of selecting the sizes of the small sphere have been imposed by Glatter (1980)

$$Q_{max} < 2\pi/d$$

where d is the distance between two neighbouring spheres. If the spheres are small enough, little error will be incurred because the total volume of the spheres is close to the volume of the true molecular shape.

Sometimes an arbitrary shape may be represented by two or three simple subunits (figure 1). In our calculational method the overlapping of subunits is allowed to approximate the arbitrary molecules whereas in Glatter's calculation such a provision is absent and thus the present method is an improvement over the other. This facility allows us to approximate the arbitrary bodies with small number of subunits. When an arbitrary molecule can be approximated by a combination of three of the simple subunits, sphere, ellipsoids or cylinders, the adjustable parameters are the coordinates of the centres and dimensions of these subunits. As the dimensions of the subunits are adjusted in the filling procedure the program automatically adjusts the appropriate number of small spheres.

CC-0. In Public Domain. Gurukul Kangri Collection, Haridwar

Digitized by Arya Samaj Foundation Chennai and eGangotri

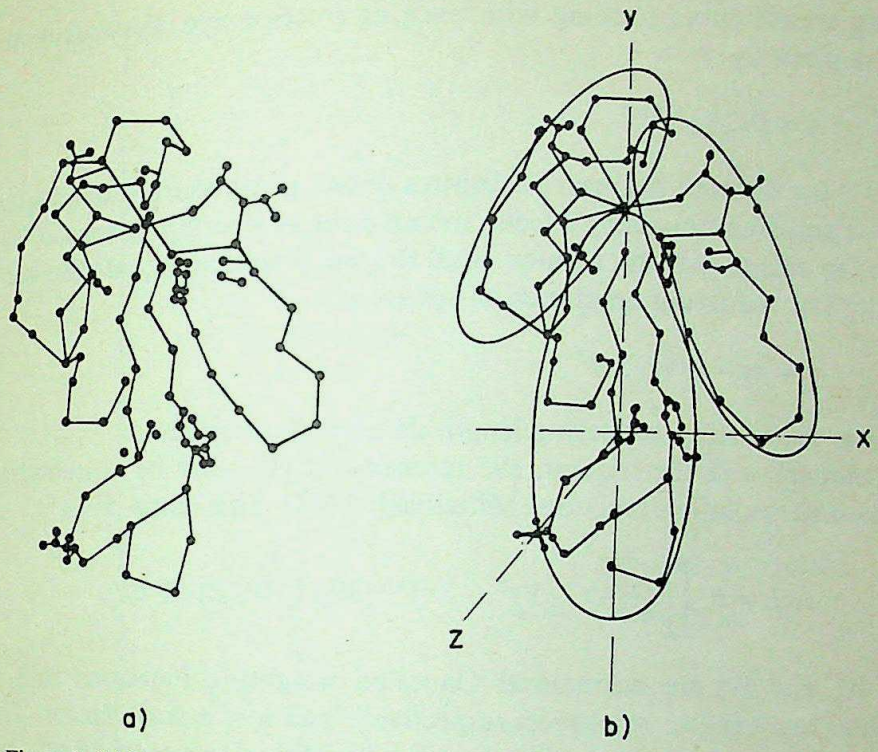

Figure 1. (a) Structure of neurotoxin obtained by X-ray diffraction (Wilkinshaw *et al* 1980). (b) Our triple ellipsoid approximation.

The scattering function for an arbitrary body having different densities at different portions can be calculated using our program. As the small angle scattering is not sensitive to the small scale structure of a molecule the approximation can be made of homogeneous density within an overall molecular shape. For most large biological molecules this approximation is surprisingly good. For example, in transferring (Martel *et al* 1980) it was possible to determine its molecular weight to $\pm 3\%$.

The program identified as COBRA calculates the convoluted scattering intensity, $J(Q)$, compares it with the experimental data and gives a criterion for the quality of the fit. The language used is Fortran 77. The program currently runs on IBM 4341 at Atomic Energy Research Establishment (AERE), Savar, Dhaka as well as at the University of Dhaka and on CDC Cyber 175 at Chalk River Nuclear Labs. (CRNL), Canada.

3. Mathematical formalism

The intensity of coherently scattered neutrons, $I(Q)$, at wave-vector transfer Q, from an orientational average of an aggregate of n overlapping spheres can be computed by the Debye formula (Porod 1948)

$$I(Q) = \sum_{i=1}^{n} w_i^2 S_i^2(Q) + 2 \sum_{i=1}^{n-1} \sum_{j=i+1}^{n} w_i w_j S_i(Q) S_j(Q) \sin(l_{ij}Q)/(l_{ij}Q) \qquad (1)$$

where $Q = 4\pi \sin\theta/\lambda$, λ is the wavelength of neutrons, 2θ is the scattering angle and l_{ij} is the distance between the centres of the ith and jth spheres. The structure factor of each small sphere of radius R is

$$S(Q) = 3[\sin(QR) - (RQ)\cos(RQ)]/(RQ)^3. \qquad (2)$$

CC-0. In Public Domain. Gurukul Kangri Collection, Haridwar

Digitized by Arya Samaj Foundation Chennai and eGangotri

Assuming simple cubic packing with packing fraction $\pi/6$, the radius of the small spheres is given by

$$R = D/2 \cdot (6/\pi)^{1/3} \tag{3}$$

where D is the distance between the centres of two neighbouring small spheres which overlap. Excluding boundary effects, the amount of overlap governed by (3) is just sufficient to ensure that the volume of all the small spheres equals the volume of the molecule. The scattering amplitude of sphere is

$$w = \rho v = \rho(4\pi/3)R^3 \tag{4}$$

where ρ is the neutron scattering length density of the sphere.

To compare with experiment, the intensity of (1) must be convoluted with the experimental resolution function (Mittelbach 1962). This leads to

$$J(Q) = K \iint \{I[(Q-Y)^2 + Z^2]^{1/2}\} W_h(Y) W_v(Z)\, dY\, dZ, \tag{5}$$

where W_h and W_v are normalized Gaussian weighting functions that specify the horizontal and vertical resolution respectively and k is a scale factor. The width of W_h was determined experimentally by scanning the detector in 2θ across the direct beam and fitting the results to a Gaussian. The width of the W_v function was calculated from known collimations. The Gaussian approximations for W_h and W_v allow integration by means of a Gauss-Hermite numerical algorithm.

The experimental intensity $J(Q)$ is given by

$$\begin{aligned} J(Q) = &\{[S(Q) - C(Q))/t_S] - [(E(Q) - C(Q))/t_E]\} \\ &- \delta\{[(R(Q) - C(Q))/t_R] - [(E(Q) - C(Q))/t_E]\} \end{aligned} \tag{6}$$

where S, R and E are the observed intensities (normalized to constant monitor) of the sample plus cell, solvent plus cell and empty cell respectively and t_S, t_R and t_E are the corresponding measured transmissions. The observed intensity with the incident beam blocked by cadmium is designated by C and δ is the volume fraction of solvent in solution.

4. Results and discussion

The scattering intensity calculated for different models, and its comparison with analytical calculations have been shown in figures 2, 3, 4 and 5. Figure 6 shows the comparison of the calculated intensities for different models with experimental data. In the first four figures the neutron wavelength was 4 Å. In figure 6 the wavelength was 2·5 Å. A comparison of figures 4 and 5 provides some evidence for the necessity of utilizing as many spheres as possible. Whereas the results for a solid cylinder (figure 4) are satisfactory up to $\simeq 3{\cdot}6°$, a discrepancy at scattering angle of about 1·4° appears in the calculations illustrated in figure 5. The latter result arises because an insufficient number of spheres span the wall thickness of this hollow cylinder. In practice the number of subunits whose parameters are varied is limited. Typically it

CC-0. In Public Domain. Gurukul Kangri Collection, Haridwar

Digitized by Arya Samaj Foundation Chennai and eGangotri

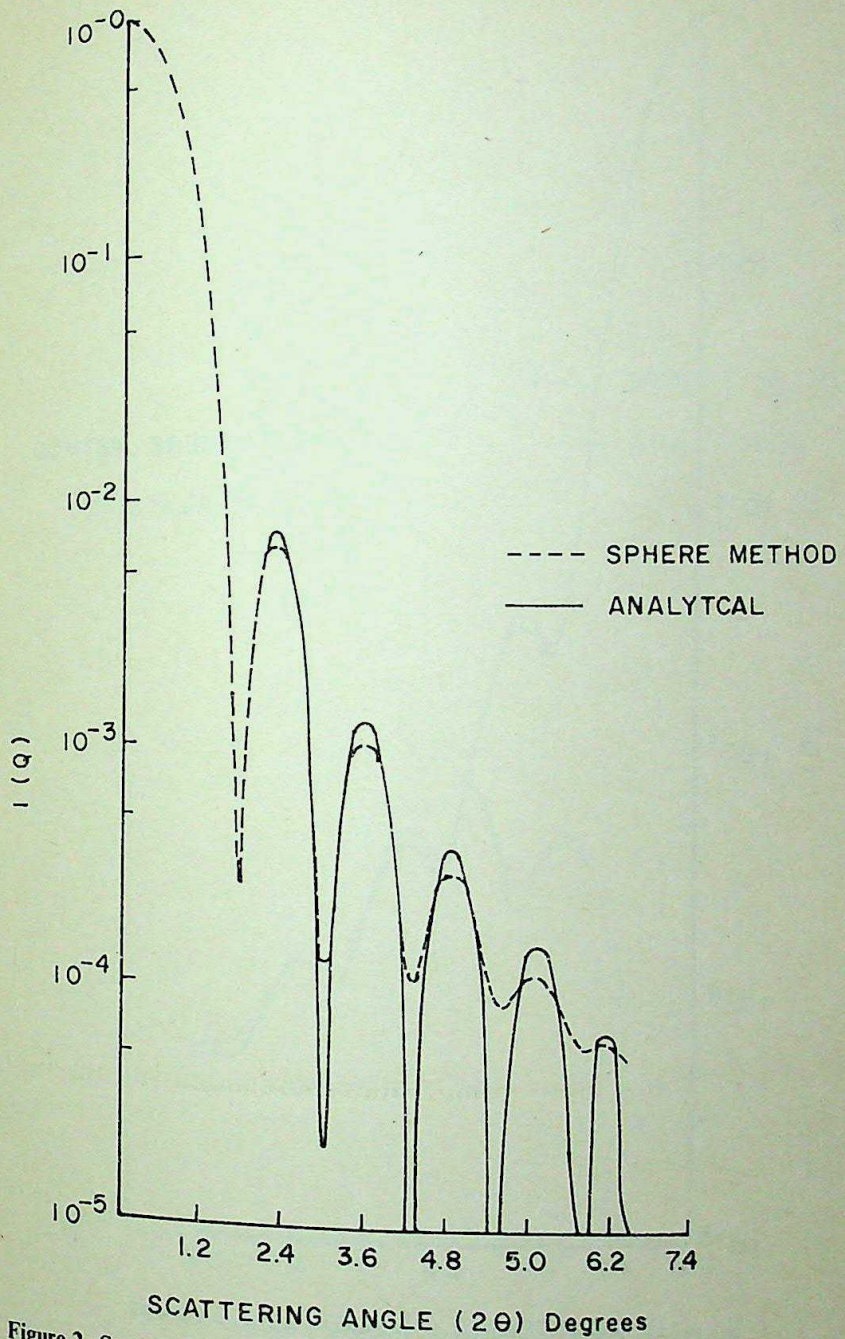

Figure 2. Scattering function from a sphere, $R = 100$ Å, $Rg = 77{\cdot}45$ Å, $R_1 = 13{\cdot}57$ Å, number of spheres = 402.

is possible to vary the size and position of one ellipsoid in a three-ellipsoid model. The program also allows calculations for mixtures of two different molecular species, a possibility where partial dimerization occurs.

Every successful run of the program produces plots of molecular profiles in the X-Y, Y-Z and Z-X planes. In the fitting procedure the quality of fit parameter is defined as

$$\chi^2 = \sum_{i=1}^{N} M_i[J(Q_i)_{\text{calc}} - J(Q_i)_{\text{expt}}]^2/(N-P) \qquad (7)$$

CC-0. In Public Domain. Gurukul Kangri Collection, Haridwar

Digitized by Arya Samaj Foundation Chennai and eGangotri

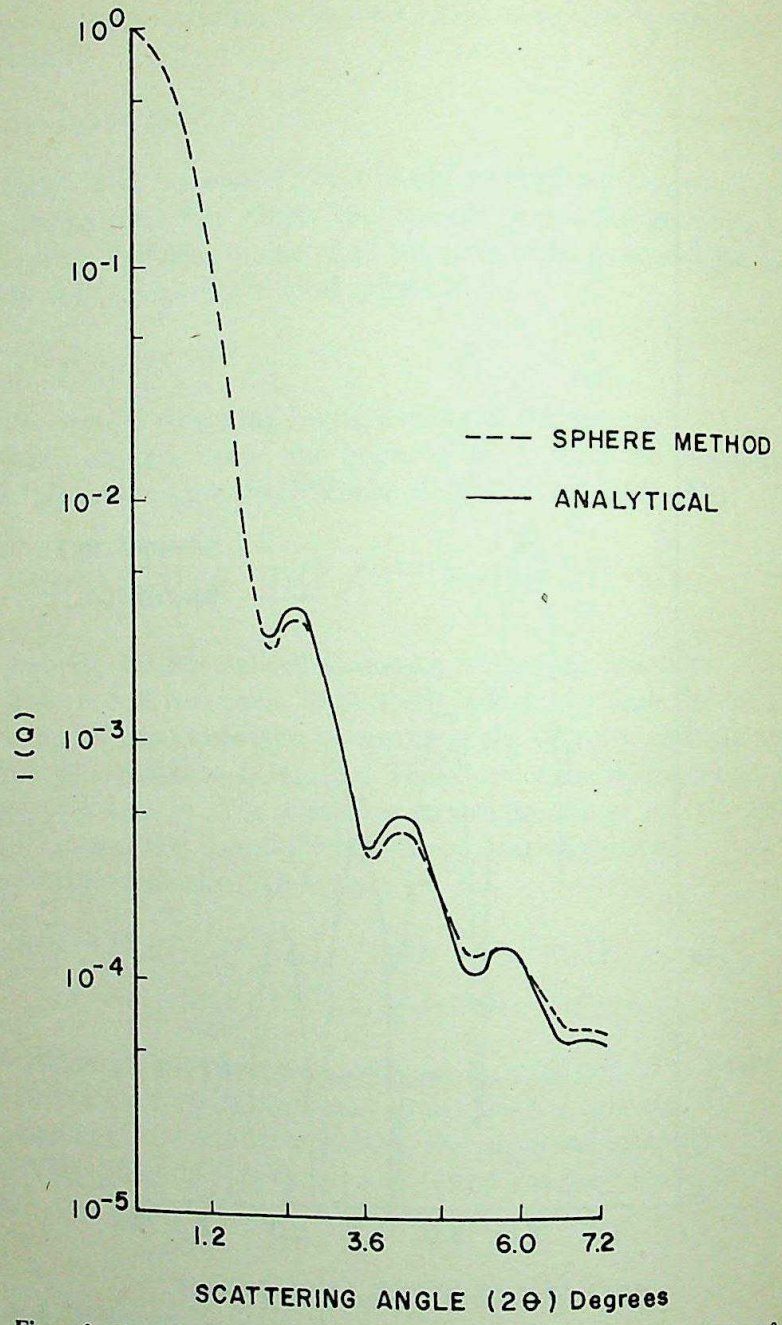

Figure 3. Scattering function from an ellipsoid, $A = 80$, $B = 80$, $C = 150$ Å, $Rg = 83{\cdot}87$ Å, $R_1 = 13{\cdot}39$ Å, number of spheres = 403.

where $J(Q_i)_{calc}$ and $J(Q_i)_{expt}$ are the calculated and experimental value respectively at the point i, N is the number of data points and P is the number of parameters which are varied. The weighting factor is $M_i = (1/J(Q_i)_{expt})^2$. The program varies the model parameters to minimize χ^2.

The running time in summing the Debye formula (eq. 1) goes up very fast as the number of small spheres, n, increases. To provide an idea of running times on an IBM 4341 computer, a fit was made of the scattering from neurotoxin molecule, measured at a concentration of 8 $g/1$. The scan data comprised 301 points. The model

CC-0. In Public Domain. Gurukul Kangri Collection, Haridwar

Digitized by Arya Samaj Foundation Chennai and eGangotri

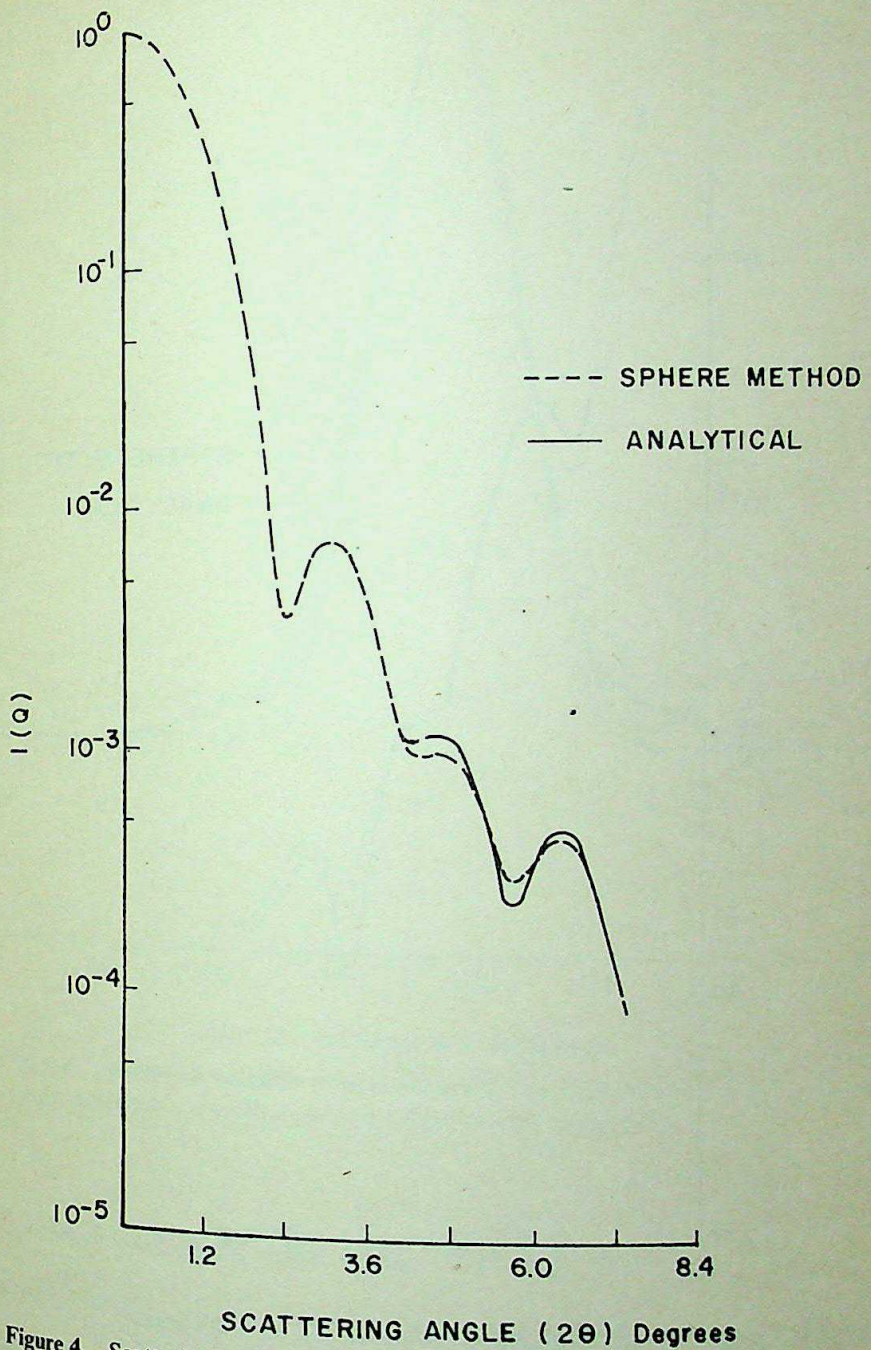

Figure 4. Scattering function from a cylinder, $R = 70$ Å, $H = 100$ Å, $Rg = 56{\cdot}93$ Å, $R_1 = 9{\cdot}15$ Å, number of spheres = 483.

chosen was an arbitrary shape as in figure 1. Time required was 360 s for convergence with $n = 20$, without convolution and with variation of four model-parameters. Time required was 12 s only without variation of model parameters. For $n = 40$, without convolution and with variation of four model parameters the time was 905 s, and without convolution and without variation of model parameters the time was only $\simeq 30$ s. When the analytic function was convoluted with the experimental resolution, the model volume increased slightly but the parameters remained the same within their combined errors. The time was 25 times greater for calculations with convolution

CC-0. In Public Domain. Gurukul Kangri Collection, Haridwar

Digitized by Arya Samaj Foundation Chennai and eGangotri

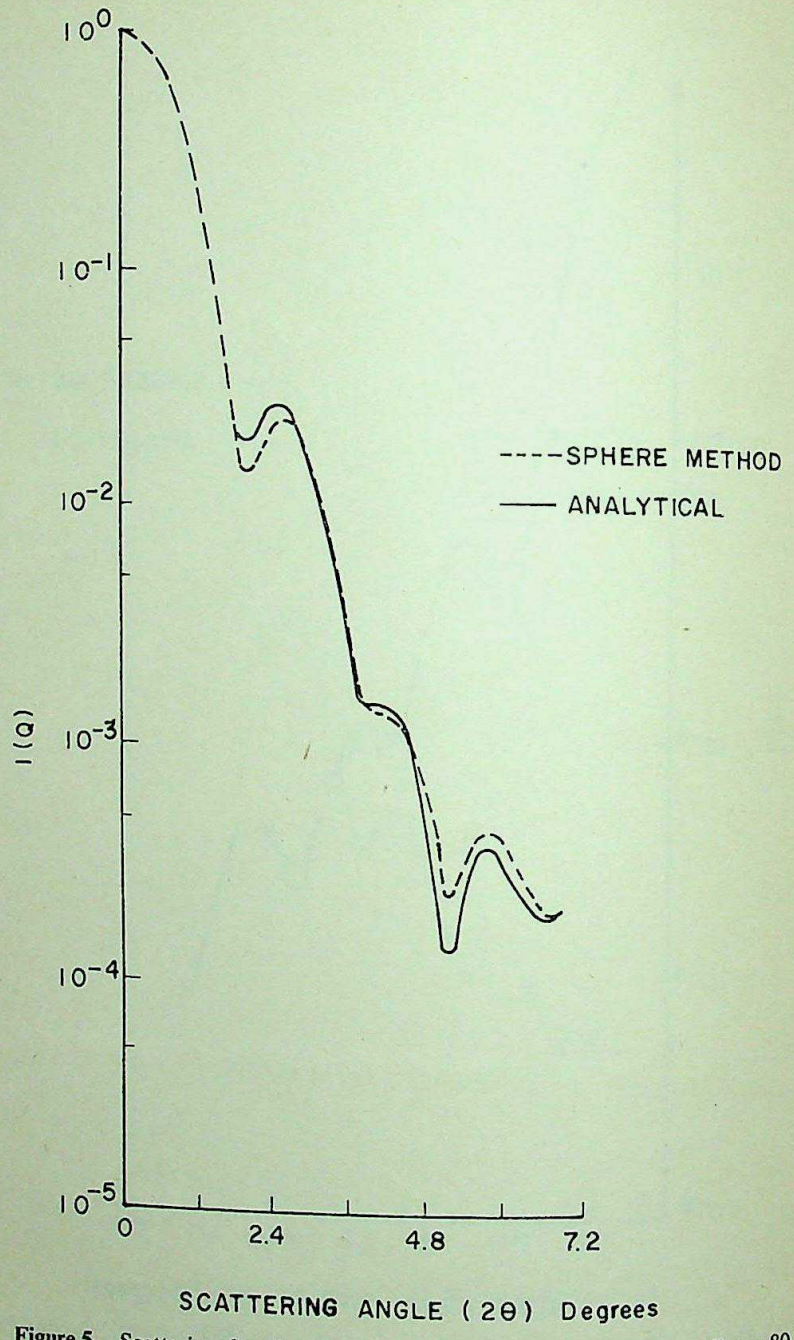

Figure 5. Scattering function from a hollow cylinder of outer radius = 80 Å and inner radius = 30 Å, $Rg = 66{\cdot}52$ Å, $R_1 = 9{\cdot}16$ Å, $H = 100$ Å, number of spheres = 537.

and with variation of four parameters for $n = 20$ and 36 times greater when $n = 40$. These results suggest that the preliminary calculations should be maintained without convolution until approximate values for model parameters are obtained.

The most reliable and commonly measured variable in small angle scattering experiments is the radius of gyration Rg. The radius of gyration is calculated from the expression

$$Rg^2 = \sum_{i=1}^{n} w_i I_{0i}^2 \Big/ \sum_{i=1}^{n} w_i \qquad (8)$$

CC-0. In Public Domain. Gurukul Kangri Collection, Haridwar

Digitized by Arya Samaj Foundation Chennai and eGangotri

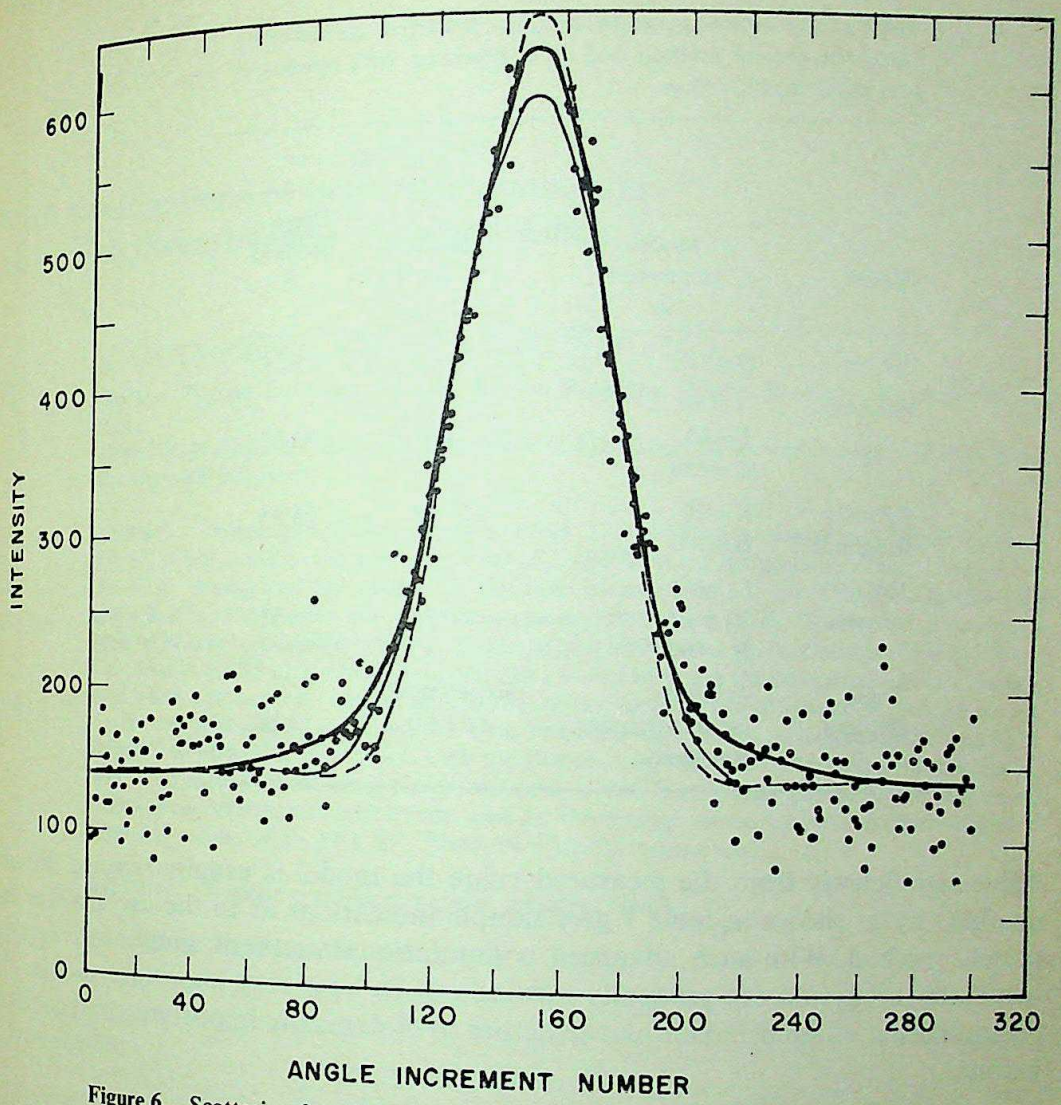

Figure 6. Scattering function from neurotoxin. The solid thick, solid thin and dashed lines represent the arbitrary, ellipsoid and sphere models respectively.

where

$$l_{0i}^2=(X_0-X_i)^2+(Y_0-Y_i)^2+(Z_0-Z_i)^2.$$

The X-coordinate, X_0, of the centre of scattering amplitude density is given by

$$X_0=\sum_{i=1}^{n} w_iX_i \Big/ \sum_{i=1}^{n} w_i. \qquad (10)$$

Analogous expressions are used for Y_0 and Z_0. The coordinates of the centres of the small spheres are X_i, Y_i and Z_i.

The radii of gyration for different shapes calculated by using the present method are compared with analytical and experimental values (table 1).

Any useful model must yield a value of Rg in agreement with the measured value as determined by the Guinier approximation to the low-Q data. A valuable feature of our program is the calculation of Rg at every iteration; this is especially desirable when complicated molecular shapes are being generated. When the calculated Rg

CC-0. In Public Domain. Gurukul Kangri Collection, Haridwar

Digitized by Arya Samaj Foundation Chennai and eGangotri

Table 1. The radii of gyration for different shapes calculated by using the present method and its comparison with analytical and experimental values.

Model	Model parameters Å	Radius of gyration: Analytical Å	Radius of gyration: Present method Å
Sphere	$R = 100$	77·46	77·45
Ellipsoid	$A = 80$ $B = 80$ $C = 150$	84·02	83·87
Cylinder (height 2H)	$R = 70$ $H = 100$	57·30	56·93
Hollow cylinder	$R_1 = 80$ $R_2 = 30$ $H = 100$	66·95	66·52
Triple ellipsoid	Arbitrary model for cobra neurotoxin	Experimental $12·2 \pm 0·2$	12·24

differs significantly from the measured value the model is usually rejected. Results obtained by us shown in table 1 give sample indications as to the usefulness of the present method. With such advanced computational methods small angle neutron scattering techniques are gradually turning out to be a very important tool for the determination of the behavior and structure of biologically important compounds in nature.

References

Ahmed F U and Martel P 1986 Analysis of Neutron Small Angle Scattering Data from Molecules of Arbitrary Shape. (Internal Report), AECL-9185, Chalk River Nuclear Labs, Canada

Debye P 1915 *Ann. Phys.* **46** 809

Glatter O 1977 *J. Appl. Crystallogr.* **52** 243

Glatter O 1980 *Acta Phys. Austriaca* **52** 415

Mittelbach P and Porod G 1961 *Acta Phys. Austriaca.* **14** 185

Mittelbach P 1962 *Acta Phys. Austriaca.* **19** 53

Martel P, Kim S M and Powell B M 1980 *Biophys. J.* **31** 371

Porod G 1948 *Acta. Phys. Austriaca.* **2** 255

Sjoberg B 1978 *J. Appl. Crystallogr.* **11** 73

Wilkinshaw M D, Saenger W and Maelicke A 1980 *Proc. Natl. Acad. Sci. U.S.A.* **77** 2400

CC-0. In Public Domain. Gurukul Kangri Collection, Haridwar

Digitized by Arya Samaj Foundation Chennai and eGangotri

Pramāṇa – J. Phys., Vol. 34, No. 4, April 1990, pp. 313–324. © Printed in India.

NMR investigations of molecular motions in *p-n*-hexyloxybenzylidene-*p'*-*n*-propylaniline

K USHA DENIZ and S R KASTURI*

Nuclear Physics Division, Bhabha Atomic Research Centre, Trombay, Bombay 400 085, India

*Solid State Physics Group, Tata Institute of Fundamental Research, Homi Bhabha Road, Bombay 400 005, India

Abstract. Proton spin-lattice relaxation times, T_1, have been measured in the smectic phases, S_G^2, S_G^1 and S_A, and in the nematic phase of HxBPA, in the temperature range, $220\,K < T < 360\,K$. In the S_G^1 and S_G^2 phases, T_1 has been measured at 15 and 40 MHz. The $(S_G^1 \rightarrow S_G^2)$ and $(S_G^2 \rightarrow S_G^1)$ transitions are clearly seen as discontinuities in T_1. The former transition is seen to be due to possible freezing or change of hydrocarbon chain motions of the molecule. Our data in the S_G^1 phase have been fitted to a model in which anisotropic rotational diffusion of the end hydrocarbon chains as also that of the rigid part of the molecule are considered. In the nematic phase, at 351 K, the observed behaviour of T_1, measured in the frequency range, 5 to 40 MHz, agrees well with the theoretical predictions of Ukleja *et al* and Freed, who take into account long range collective order fluctuations and local reorientations. Using these theories, the correlation time for short range reorientations has been calculated from our results to be $4{\cdot}3 \times 10^{-10}$ and $1{\cdot}1 \times 10^{-9}$ s respectively.

Keywords. Smectic crystals; molecular motions; NMR.

PACS Nos. 76·60; 61·30

1. Introduction

The compound, *p-n*-HexyloxyBenzylidene-*p'*-*n*-PropylAniline or HxBPA (figure 1), exhibits (Usha Deniz *et al* 1977a) two smectic crystalline and two liquid crystalline

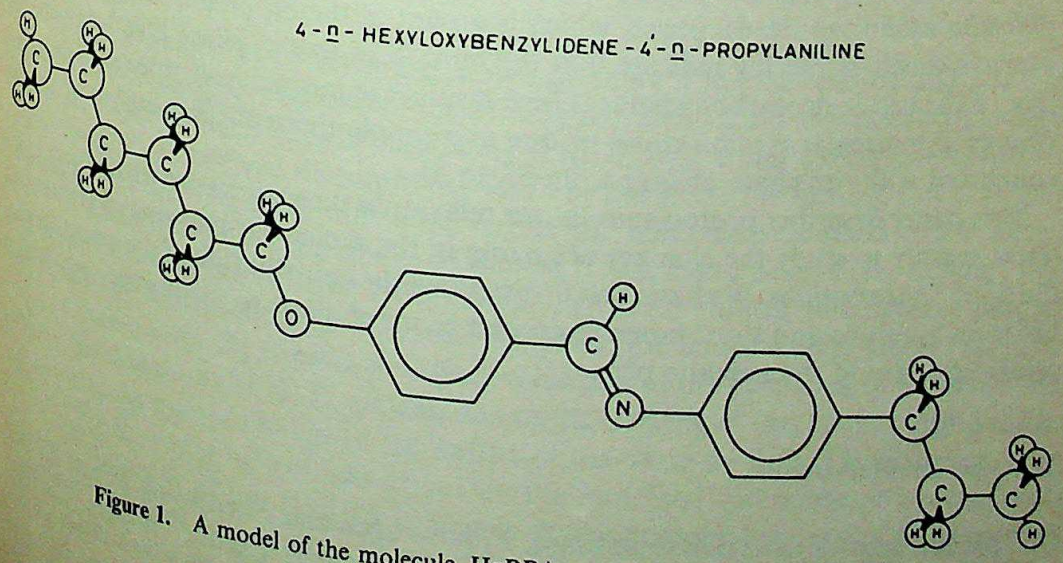

Figure 1. A model of the molecule, HxBPA.

CC-0. In Public Domain. Gurukul Kangri Collection, Haridwar

Digitized by Arya Samaj Foundation Chennai and eGangotri

phases, in the temperature range $180\,K < T < 360\,K$. Its scheme of transitions is as follows:

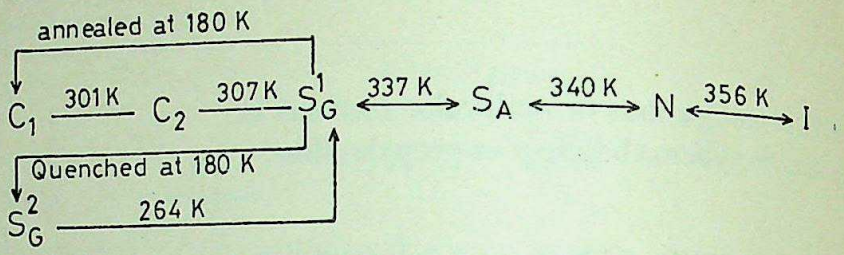

C: Crystal, S: Smectic, N: Nematic, I: Isotropic liquid. The earlier nomenclature used (Usha Deniz *et al* 1977a, b; Mehta 1980) for some of these phases is given below:

$$C_2 \equiv P_1; \quad S_G^{1*} \equiv S_H; \quad S_G^{2*} \equiv P_2, \quad S_m \text{ and } S_H.$$

The nature of the S_G^2 and C_2 phases was not known prior to 1978, hence the change of nomenclature. It has since been confirmed by X-ray diffraction (Mehta 1980; Usha Deniz and Mehta 1982), that the S_G^1 and S_G^2 phases have similar *c*-face centred monoclinic structures with the *b*-axis as the unique axis and the molecular long axis, $\hat{n}$, oriented along the *c*-axis. The molecules are packed in a pseudohexagonal manner in the smectic planes, whereas they have an almost ideal hexagonal packing in a plane perpendicular to their long axes. The lattice constant *a* increases, *b* decreases and *c* remains almost constant as the temperature is decreased in both the S_G^1 and S_G^2 phases (Usha Deniz and Mehta 1982), leading to a net decrease in the area per molecule in the smectic plane, as the sample is cooled from the S_G^1 to the S_G^2 phase. Since the intermolecular distance, *b*, perpendicular to $\hat{n}$ is smaller in the S_G^2 phase than in the S_G^1 phase, the molecular motions in these two phases could be somewhat different. Raman scattering experiments (Usha Deniz *et al* 1977b; Mehta 1980) have shown that when one goes from the S_G^2 to the S_G^1 phase, the neighbourhood of the end hydrocarbon (hc) chains of the molecule changes significantly, whereas such a change does not occur in the environment of the central rigid portion of the molecules. This change is thought to be due to chain disorder. The Raman results, however, give no clue to the nature of this disorder, which can be either static or dynamic. Neutron quasi-elastic scattering experiments (Mehta 1980; Sinha *et al* 1973) carried out at 257K (S_G^2) and 300 K (S_G^1) with HxBPA, show the presence of a rotational diffusion motion in the S_G^1 phase, which is absent in the S_G^2 phase. Form factors for neutron elastic scattering indicate that the motion in the S_G^1 phase is most probably that of the end hydrocarbon chains. These results are inconclusive since the observed change in molecular motion could be due to a simple thermal effect and need not be connected with the phase change from S_G^2 to S_G^1.

This paper describes proton spin-lattice relaxation measurements which have been done, mainly to study the changes occurring in the molecular motions of HxBPA at the $S_G^2 \rightleftarrows S_G^1$ transitions. We have also investigated the contribution of the orientational order fluctuations and short range molecular reorientations to the proton spin-lattice relaxation rate in the nematic phase.

2. Experimental details

The proton spin-lattice relaxation times, T_1 have been measured using Model CPS-2, Spin-Lock Ltd. NMR Instrument (Spin-Lock Ltd., Port Credit, Ontario, Canada)

*The phase S_H is now called S_G (Demus *et al* (1980) *Mol. Cryst. Liq. Cryst. Lett.* **56** 311)

CC-0. In Public Domain. Gurukul Kangri Collection, Haridwar

Digitized by Arya Samaj Foundation Chennai and eGangotri

and a box car signal averager (Princeton Applied Research Corporation, Model 162). The temperature of the sample was stabilized by a home-built automatic temperature controller and could be maintained to within $\pm 0{\cdot}3$ K. The accuracy in the measurement of temperature is 1 K. The temperature range investigated is 223 K $< T <$ 358 K. T_1 was determined mostly at frequencies (ν) of 15 and 40 MHz either by the $\pi/2-\tau-\pi/2$ method or progressive saturation recovery method. Both methods have been used in some measurements and yield identical results.

The temperature dependence of T_1 in S_G^1 and S_G^2 phases was determined both while heating and cooling the sample. To avoid the presence of the crystalline phase (C_1 or C_2) in the sample and to obtain it in a polycrystalline form in the S_G phase, the sample was heated to the isotropic liquid phase and quenched in liquid nitrogen, for the heating cycle. The sample was then placed in the NMR probe maintained at 223 K, before heating it to the desired temperature. For the cooling cycle, the sample was heated to the isotropic liquid phase and cooled rapidly to room temperature (RT) to obtain it in a polycrystalline form. It was then placed in the NMR probe and (a) heated to 315 K and cooled to the required temperature for measurements above 278 K and (b) cooled directly from RT for measurements below 278 K. Thermal cycling or cooling in the magnetic field from S_A, N or I phases resulted in a multidomain sample in the S_G phase from which data would have been hard to interpret. Hence the polycrystallinity of the sample was assured by the methods indicated above. In the other two phases the measurements were carried out only while heating.

3. Results and discussion

The temperature dependence of T_1 in all phases at 15 MHz is shown in figure 2 for the heating cycle. The notable features in this figure are the discontinuity in T_1 appearing at the $S_G^2 \rightarrow S_G^1$ transition and a broad minimum in the S_G^1 phase around 277 K. The limited T_1 data in the S_A phase do not permit any detailed analysis. The results obtained in the other three liquid crystalline phases are discussed in detail below.

3.1 S_G^1 *and* S_G^2 *phases*

Our results obtained at 15 MHz are shown in figure 3 for the heating and cooling cycles. The values of T_1 obtained in the heating run are in good agreement with those observed while cooling, except in the vicinity of the $S_G^2 \rightleftarrows S_G^1$ transitions, where hysteresis is observed. The observed discontinuity in T_1 at 263 K for the heating run is clearly related to the $S_G^2 \rightarrow S_G^1$ transition observed in our DSC measurements (Usha Deniz *et al* 1977a). In the light of the results of Raman (Usha Deniz *et al* 1977b; Mehta 1980) and neutron scattering (Mehta 1980; Sinha *et al* 1973) studies, one expects that (a) the dominant contribution to T_1 in the S_G^1 phase for temperatures below 328 K, is most probably from the rotational diffusion motion of the hc chains of the molecule, and (b) the discontinuity in T_1 may be due to the freezing of this chain motion in the S_G^2 phase or an abrupt change in the nature of the chain motion. The decrease of T_1 for $T > 328$ K, might be brought about by the increased rotational or translational (or both) diffusion of the HxBPA molecule in this temperature range. Evidence for increased diffusion comes from X-ray diffraction patterns (Mehta 1980) of HxBPA which show that the polycrystalline HxBPA sample at 300 K, rapidly changes into one with rather large single crystal grains on heating it to about 320 K. This would

CC-0. In Public Domain. Gurukul Kangri Collection, Haridwar

Digitized by Arya Samaj Foundation Chennai and eGangotri

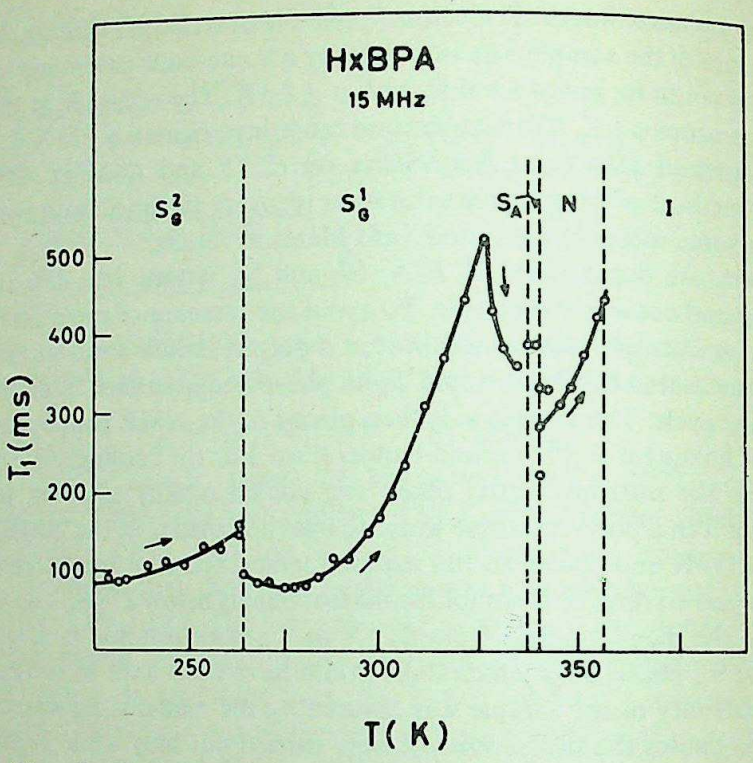

Figure 2. Temperature dependence of T_1 at 15 MHz. The lines are guides to the eye.

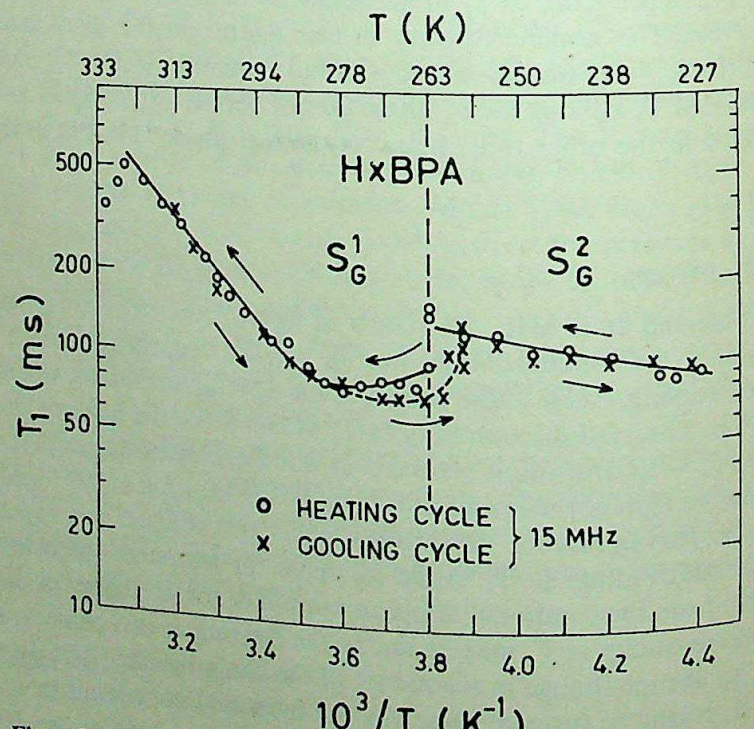

Figure 3. T_1 as a function of $10^3/T$ in the S_G^1 and S_G^2 phases for the heating and cooling cycles. The lines are guides to the eye.

CC-0. In Public Domain. Gurukul Kangri Collection, Haridwar

Digitized by Arya Samaj Foundation Chennai and eGangotri

only be possible if the translational and rotational diffusion motions were rapid for $T \geqslant 320$ K. In the cooling run, the temperature dependence of T_1 is smooth in the neighbourhood of the $S_G^2 \rightarrow S_G^1$ transition temperature, but changes rapidly at 257 K, indicating a change in the molecular (probably chain) motion at this temperature. In the S_G^1 phase, for $282\text{ K} < T < 320\text{ K}$, the T_1 values from both cycles are almost identical. The average activation energy, E_A, for this motion, obtained from our data in this temperature region, is $37{\cdot}3 \pm 1{\cdot}3$ kJ/mol. The close agreement between T_1 values of the heating and cooling runs below 257 K, shows that in these runs, there is no difference in the molecular motions contributing to T_1. This implies that while cooling, the entire sample gets converted into the S_G^2 phase at 257 K. Further, the abrupt change in the slope, dT_1/dT, at the $S_G^2 \rightleftarrows S_G^1$ transition, both while heating and cooling, clearly indicates that at this transition there is a sudden change in the motion(s) contributing to the relaxation rate. It is interesting to note that the cooling transition was not observed in DSC, possibly because calorimetry is not sensitive to the change of molecular motions occurring at this point, in HxBPA.

The T_1 data at 15 and 40 MHz in the heating cycle is given in figure 4. As stated before, a well defined, though somewhat shallow, minimum is observed at 277 K for the 15 MHz data. If a molecular motion with a single correlation time, τ, is assumed to contribute to the relaxation rate, one obtains $\tau \approx 6 \times 10^{-8}$ s (since $\omega\tau \sim 1$, where $\omega = 2\pi\nu$) at 277 K and the minimum in T_1 is expected to shift to 305 K for 40 MHz. Instead, a very shallow minimum which is hardly shifted with respect to the one observed at 15 MHz, is seen. It seems, therefore, that molecular motions with more

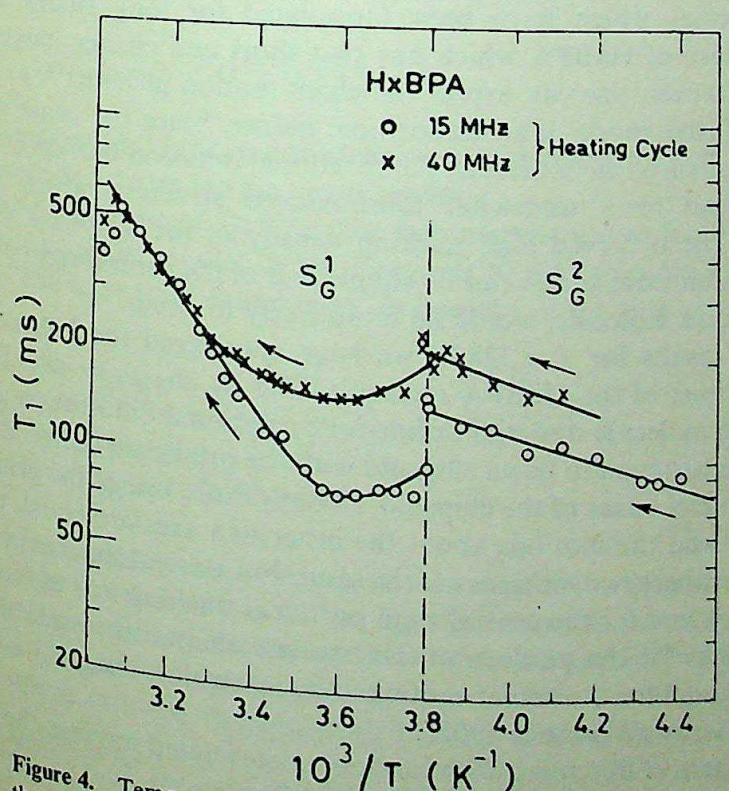

Figure 4. Temperature dependence of T_1 in the S_G^1 and S_G^2 phases, at 15 and 40 MHz, for the heating cycle. The lines are guide to the eye.

CC-0. In Public Domain. Gurukul Kangri Collection, Haridwar

Digitized by Arya Samaj Foundation Chennai and eGangotri

than one correlation time, are contributing to the relaxation rate. For $T > 307$ K, the relaxation rate is independent of frequency, indicating that in this temperature region, the molecular motions are very fast ($\omega\tau \ll 1$) (Noack 1971). On the other hand, in the S_G^2 phase, the frequency dependence of T_1 suggests that the molecular motion is slow.

3.2 *Models for molecular motions in the* S_G^1 *phase* ($T < 328$ K)

Various molecular motions such as the translational diffusion of molecules, collective lattice vibrational modes, undulation modes of the smectic planes and the rotational diffusion of the hc chains or of the entire molecule, might contribute to T_1 in the S_G^1 phase. Translational diffusion motion and undulation modes, if present, would be very slow due to the nearly 3-dimensional order in the S_G^1 phase, and their contribution to the relaxation rate, T_1^{-1} would be negligible. No abrupt change would be expected in the lattice vibrational modes at the $S_G^1 \rightleftarrows S_G^2$ transitions, both while heating and cooling, since no structural change is observed (Usha Deniz and Mehta 1982) at these transitions. The fact that T_1 shows sudden changes at these transition temperatures, indicates that the main contribution to the relaxation rate is not from structural changes. The above considerations indicate that rotational diffusion motions make the dominant contribution to $1/T_1$ in the S_G^1 phase for $T < 328$ K.

In HxBPA, anisotropic rotational diffusion motions of the end hc chains, of the entire molecule or of just the central rigid portions, are possible. Several CH_2 groups are present in the end hc chains of HxBPA and hence several rotational diffusion modes of these chains could be present, leading to as many values of the correlation time, τ. Various theories (Rouse 1953; Agreen 1972; Kimmich and Peters 1975) have considered such modes in chain-like molecules (polymers and lipids). It is doubtful whether these theories which have been formulated for long chains, would be applicable to the case of HxBPA which has two short end chains, having six and three segments. However, one can expect the chain motion in HxBPA to consist of more than one diffusive mode of an anisotropic nature. Since the chain axis is not parallel to the long axis of the molecule, the rotational diffusion motion of the entire molecule would lead to a somewhat loose-packed structure which would be incompatible with the observed high packing density of the S_G phase. Hence, the rotational diffusion motions of the end hc chains and of the central rigid part, rather than that of the entire molecule, would be more likely to occur.

To explain our results for $T < 328$ K, we have considered the following simple model for the motions of the HxBPA molecule. The hc chains as also the central rigid portion of the molecule undergo anisotropic rotational diffusion motion. Each of these two parts is assumed to be an ellipsoid with the rotational diffusion occurring about the three principal axes of the ellipsoid. In both cases, one of the principal axes is a symmetry axis and the motions about the other two axes are equal, that is, the correlation times for these two motions are the same. For the end chains, the symmetry axis is the chain axis and for the central rigid part, it is the long axis of the molecule. The correlation times for the motions of the two end chains are assumed to be the same. Using this model for molecular motions, the relaxation time, T_1, is calculated from Woessner's theory (Woessner 1962).

In a two-spin system of like spins, with random uncorrelated motion, the relaxation rate turns out to be (Woessner 1962; Abragam 1961),

$$T_1^{-1} = \frac{3}{2}\frac{\gamma^4\hbar^2}{b^6} I(I+1)\{J^{(1)}(\omega) + J^{(2)}(2\omega)\} \qquad (1)$$

CC-0. In Public Domain. Gurukul Kangri Collection, Haridwar

Digitized by Arya Samaj Foundation Chennai and eGangotri

where γ = magnetogyric ratio, b is the internuclear separation, I = nuclear spin which is 1/2 for protons and $J^{(i)}(\omega)$ is the ith spectral density. For our model, in which the motion is an anisotropic rotational diffusion motion which is equal about two of the principal axes, Woessner's theory gives,

$$J^{(i)}(\omega) = 2F_i \left\{ A\left[\frac{\tau_A}{1+\omega^2\tau_A^2}\right] + B\left[\frac{\tau_B}{1+\omega^2\tau_B^2}\right] + C\left[\frac{\tau_C}{1+\omega^2\tau_C^2}\right]\right\} \tag{2}$$

where, $F_1 = 2/15$ and $F_2 = 8/15$ and

$$A = \tfrac{1}{4}(3l^2-1)^2, \quad B = 3l^2(1-l^2), \quad C = \tfrac{3}{4}(l^2-1)^2 \tag{3}$$

where l is the direction cosine of the internuclear vector with respect to the symmetry axis of the ellipsoid. τ_A, τ_B and τ_C are correlation times, related to the diffusion coefficients, D_1, D_2 and D_3, for rotation about the three principal axes. Because the ellipsoid possesses a symmetry axis, $D_2 = D_3$, and

$$1/\tau_A = 6D_2, \quad 1/\tau_B = D_1 + 5D_2, \quad 1/\tau_C = 4D_1 + 2D_2 \tag{4}$$

For the end chains of HxBPA, since the internuclear vector for the chain protons are perpendicular to the chain axis, $A = 1/4$, $B = 0$ and $C = 3/4$. The relaxation rate due to chain motion is then,

$$\begin{aligned} T_1^{-1} &= \frac{3}{40}\frac{\gamma^4\hbar^2}{b_C^6}\left\{\left[\frac{\tau_A(c)}{1+\omega^2\tau_A(c)^2} + \frac{4\tau_A(c)}{1+4\omega^2\tau_A(c)^2}\right]\right. \\ &\quad \left. + 3\left[\frac{\tau_C(c)}{1+\omega^2\tau_C(c)^2} + \frac{4\tau_C(c)}{1+4\omega^2\tau_C(c)^2}\right]\right\} \\ &= \frac{3}{40}\frac{\gamma^4\hbar^2}{b_C^6} F_C[\omega, \tau_A(c), \tau_C(c)], \end{aligned} \tag{5}$$

where b_c = magnitude of the internuclear vector for chain protons, and $\tau_A(c)$ and $\tau_C(c)$ are the correlation times for the chain motion.

For the rigid portion of HxBPA, the internuclear vector for the orthoprotons of the aromatic rings, is parallel to the long axis of the molecule. Hence, $A = 1$, $B = 0$ and $C = 0$. The relaxation rate due to the motion of the ring proton is then,

$$\begin{aligned} T_1^{-1} &= \frac{3}{10}\frac{\gamma^4\hbar^2}{b_r^6}\left[\frac{\tau_A(r)}{1+\omega^2\tau_A(r)^2} + \frac{4\tau_A(r)}{1+4\omega^2\tau_A(r)^2}\right] \\ &= \frac{3}{10}\frac{\gamma^4\hbar^2}{b_r^6} F_r[\omega, \tau_A(r)] \end{aligned} \tag{6}$$

where b_r = magnitude of the internuclear vector for the orthoprotons and $\tau_A(r)$ is the correlation time for the motion of the rigid portion. One would have obtained the same expression as (6), if it were assumed that the rigid part had an isotropic rotational diffusion motion with a single correlation time, $\tau_A(r)$.

The relaxation rate due to both contributions is therefore,

where, $$T_1^{-1} = L\{F_c[\omega, \tau_A(c), \tau_C(c)] + RF_r[\omega, \tau_A(r)]\} \tag{7}$$

$$L = \frac{3}{40} f_c \frac{\gamma^4\hbar^2}{b_c^6} \text{ and } R = 4\frac{f_r}{f_c}\frac{b_c^6}{b_r^6} \tag{8}$$

CC-0. In Public Domain. Gurukul Kangri Collection, Haridwar

Digitized by Arya Samaj Foundation Chennai and eGangotri

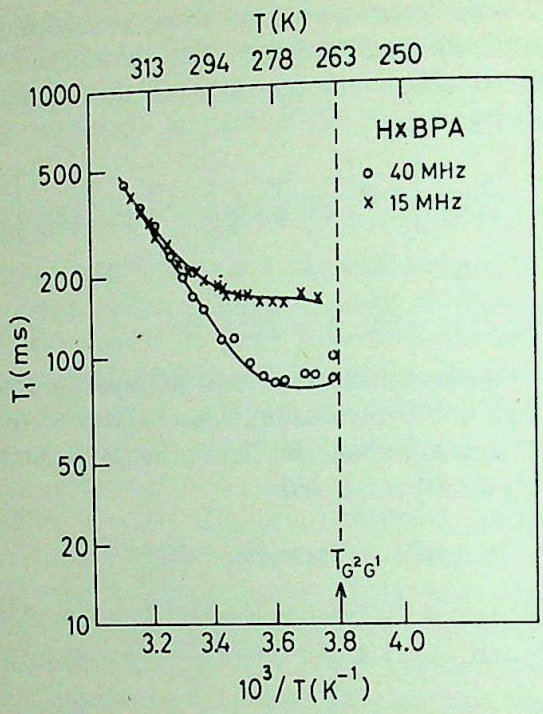

Figure 5. T_1 versus $10^3/T$ in the S_G^1 phase at 15 and 40 MHz. The lines represent best fits of our model (eq. (7)) to the experimental data.

and,

$$f_c = \frac{n_c}{n_c + n_r} \quad \text{and} \quad f_r = \frac{n_r}{n_c + n_r}$$

n_c and n_r are the number of chain and ring protons respectively. Since we have considered the diffusion motion to be thermally activated, the following expressions have been used for the temperature dependences of the correlation times:

$$(6D_2)^{-1} = \tau_A = \tau_2 = \tau_2^0 \exp(E_{A2}/k_B T) \tag{9a}$$

$$(6D_1)^{-1} = \tau_1 = \tau_1^0 \exp(E_{A1}/k_B T). \tag{9b}$$

Equation (7) was fitted to our data using L, $\tau_1^0(c)$, $\tau_2^0(c)$, $\tau_2^0(r)$, $E_{A1}(c)$, $E_{A2}(c)$, and $E_{A2}(r)$ as fitting parameters. The value of b_r was taken to be 2·46 Å. The curve calculated, using the best fit parameters is given in figure 5 and it is found that there is good agreement between our results and the calculations. The best fit parameters are given in table 1. The value of b_c, calculated from the constant L, is also given in table 1. Its value, 1·92 Å, agrees fairly well with that of 1·78 Å, the distance between the methylene protons. An attempt to fit (7) with a fixed value of L (taking $b_c = 1{\cdot}78$ Å), did not lead to such a good agreement. Models assuming chain motions alone (eq. (5)) and motion of the rigid portions alone (eq. (6)) were also fitted to the data. The model considering chain motions alone (eq. 5) gives a reasonably good fit to our data, whereas that with the motion of the rigid portions alone fails to do so. However, neither of these models gives as good an agreement with our results as does (7). In the temperature region where $\omega\tau \ll 1$, it can be seen from (1) and (2) that $T_1^{-1} \sim \exp(E_A/k_B T)$, if one assumes a single correlation time, τ, to exist. We have calculated E_A from our data at 15 and 40 MHz in such a temperature region

CC-0. In Public Domain. Gurukul Kangri Collection, Haridwar

Digitized by Arya Samaj Foundation Chennai and eGangotri

Table 1. Correlation times and activation energies for molecular motions in the S_G^1 phase.

	$\tau_1^0(c) \times 10^{13}$ (s)	$\tau_2^0(c) \times 10^{14}$ (s)	$\tau_2^0(r) \times 10^{15}$ (s)	$E_{A1}(c)$ (kJ/mol)	$E_{A2}(c)$ (kJ/mol)	$E_{A1}(r)$ (kJ/mol)	$L \times 10^5$ (s^{-2})	b_c (Å)
Model	15·04 ± 0·27	0·444 ± 0·005	34·54 ± 10·4	22·4 ± 0·04	42·6 ± 0·04	20·3 ± 0·6	6·34 ± 0·03	1·92 ± 0·04
Directly calculated*		0·590			37·3 ± 1·3			

*See text

CC-0. In Public Domain. Gurukul Kangri Collection, Haridwar

Digitized by Arya Samaj Foundation Chennai and eGangotri

($307\,\mathrm{K} \leqslant T < 328\,\mathrm{K}$) and its value is given in table 1, in the row labelled 'Directly Calculated'. This value of E_A agrees fairly well with that of E_{A1} obtained from our fit (see table 1). Similar agreement can be noticed from this table in the case of the corresponding correlation times. Thus, the dominant contribution to T_1 in this temperature range, seems to be from the chain motion. The fact that a really good fit to our results could not be obtained when the value of b_c and hence of L in (7) was fixed, could be due to the assumption that the two end chains of HxBPA have the same correlation times.

3.2 *Nematic phase*

It can be seen from figure 2 that at 15 MHz, T_1 has a strong temperature dependence in the nematic phase of HxBPA and it increases with increasing temperature. The frequency dependence of T_1 at 351 K is shown in figure 6.

3.2.1. *Molecular motions in the nematic phase*: The reorientations of the molecule as a whole can be thought of as due to (a) collective long range orientational (nematic) order fluctuations i.e. fluctuations of a local preferred direction of orientation, $\hat{n}(\mathbf{r}, t)$ of the molecular long axis about the nematic director $\hat{n}_0$, and (b) short range reorientations of the molecular long axis about $\hat{n}(\mathbf{r}, t)$ which are quite rapid (correlation time $\sim 10^{-10}$ s).

In molecules such as HxBPA, the orthoprotons of the aromatic rings would be sensitive to molecular reorientations. Several theories (Doane and Johnson 1970; Doane *et al* 1974; Blinc 1976) have considered such a two spin system in which the spin-lattice relaxation is due to molecular reorientations but with the short range (local) reorientations being neglected. Both types of molecular reorientational motions have been taken into account in some of them (Sung 1971; Ukleja *et al* 1976; Freed 1977). We consider here the theories of Ukleja *et al* (UPD) (Ukleja *et al* 1976) and Freed (Freed 1977). Both UPD and Freed make the one elastic constant approximation. UPD assume statistical independence of the two molecular motions but Freed does not do so. They both obtain,

$$T_1^{-1} = (T_1^{-1})_a + (T_1^{-1})_b + (T_1^{-1})_c \tag{10}$$

where $(T_1^{-1})_a$, $(T_1^{-1})_b$ and $(T_1^{-1})_c$ are contributions due to long range collective fluctuations, local reorientations and the cross term between the two, respectively.

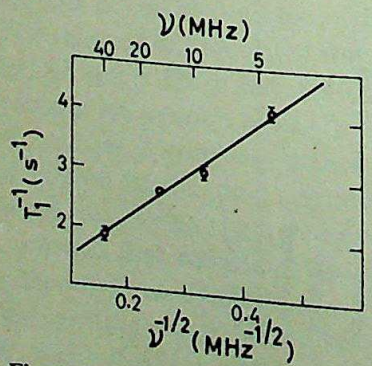

Figure 6. Frequency dependence of T_1^{-1} at 351 K in the nematic phase, fitted to eq. (13).

CC-0. In Public Domain. Gurukul Kangri Collection, Haridwar

Digitized by Arya Samaj Foundation Chennai and eGangotri

The two theories give identical expressions for $(T_1^{-1})_a$ whereas $(T_1^{-1})_b$ and $(T_1^{-1})_c$ given by them are quite different. For the intramolecular case where (1) the internuclear vector is parallel to $\hat{n}_0$, (2) $\omega \ll \omega_c$, where ω_c is a cut-off frequency for the order fluctuation modes, and (3) $\hat{n}_0$ is parallel to **H** (these conditions hold good in our experiments), these theories give,

$$(T_1^{-1})_a^{\text{UPD}} = (T_1^{-1})_a^{\text{Freed}} = \frac{9}{8\sqrt{2\pi}} \frac{\gamma^4 \hbar^2}{b_r^6} \frac{k_B T}{(K/\eta)^{1/2}} \frac{S^2}{K} \omega^{-1/2}$$

$$= A(T)\omega^{-1/2} \tag{11}$$

$S = \frac{1}{2}\langle 3\cos^2\theta - 1\rangle$, where θ is the angle between the nematic director and the long axis of the molecule and $\langle \cdots\cdots \rangle$ signifies thermal average. K is the elastic deformation constant of the nematic and η is its viscosity. Since S^2/K and $k_B T(K/\eta)^{-1/2}$ vary little with temperature, $A(T)$ is a slowly varying function of temperature.

For $\omega\tau \ll 1$, where τ is the correlation time for molecular reorientation, which is a condition that is valid in many cases,

$$(T_1^{-1})_b^{\text{UPD}} = \frac{3}{2} \frac{\gamma^4 \hbar^2}{b_r^6} (1 - S)\tau = B(T)^{\text{UPD}} \tag{12a}$$

whereas,

$$(T_1^{-1})_b^{\text{Freed}} = \frac{3}{5} \frac{\gamma^4 \hbar^2}{b_r^6} (1 - S)\tau = \text{B}(T)^{\text{Freed}}. \tag{12b}$$

It should be noted that while writing (12b), we have used the approximation, $\langle \cos^4\theta \rangle \approx \frac{1}{5}(4S + 1)$, made by UPD. Neglecting the cross term $(T_1^{-1})_c$ which is very different in the two cases, when conditions (1) to (3) hold good and when $\omega\tau \ll 1$, both theories give,

$$T_1^{-1} = \text{A}(T)\omega^{-1/2} + \text{B}(T). \tag{13}$$

Since $\text{B}(T) \propto \tau$ in both theories and the reorientational motion is thermally activated, one would expect $\text{B}(T)$ to be exponential in T. Expressions similar to (13) are obtained in the intermolecular case, but we shall not consider them here.

Equation (13) has been fitted to the T_1 data at 351 K, using A and B as adjustable parameters. The line shown in figure 6 is calculated from (13) using the parameters obtained for the best fit which are given below

$$\text{A}(T) = (1{\cdot}87 \pm 0{\cdot}08) \times 10^4\ \text{s}^{-3/2}$$

$$\text{B}(T) = (0{\cdot}72 \pm 0{\cdot}07)\ \text{s}^{-1}.$$

It is seen that agreement between our data and (13) is very good, showing that at 351 K, the major contribution to the spin-lattice relaxation is from the nematic order fluctuations and local molecular reorientations with $\omega \ll \omega_c$. Using the above value of $\text{B}(T)$ in the expression of UPD (eq. (12a)), we obtain a correlation time,

$$\tau = (4{\cdot}3 \pm 0{\cdot}4) \times 10^{-10}\ \text{s},$$

whereas using it in Freed's theory (eq. (12b)), we obtain,

$$\tau = (1{\cdot}1 \pm 0{\cdot}1) \times 10^{-9}\ \text{s}.$$

CC-0. In Public Domain. Gurukul Kangri Collection, Haridwar

Digitized by Arya Samaj Foundation Chennai and eGangotri

4. Conclusions

The proton spin-lattice relaxation times, measured in HxBPA, reveal the following interesting features:

(a) The $S_G^1 \rightleftarrows S_G^2$ transitions are well-defined ones, as far as molecular motions are concerned. However, thermal studies do not indicate the presence of $S_G^1 \rightarrow S_G^2$ transition. From the behaviour of T_1, we have deduced that this transition is related to the freezing or change of some molecular motions, most probably the chain motions.
(b) In the S_G^1 phase, the T_1 data at 15 and 40 MHz can be fitted fairly well by a model considering anisotropic rotational diffusion motion of the rigid portion of the molecule and the hydrocarbon chains. However, the value obtained for b_c from this model, is slightly higher than the actual value for the methylene protons. This may be due to the reason that our model for molecular motion assumes decoupling of the chain motions and that of the central rigid portion of the molecule.
(c) In the nematic phase, the frequency dependence of T_1 at 351 K is very well explained by considering the nematic order fluctuations and short range molecular reorientations as the main mechanisms for spin-lattice relaxation. The correlation time for short range reorientations is calculated to be $\sim 10^{-10}$ s using UPD's theory whereas with Freed's theory it is $\sim 10^{-9}$ s.

Acknowledgements

We thank R Vijayaraghavan for his interest in this work. We also thank S K Sinha, D L Fishel and J R Merchant for kindly giving us the samples.

References

Abragam A 1961 *The principles of nuclear magnetism* (Oxford: University Press)
Agreen G 1972 *J. Phys.* **33** 887
Blinc R 1976 *NMR basic principles and progress* in Introductory Essays (Eds) P Diehl, E Fluck and R Kosfeld (Berlin: Springer-Verlag) **13** 97
Doane J W and Johnson D L 1970 *Chem. Phys. Lett.* **6** 29
Doane J W, Tarr C E and Nickerson M E 1974 *Phys. Rev. Lett.* **33** 620
Freed J H 1977 *J. Chem. Phys.* **66** 4183
Kimmich R and Peters A 1975 *J. Magn. Reson.* **19** 144
Mehta A I 1980 *Studies on the structured smectics* Ph.D. Thesis, Bombay University, India
Noack F 1971 *NMR basic principles and progress* (Eds) P Diehl, E Fluck and R Kosfeld (Berlin: Springer-Verlag) **3**
Rouse P E 1953 *J. Chem. Phys.* **21** 1272
Sinha S K, Usha Deniz K, Venkataraman G, Dasannacharya B A, Paranjpe A S and Parvathanathan P S 1973 *Proc. Nucl. Phys. Solid State Phys. Symp.* **C16** 197
Sung C C 1971 *Chem. Phys. Lett.* **10** 35
Ukleja P, Pirs J and Doane J W 1976 *Phys. Rev.* **A14** 414
Usha Deniz K, Rao U R K, Mehta A I, Paranjpe A S and Parvathanathan P S 1977a *Mol. Cryst. Liq. Cryst.* **42** 1137
Usha Deniz K, Mehta A I, Rao U R K, Parvathanathan P S and Paranjpe A S 1977b *Phys. Lett.* **A63** 105
Usha Deniz K and Mehta A I 1982 *Phys. Lett.* **A89** 411
Woessner D E 1962 *J. Chem. Phys.* **37** 647

CC-0. In Public Domain. Gurukul Kangri Collection, Haridwar

Digitized by Arya Samaj Foundation Chennai and eGangotri

Pramāṇa – J. Phys., Vol. 34, No. 4, April 1990, pp. 325–331. © Printed in India.

Study of electric potentials across a moving solid-liquid interface

A K BHUNIYA, N PRASAD*, LAKSHMAN PANDEY** and P RAMACHANDRARAO†

*Department of Metallurgical Engineering, †School of Materials Science & Technology, Institute of Technology, Banaras Hindu University, Varanasi 221 005, India
**Present address: Department of Physics, Rani Durgavati Vishwavidyalaya, Jabalpur 482 001, India

MS received 29 August 1989; revised 16 January 1990

Abstract. The electric potential across a melting sample of pure lead was measured as a function of time. A difference of the order of a few hundred microvolts was seen between the measured values of the potential and those calculated using the temperature gradients and the thermopowers of the solid and the liquid phases. This difference persists as long as the solid-liquid interface moves and is attributed to the Galvani potential present at the solid-liquid interface. It is suggested that such measurements can be used to obtain the value of the Fermi energy for liquids.

Keywords. Solid-liquid interface; Galvani potential; Fermi energy; lead; thermopower.

PACS Nos 64·70; 71·25; 81·30; 72·15

1. Introduction

Consider two dissimilar metals which are characterized by Fermi energies E_{F1} and E_{F2} and work functions ϕ_1 and ϕ_2 such that $\phi_1 > \phi_2$ and the Fermi energy E_{F2} is at a level higher than E_{F1}. If these metals are brought into contact with each other at one end, electrons will flow from the metal 2 to metal 1. Metal 2 will get positively charged such that metal 2 is at a potential V_c with respect to metal 1 given by

$$V_c = (\phi_1 - \phi_2)/e, \tag{1}$$

where e is the charge on the electron. V_c is called the contact potential difference. The difference in Fermi energies between the two metals can also be expressed in terms of the so-called Galvani potential, V_g, given by

$$V_g = (E_{F1} - E_{F2})/e. \tag{2}$$

It may be noted that a contact potential results due to the difference in the work functions while the Galvani potential is due to Fermi level differences. This aspect is highlighted in figure 1 and further discussed by Van der Ziel (1968).

It is generally believed that V_c is measurable directly while V_g is perceived only by

†To whom correspondence should be addressed

CC-0. In Public Domain. Gurukul Kangri Collection, Haridwar

Digitized by Arya Samaj Foundation Chennai and eGangotri

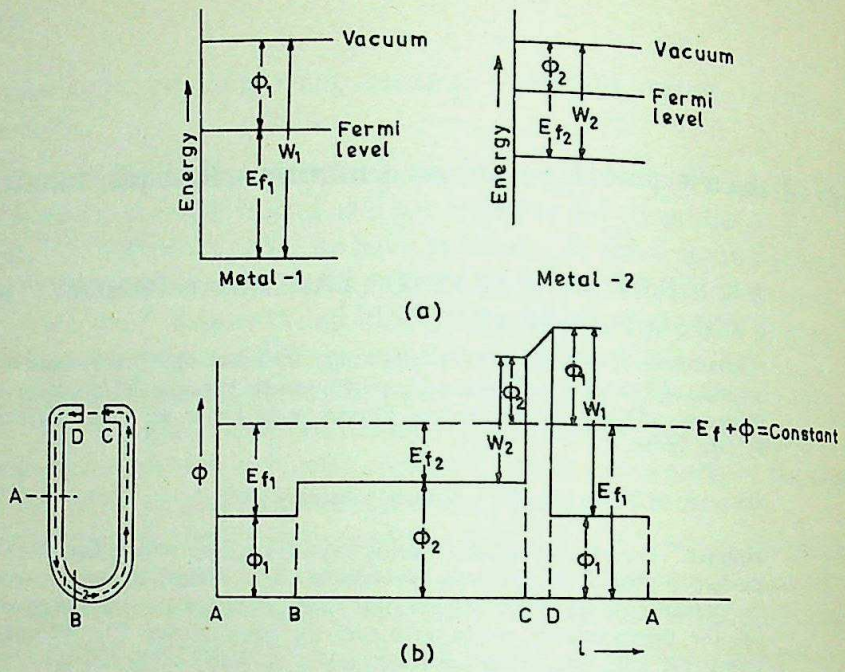

Figure 1. Schematic representation of Fermi energy levels (E_{F1} and E_{F2}) and work functions (ϕ_1 and ϕ_2) for two metals 1 and 2 when they are (**a**) separate and (**b**) in contact with the electron moving around from A. Note the existence of Galvani potential at B and contact potential between D and C.

its temperature dependence which manifests itself as the contact component of the thermoelectric e.m.f. (Van der Ziel 1968).

The Fermi levels of metal in the solid and liquid states are expected to be different. Since most metals expand on fusion, one anticipates a lower Fermi level in the liquid state. By virtue of the Fermi level difference, a Galvani potential arises at a solid-liquid interface. Whenever a solid phase is brought into physical contact with its own liquid, an instantaneous electron flow will ensue from the solid to the liquid and establishes the Galvani potential. When the solid-liquid interface moves i.e. whenever the solid melts or the liquid freezes at the interface it is accompanied by an electron flow in an appropriate direction. The latter type of electron flow affords a method of measuring the Galvani potential by monitoring the potential across a solid-liquid interface in continuous motion. The present report is in continuation of our earlier efforts at measuring the potential across a solid-liquid interface through the design of appropriate cells (Gupta *et al* 1987; Bhuniya 1989).

2. Experimental procedure

A cell was fabricated for the purpose of detecting the interface voltage. As shown in figure 2 the cell consists of two electrodes for measuring the potential and two thermocouples for measuring the temperature. The choice of the electrodes was limited by the following criteria:

(a) The material should not interact either chemically or by way of dissolution in the sample: Perusal of literature, especially phase diagrams, shows that most electrode

CC-0. In Public Domain. Gurukul Kangri Collection, Haridwar

Digitized by Arya Samaj Foundation Chennai and eGangotri

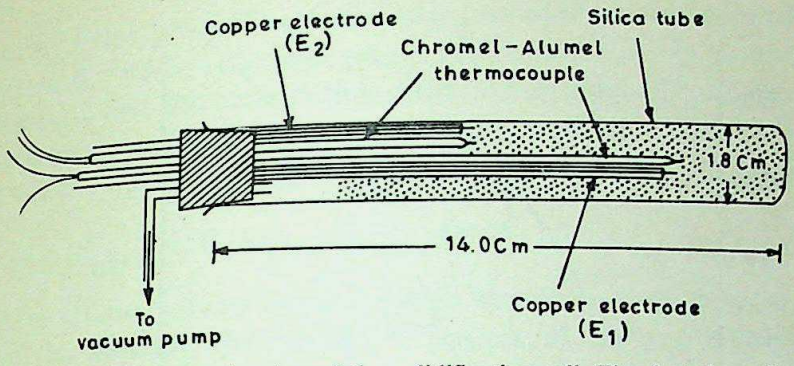

Figure 2. Schematic drawing of the solidification cell. The dotted portion represents the sample.

materials form monotectics/eutectics with lead. Only copper dissolves to a negligible extent at the temperatures of our interest. In a few cases, no phase diagram information was available thus preventing the selection of such materials.

(b) The thermopower of the electrode material should be smaller than or comparable to that of the sample for greater accuracy. Otherwise, the small interface potentials tend to get lost in the associated experimental errors. From this point of view as well, copper is the most suitable electrode for lead.

The two copper electrodes of circular cross-section with a diameter of 0·8 mm were held at a vertical separation of 5 cm in a silica tube of length 14 cm and internal dia of 1·8 cm (figure 2). These were sheathed in glass tube (with only the tip being exposed) and held in place with the aid of a rubber stopper. Two sheathed and fine chromel-alumel thermocouples were located very close to the two electrodes to monitor the temperatures.

The tube was initially filled with metal to be studied and heated until a pool of liquid metal is formed. The rubber stopper was then positioned and sealed. The output from the thermocouples was monitored using a digital microvoltmeter (model DMV 001). The output from the electrodes was amplified using a d.c. amplifier fabricated and calibrated by us and fed to a Perkin–Elmer 56 chart recorder. A typical experiment using this cell consisted of inserting the bottom end of the assembly vertically into a pre-heated resistance furnace which was maintained at a temperature above the melting point of metal to be studied. Initially the portion below electrode E_1 melts (see figure 2) and a solid-liquid interface is formed. It then progressively moves towards E_2 during which time the temperatures and the voltage between E_1 and E_2 are monitored.

3. Results

Figure 3 shows the output across the electrodes E_1 and E_2 (figure 2) and the temperature profiles of these electrodes during the melting of pure lead. It may be noted that the temperature in the region near E_1 rises linearly and attains the melting temperature (T_m) of lead (600·5 K). Temperature of electrode E_2 lags behind and attains 600·5 K after a lapse of about 360 seconds. This is the time it takes for the interface to move from electrode E_1 to electrode E_2. The potential recorded between E_1 and E_2 rises linearly, stabilizes prior to E_1 attaining T_m of lead, shows precursor

CC-0. In Public Domain. Gurukul Kangri Collection, Haridwar

Digitized by Arya Samaj Foundation Chennai and eGangotri

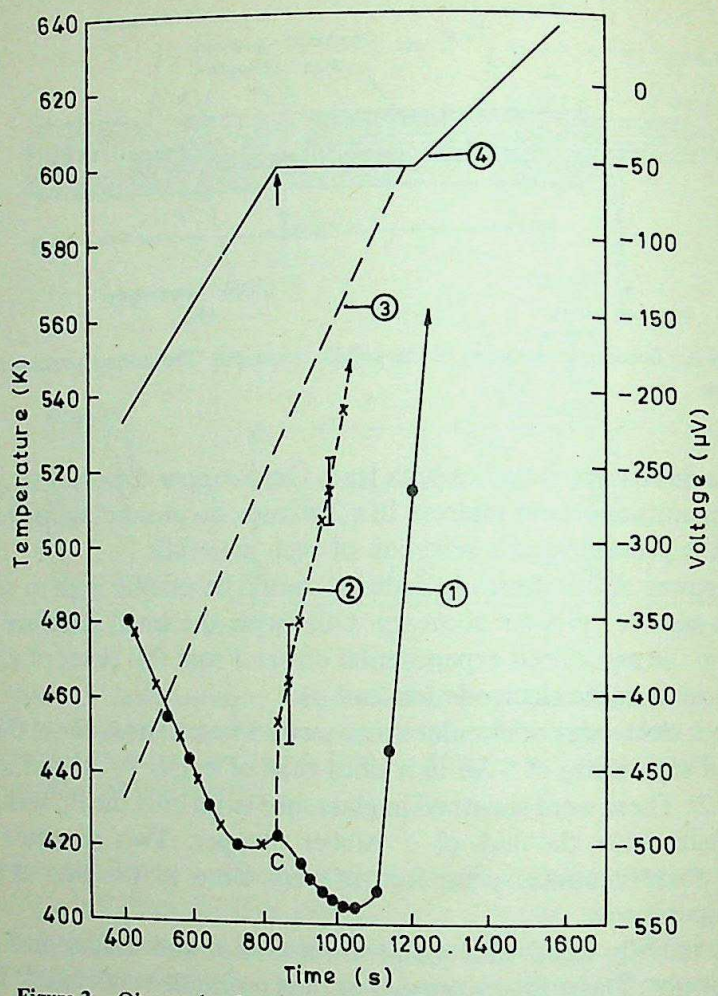

Figure 3. Observed voltage (curve 1) across the electrodes E_1 and E_2 (figure 2) plotted as a function of time. The calculated thermo e.m.f. is shown by curve 2 while the temperatures near the electrodes E_1 and E_2 are shown by curves 3 and 4 respectively.

effects (point C in figure 3) and then rises almost linearly until E_2 attains T_m after which it drops suddenly (see curve 3 in figure 3).

The thermopower of the solid phase with respect to the pure copper electrode could be readily evaluated from the portions of e.m.f. plot prior to melting. The value obtained by us for solid lead near T_m is $-5{\cdot}39 \pm 0{\cdot}83\ \mu VK^{-1}$ and compares very favourably with the value of $-5{\cdot}50\ \mu VK^{-1}$ reported earlier (Verhoeven and Gibson 1969; Blatt *et al* 1976). The thermopower of the liquid phase could not be determined with the same accuracy due to the very small gradients in the liquid phase. We, therefore, use the value of $-7{\cdot}0\ \mu VK^{-1}$ reported by them.

4. Discussion

What potential differences are expected between electrodes E_1 and E_2? In a cell of the type described above, the solid and/or liquid phases are maintained in a temperature gradient before, during and after melting. The observed gradients (as evaluated from the temperature near E_1 and E_2) are greater in the initial solid phase

CC-0. In Public Domain. Gurukul Kangri Collection, Haridwar

Digitized by Arya Samaj Foundation Chennai and eGangotri

than in the final liquid phase. These gradients lead to thermoelectric e.m.f.s. When the region between E_1 and E_2 is a single phase, the thermo e.m.f. is given by the product of thermopower S and the temperature difference between E_1 and E_2. The expected thermo e.m.f. was calculated from the following expression due to Verhoeven and Gibson (1969).

$$V = (S_p - S_l)\delta f G_l + (S_p - S_s)(1-f)G_s\delta, \tag{3}$$

where f is the fraction of the length between the probes which is the liquid. S_p, S_l and S_s are the absolute thermoelectric powers of the probe, liquid and solid respectively, δ is the separation between probes and G_s and G_l are the values of thermal gradient in solid and liquid respectively. It can be shown that equation (3) reduces to

$$V = (S_p - S_l)(T_2 - T_m) + (S_p - S_s)(T_m - T_1), \tag{4}$$

where T_m is the melting temperature of the metal and T_1 and T_2 are the temperatures at E_1 and E_2 respectively. One normally expects the output between E_1 and E_2 to be entirely due to the thermo e.m.f.s.

In figure 3 is also shown the thermo e.m.f. calculated from equation (4). While the general trend of the plot is reproduced, there are significant and inexplicable differences between the observed e.m.f. and the expected e.m.f. when the region between E_1 and E_2 is partially liquid and partly solid. Attempts at compensating for the difference by altering the thermopowers of the liquid and solid phases lead to unreasonable values for these parameters. In an earlier study on the freezing of an aqueous solution Zhekhamukov and Kambiev (1985) attributed potentials of the order of 100 μV, observed during the movement of the solid-liquid interface to change separation at the interface. In the present case where we are dealing with a highly conducting material such processes of charge separation are unlikely and an alternate explanation is required.

We propose that the discrepancy is due to the existence of a Galvani potential. It is well known that the Galvani potential at a single interface cannot be measured since any such attempt will introduce additional interfaces between the probes and the phases concerned (Bockris and Reddy 1973). However, in the present set of experiments, such additional interfaces are present both when the interfaces are stationary and when they are mobile. Any contributions from these interfaces are eliminated when we take the differences between the observed and calculated potentials since the thermopowers used in the calculation also refer to the same electrodes. From our observations it can be said that subtracting the thermo e.m.f. due to gradients is equivalent to subtracting the effects at a stationary interface in the present experiments. Since the equilization of Fermi levels is being slowed down to match the rate of movement of the interface, it is likely that the Galvani potential at the interface is being sensed in the present experiments. This conclusion is in agreement with Sommerfeld's arguments (Sommerfeld 1964) that the electric field present in a conductor carrying a current I and placed in a thermal gradient is given by,

$$E = (1/\sigma)I - S\,\mathrm{grad}\,T - \mathrm{grad}\,(\mu/e), \tag{5}$$

where σ is the electrical conductivity and μ is the chemical potential per electron. Even in the absence of temperature gradients and electric current a potential given

CC-0. In Public Domain. Gurukul Kangri Collection, Haridwar

Digitized by Arya Samaj Foundation Chennai and eGangotri

by $\Delta\mu/e$ can arise due to a finite difference ($\Delta\mu$) in chemical potential of the two phases at a moving interface. In metals, in the absence of any external fields, ($\Delta\mu/e$) can be equated to the Galvani potential ($\Delta E_f/e$). The interface temperature T_i deviates from T_m when the interface moves and leads to the differences in chemical-potentials of electrons. The difference may be expected to be dependent on the rate of interface movement.

The Galvani potential can be expanded as a function of temperature with respect to its value at T_m by the use of Taylor series. To a first approximation,

$$V_g(T) = \left(\frac{E_{F1} - E_{F2}}{e}\right)_{T_m} + \left[\frac{\partial}{\partial T}\left(\frac{E_{F1} - E_{F2}}{e}\right)\right]_{T_m} (T_m - T_i). \tag{6}$$

The second term on the right hand side of the above expression is the contact component of the thermo e.m.f. (Yepifanov and Moma 1984). One can now express the total observed output (V_{obs}) from the electrodes E_1 and E_2 as

$$V_{obs} = V_1 + V_2, \tag{7}$$

where V_1 is the component arising from the Galvani potential V_g and is given by equation (2) for $T = T_m$ i.e. the first term of equation (6). V_2 is the contribution for thermoelectric e.m.f. from all causes including the second term on the right hand side of (6). The difference, $V_{obs} - V_2$, must then correspond to V_g at T_m. If so the observed discrepancy of about 100–400 μV implies a Fermi level difference of 0·1 MeV between the solid and liquid states of lead. T_i will be a function of the rate of interface movement. V_2 will therefore be a function of the rate at which the interface moves. On the basis of the above arguments, the discrepancy between observed and calculated e.m.f.s should be a constant for a constant rate of interface movement. However, the difference changes from 100 μV at the beginning of melting to 400 μV at the end. This would imply a progressively increasing rate of melting. Such an increase may be expected following improvement in heat transfer from the furnace to the sample in the presence of a liquid phase.

The present analysis indicates the possibility of estimating the Fermi level difference between the solid and liquid phases of a pure metal and consequently the Fermi level in the liquid state. The present experimental set-up permitted only the use of low melting metals. Suitable modifications of the system and careful selection of electrodes should enable us to extend the study to other high melting metals. In the case of alloys, the situation will be further modified by the rejection of solute at the solid-liquid interface. Study of such situations will help in understanding the role of the observed potential in controlling the microstructure through feedback and superimposition of appropriate external potentials.

5. Conclusions

The present investigation shows that the electric potential measured across suitably located electrodes in a cell in which solidification takes place cannot be accounted for in terms of thermoelectric phenomena. The difference between the observed potential and that expected from temperature gradients and thermoelectric power of

CC-0. In Public Domain. Gurukul Kangri Collection, Haridwar

Digitized by Arya Samaj Foundation Chennai and eGangotri

the solid and liquid phases is of the order of few hundred microvolts in case of pure lead. The discrepancy is attributed to the contribution due to a Galvani potential across the moving solid-liquid interface. This potential is found to be dependent on the rate of solidification.

Acknowledgements

The authors are grateful to their colleague Professor V B Tare and Professor M Shakuntala for their critical comments.

References

Bhuniya A K 1989 *Electric potentials across a moving solid-liquid interface* M. Tech. (Mat. Tech) dissertation, Banaras Hindu University

Blatt F J, Schroeder P A, Foiles C L and Greig D 1976 *Thermoelectric power of metals* (New York: Plenum Press) Vol. 5

Bockris J O M and Reddy A K N 1973 *Modern electrochemistry* (New York: Plenum Press) Vol. 2

Gupta T K S P, Pandey L and Ramachandrarao P 1987 *Scr. Metall.* **21** 1455

Sommerfeld A 1964 *Thermodynamics and statistical mechanics* (New York: Academic Press) p. 159

Van der Ziel A 1968 *Solid state physical electronics* (New Delhi: Prentice-Hall of India)

Verhoeven J D and Gibson E D 1969 *J. Cryst. Growth* **5** 235

Yepifanov G I and Moma Yu A 1984 *Introduction to solid state electronics* (Moscow: Mir Publications)

Zhekhamukhov M K and Kambiey M M 1985 *Russ. J. Phys. Chem.* **59** 1729

CC-0. In Public Domain. Gurukul Kangri Collection, Haridwar

Digitized by Arya Samaj Foundation Chennai and eGangotri

CC-0. In Public Domain. Gurukul Kangri Collection, Haridwar

Digitized by Arya Samaj Foundation Chennai and eGangotri

Pramāṇa – J. Phys., Vol. 34, No. 4, April 1990, pp. 333–345. © Printed in India.

Evaluation of downstream-mixing scheme for 9·4-μm CO_2 gasdynamic laser

P CHAKRAVARTY, N M REDDY and K P J REDDY
Department of Aerospace Engineering, Indian Institute of Science, Bangalore 560 012, India

MS received 9 August 1989; revised 4 January 1990

Abstract. A theoretical analysis of a downstream-mixing 16-μm CO_2 gasdynamic laser revealed the possibility of utilizing the downstream-mixing scheme for the generation of 9·4-μm radiation using a CO_2 gasdynamic laser. The flow-field has been analyzed using complete two-dimensional, unsteady laminar form of Navier-Stokes equations coupled with the finite rate vibrational kinetic equations. The analysis showed that integrated small-signal gain of 11·5 m^{-1} for Lorentzian broadening and 4·8 m^{-1} considering Voigt function can be obtained for N_2 reservoir temperature of 2000°K and velocity ratio 1:1 between the CO_2 and N_2 mixing streams. These results (presented in graphs) clearly highlight the large potential of downstream-mixing CO_2 gasdynamic laser for 9·4-μm laser generation.

Keywords. Downstream-mixing gasdynamic laser; small-signal gain.

PACS Nos 42·55; 51·70; 42·80

1. Introduction

Since the first proposal for the generation of 16-μm laser beam in CO_2 gasdynamic laser (GDL), which can effectively be used for the laser isotope separation of uranium, there has been a lot of interest in the study of this system. Majority of publications in this field are theoretical and the results are very encouraging. The laser action at 16-μm is achieved by creating the population inversion between (02^00) and (01^10) levels of CO_2 molecule. One of the important assumptions in these studies is that an intense, saturating laser pulse of 9·4-μm is injected into the laser mixture downstream of the nozzle throat to induce transition of molecules from (00^01) level to (02^00) level such that, for a short time a net population inversion is created between (02^00) and (01^10) levels which results in 16-μm laser generation. However, this puts serious constraints on to the system experimentally in terms of choosing 9·4-μm laser pulse of right power, shape and duration. Thus, because of the complex optics involved in this technique, the system becomes very complicated and the overall efficiency goes down.

An effective way of evading this problem is to generate 16-μm beam through cascading process where the population inversion for this transition is achieved by generating a 9·4-μm laser internally from the transition between (00^01) and (02^00) levels of CO_2 molecule. Such a scheme has been investigated theoretically for a premixed cascading 16-μm CO_2 GDL (Saito *et al* 1982), and has been found to be able to render better performance than the above mentioned earlier system. A possible approach for further improvement of performance is the use of downstream-mixing

CC-0. In Public Domain. Gurukul Kangri Collection, Haridwar

Digitized by Arya Samaj Foundation Chennai and eGangotri

scheme in cascaded 16-μm CO_2 GDL. This downstream-mixing scheme is already well known for high performance at 10·6-μm for CO_2 GDLs (Cassady 1980; Murthy 1975; Losev 1981 and Anderson 1976). Further, this approach for the 9·4-μm pulse injected 16-μm CO_2 GDL, has also been proved analytically to be able to produce very high gain values for 16-μm (Chakravarty and Reddy 1986). However, to employ this scheme in actual practice for cascading 16-μm CO_2 GDL requires the generation of 9·4-μm lasing inside a CO_2-N_2 downstream-mixing GDL. This process is quite complex physically. In actual mixing region there is rise in static temperature due to total temperature recovery and consequent increase in the lower laser level (02^00) population. Thus this rise can reduce the population inversion between (00^01) and (02^00) laser levels and in turn degrade the laser action. Moreover, throughout the finite mixing region of the flow, vibrational deactivation can also decrease the lasing action. Furthermore, in actual practice it takes a finite amount of time for mixing, and hence for the molecular collision to occur, before N_2 can pump the CO_2 molecules to higher levels. Thus due to the lapse of this finite amount of time in the process of getting vibrationally excited CO_2 molecules, the 9·4-μm laser action may get affected badly due to the temperature rise. This may in turn jeopardize the 16-μm generation through cascading process. Therefore, before attempting to study such a cascade operation it is essential to evaluate the potential of 9·4-μm generation from a CO_2 downstream-mixing GDL. Also, its properties and characteristics along and across the flow-field are required to be known. In this connection, no detailed study for 9·4-μm has been reported in the literature except for some feasibility studies indicating only the possibility of generation of 9·4-μm lasing for generating 16-μm, theoretically using one-dimensional approaches from premixed CO_2 GDLs by Saito *et al* (1982), Biryukov *et al* (1981), (1984) and also from CO_2 electric discharge lasers by Zaroslov *et al* (1982), and experimentally from a CO_2 after mixing type electric discharge GDL by Wexler *et al* (1977) and Wexler and Waynant (1979). Also, no work has been reported on CO_2 downstream-mixing GDL for generation of 9·4-μm lasing action when this system is well proven to have high performance for other lasing wavelengths of CO_2 i.e., 10·6-μm and 16-μm, as mentioned above. Therefore, it is in this spirit that a study of the 9·4-μm generation from CO_2 downstream-mixing GDL has been carried out and the results of this study are presented in this paper.

The flow-field of a 9·4-μm CO_2 downstream-mixing GDL has been analyzed, using a model utilizing the complete two-dimensional, unsteady, laminar Navier-Stokes equations, fully coupled with the finite rate vibrational kinetic equations. This analysis emphasizes the fluid dynamic and kinetic aspects of the mixing flow taking into consideration the detailed collisional deactivation rate processes in the mixing region. Further, this work contributes to the understanding of 9·4-μm CO_2 downstream-mixing GDL largely by giving a detailed analysis of the various properties of it along the flow-field, and also the effect of variation of different flow-field parameters on the 9·4-μm small-signal gain. The results of numerical study clearly show for the first time the high potential of "downstream-mixing" scheme for 9·4-μm CO_2 GDL and thereby highlighting, that, a 9·4-μm CO_2 laser of such type can further be used for the generation of a 16-μm laser through the cascade process.

2. Simulation model and governing equations

The simulation model used for the present analysis is explained in detail by

CC-0. In Public Domain. Gurukul Kangri Collection, Haridwar

Digitized by Arya Samaj Foundation Chennai and eGangotri

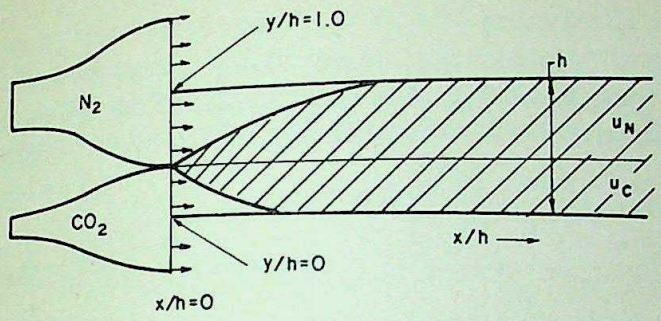

Figure 1a. Schematic diagram of a downstream-mixing gasdynamic laser.

Chakravarty and Reddy (1986) and Chakravarty (1989). Figure 1(a) illustrates the physical setup of the downstream-mixing GDL used for the present analysis. The two nozzles shown are assumed to be only part of a bank of multiple nozzles characteristics of GDLs; thereby the two centrelines are lines of symmetry. The region of interest for the present analysis starts from the nozzle exits, extends downstream and remains confined between two centrelines. This region for the sake of simplicity is referred as duct. A supersonic stream of vibrationally excited pure N_2 is mixed tangentially with a supersonic stream of cold CO_2 at the nozzle exits. Due to mixing through molecular collisions, vibrational energy is transferred from N_2 to cold CO_2. The flow-field has been assumed to be laminar (by keeping the Reynolds number low) and two-dimensional in spatial directions x and y as shown in Figure 1(a).

In the present analysis both the streams are considered to be compressible and viscous, with varying viscosity, thermal conductivity and diffusivity. They are also non-radiating and have non-equilibrium vibrational energy exchange between themselves. Thus the basic set of equations are unsteady, two-dimensional form of laminar Navier-Stokes equations, augmented with appropriate species continuity, global continuity, energy, state equation and the vibrational relaxation equations, which can be expressed as:

Continuity

$$\frac{\partial \rho}{\partial t}+\frac{\partial}{\partial x}(\rho u)+\frac{\partial}{\partial y}(\rho v)=0. \tag{1}$$

Species continuity

$$\frac{\partial}{\partial t}(\rho c_i)+\frac{\partial}{\partial x}(\rho u c_i)+\frac{\partial}{\partial y}(\rho v c_i)+\frac{\partial}{\partial x}(\rho_i u_i)+\frac{\partial}{\partial y}(\rho_i v_i)=0. \tag{2}$$

x-momentum

$$\frac{\partial}{\partial t}(\rho u)+\frac{\partial}{\partial x}\left[\rho uu+p+\frac{2}{3}\mu\left(\frac{\partial u}{\partial x}+\frac{\partial v}{\partial y}\right)-2\mu\frac{\partial u}{\partial x}\right]+\frac{\partial}{\partial y}\left[\rho uv-\mu\left(\frac{\partial u}{\partial y}+\frac{\partial v}{\partial x}\right)\right]=0. \tag{3}$$

CC-0. In Public Domain. Gurukul Kangri Collection, Haridwar

Digitized by Arya Samaj Foundation Chennai and eGangotri

y-momentum

$$\frac{\partial}{\partial t}(\rho v)+\frac{\partial}{\partial y}\left[\rho vv+p+\frac{2}{3}\mu\left(\frac{\partial u}{\partial x}+\frac{\partial v}{\partial y}\right)-2\mu\frac{\partial v}{\partial y}\right]$$
$$+\frac{\partial}{\partial x}\left[\rho uv-\mu\left(\frac{\partial u}{\partial y}+\frac{\partial v}{\partial x}\right)\right]=0. \tag{4}$$

Energy

$$\frac{\partial}{\partial t}(\rho h)+\frac{\partial}{\partial x}(\rho uh)+\frac{\partial}{\partial y}(\rho vh)$$
$$=\frac{\partial}{\partial x}\left(k\frac{\partial T}{\partial x}\right)+\frac{\partial}{\partial y}\left(k\frac{\partial T}{\partial y}\right)-\frac{\partial}{\partial x}\left(\sum_i \rho_i u_i h_i\right)$$
$$-\frac{\partial}{\partial y}\left(\sum_i \rho_i v_i h_i\right)+\frac{\partial p}{\partial t}+u\frac{\partial p}{\partial x}+v\frac{\partial p}{\partial y}$$
$$+\mu\left[2\left[\left(\frac{\partial u}{\partial x}\right)^2+\left(\frac{\partial v}{\partial y}\right)^2\right]+\left(\frac{\partial v}{\partial x}+\frac{\partial u}{\partial y}\right)^2-\frac{2}{3}\left(\frac{\partial u}{\partial x}+\frac{\partial v}{\partial y}\right)^2\right]. \tag{5}$$

State

$$p=\rho RT. \tag{6}$$

In addition to these equations, as explained earlier, a set of vibrational relaxation equations are added to find out the vibrational energies of the appropriate levels of CO_2, taking into consideration the non-equilibrium vibrational energy exchange between the two mixing streams. The present system being a downstream-mixing GDL, the pumping rate of the (001) level of CO_2 by N_2 is the controlling factor in the evaluation of laser gain as the flow moves downstream of the nozzle exits. Hence, the detailed vibrational kinetic model by Munjee (1972), where the ν_3 mode of CO_2 is kept separate from N_2, has been considered for the present analysis (figure 1(b)). In this model due to strong Fermi resonance between the ν_1 and ν_2 modes of CO_2, they are combined together as ν_{12}, with associated vibrational energies and

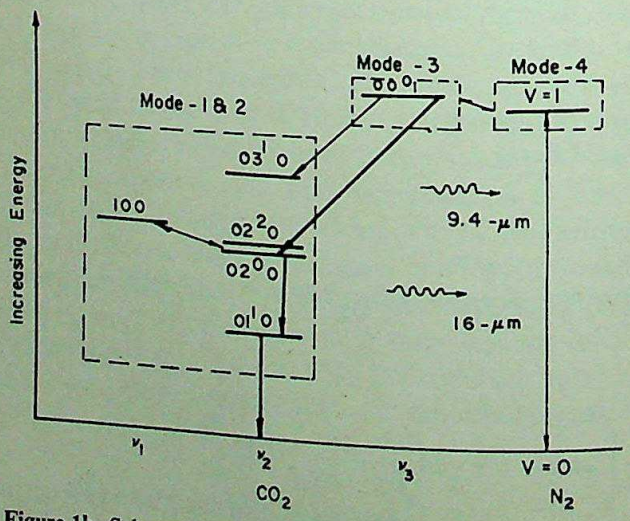

Figure 1b. Schematic diagram of vibrational energy levels of CO_2 and N_2 molecules.

CC-0. In Public Domain. Gurukul Kangri Collection, Haridwar

Digitized by Arya Samaj Foundation Chennai and eGangotri

temperatures as $e_{12} = e_1 + 2e_2$ and $T_{12} = T_1 = T_2$ respectively. However, the present system being a flowing system where, the vibrational energy in a given mode changes not only due to collisions but also due to convection and viscous diffusion, the time rates of net energy transfer into or out of these modes derived using the above model can be expressed as

$$\frac{\partial}{\partial t}(\rho e_{\text{vib}_{12}}) = -\frac{\partial}{\partial x}(\rho e_{\text{vib}_{12}} u) - \frac{\partial}{\partial y}(\rho e_{\text{vib}_{12}} v) + \frac{\partial}{\partial x}\left(\rho D_{12}\frac{\partial c_{\text{CO}_2}}{\partial x} e_{12}\right) + \frac{\partial}{\partial y}\left(\rho D_{12}\frac{\partial c_{\text{CO}_2}}{\partial y} e_{12}\right) + \rho_{\text{CO}_2}\dot{w}_{12} \tag{7}$$

$$\frac{\partial}{\partial t}(\rho e_{\text{vib}_3}) = -\frac{\partial}{\partial x}(\rho e_{\text{vib}_3} u) - \frac{\partial}{\partial y}(\rho e_{\text{vib}_3} v) + \frac{\partial}{\partial x}\left(\rho D_{12}\frac{\partial c_{\text{CO}_2}}{\partial x} e_3\right) + \frac{\partial}{\partial y}\left(\rho D_{12}\frac{\partial c_{\text{CO}_2}}{\partial y} e_3\right) + \rho_{\text{CO}_2}\dot{w}_3 \tag{8}$$

$$\frac{\partial}{\partial t}(\rho e_{\text{vib}_4}) = -\frac{\partial}{\partial x}(\rho e_{\text{vib}_4} u) - \frac{\partial}{\partial y}(\rho e_{\text{vib}_4} v) + \frac{\partial}{\partial x}\left(\rho D_{12}\frac{\partial c_{\text{N}_2}}{\partial x} e_4\right) + \frac{\partial}{\partial y}\left(\rho D_{12}\frac{\partial c_{\text{N}_2}}{\partial y} e_4\right) + \rho_{\text{N}_2}\dot{w}_4. \tag{9}$$

Here, u, v are the velocities of the mixture relative to the laboratory or fixed frame, u_i, v_i are the diffusion velocities of species i relative to the mass-motion of the mixture, ρ_i is the density of species i, ρ and p are the static density and static pressure of the mixture, T is the static temperature, c_i is the mass-fraction of species i, h_i is the static enthalpy of species i, h is the static enthalpy of the mixture, μ is the dynamic viscosity coefficient of the mixture, k is the coefficient of thermal conductivity of the mixture, R is the specific gas constant of the mixture, D_{12} is the binary diffusion coefficient, e_{12}, e_3 are the vibrational energies per unit mass of CO_2 in mode-12 and mode-3 respectively, e_4 is the vibrational energy in mode-4 per unit mass of N_2, $e_{\text{vib}_{12}}, e_{\text{vib}_3}, e_{\text{vib}_4}$ are the vibrational energies per unit mass of the mixture in modes 12, 3 and 4 respectively, $\dot{w}_{12}, \dot{w}_3, \dot{w}_4$ are the time rates of net energy transfer into our out of modes 12, 3 and 4 respectively from Munjee's model.

The above equations are nondimensionalized and solved numerically following the method given by Chakravarty *et al* (1986), (1987) and Chakravarty (1989), using an explicit, time-dependent, second-order accurate, finite-difference, computer code, based on the predictor-corrector approach of MacCormack to find out the steady-state values of flow-field variables. The flow-field properties are calculated as functions of x (in the flow direction) and y (normal to the flow direction i.e., the laser beam direction) as shown in figure 1(a). These steady-state values are further used to calculate the population inversion between $(00^0 1)$ and $(02^0 0)$ levels of CO_2 (Fig. 1(b)) and in turn the 9·4-μm small-signal gain. The small-signal gain expression for $P(14)$ line of $(00^0 1)$–$(02^0 0)$ transition considering only Lorentzian broadening with rotational correction can be expressed as:

$$G_{L9\cdot4} = \frac{\lambda^2}{4\pi\tau_{12}Z}\left(\frac{32\cdot546842}{T}\right)(N_{00^0 1} - N_{02^0 0})\exp(-117\cdot84201/T) \tag{10}$$

CC-0. In Public Domain. Gurukul Kangri Collection, Haridwar

Digitized by Arya Samaj Foundation Chennai and eGangotri

where $\lambda = 9{\cdot}4$-μm is the wavelength of the laser, $\tau_{12} = 5{\cdot}0$ s is the radiative life time (Manuccia *et al* 1976), Z is the molecular collision frequency, N_i is the population of the ith level.

However, for a gas which is expanded from high stagnation pressure to very low static pressures at the optical cavity, as in a GDL especially of the kind simulated in the present analysis, consideration of both Lorentz and Doppler line-broadening mechanisms become important for the evaluation of line shape function. Therefore, in this investigation the 9·4-μm small-signal gain values have been recalculated using Voigt function $H(a, 0)$, which combines the effect of both the line-broadening mechanisms. With the above modification the 9·4-μm small-signal gain expression with rotational correction is:

$$G_{V9\cdot4} = \frac{\lambda^2}{8\pi\tau_{12}}\left(\frac{32{\cdot}546842}{T}\right)(N_{00^01} - N_{02^00})\exp\left(\frac{-117{\cdot}84201}{T}\right) \times \left(\frac{\ln 2}{\pi}\right)^{1/2}\frac{H(a,0)}{\Delta\nu_D}. \tag{11}$$

Where $\Delta\nu_D$ is the Doppler half-width. The method of evaluation of Voigt function $H(a, 0)$, is given in detail in Chakravarty (1989) and also in Gross and Bott (1976).

3. Results and discussion

The initial conditions used for the present analysis are $T_{o_{N_2}} = 2000$°K, $p_{o_{N_2}} = 2 \times 10^6$ N/m^2, reference temperature at the nozzle exists = 141·94°K, reference pressure at the nozzle exits = 199·5 N/m^2, Mach number = 8·09 and velocity ratio between the CO_2 and N_2 streams $u_C{:}u_N = 1{:}1$. The N_2 vibrational temperature is assumed to be frozen during the nozzle expansion process, so that, $T_{vib_{N_2}} = T_{o_{N_2}} = 2000$°K. The CO_2 vibrational modes are assumed to be in equilibrium with the translational and rotational modes during the nozzle expansion process, hence $T_{vib_{CO_2}}$ = reference static temperature = 141·94°K. During the computation, grid points in the transverse direction have been assumed such that the CO_2 stream extends from $y/h = 0{\cdot}0$ to $y/h = 0{\cdot}35$, and there is only N_2 stream beyond this range.

In the present analysis though the numerical method used to solve the flow-field equations is a time dependent method, all results presented in this section are the final steady-state values. The intermediate transients are of no particular interest and are not given here. In the figures the parameters with subscript R are the reference quantities used for non-dimensionalising the variables in the governing equations. These reference quantities are the N_2 stream values at the nozzle exit.

The steady-state transverse velocity distribution profiles of the system shown in figure 1(a) having velocity ratio $u_C{:}u_N = 1{:}1$ are shown in figure 2. It has already been established from our earlier investigation (Chakravarty and Reddy 1986 and Chakravarty *et al* 1987), that velocity ratio 1:1 leads to best possible gain values for 16-μm. In this study since the system configuration and initial conditions are kept same as in the previous studies, the velocity ratio has been chosen as 1:1. It can be observed here that there is no velocity discontinuity even till far downstream at $x/h = 200$. This leads to many advantages as will be elaborated in the following discussion. Further, figure 3 presents the transverse mixture-density distribution

CC-0. In Public Domain. Gurukul Kangri Collection, Haridwar

Digitized by Arya Samaj Foundation Chennai and eGangotri

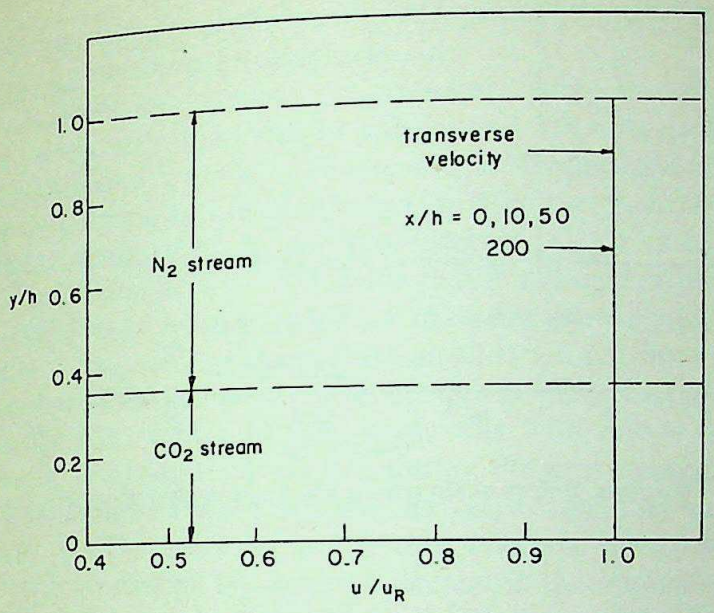

Figure 2. Transverse velocity distribution profiles at various axial locations in the cavity.

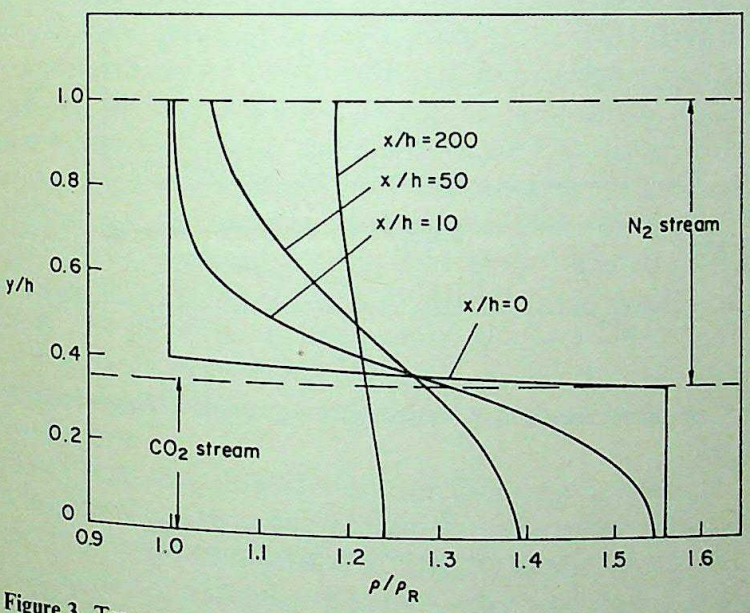

Figure 3. Transverse mixture-density distribution profiles at various axial locations in the cavity.

profiles at various axial locations. The large initial density gradients near the inlet become almost uniform by $x/h = 200$. The peak value of $\Delta\rho/\rho$ at $x/h = 200$ is only 5·2%. Such uniform mixed region with low values of density distributions are necessary for good optical quality of the laser beam.

The vibrational energy profiles of the CO_2-N_2 system under consideration are presented in figures 4, 5 and 6. The vibrational energy transfer process is a complex phenomenon. Furthermore, the vibrational energy of the molecules inside a moving fluid element in the mixing flow-field is changed by convection and diffusion of vibrational species across the fluid element boundaries and by vibrational energy exchange with other molecules that are inside the fluid element as well as with those

CC-0. In Public Domain. Gurukul Kangri Collection, Haridwar

Digitized by Arya Samaj Foundation Chennai and eGangotri

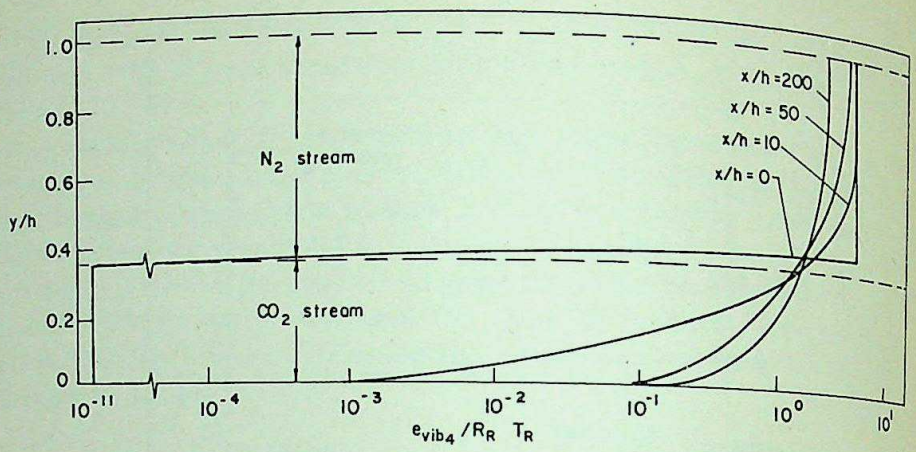

Figure 4. Transverse profiles of vibrational energy in mode-4 at various axial locations in the cavity.

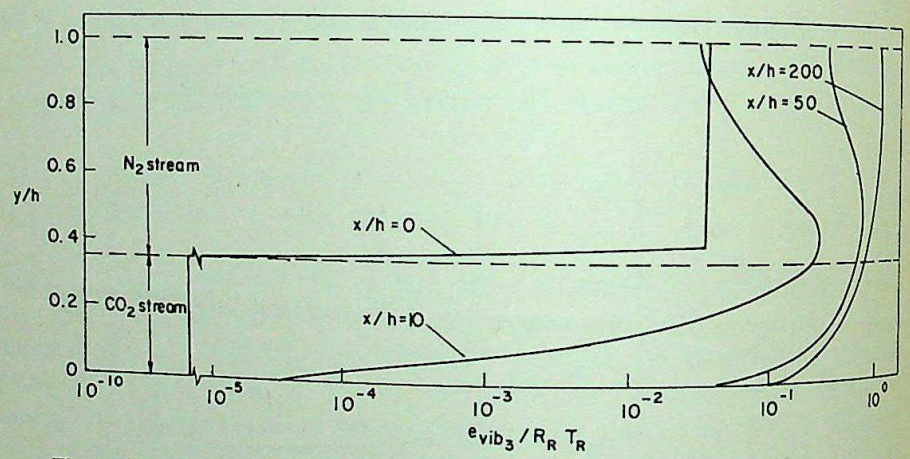

Figure 5. Transverse profiles of vibrational energy in mode-3 at various axial locations in the cavity.

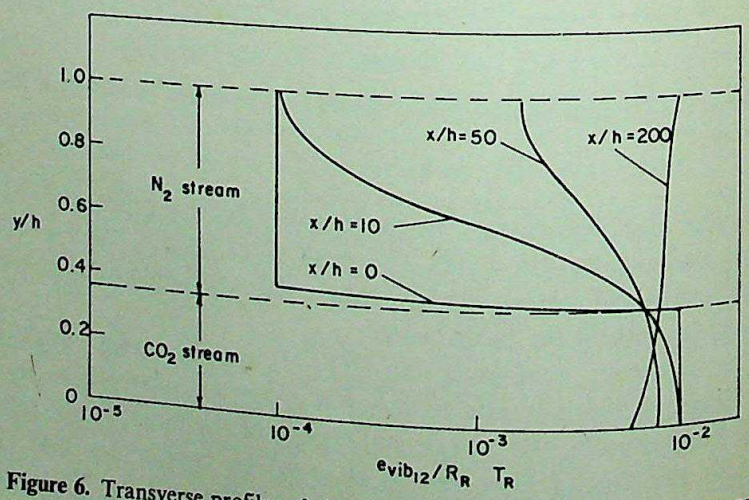

Figure 6. Transverse profiles of vibrational energy in mode-12 at various axial locations in the cavity.

CC-0. In Public Domain. Gurukul Kangri Collection, Haridwar

Digitized by Arya Samaj Foundation Chennai and eGangotri

that diffuse across the boundaries. It is the result of these complex processes that are reflected in the vibrational energy profiles.

Figure 4 shows the profiles of vibrational energy in mode-4. The energy e_{vib_4} increases from a very low value at $y/h = 0$ and $x/h = 10$, to an appreciably higher value at $y/h = 0$ and $x/h = 200$. This is due to the presence of vibrationally excited N_2 in the CO_2 stream as a result of diffusion from the N_2 stream. On the other hand, due to the existence of N_2 in the upper stream, e_{vib_4} does not change appreciably even far downstream at $x/h = 200$, a fact that is reflected in the upper portion of the curve at $y/h = 1{\cdot}0$. An interesting feature of the initial steady-state distribution profile in this figure is that, the e_{vib_4} is negligibly small at $x/h = 0$, from $y/h = 0$ to 0·35. This is attributed to the fact that there are practically no vibrationally excited N_2 molecules present in the CO_2 stream at the nozzle exits. This means that, in the process of attainment of steady-state at $x/h = 0$, during the time elapsed, even if a handful of excited N_2 molecules have diffused into the CO_2 stream, they have quickly transferred their energy to CO_2 molecules due to near resonant energy transfer collision. As a result, there is no excited N_2 molecule present in that region to contribute for e_{vib_4}. On the other hand, e_{vib_4} is quite large in the N_2 stream region i.e., $y/h = 0{\cdot}4$ to 1·0 at $x/h = 0$, due to the presence of large number of excited N_2 molecules.

The profiles of vibrational energy in mode-3 are presented in figure 5. These profiles of e_{vib_3} are the direct measure of population in the (001) level of CO_2, which gives rise to 9·4-μm laser emission. Thus, higher e_{vib_3} means higher gain for 9·4-μm transition. Here at $x/h = 0$, up to $y/h = 0{\cdot}35$ the e_{vib_3} is very small, which implies that in a downstream-mixing GDL at the exit of the nozzle, CO_2 is very cold and hence mode-3 is practically empty. However, at $y/h = 0{\cdot}4$ onwards (at the same $x/h = 0$) there is large increase in e_{vib_3}. By similar reasoning as given for figure 4 in the process of attainment of steady-state at $x/h = 0$, during the time elapsed a few of the CO_2 molecules diffuse into the N_2 stream and give rise to increase in e_{vib_3}. There is a large increase in e_{vib_3} far downstream due to mixing at $x/h = 200$ and $y/h = 0$. Also, from $y/h = 0{\cdot}4$ and upwards, distribution of e_{vib_3} is uniform. This is a very important feature, since it leads to almost uniform small-signal gain profiles as will be explained in the following discussion.

Figure 6 is a representation of vibrational energy in mode-12. This mode due to its lower energy level is in near equilibrium with the translational mode, and it reflects the changes in the static temperature T. The change in the $e_{vib_{12}}$ in the region $y/h = 0$ to 0·35 is negligible for various x/h values, which implies that, the change in static temperature of the system is negligible even far downstream at $x/h = 200$, compared to that at $x/h = 0$. This fact will be elaborated later during the discussion of figures 7 and 8. However, the little decrease of $e_{vib_{12}}$ in this region as seen in figure 6 can be attributed to the following reasons. The diffusion of $e_{vib_{12}}$ to other parts of the stream is one reason, due to which there is appreciable increase in $e_{vib_{12}}$ above $y/h = 0{\cdot}35$ at $x/h = 200$. Also collisionally deactivated CO_2 molecules to the ground state have a higher probability of being pumped to the (001) level because of the increased amount of vibrationally excited N_2 that has diffused into the CO_2 stream. In the N_2 stream region, between $y/h = 0{\cdot}35$ to $y/h = 1{\cdot}0$, from $x/h = 0$ to 10, there are very few CO_2 molecules and hence $e_{vib_{12}}$ is low. This $e_{vib_{12}}$ in this region increases at $x/h = 200$, as explained earlier, due to mixing.

All these observations are further borne out by the plots of static temperature T and the vibrational temperatures T_{12}, T_3 and T_4 for the modes 12, 3 and 4 given in

CC-0. In Public Domain. Gurukul Kangri Collection, Haridwar

Digitized by Arya Samaj Foundation Chennai and eGangotri

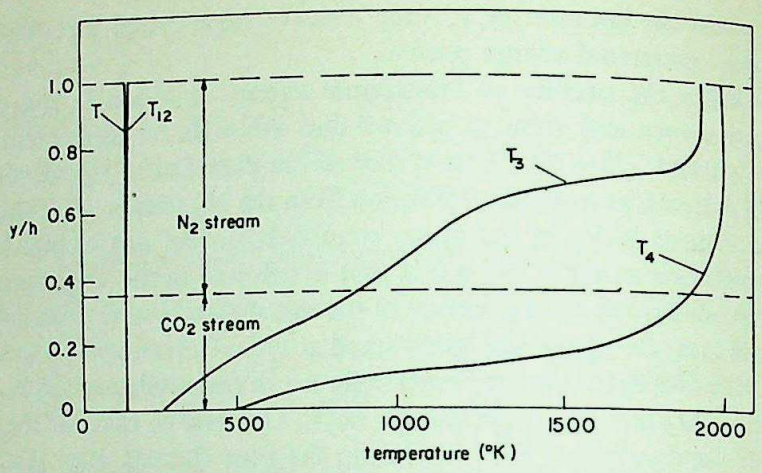

Figure 7. Transverse profiles of static temperature (T) and vibrational temperatures of the modes (12), (3) and (4) at $x/h = 10$.

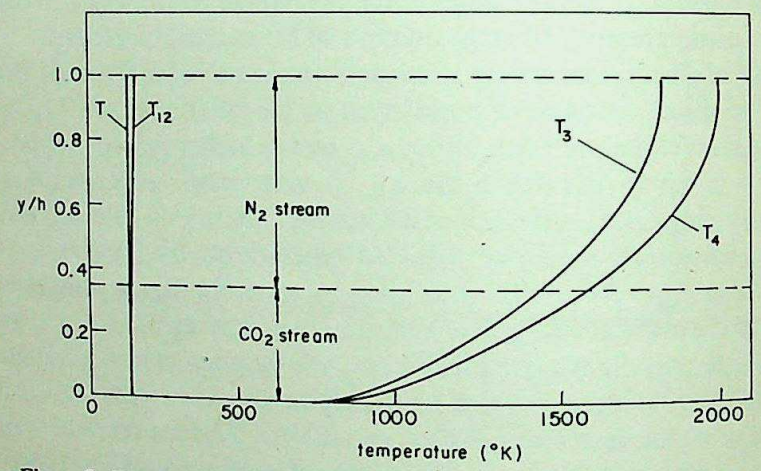

Figure 8. Transverse profiles of static temperature (T) and vibrational temperatures of the modes (12), (3) and (4) at $x/h = 200$.

figures 7 and 8. It can be seen, that in support of earlier discussion on figure 6, the static temperature T remains almost constant from $x/h = 10$ to far downstream $x/h = 200$ as shown in figures 7 and 8. This is due to the reason that the effect of viscous dissipation in increasing the static temperature has been completely eliminated because there is no velocity discontinuity between the two streams as shown in figure 2. The mixing of two streams in this case is only by diffusion. Hence there is no appreciable rise in static temperature. It can be noticed that the temperature T_{12} is slightly different from the static temperature above $y/h = 0{\cdot}35$ at $x/h = 200$. This supports the earlier explanation that some of the CO_2 molecules that diffuse into the N_2 streams are vibrationally excited not only into mode 3 but also into mode 12. Further, at $x/h = 10$ in figure 7, the temperature T_3 and T_4 are far apart indicating that the resonant transfer of vibrational energy from N_2 to CO_2 has not occurred to any significant extent. However, at $x/h = 200$ in figure 8, the T_3 and T_4 temperature profiles lie very close to each other indicating that the pumping of CO_2 molecules by N_2 is nearly complete. Thus these profiles show that the (001) level of CO_2 and ($V = 1$) level of

CC-0. In Public Domain. Gurukul Kangri Collection, Haridwar

Digitized by Arya Samaj Foundation Chennai and eGangotri

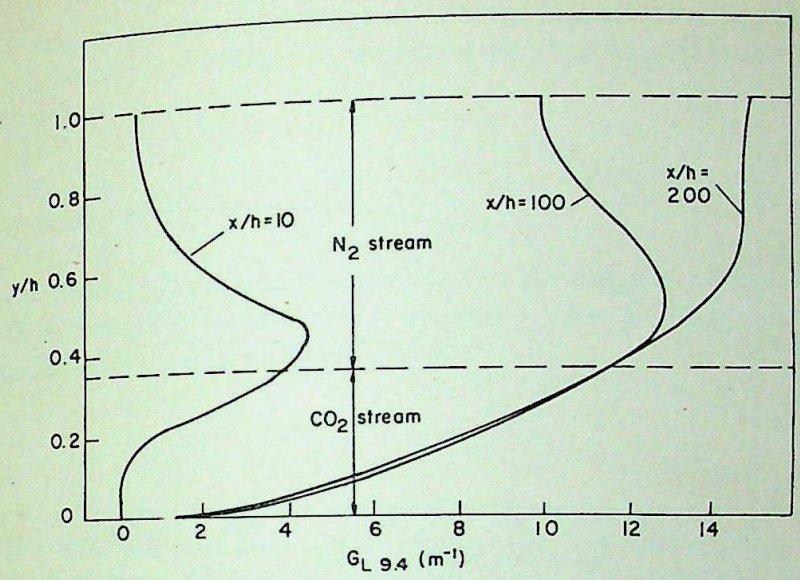

Figure 9. Transverse profiles of local small-signal gain at various axial locations in the cavity.

N_2 equilibrate while mode 12 closely follows the translational mode indicating a population inversion between the two laser levels namely ($00^0 1$) and ($02^0 0$) especially at far downstream.

The testimony of this population inversion is finally brought out in the local small-signal gain $G_{L9\cdot4}$ profiles as shown in figure 9. These plots are obtained using (10). The strong gradients in $G_{L9\cdot4}$ near the inlet are attenuated as the two streams mix farther downstream. These strong gradients near the initial axial locations appear in the good mixing region i.e., in the middle of the flow, between $y/h = 0{\cdot}4$ to $0{\cdot}6$, due to the availability of more number of excited CO_2 molecules, which contribute to the gain. However, in support of our earlier observations (figures 3 and 5), more uniform gain region evolves only at far downstream due to creation of homogeneously mixed total flow-field, as shown by the upper portion of the curve at $x/h = 200$, reflecting the point that far downstream, the flow gradually tends towards that of a conventional 9·4-μm GDL. The highest value of local small-signal gain obtained from the present analysis, at $x/h = 200$ is $14{\cdot}9\ m^{-1}$. This value of $G_{L9\cdot4}$ at N_2 reservoir temperature 2000°K is even when the detailed collisional deactivation rate processes in the mixing zone are considered in the analysis. Further, from the previous experience of the authors for the 9·4-μm induced 16-μm CO_2-N_2 downstream mixing GDL (Chakravarty *et al* 1986, 1987), it is expected that the above mentioned value of $G_{L9\cdot4}$ for the present CO_2 downstream-mixing GDL is higher than a conventional CO_2 GDL with the same reservoir temperature of 2000°K. However, no quantitative comparison of this result can be made at present due to lack of data.

Figure 10 presents the variation of integrated gain with distance along the flow. These plots are obtained by integrating the local small-signal gain profiles individually, along y/h, at particular x-location. Hence, such a plot represents the average small-signal gain axially, as a result it can express the overall laser quality of the mixing flow. The upper plot (a) in this figure corresponds to figure 9 i.e., the integrated gain obtained from the local small-signal gain $G_{L9\cdot4}$ distribution, computed using eqn. (10). Whereas, the lower plot (b) is corresponding to the local small-signal gain $G_{V9\cdot4}$ distribution, obtained using Eqn. (11), i.e., considering the effect of Voigt

CC-0. In Public Domain. Gurukul Kangri Collection, Haridwar

Digitized by Arya Samaj Foundation Chennai and eGangotri

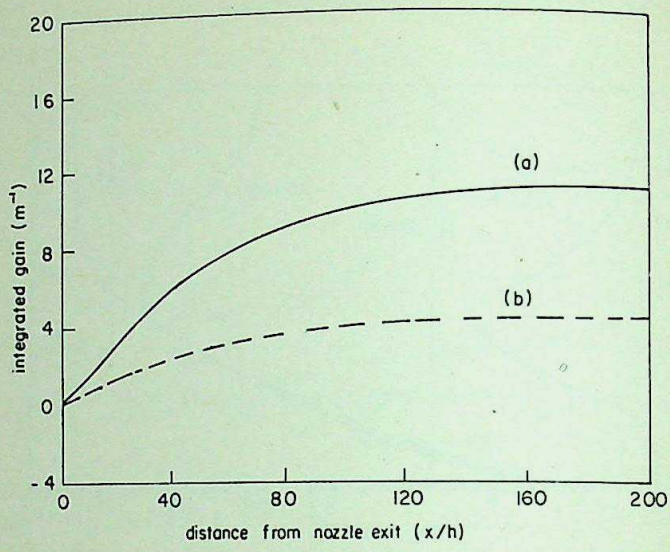

Figure 10. Variation of average small-signal gain (integrated gain) along the flow for (**a**) Lorentzian broadening and (**b**) Lorentzian-Doppler broadening.

function. The highest value of integrated gain for the upper and lower plot at $x/h = 200$ is $11{\cdot}5\,m^{-1}$ and $4{\cdot}8\,m^{-1}$ respectively. Although, there is a definite decrease in the gain results as shown by plot (b) compared to plot (a), however, they are still large and also due to the reasons mentioned earlier these results are definitely more accurate than the results of plot (a) computed assuming pure Lorentzian broadening. Also, in support of our earlier obervations (figures 3 and 5), the peak integrated gain tends to become constant downstream of $x/h = 140$, this behaviour is beneficial to good laser quality. Another important inference is that from station $x/h = 140$ onwards enough population inversion is expected to buildup upon resuming the 9·4-μm lasing to give rise to a 16-μm laser action.

4. Conclusions

The theoretical analysis of the 9·4-μm CO_2 downstream-mixing GDL is presented in detail. From the analysis it is shown that such a GDL can easily produce the power levels required for industrial applications with 9·4-μm radiation. It has been shown that the peak integrated gain value of $11{\cdot}5\,m^{-1}$ considering Lorentzian broadening is achievable on the $P(14)$ line of the (001)–(020) transition. However, this gain value reduces to $4{\cdot}8\,m^{-1}$ when Voigt function is considered for line shape, which is more realistic for the experimental set up simulated in the present investigation. The study of variation of peak gain along the downstream of the nozzle has shown that the gain remains constant after reaching a maximum value. The gain values reported here are higher than the conventional 9·4-μm CO_2 GDL gain values. In addition, these high values of 9·4-μm gain are clear indication of the possibility of internal generation of 9·4-μm lasing action which in turn may generate 16-μm lasing through cascading process.

It is recommended to have 1:1 velocity ratio between the CO_2 and N_2 mixing streams to reduce the viscous heating and hence the total temperature recovery in

CC-0. In Public Domain. Gurukul Kangri Collection, Haridwar

Digitized by Arya Samaj Foundation Chennai and eGangotri

the mixing region. Further, the laminar mixing, though slow, is found to be very efficient as it gave rise to uniform mixed regions with homogeneous density distribution at large distances.

Acknowledgement

One of the authors (PC) gratefully acknowledges the financial assistance provided by the Council of Scientific and Industrial Research, New Delhi by awarding him the Senior Research Fellowship in Engineering.

References

Anderson J D Jr 1976 *Gasdynamic lasers: An introduction* (New York: Academic Press)
Biryukov A S and Shcheglov V A 1981 *Sov. J. Quantum Electron.* (*Engl. Transl.*) **11** 1450
Biryukov A S, Serikov R I, Starik A M and Shcheglov V A 1984 *Sov. J. Quantum Electron.* (*Engl. Transl.*) 14 575
Cassady P E 1980 *J. Energy* **4** 145
Chakravarty P and Reddy N M 1986 *Appl. Phys. Lett.* **48** 263
Chakravarty P, Reddy N M and Reddy K P J 1987 *AIAA J.* **25** 713
Chakravarty P 1989 *Analysis of two-dimensional downstream-mixing* 16-μm CO_2 *gasdynamic laser* (Ph.D Thesis), Indian Institute of Science, Bangalore, India
Gross R W F and Bott J F 1976 *Handbook of chemical lasers* (New York: John Wiley and Sons)
Losev S A 1981 *Gasdynamic laser*, Springer Series in Chemical Physics, (Berlin: Springer-Verlag) Vol. 12
Manuccia T J, Stregack J A, Harries N W and Wexler B L 1976 *Appl. Phys. Lett.* **29** 360
Munjee S A 1972 *Phys. Fluids* **15** 506; Erratum 1973 *Phys. Fluids* **16** 160
Murthy S N B 1975 *High-power gas lasers*, Inst. Phys. Conf. Ser. (London) No. **29** 222
Saito S, Obara M and Fujioka T 1982 *J. Appl. Phys.* **53** 4616
Wexler B L, Manuccia T J and Waynant R W 1977 *Appl. Phys. Lett.* **31** 730
Wexler B L and Waynant R W 1979 *Appl. Phys. Lett.* **34** 674
Zaroslov D Yu, Islamov R Sh, Karlov N V, Kovalev I O, Konev Yu B, Kuz'min G P and Prokhorov A M 1982 *Sov. J. Quantum Electron.* (*Engl. Transl.*) **12** 1107

CC-0. In Public Domain. Gurukul Kangri Collection, Haridwar

Digitized by Arya Samaj Foundation Chennai and eGangotri

CC-0. In Public Domain. Gurukul Kangri Collection, Haridwar

Digitized by Arya Samaj Foundation Chennai and eGangotri

Pramāṇa – J. Phys., Vol. 34, No. 4, April 1990, pp. 347–358. © Printed in India.

Beam propagation method and its application to integrated optic structures and optical fibers

SHIVA KUMAR, T SRINIVAS and A SELVARAJAN

Department of Electrical Communication Engineering, Indian Institute of Science, Bangalore 560012, India

MS received 28 July 1989; revised 10 November 1989

Abstract. Practical applications of integrated optics require understanding of light propagation in dielectric waveguides of various geometries and calls for elegant and quick methods of analysis. In this paper, we use beam propagation method to analyse some integrated optic waveguiding elements such as waveguide with bend and branching waveguide. The method is extended to cylindrical co-ordinates, so that structures with circular symmetry can be easily solved. We first present a general beam propagation method algorithm, followed by results taking typical values for various parameters. Our studies show that the efficiency of the method depends on the z-propagation steps and on the number of points chosen for the Fourier transform. The algorithm developed can be used to analyse many other integrated optic structures and to study the effect of other input beam profiles.

Keywords. Integrated optics; branching waveguide; Hankel transform; fast fourier transform.

PACS No. 42·82

1. Introduction

Beam propagation method is basically a numerical modelling method for the propagation of an optical beam through a medium with small variations of refractive index (Feit and Fleck 1978; Van Roey *et al* 1981). The method consists of propagating the input beam over a small distance through a homogeneous space and then correcting for the refractive index variations seen by this beam during the propagation step. In this paper we give an algorithm for generalized beam propagation method (BPM) and apply it to some integrated optic structures and optical fibers. To solve the wave equation of the homogeneous medium, the Fourier transform pair has to be evaluated. Instead of using fast Fourier transform (FFT) directly, it is suggested that FFT combined with Simpson's 1/3 rule can be used which improves the accuracy. Also, for optical fibers the Hankel transform method can be used instead of the two-dimensional FFT.

2. Theory

The propagation of light in a waveguide can be described by the wave equation

$$\frac{\partial^2\psi}{\partial x^2}+\frac{\partial^2\psi}{\partial z^2}+k_0^2n^2(\omega,x)\psi=0, \tag{1}$$

CC-0. In Public Domain. Gurukul Kangri Collection, Haridwar

Digitized by Arya Samaj Foundation Chennai and eGangotri

where $k_0 = \omega/c$, n the refractive index and the ω circular frequency of light. The solution to equation (1) at $z = \Delta z$ may be written in terms of field at $z = 0$ as,

$$\psi(x, \Delta z) = \exp\left[-i\Delta z\{\nabla_T^2 + k_0^2 n^2\}^{1/2}\right]\psi(x, 0), \tag{2}$$

where $\nabla_T^2 = \partial^2/\partial x^2$. The solution ψ can be expressed in the form,

$$\psi(x, z) = \xi(x, z)\exp(-ikz), \tag{3}$$

where $k = n_0\omega/c$ and n_0 is the refractive index of the homogeneous medium. ξ can be written in the symmetrized split operator form to second order Δz (Feit and Fleck 1976) as

$$\xi(x, \Delta z) = \exp\left\{-\frac{i\Delta z}{2}\left[\frac{\nabla_T^2}{(\nabla_T^2 + k^2)^{1/2} + k}\right]\right\}\exp(-i\Delta z\chi)$$
$$\times \exp\left\{\frac{-i\Delta z}{2}\left[\frac{\nabla_T^2}{(\nabla_T^2 + k^2)^{1/2} + k}\right]\right\}\xi(x, 0) + 0(\Delta z)^3, \tag{4}$$

where $\chi = k_0 * [n(x) - n_0]$. The operation

$$\exp\left\{-i\Delta z\left[\frac{\nabla_T^2}{(\nabla_T^2 + k^2)^{1/2} + k}\right]\right\}\xi(x, 0)$$

is equivalent to solving the wave equation

$$\frac{\partial^2\psi}{\partial x^2} + \frac{\partial^2\psi}{\partial z^2} + k_0^2 n_0^2\psi = 0 \tag{5}$$

with $\psi(x, 0)$ as an initial condition. Van Roey *et al* (1981) and Van der Donk (1982) have however used a simple correction factor

$$\psi(x, z_0 + \Delta z) = \eta(x, z_0 + \Delta z)\exp(-ik_0 * \Delta n(x) * \Delta z), \tag{6}$$

where $\Delta n(x) = n(x) - n_0$ and $\eta(x, z)$ satisfies,

$$\frac{\partial^2\eta}{\partial x^2} + \frac{\partial^2\eta}{\partial z^2} + k_0^2 n_0^2\eta = 0 \tag{7}$$

and $\eta(x, z_0) = \psi(x, z_0)$. Equation (7) can be solved by Fourier transform pairs (Lee 1986)

$$\eta(x, z_0 + \Delta z) = \frac{1}{2\pi}\int_{-\infty}^{\infty}\bar{\eta}(k_x, z_0 + \Delta z)\exp(jk_x x)\,dk_x, \tag{8}$$

$$\bar{\eta}(k_x, z_0) = \int_{-\infty}^{\infty}\eta(x, z_0)\exp(-jk_x x)\,dx, \tag{9}$$

$$\bar{\eta}(k_x, z_0 + \Delta z) = \bar{\eta}(k_x, z_0)\exp(-j\beta\Delta z), \tag{10}$$

where $\beta = (k_0^2 n_0^2 - k_x^2)^{1/2}$. Equation (8) is substituted in (6) to get the desired field ψ at

CC-0. In Public Domain. Gurukul Kangri Collection, Haridwar

Digitized by Arya Samaj Foundation Chennai and eGangotri

$z_0+\Delta z$. It is known that the error introduced while using (4) is $\sim\Delta z^3$ and while using (6) is $\sim\Delta z^2$. Equation (8) has to be solved in both the cases. To solve (8) and (9), Simpson's 1/3 rule can be used. But it would need $2N+1$ complex multiplications and additions for each value of k_x where $2N$ is the number of samples taken for integration. If $\bar{n}(k_x)$ is calculated $2N$ times, then $2N(2N+1)$ complex multiplication and addition will be needed. To reduce the number of complex multiplications, Simpson's 1/3 rule is combined with FFT so that the total number of complex multiplications reduces to $4N\log N$ (Appendix A). Thus we get the accuracy of Simpson's 1/3 rule and the speed of FFT at the same time.

3. Extracting mode data

The complex field amplitude can be expressed as a superposition of orthogonal mode eigen functions,

$$\psi(x,z)=\sum_{n,j}A_{nj}u_{nj}(x)\exp(-i\beta_n z), \tag{11}$$

where n is a mode index, j the distinguishing members of degenerate group and A_{nj} is determined by the input field $\psi(x,0)$; The mode propagation constant β_n can be determined from computation of correlation function, (Feit and Fleck 1978)

$$P_1(z)=\int_{-\infty}^{\infty}\psi^*(x,0)\psi(x,z)\,dx. \tag{12}$$

Using (11) and the orthogonality of mode eigen functions, (12) reduces to,

$$P_1(z)=\sum_{n,j}|A_{nj}|^2\exp(-i\beta_n z). \tag{13}$$

Multiplying (13) by the Hanning window function,

$$\begin{aligned} w(z)&=1-\cos(2{\cdot}0*\pi*z/Z_1) \quad 0<=z<=Z_1\\ &=0 \qquad\qquad\qquad\qquad\quad \text{otherwise}\end{aligned} \tag{14}$$

and taking Fourier transform w.r.t. z,

$$\begin{aligned}\bar{P}_1(\beta)&=\frac{1}{Z_1}\int_0^{Z_1}P_1(z)w(z)\exp(-i\beta z)\,dz\\ &=\sum_{n,j}|A_{nj}|^2\mathscr{L}(\beta-\beta_n),\end{aligned} \tag{15}$$

$$\begin{aligned}\mathscr{L}(\beta-\beta_n)=&\frac{\exp[i(\beta-\beta_n)z_1]-1}{i(\beta-\beta_n)z_1}\\ &-\frac{1}{2}\left\{\frac{\exp[i(\beta-\beta_n)z_1+2\pi]-1}{i(\beta-\beta_n)z_1+2\pi}+\frac{\exp[i(\beta-\beta_n)z_1-2\pi]-1}{i(\beta-\beta_n)z_1-2\pi}\right\}.\end{aligned}$$

The eigenvalue β_n can be determined by locating the local maxima of $\bar{P}_1(\beta)$.

CC-0. In Public Domain. Gurukul Kangri Collection, Haridwar

Digitized by Arya Samaj Foundation Chennai and eGangotri

4. Extensions of BPM to cylindrical coordinates

Consider the wave equation in cylindrical co-ordinates.

$$\frac{\partial^2\psi}{\partial r^2}+\frac{1}{r}\frac{\partial\psi}{\partial r}+\frac{1}{r^2}\frac{\partial^2\psi}{\partial\theta^2}+\frac{\partial^2\psi}{\partial z^2}+k_0^2n^2(r)\psi=0, \tag{16}$$

which can be written as (Feit and Fleck 1976)

$$\psi(r,\theta,z)=\exp(-i(\nabla_T^2+k_0^2n^2)^{1/2}z)\psi(r,\theta,0) \tag{17}$$

where $\nabla_T^2=\partial^2/\partial r^2+1/r\ \partial/\partial r+(1/r^2)\ \partial^2/\partial\theta^2$ $(\nabla_T^2+k_0^2n^2)^{1/2}$ can be written in the form,

$$\frac{(\nabla_T^2+k_0^2n^2)^{1/2}[(\nabla_T^2+k_0^2n^2)^{1/2}+k_0n]}{[(\nabla_T^2+k_0^2n^2)^{1/2}+k_0n]}=\frac{\nabla_T^2}{[(\nabla_T^2+k_0^2n^2)^{1/2}+k_0n]}+k_0n. \tag{18}$$

If n in the first term of the right hand side is approximated by n_0, where n_0 is the refractive index of the unperturbed medium, equation (18) becomes

$$(\nabla_T^2+k_0^2n^2)^{1/2}\cong\left[\frac{\nabla_T^2}{(\nabla_T^2+k_0^2n_0^2)^{1/2}+k_0n_0}+k_0n_0\right]+k_0[n(r)-n_0]$$

$$\cong[\nabla_T^2+k_0^2n_0^2]^{1/2}+k_0\Delta n(r) \text{ from (18)}$$

where $\Delta n(r)=n(r)-n_0$. Substituting in (17),

$$\psi(r,\theta,z)=\exp[\{-iz(\nabla_T^2+k_0^2n_0^2)^{1/2}\}-\{iz*k_0*\Delta n(r)\}]\psi(r,\theta,0). \tag{19}$$

By neglecting the error due to non-commutation of operators, (19) can be written as,

$$\psi(r,\theta,z)\cong[\exp[-iz(\nabla_T^2+k_0^2n_0^2)^{1/2}]\psi(r,\theta,0)]\exp[-iz*k_0*\Delta n(r)]$$

$$\cong\phi(r,\theta,z)*\exp[-iz*k_0\Delta n(r)], \tag{20}$$

where ϕ satisfies the wave equation

$$\frac{\partial^2\phi}{\partial r^2}+\frac{1}{r}\frac{\partial\phi}{\partial r}+\frac{1}{r^2}\frac{\partial^2\phi}{\partial\theta^2}+\frac{\partial^2\phi}{\partial z^2}+k_0^2n_0^2\phi=0 \tag{21}$$

with $\phi(r,\theta,0)$ as initial condition. Let

$$\phi=R(r,z)*[A\cos m\theta+B\sin m\theta]. \tag{22}$$

Then, (21) becomes,

$$\frac{\partial^2R}{\partial r^2}+\frac{1}{r}\frac{\partial R}{\partial r}+\frac{\partial^2R}{\partial z^2}+\left[k_0^2n_0^2-\frac{m^2}{r^2}\right]R=0. \tag{23}$$

Taking the Hankel transform,

$$\frac{d^2\bar{R}(\alpha,z)}{dz^2}+(k_0^2n_0^2-\alpha^2)\bar{R}(\alpha,z)=0, \tag{24}$$

CC-0. In Public Domain. Gurukul Kangri Collection, Haridwar

Digitized by Arya Samaj Foundation Chennai and eGangotri

where

$$\bar{R}(\alpha, z) = \int_0^\infty R(r, z) r J_m(\alpha r)\, dr,$$

$$\bar{R}(\alpha, z) = \bar{R}(\alpha, 0) \exp(-j\beta z) \text{ where } \beta = (k_0^2 n_0^2 - \alpha^2)^{1/2}.$$

Taking the inverse Hankel transform,

$$R(r, z) = \int_0^\infty [\bar{R}(\alpha, 0) \exp(-j\beta z)] \alpha J_m(\alpha r)\, d\alpha. \tag{25}$$

For structures such as weakly guiding single-mode fibers, we can set $m = 0$.

$$R(r, z) = \int_0^\infty [\bar{R}(\alpha, 0) \exp(-j\beta z)] \alpha J_0(\alpha r)\, d\alpha \tag{26}$$

$$\bar{R}(\alpha, 0) = \int_0^\infty R(r, z) r J_0(\alpha r)\, dr. \tag{27}$$

To evaluate (26) and (27), the Fast Hankel transform technique is used (Appendix B). Hence ϕ is calculated and substituted in (20) to get the desired field.

5. Results

To verify the above equations, a step index fiber is considered. The fiber is excited with step input, i.e. the field within the fiber is uniform and is zero outside. The fiber has the following parameters: core refractive index of 1·45, cladding refractive index of 1·44, a radius of 2 μm and a wavelength of 1·32 μm. To find the eigenvalues, instead of (12)

$$P_1(z) = \int_0^\infty R^*(r, 0) R(r, z) r\, dr$$

is used. It is found to excite only single-guided mode $\beta_1 = 6{\cdot}868$ rad/μm. The propagation constant obtained after solving the characteristic equation for weakly guiding fibers is, $\beta_1 = 6{\cdot}8676$ rad/μm.

To find the field in the integrated optic structures, we have used the simple correction factor of (6) instead of (4) since the propagation distance is 1000 μm.

From figure 1(a), it can be seen that the given power input is carried through bent guiding region. The bent waveguide is excited as shown. Power output is calculated for different angles. Power in the bent waveguide for different angles of bend is shown in figure 1(b). For angles greater than 10°, most of the power is radiated out of the waveguide.

Figure 2 shows the field in a branching waveguide. Yajima (1973) experimentally showed that modes incident on an asymmetric planar-dielectric branching waveguide with a shallow taper propagate such that the mode power is transferred to one arm of the branch or the other. The branching waveguide acts like a power divider (non-adiabatic) when tapers are steep and it acts like a mode-splitter (adiabatic) when

CC-0. In Public Domain. Gurukul Kangri Collection, Haridwar

Digitized by Arya Samaj Foundation Chennai and eGangotri

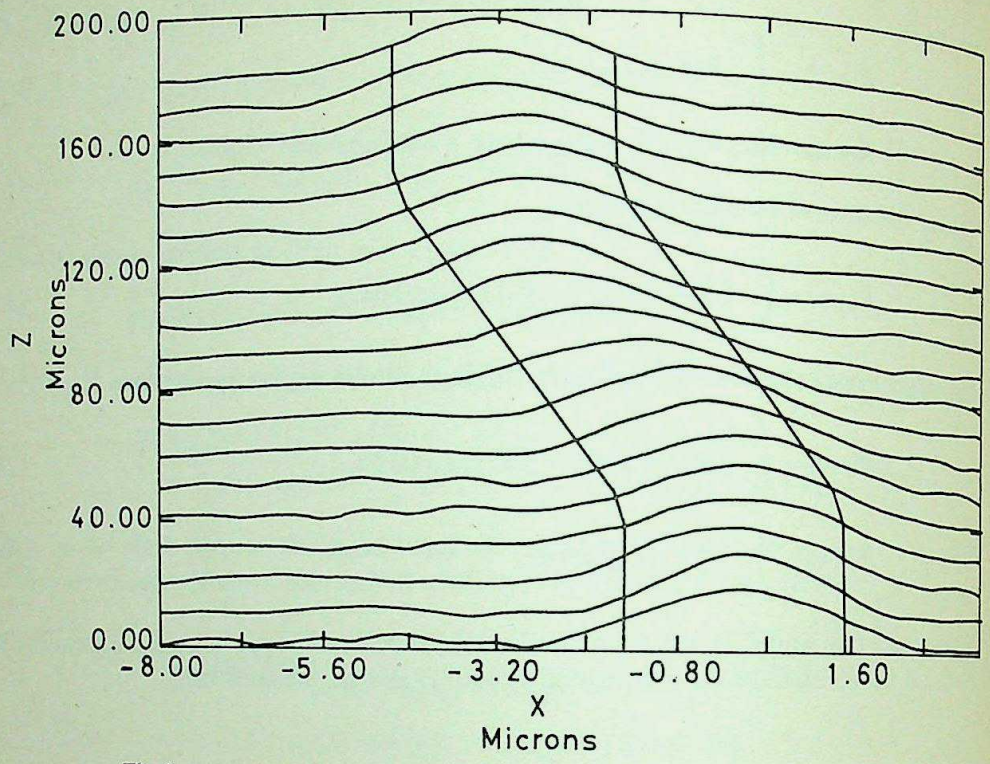

Fig. 1a.

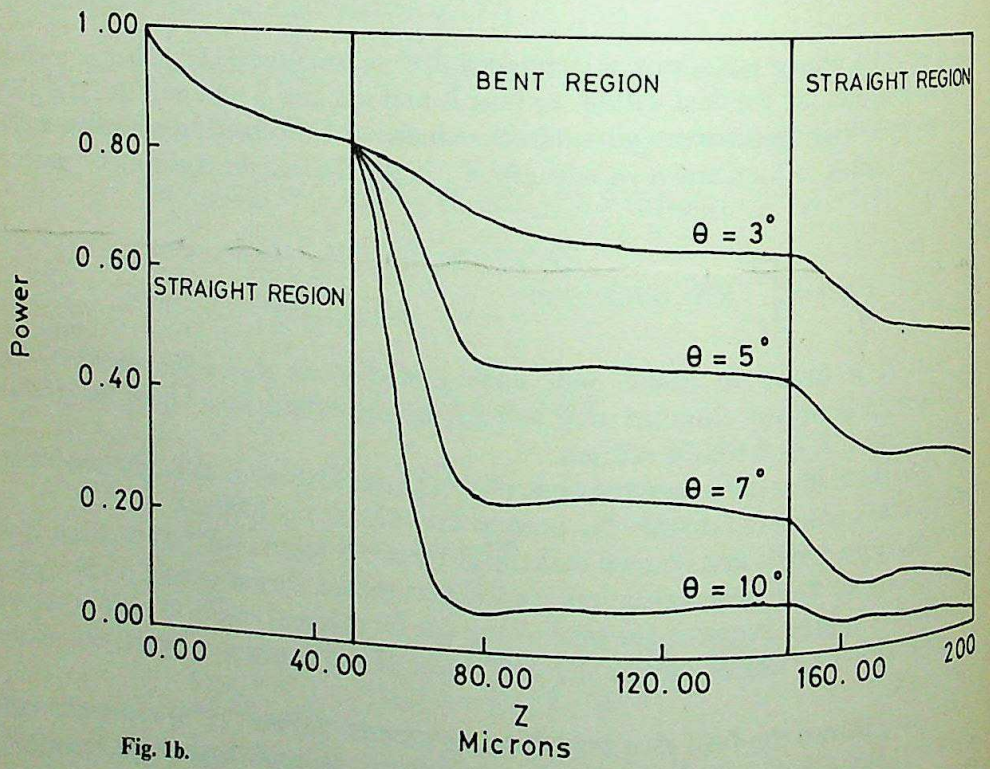

Fig. 1b.

Figure 1a. Field in a bent waveguide for Gaussian input with $1/e$ depth 2μm. $n_s = 2{\cdot}1398$. $\Delta n = 0{\cdot}1\%$. **b.** Power in a bent waveguide for different angles of bend.

CC-0. In Public Domain. Gurukul Kangri Collection, Haridwar

Digitized by Arya Samaj Foundation Chennai and eGangotri

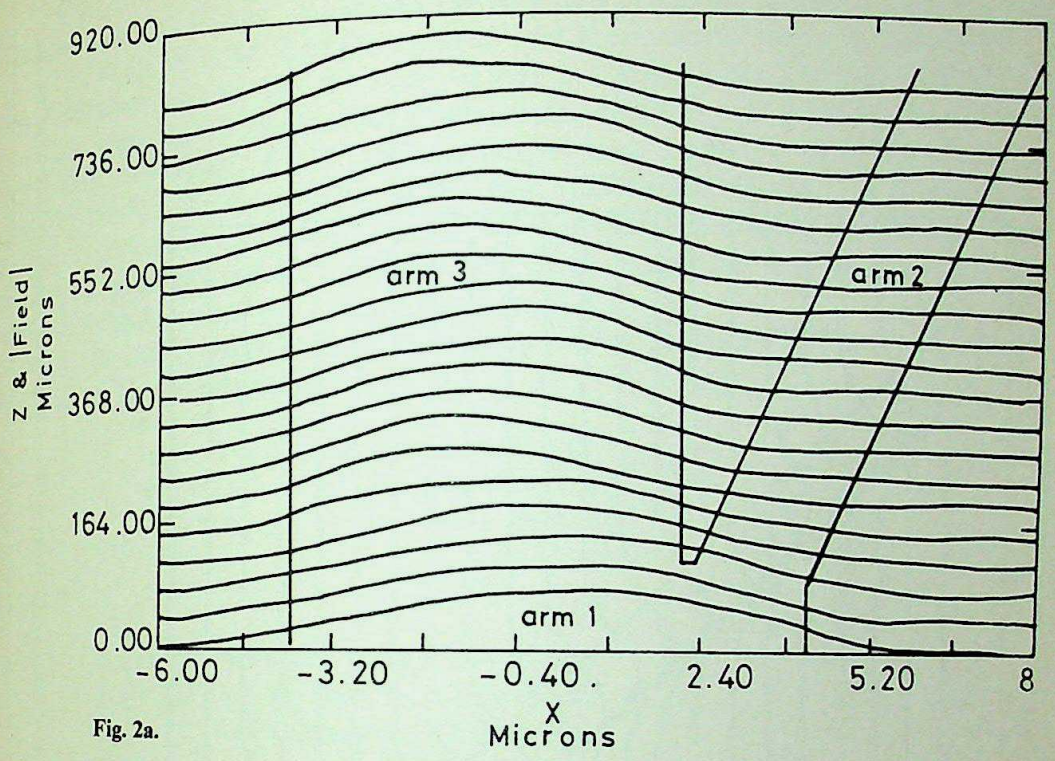

Fig. 2a.

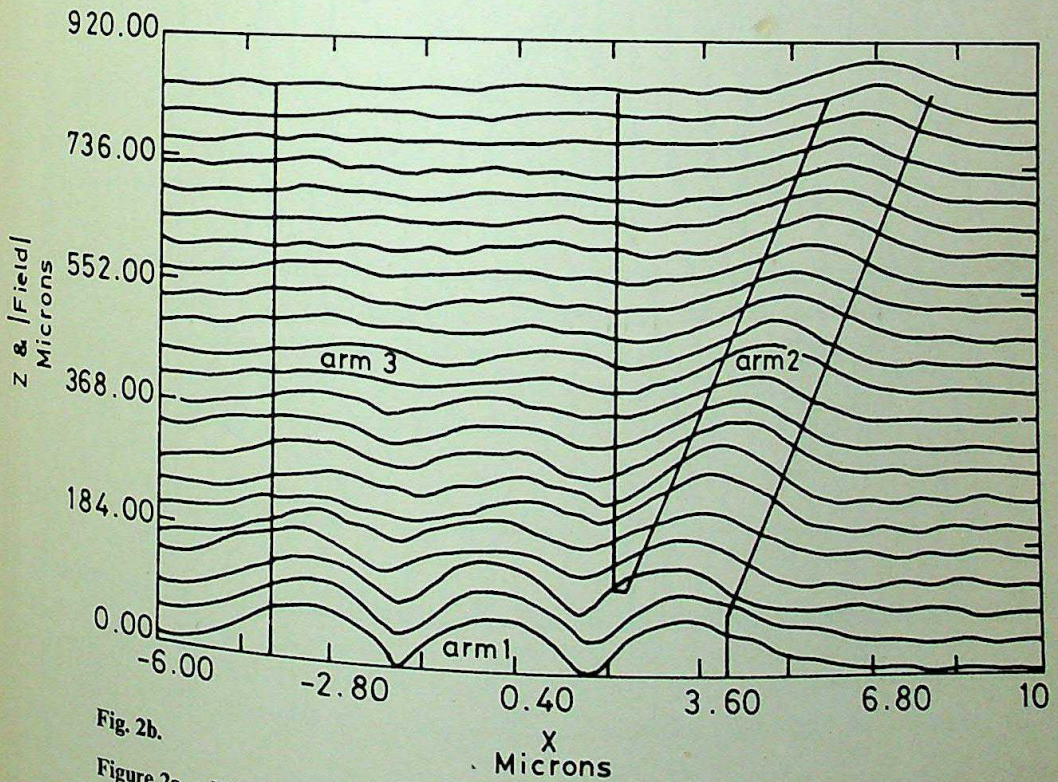

Fig. 2b.

Figure 2a. Field in a branching waveguide with the fundamental mode excitation into arm 1. The angle is 1/200 radians. The guide thickness for arm 1 and arm 2 is 8 μm and 2 μm respectively. For arm 1 and arm 3, the refractive indices (RI) within the guide are 2·155 and 2·1398 outside. For arm 2, RI is 2·155 within the guide on the right side and 2·1398 on the left side.

Figure 2b. Field in a branching waveguide with the TE03 mode excitation into arm 1. The parameters are same as figure 2a.

CC-0. In Public Domain. Gurukul Kangri Collection, Haridwar

Digitized by Arya Samaj Foundation Chennai and eGangotri

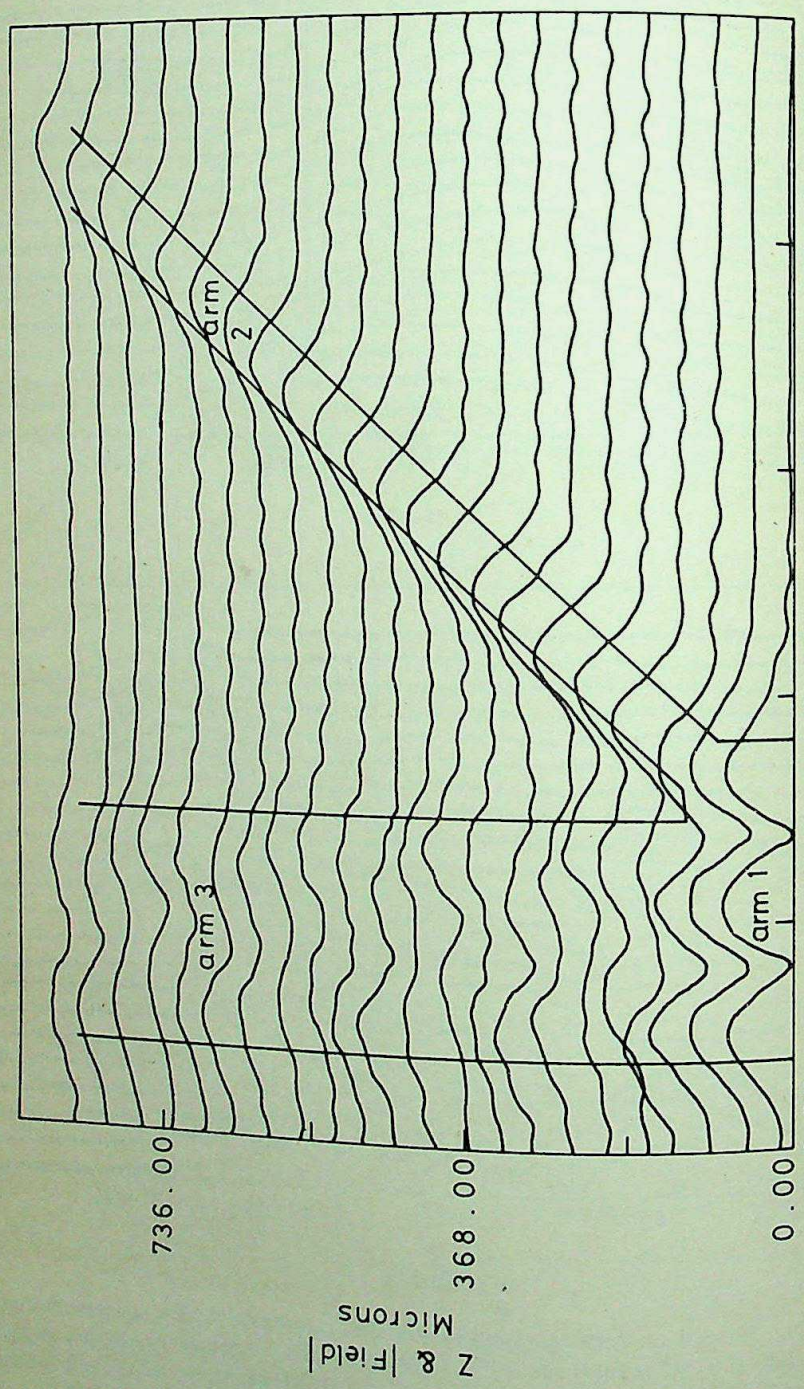

Figure 2c. Field in a branching waveguide with the TE03 mode excitation into arm 1. The angle of bend is 1/50 radians. The other parameters are the same as figure 2a.

CC-0. In Public Domain. Gurukul Kangri Collection, Haridwar

Digitized by Arya Samaj Foundation Chennai and eGangotri

tapers are gradual. Figure 2(a) shows the field in a branching waveguide for shallow taper. The angle of bend is 1/200 radians. The fundamental mode is launched into arm 1 of the waveguide. The thickness of arm 2 is made much less than that of arm 3 so that propagation constant for fundamental mode in arm 2 is less than that of arm 3. For $\lambda = 1{\cdot}32\,\mu m$, $\beta = 10{\cdot}2190$ rad/μm for arm 2 and $\beta = 10{\cdot}2494$ rad/μm for arm 3 for the fundamental mode. In this case, TE01 mode in arm 1 is converted to the TE01 mode in arm 3. Hence, it can be seen that TE01 mode in arm 1 chooses the arm of larger propagation constant for TE01 mode. We can see from 2(a) that power launched in arm 1 is coming out of arm 3.

Figure 2(b) shows the field in the branching waveguide with TE03 mode excitation. The propagation constant for arm 1 is,

$\beta_{11} = 10{\cdot}2524$ rad/μm for TE01 mode,
$\beta_{12} = 10{\cdot}2372$ rad/μm for TE02 mode,
$\beta_{13} = 10{\cdot}2132$ rad/μm for TE03 mode.

For arm 3,

$\beta_{31} = 10{\cdot}2494$ rad/μm for TE01 mode,
$\beta_{32} = 10{\cdot}2258$ rad/μm for TE02 mode,
$\beta_{33} = 10{\cdot}1924$ rad/μm for TE03 mode.

For arm 2,

$\beta_{21} = 10{\cdot}2190$ rad/μm for TE01 mode.

It can be seen that TE03 mode of arm 1 is converted into TE01 mode of arm 2 since the propagation constant for TE01 mode of arm 2 is closest to that for TE03 mode of arm 1.

Figure 2(c) shows the field in the branching waveguide when the tapers are steep. The angle of bend is 1/50 radians. Now, the waveguide acts like a power splitter. After doing the modal analysis, it is found that, in arm 3, the odd mode with $\beta = 10{\cdot}2257$ rad/μm is excited. In arm 2, the even mode with $\beta = 10{\cdot}219$ rad/μm is excited. The ratio of power in arm 2 to arm 3 is found to be 36:64.

6. Conclusions

Beam propagation method is a powerful tool for the numerical modelling of scalar wave propagation through media with arbitrary but slow and small variations in refractive index. For structures with circular symmetry, the Hankel transform method can be used which reduces the computational time against the two-dimensional Fourier transform.

Appendix A

Multiply equation (7) by $\exp(-j*2\pi kx/T)$ and integrate w.r.t. x with limits $-T/2$ to

CC-0. In Public Domain. Gurukul Kangri Collection, Haridwar

Digitized by Arya Samaj Foundation Chennai and eGangotri

$T/2$ where T is a large number such that

$$\eta(\pm T/2) \cong \frac{\partial \eta(\pm T/2)}{\partial x} \simeq 0.$$

$$\frac{\partial^2 \bar{\eta}(k,z)}{\partial z^2} + \left[k_0^2 n_0^2 - \left(\frac{2\pi k}{T} \right)^2 \right] \bar{\eta}(k,z) = 0, \tag{A1}$$

where

$$\bar{\eta}(k,z) = \frac{1}{T} \int_{-T/2}^{T/2} \eta(x,z) \exp(-i2\pi kx/T)\, dx. \tag{A2}$$

$$\bar{\eta}(k,\Delta z) = \bar{\eta}(k,0) \exp(-j\beta_k \Delta z) \text{ where } \beta_k = [(k_0^2 n_0^2) - (2\pi k/T)^2]^{1/2}. \tag{A3}$$

$$\bar{\eta}(x,\Delta z) = \sum_{k=-L}^{L} \bar{\eta}(k,0) \exp(-j\beta_k \Delta z) \exp(i2\pi kx/T), \tag{A4}$$

where $2L$ is the total number of prominent Fourier spectral components. To evaluate (A2), Simpson's 1/3 rule is used. Let h be the interval between samples and $2N$ be the total number of samples. Then (A2) can be written as,

$$\bar{\eta}(k,0) = \frac{1}{6N} \{ w_0 + 4{\cdot}0(w_1 + w_3 \cdots + w_{2N-1}) + 2{\cdot}0(w_2 + w_4 + \cdots w_{2N-2} + w_{2N}) \} \tag{A5}$$

where $w(x) = \eta(x,0) \exp(-j*2\pi k*x/T)$. Replacing the continuous variable x with a discrete variable $x = (T*n/2N) - T/2$ (A5) can be written as,

$$\bar{\eta}(k,0) = \frac{\exp(j\pi k)}{6N} \left[4{\cdot}0 \sum_{\substack{n \\ \text{odd}}} \eta_n \exp\left(\frac{-i2\pi kn}{2N} \right) + 2{\cdot}0 \sum_{\substack{n \\ \text{even}, \neq 0, 2N}} \eta_n \exp\left(\frac{-i2\pi kn}{2N} \right) + \eta_0 + \eta_{2N} \right]. \tag{A6}$$

Putting $m = (n-1)/2$ for the odd terms and $m = (n-2)/2$ for the even terms, we get

$$\begin{aligned} \bar{\eta}(k,0) &= \frac{\exp(j\pi * k)}{6N} \left[4{\cdot}0 \sum_{m=0}^{N-1} \eta_{2m+1} \exp\left(\frac{-j2\pi km}{N} \right) \exp(-j\pi k) \right. \\ &\quad \left. + 2{\cdot}0 \sum_{m=0}^{N-1} \eta_{2m+2} \exp\left(\frac{-i2\pi km}{N} \right) + \eta_0 - \eta_{2N} \right] \\ &= \frac{1}{6N} \left[4{\cdot}0 \sum_{m=0}^{N-1} \eta_{2m+1} \exp\left(\frac{-i2\pi km}{N} \right) \right. \\ &\quad \left. + 2{\cdot}0 * (-1)^k \sum_{m=0}^{N-1} n_{2m+2} \exp\left(\frac{-i2\pi km}{N} \right) + \eta_0 - \eta_{2N} \right] \end{aligned} \tag{A7}$$

Using FFT algorithms (Oppenheim and Schafer 1975) for summations in (A7), $\bar{\eta}$ can be evaluated. Each FFT takes $2N \log N$ complex multiplications. Therefore, the total complex multiplication will be $4N \log N$.

CC-0. In Public Domain. Gurukul Kangri Collection, Haridwar

Digitized by Arya Samaj Foundation Chennai and eGangotri

Appendix B

The fast Hankel transform (Siegman 1977) reduces the effort required to calculate Bessel functions for every iteration. r and α of (27) can be replaced by,

$$r = r_0 \exp(px), \quad \alpha = \alpha_0 \exp(py), \tag{B1}$$

and

$$rR(r) \equiv f(x); \quad \alpha \bar{R}(\alpha) \equiv g(y), \tag{B2}$$

The Hankel transform,

$$\alpha \bar{R}(\alpha) = \int_0^\infty J_0(\alpha r) \alpha r R(r)\, dr, \tag{B3}$$

i.e.

$$\alpha \bar{R}(\alpha) \equiv g(y) = \int_{-\infty}^{\infty} j(x+y) f(x)\, dx, \tag{B4}$$

where

$$j(r) = J_0(\alpha_0 r_0 \exp(pr)) p r_0 \alpha_0 \exp(pr). \tag{B5}$$

This change of variable may be called Gardner Transform (Gardner *et al* 1959). Taking the Fourier transform of (B4),

$$\begin{aligned} G(k) = \int_{-\infty}^{\infty} g(y) \exp(-iky)\, dy &= \int_{-\infty}^{\infty} j(x+y) \exp[-ik(x+y)] \\ &\times \int_{-\infty}^{\infty} f(x) \exp(iky)\, dx\, dy \\ &= J(k) * F(-k). \end{aligned} \tag{B6}$$

where $J(k)$ and $F(k)$ are the Fourier transforms of j and f respectively. Finally, $g(y)$ can be found by taking the inverse Fourier transform of $G(k)$.

$$g(y) = \frac{1}{2\pi} \int_{-\infty}^{\infty} J(k) F(-k) \exp(iky)\, dk.$$

Thus, the Hankel transform of $R(r)$ requires an FFT on $f(x)$, FFT on $j(x)$, and an inverse FFT to get $g(y)$ or $\bar{R}(\alpha)$. The Fourier transform of the Bessel function needs to be obtained only once. Hence, the calculation of Bessel function for every iteration is avoided.

Acknowledgements

The authors wish to thank the referee for valuable suggestions to improve the paper.

References

Feit M D and Fleck Jr J A 1978 *Appl. Opt.* **17** 3990
Feit M D and Fleck Jr J A 1979 *Appl. Opt.* **18** 2843

CC-0. In Public Domain. Gurukul Kangri Collection, Haridwar

Digitized by Arya Samaj Foundation Chennai and eGangotri

Gardner D G, Gardner J C, Lausch G and Meinke W W 1959 *J. Chem. Phys.* **31** 987
Lee D L 1986 *Electromagnetic principles of integrated optics* (New York: John Wiley) ch. 2
Oppenheim A V and Schafer R W 1975 *Digital signal processing* (New Delhi: Prentice-Hall of India) ch. 6
Siegman A E 1977 *Opt. Lett.* **1** 13
Van der Donk J 1982 *The beam propagation method in integrated optics* Ph.D. Thesis, University of Gent, Gent, Belgium
Van Roey J, Van der Donk J and Lagasse P E 1981 *J. Opt. Soc. Am.* **71** 803
Yajima H 1973 *Appl. Phys. Lett.* **22** 647

CC-0. In Public Domain. Gurukul Kangri Collection, Haridwar

Digitized by Arya Samaj Foundation Chennai and eGangotri

Pramāṇa – J. Phys., Vol. 34, No. 4, April 1990, pp. 359–367. © Printed in India.

Differential temperature sensors method for simultaneous determination of thermal conductivity and diffusivity

L S VERMA*, A K SHROTRIYA, RAMVIR SINGH and D R CHAUDHARY

Department of Physics, University of Rajasthan, Jaipur 302004, India
*R L Saharia College, Kaladera (Jaipur) Rajasthan 303801, India

MS received 17 August 1989; revised 29 November 1989

Abstract. An attempt has been made to minimize the sources of error involved in the transient probe method for thermal conductivity determination. Two sensors (thermocouples) are mounted parallel to the needle probe at known distances. This modification makes it a device for simultaneous conductivity and diffusivity determination. Thermal conductivity and diffusivity for glycerine, dune sand and mustard seed are determined by this method. Results obtained are compared with those obtained by a calibrated transient probe for conductivity and by a parallel wire method for diffusivity. Analysis of the results prove it to be a better instrument over the traditional ones. The technique can also be used as a direct reading device for conductivity and diffusivity measurements.

Keywords. Thermal conductivity; thermal diffusivity; differential temperature sensors.

PACS Nos 44·10; 44·90; 66·70; 72·15

1. Introduction

Transient methods are under constant use for determination of thermal conductivity and diffusivity of liquids, granular substances and insulators in powder form. Various authors (Chaudhary 1968; Lozano *et al* 1979; Singh *et al* 1988a, b; Inaba 1983; Singh *et al* 1985a; Penner *et al* 1975) have used probes of different designs and dimensions according to their need. Wechsler (1966) has described two main sources of error associated with transient probes and the following correction has been suggested.

1.1 *Initial lag error* ($2K/bH$)

It arises due to thermal mass of the probe and contact resistance between the probe and the sample. For small experimental time t, corrected expression giving the temperature rise of the point under consideration become

$$\theta = \frac{q}{4\pi K}\left[\ln\frac{4\alpha t}{r^2} - \gamma + \frac{2K}{bH}\right],$$

where K is the thermal conductivity of the medium, α is its thermal diffusivity, b is the probe radius and H is the contact conductance at the probe medium interface, γ being Euler's constant = 0·5772.

CC-0. In Public Domain. Gurukul Kangri Collection, Haridwar

Digitized by Arya Samaj Foundation Chennai and eGangotri

1.2 *Time correction term* (t_c)

This is due to the finite time required for heating of the probe mass. This error becomes significant for heavier probes of large diameter. For small experimenal time, a correction term should be considered for precise measurements.

If at any point in the medium the rise in temperature is θ_1 at time t_1 and θ_2 at time t_2, then

$$(\theta_2 - \theta_1) = \frac{q}{4\pi K}\left[\ln \frac{t_2 - t_c}{t_1 - t_c}\right].$$

No such correction term has so far been applied for diffusivity measurements. Authors (Sharma *et al* 1984; Kerrisk 1971) have determined diffusivity of substances by independent experiments, but the need for simultaneous determination of these two coefficients has always been felt for exactness of the sample. Many (Agarwal and Bhandari 1970; Singh *et al* 1985b) have described methods for simultaneous determination of these coefficients. But no method could gain acceptance because of either complexity of the apparatus involved or larger time duration needed for experiment.

The method presented here determine both the constants simultaneously by a single experiment of short duration (5–6 min). Two temperature sensors (thermocouples) are mounted parallel, diametrically opposite to the needle. This arrangement improves its performance by eliminating the sources of error discussed above.

To test the performance of the probe, proper substances from various material groups were taken and their thermal coefficients were determined. Glycerine was selected to represent liquids. Dune sand (particle size, mesh No. 80–100) and mustard pusa bold (grain size, mesh No. 5–10) were taken from granular substances. Their thermal conductivity and diffusivity were also determined by transient probe and parallel wire method. All the measurements were done under identical conditions.

2. Theory

When a line source of heat is placed in an inifnite medium, the rise in temperature θ at a near point is given by the expression (Chaudhary 1968, Carslaw and Jaeger 1959)

$$\theta = \frac{q}{2\pi K}\left[-\frac{\gamma}{2} - \ln \frac{r}{\sqrt{4\alpha t}} + \frac{1}{2}\frac{r^2}{4\alpha t} - \frac{1}{8}\frac{r^4}{(4\alpha t)^2}\right]. \quad (1)$$

where r is the distance of the point from the line source, q, the power generated per unit length of probe, K being thermal conductivity of sample, α being its diffusivity and γ the Euler's constant ($= 0{\cdot}5772$). The terms containing third and higher powers of $(1/t)$ have been neglected.

2.1 *Lag error correction*

Considering this correction term the rise in temperature will be

$$\theta = \frac{q}{2\pi K}\left[-\frac{\gamma}{2} - \ln \frac{r}{\sqrt{4\alpha t}} + \frac{1}{2}\frac{r^2}{4\alpha t} - \frac{1}{8}\frac{r^4}{(4\alpha t)^2} + \frac{K}{bH}\right]. \quad (2)$$

CC-0. In Public Domain. Gurukul Kangri Collection, Haridwar

Digitized by Arya Samaj Foundation Chennai and eGangotri

Determining the respective rise in temperatures θ_1 and θ_2 at same time t, at two near points r_1 and r_2 from the above equation and subtracting the two we get,

$$(\theta_1 - \theta_2) = \frac{q}{2\pi K}\left[\ln\left(\frac{r_2}{r_1}\right) - \frac{r_2^2 - r_1^2}{8\alpha}\cdot\frac{1}{t} + \frac{r_2^4 - r_1^4}{128\alpha^2}\cdot\frac{1}{t^2}\right]. \tag{3}$$

So the lag error term is eliminated from the final expression.

2.2 *Time correction term* (t_c)

This term is to be subracted from the observed time t, Hence the (3) becomes

$$(\theta_1 - \theta_2) = \frac{q}{2\pi K}\left[\ln\left(\frac{r_2}{r_1}\right) - \frac{r_2^2 - r_1^2}{8\alpha}\cdot\frac{1}{(t-t_c)} + \frac{r_2^4 - r_1^4}{128\alpha^2}\cdot\frac{1}{(t-t_c)^2}\right].$$

As $t \gg t_c$, hence, simplifying and neglecting higher power terms of (t_c/t) in the above equation we get

$$(\theta_1 - \theta_2) = \frac{q}{2\pi K}\left[\ln\left(\frac{r_2}{r_1}\right) - \frac{r_2^2 - r_1^2}{8\alpha}\frac{1}{t} + \frac{r_2^2 - r_1^2}{8\alpha}\left(\frac{r_2^2 + r_1^2}{16\alpha} - t_c\right)\frac{1}{t^2}\right]. \tag{4}$$

Here we have retained terms up to second power of $(1/t)$. Equation (4) shows that correction term appears in the coefficient of $(1/t^2)$. The values of the coefficient can be determined by data fitting technique by a computer.

2.3 *Computation of thermal conductivity and diffusivity*

Equation (4) between $(\theta_1 - \theta_2)$ and reciprocal of time $(1/t)$, represents parabola of the form

$$y = B_0 + B_1 x + B_2 x^2. \tag{5}$$

The coefficients B_0, B_1, and B_2 lead to the following expressions for obtaining thermal conductivity and thermal diffusivity

$$K = \frac{q}{2\pi B_0}\ln\left(\frac{r_2}{r_1}\right) \tag{6}$$

$$\alpha = \frac{1}{8}\frac{B_0}{B_1}\frac{(r_2^2 - r_1^2)}{\ln(r_2/r_1)} \tag{7}$$

$$\alpha = \frac{1}{16}\frac{B_1}{B_2}(r_2^2 + r_1^2) \tag{8}$$

$$\alpha = \frac{1}{8}\left[\frac{B_0}{B_2}\frac{(r_2^4 - r_1^4)}{2\ln(r_2/r_1)}\right]^{1/2}. \tag{9}$$

The correction term t_c in (4) has been omitted for sake of simplicity while evaluating (8) and (9). Its order can be estimated by the knowledge of constant B_1 and B_2. It

CC-0. In Public Domain. Gurukul Kangri Collection, Haridwar

Digitized by Arya Samaj Foundation Chennai and eGangotri

comes out to be,

$$t_c = \frac{(r_2^2 + r_1^2)}{16\alpha} + \left(\frac{B_2}{B_1}\right).$$

For the probe used for glycerine, correction term comes out to be 5·8 s, whereas the term $(r_2^2 + r_1^2)/(16\alpha)$ works out to be 25·3 s.

3. Fabrication of differential sensor probe

A hypodermic needle of 13·5 cm long and 2 mm diameter was selected for the purpose. A silk insulated constantan wire (SWG 42) of about 6 times the needle length was taken as the heater of probe. It is made into six folds and wrapped on 13·3 cm long insulated copper wire (SWG 32). The ends of the heater wire are connected to heavy copper leads. The junctions are soldered and insulated by a sticking tape. The whole assembly was then pushed inside the needle carefully. Air pockets left if any, were filled by zircona powder and ends of the needle were sealed.

The needle was mounted in the centre of a triangular bakelite plate of side 5 cm each. The ends of the plate were rounded off to remove sharp corners. Two such identical plates were also taken for mounting the sensor assembly. These were supported on 14.5 cm long iron bars, such that distance between them was 13.5 cm. Holes were drilled at the centre for insertion of the needle. The thermocouples are made by soldering constantan wire and steel wire (each SWG 28). Steel wire meant for string musical instruments were selected for the purpose. Such thermocouples could be easily stretched without producing a sag up to 100°C. The thermo emf generated for these thermocouples is 39.45 μV/°C, not very much different to that produced by copper constantan thermocouples (40.8 μV/°C). Two similar sensors were mounted at distances 0.2 cm and 0.6 cm from the central hole. Their junctions were placed midway between the two plates. The sensors were kept tight by inserting springs in the supporting rods. The needle is then inserted within the assembly and screwed properly. Distance of the thermocouples from the needle is determined accurately by a travelling microscope. In figure 1 the design of the probe is given.

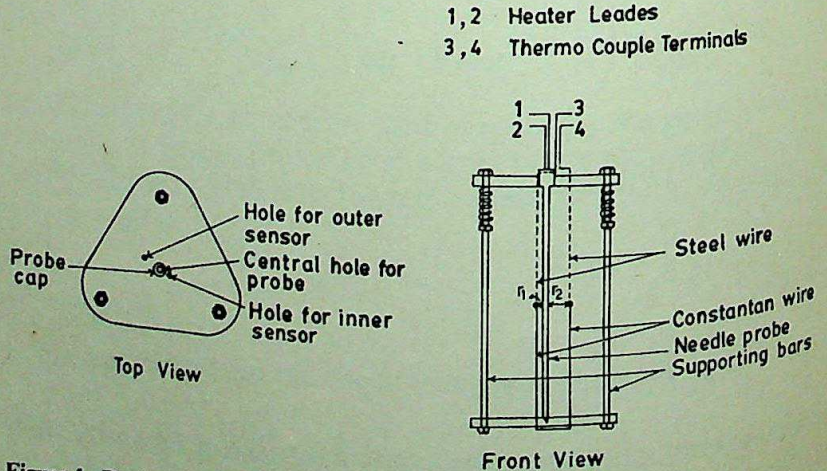

Figure 1. Design of differential temperature sensors probe.

CC-0. In Public Domain. Gurukul Kangri Collection, Haridwar

Digitized by Arya Samaj Foundation Chennai and eGangotri

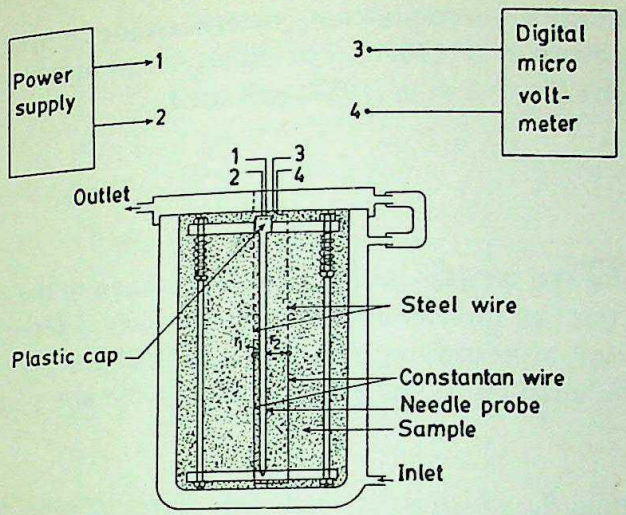

Figure 2. Experimental arrangement for conductivity and diffusivity determination.

4. Experimental set-up

The experimental arrangement consisted of mainly three parts.

4.1 *Constant current power supply*

It provides a constant current to the probe heater wire.

4.2 *Sample container*

It consists of a cylindrical copper vessel 15.5 cm long and diameter of 7 cm. It is placed in a chamber maintained at constant temperature. The temperature of the container can be kept constant at a desired value within $\pm 1°C$ by circulating liquid from a constant temperature bath.

4.3 *Temperature measuring unit*

The thermo emf generated at the two ends of thermocouple assembly can be registered by a digital microvoltmeter with an accuracy of 0.1 μV. In figure 2 the experimental arrangement is shown schematically.

5. Procedure

After switching on the current in the heater wire, the temperature difference in the sample at the midpoints of the sensors is noted with time. A plot between reciprocal of time ($1/t$) and temperature difference ($\theta_1 - \theta_2$) will be a parabola. Its coefficients are determined by data fitting technique by a personal computer.

Conductivity and diffusivity can be determined by formulae discussed above. The computer programme is designed to display the values of various coefficients, i.e., thermal conductivity and diffusivity directly.

CC-0. In Public Domain. Gurukul Kangri Collection, Haridwar

Digitized by Arya Samaj Foundation Chennai and eGangotri

The experimental arrangement for conductivity determination by transient probe is similar to that used by Singh *et al* (1988b). For diffusivity measurements parallel wire method as described by Sharma *et al* (1984) was used.

6. Results and discussion

Two sets of observations for the samples investigated were taken in the temperature range $-20°C$ to $90°C$. Equation (6) was used for conductivity determination. For diffusivity measurements any expression represented by (7), (8) and (9) can be used, but (7) was preferred for calculations. Equations (8) and (9) were not used because of the following reasons.

6.1. Both expressions contain B_2, which is the coefficient of second order term in $(1/t)$. Thus any error in time measurement will have two fold effect on it. It also includes the time correction term, so diffusivity given by these expressions will not be accurate.

6.2. Equation (8) contains the sum of squares of distances r_1 and r_2. Any error in their measurement will have additive effect on the final result. Similar reasoning rejects (9) which contain fourth power of r_1 and r_2.

Equation (7) is free from such discrepancies. Moreover here occurrence of squares of r_1 and r_2 is in subtractive mode, so the inaccuracy due to errors involved in measurement of r_1 and r_2 is minimum.

The results of conductivity and diffusivity determination by two methods are shown by graphs in figures 3 and 4. To ascertain the closeness of the results with the mean

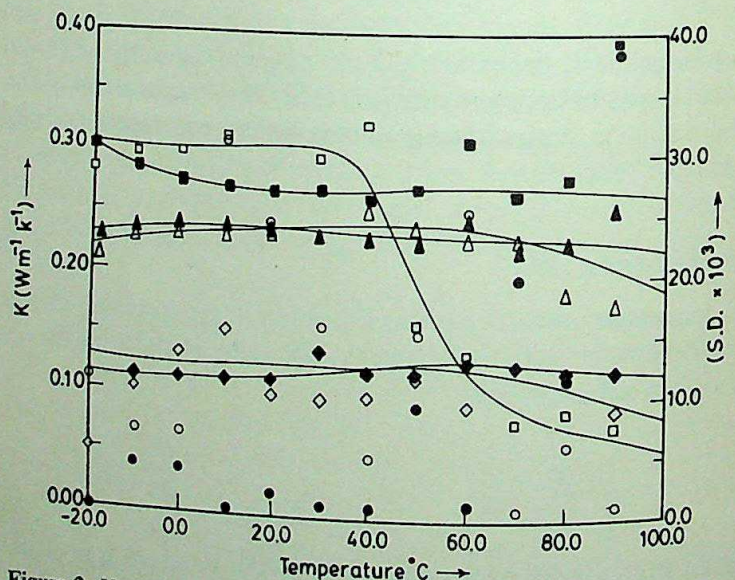

Figure 3. Variation in thermal conductivity of substances with temperature.

	Differential temp. sensors probe	Transient probe
K Glycerine	■	□
K Dune sand	▲	△
K Mustard pusa bold	◆	◇
Standard deviation for glycerine	●	○

CC-0. In Public Domain. Gurukul Kangri Collection, Haridwar

Digitized by Arya Samaj Foundation Chennai and eGangotri

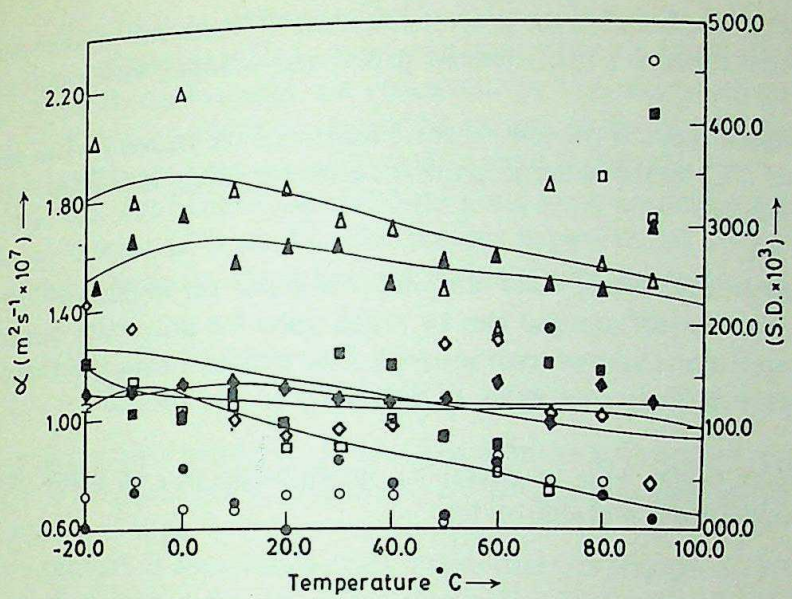

Figure 4. Variation in thermal diffusivity of substances with temperature.

	Differential temp. sensors probe	Parallel wire method
Glycerine	■	□
Dune sand	▲	△
Mustard pusa bold	◆	◇
Standard deviation for glycerine	●	○

values, the standard deviation was also calculated for all the samples. But here on graphs, standard deviation for glycerine alone is depicted, to avoid too much accumulation of points on graphs.

The two graphs show that the values of the respective thermophysical constants determined by differential temperature sensors probe are relatively closer to the expected behaviour of the samples. Moreover the comparison of standard deviation also indicate that the values given by it are nearer to the mean value. The same is found true for other substances also. The following considerations also favour its superiority over the traditional probes.

6.3. Heat transfer by convection and radiation in the proposed technique is minimum. In this method a low heat flux ($q = I^2R/L$) is required for obtaining a measurable rise in temperature between the sensors, where R is the resistance of the probe heater and L being its length. So a low current ($I = 45$ mA) is needed during an experimental run. This causes a rise in temperature of nearly 3°C in the vicinity of the probe. Whereas in parallel wire method a current ($I = 120$ mA) was required to obtain a measurable temperature rise at the sensor. This gives rise to a temperature increase as high as 15°C in the probe surroundings. Luikov (1966) has shown that when temperature difference is small, the transfer of heat by convection and radiation in the pores of the substances is negligibly small in comparison with the heat transfer by conduction. It is evident that, convective and radiative heat transfer in parallel wire method is on higher side which is not desirable. Such errors are minimum in the proposed method.

CC-0. In Public Domain. Gurukul Kangri Collection, Haridwar

Digitized by Arya Samaj Foundation Chennai and eGangotri

These errors are reflected in the graphs above 50°C where the plotted points deviate from the normal trend, for the transient probe and parallel wire methods.

6.4. In the present method the temperature difference measured by two sensors never exceed beyond 2°C, so the same step microvoltmeter range is needed over the entire temperature range.

6.5. In the literature, much data are not available for diffusivity of substances investigated. The present method can be relied upon for diffusivity measurements. If for a set of observations, sum of error square is least in data fitting, thermal conductivity is precise, then it is likely that value of diffusivity is also precise.

6.6. The present probe with its accessory instruments can be calibrated for direct reading of conductivity and diffusivity.

7. Calibration for direct measurement

7.1 *Conductivity determination*

From (3) one finds that for large time, the temperature difference i.e. microvoltmeter reading approaches a constant value (say ϕ) given by

$$\phi = \frac{q}{2\pi K} \ln\left(\frac{r_2}{r_1}\right),$$

so for a constant value of current in the heater wire the final reading of microvoltmeter

$$\phi \propto \frac{1}{K},$$

so the microvoltmeter can be calibrated for direct measurements.

Experimentally it takes about 7 to 8 min for attainment of almost a constant microvoltmeter reading.

7.2 *Diffusivity measurement*

Diffusivity is the property of a substance undergoing transient changes. For reading it directly from the instrument, a time, say 90 s is specified. At such time values, the effect of second order term is almost negligible. Hence the (4) reduces to

$$(\theta_1 - \theta_2) = \frac{q}{2\pi K} \ln\left(\frac{r_2}{r_1}\right) - \frac{q}{2\pi K} \frac{(r_2^2 - r_1^2)}{720\alpha}$$

or

$$\alpha = \frac{p \cdot q}{2\pi K} \cdot \frac{(r_2^2 - r_1^2)}{720} \cdot \left[\frac{1}{\frac{p \cdot q}{2\pi K} \ln\left(\frac{r_2}{r_1}\right) - \phi}\right],$$

where $\phi = (\theta_1 - \theta_2)$ is being measured in μV. p is the calibration constant of

CC-0. In Public Domain. Gurukul Kangri Collection, Haridwar

Digitized by Arya Samaj Foundation Chennai and eGangotri

the thermocouple. In our case $p = 39{\cdot}45\,\mu\text{VK}^{-1}$. Now an initial bias emf of $=(p{\cdot}q/2\pi K)\ln(r_2/r_1)\,\mu\text{V}$ is applied to the microvoltmeter, to give a constant reading. If the ends of the thermocouples are connected to the microvoltmeter, such that thermo emf produced oppose the bias emf its reading at 90 ths will give the thermal diffusivity. The instrument can be calibrated to read it directly.

It is obvious that this calibration will hold good for a particular value of current for a particular instant of time. For the present experimental set-up for glycerine (current $I = 0{\cdot}043$ mA, time -90 s) the expression works out to be

$$\alpha = \frac{1{\cdot}03 \times 10^{-6}}{(23{\cdot}1 - \phi)}\,\text{m}^2\text{s}^{-1}.$$

The electronic circuitry can be so designed to produce a single unit to give constant current supply to the probe heater, bias emf to microvoltmeter and register observation at required instant of time.

Such an instrument in association with differential temperature sensors probe will be a direct reading instrument for obtaining thermal characteristics of substances.

It might prove to be a useful handy apparatus for in situ measurements.

Acknowledgments

The authors thank Dr (Mrs) Usha Singh for her valuable suggestions. Authors also thank Mr P G Suradas (Mechanic) for preparation of probes and typing the manuscript. Financial assistance from DNES and ICAR, New Delhi is gratefully acknowledged.

References

Agrawal M P and Bhandari R C 1970 *Appl. Sci. Res.* **23** 113

Carslaw H S and Jaeger J C 1959 *Conduction of heat in solids* (Oxford: Clarendon) 2 ed., p. 261

Chaudhary D R 1968 *Some problems of heat transfer in disperse and porous media: Rajasthan desert sand.* Ph.D. thesis University of Rajasthan, Jaipur, India

Inaba H 1983 *Trans. ASME* **105** 268

Kerrisk J F 1971 *J. Appl. Phys.* **42** 268

Lozano J E, Urbicain M and Rostein E 1979 *J. Food. Sci.* **44** 198

Luikov A V 1966 *Heat and mass transfer in capillary-porous media.* (Translated by Harrison P W B, Translation (ed) W M Pun) (Oxford: Pergamon Press) First English ed., p. 263

Penner E, Johnsion G H, Goodrich L E 1975 *Can. Geotech. J.* **12** 271

Sharma R G, Pandey R N and Chaudhary D R 1984 *Indian J. Pure Appl. Phys.* **22** 658

Singh A K, Singh R, Beniwal R S and Chaudhary D R 1988a *Natl. Acad. Sci. Lett.* (India) **11** 261

Singh A K, Singh R and Chaudhary D R 1988b *Pramāṇa – J. Phys.* **31** 523

Singh R, Beniwal R S, Chaudhary D R 1985a *Indian J. Pure Appl. Phys.* **23** 630

Singh R, Saxena N S and Chaudhary D R 1985b *J. Phys.* **D18** 1

Wechsler A E 1966 *Development of thermal conductivity for Soil and Insulation.* Technical Report 182 U S Army Material Command, Cold Region Research and Engineering Laboratory Hanover, New Hampshire. p. 4

CC-0. In Public Domain. Gurukul Kangri Collection, Haridwar

Digitized by Arya Samaj Foundation Chennai and eGangotri

CC-0. In Public Domain. Gurukul Kangri Collection, Haridwar

Digitized by Arya Samaj Foundation Chennai and eGangotri

Pramāṇa – J. Phys., Vol. 34, No. 4, April 1990, pp. L369–L375. © Printed in India.

Mössbauer study of the stability of quasicrystalline phases: $Al_{78}Fe_{22}$ and $Al_{82}Fe_{18}$

K R P M RAO
Nuclear Physics Division, Bhabha Atomic Research Centre, Bombay 400 085, India

MS received 18 December 1989

Abstract. A quasicrystal of Al-Fe with a stoichiometric composition very close to a crystalline phase is shown to transform to the crystalline phase with simple thermal cycling from 300 K through 78 K and 300 K.

Keywords. Mössbauer spectroscopy; instability of quasicrystals; phase transition at low temperature; Al-Fe alloys.

PACS No. 76·80

1. Introduction

Generally the quasicrystals belonging to the icosahedral phase are metastable. Recently a few i-phase quasicrystals were shown to be thermodynamically more stable (Sanyal *et al* 1987; Eibschutz *et al* 1989) than their corresponding crystalline phases. Al-Fe alloys with Fe concentration less than 14% are known to form icosahedral phase and those with concentration greater than 14%, the so-called T-phase or decagonal phase. It is of interest to investigate the nature of quasicrystals with a stoichiometric composition very near to that of a crystalline phase of the alloys from the point of their stability. In this connection, we carried out Mössbauer spectroscopy studies on two alloys, viz., $Al_{78}Fe_{22}$ and $Al_{82}Fe_{18}$, the former being very close to the crystalline phase $Al_{13}Fe_4$.

2. Experimental details

The samples were prepared following standard melt spinning techniques and their quasicrystalline nature was verified using X-ray diffraction measurements. A small impurity phase was present in the samples. A source of ^{57}Co in Rh matrix was utilized for Mössbauer measurements. The Mössbauer spectra of the quasicrystals recorded at several temperatures are shown in figures 1, 2 and 3.

3. Analysis of the data

The spectra of the fresh $Al_{78}Fe_{22}$ (figure 1a) recorded at 300 K and those of $Al_{82}Fe_{18}$ (figures 2a, b, c) are very similar to those reported for the quasicrystals of Al-Fe,

CC-0. In Public Domain. Gurukul Kangri Collection, Haridwar

Digitized by Arya Samaj Foundation Chennai and eGangotri

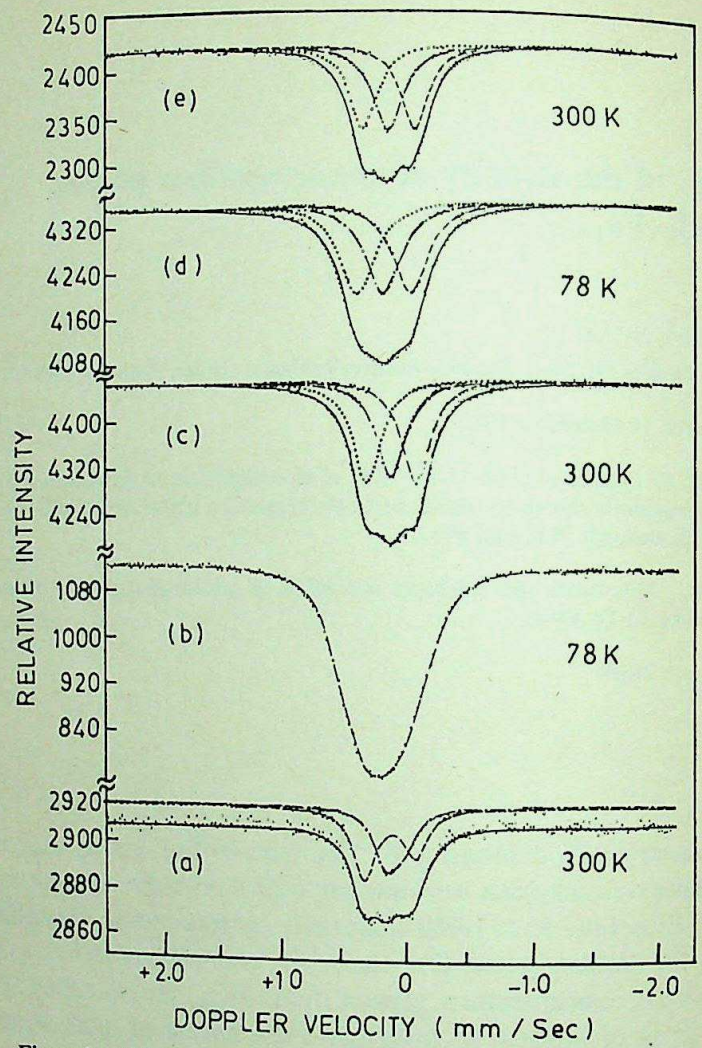

Figure 1. Mössbauer spectra of $Al_{78}Fe_{22}$: (**a**) Fresh sample at 300 K, (**b**) at 78 K, (**c**) at 300 K, after cycling through 78 K, (**d**) at 78 K, after cycling through 78 K and 300 K, (**e**) at 300 K after annealing the fresh sample at 977 K for more than 20 h.

$Al_{86}(Fe_{.02}Mn_{.98})_{14}$, $Al_6(Cr_{.7}Fe_{.3})$, $Al_7(Mn_{1-x}Fe_x)_2$, Al-5%Fe, $Al_{86}Cr_8Fe_6$ etc. (van der Woude and Schurer 1987; Eibschutz *et al* 1989; Ajay Gupta *et al* 1989).

It is seen from literature that the isomer shifts of the quasicrystalline phases were insensitive to the substitution of other transition metal atoms like Mn, Cr, for Fe (van der Woude and Schurer 1987). This observation indicates that Fe is surrounded by only Al atoms in all these samples. We believe that even in the present case, such a situation prevails and that Fe is randomly occupying the oblate and prolate rhombohedra of the icosahedral phase. Thus one would expect two Fe inequivalent sites and in an ideal case, with a relative occupation in the ratio of $\tau = 1{\cdot}618$, the Golden mean. Hence, the above spectra of the quasicrystalline phases were analysed as consisting of two quadrupole doublets arising from two inequivalent sites.

An appreciable anisotropy in the intensity of the Mössbauer spectra of quasicrystalline phases was observed. The apparent anisotropy of Mössbauer spectra of quasicrystals observed was interpreted and reported (von der Woude and Schurer 1987; Dunlap *et al* 1988; Ajay Gupta *et al* 1989) as arising due to the presence of two inequivalent sites each giving rise to a symmetric quadrupole doublet with different

CC-0. In Public Domain. Gurukul Kangri Collection, Haridwar

Digitized by Arya Samaj Foundation Chennai and eGangotri

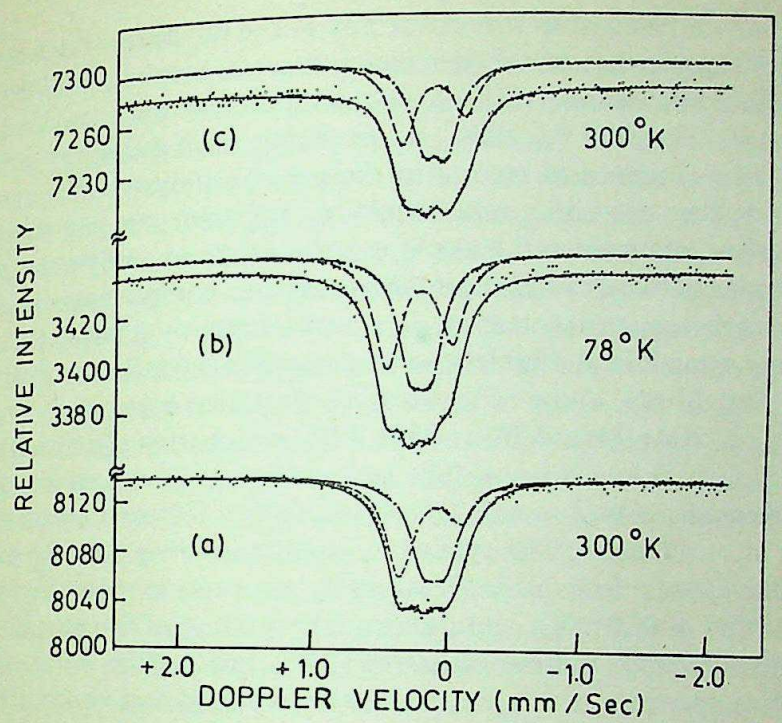

Figure 2. Mössbauer spectra of $Al_{82}Fe_{18}$: (**a**) fresh sample at 300 K, (**b**) at 78 K, (**c**) at 300 K after cycling through 78 K.

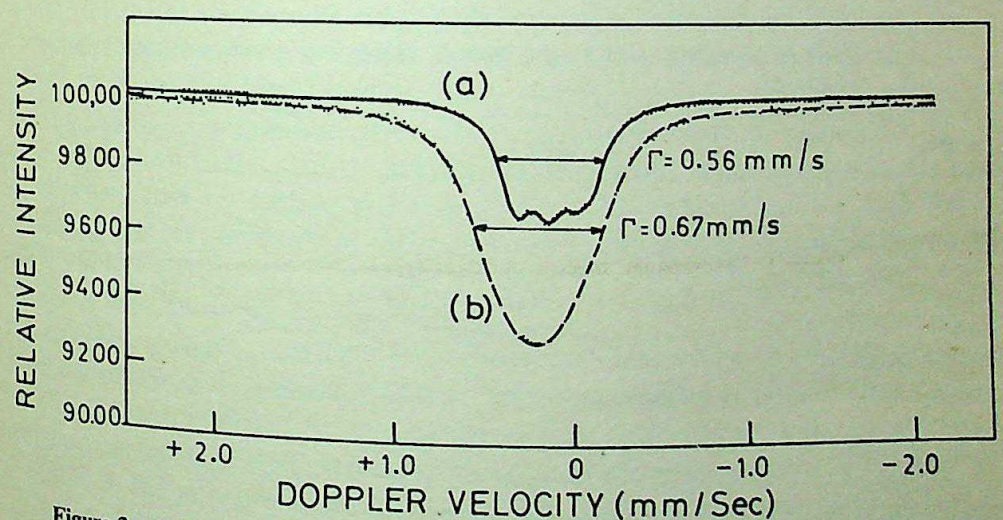

Figure 3. Mössbauer spectra of $Al_{78}Fe_{22}$: (**a**) Fresh sample at 300 K, (**b**) at 78 K.

isomer-shift and quadrupole splitting parameters or alternatively as arising due to a distribution of environments around iron with a definite correlation between the isomer-shift and quadrupole splitting for each of the environments (Eibschutz *et al* 1986; Stadnik *et al* 1989). The anisotropy observed can also arise due to the anisotropy of the lattice vibrations or due to the presence of texture in the samples. Splat-cooled alloys of Al containing Fe 14% are known to give rise to decagonal phases. It is also known that in the decagonal phase, the force constants along the *c*-axis can be very different from those in the basal plane (Bendersky 1989). This can lead to an anisotropy in the lattice vibrations. Hence it is not unreasonable to expect that this anisotropy

CC-0. In Public Domain. Gurukul Kangri Collection, Haridwar

Digitized by Arya Samaj Foundation Chennai and eGangotri

of lattice vibrations is reflected in the anisotropy of the quadrupole doublet through the Goldanskii-Karyagin effect in the Mössbauer spectra. Macko *et al* (1989) attribute the discrepancies in the intensity of their X-ray diffraction patterns of powder and ribbon samples of decagonal $Al_{79}Mn_{21}$ as probably arising due to texture in the ribbon sample. The existence of texture in the present alloys cannot be ruled out. The above two factors can either individually or together give rise to asymmetric quadrupole doublets observed and hence it is appropriate to analyse the Mössbauer spectra as consisting of two quadrupole doublets, the two components of each doublet being not necessarily equal in intensity. It is not correct to analyse the spectra as consisting of two symmetrical doublets as was assumed by earlier workers.

It is known that Al-rich alloys with Fe when annealed precipitate to crystalline monoclinic $Al_{13}Fe_4$ (Gonser and Ron 1980). $Al_{13}Fe_4$ has two significantly different iron lattice sites. One Fe site is completely surrounded by Al atoms (monomer) and gives rise to essentially a singlet with an isomer shift of 0·20 mm/s and with a very small splitting of $<0{\cdot}06$ mm/s. The second Fe site has another Fe atom as a nearest neighbour (a dimer) apart from other Al atoms. It gives rise to a quadrupole doublet with an isomer shift of 0·20 mm/s and quadrupole splitting of 0·40 mm/s.

The spectrum of the specimen annealed at 977 K for more than 20 h is very similar to the Mössbauer spectrum of $Al_{13}Fe_4$ as can be expected and hence it is analysed as consisting of a singlet and a quadrupole doublet. The Mössbauer parameters obtained from computer fitting are in very good agreement with those reported for the crystalline $Al_{13}Fe_4$ (table 1).

Table 1. Mössbauer parameters obtained from a least-square analysis of the various spectra recorded.

Sample	Doublet 1			Doublet 2/singlet			
$Al_{78}Fe_{22}$	I.S. (w.r.t. α-Fe)	E_q	Γ	I.S. (w.r.t. α-Fe)	E_q	Γ	A_1/A_2
300 K	0·20	0·41	0·23	0·07	0·15	0·23	1·36
78 K	----------	Gaussian	----------				
300 K (cycled through 78 K)	0·15	0·39	0·28	0·16	0·0	0·28	2·0
78 K (cycled through 300–78–300 K)	0·21	0·43	0·33	0·21	0·0	0·34	1·91
300 K (sample annealed at 977 K)	0·17	0·40	0·27	0·18	0·0	0·30	1·76
$Al_{82}Fe_{18}$							
300 K	0·23	0·45	0·25	0·07	0·15	0·25	0·92
78 K	0·24	0·48	0·23	0·08	0·15	0·23	1·02
300 K (cycled through 78 K)	0·24	0·47	0·23	0·09	0·17	0·23	0·89
$Al_{13}Fe_4$ 300 K Crystalline phase Ref. Fujita (1975)	0·20	0·40 (Doublet)	0·26	0·20	0·0 (singlet)	0·32	2·0

All in mm/s and $\leqslant \pm 0{\cdot}025$ mm/s.

CC-0. In Public Domain. Gurukul Kangri Collection, Haridwar

Digitized by Arya Samaj Foundation Chennai and eGangotri

The spectrum of $Al_{78}Fe_{22}$ cooled to 78 K (figure 1b) shows a very broad non-Lorentzian single line indicating a change in the quasicrystalline nature of the sample. It appears that there is a continuous distribution of the local environment with different isomer shifts and quadrupole splittings around the iron atoms in the sample. The shape of the line appears to be Gaussian. The overall line width has increased to 0·67 mm/s from the value of 0·56 mm/s observed for the spectrum at 300 K (figure 3). The overall line width of the Mössbauer spectrum of $Al_{78}Fe_{22}$ is relatively narrower for the quasicrystalline phase, it broadens in the case of the intermediate phase (figure 1b) and once again becomes narrower for the crystalline phases. The phase transition from the quasicrystalline to the crystalline phase can take place through a movement or adjustment of atoms over small distances of the order of one or two lattice spacings. The surroundings of Fe in both the quasicrystalline and crystalline phases appear to be well defined giving rise to relatively narrower overall line width while the surroundings of Fe atoms in the intermediate phase seem to be varied giving rise to the observed broader line at 78 K.

The broader width observed at 78 K compared to that at 300 K could also arise as a consequence of the onset of magnetic ordering at about 78 K. However, the irreversible nature of the spectra obtained rules out magnetic ordering as the possible cause for the line broadening.

The room-temperature spectrum of $Al_{78}Fe_{22}$ cycled through 78 K, (figure 1c) is very similar to that of the crystalline phase $Al_{78}Fe_{22}$ (Gonser and Ron 1980) obtained after the sample was annealed at 977 K for more than 20 h (figure 1e). The spectrum recorded at 78 K after the sample was cycled through 78 K and 300 K (figure 1d) is also very similar to the annealed sample, but is drastically different from the spectrum recorded at 78 K of the fresh sample. This clearly indicates that an irreversible transition of the quasicrystalline phase (via an intermediate phase consisting of continuous distribution of local environment around a given Fe atom) to the crystalline phase is obtained just by cycling the sample from 300 K through 78 K and 300 K without raising the temperature of the sample beyond 300 K. The stoichiometry of the quasicrystal $Al_{78}Fe_{22}$ is very close to that of the crystalline $Al_{13}Fe_4$. This composition is seen to be highly metastable.

In certain cases, a phase transition from quasicrystalline phase to crystalline phase can be the consequence of nucleation and growth phenomenon (Fujita 1975; Knowles 1989) which has been initiated by the presence of an impurity of a crystalline phase.

The various computer-fitted parameters obtained are given in table 1. It may be pointed out that the spectra of the quasicrystalline phases can also be analysed in terms of one singlet and one doublet as in the case of crystalline phases. However, physical considerations, based on consistency with X-ray data and various data reported in literature, favour analysis of the quasicrystal phases as consisting of two quadrupole doublets and the crystalline phases as consisting of one singlet and one quadrupole doublet.

The relative occupation of the sites with larger quadrupole splitting is seen to increase with higher Fe concentration in the Al–Fe quasicrystals. The relative population of the two Fe sites as obtained from our analysis is about 1·4 in the case of $Al_{78}Fe_{22}$ and near about 1·0 in the case of $Al_{82}Fe_{18}$ as against 1·618 in the ideal case of icosahedral phases.

It is well known (Goldanskii 1968; Gonser 1975) that the anisotropy, arising due to Goldanskii-Karyagin effect, increases with temperature. In the case of $Al_{78}Fe_{22}$,

CC-0. In Public Domain. Gurukul Kangri Collection, Haridwar

Digitized by Arya Samaj Foundation Chennai and eGangotri

it is seen that the low temperature spectrum does not show any anisotropy while the room temperature spectrum shows considerable anisotropy. Although there is a change in the crystalline nature of the sample, it is significant that anisotropy is present in the decagonal phase and is absent in the intermediate phase. It is also gratifying to note that the quasicrystal $Al_{82}Fe_{18}$, which does not show any transition to the crystalline phase at low temperature, gives rise to anisotropy in all the spectra and that the anisotropy of the 78 K spectrum is less compared to that of the 300 K spectrum. This clearly indicates that anisotropy increases with temperature in both the quasicrystals. Such variation of the anisotropy with temperature is indicative of the presence of Goldanskii-Karyagin effect in the present quasicrystals.

The spectra of fresh $Al_{82}Fe_{18}$ are typical of quasicrystalline phase, without the kind of changes seen in the case of $Al_{78}Fe_{22}$.

3. Conclusions

The sample $Al_{78}Fe_{22}$ contains 22% Fe and this is close to the 23·5% Fe present in the crystalline phase of $Al_{13}Fe_4$. This favourable composition of $Al_{78}Fe_{22}$ is quite conducive for the transformation of the quasicrystalline phase, $Al_{78}Fe_{22}$, on thermal cycling from 300 K through 78 K and 300 K, to the crystalline phase of $Al_{13}Fe_4$. In the case of $Al_{82}Fe_{18}$, the Fe content is only 18%, quite away from the 23·5% required for the precipitation of $Al_{13}Fe_4$ phase and consequently the phase is not susceptible to any change in its nature on thermal cycling.

This appears to be the first time that a phase transition from a quasicrystalline phase to a crystalline phase has been observed when a fresh sample at room temperature is subjected to thermal cycling through 78 K and 300 K. The present measurements show that a quasicrystal with a composition very near to the stoichiometry of a crystalline phase is highly metastable.

Acknowledgements

The author is grateful to Drs K R Rao and B A Dasannacharya for their keen interest, critical comments and very helpful suggestions. He would like to thank Dr K R Rao for providing the samples. Sincere thanks are due to Shri Y D Dande and S R Chinchanikar for technical help.

References

Ajay Gupta, Jayaraj M E and Rama Reddy K 1989 *Phys. Rev.* **39** 8757

Bendersky L 1989 *Phys. Rev. Lett.* **55** 1461

Dunlap R A, Lawther P W and Lloyd D J 1988 *Phys. Rev.* **38** 3649

Eibschutz M, Chen H S and Hauser J J 1986 *Phys. Rev. Lett.* **56** 169

Fujita F E 1975 in *Topics in applied physics Vol. 5 Mössbauer spectroscopy*. Chap. 6 (ed.) U Gonser (Heidelberg: Springer-Verlag)

Goldanskii V I 1968 in *Chemical application of Mössbauer spectroscopy* (eds) V I Goldanskii and R H Herber (New York: Academic Press)

CC-0. In Public Domain. Gurukul Kangri Collection, Haridwar

Digitized by Arya Samaj Foundation Chennai and eGangotri

Gonser U and Ron M 1980 in '*Applications of Mössbauer spectroscopy*' (ed.) R L Cohen (New York: Academic Press) Vol. 2
Gonser U 1975 in *Topics in applied physics Vol. 5 Mössbauer spectroscopy*. Chap. I (ed.) U Gonser (Heidelberg: Springer-Verlag)
Knowles K M 1989 *Bull. Mater. Sci.* **12** 271
Macko D, Hudak O and Hajko Jr V 1989 *Phys. Lett.* **A136** 327
Sanyal M K, Sahni V K and Dey G K 1987 *Nature* (*London*) **328** 704
Stadnik M, Stroink G, Ma H and Williams G 1989 *Phys. Rev.* **B39** 9797
Van der Woude F and Schurer P J 1987 *Can. J. Phys.* **65** 1301

CC-0. In Public Domain. Gurukul Kangri Collection, Haridwar

Digitized by Arya Samaj Foundation Chennai and eGangotri

CC-0. In Public Domain. Gurukul Kangri Collection, Haridwar

Digitized by Arya Samaj Foundation Chennai and eGangotri

Pramāṇa – J. Phys., Vol. 34, No. 4, April 1990, pp. L377–L381. © Printed in India.

Detection limits of high temperature superconducting materials on various substrates by energy dispersive X-ray fluorescence and proton induced X-ray emission methods

M LAL, H N BAJPAI*, D JOSEPH and R K CHOUDHURY

Nuclear Physics Division,* Analytical Chemistry Division, Bhabha Atomic Research Centre, Bombay 400 085, India

MS received 22 November 1989; revised 3 February 1990

Abstract. Application of energy dispersive X-ray fluorescence (EDXRF) and proton induced X-ray emission (PIXE) methods has been demonstrated for determining the elemental composition of thin film superconducting materials. The results of analysis carried out by EDXRF method have been compared with those obtained by PIXE method. Thin films of $YBa_2Cu_3O_7$ superconducting material were deposited on various substrates such as thin mylar sheet and thick substrates of $SrTiO_3$, MgO and Al_2O_3. In thin backing the minimum detection limits obtained for Cu, Y, Ba by the PIXE method are 20 ng, 70 ng and 800 ng respectively and the corresponding values by the EDXRF method are 3000 ng, 600 ng and 1000 ng. Detection limits for samples on thick backings deteriorated to a large extent by both methods.

Keywords. High temperature superconductivity; $YBa_2Cu_3O_7$; thin film deposition; substrates: EDXRF analysis; PIXE analysis; minimum detection limits.

PACS No. 73·60

The development of high temperature superconducting materials in recent years evoked interest in the formation of thin film superconductors for a variety of applications. To optimize various parameters involved in the evaporation method to obtain the composition of the original material with superconducting properties it becomes necessary to choose a method for rapid characterization of the composition of the thin film deposited on any given substrate. A number of methods such as Rutherford backscattering (Dijjkamp *et al* 1987) and X-ray photoelectron spectroscopy (Jin *et al* 1987) have been employed to characterize thin films of the deposited superconducting materials. EDXRF method has been widely employed (Gianelos 1974; Stine and Leidl 1974; Laguitton 1977; Huang and Parush 1979 and Lal and Choudhury 1987) for a rapid non-destructive determination of the elemental composition of any material. This method is particularly suitable for analysis of thin films down to elemental thickness of the level of a few angstroms. Earlier we have reported (Lal and Choudhury 1988) the application of the EDXRF method for monitoring the composition of the films of $YBa_2Cu_3O_7$ superconducting material deposited by laser evaporation. In the present work we have made use of both EDXRF and PIXE methods for monitoring of the thin film composition of $YBa_2Cu_3O_7$ using various substrates and evaluated application of these methods with regard to the level of detection of the elements present in thin films using both

CC-0. In Public Domain. Gurukul Kangri Collection, Haridwar

Digitized by Arya Samaj Foundation Chennai and eGangotri

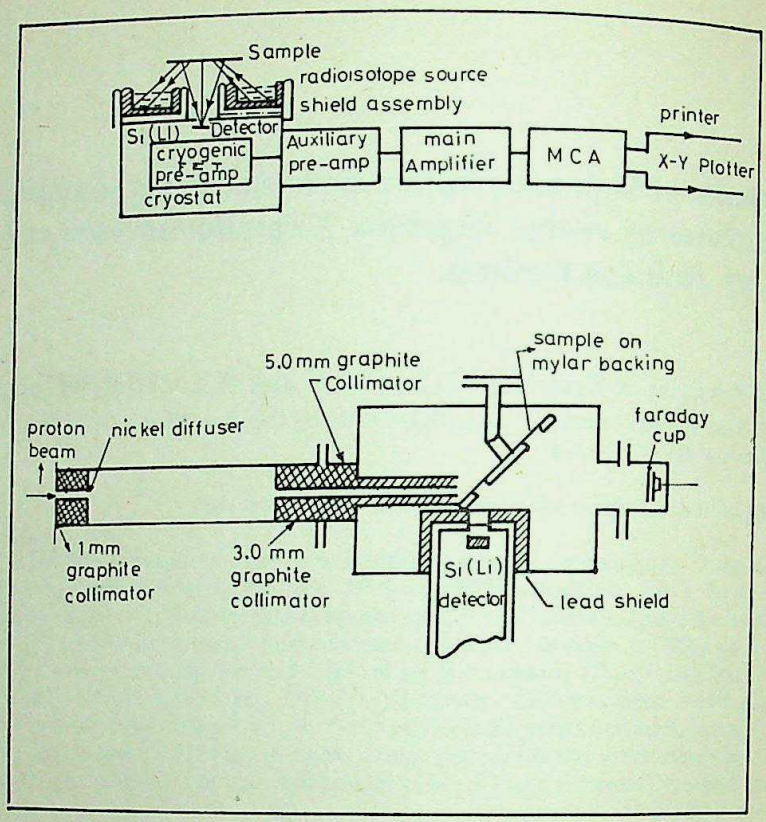

Figure 1. Schematic arrangement of Si(Li) detector X-ray system employing (a) photon excitation from radioisotope sources. (b) proton beam from Van de Graaff accelerator.

thin and thick substrates. The thick substrates used were $SrTiO_3$, MgO and Al_2O_3 in the form of 5 mm thick disks and the thin substrate used was 6 μm mylar sheet.

The EDXRF set up employed for monitoring these thin film deposits comprises of a high resolution lithium drifted silicon, Si (Li) detector along with radioisotope sources of ^{109}Cd (2·0 mc) and ^{241}Am (100 mc) for excitation of characteristic X-rays. The sources are mounted in an annular geometry as shown in figure 1(a). The signals of the X-rays detected by Si(Li) detector are amplified by high resolution electronics and the spectrum is stored in the multi-channel analyzer. Figure 1(b) shows the PIXE set up (Lal *et al* 1989) at the 5·5 MeV Van de Graaff accelerator, Trombay. The beam from the accelerator is diffused by passing through a thin Ni foil located 0·5 m from the sample target. The diffused beam passes through a set of collimators before striking the sample over a well-defined area. The X-rays from the sample are detected at 90° with respect to the beam by a Si(Li) detector which is shielded against the proton induced γ-ray background from all sides except the Be window which interfaces the sample and the detector.

Figures 2 and 3 show the X-ray spectra of the high T_c superconducting material deposited on thin mylar backing obtained with the EDXRF and PIXE methods. In EDXRF method both ^{109}Cd and ^{241}Am were used to excite the samples. In PIXE method, proton beam of 2·5 MeV was used from the Van de Graaff accelerator. The sample of 500 $\mu g/cm^2$ thickness was deposited by micropippeting the $YBa_2Cu_3O_7$ solution. From the observed intensities of the K X-rays of all the elements, the minimum detection limits (MDL) were evaluated. The MDL of an element was

CC-0. In Public Domain. Gurukul Kangri Collection, Haridwar

Digitized by Arya Samaj Foundation Chennai and eGangotri

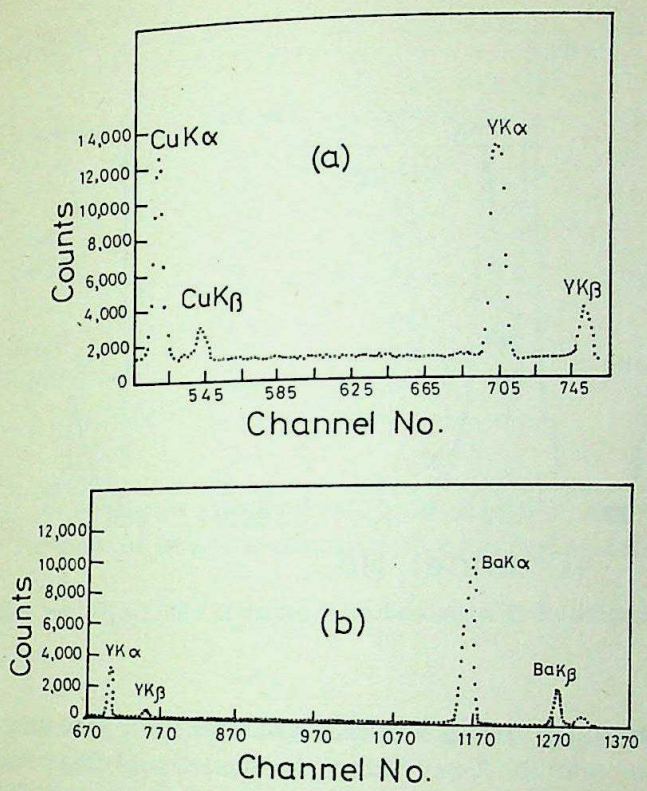

Figure 2. EDXRF spectra of thin superconducting material $YBa_2Cu_3O_7$ on mylar backing excited by (**a**) ^{109}Cd (**b**) ^{241}Am.

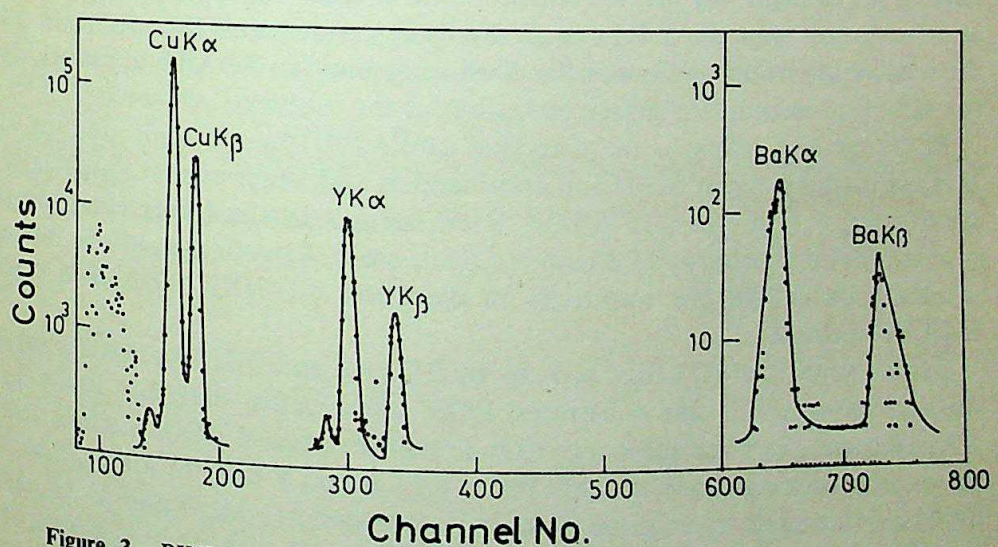

Figure 3. PIXE spectrum of thin superconducting materials $YBa_2Cu_3O_7$ on mylar backing.

calculated as the equivalent of the element concentration corresponding to the total counts of $2\sqrt{N_B}$, where N_B is the background counts under the X-ray peak. Similar analysis was carried out for samples deposited on thick substrates. The detection limits deteriorated to a large extent for the thick substrates. However in $SrTiO_3$ substrate, the K X-rays of Sr were found to heavily interfere with the Y K X-rays (figure 4). The results on detection limits for substrates of mylar, MgO, Al_2O_3 are discussed below.

CC-0. In Public Domain. Gurukul Kangri Collection, Haridwar

Digitized by Arya Samaj Foundation Chennai and eGangotri

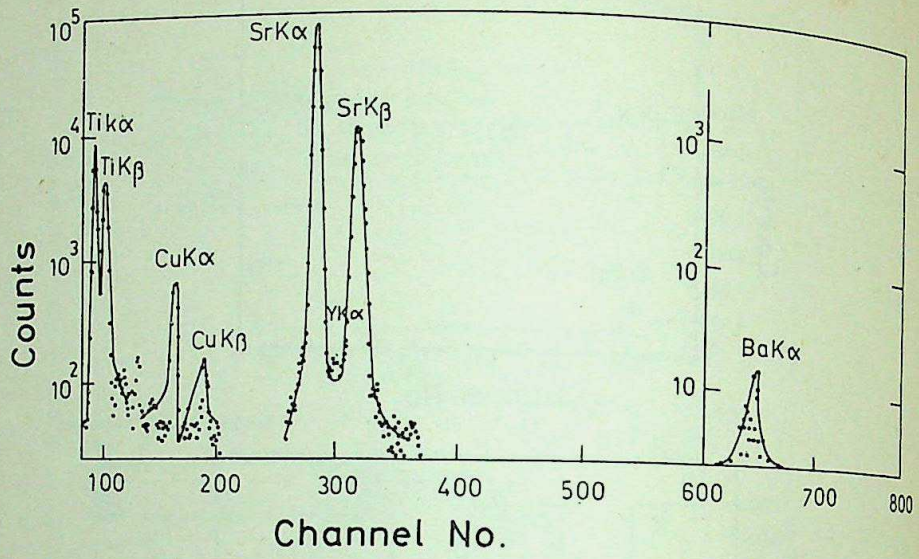

Figure 4. PIXE spectrum of superconducting material $YBa_2Cu_3O_7$ on thick substrate of $SrTiO_3$.

To achieve good detection limits in EDXRF analysis, it is essential to employ suitable exciting source energies for X-ray lines to be excited and also to minimize the background under the X-ray peak of the elements to be measured. Better detection limits are obtained by employing the excitation source energy closer to the absorption edge of the element and for this reason ^{109}Cd is used for Cu and Y and ^{241}Am for Y and Ba. In this way, the Y K_α counts are used to normalize the spectra to determine the relative intensities of Cu and Ba. The background in EDXRF arises mainly due to the tailing of incomplete charge collection of the scattered photons.

PIXE method offers better detection limits for lower atomic number elements because of much higher excitation cross section and easier availability of large flux of proton beam from the accelerator. Even though in the lower energy region the bremsstrahlung background due to electrons emitted in charge particle interaction is predominantly high, the sensitivity of detection by PIXE method is superior to EDXRF method.

Table 1 gives the MDL for Cu, Y, Ba by EDXRF and PIXE methods using thin and thick substrates. For thin substrates, PIXE offers better detection limits for all the three elements. In thick substrates though performance of PIXE method deteriorates by an order of magnitude, it is still better for Cu and Y but not for Ba. The detection limits for thick substrates given in table 1 correspond to MgO and Al_2O_3 substrates. In $SrTiO_3$ there was heavy interference of Sr K X-rays with the Y K X-rays obscuring their proper detection. For an element to be detected, its concentration has to be higher than the MDL as quoted above. The error in the determination of the concentration of an element will however, depend on the counting statistics of the K X-ray peak including the background under it.

In summary we have applied the PIXE and EDXRF methods for characterizing the composition of elements of high T_c superconducting films on various substrates. As a typical case the material of $YBa_2Cu_3O_7$ was used in the present analysis. It was observed that in general PIXE gives better detection limits than EDXRF except for the measurement of Ba on thick substrates. Depending upon the elemental thickness

CC-0. In Public Domain. Gurukul Kangri Collection, Haridwar

Digitized by Arya Samaj Foundation Chennai and eGangotri

Table 1.

Substrate	Elements	Minimum detection limits ($\mu g/cm^2$)	
		EDXRF	PIXE
Thin (Mylar)	Cu	3·0	0·02
	Y	0·6	0·07
	Ba	1·0	0·8
Thick (Al_2O_3, MgO)	Cu	10·0	0·2
	Y	7·0	0·5
	Ba	0·7	4·0

required for a particular application both EDXRF and PIXE methods can be employed. The present analysis can also be extended to other high T_c materials.

References

Dijkkamp P, Venkatesan T, Wu X D, Shaheen S A, Jisrawi N, Min-Lee Y H, McLean W L and Croft M 1987 *Appl. Phys. Lett.* **51** 819

Gianelos J 1974 *Adv. X-ray Anal.* **17** 325

Huang T C and Parush W 1979 *Adv. X-ray Anal.* **22** 43

Jin B Y, Lee S J, Song S N, Hwu S J, Thul J, Poeppelmeir K R and Ketterson J B 1987 *Advanced Ceramic materials* (special issue) Vol 2, No 3B, 436

Laguitton D 1977 *X-ray spectrometry* Vol 6, No 4 p. 187

Lal M and Choudhury R K 1987 National symposium on advances in surface treatment of metals ASTOM, BARC 472

Lal M and Choudhury R K 1988 *Pramāṇa–J. Phys.* **30** 463

Lal M, Choudhury R K, Nayak B K, Bamane V S, Trivedi P N and Ranade S S 1989 The science of the total environment **78** 167

Stine P A and Leidl S J 1974 *Adv. X-ray Anal.* **17** 48

CC-0. In Public Domain. Gurukul Kangri Collection, Haridwar

Digitized by Arya Samaj Foundation Chennai and eGangotri

CC-0. In Public Domain. Gurukul Kangri Collection, Haridwar

Digitized by Arya Samaj Foundation Chennai and eGangotri

Pramāṇa – J. Phys., Vol. 34, No. 5, May 1990, pp. 383–396. © Printed in India.

Spherical shells of positive density – can they be of non-positive mass?†

A K RAYCHAUDHURI and S BANERJEE*

Department of Physics, Presidency College, Calcutta 700 073, India
*Department of Physics, The University of Burdwan, Burdwan 713 104, India

MS received 18 September 1989

Abstract. Spherical shells of fluid in general relativity are considered. The density is assumed to be spatially uniform and it is found that there may be three cases of positive, negative and vanishing Schwarzschild mass of the shell although the density and the pressure are both positive throughout. However the negative mass case has to be associated with a singularity representing a negative mass particle and so is unphysical. The zero mass solution has the intriguing feature that the geometry on either side of the shell is Minkowskian and the space is closed. This closure of the space saves the present result from being in contradiction with the positive energy theorems. Earlier investigations claiming zero-mass distributions are also discussed.

Keywords. Zero mass; negative mass; spherical shells.

PACS No. 04·20

1. Introduction

The problem arose out of a consideration of the fit between the Schwarzschild metric of empty space

$$ds^2 = \frac{(1-2m/\hat{r})^2}{(1+2m/\hat{r})^2}d\hat{t}^2 - \left(1+\frac{m}{2\hat{r}}\right)^4 (d\hat{r}^2 + \hat{r}^2 d\theta^2 + \hat{r}^2 \sin^2\theta\, d\phi^2) \quad (1)$$

and the Friedmann metric

$$ds^2 = dt^2 - \frac{e^g}{\left[1+\frac{kr^2}{4}\right]^2}(dr^2 + r^2 d\theta^2 + r^2 \sin^2\theta\, d\varphi^2) \quad (2)$$

where $g=g(t)$ and $k=0, +1$ or -1 and the constant m signifies the mass of the Schwarzschild field source. The particular coordinate systems are characterized by the condition that in both (1) and (2), the three spaces have a conformally flat metric.

The problem of fitting a Schwarzschild metric with the Friedmann metric was first considered by Einstein and Straus (1945, 1946) who showed the existence of a transformation which renders the two metrics continuous. While in their case, the Schwarzschild vacuum was a hole in the universe, Raychaudhuri (1953) considered a dust sphere cut out of a homogeneous universe placed in a vacuum and showed

†A short report giving some of the results of the present paper is published in *Phys. Lett.* **A140** 285 (1989).

CC-0. In Public Domain. Gurukul Kangri Collection, Haridwar

Digitized by Arya Samaj Foundation Chennai and eGangotri

that the metric (2) valid within the dust sphere may be fitted to the metric (1) at $r=r_1$, if,

$$m=\tfrac{4}{3}\pi\rho\frac{r_1^3\exp(3g/2)}{\left[1+\dfrac{kr_1^2}{4}\right]^3}. \tag{3}$$

where ρ is mass density of the dust in the sphere. The relation (3) shows that in $k=1$, the mass m of the dust sphere has a maximum for $r_1=2$ and then decreases to zero as $r_1\to\infty$. Thus one cannot obtain in this way a sphere of negative mass and in case $r_1\to\infty$, the sphere fills up the entire space leaving no empty space outside. However the decrease of m with increasing r_1, even though the density is positive everywhere, seems somewhat intriguing and here we investigate the problem whether we can obtain a spherical shell of positive density everywhere but nevertheless having a Schwarzschild field of negative or vanishing mass in the neighbouring vacuum.

Zero mass solutions have previously been proposed by Zel'dovich (1962) and Harrison *et al* (1965). But these models have been criticized by Leibovitz and Israel (1970) which we discuss in concluding section.

2. Field equations

We consider three regions (a) an internal vacuous region extending from $r=0$ to $r=r_1$ (i.e. $0\leqslant r\leqslant r_1$). (b) A shell of uniform positive density and (non-uniform) positive pressure from $r=r_1$ to r_2. (c) An external vacuous region extending beyond $r_2(r>r_2)$.

We consider a spherically symmetric system and assume that the matter which is a perfect fluid has a shearfree motion. Thus we can introduce a comoving coordinate system in which the metric assumes the form

$$ds^2=e^{\nu}dt^2-e^{\mu}(dr^2+r^2\,d\theta^2+r^2\sin^2\theta\,d\phi^2) \tag{4}$$

where ν and μ are functions of r and t. The velocity vector v^μ of the fluid is given by $v^\mu=\exp(-\nu/2)\,\delta^\mu_0$ (the coordinates t, r, θ, ϕ being numbered 0, 1, 2, 3 respectively). In the above metric the coordinate r is uniquely defined up to a trivial constant multiplier in the fluid filled region and in the empty spaces by the conditions of continuity of $\exp(\nu)$ and $\exp(\mu)$ and their first derivatives.

The Einstein field equations

$$R^\mu_{\ \nu}-\tfrac{1}{2}R\delta^\mu_{\ \nu}=-8\pi T^\mu_{\ \nu} \tag{5}$$

give four non-trivial equations with the metric (4):

$$\begin{aligned}8\pi p\equiv -8\pi T^1_{\ 1}&=\exp(-\mu)\left[\frac{\mu'^2}{4}+\frac{\mu'\nu'}{2}+\frac{\mu'+\nu'}{r}\right]\\&\quad-\exp(\nu)\left(\ddot{\mu}+\frac{3\dot{\mu}^2}{4}-\frac{\dot{\mu}\dot{\nu}}{2}\right)\end{aligned} \tag{6}$$

CC-0. In Public Domain. Gurukul Kangri Collection, Haridwar

Digitized by Arya Samaj Foundation Chennai and eGangotri

$$8\pi p \equiv -8\pi T^2{}_2 = -8\pi T^3{}_3 = \exp(-\mu)\left[\frac{\mu''+\nu''}{2}+\frac{\nu'^2}{4}+\frac{\mu'+\nu'}{2r}\right] - \exp(\nu)\left(\ddot{\mu}+\frac{3\dot{\mu}^2}{4}-\frac{\dot{\mu}\dot{\nu}}{2}\right) \tag{7}$$

$$8\pi\rho \equiv 8\pi T^0{}_0 = \exp(-\mu)\left(\mu''+\frac{\mu'^2}{4}+\frac{2\mu'}{r}\right)+\tfrac{3}{4}\exp(-\nu)\dot{\mu}^2 \tag{8}$$

$$0 = 8\pi T_{10} = -\left(\dot{\mu}'-\frac{\dot{\mu}\nu'}{2}\right). \tag{9}$$

We shall assume that the density ρ is uniform throughout the shell but leave the pressure free except that we require it to vanish at the two boundaries of the shell ($r=r_1$ and $r=r_2$—this is necessary if the continuity conditions at the boundary are to be satisfied) and further that the pressure of the fluid is positive everywhere else. Still, the association of a non-uniform pressure with a uniform density appears to be somewhat unphysical but the assumption of a uniform density has been introduced to make the mathematics tractable and presumably the assumption does not vitiate the final results.

Equation (9) is readily integrated to give

$$\exp(-\nu)\dot{\mu}^2 = \dot{g}^2 \tag{10}$$

where g is an arbitrary function of t alone. We now recall some results in Raychaudhuri's paper (1953). Introducing new variables ξ and x defined by

$$\exp(\mu)r^2 = \xi^4, \quad x = \ln r \tag{11}$$

equation (8) reduces to

$$\xi_{xx} \equiv \frac{\partial^2\xi}{\partial x^2} = \tfrac{1}{4}\xi + \tfrac{3}{16}\dot{g}^2\xi^5 \quad \text{(in vacuo)} \tag{12a}$$

$$= \tfrac{1}{4}\xi + \tfrac{3}{16}\left(\dot{g}^2 - \frac{32\pi\rho}{3}\right)\xi^5 \text{ (for fluid filled region).} \tag{12b}$$

The first integrals of equation (12a) are

$$\xi_x^2 \equiv \left(\frac{\partial\xi}{\partial x}\right)^2 = \frac{\xi^2}{4}+\tfrac{1}{16}\dot{g}^2\xi^6 \quad (r \leqslant r_1) \tag{13a}$$

$$= \frac{\xi^2}{4}+\frac{1}{16}\left(\dot{g}^2-\frac{32\pi\rho}{3}\right)\xi^6 + K_1 \quad (r_1 \leqslant r \leqslant r_2) \tag{13b}$$

$$= \frac{\xi^2}{4}+\frac{1}{16}\dot{g}^2\xi^6 + K_2 \quad (r \geqslant r_2) \tag{13c}$$

where the subscript x indicates partial differentiation with respect to x and K_1, K_2

CC-0. In Public Domain. Gurukul Kangri Collection, Haridwar

Digitized by Arya Samaj Foundation Chennai and eGangotri

are integration 'constants' which are at most functions of t. However the condition of isotropy of pressure ($T^1{}_1 = T^2{}_2$) gives from (6) and (7) on eliminating ν' by (9):

$$\frac{\mu'^2}{4} + \frac{\mu'\dot{\mu}'}{\dot{\mu}} + \frac{\mu'}{2r} + \frac{\dot{\mu}'}{\dot{\mu}r} - \frac{\mu''}{2} - \frac{\dot{\mu}''}{\dot{\mu}} = 0.$$

This on integration yields

$$\exp(\mu/2)\left(\frac{\mu'^2}{2} + \frac{\mu'}{r} - \mu''\right) = f(r) \tag{14}$$

where $f(r)$ is an undetermined function of r alone. Now using (11), (12) and (13), eq. (14) reduces to

$$12K_1/r^3 = f(r), \quad 12K_2/r^3 = g(r)$$

or K_1 and K_2 are constants independent of t as well. The conditions of continuity of ξ and ξ_x at r_1 and r_2 give

$$\begin{aligned} K_1 &= \tfrac{2}{3}\pi\rho_1\xi_1{}^6 \\ K_2 &= \tfrac{2}{3}\pi\rho(\xi_1{}^6 - \xi_2{}^6) \end{aligned} \tag{15}$$

where ξ_1 and ξ_2 are the values of ξ at r_1 and r_2 respectively. From the divergence relation $T^{0\mu}{}_{;\mu} = 0$, one gets:

$$\dot{\rho} = -\tfrac{3}{2}(p+\rho)\dot{\mu}$$

so that at r_1 and r_2 where the pressure is to vanish,

$$\frac{\partial}{\partial t}(\rho\exp(3\mu/2)) = 0.$$

Thus $\rho\xi_1{}^6$ and $\rho\xi_2{}^6$ are constants —a conclusion which follows from the constancy of K_1 and K_2 also. We have omitted a constant in (13a) to avoid a singularity at the origin $r=0$. We may now write the solution as

$$\exp(\mu) = \xi^4 r^{-2}, \quad \exp(\nu) = 16\dot{\xi}^2/(\xi^2\dot{g}^2) \tag{16}$$

with ξ determined by (13). Of course an additional function of time will come from the integration of (13). This may be fixed up from the following consideration.

The divergence relation $T^{1\nu}{}_{;\nu} = 0$ gives

$$p' = -(p+\rho)\nu'/2 \tag{17}$$

and as ρ is independent of r, we may integrate the above equation to get

$$(p+\rho)\exp(\nu/2) = \text{function of } t \text{ alone.}$$

Now at r_1 and r_2, $p=0$, and ρ is independent of r. Hence, from the above

$$\exp(\nu/2)_{r_1} = \exp(\nu/2)_{r_2}$$

CC-0. In Public Domain. Gurukul Kangri Collection, Haridwar

Digitized by Arya Samaj Foundation Chennai and eGangotri

Or, using (16)

$$(\dot{\xi}/\xi)_{r_1} = (\dot{\xi}/\xi)_{r_2}. \tag{18}$$

From (13b), it is obvious that the integral will be of the form

$$\xi = \xi[(x + C), \eta, K_1]$$

where C is a function of t alone and we have written η for

$$\frac{1}{16}\left(\dot{g}^2 - \frac{32\pi\rho}{3}\right)$$

so that η also is a function of t alone. Hence

$$\frac{\dot{\xi}}{\xi} = \frac{1}{\xi}\left[\frac{\partial\xi}{\partial(x+C)}\dot{C} + \frac{\partial\xi}{\partial\eta}\dot{\eta}\right].$$

$$= \frac{1}{\xi}\left[\xi_x\dot{C} + \frac{\partial\xi}{\partial\eta}\dot{\eta}\right].$$

Consequently (18) gives

$$\left[\left(\frac{\xi_x}{\xi}\right)_{r_1} - \left(\frac{\xi_x}{\xi}\right)_{r_2}\right]\dot{C} + \left[\left(\frac{1}{\xi}\frac{\partial\xi}{\partial\eta}\right)_{r_1} - \left(\frac{1}{\xi}\frac{\partial\xi}{\partial\eta}\right)_{r_2}\right]\dot{\eta} = 0. \tag{19}$$

This equation will determine C (except when the coefficient of C vanishes) if η is given and ensure that (18) is satisfied. We shall see in the next section that $(\xi_x/\xi)_{r_1}$ and $(\xi_x/\xi)_{r_2}$ are of opposite signs and the question of vanishing of the coefficient of C does not arise. Note that the constancy of $\rho\xi_1{}^6$ and $\rho\xi_2{}^6$ as follows from (15) automatically leads to (18). Equation (19) serves to determine C and is consistent with (15).

Note that if η is a constant, then C will also be a constant and ξ would be independent of t. Obviously there cannot be any static solution of the type we are considering and this is indicated by the vanishing of e^{ν} for $\dot{\xi} = 0$.

The vanishing of pressure at the two boundaries r_1 and r_2 is automatically ensured if the continuity conditions with the vacuum fields at these two surfaces are satisfied. However the requirement that the pressure is positive inside requires, in view of equation (17), that ν' is negative at r_1 and positive at r_2. From (16), (13a, c) we get

$$\frac{\nu'}{2} = \frac{\xi^6}{8r\dot{\xi}\xi_x}\left(\dot{g}^2\frac{\dot{\xi}}{\xi} + \frac{\dot{g}\ddot{g}}{2}\right) \quad [\text{for } r \leqslant r_1] \tag{20a}$$

$$= \frac{\xi^6}{8r\dot{\xi}\xi_x}\left(\dot{g}^2\frac{\dot{\xi}}{\xi} + \frac{\dot{g}\ddot{g}}{2} - \frac{8K_2\dot{\xi}}{\xi^7}\right) \quad [\text{for } r \geqslant r_2] \tag{20b}$$

ξ_x will be positive at r_1 and negative at r_2, hence the condition on ν' requires that the expression within the brackets in (20a) and (20b) should be negative at r_1 and r_2 respectively (we are taking $\dot{\xi}$ to be positive – this does not mean any loss of generality owing to the time reversal symmetry). Due to (18), if $K_2 \geqslant 0$, (20b) will be automatically positive if (20a) is negative, while if $K_2 \leqslant 0$, (20a) would be negative if (20b) is positive.

CC-0. In Public Domain. Gurukul Kangri Collection, Haridwar

Digitized by Arya Samaj Foundation Chennai and eGangotri

Specifically, the conditions are

$$\left(\frac{\dot{\xi}}{\xi}\right)_b + \frac{\ddot{g}}{2\dot{g}} < 0 \quad \text{if } \xi_1 \geqslant \xi_2$$

$$\left(\frac{\dot{\xi}}{\xi}\right)_b + \frac{\ddot{g}}{2\dot{g}} - \frac{16\pi\rho}{3}\frac{(\xi_1^6 - \xi_2^6)}{\dot{g}^2\xi^7} < 0 \quad \text{if } \xi_2 \geqslant \xi_1$$

where the subscript b indicates that the values at the boundaries are to be taken.

3. The behaviour of ξ within the fluid region

In general an integration of (13b) will bring in elliptic functions which will degenerate into trigonometric functions only if the rhs of (13b) has two identical roots. However such identical roots can only occur if η is a constant; but as already noted, in that case we do not have any solution. Without writing out the integral in terms of elliptic functions, we attempt to study the qualitative behaviour of ξ in different cases, depending on whether η is positive or negative.

Case I: $\eta \equiv \frac{1}{16}\left(\dot{g}^2 - \frac{32\pi\rho}{3}\right) \geqslant 0$

In Friedmann metric, the above condition corresponds to negative or zero spatial curvature and an ever-expanding space and the inequality, if true at one epoch, is maintained at all times. In the present case, however, there does not seem to be any guarantee that the inequality will be preserved. However at the epoch when this inequality holds, we find that ξ_x starting from a positive value at r_1 will have a monotonic increase with x (see (12a)) and hence $\xi_2 > \xi_1$ and K_2 will be negative. We shall see that this corresponds to a positive Schwarzschild mass for the shell.

Case II: $\eta \equiv \frac{1}{16}\left(\dot{g}^2 - \frac{32\pi\rho}{3}\right) < 0$

In ξ_x starting from a positive value will lead to an increasing ξ which will finally make ξ_x vanish and ξ having a maximum. With further increase of x, ξ will show a monotone decrease [see (12b) and (13b)]. Again we may consider three subcases. Case IIa: Let r_2 be such that $\xi_2 > \xi_1$; K_2 is negative in this case and the situation is not significantly different from case I considered above. Case IIb: $\xi_2 < \xi_1$, so that $K_2 > 0$. In this case ξ_x would not have any zero in the region $r > r_2$. Hence it will continue to be negative and as $|\xi_x| > (K_2)^{1/2}$ will vanish at a finite value of x in the vacuous region extending beyond r_2. Case IIc: $\xi_2 = \xi_1$ so that $K_2 = 0$: In this case also ξ shows a monotone decrease for $r > r_2$ but approaches zero only asymptotically for $r \to \infty$.

To have positive pressure in the fluid region, we have insisted that v' must be negative at r_1 and positive at r_2. In between, v' will have a zero where the pressure will have the maximum value and $\exp(v)$ its minimum.

From (15), the condition for the vanishing of v' is

$$\frac{\dot{\xi}_x}{\dot{\xi}} - \frac{\xi_x}{\xi} = 0 \tag{21}$$

CC-0. In Public Domain. Gurukul Kangri Collection, Haridwar

Digitized by Arya Samaj Foundation Chennai and eGangotri

or, $$\dot{\xi}_x\xi\xi_x - \xi_x{}^2\dot{\xi} = 0 \tag{22}$$

(Note that (22) does not lead to (21) if $\xi_x = 0$; hence (22) is a necessary but not a sufficient condition for the vanishing of v'). Substituting from (13b) we get from (22)

$$-\left(\frac{\pi\rho\xi^6}{3}\right)^{\cdot} + \tfrac{1}{8}\dot{g}^2\xi^5\dot{\xi} + \tfrac{1}{16}\dot{g}\ddot{g}\xi^6 + \frac{2\pi\rho}{3}\xi^5\dot{\xi} - \frac{K_1\dot{\xi}}{\xi} = 0.$$

Using the divergence relation $(\rho\xi^6)^{\cdot} = -6p\xi^6\dot{\xi}$, we get the expression for the maximum pressure (see (15)).

$$8\pi p = -\left[\frac{\dot{g}^2}{2} + \frac{\dot{g}\ddot{g}}{4}\frac{\xi}{\dot{\xi}} + \frac{8\pi\rho}{3}\left(1 - \frac{\xi_1{}^6}{\xi^6}\right)\right].$$

4. The fields in the vacuous regions

Equation (13a) may be readily integrated to give

$$\xi^4 = \frac{16a^2}{\dot{g}^2}\frac{u^2}{(a^2u^2-1)^2} \tag{23}$$

where

$$u = r^{-1} \quad \text{for } \xi_x > 0$$
$$= r \quad \text{for } \xi_x < 0$$

and 'a' is a function of t alone.

We shall take $\xi_x > 0$ in the region (1) so that ξ starting from zero at the origin will be positive. The function 'a' of t is fixed by the condition of continuity of ξ at $r = r_1$. We have already seen that the field in region $r_1 \leqslant r \leqslant r_2$ has been completely determined, the function C being determined by (19). Hence the continuity of ξ at r_1 will now determine 'a'. Once ξ is made continuous, the choice of K_1 by (15) ensures the continuity of ξ_x.

In the region $r > r_2$, the nature of the integral will depend on K_2. In case $K_2 \neq 0$, we shall have an elliptic function of the form, $\xi = f(x + b, \eta, K_2)$ and the arbitrary function b of t will be chosen so as to obtain the continuity of ξ at r_2. Again the choice of K_2 by (15) will ensure the continuity of ξ_x.

As is to be expected, in view of Birkhoff's theorem, the metric in this region may be transformed to the Schwarzschild form. The requisite transformations are (Raychaudhuri 1953)

$$\left(1 + \frac{m}{2\hat{r}}\right)^4 \hat{r}^2 = \xi^4 \tag{24}$$

$$\mathrm{d}\hat{t} = \left|\frac{8\dot{\xi}\xi_x}{\dot{g}(\xi^2 - 2m)}\right| \mathrm{d}t + \left|\frac{\xi^6\dot{g}}{2r(\xi^2 - 2m)}\right| \mathrm{d}r. \tag{25}$$

with $m = -2k_2$. The metric then assumes the form (1). Thus the Schwarzschild mass is related with the constant K_2. It is useful to note also that the so-called curvature

CC-0. In Public Domain. Gurukul Kangri Collection, Haridwar

Digitized by Arya Samaj Foundation Chennai and eGangotri

coordinate $\bar{r}$ which appears in the metric

$$ds^2 = \left(1 - \frac{2m}{\bar{r}}\right) dt^2 - \left(1 - \frac{2m}{\bar{r}}\right)^{-1} d\bar{r}^2 - \bar{r}^2(d\theta^2 + \sin^2\theta\, d\varphi^2) \tag{26}$$

is related with ξ by

$$\bar{r}^2 = \xi^4.$$

Consider now the case $\xi_2 > \xi_1$. In view of (15) and (25), the Schwarzschild mass is positive. Then at r_2, one may have $\xi_x > 0$, with either sign of η (see figures 1 and 2). In any case, an increasing ξ will increase the value of ξ_x and for large values of ξ,

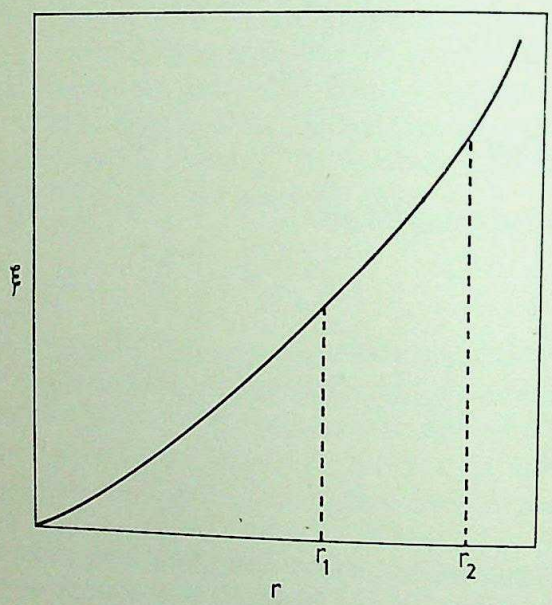

Figure 1. (not to scale) Case $\eta > 0$ $\xi_2 > \xi_1$.

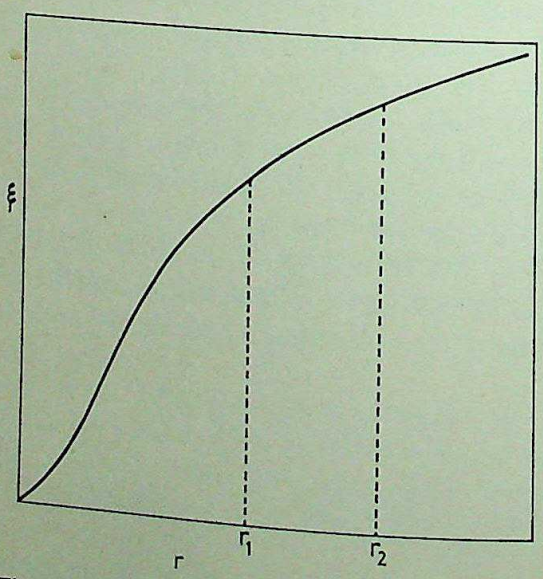

Figure 2. (not to scale) Case $\eta < 0$, $\xi_2 > \xi_1$, $(\delta\xi/\delta x)_2 > 0$.

CC-0. In Public Domain. Gurukul Kangri Collection, Haridwar

Digitized by Arya Samaj Foundation Chennai and eGangotri

(13c) will have the asymptotic form

$$\xi_x^2 = \tfrac{1}{16}\dot{g}^2\xi^6.$$

The above equation integrates to give

$$\frac{2}{\dot{g}\xi^2} = q(t) - x.$$

Thus at a finite value of $x = q$, ξ^2 will blow up. This apparent singularity is however easily understood, when one notes that in view of (27) the corresponding $\bar{r} \to \infty$. Thus the singularity appears only because the sphere at infinity is mapped out at a finite value of ξ.

If however $\xi_x < 0$ at ξ_2 as may be the case with $\eta < 0$, ξ will have a minimum at ξ_0 where

$$\tfrac{1}{4}\xi_0{}^2 + \tfrac{1}{16}\dot{g}^2\xi_0{}^6 = \frac{m}{2}. \tag{27}$$

or,

$$\xi_0{}^2 < 2m.$$

Beyond this minimum, ξ will have a monotone increase, tending to ∞ as $r \to \infty$ (see figure 3). As $\xi_0{}^6 < 2m$ corresponds to $\bar{r} < 2m$, one has the interesting situation that there is a Schwarzchild horizon but no Schwarzschild singularity corresponding to ($\xi^2 = \bar{r} = 0$).

Next let us suppose $\xi_2 < \xi_1$. In this case, we must have $\eta < 0$ and $\xi_x < 0$ at r_2. K_2 is now positive and the Schwarzschild mass negative. Equation (13c) shows that ξ_x cannot have any zero in the region $r > r_2$ and as $|\xi_x| > (K_2)^{1/2}$, ξ will vanish at a finite value of r (figure 5). The vanishing of ξ corresponds to $r = 0$ where there is a physical singularity as evident from the blowing up of the Riemann scalar $R_{\alpha\beta\gamma\delta}R^{\alpha\beta\gamma\delta}$. Thus one has to interpret the situation in the following manner—at $r = 0$, there is a negative mass particle, it is covered by a shell of positive mass exactly equal in magnitude to the negative mass of the particle. The resulting system has a vanishing

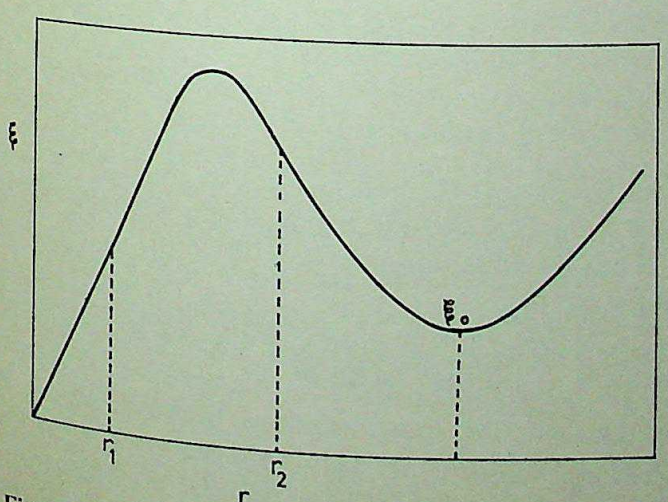

Figure 3. Case $\eta < 0$, $\xi_2 > \xi_1$. $(\delta\xi/\delta x)_2 < 0$. Note minimum at ξ_0 [$(\xi_0{}^2 < 2m)$].

CC-0. In Public Domain. Gurukul Kangri Collection, Haridwar

Digitized by Arya Samaj Foundation Chennai and eGangotri

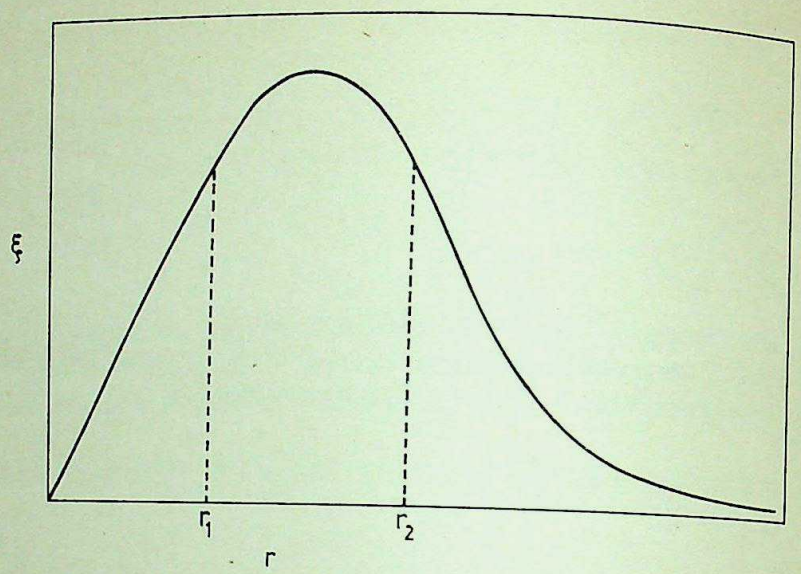

Figure 4. Case $\eta < 0$, $\xi_2 = \xi_1$, $K_2 = 0$ (zero mass case) $\xi \to 0$ as $r \to \infty$.

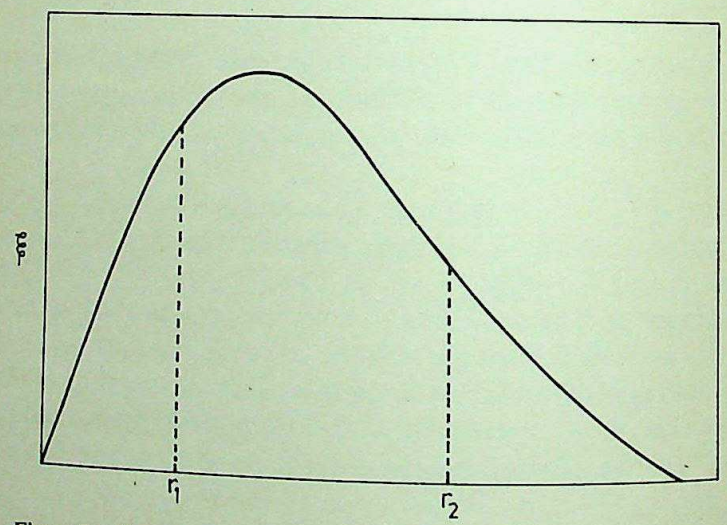

Figure 5. Case $\eta < 0$, $\xi_2 < \xi_1$, $K_2 > 0$ (negative mass case) ξ vanishes at finite r.

mass and thus one has a flat space-time beyond. In this picture the negative mass particle is at the centre of symmetry and the region which we have termed region I is euclidean but closed. In any case this situation does not allow us to assign a negative mass for a shell of positive density.

If however $\xi_2 = \xi_1$, $(\xi_x)_{r_2} < 0$, $K_2 = 0$; the Schwarzschild mass vanishes and (13c) reduces to (13a) (see figure 4). ξ will then be given by

$$\xi^4 = \frac{16S^2}{\dot{g}^2} \frac{\dot{r}^2}{(S^2r^2 - 1)^2} \quad (r \geq r_2) \tag{28}$$

where the function $S(t)$ is to be determined by the continuity of ξ at r_2. In fact the

CC-0. In Public Domain. Gurukul Kangri Collection, Haridwar

Digitized by Arya Samaj Foundation Chennai and eGangotri

relation between S and a can be easily written out

$$\frac{S^2 r_2^{\,2}}{(S^2 r_2^{\,2}-1)^2} = \frac{a^2}{r_1^{\,2}\left(\frac{a^2}{r_1^{\,2}}-1\right)^2}.$$

This leads to a quadratic equation for S which may be solved to give S in terms of a. It is clear from (28) that ξ will vanish as $r\to\infty$; however, the space-time in this region is euclidean as follows from the transformation to the Schwarzschild form with $m=0$. Only the space is now closed. Thus the shell although has a positive density and pressure everywhere does not produce any departure from euclidean geometry in the adjoining space except bringing about a closure ($e^{\mu}\to 0$ as $r\to\infty$).

One may be tempted to give an alternative interpretation as suggested by the transformation to the Schwarzschild coordinate $\bar{r}$ ($\bar{r}^2=\xi^4$). The two regions which we have considered to be on opposite sides of the shell then get mapped in the same domain of $\bar{r}$—the sphere at infinity ($r\to\infty$, $\xi\to 0$) goes to the origin and the surface $r_2(\xi_2)$ to the surface r_1 (ξ_1). One may then suggest that the situation pictured above is merely of a vacuous region with the shell appearing as a singular boundary of the space.

However, the transformation to Schwarzschild coordinate bringing about a merging of two apparently distinct regions may be criticized as suppressing some aspects of the situation. One may cite the Schwarzschild black hole as an analogous case. The black hole and the white hole which appear separated in (say) the Kruskal–Szekeres coordinates are fused into a single region in the Schwarzschild coordinates and altogether disappear in the isotropic coordinates $\hat{r}$. There one prefers the Kruskal–Szekeres picture as giving the maximal extension. Here also we argue that the picture given by ξ is a maximal extension and the present discussion has indeed revealed an intriguing situation where a system of positive mass density and pressure appear to have vanishing mass to outside observers.

5. Newtonian analogue

Although it is quite conceivable that general relativity situations where the field is not weak may not have any newtonian analogue, it is interesting to explore the possibility of such analogues. In the newtonian case one may consider the energy to consist of three distinct parts—the kinetic energy (the random part being associated with pressure) which is positive definite, the negative gravitational potential energy and the rest mass energy which again is assumed to be positive. Thus the possibility of a non-positive total energy arises from the gravitational potential energy which varies as the fifth power of the radius for a given density (recall the expression for potential energy $\sim GM^2 r^{-1} \approx G\rho^2 r^5$). The rest mass energy $M_c^{\,2}\sim \rho r^3 C^2$. Hence with r sufficiently large one sees the possibility of the total energy being negative.

However with the physically realistic equations of state, one knows that the equilibrium condition sets upper bounds to the mass and radius and consequently one cannot have a non-positive energy for systems in equilibrium.

The situation may be different for dynamic systems as considered in the present investigation.

CC-0. In Public Domain. Gurukul Kangri Collection, Haridwar

Digitized by Arya Samaj Foundation Chennai and eGangotri

6. Concluding remarks—earlier models of zero-mass

The integration of the field equations have brought in a number of undetermined functions of time e.g. $\dot{g}, a, b, c$ and S. However the conditions of continuity have linked up a, b, c, S with $\dot{g}$ and ρ (cf eq. (19)). Thus finally there remain two free functions of time $\dot{g}$ and ρ and two free parameters r_1 and r_2. It is natural to pose the question as to whether there is any constraint on their choice and the nature of the dependence of the solution on these functions and parameters. While it is not possible to spell out clearly the constraints on these, it is fairly obvious that they are not quite free, e.g. in the Friedmann case one cannot take ρ to be a constant as that would lead to a negative pressure. Again it is not possible to get rid of the function $\dot{g}$ by a mere scaling of the time coordinate as may appear from (16). This is because (10) can be written as

$$\left(\frac{\mathrm{d}\mu}{\mathrm{d}S}\right)^2 = \dot{g}^2$$

where $\mathrm{d}s\,(\equiv \exp(\nu/2)\,\mathrm{d}t)$ is the proper time interval as measured by an observer moving with the fluid. Thus for a simple transformation $t \to f(t)$, $\dot{g}$ is an invariant.

Lake and Roeder (1978) have attempted to establish a distinction between interior and exterior across a surface Σ of discontinuity. Thus they argue "whereas an exterior field arises due to the matter distribution interior to Σ, an interior field does not arise due to the matter distribution exterior to Σ". However in our case, this distinction disappears as the metrics in the interior and exterior vacua are both reducible to the Minkowski form. The same situation holds regarding the other criteria put forward by Lake and Roeder. Indeed one may be tempted to conclude that Lake and Roeder's work suggests an identification of the two vacua but as we have already pointed out, this appears to be an incomplete description of the space-time.

We next consider the zero-mass situations that appear already in the literature. Zel'dovich (1962) considers a star passing through a momentarily static configuration such that each element is just beyond the horizon i.e. if $m(\bar{r})$ represents the mass of the system up to the (curvature) coordinate $\bar{r}$, $\bar{r} = 2m\,(\bar{r}) + 0$. Now the metric is of the form

$$\mathrm{d}s^2 = \left(1 - \frac{2m}{\bar{r}}\right)\exp(2\psi)\,\mathrm{d}t^2 - \left(1 - \frac{2m}{\bar{r}}\right)^{-1}\mathrm{d}\bar{r}^2 - \bar{r}^2(\mathrm{d}\theta^2 + \sin^2\theta\,\mathrm{d}\varphi^2) \tag{29}$$

where m and ψ are functions of r and t with

$$m = 4\pi\int_0^r T^0_0\bar{r}^2\,\mathrm{d}\bar{r}. \tag{30}$$

The baryon number A can be expressed in terms of their number density n:

$$A = 4\pi\int nv^0\exp(\psi)\bar{r}^2\,\mathrm{d}\bar{r}. \tag{31}$$

For a perfect fluid, one has

$$T^{\mu}{}_{r} = (p+\rho)v^{\mu}v_r - p\delta^{\mu}{}_{r}. \tag{32}$$

CC-0. In Public Domain. Gurukul Kangri Collection, Haridwar

Digitized by Arya Samaj Foundation Chennai and eGangotri

Using this expression in (30) and changing the integration variable from r to A by (31) we get

$$m = \int \frac{\rho}{n} \exp(-\psi) v_0 \, dA + 4\pi \int p \left(1 - \frac{2m}{\bar{r}}\right) v_1{}^2 \, d\bar{r}. \tag{33}$$

It is argued that for a momentarily static situation $v_1 = 0$, so that the second integral vanishes. Also, then

$$\exp(-\psi) v_0 = \left[1 - \frac{2m}{\bar{r}}\right]^{\frac{1}{2}} \to 0 \tag{34}$$

as $\bar{r} \to 2m$. Thus from (33) $m = 0$. But with (34), $A \to \infty$ (see (31)). Thus the Zel'dovich configuration, admittedly artificial as pointed out by Leibovitz and Israel (1970), is not at all realisable for finite baryon number.

Indeed from (30) and (31) it follows that with p and ρ non-negative, m can vanish only if $d\bar{r}$ changes sign within the domain of integration. This is the case in our solution as well as in the model of Harrison *et al* (1965) who change the variable from $\bar{r}$ to χ by the relation

$$\bar{r} = \left(\frac{8\pi\rho}{3}\right)^{-\frac{1}{2}} \sin\chi$$

the domain of χ being set as $0 \leqslant \chi \leqslant \pi$. Obviously $d\bar{r}$ changes sign at $\chi = \pi/2$. Thus for a momentarily static sphere of uniform density

$$m = 4\pi\rho \int \bar{r}^2 \, d\bar{r} = 4\pi\rho \left(\frac{8\pi\rho}{3}\right)^{-3/2} \int_0^{\pi} \sin^2\chi \cos\chi \, d\chi$$

now vanishes. However $\chi = \pi$ makes the space closed. Thus while in our solution, there exists an outside vacuum where the Schwarzschild mass vanishes, in the situation conceived by Harrison *et al*, there is no outside vacuum and so it is not meaningful to talk of a Schwarzschild mass. Leibovitz and Israel have argued that the Harrison *et al* distribution is in the left quadrant of the Kruskal diagram while we, the observers, are in the right quadrant; so no communication is possible. However, it seems more natural to say that the distribution covers all space and thus there is no outside rather than invoking oddities of the Kruskal diagram.

Acknowledgements

Thanks are due to the UGC for financial support to one of the authors (SB) under the special assistance programme and to the INSA for the award of a Senior Scientist position to AKR.

Appendix

A special class of solutions

$$\xi_x^2 = \gamma(\xi^2 - \alpha)^2 (\beta - \xi^2).$$

CC-0. In Public Domain. Gurukul Kangri Collection, Haridwar

Digitized by Arya Samaj Foundation Chennai and eGangotri

The above form obtains if there are two equal roots α. Here

$$\gamma = \frac{1}{16}\left(\frac{32\pi\rho}{3} - \dot{g}^2\right)$$

$$\alpha^2\beta\gamma = K_1$$

$$2\alpha + \beta = 0 \rightarrow \beta = -2\alpha$$

$$-\gamma\alpha(2\beta + \alpha) = \tfrac{1}{4}.$$

One can solve these equations

$$\alpha = -6K_1, \quad \beta = 12K_1, \quad \gamma = \frac{1}{432{K_1}^2}.$$

Note that γ is independent of t. As noted, in this case no solution can occur. However the integration can be performed to give

$$\frac{\beta}{\xi^2} = 1 + 3\cot^2\left(\frac{x + C}{2}\right)$$

where C is apparently a function of time but if we impose (19), C must be a constant and the solution does not exist (for then $\dot{\xi} = 0$ or $e^{\nu} = 0$).

References

Einstein A and Straus E G 1945 *Rev. Mod. Phys.* **17** 120
Einstein A and Straus E G 1946 *Rev. Mod Phys.* **18** 148
Harrison B K, Thorne K S, Wakano M and Wheeler J A 1965 *Gravitation theory and gravitational collapse* (Chicago: University of Chicago Press) pp. 73–75
Lake K and Roeder R C 1978 *Phys. Rev.* **D17** 1935
Leibovitz C and Israel W 1970 *Phys. Rev.* **D1** 3226
Raychaudhuri A K 1953 *Phys. Rev.* **89** 417
Zel'dovich Ya B 1962 *Zh. Eksp. Teor. Fiz.* **42** 641; *Sov. Phys. JETP* **15** 446

CC-0. In Public Domain. Gurukul Kangri Collection, Haridwar

Digitized by Arya Samaj Foundation Chennai and eGangotri

Pramāṇa – J. Phys., Vol. 34, No. 5, May 1990, pp. 397–401. © Printed in India.

Spherically symmetric solutions with heat flow in general relativity

A BANERJEE, S B DUTTA CHOUDHURY and B K BHUI
Department of Physics, Jadavpur University, Calcutta 700 032, India

MS received 1 September 1989; revised 6 January 1990

Abstract. Some new solutions of shear-free imperfect fluid spheres with heat flux in the radial direction are obtained. They have isotropic pressure and could be the generalizations of earlier solutions of Nariai and of Banerjee and Banerji for perfect fluid without dissipation.

Keywords. Cosmology; imperfect fluid; general relativity; spherically symmetric solution.

PACS Nos 04·20; 95·30

1. Introduction

It is interesting to investigate the problem of gravitational collapse of stars with dissipation in the form of radial heat flow in the sense that it gives a more general picture of the collapse problem that what is described in a simple adiabatic fluid. Such models were proposed by Bergmann (1981) and later generalized by Modak (1984). The problem of matching the interior solutions with the exterior Vaidya (Vaidya 1953) metric representing a radial unpolarized radiation flux was studied by Santos (1985), as well as by de Oliveria *et al* (1986).

In the present paper we present some new interior solutions for an isotropic spherically symmetric dissipative fluid with heat flow in the radial direction which is an extension of the previous perfect fluid solutions of Buchdahl (1964), Nariai (1967) and Banerjee and Banerji (1976) to include the heat flow terms in the energy momentum tensor. The condition of fit at the boundary in one of the simple cases discussed. The density, pressure and heat flux terms are also calculated in this particular class of solutions. In other cases these expressions are rather complicated and definite conclusions cannot be derived without suitable assumptions.

2. Einstein's fixed equations and their solutions

We start with the well-known isotropic form of the spherically symmetric metric

$$\mathrm{d}S^2 = A^2\,\mathrm{d}t^2 - B^2(\mathrm{d}r^2 + r^2\,\mathrm{d}\theta^2 + r^2\sin^2\theta\,\mathrm{d}\phi^2), \tag{1}$$

where A, B are functions of r and t. The energy momentum tensor for a fluid with heat flux is expressed in the standard form as

$$T^{\mu}_{\nu} = (\rho + p)v^{\mu}v_{\nu} - p\delta^{\mu}_{\nu} + q^{\mu}v_{\nu} + v^{\mu}q_{\nu}, \tag{2}$$

CC-0. In Public Domain. Gurukul Kangri Collection, Haridwar

Digitized by Arya Samaj Foundation Chennai and eGangotri

where q^μ represents the heat flow vector which is orthogonal to the velocity vector v^μ. In the present spherically symmetric case the radial component q^1 is nonvanishing. In comoving coordinates we have $v^\mu = \delta^\mu_4 A^{-1}$ and in Einstein's field equations the isotropy of pressure leads to the following equation (see Bergmann 1981)

$$A_{xx} + 2(F_x/F)A_x - (F_{xx}/F)A = 0, \tag{3}$$

where F is written for B^{-1} and x for r^2. For adiabatic motion, that is when there is no heat flux, the solutions must satisfy another field equation $G^1_4 = 0$ and this combined with (3) yields the perfect fluid solutions. The solutions of equation (3) for which $G^1_4 \neq 0$ allow heat flux through the fluid and were previously obtained by others as mentioned in §1. These solutions may be astrophysically interesting and more such solutions are worth investigating.

One of the groups of solutions is obtained by imposing simplifying assumptions regarding A and F in (3). Some such solutions are as follows:

(i) *Bergmann solution*:

$A = A(t)$, which results in $F_{xx} = 0$ and yields without any loss of generality

$$A = 1, \quad B = \frac{R(t)}{1 + \xi(t)r^2}, \tag{4}$$

$\xi(t)$ being an arbitrary function of time.

(ii) *Modak solution*:

$F_{xx} = 0$, so that one gets the solutions in the form

$$A = \left(1 + \frac{a(t)}{1 + \xi(t)r^2}\right), \quad B = \frac{R(t)}{1 + \xi(t)r^2}. \tag{5}$$

This solution is conformally flat and is the most general conformally flat solution of the above type for the metric (1). A special case of (5) was given by Maiti (1982) with $\xi(t) =$ constant.

(iii) The assumption $A_{xx} = 0$ yields the solutions

$$A = [1 + \xi(t)r^2], \quad B = \frac{R(t)}{[1 + \xi(t)r^2]^3}, \tag{6}$$

where ξ and R are arbitrary functions of time.

(iv) Another class of solutions for the metric (1) representing fluid with heat flux in the radial direction is obtained by generalizing the perfect fluid solutions of Nariai and of Banerjee and Banerji.

These solutions are completely new. The metric chosen in this case is in the form originally given by Buchdahl (1964) for his static solutions. These are

$$A = (1 - f)/(1 + f), \quad B = S(t)(1 + f)^2. \tag{7}$$

CC-0. In Public Domain. Gurukul Kangri Collection, Haridwar

Digitized by Arya Samaj Foundation Chennai and eGangotri

The function f is assumed to be the form $f=[R(r)\cdot K(t)]$ suggested originally by Nariai. The isotropy of the pressure then demands that R and K must satisfy the following equation

$$2R^3R''K^4-2RR''K^2+6R'^2K^2-6R^2R'^2K^4+\frac{2RR'K^2}{r}-\frac{2R^3R'K^4}{r}=0. \quad (8)$$

It is easy to show that the above equation is satisfied if we have the following simple equation satisfied

$$(R''/R')-(3R'/R)-(1/r)=0. \quad (9)$$

The dash sign stands for the derivative with respect to r. The solutions of (9) will satisfy (8). Equation (9) with $R'\neq 0$ yields the solutions, in view of (7) as follows

$$A=\frac{(Tz^{1/2}-1)}{(Tz^{1/2}+1)}, \quad B=\frac{(Tz^{1/2}+1)^2}{T_1 z}, \quad (10)$$

where $z=1+ar^2$, a being an arbitrary constant, $T(t)=K^{-1}$ and T_1 is another arbitrary function of time. In the special case $T_1=T$ we get Nariai's inhomogeneous perfect fluid solution, otherwise when $T_1\neq T$ there is heat flux. We calculate the pressure, density and heat flux for a simple case where $T_1=1$. These are

$$8\pi p=\frac{4a}{X^5Y}-\frac{4z^{1/2}}{Y^3}[\ddot{T}XY-4\dot{T}^2z^{1/2}+2T\dot{T}^2z], \quad (11)$$

$$8\pi\rho=(12a/X^5)+(12\dot{T}^2z/Y^2), \quad (12)$$

$$8\pi q^1B=-(4\dot{T}z^{1/2}ar/X^2Y^2), \quad (13)$$

where we have written $X=(Tz^{1/2}+1)$ and $Y=(Tz^{1/2}-1)$. The contraction takes place for $\dot{T}<0$. The constant a is chosen to be positive in order that ρ remains positive even when $\dot{T}=0$ at the turning point. One can refer to the matching conditions at the boundary where the interior metric can fit with the exterior radiating Vaidya metric. Here the interior spacetime V^- of the system is represented by a nonadiabatic spherically symmetric shear-free collapsing fluid undergoing dissipation in the form of a radial heat flow. While the fluid collapses it produces unpolarized radiation and hence the exterior space-time V^+ of the sphere is described by the Vaidya metric. We have therefore in the interior the metric (1), but the exterior is represented by the Vaidya metric

$$dS^2=\left(1-\frac{2m(v)}{\bar{r}}\right)dv^2-2\,dv\,d\bar{r}+\bar{r}^2(d\theta^2+\sin^2\theta\,d\phi^2),$$

where m, the total energy of the system, is a function of the retarded time v. The intrinsic metric to the hyper-surface Σ as a part of their boundaries is given by

$$dS_\Sigma^2=g_{ij}\,d\xi^i\,d\xi^j=d\tau^2-A^2(\tau)(d\theta^2+\sin^2\theta\,d\phi^2).$$

The conditions of fit need the continuity of the first and second fundamental forms

CC-0. In Public Domain. Gurukul Kangri Collection, Haridwar

Digitized by Arya Samaj Foundation Chennai and eGangotri

at the boundary hypersurface (Santos 1985) which in turn lead to a relation

$$(p + Bq^1)_\Sigma = 0,$$

where the subscript Σ indicates the value at the boundary surface $r = r_\Sigma$.

It is evident from the above boundary condition that the pressures does not vanish at the boundary as long as there is a heat flux across it. The interior matches with the Schwarzschild's exterior solution only in the absence of the heat flow. In the present case the exterior is the Vaidya metric which includes a time-dependent mass function $m(v)$. This function, however, decreases with time as the energy flows across the boundary in the radial direction.

The behaviour of the sphere now depends on the choice of the function $T(t)$. Consider the instant $\dot{T} = 0$, when the pressure-heat flux relation at the boundary mentioned above reduces in view of (11) and (13), to

$$\ddot{T} = aY_\Sigma/(X_\Sigma^6 Z_\Sigma^{1/2}). \tag{14}$$

Since the relation (14) corresponds to the situation $\dot{T} = 0$, which means a turning point in the motion of the sphere, we get a maximum or a minimum to the dimension according as $\ddot{T} < 0$ or $\ddot{T} > 0$. Again we note that for $\ddot{T} < 0$ the constant a turns out to be negative and as a result the density ρ can attain only negative magnitude at this turning point, which however, does not give a physically realistic model. So for a reasonable model one should choose the function T in such a way that it must possess the property $\ddot{T} > 0$ at the moment $\dot{T} = 0$ (if it has at all a turning point). It can, therefore, represent only a minimum putting a lower limit to the dimension of a contracting sphere. One further notes that apart from a singularity of the type $X = 0$, there may be another kind of singularity given by

$$Y = 0 \text{ that is } Tz^{1/2} = 1.$$

The other classes of solutions of equation (3) we wish to present, are the direct generalizations of the perfect fluid solutions given previously by Nariai and Banerjee and Banerji. In the first case the solutions of (3) are

$$A = \frac{Tz^{1/2} - \alpha}{Tz^{1/2} + \alpha}, \quad B = \frac{(Tz^{1/2} + \alpha)^2}{Tz}. \tag{15}$$

In the second case the appropriate solutions are given by

$$A = \frac{1}{T}\frac{z}{(z + a/T)}, \quad B = \frac{T^2}{z^3}(z + b/T)^2, \tag{16}$$

where in both cases $z = 1 + \eta(t)\, r^2$, with $\eta(t)$ an arbitrary function of time and b, α are constants. Putting $\eta(t) =$ constant one gets back Nariai's perfect fluid solution from (15) and that of Banerjee and Banerji from (16). We have not investigated in detail the scalars like pressure and density which we hope to do in a subsequent paper.

Acknowledgement

Thanks are due to CSIR, New Delhi for financial support.

CC-0. In Public Domain. Gurukul Kangri Collection, Haridwar

Digitized by Arya Samaj Foundation Chennai and eGangotri

References

Banerjee A and Banerji S 1976 *Acta Phys. Pol.* **B7** 389
Bergmann O 1981 *Phys. Lett.* **A82** 383
Buchdahl H A 1964 *Astrophys. J.* **140** 1512
de Oliveria A K G, de F Pacheco J A and Santos N O 1986 *Mon. Not. R. Astron. Soc.* **220** 405
Maiti S R 1982 *Phys. Rev.* **D25** 2518
Modak B 1984 *J. Astrophys. Astron.* **5** 317
Nariai H 1967 *Prog. Theor. Phys.* **38** 92
Santos N O 1985 *Mon. Not. R. Astron. Soc.* **216** 403
Vaidya P C 1953 *Nature (London)* **171** 260

CC-0. In Public Domain. Gurukul Kangri Collection, Haridwar

Digitized by Arya Samaj Foundation Chennai and eGangotri

CC-0. In Public Domain. Gurukul Kangri Collection, Haridwar

Digitized by Arya Samaj Foundation Chennai and eGangotri

Pramāṇa – J. Phys., Vol. 34, No. 5, May 1990, pp. 403–414. © Printed in India.

Wave function with second order correction and inflationary solutions in quantum cosmology

SUBENOY CHAKRABORTY
Department of Mathematics, Jadavpur University, Calcutta 700032, India

MS received 3 August 1989

Abstract. A brief account for the higher order wave function in Hartle-Hawking (H–H) proposal is given which is compared with the tunneling wave function due to Vilenkin. The probability distributions are determined for both types of wave functions. Also a class of solutions are evaluated using H–H approach for Kantowski–Sachs metric with a scalar field and inflation is observed.

Keywords. Path-integral; tunneling; wave function; inflation; saddle point.

PACS Nos 04·20; 98·90

1. Introduction

In recent years exciting developments have taken place in quantum cosmology. To know the early stages of the evolution of the universe (where quantum effects are important) two appealing approaches have been suggested. In the first proposal, Vilenkin (1988) has considered quantum tunneling from nothing, i.e. creation of the universe from nothing to describe the spontaneous nucleation of the universe and then evolves in an inflationary manner using the idea of Linde (1984). The second method has been developed by Hartle and Hawking (1983), combining ideas of canonical and path-integral quantization of general relativity. In this proposal, the wave function of the universe is given by a path integral over compact Euclidean geometries. They showed that for conformally non-invariant field, the desirable cosmological phenomenon of inflation can occur at early stages of the evolution without any phase transition. A comparison between these two approaches has been studied by Vilenkin (1988). The tunneling boundary conditions can be written as "at singular boundaries of superspace, includes only outgoing modes". On the other hand, in the H–H approach the boundary condition is that it has no boundary.

In this paper I consider the H–H approach with higher order correction to the wave function, by the saddle point method (Morse and Feshback 1953) and discuss the cosmological predictions. The tunneling wave functions are also evaluated using the approach of Vilenkin by analytic continuation and the probability distributions are calculated for both types of wave functions. An exhaustive set of solutions for Kantowski–Sachs model are evaluated using H–H proposal for a scalar potential in the field $\frac{1}{2}\lambda\phi^n$. The paper is organised as follows:

Section 2 reviews the basic formalism of H–H proposal and compared with tunneling approach. A collection of solutions for both classical and classically forbidden region are given in §3. The conclusions are given in §4.

CC-0. In Public Domain. Gurukul Kangri Collection, Haridwar

Digitized by Arya Samaj Foundation Chennai and eGangotri

2. Wave function with second order correction in H–H approach and comparison with tunneling wave function

The wave function of the universe is defined by the Euclidean path integral (Fang and Ruffinm 1987).

$$\psi_{HH}(h_{ij}, \phi) = \int \mathrm{d}[g_{\mu\nu}]\,\mathrm{d}[\phi]\exp[-I_E(g_{\mu\nu}, \phi)]. \tag{1}$$

The integral is taken over all compact-Euclidean 4-geometries $g_{\mu\nu}$ and regular matter fields ϕ. The three metric h_{ij} and ϕ, appearing in the argument of ψ_{HH} are boundary condition of the Wheeler–De-Witt equation

$$\hat{H}_{\perp}\psi = 0. \tag{2}$$

It also satisfies the supermomentum constraints

$$\hat{H}_i\psi = 0. \tag{3}$$

As the path integral (1) has no precise definition so its qualitative behaviour can be obtained using semi-classical techniques in simple cosmological models. Equivalently the Wheeler–De-Witt equation is a second order hyperbolic differential equation on superspace. To solve it one restricts to minisuperspace. So the boundary conditions in the semi classical approximation to the wave function is in the form (Fang and Ruffinm 1987).

$$\psi[h_{ij}, \phi] = N_0 \sum A_i \exp(-B_i), \tag{4}$$

where N_0 is a normalization constant and B_i is the action of the classical solution with arguments of ψ on the boundary. The prefactors A_i denote fluctuations about classical solutions.

Hartle and Hawking has started with four geometrics to be spatially homogeneous, isotropic and closed and is given in a useful co-ordinate system by

$$\mathrm{d}s^2 = \sigma^2[-N^2(t)\cdot\mathrm{d}t^2 + a^2(t)\cdot\mathrm{d}\Omega_3^2], \tag{5}$$

where $\mathrm{d}\Omega_3^2$ is the metric on the unit three sphere S^3. The overall prefactor is taken to be

$$\sigma^2 = 2G/3\pi,$$

where G is Newton's constant ($\hbar = c = 1$), $a(t)$ is the cosmic scale factor. For matter degrees of freedom they consider a single conformally invariant scalar field $\phi = \phi(t)$.

The Lorentzian action with positive cosmological constant Λ is given by

$$S = \tfrac{1}{2}\int Na^3\left(-\frac{\dot{a}^2}{N^2a^2} + \frac{1}{a^2} + \lambda + \frac{\dot{\chi}^2}{N^2a^2} - \frac{\dot{\chi}^2}{a^4}\right)\mathrm{d}t, \tag{6}$$

where

$$\chi = (2\pi^2\sigma^2)^{1/2}a\phi, \quad \text{and } \lambda = \tfrac{1}{3}\sigma^2\Lambda.$$

The Wheeler–De-Witt equation is

$$\frac{1}{2}\left[\frac{1}{a^p}\frac{\partial}{\partial a}\left(a^p\cdot\frac{\partial}{\partial a}\right) - a^2 + \lambda a^4 - \frac{\partial^2}{\partial\chi^2} + \chi^2\right]\psi(a, \chi) = 0. \tag{7}$$

CC-0. In Public Domain. Gurukul Kangri Collection, Haridwar

Digitized by Arya Samaj Foundation Chennai and eGangotri

The index p represents some (not all) of the factor ordering ambiguity in the above equation. Its value will not make great difference in the nature of the solution. Then according to H–H proposal the wave function is given by the path integral

$$\psi_0(a_0, \chi_0) = \int \delta a \delta \chi \exp(-I_E(a, \chi)), \tag{8}$$

over compact 4-geometrics and matter field configuration $\chi(\tau)$, which has the value χ_0 on the boundary. The compact 4-geometry is given by

$$ds^2 = \sigma^2[d\tau^2 + a^2(\tau)\, d\Omega_3^2], \tag{9}$$

for which $a(\tau)$ matches a_0 on the given boundary. The Euclidean action I_E is given by

$$I_E = \tfrac{1}{2}\int d\eta \left[-\left(\frac{da}{d\eta}\right)^2 + a^2 + \lambda a^4 + \left(\frac{d\chi}{d\eta}\right)^2 + \chi^2 \right], \tag{10}$$

with

$$\eta = \int \frac{d\tau}{a}.$$

In the K-representation (Hartle *et al* (1983)) the wave function is given by

$$\phi_0(k_0, \chi_0) = \int \delta a \delta \chi \exp(-I^k(a, \chi)). \tag{11}$$

The sum is over the same class of 4-geometry and matter field but on the boundary $k = k_0$ is prescribed instead of $a = a_0$. Here $k = \sigma K/9$ is the simplifying measure of K (extrinsic curvature) and is related to a (τ) by the relation

$$k = \frac{1}{3a}\frac{da}{d\tau}. \tag{12}$$

The action I^k is related to I_E as

$$I^k = K_0 a_0^3 + I_E. \tag{13}$$

So the ground state wave function may be recovered by inverse Laplace transform as

$$\psi_0(a_0, \chi_0) = -\frac{1}{2\pi^2}\int_c dk \exp(k a_0^3)\phi_0(k, \chi_0), \tag{14}$$

where the contour runs from $-i\infty$ to $+i\infty$ to the right of any singularity of $\phi_0(k, \chi_0)$. Now separating the gravitational and field part in the action (10) the wave function $\psi_0(a)$ for pure gravitational part can be written as

with
$$\psi_0(a) = -\frac{N}{2\pi i}\int_c dK \exp[Ka^3 - I_E^k(k)], \tag{15}$$

$$I_E^k(k) = -\frac{1}{3H^2}\left(1 - \frac{3K}{(9K^2 + H^2)^{1/2}}\right) \text{ and } H^2 = \lambda. \tag{16}$$

CC-0. In Public Domain. Gurukul Kangri Collection, Haridwar

Digitized by Arya Samaj Foundation Chennai and eGangotri

The contour integral in (15) is now evaluated by the saddle point method retaining terms up to 2nd order (which indicates fluctuation about classical solution).

For $aH < 1$, the dominant contribution to the integral (15) comes from the stationary phase point

$$K = \frac{H}{3}\tan\alpha, \quad \text{with } \cos\alpha = aH.$$

(There are also complex extrema but all have real part less than $(H/3)\tan\alpha$).

So by distorting the contour (as H–H) into the steepest-descent path $u = (H/3)\tan\alpha$ (near the saddle point) in the k-plane ($k = u + iv$) (see figure 1(a)), we obtain the ground state wave function in the classically forbidden region ($aH < 1$) as

$$\psi_{HH}(a) = \frac{N}{3\sqrt{2\pi}a^2(1-a^2H^2)^{1/4}} \exp\left[\{1-(1-a^2H^2)^{3/2}\}/3H^2\right]. \tag{17}$$

Moreover, at the tunneling point ($aH = 1$) we have

$$\psi_{HH}(a) = \frac{N}{\sqrt{2\pi}} \exp(-1/3H^2), \tag{18}$$

where $k = 0$ is the saddle point with dominant real part. In this case the whole of $u = 0$ can be taken as the path of integration (see figure 1(b)). Lastly, in the classical region i.e. for $aH > 1$ there are no real extrema. This is expected as it is not possible to bound a 4-sphere of radius $1/H$ by a 3-sphere of radius a. Hence we obtain two complex saddle points with larger real part and are given by

$$k = \pm(ih/3)\tanh\alpha, \text{ where } \cosh\alpha = aH.$$

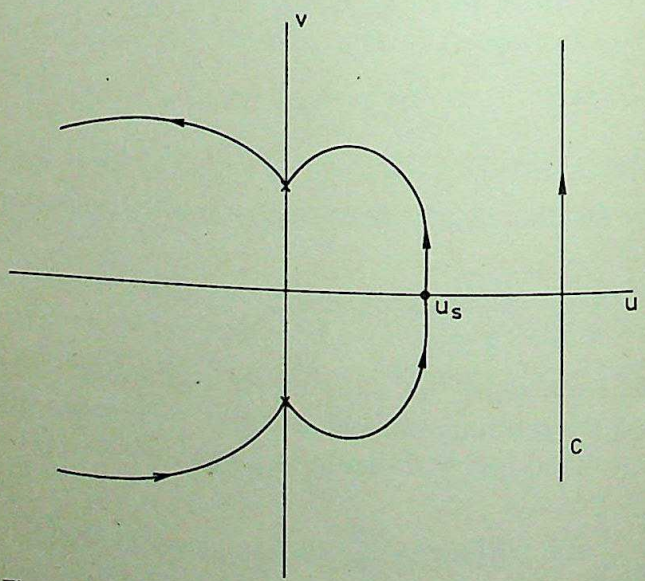

Figure 1(a). The steepest descent contour for the ground-state wave function of FRW model in $Ha < 1$. Near the saddle point $k = (H/3)\tan\alpha$ on the real axis of k-plane, the path is the straight line $u = (H/3)\tan\alpha$. The contour also passes through the branch points $k = \pm i$, located by crosses.

CC-0. In Public Domain. Gurukul Kangri Collection, Haridwar

Digitized by Arya Samaj Foundation Chennai and eGangotri

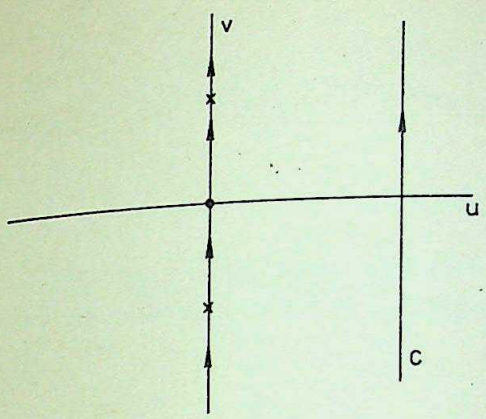

Figure 1(b). For $aH=1$, the whole of v-axis is the path of the saddle point method with $k=0$ as the saddle point.

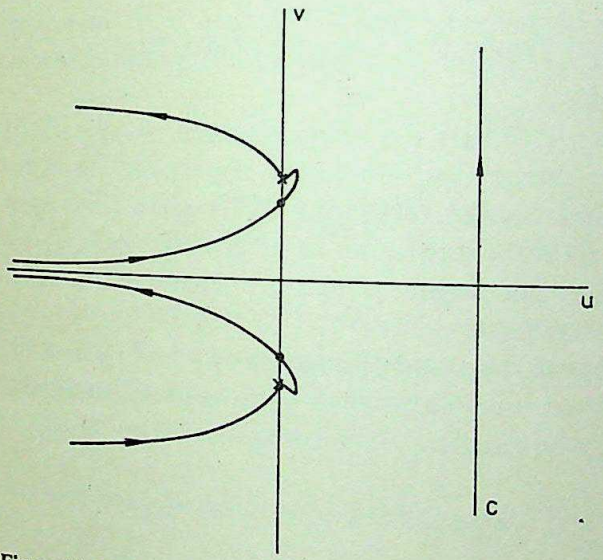

Figure 1(c). There are two complex extrema at $k=\pm i(H/3)\tanh\alpha$ for $aH>1$. The paths near the saddle points are the straight lines $v\mp(H/3)\tanh\alpha=u$ making 45° with real axis and also passes through the branch points $\pm i$.

The deformed contours near the saddle points are given by

$v\mp(H/3)\tanh\alpha=u$, as shown in figure 1(c).

So the wave function using these steepest-descent path can be obtained from (15) as

$$\psi_{HH}(a)=\frac{2N}{3(2\pi)^{1/2}a^2(a^2H^2-1)^{1/4}}\cos\left[\frac{(a^2H^2-1)^{3/2}}{3H^2}-\frac{\pi}{4}\right]. \tag{19}$$

Now we shall evaluate the tunneling wave functions using the analytic continuation technique employed by Vilenkin (1988). According to him the tunneling wave function ψ_T obtained from ψ_{HH} by the relation

$$\psi_T=\psi_{HH}(H^2\to\exp(i\pi)H^2,\ a\to\exp(-i\pi/2)a).$$

CC-0. In Public Domain. Gurukul Kangri Collection, Haridwar

Digitized by Arya Samaj Foundation Chennai and eGangotri

Thus we obtained,

$$\psi_T = \frac{N\exp(i\pi)}{3(2\pi)^{1/2}a^2(1-a^2H^2)^{1/4}}\exp\left[\frac{(1-a^2H^2)^{3/2}-1}{3H^2}\right], \quad \text{for } aH<1, \tag{20}$$

$$= \frac{N}{(2\pi)^{1/2}}\exp(1/3H^2), \quad \text{for } aH=1, \tag{21}$$

$$= \frac{N\exp(-3i\pi/4)}{3(2\pi)^{1/2}a^2(a^2H^2-1)^{1/4}}\exp\left[-\frac{1+i(a^2H^2-1)^{3/2}}{3H^2}\right], \quad \text{for } aH>1. \tag{22}$$

An estimate of factor ordering is obtained by comparison of wave function in the region $a \gg H^{-1}$. According to Hawking (1983) the prefactor is

$$A \simeq a^{-(1+p/2)}, \quad \text{for } a \gg H^{-1}. \tag{23}$$

But from (19) the prefactor is of the order of $a^{-5/2}$ for $a \gg H^{-1}$. So we can take p to be 3. Hence a partial information about the factor ordering ambiguity in Wheeler-De-Witt equation is obtained.

Moreover it is evident from (17) that the wave function diverges in the limit of small three volume, which is a direct contradiction to the Hartle-Hawking boundary condition. A zeta function regularization (Hawking 1977) scheme has been employed by Schleich (1985) and Louko (1988) separately to determine the prefactor in higher order correction by adopting a scale invariant measure. However, none of them have given any explicit wave function form.

An interesting observation is that instead of conformally invariant scalar field with a positive cosmological constant if we consider a homogeneous and isotropic scalar field $\tilde{\phi}$ in a potential field $V(\tilde{\phi})$ the identical wave functions will be obtained except here

$$H^2 = V(\phi) = (2\pi\sigma^2)^2\tilde{V},$$

and

$$\phi = (4\pi\sigma/3)^{1/2}\tilde{\phi}.$$

Finally we determine the probability distribution for the initial states of the universe. The current vector

$$\mathbf{J} = \frac{i}{2}a^p(\psi^*\nabla\psi - \psi\nabla\psi^*),$$

has two components

$$J^a = \frac{i}{2}a^p(\psi^*\partial_a\psi - \psi\partial_a\psi^*),$$

$$J^\phi = -\frac{i}{2}a^{p-2}(\psi^*\partial_\phi\psi - \psi\partial_\phi\psi^*),$$

and the continuity equation

$$\operatorname{div}\mathbf{J} = 0,$$

CC-0. In Public Domain. Gurukul Kangri Collection, Haridwar

Digitized by Arya Samaj Foundation Chennai and eGangotri

becomes $\partial_a J_a + \partial_\phi J_\phi = 0$, for the minisuperspace model given by (5). So J^a is the probability density for ϕ at a particular value of the scale factor a. The conservation of probability is guaranteed by the relation

$$\partial_a \int J^a \, d\phi = 0.$$

So with our estimated value of p (i.e. $p = 3$) the probability density $\rho(a, \phi)$ (i.e. $\rho(a, \phi)\, d\phi$ is the probability for the scalar field to be between ϕ and $\phi + d\phi$ and scale factor be a) is given by

$$\rho(a, \phi) = N_T \exp\left[-\frac{2}{3H^2} \right], \text{ for tunneling wave function,}$$

$$= N_H \exp\left[+\frac{2}{3H^2} \right] \text{ for H–H wave function.}$$

where the normalization constants have the following expressions

$$N_T = \left\{ \int_{H>0} d\phi \exp\left[-2/3H^2 \right] \right\}^{-1},$$

$$N_H = \left\{ \int_{H>0} d\phi \exp\left[2/3H^2 \right] \right\}^{-1}.$$

These results for probability distribution are identical to those obtained by Vilenkin (1988). So all the conclusions regarding convergence of the integrals and inflation in H–H wave function obtained by Vilenkin will also hold here.

3. Inflationary solutions in Kantowski-Sachs model

The 4-metric in Kantowski-Sachs model is

$$ds^2 = -N^2(t)\, dt^2 + a^2(t)\, dr^2 + b^2(t)\, d\Omega^2, \tag{24}$$

where $d\Omega^2$ is the metric on the unit 2-sphere and r is identified periodically.

In this section, I shall give a series of solutions for Kantowski–Sachs metric using H–H approach. The results are similar to the solutions for FRW-model by Esposito *et al* (1988). If we consider a scalar field $\phi'(t)$ having a potential of the form $V(\phi) \frac{1}{2}\lambda'(\phi')^n$, then the action is

$$I = -\tfrac{1}{2} \int N a b^2 \left(\frac{2}{N^2} \frac{\dot{a}}{a} \frac{\dot{b}}{b} + \frac{\dot{b}^2}{N^2 b^2} - \frac{1}{b^2} - \frac{\dot{\phi}^2}{N^2} + \lambda \phi^n \right) dt$$

$$= \int L \, dt, \tag{25}$$

where $\phi(t) = \phi'(t) \sqrt{2}\pi\sigma$, is dimensionless and

$$\lambda = \lambda' \sigma^{-n+4} (\pi \sqrt{2})^{-n+2}.$$

CC-0. In Public Domain. Gurukul Kangri Collection, Haridwar

Digitized by Arya Samaj Foundation Chennai and eGangotri

The Lorentzian field equations are

$$2\frac{\ddot{b}}{b}+\frac{\dot{b}^2}{b^2}+\frac{1}{b^2}+\dot{\phi}^2-\lambda\phi^n=0, \tag{26}$$

$$\frac{\ddot{a}}{a}+\frac{\ddot{b}}{b}+\frac{\dot{a}\dot{b}}{a b}+\dot{\phi}^2-\lambda\phi^n=0, \tag{27}$$

and

$$\ddot{\phi}+\left(\frac{\dot{a}}{a}+\frac{2\dot{b}}{b}\right)\dot{\phi}+\lambda\cdot\phi^n=0, \tag{28}$$

which is the equation of continuity. The Wheeler-De-Witt equation is

$$\left[2\frac{\partial^2}{\partial\alpha\partial\beta}-\frac{\partial^2}{\partial\alpha^2}-\frac{\partial^2}{\partial\phi^2}+(\lambda\phi^n\exp(2(\alpha+2\beta)))\right.$$
$$\left.-\exp(2(\alpha+\beta))\right]\psi(\alpha,\beta,\phi)=0, \tag{29}$$

where $a=e^{\alpha}$, $b=e^{\beta}$ and the operator ordering for P_a^2 is taken to be $+1$.

According to Hartle-Hawking proposal there should be an effective cosmological constant at early stages of the universe leading to inflation and also the parameter (cosmological constant) has to decay and finally vanishes with the evolution of the universe as our universe is not expanding exponentially today. In the present case the scalar field ϕ is initially very large and almost constant. So $\phi\simeq$ constant $=\phi_0$ at very early stages of the evolution. Then the potential term can be viewed as an effective cosmological constant. This region is known as Euclidean or classically forbidden. The Euclidean field equations are

$$2\frac{\ddot{b}}{b}+\frac{\dot{b}^2}{b^2}+\dot{\phi}^2-\frac{1}{b^2}+\lambda\phi^n=0, \tag{30}$$

$$\frac{\ddot{b}}{b}+\frac{\ddot{a}}{a}+\frac{\dot{a}\dot{b}}{a b}+\dot{\phi}^2+\lambda\phi^n=0, \tag{31}$$

and the constraint equation is

$$2\frac{\dot{a}\dot{b}}{a b}+\frac{\dot{b}^2}{b^2}-\frac{1}{b^2}-\dot{\phi}^2+\lambda^2\phi^n=0. \tag{32}$$

(the dot $=\mathrm{d}/\mathrm{d}\tau$).

The initial conditions for the solution of (30)–(32) is implied by H–H proposal. According to this proposal the ground state is a Euclidean functional integral taken over compact 4-metrics and regular matter fields. Hence the semi classical approximation for the wave function reduces to

$$\psi=C\cdot\exp(I_E), \tag{33}$$

with

$$I_E=-ab(1-\tfrac{1}{3}H^2b^2)^{1/2}, \tag{34}$$

CC-0. In Public Domain. Gurukul Kangri Collection, Haridwar

Digitized by Arya Samaj Foundation Chennai and eGangotri

and $$H = (\lambda \cdot \phi_0^n)^{1/2}. \tag{35}$$

So the initial conditions are

$$b(0) = 0, \quad \phi(0) = \phi_0, \qquad \dot{b}(0) = 1, \quad \dot{\phi}(0) = 0. \tag{36}$$

(the argument '0' denote $\tau = 0$). So from (30) neglecting $\dot{\phi}$ term and substituting $H^2 = \lambda\phi^n$ we obtain the solution

$$b(\tau) = \frac{1}{\delta}\sin(\delta\tau), \quad \delta = \frac{H}{\sqrt{3}}. \tag{37}$$

Also from (30) and (32) we obtain the relation

$$a = \mu\dot{b}, \ \mu \text{ is arbitrary.} \tag{38}$$

So we can write

$$a = \mu\cos(\delta\tau), \tag{39}$$

with initial conditions $a(0) = \mu$, $\dot{a}(0) = 0$.

Now for the classically allowed region in which the wave function is oscillatory, the WKB ansatz gives

$$\psi = \mathrm{Re}(C\exp(iS)), \tag{40}$$

where we assume

$$\frac{\nabla^2 C}{C} \ll (\nabla S)^2. \tag{41}$$

So that the prefactor varies slowly compared to S. Substituting (40) in Wheeler-De-Witt equation one obtains

i.e. $$(\nabla S)^2 + V \simeq 0$$

$$-2\left(\frac{\partial S}{\partial\alpha}\right)\left(\frac{\partial S}{\partial\beta}\right) + \left(\frac{\partial S}{\partial\alpha}\right)^2 + \left(\frac{\partial S}{\partial\phi}\right)^2$$

and $$= \exp 2(\alpha+\beta) - \lambda\phi^n \cdot \exp 2(\alpha + 2\beta), \tag{42}$$

$$2\nabla S\cdot\nabla C + \nabla^2 S = 0. \tag{43}$$

Equation (42) is the Hamilton-Jacobi equation for general relativity and (43) is the continuity equation. The gradient S will be the direction of the classical trajectories in superspace. The particular Hamilton-Jacobi function which is the analytic continuation of Euclidean action, will be the desire action according to H–H proposal. The analytic continuation is obtained by rotating to imaginary time,

$$\tau = \frac{\pi}{2H} + it,$$

CC-0. In Public Domain. Gurukul Kangri Collection, Haridwar

Digitized by Arya Samaj Foundation Chennai and eGangotri

and we obtain

$$b(t) = \frac{1}{\delta}\cosh(\delta t),$$
$$a(t) = \mu \sinh(\delta t),$$
$$\phi(t) = \phi_0, \tag{44}$$

for small time t.

Thus the initial conditions for the Lorentzian trajectories which are analytic continuation of Euclidean paths are

$$a(0) = 0, \quad b(0) = 1/\delta, \quad \phi(0) = \phi_0,$$
$$\dot{a}(0) = \mu\delta, \quad \dot{b}(0) = 0, \quad \dot{\phi}(0) = 0. \tag{45}$$

(here argument '0' stands for $t = 0$). These are identical to those of Laflamme and Shellard (1987).

Now by analytic continuation of (34), the action for classical region is given by

$$S \simeq -ab(\tfrac{1}{3}\lambda\phi^n b^2 - 1)^{1/2}. \tag{46}$$

Since S is real, so negative $\dot{\phi}$ for odd n is not possible. Expressing momenta in terms of H–J function S, the 1st integral of the system is

$$p_a = \frac{\partial S}{\partial a} = \frac{\partial L}{\partial \dot{a}}, \quad p_b = \frac{\partial S}{\partial b} = \frac{\partial L}{\partial \dot{b}}, \quad p_\phi = \frac{\partial S}{\partial \phi} = \frac{\partial L}{\partial \dot{\phi}}, \tag{47}$$

where L is given by (25). So we obtain ($N = 1$) the differential equations

$$\dot{b} = (\tfrac{1}{3}\lambda\phi^n b^2 - 1)^{1/2}, \tag{48}$$
$$\dot{a} = \tfrac{1}{3}(\lambda\phi^n ab)/(\tfrac{1}{3}\lambda\phi^n b^2 - 1)^{1/2}, \tag{49}$$
$$\dot{\phi} = -n\dot{a}/2a\phi, \tag{50}$$

which are in agreement with the boundary conditions (45).

As t increases, exponential with positive t becomes dominant and $a(t)$ and $b(t)$ become identical (except for prefactor) (see (44)). In this situation the action (46) takes the approximate form

$$S \simeq -\frac{1}{\sqrt{3}}\lambda^{1/2}\phi^{n/2}ab^2, \tag{51}$$

which holds when either $\dot{\phi} \gg 1$ or b is very large.

Let $[0, t_1]$ be the time interval during which the Lorentzian action is given by (46). So the solutions are represented by (44). We shall now try to find out the solutions in the interval $[t_1, t_2]$ during which S can be approximated by (51). Thus the system of eqs (48)–(50) now give

$$\dot{b} = \frac{b\lambda^{1/2}}{\sqrt{3}}\phi^{n/2}, \tag{52}$$

CC-0. In Public Domain. Gurukul Kangri Collection, Haridwar

Digitized by Arya Samaj Foundation Chennai and eGangotri

$$\dot{a} = \frac{a\lambda^{1/2}}{\sqrt{3}}\phi^{n/2}, \tag{53}$$

$$\dot{\phi} = -\frac{n}{2\sqrt{3}}\lambda^{1/2}\phi^{(n/2-1)}. \tag{54}$$

From (54) we have on integration

$$\phi(t) = \left[\phi_0^{(4-n)/2} - \left(\frac{4-n}{2}\right)\frac{n\lambda^{1/2}}{2\sqrt{3}}(t-t_1)\right]^{2/(4-n)}, \quad n \neq 4 \tag{55}$$

$$= \phi_0 \exp\left[-\frac{2}{\sqrt{3}}\lambda^{1/2}(t-t_1)\right], \quad n = 4 \tag{56}$$

where we have assumed $\phi(t = t_1) = \phi_0$. So

$$b(t) = b_1 \exp\left(\frac{\lambda^{1/2}}{\sqrt{3}}\int_{t_1}^{t}[\phi(t')]^{n/2}\,dt'\right), \tag{57}$$

$$a(t) = a_1 \exp\left(\frac{\lambda^{1/2}}{\sqrt{3}}\int_{t_1}^{t}[\phi(t')]^{n/2}\,dt'\right), \tag{58}$$

where,

$$a_1 = \mu \sinh(\delta t_1) \simeq \frac{\mu}{2}\exp(\delta t_1),$$

$$b_1 = \frac{1}{\delta}\cosh(\delta t_1) \simeq \frac{1}{2\delta}\exp(\delta t_1).$$

Thus for $t > t_1$, a and b have same expression (except for arbitrary multiplicative constant) and satisfy identical differential equation. Further we can approximate (57) and (58) as

$$b(t) \simeq b_1 \exp\left(\frac{\lambda^{1/2}}{\sqrt{3}}\phi_0^{n/2}t\right),$$

$$a(t) \simeq a_1 \exp\left(\frac{\lambda^{1/2}}{\sqrt{3}}\phi_0^{n/2}t\right),$$

for small $(t - t_1)$. These are the correct inflationary form as expected. Therefore the Lorentzian trajectories in H–H proposal gives inflationary solutions by the scalar field.

4. Conclusions

In this paper we have considered the 2nd order corrections to the wave function by the method of steepest descent along the line of approach of Hartle–Hawking and compare with tunneling wave function. The probability distributions are calculated for both types of wave functions. The results show an initial singularity at $a = 0$ in both the wave functions. So Hartle–Hawking boundary conditions seem to be

CC-0. In Public Domain. Gurukul Kangri Collection, Haridwar

Digitized by Arya Samaj Foundation Chennai and eGangotri

contradictory and initial singularity cannot be avoided. Also this 2nd order correction (which gives the initial singularity) indicates fluctuation about classical solutions and is important at very early stages of the universe. The factor ordering problems is partially overcome and there are no definite reasons to take $p = +1$ (in H–H approach) or $p = -1$ (by Vilenkin).

Lastly from the series of solutions in §3 we observe that inflation can be originated by the introduction of a scalar field but there are no means to stop it. So universe expands exponentially with time forever, which is contrary to our present state of universe. This point was also discussed by Vilenkin and according to him. "The universe had a beginning but it will have no end, and we live in a region which thermalized about 10^{10} years ago."

Acknowledgements

This research was supported in part by the UGC–DSA program in Mathematics Department of Jadavpur University.

References

Esposito G and Platania G 1988 *Class. Quan. Grav.* **5** 937

Fang L Z and Ruffinm R 1987 "*Quantum Cosmology, Advanced Series in Astrophysics and Cosmology*" (World Scientific) **3**

Hartle J B and Hawking S W 1983 *Phys. Rev.* **D28** 2960

Hawking S W 1977 *Commun. Math. Phys.* **55** 133

Hawking S W 1983 *Relativity, groups and topology II* Les Houches (eds) B S Dewitt and R Stora, p. 336

Laflamme R and Shellard P E 1987 *Phys. Rev.* **D35** 2315

Linde A D 1984 *Nuovo Cimento Lett.* **39** 401

Louko Jorma 1988 *Ann. Phys.* **181** 318

Morse P M and Feshback 1953 *Methods of Theoretical Physics* (N. York, Toronto, London: McGraw-Hill book Company) INC. Vol. 1.

Schleich Kristin 1985 *Phys. Rev.* **D32** 1889

Vilenkin A 1988 *Phys. Rev.* **D37** 888

CC-0. In Public Domain. Gurukul Kangri Collection, Haridwar

Digitized by Arya Samaj Foundation Chennai and eGangotri

Pramāṇa – J. Phys., Vol. 34, No. 5, May 1990, pp. 415–422. © Printed in India.

Cosmological models consistent with supersymmetric compactification of superstring theories

SANJAY KUMAR, S MAHAJAN*, A MUKHERJEE, N PANCHAPAKESAN and R P SAXENA

Department of Physics and Astrophysics, University of Delhi, Delhi 110007, India
*St. Stephen's College, University of Delhi, Delhi 110007, India

MS received 21 September 1989; revised 1 February 1990

Abstract. The compactification of 10-dimensional supergravity, coupled to super Yang–Mills theory, to curved 4-dimensional spacetimes is investigated. The requirement of unbroken supersymmetry leads to a set of consistency conditions. These are fairly restrictive, but nevertheless permit some nontrivial solutions, including the Milne universe. More general time-dependent metrics are also not ruled out.

Keywords. Superstrings; compactification; unbroken supersymmetry; spherical symmetry.

PACS Nos 11·17; 98·80

1. Introduction

In recent times, superstring theories (Green *et al* 1987) have raised hopes of providing a unification of all forces in nature. They do also seem to offer, for the first time, a consistent way of quantizing gravity. In the limit of infinite string tension, these theories correspond to 10-dimensional supergravity coupled to super Yang–Mills theory. To make contact with 4-dimensional physics, the extra six dimensions have to be compactified. The paper of Candelas *et al* (1985) is an important landmark in this direction. It is an open question whether the sequence

$$\text{String theory} \rightarrow \text{10-dimensional field theory} \rightarrow \text{4-dimensional field theory} \tag{1}$$

is actually the correct and unique description of the process by which string theories make contact with low-energy physics. However, in spite of recent progress in formulating string theories directly in four dimensions (Antoniadis 1988), the above sequence remains interesting since it leads to definite predictions for the low-energy theory. Within this approach, Candelas *et al* (1985) derive restrictions on the compact 6-manifold by assuming that (i) the 10-dimensional geometry is of the form $M \times K$, where M is maximally symmetric and K is compact, and (ii) there is unbroken $N = 1$ supersymmetry in four dimensions. In this paper, we investigate the consequences of relaxing assumption (i), while maintaining (ii).

We seek vacuum states of the 10-dimensional theory such that the 4-dimensional metric has a nonvanishing background value

$$\langle g_{\mu\nu} \rangle = g^{cl}_{\mu\nu}(x). \tag{2}$$

CC-0. In Public Domain. Gurukul Kangri Collection, Haridwar

Digitized by Arya Samaj Foundation Chennai and eGangotri

We assume $g^{cl}_{\mu\nu}(x)$ to be of a general spherically symmetric form, given by the line element

$$ds^2 = -R_1(r,t)dt^2 + R_2(r,t)dr^2 + R_3(r,t)d\Omega^2, \tag{3}$$

where

$$d\Omega^2 = d\theta^2 + \sin^2\theta\, d\phi^2.$$

The requirement of unbroken supersymmetry implies certain restrictions on the metric coefficients R_i. We attempt to satisfy these requirements under various ansatze. However, it turns out that the compactness of the 6-manifold K severely restricts the 4-dimensional background geometry. In almost all cases, we find that the simultaneous requirements of supersymmetry and compactness of K leaves us with only flat 4-geometry. We have an interesting case of a flat geometry in a nonflat coordinatization (§4), as well as a class of solutions which does not appear to reduce to flat spacetime (§5). We are yet to work out the physical implications of such background configurations.

In §2 we consider the conditions for unbroken supersymmetry and obtain the coupled set of differential equations satisfied by R_i. In the subsequent sections, we look for solutions to these equations under various ansatze. In §3, we consider time-independent metrics. In §4, we consider metrics of the Friedmann–Robertson-Walker type. In §5 a more general class of time-dependent metrics is considered, where the R_i's are products of functions of r and t. Section 6 contains some concluding remarks.

2. The consistency conditions

Following Candelas *et al* (1985), we assume vanishing background values for all fermion fields in the ground state configuration. For unbroken supersymmetry in four dimensions we require (Candelas *et al* 1985; Gates and Nishino 1986)*

$$0 = \delta\psi_\mu = \nabla_\mu\varepsilon + \frac{\sqrt{2}}{32}\exp(2\phi)(\gamma_\mu\gamma_5 \otimes H)\varepsilon \tag{4}$$

$$0 = \delta\psi_m = \nabla_m\varepsilon + \frac{\sqrt{2}}{32}\exp(2\phi)(\gamma_m H - 12H_m)\varepsilon \tag{5}$$

$$0 = \delta\lambda = \sqrt{2}(\gamma^m\nabla_m\phi)\varepsilon + \tfrac{1}{8}\exp(2\phi)H\varepsilon \tag{6}$$

$$0 = \delta\chi^\alpha = -\tfrac{1}{4}\exp(\phi)F^\alpha_{mn}\gamma^{mn}\varepsilon. \tag{7}$$

We assume (3) for the vacuum expectation value of the metric of 4-dimensional spacetime. The following special cases may be noted:

---

* As a matter of fact, these equations are not exact (Gates and Nishino 1986), and there are additional terms on the r.h.s. of eqs (4)–(7). We ignore them here, since within the framework of (1) there is a regime where the relevant length scales are large compared to the Planck length, but small compared to the compactification length, so that (curvature)^2 terms can be neglected. As pointed out in the first paragraph, this is really an open question, and interesting physics may emerge from the consideration of these terms. This is currently under investigation.

CC-0. In Public Domain. Gurukul Kangri Collection, Haridwar

Digitized by Arya Samaj Foundation Chennai and eGangotri

i) Flat spacetime: $R_1 = R_2 = 1, R_3 = r^2$, ii) Schwarzschild spacetime: $R_1 = (1-2M/r) = R_2^{-1}, R_3 = r^2$, iii) Robertson–Walker universe: $R_1 = 1, R_3 = R^2(t)r^2, R_2 = R^2(t)/(1-kr^2)$, and iv) static de Sitter universe:

$$R_1 = (1 - kr^2) = R_2^{-1}, \quad R_3 = r^2.$$

As in Candelas *et al* (1985), (4) implies

$$[\nabla_\mu, \nabla_\nu]\varepsilon = -\frac{1}{(16)^2}\exp(4\phi)(\gamma_{\mu\nu} \otimes H^2)\varepsilon$$

i.e.

$$\frac{1}{4}R_{\mu\nu\lambda\sigma}(\gamma^{\lambda\sigma} \otimes \mathbb{1})\varepsilon = -\frac{1}{(16)^2}\exp(4\phi)(\gamma_{\mu\nu} \otimes H^2)\varepsilon \tag{8}$$

where $R_{\mu\nu\lambda\sigma}$ is the Riemann curvature tensor and

$$\gamma^{\mu\nu} = \gamma^{[\mu}\gamma^{\nu]}.$$

For a diagonal metric tensor, $R_{\mu\nu\lambda\sigma}$ is diagonal in pairs of indices, so that the product $R_{\mu\nu\lambda\sigma}\gamma^{\lambda\sigma}$ is proportional to $\gamma_{\mu\nu}$ for each μ and ν. Equations (5)–(7) do not explicitly involve $g_{\mu\nu}$; thus they can be handled as in Birrell and Davies (1982).

For the general metric of (3) we have, using the notation

$$R_i = \exp(f_i(r,t)), \quad i = 1,2,3, \tag{9}$$

the following expressions for $1/4R_{\mu\nu\lambda\sigma}\gamma^{\lambda\sigma}$ (here primes and dots refer to differentiation with respect to r and t respectively):

$$\mu = t, \nu = r: \{[1/2f_1'f_2' - 1/2f_1'^2 - f_1'']4R_2 + [\ddot{f}_2 + 1/2\dot{f}_2^2 - 1/2\dot{f}_1\dot{f}_2]/4R_1\}\gamma_{tr} \tag{10}$$

$$\mu = t, \nu = \theta: \{[\ddot{f}_3 + 1/2\dot{f}_3^2 - 1/2\dot{f}_3\dot{f}_1]/4R_1 - f_3'f_1'/8R_2\}\gamma_{t\theta} \tag{11}$$

$$\mu = r, \nu = \theta: \{[1/2f_2'f_3' - f_3'' - 1/2f_3'^2]/4R_2 + \dot{f}_2\dot{f}_3/8R_1\}\gamma_{r\theta} \tag{12}$$

$$\mu = \theta, \nu = \phi: \{1/2R_3 - f_3'^2/8R_2 + \dot{f}_3^2/8R_1\}\gamma_{\theta\phi} \tag{13}$$

while the other components vanish or are proportional to these. In order that factoring out $\gamma_{\mu\nu}$ from (8) leave an eigenvalue equation for the 8×8 matrix H^2, all the expressions in braces in (10) must be equal, although they may depend upon r and t. This leads to a set of three consistency conditions which can be written in the following form

$$[(\ddot{f}_2 - \ddot{f}_3) + 1/2(\dot{f}_2^2 - \dot{f}_3^2) + 1/2\dot{f}_1(\dot{f}_2 - \dot{f}_3)]/4R_1 = [f_1'' - 1/2f_1'^2 - 1/2f_1'(f_2' + f_3')]/4R_2 \tag{14}$$

$$[\ddot{f}_3 + 1/2\dot{f}_1\dot{f}_3]/4R_1 = 1/2R_3 - [f_3'^2 + f_1'f_3']/8R_2. \tag{15}$$

$$[\dot{f}_3(\dot{f}_2 - \dot{f}_3)]/8R_1 = [f_3'' - 1/2f_2'f_3']/4R_2 + 1/2R_3. \tag{16}$$

The possibility of a consistent string compactification with unbroken supersymmetry in nonflat background spacetimes depends on finding a nontrivial set of f_i (or R_i)

CC-0. In Public Domain. Gurukul Kangri Collection, Haridwar

Digitized by Arya Samaj Foundation Chennai and eGangotri

satisfying the consistency conditions of (14)–(16) together with the requirement that K be compact. A priori, there seems to be no argument to suggest that this is impossible. However, the technical difficulty of the problem (three coupled nonlinear partial differential equations) makes it unlikely that the most general solution to (14–16) can be found analytically. In the following sections, we subject (14)–(16) to a series of simplifying ansatze and look for solutions.

3. Time-independent geometries

When f_i's are independent of t, (14)–(16) become

$$f_1'' + 1/2 f_1'^2 - 1/2 f_1'(f_2' + f_3') = 0 \tag{17}$$

$$f_3'' + 1/2 f_3'^2 - 1/2 f_3'(f_1' + f_2') = 0 \tag{18}$$

$$1/2R_3 + (f_3'' - 1/2 f_2' f_3')/4R_2 = 0. \tag{19}$$

These equations are still too complicated to permit an analytical solution, so we make the following simplifying ansatz:

$$f_1 + f_2 = 0. \tag{20}$$

Note that this condition is satisfied by the Schwarzschild and static de Sitter geometries.

On substituting (20) into (18), we obtain

$$f_3'' + 1/2 f_3'^2 = 0$$

with the general solution

$$f_3 = 2 \ln [A(r + B)],$$

i.e.

$$R_3 = A(r + B)^2. \tag{21}$$

Substituting (21) into (17), we obtain

$$f_1'' + f_1'^2 - f_1'/(r + B) = 0,$$

with the general solution

$$R_i = \exp(f_1) = \lambda(1/2r^2 + Br) + \mu. \tag{22}$$

Equation (19) is now simply a consistency condition on the solution in (21) and (22), yielding

$$[1/2\lambda AB^2 - A\mu + 1]/2A(r + B)^2 = 0.$$

Therefore the complete solution to (17)–(19) and (20) is given by (21) and (22), together with

$$1/2\lambda AB^2 - A\mu + 1 = 0. \tag{23}$$

CC-0. In Public Domain. Gurukul Kangri Collection, Haridwar

Digitized by Arya Samaj Foundation Chennai and eGangotri

This condition can be satisfied in infinitely many ways; thus, within these ansatze, there are infinitely many solutions to (14)–(16).

Substituting the above general solution into the expression in braces in (13), we obtain

$$1/4R_{\mu\nu\lambda\sigma}\gamma^{\lambda\sigma} = -\lambda/4\gamma_{\mu\nu}. \tag{24}$$

Since the coefficient of $\gamma_{\mu\nu}$ in (24) is a constant, the compactness of K implies, by the argument of Candelas *et al* (1985), exploiting (4)–(6), that it must be zero, corresponding to flat spacetime. It should be noted that the general solution above is related to the de Sitter metric (corresponding to $A=1$, $B=0$, $\mu=1$) by a redefinition of r.

It is amusing to note that (17)–(19) can also be solved exactly by means of the ansatz $f_2+f_3=0$, leading to the general solution

$$R_1 = A(r+B)^2$$
$$R_3 = R_2^{-1} = \lambda(1/2r^2 + Br) + \mu \tag{25}$$

with the relation

$$1 + 1/2\mu\lambda - 1/4\lambda^2 B^2 = 0. \tag{26}$$

However, substituting (25) and (26) in the expression in braces in (13), we again obtain (24)!

4. Friedmann–Robertson–Walker (FRW) metric

The FRW geometries correspond to the following special case of (3):

$$R_1 = 1, \quad R_2 = R^2(t)/(1-kr^2), \quad R_3 = R^2(t)r^2. \tag{27}$$

Equations (14) and (16) turn out to be identically satisfied under this ansatz. The remaining consistency condition, (15), reduces to

$$R\ddot{R} = \dot{R}^2 + k. \tag{28}$$

This equation can be integrated once, to obtain

$$(\mathrm{d}R/\mathrm{d}t)^2 = AR^2 - k \tag{29}$$

where A is a constant of integration. The final form of the solution depends on the values of A and k. There are three kinds of solution for $R(t)$: (a) exponentially growing (for $A>0$), (b) linear including a constant (for $A=0$), and (c) oscillatory (for $A<0$). Solutions of type (a) exists for all values of k, while those of types (b) and (c) exists only for $k<0$. In all cases it is trivial to show, from (28) and (29), that

$$\ddot{R}/R = A. \tag{30}$$

Further, for the FRW metric, the expression in braces in (10)–(13) all reduce to $\ddot{R}/2R$, so that (8) takes the form of an eigenvalue equation for H^2, with eigenvalue

CC-0. In Public Domain. Gurukul Kangri Collection, Haridwar

Digitized by Arya Samaj Foundation Chennai and eGangotri

proportional to the constant A. Since H is anti-Hermitian, the solutions with $A>0$ are ruled out. Finally, since the eigenvalue is a constant, by the argument of §3 it must be zero. Then by (29) the only surviving solution for $R(t)$ is)

$$R(t)=(-k)^{1/2}t+B \tag{31}$$

where B is a constant. This is the well-known Milne universe (Milne 1932), which is a solution to the vacuum Einstein equations. It is a linearly growing, spherically symmetric universe which is empty of matter. Note that we have not used the Einstein equations anywhere.

The emergence of a truly cosmologically interesting solution from our consistency requirements [eqs (14)–(17)] can also be understood as follows. The Einstein equations under the FRW ansatz, with homogeneous matter density ρ and pressure p, are (Gibbons *et al* 1983)

$$\ddot{R}/R=-4\pi G(\rho+3p)/3 \tag{32}$$

$$(\dot{R}^2+k)/R=8\pi G\rho/3. \tag{33}$$

Because of the consistency requirement (28), these can be satisfied only if

$$p=-\rho.$$

A negative pressure is characteristic of an inflationary universe (Brandenberger 1985). Unfortunately, this possibility does not survive the compactification requirement, which by (31) yields $\rho=0$. Thus we are left with the vacuum Einstein equations.

As is clear from (31), the Milne universe is a linearly growing, spherically symmetric universe which is empty of matter. It is well known (Birrell and Davies 1982) that by choosing a suitable frame of reference the Milne universe can be seen to be flat. Classically, therefore, the solution (31) is nothing but Minkowski space in disguise. It must be remembered, however, that our arguments are semiclassical in nature: we are dealing with quantum fields in a background gravitational metric. In order to define particle states, one has to consider positive frequency solutions defined with respect to a particular choice of the time coordinate t. Since a choice of t corresponds to a choice of the vacuum, the latter is not invariant under general coordinate transformations. Equation (2) presupposes a choice of the vacuum. (More technically, the 4-dimensional vacuum of the comoving Milne observer is inequivalent to the Minkowski vacuum (Birrell and Davies 1982, p. 121).) For this reason, the solution (31) must be regarded as nontrivial. Moreover, note that the Einstein equations with a 'small' matter term admit a solution of the FRW type that has $k=-1$, is nonflat, and goes over to (31) in the limit $p\to 0$, $\rho\to 0$. Such a term will arise as the first quantum correction to (2).

5. Separable metrics

In this section, we consider geometries where the r and t dependences of the R_i's are factorizable. Thus

$$R_i(t)=\exp(g_i(t))\exp(h_i(r)) \tag{34}$$

CC-0. In Public Domain. Gurukul Kangri Collection, Haridwar

Digitized by Arya Samaj Foundation Chennai and eGangotri

or $$f_i(r,t) = g_i(t) + h_i(r). \tag{35}$$

Notice that the FRW metric, considered in the previous section, is a special case of this class. Under this general ansatz, (14)–(16) take the form

$$[\ddot{g}_2 - \ddot{g}_3 - 1/2\dot{g}_1(\dot{g}_2 - \dot{g}_3) + 1/2(\dot{g}_2^2 + \dot{g}_3^2)]\exp(g_2 - g_1)$$
$$= [h_1'' + 1/2(h_1'^2 - h_1'h_2' - h_1'h_3')]\exp(h_1 - h_2) = C_1 \tag{36}$$

$$[\ddot{g}_3 - 1/2(\dot{g}_3^2 + \dot{g}_1\dot{g}_3 + \dot{g}_2\dot{g}_3)]\exp(g_2 - g_1)$$
$$= -[h_3'' + 1/2(h_3'^2 - h_2'h_3' - h_1'h_3')]\exp(h_1 - h_2) = C_2 \tag{37}$$

$$1/2[\dot{g}_2\dot{g}_3 - \dot{g}_3^2]\exp(g_2 - g_1) = 2\exp(g_2 - g_3)\exp(h_1 - h_3)$$
$$+ [h_3'' - 1/2h_2'h_3']\exp(h_1 - h_2) \tag{38}$$

where C_1 and C_2 are separation constants. Unlike (36) and (37), (38) does not separate into a t-dependent and an r-dependent part. This separation can however be achieved by imposing the additional condition

$$g_2 = g_3. \tag{39}$$

This is assumed in the subsequent discussion.

On substituting (39) in (36, 37) we obtain, for the time dependent parts,

$$\dot{g}_2^2\exp(g_2 - g_1) = C_1 \tag{40}$$

$$(\ddot{g}_2 - \dot{g}_2^2 - 1/2\dot{g}_1\dot{g}_2)\exp(g_2 - g_1) = C_2. \tag{41}$$

The solution of (40) can be written in the implicit form

$$\exp(g_2/2) = 1/2(C_1)^{1/2}\int \exp(g_1/2)\,dt + C_3. \tag{42}$$

Note that the allowed FRW solution of (31) is a special case of (42). On substituting (42) in (41), the latter is identically satisfied provided $-3C_1 = 2C_2$.

The space dependent parts now satisfy

$$h_1'' + 1/2(h_1'^2 - h_1'(h_2' + h_3')) = C_1\exp(h_2 - h_1) \tag{43}$$

$$h_3'' + 1/2(h_3'^2 - h_3'(h_1' + h_2')) = 3/2C_1\exp(h_2 - h_1) \tag{44}$$

$$h_3'' - 1/2h_2'h_3' + 2\exp(h_2 - h_3) = 0. \tag{45}$$

While (43)–(45) are simpler than (14)–(16), they are still too complex to permit a general analytical solution. From the result of §4, we know that (43)–(45) do possess a nontrivial solution. Presumably there may be other exact nontrivial solutions, but we have been unable to find any.

A physically reasonable special case occurs when $h_3 = r^2$. In that case (43)–(45) can be solved exactly, leading to

$$\exp(h_1) = -3C_1/4\alpha - (1 - \beta r^2) \tag{46}$$

$$\exp(-h_2) = (1 - \alpha r^2) \tag{47}$$

CC-0. In Public Domain. Gurukul Kangri Collection, Haridwar

Digitized by Arya Samaj Foundation Chennai and eGangotri

where α and β are constants. Clearly flat space, de Sitter space as well as the FRW spacetime are all special cases of (46)–(47). Of course, on imposing the requirements of (5)–(7), de Sitter space reduces to flat space and the FRW geometries reduce to the solution of (31).

6. Conclusions

We have considered the compactification of 10-dimensional supergravity in a class of background 4-geometries. We have imposed the requirement of unbroken supersymmetry, and found some solutions to the resulting consistency conditions. In all these cases, the geometry of the 6-manifold, and hence the field content of the 4-dimensional theory, is identical to that found by Candelas *et al* (1985); thus there are no new consequences for low energy physics. However, the vacuum of the Milne universe is different, in a semiclassical sense, from the Minkowski vacuum. The fact that the Milne universe is also a solution of the consistency conditions is encouraging for applications to cosmology using FRW metrics.

Our work can be extended and generalized in several ways. The coupled eqs (43)–(45) may be solved numerically; work on this is in progress. Of course, the separable solutions of §5 are not the most general solutions of (14)–(16), though it is not easy to see how to look after nonseparable solutions. Generalizing even further, (3) could be relaxed. Indeed, there are respectable cosmological models that do not fall in this class.

It should be emphasized that the Einstein equations have not been used anywhere as inputs. Indeed they emerge as solutions to the conditions imposed in §4. Thus the geometries found here are true vacuum solutions to the classical equations of motion (e.g. the de Sitter and Milne solutions). Since superstring theory is a "theory of everything", it should explain things like galaxy formation. Presumably, quantum fluctuations about these vacuum solutions are responsible for the creation of matter.

References

Antoniadis I 1988 *Status report on four dimensional strings*, CERN-TH 5199/88 (invited talk at XXIV International Conference on High Energy Physics, Munich, August 1988)
Birrell N D and Davies P C W 1982 *Quantum fields in curved space* (Cambridge: University Press)
Brandenberger R 1985 *Rev. Mod. Phys* **57** 1
Candelas P, Horowitz G T, Strominger A and Witten E 1985 *Nucl. Phys.* **B258** 46
Ellis J 1988 *Aspects of superstring model—building* CERN-TH 5103/88 (Trieste Lectures 1988)
Gates S J and Nishino H 1986 *Phys. Lett.* **B17** 52
Gibbons G W, Hawking S W and Siklos S T 1983 *The very early universe* (Cambridge: University Press)
Green M B, Schwarz J H and Witten E 1987 *Superstring theory* (Cambridge: University Press) 1 and 2
Milne E A 1932 *Nature (London)* **130** 9

CC-0. In Public Domain. Gurukul Kangri Collection, Haridwar

Digitized by Arya Samaj Foundation Chennai and eGangotri

Pramāṇa – J. Phys., Vol. 34, No. 5, May 1990, pp. 423–432. © Printed in India.

Spherically symmetric anisotropic and inhomogeneous cosmological models*

J KRISHNA RAO
Department of Mathematics, Bhavnagar University, Bhavnagar 364002, India

MS received 17 June 1989; revised 7 February 1990

Abstract. Spherically symmetric cosmological models filled with dust (pressure-free fluid) content are analyzed. It has been pointed out that these models are anisotropic (of non-vanishing shear) and inhomogeneous ($\partial\rho/\partial r \neq 0$), the characteristics related directly to the presence of the free gravitational field. It is demonstrated that when the free gravitational field vanishes these models degenerate to the corresponding Friedmann–Robertson–Walker (FRW) models. It is further shown that the energy density of the free gravitational field can be introduced into observational cosmology as a new parameter since it enters into the expansion and deceleration equations, as well as conservation law for total energy, implying that the present Hubble velocity can be reached in a shorter time from the big bang. Finally, the effect of shear on the redshift is also discussed.

Keywords. Cosmology; gravitational radiation; energy density of the free gravitational field.

PACS Nos 04·30; 98·80

1. Introduction

Spherically symmetric inhomogeneous cosmological models have been discussed by many authors including Tolman (1934, 1949), Omer (1949), Bondi (1947) and Bonnor (1972, 1974). These investigations have acquired importance due to both theoretical and observational considerations. Some of the objections for the homogeneous and isotropic FRW models are, for example, instability against small perturbations, existence of horizons, inability to explain the formation of galaxies and evidence for considerable anisotropy in expansion velocities among galaxies. Inhomogeneities in cosmology may also arise due to the propagation of gravitational waves. As a consequence of the big bang, *thermal* gravitational radiation should pervade the universe. If one assumes that the present energy density of these waves is comparable with 3°K microwave background (black-body) radiation, it is natural to treat gravitational radiation as a homogeneous and isotropic fluid with $P_r = \rho_r/3$. It was pointed out by Rees *et al* (1974) that even if the frequencies of such waves are of the order 10^{11} Hz and the energy density 10^{-36} g/cm^3, they may as well go undetected by the present day techniques. Isaacson and Winicour (1973) studied in detail *thermal* gravitational radiation emanating from within the galaxies. A geometrical framework for the propagation of such thermal gravitational radiation on the FRW background geometry was provided by Swinerd (1977). On the other hand gravitational waves

*This paper is dedicated to my teacher Professor V V Narlikar on the occasion of his 81st birthday.

CC-0. In Public Domain. Gurukul Kangri Collection, Haridwar

Digitized by Arya Samaj Foundation Chennai and eGangotri

associated with the premordial fluctuations with energy density 10^{-29} g/cm^3 are more interesting. Such a situation would fit nicely with an inhomogeneous and anisotropic universe. The presence of a gravitational wave field should have important effects on the appearance of distant galaxies and clusters as well as the linear Hubble law. In an epoch-making paper Kristian and Sachs (1966) analyzed the cosmological effects of the incident field, the contribution of the conformal Weyl tensor to the Riemann curvature tensor. It was pointed out by them that gravitational waves with periods of the order of 10^9 light years would contribute to the incident field and they estimated the maximum size of this incident field as about 10^{-16}/(light-year)^2. In a parallel development Szekeres (1966) studied the propagation of gravitational radiation in perfect fluid distributions. His analysis was based on the fact that Riemann curvature tensor can be decomposed into the conformal Weyl tensor and a certain combination of terms arising from the Ricci tensor and its spur. The matter terms enter the Riemann curvature tensor through the Ricci tensor and the conformal Weyl tensor having all the symmetry properties of the Riemann tensor is to be thought of as representing the free gravitational field. The interaction between the matter field and the free gravitational field arises from the general Bianchi identities

$$C_{ab}{}^{cd}{}_{;d} = R_{[a;b]}{}^{c} - \frac{1}{6} g_{[a}{}^{c} R_{;b]} = J_{ab}{}^{c},$$

where $J_{ab}{}^{c}$ is called the matter current satisfying the conservation equation, $J_{ab}{}^{c}{}_{;c} = 0$. Those parts of matter which contribute to $J_{ab}{}^{c}$ are called gravitationally active and they represent the interaction between the matter and free gravitational fields. When the material distribution is represented by a perfect fluid, the gravitationally active part is given by the shear and rotation of the congruence of fluid lines as well as the spatial gradient of density. Hence these three characteristics are important to identify the presence of gravitational radiation propagating through a perfect fluid medium.

In the present paper we wish to discuss the propagation of gravitational radiation on a cosmological background. The assumptions of spatial isotropy (congruence of world-lines of the material particles being non-shearing) and homogeneity (uniform material density) give a conformally flat geometry for the FRW models (Krishna Rao 1971, 1972, 1973). Since the Weyl tensor vanishes identically, the free gravitational (incident) field is totally absent and hence the Friedmann–Robertson–Walker cosmological models are devoid of gravitational radiation. Hence, we focus our attention on spherically symmetric models which are both anisotropic (shearing) and inhomogeneous ($\partial\rho/\partial r \neq 0$) since by Szekeres' criteria they contain gravitational radiation (only Coloumb field in the present case). Thus, one would expect the abundance of gravitational radiation in those parts of the universe where anisotropy and inhomogeneity are still dominant features. But as suggested by Misner (1967, 1968) dissipative processes would tend to smooth out anisotropy and inhomogeneity providing a mechanism to explain a high degree of homogeneity and isotropy observed in the present epoch. Thus, perhaps, experiments to detect gravitational radiation will not meet with success since all gravitational radiation emitted in an earlier spoch has already been absorbed by the cosmos or died down. Also, gravitational radiation which is abundant in distinct parts of the universe may meet the same fate before reaching the earth. However, in a universe in which gravitational radiation is present the rate of expansion per unit distance $\dot{R}/R$, is always greater than the corresponding

CC-0. In Public Domain. Gurukul Kangri Collection, Haridwar

Digitized by Arya Samaj Foundation Chennai and eGangotri

quantity in the FRW models (see (9)). Also, the energy density of the free gravitational field appearing in the deceleration equation implies that the present Hubble velocity can be reached in a shorter time from the big bang.

Assuming equations governing the evolution of spherically symmetric systems filled with perfect fluids (Rao and Annapurna 1986), in §2 we discuss three types of solutions (corresponding to parabolic, hyperbolic and elliptic motion of dust particles) representing anisotropic and inhomogeneous cosmological models filled by dust and their degeneracy to the FRW models. We compare and contrast our procedure with that of Isaacson and Winicour (1973) in §3 and the effect of anisotropy and inhomogeneity on the Z-r relation is discussed in §4. In §5 we give concluding remarks.

2. Inhomogeneous and anisotropic cosmological models

The equations governing the evolution of spherically symmetric space-times with the metric

$$ds^2 = -\exp\lambda\,dr^2 - R^2(d\theta^2 + \sin^2\theta\,d\phi^2) + \exp\nu\,dt^2 \tag{2}$$

λ, R, ν being functions of r and t only and filled with a perfect fluid of energy-momentum tensor

$$T_a^{\ b} = (\rho + p)u_a u^b - p g_a^{\ b},\ u^a = (0, 0, 0, e^{-\nu/2}) \tag{3}$$

were given by Misner and Sharp (1964). A different formalism more geometrical in nature, is developed by Rao and Annapurna (1986) by introducing into the scheme a new variable called the energy density of the free gravitational field which is nothing but the eigenvalue of the conformal Weyl tensor (Rao 1966). For the present purpose we make use of the latter work and follow the same notations.

It is well-known that the assumption of the fluid lines being geodetic leads to $\nu = 0$ which on substitution in the equation for pressure gradient gives $p = p(t)$. Since we are interested in inhomogeneous models, we neglect uniform pressure and take $p = 0$.

Similarly, from

$$D_t\Gamma = UD_r\nu = 0,$$

we get $\Gamma = \Gamma(r)$, so that

$$\exp\lambda = R'^2/\Gamma^2(r). \tag{5}$$

Writing $E = (\Gamma^2 - 1)/2$, the three cases $E > 0$ (positive energy), $E = 0$ (zero energy) and $E < 0$ (negative energy) correspond respectively to hyperbolic, parabolic and elliptic motion of dust particles.

Also, the conservation equation for the combined energy of the fluid and field

$$D_t\{4\pi(\rho + \varepsilon)R^3/3\} = -pD_t(4\pi R^3), \tag{6}$$

reduces to

$$4\pi(\rho + \varepsilon)R^3 = 3M(r), \tag{7}$$

CC-0. In Public Domain. Gurukul Kangri Collection, Haridwar

Digitized by Arya Samaj Foundation Chennai and eGangotri

where $M(r)$ is of class c^2 and $M'(r) > 0$. Also, the expression for acceleration is given by

$$\ddot{R}/R = -4\pi(\rho + \varepsilon)/3 = -M(r)/R^3, \tag{8}$$

which shows that the presence of the energy density of the free gravitational field ε increases the rate of deceleration per unit distance. This may be interpreted that the free gravitational field affects the motion of dust particles by inducing shear in their world-lines and tending to cause them to converge.

Define a new parameter α as

$$\alpha \equiv \dot{R}/R = [\{8\pi(\rho + \varepsilon)/3\} + (2E/R^2)]^{1/2},$$
$$= [(2M/R^3) + (2E/R^2)]^{1/2}. \tag{9}$$

The expressions for shear invariant σ, expansion θ, proper density of dust particles ρ and energy density of the free gravitational field ε are written as

$$\sigma = R\alpha'/R', \tag{10}$$

$$\theta = (\sigma + 3\alpha) \tag{11}$$

$$8\pi\rho = 3M'/R'R^3 \tag{12}$$

$$8\pi\varepsilon = (R/R')(\dot{\alpha}' + \alpha\alpha') + (E'/R'R) - (2E/R^2). \tag{13}$$

The parameter α $(= \dot{R}/R)$ introduced in (9) represents the rate of expansion per unit distance (in a coordinate system using R as a coordinate) and at a particular time t, it has different values on different shells of the model (recalling that r is our labelling coordinate). Thus, all parts of the universe do not undergo the same expansion rate per unit distance.

It may also be pointed out that the rates of expansion per unit distance along the radial and transverse directions are given respectively by $(\dot{R}'/R')$ and $(\dot{R}/R)$. De Vaucouleurs (1958) found evidence for a considerable anisotropy of expansion velocities among galaxies. In our case it is easy to check that the anisotropy of expansion is due to shear. Kristian and Sachs (1966) discussed such a velocity anisotropy as shear velocity field and Stewart and Sciama (1967) were interested in it from the point of view of finding earth's velocity with respect to the distant background (see also Sciama 1971).

Now, integrating (9), we obtain $R(r, t)$ and the expressions for σ, θ, ρ and ε are computed from (10)–(13). The cases $E = 0$ and $E \neq 0$ are considered separately.

Case (*i*): $E = 0$ (parabolic motion)

For this case $R(r, t)$ can be obtained by simple integration of (9). Thus,

$$R(r, t) = [9M(r)/2]^{1/3}\{t + f(r)\}^{2/3}, \tag{14}$$

and

$$\exp\lambda = (R')^2 = X_1^{\,2}\{6M^2(t + f)\}^{-2/3}, \tag{15}$$

$$\sigma = -2M(r)f'/(t + f)X_1, \tag{16}$$

$$\theta = -(\dot{\rho}/\rho) = 2\{1 - M(r)f'X_1^{\,-1}\}/(t + f), \tag{17}$$

$$\rho = M'(r)/6\pi(t + f)X_1, \tag{18}$$

$$\varepsilon = M(r)f'/3\pi(t + f)^2X_1, \tag{19}$$

CC-0. In Public Domain. Gurukul Kangri Collection, Haridwar

Digitized by Arya Samaj Foundation Chennai and eGangotri

where a prime for f denotes a differentiation with respect to r and $X_1 = (t+f)M'(r) + 2M(r)f'(r)$. From (18) we note that since ρ and $M'(r)$ are both positive, $(t+f)X_1 > 0$. Thus from (19) it is obvious that $f'/(t+f) > 0$. From (17), it is clear that the expansion rate is slowing down due to shear terms. The expression for $(\rho + \varepsilon)$ takes a simple form

$$\rho + \varepsilon = 1/6\pi(t+f)^2, \tag{20}$$

showing that whereas the metric, ρ and ε are singular on two surfaces $t+f=0$ and $X_1 = 0$, $(\rho+\varepsilon)$ is singular only on $t+f=0$. It may be pointed out that the presence of both anisotropy $(\sigma \neq 0)$ and inhomogeneity $(\partial\rho/\partial r \neq 0)$ are characterized by the function $f(r)$.

Without loss of generality we can choose the radial coordinate r such that

$$M(r) = 2r^3/9, \tag{21}$$

so that,

$$R(r,t) = r\{t + f(r)\}^{2/3}. \tag{22}$$

Thus, the metric takes the form

$$ds^2 = dt^2 - (t+f)^{4/3}\{Y^2 dr^2 + r^2(d\theta^2 + \sin^2\theta\, d\phi^2)\}, \tag{23}$$

where

$$Y = [1 + \{2rf'/3(t+f)\}]. \tag{24}$$

Consequently, (16)–(19) take the form

$$\sigma = -2rf'/3Y(t+f)^2, \tag{25}$$

$$\theta = -\dot{\rho}/\rho = 2(t+f)^{-1}[1 - \{rf'/3Y(t+f)\}], \tag{26}$$

$$\rho = 1/6\pi Y(t+f)^2, \tag{27}$$

$$\varepsilon = rf'/9\pi Y(t+f)^2. \tag{28}$$

For $f(r) = 0$, we get $\sigma = 0$, $\varepsilon = 0$ and as pointed out by Bonnor (1974), the expressions given by (22)–(27), reduce to those corresponding to the Einstein-de Sitter model.

Case (ii): $E \neq 0$

For this case we get

$$R = \begin{cases} M(r)(\cosh u - 1)/2E, & E > 0, \quad (29a) \\ -M(r)(1 - \cos u)/2E, & E < 0, \quad (29b) \end{cases}$$

$$t + g(r) = \begin{cases} M(r)(\sinh u - u)/(2E)^{3/2}, & E > 0, \quad (30a) \\ M(r)(u - \sin u)/(-2E)^{3/2}, & E < 0, \quad (30b) \end{cases}$$

u being a parameter. Thus, once again (10)–(13) take the form

$$\sigma = \begin{cases} (1/4M)\,\mathrm{cosech}^4(u/2)\tanh(u/2)[2A^{-1}\{EM' + ME'\sinh^2(u/2)\} \\ \quad -(2E)^{3/2}\{1 + 2\cosh^2(u/2)\}], \quad E > 0, \quad (31a) \\ (1/4M)\,\mathrm{cosec}^4(u/2)\tan(u/2)[2A^{-1}\{-EM' + ME'\sin^2(u/2)\} \\ \quad -(-2E)^{3/2}\{1 + 2\cos^2(u/2)\}], \quad E < 0, \quad (31b) \end{cases}$$

CC-0. In Public Domain. Gurukul Kangri Collection, Haridwar

Digitized by Arya Samaj Foundation Chennai and eGangotri

$$\theta = -(\dot{\rho}/\rho) = \begin{cases} \sigma + (3/2M)(2E)^{3/2} \coth(u/2)\,\mathrm{cosech}^2(u/2), & E>0, \quad (32a) \\ \sigma + (3/2M)(-2E)^{3/2} \cot(u/2)\,\mathrm{cosec}^2(u/2), & E<0, \quad (32b) \end{cases}$$

$$8\pi\rho = \begin{cases} (1/4M^2A)(2E)^{3/2}M' \,\mathrm{cosech}^6(u/2), & E>0, \quad (33a) \\ (1/4M^2A)(-2E)^{3/2}M' \,\mathrm{cosec}^6(u/2), & E<0, \quad (33b) \end{cases}$$

$$8\pi\varepsilon = \begin{cases} (1/8M^2)(2E)^{5/2}\{3(2E)^{1/2} - A^{-1}M\}\,\mathrm{cosech}^6(u/2), & E>0, \quad (34a) \\ (1/8M^2)(-2E)^{5/2}\{3(-2E)^{1/2} - A^{-1}M\}\,\mathrm{cosec}^6(u/2), & E<0, \quad (34b) \end{cases}$$

where

$$A = \begin{cases} (2E)^{-3/2}[\{(3/2)ME' - EM'\}(\sinh u - u)\coth(u/2)\,\mathrm{cosech}^2(u/2) \\ \quad + 2(EM' - ME')] + Eg' \coth(u/2)\,\mathrm{cosech}(u/2), & E>0, \quad (35a) \\ (-2E)^{-3/2}[\{(3/2)ME' + EM'\}(u - \sin u)\cot(u/2)\,\mathrm{cosec}^2(u/2) \\ \quad - 2(EM' + ME')] - Eg' \cot(u/2)\,\mathrm{cosec}(u/2), & E<0, \quad (35b) \end{cases}$$

and a prime for g denotes a differentiation with respect to r. It may be noted that the function $g(r)$ characterizes both anisotropy ($\sigma \neq 0$) and inhomogeneity ($\partial\rho/\partial r \neq 0$).

As earlier the role of $g(r)$ will become more transparent if we compare the present models with the corresponding FRW models by making the following simplifications (see Bonnor 1974). For small $r(\to 0)$, we take

$$M(r) = br^3, \quad E = 2r^2 (-2r^2 \text{ for the elliptic case}), \quad rg' \to 0, \quad (36)$$

b being a constant, so that

$$R = \begin{cases} br(\cosh u - 1), & E>0, \quad (37a) \\ -br(1 - \cos u), & E<0, \quad (37b) \end{cases}$$

$$t + g(r) = \begin{cases} b(\sinh u - u), & E>0, \quad (38a) \\ -b(u - \sin u), & E<0, \quad (38b) \end{cases}$$

$$\sigma = \begin{cases} -(rg'/4Bb)\,\mathrm{cosech}^6(u/2)\{1 + 2\cosh^2(u/2)\}, & E>0, \quad (39a) \\ -(rg'/4Bb)\,\mathrm{cosec}^6(u/2)\{1 + 2\cos^2(u/2)\}, & E<0, \quad (39b) \end{cases}$$

$$\theta = -(\dot{\rho}/\rho) = \begin{cases} \sigma + (3/2b)\coth(u/2)\,\mathrm{cosech}^2(u/2), & E>0, \quad (40a) \\ \sigma + (3/2b)\cot(u/2)\,\mathrm{cosec}^2(u/2), & E<0, \quad (40b) \end{cases}$$

$$8\pi\rho = \begin{cases} (3/2Bb)\,\mathrm{cosech}^6(u/2), & E>0, \quad (41a) \\ (3/2Bb)\,\mathrm{cosec}^6(u/2), & E<0, \quad (41b) \end{cases}$$

$$8\pi\varepsilon = \begin{cases} (3/4Bb^2)rg' \coth(u/2)\,\mathrm{cosech}(u/2), & E>0, \quad (42a) \\ (3/4Bb^2)rg' \cot(u/2)\,\mathrm{cosec}(u/2), & E<0, \quad (42b) \end{cases}$$

where

$$B = \begin{cases} 2b + rg' \coth(u/2)\,\mathrm{cosech}^2(u/2), & E>0, \quad (43a) \\ 2b + rg' \cot(u/2)\,\mathrm{cosec}^2(u/2), & E<0. \quad (43b) \end{cases}$$

Thus, $g(r) = 0$ implies $\sigma = \varepsilon = 0$ and the present models reduce to the corresponding FRW models.

CC-0. In Public Domain. Gurukul Kangri Collection, Haridwar

Digitized by Arya Samaj Foundation Chennai and eGangotri

3. A new parameter in observational cosmology

Isaacson and Winicour (1973) introduced a new parameter into observational cosmology: the present fractional conversion rate of matter into radiation. They have assumed that the thermal gravitational radiation thus produced is a homogeneous and isotropic fluid obeying the pressure-density relation $P_r = \rho_r/3$. Defining the fractional mass loss f due to radiative burning as

$$f = -\mathrm{d}(\log \mu)/\mathrm{d}t, \quad \mu = \rho S^3(t), \tag{44}$$

where $S(t)$ is the cosmological radius in the FRW models, the energy conservation equation

$$\frac{\mathrm{d}}{\mathrm{d}t}(\rho S^3) + \frac{1}{S}\frac{\mathrm{d}}{\mathrm{d}t}(\rho_r S^4) = 0, \tag{45}$$

takes the form

$$\frac{1}{S}\frac{\mathrm{d}\xi}{\mathrm{d}t} = -\frac{\mathrm{d}\mu}{\mathrm{d}t}, \quad \xi = \rho_r S^4. \tag{46}$$

Thus, in case of non-burning of matter into gravitational radiation ($f = 0$), ξ and μ are conserved. Also, the cosmological expansion is given by

$$(\dot{S}/S)^2 = (8\pi/3)(\rho + \rho_r) - (k/S^2). \tag{47}$$

The acceleration equation takes the form

$$\ddot{S}/S = -4\pi(\rho + 2\rho_r)/3, \tag{48}$$

giving an increased deceleration rate due to the presence of the ρ_r term. This implies that the present Hubble velocity can be reached in a shorter time from the big bang.

In contrast to the above scenario, Szekeres (1966) as well as Kristian and Sachs (1966) relate the presence of gravitational radiation with (the non-vanishingness of) the Weyl conformal tensor because it characterizes (through the geodesic equation) the inhomogeneities in the matter filled space-times. Thus, the FRW models with their conformally flat geometry can never describe propagation of gravitational radiation. Also Isaacson and Winicour's treatment of gravitational radiation as an isotropic fluid is difficult to accept since gravitational waves are transverse in character and their propagation must result in anisotropy (see Krauss 1986). Thus, one expects that any cosmological model in which gravitational radiation is propagated must be both inhomogeneous and anisotropic.

The models discussed in §2 are both inhomogeneous and anisotropic. Also, ε fits naturally as a new parameter in observational cosmology since it enters into the conservation law

$$\frac{\mathrm{d}}{\mathrm{d}t}\{4\pi(\rho + \varepsilon)R^3/3\} = 0. \tag{49}$$

It may be noted that although $(\rho + \varepsilon)$ is of the order R^{-3}, ε has the typical R^{-4}

CC-0. In Public Domain. Gurukul Kangri Collection, Haridwar

Digitized by Arya Samaj Foundation Chennai and eGangotri

spherical fall-off (see Eq. (19)). The factor $f'/\{2Mf' + (f+t)M'\}$ may be identified as representing the type N gravitational wave superposed on the traditional Coulomb field: $M/3\pi(f+t)^2$. This interpretation holds for hyperbolic and elliptic models also.

The new parameter ε enters the expansion eq. (9) and the deceleration eq. (8) and these equations are similar to (47) and (48) respectively. Hence, Isaacson and Winicour's remark that the presence of gravitational radiation increases the deceleration rate and hence the present Hubble velocity is reached in a shorter time from the big bang is true in our case also.

4. Effect of shear on redshift

In the FRW models the linear relation between the observed redshift of a galaxy and its distance from the observer is given by

$$Z = (\dot{S}/S)r = Hr, \tag{50}$$

H being the Hubble constant. In (50) the redshift is essentially due to the expansion of the Universe. However, in the more general cosmological models discussed in §2 shear also plays an important role in the computation of redshifts.

Following Kristian and Sachs (1966) we write the r-dependence of redshifts in the form

$$Z = Wr, \tag{51}$$

where

$$W = (\theta/3) + \sigma_{\alpha\beta}e^{\alpha}e^{\beta}, \tag{52}$$

e^{α} being a unit vector in the direction of observation. The expressions for the redshift of galaxies in the three cases can be computed by using the expressions given in §2. Thus, for the case $E=0$, we get

$$Z = \{2/3(f+t)\}[1 + 2M(r)f'(r)X_1^{-1}]r, \tag{53}$$

showing that the terms containing f' are indicative of the presence of shear terms in the redshift formula. Similarly for the case $E \neq 0$, we obtain

$$Z = \begin{cases} [(2E)^{3/2}\operatorname{cosech}^2(u/2)]/[2M(r)\tanh(u/2)] \\ \quad \times [1 + \tfrac{1}{6}\operatorname{sech}^2(u/2)\{(X_2/A) - (1 + 2\cosh^2(u/2))\}]r, & E>0, \quad (54a) \\ [(-2E)^{3/2}\operatorname{cosec}^2(u/2)]/[2M(r)\tan(u/2)] \\ \quad \times [1 + \tfrac{1}{6}\sec^2(u/2)\{(X_2/A) - (1 + 2\cos^2(u/2))\}]r, & E<0, \quad (54b) \end{cases}$$

where

$$X_2 = \begin{cases} 2(2E)^{-3/2}\{EM' + ME'\sinh^2(u/2)\}, & E>0, \quad (55a) \\ 2(-2E)^{-3/2}\{-EM' + ME'\sin^2(u/2)\}, & E<0. \quad (55b) \end{cases}$$

It may be noted that in (54a) and (54b) the shear terms appear through X_2.

It may be mentioned here that the force distribution for a free gravitational field has the effect of distorting a sphere into an ellipsoid which has the r-direction as the

CC-0. In Public Domain. Gurukul Kangri Collection, Haridwar

Digitized by Arya Samaj Foundation Chennai and eGangotri

principal axis and is degenerate in the (θ, ϕ)-plane (see Szekeres 1965). Kristian and Sachs (1966) have pointed out that the distortion effect is important in relativistic cosmology since an intrinsically spherical distant object appears as an ellipse in the photographic plates. This effect, even though proportional to r^2, depends on the Weyl conformal curvature tensor. Hence, any observed distortion favours the anisotropic and inhomogeneous cosmological models rather than the FRW models for which the conformal curvature tensor vanishes identically. However, it may be cautioned that in the spherically symmetric case the incident field is only of electric type.

5. Conclusion

The foregoing analysis of spherically symmetric inhomogeneous and anisotropic cosmological models strengthens the view that the FRW models have evolved from more general situations. In fact, perturbation of the FRW models (see Niedra and Janis 1983) leads to non-vanishing Weyl conformal tensor, even at first order of approximation, which again depends on shear terms. However, spherical symmetry does not permit to have explicitly a true radiation type of effect in the Weyl tensor which represents the propagated part of the gravitational field. A more realistic view of the universe is possible by relaxing spherical symmetry. Inhomogeneous and anisotropic cosmological models with axial symmetry and which are of Petrov type I will be discussed in a subsequent paper.

Acknowledgement

The author thanks the referees for their critical comments.

References

Bondi H 1947 *Mon. Not. R. Astron. Soc.* **107** 410
Bonnor W B 1972 *Mon. Not. R. Astron. Soc.* **159** 261
Bonnor W B 1974 *Mon. Not. R. Astron. Soc.* **167** 55
De Vaucouleurs G 1958 *Astron. J.* **63** 253
Isaacson R A and Winicour J 1973 *Astrophys. J.* **184** 49
Krauss L M 1986 *Gen. Relativ. Gravit.* **18** 723
Krishna Rao J 1966 *Curr. Sci.* **35** 589
Krishna Rao J 1971 *Gen. Relativ. Gravit.* **2** 385
Krishna Rao J 1972 *J. Phys. (London)* **A5** 479
Krishna Rao J 1973 *Gen. Relativ. Gravit.* **4** 351
Krishna Rao J and Annapurna M 1986 *Pramana – J. Phys.* **27** 637
Kristian J and Sachs R K 1966 *Astrophys. J.* **143** 379
Misner C W and Sharp D H 1964 *Phys. Rev.* **B136** 571
Misner C W 1967 *Nature (London)* **21** 357
Misner C W 1968 *Astrophys. J.* **151** 431
Niedra J M and Janis A I 1983 *Gen. Relativ. Gravit.* **15** 241
Omer G C (Jr) 1949 *Astrophys. J.* **109** 164

CC-0. In Public Domain. Gurukul Kangri Collection, Haridwar

Digitized by Arya Samaj Foundation Chennai and eGangotri

Rees M, Ruffini R and Wheeler J A 1974 *Black holes, gravitational waves and cosmology* (New York: Gordon and Breach)
Sciama D W 1971 *General relativity and cosmology* (ed.) R K Sachs (New York: Academic Press)
Stewart J M and Sciama D W 1967 *Nature* (*London*) **216** 748
Swinerd G G 1977 *Gen. Relativ. Gravit.* **8** 379
Szekeres P 1965 *J. Math. Phys.* **6** 1387
Szekeres P 1966 *J. Math. Phys.* **7** 751
Tolman R C 1934 *Proc. Natl. Acad. Sci. U.S.A.* **20** 169
Tolman R C 1949 *Rev. Mod. Phys.* **21** 374

CC-0. In Public Domain. Gurukul Kangri Collection, Haridwar

Digitized by Arya Samaj Foundation Chennai and eGangotri

Pramāṇa – J. Phys., Vol. 34, No. 5, May 1990, pp. 433–440. © Printed in India.

Q matter in the field of an abelian dyon admitting parity violating anomalous couplings

C WOLF
Department of Physics, North Adams State College, North Adams, MA 01247, USA

MS received 11 October 1989

Abstract. The properties of a configuration of two scalar doublets admitting a global SO(2) symmetry is studied in the presence of an abelian dyon core when the scalar doublets are coupled to the electromagnetic field through parity violating and parity preserving terms. The mass and the conserved global charge of the Q configuration are computed in terms of the parameters of the lagrangian.

Keywords. Soliton; dyon; parity violation.

PACS No. 04·90

1. Introduction

The existence of global symmetries in nature prods us to think if they are really the result of a precise gauge theory at a high energy scale with the global symmetry of the theory remaining after the gauge symmetry has been broken (Peccei 1986). In fact, many theorists believe that changing the field by the same amount in causally disconnected regions is very unnatural and cannot have any dynamical properties associated with it (Safian, Personal Communication). In spite of this fact, global symmetries have been useful in studying certain problems in particle theory, notably, the $U(1)_{PQ}$ (Peccei Quinn) symmetry to resolve the strong CP problem (Sikvie 1982) and $SU(3)_L \times SU(3)_R$ chiral flavor symmetry to aid in the understanding of the mechanism of quark mass generation (Wilczek 1982). With conserved global charges like baryon and lepton number being unavoidable consequences of the structure of particle theory, it seems relevant that we look for situations where these conserved charges play a role when a large number of particles are present. In response to this sentiment, Coleman suggested that conserved global charges might stabilize a configuration of fields against collapse or decay (Coleman 1984). This is the essential idea of the Q ball, namely a configuration of fields admitting a global symmetry wherein the mass of the configuration is less than that of the corresponding pions of the theory specified by the global charge Q. The original discussion of Coleman drew analogy with a conserved angular momentum preventing a particle's orbit from destabilizing. In an interesting paper, Cohen *et al* discuss the stability of L balls which are configurations of fermi fields and scalar fields inspired by the Gelmini Roncadelli model of neutrino mass generation (Cohen *et al* 1986). The result of their analysis was that L balls were stable except for slow decay into fermions at the surface. Also, in curved space, we have discussed the stability of Q balls in general relativity with

CC-0. In Public Domain. Gurukul Kangri Collection, Haridwar

Digitized by Arya Samaj Foundation Chennai and eGangotri

the result that the Q ball is stable providing its radius remains small (Wolf 1986). If gauge forces come into play, Q balls or "Q matter" has the additive feature of admitting internal repulsive forces in much the same way that a high Z nucleus becomes unstable to electrostatic repulsion. In this spirit, Lee *et al* have discussed gauged Q balls with a charged scalar field carrying the Q charge, the configuration is indeed stable provided the gauge charge does not grow large enough to destabilize the configuration (Lee *et al* 1989). In a previous note, we studied a shell of Q matter in the field of an abelian dyon with anomalous couplings between the scalar fields and electromagnetic field (Wolf 1989), the couplings we studied violated parity and in the present paper we study the more general case with both parity violating terms and parity conserving terms present. The interesting feature of this study is that the conserved Q charge is coupled to the magnetic charge of the central dyon core. Such a result suggests the indirect effect of magnetic charge on astrophysical situations. Of interest, also, is the fact that all non-abelian dyons appear as abelian for distances far removed from the dyon core, this justifies us describing the dyon as abelian when it interacts with the Q matter (Prassard and Sommerfield 1975). The interest in this investigation lies in the fact that it may simulate a configuration of Higgs fields when GUT dyons are present in the early universe. Such dyons or monopoles are inevitable consequences of GUT theories when the GUT group is broken to a sub-group with surviving U(1) factor, the simple problem we study here could serve as a spring-board from which we may investigate more complex Q configurations in the presence of a dyon core.

2. Q matter in the presence of a dyon core admitting anomalous scalar EM couplings

We begin our discussion by considering two scalar doublets transforming under the same SO(2) symmetry.

$$\phi = \begin{pmatrix} \phi_1 \\ \phi_2 \end{pmatrix}, \quad \psi = \begin{pmatrix} \psi_1 \\ \psi_2 \end{pmatrix}$$

$$\phi \to \left[1 + \varepsilon \begin{pmatrix} 0 & -1 \\ 1 & 0 \end{pmatrix} \right] \begin{pmatrix} \phi_1 \\ \phi_2 \end{pmatrix}$$

$$\psi \to \left[1 + \varepsilon \begin{pmatrix} 0 & -1 \\ 1 & 0 \end{pmatrix} \right] \begin{pmatrix} \psi_1 \\ \psi_2 \end{pmatrix}. \tag{1}$$

For the lagrangian of scalar fields interacting with electromagnetism and gravity, we have

$$\begin{aligned} \mathcal{L} = \frac{C^4}{16\pi G} R\sqrt{-g} + \Bigg[& \frac{\partial^\mu \phi^T \partial_\mu \phi}{2} + \frac{\partial^\mu \psi^T \partial_\mu \psi}{2} - \frac{A_2}{4}\left(\phi^T \phi - \frac{A_1}{A_2} \right)^2 \\ & - \frac{\bar{A}_2}{4}\left(\psi^T \psi - \frac{\bar{A}_1}{\bar{A}_2} \right)^2 + \alpha \left(\frac{\varepsilon^{\mu\nu\alpha\beta} F_{\alpha\beta} \partial_\mu \phi^T \partial_\nu \psi}{\sqrt{-g}} \right) \\ & + \beta \left(\frac{\varepsilon^{\mu\nu\alpha\beta} F_{\alpha\beta} \partial_\mu \phi^T \partial_\nu \psi}{\sqrt{-g}} \right)^2 \Bigg] \sqrt{-g} - \frac{1}{16\pi} F_{\mu\nu} F^{\mu\nu} \sqrt{-g}. \end{aligned} \tag{2}$$

Here, $F_{\mu\nu} = (\partial A_\mu / \partial x^\nu) - (\partial A_\nu / \partial x^\mu)$ where A_μ = vector potential and $A_1, A_2, \bar{A}_1, \bar{A}_2$ are

CC-0. In Public Domain. Gurukul Kangri Collection, Haridwar

Digitized by Arya Samaj Foundation Chennai and eGangotri

the parameters in the scalar potentials. The constants α, β measure the anomalous scalar—EM couplings with the α term being parity violating. The anomalous terms are phenomenological but can be thought of as generated by a Feynmann diagram representing a photon coupled to a quark look with two external scalars. The same type of term arises in an axion-photon coupling only in our case we may think of replacing the axion with a photon and the two photons in the axion diagram with the scalars in the present theory (Sikivie 1984). In this paper, we understand these couplings to be purely phenomenological and study what effect they have on the configuration of scalar fields.

For the boundary conditions, we put an abelian dyon at $r=0$ with electric charge e and magnetic charge q. The mass of the dyon we represent by M_x. For the region $R_1 > r > 0$ we have the true vacuum of each scalar and have the static solution

$$\phi = \begin{pmatrix} \sqrt{A_1/A_2} \\ 0 \end{pmatrix}, \quad \psi = \begin{pmatrix} \sqrt{\bar{A}_1/\bar{A}_2} \\ 0 \end{pmatrix}. \tag{3}$$

For the region of $R_2 \geqslant r \geqslant R_1$ we have the stationary Q matter solution

$$\phi = \begin{pmatrix} \phi(r)\cos wt \\ \phi(r)\sin wt \end{pmatrix}, \quad \psi = \begin{pmatrix} -\psi(r)\sin wt \\ \psi(r)\cos wt \end{pmatrix}. \tag{4}$$

We choose the true vacuum at $r = R_1$, $\phi, (R_1) = \sqrt{A_1/A_2}$, $\psi(R_1) = \sqrt{\bar{A}_1/\bar{A}_2}$, at $r = R_2$ we have the false vacuum $\phi(R_2) = 0$, $\psi(R_2) = 0$. For $r > R_2$ we have the static false vacuum

$$\phi = \begin{pmatrix} 0 \\ 0 \end{pmatrix}, \quad \psi = \begin{pmatrix} 0 \\ 0 \end{pmatrix}. \tag{5}$$

The metric takes the spherically symmetric form

$$(ds)^2 = e^{\nu}(dx^4)^2 - e^{\lambda}(dr)^2 - r^2\,d\theta^2 - r^2\sin^2\theta(d\phi)^2 \tag{6}$$

with $x^4 = ct$, $x^1 = r$, $x^2 = \theta$, $x^3 = \phi$. The radial electric and magnetic fields are related to the field tensor as $F_{14} = E(r)$, $F_{23} = r^2\sin\theta B_r$. The antisymmetry of $F_{\mu\nu}$ implies

$$\frac{\partial}{\partial x^{\nu}}(\varepsilon^{\mu\nu\alpha\beta}F_{\alpha\beta}) = 0 \tag{7}$$

$$\frac{\partial}{\partial r}(r^2\sin\theta B_r) = 0,$$

$$B_r = \frac{q}{r^2} \tag{8}$$

for all $r > 0$. Here q is the magnetic charge of dyon. Varying (2) with respect to the electromagnetic field gives

$$\frac{\partial}{\partial x^{\nu}}\left(\frac{1}{4\pi}\sqrt{-g}\,F^{\mu\nu}\right) - \frac{\partial}{\partial x^{\nu}}(2\varepsilon^{ab\mu\nu}\partial_a\phi^T\partial_b\psi)$$
$$-\frac{\partial}{\partial x^{\nu}}\left(4\frac{(\varepsilon^{ab\alpha\beta}F_{\alpha\beta}\partial_a\phi^T\partial_b\psi)}{\sqrt{-g}}\varepsilon^{st\mu\nu}\partial_s\phi^T\partial_t\psi\right) = 0 \tag{9}$$

CC-0. In Public Domain. Gurukul Kangri Collection, Haridwar

Digitized by Arya Samaj Foundation Chennai and eGangotri

since ϕ, ψ are independent of θ, ϕ the anomalous terms do not contribute in (9) giving

$$\frac{\partial}{\partial x^{\nu}}\left(\frac{1}{4\pi}\sqrt{-g}\,F^{\mu\nu}\right)=0. \tag{10}$$

We next calculate the energy momentum tensor from the matter part of the lagrangian in (2),

$$\begin{aligned}T_{\mu\nu}&=\frac{2}{\sqrt{-g}}\frac{\partial\mathscr{L}}{\partial g^{\mu\nu}}\\&=\partial_{\mu}\phi^{T}\partial_{\nu}\phi+\partial_{\mu}\psi^{T}\partial_{\nu}\psi-\frac{q_{\mu\nu}}{2}(\partial^{\alpha}\phi^{T}\partial_{\alpha}\phi+\partial^{\alpha}\psi^{T}\partial_{\alpha}\psi)\\&\quad+g_{\mu\nu}\frac{A_2}{4}\left(\phi^{T}\phi-\frac{A_1}{A_2}\right)^{2}+\frac{q_{\mu\nu}}{4}\bar{A}_2\left(\psi^{T}\psi-\frac{\bar{A}_1}{\bar{A}_2}\right)^{2}\\&\quad+\frac{1}{16\pi}g_{\mu\nu}F_{\alpha\beta}F^{\alpha\beta}-\frac{1}{4\pi}F_{\mu\alpha}F_{\nu}{}^{\alpha}+\beta\frac{(\varepsilon^{ab\alpha\beta}F_{\alpha\beta}\partial_{a}\phi^{T}\partial_{b}\psi)^{2}}{(-g)}g_{\mu\nu}.\end{aligned}$$

For $R_1>r$ and $r>R_2$ we have from (11), $T_1^1=T_4^4$, this implies $\lambda+\nu=0$ from the Einstein equation for the metric. From (10) we have

$$\frac{\partial}{\partial r}(r^2\exp[(-\nu+\lambda)/2]E(r)\sin\theta)=0,\quad\text{or } E(r)=e/r^2 \tag{12}$$

for $R_1>r, r>R_2$. Here $e=$ electric charge of dyon. To calculate the metric for $R_1>r$, we have, from $(^1_1)$ and the $(^4_4)$ component of the Einstein equation

$$\begin{aligned}&\frac{\mathrm{d}}{\mathrm{d}r}(r\exp(-\lambda))=1-\frac{8\pi G}{C^4}T_4^4r^2\\&T_4^4=\frac{E^2}{8\pi}+\frac{B^2}{8\pi}.\end{aligned} \tag{13}$$

Integrating gives

$$\exp(-\lambda)=1-\frac{2GM_x}{rC^2}+\frac{Gg^2}{r^2C^4}+\frac{Ge^2}{r^2C^4}. \tag{14}$$

Here we identify M_x as the mass of the dyon. For $r>R_2$ we have

$$T_4^4=\frac{E^2}{8\pi}+\frac{B^2}{8\pi}+\frac{A_1^2}{4A_2}+\frac{\bar{A}_1^2}{4\bar{A}_2}$$

this gives upon integrating (13)

$$\begin{aligned}\exp(-\lambda)=1&-\frac{2G(M_x+M_Q)}{rC^2}+\frac{Ge^2}{r^2C^4}+\frac{Gq^2}{r^2C^4}\\&-\frac{8\pi G}{3C^4}r^2\left(\frac{A_1^2}{4A_2}+\frac{\bar{A}_1^2}{4\bar{A}_2}\right).\end{aligned} \tag{15}$$

CC-0. In Public Domain. Gurukul Kangri Collection, Haridwar

Digitized by Arya Samaj Foundation Chennai and eGangotri

Where M_Q = mass of Q matter, and the false vacuum is present for $r > R_2$. For the region $R_2 \geqslant r \geqslant R_1$ we have $\lambda + v \neq 0$ since $T_1^1 \neq T_4^4$ from (11), however we will approximate $E_r = e/r^2$ in this region and also have $B = q/r^2$ from (8) which is an exact result following from the anti-symmetric condition in (7). We next proceed to solve for the field $\phi(r)$, $\psi(r)$ for $R_1 \leqslant r \leqslant R_2$, from the lagrangian (2) and the stationary solution in (4) we have upon substituting in (2) for the matter electromagnetic part of the lagrangian

$$\mathscr{L} = \left[\begin{array}{c} \dfrac{\exp(-v)(\phi(r))^2 w^2}{2c^2} + \dfrac{\exp(-v)(\psi(r))^2 w^2}{2c^2} - \dfrac{\exp(-\lambda)(\phi_{,r})^2}{2} \\ \dfrac{-\exp(-\lambda)(\psi_{,r})^2}{2} - \dfrac{A_2}{4}\left(\phi^2 - \dfrac{A_1}{A_2}\right)^2 - \dfrac{\bar{A}_2}{4}\left(\psi^2 - \dfrac{\bar{A}_1}{\bar{A}_2}\right)^2 \end{array} \right] r^2 \exp\left(\frac{\lambda + v}{2}\right) \sin\theta$$

$$+ \frac{\alpha}{c}(2r^2 B(r))\left[\frac{w\phi\psi_{,r}}{c} + \frac{w\phi_{,r}\psi}{c}\right]\sin\theta$$

$$+ \beta 4(B(r))^2 \left[\frac{w\phi\psi_{,r}}{c} + \frac{w\phi_{,r}\psi}{c}\right]^2 r^2 \exp\left(\frac{\lambda + v}{2}\right)\sin\theta \tag{16}$$

where we have approximated $(\lambda + v) = 0$ in the denominator of the second anomalous term, varying (16) with respect to ϕ, ψ gives upon setting $e^v \simeq e^\lambda \simeq 1$.

$$r^2\phi_{,rr} + 2r\phi_{,r} + \frac{r^2 w^2}{c^2}\phi - r^2 A_2 \phi\left(\phi^2 - \frac{A_1}{A_2}\right)$$

$$+ 8\beta\left(\frac{q^2}{r^2}\right)\left(\frac{w^2}{c^2}\right)(\phi(\psi_{,r})^2 + \psi\psi_{,r}\phi_{,r})$$

$$+ 16\beta\left(\frac{q^2}{r^3}\right)\left(\frac{w^2}{c^2}\right)(\phi\psi\psi_{,r} + \phi_{,r}(\psi)^2)$$

$$- \frac{8\beta q^2}{r^2}\left(\frac{w^2}{c^2}\right)(3\psi\psi_{,r}\phi_{,r} + \phi(\psi_{,r})^2 + \phi\psi\psi_{,rr} + \phi_{,rr}(\psi)^2) = 0 \tag{17}$$

$$r^2\psi_{,rr} + 2r\psi_{,r} + \frac{r^2 w^2 \psi}{c^2} - r^2 \bar{A}_2 \psi(\psi^2 - (\bar{A}_1/\bar{A}_2)$$

$$+ 8\beta\left(\frac{q^2}{r^2}\right)\left(\frac{w^2}{c^2}\right)(\psi(\phi_{,r})^2 + \phi\phi_{,r}\psi_{,r})$$

$$+ 16\beta\left(\frac{q^2}{r^3}\right)\left(\frac{w^2}{c^2}\right)(\psi\phi\phi_{,r} + \psi_{,r}\phi^2)$$

$$- \frac{8\beta q^2}{r^2}\left(\frac{w^2}{c^2}\right)\left(\begin{array}{c} 3\phi\phi_{,r}\psi_{,r} + \psi(\phi_{,r})^2 \\ + \psi\phi\phi_{,rr} + \psi_{,rr}\phi^2 \end{array}\right) = 0. \tag{18}$$

In (17) and (18) we have approximated $e^v \simeq e^\lambda \simeq 1$. To solve these equations we obtain an approximate solution as follows, we set

$$\phi = a_0 + a_1 r + a_2 r^2 + a_3 r^3$$
$$\psi = b_0 + b_1 r + b_2 r^2 + b_3 r^3 \tag{19}$$

CC-0. In Public Domain. Gurukul Kangri Collection, Haridwar

Digitized by Arya Samaj Foundation Chennai and eGangotri

we next insist that (19) obeys (17), (18) up to the third order in r, we also insist that (19) obeys the boundary condition

$$\phi(R_1)=\sqrt{\frac{A_1}{A_2}},\quad \phi(R_2)=0$$
$$\psi(R_1)=\sqrt{\frac{\bar{A}_1}{\bar{A}_2}},\quad \psi(R_2)=0. \tag{20}$$

To solve for the coefficients we must impose a relation between the coefficient a_0, b_0 given by $a_0=\bar{\alpha}b_0$ because of the finite number of terms we use. The results up to the cubic term are for ϕ, ψ

$$\phi=a_0+a_1r+a_2r^2+a_3r^3$$
$$a_0=-\frac{R_2^3}{R_1^3}\sqrt{\frac{A_1}{A_2}}+\frac{R_2^3}{R_1^3}\left(\frac{\bar{\alpha}}{2}\right)\left(\frac{1}{\bar{A}}\sqrt{\frac{A_1}{A_2}}-\sqrt{\frac{\bar{A}_1}{\bar{\alpha}_2}}\right)$$
$$a_1=0$$
$$a_2=\frac{-\frac{R_2^3}{R_1^3}\left[\sqrt{\frac{\bar{A}_1}{\bar{A}_2}}-\frac{1}{\bar{\alpha}}\sqrt{\frac{A_1}{A_2}}\right]}{\frac{2}{\alpha}\left(\frac{R_2^3}{R_1}-R_2^2\right)} \tag{21}$$
$$a_3=\frac{1}{R_1^3}\left[\sqrt{\frac{A_1}{A_2}}-a_0-a_2R_1^2\right]$$
$$\psi=b_0+b_1r+b_2r^2+b_3r^3$$
$$b_0=\frac{1}{\bar{\alpha}}a_0$$
$$b_1=0$$
$$b_2=-\frac{1}{\bar{\alpha}}a_2$$
$$b_3=\frac{1}{R_1^3}\left[\sqrt{\frac{\bar{A}_1}{\bar{A}_2}}-\frac{1}{\bar{\alpha}}a_0+\frac{1}{\bar{\alpha}}a_2R_1^2\right]. \tag{22}$$

Our next task is to evaluate the conserved Q charge, we have from the invariance under SO(2) of the lagrangian in (2)

$$\frac{\partial\mathcal{L}}{\partial\phi_1}\delta\phi_1+\frac{\partial\mathcal{L}}{\partial\phi_2}\delta\phi_2+\frac{\partial\mathcal{L}}{\partial\phi_{1,\mu}}\delta\phi_{1,\mu}+\frac{\partial\mathcal{L}}{\partial\phi_{2,\mu}}\delta\phi_{2,\mu}$$
$$+\frac{\partial\mathcal{L}}{\partial\psi_1}\delta\psi_1+\frac{\partial\mathcal{L}}{\partial\psi_2}\delta\psi_2+\frac{\partial\mathcal{L}}{\partial\psi_{1,\mu}}\delta\psi_{1,\mu}+\frac{\partial\mathcal{L}}{\partial\psi_{2,\mu}}\delta\psi_{2,\mu}=0 \tag{23}$$

Inserting the field equations for $\phi_1, \phi_2, \psi_1, \psi_2$ into (23) and integrating over r, θ, ϕ gives the conserved Q charged

CC-0. In Public Domain. Gurukul Kangri Collection, Haridwar

Digitized by Arya Samaj Foundation Chennai and eGangotri

$$Q=\frac{4\pi w}{c}\int_{R_1}^{R_2}|\phi(r)|^2r^2\,\mathrm{d}r+\frac{4\pi w}{c}\int_{R_1}^{R_2}|\psi(r)|^2r^2\,\mathrm{d}r$$
$$+8\pi q\alpha\int_{R_1}^{R_2}(\psi_{,r}\phi+\phi_{,r}\psi)\,\mathrm{d}r$$
$$+\frac{32\pi q^2\beta}{C}\int_{R_1}^{R_2}\frac{w}{r^2}(\psi_{,r}\phi+\phi_{,r}\psi)^2\,\mathrm{d}r. \tag{24}$$

Here, we have approximated $e^{\nu}\simeq e^{\lambda}\simeq 1$ and used the fact that the spatial component of the conserved current generated from (23) gives zero contribution to the spatial integral from the invariance condition in (1). The global charge in (24) we see is coupled both to the magnetic charge and the square of the magnetic charge, the linear dependence on the magnetic charge is parity violating while the quadratic coupling is parity respecting. Equation (24) can be used to solve for ω in terms of the global charge Q and the magnetic charge q. Our next task is to evaluate the mass of the Q matter, we first write down the $\binom{4}{4}$ component of the energy momentum tensor from (11) for $R_2\geqslant r\geqslant R_1$

$$T_4^4=\frac{(\phi(r))^2w^2}{2c^2}+\frac{(\psi(r))^2w^2}{2c^2}+\frac{(\phi_{,r})^2}{2}+\frac{(\psi_{,r})^2}{2}$$
$$+\frac{A_2}{4}\left((\phi(r))^2-\frac{A_1}{A_2}\right)^2+\frac{\bar{A}_2}{4}\left((\psi(r))^2-\frac{\bar{A}_1}{\bar{A}_2}\right)^2$$
$$+\frac{E^2}{8\pi}+\frac{B^2}{8\pi}+4\beta(B^2)\left(\frac{\phi\psi_{,r}}{c}+\frac{\psi_{,r}\phi}{c}\right)^2w^2. \tag{25}$$

Here, once again, we have approximated $e^{\nu}\simeq e^{\lambda}\simeq 1$ for $R_2\leqslant r\leqslant R_1$. We can now insert into (25) E, B from

$$B=\frac{q}{r^2},\quad E=\frac{e}{r^2}$$

where we are using the approximate solution for E for $R_2\leqslant r\leqslant R_1$, we also use the expression for $\phi(r)$, $\psi(r)$ from (21) and (22) with w being expressible in terms of the Q charge from (24). This series of substitutions will specify T_4^4 in terms of e, q, α, β and the parameters in the two scalar potentials for $R_2\geqslant r\geqslant R_1$. Inserting (25) into the $\binom{4}{4}$ component of the Einstein equations gives

$$\frac{\mathrm{d}}{\mathrm{d}r}(re^{-\lambda})=1-\frac{8\pi G}{c^4}T_4^4r^2, \tag{26}$$

integrating between R_2 and R_1 gives

$$(re^{-\lambda})_{R_2}-(re^{-\lambda})_{R_1}=R_2-R_1-\frac{8\pi G}{c^4}\int_{R_1}^{R_2}r^2T_4^4\,\mathrm{d}r. \tag{27}$$

Substituting (14) for the metric $e^{-\lambda}$ at $r=R_1$ and (15) for the metric $e^{-\lambda}$ at $r=R_2$ allows us to solve (27) for the mass of the Q matter since T_4^4 is known from (25).

CC-0. In Public Domain. Gurukul Kangri Collection, Haridwar

Digitized by Arya Samaj Foundation Chennai and eGangotri

3. Conclusion

The above calculation provides an interesting model upon which to build Q matter calculations whenever a central dyon or monopole core interacts with the scalar fields through the above anomalous coupling. Such a coupling might arise in super-symmetric extensions of the standard model where two Higgs doublets are required, to form such a Q matter configuration about a dyon core we need only have a gradient in the potential between the outer and inner boundary as well as the condition that the mass of the configuration is less than that of the free pions of the theory. Even if this last condition is not met, the above solution represents an interesting classical configuration of scalar fields. If the above configuration becomes unstable, either gravitationally, or through surface effects, it could provide a source of high energy gamma rays or massive particles with the energy liberated being a function of the global charge Q and the magnetic charge of the central dyon. It would be interesting to speculate that a series of these objects might appear in a cosmological setting with the energy liberated having the characteristic dependence on Q and q mentioned above.

Acknowledgements

I would like to thank the Physics Departments at Harvard University and Williams College for the use of their facilities.

References

Cohen A, Coleman S, Georgi H and Monohar A *Nucl. Phys.* 1986 **B272** 301
Coleman S 1984 *Lecture on Q Balls*, M.I.T.
Lee K, Stein-Schabes J A, Watkins R and Widrow L M 1989 *Phys. Rev.* **D1665**
Peccei R D 1986 *Proc. of XXIII Int. Conf. on High Energy*, (Singapore: World Scientific) p. 119
Prassard M K and Sommerfield E M 1975 *Phys. Rev. Lett.* **35** 760
Sikivie P 1982 *Phys. Rev. Lett.* **48** 1156
Sikivie P 1984 *Phys. Lett.* **B137** 355
Wilczek F 1982 *Phys. Rev. Lett.* **49** 1549
Wolf C 1986 *Phys. Lett.* **A117** 443
Wolf C 1989 *Can. J. Phys.* (submitted)

CC-0. In Public Domain. Gurukul Kangri Collection, Haridwar

Digitized by Arya Samaj Foundation Chennai and eGangotri

Pramāṇa – J. Phys., Vol. 34, No. 5, May 1990, pp. 441–445. © Printed in India.

The wavefunction envelope in one-dimensional random potentials

A MOOKERJEE and A M JAYANNAVAR*

S N Bose National Centre for Basic Sciences, DB-17, Sector I, Salt Lake City, Calcutta 700 064, India

*International Centre for Theoretical Physics, Trieste, Italy

MS received 19 December 1989; revised 8 February 1990

Abstract. We propose a formalism for the study of mean resistance of a one dimensional chain of random potentials. We obtain the resistance as a function of the length of the chain. In the asymptotic limit, this is related to the wavefunction envelope. The formalism demands loss of translational symmetry, but is general enough to include potentials with spatial correlations which are not long ranged and also those whose randomness is inhomogeneous.

Keywords. One-dimensional random potentials; inhomogeneous disorder; wavefunction envelopes.

PACS Nos 02·70; 62·10

The spectrum of random Hamiltonians has been a subject of intense study for the last two decades, following the pioneering work of Anderson (1958). Related to the above problem is the behaviour of the wavefunction for a given energy. One of the most interesting results in this connection is the fact that in one dimensional potentials even infinitesimal randomness in the potential leads to a pure point spectrum for almost all realisations of the potential, with exponentially decaying wavefunction envelopes (Kunz and Souillard 1980; Royer 1982; Delyon *et al* 1983). Delyon *et al* presented a formalism that allows generalization to random potentials which do not possess statistical homogeneity, or which have short ranged correlations in space. This is the subject matter of our study.

Several situations on non-homogeneous random potentials have been studied in the literature. A typical such potentials is $V(x) = f|x|^{-a}v(x)$, where $v(x)$ is a homogeneously random potential. The problem is closely related to the physically interesting problem of an independently random Kronig-Penny model in the presence of a uniform electric field, such that we have $V(x) = \Sigma v_n\, \delta(x-n) - Fx$ (Delyon *et al* 1983). For the former, Delyon *et al* have given a proof that almost surely

(i) if $0 < a < 1/2$, the entire spectrum is pure point with eigenfunction envelopes decaying as stretched exponentials of the form $\exp(-|x|^{-a})$. (ii) If $a = 1/2$, the spectrum is pure point with power law decaying states if $x > x_1$ and singularly continuous if $x < x_2$ in $|E| < 2$. (iii) If $a > 1/2$, the spectrum is absolutely continuous (Kotani 1986; Souillard 1986) with extended eigenstates.

In Kronig-Penny model Souillard finds that (i) $0 < F < F_1$ almost surely we have a point spectrum with power law decaying eigenstates. (ii) $F > F_2$ almost surely we have an absolutely continuous spectrum with extended states.

Vijaygovindan *et al* (1986) have studied the mean resistance of the same model.

CC-0. In Public Domain. Gurukul Kangri Collection, Haridwar

Digitized by Arya Samaj Foundation Chennai and eGangotri

They observe a smooth crossover from the power law to exponentially decaying states. The former is relevant at large fields and large lengths.

We shall develop a formalism to study the mean resistance of a one-dimensional potential. It would include non-homogeneously random potentials as well as those with spatially correlated potentials which are nevertheless without translational symmetry. A classic example of this is the Fibonacci chain (Mookerjee and Singh 1986). Our approach will be based on the invariant embedding principle (Chandrasekhar 1960; Bellman and Wing 1975). In particular, we shall use the variant used by Heinrichs (1986) involving the potential, rather than Kumar's (1985) version involving the potential derivatives.

The model Hamiltonian is given by

$$H = (-\hbar^2/2m)\,\mathrm{d}^2/\mathrm{d}x^2 + V(x)$$
$$V(x) = f(x)v(x) \tag{1}$$

where $f(x)$ is a non-random function which describes the non-homogeneity of the potential distribution (it is a constant for homogeneously random potentials). $v(x)$ is a Gaussian random function with

$$\langle v(x)\rangle = 0; \quad \langle v(x)v(x')\rangle = g(x-x'). \tag{2}$$

The disordered potential stretches from $x=0$ to $x=L$. A plane wave is incident at one end, partially reflected and partially transmitted. In our approach we address ourselves only to emergent quantities like the transmission and reflection coefficients. The complex amplitude reflection coefficient $R(x)$ obeys the Stochastic-Riccati equation

$$ik\frac{\mathrm{d}R(x)}{\mathrm{d}x} = V(x)[R(x)^2+1] - 2[k^2 - V(x)]R(x), \tag{3}$$

where k is the wavenumber of the incident wave related to the energy by $k=\sqrt{|E|}$ in atomic units (Bellman and Wing 1975).

If $R(x) = r(x)\exp[ip(x)]$ where $r(x)$ and $p(x)$ are real functions, then the Landauer (1970) expression for the resistance $\rho(x)$ in natural units of $(\hbar/e^2)$ is

$$\rho(x) = \frac{r^2(x)}{1-r^2(x)}. \tag{4}$$

The Riccati eq. (3) with the transformation (4) may be written as a pair of coupled non-linear stochastic equations

$$\frac{\mathrm{d}p(x)}{\mathrm{d}x} = -\frac{V(x)}{k}\left(r(x)+\frac{1}{r(x)}\right)\cos p(x) + 2\left(k-\frac{V(x)}{k}\right)$$
$$\frac{\mathrm{d}\rho(x)}{\mathrm{d}x} = -\frac{2V(x)}{k}(\rho(x)[\rho(x)+1])^{1/2}\sin p(x). \tag{5}$$

For deterministic potentials the phase $p(x)$ is a specific function of x. Equations (5) have in no way made use of the randomness in the potentials. Such equations have been used as the basis of elaborate numerical calculations on one dimensional quantum

CC-0. In Public Domain. Gurukul Kangri Collection, Haridwar

Digitized by Arya Samaj Foundation Chennai and eGangotri

wells both periodic as well as incommensurate. In random one-dimensional potentials, the phase $p(x)$ rapidly becomes random with increasing x and the phase memory is lost. The equations may then be decoupled by averaging over the random phase in addition to averaging over the different realizations of the potential. This has been implicitly done in all the work quoted above on random one-dimensional systems. The averaging is carried out using the Novikov theorem (Novikov 1964; Madhukar and Post 1977) for Gaussian random functions

$$\frac{\mathrm{d}}{\mathrm{d}x}\langle\rho(x)\rangle_{vp} = -(2/k)\langle V(x)F[V(x)]\rangle_{vp}$$

$$F[V(x)] = \sin p(x)\rho(x)[\rho(x)+1].$$

Note that $V(x)$ and $p(x)$ are not independently random functions but are related via the first of (5). Using (5)

$$\mathrm{d}F(x)/\mathrm{d}x = [V(x)/k][1+2\rho(x)] + 2[k - V(x)/k]\rho(x)[\rho(x)+1]\cos p(x).$$

It is at this point that we have to invoke randomness. In the second term above the factors $V(x)$, $\rho^2(x)$ and $\cos p(x)$ vary in a strongly correlated manner. In fact in systems where phase memory is retained, the pair of non-linear equations need to be solved. However, in systems where the phase memory is lost for large enough values of x (and this includes random variation in $V(x)$, homogeneous or otherwise, including short ranged order or not) phase averaging leads to this term dropping out, provided we apply the equations for large enough values of x. For periodic potentials this approximation is strictly untrue. For quasi-periodic systems, the validity of this assumption is uncertain

Thus, $$\langle \mathrm{d}F(x)/\mathrm{d}x\rangle = -[V(x)/k][1+2\rho(x)\rangle].$$

or $$F(x) = -(1/k)\int^x V(x')[1+2\langle\rho(x')\rangle\,\mathrm{d}x'$$

$$\langle\delta F/\delta V\rangle = -(1/k)[1+\langle\rho(x)\rangle].$$

Novikov's theorem states that

$$\langle V(x)F[V(x)]\rangle = \int^x \mathrm{d}x'\langle V(x)V(x')\rangle\langle\delta F/\delta V\rangle.$$

Using these equations and averaging over different realizations of the random potential, we obtain the basic equation for the averaged resistance $\langle\rho(x)\rangle = \bar{\rho}$

where $$\mathrm{d}\bar{\rho}/\mathrm{d}x = (2/k^2)\int^x \mathrm{d}x' G(x,x')[1+2\bar{\rho}(x')]$$

$$G(x,x') = \langle V(x)V(x')\rangle = f(x)f(x')g(x-x') \qquad (6)$$

$g(x-x') = \langle v(x)v(x')\rangle$ is the homogeneous part of the spatial correlations of the potential.

CC-0. In Public Domain. Gurukul Kangri Collection, Haridwar

Digitized by Arya Samaj Foundation Chennai and eGangotri

We shall now apply the above equation to different situations of interest

(1) Let $f(x)=f$, and $g(x-x')=\delta(x-x')$. This occurs if we have a purely homogeneously random potentials with no short ranged correlations at all. Here $d\bar{\rho}/dx=(2f^2/k^2)(1+\bar{2}\rho)$, with $\bar{\rho}=0$ at $x=0$. This gives

$$\bar{\rho}(x)=(1/2)[\exp(x/x_0)-1] \quad \text{with } x_0=k^2/f^2. \tag{7}$$

This result is identical with that of Kumar (1985), although a different embedding technique is used.

(2) The inhomogeneously random potential with $f(x)=f|x|^{-a}$ and $g(x-x')=\delta(x-x')$ (studied by Souillard), so that

$$d\bar{\rho}/dx=(2f^2/k^2)|x|^{-2a}(1+2\bar{\rho}) \quad \text{with } \bar{\rho}=0 \text{ at } x=0$$

(a) for $0<a<1/2$ $\bar{\rho}=(1/2)[\exp(c|x|^{1-2a})-1]$ with the factor $c=(4f^2/k^2)\{1/(1-2a)\}$. The average resistance diverges non-ohmically and the resistivity is infinite. This is characteristic of localized states and pure point spectra. Since, for large x, $\rho\simeq 1/T(x)$ where $T(x)$ is the transmission coefficient, which itself reflects the decay of the wavefunction envelope decay, the above expression indicates that this decay is of the stretched exponential type. This result is identical to that of Souillard but based on completely different arguments. (b) for $a=1/2$, if $\bar{\rho}=\rho_0$ at $x=x_0$ $\bar{\rho}=(1/2)[(1+2\rho_0)\cdot(x/x_0)^{4f^2/k^2}-1]$ again, using the above arguments, the wavefunction decay is power law, agreeing with Souillard's result. (c) For $a>1/2$ $\bar{\rho}=(1/2)[(1+2\bar{\rho}_0)\exp\{(2f^2/k^2)\cdot|x|^{1-2a}\}-1]$ since $a>1/2$, $\bar{\rho}$ becomes a constant as x becomes large. Thus the resistivity vanishes. This is characteristic of extended states and absolutely continuous spectra.

(3) Finally we wish to apply the ideas of (6) to a homogeneously random potential with $f(x)=f$, but $g(x-x')=(1/a)\exp\{-a(x-x')\}$ so that $1/a$ is a measure of the extent of spatial correlation (or short ranged order) of the potentials. In (6) we change the variable $\bar{\rho}$ to $y=(1+2\bar{\rho})$ and take the Laplace transform of both sides

$$s\tilde{y}(s)=2\tilde{g}(s)\tilde{y}(s) \quad \text{or} \quad \tilde{y}(s)=1/[s-g(s)]. \tag{8}$$

For our case $\tilde{g}(s)=(2f^2/k^2a)(s+a)$ which leads to the solution $\tilde{y}(s)=(1/2)[(1+a/D)\cdot(s-s_1)+(1-a/D)(s-s_2)]$ where $s_1=(D-a)/2$ and $s_2=(D+a)/2$ and $D=[a^2+16(f^2/ak^2)]^{1/2}$. Inverse transform yields

$$\bar{\rho}(x)=(1/2D)[s_2\exp(s_1x)+s_1\exp(s_2x)-1] \tag{9}$$

for large values of x, $\bar{\rho}=(s_2/2D)\exp(x/x_0)$, where $x_0=1/s_1$. Thus although the potentials have an extent of spatial correlations, the result is substantially similar to the case (1) without any spatial correlation. We have shown that short ranged order does not destroy localization in a one-dimensional system and we still have exponentially decaying wavefunction envelope and pure point spectra.

The aim of the present communication is to study the mean resistance of linear random systems as a means of examining the wavefunction envelopes. We propose (6) as the basis of further study. The examples quoted illustrate that the results of this analysis agree substantially with more detailed and involved mathematical analysis of the same problems. The added advantage is that in the process we also have information about the physical response of the one-dimensional systems.

CC-0. In Public Domain. Gurukul Kangri Collection, Haridwar

Digitized by Arya Samaj Foundation Chennai and eGangotri

Conjectures have been made about the spectrum of quasi-crystalline one-dimensional systems (Valsakumar and Ananthakrishna 1986). Such one-dimensional systems have potentials which lack translational symmetry and long ranged correlations, but whose correlations are different from random one-dimensional systems. We propose to make confirmatory studies on the basis of this formalism.

Acknowledgements

The authors would like to thank Prof. Abdus Salaam and the ICTP, Trieste, Italy for kind hospitality in Trieste, where a major part of the discussion leading to this work took place. One of us (AMJ) would like to thank Prof. B Souillard for making available several preprints.

References

Anderson P W 1958 *Phys. Rev.* **109** 1492
Bellman R and Wing G M 1975 *An introduction to invariant embedding* (New York: Wiley)
Chandrasekhar S 1960 *Radiative transfer* (New York: Dover)
Delyon F, Kunz H and Souillard B 1983 *J. Phys.* **A16** 25
Heinrichs H 1986 *Phys. Rev.* **B33** 5261
Kotani S 1986 (private communication, see paper *by Souillard*)
Kumar N and Jayannavar A M 1986 *J. Phys.* **C19** L85
Kunz H and Souillard B 1980 *Commun. Math. Phys.* **78** 201
Landauer R 1970 *Philos. Mag.* **21** 863
Madhukar A and Post P 1977 *Phys. Rev. Lett.* **39** 1424
Mookerjee A and Singh V A 1986 *Phys. Rev.* **B34** 7433
Novikov E A 1964 *Zh. Eksp. Teor. Fiz.* **47** 1919
Royer G 1982 *Bull. Soc. Math. Fr.* **110** 201
Souillard B 1986 *Proc. Conf. on random media* (Minnesota, USA)
Valsakumar M C and Ananthakrishna G 1987 *J. Phys.* **C20** 9
Vijayagovindan A, Kumar N and Jayannavar A M 1987 *Phys. Rev.* **B35** 2029

CC-0. In Public Domain. Gurukul Kangri Collection, Haridwar

Digitized by Arya Samaj Foundation Chennai and eGangotri

CC-0. In Public Domain. Gurukul Kangri Collection, Haridwar

Digitized by Arya Samaj Foundation Chennai and eGangotri

Pramāṇa – J. Phys., Vol. 34, No. 5, May 1990, pp. 447–460. © Printed in India.

The effect of the relativistic Hartree–Fock–Roothaan momentum distribution in the binary encounter approximation for inner shell ionization

V KUMAR, S N CHATTERJEE and B N ROY
Department of Physics, Bihar University, Muzaffarpur 842001, India

MS received 25 September 1989; revised 31 January 1990

Abstract. K- and L-shell ionization cross sections of gold due to impact of proton and alpha particles have been calculated in the binary encounter approximation incorporating the effects of Coulomb deflection of the projectile, of increase in binding of the target electron, and of polarization and relativity. Relativistic Hartree–Fock–Roothaan (RHFR) momentum distributions for the target electron along with an approximate relativistic correction to the collision dynamics have been used in the present calculations. A comparison with the corresponding calculations using non-relativistic Hartree–Fock–Roothaan wave functions, experimental results and other available calculations is presented.

Keywords. Alpha particle; proton; K-shell ionization; L-shell ionization; relativistic.

PACS No. 34·50

1. Introduction

Ionization from inner shells of atoms, particularly K and L shells due to impact of charged particles has been a subject of intensive study because of its wide applications (Hardt and Watson 1976; Starter *et al* 1981). A systematic study of experimental and theoretical cross sections for light ion impact K-shell ionization of different atoms are available in literature (e.g. Paul and Obermann 1983; Paul 1984, 1987, 1989). In this context the two review articles, Paul (1984) and Paul and Muhr (1986), are important. The experimental cross sections available in literature have been systematically studied for proton impact L-shell ionization of atoms, in the recent past by Braziewicz and Braziewicz (1988). These studies indicate that the ion impact inner shell ionization process is best described in the intermediate energy region by ECPSSR method which is a modified version of plane wave born approximation (PWBA) including corrections for the energy loss (E), Coulomb deflection (C), perturbed stationary state effect (PSS) and the relativistic effect (R). However, a direct calculation by this method is involved and requires much computation. On the other hand the binary encounter approximation (BEA) has been successfully used for a theoretical investigation of these processes with comparatively much small computer time (for example Chatterjee *et al* 1983; Srivastava *et al* 1984; Shrivastava and Roy 1986). In fact the BEA, apart from its simplicity, is essentially linked with the plane wave Born approximation (PWBA) and gives results which are in agreement with PWBA (Langenberg 1978). However, in most of the previous BEA calculations on inner-shell ionization cross sections by charged particle impact of atoms the relativistic

CC-0. In Public Domain. Gurukul Kangri Collection, Haridwar

Digitized by Arya Samaj Foundation Chennai and eGangotri

nature of the target electron has been ignored. But this must be taken into account especially for heavy targets. For heavy targets the relativistic effects have been found to increase the cross sections significantly, particularly at low impact energy (Avaldi *et al* 1982). Avaldi *et al* (1982) have reported their BEA calculations on proton impact K-shell ionization cross section for Au. They have incorporated the effect of relativity using relativistic collision dynamics and a relativistic hydrogenic momentum distribution for the bound electron. Sheth (1984) has reported BEA calculations on proton impact K-shell ionization of Ti and Cu incorporating relativistic effects for the bound electron following a different approach. He has used the relativistic version of the Rutherford cross section up to the first order Born approximation, incorporating the correction due to relativity and spin along with the Dirac wave function. Although, the use of hydrogenic functions is approximately correct in K-shell electrons, it is not at all physically justified for other shells. We have used RHFR wave functions for both K and L shell electrons in the present calculations.

In the present work, Vrien's (1967) expressions for the ionization cross section of an atom due to impact of heavy charged particles have been used. The effects of Coulomb repulsion of the projectile due to the target nucleus and of the change in binding of the target electron due to presence of the projectile have been incorporated following the method of Thomas and Garcia (1969) and Brandt and Lapicki (1979) respectively. In order to account for relativistic effects of the target electron, approximate relativistic collision dynamics introduced by Avaldi *et al* (1982) has been used along with the RHFR momentum distribution function for the bound electron which have been developed as suggested by Mukoyama and Kagawa (1983).

2. Theoretical consideration

Using atomic units, with energy expressed in rydbergs, Vriens's expression (1967) for ionization cross section due to impact of a heavy charged particle, incorporating the modification for Coulomb repulsion of the projectile and change in the binding energy of the target electron may be written as

$$Q=\begin{cases}\dfrac{(s+s')^2 Z_1^2}{s^2 s'^2 U_c^2 m}\left\{1+\dfrac{2}{3}mt^2-\dfrac{1}{4m(s'^2-t^2)}\right\}(\pi a_0^2); & 1\leqslant 4ms'(s'-t)\\ \dfrac{(s+s')^2}{2s^2 s'^2 U_c^2 tm} Z_1^2\left[\dfrac{1}{4m(s'+t)}+t+\dfrac{2}{3}m\left\{2s'^3+t^3-\left(\dfrac{1}{m}+t^2\right)^{3/2}\right\}\right](\pi a_0^2); & \\ 0; \quad 4ms'(s'-t)\leqslant 1\leqslant 4ms'(s'+t) & \\ \qquad 1\geqslant ms'(s'+t) & \end{cases} \tag{1}$$

where

$$t^2=v_{2s}^2/U_c, \quad s^2=v_1^2/U_c$$

$$s'^2=s^2-(1{\cdot}058Z_1Z_{2s})/(1836Ma_{2s}U_c),$$

with v_1 and v_{2s} (subscript s stand for K, L_1, L_2, L_3) the velocity of the projectile and bound electron, respectively, Z_1 and M, the charge and mass (in units of proton mass) of the projectile, a_{2s} the radius of the shell considered, $Z_{2s}=Z_2-S_{2s}$ with Z_2 the nuclear charge of the target and S_{2s} the screening constant of the shell, and m the

CC-0. In Public Domain. Gurukul Kangri Collection, Haridwar

Digitized by Arya Samaj Foundation Chennai and eGangotri

ratio of relativistic to non-relativistic mass of the electron. In (1) $U_c = \varepsilon U_{2s}$ is the binding energy of the target electron corrected for the presence of the projectile whereas U_{2s} is the unperturbed binding energy of the target electron. The correction factor ε (Brandt and Lapicki 1979), incorporating the effects of increase in binding energy of the target electron and the polarization of the orbital, is given by

$$\varepsilon = 1 + (2Z_1/Z_{2s}\theta_{2s}) \quad (g - h),$$

with $\theta_{2s} = (U_{2s}/Z_{2s}^2)$ (13·6), and, for K shell:

$$g = (1 + 5x + 7{\cdot}14x^2 + 4{\cdot}27x^3 + 0{\cdot}947x^4)/(1 + x)^5,$$

for L_1 shell:

$$g = (1 + 9x + 31x^2 + 49x^3 + 162x^4 + 63x^5 + 18x^6 + 1{\cdot}97x^7)/(1 + x)^9,$$

and for L_2 and L_3 sub shells:

$$g = (1 + 10x + 45x^2 + 102x^3 + 331x^4 + 6{\cdot}7x^5 + 58x^6 + 7{\cdot}8x^7 + 0{\cdot}888x^8)/(1 + x)^{10}$$

where $x = v_1/(\frac{1}{2}\theta_{2s}v_{2s})$,

$$h = (2n_2/\theta_{2s}x^3)I(C_s n_2/x),$$

$$I(\kappa) = 2\exp(-2\kappa)/\kappa^{1\cdot 6},$$

$$C_K = C_{L_1} = 3/2 \text{ and } C_{L_2} = C_{L_3} = 5/4.$$

Cross sections have been obtained by integrating the above expressions over the Hartree-Fock-Roothaan (HFR) and RHFR momentum distribution for the target electron. In principle, for relativistic considerations, the upper limit of the velocity of the target electron should be c, the speed of light in vacuum. However, the contributions from large values of t (and hence v_{2s} the velocity of the target electron) are negligibly small. Hence during the course of evaluting the integrals over the momentum distribution we have used a cut off for t determined by a fixed accuracy limit of the cross sections, in order to obtain convergence of the integral. The HFR momentum distribution for the target electron has been constructed using the double zeta function taken from the table of Mclean and Mclean (1981).

Here we would like to present a brief discussion on the method of constructing RHFR momentum distribution function for the target electron. In the configuration space the RHFR wave function is given as (Kagawa 1975)

$$\psi_{s\kappa u}(\gamma) = \frac{1}{\gamma}\begin{pmatrix} P_{s\kappa}(\gamma) & \chi^u_\kappa(\gamma) \\ iQ_{s\kappa}(\gamma) & \chi^u_{-\kappa}(\gamma) \end{pmatrix} \tag{2}$$

where $P_{s\kappa}(\gamma)$ and $Q_{s\kappa}(\gamma)$ are the large and small components of the radial wave function, $\chi^u_\kappa(\hat{\gamma})$ is the spin angular wave function and S is the principal quantum number. The relativistic quantum number κ is expressed as $\kappa = \pm(j + \frac{1}{2})$ for $j = l \pm \frac{1}{2}$, where j is the total angular momentum and l is the orbital angular momentum. The radial wave functions are given in terms of the STO with non-integral principal quantum

CC-0. In Public Domain. Gurukul Kangri Collection, Haridwar

Digitized by Arya Samaj Foundation Chennai and eGangotri

number

$$P_{s\kappa}(\gamma) = \sum_q \xi_{sq}^{(l)} f_{\kappa q}(\gamma) \tag{3}$$

and

$$Q_{s\kappa}(\gamma) = \sum_q \xi_{sq}^{(s)} f_{\kappa q}(\gamma). \tag{4}$$

Here $\xi_{sq}^{(l)}$ and $\xi_{sq}^{(s)}$ are the expansion coefficients.

The STO $f_{\kappa q}(\gamma)$ is given by

$$f_{\kappa q}(\gamma) = (2\zeta_{\kappa q})^{n'_{\kappa q}+\frac{1}{2}}[\Gamma(2n'_{\kappa q}+1)]^{-1/2}\gamma^{n'_{\kappa q}}\exp(-\zeta_{\kappa q}\gamma) \tag{5}$$

where

$$n'_{\kappa q} = n_{\kappa q} + (\kappa^2 - z^2\alpha^2) \quad n_{\kappa q} = 0, 1, \ldots . \tag{6}$$

and $\zeta_{\kappa q}$, $\Gamma(x)$, z and α are orbital exponent, gamma function, atomic number and fine structure constant, respectively.

The momentum representation of the wave function of (2) is given by (Rubinowicz 1948)

$$\psi_{szu}(p) = \begin{pmatrix} N_{s\kappa}(p) & \chi_\kappa^u(p) \\ iM_{s\kappa}(p) & \chi_\kappa^u(p) \end{pmatrix}. \tag{7}$$

The radial wave functions are obtained from those in the configuration space through the Fourier Bessel transformation

$$N_{s\kappa}(p) = i^{-l}\left(\frac{2}{\lambda}\right)^{1/2}\int_0^\infty j_l(p\gamma)P_{s\kappa}(\gamma)\,d\gamma \tag{8a}$$

$$M_{s\kappa}(p) = i^{-\bar{l}}\left(\frac{2}{\lambda}\right)^{1/2}\int_0^\infty j_{\bar{l}}(p\gamma)Q_{s\kappa}(\gamma)\,d\gamma \tag{8b}$$

where $j_l(x)$ is the spherical Bessel function of the first kind and $\bar{l}$ denotes the orbital angular momentum corresponds to $-\kappa$.

Using (3) and (4), eqs. (8a) and (8b) reduce to

$$N_{s\kappa}(p) = i^{-l}\sum_q \xi_{sq}^{(l)} C_{\kappa q} I(n'_{\kappa q}, \zeta_{\kappa q}, l) \tag{9a}$$

$$M_{s\kappa}(p) = i^{-\bar{l}}\sum_q \xi_{sq}^{(s)} C_{\kappa q} I(n'_{\kappa q}, \zeta_{\kappa q}, \bar{l}) \tag{9b}$$

where

$$C_{\kappa q} = (2\zeta_{\kappa q})^{n'_{\kappa q}+(1/2)}/[\Gamma(2n_{\kappa q}^1+1)]^{1/2} \tag{10}$$

and

$$I(n,\zeta,l) = \frac{\Gamma(m)p^l}{2^{l+2}\zeta^m\Gamma(l+\frac{3}{2})}F\left(\frac{m}{2}, \frac{m+1}{2}; l+\tfrac{3}{2}; \frac{-p^2}{\zeta^2}\right)$$

with $m = n + l + 2$.

Finally the RHFR momentum distribution for an orbital is given by $P(p) = |N_{s\kappa}(p)|^2 + |M_{s\kappa}(p)|^2$ (see Mukoyama and Kagawa 1983). For these calculations, parameters made available by Mukoyama (private communication) have been used. These parameters were made available by Mukoyama only for gold and hence it was not possible to extend the calculations for other systems in the present work. The

CC-0. In Public Domain. Gurukul Kangri Collection, Haridwar

Digitized by Arya Samaj Foundation Chennai and eGangotri

binding energies of the target electron and the quantum mechanical values of the screening constant have been taken from Lotz (1968) and Fischer (1972) respectively. For the shell radii of atoms the quantum mechanical values of points of maximum radial probability density reported by Desclaux (1973) have been used.

3. Results and discussion

We have calculated proton and alpha particle impact K-shell and L-shell ionization cross sections of gold following the method outlined in § 2. Two sets of calculations have been carried out for each projectile. The results have been presented in the figures. In the first set of calculations the effects of the Coulomb repulsion of the projectile, the increase in the binding energy of the target electron and polarization effects have been incorporated along with a non-relativistic HFR wave functions for the bound electron. In the second set of calculations the effects of relativity have also been incorporated. The calculated results have been compared with available experimental observations and other theoretical calculations, particularly the ECPSSR originally formulated by Brandt and Lapicki (1979).

The present results for proton and alpha particle impact K-shell ionization cross sections have been shown in figures 1 and 2 respectively. The BEA calculations for proton impact by Avaldi *et al* (1982) overestimate the cross sections. This is as expected because they have used a relativistic hydrogenic wave function for the bound electron. In the present work the target electron has been described by a RHFR wave function.

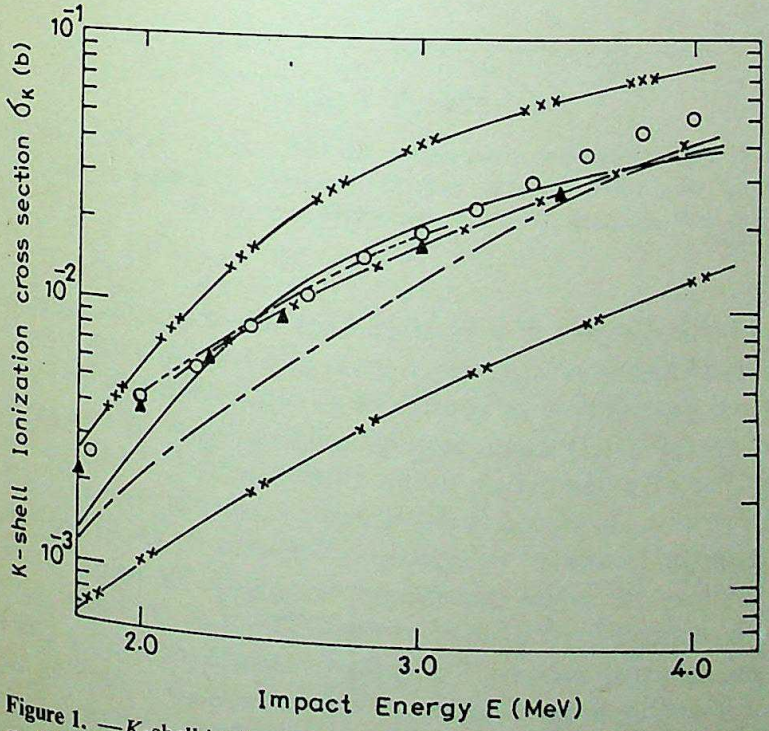

Figure 1. —K-shell ionization cross sections for H^+ impact. Experimental data: O, Kamiya *et al* (1977); Δ, Castro Faria *et al* (1984). Theoretical curves: —— × × × ——, BEA with relativistic hydrogenic wave functions (Avaldi *et al* (1982) —— × × ——, Present non-relativistic results; —— — — ——, PWBA with electronic relativistic wave functions (Jamnik and Zupanic 1957); ——————, Present relativistic results; —— × ——, ECPSSR Theory (Cohen and Harrigan 1985) —— — — — —— RPWBA-BC (Chen and Crasemann 1985).

CC-0. In Public Domain. Gurukul Kangri Collection, Haridwar

Digitized by Arya Samaj Foundation Chennai and eGangotri

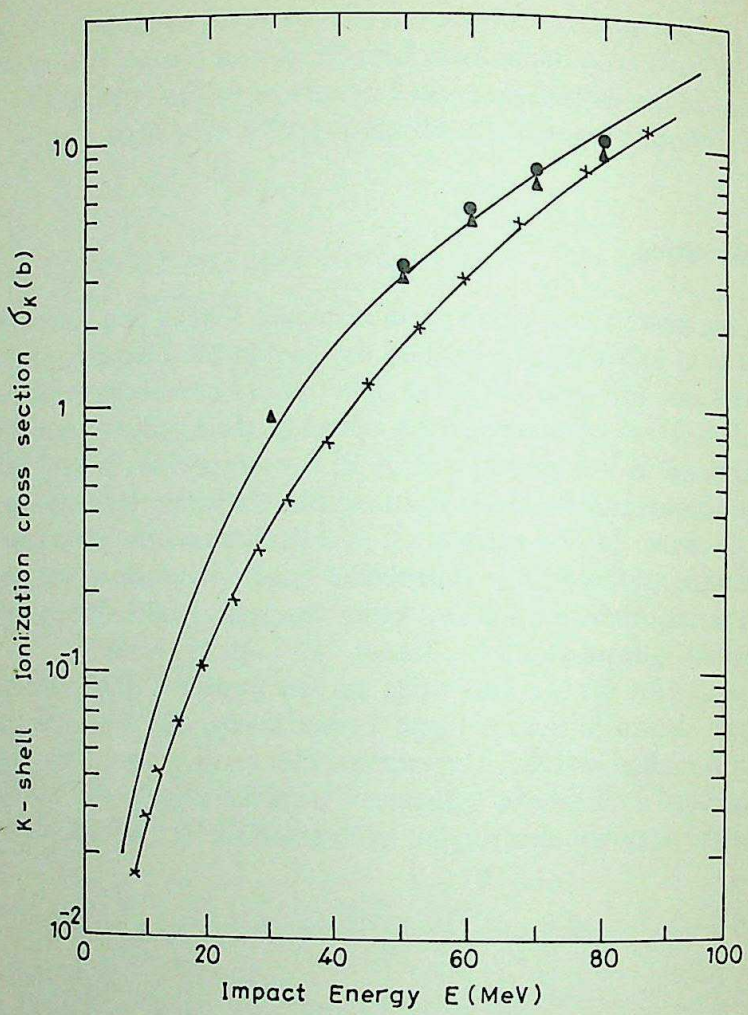

Figure 2. *K*-shell ionization cross section for He^{2+} impact. Experimental data: ● and Δ, Hardt and Watson (1973) – × – × –, present results incorporating effects of relativistic collision dynamics only (see text); ———, present relativistic results.

It has been found that the use of a Hartree-Fock wave function lowers the cross sections, especially at low impact energies (Kumar and Roy 1981). Further, the present results are closer to experiments as compared to relativistic PWBA calculations of Jamnik and Zupancic (1957). It is also seen from figure 1 that relativistic treatment of the collision and use of a relativistic momentum function for the bound electron increases the cross sections, leading to a closer agreement with experiment. To examine the effects of relativistic treatment of collision dynamics on cross sections, we have carried out calculations for alpha particle impact (figure 2), using relativistic wave functions only. As expected, relativistic consideration of collision gives rise to a significant increase in cross section. The present results for alpha particle impact including all corrections are in close agreement with other experimental and theoretical results. Figures 3 and 4 show the results for L_1 sub-shell. The present calculations for proton impact (incorporating all physical effects) overestimate most of the experimental cross sections throughout the energy range investigated. However, different sets of experimental results show significant differences among themselves and hence more experimental and theoretical investigations are needed to understand the reason

CC-0. In Public Domain. Gurukul Kangri Collection, Haridwar

Digitized by Arya Samaj Foundation Chennai and eGangotri

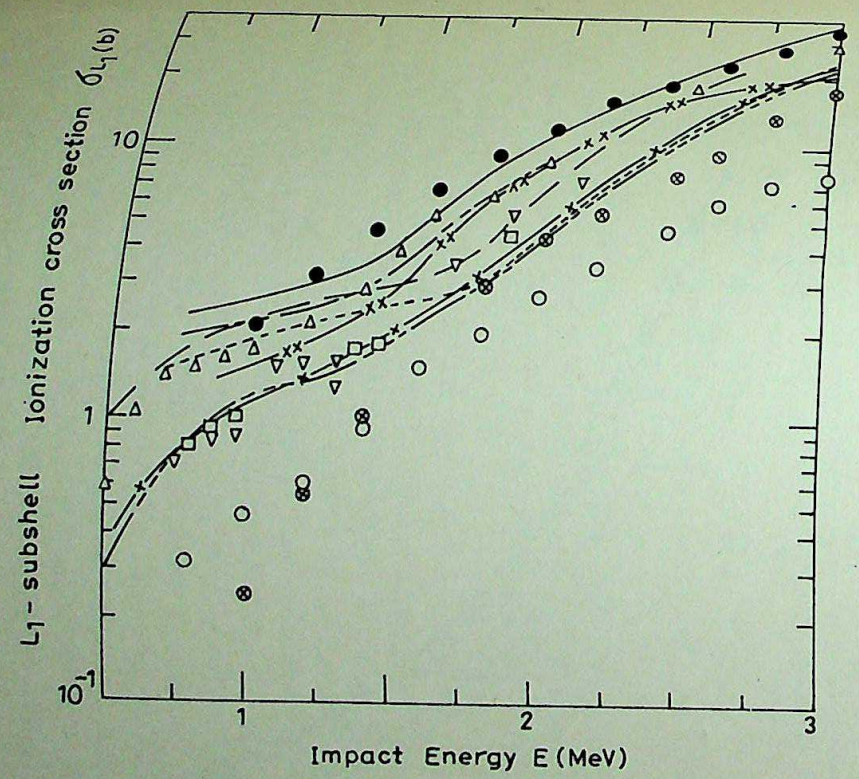

Figure 3. L_1 subshell ionization cross sections for H^+ impact. Experimental data: ○ and ⊗, Cohen (1980); □, Chen (1977); ∇, Datz *et al* (1974); ● and Δ, Cohen and Pinho respectively (reported by Sokhi and Crumpton (1984)). Theoretical curves: ---, ———, calculations in PWBA, and PWBAR respectively (reported by Cohen 1980); ------, PWBA-DHS (Chen 1984):—— × × ——, present non-relativistic results; ————, Present relativistic results; ————, RPWBA-BC (Chen and Crasemann 1985)— × —ECPSSR theory (Cohen and Harrigan 1985).

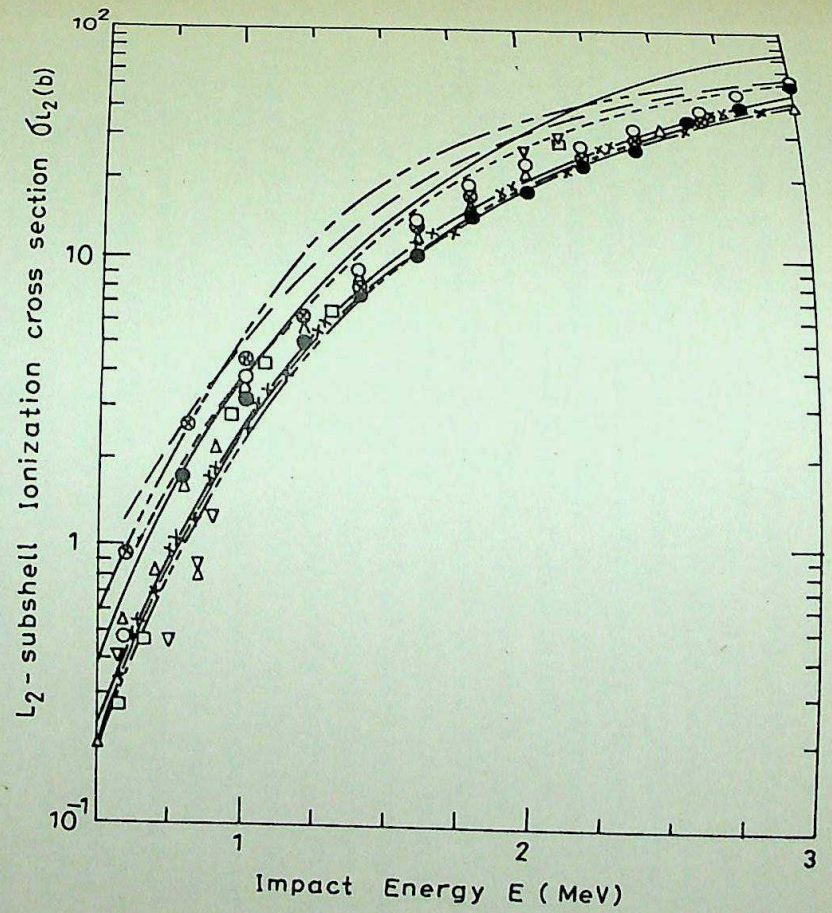

Figure 4. L_1 Subshell ionization cross sections for He^{2+} impact. --- × ---, present non-relativistic result; ——— present relativistic results; ——— × ———, ECPSSR theory (Cohen and Harrigan 1985). Experimental ●, Chang *et al* (1975) reported by Hardt and Watson (1976).

CC-0. In Public Domain. Gurukul Kangri Collection, Haridwar

Digitized by Arya Samaj Foundation Chennai and eGangotri

behind this discrepancy. In fact all the available theoretical calculations (shown in figure 3) overestimate the experimental cross sections considerably. As observed in experiments, an inflexion has been obtained in the present cross section curve which has been attributed to the presence of an extra node in the L_1 sub-shell wave function. The position of the inflexion in our work is close to the experimental counterpart. As is seen from the figure, results of theoretical calculations using different approximations differ significantly. The present results are closer to the recent calculations of Chen (1984) in the relativistic plane wave Born approximation (RPWBA) using relativistic Hartree-Slater (RHS) wave function for the target electron. For alpha particle impact (Figure 4) also our calculations show good agreement with other results. From the figure it is clear that, as expected, incorporation of relativity in the calculation enhances the cross sections considerably.

Cross sections for L_2 sub-shell have been presented in figures 5 and 6. The present results for proton impact are in reasonable agreement with the experimental cross sections (figure 5). Our results also show agreement with other theoretical calculations. Recent relativistic calculations in RPWBA along with RHS wave function for the bound electron reported by Chen (1984) are larger than experimental as well as theoretical cross sections at low impact energies; however, with increase in impact energy RPWBA results improve. Our results for alpha particle impact (figure 6) have been compared with the theoretical results in ECPSSR reported by Cohen and Harrigan (1985) and experimental data of Chang *et al* (1975). Present calculations are larger than experimental as well as other theoretical cross sections.

The present results for proton impact L_3 sub-shell ionization cross sections (figure 7) are within a factor of 2 as compared to the experimental cross sections throughout

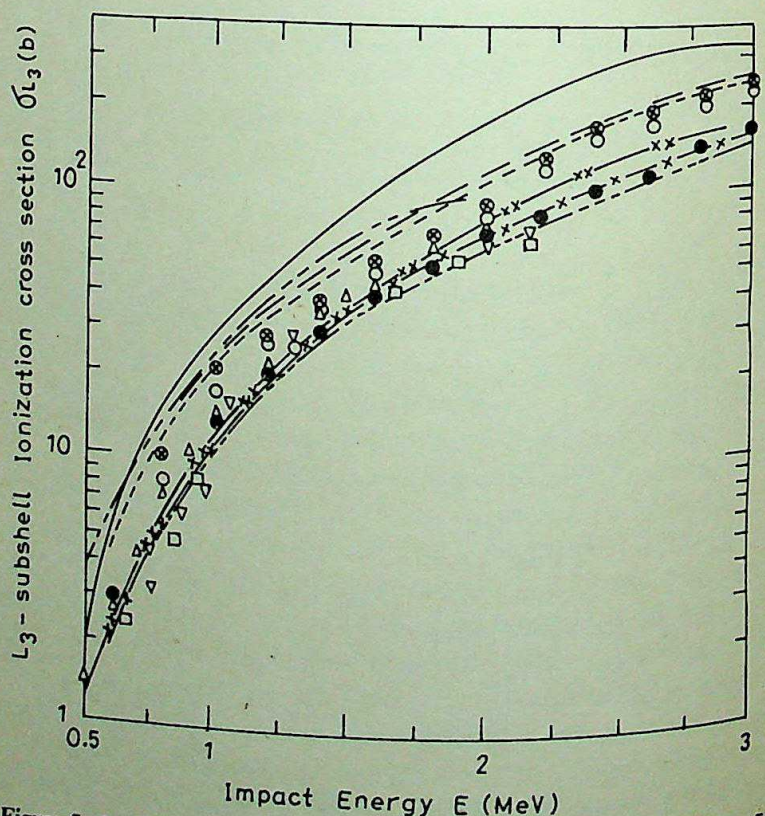

Figure 5. L_2 subshell ionization cross sections for H^+ impact. Same as in fig 3.

CC-0. In Public Domain. Gurukul Kangri Collection, Haridwar

Digitized by Arya Samaj Foundation Chennai and eGangotri

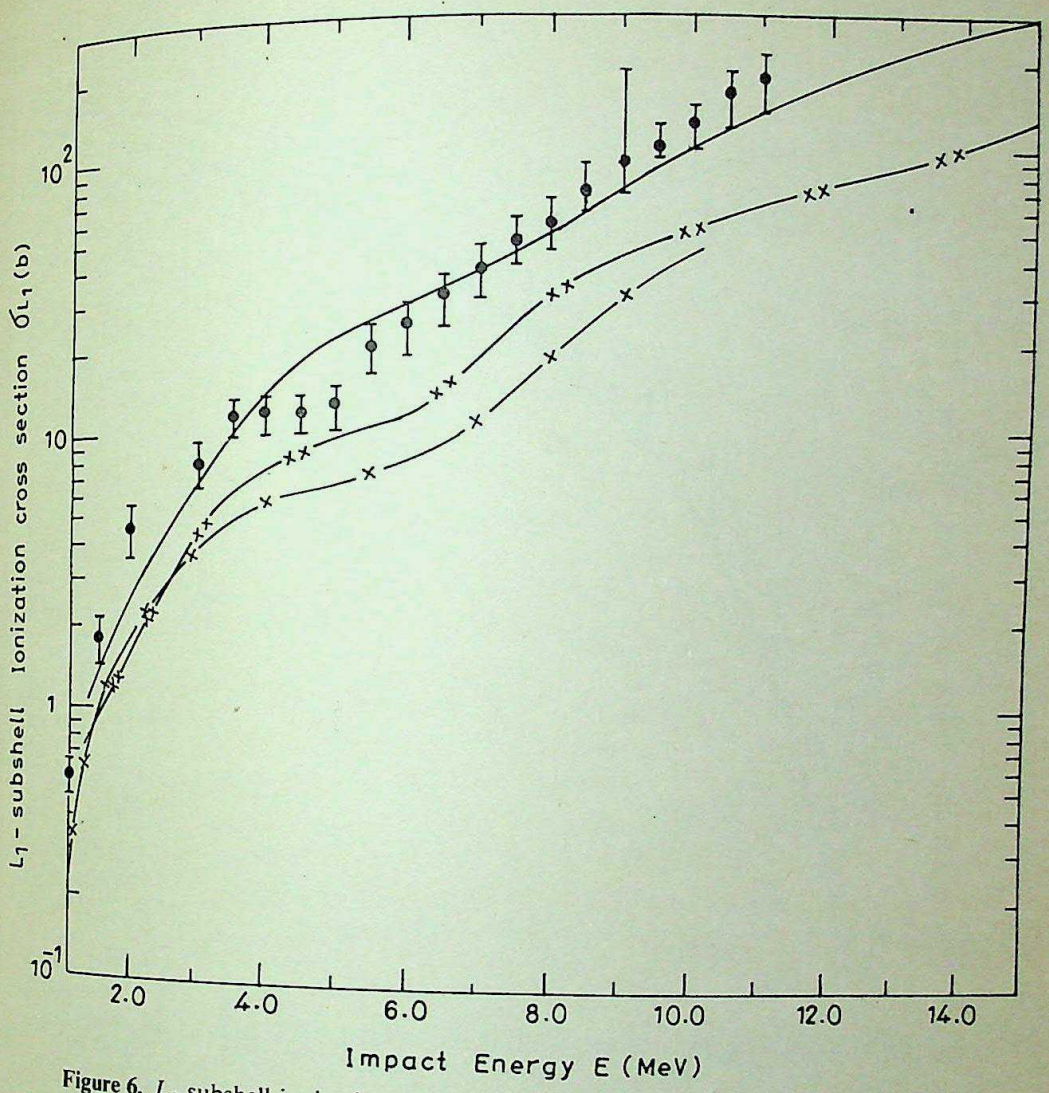

Figure 6. L_2 subshell ionization cross sections for He^{2+} impact. Same as in figure 4.

the energy range investigated. Except the recent RPWBA calculation of Chen (1984) using RHS wave function for the target electron, all theoretical calculations show almost similar type of variation of cross sections with energy, in agreement with experiments.

From our calculated cross sections we have obtained the values $\sigma_{L_1}/\sigma_{L_2}$ and $\sigma_{L_1}/\sigma_{L_3}$ for proton and alpha particle impact and have compared them with the available experimental observations and other theoretical calculations (Figures 9–12). The proton impact experimental values of these ratios, obtained by different workers, show marked differences among themselves. The present calculations of $\sigma_{L_1}/\sigma_{L_2}$ are slightly higher than the results of ECPSSR reported by Cohen and Harrigan (1985) but in $\sigma_{L_1}/\sigma_{L_3}$ the present values are in close agreement with other results. Our results for $\sigma_{L_1}/\sigma_{L_2}$ and $\sigma_{L_1}/\sigma_{L_3}$ in He^{2+} impact show good agreement with the experimental observations and other theoretical calculations. In fact the present results are always within a factor of 2 as compared to experimental values.

From a close inspection of the figures it is concluded that the present method, in spite of being simple, gives satisfactory description of the relativistic effects for heavy particle impact inner shell ionization of atoms. Our results, in most cases, are higher

CC-0. In Public Domain. Gurukul Kangri Collection, Haridwar

Digitized by Arya Samaj Foundation Chennai and eGangotri

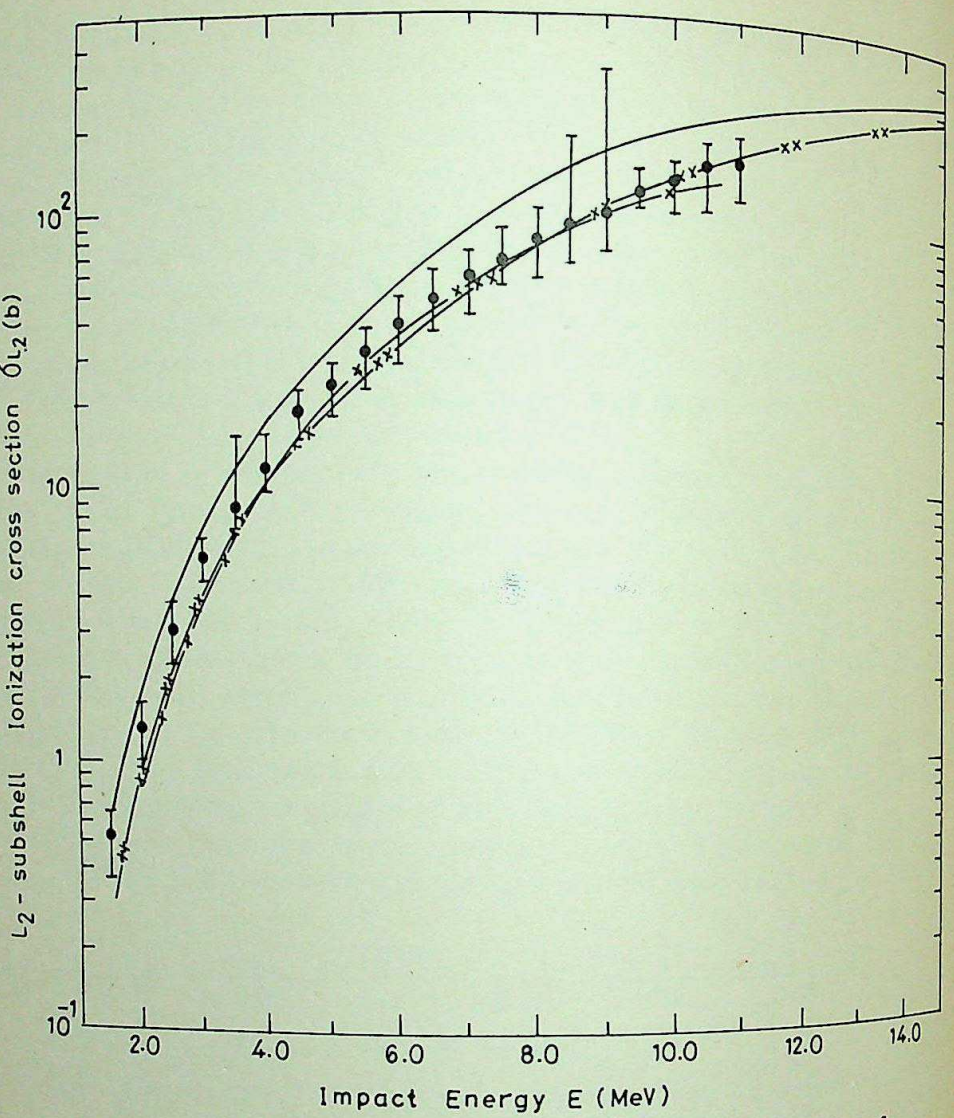

Figure 7. L_3 subshell ionization cross sections for H^+ impact. Same as in figure 3.

CC-0. In Public Domain. Gurukul Kangri Collection, Haridwar

Digitized by Arya Samaj Foundation Chennai and eGangotri

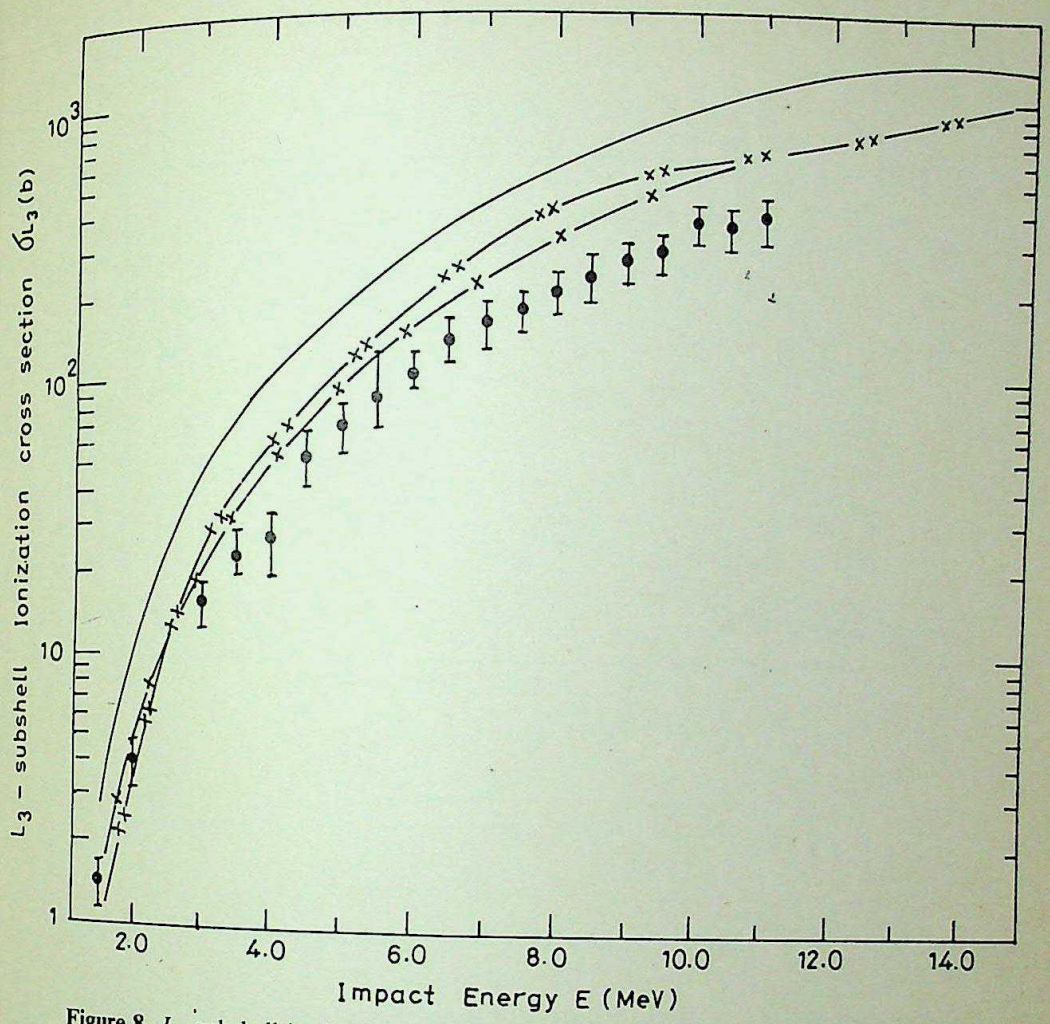

Figure 8. L_3 subshell ionization cross sections for He^{2+} impact. Same as in figure 4.

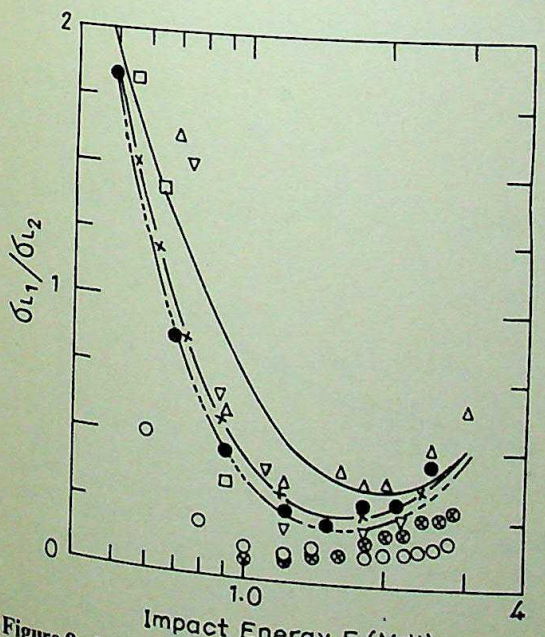

Figure 9. Ionization cross section ratio $\sigma_{L_1}/\sigma_{L_2}$ for H^+ impact. Experimental data: ●, Jitchin *et al* (1982); □, Chen (1977); ∇, Datz *et al* (1974); ○ and × Thin and Thick target measurements (Cohen 1980); Δ, Sokhi and Crumpton (1984). Theoretical curves: ————, – – – – –, RPWBA-BC (Chen and Crasemann 1985); —— × ——, ECPSSR Theory (Cohen and Harrigan 1985); Present relativistic results;

CC-0. In Public Domain. Gurukul Kangri Collection, Haridwar

Digitized by Arya Samaj Foundation Chennai and eGangotri

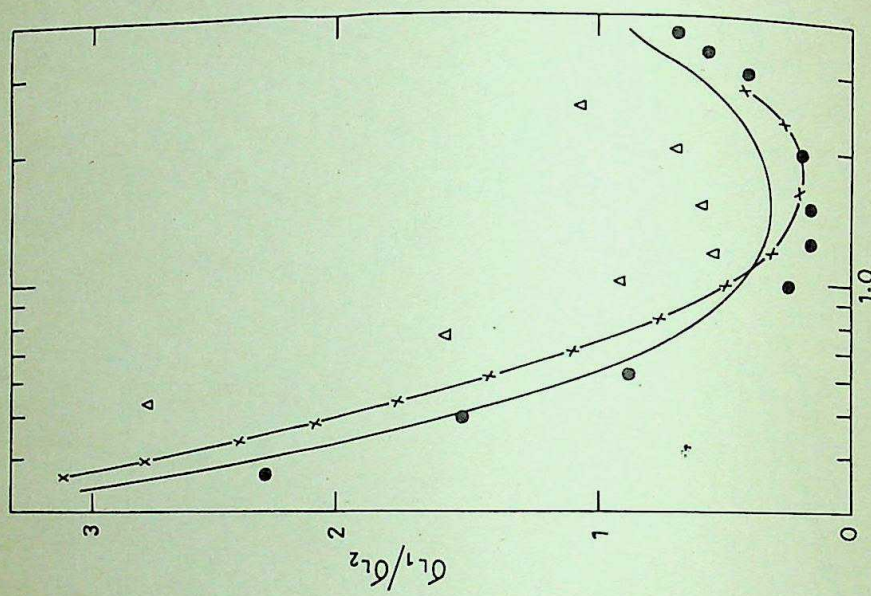

Figure 11. Ionization cross section ratio $\sigma_{L_1}/\sigma_{L_2}$ for He^{2+} impact. ●, *Experimental data* (Jitchin *et al* 1983); Δ, Hardt and Watson (1976). *Theoretical curves:* ————, present relativistic results. ———— × ————, *ECPSSR Theory (Cohen and* Harrigan 1985).

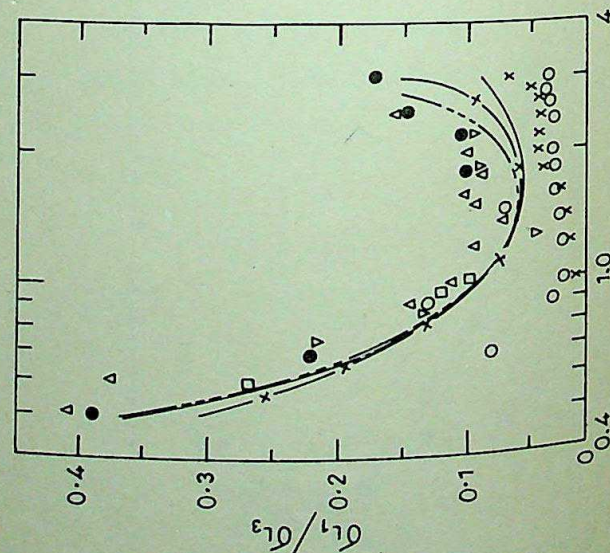

Figure 10. Ionization cross section ratio $\sigma_{L_1}/\sigma_{L_3}$ for H^+ impact. Same as in figure 9.

CC-0. In Public Domain. Gurukul Kangri Collection, Haridwar

Digitized by Arya Samaj Foundation Chennai and eGangotri

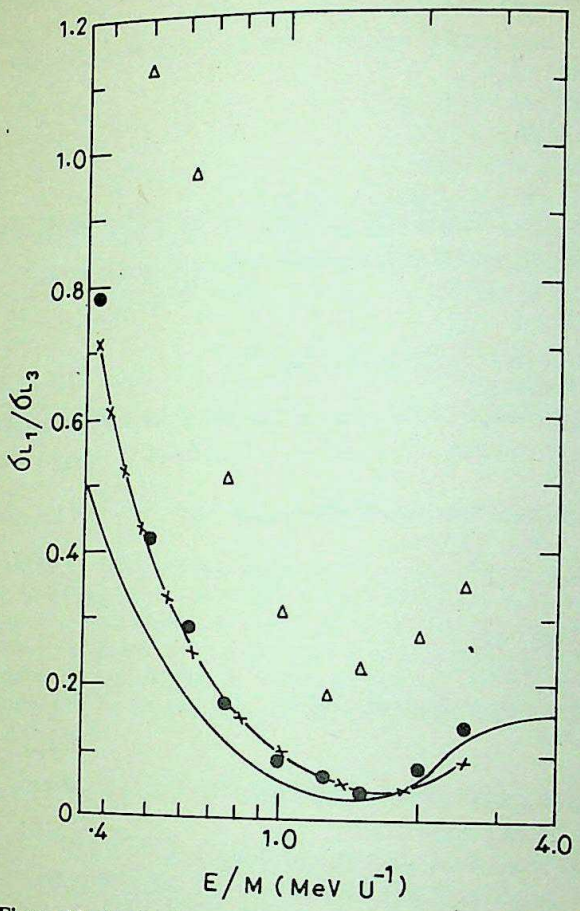

Figure 12. Ionization cross section ratio $\sigma_{L_1}/\sigma_{L_3}$ for He^{2+} impact. Same as in figure 11.

than the cross sections obtained experimentally or calculated using different quantal approximations, particularly at low impact energies. This might be due to the use of the binary encounter approximation in the present work.

Acknowledgement

One of us (SNC) is grateful to CSIR, New Delhi, India for the award of a Research Associateship.

References

Avaldi L, Locarno G and Milazzo M 1982 *J. Phys.* **L15** 129
Brandt W and Lapicki G 1979 *Phys. Rev.* **A20** 465
Braziewicz E and Braziewicz J 1988 *J. Phys.* **B21** 1537
Castro Faria N V de, Freir Jr F L, Montenegro, Pinho A G de and Silveira E F da 1984 *J. Phys.* **B17** 2304
Chang, C N, Morgan J F and Blatt S L 1975 *Phys. Rev.* **A11** 607
Chatterjee S N, Kumar A and Roy B N 1983 *Physica* **C122** 275
Chen J R 1977 *Phys. Rev.* **A15** 487
Chen M H 1984 *Phys. Rev.* **A30** 2082
Chen M H and Crasemann B 1985 *At. Data Nucl. Data Tables* **33** 217
Cohen D D 1980 *J. Phys.* **B13** 2953

CC-0. In Public Domain. Gurukul Kangri Collection, Haridwar

Digitized by Arya Samaj Foundation Chennai and eGangotri

Cohen D D and Harrigan M 1985 *At. Data Nucl. Data Tables* **33** 255
Datz S, Duggan J L, Feldmann L C, Laegsgaard E and Andersen J U 1974 *Phys. Rev.* **A9** 192
Desclaux J P 1973 *At. Data Nucl. Tables* **12** 325
Fisher C F 1972 *At. Data Nucl. Data Tables* **4** 301
Hardt T L and Watson R L 1973 *Phys. Rev.* **A7** 1917
Hardt T L and Watson R L 1976a *Phys. Rev.* **A14** 137
Hardt T L and Watson R L 1976b *At. Data Nucl. Data Tables* **17** 107
Jamnik D and Zupancic C 1957 *Kgl. Danske Videnskab. Selskab. Mat. Fys. Meddr.* **31**
Jitchin W, Kaschuba A, Hippler R and Lutz H O 1982 *J. Phys.* **B15** 763
Jitchin W, Hippler R, Finck K, Schuch R and Lutz H O 1983 *J. Phys.* **B16** 4405
Kagawa T 1975 *Phys. Rev.* **A12** 2245
Kamiya M, Tshii K, Sera K and Morita S 1977 *Phys. Rev.* **A16** 2295
Kumar A and Roy B N 1981 *J. Phys.* **B14** 501
Langenberg A 1978 *Atomic innershell ionization: X-ray emission cross sections and fluorescence yields* Ph.D. Thesis, Phys. Lab. Rijksuni Versiteit Utrecht
Lotz W 1968 *J. Opt. Soc. Am.* **58** 236
Mclean A D and Mclean R S 1981 *At. Data Nucl. Data Tables* **26** 197
Mukoyama T and Kagawa T 1983 *J. Phys.* **16** 1875
Paul H 1984 *Nucl. Instrum. Methods* **B4** 211
Paul H 1987 *Z. Phys.* **D4** 249
Paul H 1989 *Nucl. Instrum. Methods* **B42** 443
Paul H and Muhr J 1986 *Phys. Rep.* **135** 47
Paul H and Obermann W 1983 *Nucl. Instrum. Methods* **214** 15
Rubinowicz A 1948 *Phys. Rev.* **73** 1330
Sheth C V 1984 *Phys. Rev.* **A29** 1151
Shrivastava S K, Kumar A and Roy B N 1984 *Physica* **C124** 127
Shrivastava S K and Roy B N 1986 *Physica* **C138** 219
Sokhi R S and Crumpton D 1984 *At. Data Nucl. Data Tables* **30** 49–124
Starter W, Mommson M, Sarkar M, Schurkes P and Weller A 1981 *J. Phys.* **B14** 2843
Thomas B K and Garcia J D 1969 *Phys. Rev.* **A179** 94
Vriens L 1967 *Proc. Phys. Soc.* **90** 935

CC-0. In Public Domain. Gurukul Kangri Collection, Haridwar

Digitized by Arya Samaj Foundation Chennai and eGangotri

Pramāṇa – J. Phys., Vol. 34, No. 6, June 1990, pp. 461–471. © Printed in India.

Wavelength dependence of phase conjugate reflectivity in absorbing media and thermal grating studies by four wave mixing

R KRISHNA MOHAN, B RAGHAVENDRA PRASAD, C K SUBRAMANIAN and P S NARAYANAN
Department of Physics, Indian Institute of Science, Bangalore 560012, India

MS received 26 May 1989; revised 21 November 1989

Abstract. The development of optical phase conjugation using thermally formed gratings in absorbing media, especially the dye solutions, has besides the high efficiencies, many other characteristics which are worthy of study. Here the wavelength dependence of phase conjugate reflectivity in relation to absorption spectrum of rhodamine-6G and rhodamine-B in water, methanol and ethanol is reported. Further the Bragg condition has been verified for the dominant diffracted beam which shows that the thermal grating behaves like an optically thick grating.

Keywords. Optical phase conjugation; absorbing media; thermal grating; Bragg condition.

PACS No. 42·65

1. Introduction

Optical phase conjugation (OPC) has been achieved in several ways. These methods of generating phase conjugated wavefronts, their efficiencies, utilities, shortcomings, and applications have been dealt with in many articles (Fisher 1983; Zel'dovich *et al* 1985). We have investigated optical phase conjugation using degenerate and non-degenerate four wave mixing (FWM) in absorbing media with particular reference to rhodamine-6G (Rh6G) and rhodamine-B (RhB) in various solvents. The effects of concentration, angle of interaction and the pump-probe intensities on phase conjugate reflectivity have been dealt with earlier (Prasad *et al* 1988). The present paper deals with (i) the effect of changing the wavelength used for writing the grating on conjugate reflectivity and (ii) characterization of the thermal grating (Shen 1986).

2. Principle

The underlying principle in the technique of OPC-FWM in absorbing media is the creation of a thermal grating in the medium using high power laser beams. The dye molecules absorb the incident light energy and undergo transitions to higher energy states. Subsequent radiationless relaxation of some of the optically excited molecules, and transfer of energy to the solvent molecules causes local heating or thermalization of the solvent giving rise to periodic temperature or entropy fluctuations. These result in spatial modulation of the refractive index of the solvent which then acts as a phase

CC-0. In Public Domain. Gurukul Kangri Collection, Haridwar

Digitized by Arya Samaj Foundation Chennai and eGangotri

grating in the scattering of incident light and is termed as stimulated thermal Rayleigh scattering (STRS).

Most of the experiments on OPC-FWM in dyes show that pure thermal effects play a major role in the recording of the interference pattern, particularly if the absorbed energy relaxes into heat immediately. The dyes were chosen as absorbing media for these investigations because of their high absorption coefficient at the operating wavelengths. This plays a major role in yielding high phase conjugate reflectivities as will be seen later. The present investigations are also aimed at studying the grating characteristics especially to study whether a thermal grating in absorbing media behaves like an ordinary grating obeying the Bragg's law of diffraction.

3. Theory

The theoretical model as presented by Hoffman (1986a, b) was taken as the working model for our investigations. From her model, one obtains an expression for the phase conjugate reflectivity R given by,

$$R = f^2 Q^2 \exp(-\alpha L/\cos\theta)\{1-\exp(-\alpha L)\}^2 I_1 I_2 G(t_D) \tag{1}$$

where I_1, I_2 are the intensities of the forward propagating pump and the backward propagating read beams respectively, α is the absorption coefficient, L is the interaction length and θ is the angle of interaction or the angle between the forward propagating pump and probe beams. f is a phenomenological factor related to quantum yield of fluorescence of the dye which gives an estimate of the fraction of absorbed light energy converted into heat. Further,

$$Q = \frac{2n(\mathrm{d}n/\mathrm{d}T)}{\lambda \rho_0 C_p}$$

is a factor which is characteristic of the solvent and contains all the solvent dependent parameters viz. ρ_0 the density, C_p the specific heat at constant pressure, $\mathrm{d}n/\mathrm{d}T$ the change in refractive index of the solvent with temperature etc.

The details of the thermal grating build up and decay along with various time scales involved in the process are contained in the factor $G(t_D)$ of (1). Since our experiment was carried out in a near zero time delay condition, the $G(t_D)$ factor for small time delay regions can be written as (Hoffman 1986b)

$$G(t_D) = \frac{t_p'^2}{3\tau_{\mathrm{eff}}^2 \Gamma_\mu^2}\left[1 + \frac{3t_D(t_D+t_p')}{t_p'^2}\right] \tag{2}$$

where

$$\tau_{\mathrm{eff}}\Gamma_u = 1 + \tau_{\mathrm{eff}} D q^2$$

where t_p' is the conjugate pulse width which can be smaller or equal to the laser pulse width t_p, t_D is the time delay of the backward propagating 'read' beam with respect to the forward propagating beams, τ_{eff} is the effective thermalization time of the solute, $1/\Gamma_u$ is the thermalization time due to noninstantaneous and nonlocal solute-solvent energy transfer, also called the energy transfer time, q, defined as $q = 2k \sin(\theta/2)$, is the grating vector and D the diffusion constant.

CC-0. In Public Domain. Gurukul Kangri Collection, Haridwar

Digitized by Arya Samaj Foundation Chennai and eGangotri

3.1 *Wavelength dependence*

The above expression (1) for reflectivity can be rewritten, to suit our measurements, in terms of two factors; one containing the information about the dye solvent combination, the various time-scales involved in the process, the geometrical arrangement and the intensities of the beams while the other pertaining to the explicit and implicit dependence of reflectivity (R) on the wavelength. The expression can be rewritten as

$$R = A \exp(-\alpha L/\cos\theta)\{1-\exp(-\alpha L)\}^2/\lambda^2 \tag{3}$$

$$A = \frac{4n^2 f^2 (\mathrm{d}n/\mathrm{d}T)^2}{\rho_0^2 C_p^2} I_1 I_2 G(t_D)$$

While the explicit dependence is λ^{-2}, the implicit dependence of reflectivity of the process on wavelength comes due to the fact that R depends on α which in turn is a function of wavelength and any dispersion effect in $(\mathrm{d}n/\mathrm{d}T)$. f is assumed to be constant. The variation of the intensities I_1 and I_2 with wavelength is not considered in (3) because, experimentally, the dye laser output, which governs these intensities, can be maintained at the same value of intensity irrespective of the wavelength of the output throughout the operating wavelength range by adjusting the Nd:YAG laser output, which pumps the dye laser. The theoretical plot of normalized reflectivity against wavelength superimposed on the plot of normalized α against wavelength for Rh6G in water is given in figure 1. The normalization is done with respect to the corresponding peak values. The figure shows that the variation of R with wavelength follows the absorption spectrum of the dye-solvent combination in the spectral region 550–580 nm.

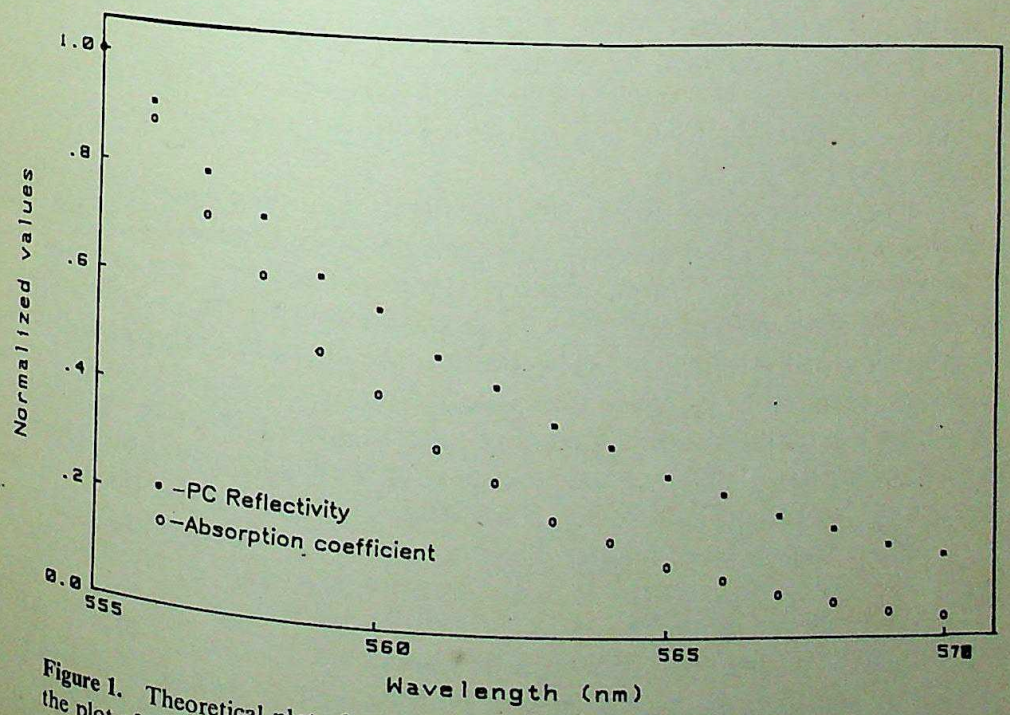

Figure 1. Theoretical plot of normalized reflectivity against wavelength superimposed on the plot of normalized absorption coefficient against wavelength for Rh6G in water.

CC-0. In Public Domain. Gurukul Kangri Collection, Haridwar

Digitized by Arya Samaj Foundation Chennai and eGangotri

3.2 *Thermal grating*

To study the thermal grating characteristics, a slightly modified technique termed as non-degenerate four wave mixing (NFWM) was employed. As the name suggests one of the three beams interacting in the sample cell should be of a different wavelength. An important feature of this technique is a broad acceptance angle for phase matching. In other words the process is phase matched for the 'read' beam wavelength over a range of hundreds of wave numbers for fixed pump and probe beams. It is assumed that at the power levels used, only the pump and the 'probe' beams couple to form the grating and read beam was just diffracted off the transient grating.

4. Experiment

As mentioned earlier, dyes Rh6G and RhB were chosen as the absorbing media because of their high absorption at this range of wavelengths i.e., 530 to 580 nm and their properties are well known. The experimental investigation was carried out in the wavelength interval from 555 to 575 nm as the output intensity of the dye laser falls off very rapidly beyond this interval and is not sufficient to yield an easily detectable signal.

4.1 *Absorption dependence*

Since the investigations were aimed at studying the effect of wavelength on reflectivity, all other parameters regarding the geometrical arrangement like the read beam time delay and the interaction angle etc. the medium parameters like the concentration, the interaction length etc. were fixed. The absorption spectra of different dye-solvent systems were taken by a Hitachi (model 150–20) spectrophotometer.

The experimental investigations were conducted using the output of the dye laser (PDL-II) which is pumped by frequency-doubled Nd:YAG laser (DCR-2A) with filled-in beam mode. The tunable wavelength range was 550–580 nm with the pulse duration between 6 and 8 ns and the power density used for the experiments was about 2 MW/cm^2 per pulse.

The experimental set-up used for the investigations is shown in figure 2. The incident laser beam is split up into two vertically (or s-) polarized beams by the 10% reflecting beam-splitter BS1. The transmitted beam is then split into two beams of equal intensity by the 50% beam splitter BS2. The beam transmitted by BS2 is reflected on to the sample cell SC by a mirror M1. This beam is the backward propagating read beam. The beam reflected by BS2 is in turn reflected on to the sample cell by a mirror M2. This beam is referred to as the forward propagating pump beam or write beam. These two beams are made collinear and counter-propagating by careful adjustments of the mirrors M1 and M2. The reflected beam from the beam-splitter BS1 is further split by a 30% reflecting beam-splitter BS3 to maintain a high pump-probe ratio. The beam reflected by BS3 referred to as the forward propagating 'probe' beam, is made to interact with the 'pump' beam in the sample cell to form the thermal grating. It is mandatory to satisfy the coherence requirements for the two beams forming the grating by adjusting the path lengths of both the beams. The angle of interaction or the angle between the pump and the probe beam was maintained at 10°. The concentration of each of the dye-solvent systems was chosen to be 5×10^{-5} mol/l.

CC-0. In Public Domain. Gurukul Kangri Collection, Haridwar

Digitized by Arya Samaj Foundation Chennai and eGangotri

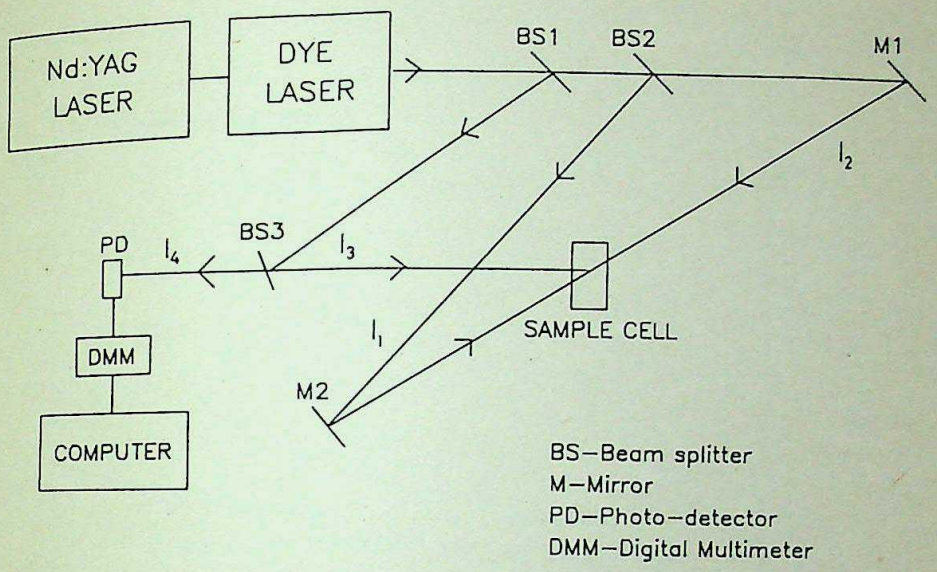

Figure 2. Experimental arrangement for studying dependence of phase conjugate reflectivity on absorption spectrum by DFWM.

The beam intensities at various stages in the set up, were monitored by photo-detectors PD.

The experimental results shown in the figures reveal an interesting pattern which agrees very well with the theoretical predictions. Figures 3a to 3c show the variation of the α with wavelength for Rh6G in water, methanol and ethanol. The plots also show the variation of phase conjugate reflectivity for the same system. It is clear that the variation of reflectivity follows that of the absorption coefficient. This behaviour is identical for RhB in various solvents as shown in figures 4a–4c. In figures 5 and 6 the percentage reflectivities as function of wavelength are plotted for Rh6G and RhB in various solvents under identical experimental conditions. The highest reflectivity is observed in the case of Rh6G in ethanol, and water gives the least reflectivity. In figure 6, the situation is completely reversed with RhB in water giving the highest reflectivity which is much more than the peak reflectivity of Rh6G. RhB in ethanol gives consistently lower reflectivity than RhB in water. This dramatic change can be explained by the fact that the reflectivity is dependent on α which in turn is dependent on wavelength. At the initial operating wavelength of the dye laser i.e., at about 555 nm, the α of Rh6G in ethanol is much higher than that of Rh6G in water. Thus ethanol is a better solvent for Rh6G. But in the case of RhB, in any solvent the absorption peak is centered around 554 nm. Consequently absorption is much higher than that of Rh6G in any solvent in this range of 550–580 nm. Thus the overall higher reflectivity for RhB over Rh6G can be explained. For RhB in water the α is much higher compared to that of RhB in ethanol throughout the wavelength range and hence the reflectivity is correspondingly higher.

4.2 *Grating studies*

The experimental layout for studying the grating characteristics is given in figure 7. Non-degeneracy was introduced in the backward propagating read beam. The forward propagating pump and probe beams were kept at the same wavelength obtained from

CC-0. In Public Domain. Gurukul Kangri Collection, Haridwar

Digitized by Arya Samaj Foundation Chennai and eGangotri

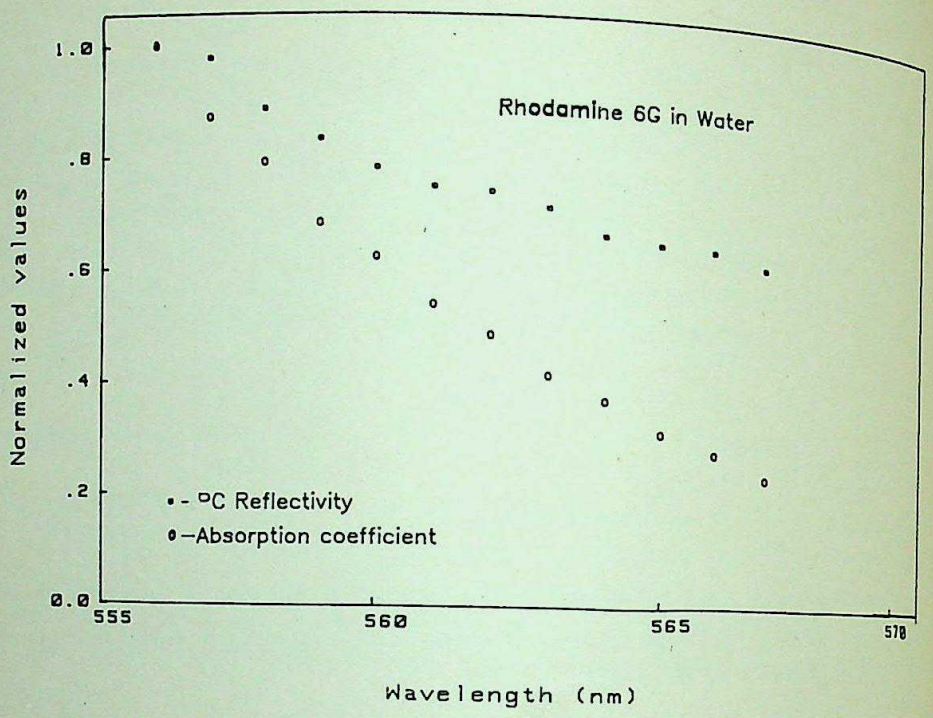

Figure 3a.

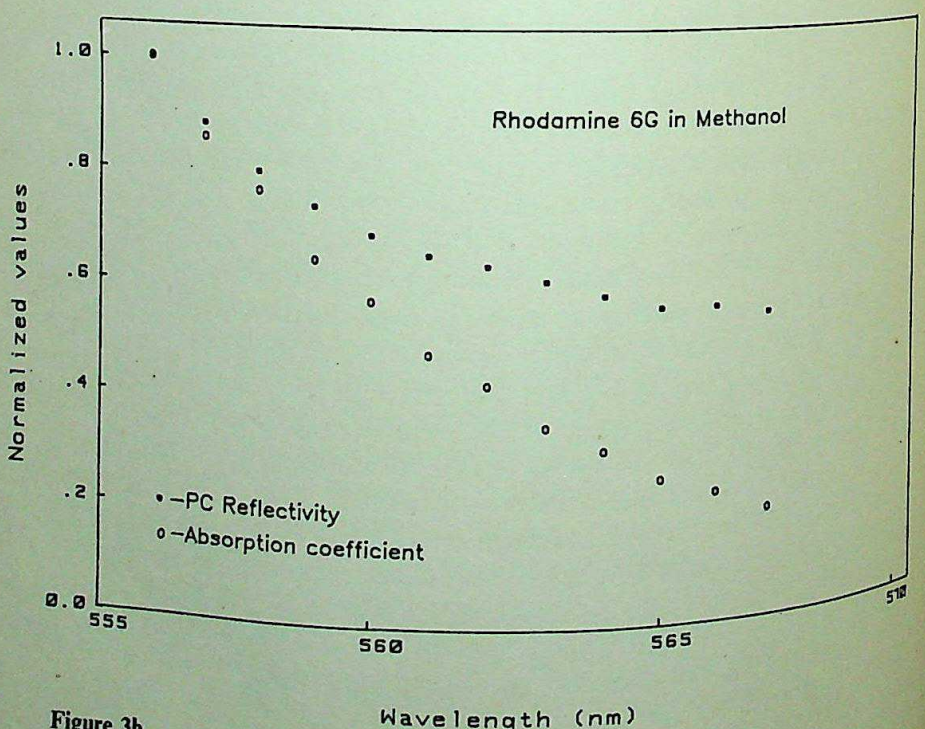

Figure 3b.

CC-0. In Public Domain. Gurukul Kangri Collection, Haridwar

Digitized by Arya Samaj Foundation Chennai and eGangotri

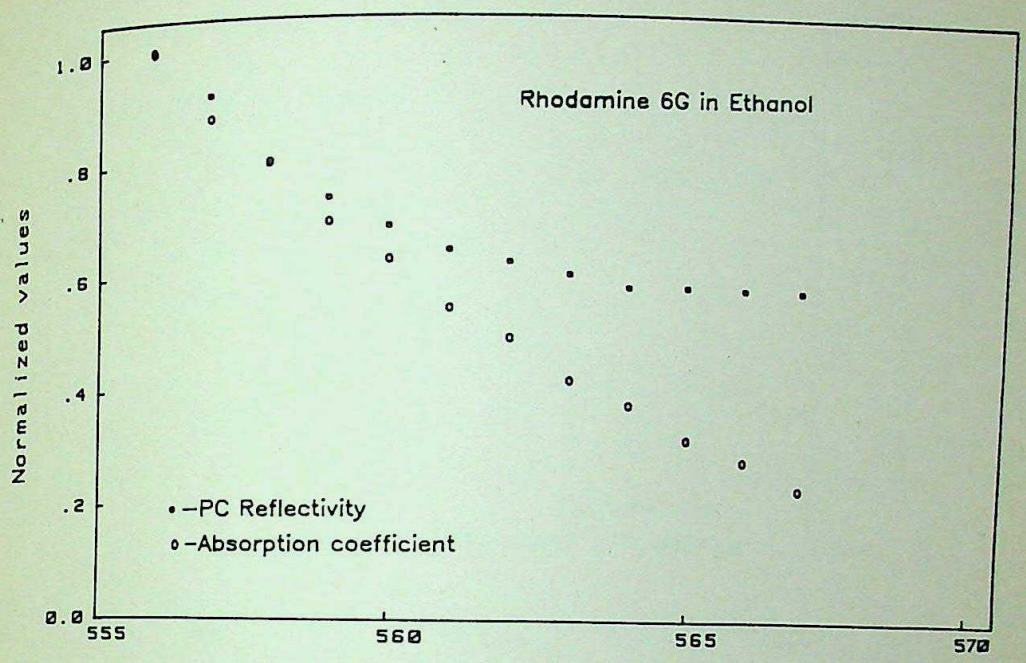

Figure 3c.

Figure 3a-c. Variation of absorption coefficient and phase conjugate reflectivity with wavelength for Rh6G in water, methanol and ethanol.

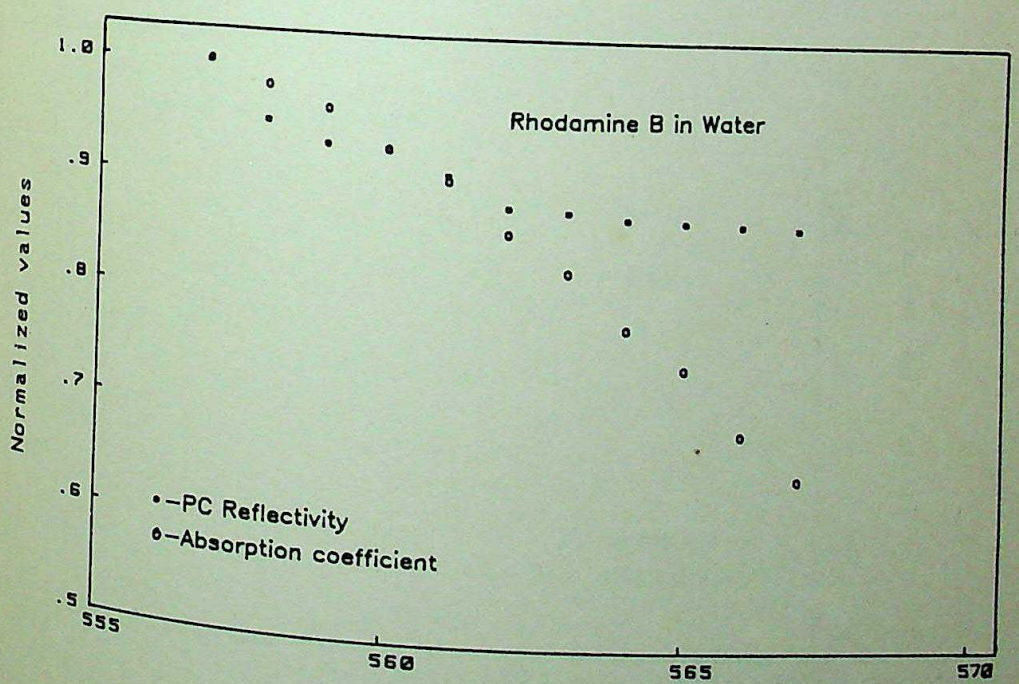

Figure 4a.

CC-0. In Public Domain. Gurukul Kangri Collection, Haridwar

Digitized by Arya Samaj Foundation Chennai and eGangotri

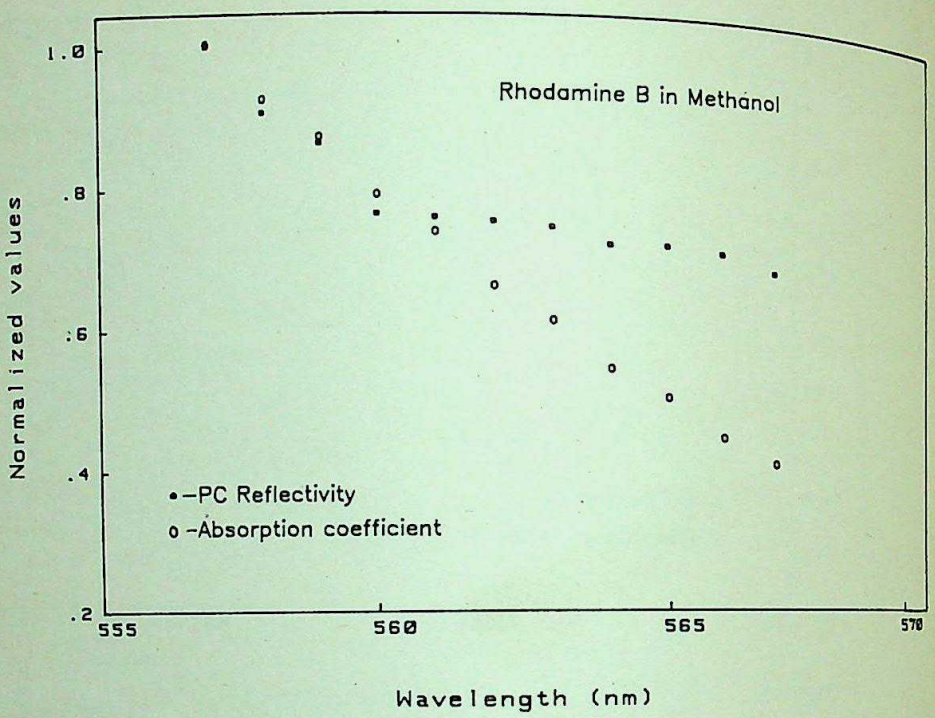

Figure 4b.

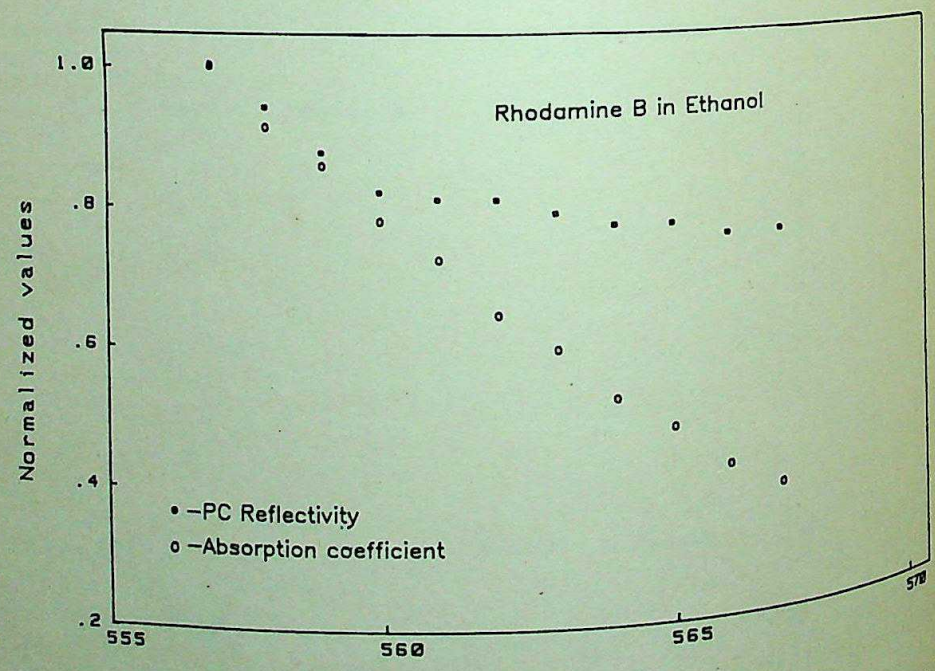

Figure 4c.

Figure 4a-c. Variation of absorption coefficient and phase conjugate reflectivity with wavelength for RhB in water, methanol and ethanol.

CC-0. In Public Domain. Gurukul Kangri Collection, Haridwar

Digitized by Arya Samaj Foundation Chennai and eGangotri

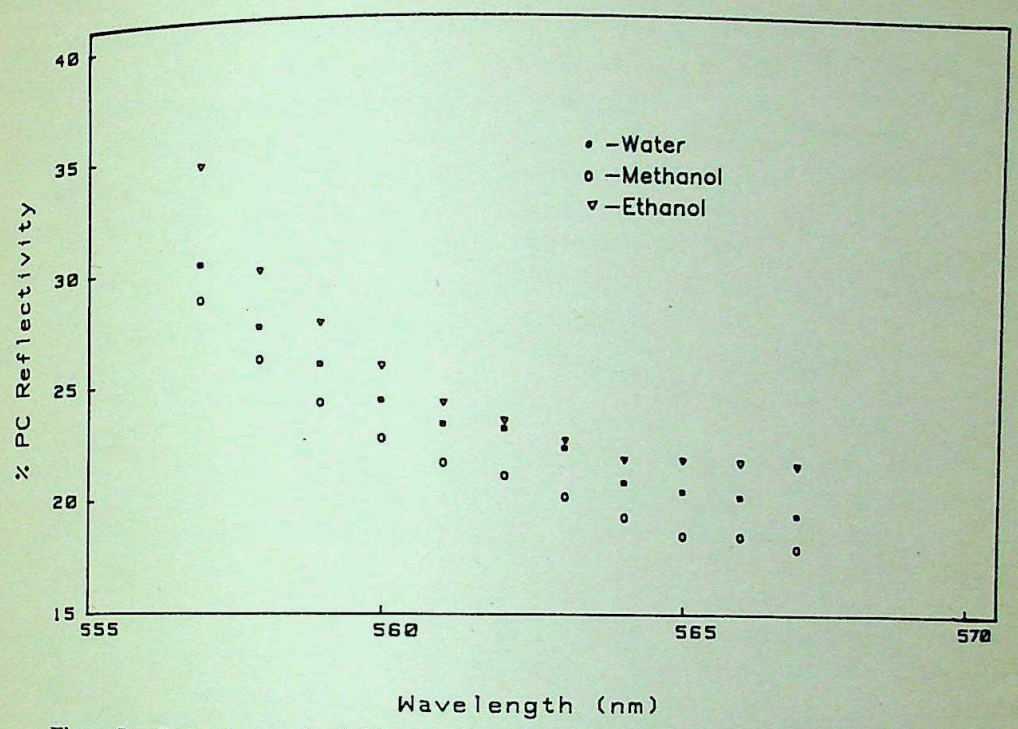

Figure 5. Percentage reflectivities as a function of wavelength for Rh6G in different solvents.

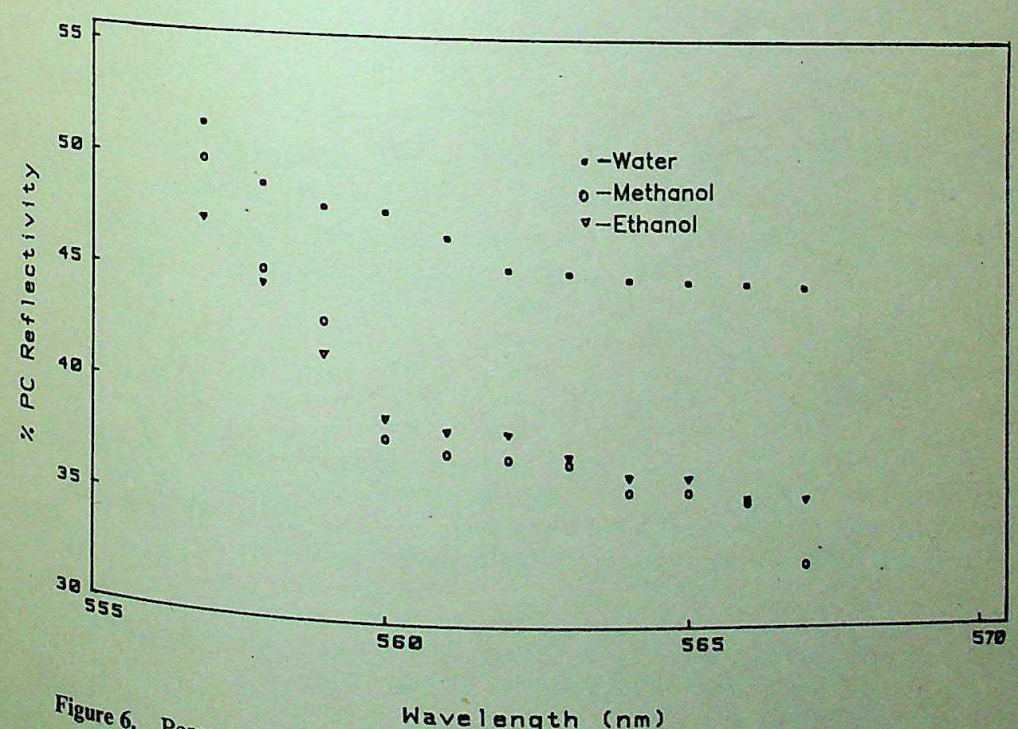

Figure 6. Percentage reflectivities as a function of wavelength for RhB in different solvents.

CC-0. In Public Domain. Gurukul Kangri Collection, Haridwar

Digitized by Arya Samaj Foundation Chennai and eGangotri

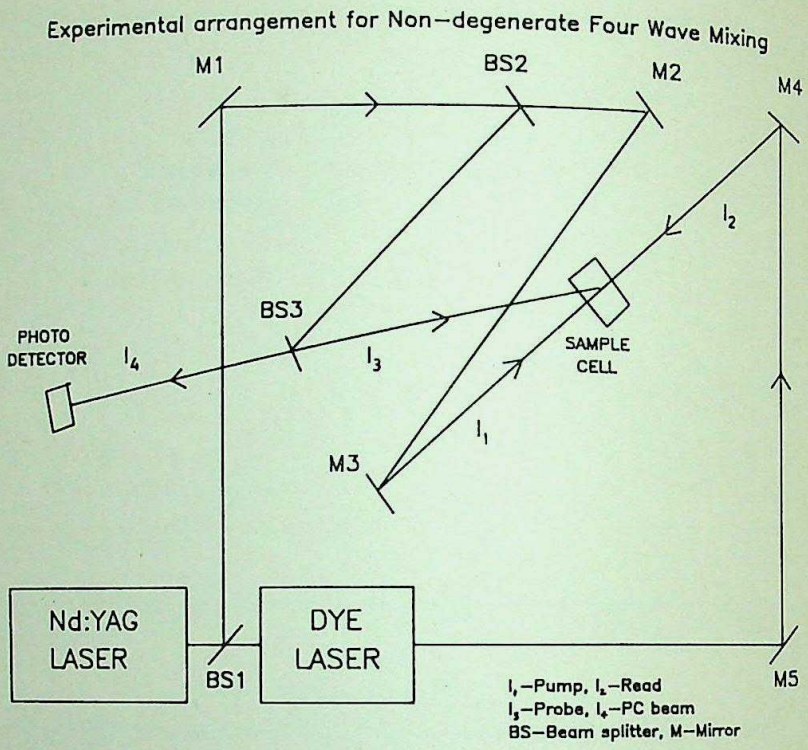

Figure 7. Experimental arrangement to study the thermal grating characteristics using NFWM.

Table 1. Theoretical calculations and experimental measurement of angular shift of read beam with wavelength in NFWM.

Read beam λ(nm)	$\theta = \sin^{-1}(\lambda/2d)$	$\Delta\theta$ (Theor)	$\Delta\theta$ (Expt.)
550	5·174		
		0·0472	0·047
555	5·2211		
		0·0472	0·047
560	5·2683		
		0·0472	0·047
565	5·3155		
		0·0472	0·047
570	5·3627		
		0·0472	0·047
575	5·4098		
		0·0472	0·047
580	5·457		

Grating forming wavelength = 532 nm, L = 332 cm., Interaction angle = 5·0 deg., Grating spacing, d = 3049·4 nm

the frequency-doubled Nd:YAG output at 532 nm. The read beam was taken from the output of the tunable dye laser PDL-II pumped by the 532 nm of Nd:YAG laser. The tunable range of the dye laser is 550–580 nm. The power density used in the experiment was about 4 MW/cm^2 per pulse.

CC-0. In Public Domain. Panini Kanya Maha Vidyalaya Collection, Haridwar

Digitized by Arya Samaj Foundation Chennai and eGangotri

Various dye-solvent combinations were used as the absorbing media. The concentration of the solution was kept at 3×10^{-5} mol/l to get the optimum reflectivity. The diffracted read beam was obtained as the phase conjugate signal. The read beam was tuned from 550–580 nm in steps of 5 nm. The phase conjugate beam at each of these wavelengths was detected by a photodetector mounted on a precision XY-mount placed about 3 m away from the sample cell. In all cases of the dye-solvent combination it was found that the shift in the position ΔL was equal for equal shifts in the wavelength. The angular shift was calculated from ΔL and L, where L is the distance of the detector from the sample cell using the formula,

$$\theta = \tan^{-1}(\Delta L/L). \tag{4}$$

The value of the angular shift was also calculated using the Bragg diffraction condition. The experimental and theoretical values of the angular shift with the read beam wavelength were found to be in excellent agreement with each other.

5. Conclusion

The investigations show that the phase conjugate reflectivity of absorbing media depends to a very large extent on the absorption coefficient of the medium. The variation of the reflectivity with wavelength closely follows that of the absorption coefficient with all other experimental parameters being fixed. Further the thermal grating formed in these absorbing media behaves like a Bragg grating or an optically thick grating.

Acknowledgements

The work was carried out with the financial support from the Defence Research and Development Organization (Research and Training scheme). We also thank the Chairman, Department of Physics, Indian Institute of Science, Bangalore, for encouraging us to carry out these investigations.

References

Fisher R A (ed) 1983 *Optical phase conjugation* (New York: Academic Press)

Hoffman H J 1986a *IEEE J. Quantum Electron.* **QE-22** 552

Hoffman H J and Perkins P E 1986b *IEEE J. Quantum Electron.* **QE-22** 563

Prasad B R, Krishna Mohan R, Narayanan P S, Subramanian C K and Chandra Sekhar P 1988 *Curr. Sci.* 57 648

Shen Y R 1986 *IEEE J. Quantum Electron.* **QE-22** 1196

Zel'dovich B Ya, Pilipetskii N F and Shkunov V V 1985 *Principles of phase conjugation* (Berlin: Springer Verlag)

CC-0. In Public Domain. Gurukul Kangri Collection, Haridwar

Digitized by Arya Samaj Foundation Chennai and eGangotri

CC-0. In Public Domain. Gurukul Kangri Collection, Haridwar

Digitized by Arya Samaj Foundation Chennai and eGangotri

Pramāṇa – J. Phys., Vol. 34, No. 6, June 1990, pp. 473–489. © Printed in India.

Analysis of the absorption mechanism during laser-metal interaction

B S YILBAS, R DAVIES, Z YILBAS and A KOC

The University of Erciyes Institute of Science and Engineering, Erciyes Universitesi, Fen Bilimleri Enstitüsü, Kayseri-Turkey

MS received 8 September 1989; revised 19 December 1989

Abstract. The present study examines the absorption of a laser beam at different wavelengths by a partially-ionized vapour during the interaction mechanism. The applicability of the theoretical models developed is discussed in detail. The interaction of the high- and low-power intensities of a laser beam with plasma is distinguished. It is shown that different metal vapours at similar temperatures and densities have absorption depths which may differ by an order of magnitude. Even more substantial is the difference between the absorption depths of light from different lasers in common use. It is also shown that the free electron temperature becomes significantly different from the heavy particle temperature for power intensities above the critical level which is typically $> 10^{14}$ W/m^2. The free electron velocity distribution has an isotropic part which becomes non-Maxwellian for power intensities greater than the critical power intensity.

Keywords. Laser; absorption; laser-metal interaction.

PACS No. 52·50

1. Introduction

The present work is presented in two sections: In §§2–4, the theory of the absorption of electromagnetic radiation by a partially-ionized vapour is considered in the context of the interaction between a single temperature, homogeneous, steady-state vapour and a low-power intensity laser beam. In §§5–8, the applicability of the theory to laser interactions in general is considered and some analytical restrictions are discussed.

The absorption property of the vapour depends critically on the vapour state which in turn depends on the beam power intensity. Previous work (Robin 1971) on high power intensity ($I > 10^{-14}$ W/m^2) beam vapour interactions showed that the vapour becomes a high temperature, fully-ionized plasma with a high absorption coefficient. However, the lower power intensities suitable for drilling operations (10^{10}–10^{12} W/m^2) also produce vapour plumes which have significant attenuation properties even though the vapour state is considerably different. Our investigation was necessitated on account of this difference. The results used by Robin (1971) and Culliford *et al* (1974), for example, are unsatisfactory under some conditions which are of interest here, since they both use high power intensity beam vapour interactions.

2. Absorption analysis

The absorption law for a laser beam with a local power intensity I is of the form:

$$(1/I) \times (\mathrm{d}I/\mathrm{d}x) = -1/d, \tag{1}$$

CC-0. In Public Domain. Gurukul Kangri Collection, Haridwar

Digitized by Arya Samaj Foundation Chennai and eGangotri

where d is the absorption depth which is determined from

$$d = 1/(2\Sigma\alpha), \tag{2}$$

where $\Sigma\alpha$ is the summation of attenuation coefficients for electron-neutral atom and electron-ion collisional absorption and photoionization absorption respectively.

In the following sections a classical derivation of the effective electron-neutral atom collision frequency is found to be valid which allows kinetic theory to be used to deduce the electron-neutral atom collisional attenuation coefficient. The same approach is found to be valid when used to describe electron-ion absorption in which the corresponding attenuation coefficient is determined from quantum mechanical/classical theory. This is also used to determine the attenuation coefficient for photoionization absorption.

3. Classical description of absorption

Considerations of the interaction mechanism can be based either on the concept of an electromagnetic wave or on the photon gas description of the laser beam. Only a quantum-mechanical approach using the photon gas description offers a complete explanation of the absorption processes. However, the classical theory is simpler and useful in interpreting the limitations of the theory. The attenuation coefficient is (Yilbas 1988)

$$\alpha = \frac{\omega}{c}\left\{\frac{\omega^2 + \nu_{av}^2 - \omega_p^2}{2(\omega^2 + \nu_{av}^2)}\left[\left\{1 + \left(\frac{\omega_p^2 \nu_{av}}{\omega(\omega^2 + \nu_{av}^2 - \omega_p^2)}\right)^2\right\}^{1/2} - 1\right]\right\}^{1/2}. \tag{3}$$

This expression may be used to describe electron-neutral atom and electron-ion collisional absorption if the respective effective collision frequency ν_{av} can be calculated. This is defined as:

$$\nu_{av} = -\frac{4\pi}{3}\int_0^\infty v \frac{\partial f_0}{\partial v} v^3 \, dv. \tag{4}$$

The evaluation of ν_{av} is considered in the following section.

3.1 *Conditions of validity of classical treatment for electron-neutral atom collisions*

An expression for the collision frequency is required before the integral in equation (4) may be evaluated. The semi-classical results described by Zeldovich and Raizer (1967) are limited by the condition $h \cdot \omega \ll 1/2\,mV^2$ which is too restrictive to be satisfactory in the range of conditions of interest. Bekifi (1966) gives a result which requires numerical integration to relate it to the effective collision frequency. A more complete work by Koch and Motz (1959) presents a comprehensive review of bremsstrahlung results, but these require an unjustified increase in complexity in view of the uncertainty of cross-section values.

For a classical analysis to be valid, the electron-atom collisions are required to be effectively instantaneous and elastic. The former condition is satisfied if the periodic time of the electromagnetic wave is large compared to the characteristic electron-atom

CC-0. In Public Domain. Gurukul Kangri Collection, Haridwar

Digitized by Arya Samaj Foundation Chennai and eGangotri

interaction time, τ, which may be expected to be of the order:

$$\tau \sim a_0/v, \tag{5}$$

where a_0 is the atom radius and v the electron velocity. The wave period is given by $2\pi/\omega$. Using the arithmetic mean velocity, which according to kinetic theory is related to the vapour temperature by $V = (8kT/\pi m)^{1/2}$, gives a condition for instantaneous collisions:

$$T > (\omega a_0/2\pi)^2 (m\pi/8k), \tag{6}$$

which for $a_0 = 0{\cdot}5 \times 10^{-10}$ m (Bohr's radius of the hydrogen atom) and $\omega = 1{\cdot}78 \times 10^{15}\,s^{-1}$ (Nd YAG laser light frequency) reduces to $T > 10$ K.

The elastic collision approximation is reasonable if the number of inelastic collisions is small compared to the total number of collisions in a given period.

If photoionization is neglected, the absorption of a laser beam photon requires an inelastic collision and so the laser beam absorption rate corresponds to a minimum rate of inelastic collisions per free electron given by

$$\nu_{\text{inelastic}} = 2\alpha I/n_e \hbar\omega.$$

Since this frequency is small compared to the total collision frequency under the conditions of interest, its effect on the elastic collision approximation is small.

3.2 *Effective electron-neutral atom collision frequency*

There are no results available for metal-vapour momentum transfer cross-sections for electron energies of the order of 10^0 eV. Consequently it is necessary to resort to the elementary "hard sphere" result for which the momentum transfer and total cross-sections Q are equal, i.e.

$$Q = \pi a_0^2. \tag{7}$$

The collision frequency is given by

$$\nu = + Q \cdot n_n \cdot V, \tag{8}$$

where n_n is the number density of neutral atoms. For a Maxwellian f_0 component of the electron velocity distribution,

$$\partial f_0/\partial v = \frac{-v}{(2\pi)^{3/2}} (m/kT)^{5/2} \exp(-mv^2/2kT). \tag{9}$$

Substituting equations (9) and (8) in (4), and using the relationship (Chapman and Cowling 1952)

$$\int_0^\infty \exp(-\alpha v^2) v^r \, dv = \tfrac{1}{2}\alpha^{-(r+1)/2} \Gamma\left(\frac{r+1}{2}\right), \tag{10}$$

equation (4) may be evaluated to give

$$\nu_{en} = \frac{8\pi^{1/2}}{3} (m/2kT)^{-1/2} a_0^2 n_n, \tag{11}$$

CC-0. In Public Domain. Gurukul Kangri Collection, Haridwar

Digitized by Arya Samaj Foundation Chennai and eGangotri

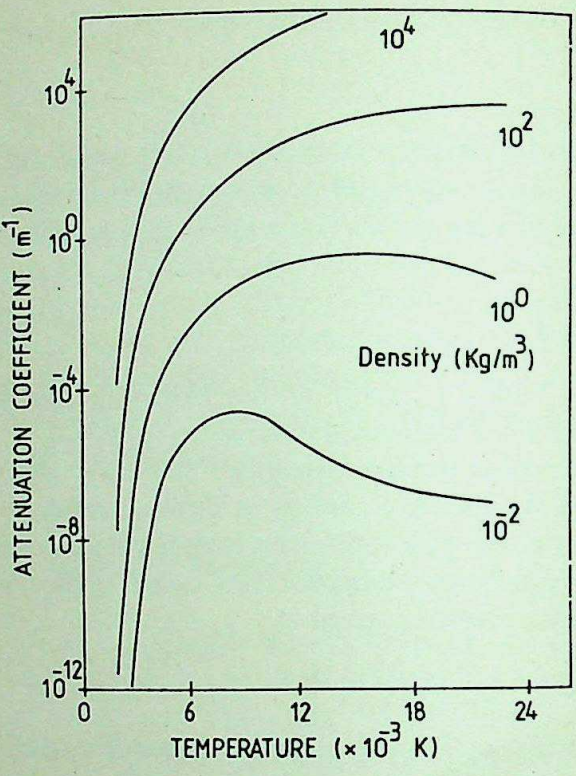

Figure 1. Attenuation coefficient due to electron-neutral atom collisions in steady-state copper vapour for 10·6 μm radiation.

taking $a_0 = 0{\cdot}5 \times 10^{-10}$ m (Bohr's radius of hydrogen atom)

$$\nu_{en} = 7{\cdot}3 \times 10^{-11} n_n(\mathrm{cm}^{-3}) T^{1/2}(\mathrm{K}), \tag{12}$$

where ν_{en} is the effective collision frequency, defined by equation (4) for electron-neutral atom collisions.

3.3 *Attenuation coefficient for electron-neutral atom collision absorption*

This may be calculated by substituting equation (12) for the effective collision frequency, into equation (3). The attenuation coefficient has been calculated for copper vapour, for a range of vapour states and the results are plotted in figure 1.

3.4 *Effective electron-ion frequency calculated using the classical Coulomb interaction*

The effective electron-ion collision frequency may be calculated by the same method used to determine the effective electron-neutral collision frequency. However the result, which is given below, has a limited validity which restricts its use in the study of vapour beam interactions at drilling power intensities. The theory of electron-ion coulomb interactions is well known, giving the electron-ion collision frequency to be (Chapman and Cowling 1952):

$$\nu = (4\pi n_e z/v^3)(e^2/4\pi\varepsilon_0 m)^2 \ln \Lambda, \tag{13}$$

where ε_0 is the permittivity of free space and Λ is the cut-off ratio. Substituting (13)

CC-0. In Public Domain. Gurukul Kangri Collection, Haridwar

Digitized by Arya Samaj Foundation Chennai and eGangotri

and (9) in (4) gives the effective collision frequency for electron-ion collisions:

$$\nu_{ei} = \frac{4(2\pi)^{1/2}}{3} Z n_e (e^2/4\pi\varepsilon_0 m)^2 (m/kT)^{3/2} \ln \Lambda. \tag{14}$$

Substituting the numerical values gives:

$$\nu_{ei}(\mathrm{s}^{-1}) = \frac{3{\cdot}64 Z n_e(\mathrm{cm}^{-3}) \ln \Lambda}{T^{3/2}(\mathrm{K})}. \tag{15}$$

This ratio is (Spitzer 1962)

$$\Lambda = \frac{3}{2Ze^3} \frac{(4\pi\varepsilon_0 kT)^{3/2}}{(\pi n_e)^{1/2}}, \tag{16}$$

which is the ratio of the Debye shielding length to the impact parameter for which the impinging electron is deflected through 90°. This represents the ratio of maximum to minimum limits of the impact parameter for a collision. The Debye length is approximately the distance at which the ion charge is effectively shielded by other particle fields, so at this distance the collision deflection tends to zero.

The cut-off ratio is subjected to modifications to account for quantum- and high-frequency effects. The quantum effects are negligible up to electron energies of the order of 10 eV, which exceeds the range of electron energies reached in laser machining processes. The high-frequency effect occurs when the electromagnetic wave period is less than the duration of a collision as for $\omega \gg \omega\rho$. In this case the ion charge is effectively shielded in a distance z so that (16) needs to be modified, according to Bekifi (1966), and Shkarofsky *et al* (1966):

For $\omega > \omega_p$

$$\Lambda_{\mathrm{h.f.}} = (\omega_p/\omega)\Lambda. \tag{17}$$

Substituting the numerical values in (16) and (17) gives

$\omega < \omega_p$,

$$\Lambda = 1{\cdot}24 \times 10^4 \times T^{3/2}(\mathrm{K})/n_e^{1/2}(\mathrm{cm}^{-3}), \tag{18}$$

$\omega > \omega_p$,

where
$$\Lambda = 7{\cdot}01 \times 10^8 \times T^{3/2}(\mathrm{K})/\omega(\mathrm{s}^{-1}), \tag{19}$$

$$\omega_p(\mathrm{s}^{-1}) = 5{\cdot}64 \times 10^4 \times n_e^{1/2}(\mathrm{cm}^{-3}). \tag{20}$$

A condition for the validity of the theory is:

$$\ln \Lambda \gg 1. \tag{21}$$

The following shows this limitation to be restrictive for laser-drilling interactions. Nd YAG solid state laser light, commonly used in machining applications, has a frequency of $\omega = 1{\cdot}78 \times 10^{-5}\ \mathrm{s}^{-1}$. From equation (20) the free electron number density n_e for $\omega = \omega_p$ is found to be $n_e = 1 \times 10^{21}(\mathrm{cm}^{-3})$, which corresponds to a density of about $10^2\ \mathrm{kg/m}^3$ for most fully, single-ionized metals. Since the vapour expands to

CC-0. In Public Domain. Gurukul Kangri Collection, Haridwar

Digitized by Arya Samaj Foundation Chennai and eGangotri

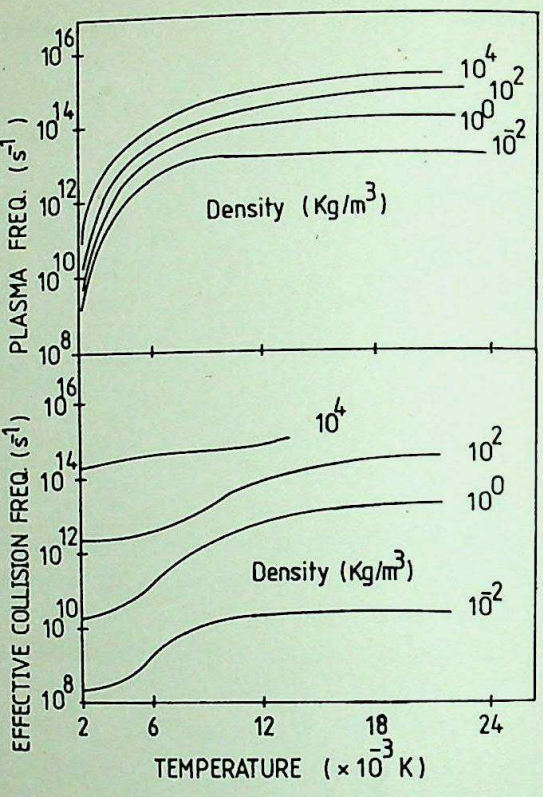

Figure 2. Effective collision frequency and plasma frequency for copper vapour.

densities an order of magnitude less than this distances from the surface of 10^{-4}–10^{-5} m, the vapour that is studied in this work is generally underdense (i.e. has a free electron density less than critical). The plasma frequency is plotted as a function of temperature for a range of vapour densities and for various equilibrium conditions in figure 2, for copper. For underdense vapour, equation (19) applies. It follows that the vapour temperature must satisfy the condition:

$$\ln T \gg \ln 3600.$$

This is not generally the case for machining power intensities. For the region close to the surface when $\omega_p > \omega$, the minimum temperature limit is increased whereas the vapour temperature is likely to be cooler. Consequently the limit equation (21) is even less likely to be satisfied.

The preceding discussion indicates that a quantum-mechanical approach is necessary to determine the attenuation coefficient for electron-ion collisions. However, the collision frequency provides an indication of whether for, example, the vapour reaches an equilibrium condition in a given time, and so a measure of this frequency is desired.

An expression for the attenuation coefficient was given earlier, equation (3):

$$\alpha = \frac{\omega}{c}\left\{\frac{\omega^2+\nu_{av}^2-\omega_p^2}{2(\omega^2+\nu_{av}^2)}\left[\left\{1+\left(\frac{\omega_p^2\nu_{av}}{\omega(\omega^2+\nu_{av}^2-\omega_p^2)}\right)^2\right\}^{1/2}-1\right]\right\}^{1/2},$$

for a range of conditions $\omega \gg \omega_p$ and $\omega \gg \nu_{av}$ so that (22)

$$\alpha = \frac{\omega}{c}\left\{\frac{1}{2}\left[\left\{1+\left(\frac{\omega_p^2\nu_{av}}{\omega^3}\right)^2\right\}^{1/2}-1\right]\right\}^{1/2}.$$

CC-0. In Public Domain. Gurukul Kangri Collection, Haridwar

Digitized by Arya Samaj Foundation Chennai and eGangotri

Using the binomial series expansion:

$$\alpha \simeq \frac{\omega}{c}\left\{\frac{1}{2}\left[1+\frac{1}{2}\left(\frac{\omega_p^2 \nu_{av}}{\omega^3}\right)^2-1\right]\right\}^{1/2}$$

or

$$\alpha \simeq \omega_p^2 \nu_{av}/2c\omega^2. \tag{23}$$

which may be rearranged to give

$$\nu_{av} \simeq \omega^2 2\alpha/\omega_p^2 c. \tag{24}$$

Consequently the collision frequency may be determined if the attenuation coefficient is known for quantum-mechanical calculation for the absorption coefficient (A_f) for electron-ion absorption where

$$A_f \equiv 2\alpha. \tag{25}$$

The value of A_f may be determined from (24).

As an illustration, the total effective collision frequency

$$\nu_{av} = (\nu_{av})_{\text{electron-ion}} + (\nu_{av})_{\text{electron-neutral}}$$

is given in figure 2 for copper.

4. Quantum-mechanical/classical methods

In this section the results of the quantum-mechanical/classical Krammer's theory are given, with a minor modification, for absorption involving electron-ion collisions and photoionization. It is assumed that the metal atoms will be hydrogen-like which requires the outer bound electrons to have a large orbit radius to the other bound electrons of the atom. Details of the theory for hydrogenic atoms may be found in Landau and Lifshitz (1960), Zeldovich and Raizer (1967) and Karzas and Latter (1961).

4.1 *Inverse Bremsstrahlung absorption*

The absorption coefficient A, for beam frequency ω and power intensity I is

$$A = -(1/I) \times (\mathrm{d}I/\mathrm{d}x) \tag{26}$$

where x is the spatial coordinate in the direction of propagation. The absorption coefficient for electron-ion inverse bremsstrahlung A_f for a hydrogenic atom is

$$A_f = \zeta \cdot \frac{16\pi^2}{3}\left(\frac{2\pi}{3mkT}\right)^{1/2} Z^2 \left(\frac{e^2}{4\pi\varepsilon_0}\right)^3 \frac{n_i n_e}{\hbar c m \omega^3}. \tag{27}$$

In the present work this equation is modified by replacing the theoretical ionization for a hydrogen-like atom with the actual ionization potential U which gives

$$A_f = \zeta \cdot \frac{32\pi^2}{3}\left(\frac{2\pi}{3mkT}\right)^{1/2} \left(\frac{e^2}{4\pi\varepsilon_0}\right) \frac{\hbar U n_i n_e}{cm^2\omega^3}. \tag{28}$$

CC-0. In Public Domain. Gurukul Kangri Collection, Haridwar

Digitized by Arya Samaj Foundation Chennai and eGangotri

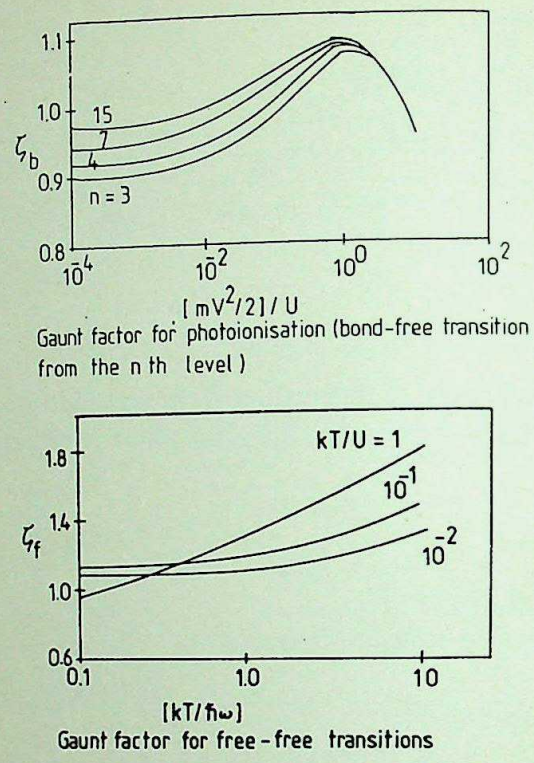

Figure 3. Effective Gaunt Factors computed by Karzas and Latter (1961).

The Gaunt factor ζ relates the quantum-mechanical result and the Krammer's theory result. Values for ζ have been computed by Karzas and Latter (1961). These are plotted in a convenient form in figure 3, showing that ζ is of the order of unity in the range of conditions of interest and so deviations from unity are neglected. Substituting the numerical values in (28) gives:

$$A_f(\mathrm{cm}^{-1}) = 6{\cdot}7 \times 10^9 \times n_e(\mathrm{cm}^{-3}) n_i(\mathrm{cm}^{-3}) U(\mathrm{eV}) / T^{1/2}(\mathrm{K}) \omega^3.$$

The attenuation coefficient $\alpha = (A_f/2)$ for electron-ion inverse bremsstrahlung is given in figure 4 for copper vapour.

4.2 *Photoionization absorption*

The absorption coefficient for light of frequency ω due to photoionization may also be calculated using the same theory. Replacing the theoretical ionization potential for a hydrogenic atom with the actual ionization potential U the modified result is

$$A_b = \zeta \cdot \frac{16\pi k T n_n U}{3\sqrt{3} m c \omega^3 \hbar^2} \left(\frac{e^2}{4\pi\varepsilon_0} \right) \exp(-U/kT) [\exp(\hbar\omega/kT) - 1]. \tag{30}$$

The Gaunt factor ζ for photoionization transitions (bound-free transitions) calculated by Karzas and Latter (1961) is close to unity for the conditions of interest as figure 3 shows and so ζ may be taken as unity.

CC-0. In Public Domain. Gurukul Kangri Collection, Haridwar

Digitized by Arya Samaj Foundation Chennai and eGangotri

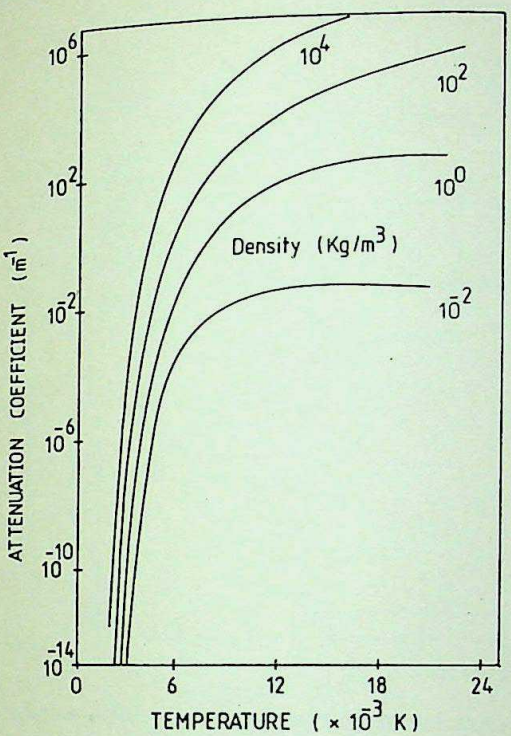

Figure 4. Attenuation coefficient due to electron-ion collisions in steady-state copper vapour for 10·6 μm radiation.

Substituting the numerical values for constants gives:

$$A_b(\mathrm{cm}^{-1}) = 1{\cdot}6 \times 10^{25} \frac{T(\mathrm{K}) n_n(\mathrm{cm}^{-3}) U(\mathrm{eV})}{\omega^3} \exp\left(\frac{-11605 U(\mathrm{eV})}{T(\mathrm{K})}\right) \times \left\{\exp\left(\frac{7{\cdot}637 \times 10^{-12} \times \omega}{T(\mathrm{K})}\right) - 1\right\}. \tag{31}$$

The attenuation coefficient for bound-free electron transitions (photoionization), $\alpha = A_b/2$, is given in figure 5 for copper.

4.3 *Effective absorption depth*

The effective absorption depth d for the vapour is dependent on the combined effects of absorption due to electron-ion and electron-neutral atom collisions and photoionization

$$d = 1/2\Sigma\alpha,$$

where $\Sigma\alpha$ is the summation of attenuation coefficients which may be calculated using (28), (30), (3) and (11).

The effective absorption depth for a laser light frequency of $1{\cdot}78 \times 10^{15}$ (Nd YAG laser) has been plotted for a range of conditions and materials. The results for tantalum, titanium and copper are shown in figures 6, 7 and 8 respectively.

As an indication of how d varies with the ω of the laser light, d has been calculated in the frequency range spanning $1{\cdot}78 \times 10^{14}\,\mathrm{s}^{-1}$ $1{\cdot}78 \times 10^{15}\,\mathrm{s}^{-1}$, and $2{\cdot}977 \times 10^{15}\,\mathrm{s}^{-1}$ which are the respective frequencies for CO_2, Nd YAG and He-Ne laser light. The

CC-0. In Public Domain. Gurukul Kangri Collection, Haridwar

Digitized by Arya Samaj Foundation Chennai and eGangotri

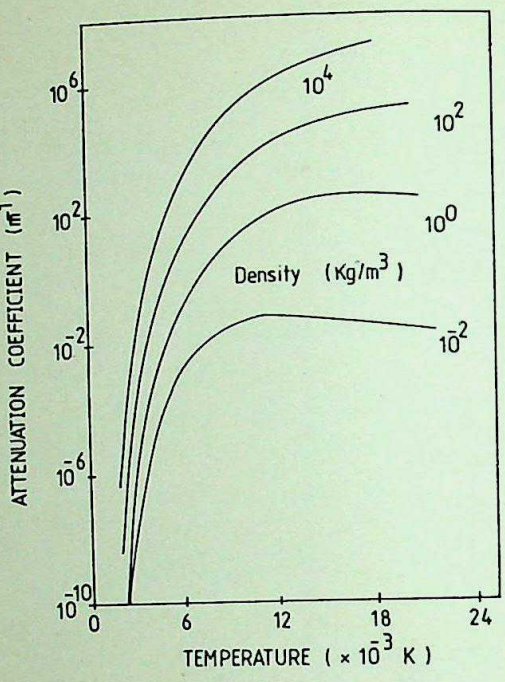

Figure 5. Attenuation coefficient due to photoionisation in steady-state copper vapour for 10·6 μm radiation.

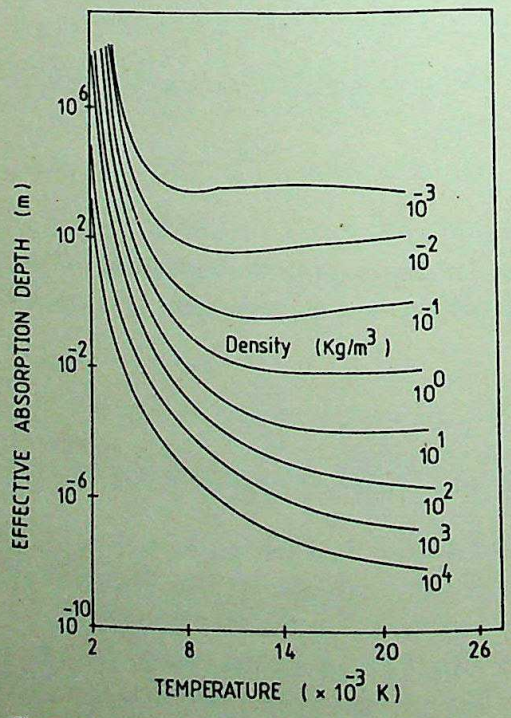

Figure 6. Effective absorption depth in tantalum vapour for 1·06 μm radiation.

CC-0. In Public Domain. Gurukul Kangri Collection, Haridwar

Digitized by Arya Samaj Foundation Chennai and eGangotri

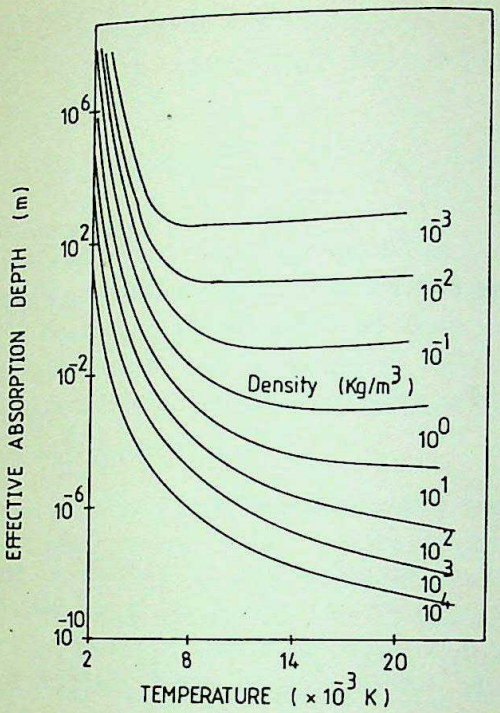

Figure 7. Effective absorption depth in titanium vapour for 1·06 μm radiation.

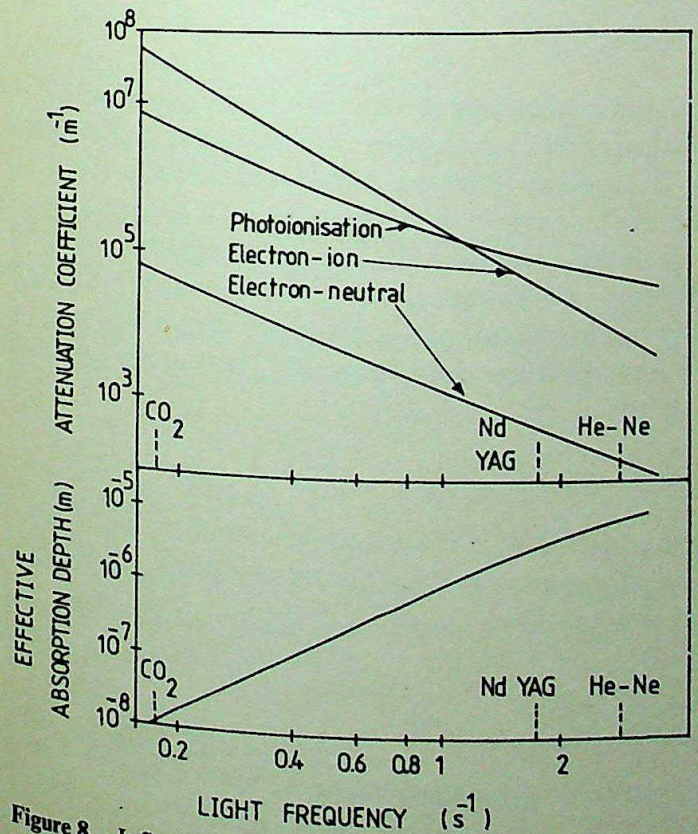

Figure 8. Influence of light frequency on absorption properties of copper vapour (density 1 kg/m and temperature 12000 K).

CC-0. In Public Domain. Gurukul Kangri Collection, Haridwar

Digitized by Arya Samaj Foundation Chennai and eGangotri

computed results and the corresponding attenuation coefficients are plotted in figure 8, for copper vapour with a density and temperature of 1 kg/m^3 and 12000 K respectively.

4.4 *Line absorption*

The absorption of radiation due to bound-bound electron transitions is not accounted for in this work. If the laser light frequency coincides with a strong absorption line, the overall attenuation coefficient could be significantly increased and the line absorption would have to be considered. However in view of the wide separation of absorption lines, this case is unlikely to arise for monotonic metal vapours.

5. Evaluation of theory limits for laser interaction problem

We have considered in an earlier section the processes involved in the absorption of electromagnetic radiation and some checks on the validity of laser interaction problems were incorporated in the derivation of results. However, the theory was developed for a homogeneous steady state vapour in which the free electrons and heavy particles have a Maxwellian velocity distribution function and the same temperature. Since laser machining and drilling interactions do not produce vapour which obviously satisfies these conditions, the restriction on the validity of the theory is considered in the following sections.

6. Influence of power density

High power density focused laser beams have a high electric field strength which may affect the electron velocity distribution function and the equality of electron and heavy particle temperatures. These possibilities are considered below where it is shown that the effects may be neglected for power intensities below a characteristic value.

The magnitude of the electric intensity and the power intensity may be related for a beam propagating through a vacuum or, to a good approximation, through air by equating expressions for the electromagnetic wave per unit volume.

In terms of electric and magnetic field intensity, the energy per unit volume is (Lifshitz and Pitoevskii 1981)

$$W = \tfrac{1}{2}(\varepsilon_0 \kappa E^2 + \mu_0 \kappa_m H^2), \tag{32}$$

where κ is the dielectric constant, κ_m the relative permeability and E the electric field intensity. Averaging over the period of the wave and introducing the ratio of electric and magnetic intensity amplitudes:

$$H_0 = \frac{(\alpha^2 + \eta^2)^{1/2}}{\mu_0 \kappa_m \omega} E_0, \tag{33}$$

where η is the phase coefficient. Equation (32) becomes

$$W_{av} = \tfrac{1}{4}\varepsilon_0 \kappa E_0^2 \left(1 + \frac{\alpha^2 + \eta^2}{\varepsilon_0 \mu_0 \kappa \kappa_m \omega^2}\right). \tag{34}$$

CC-0. In Public Domain. Gurukul Kangri Collection, Haridwar

Digitized by Arya Samaj Foundation Chennai and eGangotri

For a vacuum $\alpha = 0$ and $\eta = \omega/c$, so that

$$W_{av} = \tfrac{1}{2}\varepsilon_0 E_0^2.$$

Since the velocity of energy flow is the speed of light c, in a vacuum,

$$W_{av} = I/c, \tag{35}$$

where I is the power intensity. Equating (34) and (35) gives:

$$E_0 = (2I/\varepsilon_0 c)^{1/2}. \tag{36}$$

6.1 *Electron heavy particle ratio*

To determine whether the free electron temperature is sufficiently different from the heavy particle temperature to warrant treating the vapour as having a two-temperature state, the temperature ratio is determined as a function of power intensity for conditions when the respective species temperature difference is constant. This maximises the temperature ratio for a particular heavy particle temperature in the case a vapour whose specific internal energy is constant or increasing.

The free electrons gain as internal energy the electromagnetic wave energy dissipated by ohmic heating. The rate at which this occurs may be determined for the effective current density:

$$J = \frac{n_e e^2 E}{m(i\omega + \nu_{av})} \tag{37}$$

The power dissipated by ohmic heating is

$$Q = \mathrm{Re}(J)\cdot\mathrm{Re}(E)$$

$$= \frac{n_e e^2 E_0^2}{m(\omega^2 + \nu_{av}^2)}(\nu_{av}\cos^2\omega t + \omega\cos\omega t\sin\omega t). \tag{38}$$

Since the period of the electromagnetic wave is short compared to the characteristic times of the other processes involved, the time-averaged value over a time $1/\omega$ is sufficient

$$Q_{av} = \frac{n_e e^2 E_0^2 \nu_{av}}{2m(\omega^2 + \nu_{av}^2)}. \tag{39}$$

When the temperature difference is the maximum possible, the rate of energy gain of the free electrons is equal to the rate at which energy is transferred to the heavy particle species, at temperature T:

$$Q = \nu_{av}\left(\frac{2m}{M}\right)\tfrac{3}{2}n_e k(T_e - T), \tag{40}$$

where $(2m/M)$ is the fraction of the average excess energy $3/2n_e\, k(T_e - T)$ transferred in a collision with a heavy rigid particle of mass M. Equating (30) and 40 and

CC-0. In Public Domain. Gurukul Kangri Collection, Haridwar

Digitized by Arya Samaj Foundation Chennai and eGangotri

rearranging:

$$T_e/T = 1 + \frac{Me^2E_0^2}{6m^2kT(\omega^2 + v_{av}^2)}. \tag{41}$$

For laser light frequencies, $\omega^2 \gg v_{av}^2$ will usually be satisfied so that

$$T_e/T = 1 + (Me^2E_0^2)/(6m^2kT\omega^2). \tag{42}$$

Using equation (36),

$$T_e/T \simeq 1 + (I/I_{crit}), \tag{43}$$

where

$$I_{crit} = (6m^2kT\omega^2)/(M\varepsilon_0 ce^2). \tag{44}$$

I_{crit} is the power intensity indicating the threshold for a free electron temperature which is significantly different from the heavy particle temperature. Substituting the numerical values for constants and taking the mass of the heavy particles for metals to be $M = 10^{-25}$ kg

$$I_{crit} = 10^{-17} \times T \times \omega^2.$$

For CO_2 laser radiation, which has a low light frequency ($\omega^2 = 3{\cdot}2 \times 10^{28}\,s^{-2}$), and taking $T = 1000$ K the value of I_{crit} is $\sim 3 \times 10^{14}$ W/m^2. This is typically two or three orders of magnitude greater than the power intensities commonly used for machining applications.

6.2 *Effect of power intensity on electron velocity distribution function*

The free electron velocity distribution function f is governed by the Boltzmann equation. This equation may be solved approximately for f by assuming a solution of the form:

$$f = f_0 + \bar{v}/v \times \bar{f}_1 + \cdots,$$

where f_0 represents the isotropic part f, and $\bar{f}_1$ together with succeeding terms present the directed part of f. Substituting this series into the Boltzmann equation yields a chain of equations for f_0, $\bar{f}_1$, etc. The respective equations for f_0 and $\bar{f}_1$ may be found (Waldrom 1987).

In the derivation of results presented earlier, f_0 was assumed to be Maxwellian. This is valid if the free electron motion is dominated by electron-electron collisions. If, however, the degree of ionization is low or the power intensity sufficiently high, f_0 may be non-Maxwellian. For this case f_0 is determined by solving the simplified equation in which the electron-electron collision term is dropped:

$$-\frac{en_e\bar{E}}{3mv^2}\frac{\partial(v^2\bar{f}_1)}{\partial v} = \frac{n_e m}{Mv^2}\frac{\partial}{\partial v}\left\{vv^3\left(f_0 + \frac{kT}{mv}\frac{\partial f_0}{\partial v}\right)\right\}. \tag{45}$$

Integrating

$$-\frac{eM\bar{E}\cdot\bar{f}_1}{3m^2vv} = f_0 + \frac{kT}{mv}\frac{\partial f_0}{\partial v}. \tag{46}$$

CC-0. In Public Domain. Gurukul Kangri Collection, Haridwar

Digitized by Arya Samaj Foundation Chennai and eGangotri

Using equation (29) for $\bar{f}_1$

$$\bar{f}_1 = \frac{e\bar{E}}{m(i\omega + \nu)} \frac{\partial f_0}{\partial v}. \tag{47}$$

Equation (46) becomes

$$\frac{\mathrm{d}f_0}{f_0} = \frac{mv\,\mathrm{d}v}{kT\left(1 + \dfrac{MeE^2}{3m^2(\omega^2 + \nu^2)kT}\right)}, \tag{48}$$

or, using equations (36) and (44)

$$\mathrm{d}f_0/f_0 = mv\,\mathrm{d}v/\{kT[1 + (I/I_{\mathrm{crit}})]\}. \tag{49}$$

Equation (49) gives a Maxwellian f_0 only when $I \ll I_{\mathrm{crit}}$, which is the same criterion for a single-temperature fluid.

7. Effect of temporal changes and spatial gradients in the vapour

In practice the vapour has a transient state and may be inhomogenous. The absorption theory developed earlier may therefore be inadequate. An indication of the validity of the theory is provided by examining the equation for the directed part of the electron distribution function $\bar{f}_1$ which in the earlier analysis was taken to be of the form:

$$\frac{\partial \bar{f}_1}{\partial t} + \nu \bar{f}_1 = \frac{e\bar{E}}{m} \frac{\partial f_0}{\partial v}. \tag{50}$$

When the temporal and spatial gradients are included, (50) becomes:

$$\frac{\partial}{\partial t}(n_e \bar{f}_1) + v\nabla(n_e f_0) - \left(\frac{e\bar{E}}{m} + \frac{D\bar{u}}{Dt}\right) n_e \frac{\partial f_0}{\partial v} = -n_e \nu \bar{f}_1. \tag{51}$$

where the heavy particle diffusion and the magnetic field effect terms have been dropped from the full equation given in the previous work (Waldram 1987).

A general solution of (51) is, fortuitously, unnecessary for a one-dimensional expansion along the axis of the laser beam, since the electric field lies in a plane perpendicular to the direction of expansion. Assuming, for simplicity, the electric field is linearly polarized the component equations of (51) are

$$\frac{\partial}{\partial t} f_1' + \left(\frac{\partial}{\partial t} \ln n_e\right) + \nu\Bigg) f_1' = \frac{\partial f_0}{\partial v} \frac{eE}{M}, \tag{52}$$

$$\frac{\partial f_1''}{\partial t} + \left(\frac{\partial}{\partial t}(\ln n_e) + \nu\right) f_1'' = \frac{\partial f_0}{\partial v} \cdot \frac{Du}{Dt} - v f_0 \frac{\partial}{\partial z}(\ln n_e) - v \frac{\partial f_0}{\partial z}, \tag{53}$$

where z and u are the spatial coordinate and vapour velocity along the beam axis respectively. Equation (52) governs the absorption of the laser beam, and comparing

CC-0. In Public Domain. Gurukul Kangri Collection, Haridwar

Digitized by Arya Samaj Foundation Chennai and eGangotri

(50) and (52) the restriction on the analysis using (50) is that

$$\nu \gg \frac{\partial}{\partial t}(\ln n_e) \tag{54}$$

or

$$\nu \gg \Delta n_e / n_e \Delta t. \tag{55}$$

This condition is generally satisfied since for the times of interest $\Delta t \sim 10^{-9}$, $\Delta n_e/n_e < 1$. Values for the effective collision frequency ν_{av} are given in figure 2 for copper.

8. Discussion

Electron-ion and electron-neutral atom collisional absorption and photoionization absorption for electromagnetic radiation have been discussed. Results are presented graphically to indicate the relative importance of each process, for a range of conditions, and also to indicate the effective absorption depth. These results show that absorption due to electron-neutral atom collisions is significant only at low temperatures ($T < 4000$ K). The contributions of electron-ion and photoionization absorption are usually of similar magnitude owing to the fact that $\hbar\omega \sim kT$. For $\hbar\omega > 0{\cdot}7kT$ photoionization dominates electron-ion collisional absorption and vice-versa for $\hbar\omega < 0{\cdot}7\,kT$.

Different metal vapours at similar temperatures and densities have absorption depths which may differ by an order of magnitude. Even more substantial is the difference between the absorption depths of light from different lasers in common use. For example, when electron-ion or photoionization absorption processes dominate, the absorption coefficient is dependent on ω^3 and the absorption depth of CO_2 laser light is approximately three orders of magnitude smaller than Nd YAG laser light.

In §§5–8, it was shown that the free electron temperature becomes significantly different from the heavy particle temperature for power intensities above a critical level which is typically $> 10^{14}$ W/m^2. The free electron velocity distribution has an isotropic part and becomes non-Maxwellian for power intensities of the order or of greater than the same critical power intensity.

For one-dimensional vapour expansions the restrictions on the analysis of §§2–4 due to the assumption that the vapour is stationary and homogeneous are generally satisfied for the conditions of interest in this work.

References

Bekefi G 1966 *Radiation processes in plasmas* (Series in plasma physics) (New York: Wiley)

Chapman S and Cowling T G 1952 *The mathematical theory of non-uniform gases, an account of the kinetic theory of viscosity, thermal conductivity, and diffusion in gases* (Cambridge: University Press) 2nd ed.

Culliford E R, McMordie J A, Roberts P D and Sentance G W 1974 The interaction of pulsed CO_2 laser radiation with aluminium LDPN4174, AWRE Preliminary report

Karzas W J and Latter R 1961 *Astrophys. J. Suppl. Ser.* **16** 167

Koch H W and Motz J W 1959 *Rev. Mod. Phys.* **31** 921

Landau L D and Lifshitz E M 1960 *Electrodynamics of continuous media* (Translated by J B Svkes and J B Bell) Course of Theoretical Physics, (Oxford) Vol. 8

CC-0. In Public Domain. Gurukul Kangri Collection, Haridwar

Digitized by Arya Samaj Foundation Chennai and eGangotri

Lifshitz E M and Pitoevskii L D 1981 *Physical kinetics* (Oxford: Pergamon Press)
Robin J L 1971 *Phys. Fluids* **14** 2341
Shkarofsky I P, Johnston T W and Bachvncki M P 1966 *The particle kinetics of plasmas* (New York: Addison-Wesley)
Spitzer L 1962 *Physics of fully ionised gases* (*Tracts on physics and astronomy*) 2nd ed. No. 3 (New York: Interscience)
Waldram J R 1987 *The theory of thermodynamics* (Cambridge: University Press)
Yilbas B S 1988 *Pramana – J. Phys.* **31** 365
Zeldovic Y B and Raizer Y P 1967 *Physics of shock waves and high temperature hydrodynamics phenomena* (New York: Probstein and Haves) Vol. 2

CC-0. In Public Domain. Gurukul Kangri Collection, Haridwar

Digitized by Arya Samaj Foundation Chennai and eGangotri

CC-0. In Public Domain. Gurukul Kangri Collection, Haridwar

Digitized by Arya Samaj Foundation Chennai and eGangotri

Pramāṇa – J. Phys., Vol. 34, No. 6, June 1990, pp. 491–506. © Printed in India.

Anisotropic ESR parameters of Cu(II) complexes in solutions and dynamics of solvent coordination: use of "minimum linewidths"

B S PRABHANANDA

Chemical Physics Group, Tata Institute of Fundamental Research, Bombay 400005, India

MS received 25 November 1989; revised 7 March 1990

Abstract. The "minimum linewidths" seen in the ESR linewidths against temperature plots, the dependence of line widths on the ^{63}Cu nuclear magnetic quantum numbers and the Hubbard relation provide sufficient number of equations to determine the anisotropic ESR parameters in the case of axially symmetric Cu(II) complexes even when unresolved hyperfine structures make contributions to linewidths. After testing the method by reanalysing the literature data on Cu(II) bis-acetylacetonate, it has been used to obtain the anisotropic ESR parameters in the case of bis-salicylaldehydate of Cu(II). Linewidth contributions from unresolved hyperfine structures associated with the ^{1}H of coordinating $CHCl_3$ inferred in these studies, were confirmed by comparing the widths in $CHCl_3$ and $CDCl_3$ under ideal conditions. The temperature dependence of this contribution and the estimate of rate constant at room temperature ($\sim 10^{10}\,s^{-1}$) suggest that the coordinating solvent exchange is diffusion controlled.

Keywords. Electron spin resonance; Cu(II) complex; electron spin resonance linewidth; dynamics of solvent-solute interaction.

PACS Nos 33·35; 82·30

1. Introduction

Determination of **g** tensor and hyperfine tensor **A** is an important task in ESR spectroscopy. Study of paramagnetic molecules in diamagnetic host crystals is the best way of obtaining these tensors. However, this type of study cannot be carried out easily in several situations due to practical difficulties. In addition, strains in solid matrices may alter the ESR parameters (Froncisz and Hyde 1980). Such strains can be expected to be less in liquid solutions and hence a determination of the anisotropic ESR parameters in solutions is desirable. The simplicity of ESR spectra obtained in liquid solutions and the theoretical studies which have established relations between ESR linewidths and the anisotropies of the **g** and **A** tensors (McConnell 1956; Wilson and Kivelson 1966; Atkins and Kivelson 1966; Campbell and Freed 1980) have inspired attempts to obtain these anisotropies from ESR linewidths in liquid solutions (Hudson and Luckhurst 1969; Symons and Wilkinson 1972; Atherton and Waldrum 1972; Prabhananda 1979). In the case of Cu(II) complexes, the method which makes use of the Hubbard relation (Hubbard 1963) has been found to be particularly useful (Prabhananda 1979). The major stumbling blocks in the application of this method are: (i) unresolved hyperfine structures which make an apparent contribution to linewidths, and (ii) linewidth contributions from dynamic solvent perturbation of the

CC-0. In Public Domain. Gurukul Kangri Collection, Haridwar

Digitized by Arya Samaj Foundation Chennai and eGangotri

ligand field and other unidentified factors. Such contributions could be temperature dependent increasing the complication. This outstanding problem can be solved by devising a method to detect the presence of such contributions and estimate their magnitude. In an earlier work (Prabhananda 1980), it was shown that nearly isotropic ligand hyperfine structures when unresolved, contribute dominantly to the nuclear spin state independent term in the linewidth expression. It was also suggested that an estimate of unresolved hyperfine constants could be obtained from spin density distributions determined with the help of **g** and **A**. (These are first determined from linewidths neglecting unresolved hyperfine structures. Subsequently they are refined by iteration after including the hyperfine structures determined with the help of **g** and **A** of the previous iteration in the computer simulations of spectra to obtain true linewidths.) The work described below shows, how the minimum linewidths determined from a temperature dependent study of ESR spectra in liquid solutions could offer a simple and useful solution to the above mentioned problem. Additional help could also come from multifrequency ESR linewidth studies.

The new method primarily rests on the equations derived by Kivelson and coworkers (Wilson and Kivelson 1966a; Atkins and Kivelson 1966) and the contention that in the limited temperature range in which observations on minimum linewidths are made, the variations in the anisotropy parameters are not significant as far as linewidths in liquid solutions are concerned. (This could be verified by examining the straight line plot predicted by eq. (8) given below.) The method has been tested for Cu(II) complexes, by first analysing the literature data (Wilson and Kivelson 1966b) on the *X*-band ESR linewidths of bis-acetylacetonate of Cu(II), ($Cu(ac.ac)_2$) in toluene using the new method, and predicting the *K*-band ESR linewidth parameters. The excellent agreement between the predicted values and those reported in literature (Wilson and Kivelson 1966b), could be taken as a support for the validity of the method. The method has also been used to infer the presence of the second type of linewidth contributions in the *X*-band ESR spectra of $Cu(ac.ac)_2$ and bis-salicylaldehydate of Cu(II), ($Cu(Sal)_2$) in $CHCl_3$. The assignment of the additional linewidth contributions to unresolved ligand hyperfine structures from the coordinating $CHCl_3$ molecules and its subsequent confirmation from the linewidths measured in $CDCl_3$ demonstrates the usefulness of the method. The estimate of additional linewidth, enables us to discuss the dynamics of solvent coordination.

2. Experimental

The complex $Cu(Sal)_2$ (figure 1) prepared by the reaction of cupric acetate (enriched to > 99% with ^{63}Cu) and salicylaldehyde (purified by distillation) in aqueous solutions was extracted in chloroform. Degassed solutions were used in the experiments to eliminate broadening of the ESR lines due to dissolved oxygen. Sufficiently dilute solutions ($\sim 5{\cdot}10^{-4}$ M) were used to minimize the concentration dependent contributions to linewidths. *X*-band ESR spectra at different temperatures were obtained using the spectrometer described elsewhere (Prabhananda *et al* 1972). Computer simulated spectra with Lorentzian line shapes were obtained to analyse the liquid solution spectra using a Fortran program developed earlier (Baratova *et al* 1982). Frozen solution spectra were analysed using a powder spectrum computer program (Pilbrow and Winfield 1973), suitably modified to include hyperfine structures from

CC-0. In Public Domain. Gurukul Kangri Collection, Haridwar

Digitized by Arya Samaj Foundation Chennai and eGangotri

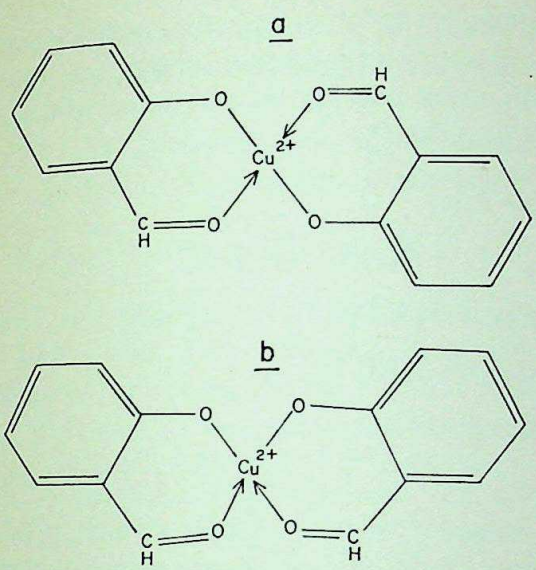

Figure 1. Two possible isomers of $Cu(Sal)_2$.

^1H on the ligands. The minimum linewidths were used to obtain the **g** and **A** anisotropy estimates using a Fortran program (available from the author on request), which makes use of the method and equations discussed below. A CDC Cyber computer was used in all simulations and calculations.

3. Theory

In this paper we restrict ourselves to axially symmetric **g** and **A** tensors with their symmetry axes coincident. The dependence of peak to peak derivative ESR linewidth W_j of the hyperfine transition "j", on the rotational correlation time τ is well known (Wilson and Kivelson 1966b). Unresolved hyperfine structures make an additional spin state independent contribution to linewidths (Prabhananda 1980). If F is this additional contribution at the temperature of observation,

$$W_j = C/\tau + D_j\tau + F. \tag{1}$$

Since the dynamic processes responsible for a possible temperature dependence of F are not correlated with the tumbling motion (with which τ is associated), we do not have any additional cross term in (1). A minimum linewidth W_j^* corresponding to the minimum value of $(W_j - F)$ should satisfy,

$$\partial[W_j - F]/\partial\tau = 0$$

which enables us to write,

$$W_j^* = 2(CD_j)^{0\cdot5} + \alpha_{4j} \tag{2}$$

where α_{4j} is the magnitude of F at the temperature of minimum linewidth. The corresponding rotational correlation time is given by

$$\tau_j^* = (C/D_j)^{0\cdot5}. \tag{3}$$

CC-0. In Public Domain. Gurukul Kangri Collection, Haridwar

Digitized by Arya Samaj Foundation Chennai and eGangotri

In a first approximation the experimentally observed minimum linewidths can be used for W_j^*. These values can be corrected in the subsequent iterations. The dependence of linewidth on the quantum number m_j associated with the hyperfine transition is included in the expression for D_j.

$$\begin{aligned}
&D_j = \alpha_0 + \beta_0 m_j + \gamma_0 m_j^2 + \delta_0 m_j^3 \\
&\alpha_0 = \alpha_1 + \alpha_2 + \alpha_3; \quad \beta_0 = \beta_1 + \beta_2; \quad \gamma_0 = \gamma_1 + \gamma_2 \\
&\alpha_1 = 3^{-0.5}\{(8/45)(B\Delta g/g_0)^2 + (3/20)I(I+1)b^2\}\{\omega/B\} \\
&\beta_1 = 3^{-0.5}\{(8/15)(B\Delta g/g_0)b\}\{\omega/B\} \\
&\gamma_1 = 3^{-0.5}\{b^2/4\}\{\omega/B\}.
\end{aligned} \tag{4}$$

$\Delta g_0 = g_0 - 2{\cdot}0023$; $\Delta g = g_z - (g_x + g_y)/2$; $b = \{A_z - (A_x + A_y)/2\}\{B/\omega\}/1{\cdot}5$; $\omega = 2\pi\cdot$ resonant frequency; $B = \hbar\omega/g_0\beta_0$ where g_0 is the isotropic g-value, g_x, g_y, g_z are the principal components of the **g** tensor, A_x, A_y and A_z are the principal components of the **A** tensor in units of rad s^{-1}. However, b is in gauss. I is the nuclear spin giving the hyperfine splittings and β_e is the Bohr magneton. $\delta_0, \alpha_2, \beta_2$, and γ_2 are the small contributions, the expressions for which are given below. In these expressions A_0 is the isotropic part of the hyperfine constant in units of rad s^{-1} (Wilson and Kivelson 1966a).

$$\begin{aligned}
\alpha_2 &= (2/3^{0.5})\{(B\Delta g/g_0)^2 U/15 + b^2 I(I+1)U\{7 - 5f(A_0/\omega)\}/40 \\
&\quad - (B\Delta g/g_0)b(1+U)I(I+1)(A_0/\omega)/30\}\{\omega/B\} \\
\beta_2 &= (2/3^{0.5})\{-(B\Delta g/g_0)^2(8 + 6U + 6Uf)/45(A_0/\omega) \\
&\quad - b^2\{2I(I+1)(1+U+7Uf) + (3+2U)\}\{A_0/\omega\}/40 \\
&\quad + (B\Delta g/g_0)b\,U/5\}\{\omega/B\} \\
\gamma_2 &= (2/3^{0.5})\{-b^2\{U/40 - (Uf/8)(A_0/\omega)\} \\
&\quad - (B\Delta g/g_0)b\{7 + 5U + 12Uf\}/30\}\{\omega/B\} \\
\delta_0 &= (2/3^{0.5})\{(b^2/20)(A_0/\omega)(1+U+Uf)\}\{\omega/B\} \\
U &= 1/(1+\omega^2\tau^2); \quad f = \omega^2\tau^2.
\end{aligned} \tag{5}$$

α_3 is included to take care of additional small terms which have the same temperature dependence as τ. We also have the spin rotational contribution to linewidths (Atkins and Kivelson 1966):

$$C = 3^{-0.5}\{(2/27)(B/\omega)\}\{g\,\Delta g_0^2 + 2\Delta g^2\}. \tag{6}$$

In the above expressions, B and ω are noted during the course of experiments and the values of g_0 and A_0 are determined from the spectra. To determine the other parameters, $\Delta g, b, \tau_j^*$ corresponding to the minimum linewidth of "m_j" hyperfine transition, α_3 and α_{4j} we require at least five independent equations. Equation (2) for minimum linewidths of three hyperfine transitions, use of the Hubbard relation for the situation corresponding to τ_j^* and the experimentally determined β_0/γ_0 provide the required number of equations for the determination of above mentioned

CC-0. In Public Domain. Gurukul Kangri Collection, Haridwar

Digitized by Arya Samaj Foundation Chennai and eGangotri

parameters. Equations generated by additional measurements help in the determinations of the parameters to a better accuracy. The procedure followed by us is given below.

If W_j^* and W_i^* are the minimum linewidths associated with two hyperfine transitions of quantum numbers m_j and m_i, we can define,

$$X_{ji} = [(W_j^* - \alpha_{4j})/(W_i^* - \alpha_{4i})]^2. \tag{7}$$

The additional subscripts j or i are added in α_4 above and in $\alpha_2, \beta_2, \gamma_2$ and δ_0 below to indicate their values at the temperature at which W_j or W_i^* are observed (since they are dependent on τ). In (7) spin rotational interaction C does not occur. This enables us to write the following simultaneous equations, since the small term involving δ_{0j} could be neglected compared to other terms.

$$Y = -(\alpha_1 + \alpha_3)/\gamma_1 - S\beta_1/\gamma_1 \tag{8}$$

where,

$$S = f_1(m_j - X_{ji} m_i f_2)/(1 - X_{ji} f_0)$$

$$Y = f_3(m_j^2 - X_{ji} m_i^2 f_4)/(1 - X_{ji} f_0). \tag{9}$$

$$f_0 = \{1 + \alpha_{2i}/(\alpha_1 + \alpha_3)\}/\{1 + \alpha_{2j}/(\alpha_1 + \alpha_3)\}$$

$$f_1 = \{1 + \beta_{2j}/\beta_1\}/\{(1 + \alpha_{2j})/(\alpha_1 + \alpha_3)\}$$

$$f_2 = (1 + \beta_{2i}/\beta_1)/(1 + \beta_{2j}/\beta_1)$$

$$f_3 = \{1 + \gamma_{2j}/\gamma_1\}/\{(1 + \alpha_{2j})/(\alpha_1 + \alpha_3)\}$$

$$f_4 = (1 + \gamma_{2i}/\gamma_1)/(1 + \gamma_{2j}/\gamma_1). \tag{10}$$

When g and A anisotropies have negligible temperature dependence, (8) represents an equation for a straight line the slope of which gives β_1/γ_1 and the intercept gives $(\alpha_1 + \alpha_3)/\gamma_1$. If it is possible to make minimum linewidth measurements on N hyperfine transitions, we can write $N(N-1)/2$ equations of the type shown in (8). A least square anaysis of the data could be carried out to determine the best fit values for the slope and intercept. However, for this purpose we need estimates of small terms such as α_{2j}, β_{2j} etc. In the first approximation these small terms could be neglected and approximate estimates β_1/γ_1 and $(\alpha_1 + \alpha_3)/\gamma_1$ determined. The following equation enables us to write b in terms of Δg in (4).

$$(B/g_0)(\Delta g/b) = (15/32)(\beta_1/\gamma_1). \tag{11}$$

A quadratic equation in Δg is obtained from the minimum linewidth of a hyperfine transition from the following expression (written using (2) (4) and (11)).

$$4C\alpha_1(1 + \alpha_2/\alpha_1 + \alpha_3/\alpha_1)(1 + m_j\beta_0/\alpha_0 + m_j^2\gamma_0/\alpha_0) = [W_j^* - \alpha_{4j}]^2. \tag{12}$$

Solving the equation neglecting the small terms and using (11) first estimates of Δg and b could be determined. The corresponding estimate of $\omega\tau_j^*$ can be obtained from the following expression

$$\omega\tau_j^* = 2CB/(W_j^* - \alpha_{4j}). \tag{13}$$

The above equation could be readily obtained using (1) and (2). Estimate of α_3 could

CC-0. In Public Domain. Gurukul Kangri Collection, Haridwar

Digitized by Arya Samaj Foundation Chennai and eGangotri

be obtained from $(\alpha_1 + \alpha_3)/\gamma_1$ using (4) for α_1 and γ_1. Other small terms which had been neglected in the first approximation are determined using (13) and (5). By iteration the estimates are refined. α_{4j} could be determined by varying it until the calculated β_0/γ_0 at different temperatures are in good agreement with the values directly determined from the widths. Since the magnitude of δ_0 is small compared to other terms, β_0/γ_0 at a particular temperature could be obtained from the widths of hyperfine transitions, by a least square analysis of the following equations

$$(m_j^2 - m_i^2)/(W_j - W_i) = -(\beta_0/\gamma_0)\cdot((m_j - m_i)/(W_j - W_i)) + 1/\gamma_0. \tag{14}$$

In practice it is more convenient to include the temperature dependent α_3 in α_{4j} itself (in which case all the additional width contributions are in α_{4j}) by writing a suitable expression. We could vary the parameters of such an expression until the above procedure yields $\alpha_3 = 0$ and β_0/γ_0 is in good agreement with the experimentally observed values.

When the observations are restricted to only two hyperfine transitions, we have only one equation of the type (9). Even in this case it is possible to proceed if some criteria could be used to give estimates of α_3 and α_{4j}, since α_1/γ_1 could be expressed in terms of β_1/γ_1. If α_3 is zero or is already included in α_{4j}, (4) and (8) can be used to write the following quadratic equation, whose realistic solution could be used as an estimate of β_1/γ_1 in the above calculations

$$(5/32)(\beta_1/\gamma_1)^2 + S(\beta_1/\gamma_1) + (3/5)\,I(I+1) - Y = 0. \tag{15}$$

4. Results and discussion

4.1 *Reliability test; Cu(ac.ac)$_2$ in toluene*

The usefulness of the above mentioned method was tested using the data on Cu(ac.ac)$_2$ in toluene reported in the literature (Wilson and Kivelson 1966b). Since there is no reason to expect abrupt changes in linewidths with temperature, we have determined the widths from the smooth curve, which has the least square deviation from the experimental points given in figure 10 of paper by Wilson and Kivelson (1966b). The minimum linewidths associated with the four hyperfine transitions and the experimental β_0/γ_0 at one of the minima (which has the least experimental error) are given in table 1. The values of g_0, A_0, and B used in the calculations are given in the footnote of table 1. Use of $\alpha_{4j} = 0$ gave $\alpha_3 \approx 0$ and β_0/α_0 estimate close to the experimental value. Thus, in this case, there appears to be no additional width contributions. The Y against S plot obtained in this case (see (8)) is given in figure 2 and is a good straightline. (This supports the contention that the variations in the anisotropies are small within the temperature range of interest.) The anisotropies and $\omega\tau_j^*$ determined from "minimum linewidths" are given in table 2.

The value of $\omega\tau$ ($= 1{\cdot}12$) corresponding to 300°K was determined by comparing the observed widths at this temperature and the widths calculated for different values of $\omega\tau$ using the parameters given in table 2. A confirmation of the correctness of the parameters could be made by predicting the K-band linewidths at 300 K and comparing with the data reported in the literature (Wilson and Kivelson 1966b). The X-band and K-band frequencies given by Wilson and Kivelson (1966c) were used in predicting the K-band linewidth parameters at 300°K given in table 3. Table 3 also

CC-0. In Public Domain. Gurukul Kangri Collection, Haridwar

Digitized by Arya Samaj Foundation Chennai and eGangotri

Table 1. X-band ESR linewidths.[a]

System	Temperature °K	$m_j =$	Linewidths (in Gauss) 3/2	1/2	−1/2	−3/2	$-\beta_0/\gamma_0$ Exptl[b]	Calcd[c]
$Cu(ac.ac)_2$ in toluene	208·0		7·60	—	—	—		
	244·0		—	16·80	—	—		
	261·0		—	—	24·90	—		
	275·0		16·50	20·60	26·20	33·10	7·82 ±0·14	8·20 ±0·41
$Cu(ac.ac)_2$ in $CHCl_3$	229·0		10·30					
	256·0		12·00	18·95	28·00	39·40	8·26 ±0·12	7·89 ±0·24
	271·5		14·30	19·90	26·85	35·80	8·66 ±0·45	8·78 ±0·26
	289·5		17·70	22·50	27·70	34·60	10·08 ±1·80	9·79 ±0·30
$Cu(Sal)_2$ in $CHCl_3$	245·0		12·40	—	—	—		
	275·0		14·1	21·00	30·70	41·40	8·70 ±1·00	9·99 ±0·31
	300·0		—	—	28·80	—		
	315·0		—	—	—	36·40		

[a]Minimum linewidths are underlined in the table.
[b]Determined from the linewidths observed at that temperature.
[c]Calculated from the minimum linewidths of the four hyperfine transitions, $g_0 = 2{\cdot}123, 2{\cdot}12$ $A_0 = -76{\cdot}4$ G, $-57{\cdot}0$ G for the two complexes and $B = 3117{\cdot}0$ G.

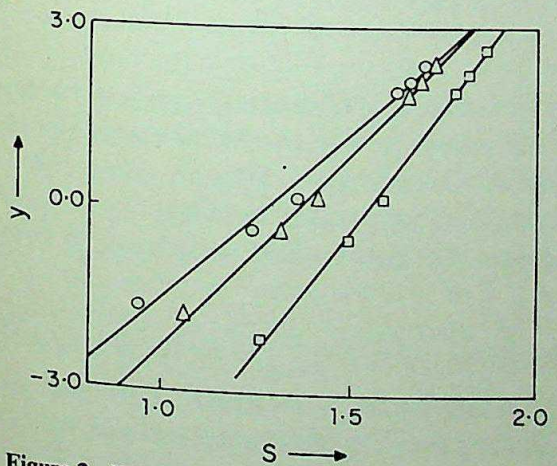

Figure 2. Y against S plot (see expressions (7)–(9) for Y and S with linewidths expressed in gauss) obtained in the case of $Cu(ac.ac)_2$ in toluene, ∘, $Cu(ac.ac)_2$ in $CHCl_3$, Δ, and $Cu(Sal)_2$ in $CHCl_3$, □.

gives the K-band linewidth parameters obtained by using Δg and b slightly different from those given in table 2. Three comments about table 3 are relevant. (i) The agreement between the experimental and calculated linewidth parameters is better in the present work, (where the anisotropies given in table 2 are used). (The errors in the estimation of γ from experimental widths are large, especially in the K-band, since they are determined by subtracting one large number from another large number of similar magnitude.) (ii) The spin rotational contribution estimated in this work is

CC-0. In Public Domain. Gurukul Kangri Collection, Haridwar

Digitized by Arya Samaj Foundation Chennai and eGangotri

Table 2. ESR anisotropy, $\omega\tau_j^*$ and parameters associated with α_{4j} in eq. [16], determined from the "minimum ESR linewidths" at *X*-band.

System	Δg	$-b$ (G)	α_{4j}^0 (G)	ΔE (kcal M^{-1})	$\omega\tau_j$ $m_j=3/2$	1/2	−1/2	−3/2
$Cu(ac.ac)_2$ in toluene	0·183 ±0·002	104·2 ± 1·3	0·0	0·0	6·88	3·17	2·12	1·60
$Cu(ac.ac)_2$ in $CHCl_3$	0·198 ±0·001	96·5 ± 0·4	10.0	1·67	6·47	3·13	2·15	1·65
$Cu(Sal)_2$ in liquid $CHCl_3$	0·222 ±0·001	86·6 ± 0·3	11·2	1·67	5·41	2·96	2·12	1·66
$Cu(Sal)_2$ in frozen $CHCl_3$	0·206	92·9	—	—	—	—	—	—

Table 3. K-band linewidth parameters[a] for $Cu(ac.ac)_2$ in toluene at 300°K.

Parameter	Experimental[b]	Predicted[c]	Predicted[d]
$\beta_0\cdot\tau$	−8·16	−8·26	−8·13
$\gamma_0\cdot\tau$	0·39	0·47	0·43
$C/\tau+\alpha_0\cdot\tau$	45·83	44·93	45·73
C/τ		23·58	23·85

[a]Calculated using $\omega\tau=2{\cdot}943$ at $B=8193{\cdot}0$ G corresponding to $\omega\tau=1{\cdot}12$ at $B=3117{\cdot}0$ G. $g_0=2{\cdot}123$, $A_0=-76{\cdot}4$ G.
[b]From Wilson and Kivelson (1966b)
[c]Calculated using the anisotropies given in table 2.
[d]Calculated using $\Delta g=0{\cdot}186$ and $b=-100{\cdot}0$ G.

substantially higher than that reported earlier (Wilson and Kivelson 1966b). (iii) There appears to be no magnetic field dependent residual linewidth (speculated by Wilson and Kivelson (1966b)) in the case of $Cu(ac.ac)_2$ in toluene, when the anisotropies given in table 2 are used. The excellent agreement between the experimental and calculated *K*-band linewidth suggests that the method used by us is reliable.

4.2 *Additional width contributions in the ESR spectra of $Cu(ac.ac)_2$ in $CHCl_3$*

The linewidth data for $Cu(ac.ac)_2$ in $CHCl_3$ were obtained from figure 5 of paper by Wilson and Kivelson (1966b) following the procedure outlined above. The minimum linewidths and β_0/γ_0 at three of these minima are given in table 1. The *Y* against *S* plot in this case is also a good straight line and is given in figure 2. The anisotropies and $\omega\tau_j^*$ determined by the analysis of the experimental data, by varying the parameters of α_{4j} until α_3 estimated was close to zero and β_0/γ_0 were in close agreement with the observed values (as suggested in the procedure above), are given in table 2. This was possible when the temperature (T_j) dependence of α_{4j} was expressed as,

$$\alpha_{4j}=\alpha_{4j}^0\{\exp(\Delta E/RT_j)/T_j\} \tag{16}$$

with $\alpha_{4j}^0=10{\cdot}0$ G and $\Delta E=1{\cdot}67$ k cal M^{-1}. It was also possible to get α_3 close to zero

CC-0. In Public Domain. Gurukul Kangri Collection, Haridwar

Digitized by Arya Samaj Foundation Chennai and eGangotri

by choosing $\alpha_{4j} = 2{\cdot}78$ G and independent of temperature. However, $-\beta_0/\gamma_0$ calculated under this condition ($= 6{\cdot}26$, $6{\cdot}80$, $7{\cdot}55$, $8{\cdot}42$) did not agree with those determined from experimental linewidths at the temperatures of minimum linewidths (table 1).

Two comments are relevant when comparing our results with those reported in the literature. (i) The anisotropies given in table 2 are slightly different from the values assumed by Wilson and Kivelson (1966b). Calculations show that even when departures from axial symmetry to the extent observed in single crystal studies (Maki and McGarvey 1958) are included with the help of relevant expressions (2), other parameters required to account for the observed data are not significantly different from those given in table 2. (ii) Wilson and Kivelson (1966b) have not considered the possibility of additional linewidth contributions while analysing the data. Our analysis has suggested a temperature dependent additional linewidth contributions in $CHCl_3$. The following arguments could be used in identifying the source of α_{4j} in this case.

(i) The additional linewidth contribution observed in the ESR spectra of $Cu(ac{\cdot}ac)_2$ in $CHCl_3$ was absent in the data obtained with toluene as the solvent. Therefore, α_{4j} in this case must be associated with the interaction of $CHCl_3$ with the Cu(II) complex. (ii) The temperature dependence of α_{4j} is similar to that of correlation times associated with diffusion controlled rate processes (which varies as viscosity/temperature). Such a process could be the diffusion controlled coordination and dissociation dynamics involving $CHCl_3$ and $Cu(ac.ac)_2$. (iiia) The modulation of the **g** and **A** tensors by the coordination and dissociation equilibrium could be a source of α_{4j} if the concentrations of solvent coordinated and uncoordinated $Cu(ac.ac)_2$ are comparable. Such a process would also make additional contributions to the parameters β_0 and γ_0. However, since the concentration of solvent molecules is large in liquid solutions, the situation (iiia), appears unrealistic. (iiib) Unresolved hyperfine structures from the coordinating $CHCl_3$ could also be a source of α_{4j}. The diffusion controlled exchange of coordinating $CHCl_3$ will be fast compared to the nuclear spin relaxation rate associated with the nuclei causing the unresolved hyperfine structures. Furthermore, during the exchange of coordinating solvent molecule the nuclear spin states seen by the unpaired electron are not conserved. Such a situation is similar to the "chemical exchange" seen in the case of free radicals in solutions (Atherton 1973), and would result in the collapse of the unresolved hyperfine structures progressively as the correlation time associated with the exchange is decreased. Therefore, such a process would make α_{4j} decrease as the temperature is increased, which is consistent with our observations. Furthermore, it should be possible to increase the magnitude of α_{4j} substantially by substituting Cl with Br (by changing the solvent from $CHCl_3$ to $CHBr_3$) if the halogens are responsible for the unresolved hyperfine structures or decrease the magnitude of α_{4j} by changing the solvent from $CHCl_3$ to $CDCl_3$ if the unresolved structures are due to ^1H of the solvent (see Atkins and Symons (1967) for the relative magnitudes of hyperfine constants associated with different nuclei). Changing the solvent to $CHBr_3$ did not change α_{4j} significantly. However, a significant reduction in the width of $m_j = 3/2$ line could be seen on changing the solvent to $CDCl_3$ in the 227°K spectra (figure 3). The magnitude of the change was also consistent with the expected reduction in α_{4j}. (A comparison of the relative heights of $m_j = 1/2$ and $3/2$ transitions were made to ensure that the temperatures at which the two spectra were recorded were close.) The observed decrease is only $\sim 10\%$ of the total width even at the temperature of minimum linewidth. The temperature dependence of α_{4j} is such that at room temperature the difference in widths on deuterating the solvent is still smaller.

CC-0. In Public Domain. Gurukul Kangri Collection, Haridwar

Digitized by Arya Samaj Foundation Chennai and eGangotri

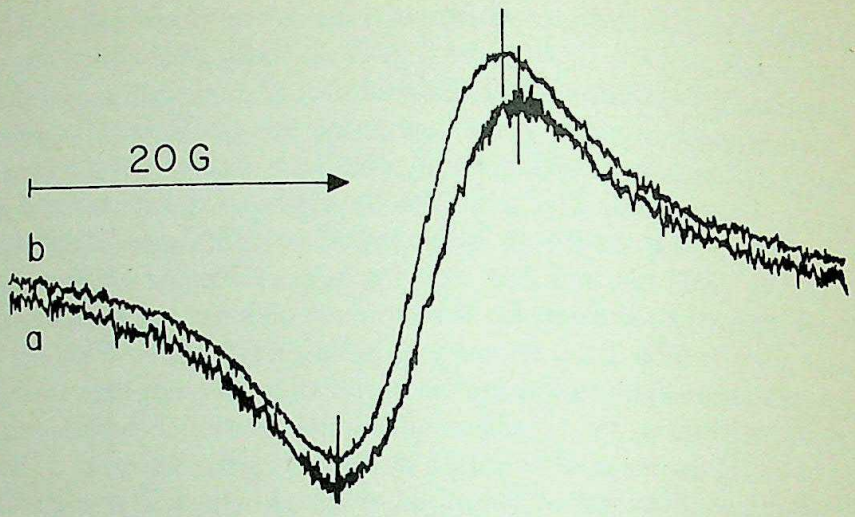

Figure 3. The $m_j = 3/2$ lines in the ESR spectrum of $Cu(ac.ac)_2$ (**a**) in $CHCl_3$ and (**b**) in $CDCl_3$ at 227°K showing the reduction in linewdiths on deuterating the solvent. The concentration of the Cu(II) complex $\sim 5 \times 10^{-4}$ M.

Significant differences in widths on deuterating the solvents had not been observed in the case of vanadyl complexes (Wilson and Kivelson 1966c). These three factors might have influenced Wilson and Kivelson (1966b), who do not appear to have done experiments on $Cu(ac.ac)_2$ in $CDCl_3$.

4.3 *Additional width contributions in the ESR spectra of $Cu(Sal)_2$ in $CHCl_3$*

In view of the results mentioned above, it is possible to suggest that even in the case of other complexes where four oxygens coordinate to the Cu(II), unresolved hyperfine structures from the coordinating solvent $CHCl_3$ should make contributions of similar magnitude to ESR linewidths. Such a suggestion has been examined from a study of $Cu(Sal)_2$ in $CHCl_3$ and $CDCl_3$. The ESR spectra from solutions of $Cu(Sal)_2$ are more complex than those from $Cu(ac.ac)_2$: they reveal nearly overlapping spectra (figure 4) from two possible isomers (figure 1) and unresolved hyperfine structures from a proton on each of the "Sal" ligand make an additional contribution to linewidths. Therefore, a study of this system could be considered to be a test of the usefulness of the new method in a more complex situation. Furthermore, we are not aware of a detailed report on the ESR studies on this system, although unpublished ESR anisotropy data had been used by us (Ugrankar and Prabhananda 1988).

X-band ESR spectra from $Cu(Sal)_2$ in $CHCl_3$, at 301°K and 251°K and in $CDCl_3$ at 251°K are shown in figures 4a–c. The spectra could be interpreted as coming from two Cu(II) species. The relative concentrations of the two species did not change on dilution. But it was temperature dependent (figure 5). Eventhough, the isotropic A_0 differed in the case of two complexes (which could come from differences in the 4*s*-mixing (Kuska 1970)), the ESR linewidths were nearly equal. Therefore, the ESR anisotropies and hence the coordination at the metal are likely to be similar in the two complexes. These observations are consistent with an assignment of the spectra to the two possible isomers of $Cu(Sal)_2$ (figure 1). The two isomers IS_1 and IS_2 are in equilibrium with each other

$$IS_1 \overset{K}{\rightleftharpoons} IS_2. \tag{17}$$

CC-0. In Public Domain. Gurukul Kangri Collection, Haridwar

Digitized by Arya Samaj Foundation Chennai and eGangotri

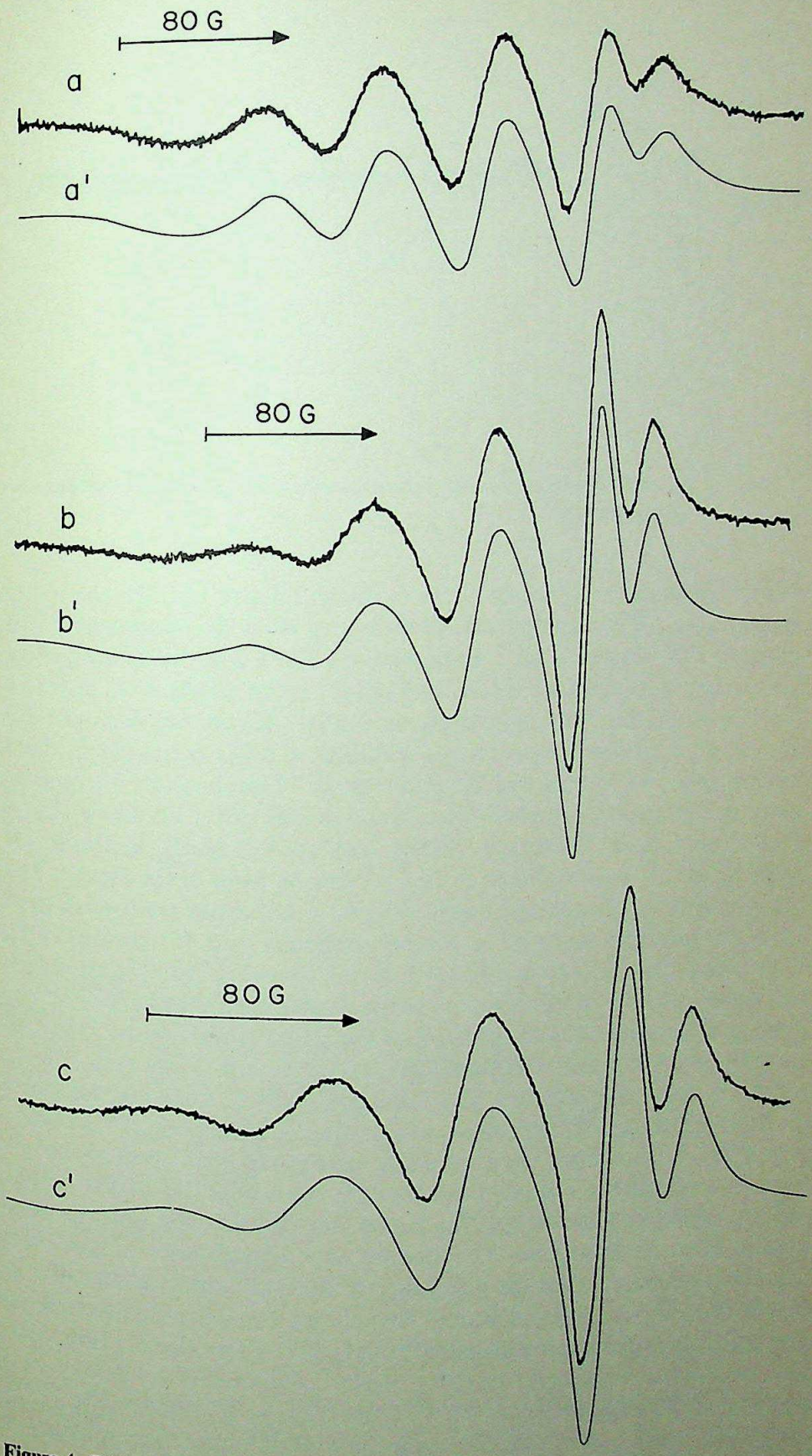

Figure 4. ESR spectrum of $Cu(Sal)_2$ in $CHCl_3$ at (**a**) 301°K, (**b**) 251°K and in $CDCl_3$ at (**c**) 251°K. The corresponding computer simulated spectra (*a'*),(*b'*) and (*c'*) used in the determination of widths.

CC-0. In Public Domain. Gurukul Kangri Collection, Haridwar

Digitized by Arya Samaj Foundation Chennai and eGangotri

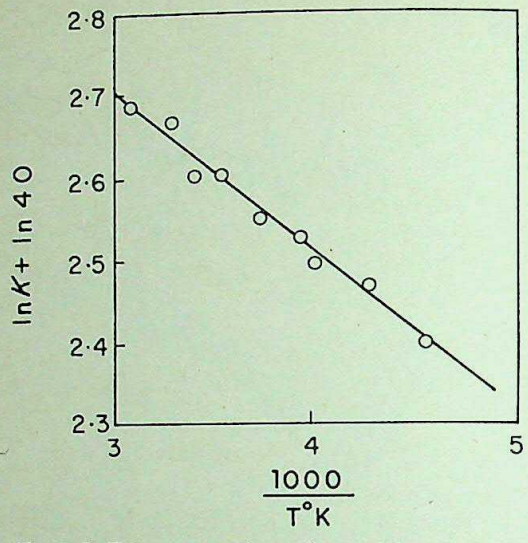

Figure 5. Temperature dependence of the constant K associated with the equilibrium between the two isomers.

It is not possible to say which of the isomers of figure 1 is IS_1, the species at higher concentration. The enthalpy change estimated from the temperature dependence of K (figure 5) is $\sim 0{\cdot}4$ k cal M^{-1}. Extrapolating figure 5 to the freezing temperature, we can expect the prominent species of $Cu(Sal)_2$ to be nearly 85% in frozen solutions. The frozen solution ESR spectrum from $Cu(Sal)_2$ (figure 6a), obtained just below the freezing point of the solvent reveals splittings $\sim 5{\cdot}5$ G especially in the 45° and 90° spectral regions (Neiman and Kivelson 1961). There could be three sources of such splittings: (i) A Cu(II) complex with a ligand similar to Sal, bis-salicylaldehydeaminato Cu(II) (Maki and McGarvey 1958b), had shown nearly isotropic ^1H hyperfine splittings of similar magnitude from a proton on each of the ligand. Therefore, it is reasonable to assign splittings seen in figure 6 to similar proton on the ligands Sal. Since the splittings observed in the perpendicular and 45° regions of the spectrum have similar values, we could say that this hyperfine splitting is nearly isotropic. (ii) Slightly different conformations of the complex stabilized in the frozen solutions, causing a discontinuous distribution of the **g** and **A** anisotropy could also manifest themselves as apparent splittings. (iii) Hyperfine structures from the coordinating solvent is another possibility. The third possibility is unlikely since the magnitudes of these splittings did not show a decrease on changing the solvent to $CDCl_3$. Figure 6b was simulated using the anisotropy parameters given in table 2 and ligand hyperfine splittings ($= 5{\cdot}5$ G) from the two equivalent ^1H of Sal without invoking any m_j dependent linewidths. The agreement between the observed and simulated spectra is reasonably good. The absence of m_j dependence of linewidths in frozen solutions spectra rule out the possibility of "strains" which could cause a continuous distribution of **g** and **A** (Froncisz and Hyde 1980). The differences between the observed and calculated spectra are attributable to at least two species of similar concentrations and with small differences in the **g** tensor components ($\sim 0{\cdot}006$). In view of the peak-to-peak derivative linewidth 4·5 G used in the simultations to get the observed resolution, we can say that the magnitude of ^{1}H hyperfine splitting if any, from coordinating $CHCl_3$ should be less than this magnitude. The presence of contribution to the linewidths from solvent proton hyperfine splittings could be inferred from the

CC-0. In Public Domain. Gurukul Kangri Collection, Haridwar

Digitized by Arya Samaj Foundation Chennai and eGangotri

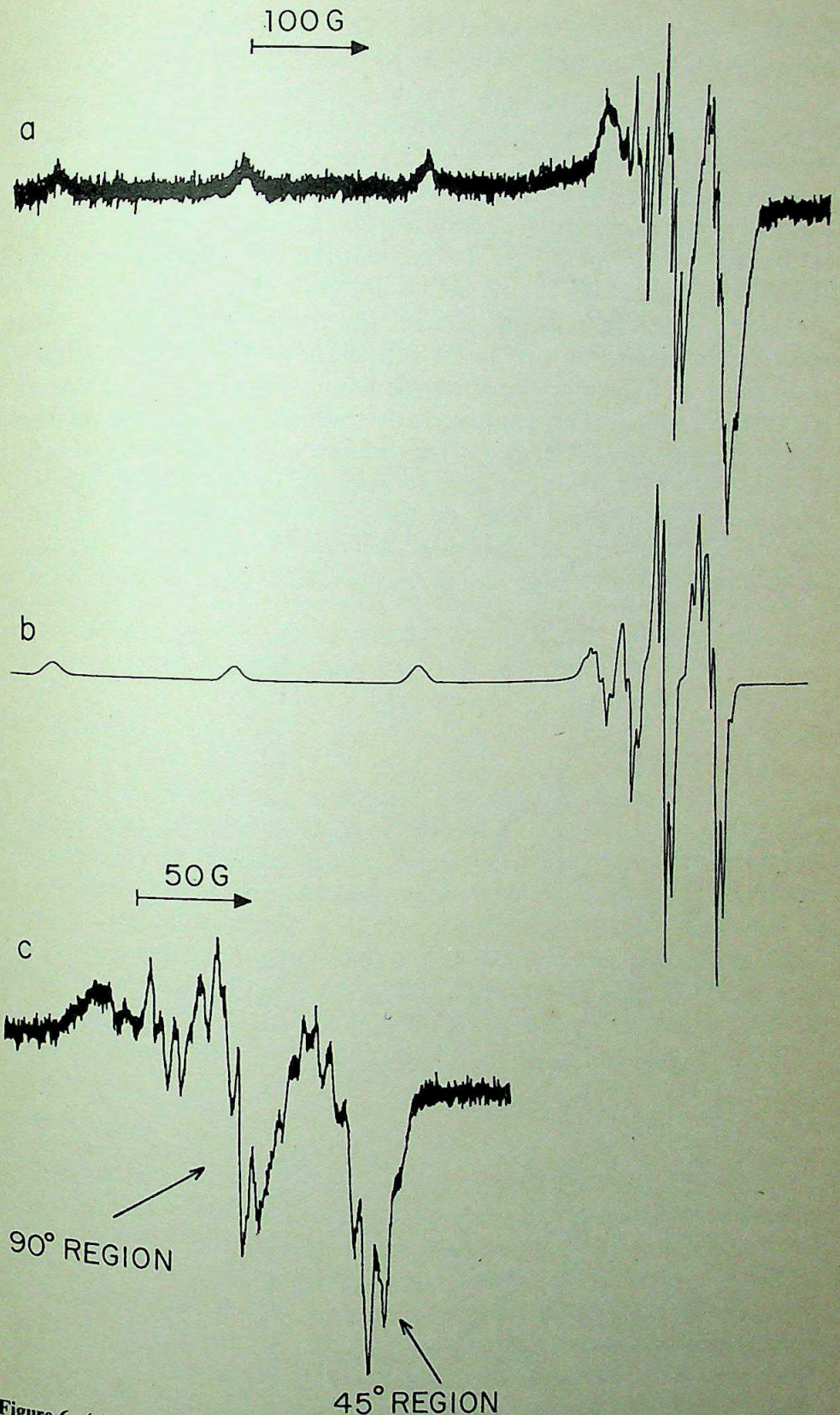

Figure 6. **(a)** ESR spectrum of $Cu(Sal)_2$ in frozen $CHCl_3$ at 153°K. **(b)** Simulated spectrum at 9·25 GHz using $g_x = g_y = 2{\cdot}0042$, $g_z = 2{\cdot}248$; $A_x = A_y = -27 \times 10^{-4}\,cm^{-1}$, $A_z = -165 \times 10^{-4}\,cm^{-1}$ for the species with 85% concentration and $A_x = A_y = -38{\cdot}8 \times 10^{-4}\,cm^{-1}$, $A_z = -171{\cdot}8 \times 10^{-4}\,cm^{-1}$ for the species with 15% concentrations. **(c)** the high field region showing the hyperfine splitting from the ^1H of "Sal" ligands.

CC-0. In Public Domain. Gurukul Kangri Collection, Haridwar

Digitized by Arya Samaj Foundation Chennai and eGangotri

frozen solution spectrum obtained with $CDCl_3$ as solvent. This spectrum was similar to figure 6a, but had smaller linewidths (~ 2.2 G), and enabled the resolution of some of the splittings attributable to the presence of different species mentioned in (ii) above.

The 'minimum' linewidths corresponding to the four ^{63}Cu hyperfine transitions of $Cu(Sal)_2$ were determined by comparing the observed spectra and those simulated after including the above mentioned ^1H splittings. (The simulated spectra corresponding to the experimental spectra are also given in figure 4.) Thus the minimum linewidths given in table 1 do not contain the contributions from the unresolved hyperfine splittings from the ^1H on Sai. Figure 2 gives the Y against S plot (see (8)) obtained with the help of these widths. The observed straight line behaviour again supports our contention that in the temperature range of interest the temperature dependence of anisotropy parameters is not significant as far as linewidth data are concerned. The anisotropy parameters determined using the method described above and the parameters associated with the temperature dependent α_{4j} (which gave $\alpha_3 = 0$), are given in table 2. The agreement between the frozen solution and liquid solution anisotropy data is good. Since, we have similar coordination situations in both $Cu(ac.ac)_2$ and $Cu(Sal)_2$ it is not surprising that the α^0_{4j} and ΔE estimates for $CHCl_3$ in both the complexes have similar magnitudes. Figure 7 gives the experimentally

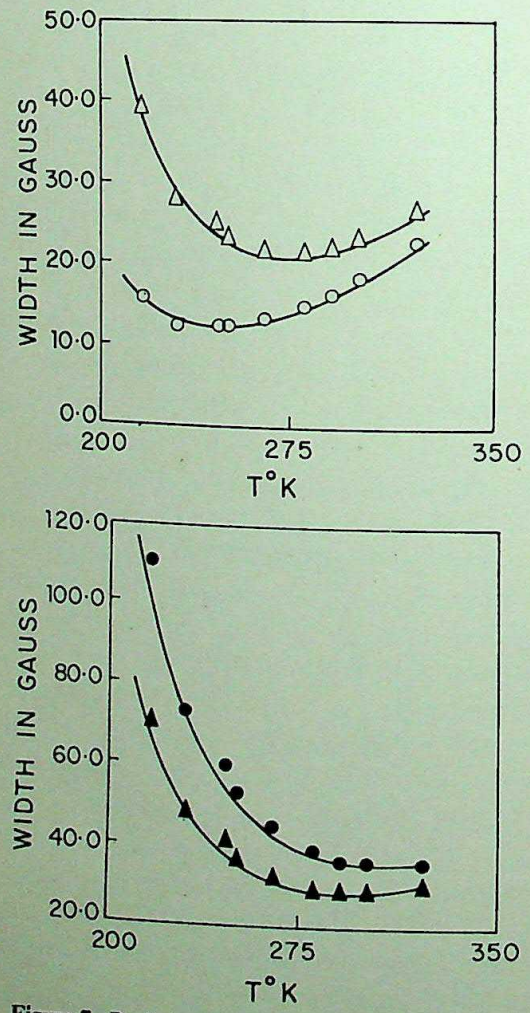

Figure 7. Peak-to-peak derivative ESR widths of the hyperfine lines ($m_j = 3/2$, ○, $1/2$, △, $-1/2$, ▲, $-3/2$, ●.) of 8×10^{-4} M $Cu(Sal)_2$ in $CHCl_3$ at X-band (9·25 GHz). Solid lines calculated from the ESR anisotropy parameters (table 2) determined with the help of minimum linewidths.

CC-0. In Public Domain. Gurukul Kangri Collection, Haridwar

Digitized by Arya Samaj Foundation Chennai and eGangotri

determined linewidths and those calculated using the parameters given in table 2. (Inclusion of temperature dependence of A_0 and g_0 alter the calculated widths to the extent of experimental errors.)

A visual examination of the spectra of $Cu(Sal)_2$ at 251°K (Figure 4) shows that the linewidth of the $m_j = 3/2$ component is smaller in $CDCl_3$ when compared to that in $CHCl_3$ (as indicated by the increased resolution). The magnitude of the reduction in width by ~ 1.4 G is consistent with the assignment of the additional linewidths α_{4j} to the unresolved hyperfine structure from the ^1H of the coordinating $CHCl_3$, when the differences in the magnetic moments and spins of ^1H and ^2D, as well as the dynamic nature of the solvent coordination mentioned above are noted. This observation is also similar to that made in the case of $Cu(ac.ac)_2$ in these solvents.

4.4 *Dynamics of solvent coordination*

It is also possible to give an estimate of the magnitude of the rate constant associated with the coordinating solvent exchange from the estimates of additional linewidth contributions. A fast exchange of a coordinating $CHCl_3$ would cause fluctuations in the magnetic environment of the unpaired electron and a fluctuation in its precession frequency between ω_1 and ω_2 (corresponding to the two spin states of the solvent ^1H) with a correlation time τ_c. For fast exchange, $(\omega_1 - \omega_2)\tau_c/2 < 1$. The additional linewidth contribution ΔW could be related to $(\omega_1 - \omega_2)$ and τ_c (Pake 1962).

$$\Delta W \approx 0{\cdot}5\,\tau_c(\omega_1 - \omega_2)^2/3^{0{\cdot}5}. \tag{18}$$

As the temperature is increased τ_c decreases and ΔW decreases. The observed temperature dependence of our estimates of ΔW shows such a behavior. The rate constant k associated with the fast exchange is $\sim 1/\tau_c$. The ^1H solvent hyperfine splitting estimated from the widths of frozen solution spectrum is ~ 4 G. Therefore, the observed additional linewidth at ~ 300°K ($= 0.6$ G) can be used to say that at this temperature the rate constant associated with coordinating solvent exchange (in square planar Cu(II) complexes with ligands coordinating through oxygens) is $\sim 10^{10}\,s^{-1}$. The magnitude of k and its temperature dependence are similar to those expected for diffusion controlled rate processes.

4.5 *Out of plane bonding*

Unresolved hyperfine structures from the coordinating solvent molecules suggest a spin transfer in a direction perpendicular to the plane of the complex. Such spin transfers could come from the covalent bonding involving the solvent orbitals and the metal d_{yz} and d_{xz} orbitals and a configuration interaction mechanism (Kivelson and Lee 1964; Krishnamoorthy and Prabhananda 1978), which induces a negative spin density in these orbitals. Another mechanism which could contribute to the spin density on the coordinating solvents is the covalent bonding involving the 4*s* orbital part of the unpaired electron orbital and the solvent orbitals. In this case the spin density on the solvent will be positive in sign. With the help of present results it is not possible to decide between the two mechanisms. Nevertheless, the **g** anisotropy data could tell us about the covalent bonding involving the metal d_{yz} and d_{xz} orbitals. Expressions for **g** show that increased covalent bonding involving these orbitals should result in a decrease in g_x and g_y or an increase in Δg (Kivelson and Neiman 1961).

CC-0. In Public Domain. Gurukul Kangri Collection, Haridwar

Digitized by Arya Samaj Foundation Chennai and eGangotri

The relative magnitudes of Δg determined in toluene and chloroform are consistent with such expectations.

5. Conclusions

In dilute degassed $CHCl_3$ solutions of $(Cu(ac.ac)_2$ and $Cu(Sal)_2$ ESR linewidth is due to (i) modulation of **g** and **A** tensors by the tumbling motion of the complex and (ii) unresolved hyperfine structure associated with solvent-solute interaction. Minimum linewidths are useful in the determination of anisotropic ESR parameters in liquid solutions, which enable us to get an estimate of the first contribution. The agreement between the additional width contributions and the difference in widths obtained in $CHCl_3$ and $CDCl_3$ shows that additional width contributions from other sources such as the modulation of ligand field or unknown mechanisms are negligibly small. Due to the temperature dependent fast exchange of coordinating solvent molecules, the linewidth contribution from unresolved hyperfine structure decreases with increase in temperature.

Acknowledgement

The author thanks Ms. M M Ugrankar for technical assistance in the preparation of samples and in recording the ESR spectra.

References

Atherton N M 1973 *Electron spin resonance* (Chichester: Ellis Horwood) p. 302
Atherton N M and Waldrum D 1972 *J. Chem. Soc. Faraday Trans.* II **68** 413
Atkins P W and Kivelson D 1966 *J. Chem. Phys.* **44** 169
Atkins P W and Symons M C R 1967 *Structure of inorganic radicals* (Amsterdam: Elsevier) p. 21
Baratova Z R, Semenov E V, Solozhenkin P M and Prabhananda B S 1982 *Inorg. Chem.* **21** 57
Campbell R F and Freed J H 1980 *J. Phys. Chem.* **84** 2668
Froncisz W and Hyde J S 1980 *J. Chem. Phys.* **73** 3123
Hubbard P S 1963 *Phys. Rev.* **131** 1155
Hudson A and Luckhurst G R 1969 *Chem. Rev.* **69** 191
Kivelson D and Neiman R 1961 *J. Chem. Phys.* **35** 149
Kivelson D and Lee S K 1964 *J. Chem. Phys.* **41** 1896
Krishnamurthy G and Prabhananda B S 1978 *J. Magn. Reson.* **30** 273
Kuska H A 1970 *J. Am. Chem. Soc.* **97** 2289
Maki A H and McGarvey B R 1958a *J. Chem. Phys.* **29** 31
Maki A H and McGarvey B R 1958b *J. Chem. Phys.* **29** 35
McConnell H M 1956 *J. Chem. Phys.* **25** 709
Neiman R and Kivelson D 1961 *J. Chem. Phys.* **35** 156
Pake G E 1962 *Paramagnetic resonance* (New York: Benjamin) p. 106
Pilbrow J R and Winfield M F 1973 *Mol. Phys.* **25** 1073
Prabhananda B S 1979a *Mol. Phys.* **38** 209
Prabhananda B S 1979b *Indian J. Chem.* **18** 290
Prabhananda B S 1980 *Indian J. Pure Appl. Phys.* **18** 823
Prabhananda B S, Shah S J and Venkataraman B 1972 *Indian J. Pure Appl. Phys.* **10** 365
Symons M C R and Wilkinson J G 1972 *J. Chem. Soc. Faraday Trans. II* **68** 1265
Ugrankar M M and Prabhananda B S 1988 *Proc. Indian Acad. Sci. (Chem. Sci.)* **100** 425
Wilson R and Kivelson D 1966a *J. Chem. Phys.* **44** 154
Wilson R and Kivelson D 1966b *J. Chem. Phys.* **44** 4445
Wilson R and Kivelson D 1966c *J. Chem. Phys.* **44** 4440

CC-0. In Public Domain. Gurukul Kangri Collection, Haridwar

Digitized by Arya Samaj Foundation Chennai and eGangotri

Pramāṇa – J. Phys., Vol. 34, No. 6, June 1990, pp. 507–523. © Printed in India.

A quantitative study of diffracted X-ray intensities from type I natural diamond crystals by high resolution X-ray diffractometry and comparison with nearly perfect silicon single crystals

KRISHAN LAL, S NIRANJANA N GOSWAMI and AJIT RAM VERMA

National Physical Laboratory, Dr K S Krishnan Road, New Delhi 110012, India

MS received 13 October 1989; revised 12 February 1990

Abstract. Results of accurate measurements of peak and integrated intensities of $\bar{2}20$, $\bar{4}40$, $\bar{2}\bar{2}4$, $\bar{1}\bar{1}3$, 111 and 333 reflections of natural diamonds of type I and nearly perfect silicon single crystals are reported. Highly monochromated and collimated MoK_{α_1} exploring beam was used. A quadrupole crystal X-ray diffractometer was employed in $(+,-,+)$ and $(+,-,+,-)$ settings. (111) platelets of diamond and silicon crystals with thicknesses of about 1 mm were selected. High resolution diffraction curves, stationary and traverse topographs were recorded. Diffraction curve half widths of diamond and silicon crystals were in the range: 45–200 arc sec and a few arc sec respectively. The experimental values of integrated intensities ρ for diamond crystals were found to lie between the theoretical values for ideally perfect and ideally imperfect crystals. Experimental values of ρ for silicon were closer to the "perfect crystal" values. This is consistent with the results of diffractometric and topographic evaluation. The peak intensities of all reflections were higher for diamond crystals in comparison to the silicon crystals. The ratio I_C/I_{Si} lies in the range 1·3 (111 reflection) to 10·5 ($\bar{1}\bar{1}3$) and (333) reflections. This is anomalous and cannot be accounted for by considering the degree of perfection, structure factor and difference in absorption coefficient.

Keywords. Natural diamonds; silicon single crystals; high resolution X-ray diffractometry and topography; accurate diffraction peak intensities; accurate integrated X-ray intensities.

PACS Nos 61·10; 61·55; 61·70

1. Introduction

Natural diamonds were among the first few crystals to be extensively investigated by X-ray diffraction techniques (Bragg 1914; Renninger 1935, 1937; Brill *et al* 1939; Ehrenberg *et al* 1928; Brindley 1932, 1933). The early investigations were aimed at quantitative understanding of the observed intensities in terms of a "mosaic" crystal model. Some of the crystals were found to possess reasonably high degree of perfection (Bragg 1921) while others were found to be closer to the mosaic model. Crystals with intermediate degree of perfection were also detected. Some of the investigators used double crystal diffractometers in the $(+,-)$ configuration and obtained very narrow diffraction curves (Bragg 1921). In recent times real structure of diamond has been studied by Lang and his co-workers by using X-ray diffraction topographic method (Lang 1974).

Considerable advances have been made in the techniques and equipments used for high resolution X-ray diffractometric experiments (Bonse and Hart 1965; Hart 1971;

CC-0. In Public Domain. Gurukul Kangri Collection, Haridwar

Digitized by Arya Samaj Foundation Chennai and eGangotri

Pinsker 1978; Patel and Battermann 1963; Lal 1982, 1988). It is possible to achieve highly monochromated and well collimated X-ray beams of appreciable intensities which can be used for precise X-ray diffraction studies (Lal *et al* 1979). High resolution X-ray diffractometric and topographic techniques developed in our group at National Physical Laboratory, have been very successfully used to study imperfections in crystals (Lal *et al* 1979; Lal and Thoma 1983; Lal and Goswami 1987). Here we describe results of a high resolution X-ray diffractometric study on natural diamond crystals and report anomalously higher diffracted intensities from these crystals in comparison to nearly perfect silicon single crystals.

2. Experimental details

2.1 *Specimen*

The diamond specimens were platelet-shaped natural crystals with surface along (111) having areas of a few mm^2. The thicknesses of the crystals were about 1 mm. Infrared and EPR absorption measurements carried out in our laboratory showed that these crystals contain nitrogen and are of type I. Silicon single crystal specimens were (111) discs cut out of a Czochralski grown *n*-type boule of 50 Ω cm resistivity.

2.2 *Experimental set-up*

A quadruple crystal X-ray diffractometer developed in our group has been employed in three-crystal and four-crystal modes in these experiments. Figures 1(a) and (b) show schematic line diagrams of these triple and the quadruple crystal X-ray diffractometers, respectively. Fine focus X-ray source of following specifications was used: Philips sealed tube; 2 kW; molybdenum and source size foreshortened to $0{\cdot}4 \times 0{\cdot}4\ mm^2$. X-ray beam emerging from the source is collimated with the help of a long collimator which is fitted with a fine slit at its end away from the source. The collimated X-ray beam is diffracted from two dislocation free plane (111) silicon single crystal monochromators set in the (+, −) configuration (Bonse–Hart type). With this combination of source, collimator and the monochromators, $K_{\alpha 1}$ and $K_{\alpha 2}$ components of the characteristic K_α doublet are conveniently resolved. The more intense $K_{\alpha 1}$ beam is highly collimated and monochromated and is used as the exploring beam. All the

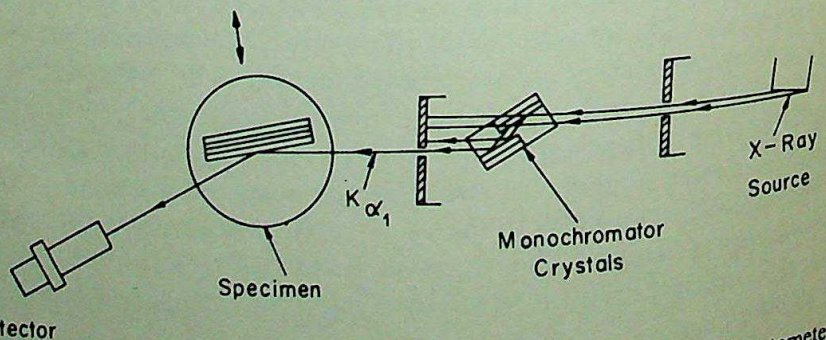

Figure 1 (a). A schematic line diagram of the quadruple crystal X-ray diffractometer when set in (+, −, +) configuration.

CC-0. In Public Domain. Gurukul Kangri Collection, Haridwar

Digitized by Arya Samaj Foundation Chennai and eGangotri

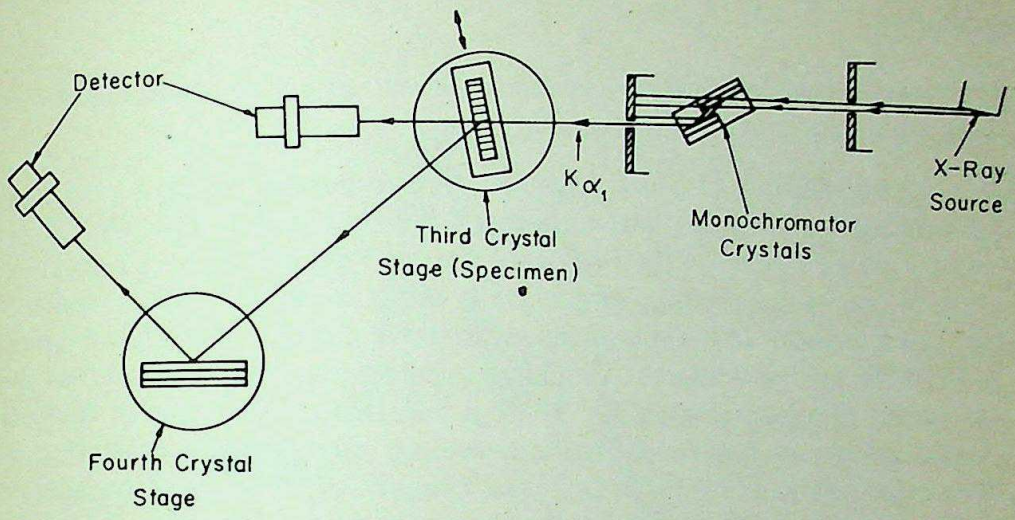

Figure 1 (b). A schematic line diagram of the quadruple crystal X-ray diffractometer when set in (+, −, +, −) configuration.

experiments reported have been performed with the $MoK_{\alpha 1}$ radiation. The specimen crystal formed the third crystal of the diffractometer in the (+, −, +) configuration. Some experiments with the specimen at the fourth crystal position have also been performed in the (+, −, +, −) setting. The width of the exploring beam was 0·2 mm in the plane of diffraction. The height of the irradiated area of the specimen was adjusted according to different requirements. For recording traverse topographs, the height of the beam was increased to bathe the entire specimen. For quantitative diffracted X-ray intensity measurements, the height was adjusted to 1·2 mm. This is much smaller than the size of the specimen.

Specimen is mounted on a special goniometer which is fixed on top of a traversing mechanism. This assembly is mounted on a special turntable, which provides precise rotations around a vertical axis. The special goniometer provides rotations to the specimen around a horizontal axis with minimum rotation of 10 arc sec. Minimum rotations of 0·4 arc sec can be given about the vertical axis with the help of a fine angular movement attachment. Details of the quadruple crystal X-ray diffractometer are reported in Lal (1985). The specimen is aligned for diffraction from any desired set of lattice planes. Diffraction curves are recorded from different regions of the specimen. High resolution traverse topographs are recorded on photographic films by traversing the specimen and the film together across the exploring beam while maintaining the angular orientation of the crystal at the diffraction peak position. It may be mentioned that in this case the diffraction curves are significantly sharper as compared to the Lang technique. Radius of curvature of the specimen is measured from the plots of the orientation of the diffraction vector versus linear position of the specimen.

Diffraction from $(\bar{2}20)$, $(\bar{4}40)$, $(\bar{2}\bar{2}4)$ lattice planes was studied in the symmetrical Laue (transmission) geometry. 111 and 333 reflections were studied in the symmetrical Bragg (reflection) geometry. Measurements were also made with $\bar{1}\bar{1}3$ reflection in asymmetric Laue geometry.

The integrated intensities were determined by the standard method (James 1950). The area of the diffraction curve was obtained from the experimentally measured diffraction curves and the intensity of the exploring beam was accurately measured.

CC-0. In Public Domain. Gurukul Kangri Collection, Haridwar

Digitized by Arya Samaj Foundation Chennai and eGangotri

3. Results

3.1 *Determination of crystalline perfection of the natural diamond crystals and comparison with silicon single crystals*

First of all, natural diamond crystals were examined by high resolution X-ray diffractometry and topography to evaluate their crystalline perfection. These experiments were performed in the (+, −, +) setting. Figure 2 shows a typical diffraction curve of one of the crystals. This curve is rather broad with a half width of 58 arc sec. The half width of the specimens investigated during this study were in the range of 45 to 200 arc sec. These are very large in comparison to the theoretical half widths for perfect diamond crystals for $MoK_{\alpha 1}$ radiation on the basis of the plane wave approximation of dynamical theory calculated for the reflections studied here. The theoretical values are 0·35 to 2 arc sec (Tanner 1976). A small broadening of the diffraction curve is expected due to dispersion as the interplanar spacings of the diamond crystals and those of the silicon monochromators are different. However, the observed difference is too large to be explained on this basis. Diffraction curves from some parts of these crystals show more than one peak due to the presence of low angle boundaries. Figure 3 shows one such diffraction curve. Two well resolved peaks and a shoulder on low glancing angle side are clearly seen.

A typical high resolution traverse topograph of a diamond crystal is shown in Figure 4. The diffracted intensity is not uniformly distributed in this topograph. The strain is quite large and hence individual line defects could not be resolved. These

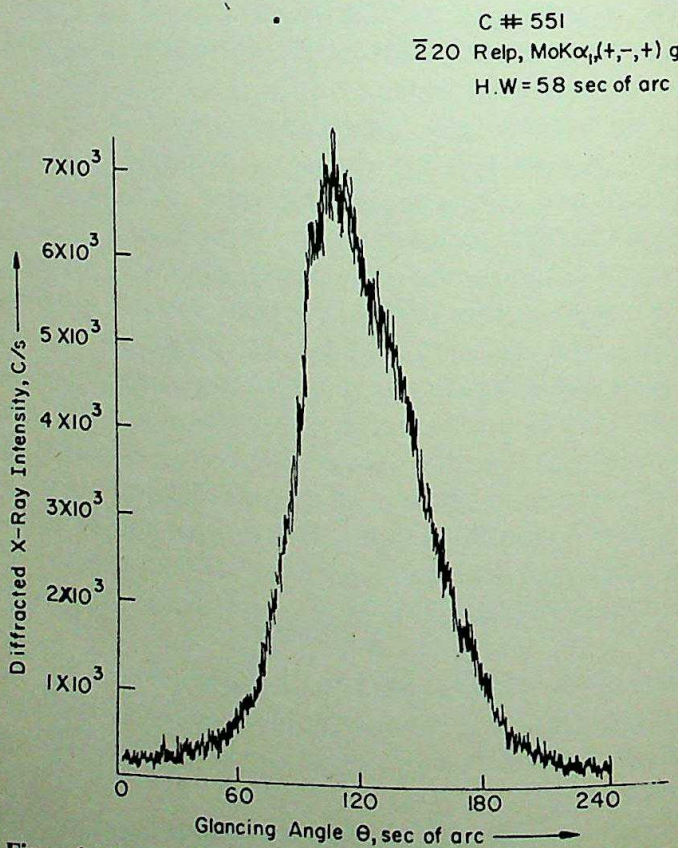

Figure 2. A typical diffraction curve of a natural diamond crystal. $\bar{2}20$ Relp; $MoK_{\alpha 1}$ beam, symmetrical Laue geometry and (+, −, +) settings were used.

CC-0. In Public Domain. Gurukul Kangri Collection, Haridwar

Digitized by Arya Samaj Foundation Chennai and eGangotri

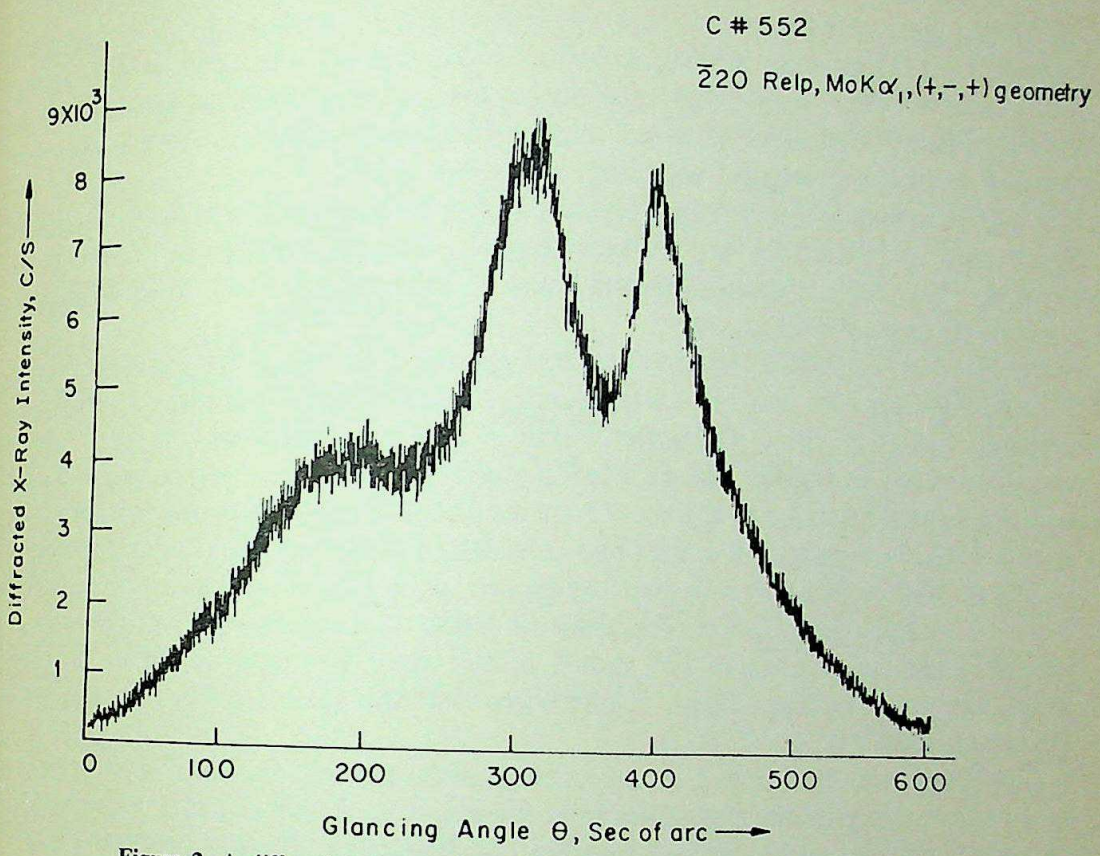

Figure 3. A diffraction curve of a natural diamond specimen with low angle boundaries. Experimental conditions are the same as in figure 2.

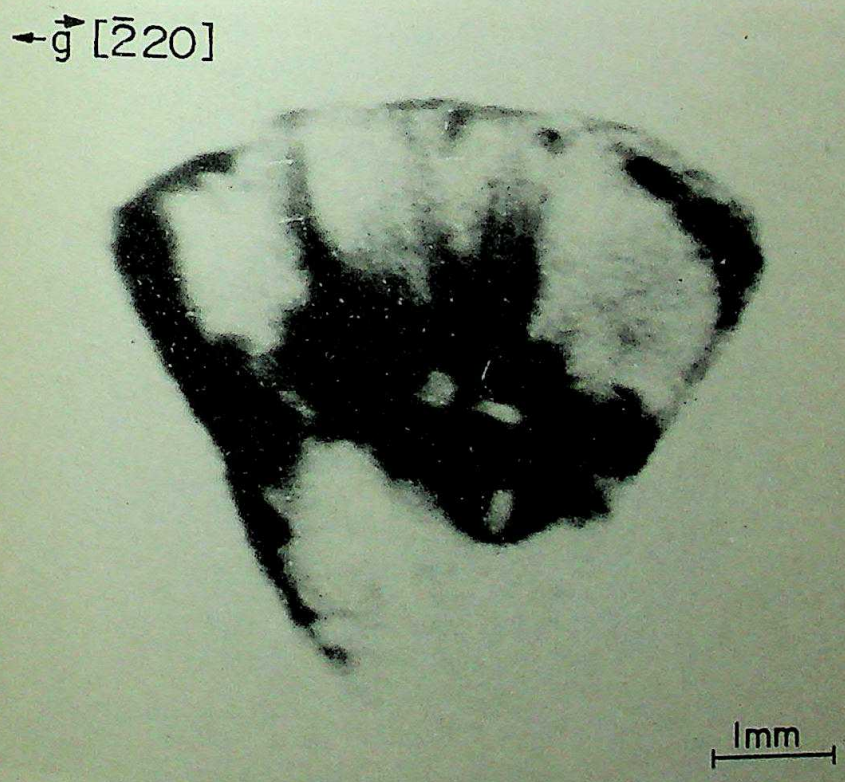

Figure 4. A high resolution traverse topograph of a natural diamond crystal. Experimental details as in figure 2.

CC-0. In Public Domain. Gurukul Kangri Collection, Haridwar

Digitized by Arya Samaj Foundation Chennai and eGangotri

results are understandable as these crystals have grown in nature in an uncontrolled fashion. One can observe a small inclusion in the middle of the photograph. So far, it is considered that transition metal elements like nickel promote growth of diamond crystals. The absorption of X-rays of relatively short wavelength (0·709 Å in this case) shows that this is a material with high atomic number.

Curvature plots of the diamond crystals also show the presence of many subgrains. The radii of curvature for any of these subgrains is small and lies in the range of 3 to 10 m. This result is consistent with those of the diffractometric and topographic characterizations reported above.

For comparison, diffractometric and topographic evaluation of a few nearly perfect silicon single crystals was also carried out under identical experimental conditions. Figure 5 shows a typical diffraction curve of a nearly perfect silicon single crystal recorded with ($\bar{2}20$) lattice planes, $MoK_{\alpha 1}$ radiation and $(+,-,+)$ setting. The half width of this diffraction curve is about 5 arc sec. In the four crystal geometry, diffraction curves from the same set of planes have a width of only 3 arc sec (Lal and Goswami 1987). A high resolution traverse topograph of a silicon specimen is shown in Figure 6. In this topograph, no line defect is visible. Curvature plots for silicon single crystals were also recorded. The radius of curvature was determined to be about 240 m for this specimen. These results show that the silicon specimens are nearly perfect crystals.

The results reported above clearly show that the natural diamond crystals have a low degree of crystalline perfection in comparison to silicon crystals. However, the diamond crystals exhibit very high intensity of diffraction at the peak position. Figure 7 shows diffraction curves of a silicon crystal and a diamond crystal drawn on the same scale and normalized for approximately the same diffracting volume for $\bar{2}20$ reflection. The peak intensity is much higher in the case of diamond in comparison to that of the silicon. The peak intensity ratio is 5:1. This is anomalous. It is well established that with decrease in perfection of atomic arrangement the intensity of diffraction

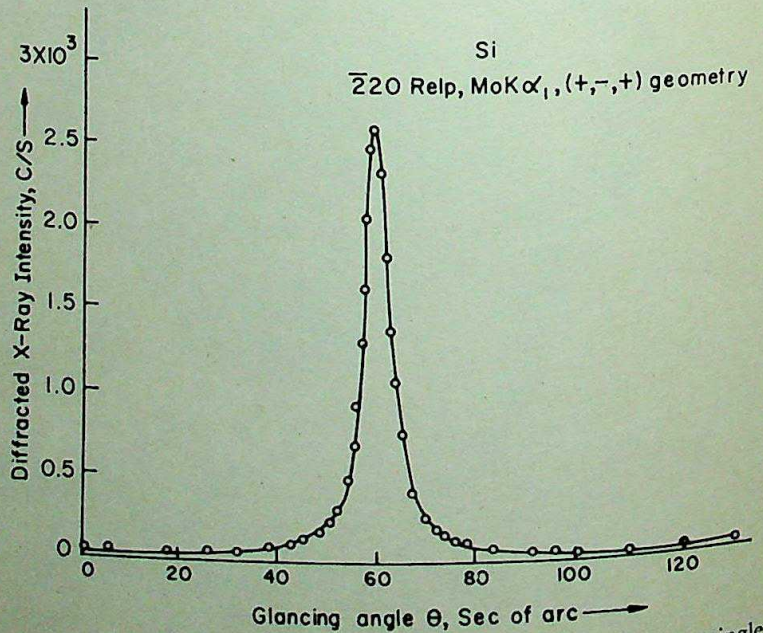

Figure 5. A typical diffraction curve of a dislocation free silicon single crystal. $\bar{2}20$ Relp, $MoK_{\alpha 1}$ and $(+,-,+)$ setting were used.

CC-0. In Public Domain. Gurukul Kangri Collection, Haridwar

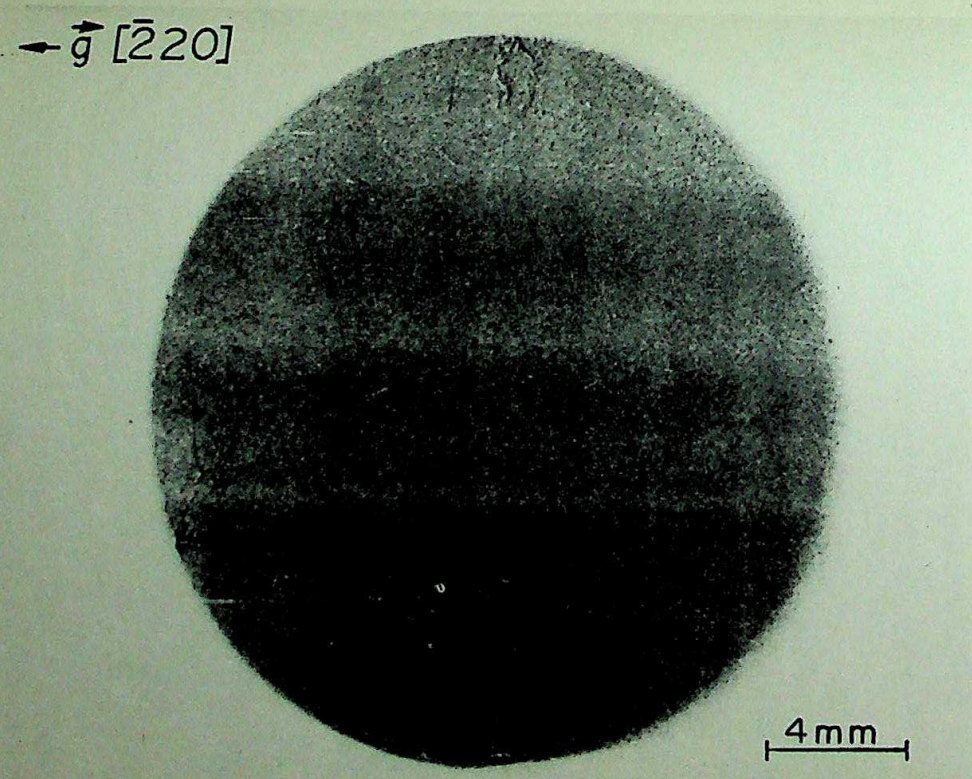

Figure 6. A high resolution traverse topograph of a dislocation free silicon single crystal. Experimental details are as given in figure 5.

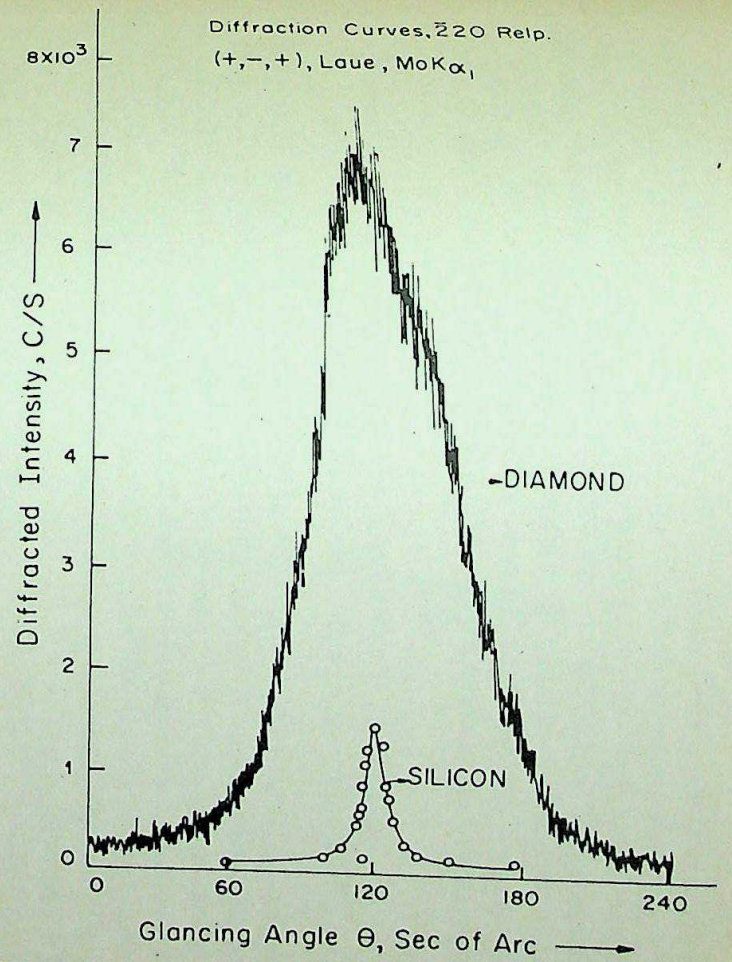

Figure 7. Diffraction curves of a diamond and a silicon single crystal plotted on the same scale. Diffracting volumes of both the specimens are approximately the same. $\bar{2}$20 Relp, MoK$_{\alpha 1}$ beam, symmetrical Laue geometry and (+, −, +) setting were used.

CC-0. In Public Domain. Gurukul Kangri Collection, Haridwar

Digitized by Arya Samaj Foundation Chennai and eGangotri

Digitized by Arya Samaj Foundation Chennai and eGangotri

maxima decreases (James 1950, p. 271). We shall consider this further in §3.3. Moreover, the atomic scattering factor for carbon is much smaller in comparison to that for silicon. This further enhances the discrepancy. Even when the difference in the absorption coefficients of the two crystals for $MoK_{\alpha 1}$ radiation are taken into consideration the anomaly cannot be explained. Therefore, a detailed quantitative comparative study of the diffracted X-ray intensities, both peak as well as integrated was undertaken. Results of these experiments are described in the following.

3.2 *Quantitative measurements of diffracted X-ray intensities from natural diamond and comparison with those of nearly perfect silicon single crystals*

To understand the cause of anomalous ratio of peak intensities of diamond and silicon crystals, systematic quantitative measurements of intensities of diffracted *X*-rays, both peak as well as integrated, for a number of reflections from natural diamond and silicon crystals have been made. The irradiated area (Bragg geometry) and volume (Laue geometry) for diamond and silicon crystals was nearly identical. It was small in comparison to the total area/volume of the specimen crystals. The results are described in the following.

3.2.1 *Results of experiments performed in the Bragg (reflection) geometry*: Experiments were performed with (111) and (333) diffracting planes. Both these reflections were studied in the symmetrical Bragg geometry with (+, −, +) setting of the diffractometer. Figure 8 shows typical diffraction curves obtained with a diamond and a silicon crystal for 111 reflection. The peak intensity for diamond crystal is higher than that for silicon crystal as reported above. The peak intensity ratio is $I_C/I_{Si} = 1{\cdot}3$. Here I_C and I_{Si} are the peak intensities for diamond and silicon, respectively.

Figure 9 shows results obtained with a high order reflection 333. The ratio of diffracted intensities from diamond and silicon has considerably increased when we compare this result with that reported in Figure 8. The value of I_C/I_{Si} is 10·5.

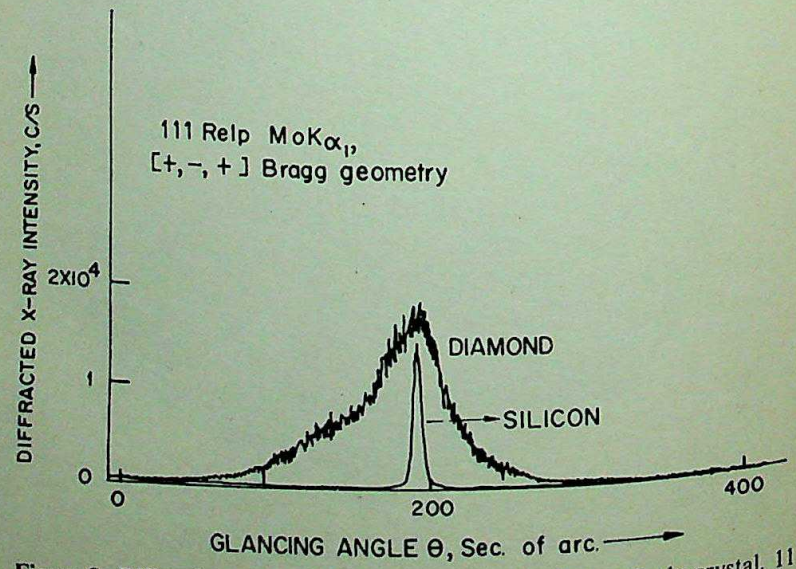

Figure 8. Diffraction curves of a diamond and a silicon single crystal. 111 Relp, $MoK_{\alpha 1}$ radiation, symmetrical Bragg geometry and (+, −, +) setting were used.

CC-0. In Public Domain. Gurukul Kangri Collection, Haridwar

Digitized by Arya Samaj Foundation Chennai and eGangotri

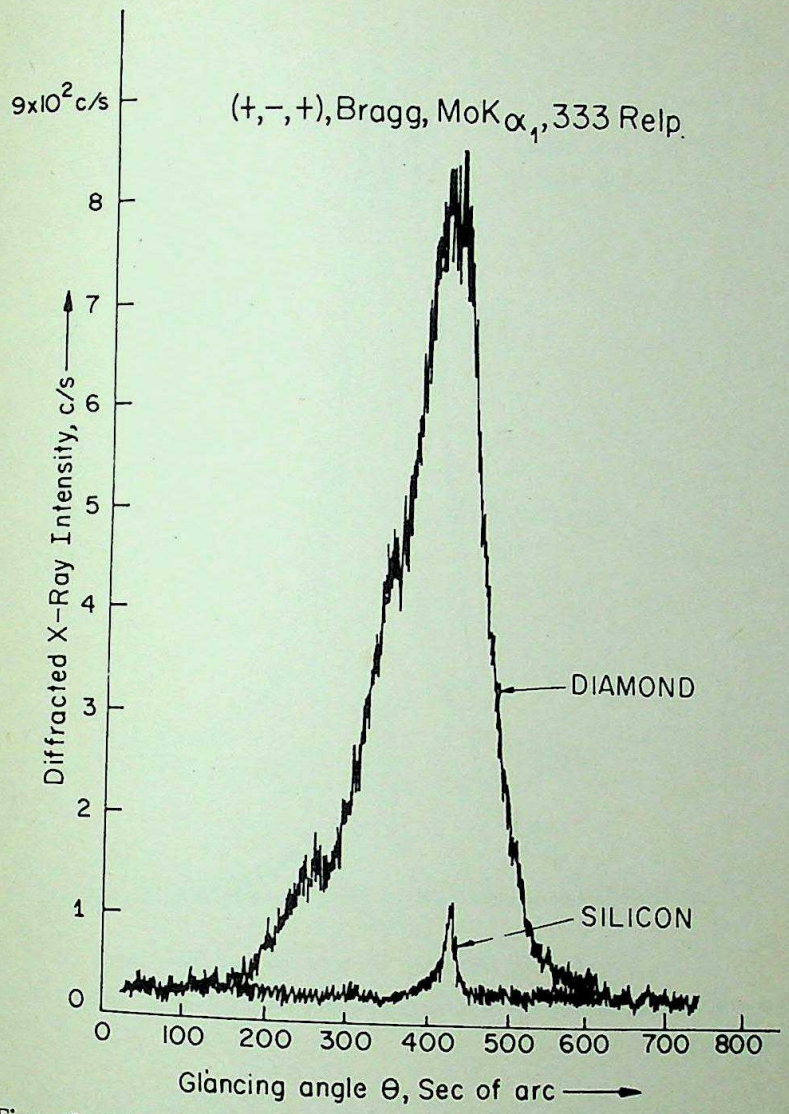

Figure 9. Diffraction curves of a diamond and a silicon single crystal. 333 Relp, $MoK_{\alpha 1}$ radiation, symmetrical Bragg geometry and (+, −, +) setting were used.

3.2.2 *Results of experiments performed in the Laue (transmission) geometry*: Figure 10 shows diffraction curves of diamond and silicon crystal for $\bar{2}20$ reflection. (+, −, +) setting of the diffractometer was used. The diffracted X-ray intensity is much higher for the diamond crystal in the entire angular range. The peak intensity for this diamond specimen is 4·5 times that of silicon crystal. In all the specimen crystals examined by us, peak intensity for diamond I_C was always higher than that observed for silicon I_{Si}. The ratio was in the range 4·5 to 5.

Experiments have been performed with higher order reflections. Figure 11 shows diffraction curves for diamond and silicon crystals recorded with $(\bar{4}40)$ diffracting planes. The peak intensity of $\bar{4}40$ reflection for silicon crystals with the normal size of the exploring beam, an area of $1{\cdot}2 \times 0{\cdot}2\,mm^2$, is rather small. It is only 90 c/s. With this small intensity, it is not possible to get good quality diffraction curves. Therefore, the vertical slit opening was increased from 1·2 mm to 5·6 mm to enhance the intensity of the exploring beam. This helped in recording a curve with good statistics, and having the peak intensity comparable to that of the diamond crystal for a beam of

CC-0. In Public Domain. Gurukul Kangri Collection, Haridwar

Digitized by Arya Samaj Foundation Chennai and eGangotri

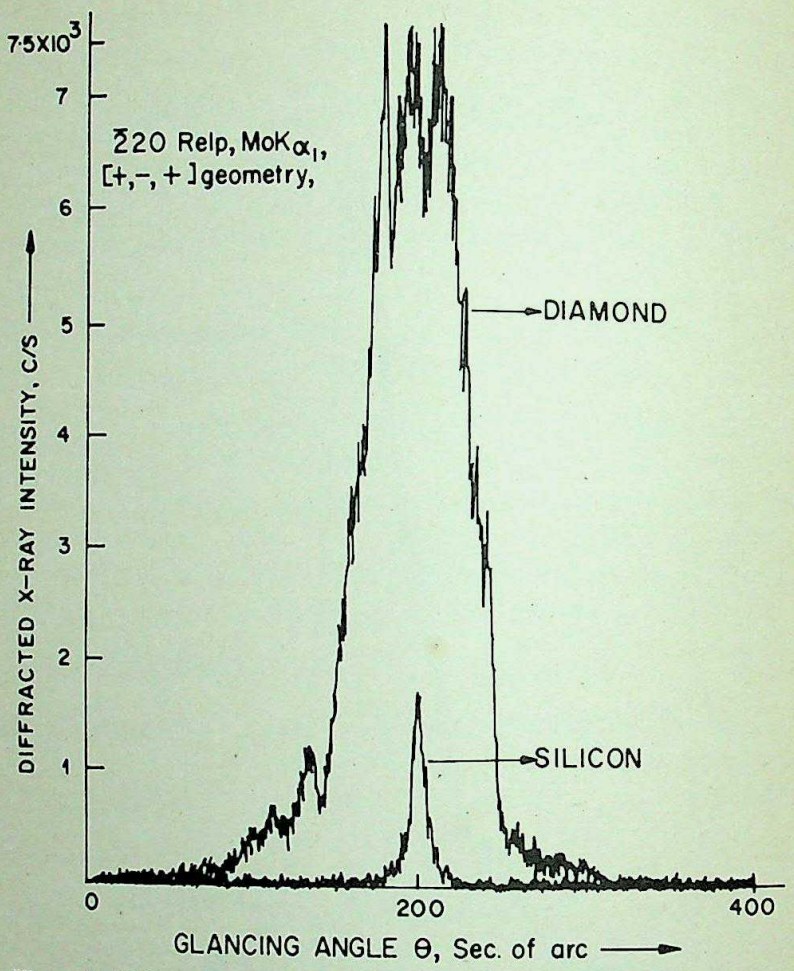

Figure 10. Diffraction curves of a diamond and a silicon single crystal recorded with ($\bar{2}20$) diffracting planes.

fixed height (1·2 mm). From the experimental curve, intensities for different glancing angles were calculated for the normal irradiated area (1·2 × 0·2 mm^2) and a normalized diffraction curve was obtained. This is the silicon curve shown in figure 11. The peak intensity for the diamond crystal is seven times higher than that of the silicon crystal.

A weak reflection like $\bar{2}\bar{2}4$ was also studied in the symmetrical Laue geometry. Figure 12 shows typical diffraction curves for diamond and silicon crystals for $\bar{2}\bar{2}4$ reflection. It is seen that even in these diffraction curves, the peak intensity for diamond is very high (7·5 times) as compared to that for silicon crystal.

In addition to the experiments described above, we have made measurements with $\bar{1}\bar{1}3$ reflection in the asymmetric transmission mode (Laue geometry). ($\bar{1}\bar{1}3$) lattice planes are inclined at an angle of 79° 58′ to the surfaces of these crystals which are along (111) planes. Figure 13 shows typical diffraction curves obtained with diamond and silicon crystals for this reflection. The diffracted X-ray intensity from diamond crystal in this case also is much higher as compared to that from silicon crystal. The peak intensity ratio I_C/I_{Si} is 10·5:1.

3.2.3 *Results of experiments performed with the specimen crystals at the fourth crystal position of the quadruple crystal X-ray diffractometer*: To further improve upon the resolution of the experimental arrangement, the specimens were placed at the fourth

CC-0. In Public Domain. Gurukul Kangri Collection, Haridwar

Digitized by Arya Samaj Foundation Chennai and eGangotri

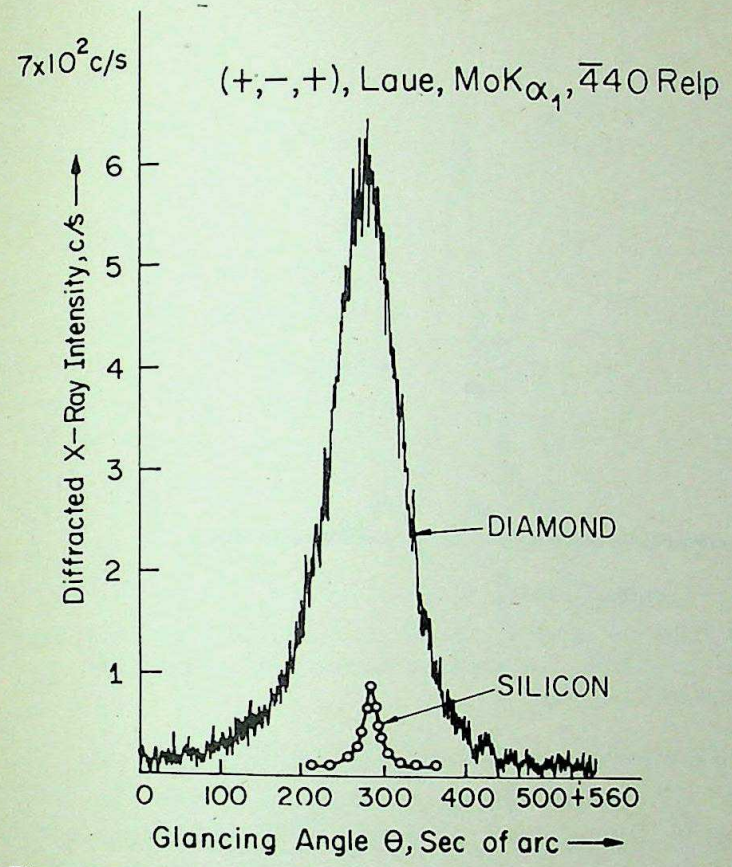

Figure 11. Diffraction curves of a diamond and a silicon single crystal recorded with ($\bar{4}40$) diffracting planes.

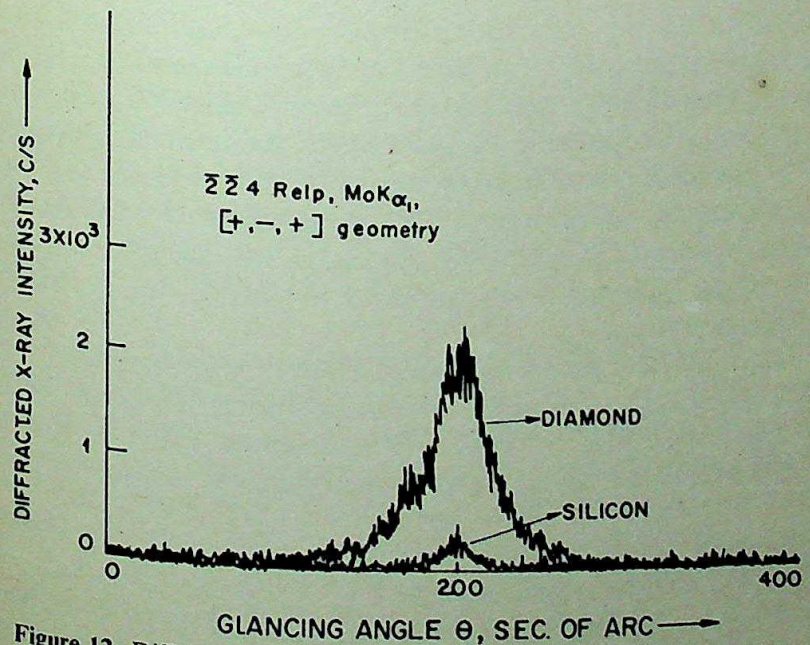

Figure 12. Diffracting curves of a diamond and a silicon single crystal recorded with ($\bar{2}\bar{2}4$) diffracting planes.

CC-0. In Public Domain. Gurukul Kangri Collection, Haridwar

Digitized by Arya Samaj Foundation Chennai and eGangotri

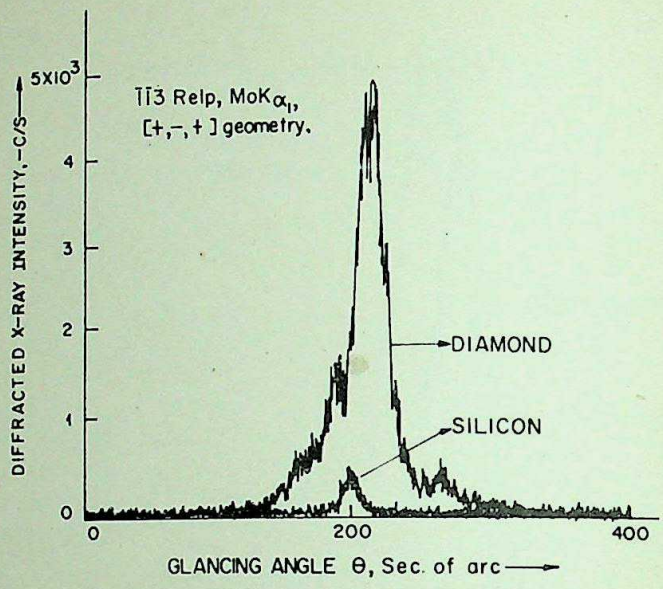

Figure 13. Diffraction curves of a diamond and a silicon single crystal recorded with $(\bar{1}\bar{1}3)$ diffracting planes. $MoK_{\alpha 1}$ radiation; asymmetric Laue geometry and $(+,-,+)$ setting of the diffractometer were used.

crystal position and diffraction curves were recorded with the $(+, -, +, -)$ setting of the diffractometer. Symmetrical Bragg geometry was used. The third crystal was a dislocation free (111) silicon single crystal aligned for diffraction from $(\bar{2}20)$ planes in the symmetrical Laue geometry. Figure 14 shows the diffraction curves recorded with the (111) diffracting planes of diamond and silicon single crystals. The difference between the peak intensities of these curves is quite small. The peak intensities are in the ratio $I_C/I_{Si} = 1{\cdot}1$.

3.3 *A comparison of the absolute values of the integrated intensities of diamond and silicon crystals*

The absolute value of the integrated intensity of a reflection can be determined experimentally by following the well known procedure (James 1950). The intensity of the exploring beam is carefully measured and maintained constant in these experiments. The area under the diffraction maxima is obtained from the curves shown in figure 8–13. The crystal was rotated with a constant velocity while recording these curves. The values of integrated intensity ρ, obtained by dividing the area of the curve by the intensity of the exploring beam, are given in tables 1 and 2, respectively, for diamond and silicon crystals.

For comparison with the experimental data, we have also calculated the values of the integrated intensities by assuming the crystals as: (i) ideally "perfect" and (ii) ideally "mosaic" crystals. For "perfect crystals" with moderate value of the absorption coefficient μ for the exploring beam, the integrated intensity is given by (James 1950)

$$\rho = \frac{8}{3\pi} N\lambda^2 |F| \frac{e^2}{mc^2} \frac{1+|\cos 2\theta|}{2\sin 2\theta} . \tag{1}$$

Here N = number of unit cells per unit volume, λ = wavelength of the exploring radiation, F = structure factor for the reflection under consideration; e, m = charge

CC-0. In Public Domain. Gurukul Kangri Collection, Haridwar

Digitized by Arya Samaj Foundation Chennai and eGangotri

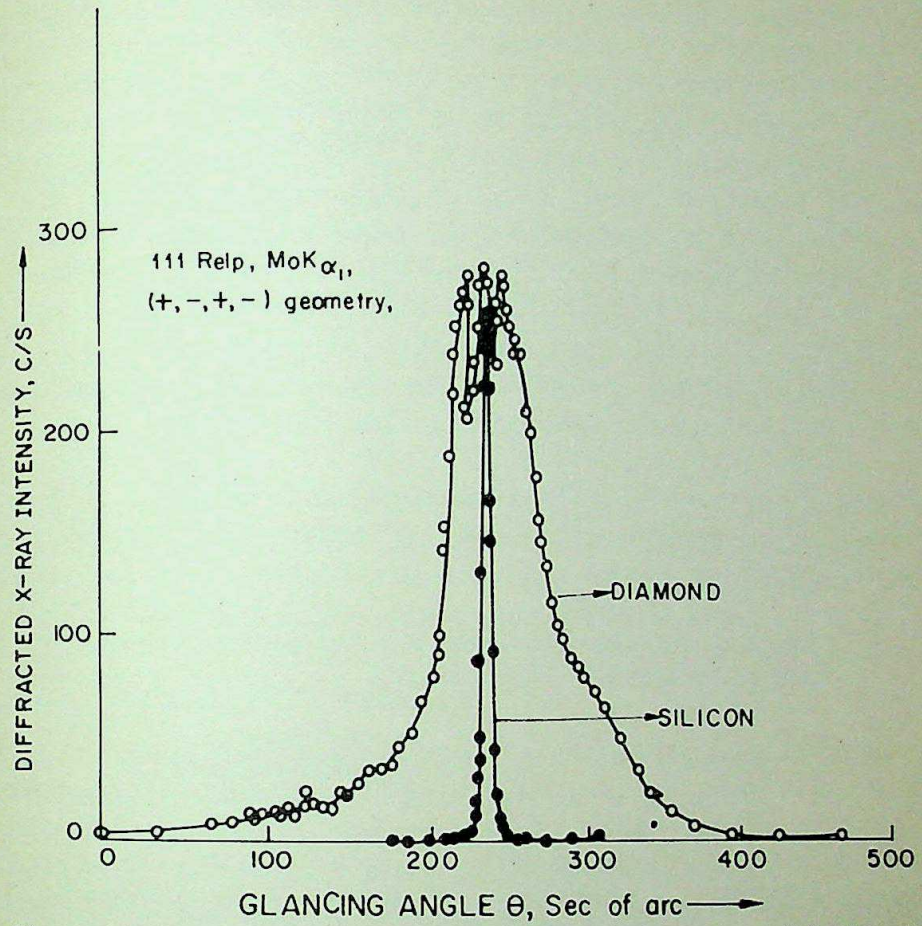

Figure 14. Diffraction curves of a diamond and a silicon single crystal recorded with specimen at the fourth crystal position of the diffractometer in the (+,−,+,−) setting. 111 Relp, $MoK_{\alpha 1}$ radiation and symmetrical Bragg geometry were used. The curves were plotted after normalizing the intensities for equal area of irradiation for both types of crystals.

and mass of the electron, c = velocity of light, and θ = glancing angle = $\theta_B + \varepsilon$; θ_B being the Bragg angle and ε the angular deviation from that orientation. The exploring beam has been assumed to be unpolarized.

For an ideally imperfect or 'mosaic' crystal the integrated intensity is given by the following expression when the X-ray beam is unpolarized (James 1950):

$$\rho = \frac{N^2\lambda^3}{2\mu}|F|^2\left(\frac{e^2}{mc^2}\right)^2\frac{1+\cos^2 2\theta}{2\sin 2\theta}. \qquad (2)$$

We have used (1) and (2) for determining the theoretical values of ρ for all reflections. These are given in tables 1 and 2.

It is seen from table 1 that the experimental values of integrated intensities for diamond crystals lie between the values expected for ideally mosaic and perfect crystals. This is to be expected as all the specimens were moderately perfect (§ 3.1). From table 2 we find that the integrated intensities for silicon determined experimentally are closer to the theoretical values for a perfect crystal. In fact most of the values are even smaller than those calculated for nearly perfect crystals. This is rather surprising. It is another interesting anomaly revealed by this investigation. Further, work is in progress to understand this discrepancy.

CC-0. In Public Domain. Gurukul Kangri Collection, Haridwar

Digitized by Arya Samaj Foundation Chennai and eGangotri

Table 1. Absolute values of integrated intensities of different reflections from diamond single crystals at 27°C for $MoK_{\alpha 1}$ radiation.

Reflection *hkl*	Temperature correction $\exp[-(B\sin^2\theta/\lambda^2)]$	Theoretical values of integrated intensities		Experimental values of integrated intensities ($\times 10^{-6}$)
		Perfect crystal model ($\times 10^{-6}$)	Mosaic crystal model ($\times 10^{-6}$)	
111	0·987	12·5	2455	229·2
333	0·925	1·61	108	83·0
$\bar{2}20$	0·977	2·01	117	90·6
$\bar{4}40$	0·911	1·92	189	50.0
$\bar{1}\bar{1}3$	0·969	3·78	403	31·3
$\bar{2}\bar{2}4$	0·933	2·57	281	16·6

Table 2. Absolute values of integrated intensities of different reflections from silicon single crystals at 27°C for $MoK_{\alpha 1}$ radiation.

Reflection *hkl*	Temperature correction $\exp[-(B\sin^2\theta/\lambda^2)]$	Theoretical values of integrated intensities		Experimental values of integrated intensities ($\times 10^{-6}$)
		Perfect crystal model ($\times 10^{-6}$)	Mosaic crystal model ($\times 10^{-6}$)	
111	0·992	19·75	616·2	20·8
333	0·926	3·57	58·1	1·43
$\bar{2}20$	0·978	14·04	503·9	2·60
$\bar{4}40$	0·913	4·23	88·6	1.46
$\bar{1}\bar{1}3$	0·969	7·83	182·7	1·46
$\bar{2}\bar{2}4$	0·934	5·67	138·7	1·04

We have considered here theoretical expressions for integrated intensity from ideally perfect as well as from ideally mosaic crystals. It may be stressed that from this one cannot directly deduce the relationship between peak intensities at diffraction maxima of absolutely perfect crystals and ideally imperfect crystals. In this connection, one may quote James (1950) "... It must be borne in mind throughout this discussion (on integrated intensities) that we are considering the integrated reflection, and not the reflecting power when the crystal is set so as to reflect most strongly. This will always be greatest for the most perfect crystal, whereas, as we have just seen, the integrated reflection is increased by the introduction of imperfections."

4. Discussion

Results of experiments reported above have clearly established that the observed peak intensities of diffraction are higher for diamond crystals in comparison to those for

CC-0. In Public Domain. Gurukul Kangri Collection, Haridwar

Digitized by Arya Samaj Foundation Chennai and eGangotri

silicon crystals. For higher order reflections like 333 the diamond peak intensity is more than ten times that of the silicon crystals. It may be emphasized that these experiments have been performed by using recently developed high resolution techniques employing highly collimated and monochromated $K_{\alpha 1}$ beam. Therefore, there is no possibility of experimental factors being responsible for these observations.

This result is new and anomalous due to the following two reasons. The atomic scattering factor of silicon atoms is considerably higher than that of the carbon atoms due to their widely different atomic numbers. Further, the degree of perfection of silicon crystals is much higher than that of diamond crystals. This fact has been well established by the diffractometric and topographic evaluations (§ 3.1) and integrated intensity measurements (§ 3.4). For a given reflection the ratio of peak intensities for diamond and silicon $-I_C/I_{Si}$ varies from specimen to specimen, yet the overall result is the same.

The absorption coefficient of the exploring beam is different for diamond and silicon. Correction for absorption has been applied. The observed peak intensity had already been reduced due to absorption and, therefore, (observed) $I_C = I_C^0 \exp(-\mu_C t'_C)$ or $I_C^0 = I_C \exp(\mu_C t'_C)$. Similarly, $I_{Si}^0 = I_{Si} \exp(\mu_{Si} \cdot t'_{Si})$. Here $t' = t \sec\theta_B$.

Hence

$$I_C^0/I_{Si}^0 = I_C/I_{Si} \exp(\mu_c t'_C - \mu_{Si} t'_{Si}). \tag{3}$$

The values of I_C/I_{Si} and I_C^0/I_{Si}^0 have been calculated and are given in table 3 for different reflections. It is very tempting to compare the experimentally observed intensities with theoretically calculated values. It is possible to make calculations of diffracted intensities at diffraction maxima for ideally perfect crystals in the case of idealised experimental conditions conforming to plane wave conditions and ideal monochromaticity (Pinsker 1978). However, it is not possible to calculate intensities at diffraction maxima in moderately perfect crystals. Even in an ideally imperfect or mosaic crystal, theoretical expressions for peak intensities are not available. Therefore, a comparison between theoretically expected peak values for perfect and imperfect crystals is not possible at present. However, even if such a quantitative comparison is made theoretically it will not explain the observed anomaly. The peak intensity for perfect crystals will always be higher than that of imperfect crystals. It may be mentioned that experimental comparison of intensities of nearly perfect and not so perfect crystals has been made several times in our group. Some of these results have been published showing that the peak intensities of perfect crystals are higher than those of less perfect crystals of the same substance (Lal *et al* 1979; Lal 1981).

Integrated intensities of diffraction from diamond crystals have been studied extensively by Raman group (Ramachandran 1944 and Hariharan 1944). It is well established that the values of ρ_C vary from specimen to specimen. The variation for

Table 3. Values of I_C/I_{Si} and I_C^0/I_{Si}^0 for different reflections.

Reflection	Observed value of I_C/I_{Si}	Value of I_C^0/I_{Si}^0
$\bar{2}20$	4·5	1·37
$\bar{4}40$	7·0	2·02
$\bar{2}\bar{2}4$	7·5	2·21
$\bar{1}\bar{1}3$	10·5	3·10

CC-0. In Public Domain. Gurukul Kangri Collection, Haridwar

Digitized by Arya Samaj Foundation Chennai and eGangotri

111 reflection can be in the range: 4×10^{-5} to 2×10^{-3}, a factor of 50 for CuK_α radiation (Lonsdale 1948). The experimental results on ρ reported in table 1 are in agreement with this keeping in view the wavelength of the exploring radiation and the structure factors of the reflections studied. However, in the present investigation emphasis has been on comparison of peak intensities from two crystals having same structure but widely different structure factors. The peak intensity is a direct manifestation of the quality of atomic ordering inside a crystal and the range over which it extends. All the experimental data reported here establish that the degree of perfection of silicon crystals is close to the ideally perfect state and yet its peak intensities are lower than those of diamond crystals which are moderately perfect. The consideration of structure factor values further enhance this anomaly.

One may argue that the observed anomaly could be partly due to large size of mosaics in diamond crystals in comparison to primary extinction distance and/or due to the resolution width of the experimental system being larger than the silicon diffraction peaks but smaller than the diamond peaks. Even if one assumes that the mosaic size in a diamond crystal is greater than the primary extinction distance, the observed anomaly cannot be accounted for due to the following reasons. In an ideally perfect crystal all mosaics are oriented identically and therefore the entire crystal can be treated as one single mosaic. In a mosaic crystal like the diamond specimens investigated here, the individual mosaics, small or big, are misoriented with respect to each other and their orientation lies in a wide angular range. Therefore, in a mosaic crystal, at any given orientation of the specimen on the diffraction curve, only a fraction of all mosaics would be oriented to satisfy the diffraction condition. Hence, the diffracted intensity will be much lower than that expected when all of them would be oriented identically, as in the case of a perfect crystal. In the present experiments, the diffraction curves of diamond crystals are broad with half widths of about 100 arc sec or so as compared to the theoretical values of a few arc sec for a perfect diamond crystal. Therefore, by these considerations, one cannot explain the observed anomaly. It is true that in all experimental systems, there is a finite divergence and wavelength spread in the exploring X-ray beam leading to a finite resolution width. This width in our experimental system has been estimated as 3 arc sec, as measured by direct experiments. This limit is comparable with the diffraction curve half widths for low order reflections of perfect crystals of silicon as well as diamond. For example, theoretical values of half widths of diamond and silicon crystals for different reflections are given below:

Theoretical half widths of diffraction curves (arc sec)

Reflection	Silicon	Diamond
111	2·97	1·96
333	0·67	0·35
220	2·19	1·14
440	0·79	0·46
224	0·99	0·54
113	1·25	0·65

These values have been calculated by us for plane polarized incident wave front (Pinsker 1978). It is seen that the resolution width is not small compared to the

CC-0. In Public Domain. Gurukul Kangri Collection, Haridwar

Digitized by Arya Samaj Foundation Chennai and eGangotri

theoretical half widths of diamond crystals and larger compared to that for silicon crystals. The observed broad curves for diamond crystals are due to mosaic spread. Therefore, the observed anomaly cannot be explained on the basis of different values of resolution width in relation to diffraction curve half widths of diamond and silicon crystals.

The results reported in this paper have established interesting anomalies which deserve further work for complete understanding. In this connection we have borrowed several diamond crystals from Professor C V Raman's collection at Raman Research Institute, Bangalore, for which we are grateful to the Director, Professor V Radhakrishnan and Professor S Ramaseshan.

Acknowledgements

One of the authors (ARV) would like to thank the Council of Scientific and Industrial Research, New Delhi and Indian National Science Academy, New Delhi, for partial financial assistance. Thanks are due to Dr S K Gupta for EPR measurements on diamond crystals.

References

Bonse U and Hart M 1965 *Appl. Phys. Lett.* **7** 238
Bragg W H 1914 *Philos. Mag.* **12** 881
Bragg W H 1921 *Proc. Phys. Soc. London* **33** 304
Brill R, Grimm H G, Hermann C and Peters C L 1939 *Ann. d. Phys.* **34** 393
Brindley G W 1932 *Proc. Leeds Philos. Soc.* **2** 271
Brindley G W 1933 *Proc. R. Soc.* (London) **A140** 301
Ehrenberg W, Ewald P P and Mark H 1928 *Z. Kristallogr.* **66** 547
Hariharan P S 1944 *Proc. Indian Acad. Sci.* **A19** 261
Hart M 1971 *Rep. Prog. Phys.* **34** 435
James R W 1950 *The optical principles of the diffraction of X-rays* (London: G Bell and Sons) p. 271
Lal Krishan, Singh B P and Verma A R 1979 *Acta Crystallogr.* **A35** 286
Lal Krishan 1981 *Proc. Indian Natl. Sci. Acad. Suppl.* **A47** 20
Lal Krishan 1982 *Synthesis, crystal growth and characterization* (ed.) Krishan Lal (Amsterdam, New York, Oxford: North Holland) p. 287
Lal Krishan and Thoma P 1983 *Phys. Status Solidi.* **A80** 491
Lal Krishan 1985 *NPL Research Report* No. NPL-85-B4-0051
Lal Krishan 1988 *Crystal properties & preparation* **16** 143
Lal Krishan and Goswami S N N 1987 *Materials science and engineering* **85** 147
Lang A R 1974 *J. Cryst. Growth* **24/25** 108
Lonsdale K 1948 *Crystals and X-rays* (London: G. Bell and Sons) p. 138
Patel J R and Betterman B W 1963 *J. Appl. Phys.* **34** 2716
Pinsker Z G (1978) *Dynamical scattering of X-rays in crystals* (Berlin, Heidelberg, New York: Springer-Verlag)
Ramachandran G N 1944 *Proc. Indian Acad. Sci.* **A19** 304
Renninger M 1935 *Z. Tech. Phys.* **16** 440
Renninger M 1937 *Z. Phys.* **106** 141
Tanner B K 1976 *X-ray diffraction topography* (Oxford: Pergamon Press) p. 18

CC-0. In Public Domain. Gurukul Kangri Collection, Haridwar

Digitized by Arya Samaj Foundation Chennai and eGangotri

CC-0. In Public Domain. Gurukul Kangri Collection, Haridwar

Digitized by Arya Samaj Foundation Chennai and eGangotri

Pramāṇa – J. Phys., Vol. 34, No. 6, June 1990, pp. 525–536. © Printed in India.

Diffraction properties of one-dimensional finite size Fibonacci quasilattice

V S K BALAGURUSAMY, S BARANIDHARAN, E S R GOPAL*, and V SASISEKHARAN†

Department of Physics, †Molecular Biophysics Unit, Indian Institute of Science, Bangalore 560012, India

MS received 9 August 1989; revised 5 December 1989

Abstract. The diffraction patterns from Fibonacci quasilattices have been calculated. Finite-size effects are evaluated for weak and strong peaks. For a smaller number of scatterers (<100) there are fluctuations in the intensities of weak and strong peaks. The fluctuations in weak peaks are greater than that in strong peaks. The fluctuations in intensities of weak and strong peaks near the origin are larger than in the corresponding cases of weak and strong peaks far away from the origin. Small shifts in peak-positions are unexpectedly found, the shifts being proportional to $N^{-3/2}$ for a large number of scatterers. The diffraction pattern of a one-dimensional crystal and random structure is compared with that of the Fibonacci quasilattice. The strong peaks observed in the diffraction pattern of 1-d crystal show negligible peak-shifts, they being comparable with computational errors even when the number of scatterers is as small as 5. The implications for analysing the experiments are briefly indicated.

Keywords. Quasilattice; diffraction; quasicrystal.

PACS Nos 61·50; 61·55

1. Introduction

Soon after the discovery of rapidly quenched Al-Mn alloys showing the crystallographically forbidden 5-fold symmetry in the electron diffraction patterns (Shechtman *et al* 1984), quasiperiodic structures were proposed (Levine and Steinhardt 1984) as possible models for the atomic structure of these phases. The numerically computed diffraction patterns of these models show the features of the experimentally observed diffraction patterns. Quasilattices in one-, two- and three-dimensions can be obtained by projecting higher dimensional periodic lattices onto a lower dimensional space (Kramer and Neri 1984; Duneau and Katz 1985; Zia and Dallas 1985; Elser 1985, 1986; Gratias and Cahn 1986; Janssen 1986; Levine and Steinhardt 1986; Valsakumar and Vijaykumar 1986; Prince 1987). The method of generating quasilattices using a self-similarity principle is also known (Penrose 1974; Sasisekharan 1986). Quasilattices can also be obtained by the generalized dual method or multigrid method (de Bruijn 1981; Socolar *et al* 1985).

Long before the experimental observation of quasicrystals, tiling a plane aperiodically with two kinds of rhombuses preserving the 5-fold rotational symmetry had been

*To whom correspondence should be addressed

CC-0. In Public Domain. Gurukul Kangri Collection, Haridwar

Digitized by Arya Samaj Foundation Chennai and eGangotri

suggested (Penrose 1974). Starting with a pattern, having 5-fold rotational symmetry, consisting of these two kinds of rhombi an aperiodic tiling can be generated by following a rule while matching the rhombuses. The number of rhombi of each kind generated after n substitutions follows the Fibonacci sequence: 1, 1, 2, 3, 5, 8, 13, 21, 34, 55, 89, 144,... The ratio of the number of one kind of rhombi to the other converges to the golden mean, as the number of substitutions applied to generate the tiling tends to infinity.

Fibonacci superlattices have been grown experimentally using GaAs/AlAs layers (Todd *et al* 1986) and Nb/Cu layers (Hu *et al* 1986) and their diffraction properties have been studied. The present work is concerned with these situations.

2. Model calculations

The one-dimensional (1-d) Fibonacci quasilattice can be generated using two length-scales by the following substitution rule: L goes to LS, S goes to L. Thus we get the following sequence of L's and S's: S; L; LS; LSL; LSLLS; LSLLSLSL; LSLLSLSLLSLLS... The total number of L's and S's generated by the above substitution rule follows the Fibonacci sequence. The ratio of the number of L's to the number of S's converges to the golden mean $\tau=(1+\sqrt{5})/2$. The numbers forming the Fibonacci sequence can be generated from the recursion rule: $F_n=F_{n-1}+F_{n-2}$, $n>2$ (with $F_1=1$, $F_2=1$) where F_n refers to the nth term of the sequence. The ratio F_n/F_{n-1} oscillates about the value of τ and converges to τ as n tends to infinity. The 1-d Fibonacci quasilattice is obtained by placing δ-function scatterers at the positions given by the formula:

$$x_n = A + n + (1/\tau)\,[B + n*(1/\tau)]$$

where x_n is the position of the nth scatterer, $A=0{\cdot}0$ and $B=1{\cdot}0$, $[....]$ denotes the integer part. A segment of the 1-d quasilattice is shown in figure 1.

The diffraction pattern was numerically calculated by numerical Fourier transformation: $F(k)=\sum_n \exp(ikx_n)$. The diffraction pattern obtained from 610 scatterers by scanning the $x^*(x^*=k/2\pi)$ axis is shown in figure 2. The peaks with intensity less than 1% are not shown in the figure. The peaks could be indexed using the infinite-quasilattice formula: $k_{pq}=(2\pi/d)*(p+q/\tau)$, $(x^*_{pq}=k_{pq}/2\pi)$ where p and q are integers and d is defined to be the average spacing between the scatterers. For the infinite Fibonacci quasilattice, $d=d_{\text{ideal}}=1+(1/\tau^2)$. For the finite Fibonacci quasi-

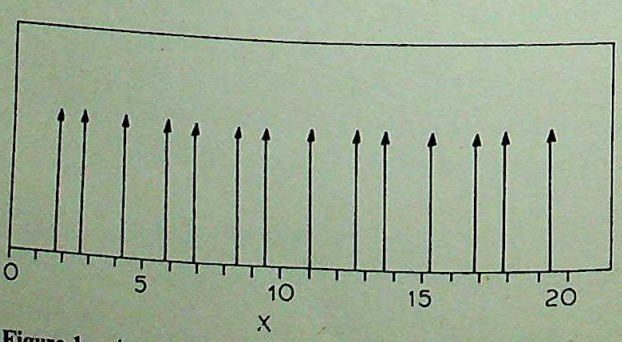

Figure 1. A segment of the one-dimensional Fibonacci quasilattice with unit δ-function scatterers.

CC-0. In Public Domain. Gurukul Kangri Collection, Haridwar

Digitized by Arya Samaj Foundation Chennai and eGangotri

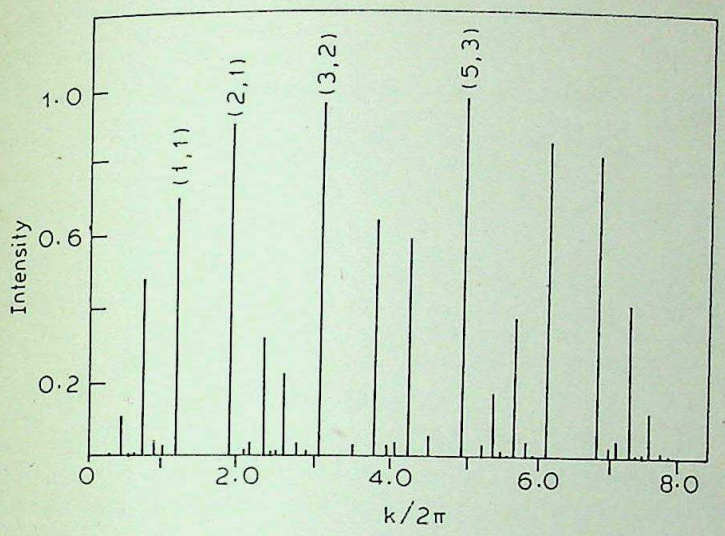

Figure 2. Diffraction from the Fibonacci quasilattice with 610 scatterers. Peaks with intensity less than 1% of the central peak ($x^*=0$) are not shown.

lattice $d=d_{\text{finite}}=(N_L\tau+N_S)/(N_L+N_S)$, where N_L=number of long intervals and N_S=number of short intervals. Some of the peaks indexed by the above formula can be seen in figure 2. When p and q are consecutive Fibonacci integers, it is found that they index the strong peaks. The weak peaks are found to be indexable when p and q are non-Fibonacci integers.

3. Results and discussion

In order to evaluate the finite size effects of the quasilattice on its diffracting property the ratio of intensity of peak to the square of number of scatterers (I/N^2) was calculated for a number of peaks (peaks near the origin and far away from the origin). It was calculated for different number of scatterers N. For a strong peak near the origin ($p=3$, $q=2$) the intensity has been followed as a function of the number of scatterers (figure 3). The fluctuations tend to settle down when the number of scatterers is greater than 50. Figure 4 shows the plot of I vs N^2 for the strong peak ($p=610$, $q=377$) far away from the origin. It can be seen that the fluctuations are within the computational error even for a small number of scatterers ($N<50$).

Figure 5 shows the plot of I vs N^2 for a weak peak ($p=2$, $q=2$) near the origin. The fluctuations tend to settle down only when the number of scatterers is greater than 800. Figure 6 shows the plot of I vs N^2 for a weak peak ($p=621$, $q=386$) far away from the origin. In this case also the intensity of the peak stabilizes around $N\sim700$. In all cases, I/N^2 approaches constant values asymptotically.

Another interesting aspect of the diffraction from the quasilattice is the shifts in peak positions as a function of the number of scatterers. The peak-positions were found out by scanning the x^*-axis starting from the position of the peak to be expected for the diffraction from an infinite quasilattice and locating the position of the peak nearest to the peak-position for the infinite quasilattice. The peaks were found unexpectedly to shift and oscillate and finally converge to a mean value with increasing number of scatterers. For example, figure 7 shows the peak-shifts as a function of number of scatterers for a strong peak near the origin ($p=3$, $q=2$). The peak-shifts

CC-0. In Public Domain. Gurukul Kangri Collection, Haridwar

Digitized by Arya Samaj Foundation Chennai and eGangotri

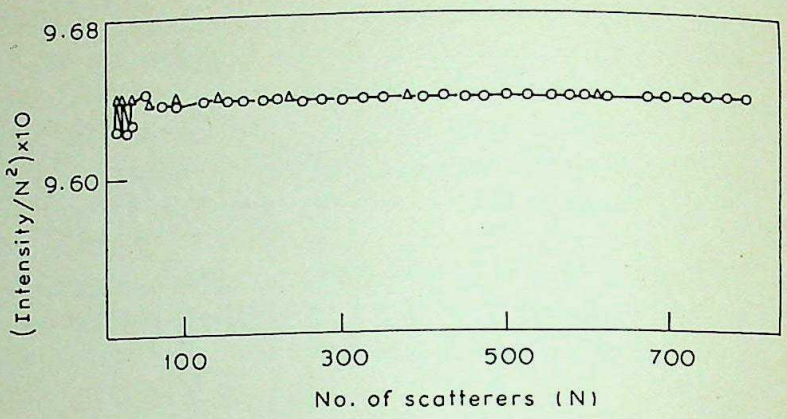

Figure 3. Plot of I/N^2 for the strong peak ($x^*_{p=3,q=2} \approx 3{\cdot}065$) nearer the origin. When the number of scatterers is around 50 the fluctuations settle down. Strong peak $p=3$, $q=2$, Circles and triangles represent non-Fibonacci and Fibonacci integers respectively.

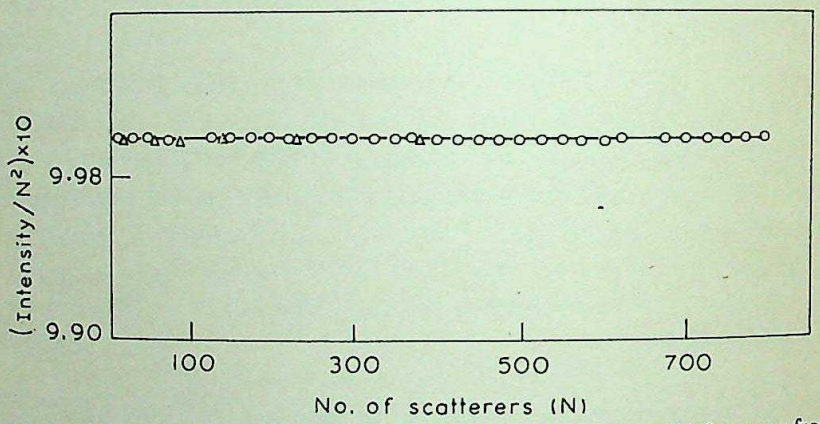

Figure 4. I/N^2 is plotted for the strong peak ($x^*_{p=610,q=377} \approx 610$) far away from the origin. Even when the number of scatterers is around 10 the fluctuations are within the computational error. Strong peak ($p=610$, $q=377$); Circles and triangles denote non-Fibonacci and Fibonacci integers respectively.

are within computational error when $N>50$. Figure 8 is the plot of peak-shifts vs N for a strong peak ($p=610$, $q=377$) far away from the origin. The peak-shifts are negligible even for a very small number of scatterers. Figure 9 shows the peak-shifts for a weak peak ($p=2$, $q=2$) near the origin. The changes in the peak position are larger and become negligible when $N>100$. Figure 10 shows the plot of peak-shifts vs N for the weak peak ($p=621$, $q=386$) far away from the origin. It is interesting to see that the peak-shifts are much larger and also persist till $N\sim300$. For the weak-peaks discussed above (figures 9 and 10), the asymptotic behaviour of peak-shifts (figures 11a and 11b) seem to be almost proportional to $N^{-3/2}$.

The formula for indexing the peaks involves the d-spacing values and the d-spacing values change due to changes in N_L and N_S. The N_L and N_S values depend on the choice of the finite segment of the quasilattice. Hence the d-spacing values for various segments of the quasi-lattice containing the same number of scatterers have been calculated. In order to see if there is any correlation between the d-spacing values and the peak-position shifts, the diffraction from various segments containing the same number of scatterers has been calculated. Figure 12 shows the d-spacing changes

CC-0. In Public Domain. Gurukul Kangri Collection, Haridwar

Digitized by Arya Samaj Foundation Chennai and eGangotri

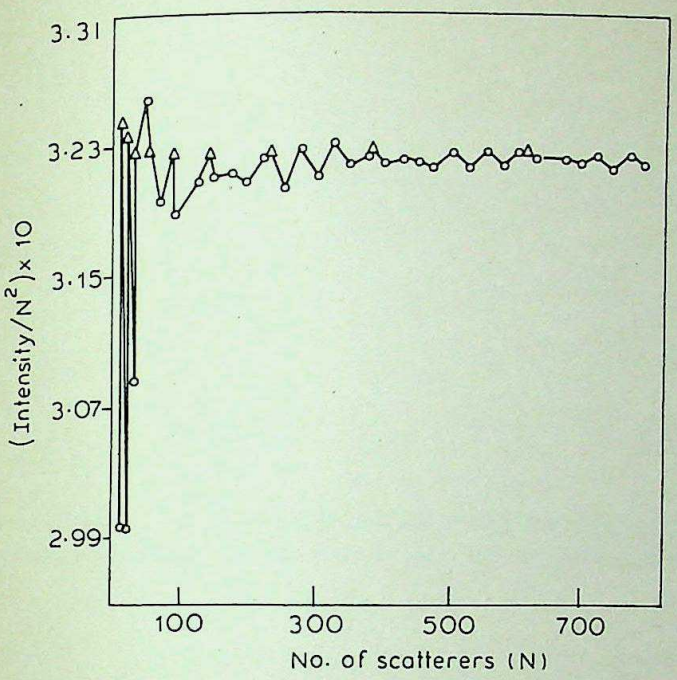

Figure 5. For the weak peak ($x^*_{p=2,q=2} \approx 2{\cdot}341$) nearer the origin, the fluctuations in I/N^2 are shown. The fluctuations tend to settle down when the number of scatterers is around 700. Weak peak ($p=2$, $q=2$).

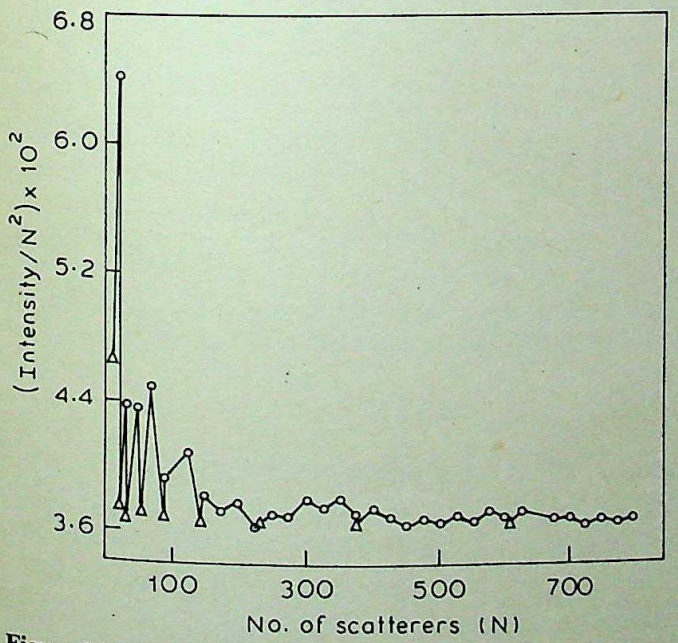

Figure 6. Plot of I/N^2 for the weak peak ($x^*_{p=621,q=386} \approx 621{\cdot}984$) far away from the origin. The fluctuations persist till $N \sim 700$. Weak peak ($p=621$, $q=386$).

for various segments with 20 scatterers along with the selected peak position shifts. Both the strong and weak peaks follow the same trend regarding the peak position shifts. It seems that there is a partial correlation of peak-shifts with the d-spacing changes. However even when the d-spacings are not changing, the peaks are found to shift in a few places. This implies the existence of contributions to the peak positions which are decided by the sequence of long and short intervals. The boundary effects

CC-0. In Public Domain. Gurukul Kangri Collection, Haridwar

Digitized by Arya Samaj Foundation Chennai and eGangotri

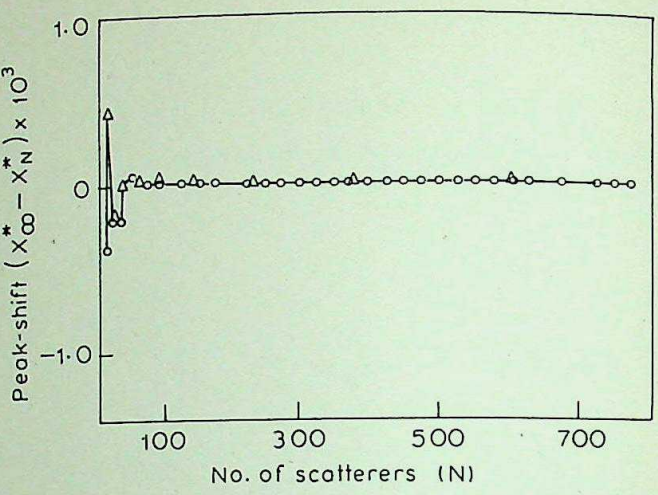

Figure 7. Shifts in peak-positions of the strong peak ($x^*_{p=3,q=2} \approx 3{\cdot}065$) nearer the origin. The peak-shifts are within the computational error when $N \sim 100$. Strong peak ($p=3$, $q=2$).

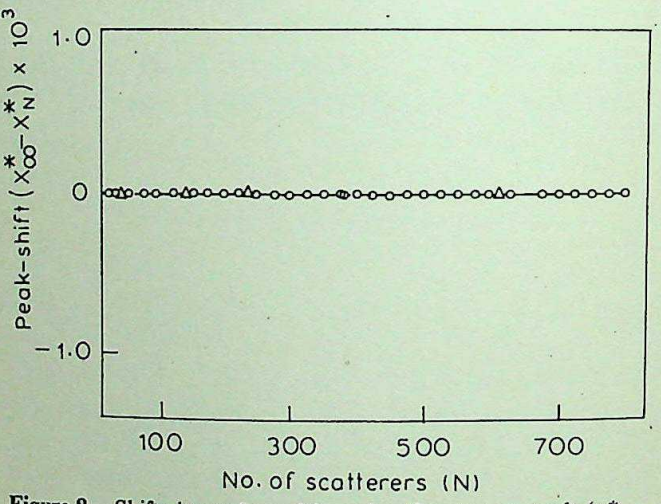

Figure 8. Shifts in peak-positions for the strong peak ($x^*_{p=610,q=377} \approx 610$) far away from the origin. Even when $N \approx 10$ the shifts are within the computational error. Strong peak ($p=610$, $q=377$).

clearly persist as the residual effect, besides the contribution from the d-spacings.

It is observed that the fluctuations in I/N^2 is larger for a weak peak than for a strong peak when both the peaks are either nearer the origin or far away from the origin. This is due to the fact that a strong peak corresponds to the constructive interference of the waves diffracted from a large number of scatterers. In the case of a weak peak, there is a partial cancellation of the many contributions. The fractional fluctuations are greater in this case of weak spots. When the size of the quasilattice changes, it may not affect the intensity of a strong peak as much as it does a weak peak.

It is found that for a weak peak or strong peak nearer the origin, the changes in peak intensities are larger than for a weak or strong peak far away from the origin, respectively. This can be understood in terms of the property of Fourier transforms. The changes in the values of the function at points far away from the origin in real space will be reflected more in the values of the transform of the function at points near the origin of the transformed space. This gives rise to the observed larger

CC-0. In Public Domain. Gurukul Kangri Collection, Haridwar

Digitized by Arya Samaj Foundation Chennai and eGangotri

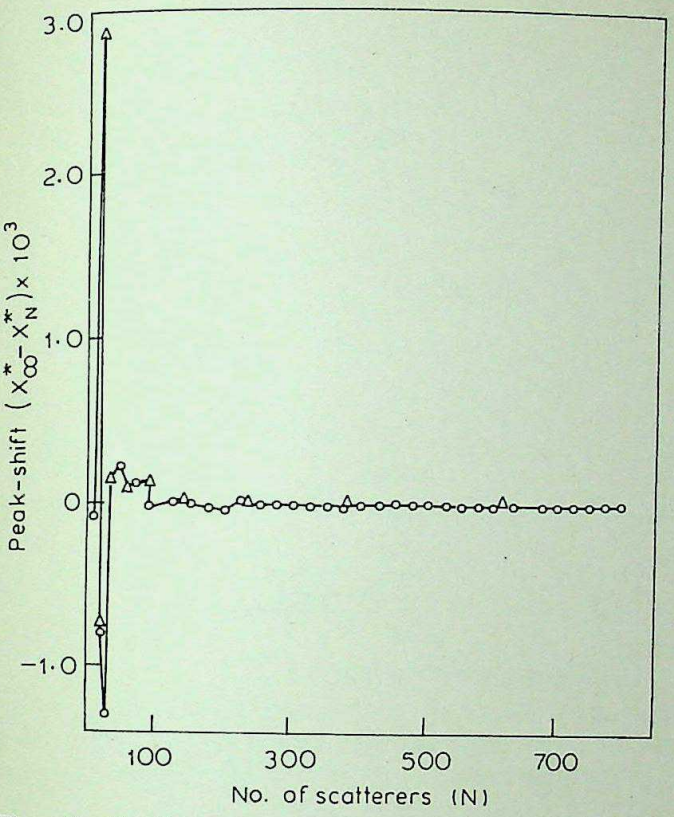

Figure 9. For the weak peak ($x^*_{p=2,q=2} \approx 2{\cdot}341$) nearer the origin, the shifts in peak-positions are shown. The peak-shifts are within the computational error when $N \sim 300$. Weak peak ($p=2$, $q=2$).

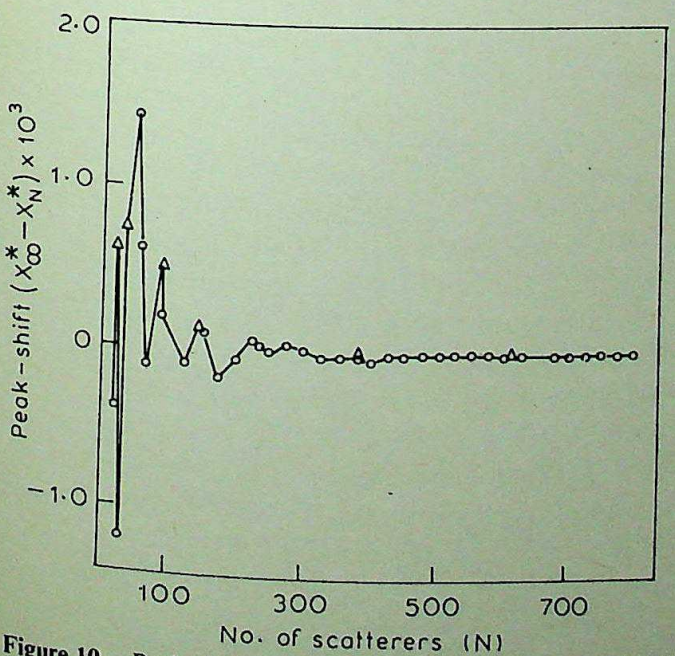

Figure 10. Peak-shifts in the weak peak ($x^*_{p=621,q=386} \approx 621{\cdot}984$) far away from the origin are shown. The peak-shifts tend to settle down when $N \sim 400$. Weak peak ($p=621$, $q=386$).

CC-0. In Public Domain. Gurukul Kangri Collection, Haridwar

Digitized by Arya Samaj Foundation Chennai and eGangotri

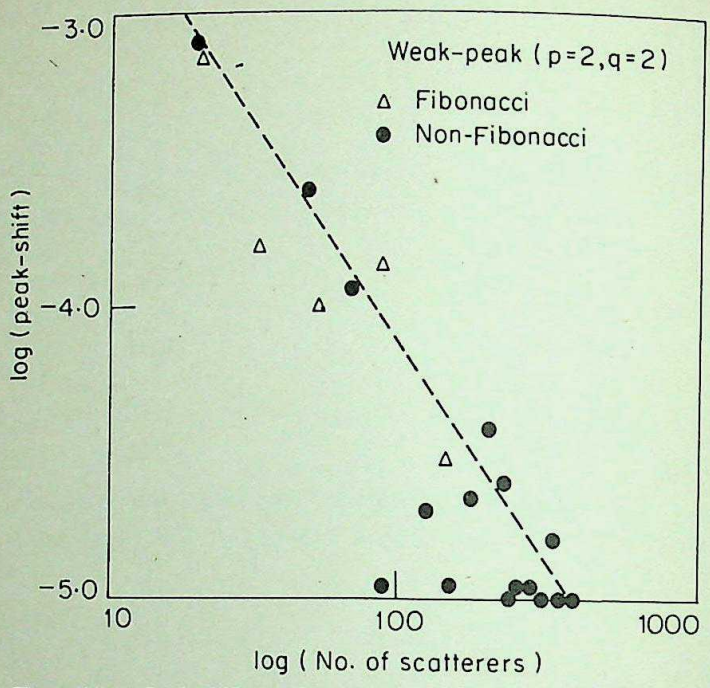

Figure 11a. Peak-shifts against number of scatterers is plotted in a log-log scale for the weak-peak ($p=2$, $q=2$). The asymptotic behaviour of the peak-shifts is shown by a dotted line. The peak-shift behaves almost like $N^{-3/2}$ for a large number of scatterers.

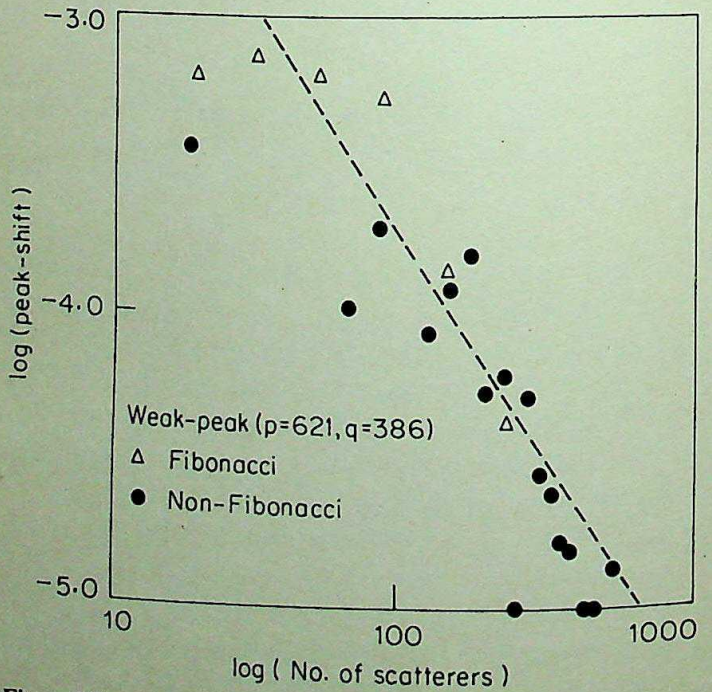

Figure 11b. Log-log plot of peak-shifts against number of scatterers for the weak peak far away from the origin ($p=621$, $q=386$). This also shows the similar asymptotic behaviour as the other weak peak.

CC-0. In Public Domain. Gurukul Kangri Collection, Haridwar

Digitized by Arya Samaj Foundation Chennai and eGangotri

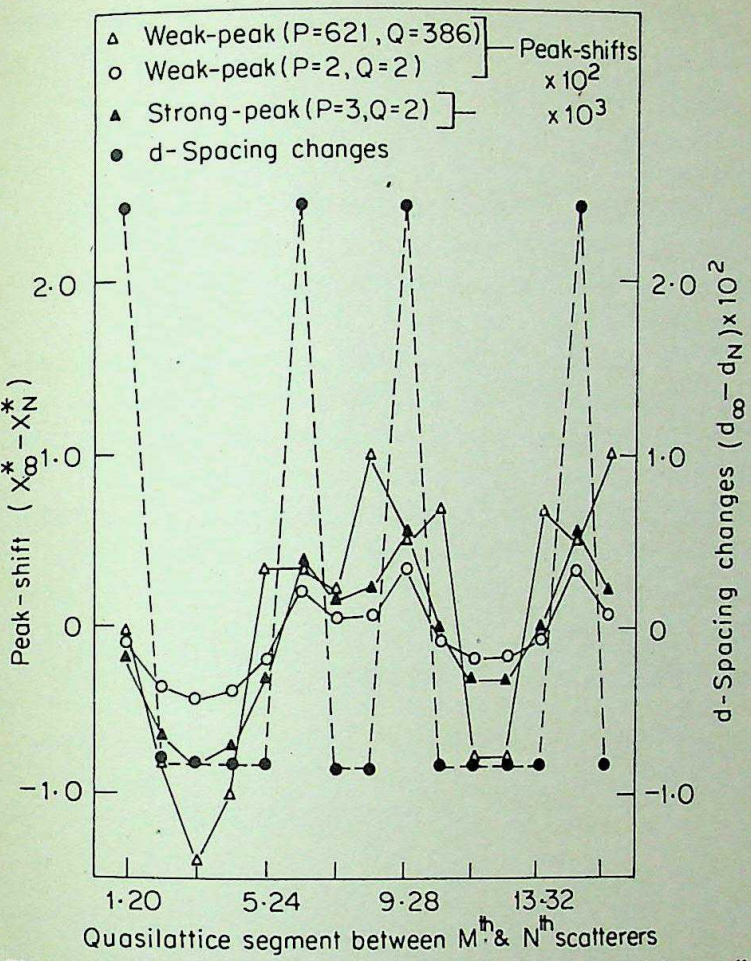

Figure 12. Peak-shifts corresponding to various segments of the quasilattice containing the same number of scatterers are shown. The dotted lines connect the d-spacings corresponding to various segments. The continuous lines connect the peak-shifts for various peaks.

peak-intensity variations nearer the origin when the size of the quasilattice and hence the boundary effects are changed.

The peak-positions of the diffraction from an infinite quasilattice have been worked out (Levine and Steinhardt 1986; Zia and Dallas 1986). But the peak-positions of the diffraction from a finite-size quasilattice will be different from that for the infinite quasilattice. The analytical methods of calculating the Fourier transforms of finite segments of Fibonacci quasilattices use the periodic boundary conditions of an infinite repetition of the finite segment. In the present case segments with a finite number of scatterers are discussed. This necessitates the use of numerical Fourier transformation to calculate the diffraction pattern. For the scattering from a truly finite number of points, the mean d-spacing and the boundary effects are noticeable.

In order to see whether similar effects are observable in the diffraction patterns of finite-size 1-d crystal, we calculated the Fourier transform of a 1-d crystal with interatomic spacings 1, τ, 1, τ, 1, τ,... (figure 13). We observed two kinds of peaks: strong and weak. Strong peaks occur at positions which are integral multiples of the inverse of the lattice spacing (Sommerfeld 1954). Weak peaks occur between the strong peaks. As the size of the crystal increases, the peak-width decreases. The strong peaks were found to have shifts in their position comparable with the computational error

CC-0. In Public Domain. Gurukul Kangri Collection, Haridwar

Digitized by Arya Samaj Foundation Chennai and eGangotri

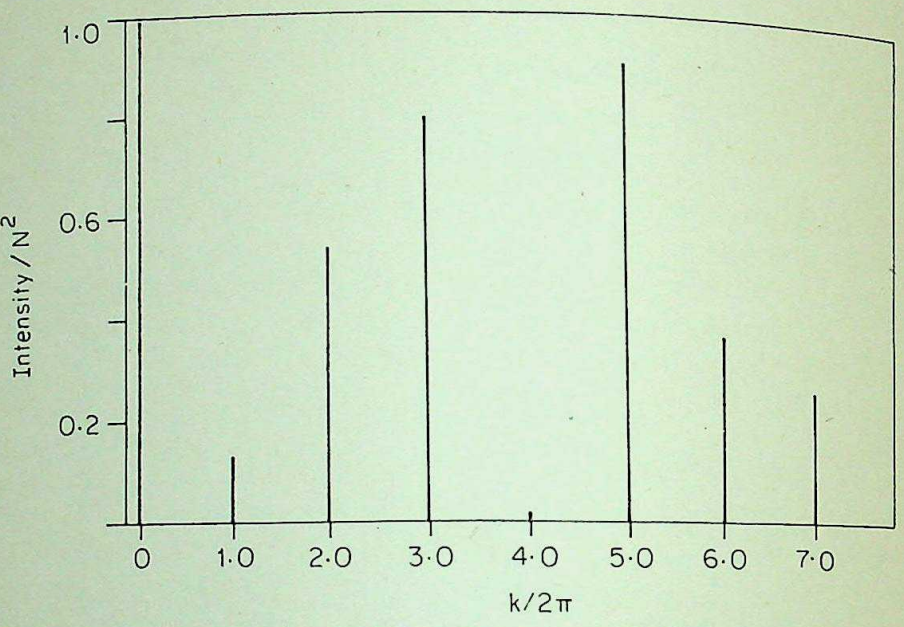

Figure 13. Diffraction pattern of 1-d crystal (1, τ, 1, τ,...) with 600 scatterers. The intensity of the strong peaks can be seen modulated in contrast to the diffraction from an undecorated lattice.

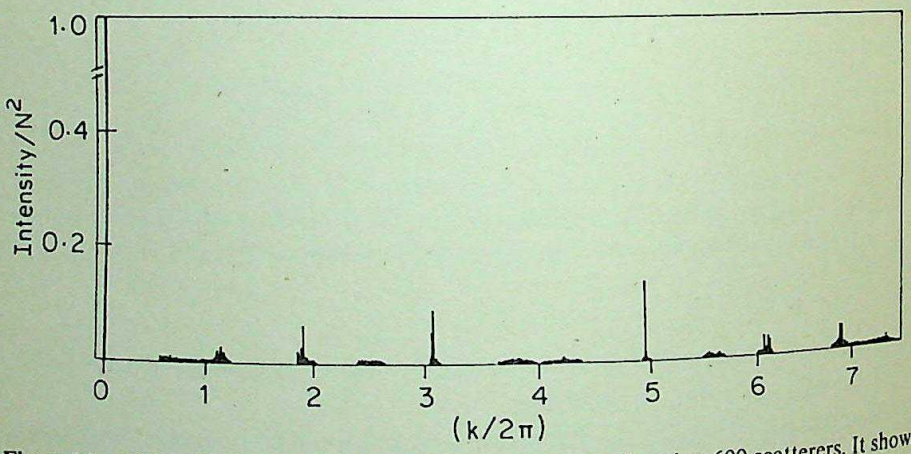

Figure 14. Diffraction from a random sequence of 1 and τ forming 600 scatterers. It shows clusters of peaks with large peak-widths.

even when the number of scatterers was as small as 5. The weak peaks were found to have shifts in their positions slightly more than that observed in the case of 1-d Fibonacci quasilattice.

In figure 14 the diffraction from a structure consisting of a random sequence of 1 and τ is shown. One can see clusters of peaks with large width compared to the 1-d Fibonacci quasilattice and also 1-d crystal. Only a few strong peaks are present when compared to the other two cases of ordered structures, within the same region of reciprocal space. The diffraction from a random structure with small number of scatterers shows many stronger peaks than from a large number of scatterers. When N is large, one tends to the situation of diffuse rings characteristic of glasses.

Recently, GaAs/AlAs and Nb/Cu Fibonacci superlattices have been grown by molecular beam epitaxial method by Todd *et al* (1986), Hu *et al* (1986), Gay and

CC-0. In Public Domain. Gurukul Kangri Collection, Haridwar

Digitized by Arya Samaj Foundation Chennai and eGangotri

Clemens (1987), and their diffraction properties have been studied using X-rays. The relevance of Fibonacci sequence to the 1-d quasicrystals (He *et al* 1988) discovered in Al-Ni-Si, Al-Cu-Mn and Al-Cu-Co has been pointed out (He *et al* 1988). Since peak-shifts are observed even when the number of scatterers is around 300, attempts to experimentally solve the sequencing of layers in one-dimensional quasicrystals, may have to take the peak-shifts into account. In fact, the finite segments of 1-d Fibonacci quasilattices have been used as the repeating unit in the structure factor calculations of vacancy ordered phases (Chattopadhyay *et al* 1987).

The distortions in the electron diffraction patterns of 3-d-quasicrystals have been explained only in terms of phason strain (Bancel and Heiney 1986; Budai *et al* 1987). Our calculations indicate that there will be considerable peak-shifts when the diffraction patterns of two different quasicrystalline grains of the same alloy or different regions of the same quasicrystalline grain are compared, even if the same amount of disorder is present. It has also been pointed out recently (Ma *et al* 1989), that ignoring the background in the diffraction pattern while calculating the Patterson function may lead to a shift in peak-positions and the disappearance or introduction of spurious peaks. It seems possible that peak-shifts can be observed experimentally at the resolution at which the X-ray diffraction experiments on Fibonacci superlattices have been performed by Terauchi *et al* (1988). The peak-positions and widths should change when the number of layers forming the Fibonacci superlattice is increased from a small value. Some attempts are being made to analytically find out the peak positions of the diffraction from finite size quasilattices.

Acknowledgements

We wish to thank Dr D Pandey for useful discussions. We are thankful to the referee for constructive comments. We thank Mr A Srinivasan for help in various ways. We are grateful to the Council of Scientific and Industrial Research and the Department of Science and Technology, India, for financial assistance.

References

Bruijn N G de 1981 *Kon. Nederl. Akad. Wetensch. Proc. Ser.* **A84** 39, 53
Bancel P A and Heiney P A 1986 *J. Phys. Colloq.* **47** C3-341
Budai J D, Tischler J Z, Habenschuss A, Ice G E and Elser V 1987 *Phys. Rev. Lett.* **58** 2304
Chattopadhyay K, Lele S, Thangaraj N and Ranganathan S 1987 *Acta. Metall.* **35** 727
Duneau M and Katz A 1985 *Phys. Rev. Lett.* **54** 2688
Elser V 1985 *Phys. Rev.* **B32** 4892
Elser V 1986 *Acta Crystallogr.* **A42** 36
Gay J G and Clemens B M 1987 *Phys. Rev. Lett.* **59** 2236
Gratias D and Michel L (Eds.) 1986 *Proc. Int. Conf. on Aperiodic Crystals*, Les Houches, (France). *J. Phys. Colloq.* **47** C3
Gratias D and Cahn J W 1986 *Scr. Metall.* **20** 1193
He L X, Li X Z, Zhang Z and Kuo K H 1988 *Phys. Rev. Lett.* **61** 1116
Hu A, Tien C, Li X, Wang Y and Feng D 1986 *Phys. Lett.* **A119** 313
Janssen T 1986 *J. Phys. Colloq.* **47** C3-85
Kramer P and Neri R 1984 *Acta. Crystallogr.* **A40** 580
Levine D and Steinhardt P J 1984 *Phys. Rev. Lett.* **53** 2477

CC-0. In Public Domain. Gurukul Kangri Collection, Haridwar

Digitized by Arya Samaj Foundation Chennai and eGangotri

Levine D and Steinhardt P J 1986 *Phys. Rev.* **B34** 596
Ma Y, Stern E A, Li X and Janot C 1989 Presented at the Int. Conf. Quasicrystals, Mexico City, May 29–2 June
Mackay A L 1982 *Physica* **A114** 609
Penrose R 1974 *Bull. Inst. Math. Appl.* **10** 216
Prince E 1987 *Acta. Crystallogr.* **A43** 393
Sasisekharan V 1986 *Pramana – J. Phys.* **26** L283
Shechtman D, Blech I, Gratias D and Cahn J W 1984 *Phys. Rev. Lett.* **53** 1951
Socolar J E S, Steinhardt P J and Levine D 1985 *Phys. Rev.* **B32** 5547
Sommerfeld A 1954 *Optics*, (New York: Academic Press)
Terauchi H, Noda Y, Kamigaki K, Matsunaka S, Nakayama M, Kato H, Sano N and Yamada Y 1988 *J. Phys. Soc. Jpn.* **57** 2416
Todd J, Merlin R, Clarke R, Mohanty K M and Axe J D 1986 *Phys. Rev. Lett.* **57** 1157
Valsakumar M C and Vijaykumar 1986 *Pramana – J. Phys.* **26** 215
Zia R K P and Dallas W J 1985 *J. Phys.* **A18** L341

CC-0. In Public Domain. Gurukul Kangri Collection, Haridwar

Digitized by Arya Samaj Foundation Chennai and eGangotri

Pramāṇa – J. Phys., Vol. 34, No. 6, June 1990, pp. 537–553. © Printed in India.

Generation of aperiodic tilings with fivefold symmetry by the method of intersecting decagons and diffraction from finite size tilings

S BARANIDHARAN, E S R GOPAL* and V SASISEKHARAN†

Department of Physics, †Molecular Biophysics Unit, Indian Institute of Science, Bangalore 560 012, India

MS received 23 November 1989; revised 26 February 1990

Abstract. A method for generating aperiodic tilings with five fold symmetry is discussed here. Basic patterns formed within decagons can be used to fill two dimensional space, by matching such suitable patterns. It appears to be possible to generate perfect tilings without retracing already established coordinates imposing conditions at the initial stages of generating them. Various possible ways to generate tilings, when perfectness is not required, are discussed. The calculated diffraction patterns for some representative finite size tilings are shown. There are subtle differences in the intensities of peaks in the diffraction patterns corresponding to different finite size tilings constructed using intersecting decagons. These effects persist for a larger number of scatterers in weak peaks than in strong peaks. They are unaffected by an introduction of systematic disorder. These effects could be termed as the finite size boundary effects. There are also small shifts in the peak positions owing to the finite size effects. The possibility of formation of large approximate square cells in large tilings is shown.

Keywords. Tilings; symmetry; nonperiodic; diffraction.

PACS No 61·50

1. Introduction

The unusual interest in the quasicrystalline materials is undoubtedly due to the observation of electron diffraction spots with fivefold symmetry, normally forbidden in classical crystallography (Shechtman *et al* 1984). Recently, the concept of aperiodic space filling in two dimensions with fivefold symmetry has been widely discussed. The extension of the ideas to the aperiodic filling of space in 3-dimensions with icosahedral or related fivefold symmetric objects is generally considered to be the basis for understanding the experimental observations. The contact with the experimental studies of the quasicrystals is generally made through the electron or the X-ray diffraction measurements. These require a consideration of the Fourier transforms of the real space structures and have been discussed by many authors. The details of the atomic positions are as yet unknown in any of the quasicrystalline materials. Nevertheless, some aspects of the transforms are of interest, if they are explicit calculations of well defined models which could be used at least as limiting cases of experimental situations. In this article we present such aspects of the problem. A preparatory section deals with the aperiodic tilings of the 2-D plane with fivefold

*To whom correspondence should be addressed

CC-0. In Public Domain. Gurukul Kangri Collection, Haridwar

Digitized by Arya Samaj Foundation Chennai and eGangotri

symmetry in a brief pedagogic way so that different results can be discussed in a compact self-contained manner.

The aperiodic tiling of a 2-D plane with 5-fold symmetry using kites and darts was first initiated by Penrose (1974) and discussed later by Mackay (1982). An algebraic analysis of Penrose tilings has been carried out by de Bruijn (1981). The possibility of tiling a plane with any given symmetry was first shown by Sasisekharan (1986) who also discussed briefly the method of intersecting decagons described in detail here. The projection from hypercubic lattices has also been a technique to produce quasiperiodic tilings (Levine and Steinhardt 1984; Kramer and Neri 1984; Kalugin *et al* 1985; Elser 1985; Prince 1987; Gratias and Michel 1986; Ostlund and Wright 1986). Similar tilings can also be obtained as cuts from six-dimensional lattices (Bak 1986). A general method to produce quasiperiodic patterns in arbitrary dimensions was shown by Duneau and Katz (1985). A generalised dual method for generating quasicrystal structures with arbitrary orientation was introduced by Socolar *et al* (1985). The diffraction properties of these tilings have been evaluated based on the reason that the tilings are of infinite size and they are obtained by a bounded projection technique. In this particle we calculate the diffraction properties of perfect Penrose tiling and other tilings, that are of finite size, generated by using the method of intersecting decagons. We show that the finite size effects are not affected by an introduction of a small amount of local disorder. When perfectness is not demanded, various tilings can be generated by different choices of the intersecting decagons.

2. Pentagonal tiling of 2-D space

The elementary idea of similar triangles forms a simple self similarity principle for inflation/deflation to tile the space completely. In a ΔABC with the $\angle BAC = \theta$ one can create a similar smaller ΔBCD with the $\angle BCD = \theta$ (figure 1a). This idea enables one to inflate or deflate regions of similar structures. While triangles can indeed be used as the basis for discussion, it is advantageous to use the more familiar rhombuses. In figure 1b, from the basic isosceles triangle OAB of a decagon a smaller similar ΔABC is formed. The juxtaposition of the similar triangles gives two different rhombuses. These rhombuses ACDB, OCAE may be called the acute $(\alpha, 4\alpha)$ and the obtuse $(2\alpha, 3\alpha)$ respectively, where the angle $\alpha = \pi/5$. Five of each type of the rhombuses are inscribed in the decagon. However this inscribing can be done in different ways. Four different ways A, B, C, D of arranging the rhombuses within a decagon are

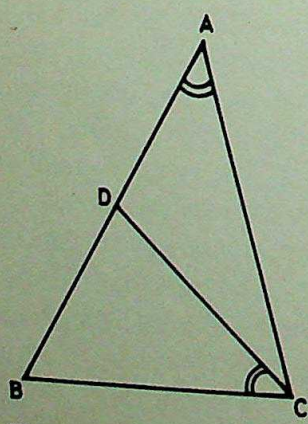

Figure 1a. The triangles ABC and BCD are similar.

CC-0. In Public Domain. Panini Kanya Maha Vidyalaya Collection, Haridwar

Digitized by Arya Samaj Foundation Chennai and eGangotri

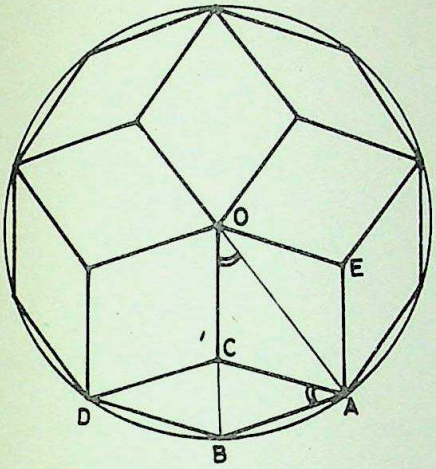

Figure 1b. The basic isosceles triangle ABO of a decagon is divided into two isosceles triangles ACO and ABC which lead to the formation of rhombuses.

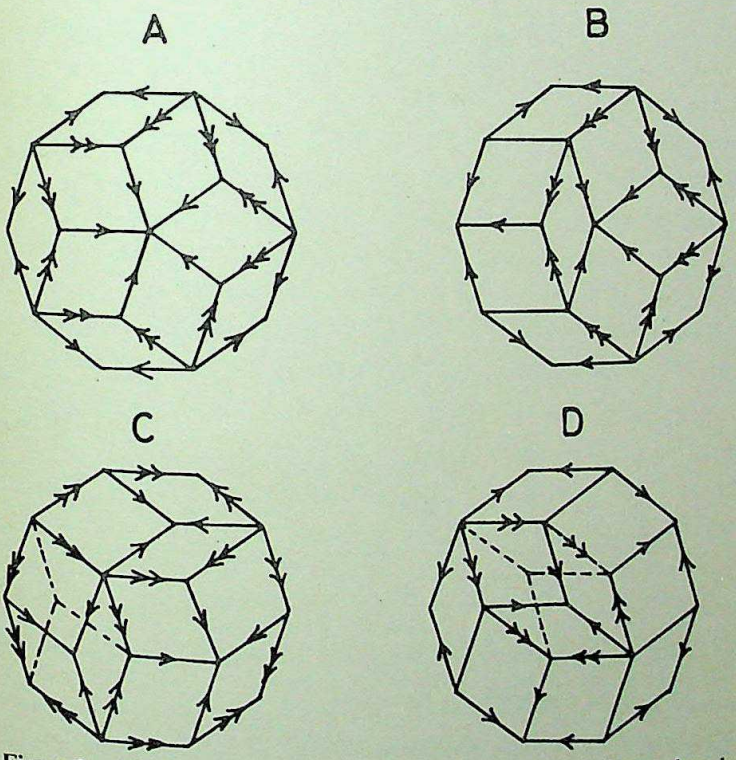

Figure 2. The four basic arrangements of the acute and obtuse rhombuses inside a decagon.

shown in figure 2. These four patterns A, B, C, D are formed so as to possess at least one mirror plane. The modifications in these patterns (shown by dotted lines) lead to very similar results. In the case of pattern C the mirror plane is destroyed during such a modification. The four different patterns A, B, C, D are shown along with the arrows indicating the Penrose matching rule. It is readily seen that the patterns A and C do not violate the matching rule while the patterns B and D do.

In order to complete the tiling of the entire plane, one proceeds to match the suitable choices of the four patterns A, B, C, D. For the clarity of illustration the decagonal patterns are inscribed in circles. It can be seen that two decagons inscribed in circles can share one, two, three or four edges such that the distance between their centres are $R1$, $R2$, $R3$ and $R4$ respectively, as shown in figure 3. Since the radius of

CC-0. In Public Domain. Gurukul Kangri Collection, Haridwar

Digitized by Arya Samaj Foundation Chennai and eGangotri

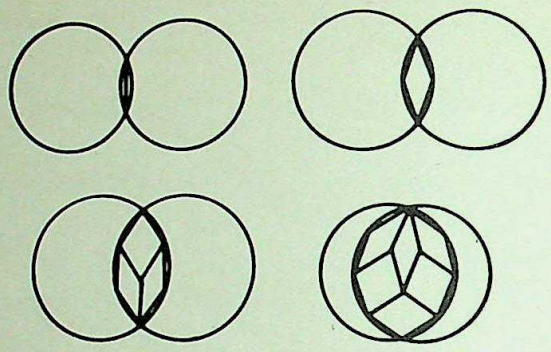

Figure 3. Two decagons inscribed in circles for clarity, can share one, two, three or four edges. Only the shared edges of the decagon are shown.

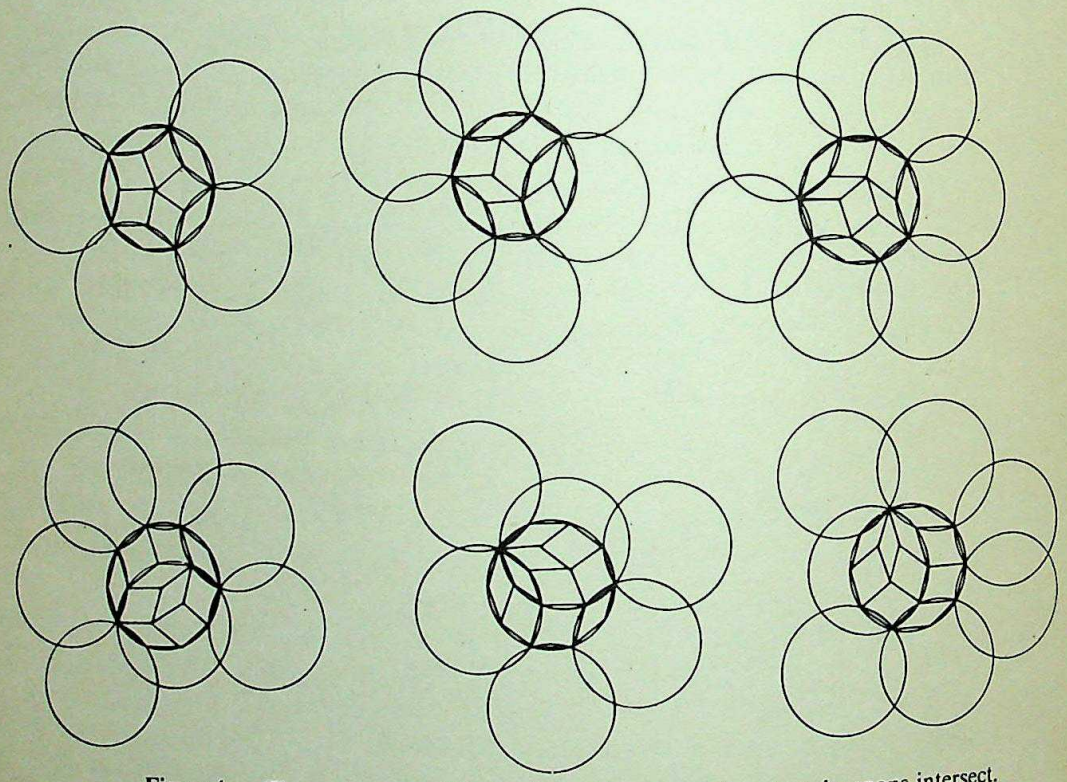

Figure 4a. The various possible sharings when more than two decagons intersect.

the circle (R), the edge of the rhombus (R/τ) where τ is the golden mean) and the distance between the centres of the two circles ($R1$, $R2$, $R3$, $R4$) bear fixed relationships, the sharings can easily be proved, the proof being omitted here for the sake of brevity. When two such circles intersect, the common area between them can be occupied by one edge of a rhombus, or, one acute rhombus, or, one obtuse plus two acute rhombuses or three acute plus three obtuse rhombuses depending upon the distance ($R1$, $R2$, $R3$, $R4$) between the centres of the circles. Next, one sees that a circle at the centre can intersect 3, 4, 5, 6 or 7 circles surrounding it as shown in figure 4a.

By a choice of intersecting decagons it is possible to generate tilings with any combination of two or more basic patterns. As stated before basic patterns A and C do not individually violate Penrose matching rule but arbitrary combination of these two patterns cannot be expected to behave so. Nevertheless, it can be stated that an arbitrary combination of A and C patterns may contain lesser disorder than other arbitrary combinations involving B and D patterns.

CC-0. In Public Domain. Gurukul Kangri Collection, Haridwar

Digitized by Arya Samaj Foundation Chennai and eGangotri

3. Random generation of patterns

Large tilings can be generated by computers to perform the operation recursively. In this example, the coordinates of the four basic patterns A, B, C, D are initially calculated numerically, with an arbitrary choice of the coordinate axes and stored in subroutines. The pattern A is chosen at the origin and the radius of the circle circumscribing it is '*R*'. The distance of the next intersecting circle can only be *R*1, *R*2, *R*3 or *R*4 (from figure 3). Starting from pattern A at the origin a random number is chosen from 1, 2, 3 and 4, that determines the distance *R*1, *R*2, *R*3 or *R*4 of the next pattern. In case there is no proper sharing between the two patterns, the new pattern is rotated by 18° successively until all possible rotations are exhausted. The next random number is called if any rotation of the new pattern is unsuitable for matching. The coordinates of the new pattern after proper rotation is stored along with the starting pattern after eliminating repetitions. Subsequent patterns are also generated in a similar fashion such that any two patterns satisfy the possible sharings. An example of a tiling generated using basic patterns A and C is shown in figure 4b. This tiling as expected does not possess a true fivefold origin. If a true fivefold axis is to be preserved at the origin, the tiling can be generated interactively with the computer by retracing some of the already generated coordinates which in a way can be thought of as a trial and error method. At this point it is appropriate to mention that while the Penrose matching rule does not permit two adjacent rhombuses to be parallel, such a situation can arise in this method of intersecting decagons. In fact figure 4b contains many local regions where two adjacent rhombuses are parallel and these configurations are termed as defects. The method of projection also does not permit this possibility (Whittaker and Whittaker 1988). The tilings with such defects cannot be classified as random (glass like) tilings because of the fact that more than

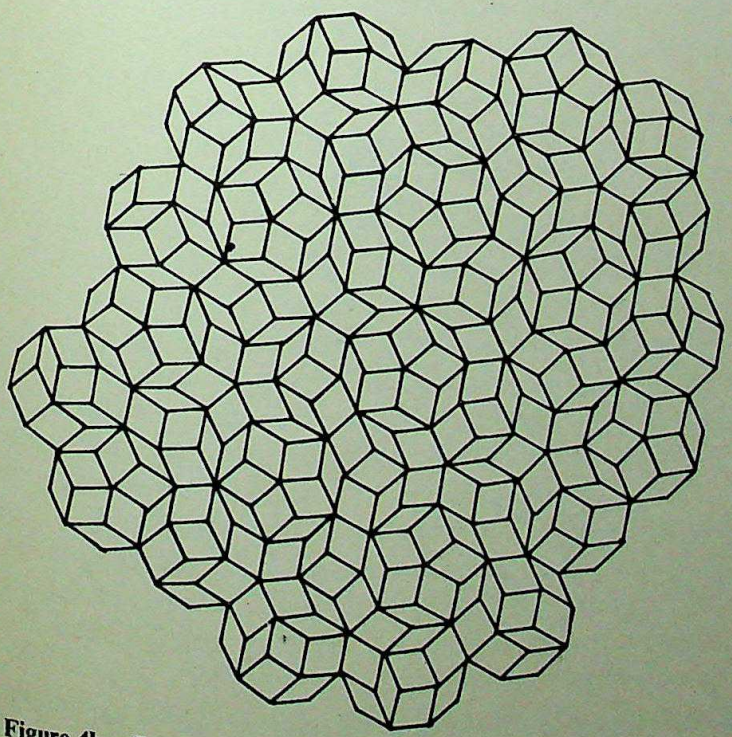

Figure 4b. Randomly generated tiling with A and C basic patterns.

CC-0. In Public Domain. Gurukul Kangri Collection, Haridwar

Digitized by Arya Samaj Foundation Chennai and eGangotri

two adjacent rhombuses will not be parallel to each other in any situation. This is because first of all the basic decagonal patterns shown in figure 2 do not contain two adjacent, parallel rhombuses and so any possible rotation of an adjacent decagonal pattern can utmost lead to only one rhombus being parallel to another adjacent rhombus. When the tiling is constructed with A and C decagonal patterns obeying the Penrose matching rule, then the final tiling obtained belongs to the Penrose local isomorphism class. The tilings generated using the other basic patterns without having adjacent rhombuses parallel, then they can also be constructed by the generalized dual grid method. Wherever adjacent rhombuses occur in parallel, they can be considered to be localized defects, since a local modification involving any one of the rhombuses can eliminate the defect.

4. Generation of perfect tilings

The generation of a perfect Penrose tiling can be achieved in two ways. One will be to follow the inflation rule procedure where basic rhombuses are inflated. The other will be the tiling approach in which either rhombuses can be matched or in a similar way the basic patterns A and C can be matched. In the latter method it is necessary to retract sometimes the already generated coordinates (Steinhardt and Ostlund 1987) when the tiling is generated using a computer. One way to avoid the retracting of coordinates would be as follows: We stated earlier that not more than two rhombuses can occur adjacent parallel to each other when the tiling is made of the basic decagonal patterns. The pattern C has more than one possible orientation inside the decagon. Hence a proper reorientation of pattern C at the first stage of generation itself will result in a perfect tiling. Figure 5a illustrates the occurrence of a defect when using the decagons and also how to rectify the defect without altering the rest

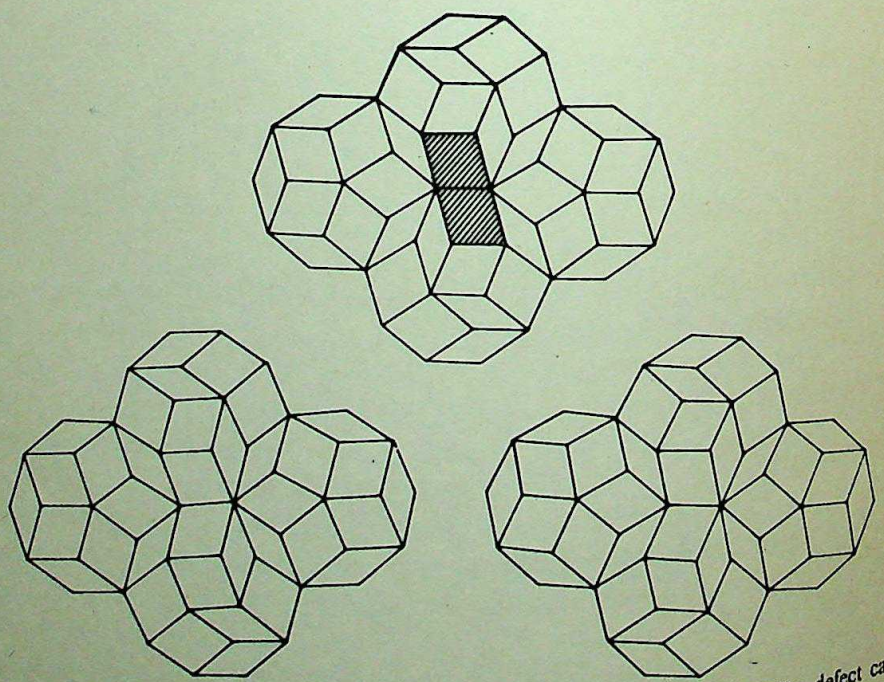

Figure 5a. Occurrence of a defect while matching patterns A and C. The defect can be eliminated by rearranging a hexagon or by reorientation of a decagon as shown in the figure.

CC-0. In Public Domain. Gurukul Kangri Collection, Haridwar

Digitized by Arya Samaj Foundation Chennai and eGangotri

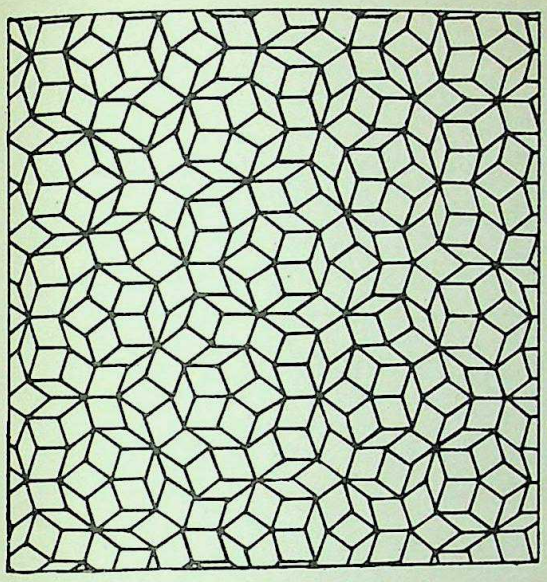

Figure 5b. A section of a perfect Penrose tiling made by matching A and C basic decagonal patterns.

of the tiling. This way to avoid defects is easily achieved with an interacting computer. Figure 5b shows a section of a perfect Penrose tiling made by matching basic patterns A and C such that they obey the Penrose matching rule by reorienting the C pattern if and when a local defect occurred.

5. Fourier transforms

The Fourier transforms are needed in diffraction studies of quasicrystalline samples of the type used experimentally with electrons or X-rays. These have been calculated numerically on the basis

$$F(h,k) = \sum_j f_j \exp\left[2\pi i(hx_j + ky_j)\right]$$

where $F(h,k)$ is the structure factor, (x_j, y_j) are the coordinates of the scatterer with an atomic scattering factor f_j. In order to get well defined situations scatterers of unit scattering factor ($f_j = 1$) have been placed at the vertices of the rhombuses. The numerical method has been resorted to because of the finite nature of the tilings and due to the possible disorder in them. The analytic techniques are useful in calculating the diffraction patterns for a generic class of tilings but they cannot be used to find subtle differences arising out of disorder of the type discussed earlier as well as the finite size of the tilings.

In order to check explicitly the coherence of the scattering from various tilings, an arbitrary tiling using the basic arrangements A and C was generated (figure 6) and a circular region containing about 200 scatterers is taken. The Fourier transform of figure 6 is shown in figure 7, where a cut-off at 4% of the peak intensity has been used in the plotting to pick out the more significant peaks. In figure 7 the size of the spot corresponds to the intensity of the diffracted spot. The diffraction pattern has the fivefold symmetry as is to be expected.

CC-0. In Public Domain. Gurukul Kangri Collection, Haridwar

Digitized by Arya Samaj Foundation Chennai and eGangotri

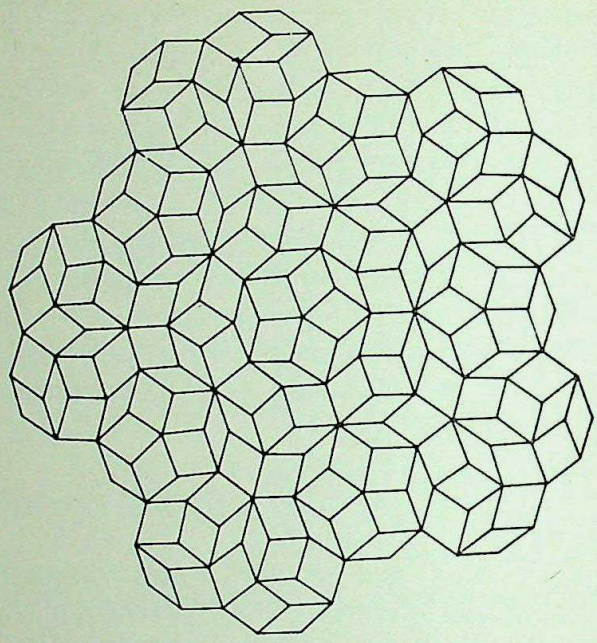

Figure 6. A small section of a tiling made of A and C patterns.

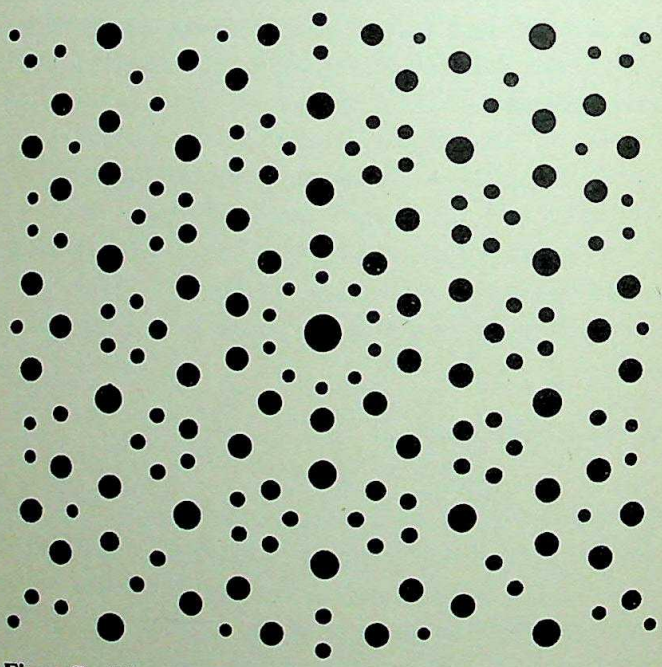

Figure 7. The diffraction pattern corresponding to the tiling shown in figure 6.

The tiling of the 2-D plane can be done with other basic patterns as mentioned earlier. As an example, figure 8 shows the tiling where patterns A and D are used to generate the tiling. A circular region containing again about 200 scatterers was chosen from the tiling and its Fourier transform was calculated. The resulting diffraction pattern is shown in figure 9 where 4% cut-off was used while plotting.

One notices specific differences though the same cut-off has been used between figures 7 and 9. In figure 7 starting from the central peak, one has two rings of 10 strong spots, followed by a third weak ring of 10 spots. However in figure 9 this third

CC-0. In Public Domain. Gurukul Kangri Collection, Haridwar

Digitized by Arya Samaj Foundation Chennai and eGangotri

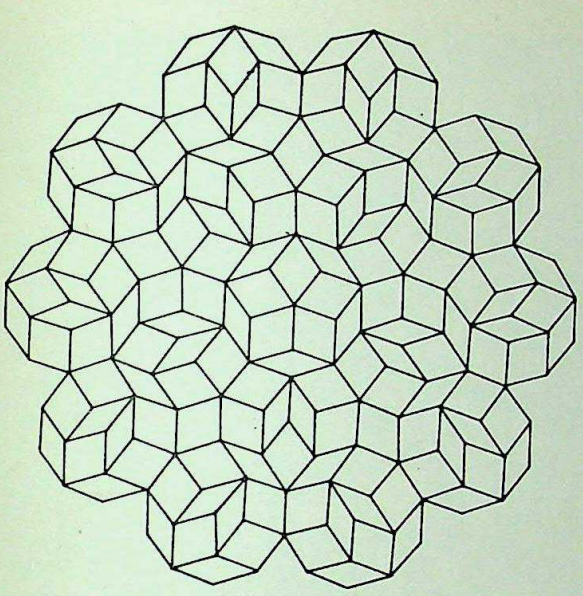

Figure 8. A small section of a tiling made of A and D patterns.

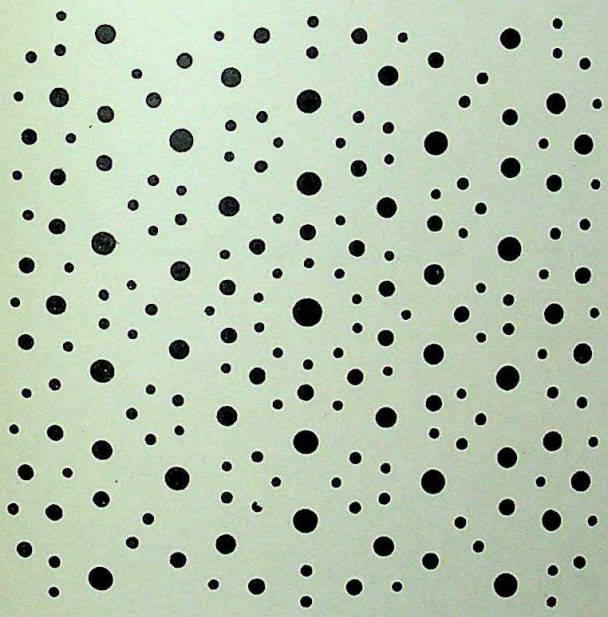

Figure 9. The diffraction pattern corresponding to the tiling shown in figure 8.

ring of 10 spots is absent at the 4% cut-off. Their intensities are about 2% of the peak values and so are not present in figure 9, while they are about 10% in figure 7. Again the pentagonal symmetrically located spots have different intensities. These differences could be interpreted as arising out of the finite nature of the tilings. A comparison of figure 7 and figure 9 with figure 10 which is an electron diffraction pattern taken from a fivefold axis of a grain of Al–Mn icosahedral phase shows that the agreement is better between figure 7 and figure 10.

It is also of great interest to see the nature of scattering from different sections of the same tiling. Figure 11 shows the circular region of a tiling with A and C patterns. This figure possesses a true fivefold axis at the origin and more than 1000 scatterers. Figure 12 shows the diffraction pattern of figure 11 with 1% cut-off. Figure 13 shows the circular region of a tiling again with A and C patterns, but the true fivefold

CC-0. In Public Domain. Gurukul Kangri Collection, Haridwar

Digitized by Arya Samaj Foundation Chennai and eGangotri

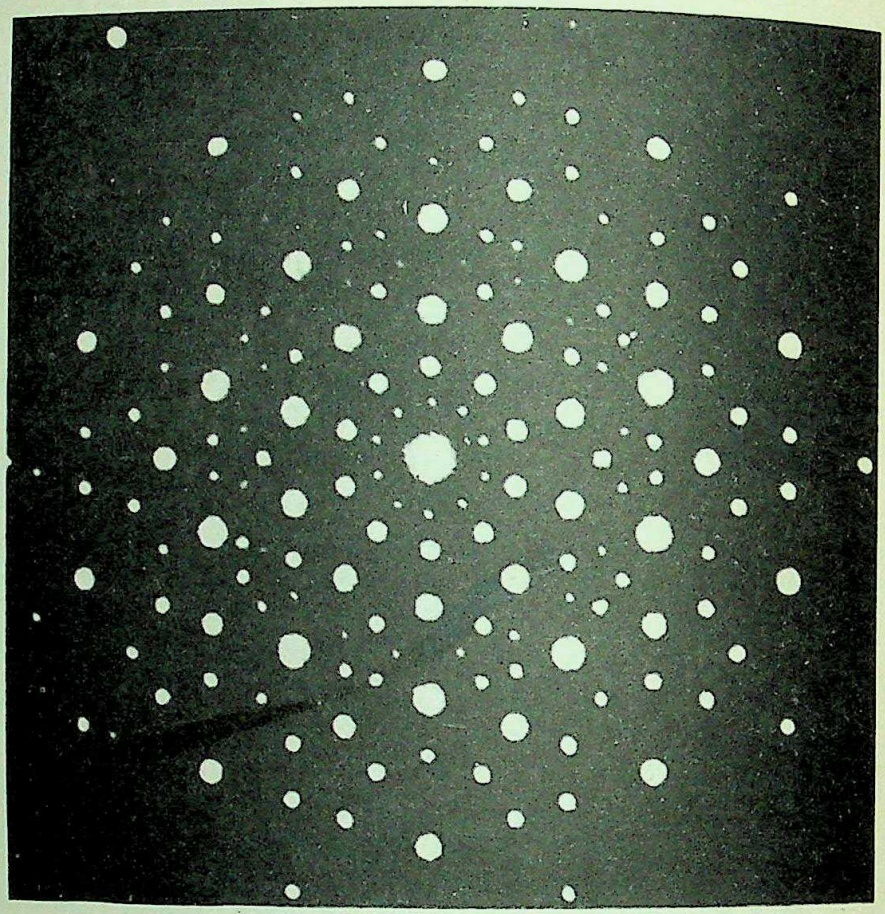

Figure 10. The electron diffraction pattern taken from a grain of Al–Mn icosahedral phase. Compare the position and intensity of the peaks with those in figure 7 and in figure 9.

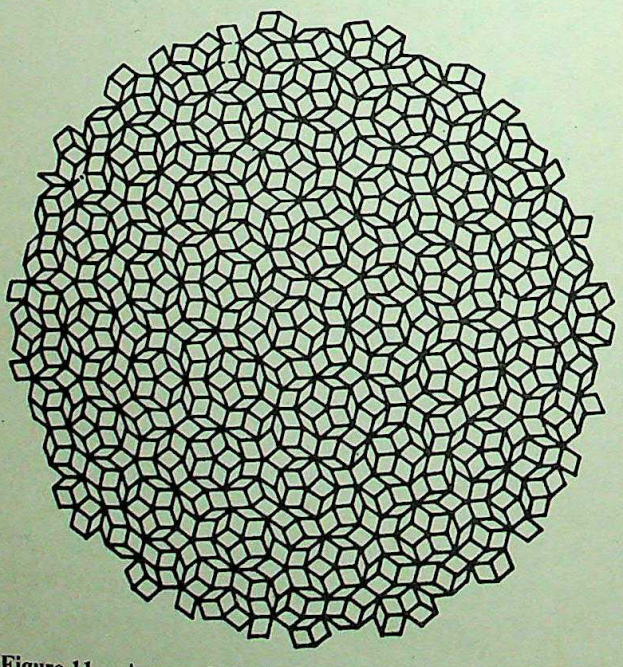

Figure 11. An aperiodic tiling with true fivefold symmetry at the origin with nearly 1000 verticies.

CC-0. In Public Domain. Gurukul Kangri Collection, Haridwar

Digitized by Arya Samaj Foundation Chennai and eGangotri

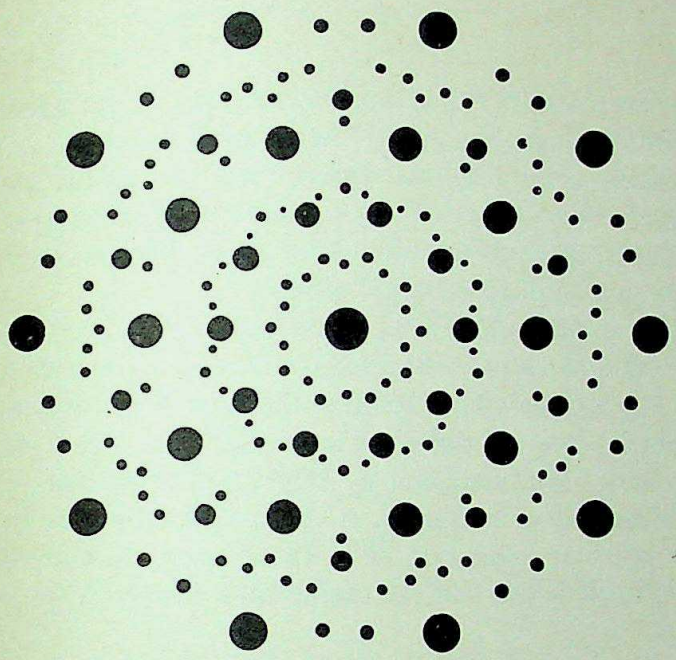

Figure 12. Diffraction pattern corresponding to the tiling shown in figure 11.

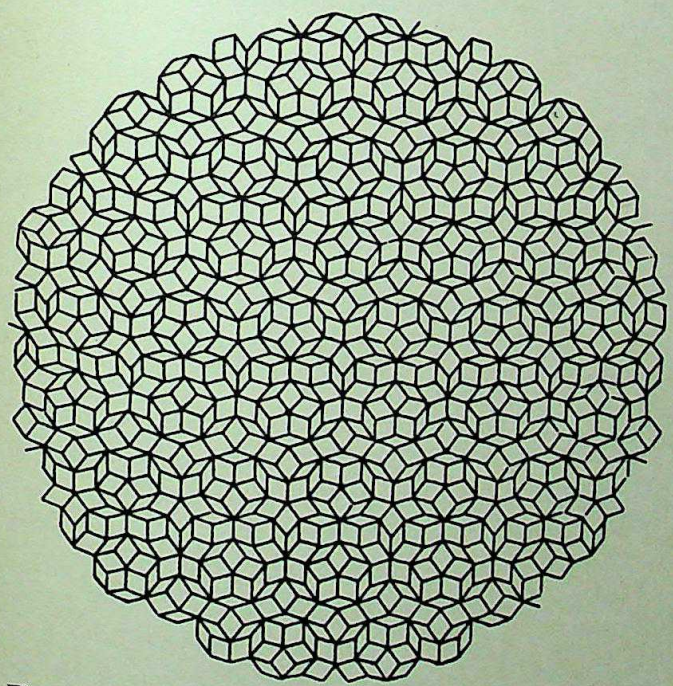

Figure 13. An aperiodic tiling without the true fivefold symmetry origin and with nearly 1000 vertices.

symmetry axis is destroyed. The true fivefold axis can be considered to be at some other arbitrary point outside the tiling. The calculated diffraction pattern of this tiling is not significantly different from the diffraction pattern (figure 12) although there are some small differences in the intensities of very weak spots. This implies that the location of the true fivefold axis is not significant as regard to the coherency of scattering.

CC-0. In Public Domain. Gurukul Kangri Collection, Haridwar

Digitized by Arya Samaj Foundation Chennai and eGangotri

6. Finite size effects

A study of finite size effects becomes important because one of the relevant models for quasicrystals is the icosahedral glass model (Stephens and Goldman 1986). If the icosahedral clusters possess a orientational order then the diffraction from the quasicrystalline phase can be considered to be as a result of diffraction from individual clusters. While the particle size effects are known for crystalline phases, such effects have not been evaluated so far for quasicrystal models.

The finite size effects on some selected peaks have been calculated by varying the number of scatterers. These effects have been calculated for the tiling with true fivefold symmetry axis (figure 11), for the tiling without the true fivefold symmetry axis (figure 13) and for the perfect Penrose tiling shown in figure 5b. These effects for the strong and weak peaks have been calculated by following the intensity of the peak, $I(N)$ as a function of the number of scatterers, N. Figure 14 shows the behaviour of the intensity of various peaks as a function of N. In all cases there are fluctuations when the number of scatterers is less and the oscillations disappear for large values

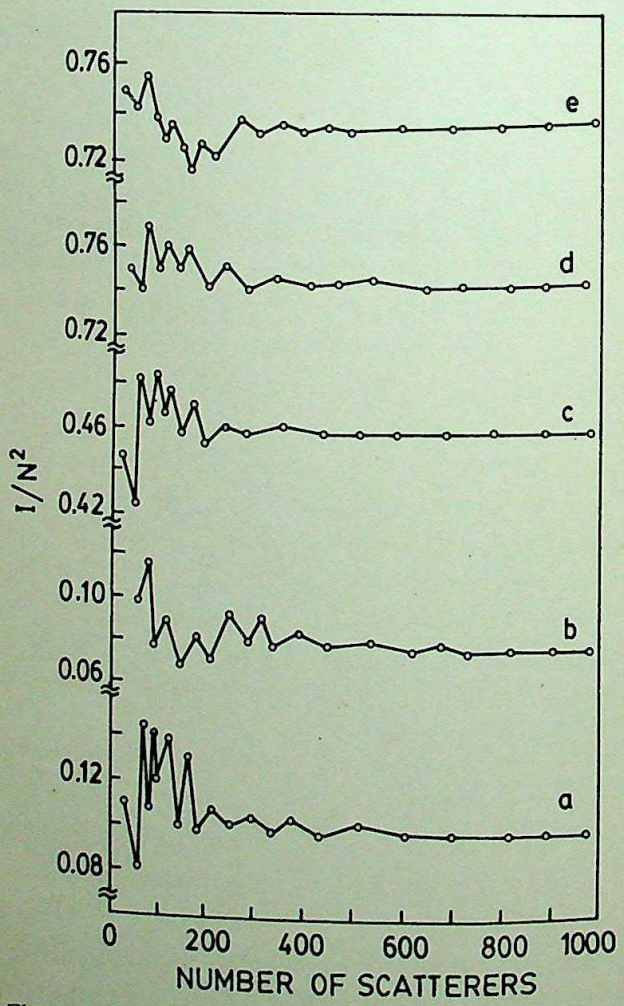

Figure 14. (a) The finite size effects on the intensity of a weak peak from the diffraction from figure 11; (b) the finite size effects on the intensity of a weak peak for figure 13; (c) the finite size effects on the intensity of a strong peak from the diffraction from the perfect Penrose tiling shown in figure 5b; (d) the finite size effects on the intensity of a strong peak for figure 11; (e) the finite size effects on the intensity of a strong peak for figure 13.

CC-0. In Public Domain. Gurukul Kangri Collection, Haridwar

Digitized by Arya Samaj Foundation Chennai and eGangotri

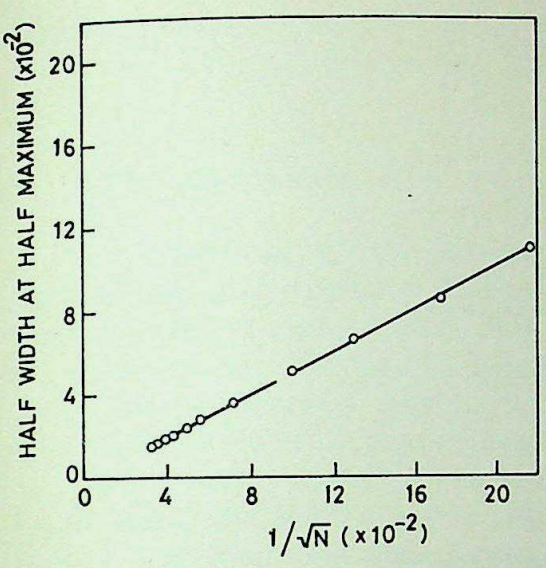

Figure 15. The half width at half maximum as a function of the number of scatterers.

of N. In the case of weak peaks the size effects last for a slightly larger number of scatterers ($N \sim 400$) as compared to the strong peaks where the effects are present up to $N \sim 300$. Also seen from figure 14 is that the size effects are present for the perfect Penrose tiling. It is clear from this figure that defects in a small proportion do not affect the intensity of the peaks as much as the size effects do.

The peak broadening of the same peak considered in the case of the perfect tiling has been monitored as a function of number of scatterers. Figure 15 shows the variations of the half width at half maximum of the peak as a function of $1/\sqrt{N}$. The slope of the straight line is an analogue of the familiar Scherrer constant. The HWHM is found to be just inversely proportional to the number of scatterers along the reciprocal vector considered very similar to the cases of crystalline materials. The experimental observation of large peak widths in quasicrystal diffraction may possibly support the icosahedral glass model where the individual icosahedral clusters could actually resemble a small tiling with a small number of scatterers. The shifts in a peak position (Socolar *et al* 1986) have also been evaluated as a function of the number of scatterers for a strong peak in the diffraction from the perfect tiling. It is seen from figure 16 that the shifts in a mean peak position become negligible when N goes above 300.

Another way of studying the finite size effects is to study the diffraction side-lobes in the fine structure of the shape of the spots. Figures 17 and 18 show the scan of the h-axis for $N = 100$ and $N = 500$ referring to the diffraction in figure 12. The sharpening of the peaks and the movements of the side-lobes towards the peak when the number of scatterers is increased, is a direct reflection of the effect of the finite size of the tiling and the coherence among the contributions from the different scatterers. The sharpening of the peaks and the movements of the side-lobes also indicate a necessity to locate the exact peak positions for every N. The exact peak positions (within an absolute error of 10^{-5} have been located for every N in all the above analyses by maximising the intensity until any further refinement in the peak positions does not affect the intensity values significantly. We have shown qualitatively that there are shifts in peak positions and fluctuations in the intensity of peaks due to finite size of the tilings irrespective of the perfect or imperfect nature of the tiling.

CC-0. In Public Domain. Gurukul Kangri Collection, Haridwar

Digitized by Arya Samaj Foundation Chennai and eGangotri

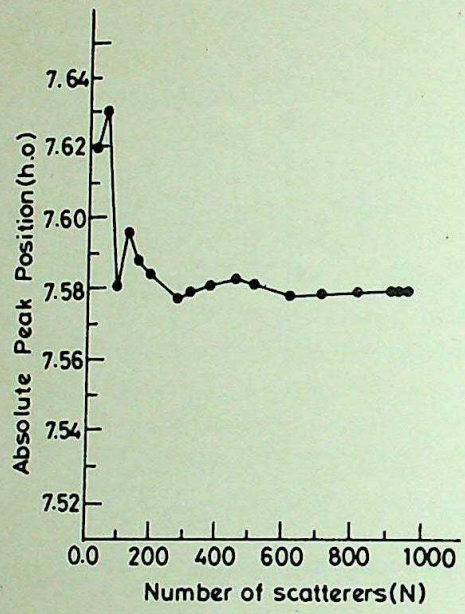

Figure 16. Shifts in a peak position as a function of number of scatterers.

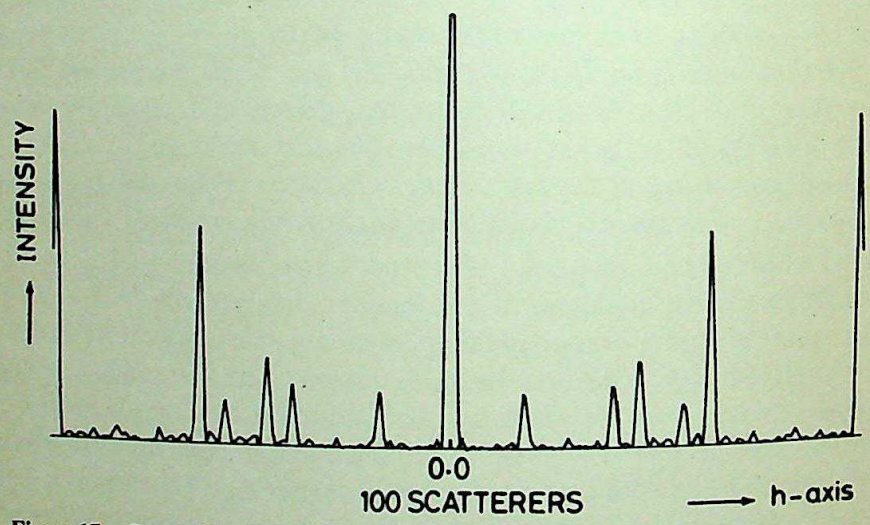

Figure 17. Scan of h-axis of figure 12 for $N = 100$.

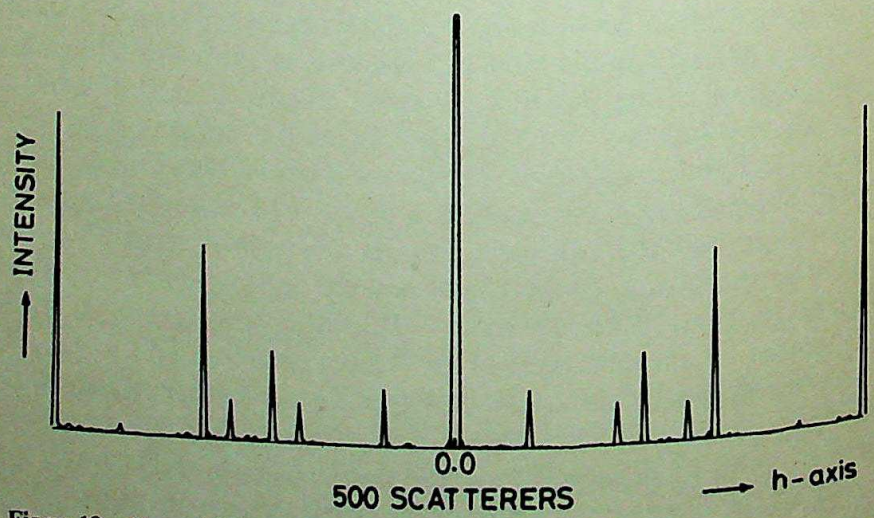

Figure 18. Scan of h-axis of figure 12 for $N = 500$.

CC-0. In Public Domain. Gurukul Kangri Collection, Haridwar

Digitized by Arya Samaj Foundation Chennai and eGangotri

Clearly the peak shifts, defects and dislocations, half widths of the peaks, peak profiles and other intensity statistics are also of interest. These will be reported in due course.

7. Formation of nearly square lattices

It was pointed out by Sasisekharan (1986) that pentagonal tilings can have regions of apparent, approximate square symmetry. This can be seen from figure 19 where a tiling with A and C basic patterns is drawn, showing the true fivefold symmetric origin and the extended region. The thick lines connecting the centres of the local fivefold symmetries form a hexagonal pattern. On the extended region of figure 19 one has marked with broken lines, the approximate square cells. One side of the cell is larger than the other side by 2·5%. The angles formed by the broken lines are exactly 90°. On extending the drawing further it is possible to have larger cells of approximate square shape with lesser error. Given the ion sizes of Al and Mn, the cell shown in figure 19 has an edge of about 30 Å, very comparable in size to the cells proposed by Pauling (1987) in the twinning model of quasicrystals. The Fourier transforms of the vertices from the square regions of figure 19 is shown in figure 20. The number of vertices within the square regions is ~ 300.

The basic patterns used in figure 19 are A and C. Therefore the diffraction pattern (figure 20) should be compared with figure 12 which is the Fourier transform of the tiling in figure 11 containing basic patterns A and C. In figure 20 the arrowed spots arranged in a twofold configuration are slightly more intense (1%), although not visually observable, than the other spots in the same layer. The vertices inside the approximate square region in figure 19 are themselves arranged with a mirror symmetry and hence the diffraction pattern shows a deviation from figure 12. Also we earlier stated that the finite size effects tend to settle down for $N > 300$. In order to determine if the boundary effects are persistent significantly for $N > 300$, a set of 4 such approximate square cells ($N \sim 1150$) adjacent to each other has been considered

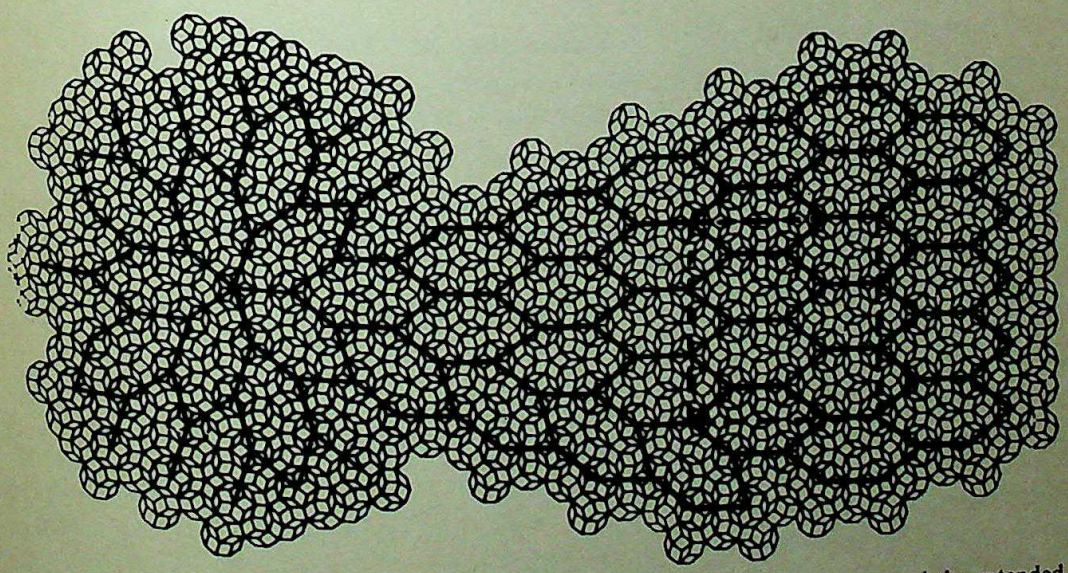

Figure 19. A large section of an aperiodic tiling with fivefold symmetry and the extended region. Also observe the hexagonal superstructure and the approximate square cell marked by the dotted lines.

CC-0. In Public Domain. Gurukul Kangri Collection, Haridwar

Digitized by Arya Samaj Foundation Chennai and eGangotri

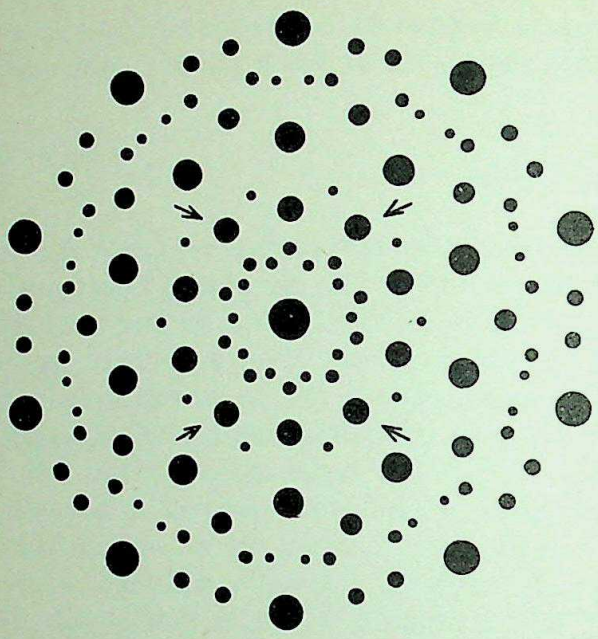

Figure 20. The computed diffraction pattern of the contents of the approximate square cell marked in figure 19.

and its Fourier transform was calculated. The resulting diffraction pattern was very similar to figure 12 within computational error. Hence we conclude that the diffraction from approximate square cells could bear resemblance to the diffraction from truly aperiodic structures. In the absence of standard methods to determine the structure of the quasicrystals either in the form of rhombohedrons or in the form of icosahedral clusters, it may be possible to approximate the structure to a near cubic symmetry and followed up experimentally.

Acknowledgements

The authors are grateful to Prof. S Ramaseshan and Prof. R Nityananda of Raman Research Institute, Bangalore for their comments and discussions on Penrose tilings. The suggestions and assistance of Messrs. V S K Balagurusamy, T Narasimhamurthy, M Sundaramoorthy and other colleagues have been invaluable and we thank them for the same. We also thank Prof. M A Viswamitra for his interest in our work on tilings and X-ray diffraction from quasicrystals. We thank the referee for explaining the peak broadening nature and for suggesting other improvements. This work is part of the research carried out on quasicrystals funded by the Department of Science and Technology, Government of India.

References

Bak P 1986 *Scr. Metall.* **20** 1199
de Bruijn N G 1981 *Proc. Ned. Acad. Wet. Ser.* **A84** 39
Duneau M and Katz A 1985 *Phys. Rev. Lett.* **54** 2688
Elser V 1985 *Phys. Rev.* **B32** 4892
Gratias D and Michel L 1986 *J. Phys.* (*Paris*) **47** C3

CC-0. In Public Domain. Gurukul Kangri Collection, Haridwar

Digitized by Arya Samaj Foundation Chennai and eGangotri

Kalugin P A, Kitayev A.Yu and Levitov L S 1985 *J. Phys. Lett.* **46** L601
Kramer P and Neri R 1984 *Acta Crystallogr.* **A40** 580
Levine D and Steinhardt P J 1984 *Phys. Rev. Lett.* **53** 2477
Mackay A L 1982 *Physica* **A114** 609
Ostlund S, Wright D C 1986 *Phys. Rev. Lett.* **56** 2068
Pauling L 1987 *Phys. Rev. Lett.* **58** 365
Penrose R 1974 *Bull. Inst. Math. & its Appln.* **10** 266
Prince E 1987 *Acta Crystallogr.* **A43** 393
Sasisekharan V 1986 *Pramana – J. Phys.* **26** L283
Shechtman D, Blech I, Gratias D, Cahn J W 1984 *Phys. Rev. Lett.* **53** 1951
Socolar J E S, Steinhardt P J and Levine D 1985 *Phys. Rev.* **B32** 5547
Socolar J E S, Lubensky T C, Steinhardt P J 1986 *Phys. Rev.* **B34** 3345
Steinhardt P J, Ostlund S 1987 *The physics of quasicrystals* (Singapore: World Scientific)
Stephens P W and Goldman A I 1986 *Phys. Rev. Lett.* **56** 1168
Whittaker E J W and Whittaker R M 1988 *Acta Crystallogr.* **A44** 105

CC-0. In Public Domain. Gurukul Kangri Collection, Haridwar

Digitized by Arya Samaj Foundation Chennai and eGangotri

CC-0. In Public Domain. Gurukul Kangri Collection, Haridwar

Digitized by Arya Samaj Foundation Chennai and eGangotri

Pramāṇa – J. Phys., Vol. 34, No. 6, June 1990, pp. 555–560. © Printed in India.

Vibrational spectra of $Na_4P_2O_7 \cdot 10H_2O$

V RAMAKRISHNAN*, S NARAYANA KALKURA† and P RAJAGOPAL†

*School of Physics, Madurai Kamaraj University, Madurai 625021, India
†Department of Physics, University of Kerala, Kariavattom 695581, India

MS received 2 December 1989; revised 26 February 1990

Abstract. The IR and Raman spectra are measured and analysed for sodium pyrophosphate decahydrate. The spectra are interpreted on the basis of $P_2O_7^{4-}$ ion and water vibrations. The observed results fit with the features predicted for the factor goup model. The appearance of two sets of frequencies in the stretching and bending regions of water suggests the existence of two kinds of water molecules in the crystal. This is confirmed by deuterium substitution.

Keywords. IR and Raman specta; $P_2O_7^{4-}$ ion; water molecules.

PACS No. 33·20

1. Introduction

Investigations on pyrophosphates have revealed that pyrophosphate ion ($P_2O_7^{4-}$) exists as a discrete unit consisting of two PO_4 tetrahedra sharing a common oxygen (Calvo 1909; Saksena 1961). It is found that the two PO_3 groups are staggered. The ion possesses six symmetries such as D_{3d}, D_{3h}, D_3, C_{2v}, C_s and C_2 depending on the nature of terminal bond lengths, free rotation of PO_3 groups and the linearity of P–O–P bridge. IR spectra of several pyrophosphates have been analysed to elucidate the possible symmetry of the pyrophosphate ion (Hanwick and Hoffmann 1951; Palmer 1961; Hezel and Ross 1967). The vibrational spectroscopic studies of different alkaline earth pyrophosphates explained the behaviour of P–O–P bridge with respect to the polymorphism (Cornilsen and Condrate 1977, 1978). The effects due to factor group and site group are also discussed to correlate the multiplicity of the observed bands. In the present study, the IR and Raman spectral analysis of $Na_4P_2O_7 \cdot 10H_2O$ is presented with the structural information about the pyrophosphate ion in this crystal.

2. Experimental

Commercially available analar grade $Na_4P_2O_7 \cdot 10H_2O$ is used for investigation. IR spectrum is measured on a Perkin Elmer 577 specrtophotometer. Both the KBr pellet and nujol mull techniques are employed to obtain IR spectrum in the 200–4000 cm^{-1}

*To whom correspondence should be addressed

CC-0. In Public Domain. Gurukul Kangri Collection, Haridwar

Digitized by Arya Samaj Foundation Chennai and eGangotri

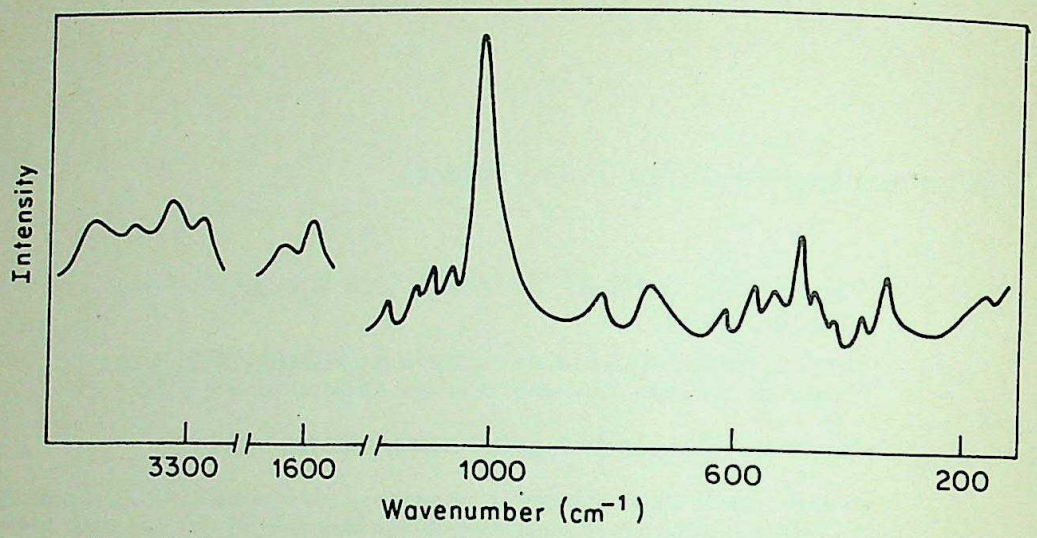

Figure 1. Raman spectrum of $Na_4P_2O_7 \cdot 10H_2O$ in the 100–3600 cm^{-1} region.

region. The wave number accuracy is within $\pm 2\,cm^{-1}$. Raman spectrum is obtained using a SPEX Ramalog 1401 double monochromator and a Spectra Physics 165 model Argon ion laser excitation source. The 4880 Å (blue) line is used with 50 mW power to obtain the illustrated spectrum (figure 1). Normal 90° collection optics is employed for the spectral measurements. The wavenumber accuracy is within $\pm 1\,cm^{-1}$. The deuterated sample is prepared by dissolving 1 g of $Na_4P_2O_7 \cdot 10H_2O$ in minimum amount of D_2O. The solution is stirred and kept under N_2 atmosphere for 1 h. Excess solvent is then removed under vacuum evaporation. This process is repeated several times. The Raman spectrum of the deuterated crystal is taken with the Raman scattering studies set up consisting of a Spectra Physics 125 A He–Ne laser, a GCA McPherson 1 metre scanning monochromator attached with a predispersing unit, a RCA C31034 PMT, a Keithley picoammeter and a strip chart recorder. The laser power at the sample is about 60 mW.

3. Results and discussion

Sodium pyrophosphate decahydrate crystallizes in the monoclinic system with space group $C2/c$ (Mac Arthur and Beevars 1957). The nonprimitive unit cell contains four molecules of $Na_4P_2O_7 \cdot 10H_2O$. In this space group, the two PO_4 groups forming the pyro ion can be related to each other by a centre of symmetry or by a two fold axis. The configuration of the pyrophosphate ion is represented with the centre P–O bonds lie at an angle 133°48′ to one another and the staggered PO_3 groups. This leads to the conclusion that the two PO_4 groups are related by a two fold axis and it gives the site symmetry of the $P_2O_7^{4-}$ ion as C_2. The sodium atoms have octahedral groups of water molecules together with some of the oxygen atoms from the $P_2O_7^{4-}$ ion. Hydrogen bonds also exist in addition to the bonds from sodium atoms to oxygen and water molecules. The OH---O distances vary between 2·66 and 2·8 Å.

3.1 *Pyrophosphate ion vibrations*

The $P_2O_7^{4-}$ ion has 21 normal modes of vibration under free ion symmetry. The model D_{3d} is centrosymmetric. The remaining models D_{3h}, D_3, C_{2v}, C_2 and C_s are

CC-0. In Public Domain. Gurukul Kangri Collection, Haridwar

Digitized by Arya Samaj Foundation Chennai and eGangotri

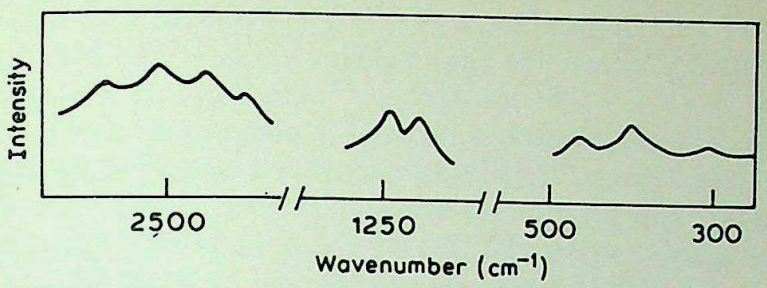

Figure 2. Raman spectrum of $Na_4P_2O_7 \cdot 10D_2O$ in the 250–2650 cm^{-1} region (Shifted bands only given).

Table 1. Correlation of free ion (C_{2v}) species with factor group (C_{2h}).

Free ion C_{2v}	Site C_2		Factor group C_{2h}	
$7A_1$	22A		A_g	11
$4A_2$			B_g	10
$6B_1$			A_u	11
$4B_2$	20B		B_u	10
Activities	C_{2v}	C_2		C_{2h}
Raman	21	42		21
IR	17	42		21

non-centrosymmetric. The higher symmetry models D_{3d}, D_{3h} and D_3 have doubly degenerate species. The activities of the vibrations under these models are given below:

	D_{3d}	D_{3h}	D_3	C_{2v}	C_s	C_2
IR	7	7	10	17	21	21
Raman	6	6	11	21	21	21

The observed spectrum can be used to find out the possible free ion symmetry for the $P_2O_7^{4-}$ ion in this crystal. The number of bands appearing both in IR and Raman spectra suggests a lower symmetry for the free ion. The absence of split components due to doubly degenerate modes also favours this. Of the C_{2v}, C_s and C_2 models, C_s and C_2 models are expected to give rise to equal number of fundamentals which are active both in IR and Raman spectra. However this is not so in the case of C_{2v} model. The observed spectrum shows that the applicability of free ion model C_{2v} is more reasonable.

Correlation of the symmetry species for the C_{2v} free ion group to C_{2v} factor group via C_2 site leads to the spectral predictions given in table 1. The spectral analysis can be made by (1) identifying bands due to different modes of $P_2O_7^{4-}$ ion (2) characterizing the bands resulting from the factor group splitting of the same site group mode which are close (3) correlating the intensities of bands to the symmetry of the vibrational modes involved.

The $P_2O_7^{4-}$ ion has a non-linear P–O–P bridge and two PO_3 groups. The P–O bond distance in P–O–P bridge and PO_3 group is different. So the stretching and bending frequencies of PO_3 group and of P–O–P bridge are expected to occur at different regions. This makes the interpretation of the observed spectra on the basis

CC-0. In Public Domain. Gurukul Kangri Collection, Haridwar

Digitized by Arya Samaj Foundation Chennai and eGangotri

of the characteristic vibrations of these groups. The frequencies of stretching modes of PO_3 group generally occur in the 1000–1200 cm^{-1} region. The three Raman bands with frequencies at 1104, 1135 and 1185 cm^{-1} are due to the asymmetric PO_3 stretching modes. The corresponding IR band is observed as a very strong broad band covering 1110–1150 cm^{-1} (IR) originate from a band with A_1 symmetry for C_{2v} free ion model. The very intense band at 1022 cm^{-1} and a weaker band at 1068 cm^{-1} are assigned to symmetric PO_3 stretching mode with A_g and B_g symmetry respectively. The very high intensity observed for the band at 1022 cm^{-1} is due to the fact that this mode is correlated with A_1 symmetry for the C_{2v} free ion. The mode possessing A_u symmetry appeared as a strong band at 1030 cm^{-1} in IR.

The strong IR bands at 980 and 910 cm^{-1} are assigned to the asymmetric P–O–P bridge stretching modes with B_u and A_u symmetry respectively. The symmetric P–O–P bridge stretching mode occurs in the 70–850 cm^{-1} region which is at lower wave number than the asymmetric P–O–P bridge stretching mode. The pair of bands at 735 (Raman) and 730 (IR) cm^{-1} is due to this mode with A_g and A_u symmetry respectively. These bands correlate with a free ion band possessing A_2 symmetry. The smaller splitting observed for these bands is because of the factor group splitting of the same site group mode.

The bands at 520 (IR) and 516 (Raman) cm^{-1} as well as those at 490 (IR) and 495 (Raman) cm^{-1} are considered as pairs of bands split from the bending modes for the B_1 and A_1 species of the free ion respectively. The lower wave number band at 495 cm^{-1} in Raman spectrum possess higher intensity and therefore assigned to the mode with A_g symmetry. Similarly the bands with medium intensity at 473 and 516 cm^{-1} in Raman spectrum are correlated to the B_g symmetry species. A normal coordinate analysis for the C_{2v} free ion group points out that the two IR bands with B_2 symmetry occur around 580 cm^{-1}. The IR band at 560 cm^{-1} is assigned with A_u symmetry originating from a mode with A_1 symmetry for C_{2v} free ion. The band at 344 cm^{-1} in Raman is due to a mode belonging to the A_g symmetry species of the factor group arising from the A_1 free ion symmetry species. The proposed assignments are given in table 2.

3.2 *Water vibrations*

A free water molecule has three normal modes of vibration corresponding to the $2A_1+B_1$ species of C_{2v} point group. The frequencies of these modes are $\nu_1 = 3650$ cm^{-1}, $\nu_2 = 1595$ cm^{-1} and $\nu_3 = 3750$ cm^{-1}. The site symmetry of water molecules is C_1 and a large number of molecules are present in the unit cell. Hence each normal mode splits into distinct vibrations corresponding to the A_g, B_g, A_u and B_u species of the C_{2h} point group. In the crystal, there are three sets of water molecules having the average O–H---O distances as 2·80 Å, 2·77 Å and 2·66 Å. There is a possibility of accidental degeneracy between the water molecules having very close hydrogen bond strength (2·80 Å and 2·77 Å). Hence two sets of frequencies for each normal mode of vibration are expected. The observed Raman and IR frequencies are given in table 3. In deuterated spectrum also (table 3) two sets of frequencies for each normal mode of vibration are observed. The ν_1 and ν_3 stretching of the water molecules in this crystal is about 350 cm^{-1} lower than the corresponding frequencies of the free molecule. This decrease is due to the reason that the hydrogen bonding reduces the effective O–H force constant. At the same time the hydrogen bond resists the bending

CC-0. In Public Domain. Gurukul Kangri Collection, Haridwar

Digitized by Arya Samaj Foundation Chennai and eGangotri

Table 2. Band assignments for $P_2O_7^{4-}$ ion.

Symmetry species		Frequencies (cm^{-1})		
Free ion	Factor group	Raman	IR	Assignment
A_2	A_g	1185		
B_1	B_g	1135		
A_1	A_u		1110–1150 s. br	$\nu_{as}\,PO_3$
	A_g	1104		
B_2	B_g	1068		
A_1	A_u		1030 s	$\nu_s\,PO_3$
	A_g	1022		
B_1	B_u		980 s	
A_1	A_u		910 vs	ν_{as} P–O–P
B_2	B_g	825		ν_s P–O–P
A_2	A_g	735		
	A_u		730 s	
B_2	B_u		575 w	
A_1	A_u		560 vs	
B_1	B_u		520 m	
	B_g	516		$\delta\,PO_3$
A_1	A_u		490 m	
	A_g	495		
B_1	B_g	473		
B_2	B_g	386		
A_1	A_g	344		δ P–O–P
A_2	A_g	161		

Table 3. Vibration of water molecules.

	Raman		
IR	H_2O	D_2O	Assignment
	3478	2582	ν_3
3400 br	3400	2506	
	3323	2456	ν_1
	3268	2409	
1620 m	1628	1240	ν_2
1590 sh	1588	1203	
610, 530, 420	600, 535, 465, 401, 421	315	Water librations

vibration of the molecule also. The slight change observed for the ν_2 frequencies shows that the hydrogen bond net work in this crystal is not contributing much to the effective H–H force constant. Librational modes of water generally fall in the 500–900 cm^{-1} region. The bands due to these modes are distinguished from deuterium substitution.

CC-0. In Public Domain. Gurukul Kangri Collection, Haridwar

Digitized by Arya Samaj Foundation Chennai and eGangotri

4. Conclusions

(1) The pyrophosphate ion possess a non-centrosymmetric structure with C_{2v} point group.
(2) The observed frequencies are assigned to the fundamentals of the $P_2O_7^{4-}$ ion with C_{2h} factor group model.
(3) The appearance of multiple bands in the stretching and bending regions explains the effect of hydrogen bonding on the vibrations of water molecules.

Acknowledgement

One of the authors (SNK) is thankful to CSIR for the award of a Senior Research Fellowship.

References

Calvo C 1909 *Acta Crystallogr.* **23** 289
Cornilsen B C and Condrate R A 1977 *J. Phys. Chem. Solids* **38** 1327
Cornilsen B C and Condrate R A 1978 *J. Solid State Chem.* **23** 375
Hanwick T I and Hoffmann P O 1951 *J. Chem. Phys.* **19** 708
Hezel A and Ros S D 1967 *Spectrochim. Acta* **A23** 1583
Mac Arthur D M and Beevars C A 1957 *Acta Crystallogr.* **10** 428
Palmer W G 1961 *J. Chem. Soc.* 1552
Saksena B D 1961 *Trans. Faraday Soc.* **57** 242

CC-0. In Public Domain. Gurukul Kangri Collection, Haridwar

Digitized by Arya Samaj Foundation Chennai and eGangotri

Pramāṇa – J. Phys., Vol. 34, No. 6, June 1990, pp. 561–563. © Printed in India.

Comments on the Meyer–Neldel rule in amorphous semiconductors

K L NARASIMHAN
Tata Institute of Fundamental Research, Homi Bhabha Road, Bombay 400 005, India

MS received 20 Janurary 1990

Abstract. In this paper, we show that the Meyer–Neldel rule can be satisfactorily explained by the temperature dependence of the fermi level. We argue that the universality of the Meyer–Neldel rule can be explained by the fact that the dangling bond is the dominant defect in amorphous silicon.

Keywords. Meyer–Neldel rule; dc conductivity; amorphous semiconductors.

PACS No. 72·80

1. Introduction

The Meyer–Neldel rule in amorphous semiconductors relates the dc conductivity prefactor σ_0 to the activation energy ΔE through the relation

$$\log \sigma_0 = \log \sigma_{00} + \Delta E/E_0. \tag{1}$$

In a-Si:H, the Fermi level position can be changed by doping and the Meyer-Neldel relation can be demonstrated quite vividly (Carlson and Wronski 1979). The Meyer–Neldel relation has been attributed at various times to (a) the presence of heterogeneities (Fritzsche and Taniellian 1981), (b) the temperature dependence of the Fermi-level (Beyer and Overhof 1983) and (c) to the temperature dependence of the mobility edge (Spear *et al* 1983). In particular, it has been very difficult to account for large values of σ_0 ($\sim 10^7$–$10^8\,\Omega^{-1}\,\mathrm{cm}^{-1}$) where the dc conductivity σ is given by

$$\sigma = \sigma_0 \exp -(\Delta E/kT). \tag{2}$$

It has recently been shown that the temperature dependence of the mobility edge is not marked in a-Si and so cannot account for the Meyer–Neldel rule (Bapat *et al* 1987; Mott 1987). We would like to emphasize that (1) is not to be interpreted in a strict mathematical sense but only as an equation emphasizing a trend. If we plot $\log \sigma_0$ vs ΔE for different amorphous semiconductors (1) is satisfied for $15\,\mathrm{eV} < E_0 < 30\,\mathrm{eV}$. In this paper we argue that the Meyer–Neldel rule can be accounted for by the temperature dependence of the Fermi-level and give a simple chemical argument to account for the universality of this relationship. In this paper we emphasize results relevant to a-Si:H alloys. We believe these arguments are also valid for other tetrahedrally bonded amorphous semiconductors.

CC-0. In Public Domain. Gurukul Kangri Collection, Haridwar

Digitized by Arya Samaj Foundation Chennai and eGangotri

2. Discussion

It is known for a-Si that doping affects the distributions of defect states (DOS) in the gap (Street *et al* 1981; Lang *et al* 1982). This can be easily understood from the following argument. The gap states can be thought of as arising from the bonding and antibonding states of weak bonds. If we attempt to fill the antibonding states (bonding states) with two electrons (2 holes), it is easy to see that the bond order tends to zero and it is energetically more favourable to have a pair of dangling bonds than occupied antibonding states (empty bonding states). In a-Si (and may be in most amorphous semiconductors), these defects tend to pile up near the middle of the gap thereby reducing the number of states near the fermi-level E_F. Thus, in the presence of defects and impurities, the DOS goes through a maximum near the midgap and decreases in the vicinity of E_F. This situation is quite different from that in crystals and we will return to this point later. When we attempt to move the Fermi level of a n-type (p type) a-Si sample by doping with group V (group III) impurities, the Fermi-level finds its equilibrium position in a pseudo local minimum of the DOS (Street 1988). (The states removed from the vicinity of E_F to create that minimum appear as dangling bonds near the midgap.) This is clearly not the situation when we counterdope the specimen to change the conductivity type. For instance, if we dope with boron a nominally undoped sample (n type) we produce dangling bonds near the midgap, the Fermi-level now moves through this peak in the density of states. Experimental confirmation of this peak exists in DLTS and luminescence measurements (Street *et al* 1981, Lang *et al* 1982). In such a case, we easily see that the temperature dependence of E_F is large as it will be driven towards the minimum in the DOS when we increase the temperature. If E_F changes linearly or pseudolinearly with temperature moving away from the midgap at elevated temperatures towards the minima in the DOS, then this will give rise to an enhanced conductivity prefactor in (1) and account for the large value of σ_0. Experimental confirmation of this result appears in the values of σ_0 obtained for virgin and electron irradiated samples (Premachandran *et al* 1984). Electron irradiation gives rise to point defects near the midgap in a-Si. These defects can be annealed out by heating to 150°C. In these experiments both dE_c/dT and σ_0 were independently monitored. After electron irradiation the value of dE_c/dT was found to remain unaltered whereas that of σ_0 increases. This increase in σ_0 is related to a change in the value of dE_F/dT before and after irradiation (Premachandran *et al* 1984). In these experiments on some samples dE_F/dT was even found to change sign after irradiation indicating the presence of a maxima in the density of states near the midgap after electron irradiation. The presence of this maxima in the density of states near midgap also shows up in space charge limited currents where at small voltages the current increases rapidly with applied voltage as the quasi fermi-level E_{Fn} is swept across to the minima in the density of states (Bhattacharya and Narasimhan 1984). We hence conclude that the temperature dependence of E_F is in fact responsible for the large values of σ_0. Beyer and Overlof (1983) come to a similar conclusion in their experiments using lithium doped samples.

In c-Si, points defects are easily generated by radiation damage. These defects, in some sense, are also dangling bonds with the difference that the energy level of the defect is dependent on the impurity – O, P, B, C etc. The defect varies in energy from $E_c - 0{\cdot}2$ eV to $E_c - 1{\cdot}0$ eV depending on the nature of the complex with the impurity (Watkins *et al* 1979). Such complexes appear to be unimportant in a-Si. Here, the

CC-0. In Public Domain. Gurukul Kangri Collection, Haridwar

Digitized by Arya Samaj Foundation Chennai and eGangotri

dominant defect seems to be the dangling bond near midgap. This accounts for the fact that the Meyer–Neldel rule relates σ_0 to ΔE as the temperature dependence of E_F depends on the DOS distribution in the vicinity of E_F which in turn depends on the position of E_F in the gap. The fact that the Meyer–Neldel rule is seen in amorphous semiconductors suggests that defects behave similarly in all amorphous semiconductors (and to that extent are different from and simpler than defects in crystalline semiconductors. This also accounts for the universality of the Meyer–Neldel rule in amorphous semiconductors.

References

Bapat D R, Narasimhan K L and Kuchibotla R 1987 *Philos. Mag.* **B56** 71
Beyer W and Overhof W 1983 *J. Non-Cryst. Solids* **59–60** 301
Bhattacharya E and Narasimhan K L 1984 (unpublished)
Carlson D E and Wronski C R 1979 *in Amorphous semiconductors* (ed.) M H Brodsky (New York: Springer), p. 287
Fritzsche H and Taniellian M 1981 *in Tetrahedrally bonded amorphous semiconductors* (eds) D K Biegelsen and J C Knights (AIP Conf. Proc. 73) p. 318
Lang D V, Cohen J D and Harbison J P 1982 *Phys. Rev.* **B25** 5285
Mott N F 1987 *J. Phys.* **C21** 3075
Premachandran V, Narasimhan K L and Bapat D R 1984 *Phys. Rev.* **B29** 7073
Spear W E, Allan D, Lecomber P G and Ghaith A 1980 *J. Non-Cryst. Solids* **35/36** 357
Street R A, Biegelsen D K and Knights J C 1981 *Phys. Rev.* **B324** 969
Street R A 1988 – Private Communication
Watkins G D, Troxell J R and Chatterjee A P 1979 in *Defects and radiation effects in semiconductors* (ed.) J H Albany (Inst. of Phys. Conf. series 46) p. 16

CC-0. In Public Domain. Gurukul Kangri Collection, Haridwar

Digitized by Arya Samaj Foundation Chennai and eGangotri

CC-0. In Public Domain. Gurukul Kangri Collection, Haridwar

Digitized by Arya Samaj Foundation Chennai and eGangotri

Pramāṇa – J. Phys., Vol. 34, No. 6, June 1990, pp. 565–573. © Printed in India.

A study of absorption characteristics in polyimide and polyimide fluorocarbon-2 polymer film

M M HOSSAIN

Department of Applied Physics and Electronics, Rajshahi University, Rajshahi, Bangladesh. Present address: Department of Physics, College of Science, University of Salahuddin, Arbil, Iraq

MS received 14 August 1989; revised 18 January 1990

Abstract. The absorption characteristics of polyimide (PM) and polyimide fluorocarbon (PMF-2) polymer film were studied at temperatures ranging from 20 to 230°C. The glass transition or critical temperature of PMF-2 was found at 160°C. Conduction of PMF-2 was observed due to the upper fluorocarbon layer below the transition temperature while the middle PM layer is important above this temperature. The time-dependent absorption/resorption current does not satisfy the traditional Curie-Von Schweidler law. The experimental results of the absorption characteristics are analysed using a simple R-C circuit.

Keywords. Absorption/resorption current; residual/discharge voltage; Curie-Von Schweidler low; conduction; R-C circuit.

PACS No. 72·20

1. Introduction

Synthetic polymers are extensively used as electrical insulators because of their good electrical and mechanical properties. They have wide applications ranging from power apparatus and cables to microelectronics. Among the possible synthetic polymers, polyimide and polyimide fluorocarbon (abbreviated hereafter as PM and PMF-2 respectively) seems quite promising.

The present paper reports the comparative study of the absorption characteristics of both these films at different temperatures. Sample films have been used for measuring the absorption/resorption currents and the residual/discharge voltages.

The applications of step voltage to dielectric causes a flow of current which decays with time before reaching a steady-state value. The time-dependent part of the current (absorption current) is due to dielectric polarization under the applied electric field. The polarization of polymeric dielectrics may be due to dipolar orientation, accumulation of charge carriers near the electrodes or trapping in the bulk (Van der Schueren and Linkens 1976; Nakumara *et al* 1976). Under certain conditions, additional charge carriers may be provided by injection from the electrodes, which also contribute to space charge polarization (Wintle 1977). A systematic study of the absorption currents can reveal the carrier injection, trapping and polarization processes which may be present in a dielectric. An understanding of the absorption currents is therefore necessary to discover the true conductivity of the material.

The resorption current usually decays with time in the direction opposite to the absorption current. This has been explained as the result of dipolar depolarization

CC-0. In Public Domain. Gurukul Kangri Collection, Haridwar

Digitized by Arya Samaj Foundation Chennai and eGangotri

or redistribution of charge carriers due to interfacial polarization or space charge polarization (Das Gupta *et al* 1980).

Considerable high voltage sometimes appears on the inner-conductor of a power transmission cable and condenser after opening a circuit which was previously electrically stressed and short-circuited for a short time. This voltage gives an electric shock when touched and is termed the residual voltage. Recently, measurement of the residual voltage was proposed as a method for detecting degradation of the cable insulation (Kalsumi *et al* 1982).

In the present study the absorption/resorption currents and the residual/discharge voltages at different temperatures were measured in PM and PMF-2 and the results analysed using simple R-C circuits.

2. Experimental

Commercial-grade polyimide (Yslovia 1972) and polyimide fluorocarbon film [(10 μm fluorocarbon- 30 μm polyimide- 10 μm fluorocarbon sandwich film commercially known as PMF-2 (Yslovia 1983)] of thickness 40 μm and 50 μm respectively were used. After washing with alcohol, aluminium electrodes of 28 mm diameter were deposited on both surfaces of the films by vacuum evaporation. The sample was then mounted in a measuring cell and the absorption/resorption currents and the residual/discharge voltages at different temperatures were measured using a BK2-16 electrometer (USSR), an x-y recorder provided with a time base, and a stabilized d.c. power supply.

The absorption/resorption currents were measured according to standard procedures, of applying a step voltage, measuring the absorption current decay for some polarization time t_p, short circuiting the sample and measuring the resorption current.

The measurement procedure of residual voltage was as follows. A voltage V_p was applied to a sample for a time t_p and the circuit shorted for a time t_s. After the circuit was opened, a voltage V_R appeared on an electrode after t. Also for measuring discharge voltage, V_p was applied to a sample for t_p, the circuit opened and the discharge voltage V_d recorded.

3. Results and discussion

Variation of the absorption and resorption current with time for PM and PMF-2 is shown in figures 1 and 2 respectively at various temperatures. No time-dependent part of the currents was soon above 180°C for PM (figure 1) while the PMF-2 film showed time-dependent currents at higher temperatures (figure 2). Figure 2 shows that absorption and resorption current for PMF-2 above and below 160°C is sharply divided into two characters and so this temperature of 160°C may be the glass transition or critical temperature for PMF-2.

Atkinson and Fleming (1980) showed that absorption currents in non-polar materials were largely due to currents flowing on the surface of the polymer from the edges of the electrode. We may therefore conclude that the time-dependent parts of the currents for PMF-2 up to 120°C is due only to the outside fluorocarbon layers of the film.

CC-0. In Public Domain. Gurukul Kangri Collection, Haridwar

Digitized by Arya Samaj Foundation Chennai and eGangotri

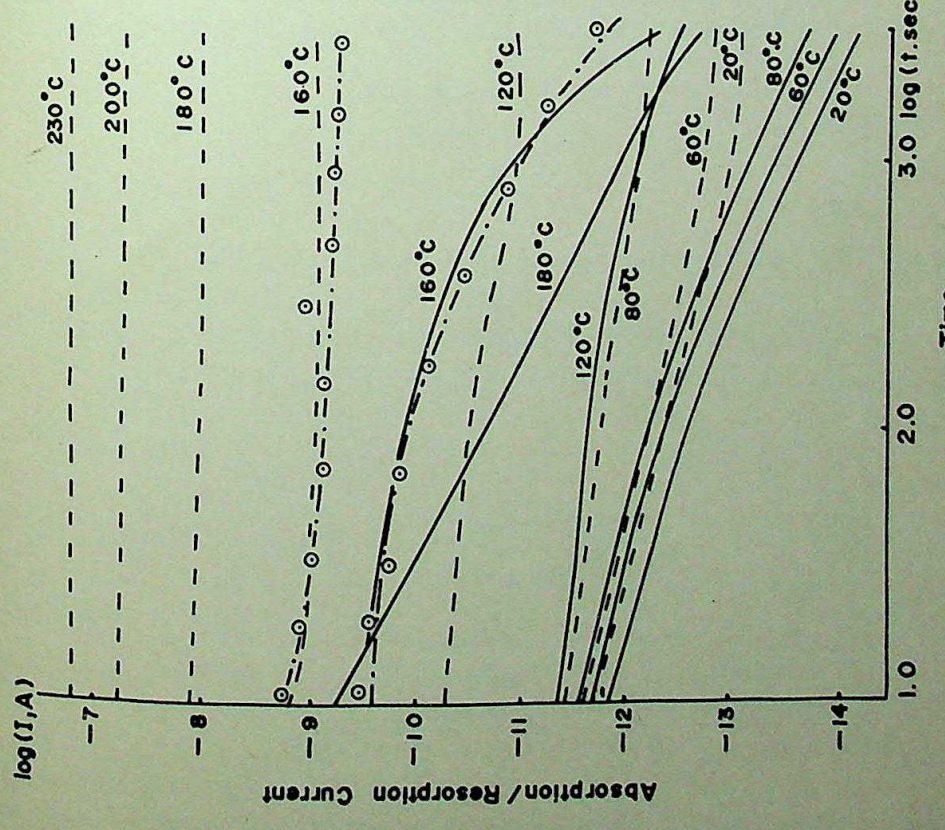

Figure 1. Time-dependent absorption/resorption currents of PM film. Absorption current (——), resorption current (– – –), calculated value of absorption and resorption current (–·–·–) $E_p = 32{\cdot}5$ kV/cm.

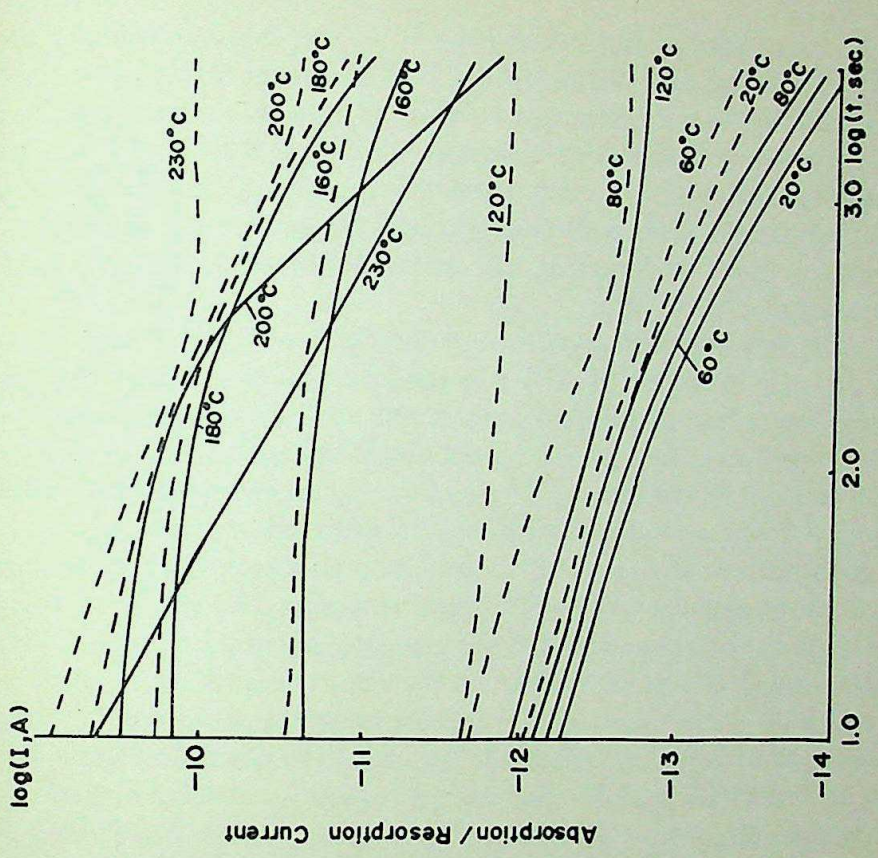

Figure 2. Time-dependent absorption/resorption currents of PMF-2 film. Details as in figure 1.

CC-0. In Public Domain. Gurukul Kangri Collection, Haridwar

Digitized by Arya Samaj Foundation Chennai and eGangotri

Above 160°C, the upper thin fluorocarbon layer (10 μm) strates to soft and becomes non-continuous, while the time-dependent parts of the currents may arise due to the contribution of the middle polyimide layer. As is evident from figures 1 and 2, at high temperatures (above 160°C) the time-dependent current of PMF-2 film is similar to the low temperature (below 160°C) time-dependent current of PM film i.e the actual temperature of the middle layer polyimide of PMF-2 may be much smaller than the upper fluorocarbon layer. In practice, the upper fluorocarbon layer is used as a heat-resistive layer of PMF-2 film.

Variation of the residual voltage with time for PM and PMF-2 films at various temperatures is shown in figures 3 and 4. The residual voltage increases with increase of temperature. The origin of residual voltage can then be explained qualitatively from experimental results as follows. Under a constant voltage and rise of temperature, the carriers pre-existing in the film or injected from the electrode, migrate within the film and establish a space charge distribution. During short-circuiting, the charge redistributes in the sample and some of the changes will be swept out of the electrode. After the circuit is opened, charge distribution is rearranged by migration of carriers in the film because of the space charge field, resulting in the appearance of residual voltage which is due to charge imbalance on the electrode and the sample.

Figures 3 and 4 show that the residual voltage increases sharply with increase of temperature but above 160°C, the PMF-2 film (figure 4) does not follow the same nature as seen in PM film (figure 3). The residual voltage for PMF-2 film takes about 1/4th time less than the simple PM film. The residual voltage for PMF-2 film at 180°C does not fall to zero at the time of measurement which agrees with the time-dependent residual voltage characteristics of PM film.

The above results indicate that there are two charge storage mechanisms in the PMF-2 film which is also seen in figure 2 in the case of time-dependent current.

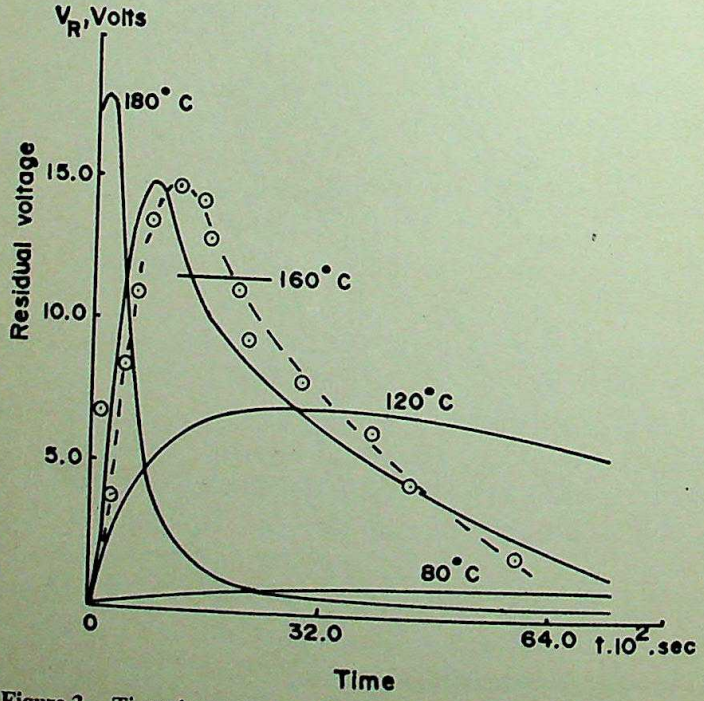

Figure 3. Time-dependent residual voltage for PM film. Experimental (——), calculated (– – –), $E_p = 32{\cdot}5$ kV/cm, $t_p = 2$ hs, $t_s = 5$ s.

CC-0. In Public Domain. Gurukul Kangri Collection, Haridwar

Digitized by Arya Samaj Foundation Chennai and eGangotri

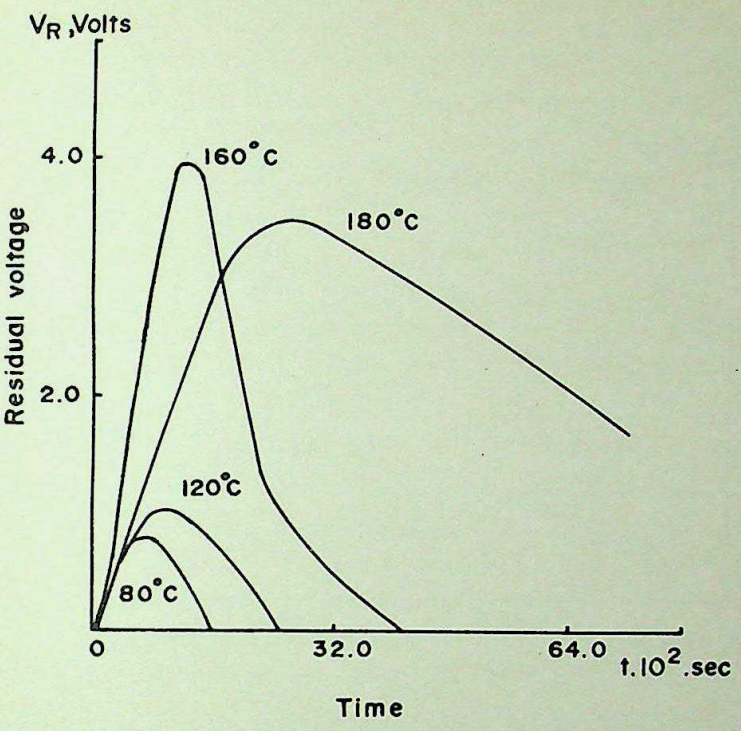

Figure 4. Time-dependent residual voltage for PMF-2 film. Details same as in figure 3.

Variation of discharge voltage with time for PM and PMF-2 films at different temperatures is shown in figures 5 and 6 respectively. The magnitude of the discharge voltages decreases with increasing temperature. It is also clear from the figures that the process of depolarization in the PMF-2 film is slower than the simple PM film.

It is seen from figures 1 and 2 that the logarithmic plots of absorption and resorption currents are not linear, i.e. the observed time dependence of the current transients does not satisfy the Curie-Von Schweidler law (Van der Schueren and Linkens 1976);

$$I(t) = A(T)t^{-n}, \tag{1}$$

where I is the absorption/resorption current, t the time and $A(T)$ the temperature-dependent factor.

The analysis of the absorption/resorption current curves (figures 1, 2) shows that it is the time-dependent summation of exponents, i.e

$$I_{A,R} = \sum_{i=1}^{n} I_{oi}^{A,R} \exp(-t/\tau_i) \tag{2}$$

where τ_i is the relaxation time for currents. The analysis of the time-dependent curves i.e. $\log V_D = f(t)$ and $\log V_R = f(t)$ for PM and PMF-2 films also shows time-dependent summation of exponents, i.e.

$$V_{D,R} = \sum_{i=1}^{n} V_{oi}^{D,R} \exp(-t/\theta_i), \tag{3}$$

where θ_i is the relaxation time for voltage.

Since the absorption/resorption currents and the residual/discharge voltages are time-dependent summation of exponents, we may conclude that the PM and PMF-2

CC-0. In Public Domain. Gurukul Kangri Collection, Haridwar

Digitized by Arya Samaj Foundation Chennai and eGangotri

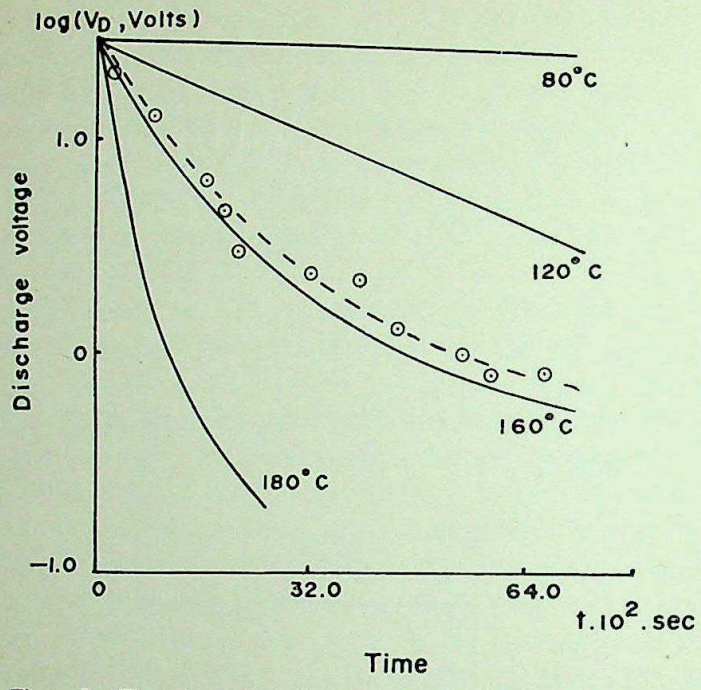

Figure 5. Time-dependent discharge voltage for PM film. Experimental (——), calculated (---) $V_p = 30$ V, $t_p = 2$ h.

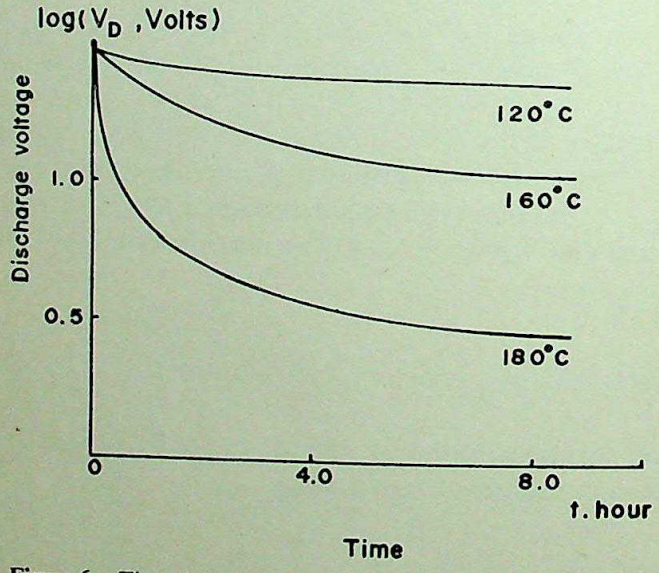

Figure 6. Time dependent discharge voltage for PMF-2 film. Details same as in figure 5.

films consist of some layers (Hossain 1988). We can therefore consider an R-C circuit to represent each layer as shown in figure 7.

The expressions for charge storage and relaxation process of this circuit (figure 7) can be written as follows;

$$I(t) = C_i \, dE_i(t)/dt + E_i(t)/R_i, \tag{4}$$

$$q_i(t) = C_{i+1} E_{i+1}(t) - C_i E_i(t), \tag{5}$$

$$V(t) = \sum_{i=1}^{n} q_i/C_i. \tag{6}$$

CC-0. In Public Domain. Gurukul Kangri Collection, Haridwar

Digitized by Arya Samaj Foundation Chennai and eGangotri

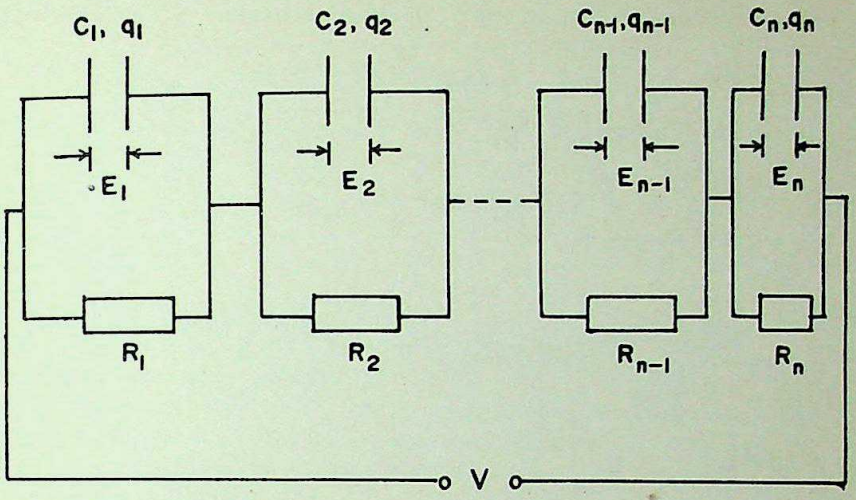

Figure 7. R-C equivalent circuit for multilayer structure of polymer film.

During the process of charging $V = V_{\text{charge}}$ and $V = 0$ we have to consider the former for the discharging voltage and the latter for the residual voltage. During charging, $q_i^0 = V.\ C_\Sigma$ and at the end of charging i.e. when the process is saturated,

$$q_i^\alpha = V\tau_i/R_\Sigma, \quad I^\alpha = V/R_\Sigma,$$

where

$$R_\Sigma = \sum_{i=1}^{n} R_i \quad \text{and} \quad C_\Sigma = \sum_{i=1}^{n} (1/C_i)^{-1}.$$

It was observed that the absorption/resorption current curve i.e. $\log I_{A,R} = f(t)$ at 160°C consists of two exponents for the PM and three exponents for the PMF-2 film; on the other hand the discharge/residual voltage curve $\log V_{D,R} = f(t)$ at that temperature is of three and four exponents for the respective film. These results indicate that the PM film consists of three layers and the PMF-2 film consists of four layers.

After solving equations (4), (5) and (6) and considering the initial and final conditions of charge storage, the following expressions can be obtained for variations of discharge/residual voltage and absorption/resorption current with time for the three-layer PM film

$$V_D(t) = V/R_\Sigma[R_1 \exp(-t/\theta_1) + R_2 \exp(-t/\theta_2) + R_3 \exp(-t/\theta_3)], \tag{7}$$

$$V_R(t) = V/R_\Sigma\left[R_1\left(1 - \frac{\theta_2\theta_3}{\tau_1\tau_2}\right)\exp(-t/\theta_1) + R_2\left(1 - \frac{\theta_1\theta_3}{\tau_1\tau_2}\right)\exp(-t/\theta_2) + R_3\left(1 - \frac{\theta_1\theta_2}{\tau_1\tau_2}\right)\exp(-t/\theta_3)\right], \tag{8}$$

$$I_A = -I_R = V/R_\Sigma\left[\frac{(\tau_1 - \theta_1)(\tau_1 - \theta_2)(\tau_1 - \theta_3)}{(\tau_2 - \tau_1)\tau_1^2}\exp(-t/\tau_1) + \frac{(\tau_2 - \theta_1)(\tau_2 - \theta_2)(\tau_2 - \theta_3)}{(\tau_1 - \tau_2)\tau_2^2}\exp(-t/\tau_2)\right] + I_s. \tag{9}$$

Here

$$I_s = V/R_\Sigma, \quad \theta_1 = R_1C_1, \quad \theta_2 = R_2C_2, \quad \theta_3 = R_3C_3$$

CC-0. In Public Domain. Gurukul Kangri Collection, Haridwar

Digitized by Arya Samaj Foundation Chennai and eGangotri

Table 1. Values of E_i, θ_i, R_i and C_i for different circuits.

i	E_i (Volts)	θ_i (s)	R_i (ohm)	C_i (10^{-11} F)	τ_i (s)
1	1,0	9090	$1{\cdot}2\times10^{11}$	7985	5880
2	10,9	1820	$10{\cdot}2\times10^{11}$	174	330
3	22·2	1110	$20{\cdot}9\times10^{11}$	52	

and

$$\tau_{1,2}=\frac{\Sigma R_i(\theta_J+\theta_k)}{2R_\Sigma}\pm\left(\frac{R_i(\theta_J+\theta_k)^2}{2R_\Sigma}-\frac{\Sigma R_i\theta_J\theta_k}{R_\Sigma}\right)^{1/2} \tag{10}$$

where

$$i\neq j\neq k.$$

From the exponents of the curve $\log V_D=f(t)$, we can find out the conductivity γ_i of each layer as follows;

$$\gamma_i=\varepsilon_0\varepsilon/\theta_i, \tag{11}$$

where ε is the dielectric constant of the sample.

If the charging process is saturated, i.e. $(E_1\gamma_1=E_2\gamma_2\cdots E_nr_n)$, then the thickness of the layers may be obtained as follows.

$$h_i/h_{i+1}=E_i\gamma_i/E_{i+1}\gamma_{i+1};\quad h=\sum_{k=1}^{n}h_k, \tag{12}$$

where h is the thickness of the whole polymer film and E_i the potential across the ith layer shown in figure 7 as a potential across the ith condensor.

From the exponent of the curve $\log V_D=f(t)$ and also from equations (11) and (12) one can easily evaluate the values of E_i, θ_i, R_i and C_i (see table 1). The above values were used for computing the variation of absorption/resorption current and the residual/discharge voltage with time. It is clear from figures 1, 3 and 5 that the calculated and experimental results are quite compatible.

If the total exponents of the discharge voltage curve are unchanged over a wide range of temperatures, then the high temperature parameters can be used to calculate the absorption characteristics at different temperatures for accelerating the process of measurements.

4. Conclusion

It is clear that charge storage mechanism in PMF-2 film above and below 160°C is sharply divided into two. The logarithmic plots of absorption and resorption currents do not satisfy the Curie-Von Schweidler law and are the time dependent summation of exponents. The charge storage and relaxation process of the polymer film have been analysed with the help of a parallel R-C circuit. The theoretical and experimental results of the absorption characteristics are quite compatible.

CC-0. In Public Domain. Gurukul Kangri Collection, Haridwar

Digitized by Arya Samaj Foundation Chennai and eGangotri

Acknowledgements

The author is grateful to Professor S N Koikov and Professor M E Baricova of the Leningrad polytechnical Institute, Leningrad, USSR for stimulating discussions.

References

Atkinson P J and Fleming R J 1980 *J. Phys.* **D13** 625
Das-Gupta D K, Doughty K and Brocklay R S 1980 *J. Phys.* **D13** 2101
Hossain M M 1988 *Indian J. Phys.* **A62** 944
Kalsumi Y, Jun K, Munsoo Y, Ken-Ichi N, Yoshio I and Nobuharu K 1982 *Jpn. J. Appl. Phys.* **21** 1333
Nakumara S, Sawa G and Idea M 1976 *Jpn. J. Appl. Phys.* **18** 995
Vander Schueren J and Linkens A 1976 *J. Appl. Phys.* **49** 4195
Yslovia T (TY) 6–05–1491–1972 (U.S.S.R)
Yslovia T (TY) 6–19–226–1983 (U.S.S.R)
Wintle H J 1977 *IEEE Trans. Electr. Insul.* **EI-12** 424

CC-0. In Public Domain. Gurukul Kangri Collection, Haridwar

Digitized by Arya Samaj Foundation Chennai and eGangotri

CC-0. In Public Domain. Gurukul Kangri Collection, Haridwar

Digitized by Arya Samaj Foundation Chennai and eGangotri

Pramāṇa – J. Phys., Vol. 34, No. 6, June 1990, pp. 575–583. © Printed in India.

A theoretical study of surface plasmon cross coupling in asymmetric corrugated metal films

M B PANDE and S DUTTA GUPTA
School of Physics, University of Hyderabad, Hyderabad 500 134, India

MS received 20 March 1990

Abstract. We investigate numerically the transmission properties of a thin sinusoidally corrugated metal film bounded by two different dielectrics in the context of the experiment of Gruhlke *et al* (1986). We study the dominant contributions from both the propagating and evanescent plane waves. A comparison with the experimental results reveals that the decisive role in cross coupling is played by the evanescent waves emitted by the molecular dipole. We extend our studies to different corrugation amplitudes and widths to show their effect on transmission.

Keywords. Surface plasmon; corrugated metal film .

PACS Nos 42·65; 78·65; 42·20; 41·10

1. Introduction

The coupling of surface plasmoms in thin metal films has drawn a considerable theoretical and experimental interest (Agarwal and Dutta Gupta 1985; Dragila *et al* 1985; Dutta Gupta *et al* 1987; Gruhlke and Hall 1988; Gruhlke *et al* 1986, 1987; Leung *et al* 1989; Raether 1977). The coupling manifests itself in various ways. In symmetric structures, the excitation of coupled surface plasmons results in high transmission of otherwise opaque metal films (Dragila *et al* 1985). In asymmetric structures involving corrugated metal films there can be cross coupling of the neighbouring spatial harmonics resulting in the partial transparency of the metal film. Besides, surface plasmons and especially coupled surface plasmons affect significantly the fluorescent lifetime and the resonance frequency of nearby molecules. In a recent series of experiments involving transmission of molecular fluorescence through corrugated thin metal films, all the above effects were demonstrated convincingly (Gruhlke *et al* 1986, 1987; Gruhlke and Hall 1988). The shift of the resonance frequencies was shown in a model experiment where the molecular dipoles were replaced by small metal particles supporting localized plasmons. Subsequently a theoretical explanation of the experimental observations was given by Agarwal and Dutta Gupta (1985). The change in the fluorescent lifetime was recently studied using a first order perturbation theory (Leung *et al* 1989). However, a systematic nonperturbative study of the wavelength dependence of the transmission has not yet been carried out. It was pointed out that the relative yield in the fluorescence transmission experiment depends on the product of two factors, namely, enhancement and transmission (Gruhlke and Hall 1988). In this paper we focus our attention on the second aspect, i.e., transmission, and present a nonperturbative study of the

CC-0. In Public Domain. Gurukul Kangri Collection, Haridwar

Digitized by Arya Samaj Foundation Chennai and eGangotri

wavelength dependence of the transmission coefficient relevant to the experimental configuration of Gruhlke *et al* 1986 (herein after referred to as I). Since the basic features of a symmetric corrugated film were studied earlier (Dutta Gupta *et al* 1987, herein after referred to as II), we pay attention to the asymmetric structure (photoresist-Ag-air) where coupling is expected to be small. We assume that the oscillating dipole emits plane propagating and evanescent waves and take into account the contributions from the dominant wave vector component (i.e., the wave vector component which is in lowest order resonance with the surface mode on the Ag-photoresist interface). The contributions from other radiative and nonradiative wave vector components are smaller and are neglected in this theory. Thus, the theory based on the Rayleigh expansions of the fields (II) is applicable and we present the numerical results in the next section. We show that the basic features and conclusions regarding transmission via cross coupling are supported by a nonperturbative theory. The calculations are extended to different corrugation amplitudes and widths to show that the resonant response of the film is extremely sensitive to the above parameters. Moreover, we compare the calculated transmission spectra for the incidence of evanescent and propagating waves with the experimental data of I. This enables us to make an important observation, namely, that the decisive role in the transmission of fluorescence through a corrugated metal film is played by the evanescent waves.

The organization of the paper is as follows. In § 2, we present the numerical results and discuss them. In § 2a, the transmission of the film for the incidence of plane propagating waves is investigated, whereas, in § 2b, we discuss the transmission of the evanescent waves and we provide the conclusions in §3.

2. Numerical results and discussion

Consider a corrugated metal film given by the surface profile functions

$$z = \begin{cases} a \sin Kx \\ -d + a \sin Kx, \end{cases} \tag{1}$$

where K is the grating vector ($K = 2\pi/\Lambda$, Λ is the grating period), a is the corrugation amplitude and d is the width of the metal film. Let the film be bounded by air on one side and by photoresist (with refractive index $n_i = 1{\cdot}6$) on the other. Let a plane TM polarized wave of unit amplitude be incident on the film from the photoresist side. Keeping in mind the experimental geometry of I we study the transmitted order at an angle θ_d with the normal to the film (i.e., the z-axis). The diffraction angle θ_d is given by the relation

$$k_0 \sin \theta_d = k_{c1} - K, \tag{2}$$

where $k_0 = 2\pi/\lambda$ (λ is the vacuum wavelength) is the wave vector in air, k_{c1} is the surface plasmon wave vector for the corrugated Ag-air interface. Note that in contrast to I we are using the surface plasmon wave vector for the corrugated surface. This is due to the fact that there may be noticeable changes in the surface plasmon dispersion due to surface corrugation. In order to have efficient cross coupling, the

CC-0. In Public Domain. Gurukul Kangri Collection, Haridwar

Digitized by Arya Samaj Foundation Chennai and eGangotri

surface plasmon wave vector for the Ag-photoresist corrugated interface k_{c2} should differ from that for Ag-air interface k_{c1} by K, i.e.,

$$k_{c2} - k_{c1} = K. \tag{3}$$

In what follows we consider two different situations namely, a) incident wave is propagating (with z-component of the incident wave vector real) and b) incident wave is evanescent (with z-component of the incident wave vector purely imaginary).

2a *Optical transmission for propagating waves*

For the incidence of a plane propagating wave, (3) implies that for a given λ the dominant contribution comes from the wave which is incident from the photoresist side at an angle θ_i given by the relation

$$k_0 n_i \sin\theta_i = k_{c1}. \tag{4}$$

Thus, for a plane wave incident on the film from the photoresist side at an angle θ_i the $+1$ order resonates with the surface mode at the Ag-photoresist interface, which subsequently gets coupled to the surface mode at the other interface (cf. eq. (3)), and radiates the -1 propagating order in air at an angle θ_d. It may be noted here that one could have a radiative mode at an angle θ_d from other higher order processes, for example, from plane wave incidence at an angle $\bar{\theta}_i$, given by

$$k_0 n_i \sin\bar{\theta}_i + K = k_{c1}. \tag{5}$$

However, the transmitted intensity at θ_d for this process is much less compared to that given by (4) for shallow gratings. In order to have numerical results we use the Rayleigh method (II) and calculate the transmitted intensity of the -1 order for a plane wave incident at an angle θ_i. For a given λ, evaluation of the angle of incidence θ_i requires the knowledge of k_{c1} (cf. eq. (4)). Therefore, we study the dispersion characteristics of Ag-air corrugated surface (and also of Ag-photoresist interface for later use). These were determined by looking at the minima of the O-th order reflectivity for the corresponding interfaces. The value of the dielectric constants of Ag at various wavelengths were determined from the interpolated experimental data of Johnson and Christy (1972). The results are displayed in figure 1 where we have plotted k_{c1} (left curve) and k_{c2} (right curve) as functions of wavelength for $a = 20$ nm. The dispersion curves were calculated using the same value of $\Lambda = 898$ nm. The same curves will be used for other values of Λ since the dispersion characteristics are almost insensitive to a change in Λ (at least for the range of Λ used in the experiment of I). Nontrivial departures from flat surface dispersion were noted. A comparison of the experimental (I) and theoretical dispersion curves reveals that the mismatch between them is significant. This may be due to the fact that the values of silver dielectric constants used in the calculations were different from the actual ones of the experiment. In fact, the dielectric constant of the deposited films depends significantly on their method of realization (Coutaz 1987). Therefore, in the forthcoming discussions we do not expect quantitative agreement with the experimental results.

In what follows, making use of the values of k_{c1} for a given λ from figure 1 and (4) we calculate the angle of incidence θ_i. The transmitted -1 order intensity T is then

CC-0. In Public Domain. Gurukul Kangri Collection, Haridwar

Digitized by Arya Samaj Foundation Chennai and eGangotri

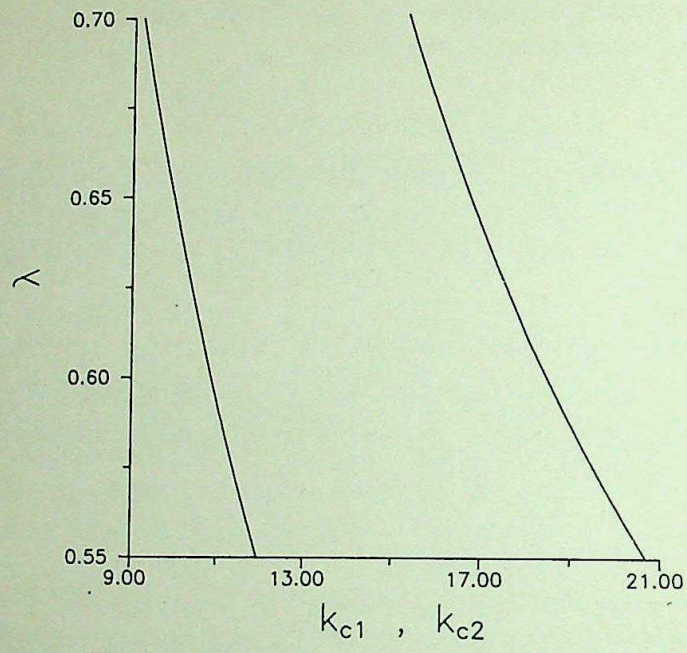

Figure 1. Surface plasmon wave vectors k_{c1} [μm^{-1}] and k_{c2} [μm^{-1}] for Ag-air (left cruve) and Ag-photoresist (right curve) corrugated interfaces, respectively, as functions of λ [μm]. Other parameters are as follows, $a = 20$ nm, $\Lambda = 898$ nm.

calculated using the coupled amplitude equations (II). Calculations have been performed for two sets of values of a and d for various Λ, namely, $\Lambda = 760$ nm, 814 nm, 898 nm, 926 nm, 976 nm. For different values of corrugation amplitude, different dispersion curves were used (figure 1 shows only one of them). The dependence of -1 order transmission coefficient as a function of λ is shown in figure 2. Figures 2a, 2b corresponds to $a = 20$ nm, $d = 100$ nm, ($a = 40$ nm, $d = 150$ nm). Curves from left to right in figure 2a, 2b are for increasing values of Λ. It may be noted from figure 2, that peaks in the transmission are preceded by dips, and the dips are prominent for lower value of a and d. The shape of the curves in figure 2 suggests that the transmitted amplitude has contributions from a complex pole and a complex zero. A change in the parameters a and d affects considerably the zeroes whereas the poles are not subject to drastic changes. An increase in a (d) shifts the poles to larger (smaller) wavelengths and results in a broadening (narrowing) of the resonances. For smaller a and d when the background radiation is strong the dips should be observed. However, the dips were not detected in the experiment of I. In the later experiments of Gruhlke and Hall (1988) involving coupled surface plasmons, dips were observed and they were ascribed to the Bragg matched interaction with other modes originating from waveguide and short range plasmon resonances. However, the occurrence of the dips before each long range plasmon resonance may have partial contribution from the complex zeroes mentioned above.

In order to have a direct evidence of cross coupling of the surface plasmons of the two interfaces we first note the wavelength $\bar{\lambda}$ at which transmission is maximum for a given Λ (figure 2a). The corresponding difference of surface plasmon wave vectors $\Delta k_c = k_{c2} - k_{c1}$ is then noted from figure 1. Next, we plot the grating vector K as a function of Δk_c. Figures 3a, 3b shows the dependence for $a = 20$ nm, $d = 100$ nm ($a = 40$ nm, $d = 150$ nm). Figures 3a, 3b clearly demonstrates that maximum trans-

CC-0. In Public Domain. Gurukul Kangri Collection, Haridwar

Digitized by Arya Samaj Foundation Chennai and eGangotri

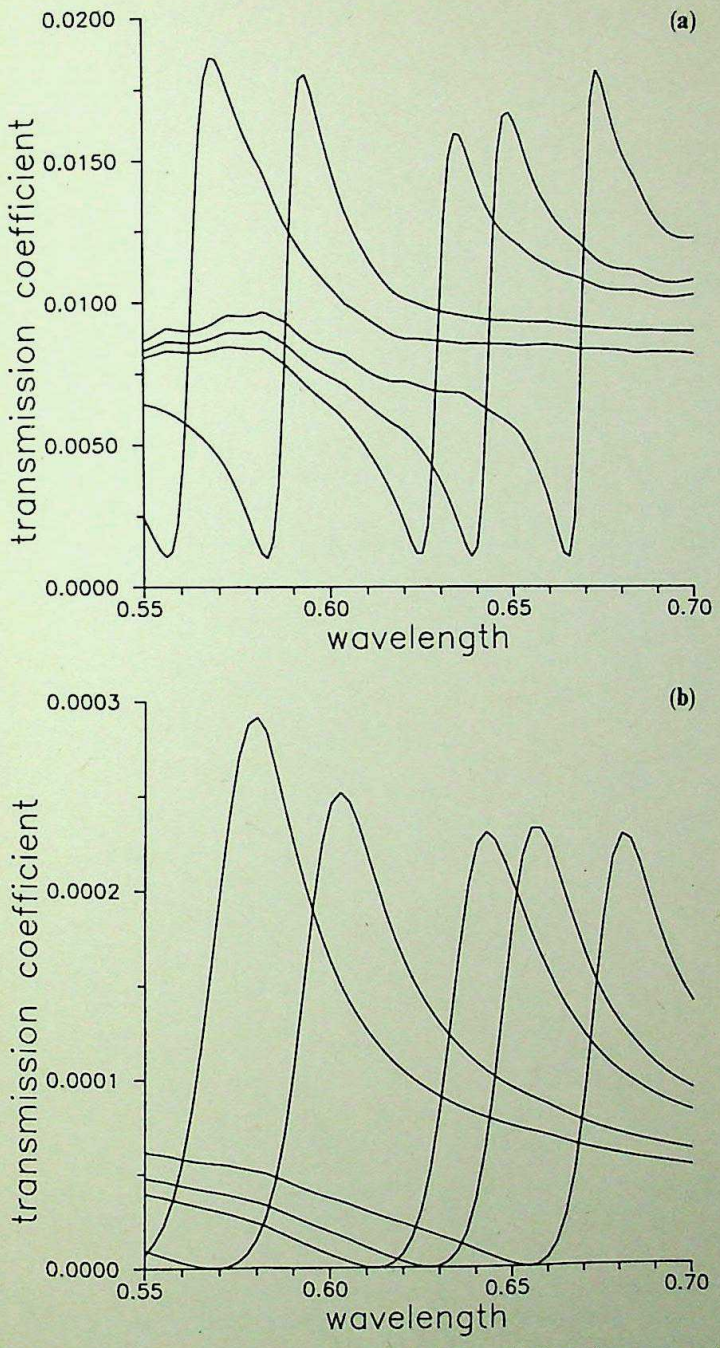

Figure 2. -1 order intensity transmission coefficient for propagating wave incidence as a function of wavelength $\lambda[\mu m]$ for **a)** $a=20$ nm, $d=100$ nm, **b)** $a=40$ nm, $d=150$ nm. Curves from left to right are for $\Lambda=760$ nm, 814 nm, 898 nm, 926 nm, 976 nm.

mission takes place at a wavelength for which the difference of the surface plasmon wave vectors at the two interfaces differ by a magnitude approximately equal to the grating vector of the structure. The deviation of the values of Δk_c from K is more for larger corrugation amplitude and width of the film. In order to emphasize the corrugation induced changes in surface plasmon dispersion, in figure 3b we show the results obtained by using flat surface dispersion curves. It is clear that the deviations from the ideal coupling condition (represented by the straight line) are larger for this case.

CC-0. In Public Domain. Gurukul Kangri Collection, Haridwar

Digitized by Arya Samaj Foundation Chennai and eGangotri

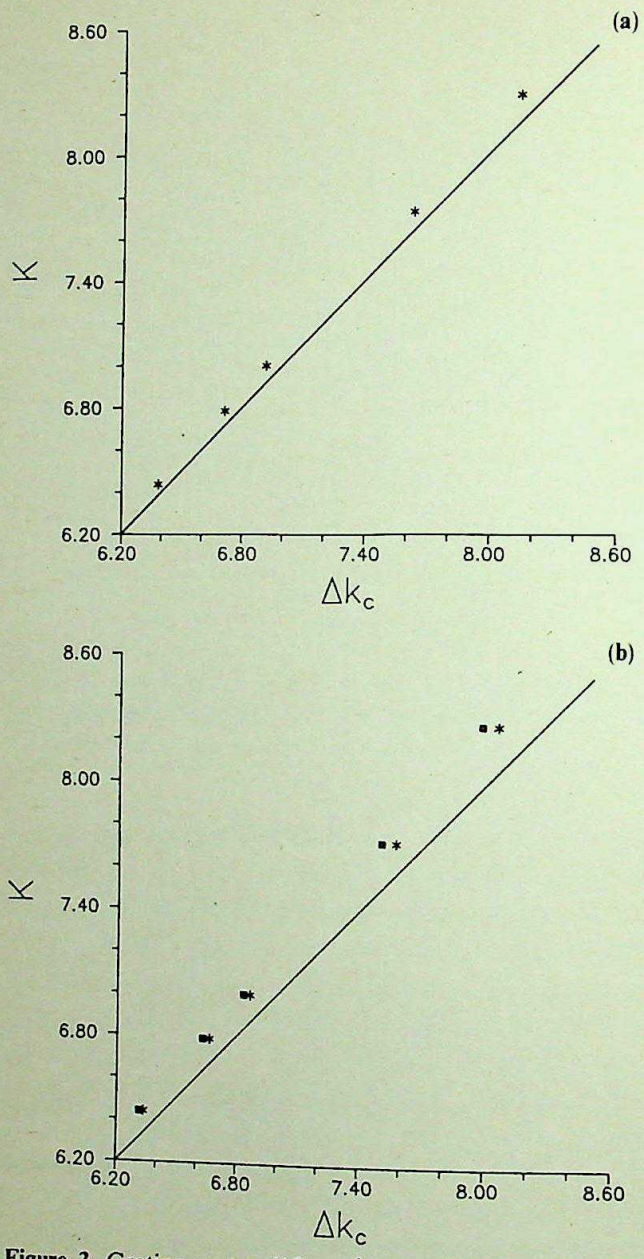

Figure 3. Grating vector $K\,[\mu m^{-1}]$ as a function of $\Delta k_c\,[\mu m^{-1}]$ for propagating wave incidence for **a)** $a = 20$ nm, $d = 100$ nm, **b)** $a = 40$ nm, $d = 150$ nm. Stars represent the calculated values. Boxes in figure 3b represent the results obtained by using flat surface dispersion curves.

2b *Optical transmission for evanescent waves*

In case of evanescent waves incident on the Ag-photoresist interface, the dominant contribution comes from the wave whose surface component of the wavevector k_{x2} matches the surface plasmon wavevector k_{c2} for that interface, i.e.,

$$k_{x2} = k_{c2}. \tag{6}$$

Note that the wave characterized by (6) represents an evanescent wave since $k_{x2} > k_0 n_i$. For such a wave the O-th order resonates with the surface mode at Ag-photoresist interface, the -1 order resonates with the surface mode at Ag-air interface and,

CC-0. In Public Domain. Gurukul Kangri Collection, Haridwar

Digitized by Arya Samaj Foundation Chennai and eGangotri

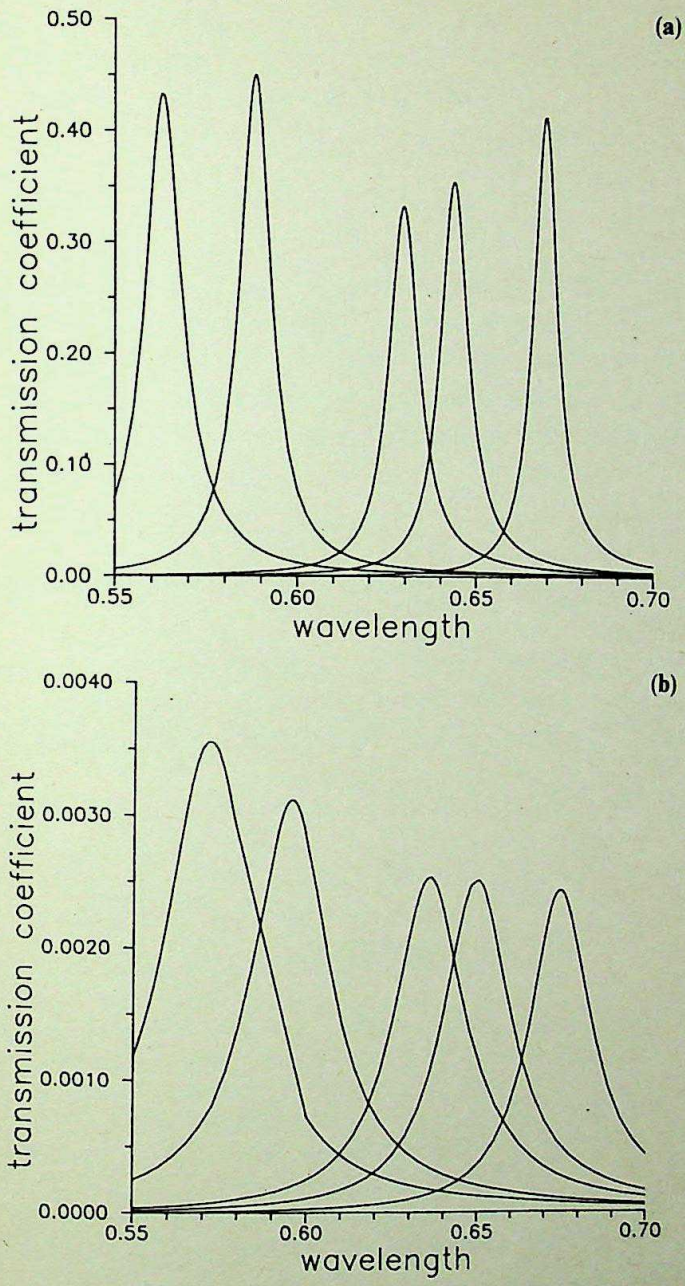

Figure 4. -2 order intensity transmission coefficient for evanescent wave incidence as a function of wavelength $\lambda[\mu m]$ for **a)** $a=20$ nm, $d=100$ nm, **b)** $a=40$ nm, $d=150$ nm. Curves from left to right are for the same values of Λ as in figure 2.

subsequently, the -2 order is radiated in air at an angle θ_d. We calculate the -2 order transmitted intensity as a function of λ using the method described in the previous subsection. The same sets of parameter values were used for calculation. The results are shown in figure 4a, 4b. It is evident from figure 4, that the wavelength dependence of transmission has an absorption-like structure (unlike the dispersion-like character for propagating wave incidence) and is close in shape to the experimentally observed transmission. Thus, one is inclined to believe that in the transmission of fluorescence the dominant role belongs to the evanescent waves emitted by the dipoles. The basis of this conclusion is reinforced if we look at the dependence of K on Δk_c (shown in figure 5a, 5b) which were calculated using the procedure outlined earlier.

CC-0. In Public Domain. Gurukul Kangri Collection, Haridwar

Digitized by Arya Samaj Foundation Chennai and eGangotri

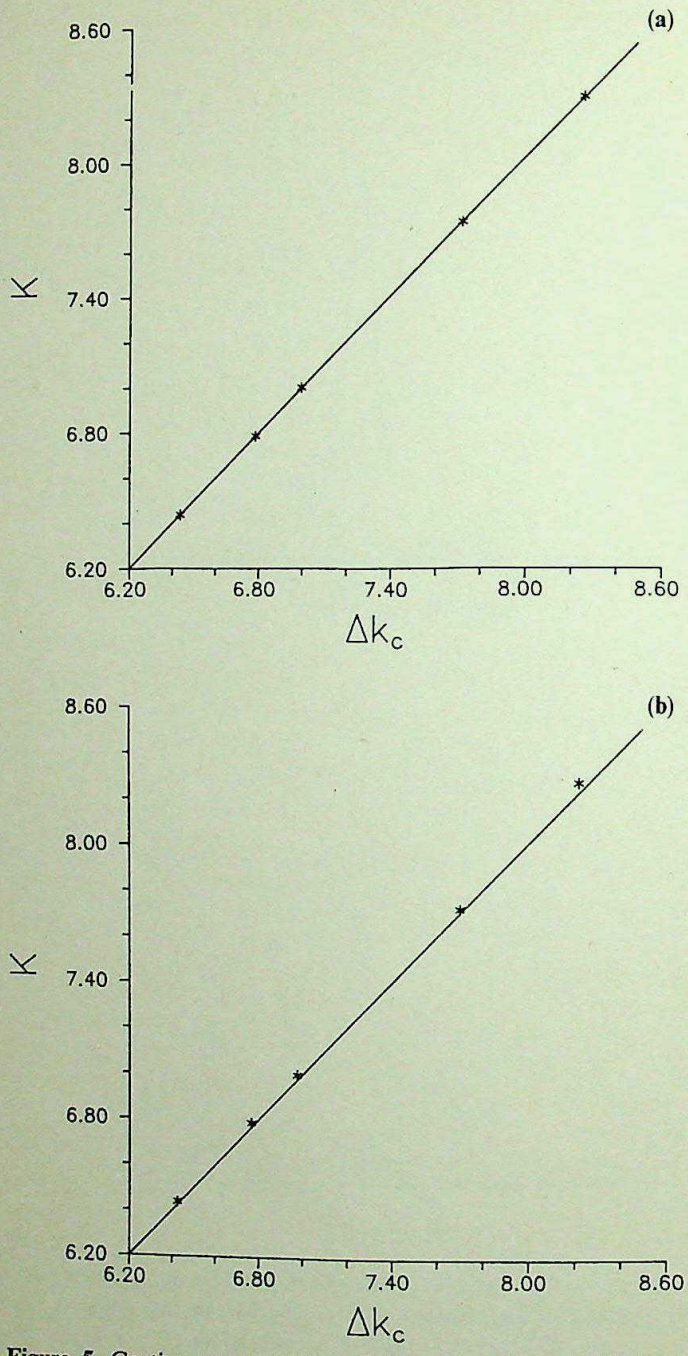

Figure 5. Grating vector $K[\mu m^{-1}]$ as a function of $\Delta k_c[\mu m^{-1}]$ for evanescent wave incidence for **a)** $a = 20$ nm, $d = 100$ nm, **b)** $a = 40$ nm, $d = 150$ nm. Stars represent the calculated values.

In fact, the calculated points given by stars (see figure 5a, 5b) lie almost on the straight line representing the ideal coupling condition. There are insignificant deviations (cf. figure 5b) for larger corrugation amplitude. This may be due to poorer convergence property of the Rayliegh method for larger a, inaccuracy of determining the maxima in figure 4, and finally, due to the fact that the dispersion curves were evaluated using the same grating period for all the structures.

It may be mentioned here that in calculating the transmission properties of the corrugated film we assumed the same amplitudes for the incident waves for both

CC-0. In Public Domain. Gurukul Kangri Collection, Haridwar

Digitized by Arya Samaj Foundation Chennai and eGangotri

propagating and evanescent cases. However, the dipole radiation amplitude has a strong wave vector dependence and hence the weight of the amplitudes for the above two different cases are not the same in general.

3. Conclusions

In conclusion, we have presented a nonperturbative analysis of the transmission from a thin corrugated metal film for the incidence of propagating and evanescent waves. A qualitative comparison with the experimental observations of Gruhlke *et al* (1986) involving transmission of fluorescence revealed that the dominant role is played by the evanescent waves. Dips in the transmission were observed for the propagating wave incidence.

Acknowledgements

The authors would like to thank G S Agarwal for many helpful discussions and for pointing out the important role of the evanescent waves in fluorescence transmission. The work was supported by the Department of Science and Technology, Government of India.

References

Agarwal G S and Dutta Gupta S 1985 *Phys. Rev.* **B32** 3607
Coutaz J L 1987 *J. Opt. Soc. Am.* **B4** 105
Dragila R, Luther-Davies B and Vukovic S 1985 *Phys. Rev. Lett.* **55** 1117
Dutta Gupta S, Varada G V and Agarwal G S 1987 *Phys. Rev.* **B36** 6331
Gruhlke R W and Hall D G 1988 *Appl. Phys. Lett.* **53** 1041
Gruhlke R W, Holland W R and Hall D G 1986 *Phys. Rev. Lett.* **56** 2838
Gruhlke R W, Holland W R and Hall D G 1987 *Opt. Lett.* **12** 364
Johnson P B and Christy R W 1972 *Phys. Rev.* **B6** 4370
Leung P T, Kim Y S and George T F 1989 *Phys. Rev.* **B39** 9888
Raether H 1977 *Physics of thin films* (New York: Academic) Vol. 9 pp. 145

CC-0. In Public Domain. Gurukul Kangri Collection, Haridwar

Digitized by Arya Samaj Foundation Chennai and eGangotri

CC-0. In Public Domain. Gurukul Kangri Collection, Haridwar

Digitized by Arya Samaj Foundation Chennai and eGangotri

Pramāṇa – J. Phys., Vol. 34, No. 6, June 1990, pp. 585–590. © Printed in India.

Fluorescence quantum yield of rhodamine 6G using pulsed photoacoustic technique

P SATHY, REJI PHILIP, V P N NAMPOORI and C P G VALLABHAN

Laser Division, Department of Physics, Cochin University of Science and Technology, Cochin 682 022, India

MS received 29 July 1989; revised 31 March 1990

Abstract. Experimental method for measuring photoacoustic(PA) signals generated by a pulsed laser beam in liquids is described. The pulsed PA technique is found to be a convenient and accurate method for determination of quantum yield in fluorescent dye solutions. Concentration dependence of quantum yield of rhodamine 6G in water is studied using the above method. The results indicate that the quantum yield decreases with increase in concentration in the quenching region in agreement with the existing reports based on radiometric measurements.

Keywords. Rhodamine 6G; pulsed photoacoustics; fluorescence; quantum yield.

PACS Nos 33·50; 33·10

The knowledge of fluorescence quantum efficiency of organic dyes is important in selecting efficient dye laser media. Even after the various corrections for system geometry, re-absorption, polarization etc., the accuracy of the quantum yield values obtained from photometric measurements is rather poor (Demas and Gosby 1971). In order to evaluate the absolute quantum efficiency we have to consider both the radiative and non-radiative relaxation processes taking place in the medium. As the contribution due to non-radiative processes is not directly measurable using the traditional optical detection methods, photoacoustic(PA) and thermal lens techniques have been adopted recently for this purpose. The viability of the PA method as a complement to fluorescence spectroscopy, and its relative advantages have been extensively described earlier (Rosencwaig 1978; David Cahen *et al* 1980; Patel and Tam 1981).

For fluorescent materials photoacoustic detection is sensitive to the total fluorescence, which means that any change in the emission characteristics will influence the PA signal. The variations in quantum yield of highly fluorescent materials can be effectively studied by this method because of the relatively large changes occurring in PA signal compared to that in fluorescence output (David Cahen *et al* 1980).

Of the several configurations possible for PA instrumentation, pulsed PA is the most sensitive, as the high peak power delivered by a pulsed laser source can generate acoustic signals of considerable magnitudes (Patel and Tam 1979). In this paper we report the results obtained from the measurements of fluorescence efficiency of the laser dye rhodamine 6G using pulsed PA technique together with fluorescence measurements.

In the case of fluorescent samples with quantum yield ϕ_F, PA signal $P(\lambda)$ can be

CC-0. In Public Domain. Gurukul Kangri Collection, Haridwar

Digitized by Arya Samaj Foundation Chennai and eGangotri

written as (Malkin and Cahen 1979),

$$P(\lambda) = \alpha(\lambda)[1 - (\phi_F/\lambda_F)\lambda]. \tag{1}$$

where λ and λ_F are the excitation wavelength and the fluorescence peak wavelength respectively. α is the fraction of light absorbed in that part of the sample that participates in the generation of the PA signal. In the case of a totally fluorescence quenched sample we can consider the entire excitation energy to be converted to non-radiative relaxation processes and hence

$$P(\lambda) = P_\alpha(\lambda) \equiv \alpha(\lambda), \quad \text{and}$$

$$\frac{P}{P_\alpha} = 1 - (\phi_F/\lambda_F)\lambda \tag{2}.$$

If λ_F is known, ϕ_F can be obtained directly (Razumova and Strarobogatov 1977; Auzel *et al* 1979) using the equation

$$\phi_F = \frac{\lambda_F}{\lambda}\left[1 - \frac{P}{P_\alpha}\right]. \tag{3}$$

Schematic experimental set up is shown in figure 1. The IR eliminated second harmonic output (532 nm) of a frequency doubled Q-switched pulsed Nd: YAG laser (quanta-ray-DCR-11) acts as the exciting light source. To prepare the samples, commercial laser grade Rh6G (exciton) was dissolved in triply distilled water without further purification. A small fraction of the beam reaches a reference photodiode PD (10 ns risetime) from a beam splitter BS1 and the major part is again split into two beams of equal strengths by a second beam splitter BS2. One part is allowed to pass through the PA cell containing the sample solution of Rh6G. A PZT transducer is screwed onto the PA cell. The design and fabrication of the PA cell and the transducer are based on earlier works (Patel and Tam 1981; Reji Philip *et al* 1988). Figure 2(a) shows the geometry of the PZT transducer. A PZT disc of 4 mm thick and 15 mm diameter is firmly mounted in a stainless steel casing, whose front diaphragm (1 mm thick) is polished on both sides. A lead disc soldered to a copper disc forms the

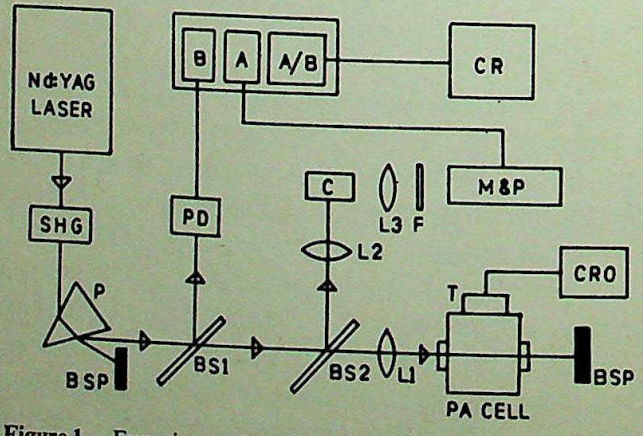

Figure 1. Experimental set-up for the determination of fluorescence quantum yield of liquids. SHG-Second harmonic generator, P-Prism, BSP-Beam stop, CR-Chart recorder, C-Cuvette, M & P-Monochromator and PMT, T-PZT Transducer.

CC-0. In Public Domain. Gurukul Kangri Collection, Haridwar

Digitized by Arya Samaj Foundation Chennai and eGangotri

backing plate of the PZT, which is spring loaded to the diaphragm as shown. This design has the advantages of high sensitivity, minimal ringing effect, excellent rejection of spurious electrical pick up and effective isolation of piezoelectric transducer from corrosive and contaminating liquid samples. Figure 2(b) shows the PA cell with the transducer screwed into it. The cell was made of stainless steel with an inner diameter of 2 cm with suitable glass windows for the entry of the laser beam. The PA signal generated in the liquid sample is detected by the transducer, which is fed to a storage oscilloscope (Tektronix, model 466). The transient PA pulses are successively monitored on the oscilloscope and the average amplitude is noted. Unlike the experimental set up of Lahmann and Ludewig (Lahmann *et al* 1977) we have used a nonresonant PA cell in conjunction with a pulsed laser source of high peak power. Hence the acoustic attenuation effects will be negligible here, and we do not expect any appreciable variation in system sensitivity with changes in concentration of the sample solution, that demands a correction for the observed values.

The other part of the laser beam from BS2 is focussed (by the cylindrical lens L2) on to a cuvette that contains the solution of same concentration as the sample taken in the PA cell, and the fluorescence emission is focussed by the convex lens L3 onto the entrance slit of a 0·5 m Jarrell-Ash monochromator. A filter *F* checks the entry of the scattered laser radiation into the monochromator. The emission is wavelength scanned in the region 530–630 nm and the optical intensity is detected by a photomultiplier tube [EMI(9684)]. The signal from the photomultiplier tube is suitably gated, and normalized to the laser power by employing the gated integrators A and B (both EG & G model 163) along with the A/B option of the boxcar averager (EG & G 162). The output is fed to a chart recorder.

Amplitudes of PA signal and fluorescence emission are plotted against concentration in the range of 10^{-6} mol/l to 10^{-4} mol/l in figure 3. The fluorescence emission has the characteristic peak near 560 nm and any specific dependence of the peak wavelength on concentration was not observed within the range studied. As seen from the figure, PA signal varies linearly in the low concentration region.

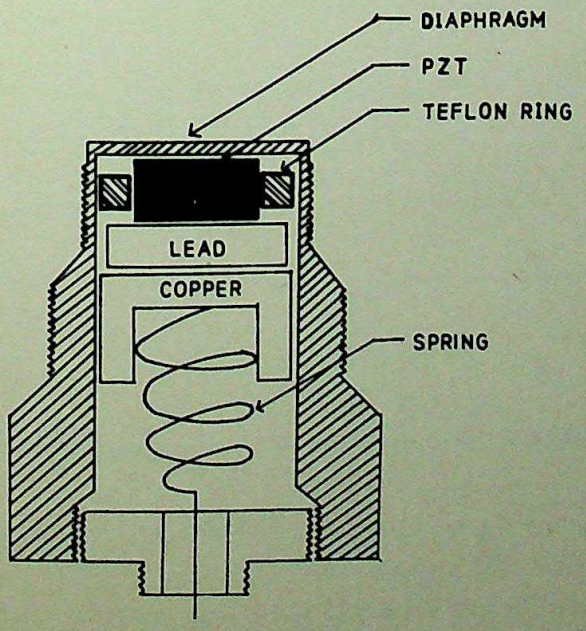

Figure 2a. The PZT transducer.

CC-0. In Public Domain. Gurukul Kangri Collection, Haridwar

Digitized by Arya Samaj Foundation Chennai and eGangotri

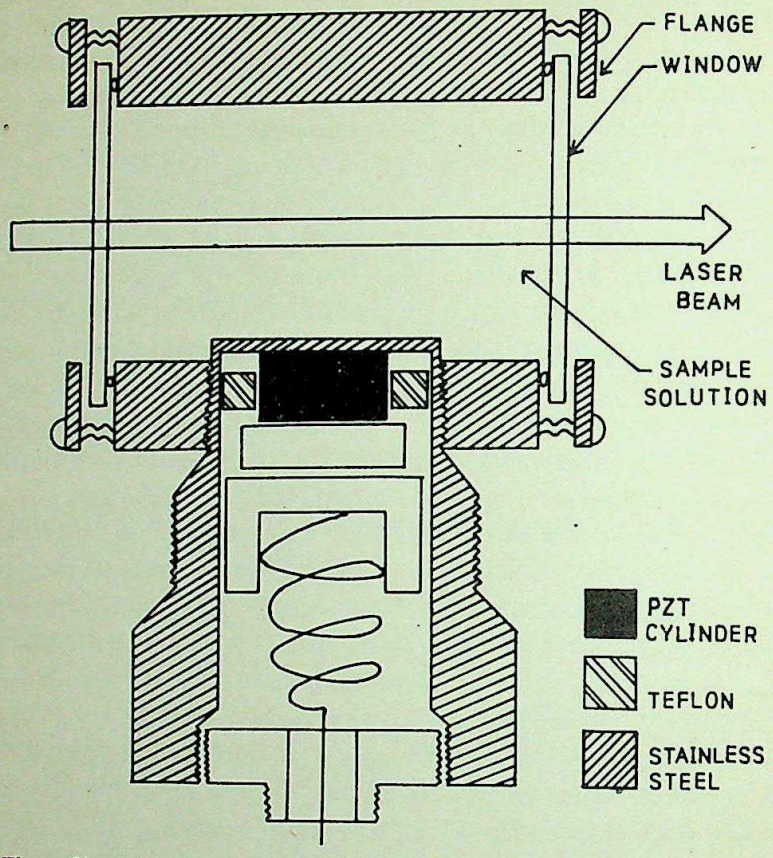

Figure 2b. The PA cell with transducer screwed in position.

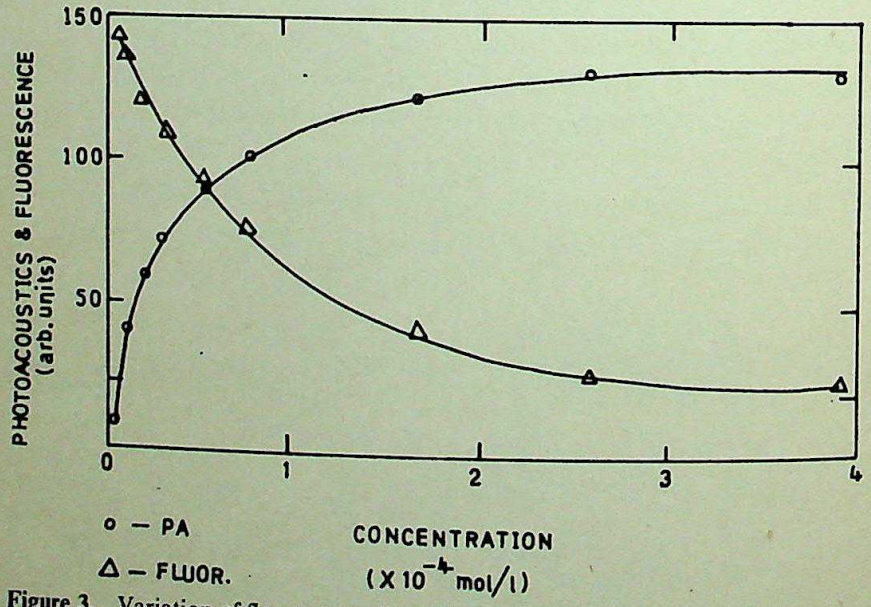

Figure 3. Variation of fluorescence intensity and PA signal amplitude with concentration.

The earlier estimates have shown that for selected concentrations, aqueous solutions of Rh6G has a quantum efficiency of 92% (Snavely 1973), 96% $\pm$ 2% (Lahmann and Ludewig 1977) etc. However, the quantum yield intimately depends on the environment of the fluorescing molecule, and the processes like internal non-radiative conversion

CC-0. In Public Domain. Gurukul Kangri Collection, Haridwar

Digitized by Arya Samaj Foundation Chennai and eGangotri

($S_1 \rightarrow S_0$), intersystem crossing ($S_1 \rightarrow T_1$), excited singlet state absorption (ESSA) and aggregation of dye molecules are strongly dependent on the solvent characteristics as well as on concentration (Drexhage 1973). The role of the excitation source also is important in this respect, as many of the above phenomena become significant in the medium when the input energy exceeds certain critical value. It has been known that Rh6G forms stable ground state dimers and higher aggregates in aqueous solution, and the decrease of Rh6G fluorescence quantum efficiency at higher concentrations is caused by Förster-type energy transfer (electric dipole-electric dipole interaction) to dimers (Penzkofer and Leupacher 1987). The equilibrium between monomers and dimers shifts to the side of the latter with increasing concentration and at 10^{-4} M concentration, the dimerization of dyes like RhB and Rh6G is severe enough to prevent laser action (Drexhage 1973) unless a deaggregating agent like hexafluoroisopropanol or ammonyx LO is added to the solution. In the present case no such deaggregating agents were added, and hence a significant reduction in fluorescence quantum yield can be expected due to dimerization. Our studies in the 10^{-4} M concentration region are generally in agreement with these earlier observations. However, we have used a pulsed laser source of high peak power for excitation of the medium in contrast with the Tungsten lamp used by Penzkofer and Leupacher (1987) and hence many of the above nonlinear processes are likely to occur here. Therefore slight departures of our results from the numerical values of previous workers are to be expected. This was actually observed, and the quantum yield was found to decrease rapidly as the concentration was increased. From figure 3 it is seen that at the highest concentration used here PA signal shows a saturation behaviour. Correspondingly, the fluorescence emission is very weak. PA signal corresponding to this concentration gives the value of $P(\alpha)$. The calculated value of the quantum yield at the lowest concentration studied ($3{\cdot}2 \times 10^{-6}$ M) is $0{\cdot}90 \pm 0{\cdot}02$, and the yield decreases rapidly at higher concentration region. Figure 4 is the plot of variation of ϕ_F with concentration. Apart from a small variation, the quantum yield is almost independent of concentration in the 10^{-6} M region, and the rapid decrease in ϕ_F at higher concentrations can be attributed mainly to the formation of dimers and higher aggregates which have zero or small fluorescence quantum yield. Also, collisional

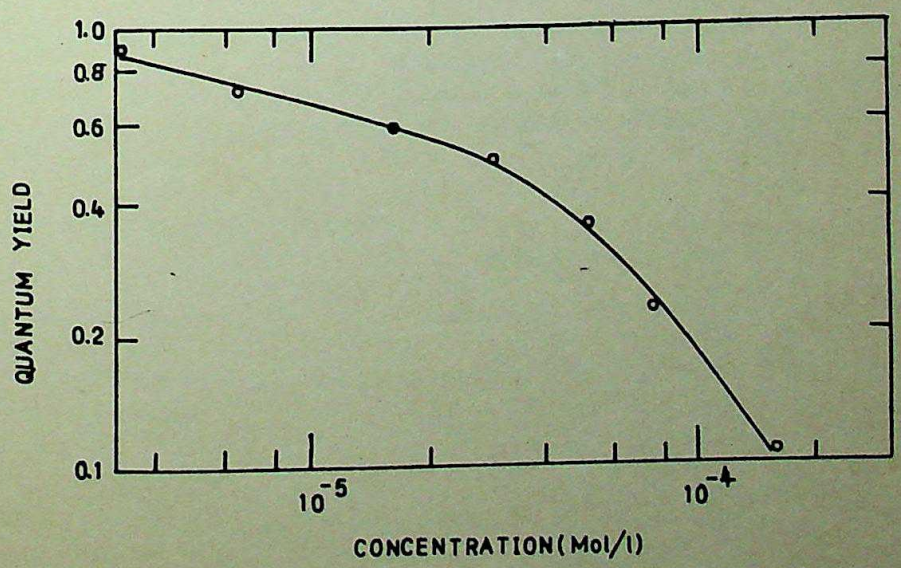

Figure 4. Variation of quantum yield of Rh6G in water with concentration.

CC-0. In Public Domain. Gurukul Kangri Collection, Haridwar

Digitized by Arya Samaj Foundation Chennai and eGangotri

quenching, occurrence of two-photon and two-step excitations in the samples when irradiated with a high power laser source (Sathy *et al* 1990) and the influence of other processes mentioned earlier can contribute to the reduction in yield.

The study of concentration dependence of the quantum yield of Rh6G solution in water using the PA technique confirms that the quantum yield decreases with increase in concentration. The simplicity of instrumentation, ease of measurement and the unambiguous nature of results clearly establish the above method as an accurate technique for the estimation of fluorescence quantum yields. For fluorescing materials like Rh6G the measurement of the quantum yield by PA technique is very convenient and useful especially in the higher concentrations, i.e. near fluorescence quenching. For example, the fluorescence quantum yield of laser dyes in various solvents at various concentrations can be measured to analyze the effect of solvent quenching and concentration quenching on the fluorescence properties of the medium.

Acknowledgement

The authors are thankful to the DST, CSIR and MHRD for financial assistance. They are also grateful to Dr Jacob Philip for his interest in this work.

References

Auzel F, Meichenin D and Michel J C 1979 *J. Lumin.* **18/19** 97
David Cahen, Halm Garty and Ralph S Becker 1980 *J. Phys. Chem.* **84** 3384
Demas J N and Crosby J A 1971 *J. Phys. Chem.* **75** 991
Drexhage K H 1973 in *Dye lasers* (ed.) F P Schafer (Berlin: Springer)
Lahmann W and Ludewig H J 1977 *Chem. Phys. Lett.* **45** 177
Malkin S and Cahen D 1979 *Photochem. Photobiol.* **29** 803
Patel C K N and Tam A C 1979 *Nature (London)* **280** 302
Patel C K N and Tam A C 1981 *Rev. Mod. Phys.* **53** 517
Penzkofer A and Leupacher W 1987 *J. Lumin.* **37** 61
Razumova T K and Strarobogatov I O 1977 *Opt. Spectrosc.* **42** 274
Strarobogatov I O 1977 *Opt. Spectrosc.* **42** 172
Reji Philip, Sathy P, Nampoori V P N, Jacob Philip and Vallabhan C P G 1988 *J. Acoust. Soc. India* **16** 223
Rosencwaig A 1978 *Adv. Electron. Electron. Phys.* **46** 207
Sathy P, Reji Philip, Nampoori V P N and Vallabhan C P G 1990 *Opt. Commun.* **74** 313
Snavely B B 1973 in *Dye lasers* (ed.) F P Schafer (Berlin: Springer)

CC-0. In Public Domain. Gurukul Kangri Collection, Haridwar

Digitized by Arya Samaj Foundation Chennai and eGangotri

SUBJECT INDEX

General Physics

Orthogonality constrained general variational calculation of excited state wavefunctions and energies: A new strategy
Priyatosh Dutta and S P Bhattacharyya 13–21

The wavefunction envelope in one-dimensional random potentials
A Mookerjee and A M Jayannavar 441–445

Relativity, Gravitation and Cosmology

String cosmology in Bianchi I space-time
A Banerjee, Abhik Kumar Sanyal and Subenoy Chakraborty 1–11

Spherical shells of positive density – can they be of non-positive mass?
A K Raychaudhuri and S Banerjee 383–396

Spherically symmetric solutions with heat flow in general relativity
A Banerjee, S B Dutta Choudhury and B K Bhui 397–401

Wave function with second order correction and inflationary solutions in quantum cosmology *Subenoy Chakraborty* 403–414

Cosmological models consistent with supersymmetric compactification of superstring theories *Sanjay Kumar, S Mahajan, A Mukherjee, N Panchapakesan and R P Saxena* 415–422

Spherically symmetric anisotropic and inhomogeneous cosmological models *J Krishna Rao* 423–432

Particle Physics

Comment on a solution of Altarelli-Parisi equations
D K Choudhury and A Saikia 85–86

On mass-independence of the minimal subtraction scheme in dimensional regularization II *Satish D Joglekar* 91–101

Phenomenology of the proton spin
M V N Murthy and V Ravindran 103–109

Stability of the S matrix pole *G Rajasekaran and S S Vasan* 183–192

Q matter in the field of an abelian dyon admitting parity violating anomalous couplings *C Wolf* 433–440

CC-0. In Public Domain. Gurukul Kangri Collection, Haridwar

Digitized by Arya Samaj Foundation Chennai and eGangotri

Nuclear Physics

Bonding potential between two ^{12}C nuclei
P Sarangi, S Ali and L Satpathy 111–115

Triad of homogeneous and inhomogeneous three particle Lippmann–Schwinger equations *Suprokash Mukherjee* 173–182

Atomic and Molecular Physics

High energy elastic e^+-O_2 scattering *K N Joshipura* 87–90

Interaction of strong laser beam with He-atom using non-perturbative Floquet method
Man Mohan, Vinod Prasad and Bhupat Sharma 117–122

The effect of the relativistic Hartree-Fock-Roothaan momentum distribution in the binary encounter approximation for inner shell ionization *V Kumar, S N Chatterjee and B N Roy* 447–460

Statistical Physics

Thermodynamic properties of hard ellipsoid square-well fluid
A K Singh, T K Dey and S K Sinha 123–131

Lasers, Optics and Spectroscopy

Time-resolved spectra of coumarin 30-rhodamine 6G dye mixture
R D Singh, D Mohan, A K Sharma and N V Unnikrishnan 77–83

Rotational analysis of 3664 Å band of NiCl
A B Darji and M B Suresh Kumar 165–171

Evaluation of downstream-mixing scheme for 9·4 μm CO_2 gas-dynamic laser *P Chakravarty, N M Reddy and K P J Reddy* 333–345

Beam propagation method and its application to integrated optic structures and optical fibers
Shiva Kumar, T Srinivas and A Selvarajan 347–358

Wavelength dependence of phase conjugate reflectivity in absorbing media and thermal grating studies by four wave mixing
R Krishna Mohan, B Raghavendra Prasad, C K Subramanian and P S Narayanan 461–471

Analysis of the absorption mechanism during laser-metal interaction
B S Yilbas, R Davies, Z Yilbas and A Koc 473–489

Vibrational spectra of $Na_4P_2O_7 \cdot 10H_2O$
V Ramakrishnan, S Narayana Kalkura and P Rajagopal 555–560

Fluorescence quantum yield of rhodamine 6G using pulsed photo-acoustic technique
P Sathy, Reji Philip, V P N Nampoori and C P G Vallabhan 585–590

CC-0. In Public Domain. Gurukul Kangri Collection, Haridwar

Digitized by Arya Samaj Foundation Chennai and eGangotri

Condensed Matter Physics

Structure factor of charged colloidal suspensions using Brownian-dynamics simulation: Comparison of Yukawa and Sogami pair potentials *B V R Tata, A K Sood and R Kesavamoorthy* 23–32

Positron annihilation in copper *V Sundararajan and D G Kanhere* 33–49

Effect of variation of dielectric constant on the magnetic field modulation of exciplex luminescence *Deb Narayan Nath and Mihir Chowdhury* 51–66

Effect of annealing on the opto-electronic properties of $Cu_{0\cdot9}In_{1\cdot0}Se_{2\cdot0}$ films *R P Sharma, Pankaj Garg and J C Garg* 67–75

Electron crystallization using localized representation *K Iyakutti and Jean Louis Calais* 133–149

Indentation studies on alkaline earth fluoride crystals at elevated temperatures *K Kishan Rao and D B Sirdeshmukh* 151–156

Ultrasonic absorption studies in solutions of ortho and para hydroxy benzoic acid in dioxan *V Balasubramanian and A Srinivasa Rao* 157–163

A relation between X-ray diffraction based liquid structure and packing coefficient *A Mikusinska-Planner* 193–199

Convexity of internal energy of cubic crystal deformed to orthorhombic structure *K P Thakur, R K Jha and O P Thakur* 201–215

Anharmonic effects on lattice resonant modes of impure metallic crystals *S K Roy and N Kundu* 217–224

The Young–Hoshino pseudopotential for lithium: calculations of structure and thermodynamics *T Das and R N Joarder* 225–233

Melting temperatures of some alkali halide mixed crystal systems *D B Sirdeshmukh, K G Subhadra and K A Hussain* 235–241

Electrical conductivity, thermoelectric power and figure of merit of doped Bi–Sb tapes produced by melt spinning technique *T K Dey* 243–248

Layered superconductors with anisotropic energy gap: specific heat and infrared absorption *Sudhanshu S Jha* 259–277

Field and temperature dependence of intergranular hysteresis in $YBa_2Cu_3O_7$ *Shailendra Kumar, G Ravikumar, P K Mishra, P Chaddah, B A Dasannacharya, Ram Prasad and N C Soni* 279–287

Electrical resistivity of the alkaline earth metals Ca, Sr and Ba in the 50–300 K temperature region *O Akinlade, U Marte and L A Hussain* 289–295

CC-0. In Public Domain. Gurukul Kangri Collection, Haridwar

Digitized by Arya Samaj Foundation Chennai and eGangotri

Elastic behaviour of lead fluoride under pressure
R K Singh and C N Rao 297–302

Computation of small angle neutron scattering functions for molecules of arbitrary shapes *F U Ahmed, P Martel and A M Khan* 303–312

NMR investigations of molecular motions in *p-n*-hexyloxybenzylidene-*p'-n*-propylaniline *K Usha Deniz and S R Kasturi* 313–324

Study of electric potentials across a moving solid-liquid interface
A K Bhuniya, N Prasad, Lakshman Pandey and P Ramachandrarao 325–331

Mössbauer study of the stability of quasicrystalline phases: $Al_{78}Fe_{22}$ and $Al_{82}Fe_{18}$ *K R P M Rao* L369–L375

Anisotropic ESR parameters of Cu(II) complexes in solutions and dynamics of solvent coordination: use of "minimum" linewidths"
B S Prabhananda 491–506

A quantitative study of diffracted X-ray intensities from type I natural diamond crystals by high resolution X-ray diffractometry and comparison with nearly perfect silicon single crystals
Krishan Lal, S Niranjana N Goswami and Ajit Ram Verma 507–523

Diffraction properties of one-dimensional finite size Fibonacci quasilattice *V S K Balagurusamy, S Baranidharan, E S R Gopal and V Sasisekharan* 525–536

Generation of aperiodic tilings with five fold symmetry by the method of intersecting decagons and diffraction from finite size tilings
S Baranidharan, E S R Gopal and V Sasisekharan 537–553

Comments on the Meyer–Neldel rule in amorphous semiconductors
K L Narasimhan 561–563

A study of absorption characteristics in polyimide and polyimide fluorocarbon-2 polymer film *M M Hossain* 565–573

A theoretical study of surface plasmon cross coupling in asymmetric corrugated metal films *M B Pande and S Dutta Gupta* 575–583

Experimental Techniques and Instrumentation

Design and the operational characteristics of a 16 μm CF_4 laser
P K Gupta, V P Singhal, N S Shikarkhane, S Sinha, S Sasikumar, U Nundy and U K Chatterjee 249–257

Differential temperature sensors method for simultaneous determination of thermal conductivity and diffusivity
L S Verma, A K Shrotriya, Ramvir Singh and D R Chaudhary 359–367

Detection limits of high temperature superconducting materials on various substrates by energy dispersive X-ray fluorescence and proton induced X-ray emission methods
M Lal, H N Bajpai, D Joseph and R K Choudhury L377–L381

CC-0. In Public Domain. Gurukul Kangri Collection, Haridwar

Digitized by Arya Samaj Foundation Chennai and eGangotri

AUTHOR INDEX

Ahmed F U
Computation of small angle neutron scattering functions for molecules of arbitrary shapes 303

Akinlade O
Electrical resistivity of the alkaline earth metals Ca, Sr and Ba in the 50–300 K temperature region 289

Ali S
see Sarangi P 111

Bajpai H N
see Lal M L377

Balagurusamy V S K
Diffraction properties of one-dimensional finite size Fibonacci quasilattice 525

Balasubramanian V
Ultrasonic absorption studies in solutions of ortho and para hydroxy benzoic acid in dioxan 157

Banerjee A
String cosmology in Bianchi I space-time 1
Spherically symmetric solutions with heat flow in general relativity 397

Banerjee S
see Raychaudhuri A K 383

Baranidharan S
see Balagurusamy V S K 525
Generation of aperiodic tilings with five fold symmetry by the method of intersecting decagons and diffraction from finite size tilings 537

Bhattacharyya S P
see Dutta Priyatosh 13

Bhui B K
see Banerjee A 397

Bhuniya A K
Study of electric potentials across a moving solid-liquid interface 325

Calais Jean Louis
see Iyakutti K 133

Chaddah P
see Shailendra Kumar 279

Chakraborty Subenoy
see Banerjee A 1
Wave function with second order correction and inflationary solutions in quantum cosmology 403

Chakravarty P
Evaluation of downstream-mixing scheme for 9·4 μm CO_2 gas-dynamic laser 333

Chatterjee S N
see Kumar V 447

Chatterjee U K
see Gupta P K 249

Chaudhary D R
see Verma L S 359

Choudhury D K
Comment on a solution of Altarelli-Parisi equations 85

Choudhury R K
see Lal M L377

Chowdhury Mihir
see Nath Deb Narayan 51

Darji A B
Rotational analysis of 3664 Å band of NiCl 165

Das T
The Young-Hoshino pseudopotential for lithium: calculations of structure and thermodynamics 225

Dasannacharya B A
see Shailendra Kumar 279

Davies R
see Yilbas B S 473

Dey T K
see Singh A K 123
Electrical conductivity, thermoelectric power and figure of merit of doped Bi-Sb tapes produced by melt spinning technique 243

Dutta Choudhury S B
see Banerjee A 397

Dutta Gupta S
see Pande M B 575

Dutta Priyatosh
Orthogonality constrained general variational calculation of excited state wavefunctions and energies: A new strategy 13

Garg J C
see Sharma R P 67

Garg Pankaj
see Sharma R P 67

Gopal E S R
see Baranidharan S 537

CC-0. In Public Domain. Gurukul Kangri Collection, Haridwar

Digitized by Arya Samaj Foundation Chennai and eGangotri

see Balagurusamy V S K 525
Goswami N S N
see Lal Krishan 507
Gupta P K
Design and the operational characteristics of a 16 μm CF_4 laser 249

Hossain M M
A study of absorption characteristics in polymide and polymide fluorocarbon-2 polymer film 565
Hussain K A
see Sirdeshmukh D B 235
Hussain L A
see Akinlade D 289

Iyakutti K
Electron crystallization using localized representation 133

Jayannavar A M
see Mookerjee A 441
Jha R K
see Thakur K P 201
Jha Sudhanshu S
Layered superconductors with anisotropic energy gap: specific heat and infrared absorption 259
Joarder R N
see Das T 225
Joglekar Satish D
On mass-independence of the minimal subtraction scheme in dimensional regularization II 91
Joseph D
see Lal M L377
Joshipura K N
High energy elastic e^+-O_2 scattering 87

Kalkura S Narayana
see Ramakrishnan V 555
Kanhere D G
see Sundararjan V 33
Kasturi S R
see Usha Deniz K 313
Kesavamoorthy R
see Tata B V R 23
Khan A M
see Ahmed F U 303
Koc A
see Yilbas B S 473
Krishna Mohan R
Wavelength dependence of phase conjugate reflectivity in absorbing media and thermal grating studies by four wave mixing 461
Kumar V
The effect of the relativistic Hartree-Fock-Roothaan momentum distribution in the binary encounter approximation for inner shell ionization 447
Kundu N
see Roy S K 217

Lal Krishan
A quantitative study of diffracted X-ray intensities from type I natural diamond crystals by high resolution X-ray diffractometry and comparison with nearly perfect silicon single crystals 507
Lal M
Detection limits of high temperature superconducting materials on various substrates by energy dispersive X-ray fluorescence and proton induced X-ray emission methods L377

Mahajan S
see Sanjay Kumar 415
Man Mohan
Interaction of strong laser beam with He-atom using non-perturbative Floquet method 117
Marte U
see Akinlade O 289
Martel P
see Ahmed F U 303
Mishra P K
see Shailendra Kumar 279
Mohan D
see Singh R D 77
Mookerjee A
see Sanjay Kumar 415
The wavefunction envelope in one-dimensional random potentials 441
Mukherjee Suprokash
Triad of homogeneous and inhomogeneous three particle Lippmann–Schwinger equations 173
Mikusinska–Planner A
A relation between X-ray diffraction based liquid structure and packing coefficient 193
Murthy M V N
Phenomenology of the proton spin 103

Nampoori V P N
see Sathy P 585
Narasimhan K L
Comments on the Meyer–Neldel rule in amorphous semiconductors 561
Narayanan P S
see Krishna Mohan R 461
Nath Deb Narayan
Effect of variation of dielectric constant on the magnetic field modulation of exciplex luminescence 51
Nundy U
see Gupta P K 249

CC-0. In Public Domain. Gurukul Kangri Collection, Haridwar

Digitized by Arya Samaj Foundation Chennai and eGangotri

Panchapakesan N
see Sanjay Kumar 415
Pande M B
A theoretical study of surface plasmon cross coupling in asymmetric corrugated metal films 575
Pandey Lakshman
see Bhuniya A K 325
Philip Reji
see Sathy P 585
Prabhananda B S
Anisotropic ESR parameters of Cu(II) complexes in solutions and dynamics of solvent coordination: Use of "minimum line-widths" 491
Prasad N
see Bhuniya A K 325

Raghavendra Prasad B
see Krishna Mohan R 461
Rajagopal P
see Ramakrishnan V 555
Rajasekaran G
Stability of the *S* matrix pole 183
Ram Prasad
see Shailendra Kumar 279
Ramachandrarao P
see Bhuniya A K 325
Ramakrishnan V
Vibrational spectra of $Na_4P_2O_7 \cdot 10H_2O$ 555
Rao A Srinivasa
see Balasubramanian V 157
Rao C N
see Singh R K 297
Rao J Krishna
Spherically symmetric anisotropic and inhomogeneous cosmological models 423
Rao K Kishan
Indentation studies on alkaline earth fluoride crystals at elevated temperatures 151
Rao K R P M
Mössbauer study of the stability of quasicrystalline phases: $Al_{78}Fe_{22}$ and $Al_{82}Fe_{18}$ L369
Ravikumar G
see Shailendra Kumar 279
Ravindran V
see Murthy M V N 103
Raychaudhuri A K
Spherical shells of positive density – can they be of non-positive mass? 383
Reddy K P J
see Chakravarty P 333
Reddy N M
see Chakravarty P 333
Roy B N
see Kumar V 447

Roy S K
Anharmonic effects on lattice resonant modes of impure metallic crystals 217

Saikia A
see Choudhury D K 85
Sanjay Kumar
Cosmological models consistent with supersymmetric compactification of superstring theories 415
Sanyal Abhik Kumar
see Banerjee A 1
Sarangi P
Bonding potential betwen two ^{12}C nuclei 111

Sasikumar S
see Gupta P K 249
Sasisekharan V
see Balagurusamy V S K 525
see Baranidharan S 537
Sathy P
Fluorescence quantum yield of rhodamine 6G using pulsed photoacoustic technique 585
Satpathy L
see Sarangi P 111
Saxena R P
see Sanjay Kumar 415
Selvarajan A
see Shiva Kumar 347
Shailendra Kumar
Field and temperature dependence of intergranular hysteresis in $YBa_2Cu_3O_7$ 279
Sharma A K
see Singh R D 77
Sharma Bhupat
see Man Mohan 117
Sharma R P
Effect of annealing on the opto-electronic properties of $Cu_{0.9}In_{1.0}Se_{2.0}$ films 67
Shikarkhane N S
see Gupta P K 249
Shiva Kumar
Beam propagation method and its application to integrated optic structures and optical fibers 347

Shrotriya A K
see Verma L S 359
Singh A K
Thermodynamic properties of hard ellipsoid square-well fluid 123
Singh R D
Time-resolved spectra of coumarin 30-rhodamine 6G dye mixture 77
Singh R K
Elastic behaviour of lead fluoride under pressure 297

CC-0. In Public Domain. Gurukul Kangri Collection, Haridwar

Digitized by Arya Samaj Foundation Chennai and eGangotri

Singh Ramvir
see Verma L S 359
Singhal V P
see Gupta P K 249
Sinha S
see Gupta P K 249
Sinha S K
see Singh A K 123
Sirdeshmukh D B
see Rao K Kishan 151
Melting temperatures of some alkali halide mixed crystal systems 235
Soni N C
see Shailendra Kumar 279
Sood A K
see Tata B V R 23
Srinivas T
see Shiva Kumar 347
Subhadra K G
see Sirdeshmukh D B 235
Subramanian C K
see Krishna Mohan R 461
Sundararjan V
Positron annihilation in copper 33
Suresh Kumar M B
see Darji A B 165

Tata B V R
Structure factor of charged colloidal suspensions using Brownian-dynamics simulation: Comparison of Yukawa and Sogami pair potentials 23
Thakur K P
Convexity of internal energy of cubic crystal deformed to orthorhombic structure 201
Thakur O P
see Thakur K P 201

Unnikrishnan N V
see Singh R D 77
Usha Deniz K
NMR investigations of molecular motions in *p-n*-hexyloxybenzylidene-*p'*-*n* propylaniline 313

Vallabhan C P G
see Sathy P 585
Vasan S S
see Rajasekaran G 183
Verma A R
see Lal Krishnan 507
Verma L S
Differential temperature sensors method for simultaneous determination of thermal conductivity and diffusivity 559
Vinod Prasad
see Man Mohan 117

Wolf C
Q matter in the field of an abelian dyon admitting parity violating anomalous couplings 433

Yilbas B S
Analysis of the absorption mechanism during laser-metal interaction 473
Yilbas Z
see Yilbas B S 473

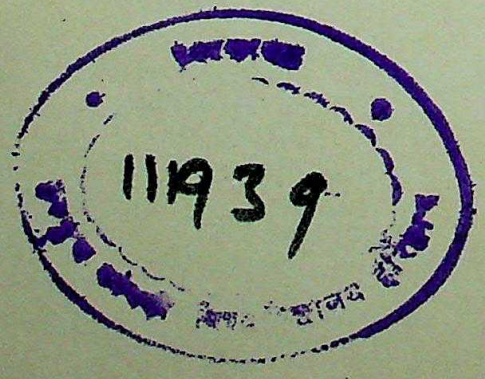

CC-0. In Public Domain. Gurukul Kangri Collection, Haridwar

Digitized by Arya Samaj Foundation Chennai and eGangotri

CC-0. In Public Domain. Gurukul Kangri Collection, Haridwar

Digitized by Arya Samaj Foundation Chennai and eGangotri

111439

Computed
1999-2000

Anish Book Binder

CC-0. In Public Domain. Gurukul Kangri Collection, Haridwar

Digitized by Arya Samaj Foundation Chennai and eGangotri

CC-0. In Public Domain. Gurukul Kangri Collection, Haridwar

Digitized by Arya Samaj Foundation Chennai and eGangotri

CC-0. In Public Domain. Gurukul Kangri Collection, Haridwar